

# Physics at *BES-III*

Editors

Kuang-Ta Chao and Yifang Wang

IHEP-Physics-Report-*BES-III*-2008-001-v1



# Physics at *BES-III*

## Editors:

Kuang-Ta Chao<sup>1</sup> and Yifang Wang<sup>2</sup>

<sup>1</sup> *Peking University, Beijing 100871*

<sup>2</sup> *Institute of High Energy Physics, P.O.Box 918, Beijing 100049*

## Working Group and Conveners

### Part One: The *BES-III* experiment and its physics

Conveners: Jian-Ping Ma, Ya-Jun Mao

### Part Two: $e^+e^-$ Collision at $\sqrt{s} = 2 - 5$ GeV

Conveners: Yuan-Ning Gao, Xiao-Yuan Li

### Part Three: Light hadron physics

Conveners: Xiao-Yan Shen, Bing-Song Zou

### Part Four: Charmonium Physics

Conveners: Cong-Feng Qiao, Changzheng Yuan

### Part Five: Charm Physics

Conveners: Hai-Bo Li, Zhi-Zhong Xing

### Part Six: Tau Physics

Conveners: Antonio Pich, Changzheng Yuan

## Authors

D. M. Asner<sup>7</sup>, T. Barnes<sup>3,24</sup>, J. M. Bian<sup>1</sup>, I. I. Bigi<sup>17</sup>, N. Brambilla<sup>11</sup>, I. R. Boyko<sup>12</sup>, V. Bytev<sup>12</sup>, K. T. Chao<sup>21</sup>, J. Charles<sup>9</sup>, H. X. Chen<sup>1</sup>, J. C. Chen<sup>1</sup>, Y. Chen<sup>1</sup>, Y. Q. Chen<sup>15</sup>, H. Y. Cheng<sup>14</sup>, D. Dedovich<sup>12</sup>, S. Descotes-Genon<sup>20</sup>, C. D. Fu<sup>26</sup>, X. Garcia i Tormo<sup>3</sup>, Y.-N. Gao<sup>26</sup>, K. L. He<sup>1</sup>, Z. G. He<sup>21</sup>, J. F. Hu<sup>25</sup>, H. M. Hu<sup>1</sup>, B. Huang<sup>1</sup>, Y. Jia<sup>1</sup>, H.-Y. Jin<sup>31</sup>, S. Jin<sup>1</sup>, Y. P. Kuang<sup>26</sup>, H. Lacker<sup>13</sup>, H. B. Li<sup>1</sup>, J. L. Li<sup>10</sup>, W. D. Li<sup>1</sup>, X. Y. Li<sup>15</sup>, B. J. Liu<sup>1</sup>, H. H. Liu<sup>1</sup>, J. Liu<sup>1</sup>, H. L. Ma<sup>1</sup>, J. P. Ma<sup>15</sup>, Y. J. Mao<sup>21</sup>, X. H. Mo<sup>1</sup>, S. L. Olsen<sup>1,27</sup>, A. Pich<sup>29</sup>, A. Pineda<sup>4</sup>, R. G. Ping<sup>1</sup>, C. F. Qiao<sup>10</sup>, G. Qin<sup>1</sup>, H. Qin<sup>1</sup>, J. M. Roney<sup>30</sup>, G. Rong<sup>1</sup>, L. Roos<sup>18</sup>, X. Y. Shen<sup>1</sup>, J. Soto<sup>6</sup>, A. Stahl<sup>2</sup>, S. S. Sun<sup>1</sup>, S. T'Jampens<sup>22</sup>, A. Vairo<sup>11</sup>, P. Wang<sup>1</sup>, Y. F. Wang<sup>1</sup>, Y. K. Wang<sup>28</sup>, N. Wu<sup>1</sup>, Y. L. Wu<sup>15</sup>, Z. Z. Xing<sup>1</sup>, G. F. Xu<sup>1</sup>, M. Xu<sup>25</sup>, M. Yang<sup>1</sup>, M. Z. Yang<sup>16</sup>, Y. D. Yang<sup>8</sup>, C. Z. Yuan<sup>1</sup>, D. H. Zhang<sup>1</sup>, D. Y. Zhang<sup>1</sup>, J. Y. Zhang<sup>1,5</sup>, Z. X. Zhang<sup>1</sup>, X. M. Zhang<sup>1</sup>, X. Y. Zhang<sup>23</sup>, Y. J. Zhang<sup>21</sup>, Q. Zhao<sup>1</sup>, A. Zhemchugov<sup>12</sup>, H. Q. Zheng<sup>21</sup>, Y. H. Zheng<sup>10</sup>, M. Zhong<sup>26,32</sup>, S.-L. Zhu<sup>21</sup>, Y. S. Zhu<sup>1</sup>, V. Zhuravlov<sup>12</sup>, B. S. Zou<sup>1</sup>, J. H. Zou<sup>23</sup>

<sup>1</sup> *Institute of High Energy Physics, Beijing 100049.*

<sup>2</sup> *III. Physikalisches Institut, RWTH Aachen University 52056 Aachen, Germany.*

<sup>3</sup> *High Energy Physics Division, Argonne National Laboratory 9700 South Cass Avenue, Argonne, IL 60439, USA.*

<sup>4</sup> *Dept. of Physics, Universitat Autonoma de Barcelona, E-08193 Bellaterra, Barcelona, Spain.*

<sup>5</sup> *China Center for Advanced Science and Technology (CCAST), Beijing 100080.*

<sup>6</sup> *Dept. d'Estructura i Constituents de la Materia, Universitat de Barcelona Diagonal 647, E-08028 Barcelona, Catalonia, Spain.*

<sup>7</sup> *Carleton University, 1125 Colonel By Drive, Ottawa, Ontario, K1S 5B6, Canada.*

<sup>8</sup> *Institute of Particle Physics, Central China Normal University, Wuhan 430079.*

<sup>9</sup> *Centre de Physique Théorique, CNRS Luminy, Case 907, F-13288 Marseille Cedex 9, France.*

<sup>10</sup> *Graduate University of the Chinese Academy of Sciences, Beijing 100039.*

<sup>11</sup> *Dipartimento di Fisica dell'Università di Milano and INFN, Milano, Italy.*

<sup>12</sup> *JINR, 141980 Dubna, Moscow region, Russian Federation.*

<sup>13</sup> *Institute für Physik, Humboldt Universität zu Berlin, Newtonstr. 15, 12489 Berlin, Germany*

<sup>14</sup> *Institute of Physics, Academia Sinica, Taipei 115.*

<sup>15</sup> *Institute of Theoretical Physics of the Chinese Academy of Sciences, Beijing 100080.*

<sup>16</sup> *Department of Physics, Nankai University, Tianjin 300071.*

<sup>17</sup> *Department of Physics, University of Notre Dame du Lac Notre Dame, IN 46556, USA.*

<sup>18</sup> *Laboratoire de Physique Nucléaire et Hautes Energies, Université Pierre et Marie Curie Paris*

- <sup>6</sup>, Université Denis Diderot Paris 7, CNRS/IN2P3, F-75252 Paris, France.
- <sup>19</sup> Physics Division, Oak Ridge National Laboratory, Oak Ridge, TN 37831, USA.
- <sup>20</sup> Laboratoire de Physique Théorique, Université Paris-Sud 11, CNRS, F-91405 Orsay Cedex, France.
- <sup>21</sup> Peking University, Beijing 100871.
- <sup>22</sup> Laboratoire d'Annecy-le-vieux de Physique des Particules, Université de Savoie, CNRS/IN2P3, F-74941 Annecy-le-Vieux, France.
- <sup>23</sup> Department of Physics, Shandong University, Jinan, Shandong 250100.
- <sup>24</sup> Department of Physics and Astronomy, University of Tennessee, Knoxville, TN 37996, USA.
- <sup>25</sup> University of Science and Technology of China, Hefei 230026.
- <sup>26</sup> Center for High Energy Physics, Tsinghua University, Beijing 100084.
- <sup>27</sup> University of Hawaii, Honolulu, HI 96822, USA.
- <sup>28</sup> Department of Physics, Wuhan University, Wuhan 430072.
- <sup>29</sup> Departament de Fisica Teorica, IFIC, Universitat de Valencia -CSIC, Apt. de Correus 22085, E-46071 Valencia, Spain.
- <sup>30</sup> Dept. of Physics, University of Victoria, P.O. Box 3055, Victoria, British Columbia Canada, V8W 3P6.
- <sup>31</sup> Institute of Modern Physics, Zhejiang University, Hangzhou 310027. <sup>32</sup> Department of Physics, National University of Defense Technology, Hunan, Changsha 410073.



## Abstract

There has recently been a dramatic renewal of interest in the subjects of hadron spectroscopy and charm physics. This renaissance has been driven in part by experimental reports of  $D^0\bar{D}^0$  mixing and the discovery of narrow  $D_{sJ}$  states and a plethora of charmonium-like  $XYZ$  states at the  $B$  factories, and the observation of an intriguing proton-antiproton threshold enhancement and the possibly related  $X(1835)$  meson state at BESII. At the same time, lattice QCD is now coming of age, and we are entering a new era when precise, quantitative predictions from lattice QCD can be tested against experimental measurements. For example, the High Precision QCD (HPQCD) and United Kingdom QCD (UKQCD) collaboration's recent high-precision, unquenched calculation of  $f_{D^+} = 208 \pm 4$  MeV has been found to agree with the CLEO-c collaboration measurement of  $f_{D^+} = 223 \pm 17 \pm 8$  MeV – a precision level of  $\sim 8\%$ . Intriguingly, this agreement does not extend to  $f_{D_s}$ , where the HPQCD + UKQCD result  $f_{D_s} = 241 \pm 3$  MeV is more than three standard deviations below the current world average experimental value  $f_{D_s} = 276 \pm 9$  MeV. Precision improvements, especially on the experimental measurements, are called for and will be of extreme interest.

The *BES-III* experiment at BEPCII in Beijing, which will start operation in summer 2008, will accumulate huge data samples of  $10 \times 10^9 J/\psi$ ,  $3 \times 10^9 \psi(2S)$ , 30 million  $D\bar{D}$  or 2 million  $D_S^+D_S^-$ -pairs per running year, respectively, running in the  $\tau$ -charm threshold region. Coupled with currently available results from CLEO-c, *BES-III* will make it possible to study in detail, and with unprecedentedly high precision, light hadron spectroscopy in the decays of charmonium states and charmed mesons. In addition, about 90 million  $D\bar{D}$  pairs will be collected at *BES-III* in a three-year run at the  $\psi(3770)$  peak. Many high precision measurements, including CKM matrix elements related to charm weak decays, decay constants  $f_{D^+}$  and  $f_{D_s}$ , Dalitz decays of three-body  $D$  meson decays, searches for  $CP$  violation in the charmed-quark sector, and absolute decay branching fractions, will be accomplished. *BES-III* analyses are likely to be essential in deciding if recently observed signs of mixing in the  $D^0\bar{D}^0$  meson system are actually due to new physics or not. *BES-III* measurements of  $f_{D^+}$  and  $f_{D_s}$  at the  $\sim 1\%$  precision level will match the precision of lattice QCD calculations and provide the opportunity to probe the charged Higgs sector in some mass ranges that will be inaccessible to the LHC. With modern techniques

and huge data samples, searches for rare, lepton-number violating, flavor violating and/or invisible decays of  $D$ -mesons, charmonium resonances, and tau-leptons will be possible. Studies of  $\tau$ -charm physics could reveal or indicate the possible presence of new physics in the low energy region.

This physics book provides detailed discussions on important topics in  $\tau$ -charm physics that will be explored during the next few years at *BES-III*. Both theoretical and experimental issues are covered, including extensive reviews of recent theoretical developments and experimental techniques. Among the subjects covered are: innovations in Partial Wave Analysis (PWA), theoretical and experimental techniques for Dalitz-plot analyses, analysis tools to extract absolute branching fractions and measurements of decay constants, form factors, and  $CP$ -violation and  $D^0\bar{D}^0$ -oscillation parameters. Programs of QCD studies and near-threshold tau-lepton physics measurements are also discussed.

# Contents

<b>Abstract</b>	<b>vii</b>
<b>I The <i>BES-III</i> experiment and its physics</b>	<b>1</b>
<b>1 Physics goal of <i>BES-III</i></b>	<b>3</b>
<b>2 The <i>BES-III</i> detector and offline software</b>	<b>9</b>
2.1 Overview of the <i>BES-III</i> Detector . . . . .	9
2.2 <i>BES-III</i> Offline Software . . . . .	9
2.2.1 Simulation . . . . .	11
2.2.2 Reconstruction . . . . .	11
2.2.3 Calibration and database . . . . .	11
2.3 Main Drift Chamber . . . . .	11
2.4 Time-Of-Flight System . . . . .	14
2.5 Electromagnetic Calorimeter . . . . .	16
2.6 Muon Identifier . . . . .	18
2.7 Trigger . . . . .	20
<b>3 Analysis Tools</b>	<b>23</b>
3.1 Monte Carlo Generators . . . . .	23
3.1.1 Introduction . . . . .	23
3.1.2 Generator framework . . . . .	24
3.1.3 <i>BES-III</i> Generators . . . . .	24
3.1.4 Summary and outlook . . . . .	28
3.2 Luminosity Measurements at <i>BES-III</i> . . . . .	28
3.2.1 Introduction . . . . .	28
3.2.2 Event selection and Algorithm . . . . .	30
3.2.3 Systematic uncertainty . . . . .	30
3.2.4 Summary . . . . .	34
3.3 Particle Identification . . . . .	34
3.3.1 Introduction . . . . .	34
3.3.2 The PID system of <i>BES-III</i> . . . . .	35
3.3.3 The Likelihood Method . . . . .	38
3.3.4 A correlation analysis of TOF PID . . . . .	42
3.3.5 Applying the ANN technique in PID algorithm at <i>BES-III</i> . . . . .	46

3.3.6	Future PID algorithms for <i>BES-III</i> . . . . .	51
3.4	Kinematic Fitting . . . . .	52
3.4.1	Introduction . . . . .	52
3.4.2	General algorithm . . . . .	52
3.4.3	Common Kinematic Constraints . . . . .	54
3.4.4	Applying Kalman filter techniques to kinematic fitting . . . . .	58
3.4.5	Limitations of Kinematic Fitting . . . . .	59
3.5	Partial Wave Analysis . . . . .	60
3.5.1	Introduction . . . . .	60
3.5.2	Decay Amplitude . . . . .	61
3.5.3	Partial Wave Analysis . . . . .	64
3.5.4	Mass, Width and Spin-parity . . . . .	65
3.5.5	Applications . . . . .	66
3.5.6	Discussions . . . . .	69
3.6	Dalitz-plot Analysis Formalism . . . . .	70
3.6.1	Barrier Factor $B_L$ . . . . .	71
3.6.2	Angular Distributions . . . . .	72
3.6.3	The Dynamical Function $T_R$ . . . . .	72
3.6.4	Breit-Wigner Formulation . . . . .	74
3.6.5	$K$ -matrix Formalism . . . . .	74
3.6.6	Flatté Formalism . . . . .	76
3.6.7	Branching Ratios from Dalitz Fits . . . . .	76
<b>Bibliography</b>		<b>79</b>
<b>II <math>e^+e^-</math> Collision at <math>\sqrt{s} = 2 - 5</math> GeV</b>		<b>87</b>
<b>4 Physics Processes and Radiative Corrections</b>		<b>89</b>
4.1	Physics Processes at BEPC-II . . . . .	89
4.2	Radiative corrections . . . . .	91
4.2.1	First order perturbation and exponentiation . . . . .	91
4.2.2	Structure function approach . . . . .	93
4.2.3	Initial and final state radiation . . . . .	96
4.2.4	MC generators: inclusive process . . . . .	97
4.2.5	MC generators: exclusive process . . . . .	98
4.2.6	MC generators: the radiative return process . . . . .	101
4.2.7	Summary . . . . .	102
<b>5 Hadronic fragmentation</b>		<b>103</b>
5.1	String fragmentation in the Lund model . . . . .	104
5.2	The Lund area law . . . . .	105
5.3	Solutions of the Lund area law . . . . .	106
5.4	Preliminary multiplicity . . . . .	107
5.5	Parameter tuning . . . . .	108

<b>6 R values and precision test of the Standard Model</b>	<b>111</b>
6.1 $e^+e^- \rightarrow$ hadrons cross sections and the $R_{had}$ value	111
6.2 Hadronic Vacuum Polarization	116
6.3 Input parameters and their uncertainties	119
6.4 Measurement of $R$ value at <i>BES-III</i>	126
6.4.1 Hadronic event selection and background subtraction	126
6.4.2 Scan of the continuum and resonances	128
6.4.3 $R$ values from radiative return	130
6.4.4 Systematic errors	132
<b>7 Experimental tests of QCD</b>	<b>133</b>
7.1 Inclusive distributions	133
7.2 Exclusive cross sections and form factors	135
7.3 Multiplicity distribution	137
7.4 Kinematical and dynamical correlations	139
7.5 Topological event shapes	140
7.6 Bose-Einstein correlations (BEC)	141
7.7 Possible fractal structure of final state phase-space	143
<b>8 Lineshapes of charmonium resonances</b>	<b>145</b>
8.1 Resonance production and $1^{--}$ charmonium states	145
8.2 Key points for precision measurements	146
8.3 An example for measuring $\psi(2S)$ and $\psi(3770)$ parameters	147
8.4 Resonance measurements at <i>BES-III</i>	151
8.5 Summary	154
<b>Bibliography</b>	<b>157</b>
<b>III Light hadron physics</b>	<b>167</b>
<b>9 Meson spectroscopy</b>	<b>173</b>
9.1 Introduction	173
9.2 Conventional meson spectrum	173
9.3 Glueball spectrum	177
9.3.1 Glueball signatures	177
9.3.2 Glueball candidates	182
9.3.3 Hunting for glueballs at <i>BES-III</i>	193
9.4 Hybrid Mesons	200
9.4.1 Theoretical models for hybrid mesons	200
9.4.2 Signatures of the hybrid mesons	217
9.4.3 Monte-Carlo simulation of $1^{+-}$ exotic state $\pi_1(1400)$	218
9.5 Multiquarks	222
9.5.1 Multiquark candidates	222
9.5.2 Simulation of the $X(1835)$ in $J/\psi$ decays at <i>BES-III/BEPCII</i>	229
9.6 Molecular states	232

<b>10 Baryon spectrum</b>	<b>233</b>
10.1 Baryons as $qqq$ states . . . . .	233
10.2 Outstanding problems in baryon spectroscopy . . . . .	239
10.3 Baryon Spectroscopy at BESI and BESII . . . . .	241
10.3.1 Partial Wave Analysis for Baryon Resonances . . . . .	246
10.4 Prospects for baryon spectroscopy at BESIII . . . . .	247
<b>11 Physics of soft pions and the lightest scalars at <i>BES-III</i></b>	<b>251</b>
11.1 Partially conserved vector current (PCAC) and soft pions . . . . .	251
11.1.1 PCAC . . . . .	251
11.1.2 Adler's theorem with one soft pion . . . . .	251
11.1.3 The linear $\sigma$ model and chiral shielding . . . . .	253
11.1.4 Why should there be a $\sigma$ resonance? . . . . .	255
11.2 Beyond the Breit–Wigner description of a broad resonance . . . . .	256
11.2.1 How to describe a light and broad resonance . . . . .	256
11.2.2 The $\sigma$ pole in the BESII experiment . . . . .	257
11.3 Final state interaction theorem and Omnés solution . . . . .	259
11.3.1 The final state interaction theorem . . . . .	259
11.3.2 $D^+ \rightarrow K^-\pi^+l\nu_l$ decays . . . . .	260
11.3.3 $D^+ \rightarrow K^-\pi^+\pi^+$ decays . . . . .	260
11.3.4 More on final state interactions in the $J/\psi \rightarrow \omega\pi\pi$ process . . . . .	261
11.3.5 The Omnés solution . . . . .	262
11.4 On the nature of the lightest scalar resonances . . . . .	263
<b>12 Two-photon physics</b>	<b>267</b>
12.1 Introduction . . . . .	267
12.2 Experimental status of two-photon processes . . . . .	270
12.3 Measurement of two-photon processes at <i>BES-III</i> . . . . .	271
12.4 Summary . . . . .	275
<b>Bibliography</b>	<b>277</b>
<b>IV Charmonium Physics</b>	<b>293</b>
<b>13 Theoretical Frameworks of Charmonium Physics</b>	<b>295</b>
13.1 Non-Relativistic QCD effective theory . . . . .	295
13.1.1 NRQCD effective theory . . . . .	296
13.1.2 Inclusive Charmonium Annihilation Decays . . . . .	297
13.2 pNRQCD and its applications . . . . .	299
13.2.1 pNRQCD . . . . .	299
13.2.2 Applications . . . . .	300
13.2.3 QCD potentials . . . . .	300
13.2.4 Precision determination of Standard Model parameters . . . . .	302
13.2.5 Gluelump Spectrum and exotic states . . . . .	303
13.2.6 Outlook . . . . .	303

<b>14 Charmonium Spectroscopy</b>	<b>305</b>
14.1 Charmonium spectroscopy . . . . .	305
14.2 Conventional charmonium states . . . . .	305
14.2.1 Particle widths . . . . .	309
14.3 Issues for <i>BES-III</i> . . . . .	310
14.3.1 Measurements related to the $\eta_c$ . . . . .	310
14.3.2 Mass and width of the $\eta'_c$ . . . . .	313
14.3.3 The $h_c$ mass . . . . .	313
14.4 Novel states . . . . .	314
14.4.1 Charm Molecules . . . . .	314
14.4.2 Charmonium Hybrids . . . . .	316
14.5 The <i>XYZ</i> mesons, recent experimental developments . . . . .	318
14.5.1 The $X(3940)$ (and $X(4160)$ ) . . . . .	318
14.5.2 The $Y(3940)$ . . . . .	319
14.5.3 The $Z(3930)$ . . . . .	319
14.5.4 $\pi^+\pi^-\psi'$ resonances at 4360 MeV/ $c^2$ and 4660 MeV/ $c^2$ . . . . .	319
14.5.5 The $Z^\pm(4430) \rightarrow \pi^\pm\psi'$ . . . . .	320
14.5.6 Evidence for corresponding states in the <i>s</i> - and <i>b</i> -quark sectors? . . . . .	322
14.5.7 Summary . . . . .	324
14.5.8 Implications for <i>BES-III</i> . . . . .	324
<b>15 Charmonium transitions</b>	<b>327</b>
15.1 Hadronic transitions . . . . .	327
15.1.1 QCD Multipole Expansion . . . . .	327
15.1.2 Hadronic Transitions Between <i>S</i> -Wave Quarkonia . . . . .	328
15.1.3 $\pi\pi$ Transitions of <i>D</i> -Wave Charmonium . . . . .	331
15.1.4 Studying the $h_c$ State . . . . .	333
15.1.5 $\pi\pi$ Transitions of <i>P</i> -Wave Quarkonia . . . . .	335
15.1.6 Summary . . . . .	337
15.2 Radiative transition . . . . .	338
15.2.1 E1 radiative transitions . . . . .	338
15.2.2 Accessing the new states near 3.9 GeV through E1 transitions . . . . .	342
15.2.3 M1 radiative transitions . . . . .	343
15.3 Channels for measurement at <i>BES-III</i> . . . . .	344
15.3.1 Introduction . . . . .	344
15.3.2 Radiative transitions . . . . .	345
15.3.3 Hadronic transitions . . . . .	348
15.3.4 Summary . . . . .	360
15.4 Monte Carlo simulation of spin-singlet charmonium states . . . . .	362
15.4.1 $\psi' \rightarrow \gamma\eta_c, \eta_c \rightarrow K_S^0 K\pi$ . . . . .	362
15.4.2 $\psi' \rightarrow \gamma\eta'_c, \eta'_c \rightarrow K_S^0 K\pi$ . . . . .	362
15.4.3 $\psi' \rightarrow \pi^0 h_c, h_c \rightarrow \gamma\eta_c, \eta_c \rightarrow K_S^0 K\pi$ . . . . .	363

<b>16 Charmonium Leptonic and EM Decays</b>	<b>365</b>
16.1 Leptonic and EM Decays in Potential Models . . . . .	365
16.1.1 $e^+e^-$ widths of $1^{--}$ states . . . . .	365
16.1.2 Two-photon couplings . . . . .	366
16.1.3 QCD radiative and relativistic corrections to EM decays . . . . .	367
16.2 Leptonic and EM Decays in Effective Field Theories . . . . .	371
16.2.1 Introduction . . . . .	371
16.2.2 Weak coupling regime . . . . .	372
16.2.3 Final discussion . . . . .	376
<b>17 Radiative decays</b>	<b>379</b>
17.1 Inclusive Radiative Decays . . . . .	379
17.1.1 Introduction . . . . .	379
17.1.2 The photon spectrum . . . . .	379
17.1.3 Extraction of $\alpha_s(M_{J/\psi})$ . . . . .	387
17.1.4 Learning about the nature of $J/\psi$ and $\psi(2S)$ . . . . .	387
17.1.5 Conclusions . . . . .	387
17.2 Exclusive Radiative Decays . . . . .	388
17.2.1 Introduction . . . . .	388
17.2.2 Radiative decays of vector charmonia . . . . .	388
17.2.3 Radiative decays of pseudoscalar charmonia . . . . .	390
17.2.4 Radiative decays of P-wave charmonia . . . . .	390
17.2.5 Discussions and conclusions . . . . .	391
<b>18 Hadronic decays</b>	<b>393</b>
18.1 Light-hadron decays . . . . .	393
18.1.1 $J/\psi, \psi'$ decay . . . . .	394
18.1.2 $\eta_c$ decay . . . . .	395
18.1.3 P-wave $\chi_{cJ}$ decay . . . . .	396
18.2 P-wave $h_c$ decay . . . . .	398
18.3 $\rho - \pi$ puzzle . . . . .	400
18.3.1 Introduction . . . . .	400
18.3.2 Review of theoretical work on the $\rho\pi$ puzzle . . . . .	400
18.3.3 Summary . . . . .	411
18.4 Open-flavor decays . . . . .	411
18.5 $\psi(3770)$ non- $D\bar{D}$ decays . . . . .	414
18.5.1 Introduction . . . . .	414
18.5.2 S-D mixing and mixing angle $\theta_{\text{mix}}$ . . . . .	415
18.5.3 Electromagnetic transitions . . . . .	417
18.5.4 Hadronic transitions . . . . .	419
18.5.5 Light hadron decays . . . . .	421
18.5.6 Studies of inclusive decays . . . . .	424
18.5.7 Summary . . . . .	427
18.6 Baryonic decays . . . . .	427
18.6.1 Introduction . . . . .	427
18.6.2 Theoretical Framework . . . . .	428

18.6.3 Two body decays . . . . .	432
18.6.4 Three body decays . . . . .	438
18.6.5 Multi-body and Semi-inclusive decay . . . . .	441
18.6.6 Summary and discussion . . . . .	444
18.7 $\psi(3770)$ and $\psi(4415)$ decays to $p\bar{p}$ . . . . .	444
<b>19 Rare and forbidden charmonium decays</b>	<b>445</b>
19.1 Weak Decays of Charmonium . . . . .	445
19.1.1 Semileptonic Decays of Charmonium . . . . .	445
19.1.2 Two-body Weak Hadronic Decays of Charmonium . . . . .	446
19.1.3 Searches at <i>BES-III</i> . . . . .	448
19.2 Search for the invisible decays of Quarkonium . . . . .	449
19.3 Search for $C$ or $P$ violating processes in $J/\psi$ decays . . . . .	454
19.4 Lepton flavor violating processes in decays of $J/\psi$ . . . . .	456
<b>20 Miscellaneous</b>	<b>459</b>
20.1 Bell inequalities in high energy physics . . . . .	459
20.2 Special topics in $B\bar{B}$ final states . . . . .	465
20.2.1 SU(3) flavor symmetry breaking effects . . . . .	465
20.2.2 $CP$ violation . . . . .	466
20.2.3 Exotic states . . . . .	469
20.2.4 Meson-nucleon bound states . . . . .	471
<b>Bibliography</b>	<b>473</b>
<b>V Charm Physics</b>	<b>499</b>
<b>21 Charm production and <math>D</math> tagging</b>	<b>503</b>
21.1 Charmed particle production cross sections . . . . .	503
21.1.1 Introduction . . . . .	503
21.1.2 The $1^{--}$ resonances around 4.0GeV . . . . .	506
21.1.3 Charmed meson cross sections below the $D^*\bar{D}$ threshold . . . . .	510
21.1.4 Charmed cross sections above the $D^*\bar{D}$ threshold . . . . .	511
21.1.5 Corrections to the observed cross sections . . . . .	514
21.2 $D$ -meson tagging . . . . .	516
21.2.1 Tag reconstruction . . . . .	517
21.2.2 Beam constrained mass . . . . .	518
21.2.3 Multiple Counting . . . . .	518
<b>22 Leptonic, semileptonic <math>D(D_S)</math> decays and CKM matrix</b>	<b>521</b>
22.1 Leptonic Decays . . . . .	521
22.1.1 Theoretical Review . . . . .	521
22.1.2 Decay Constants . . . . .	524
22.1.3 Probing for new physics in leptonic $D_{(s)}$ decays . . . . .	528
22.1.4 Measurements of Leptonic Decays at <i>BES-III</i> . . . . .	533
22.2 Semileptonic Decays . . . . .	538

22.2.1 Theoretical Review . . . . .	538
22.2.2 Exclusive Semileptonic Decays . . . . .	549
22.2.3 Inclusive Semileptonic Decays . . . . .	555
22.3 Impact on CKM Measurements . . . . .	560
22.3.1 The Role of Charm in Precision CKM Physics . . . . .	560
22.3.2 Impact of BESIII measurements . . . . .	561
<b>23 Hadronic <math>D(D_S)</math> decays</b>	<b>569</b>
23.1 Present Status and Implication for QCD . . . . .	569
23.2 Theoretical Review . . . . .	570
23.2.1 The Effective Weak Hamiltonian . . . . .	570
23.2.2 Factorization and First Generation Theoretical Techniques . . . . .	571
23.2.3 The $1/N_C$ ansatz . . . . .	572
23.2.4 Treatment with QCD sum rules . . . . .	573
23.2.5 Modern Developments . . . . .	574
23.2.6 Symmetry Analysis . . . . .	575
23.3 Two-Body Decays . . . . .	576
23.3.1 Kinematics and Topologies of Amplitudes . . . . .	576
23.3.2 $D \rightarrow PP$ , $D \rightarrow PV$ and $D \rightarrow VV$ Decays . . . . .	577
23.3.3 $D \rightarrow SP$ Decays . . . . .	579
23.3.4 $D \rightarrow AP$ Decays . . . . .	583
23.3.5 $D \rightarrow TP$ Decays . . . . .	586
23.3.6 Other Decay Modes . . . . .	587
23.4 Three-Body Decays . . . . .	589
23.4.1 Kinematics and Dalitz Plot . . . . .	589
23.4.2 Resonant Three-Body Decays . . . . .	589
23.4.3 Nonresonant Three-Body Decays . . . . .	589
23.4.4 Beyond Three-Body Decays . . . . .	590
<b>24 Charm baryon production and decays</b>	<b>593</b>
24.1 Introduction . . . . .	593
24.2 Production of charmed baryons at <i>BES-III</i> . . . . .	594
24.3 Spectroscopy . . . . .	594
24.4 Strong decays . . . . .	599
24.4.1 Strong decays of <i>s</i> -wave charmed baryons . . . . .	599
24.4.2 Strong decays of <i>p</i> -wave charmed baryons . . . . .	601
24.5 Lifetimes . . . . .	603
24.6 Hadronic weak decays . . . . .	610
24.6.1 Quark-diagram scheme . . . . .	611
24.6.2 Dynamical model calculation . . . . .	612
24.6.3 Discussions . . . . .	617
24.6.4 Charm-flavor-conserving weak decays . . . . .	619
24.7 Semileptonic decays . . . . .	620
24.8 Electromagnetic and Weak Radiative decays . . . . .	621
24.8.1 Electromagnetic decays . . . . .	621
24.8.2 Weak radiative decays . . . . .	624

<b>25 <math>D^0 - \bar{D}^0</math> Mixing</b>	<b>627</b>
25.1 Theoretical Review . . . . .	627
25.1.1 Oscillation Formalism: the Phenomenology . . . . .	627
25.1.2 Time-dependent Rate for Incoherent $D$ Decays . . . . .	629
25.1.3 Standard Model Predictions for Oscillation Parameters . . . . .	631
25.2 Experimental Review . . . . .	635
25.2.1 Semileptonic Decays . . . . .	636
25.2.2 Hadronic Final States . . . . .	637
25.2.3 $CP$ Eigenstates . . . . .	641
25.2.4 Mixing parameters from a Dalitz Plot analysis . . . . .	643
25.3 Measurements at the $\psi(3770)$ peak . . . . .	646
25.3.1 The mixing rate: $R_M$ . . . . .	650
25.3.2 Lifetime differences and the strong phase $\delta_{K\pi}$ . . . . .	652
<b>26 CP and T Violation</b>	<b>657</b>
26.1 Formalism and Review . . . . .	658
26.2 $CP$ Violation in $D^0 - \bar{D}^0$ Mixing . . . . .	660
26.3 $CP$ Violation in Decay . . . . .	662
26.4 $CP$ Violation in the interference between decays with and without mixing	663
26.5 Rate of the $CP$ Violation in the Coherent $D^0\bar{D}^0$ Pair . . . . .	666
26.6 T Violation . . . . .	667
26.6.1 Triple-Product Correlation in $D$ Decays . . . . .	667
26.6.2 Searches for $CP$ Violation via $T$ -odd moments in $D$ decays . . . . .	669
<b>27 Rare and Forbidden Charm Decays</b>	<b>673</b>
27.1 Introduction . . . . .	673
27.2 Rare charm decays in the SM . . . . .	674
27.2.1 Radiative charm decays . . . . .	674
27.2.2 GIM-suppressed decays . . . . .	675
27.3 New Physics Analysis . . . . .	678
27.3.1 $R$ -parity conserving SUSY . . . . .	678
27.3.2 $R$ -parity violating SUSY . . . . .	680
27.3.3 Large Extra Dimensions . . . . .	681
27.4 Summary . . . . .	682
<b>Bibliography</b>	<b>685</b>
<b>VI <math>\tau</math> Physics</b>	<b>707</b>
<b>28 Tau Physics near Threshold</b>	<b>709</b>
28.1 Introduction . . . . .	709
28.2 Tau Production at Threshold . . . . .	710
28.3 Physics Opportunities . . . . .	712
28.4 Running Strategy . . . . .	714

<b>29 Tau Decays</b>	<b>715</b>
29.1 Hadronic $\tau$ Decays . . . . .	715
29.1.1 A Laboratory for QCD . . . . .	715
29.1.2 Determinations of $m_s$ and $V_{us}$ in Hadronic $\tau$ Decays . . . . .	717
29.1.3 Tau Hadronic Spectral Functions . . . . .	719
29.2 Leptonic Tau decays . . . . .	722
29.2.1 Leptonic Decays and Universality Tests . . . . .	722
29.2.2 Lorentz Structure . . . . .	724
29.2.3 Study of the Lorentz structure at <i>BES-III</i> . . . . .	725
29.3 Semileptonic Decays . . . . .	731
29.3.1 Two-body Semileptonic Decays . . . . .	731
29.3.2 Decays into Two Hadrons . . . . .	731
29.4 Search for $CP$ Violation in $\tau$ decays . . . . .	734
29.4.1 $\tau \rightarrow \nu K\pi$ . . . . .	735
29.4.2 Other $\tau$ decay modes . . . . .	737
<b>30 <math>\tau</math> mass near threshold</b>	<b>739</b>
30.1 Introduction . . . . .	739
30.2 Statistical Optimization . . . . .	740
30.2.1 Methodology . . . . .	740
30.2.2 First Optimization . . . . .	742
30.2.3 Second Optimization . . . . .	743
30.2.4 Discussion . . . . .	746
30.3 Systematic uncertainty . . . . .	746
30.3.1 Theoretical accuracy . . . . .	747
30.3.2 Energy spread . . . . .	747
30.3.3 Energy scale . . . . .	748
30.3.4 Other factors . . . . .	749
30.4 Energy measurement at <i>BES-III</i> . . . . .	749
30.4.1 Laser source and optics system . . . . .	751
30.4.2 Electron beam . . . . .	752
30.4.3 Compton back-scattering principle . . . . .	752
30.4.4 A simple simulation . . . . .	753
30.5 Summary . . . . .	755
<b>Bibliography</b>	<b>757</b>
Acknowledgements . . . . .	763
<b>A Statistics in HEP data analysis</b>	<b>765</b>
A.1 Parameter estimation . . . . .	765
A.1.1 Estimators for mean and variance . . . . .	766
A.1.2 The method of maximum likelihood(ML) . . . . .	767
A.1.3 The method of least squares(LS) . . . . .	772
A.2 Interval estimation, confidence interval and upper limit . . . . .	775
A.2.1 Frequentist confidence interval . . . . .	775
A.2.2 Bayesian credible interval . . . . .	782

A.3 Tests of hypotheses . . . . .	784
A.3.1 Goodness-of-fit test . . . . .	785
A.3.2 Statistical significance of signal . . . . .	787



## Part I

# The *BES-III* Experiment and Its Physics

### Conveners

Jian-Ping Ma, Ya-Jun Mao

### Contributors

D. M. Asner, C. D. Fu, K. L. He, J. F. Hu, B. Huang,  
W. D. Li, B. J. Liu, J. P. Ma, Y. J. Mao, X. H. Mo,  
R. G. Ping, G. Qin, S. S. Sun, Y. F. Wang, N. Wu,  
M. Xu, X. Y. Zhang, H. Q. Zheng, Y. H. Zheng



# Chapter 1

## Physics Goal of *BES-III*<sup>1</sup>

The Standard Model (SM) has been successful at describing all relevant experimental phenomena and, thus, has been generally accepted as the fundamental theory of elementary particle physics. Despite its success, the SM leaves many unanswered questions. These can be classified into two main categories: one for subjects related to possible new physics at unexplored energy scales and the other for nonperturbative physics, mostly related to Quantum Chromodynamics.

The SM describes particle physics up to energies of around 100 GeV. It is expected that new particles and new interactions will appear at some higher energy scale, say 1 TeV. Those new particles and new interactions are presumably needed to solve some inconsistencies within the SM and for the ultimate unification of all interactions. Such physics issues all belong to the first category, and will be addressed by experiments at the LHC, which will start operation in 2008, and at the ILC, which is currently being planned.

The second category of unanswered questions includes those about nonperturbative effects. QCD, the fundamental theory of the strong interactions, is well tested at short distances, but at long distances nonperturbative effects become important and these are not well understood. These effects are very basic to the field of particle physics and include *e.g.*, the structure of hadrons and the spectrum of hadronic states. Lower energy facilities with high luminosity can address these questions. Among these, the Beijing Electron Positron Collider II (BEPCII), which will operate in the 2 GeV to 4.6 GeV energy range, will be an important contributor. This is because it spans the energy range where *both* short-distance and long-distance effects can be probed.

The BEPCII energy range includes the threshold of charmonia. The discoveries of the low-lying charmonium states and of open-charmed hadrons were instrumental for the acceptance of quarks as truly dynamical entities in general, and of the SM in particular. The surprising discoveries of the narrow  $D_{sJ}$  mesons, several hidden charm resonances around 4 GeV region, and the  $X(1835)$  at BESII during the past few years have considerably enhanced the interest in the study of the spectroscopy of hadrons with and without *open* charm. The high energy physics community has realized that comprehensive studies of  $e^+e^-$  annihilation in the charm-tau threshold region can teach us novel and unique lessons on hadronization and the interplay of perturbative and nonperturbative dynamics. This has great value both in its own right and for its contributions to improve the discovery

---

<sup>1</sup>By Jian-Ping Ma

potential for new physics in the decays of  $B$  mesons studied at LHCb and the  $B$ -factories. The significance of physics around the threshold of charmonia is also illustrated by the fact that the Super- $B$  factories being designed at Frascati and KEK both include the capability of running in the 4 GeV region.

Theoretical studies of physics at the energy scale accessible to BEPCII continue to be actively pursued. To provide a good understanding of physics at this scale, theoretical tools derived from QCD have been invented. For charmonia, one can use the nonrelativistic QCD (NRQCD) and potential nonrelativistic QCD (pNRQCD) models to make theoretical predictions for physics involving both short- and long-distance effects, where a factorization of the two different kinds of effects can be accomplished and predictions that do not depend on the assumptions of any particular model can be made. For charmed hadrons, one can at least partly rely on heavy quark effective theory (HQET) for their study. For physics involving long-distance effects only, one can employ QCD sum-rule methods, or lattice QCD and make predictions from first principles. It is a fortunate coincidence that the most powerful tool for the quantitative treatment of nonperturbative dynamics, namely lattice QCD, is reaching a new level of sophistication with uncertainties in calculations of charmed quark dynamics that are approaching the 1 percent level. In addition to the theoretical tools derived from QCD, many phenomenological models have been invented to deal with nonperturbative effects, especially those at the 1 GeV scale or lower, such as light hadron spectroscopy, decays of charmonia and  $D$ -mesons into light hadrons, etc. Many theoretical predictions obtained with the above-mentioned methods exist and call for tests from experiment. The BEPCII/*BES-III* facility will be ideal for carrying out the task of confirming and validating these approaches.

Fruitful physics results have been produced with the earlier Beijing Spectrometers (BESI and BESII) at BEPC. The precise measurement of the  $\tau$ -lepton mass, performed by BESI almost twenty years ago, remains the world's best measurement of this fundamentally important quantity. The  $R$ -value measurements from BESII have made an important improvement to the prediction of the mass of the still undiscovered Higgs boson. BESII also observed an anomalous  $p\bar{p}$  threshold mass enhancement in the radiative decay  $J/\psi \rightarrow \gamma p\bar{p}$ , an observation that has stimulated many theoretical speculations. The observation of non  $D\bar{D}$  decays of the  $\psi(3770)$  by BESII also confounds theoretical expectations. Violation of the notorious 12% rule has been observed in different  $J/\psi$  and  $\psi'$  decay channels. There are many other results that could be mentioned. At the same time, important results in this energy range have also been obtained by the CLEO-c collaboration in the U.S., the most important of which include: the discovery of the  ${}^1P_1$  state of charmonia (the  $h_c$ ), and a measurement of the  $D$ -meson decay constant with an 8% precision. With their large data sample of  $e^+e^- \rightarrow D\bar{D}$  events at the  $\psi(3770)$ , they are able to measure absolute hadronic branching ratios with improved precision, *e.g.*,  $B(D^0 \rightarrow K^-\pi^+)$  and  $B(D^+ \rightarrow K^-\pi^+\pi^+)$  have been measured with errors below the 5% level. It is expected that these phenomena will continue to be studied in *BES-III* with even higher precision which will provide a better understanding of non perturbative physics.

The upgraded BEPCII/*BES-III* is a unique and powerful facility for studying physics in the energy range up to 4 GeV, with a research program that covers charmonium physics,

$D$ -physics, spectroscopy of light hadrons and  $\tau$ -physics. It will also enable searches for possible new interactions. The upgraded collider will reach a luminosity of  $L = 10^{33} \text{cm}^{-2}\text{s}^{-1}$ . At the peak of the  $J/\psi$ , BEPCII will produce  $10^{10}$   $J/\psi$  events per year. These will provide *BES-III* with the world largest data sample for studying  $J/\psi$  mesons and their decays. With one-year-long runs at the design luminosity we can expect the following data samples:

	CMS Mass	Peak Lum.	$\sigma$	No. of Events
$J/\psi$	3.097	0.6	3400	$10 \times 10^9$
$\tau^+\tau^-$	3.670	1.0	2.4	$12 \times 10^6$
$\psi(2S)$	3.686	1.0	640	$3.2 \times 10^9$
$D^0D^0$	3.770	1.0	3.6	$18 \times 10^6$
$D^+D^-$	3.770	1.0	2.8	$14 \times 10^6$
$D_sD_s$	4.030	0.6	0.32	$1.0 \times 10^6$
$D_sD_s$	4.170	0.6	1.0	$2.0 \times 10^6$

It is evident from the table that there will be huge data samples of  $J/\psi$  and  $\psi(2S)$  events, and large numbers of  $D$  and  $D_s$  meson decays. These will not only enable high precision measurements, they will also provide the potential for discovering phenomena that have been overlooked at previous facilities because of statistical limitations. With these data samples, *BES-III* will have opportunities to search for new physics in rare decays of charmonia, charmed mesons,  $\tau$  leptons and to probe  $D^0 - \bar{D}^0$  oscillations and  $CP$  asymmetry. This physics yellow book gives detailed and comprehensive reviews of the relevant experimental and theoretical issues and the tools that are available or needed to address them. A brief summary of physics goals is given here.

### • Charmonium Physics

The total decay widths of the  $J/\psi$  and  $\psi'$  will be measured at a precision level that is better than 1%. The  $J/\psi$  has many different decay modes. In two-body decays, either of the final-state particles can be a pseudoscalar, a scalar, a vector, an axial vector or a tensor meson. With a  $10^{10}$   $J/\psi$  event sample, these decay modes can be measured much more precisely than before. Historically, there are some notorious problems related to decays of charmonia. Among them the most well known problems are the  $\rho\pi$  puzzle, *i.e.* violations of the 12%-rule, and non- $D - \bar{D}$  decays of the  $\psi(3770)$ . With *BES-III*'s huge data samples, more detailed experimental information will be forthcoming that will hopefully provide guidance leading to solutions of these problems. Transitions between various charmonium states will be measured with unprecedented precision. With the possibility of running at higher energies, the recently discovered  $Y(4260)$  could be accessed at BEPCII, and this would offer *BES-III* opportunities to study this unconventional charmonium state.

With such huge data samples, it will be possible to detect some Cabibbo-suppressed  $J/\psi$  decay channels. In these channels, the charmed quark decays via the weak interaction, while the anticharm quark combines with another quark to form a  $D$ -meson. This process will provide the possibility for detecting effects of new physics at BEPCII, if, for example, branching ratios of those decays are found to be larger than SM predictions. Also, one can search for evidence of flavor-changing neutral currents. This is an area where *BES-III* can make unique explorations for physics beyond the SM.

- **Light Hadron Spectroscopy and Search for New Hadronic States**

Using  $J/\psi$ -decays, one can study light hadron spectroscopy and search for new hadronic states. The large  $J/\psi$  sample makes BEPC a “glue” factory, since the charmed- and anticharmed quark constituents of the  $J/\psi$  almost always annihilate into gluons. This is very useful for glueball searches and for probing the gluon contents of light hadrons, including the low-lying scalar mesons.

QCD predicts the existence of glueballs and lattice QCD predicts their masses. For example, the  $0^{++}$  glueball is predicted to have a mass that is between 1.5 and 1.7 GeV. But to date the existence of these various glueballs has still not been experimentally confirmed. Also, since QCD is a relativistic quantum field theory, any hadron should have some gluon content if symmetries allow. These gluon contents, especially those in scalar mesons, are crucial inputs to the understanding of the properties of the light hadrons, such as the  $f_0(1500, 1700)$  scalar mesons. The rich gluon environment in  $J/\psi$  decays is an ideal place to study these issues.

Recently, evidence for exotic hadrons, *i.e.* mesons that cannot be classified as a  $q\bar{q}$  state of the traditional quark model, have been seen experimentally. In principle, QCD allows for the existence of exotic hadrons. With high-statistics data samples, comprehensive searches for exotic states can be performed and the quantum numbers of any candidates that are found can be determined.

In BESII, an anomalous near-threshold mass enhancement is seen in the  $p\bar{p}$  system produced in the radiative decay process  $J/\psi \rightarrow \gamma p\bar{p}$ ; similar enhancements are seen in other baryonic systems. Various explanations for these enhancements have been proposed, *e.g.*, there may be resonances just below the mass thresholds. However, a satisfactory and conclusive explanation has still not emerged. With *BES-III* data these enhancements can be studied more in detail and, hopefully, a satisfactory explanation can be established.

- **$D$ -Physics**

At BEPC,  $D^+$  and  $D^0$  mesons will be produced through the decays of the  $\psi(3770)$ , and  $D_s$  mesons can be produced through  $e^+e^-$  annihilation at  $s$  around  $(4.03\text{GeV})^2$ . The decay constants  $f_D$  and  $f_{D_s}$  can be measured from purely leptonic decays with expected systematic errors of 1.2% and 2.1%, respectively. Inclusive and exclusive semileptonic decays of  $D$ -mesons will also be studied to test various theoretical predictions. Moreover, through the study of the decays  $D^0 \rightarrow K^-e^+\nu_e$  and  $D^0 \rightarrow \pi^-e^+\nu_e$  one can extract the CKM matrix elements  $V_{cs}$  and  $V_{cd}$  with an expected systematic error of around 1.6%.

With *BES-III* it will be possible to measure  $D$ - $\bar{D}$  mixing and search for  $CP$ -violation. Theoretical predictions for mixing and  $CP$ -violation are unreliable; *BES-III* can provide new experimental information about them.

Rare- or forbidden decays can provide strict tests of the SM and have the potential of uncovering the effects of new physics beyond the SM. With *BES-III*, they can be studied systematically. Significant improvements of their branching ratio measurements are expected. The upper limits on branching ratios for unseen modes can be improved by factors of about  $10^{-2}$ .

- **$\tau$ -Physics**

$\tau$ -physics will also be studied at *BES-III*, where several important measurements can

be made. Experimental studies of inclusive hadronic decays can provide precise determinations of the strange quark mass and the CKM matrix element  $V_{us}$ , while the study of leptonic decays can test the universality of the electroweak interaction and give a possible hint of new physics. The measurement precision of the Michel parameter will be improved by a factor of between 2 and 4; the  $\tau$ -mass will be measured with a precision of  $\delta m_\tau \sim 0.09\text{MeV}$ , a factor of 3 improvement on the BESI result.

Beside presenting these physical goals and opportunities at the BEPCII collider with the *BES-III* detector, this yellow book also presents some useful tools that are relevant to *BES-III* analyses.



# Chapter 2

## The *BES-III* detector and offline software<sup>1</sup>

### 2.1 Overview of the *BES-III* Detector

The *BES-III* detector is designed to fulfill the physics requirements discussed in this report, and the technical requirements for a high luminosity, multi-bunch collider. Detailed descriptions of the *BES-III* detector can be found in Ref. [1]. Figure 2.1 shows a schematic view of the *BES-III* detector, which consists of the following components:

- A Helium-gas based drift chamber with a single wire resolution that is better than  $120\text{ }\mu\text{m}$  and a  $dE/dX$  resolution that is better than 6%. The momentum resolution in the 1T magnetic field is better than 0.5% for charged tracks with a momentum of 1 GeV/c.
- A CsI(Tl) crystal calorimeter with an energy resolution that is better than 2.5% and position resolution better than 6 mm for 1 GeV electrons and gammas.
- A Time-of-Flight system with an intrinsic timing resolution better than 90 ps.
- A super-conducting solenoid magnet with a central field of 1.0 Tesla.
- A 9-layer RPC-based muon chamber system with a spatial resolution that is better than 2 cm.

Details of each sub-detector and their performance, together with the trigger system, are discussed in subsequent sections.

### 2.2 *BES-III* Offline Software

The *BES-III* Offline Software System (BOSS) uses the C++ language and object-oriented techniques and runs primarily on the Scientific Linux CERN (SLC) operating system. The entire data processing and physics analysis software system consists of five functional parts: framework, simulation, reconstruction, calibration, and analysis tools.

---

<sup>1</sup>By Wei-Dong Li, Ya-Jun Mao and Yi-Fang Wang

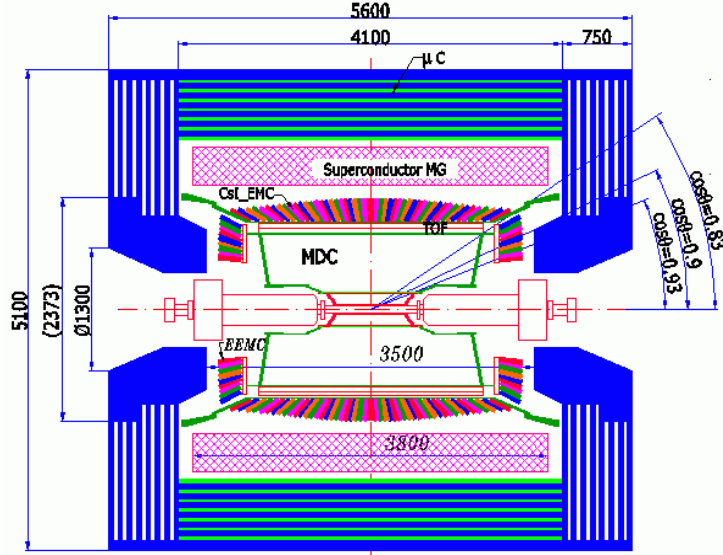


Figure 2.1: An Overview of the *BES-III* Detector.

The BOSS framework is based on the Gaudi package [2], which provides standard interfaces and utilities for event simulation, data processing and physics analysis. The framework employs Gaudi's event data service as the data manager and the event data conversion service for conversions between persistent data and transient objects. Three types of persistent event data have been defined in the BOSS system: raw data, reconstructed data and Data-Summary-Tape (DST) data. Both reconstructed data and DST data are in ROOT format for easy management and usage. Different types of algorithms can access data from Transient Event Data Store (TEDS) via the event data service. The detector's material and geometrical information are stored in GDML files, which can be retrieved by algorithms through corresponding services.

The BOSS framework also provides abundant services and utilities for various needs. For instance, the magnetic field service provides the value of the field at any space point within the detector. The navigation service helps users to trace reconstructed tracks back to their Monte Carlo origins. Using the particle property service, the particles' properties can be accessed by various software components. A performance analysis tool is instrumented to profile the execution of the code and a time measurement tool has been developed to facilitate code benchmarking. A pileup algorithm at the digital level can be used to mix a random trigger event with a simulated signal event so that the background simulation can be properly implemented.

The software is managed by CMT [3], which can define a package, maintain the dependence between different packages and produce executables and libraries.

### 2.2.1 Simulation

The *BES-III* detector simulation, based on the GEANT4 package [4], consists of four parts: event generators, detector description, particle tracking, and detector response. Event generators are discussed in Sect. 3.1. A unique description of the detector geometry and materials, used by both the simulation and reconstruction package, has been developed based on XML [5]. Particle tracking and their interactions with detector materials are handled by the GEANT4 package, while detector responses are modeled by the so-called digitization code, which takes into account detector components, including readout electronics, as well as the realistic situations such as noise, dead channels, etc. A simulation of the trigger system is also implemented.

### 2.2.2 Reconstruction

The *BES-III* reconstruction package consists mainly of the following four parts: a) a track-finding algorithm and a Kalman-Filter-based track-fitting algorithm to determine the momentum of charged particles; b) a particle identification algorithm based on  $dE/dx$  and Time-Of-Flight (TOF) measurements; c) a shower- and cluster-finding algorithm for electromagnetic calorimeter energy and position measurements; d) a muon track finder. In addition, an event timing algorithm that determines the corresponding beam bunch crossing has been developed, and a secondary vertex and track refitting algorithm has been implemented.

### 2.2.3 Calibration and database

The calibration software consists of a calibration framework and calibration algorithms. The framework provides a standard way to obtain the calibration data objects for reconstruction and other algorithms. The calibration constants for each sub-detector are produced by the associated calibration algorithm, and are then stored in a ROOT file and a database along with other information such as the run information, trigger condition, software and hardware version number, etc. The central database, which contains calibration data as well as some information from the online and slow-control databases, will be distributed to *BES-III* collaborating institutions, and will also be available by remote access. All of the databases at different sites will be synchronized via the network, and updated periodically.

## 2.3 Main Drift Chamber

The main drift chamber (MDC), one of the most important sub-detectors of *BES-III*, can determine precisely the momentum of a charged particle by measuring points along its trajectory in a well known magnetic field. It can also determine the particle type by measuring the specific energy deposits ( $dE/dx$ ) in the chamber.

The MDC is the innermost component of the *BES-III* detector, and consists of inner and outer chambers without any intervening wall. The inner chamber can be replaced at some future date in the event that it suffers severe damage due to high backgrounds. The

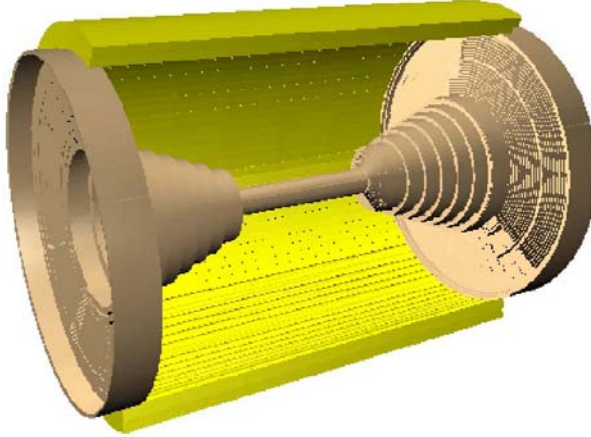


Figure 2.2: An overview of the BESIII Main Drift Chamber

absence of a chamber wall between the inner and outer chambers eliminates a potential major source of multiple scattering.

The MDC covers the polar angle  $|\cos \theta| < 0.93$ , with an inner radius of 60 mm, outer radius of 800 mm, and a maximum length of 2400 mm, as shown in Fig. 2.2. There are 43 cylindrical layers of drift cells that are coaxial with the beam pipe, 8 in the inner chamber and 35 in the outer chamber. All 8 layers in the inner chamber are stereo; 16 stereo layers and 19 axial layers are interleaved in the outer chamber. In total, there are 6796 signal wires. The average half-width of a drift cell is about 6 mm in the inner chamber and 8.1 mm in the outer chamber.

Aluminum wires ( $\phi 110 \mu\text{m}$ ) are used for field shaping and gold-plated tungsten wires ( $\phi 25 \mu\text{m}$ ) for signals. A helium-based gas mixture ( $\text{He/C}_3\text{H}_8=60/40$ ) is used as the working gas to reduce the effect of the multiple scattering, while keeping reasonable  $dE/dx$  resolution.

A superconducting solenoid magnet provides an axial 1.0 Tesla magnetic field throughout the tracking volume. The single-wire resolution in the  $R - \phi$  plane is designed to be better than  $120 \mu\text{m}$ , the resolution in  $z$ -direction at the vertex, measured with the stereo wires, is 2 mm, the  $dE/dX$  resolution from a truncated mean Landau distribution is better than 6%, and the corresponding momentum resolution is better than  $\sigma_{p_t}/p_t = 0.32\%p_t \oplus 0.37\%/\beta$ , where the first term comes from the trajectory measurement and the second term from multiple scattering. Figure 2.3 shows the single wire resolution of the MDC and truncated mean  $dE/dX$  measurements from a cosmic ray test.

## MDC Simulation

The XML descriptions of the geometry and materials of the MDC are based on the GEANT4 package. In particular, the tube class is used to describe and build endplates and axial layers, while the hype class is used for stereo layers and the twisttube class for stereo cells. During the track simulation, steps in the same cell are treated as one hit, and the digitization relies heavily on calibration parameters via the calibration service

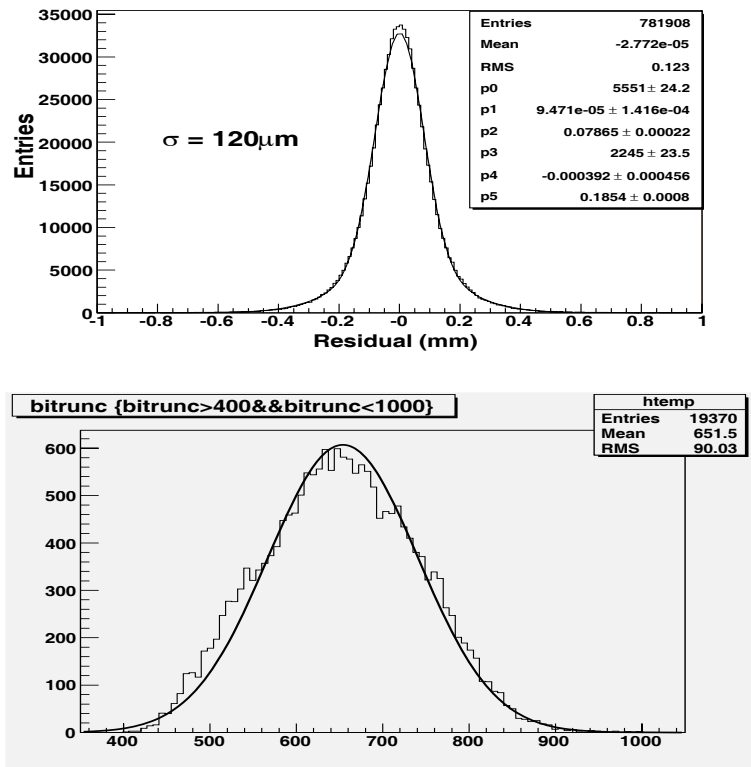


Figure 2.3: Upper plot: Single wire resolution of MDC from a cosmic-ray test; lower plot: truncated mean of  $dE/dx$  measurements from the same test.

function. Effects such as wire efficiency and resolution as a function of drift distance for each wire, noise in each layer, misalignment etc., have been modeled with parameters that can be tuned via a calibration service function.

## MDC Reconstruction and calibration

The MDC tracking algorithm starts with the formation of track segments from hits using pre-calculated patterns. It then links the found axial segments to circular tracks and applies a circular fit using the least-square method. Stereo segments are subsequently added to track candidates followed by an iterative helix fit. Finally, after collecting additional hits that might possibly belong to the track, a track refitting procedure based on the Kalman-filter technique is performed. From a Monte Carlo simulation, we determine that this algorithm can maintain a tracking efficiency of more than 98% for  $p_T > 150$  MeV/c tracks, even in the presence of severe backgrounds. The  $dE/dx$  reconstruction algorithm calculates the energy loss of each charged particle through the chamber after applying various corrections to the measured charge amplitudes, and then gives the probability of each particle identification hypothesis. A GEANT4-based algorithm is developed to extrapolate a MDC track into outer sub-detectors, taking into account the magnetic field and the ionization loss of charged particle in the detector. The associated error matrix at a given space point is calculated taking into account multiple scattering effects.

## MDC calibration

The MDC will be calibrated using  $J/\psi \rightarrow \mu^+\mu^-$  events for both position and  $dE/dX$  measurements. Since the production cross section at  $J/\psi$  peak is huge, sufficient statistics can be obtained in a short run period. The resulting calibration constants for the  $x - t$  relations, timing, alignment, absolute efficiency of wires, etc. for each run period are stored in the database for use by reconstruction algorithms. There is also a proposal to calibrate the MDC by turning off the magnetic field, so that straight tracks can be used for calibration in order to determine precisely the position of each wire [6].

## 2.4 Time-Of-Flight System

The Time-of-Flight (TOF) sub-detector, made of plastic scintillator bars and read out by fine-mesh phototubes, is placed between the drift chamber and the electromagnetic calorimeter and measures the flight time of charged particles in order to identify the particle-type. It also provides a fast trigger and helps reject cosmic-ray backgrounds.

The *BES-III* TOF consists of two parts: the barrel and endcap as shown in Fig. 2.4. The solid angle coverage of the barrel TOF is  $|\cos\theta| < 0.83$ , while that of the endcap is  $0.85 < |\cos\theta| < 0.95$ . The Barrel TOF consists of two layers of 88 plastic scintillator elements arranged in a cylinder of mean radius  $\sim 870$  mm. Each scintillator bar has a length of 2380 mm, a thickness of 50 mm and a width of 50 mm; it is read out at each end by a fine-mesh PMT. Each endcap TOF array consists of 48 fan-shaped elements with an inner radius of 410 mm and an outer radius of 890 mm; these are read out from one end of the scintillator by a single fine-mesh PMT.

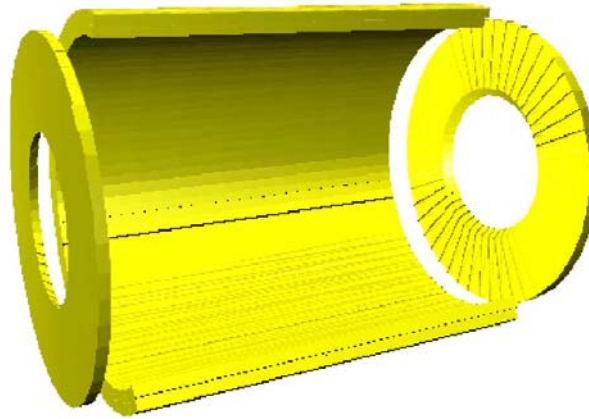


Figure 2.4: The *BES-III* Time Of Flight System

For this system, among all parameters, the time resolution is key. This mainly depends on the following contributions: the intrinsic TOF time resolution caused by the characteristics of the scintillator and the PMT, time resolution and jitter in the readout electronics, the beam-bunch length and the bunch timing uncertainty, the vertex and pathlength resolution of the track, time-walk effects, etc. The design intrinsic time resolution for a barrel counter is 90 ps and for an endcap counter is 70 ps, which have been demonstrated in beam tests as shown in Fig. 2.5. The total time resolution for the double-layer barrel TOF and the end-cap is expected to be about 100 ps.

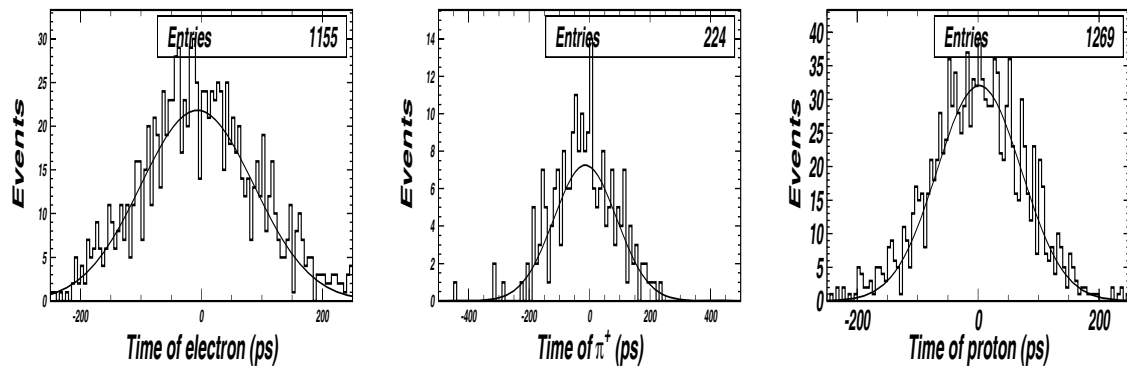


Figure 2.5: Time resolution of TOF counters from a beam test

## TOF Simulation

The TOF simulation takes into account the scintillator, wrapping materials and photo-multiplier tubes based on the GEANT4 package. A fast simulation model has been built that converts the energy loss of a particle in the scintillator into photons, propagates

them (not individual photons but the pulse and its shape) to the PMTs and generates an electronic signal. A discriminator is then applied to the pulse to yield ADC and TDC output. This algorithm has been tested with results from beam tests and further tuning will be needed when data are available. A full simulation that traces each optical photon can be activated to understand the details of the timing measurement.

## TOF Reconstruction

The TOF reconstruction starts from tracks extrapolated to the TOF and matched with a particular TOF module. The travel time of a charged particle from the interaction point to the TOF is then calculated, after a weighted average of results from PMTs at both ends of the scintillator bar and applying various corrections such as the effective light velocity in the scintillator, the light attenuation length, etc. The  $dE/dx$  measurement is also obtained for both charged and neutral particles. Energy loss in the TOF can then be added to that in the EMC in order to improve the shower energy resolution.

## TOF Calibration

The TOF calibration will be performed using  $J/\psi$  decays to leptons, both for timing and energy. The resulting calibration constants, such as effective velocity, attenuation length, muon energy loss, etc., are stored in the database for use by the reconstruction algorithms. The TOF performance and status are monitored regularly by a laser-fiberoptics pulsing system.

## 2.5 Electromagnetic Calorimeter

The Electro-Magnetic Calorimeter (EMC) measures the energies and positions of electrons and photons precisely, and plays an important role in the *BES-III* detector. The calorimeter is comprised of one barrel and two endcap sections as shown in Fig. 2.6. The barrel has an inner radius of 940 mm and a length of 2750 mm, and covers the polar angle of  $|\cos\theta| < 0.83$ . The endcaps have an inner radius of 500 mm are placed at  $z = \pm 1380$  mm from the collision point, and cover the polar angle range  $0.85 < |\cos\theta| < 0.93$ . The total acceptance is 93% of  $4\pi$ . A small gap of about 50 mm between the endcaps and the barrel is required for mechanical support structures, cables and cooling pipes. In the barrel, there are a total of 44 rings of crystals along the  $z$  direction, each with 120 crystals. All crystals except for those in two rings at the center of the detector point to  $z = \pm 50$  mm with a slight tilt angle of  $1.5^\circ$  in the  $\phi$  direction. Each endcap consists of 6 rings that are split into two tapered half-cylinders. All crystals point to  $z = \pm 100$  mm with a tilt of  $1.5^\circ$  in the  $\phi$  direction. The entire calorimeter has 6272 CsI(Tl) crystals and a total weight of about 24 tons.

The calorimeter is designed to have an energy measurement range for electrons or photons from 20 MeV to 2 GeV, with an energy resolution of about  $2.3\%/\sqrt{E(\text{GeV})} \oplus 1\%$ . The design position resolution for an electromagnetic shower is  $\sigma_{xy} \leq 6 \text{ mm}/\sqrt{E(\text{GeV})}$  and the electronics noise for each crystal is required to be less than 220 keV.

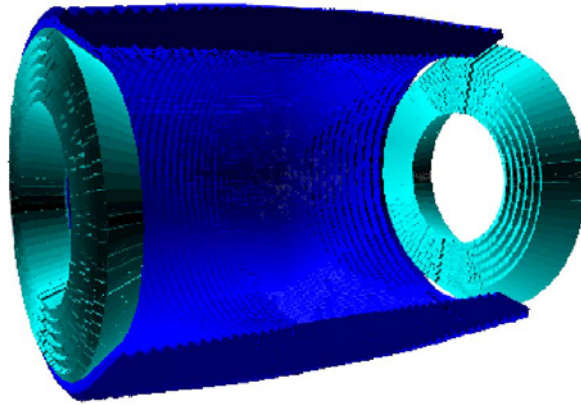


Figure 2.6: The BESIII Electromagnetic Calorimeter

## EMC Simulation

In the simulation, the EMC detector description is based on XML including crystals, casing, silicon photodiodes, preamplifier boxes, cables and the support system. The G4Trap class is used for the barrel crystals and G4IrregBox, a class implemented by *BES-III*, for the endcap crystals. The sensitive detector flag is set for crystals and photodiodes. Hit information is recorded in the sensitive detectors, and then the energy deposits summed, photon statistics computed, and the resulting photodiode response is converted into electronics signals. The waveform for the electronics signals in the time domain is obtained via an inverse Laplace transform; the sampling and peak searching process by the flash ADC is simulated to yield energy and time information. Gaussian-type electronic noise is added to each bin and the background is produced by summing the waveforms.

## EMC Reconstruction

Shower reconstruction in the EMC consists of three concatenated steps: The ADC value of each crystal is converted into energy using the corresponding calibration constants. Clusters in both the barrel and end-caps are formed around the crystals with local maximum energy deposits, called seeds. The shower energies are computed from the energy sums and the positions from energy-weighted first moments. A splitting function is invoked to split the cluster into several showers if multiple seeds are found in one cluster. Matched energy deposits found in the TOF are added to the associated showers to improve energy resolution, particularly, for low energy photons. Figure 2.7 shows the expected energy resolution for electromagnetic showers.

## EMC Calibration

The EMC high energy response will be calibrated with Bhabha electrons at energies of 1.55 GeV or more and the low energy response with  $\pi^0 \rightarrow \gamma\gamma$  decays. Each crystal has to be recalibrated periodically, and monitored frequently by a LED light pulser. Corrections

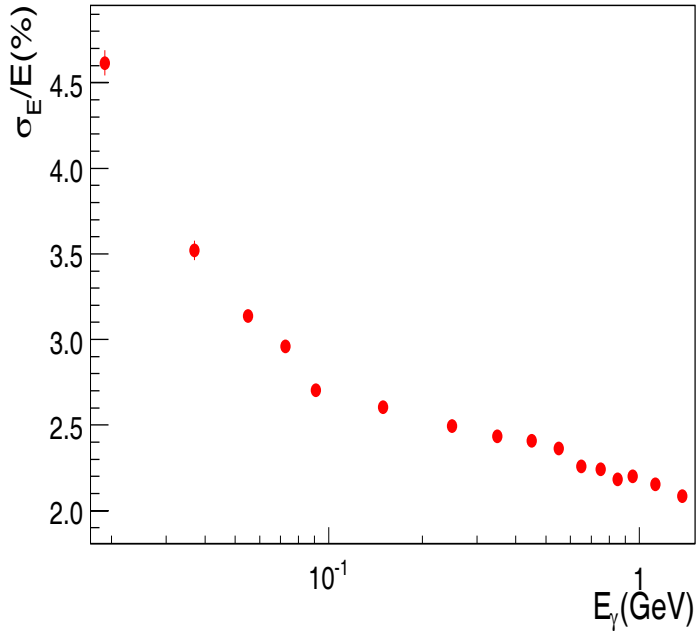


Figure 2.7: Energy resolution of EMC showers.

due to temperature variations can be applied. Calibration constants are stored in the database for use by the reconstruction algorithms.

## 2.6 Muon Identifier

The *BES-III* muon system is designed to distinguish muons from hadrons by the characteristic hit patterns they produce when penetrating the return yoke of the *BES-III* magnet. The muon counter is made of resistive plate chambers (RPC) sandwiched by iron absorbers.

The barrel part of the muon identifier is organized into octants, each of which consists of 9 layers of muon counters inserted into gaps in the iron, as shown in Fig. 2.8. Each endcap is divided into quadrants, each consisting of 8 RPC layers. Proceeding radially outward, the thicknesses of the iron absorbers are 3 cm, 3 cm, 3 cm, 4 cm, 4 cm, 8 cm, 8 cm, 8 cm and 15 cm. The muon counter insertion gap between neighboring slabs is 4 cm. The width of the RPC pickup strip is optimized at 4 cm, and only the  $z$  orientation of odd gaps and azimuthal orientation of even gaps are read out in the barrel, while in endcap, the  $x$  orientation for odd gaps and  $y$  orientation for even gaps are read out.

## MUC Simulation

The GDML technology is applied in the MUC simulation and software objects are created for each component of the detection system, including their materials, shapes, positions, sizes, etc. At the lowest level, bakelite and gas objects are used to form an RPC. A set of strip objects form a read-out plane. Objects of RPCs, read-out planes

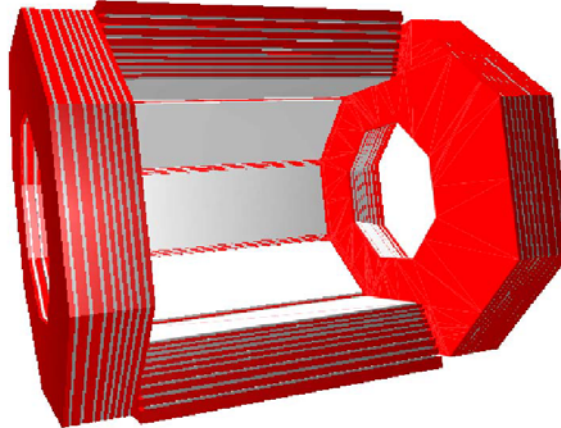


Figure 2.8: The BESIII Muon Identifier

and aluminium boxes form a muon counter module. Iron slabs and modules are finally installed in the proper position to build the muon identifier. The MUC digitization is rather simple, an algorithm is developed to select fired strips based on the distances from the tracks to strips. The detection efficiency can be set for each pad based on test results; actual values will be assigned when data are available. Noise is simulated by a Poisson distribution with a noise level determined from measurements made during the chamber construction. Again, actual values will be assigned when detector is in operation.

## MUC Reconstruction

The MUC reconstruction algorithm starts with two searches that collect hits (fired strips) in the two orientations. The two collections are then combined to form track candidates and matched with tracks reconstructed in the MDC. For low momentum muons, it may happen that too few layers in muon counters are fired. A subsequent search for tracks that looks through the remaining hits, using MDC tracks as seeds, is performed.

For each muon track candidate, a number of parameters are calculated for muon/hadron identification, such as the depth of the track in the muon identifier, the maximum number of hits among layers the track penetrates, the match between the MUC stand-alone track and the MDC track, the  $\chi^2$  of the MUC stand-alone track, etc. These parameters, together with the track momentum and exit angle from the MDC, are used as input to an Artificial Neural Network for muon/hadron analysis. Figure 2.9 shows the performance of current muon identifier from simulated single muons and pions in the momentum range between 0.5 and 1.9 GeV/c. In general, we are able to reject pions to a level of  $\sim 4\%$  while keep 90% of real muons.

## MUC Calibration

The MUC Calibration is developed within the BOSS framework. The main task is to study RPC detection efficiencies as a function of area. In addition, the cluster size and noise level are also studied. Results are stored in a database for use by reconstruction algorithms.

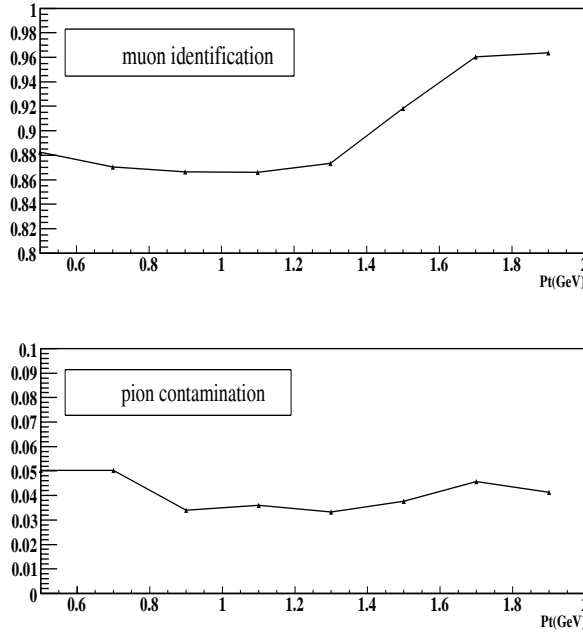


Figure 2.9: Muon/pion identification as a function of the transverse momentum

## 2.7 Trigger

The trigger system is required to select interesting physics events with a high efficiency and suppress backgrounds to a level that the data acquisition (DAQ) system can sustain. The maximum throughput of the *BES-III* DAQ system is designed to be 4000Hz, hence the trigger system should be able to reduce various backgrounds and Bhabha events to a level less than 2000 Hz while maintaining a high efficiency for signal events, which have a rate as high as 2000 Hz at the  $J/\psi$  peak.

A two-level scheme has been adopted for the *BES-III* trigger system: a level-1 hardware trigger with a level-2 software event filter. Signals from different sub-detectors are split into two, one for digitization and storage in the pipeline of the front-end electronics (FEE), and the other for the level-1 hardware trigger. Signals from sub-detectors are received and processed by the appropriate electronics modules in VME crates to yield basic trigger primitives such as the number of short and long tracks in the drift chamber, the number of fired scintillator bars in TOF, the number of clusters and their topology in the electromagnetic calorimeter, etc. Information from these primitives are assembled by the global trigger logic (GTL), which generates an L1 strobe when the trigger condition is satisfied.

Trigger conditions are pre-determined based on Monte Carlo simulations and will be adjusted based on the actual beam background conditions. Table 2.1 shows the trigger efficiencies for various signal and backgrounds based on Monte Carlo simulations using the current trigger table.

Clearly, the efficiencies for most signals with topologies containing multiple charged tracks and photons are satisfactory, even at very low momentum. The rejection power for beam backgrounds, which is estimated to have a maximum level of 40 MHz, is about

Events	Number of events simulated	Efficiency(%)
$J/\psi \rightarrow e^+e^-$	50,000	100.0
$J/\psi \rightarrow \mu^+\mu^-$	50,000	99.9
$J/\psi \rightarrow \text{Anything}$	10,000	97.7
$\psi' \rightarrow \text{Anything}$	10,000	99.5
$\psi'' \rightarrow DD \text{ Anything}$	10,000	99.9
$J/\psi \rightarrow \omega\eta \rightarrow 5\gamma$	10,000	97.9
$J/\psi \rightarrow \gamma\eta \rightarrow 3\gamma$	10,000	92.8
$J/\psi \rightarrow K^+K^-\pi^0$	10,000	97.4
$J/\psi \rightarrow \pi^0 p\bar{p}$	10,000	97.9
$J/\psi \rightarrow p\bar{p}$	10,000	95.8
Beam backgrounds	1,000,000	0.005
cosmic-ray backgrounds	100,000	9.4

Table 2.1: Estimated trigger efficiencies for different types of events.

$5 \times 10^{-5}$ , resulting in a background trigger rate of below 2000 Hz, even for extreme conditions. The trigger rate for cosmic-ray backgrounds is about 90 Hz.



# Chapter 3

## Analysis Tools

### 3.1 Monte Carlo Generators<sup>1</sup>

#### 3.1.1 Introduction

Precision measurements will be a central theme and challenge for the *BES-III* physics research program, and these will require high precision Monte Carlo (MC) generators.

High quality and precise MC simulations will be essential for minimizing experimental systematic uncertainties. They are used to determine detection efficiencies and to model backgrounds. Thus, the MC generators must simulate the underlying processes being studied as precisely as possible. Recently, high-precision generators (*e.g.* KKMC, Bhlumi etc.) based on Yennie-Frautchi-Suura exponentiation have been developed for the QED processes  $e^+e^- \rightarrow ff$  ( $f$  : fermion). The official “precision tags” of these generators are at the order of 1% or less. Generators that incorporate dynamical information into hadron decays have also been developed, most notably EvtGen, which was produced by the BaBar and CLEO collaborations to model  $B$  meson decays. These developments provide us with the luxury of being able to choose which among the existing generators is most suitable for simulating physics processes in the tau-charm threshold region.

However, most of these generators were originally intended for energies above the tau-charm threshold region. In general, MC generators are process- and model-dependent. Only a few MC generators cover the full energy scale of high energy physics experiments. So, at tau-charm threshold energies, the migration of the MC generators that were originally developed for higher energy scales requires careful tuning of parameters and further comparisons with data. In addition, the comprehensive generation of exclusive charmonium decays requires that more models are included in the EvtGen framework.

In this section, we present a general description of the *BES-III* generator framework, and give brief introductions to the *BES-III* event generators, such as KKMC, BesEvtGen, various QED generators, and some inclusive generators. For details, the reader is directed to the generator guides and/or related publications.

---

<sup>1</sup>By Rong-Gang Ping

### 3.1.2 Generator framework

The default generator framework for *BES-III* uses **KKMC** + **BesEvtGen** to generate charmonium decays. Charmonium production via  $e^+e^-$  annihilation is illustrated in Fig. 3.1. The incoming positrons and electrons can radiate real photons via initial state radiation (ISR) before they annihilate into a virtual photon. Corrections for these radiative processes are crucial in  $e^+e^-$  annihilation experiments, especially for measurements performed near a resonance or a production threshold (see chapter 5). In order to achieve precise results, generators for  $e^+e^-$  collision must carefully take ISR into account. The KKMC generator is used to simulate  $c\bar{c}$  production via  $e^+e^-$  annihilation with the inclusion of ISR effects with high precision; it also includes the effects of the beam energy spread. The subsequent charmonium meson decays are generated with BesEvtGen.

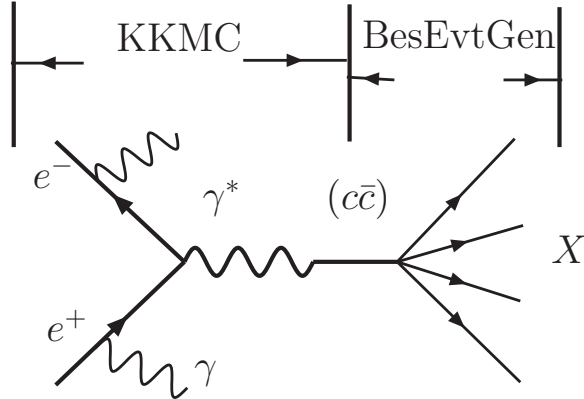


Figure 3.1: Illustration of *BES-III* generator framework.

It should be noted that the events are generated in the centre-mass-system (cms) of the  $e^+e^-$  beam. However, the  $e^+e^-$  beams at BEPCII are not aligned exactly back to back; there is a crossing angle between the two beam of about 22 mrad. Thus, the produced charmonium state is not at rest and instead moves along the  $x$ -direction with a small momentum. As a result, the generated events have to be boosted to the laboratory system before proceeding through the detector simulation. This boost is implemented outside of the generator framework.

### 3.1.3 *BES-III* Generators

Early generators used at *BES-III* were those used for BESII, which includes about 30 generators. These are now obsolete and we do not recommend their use.<sup>2</sup> In what follows, we focus on the generators currently used in the *BES-III* generator framework.

#### KKMC

KKMC [8] is an event generator for the precise implementation of the Electroweak Standard Model formulae for the processes  $e^+e^- \rightarrow f\bar{f} + n\gamma$  ( $f = \mu, \tau, d, u, s, c, b$ )

<sup>2</sup>Currently, the truth tables of these generators are not available in the simulation

at centre-of-mass energies from the  $\tau^+\tau^-$  threshold up to 1 TeV. KKMC was originally designed for LEP, SLC, and is also suitable for future Linear Colliders,  $b$ ,  $c$ ,  $\tau$ - factories etc.

The most important features of KKMC are: the implementation of ISR-FSR<sup>3</sup> interference; second-order subleading corrections; and the exact matrix element for two hard photons. Effects due to photon emission from initial beams and outgoing fermions are calculated in QED up to second order, including all interference effects, within the Coherent Exclusive Exponentiation (CEEX) scheme that is based on Yennie-Frautschi-Suura exponentiation. Electroweak corrections are included at first order with higher-order extensions using the DIZET 6.21 library. Final-state quarks hadronize according to the parton shower model using PYTHIA. Decays of the  $\tau$  lepton are simulated using the TAUOLA library, which takes spin polarization effects into account. The code and information on the program are available at the KKMC web page [9].

In the *BES-III* generator framework, KKMC is used to generate charmonium states with the inclusion of ISR effects and the beam energy spread. The resonances supported by KKMC include the  $J/\psi$ ,  $\psi(2S)$ ,  $\psi(3770)$ ,  $\psi(4030)$ ,  $\psi(4160)$ ,  $\psi(4415)$  and secondary resonances, such as the  $\rho$ ,  $\rho'$ ,  $\rho''$ ,  $\omega$ ,  $\omega'$ ,  $\phi$  and  $\phi'$ . Although KKMC supports the simulation of the decay of these particles, the models in BesEvtGen are more powerful; FSR effects can be included at the BesEvtGen level by means of the PHOTOS package.

## BesEvtGen

BesEvtGen [7] is a generator for tau-charm physics that has been developed from EvtGen,<sup>4</sup> which was originally designed to study  $B$  physics. EvtGen has a powerful interface that allows for the generation of events for a given decay using a model that is easily created by the user; it also provides access to other generators, such as PYTHIA and PHOTOS.

The EvtGen interface uses dynamical information to generate a sequential decay chain through an accept-reject algorithm, which is based on the amplitude probability combined with forward and/or backward spin-density matrix information. The EvtGen interface is designed to have the functionality to automatically calculate these spin-density matrices. As an illustration of how the event selection algorithm works, we consider the sequential decay  $J/\psi \rightarrow \rho^0\pi^0$ ,  $\rho^0 \rightarrow \pi^+\pi^-$  and  $\pi^0 \rightarrow \gamma\gamma$ .

The first chain of the decay is selected based on the probability

$$P_\psi = \sum_{\lambda_\psi, \lambda_\rho} |M_{\lambda_\psi, \lambda_\rho}^{J/\psi \rightarrow \rho^0\pi^0}|^2, \quad (3.1)$$

where  $M$  stands for the amplitude for  $J/\psi \rightarrow \rho^0\pi^0$  with the helicity indexes  $\lambda_\psi$  and  $\lambda_\rho$ . After decaying the  $J/\psi$ , one has the forward spin-density matrix

$$\mathcal{D}_{\lambda_\rho, \lambda'_\rho}^{\rho^0} = \sum_{\lambda_\psi} M_{\lambda_\psi, \lambda_\rho}^{J/\psi \rightarrow \rho^0\pi^0} [M_{\lambda_\psi, \lambda'_\rho}^{J/\psi \rightarrow \rho^0\pi^0}]^*. \quad (3.2)$$

---

<sup>3</sup>FSR stands for final state radiation.

<sup>4</sup>The version is V00-11-07

### 3. Analysis Tools

To generate the  $\rho^0 \rightarrow \pi^+ \pi^-$  decay, proceed as with the  $J/\psi$ , including also  $\mathcal{D}_{\lambda_\rho, \lambda'_\rho}^{\rho^0}$

$$P_\rho = \frac{1}{\text{Tr} \mathcal{D}^{\rho^0}} \sum_{\lambda_\rho, \lambda'_\rho} \mathcal{D}_{\lambda_\rho, \lambda'_\rho}^{\rho^0} A_{\lambda_\rho}^{\rho^0 \rightarrow \pi^+ \pi^-} [A_{\lambda'_\rho}^{\rho^0 \rightarrow \pi^+ \pi^-}]^*. \quad (3.3)$$

To decay the  $\pi^0$  with the full correlations between all kinematic variables in the decay, the EvtGen interface automatically calculates the backward spin-density matrix by

$$\tilde{\mathcal{D}}_{\lambda_\rho, \lambda'_\rho}^{\rho^0} = A_{\lambda_\rho}^{\rho^0 \rightarrow \pi^+ \pi^-} [A_{\lambda'_\rho}^{\rho^0 \rightarrow \pi^+ \pi^-}]^*, \quad (3.4)$$

then the spin-density matrix for the  $\pi^0$  is

$$\mathcal{D}^{\pi^0} = \sum_{\lambda_\psi, \lambda_\rho, \lambda'_\rho} \tilde{\mathcal{D}}_{\lambda_\rho, \lambda'_\rho}^{\rho^0} M_{\lambda_\psi, \lambda_\rho}^{J/\psi \rightarrow \rho^0 \pi^0} [M_{\lambda_\psi, \lambda'_\rho}^{J/\psi \rightarrow \rho^0 \pi^0}]^*, \quad (3.5)$$

which is a constant for a spin-0 particle. Thus the  $\pi^0$  decay is selected by the probability

$$P_{\pi^0} = \frac{1}{\text{Tr} \mathcal{D}^{\pi^0}} \sum_{\lambda_1, \lambda_2} \mathcal{D}^{\pi^0} A_{\lambda_1, \lambda_2}^{\pi^0 \rightarrow \gamma\gamma} [A_{\lambda_1, \lambda_2}^{\pi^0 \rightarrow \gamma\gamma}]^* = \sum_{\lambda_1, \lambda_2} A_{\lambda_1, \lambda_2}^{\pi^0 \rightarrow \gamma\gamma} [A_{\lambda_1, \lambda_2}^{\pi^0 \rightarrow \gamma\gamma}]^*. \quad (3.6)$$

BesEvtGen incorporates baryons up to spin=3/2, and has about 30 models for simulating exclusive decays. The amplitudes for these models are constructed using the helicity amplitude method, and constrained by imposing parity conservation. One of the most powerful models is DIY, which can generate any decays using user-provided amplitudes. Other useful models are those that generate decays using the histogram distributions, such as MassH1, MassH2 and Body3.<sup>5</sup> BesEvtGen provides access to the PYTHIA and Lund-charm inclusive generators that can be used, for example, to generate unknown decays of a given resonance.

## QED generators

- Bhlumi and Bhwide

The generators Bhlumi [10] and Bhwide [11] are used to generate the Bhabha scattering process  $e^+ e^- \rightarrow e^+ e^- + n\gamma$ . These are full energy scale generators even though they were originally designed for the high energy LEP1/SLC and LEP2 colliders. The Bhlumi generator is suitable for generating low angle Bhabha events ( $\theta < 6^\circ$ ), while the Bhwide generator is intended for wide angle Bhabha events ( $\theta > 6^\circ$ ). Here “suitable” means that when these generators work within their suitable region, they will achieve the tagged precision level; outside of that region their precision will be poorer. The precision of Bhlumi is quoted as 0.11% at the LEP1 energy scale and 0.25% for LEP2 experiments. These estimates are based on comparison with other MC calculations [10]. The precision of the Bhwide is quoted as 0.3% at the  $Z$  boson peak and 1.5% at LEP2 energies.

Bhlumi is a multiphoton Monte Carlo event generator for low angle ( $\theta < 6^\circ$ ) Bhabha events that provides four-momentum vectors of the outgoing electron, positron and

<sup>5</sup>These correspond to generating events according to a 1-D diagram, a Dalitz plot or the generation of 3-body decays according to a Dalitz plot plus two angular distribution plots.

photons. The first  $\mathcal{O}(\alpha^1)_{YFS}$  version is described in Ref. [12]. The matrix elements are based on Yennie-Frautschi-Suura (YFS) exponentiation. They include exact first-order photonic corrections and leading-log corrections at second order. The other higher-order and subleading contributions are included in an approximate form.

Bhwid is a wide angle ( $\theta > 6^\circ$ ) generator for Bhabha scattering. The theoretical formulation is based on  $\mathcal{O}(\alpha)$  YFS exponentiation, with  $\mathcal{O}(\alpha)$  virtual corrections from Ref. [13]. The YFS exponentiation is realized via Monte Carlo methods based on a Bhlumi-type Monte-Carlo algorithm, but with some important extensions: (1) QED interference between the electron and positron lines are reintroduced as they are important for large angle Bhabha scattering; (2) the full YFS form factor for the  $2 \rightarrow 2$  process, including all  $s-$ ,  $t-$  and  $u-$ channels is implemented; (3) the exact  $\mathcal{O}(\alpha)$  matrix element for the full Bhabha process is included.

Users of these generators are required to specify the centre-mass-system energy, as well as other cuts on the electrons, hard photons and soft photons in their job option file. Precisions are not given by authors for tau-charm energies, but they are the most precise generators we have for Bhabha processes.

- Babayaga [14] is a Monte Carlo event generator for  $e^+e^- \rightarrow e^+e^-$ ,  $\mu^+\mu^-$ ,  $\gamma\gamma$  and  $\pi^+\pi^-$  processes for energies below 12 GeV. It has a high-precision QED calculation of the Bhabha process and is intended for precise luminosity determinations for  $e^+e^-R$  measurements in the hadronic resonance region. The calculation is based on the matching of exact next-to-leading order corrections with a parton shower algorithm. The accuracy of the approach is demonstrated by a comparison with existing independent calculations and through a detailed analysis of the main components of theoretical uncertainty, including two-loop corrections, hadronic vacuum polarization and light pair contributions. The theoretical accuracy of Babayaga is quoted as 0.1% [15]. The current version of BABAYAGA used at *BES-III* is V3.5 [15].

To use the Babayaga generator, the user is required to specify the cms energy of the  $e^+e^-$  system, together with the cuts on the electron, positron and photons.

## Inclusive generators

The PYTHIA programs are commonly used inclusive event generators for high-energy  $e^+e^-$ ,  $pp$  and  $ep$  collisions. Historically, the family of event generators from the Lund group started with JETSET in 1978; the PYTHIA program followed a few years later. The version currently available is PYTHIA 6.4. The code and further information can be found on the Pythia web page [16].

The Lundcharm model was especially adjusted by BESII for simulating  $J/\psi$  and  $\psi(2S)$  inclusive decays.  $C-$  and  $G-$ parity constraints were imposed and comparisons with experimental data were performed [17]. As a result, *BES-III* officially decided to use this modified Lundcharm model to generate  $J/\psi$  and  $\psi(2S)$  inclusive decays in the BesEvtGen framework.

An advantage of generating inclusive MC events with Lundcharm running in the EvtGen framework is that the decay widths in the Lundcharm model can be controlled by the user. Thus, branching fractions and models for known decays can be specified in

the EvtGen decay dictionary, while unknown decays are generated with the Lundcharm model. When the Lundcharm model is called, a complete decay chain is generated, but only the first step of the  $J/\psi$  or  $\psi(2S)$  decay is read out and returned to the EvtGen interface. This interface has the functionality to check whether that particular decay is included among the EvtGen exclusive decay models. Only decays not included in the exclusive decay models are allowed to proceed; the decays of subsequent daughter particles proceed via EvtGen Models.

EvtGen also allows access to the PYTHIA model to generate the QED inclusive decays with the model "PYCONT". At tau-charm energies, the area law of the Lundcharm model should be implemented to constrain the decays, however this has not yet been done in BesEvtGen.

### 3.1.4 Summary and outlook

We present a general description on the generator framework and the event generators currently used at *BES-III*, which include KKMC, BesEvtGen, Blumi, Bhwide, Babayaga and inclusive generators. A cosmic ray generator, CORSIKA [18], is being migrated. Though some event generators for QED processes, such as  $e^+e^- \rightarrow \mu^+\mu^-$  and  $\tau^+\tau^-$  in KKMC, and  $e^+e^- \rightarrow \gamma\gamma$ ,  $\mu^+\mu^-$  and  $\pi^+\pi^-$  in Babayaga, are available, they still don't satisfy the *BES-III* requirements for hadronic cross-section measurements. The migration of other generators is necessary, for example, MCGPJ ( $\pi^+\pi^-$ ,  $K^+K^-$  and  $K_S^0K_L^0$  are available) and PHOKHARA ( $\pi^+\pi^-$ ,  $\pi^+\pi^-\pi^0$ ,  $\pi^+\pi^-\pi^+\pi^-$ ,  $K^+K^-$ ,  $K_S^0K_L^0$ ,  $p\bar{p}$ ,  $n\bar{n}$  and  $\Lambda\bar{\Lambda}$  are available) with precision levels of  $(0.1 \sim 0.2)\%$ .

## 3.2 Luminosity Measurements at *BES-III*<sup>6</sup>

### 3.2.1 Introduction

With the large data samples that will be collected at *BES-III* — typically a few  $\text{fb}^{-1}$  — unprecedented statistical precision will be achieved in the analyses of many channels. Thus, non-statistical factors and effects will be the limiting factors on the precision of many experimental results. Foremost among these limiting factors will be the luminosity, which will be an input to many precision measurements, including the  $\tau$  mass measurement,  $R$ -values,  $J/\psi$ ,  $\psi'$  and  $\psi''$  total widths etc. For these quantities, the luminosity error will directly translate into errors on their measured values. Thus, precision luminosity measurements are a very important aspect of the *BES-III* physics program.

In  $e^+e^-$  colliding beam experiments, generic physics analyses commonly require the precise knowledge of the relative luminosity accumulated on and off a resonance peak so backgrounds from continuum production can be reliably subtracted. Some analyses make internal consistency checks by dividing the full dataset into independent subsets of comparable size. Here again there will be strong reliance on the accuracy and stability of the relative luminosity measurements. In addition, events used to calculate the luminosity, such as  $e^+e^-$ ,  $\mu^+\mu^-$  and  $\gamma\gamma$ , are interesting in their own right because of their salient topologies that make them useful for online performance monitoring.

---

<sup>6</sup>By X. H. Mo, C. D. Fu, K. L. He

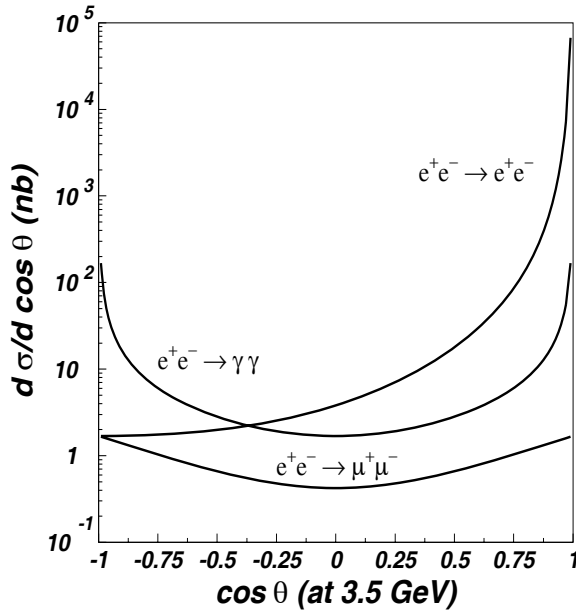


Figure 3.2: Differential cross sections for the QED processes:  $e^+e^- \rightarrow e^+e^-$ ,  $e^+e^- \rightarrow \mu^+\mu^-$ , and  $e^+e^- \rightarrow \gamma\gamma$ . The center-of-mass energy is 3.5 GeV.

In principle, any known process can be used to measure luminosity. However, in order to obtain precise results, one usually selects a process that has a characteristic experimental topology and a cross section that can be precisely calculated. The QED processes  $e^+e^- \rightarrow e^+e^-$ ,  $e^+e^- \rightarrow \mu^+\mu^-$ , and  $e^+e^- \rightarrow \gamma\gamma$  satisfy these criteria and are commonly used for luminosity measurements. Their differential cross sections, shown in Fig. 3.2, have the forms:

$$\begin{aligned} \left. \frac{d\sigma}{d\Omega} \right|_{e^+e^- \rightarrow e^+e^-} &= \frac{\alpha^2}{4s} \left( \frac{3 + \cos^2 \theta}{1 - \cos \theta} \right)^2, \\ \left. \frac{d\sigma}{d\Omega} \right|_{e^+e^- \rightarrow \mu^+\mu^-} &= \frac{\alpha^2}{4s} (1 + \cos^2 \theta), \\ \left. \frac{d\sigma}{d\Omega} \right|_{e^+e^- \rightarrow \gamma\gamma} &= \frac{\alpha^2}{4s} \left( \frac{1 + \cos^2 \theta}{(E_b/p)^2 - \cos^2 \theta} \right)^2. \end{aligned}$$

The experimental response of the detector to each of these reactions is quite distinct: their detection efficiencies rely on charged particle tracking ( $e^+e^-$  and  $\mu^+\mu^-$ ), calorimetry ( $e^+e^-$  and  $\gamma\gamma$ ), muon identification ( $\mu^+\mu^-$ ), and trigger algorithms. The expected theoretical cross sections are calculable in QED; at BEPCII energies weak interaction effects are negligible. The primary theoretical obstacle in all cases is the computation of electromagnetic radiative corrections in a way that accommodates the experimental event selection criteria with adequate precision. This is usually accomplished by Monte Carlo event generators that include diagrams with a varying number of virtual and real radiative photons. In general, the more accurate the theoretical calculation the smaller the uncertainty on the luminosity measurement.

Other factors that cannot be neglected are interference effects in the vicinity of resonance peaks. Such effects not only distort the cross sections in the peak regions but can

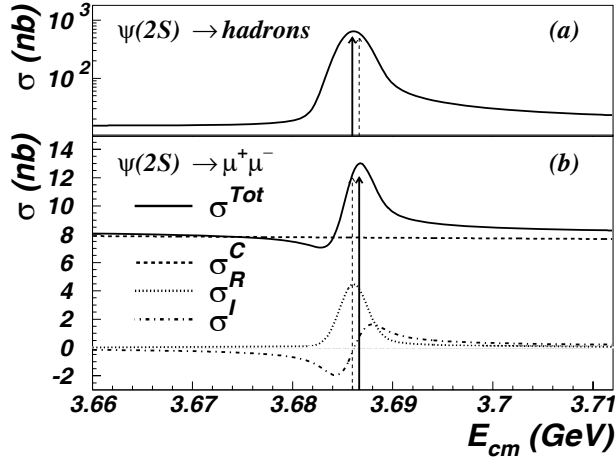


Figure 3.3: Cross sections in the vicinity of  $\psi(2S)$  for (a) inclusive hadrons and (b)  $\mu^+\mu^-$  final states. The solid line and arrow indicates the observed peak position and the dashed line and arrow the actual position of the resonance peak. In (b), the dashed line indicates the QED continuum ( $\sigma^C$ ), the dotted line the resonance ( $\sigma^R$ ), the dash-dotted line the interference ( $\sigma^I$ ), and solid line the total cross section ( $\sigma^{Tot}$ ).

also shift the resonance peak position, as the example shown in Fig. 3.3 demonstrates. Resonance-continuum cross section ratios for the  $J/\psi$ ,  $\psi'$ , and  $\psi''$  regions are listed in Table 3.1. From the table we can see that in the continuum region all three of the QED processes listed above can be used to determine the luminosity, while only  $\gamma\gamma$  and  $e^+e^-$  can be used for the  $\psi'$ , and only  $\gamma\gamma$  is suitable for the  $J/\psi$ , if high accuracy is not to be compromised.

Table 3.1: Resonance-continuum cross section ratios in the  $J/\psi$ ,  $\psi'$ , and  $\psi''$  peak regions.

Res./Con.	$J/\psi$	$\psi'$	$\psi''$
$\mu^+\mu^-$	15.3	0.625	$< 1.28 \times 10^{-5}$
$e^+e^-$	0.700	0.027	$6.0 \times 10^{-5}$
$\gamma\gamma$	$< 6 \times 10^{-3}$	$< 5.8 \times 10^{-3}$	$< 5.8 \times 10^{-3}$

### 3.2.2 Event selection and Algorithm

A detailed Monte Carlo simulation has been performed to develop the event selection criteria listed in Table 3.2. This is preliminary and is used as an example to study systematic errors and identify what further studies are needed.

### 3.2.3 Systematic uncertainty

Typical luminosity measurements at BESI and BESII are summarized in Table 3.3, where the uncertainties are around 2-3%. Comparative results from other experiments are collected in Table 3.4. To achieve the goal of the *BES-III* experiment to have better than

Table 3.2: Selection criteria for  $e^+e^-$ ,  $\gamma\gamma$ , and  $\mu^+\mu^-$  final states.

Description	$e^+e^-$	$\gamma\gamma$	$\mu^+\mu^-$
# neutral tracks		$\geq 2$	
# charged tracks	$\geq 2$ ( $< n$ , $n$ decided by detector state)	$\leq 1$	$=2$
$ \cos\theta $	$< 0.8$	$< 0.8$	$< 0.8$
Track momentum	$> 0.5E_b$		$(0.5\text{-}1.15)E_b$
Track acollinearity	$< 10^\circ$		$< 10^\circ$
$\cos\theta_1 \times \cos\theta_2 \dagger$	$< 0.02$	$< 0.001$	$< 0$
Shower Energy	$(0.5\text{-}1.1)E_b$	$> 0.5E_b$	$(0.1\text{-}0.35)$ GeV
Shower acoplanarity	$> 8^\circ$	$< 2^\circ$	$> 5^\circ$
Vertex & TOF			$ t1 - t2  < 3$ ns

$\dagger$  :  $\cos\theta_1$  and  $\cos\theta_2$  are the  $\cos\theta$  values of the two tracks with the largest momentum; the selection on their product is equivalent to a back-to-back requirement.

1% precision, effects such as backgrounds, trigger efficiency, errors in the MC simulation, data-taking stability and radiative corrections must be considered. Since *BES-III* has not yet started to take data, our systematic study is based on BESII and CLEOc experience as well as *BES-III* simulations.

Table 3.3: Luminosity measurement uncertainties using  $e^+e^-$  final states at BESI and BE-SII. The online luminosity is measured at small angles while offline luminosity is measured with large angle Bhabha events in the Barrel Shower Counter.

Energy region	$J/\psi$	$\psi'$	$\psi''$	$R$ -value
Method	online	offline	offline	offline
Uncertainty	6%	3.2%	1.83%	< 3%
Reference	[19]	[19]	[21]	[22]

Table 3.4: Luminosity errors from other experiments

Exp. Group	$E_{c.m.}$	Mode	Error	Ref.
CLEO	10 GeV	$e^+e^-$ , $\mu^+\mu^-$ , $\gamma\gamma$	1.0%	[23]
DAΦNE	1-3 GeV	$e^+e^-$	0.6%	[24]

## Background analysis

Cosmic-rays usually dominate the background in the  $\mu$ -pair sample. Tight track quality requirements minimize this contamination with almost no loss in efficiency. The remaining cosmic ray background can be estimated with two independent variables, impact parameter, *i.e.*, the distance of closest approach to the beam-axis in the plane transverse to the beam, and time-of-flight. At CLEOc the background estimates determined

by these techniques are  $(0.5 \pm 0.1)\%$  and  $(0.6 \pm 0.1)\%$ , respectively [23]. According to a KORALB [25] Monte Carlo study, background from  $\tau$ -pair decays is 0.07%, and from  $e^+e^-\mu^+\mu^-$  events [26] is  $< 0.002\%$ .

The background in the photon-pair event sample from Bhabha events where both charged tracks are missed is estimated to be  $(0.1 \pm 0.1)\%$  [26]. For Bhabha events,  $\tau$ -pairs contribute 0.03%,  $e^+e^-e^+e^-$  final states yield  $(0.05 \pm 0.05)\%$  [27], and cosmic-rays are estimated to be  $(0.1 \pm 0.1)\%$ . The backgrounds estimated by CLEOc are at the 0.1% level for all three background sources; this is also what is expected at *BES-III*.

### Trigger efficiency

A two-level filtering technique is applied in the *BES-III* data acquisition system. The first level is the hardware trigger. The second level is a software trigger with special algorithms developed to select physics events of different types [28].

Table 3.5: Trigger Efficiencies of *BES-III* at  $\sqrt{s}/2 = 1.89$  GeV.

Event type	$e^+e^-$	$\mu^+\mu^-$	$\gamma\gamma$
Condition	charge3	charge1,2&3	common,neutralA&B
Level-1	$(99.95 \pm 0.02)\%$	$(92.2 \pm 0.3)\%$	$(99.78 \pm 0.06)\%$
Level-2	$(99.999 \pm 0.001)\%$	$(98.79 \pm 0.06)\%$	$(99.5 \pm 0.3)\%$
Combined	$(99.95 \pm 0.03)\%$	$(91.1 \pm 0.4)\%$	$(98.9 \pm 0.4)\%$

The hardware trigger efficiencies are obtained using a method similar to that of BESII [29, 30] and the online software trigger efficiencies are given in Ref. [28]. The combined results are summarized in Table 3.5. A conservative estimate of the uncertainty due to the trigger efficiency is taken as 0.5% for all three processes.

### Monte Carlo simulation

The uncertainty due to Monte Carlo simulation can be analyzed by comparing the data distributions with those from MC simulation. Many different methods have been proposed to qualify the difference [23, 24]. We consider the method used in Ref. [24] to be reasonable and will adopt it for use in *BES-III*.

### Stability

Since the detector environment will change during the running period, the measured luminosity may not be stable, even after calibration. This was checked by CLEO, BES and DAΦNE and no obvious influence on the luminosity measurement was observed. Hence, no error is assigned for this for now.

### Theoretical accuracy

The theoretical accuracy is actually constrained by the accuracy of the ISR calculation. In the CLEOc analysis, radiative photons are generated above some photon energy cutoff  $k_0 = E_\gamma/E_b$ , and all diagrams with softer photons are subsumed into the two body final

state. Two generators were used for  $e^+e^-$  and  $\mu^+\mu^-$  scattering, and one for  $\gamma\gamma$  events. The BKee program [31] generates  $e^+e^-$  final states with zero or one radiative photon, yielding a cross section that is accurate to the order of  $\alpha^3$ . Higher-order corrections are available in the Bhlumi program [33], which uses Yennie-Frautschi-Suura exponentiation to generate multiple photons per event and yields a cross section with an accuracy to the order of  $\alpha^4 \ln^2(|t|/m_e^2)$ , where  $t$  is the typical momentum-transfer. Similar to BKee, the BK $\gamma\gamma$  [34] and BKJ [35] Monte Carlo programs generate events with up to one radiative photon and yields an order- $\alpha^3$  cross section for  $\gamma\gamma$  and  $\mu$ -pair respectively. Up to three radiative photons in  $\mu^+\mu^-$  events are possible (two from initial state radiation and one from final state radiation) with FPAIR [36], which has an order- $\alpha^4$  cross section accuracy. A photon cutoff of  $k_0 = 0.01$  is used for BKee, BK $\gamma\gamma$ , and BKJ, and  $k_0 = 0.001$  for Bhlumi and FPAIR. The generators used in the CLEOc analysis and the predicted cross sections at  $E_b = 5.29$  GeV are listed in Table 3.6.

Table 3.6: Generators for  $e^+e^-$ ,  $\gamma\gamma$ , and  $\mu^+\mu^-$  final states.

Item	$e^+e^-$	$\gamma\gamma$	$\mu^+\mu^-$
CLEOc: cross section at $E_b=5.29$ GeV			
$\alpha^3$ generator	BKee	BK $\gamma\gamma$	BKJ
cross section (nb)	$8.45 \pm 0.02$	$1.124 \pm 0.002$	$0.429 \pm 0.001$
$\alpha^4$ generator	BHLUMI		FPAIR
cross section (nb)	$8.34 \pm 0.02$	—	$0.427 \pm 0.001$
BESII: suitable for any energy region			
$\alpha^3$ generator	Radee	Radgg	Radmu
<i>BES-III</i> : suitable for any energy region			
$\alpha^4$ generator	KKMC, Babayaga		
DAΦNE: test at $1 \text{ GeV} < \sqrt{s} < 3 \text{ GeV}$			
$\alpha^3$ generator	Bhagenf $\sigma_{\text{eff}}(1.0195 \text{ GeV}) = (430.7 \pm 0.3) \text{ nb}$	Mcgpj	
$\alpha^4$ generator	Bhwide Babayaga $\sigma_{\text{eff}}(1.0195 \text{ GeV}) = (431.0 \pm 0.3) \text{ nb}$		

Another check to ensure the correctness of theoretical calculations is to compare the results from different generators. At DAΦNE, the event generators Babayaga [37, 38] and Bhagenf [39], both developed for large angle Bhabha scatterings and based on the cross section calculation in Ref. [31], have been evaluated, as well as their systematic uncertainties. The cross sections calculated with the two generators, including the event reconstruction efficiency, are listed in Table 3.6.

The error given in the cross section is mainly due to the Monte Carlo statistics. The theoretical uncertainty claimed by the authors is 0.5% in both cases. The radiative corrections due to the treatment of initial and final state radiation in Bhagenf and Babayaga have been compared with two other event generators: Bhwide [11] developed for LEP and Mcgpj [41] developed for VEPP-2M, which are all based on the cross section calculated

in Ref. [42]. In Ref. [43] a detailed comparison has been performed and the agreement is within 0.5%, supporting the claims from the authors of the **Bhagenc** and **Babayaga** generators.

At BESII, generators with cross section accuracy up to order- $\alpha^3$  are used. At *BES-III*, a generic Monte Carlo generator KKMC [32] has been adopted; this can provide cross sections with an accuracy up to order- $\alpha^4$ . Further checks, such as the shape of the photon energy spectrum, can be made when data are available.

### 3.2.4 Summary

Table 3.7 summarizes the errors in the luminosity measurement at CLEO [23] and estimated errors for *BES-III*. Improvements at *BES-III* includes:

- Statistics : the 0.2% statistical uncertainty corresponds to 250,000 Monte Carlo events: 1,000,000 events will accommodate a statistical uncertainty at the level of 0.1%, which can be easily realized at *BES-III*;
- Backgrounds : The same level of background as seen at CLEO, namely 0.1%, is expected at *BES-III*;
- Trigger efficiency : as discussed in Sect. 3.2.3, this uncertainty can be conservatively taken to be 0.5%;
- consistency between data and Monte Carlo: 1.0 % ;
- radiative corrections : 0.5%.

Table 3.7: Relative Error (%) in luminosity for CLEO and *BES-III*.

Exp. Group	CLEO			BES			
	Source	$e^+e^-$	$\gamma\gamma$	$\mu^+\mu^-$	$e^+e^-$	$\gamma\gamma$	$\mu^+\mu^-$
Monte Carlo Statistic		0. 2	0. 2	0. 2	0. 1	0. 1	0. 1
Backgrounds		0. 1	0. 1	0. 1	0. 1	0. 1	0. 1
Trigger Efficiency		0. 5	0. 1	1. 3	0. 5	0. 5	0. 5
Detector Modeling		1. 1	0. 9	1. 4	1. 0	1. 0	1. 0
Radiative Corrections		1. 3	1. 3	1. 0	0. 5	0. 5	0. 5
Summed in Quadrature		1. 8	1. 6	2. 2	1. 3	1. 3	1. 3
combine		1.1%			0.8%		

## 3.3 Particle Identification<sup>7</sup>

### 3.3.1 Introduction

Particle identification (PID) will play an essential role in most *BES-III* physics analyses [1]. Good  $\mu/\pi$  separation is required for precision  $f_D/f_{D_s}$  measurements. Excellent

<sup>7</sup>K. L. He, J. F. Hu, B. Huang, G. Qin, S. S. Sun, Y. H. Zheng

electron identification will help to improve the accuracy of the CKM elements  $|V_{cs}|$  and  $|V_{cd}|$ . The identification of hadronic ( $\pi/K/p$ ) particles will be a commonly used tool in *BES-III* physics analysis, and often the most crucial item to be considered.

Each part of the *BES-III* detector executes its specific functions and provides information that can be used to determine the particle identity. The PID capabilities are quite different for each sub-detector and for each different momentum range. To improve the PID performance, a powerful technique is required to combine the available information in the most optimal way, especially when some of the inputs are highly correlated. In recent years, various PID algorithms, such as the likelihood method [44], the Fisher discriminator [45], the H-Matrix estimator [46], artificial neural networks [47], and the boosted decision tree [48], have been developed. Most of the PID requirements in the *BES-III* physics program involve high quality  $e/\pi$ ,  $\mu/\pi$  and  $\pi/K$  separation.

### 3.3.2 The PID system of *BES-III*

The *BES-III* detector [1] consists of a main drift chamber (MDC), Time-Of-Flight (TOF) counters, a CsI(Tl) crystal calorimeter, and a muon identifier. All of them contribute to particle identification.

#### The $dE/dx$ measurements

The main drift chamber (MDC) consists of 43 layers of sensitive wires and operates with a 60%/40% He/C<sub>3</sub>H<sub>8</sub> gas mixture. The expected momentum resolution  $\sigma_p/p$  is about 0.5% at 1 GeV/c. The energy loss in the drift chamber provides valuable information for particle identification. The normalized pulse height, which is proportional to the energy loss of incident particles in the drift chamber, is a function of  $\beta\gamma = p/m$ , where  $p$  and  $m$  are the momentum and mass of a charged particle. Figure 3.4(a) shows the normalized pulse height variation with momentum for different particle species. From the figure, it is evident that electrons, muons and pions with momenta around 0.2 GeV/c cannot be well separated by  $dE/dx$  pulse height measurements. Similarly, the  $dE/dx$  pulse heights will not discriminate electrons from kaons in the 0.5–0.6 GeV/c momentum range.

There are a number of factors that can effect the  $dE/dx$  performance [52]: the number of hits, the average path lengths in a cell, space charge and saturation effects, electric field non-uniformities etc. After calibration, the  $dE/dx$  measurement resolution is expected to be between 6% and 7%. Using  $dE/dx$  information,  $3\sigma$   $K/\pi$  separation can be achieved for momentum below 0.6 GeV/c; good  $e/\pi$  separation can be obtained for all momenta above 0.4 GeV/c.

#### The TOF counter

Radially outside of the MDC is the TOF system, which is specialized for particle identification. It consists of a two-layer barrel array and one layer endcap array. There are two readout PMTs on each barrel scintillator and one on each endcap scintillator. The expected time resolution for the two layers combined is between 100 and 110 ps for  $K$ 's and  $\pi$ 's, providing  $2\sigma$   $K/\pi$  separation up to 0.9 GeV/c.

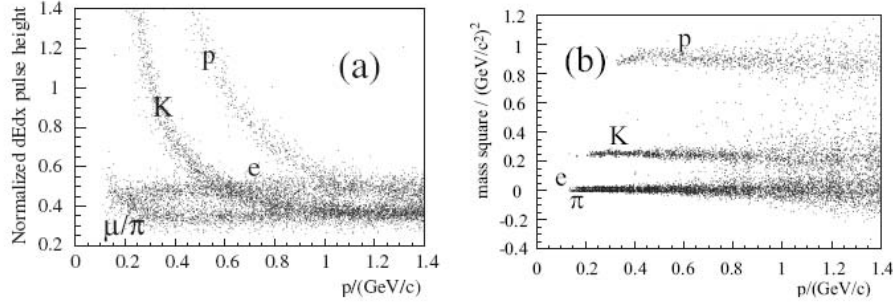


Figure 3.4: (a) The normalized pulse heights ( $dE/dx$ ) vs. momentum of charged particles; (b) The mass square distribution from TOF measurements.

The TOF system measures the flight time of charged particle. The velocity ( $\beta c$ ) and mass ( $m$ ) of the charged particle can be calculated from

$$\beta = \frac{L}{c \times t_{\text{mea}}}, \quad m^2 = p^2 \times \frac{1 - \beta^2}{\beta^2}, \quad (3.7)$$

where  $t_{\text{mea}}$  is the measured time-of-flight,  $L$  and  $p$  are the corresponding flight path and momentum of the charged particle given by MDC measurements, and  $c$  is the velocity of light in vacuum. The typical mass square distributions for electrons, pions, kaons and protons in different momentum ranges are shown in Figure 3.4(b).

The PID capability relies on good time resolution ( $\sigma_t$ ) of the TOF system.  $\sigma_t$  depends on the pulse height, hit position, and the beam status. Usually the value of  $\sigma_t$  varies for different TOF counters due to different performance of the scintillator, PMT, and electronics. Since the TOF measurements are correlated due to the common event start time, the weighted time-of-flight for two layers is obtained by a correlation analysis discussed below and in Ref. [53].

### The CsI(Tl) Calorimeter

The CsI(Tl) crystal electromagnetic calorimeter (EMC) contains 6240 crystals, and is used to measure the energy of photons precisely. The energy and spatial resolutions are 2.5% and 0.6 cm at 1 GeV, respectively. The characteristics of an electromagnetic shower is distinctive for the electron, muon and hadron, thus the energy deposited and the shape of the shower in the calorimeter can be used as discrimination variables for PID.

The energy deposited by minimum ionizing charged particles passing at normal incidence through the EMC crystals without interacting is about 0.165 GeV. Electrons and positrons lose all of their energies in the calorimeter by producing electromagnetic showers, the ratio of deposited energy to the track momentum ( $E/p$ ) will be approximately unity. Sometimes the energy deposited by hadrons will have an  $E/p$  ratio higher than that of the expected by ionization due to the nuclear interactions in the CsI material. Figure 3.5(a) shows the energy deposited *versus* momentum for  $e$ ,  $\mu$  and  $\pi$  in the EMC.

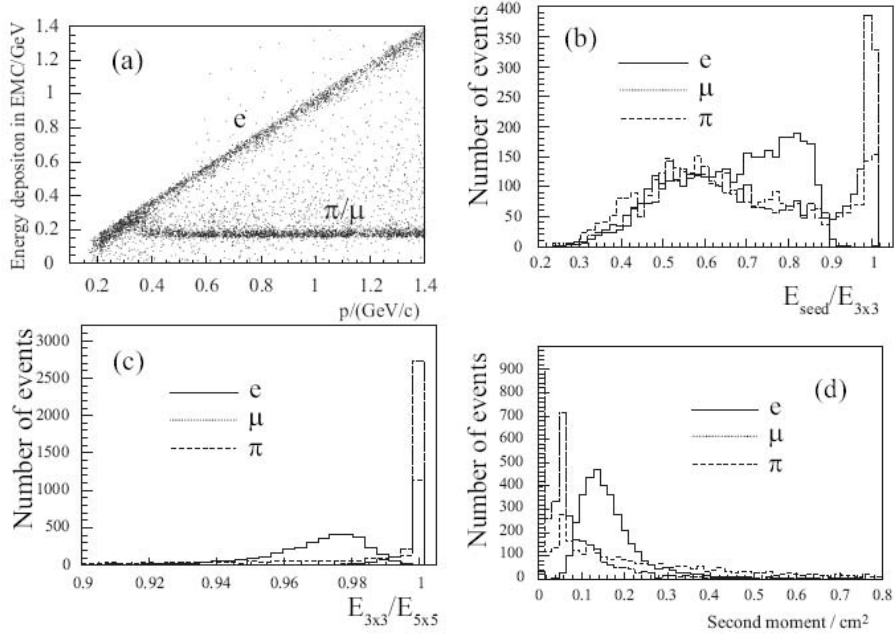


Figure 3.5: (a) Energy deposit in the EMC vs. the momentum for  $e$ ,  $\mu$  and  $\pi$ ; (b) ratio of  $E_{\text{seed}}/E_{3\times 3}$  for  $e$ ,  $\mu$  and  $\pi$ ; (c) ratio of  $E_{3\times 3}/E_{5\times 5}$  for  $e$ ,  $\mu$  and  $\pi$ ; (d) second-moment distributions for  $e$ ,  $\mu$  and  $\pi$ .

The “shape” of the shower can be characterized by the three energies:  $E_{\text{seed}}$ , the energy deposited in the central crystal;  $E_{3\times 3}$ , the energy deposited in the central  $3 \times 3$  crystal array; and  $E_{5\times 5}$ , the energy deposited in the central  $5 \times 5$  crystal array. The ratios of  $E_{\text{seed}}/E_{3\times 3}$  and  $E_{3\times 3}/E_{5\times 5}$  for  $e$ ,  $\mu$  and  $\pi$  at  $1 \text{ GeV}/c$  are plotted in Figures. 3.5(b) and 3.5(c), respectively.

The second-moment  $S$  is defined as

$$S = \frac{\sum_i E_i \cdot d_i^2}{\sum_i E_i}, \quad (3.8)$$

where  $E_i$  is the energy deposited in the  $i^{\text{th}}$  crystal, and  $d_i$  is the distance between the  $i^{\text{th}}$  crystal and the center position of reconstructed shower. The original idea of  $S$  was developed by the Crystal Ball experiment [54] to distinguish clusters generated by  $\pi^0$ 's and  $\gamma$ 's. The  $S$  distributions for  $e$ ,  $\mu$  and  $\pi$  at  $1 \text{ GeV}/c$  are shown in Figure 3.5(d).

### The muon system

The magnet return yoke has nine layers of Resistive Plate Chambers (RPC) in the barrel and eight layers in the endcap to form a muon identifier. The spatial resolution is about 16.6 mm.

An electron's energy is exhausted in the calorimeter and cannot reach the muon counter. On the other hand most of the hadrons pass through the material of calorimeter and magnet coil, and are absorbed somewhere in the iron yoke. Muons have a strong penetrating probability and usually produce one hit in each layer. Hadrons can produce

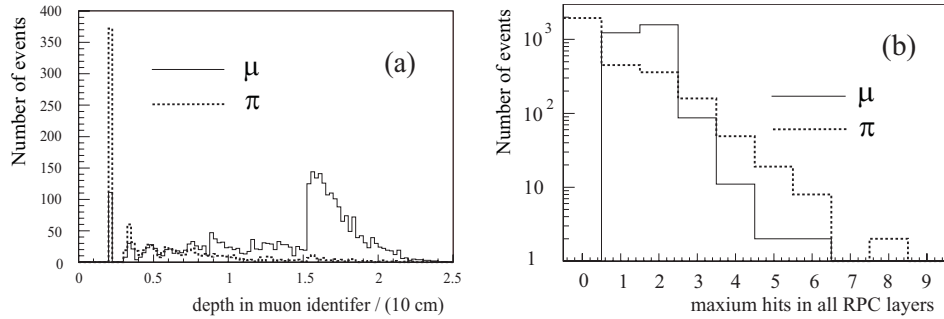


Figure 3.6: (a) The travel depth of  $\mu$  and  $\pi$  in muon counter; (b) The maximum number of hits for  $\mu$  and  $\pi$  in all RPC layers.

many hits in the layer near to where an interaction occurs. The distances between muon hits and the extrapolated positions of an MDC track are used to reduce hadron contamination to a low level, since the hits generated by secondary muons from  $\pi/K$  decay will not match the inner track very well. Figure 3.6 shows the distributions of penetration depth and the maximum number of hits in all RPC layers for  $\mu$ 's and charged  $\pi$ 's with momentum in the range 0.8–1.5 GeV/c.

### 3.3.3 The Likelihood Method

Relative likelihoods (likelihood ratios) provide the most powerful discrimination between particle identification hypotheses, and the statistical significance gives a measure of the consistency between data and the selected hypotheses.

#### Probability Density Functions

The response of a detector to each particle species is given by a probability density function (PDF), which, written as  $\mathcal{P}(x; p, H)$ , describes the probability that a particle of species  $H = e^\pm, \mu^\pm, \pi^\pm, K^\pm, p, \bar{p}$  leaves a signature  $x$  described by a vector of measurements ( $dE/dx$ , TOF,  $e/p$ , ...).  $\mathcal{P}(x; p, H)dx$  is the probability for the detector to respond to a track of momentum  $p$  and type  $H$  with a measurement in the range  $(x, x+dx)$ . As with any PDF, the integral over all possible values is unity,  $\int \mathcal{P}(x; p, H)dx = 1$ . Note that the momentum is treated as part of the hypothesis for the PDF and therefore is placed to the right of semicolon. Drift chamber momentum measurements are usually of sufficient precision that they can be treated as a given quantity. In borderline cases when the precision is marginally sufficient, the PDF is sometimes smeared by the assumption that the momentum is perfectly measured.

The vector  $x$  may describe a single measurement in one detector, several measurements in one detector, or several measurements in several detectors. The measurements may be correlated for a single hypothesis. An example of correlated measurements within a single device is  $E/p$  and the shower shape of electrons in the EMC. An example of correlated measurements in different detectors is the energy deposited in the EMC and the muon chambers by charged pions. In many cases the correlations are reasonably small and the overall PDF can be determined as a product of the PDFs for individual detectors.

For example, the specific ionization deposited by a charged track as it traverses the drift chamber has almost no influence on time-of-flight measurements in the TOF.

The challenge of PID analysis is to determine the PDFs and their correlations (if any) as well as to understand the uncertainties of these distributions.

## Likelihood

Given the relevant PDFs, the likelihood that a track with measurement vector  $x$  is a particle of species  $H$  is denoted by  $\mathcal{L}(H; p, x)$ . Although the functional forms of the PDFs and the corresponding likelihood function are identical, the difference between  $\mathcal{L}(H; p, x)$  and  $\mathcal{P}(x; p, H)$  is subtle: probability is a function of the measurable quantities ( $x$ ) for a fixed hypothesis ( $p, H$ ); likelihood is a function of particle type ( $H$ ) for a fixed momentum  $p$  and the measured value ( $x$ ). Therefore, an observed track for which  $x$  has been measured has a likelihood for each particle type. Competing particle type hypotheses should be compared using the ratio of their likelihoods. Other variables having a one-to-one mapping onto the likelihood ratio are equivalent. Two commonly used mappings of the likelihood ratios are the difference of log-likelihoods and a normalized likelihood ratio, sometimes called the likelihood fraction. For example, to distinguish between the  $K^+$  and  $\pi^+$  hypotheses for a track with measurements  $x_{\text{obs}}$ , these three quantities would be written as:

$$\mathcal{L}(K^+; p_{\text{obs}}, x_{\text{obs}}) / \mathcal{L}(\pi^+; p_{\text{obs}}, x_{\text{obs}}) \quad (3.9)$$

$$\log(\mathcal{L}(K^+; p_{\text{obs}}, x_{\text{obs}})) - \log(\mathcal{L}(\pi^+; p_{\text{obs}}, x_{\text{obs}})) \quad (3.10)$$

$$\frac{\mathcal{L}(K^+; p_{\text{obs}}, x_{\text{obs}})}{\mathcal{L}(K^+; p_{\text{obs}}, x_{\text{obs}}) + \mathcal{L}(\pi^+; p_{\text{obs}}, x_{\text{obs}})} \quad (3.11)$$

It can be shown rigorously that the likelihood ratio (Eq. (3.9) and its equivalents Eq. (3.10) and Eq. (3.11)) discriminate between hypotheses most powerfully. For any particular cut on the likelihood ratio, there exists no other set of cuts or selection procedure that gives a higher signal efficiency for the same background rejection.

There has been an implicit assumption made so far that there is perfect knowledge of the PDF describing the detector. In the real world, there are often tails on distributions due to track confusion, nonlinearities in detector response, and many other experimental sources that are imperfectly described by the PDFs. While deviations from the expected distribution can be determined from control samples of real data, the tails of these distributions are often associated with fake or badly reconstructed tracks. That is why additional consistency tests should be made.

## Weighted Likelihood

In the case (such as particle identification) that the *a priori* probabilities of competing hypotheses are known numbers,  $\mathcal{P}_{\mathcal{A}}(H)$ , likelihood can be used to calculate the expected purities of given selection criteria. Consider the case of  $K/\pi$  separation, the fraction of kaons in a sample with measurement vector  $x$  is given by

$$\mathcal{F}(K; x) = \frac{\mathcal{L}(K; x) \cdot \mathcal{P}_{\mathcal{A}}(K)}{\mathcal{L}(\pi; x) \cdot \mathcal{P}_{\mathcal{A}}(\pi) + \mathcal{L}(K; x) \cdot \mathcal{P}_{\mathcal{A}}(K)}. \quad (3.12)$$

This can be considered as a weighted likelihood ratio where the weighting factors are *a priori* probabilities. The  $\mathcal{F}(K; x)$  are also called *posteriori* probabilities, relative probabilities, or conditional probabilities, and their calculation according to Eq. (3.12) is an application of Bayes' theorem. The purity, *i.e.*, the fraction of kaons in a sample selected with, say,  $\mathcal{F}(K; x) > 0.9$ , is determined by calculating the number of kaons observed in the relevant range of values of  $\mathcal{F}$  and normalizing to the total number of tracks observed there, *e.g.*,

$$\text{fraction}(\mathcal{F}_H > 0.9) = \frac{\int_{0.9}^1 \frac{dN}{d\mathcal{F}(H;x)} \mathcal{F}(H;x) d\mathcal{F}(H;x)}{\int_{0.9}^1 \frac{dN}{d\mathcal{F}(H;x)} d\mathcal{F}(H;x)}, \quad (3.13)$$

where the integration variable is the value of  $\mathcal{F}(H; x)$ .

### An example of TOF and $dE/dx$ PID

At *BES-III*, TOF and  $dE/dx$  are most essential for hadron separation. In the TOF detector, the time-of-flight  $t$  is measured with a Gaussian resolution  $\sigma_t$  that is assumed to be a constant ( $\sim 100$  ps). Similarly, the energy loss in the drift chamber ( $dE/dx$ ) also has a Gaussian distribution with a resolution of  $\sigma_E \sim 6.5\%$ . If all incident particles are known to be either pions, kaons and protons at some fixed momentum, then the distributions of  $t$  and  $dE/dx$  will consist of the superposition of three Gaussian distributions, centered at the central values of  $(t_\pi, t_K, t_p)$  and  $((dE/dx)_\pi, (dE/dx)_K, (dE/dx)_p)$  for pions, kaons and protons. The PDF for the pion hypothesis is the normalized probability function

$$\begin{aligned} \mathcal{P}(t; \pi) &= \frac{1}{\sqrt{2\pi}\sigma_t} \exp \left[ -\frac{1}{2} \left( \frac{t - t_\pi}{\sigma_t} \right)^2 \right] \\ \mathcal{P}(dE/dx; \pi) &= \frac{1}{\sqrt{2\pi}\sigma_E} \exp \left[ -\frac{1}{2} \left( \frac{dE/dx - (dE/dx)_\pi}{\sigma_E} \right)^2 \right]. \end{aligned} \quad (3.14)$$

The PDFs for the kaon and proton hypotheses have similar forms. Using the observed time of flight  $t$  and  $dE/dx$  information, the likelihoods for pion, kaon and proton can be constructed from

$$\begin{aligned} \mathcal{L}(\pi) &= \mathcal{L}(\pi; t, dE/dx) = \mathcal{P}(t; \pi) \cdot \mathcal{P}(dE/dx; \pi), \\ \mathcal{L}(K) &= \mathcal{L}(K; t, dE/dx) = \mathcal{P}(t; K) \cdot \mathcal{P}(dE/dx; K), \\ \mathcal{L}(p) &= \mathcal{L}(p; t, dE/dx) = \mathcal{P}(t; p) \cdot \mathcal{P}(dE/dx; p). \end{aligned} \quad (3.15)$$

We consider  $K/\pi$  separation in a sample that consists of 80% pions and 20% kaons. Using the observed time of flight  $t$  and energy loss in the drift chamber, it is possible to calculate the relative probabilities of pions and kaons for these measured  $t$  and  $dE/dx$  values:

$$\begin{aligned} \mathcal{F}(\pi) &= \frac{\mathcal{P}_A(\pi)\mathcal{L}(\pi)}{\mathcal{P}_A(\pi)\mathcal{L}(\pi) + \mathcal{P}_A(K)\mathcal{L}(K)}, \\ \mathcal{F}(K) &= \frac{\mathcal{P}_A(K)\mathcal{L}(K)}{\mathcal{P}_A(\pi)\mathcal{L}(\pi) + \mathcal{P}_A(K)\mathcal{L}(K)}. \end{aligned} \quad (3.16)$$

By construction,  $\mathcal{F}(\pi) + \mathcal{F}(K) = 1$ . The calculation of relative probabilities are illustrated in Figure 3.7. As shown in Figure 3.7, the  $K/\pi$  separation at 0.6 GeV is better than it is at 1 GeV.

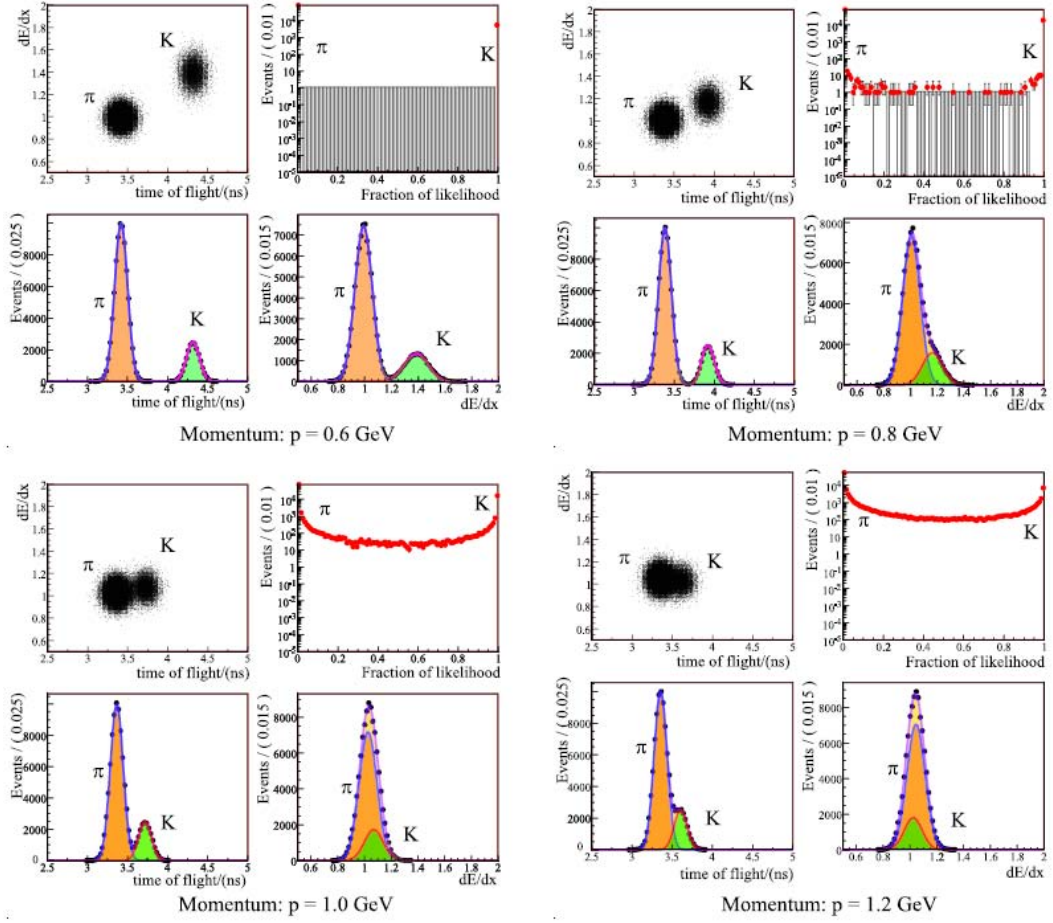


Figure 3.7: The relative likelihood constructed by combining the TOF and  $dE/dx$  information for track momenta of 0.6, 0.8 , 1.0 and 1.2 GeV/c. The time of flight distribution is calculated for a 1.0 m flight distance.

## Cell analysis

In the example presented above no correlations are assumed between the particle identification provided by TOF and that provided by  $dE/dx$ . This is an acceptable approach if the TOF is a purely passive detector and there are no other sources of correlation. An approach that takes into account all correlations explicitly is cell analysis. Basically, you make a multi-dimensional histogram of all relevant variables and compute the fraction of tracks that land in each cell for each hypothesis. You can then use these fractions as the likelihood. The result is optimal with all correlations completely accounted for, if the cells are small enough.

The trouble with this approach is that as the number of variables becomes larger, the number of cells quickly gets out of control. It becomes impossible to find enough “training events” to map out the cell distributions with adequate statistics. Still, it is a viable approach for a small number of variables and is well suited to a problem such as combining  $E/p$  and event shape in calorimeter. This would, in principle, involve three variables:  $E/p$ , shape, and the dip angle, and one might get by with relatively large cells. A judicious choice of cells that uses our knowledge of the underlying physics can greatly reduce the number of cells needed. *e.g.*, the dip angle might be eliminated as a variable if a dip-corrected shape variable could be devised. If groups of highly correlated variables can be treated together, we might be able to construct a set of relatively uncorrelated likelihoods. It may be necessary to combine information from several detectors to construct some of these variables.

### 3.3.4 A correlation analysis of TOF PID

A charged particle passing through the barrel array of scintillators will produce signals in one or two layers of the TOF counter, corresponding to two or four time-of-flight measurements. However, at *BES-III* the problem of averaging more than one TOF measurement is complicated because the different measurements are correlated due to the common event start time. A better choice would be a weighted average of the different measurements.

#### General algorithm

For the covariance matrix elements given by  $(V_t)_{ij} = \langle \delta t_i \delta t_j \rangle$ , where  $\delta t_i = t_i - \bar{t}$ ,  $\bar{t}$  is the average of  $t_i$ , the definition of the standard deviation is

$$\sigma_{\bar{t}}^2 = \sum_{ij} w_i w_j (V_t)_{ij}, \quad (3.17)$$

where  $\bar{t} = \sum_i w_i t_i$  and  $\sum_i w_i = 1$ . Using standard Lagrange multiplier techniques, we obtain:

$$w_i = \frac{\sum_k (V_t^{-1})_{ik}}{\sum_{jk} (V_t^{-1})_{jk}}. \quad (3.18)$$

#### Errors and correlations of TOF measurements

The TOF time resolution ( $\sigma_t$ ) can be factorized into the product  $\sigma_t(Q) \cdot \sigma_t(z)$ , where  $\sigma_t(Q)$  and  $\sigma_t(z)$  are functions of the pulse height  $Q$  and the hit position  $z$  [55]. The

function  $\sigma_t(Q)$  is complicated, and needs further study based on real data. On the other hand, the  $z$ -dependent time resolution  $\sigma_t(z)$  is known and similar for electrons, muons and hadrons [55]. Figure 3.8(a) shows a typical variation of  $\sigma_t(z)$  from one readout unit as a function of  $z$  for Bhabha events. The time resolution becomes poorer when the hit position is far from the readout end.

For a given barrel TOF counter, the  $t_{\text{mea}}$  in the left-end and the right-end readout units can be decomposed as

$$t_1 = t_c + (t_D)_1, \quad t_2 = t_c + (t_D)_2, \quad (3.19)$$

where  $t_1$  and  $t_2$  represent the  $t_{\text{mea}}$ 's in two readout PMTs,  $t_c$  represents the common part of  $t_1$  and  $t_2$  including the common start time, and  $(t_D)_1$  and  $(t_D)_2$  represent the uncorrelated parts of  $t_1$  and  $t_2$ . The covariance matrix for  $t_1$  and  $t_2$  can be expressed as

$$V_t = \begin{pmatrix} \sigma_1^2 & \sigma_c^2 \\ \sigma_c^2 & \sigma_2^2 \end{pmatrix}, \quad (3.20)$$

where  $\sigma_1$  and  $\sigma_2$  are the time resolution in the left-end and the right-end readout units, and  $\sigma_c$  is the uncertainty in  $t_c$ . According to the definition of the covariance matrix, we have the following expressions

$$\begin{aligned} \sigma_1^2 &= \langle \delta t_1 \delta t_1 \rangle = \langle \delta t_c \delta t_c \rangle + \langle \delta(t_D)_1 \delta(t_D)_1 \rangle, \\ \sigma_2^2 &= \langle \delta t_2 \delta t_2 \rangle = \langle \delta t_c \delta t_c \rangle + \langle \delta(t_D)_2 \delta(t_D)_2 \rangle, \\ \sigma_c^2 &= \langle \delta t_1 \delta t_2 \rangle = \langle \delta t_c \delta t_c \rangle, \end{aligned} \quad (3.21)$$

where we have used the fact that the correlations  $\langle \delta t_c \delta(t_D)_1 \rangle = 0$ ,  $\langle \delta t_c \delta(t_D)_2 \rangle = 0$  and  $\langle \delta(t_D)_1 \delta(t_D)_2 \rangle \approx 0$ .

To get  $\sigma_c$  conveniently, we define two new time variables

$$t_+ = \frac{t_1 + t_2}{2}, \quad t_- = \frac{t_1 - t_2}{2}. \quad (3.22)$$

The fluctuations of  $t_+$  and  $t_-$  can be expressed as

$$\begin{aligned} \sigma_+^2 &= \langle \delta t_+ \delta t_+ \rangle = \frac{\sigma_1^2 + \sigma_2^2}{4} + \frac{\sigma_c^2}{2}, \\ \sigma_-^2 &= \langle \delta t_- \delta t_- \rangle = \frac{\sigma_1^2 + \sigma_2^2}{4} - \frac{\sigma_c^2}{2}, \end{aligned} \quad (3.23)$$

where  $\sigma_+$  and  $\sigma_-$  are the time resolution of  $t_+$  and  $t_-$ . The value of  $\sigma_c$  can be directly extracted as  $\sigma_c = \sqrt{\sigma_+^2 - \sigma_-^2}$ . Figure 3.8(b) shows the distributions of  $\sigma_+(z)$ ,  $\sigma_-(z)$  and  $\sigma_c(z)$ , where  $\sigma_c(z)$  is approximately a constant. Substituting the expression of Eq. (3.20) into Eqs. (3.17)–(3.18), we get

$$w_1 = \frac{\sigma_2^2 - \sigma_c^2}{\sigma_1^2 + \sigma_2^2 - 2\sigma_c^2}, \quad w_2 = \frac{\sigma_1^2 - \sigma_c^2}{\sigma_1^2 + \sigma_2^2 - 2\sigma_c^2}, \quad (3.24)$$

and

$$\sigma_{\bar{t}}^2 = \frac{\sigma_1^2 \cdot \sigma_2^2 - \sigma_c^4}{\sigma_1^2 + \sigma_2^2 - 2\sigma_c^2}. \quad (3.25)$$

The resulting  $\sigma_{\bar{t}}$  as a function of  $z$  is shown in Figure 3.8.

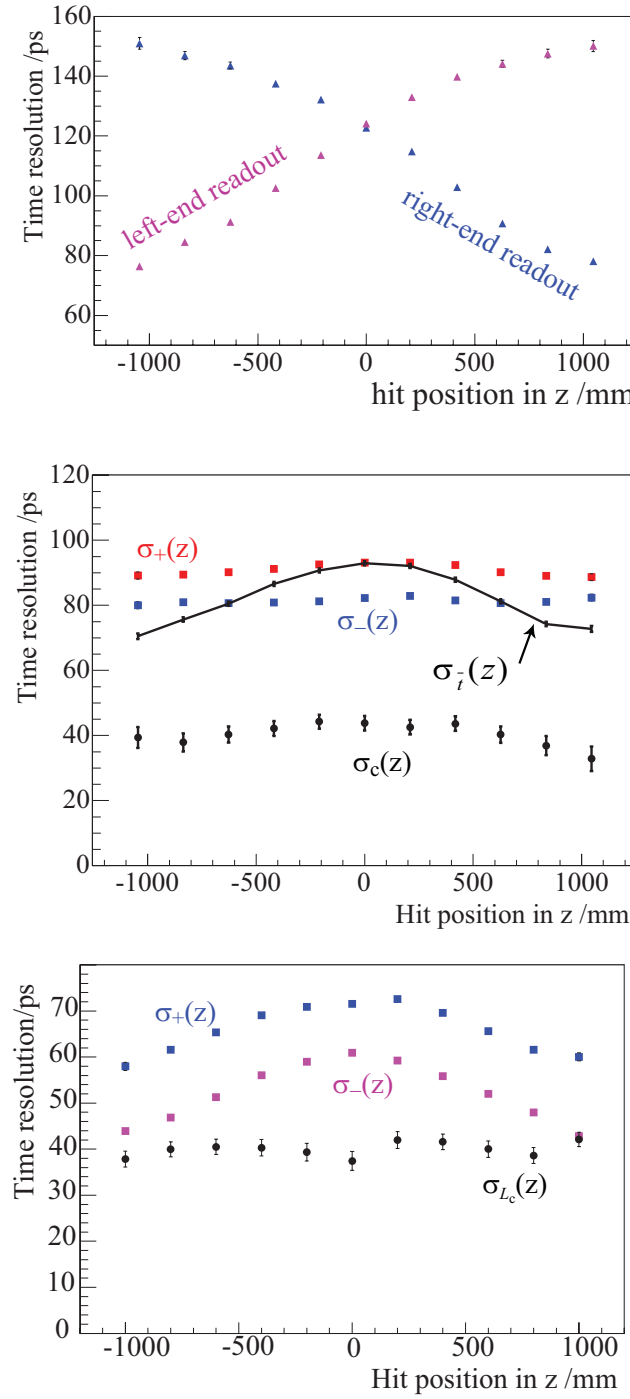


Figure 3.8: (a) The variation of  $\sigma_t(z)$  for the left-end and the right-end readout unit in a barrel TOF counter; (b) Time resolution of  $t_+$ ,  $t_-$ ,  $t_c$  and the weighted time  $\bar{t}$  for a one-layer TOF measurement; (c) The correlations between the two TOF layer measurements, where  $\sigma_{L_c}(z) = \sqrt{\sigma_+^2(z) - \sigma_-^2(z)}$ .

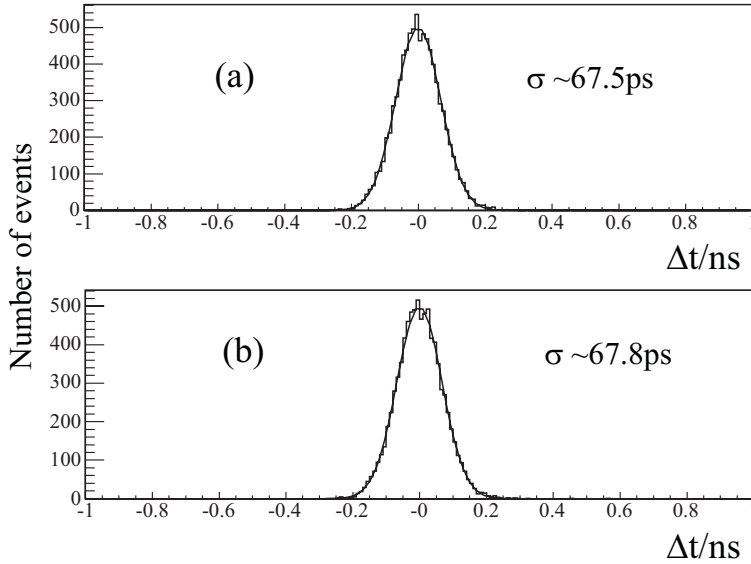


Figure 3.9:  $\Delta t = t_{\text{mea}} - t_{\text{exp}}$  distributions: (a)  $\bar{t}$  is weighted by  $\bar{t}_{L_i}$  ( $i = 1, 2$ ),  $\bar{t}_{L_i}$ 's are the average time in each layer and are weighted by  $t_{E_i}$  ( $i = 1, 2$ ),  $t_{E_i}$ 's are the TOF measurements in each end of readout units; (b)  $\bar{t}$  is directly weighted by  $t_{E_i}$  ( $i = 1, 2, \dots, 4$ ),  $t_{E_i}$ 's are the TOF measurements in the four-end of readout units.

### Combining the time-of-flight from two-layer measurements

Similar to the method adopted for the one-layer measurement, we can construct the covariance matrix for the two-layer measurement case as follows

$$V_t = \begin{pmatrix} \sigma_{L_1}^2 & \sigma_{L_c}^2 \\ \sigma_{L_c}^2 & \sigma_{L_2}^2 \end{pmatrix}, \quad (3.26)$$

where  $\sigma_{L_c}$  is the correlation between two-layer measurements. Substituting  $t_1, t_2$  with  $t_{L1}, t_{L2}$  in Eqs. (3.19) and (3.22), we get the corresponding errors and correlations. The weighted time-of-flight of two-layer measurements is easily obtained by applying the covariance matrix of Eq. (3.26) in Eq. (3.24). The resulting  $t_{\text{mea}} - t_{\text{exp}}$  are shown in Figure 3.9(a).

The apparatus of barrel TOF array can be considered as providing four independent measurements of the time-of-flight for a charged particle. The covariance matrix of TOF measurements can be constructed as

$$V_t = \begin{pmatrix} \sigma_1^2 & \sigma_c^2 & \sigma_c^2 & \sigma_c^2 \\ \sigma_c^2 & \sigma_2^2 & \sigma_c^2 & \sigma_c^2 \\ \sigma_c^2 & \sigma_c^2 & \sigma_3^2 & \sigma_c^2 \\ \sigma_c^2 & \sigma_c^2 & \sigma_c^2 & \sigma_4^2 \end{pmatrix}. \quad (3.27)$$

In Eq. (3.27),  $\sigma_i$  ( $i = 1, 2, \dots, 4$ ) are the resolutions of all readout units, the correlations ( $\sigma_c$ ) between the two-end of readout units in each layer, and the correlation between two-layer measurements are in fact the same. Employing the covariance matrix Eq. (3.27) in Eqs. (3.17)–(3.18), the weight factors  $w_i$  ( $i = 1, 2, \dots, 4$ ) can be easily calculated. The resulting  $t_{\text{mea}} - t_{\text{exp}}$  distribution is shown in Figure 3.9(b).

As shown in Figures 3.9(a) and 3.9(b), the resulting time resolutions from two weighting methods are consistent. The standard weighted method adopted in the TOF calibration/reconstruction software will be in two steps: combining the two-end TOF measurements in each layer; calculating the weighted time from the two-layer measurements.

### 3.3.5 Applying the ANN technique in PID algorithm at *BES-III*

If the variables are not highly correlated, multiplying the likelihood associated with each variable should suffice. If correlations are simple enough, a change of variables or a cell analysis may suffice. If the variables are highly correlated, neural nets and other opaque boxes might construct near-optimal discrimination variables. The PDFs for the resulting variables can be used as the basis for a likelihood analysis. Using the same formalism for neural network outputs as for conventional likelihood analyses allows modular design of analysis software with no loss of information and optimal discrimination between hypotheses.

At present, a class of Multilayer Perceptrons (MLP)[60] neural network has been applied to the *BES-III* PID algorithm and is implemented in ROOT [61]. The PID variables described in Section 3.3.2 and Section 3.3.2 are correlated each other. With no loss of information, a cell analysis may not be sufficient for the likelihood method to get an optimal result. Since the correlations of PID variables among sub-detectors are reasonably small and can be ignored, the neural networks can be configured sequentially.

#### Brief description of the artificial neural network

An artificial neural network [47] is a computational structure inspired by the study of biological neural processing. Feed-forward neural networks, also known as multilayered perceptrons, are most popular and widely used. The output of a feed-forward neural network trained by minimizing, for example, the mean square error function, directly approximates the Bayesian posterior probability without the need to estimate the class-conditional probabilities separately. A feed-forward neural network (NN) is shown schematically in Figure 3.10. Such networks provide a general framework for estimating non-linear functional mapping between a set of input variables  $\mathbf{x}(x_1, x_2, \dots, x_N)$  and an output variable  $O(\mathbf{x})$  (or a set of output variables) without requiring a prior mathematical description of how the output formally depends on the inputs.

The network is made of neurons characterized by a bias and weighted links in between, the links are called synapses. A layer of neurons makes independent computations on the data, and so it receives and passes the results to another layer. The next layer may in turn make its independent computations and pass on the results to yet another layer. Finally, the processed results of the network can be determined from the output neurons. As indicated in the sketch, all neuron inputs to a layer are linear combinations of the neuron output of the previous layer. For a given neuron  $j$  in layer  $k$ , we have the following equation

$$x_j^k = A \left( w_{0j}^k + \sum_{i=1}^{M_{k-1}} w_{ij}^k \cdot x_i^{k-1} \right), \quad (3.28)$$

where  $x_i^{k-1}(i = 1, 2, \dots, M_{k-1})$  represents the input signal from the previous layer  $k - 1$ ,

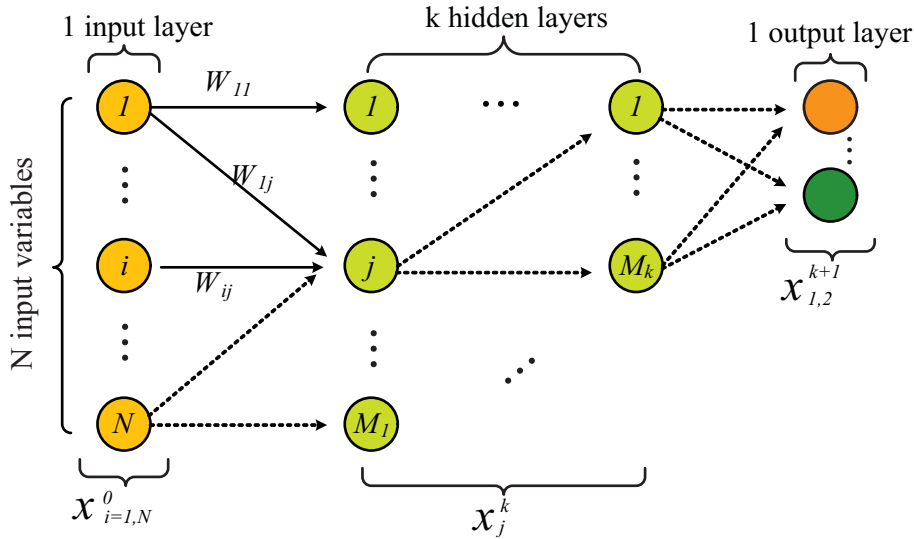


Figure 3.10: The schematic structure of a multilayered perceptrons' neural network: the input layer contains  $N$  neurons as input variables ( $x_{i=1,2,\dots,N}^0$ ); the output layer contains (two) neurons for signal and background event classes; in between the input and output layers are a number of  $k$  hidden layers with arbitrary number of neurons ( $x_{j=1,2,\dots,M_k}^k$ ).

$M_{k-1}$  is the total number of neurons in layer  $k - 1$ ,  $w_{ij}^k$ 's represent the synaptic weights of neuron  $j$ , the bias term  $w_{0j}^k$  (not shown in Figure 3.10) is acquired by adding a new synapse to neuron  $j$  whose input is  $x_{0j}^{k-1} = 1$ . The transfer from input to output within a neuron is performed by means of an “activation function”  $A(x)$ . In general, the activation function of a neuron can be zero (deactivated), one (linear), or non-linear. For a hidden layer, a typical activation function used in Eq. (3.28) is a sigmoid

$$A(x) = \frac{1}{1 + e^{-x}}. \quad (3.29)$$

The transfer function of the output layer is usually linear. As a consequence: a neural network without a hidden layer should give identical discrimination power as a linear discriminant analysis like the Fisher discriminator. In case of one hidden layer, the neural network computes a linear combination of sigmoids.

The number of parameters (the synaptic weights  $w_{ij}^k$ 's in Eq. (3.28)) need to grow only as the complexity of the problem grows. The parameters are determined by minimizing an error function, usually the mean square error between the actual output  $O^p$  and the desired (target) output  $t^p$ ,

$$E = \frac{1}{2N_p} \sum_{p=1}^N (O^p - t^p)^2, \quad (3.30)$$

with respect to the parameters. Here  $p$  denotes a feature vector or pattern. The stochastic optimization algorithm used in learning enables the model to be improved a little bit for each data point in the training sample. Neural networks provide a very practical tool because of the relatively small computational times required in their training. Their fast

convergence as well as their robustness in supervised learning of multilayered perceptrons are due to the efficient and powerful algorithms that have been developed in recent years.

### The configuration of PID networks

The PID variables selected from each sub-detector together with the incident momentum and the transverse momentum have been grouped and trained separately, each sub-detector (the barrel part and the endcap part) has one output. In this step, the neural network for each sub-detector is quite simple. Almost all sub-networks are configured with one hidden layer containing  $2N$  hidden neurons, where  $N$  is the number of the input neurons. A total of 50,000 single track events for each particle species with momentum ranging from 0.1 GeV/c to 1.6 GeV/c and  $-0.83 < \cos \theta < 0.83$  are trained for this neural network, where  $\theta$  is the incident polar angle. The output values are constrained to be 1, 2, 3, 4 and 5 for electron, muon, pion, kaon and proton, respectively. The training results for each sub-detector are shown in Figures 3.11(a)–3.11(d).

The muon and pion bands are merged into one single peak (around 2.5) in the  $dE/dx$ , TOF and EMC outputs. The EMC and MUC information is not very applicable for kaon and proton identification; the EMC output does provide some muon- pion discrimination. The MUC output can separate muons from hadrons quite clearly.

The neural network outputs from the sub-detectors can be combined in several ways to get near-optimal discrimination variables. For example, the probability density functions (PDF) for the resulting variables can be used as the basis for a likelihood analysis, or can be used as the input variables for a sequential network. At present, a conventional likelihood analysis based on the neural network output variables and a sequential neural network analysis are applied in parallel to the *BES-III* PID algorithm. The sequential neural networks consists of two input momentum variables and four input PID variables. The momentum variables are the incident momentum and the transverse momentum. The PID variables include the neural outputs from  $dE/dx$  ( $O_{dE/dx}$ ), TOF ( $O_{TOF}$ ), EMC ( $O_{EMC}$ ) and MUC ( $O_{MUC}$ ) system (the barrel part and the endcap part separately). The neural network is configured with one hidden layer of ten hidden neurons. Electron, muon, and hadron separations are studied with several simulated Monte Carlo samples through different configurations of networks. Cuts are put on the output of final discrimination variables (the output of sequential network  $O_{seq}$ ).

### Muon identification

Muon candidates are required to have some response in the  $\mu$ -identifier. The sequential neural network is trained with two PID variables: the  $O_{MUC}$  and the  $O_{EMC}$ . The  $\mu$ -ID abilities are studied in different momentum partitions by comparing the discrimination results from  $O_{MUC}$  and  $O_{seq}$ . Figures 3.12(a) and 3.12(b) show the variations of the muon identification efficiency and pion contamination rate as functions of incident track momentum, where the track momentum is required to be greater than a cut-off threshold ( $\sim 500$  MeV/c). Above 0.8 GeV/c, the muon identification efficiency is around 90%, and the pion contamination rate is about 5%. Additional information from the EMC may help improve the  $\mu$ -ID ability.

As experienced in the BaBar experiment [62], the additional variables, *e.g.*, the goodness of muon track fit and the goodness of the muon track matching to the extrapolation

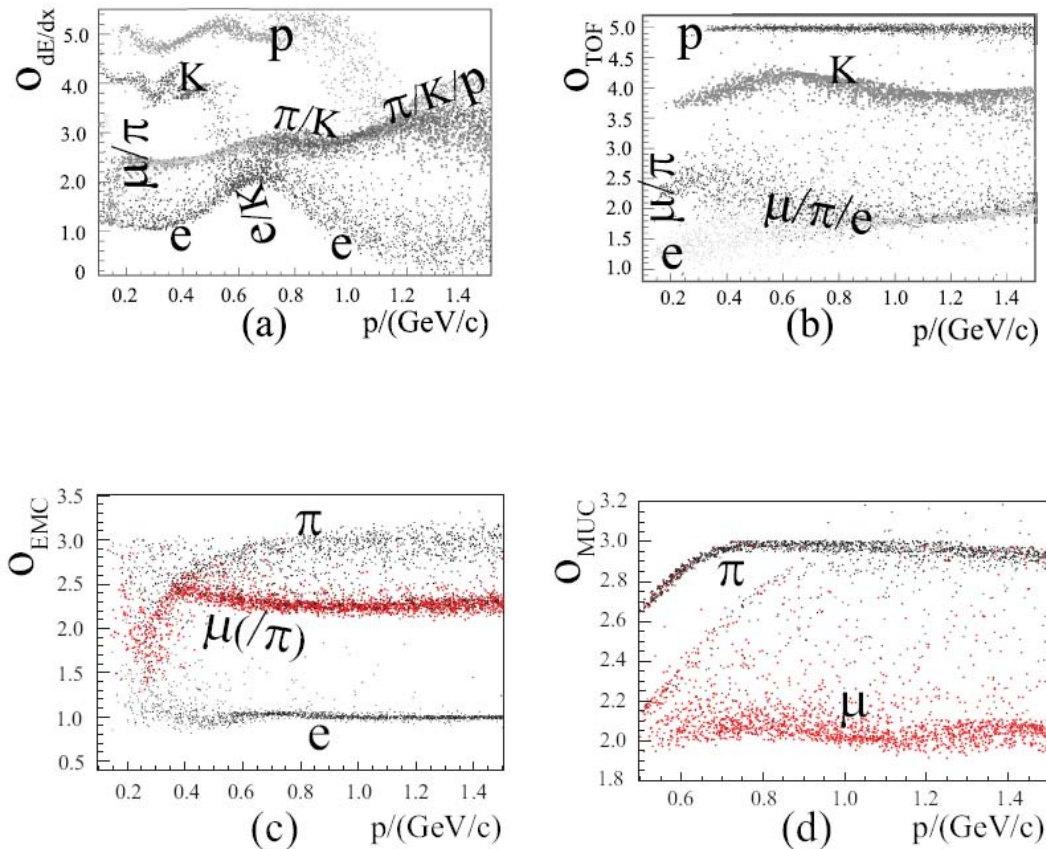


Figure 3.11: NN outputs of sub-detectors. (a)  $dE/dx$  output; (b) TOF output; (c) EMC output; (d) MUC output.

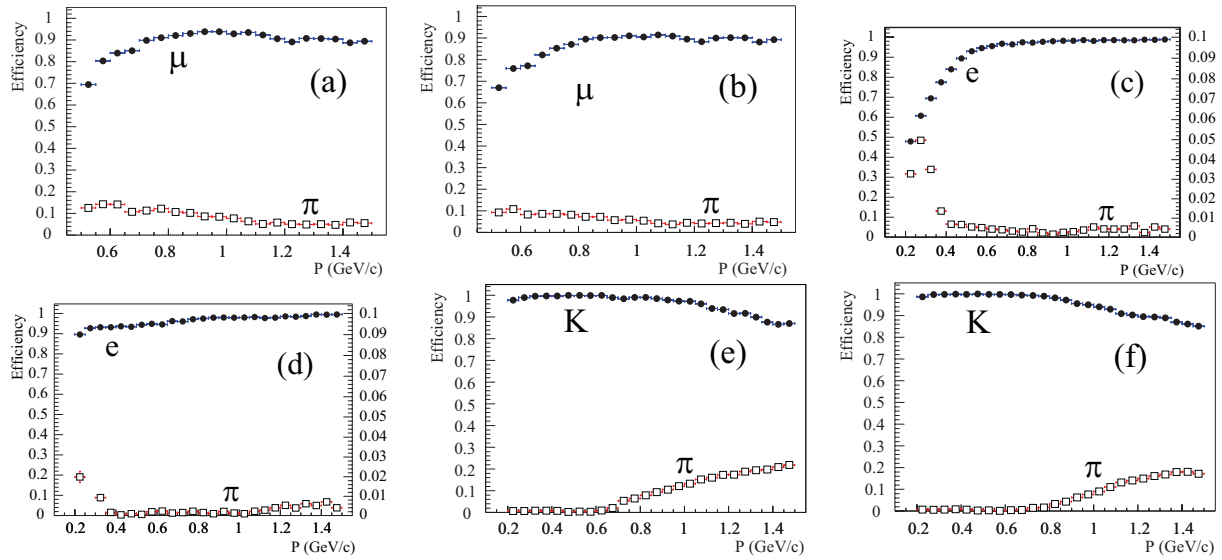


Figure 3.12: PID efficiencies and contamination rates in different momentum partitions. (a)  $\mu/\pi$  separation with  $O_{\text{MUC}}$ ; (b)  $\mu/\pi$  separation with  $O_{\text{MUC}}$  and  $O_{\text{EMC}}$ ; (c)  $e/\pi$  separation with  $O_{\text{EMC}}$ ; (d)  $e/\pi$  separation with  $O_{\text{EMC}}$ ,  $O_{\text{TOF}}$  and  $O_{\text{dE}/\text{dx}}$ ; (e)  $K/\pi$  separation with the likelihood method; (f)  $K/\pi$  separation with neural networks. In (c) and (d), the pion contamination rates are enlarged by a factor of ten.

position from inner track system, may help reduce the background contamination rates. These inputs will be studied at *BES-III* in the future.

### Electron identification

Figure 3.12(c) shows the variations of electron identification efficiency and pion misidentification rate in different momentum intervals as a function of cuts on  $O_{\text{EMC}}$ . Above 0.6  $\text{GeV}/c$ , one can see that the electron-ID efficiency is greater than 95% while the pion contamination rate can be as low as  $\sim 10^{-3}$ . On the other hand, with  $O_{\text{EMC}}$  alone, the  $e/\pi$  separation is quite poor for low momentum tracks (*i.e.* less than 0.4  $\text{GeV}/c$ ).

Both  $O_{\text{dE}/\text{dx}}$  and  $O_{\text{EMC}}$  are good discrimination variables to separate electrons from pions above 0.4  $\text{GeV}/c$ .  $O_{\text{TOF}}$  can separate  $e/\pi$  quite effectively below 0.3  $\text{GeV}/c$ . The neural network trained with  $O_{\text{dE}/\text{dx}}$ ,  $O_{\text{TOF}}$  and  $O_{\text{EMC}}$ , shown in Figure 3.12(d), offers a nearly uniform acceptance and background contamination between 0.25  $\text{GeV}/c$  and 1.6  $\text{GeV}/c$ . It is interesting to note that the acceptance hole between 0.2  $\text{GeV}/c$  and 0.4  $\text{GeV}/c$  almost vanishes after the application of an appropriate cut, even though no detector has clear discrimination power for electrons in this region. The system is obviously making the inference that the particle has to be an electron if it is not one of the others. This is the combined contribution from the sub-detectors.

### $\pi/K$ separation

It is generally believed that proton identification will be extremely good using the TOF and  $dE/dx$  information at *BES-III*. Hence, only the  $K/\pi$  separation is focused on

here. As discussed in Section 3.3.2, the  $dE/dx$  can identify  $K$ 's and  $\pi$ 's very effectively below 0.6 GeV/c; the two-layer TOF can separate  $K/\pi$  up to momenta of 0.9 GeV/c.

Traditionally, a likelihood method that combines the TOF and  $dE/dx$  information is applied to hadron identification. To construct the PDFs, data are divided into several bins in momentum and  $\cos\theta$  partitions to obtain the corresponding resolutions and offsets. Figure 3.12(e) shows the variation of kaon identification efficiency and pion contamination rate as a functions of momentum. In the real world, there are often tails on distributions due to track confusion, nonlinearities in detector response, and other experimental sources that are imperfectly described in the PDFs. In light of this, it is helpful to apply the NN technique to hadron separation.

The network is trained with two PID variables:  $O_{\text{TOF}}$  and  $O_{dE/dx}$ . The PID ability is studied as a function of cuts on the output of the sequential neural network  $O_{\text{seq}}$ . The results are shown in Figure 3.12(f). Both the likelihood method and the neural network method give similar results. Below 1 GeV/c, one can see that the kaon-ID efficiency is greater than 95% while the pion contamination rate is less than 10%. The  $K/\pi$  separation is extremely good for low momentum tracks (*i.e.*, less than 0.8 GeV/c).

### 3.3.6 Future PID algorithms for *BES-III*

The shapes of the PID variables from the EMC and MUC systems are complicated and there may exist non-linear correlations between them. It is difficult for the likelihood method to construct the PDFs analytically and handle these correlations properly. From our studies, good electron-ID and muon-ID can be easily achieved from the neural network at *BES-III* with full detector information. In a simple application, *e.g.*, for hadron separation, we get similar results from the the neural network and the likelihood methods, where the PID variables in TOF and  $dE/dx$  systems are quasi-Gaussian, and the correlation between two-layer TOF measurements is approximately linear. Hence a flexible configuration of PID neural networks is employed for both simple and complicated applications.

There are still a lot of factors that have to be taken into account while applying the artificial neural network techniques to particle identification at *BES-III*. For example, one or several input variables may have to be removed due to the imperfect consistency between data and Monte Carlo simulation. Impurities in the training samples may introduce additional systematical uncertainties. More detailed studies are needed in the future. Now the likelihood and the artificial neural network PID algorithms are being studied in parallel. The final *BES-III* PID algorithm will definitely be a combination of all the methods such as, for example, using the likelihood method to combine the neural network outputs from sub-detectors.

## 3.4 Kinematic Fitting<sup>8</sup>

### 3.4.1 Introduction

Kinematic fitting is a mathematical procedure in which one uses the physical law governing a particle interaction or decay to improve the measurements describing the process. For example, consider the decay chains,  $\psi(3770) \rightarrow D^0 \overline{D^0}$ , where  $\overline{D^0}$  decays to the  $CP$  eigenstate  $K_S^0 \pi^0$  and  $D^0$  decays to the hadronic mode  $K^- \pi^+$ . There are several constraints that can be applied: (1) the  $\pi^+ \pi^-$  pair from  $K_S^0$  decay must come from a common space point ( $2 \times 2 - 3 = 1$  constraint); (2) the momentum vector of  $\pi^+ \pi^-$  pair must be aligned with the position vector of the decay vertex relative to the interaction point ( $3 - 1 = 2$  constraints); (3) the mass of the  $\gamma\gamma$  pair has to be equal to the  $\pi^0$  mass (1 constraint); (4) energy and momentum are conserved in the  $D\overline{D}$  production (4 constraints); and (5) the mass of  $K_S^0 \pi^0$  has to be equal to the mass of  $K^- \pi^+$  (1 constraint). When the tracks are refit with these 9 constraints using the general algorithm discussed in next section, their parameters are forced to satisfy the constraints, thereby improving the mass and momentum resolution of the  $D^0$  and the  $\overline{D^0}$ . These resolution improvements will translate to a larger signal to background ratio and frequently elevate marginal signals to statistical significant results. The importance of kinematic fitting to data analysis is demonstrated by its use in virtually all modern high energy physics experiments.

### 3.4.2 General algorithm

The fitting technique is straightforward and is based on the well known Lagrange multiplier method [63]. It is assumed that the constraint equations can be linearized and summarized in two matrices,  $\mathbf{D}$  and  $\mathbf{d}$ . Let  $\alpha$  represent the parameters for a set of  $n$  tracks. It has the form of a column vector

$$\alpha = \begin{pmatrix} \alpha_1 \\ \alpha_2 \\ \vdots \\ \alpha_n \end{pmatrix}. \quad (3.31)$$

Initially the track parameters have the unconstrained values  $\alpha_0$ , obtained from the reconstruction. The  $r$  constraint functions can be written generally as

$$\mathbf{H}(\alpha) \equiv 0, \quad \text{where } \mathbf{H} = (H_1 \quad H_2 \quad \cdots \quad H_r). \quad (3.32)$$

Expanding (3.32) around a convenient point  $\alpha_A$  yields the linearized equations

$$0 = \frac{\partial H(\alpha_A)}{\partial \alpha}(\alpha - \alpha_A) + H(\alpha_A) = \mathbf{D}\delta\alpha + \mathbf{d}, \quad (3.33)$$

---

<sup>8</sup>By Kanglin He, Beijiang Liu, Min Xu, Xueyao Zhang

where  $\delta\alpha = \alpha - \alpha_A$ . Thus we have

$$\mathbf{D} = \begin{pmatrix} \frac{\partial H_1}{\partial \alpha_1} & \frac{\partial H_1}{\partial \alpha_2} & \dots & \frac{\partial H_1}{\partial \alpha_n} \\ \frac{\partial H_2}{\partial \alpha_1} & \frac{\partial H_2}{\partial \alpha_2} & \dots & \frac{\partial H_2}{\partial \alpha_n} \\ \vdots & \vdots & \ddots & \vdots \\ \frac{\partial H_r}{\partial \alpha_1} & \frac{\partial H_r}{\partial \alpha_2} & \dots & \frac{\partial H_r}{\partial \alpha_n} \end{pmatrix}, \quad \mathbf{d} = \begin{pmatrix} H_1(\alpha_A) \\ H_2(\alpha_A) \\ \vdots \\ H_r(\alpha_A) \end{pmatrix}, \quad (3.34)$$

or  $D_{ij} = \frac{\partial H_i}{\partial \alpha_j}$  and  $d_i = H_i(\alpha_A)$ . The constraints are incorporated using the method of Lagrange multipliers in which the  $\chi^2$  is written as a sum of two term

$$\chi^2 = (\alpha - \alpha_0)^T V_{\alpha_0}^{-1} (\alpha - \alpha_0) + 2\lambda^T (\mathbf{D}\delta\alpha + \mathbf{d}), \quad (3.35)$$

where  $\lambda$  is a vector of  $r$  unknown Lagrange multipliers. Minimizing the  $\chi^2$  with respect to  $\alpha$  and  $\lambda$  yields two vector equations that can be solved for parameters  $\alpha$  and their covariance matrix:

$$\begin{aligned} V_{\alpha_0}^{-1}(\alpha - \alpha_0) + \mathbf{D}^T \lambda &= 0, \\ \mathbf{D}\delta\alpha + \mathbf{d} &= 0. \end{aligned} \quad (3.36)$$

The solution can be written as:

$$\begin{aligned} \alpha &= \alpha_0 - V_{\alpha_0} \mathbf{D}^T \lambda, \\ \lambda &= V_D (\mathbf{D}\delta\alpha_0 + \mathbf{d}), \\ V_\alpha &= V_{\alpha_0} - V_{\alpha_0} \mathbf{D}^T V_D \mathbf{D} V_{\alpha_0}, \end{aligned} \quad (3.37)$$

where  $V_D = (\mathbf{D} V_{\alpha_0} \mathbf{D}^T)^{-1}$  is the  $r \times r$  constraint covariance matrix and

$$\chi^2 = \lambda^T V_D^{-1} \lambda = \lambda^T (\mathbf{D}\delta\alpha_0 + \mathbf{d}). \quad (3.38)$$

Note that the  $\chi^2$  can be written as a sum of  $r$  distinct terms, one for each constraint. It can be shown that the new covariance matrix  $V_\alpha$  has diagonal elements that are smaller than the initial covariance matrix  $V_{\alpha_0}$ . In general, the nonlinearities of the constraint equations requires that the kinematic fitting procedure be applied iteratively until satisfactory convergence is achieved. Track parameters and their errors, covariance matrices, fit information and other quantities can be obtained after fitting.

The constraints “pull” the tracks away from their unconstrained values. The “pull” of the  $i^{\text{th}}$ -track parameter is defined as:

$$(\text{pull})_i = \frac{\alpha_i - \alpha_{0i}}{\sqrt{(V_{\alpha_0})_{ii} - (V_\alpha)_{ii}}}. \quad (3.39)$$

This is an important variable to test the track parameter and its error. The resulting  $\chi^2$  that is obtained with  $r$  constraints is distributed like a standard  $\chi^2$  with  $r$  degrees of freedom, if Gaussian errors apply. Of course, since track errors are only approximately Gaussian, the actual distribution will have more events in the tail than predicted by theory. Still, knowledge of the distribution allows one to define reasonable  $\chi^2$  cuts.

It is useful to compute how far the parameters have to move to satisfy a particular constraint  $j$ . The initial “distance from satisfaction” can be characterized by the quantity  $(\mathbf{D}\delta\alpha_0 + \mathbf{d})_j$  and the number of standard deviations away from the satisfying the constraint is easily calculated to be

$$\sigma_j = \frac{D_{ji}\delta\alpha_{0i} + d_j}{\sqrt{(V_D^{-1})_{jj}}}. \quad (3.40)$$

This information can be used to provide criteria for rejecting background in addition to the overall  $\chi^2$ .

For kinematic fitting, it is important to choose a track representation that uses physically meaningful quantities and is complete. We adopt the 7-parameter  $W$  format, defined as  $\alpha_W = (p_x, p_y, p_z, E, x, y, z)$ , a 4-momentum and a point where the 4-momentum is evaluated, in the *BES-III* kinematic fitting software package. It is straight-forward to transfer the parameters of neutral tracks and their covariance to the  $W$  representation. The  $W$  format is convenient for transporting particles in a magnetic field, and well suited for vertex fitting. It has been noted that the  $W$  format also have enough information to represent the general decays of particles.

### 3.4.3 Common Kinematic Constraints

In this section, the constraints that are commonly encountered in high energy physics are described. If multiple constraints are desired, one just extends the matrices by adding additional rows, one row per constraint. This allows many constraints to be used simultaneously in the fit.

#### Invariant mass and energy-momentum constraints

The invariant mass constraint equation that forces a track to have an invariant mass  $m_c$  is

$$E^2 - p_x^2 - p_y^2 - p_z^2 - m_c^2 = 0. \quad (3.41)$$

Processes where invariant mass constraints are frequently applied in high energy physics analyses are  $\pi^0/\eta \rightarrow \gamma\gamma$ ,  $\eta \rightarrow \pi^+\pi^-\pi^0$ ,  $K_S^0 \rightarrow \pi^+\pi^-$ , and  $\Lambda \rightarrow p\pi^-$ , etc. All of these involve decays into several specific daughter particles. Since the detector resolutions for neutral particles are poorer than those for charged particles, the invariant mass constraints for  $\pi^0/\eta \rightarrow \gamma\gamma$  are almost always applied in data analyses.

In most  $J/\psi$  and  $\psi(2S)$  analyses, the final state daughter particles are fully reconstructed and are required to satisfy energy-momentum conservation:

$$\begin{aligned} p_x - p_{cx} &= 0, \\ p_y - p_{cy} &= 0, \\ p_z - p_{cz} &= 0, \\ E - E_c &= 0. \end{aligned} \quad (3.42)$$

Energy-momentum constraints are the most commonly used analysis tool. It is helpful for improving the momentum, energy and mass resolution, and for suppressing combinatorial backgrounds.

We consider the analysis of  $J/\psi \rightarrow \rho\pi \rightarrow \pi^+\pi^-\pi^0 \rightarrow \pi^+\pi^-\gamma\gamma$  as an example to illustrate the kinematic fitting procedure for energy-momentum constraints:

$$\begin{aligned} p_{x1} + p_{x2} + p_{x3} + p_{x4} &= 0, \\ p_{y1} + p_{y2} + p_{y3} + p_{y4} &= 0, \\ p_{z1} + p_{z2} + p_{z3} + p_{z4} &= 0, \\ E_1 + E_2 + E_3 + E_4 &= M_{J/\psi}, \end{aligned}$$

where the  $J/\psi$  is assumed to be at rest in the laboratory frame. Initially, the track

parameters have the values  $\alpha_0 = \begin{pmatrix} \alpha_1^0 \\ \alpha_2^0 \\ \alpha_3^0 \\ \alpha_4^0 \end{pmatrix}$ , where  $\alpha_i^0 = \begin{pmatrix} p_{x_i}^0 \\ p_{y_i}^0 \\ p_{z_i}^0 \\ E_i^0 \end{pmatrix}$ ,  $i=1, 2, 3, 4$ , represent the

four momentum vectors of  $\pi^+$ ,  $\pi^-$  and two photons. The initial track covariance matrices are denoted as  $V_{i0}$ ,  $i=1,2,3,4$ . The track parameters  $\alpha_i$  can be expanded about these values (i.e.,  $\alpha_{iA} = \alpha_i^0$ ) giving for  $\mathbf{D}$  and  $\mathbf{d}$ :

$$\mathbf{D} = \begin{pmatrix} 1 & 0 & 0 & 0 & 1 & 0 & 0 & 0 & 1 & 0 & 0 & 0 & 1 & 0 & 0 & 0 \\ 0 & 1 & 0 & 0 & 0 & 1 & 0 & 0 & 0 & 1 & 0 & 0 & 0 & 1 & 0 & 0 \\ 0 & 0 & 1 & 0 & 0 & 0 & 1 & 0 & 0 & 0 & 1 & 0 & 0 & 0 & 1 & 0 \\ 0 & 0 & 0 & 1 & 0 & 0 & 0 & 1 & 0 & 0 & 0 & 1 & 0 & 0 & 0 & 1 \end{pmatrix}, \quad \mathbf{d} = \begin{pmatrix} p_{x1}^0 + p_{x2}^0 + p_{x3}^0 + p_{x4}^0 \\ p_{y1}^0 + p_{y2}^0 + p_{y3}^0 + p_{y4}^0 \\ p_{z1}^0 + p_{z2}^0 + p_{z3}^0 + p_{z4}^0 \\ E_1^0 + E_2^0 + E_3^0 + E_4^0 - M_{J/\psi} \end{pmatrix}.$$

The updated track parameters, covariance matrices and  $\chi^2$  can be obtained by applying Eqs. (3.37) and (3.38). If one wants to apply the additional  $\pi^0 \rightarrow \gamma\gamma$  mass constraint:

$$(E_3 + E_4)^2 - (p_{x3} + p_{x4})^2 - (p_{y3} + p_{y4})^2 - (p_{z3} + p_{z4})^2 = M_{\pi^0}^2,$$

the derivative matrices  $\mathbf{D}$  and  $\mathbf{d}$  will take the forms:

$$\mathbf{D} = \begin{pmatrix} 1 & 0 & 0 & 0 & 1 & 0 & 0 & 0 & 1 & 0 & 0 & 0 & 0 & 1 & 0 & 0 & 0 \\ 0 & 1 & 0 & 0 & 0 & 1 & 0 & 0 & 0 & 1 & 0 & 0 & 0 & 0 & 1 & 0 & 0 \\ 0 & 0 & 1 & 0 & 0 & 0 & 1 & 0 & 0 & 0 & 1 & 0 & 0 & 0 & 0 & 1 & 0 \\ 0 & 0 & 0 & 1 & 0 & 0 & 0 & 1 & 0 & 0 & 0 & 1 & 0 & 0 & 0 & 0 & 1 \\ 0 & 0 & 0 & 0 & 0 & 0 & 0 & 0 & -2p_x^0 & -2p_y^0 & -2p_z^0 & 2E^0 & -2p_x^0 & -2p_y^0 & -2p_z^0 & 2E^0 \end{pmatrix},$$

and

$$\mathbf{d} = \begin{pmatrix} p_{x1}^0 + p_{x2}^0 + p_{x3}^0 + p_{x4}^0 \\ p_{y1}^0 + p_{y2}^0 + p_{y3}^0 + p_{y4}^0 \\ p_{z1}^0 + p_{z2}^0 + p_{z3}^0 + p_{z4}^0 \\ E_1^0 + E_2^0 + E_3^0 + E_4^0 - M_{J/\psi} \\ (E^0)^2 - (p_x^0)^2 - (p_y^0)^2 - (p_z^0)^2 - M_{\pi^0}^2 \end{pmatrix},$$

where  $p_x^0 = p_{x3}^0 + p_{x4}^0$ ,  $p_y^0 = p_{y3}^0 + p_{y4}^0$ ,  $p_z^0 = p_{z3}^0 + p_{z4}^0$  and  $E^0 = E_3^0 + E_4^0$ .

### Reconstruction of $K_S^0$ and $\Lambda$ decay vertex

To introduce the subject of decay vertex reconstruction, consider Figure 3.13, which shows a  $K_S^0$  that decays to  $\pi^+\pi^-$  at a secondary vertex after being produced in the beam interaction region. An accurate determination of the lifetime requires that both the

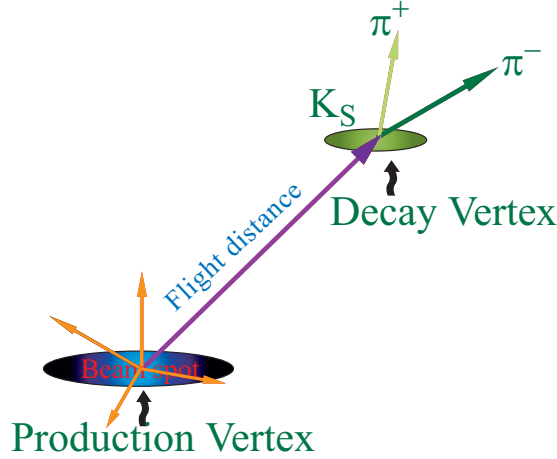


Figure 3.13: A  $K_S^0$  travels a certain distance (“the flight distance”) before decaying into its daughters. These daughters are subsequently measured by the tracking system.

beginning and endpoint of the  $K_S^0$  flight vector be determined accurately. The endpoint is determined by vertex fitting, and its measurement accuracy is controlled purely by the tracking error of the daughter particles. The beginning point is determined by the beam spot size augmented, perhaps, as shown in Figure 3.13, by other tracks produced in interaction point (IP), or by the average of preliminary vertex for lot of events.

The motion of a neutral track before its decay is a simple linear equation. We convert the flight distance ( $s$ ) measured from the production point  $(x_p, y_p, z_p)$  to the decay point  $(x_d, y_d, z_d)$ , to the proper decay time  $c\tau$  using  $s = \beta c t = \gamma \beta c \tau = (p/m)c\tau$ , yielding the new equations

$$\begin{pmatrix} x_p \\ y_p \\ z_p \end{pmatrix} = \begin{pmatrix} x_d - \frac{p_x}{m} c\tau \\ y_d - \frac{p_y}{m} c\tau \\ z_d - \frac{p_z}{m} c\tau \end{pmatrix}. \quad (3.43)$$

The lifetime  $c\tau$  is determined with Eq. (3.43) representing constraint conditions. We can apply

$$\chi^2 = (\alpha - \alpha_0)^T V_{\alpha_0}^{-1} (\alpha - \alpha_0) + 2\lambda^T (\mathbf{D}\delta\alpha + \mathbf{E}\delta c\tau + \mathbf{d}) \quad (3.44)$$

to solve for  $c\tau$  and its error, while at the same time improving the track parameters and the start point [64]. Cascade decay vertices, such as,  $\Xi^- \rightarrow \Lambda\pi^-$ , then  $\Lambda \rightarrow p\pi^-$  can also be reconstructed by applying a similar technique [65].

A cut on the ratio of decay length to its error,  $s/\sigma_s$ , is useful to suppress combinatorial backgrounds. Figure 3.14 shows the mass distribution of  $K_S^0$  ( $s/\sigma_s > 2$ ) and  $\Lambda$  ( $s/\sigma_s > 1$ ) after the secondary vertex reconstruction. The mass resolutions are  $\sim 3$  MeV for  $K_S$ , and  $\sim 1.2$  MeV for  $\Lambda$ .

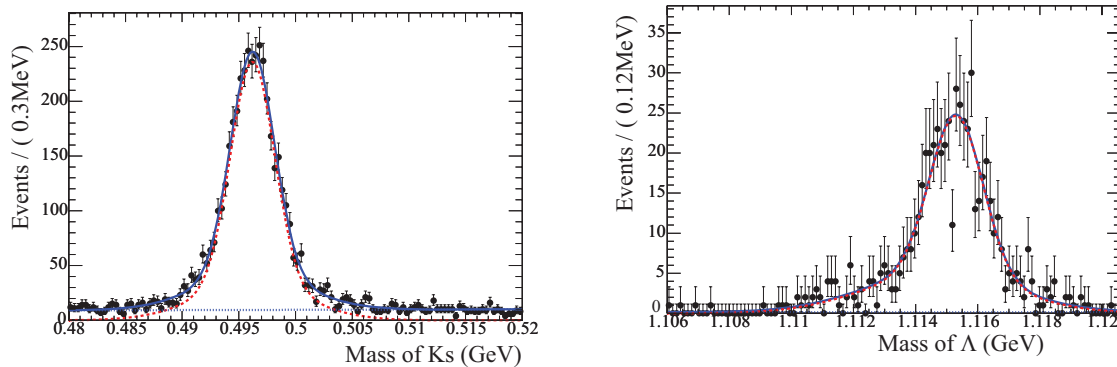


Figure 3.14: The mass distribution of reconstructed  $K_S^0$ 's and  $\Lambda$ 's from a MC simulation. The  $K_S^0$  and  $\Lambda$  mass resolutions are obtained from the weighted widths from double Gaussian fits to the histograms.

### Kinematic constraints for charm tag reconstructions

The general technique used in charm physics studies is referred to as tagging. At the peak of the  $\psi(3770)$ , charmed  $D$  mesons are pair produced with no accompanying particles. Fully reconstructing one  $D$  from a subset of tracks in an event guarantees the remaining tracks must originate from the recoiling  $\bar{D}$ .

The total energy constraints  $E = E_c(E_{\text{beam}})$  can be applied to improve the mass resolution of charm tags by the fact that each  $D$  carries one-half the total cms energy, if the cms is at rest in the laboratory frame. In this case, the reconstructed  $D$  mass is the famous, so-called “beam constrained mass.” At *BES-III*, The produced  $\psi(3770)$  is not at rest since the electron and positron beam collides with a finite crossing angle (22 mrad). The beam energy constraint can still be applied by simply boosting the tracks to the rest frame of the  $\psi(3770)$ .

The charmed particle tags can be reconstructed in an alternative way that requires the mass of the reconstructed  $D$  tag to be equal to the mass of recoiling  $\bar{D}$ . In this case we have

$$E_D^2 - p_{Dx}^2 - p_{Dy}^2 - p_{Dz}^2 = (E_\psi - E_D)^2 - (p_{\psi x} - p_{Dx})^2 - (p_{\psi y} - p_{Dy})^2 - (p_{\psi z} - p_{Dz})^2, \quad (3.45)$$

where  $(p_{Dx}, p_{Dy}, p_{Dz}, E_D)$  and  $(p_{\psi x}, p_{\psi y}, p_{\psi z}, E_\psi)$  denote the energy-momentum vectors of reconstructed  $D$  tag and produced  $\psi(3770)$ . In the  $\psi(3770)$  rest frame, the equal mass constraint is totally equivalent to the beam energy constraint.

In Dalitz-plot or partial-wave analyses, an effective recoil mass can be calculated using  $E_{\text{recoil}} = E_{\psi(3770)} - E_{\text{tag}}$  and  $\vec{p}_{\text{recoil}} = \vec{p}_{\psi(3770)} - \vec{p}_{\text{tag}}$ . One can perform a kinematic fit in which the mass of the charm tag is constrained to the  $D$  mass and the recoil mass is allowed to vary. The signal can then be seen in the recoil mass plot as a peak near the  $D$  mass. With this type of constraint, each event has the same amount of phase space for its decay throughout the recoil mass plot. This has the advantage that the kinematic boundaries of phase space are the same for the signal and sideband regions of the recoil mass plot.

### 3.4.4 Applying Kalman filter techniques to kinematic fitting

In 1960, R. E. Kalman published his famous paper describing a recursive solution to the discrete-data linear filtering problem [66]. It was introduced to the high energy physics world in a paper by Frühwirth [67]. The Kalman filter is a set of mathematical equations that provides an efficient computational (recursive) means to estimate the state of a process, in a way that minimizes the mean of the square error. It is interesting to derive the kinematic fit formalism in the Kalman filter framework [68]. This derivation is also relevant to the addition of exact constraints to a fit. At *BES-III*, there are two typical kinematic fitting problems:

- 1) constraints with a covariance matrix;
- 2) constraints with virtual particles.

that have to be processed by applying the Kalman filter technique.

#### Constraint with a covariance matrix

The exact constraints can be regarded as a measurement equation with infinite precision. Most kinematic constraints are of the exact type. But at *BES-III*, the contribution from beam energy spread should be considered if the data are taken off the peak of narrow resonance like the  $J/\psi$  and  $\psi(2S)$ . In general, we call the “measurement equation” the constraint with a covariance matrix.

Synchrotron radiation and the replacement of the radiated energy by the accelerating cavities generate an energy spread for each beam that results in an essentially Gaussian distribution in beam energies  $E'_b$  centered on the nominal value ( $E_b$ )

$$G(E_b, E'_b) = \frac{1}{\sqrt{2\pi}\Delta} \exp \left[ -\frac{(E_b - E'_b)^2}{2\Delta^2} \right], \quad (3.46)$$

where  $\Delta$  represents the beam energy spread.

Suppose that the electron and positron beams collide with a crossing angle  $2\theta$  in the  $x$ - $z$  plane (at *BES-III*,  $\theta = 11$  mrad). In the case we have the measurement equation:

$$(p_x \ p_y \ p_z \ E) = \begin{pmatrix} \sqrt{s} \tan \theta & 0 & 0 & \frac{\sqrt{s}}{\cos \theta} \end{pmatrix} \quad (3.47)$$

where  $E = 2E_b$ ,  $\delta E = \sqrt{2}\Delta$  and  $\delta\sqrt{s} = \sqrt{2}\Delta \cos \theta$ . The corresponding covariance matrix

is given by  $2 \cdot \Delta^2 \cdot \begin{pmatrix} \sin^2 \theta & 0 & 0 & \sin \theta \\ 0 & 0 & 0 & 0 \\ 0 & 0 & 0 & 0 \\ \sin \theta & 0 & 0 & 1 \end{pmatrix}$ . Clearly, the correlation between  $p_x$  and  $E$  are included.

#### Constraint with virtual particles

At *BES-III*, three kinds of constraints with virtual particles will commonly be encountered in data analysis. (In the following discussion, we suppose that a virtual particle is represented by a 4-momentum vector  $q = (q_x, q_y, q_z, W)$  and all detected particles are represented by a 4-momentum vector  $p = (p_x, p_y, p_z, E)$ .)

- No detection information available; the virtual particle is connected to kinematic fitting with some mass constraints. Energy-momentum conservation gives:

$$\begin{aligned} p_x + q_x &= p_{cx}, \\ p_y + q_y &= p_{cy}, \\ p_z + q_z &= p_{cz}, \\ E + W &= E_c. \end{aligned}$$

In the analysis of  $J/\psi \rightarrow \bar{p}n\pi^+$ , where the  $n$  is not detected, the mass of the virtual particle  $n$  provides an additional constraint. In the analysis of  $\psi(3770) \rightarrow D\bar{D}$ , where one  $D$  is reconstructed in one of its decay modes  $X$  and  $\bar{D}$  is not required to be reconstructed, an equal mass constraint  $m_X = m_{\text{missing}}$  can be employed to improve the  $D$  tag mass resolution.

- Only position information is available; the virtual particle is connected to the kinematic fitting with a set of measurement equations. Some particles, e.g.,  $K_L^0$ , will register reliable position information when it interacts in the detector. In this situation, we may construct “measurement equations” as additional constraints to the energy-momentum conservation:

$$\begin{aligned} x_v + \lambda q_x &= x_{\text{clus}}, \\ y_v + \lambda q_y &= y_{\text{clus}}, \\ z_v + \lambda q_z &= z_{\text{clus}}, \end{aligned}$$

where  $(x_v, y_v, z_v)$  is the position of interaction or decay vertex,  $(x_{\text{clus}}, y_{\text{clus}}, z_{\text{clus}})$  is the position vector of the neutral cluster with the covariance matrix  $V_{\text{clus}}$ , and  $\lambda$  is the flight path. The value of the parameter  $\lambda$  is not very interesting, it can be easily substituted with

$$\lambda = \frac{q^T V_{\text{clus}}^{-1} \Delta x}{q^T V_{\text{clus}}^{-1} q},$$

where  $\Delta x = (x_v - x_{\text{clus}}, y_v - y_{\text{clus}}, z_v - z_{\text{clus}})$ .

- The virtual particle is built by merging a set of tracks. Frequently, one wants to build virtual particles with a vertex constraint (e.g.  $K_S^0 \rightarrow \pi^+\pi^-$ ), or with a mass constraint (e.g.,  $\pi^0 \rightarrow \gamma\gamma$ ). The pre-fitted  $K_S^0$ 's and  $\pi^0$ 's can be directly applied in physics analyses.

### 3.4.5 Limitations of Kinematic Fitting

The precision of kinematic fitting is governed by the model of constraint/measurement equations and the model of track parameters and their covariance matrices. To understand the power and limitations of the kinematic fitting, one has to understand these models well.

Since the natural widths of the narrow resonance such as the  $J/\psi$  and  $\psi(2S)$  are much smaller than the detector resolution, the imperfection of energy-momentum constraints could be ignored. For broad resonances above charm threshold or for data-taking off of resonance peaks, effects due to beam energy spread and initial state radiation must be taken into account.

Unlike the real world, the errors of track parameters are assumed to be Gaussian in the kinematic fitting procedure. In some experiments, the track errors are poorly understood, making kinematic fitting be of little use. On the other hand, Kalman fitted tracks at *BES-III* have better-understood tracking errors and are well suited for kinematic fitting. As is known, it is quite difficult to obtain “ideal” track error in an experiment since there are many approximations in the Kalman track fitting error models, such as the wire resolution, fluctuations of energy losses and multiple scattering. Tight  $\chi^2$  cuts can cause large systematic uncertainties into an analysis because of a long tail in the  $\chi^2$  distribution.

For neutral tracks, the energy deposited in the crystal calorimeter is distributed asymmetrically. If one is to avoid large inefficiencies in kinematic fits, the Gaussian error model for neutrals has to be modified. A solution may be carried out in the near future by application of the method of dynamic noise adjustment [69].

## 3.5 Partial Wave Analysis<sup>9</sup>

### 3.5.1 Introduction

Partial Wave Analysis (PWA) is widely used in high energy experimental physics. It is a useful method for analyzing the correlation between the momenta of final state particles in order to determine the masses, widths and spin-parities of intermediate resonances. The basis of PWA is relativistic kinematics.

It is known that all quantum states form a Hilbert space that is a representation of inhomogeneous Lorentz space. Physicists are used to studying quantum states from the point of view of group theory. In this context, the quantum state of a fundamental particle corresponds to an irreducible representation of the Poincare group. The quantum state of a composite particle consisting of more fundamental constituents is represented by a state vector of the irreducible representation of the Poincare group reduced is reduced from the direct product of the states of its component particles. Hence, the Poincare group and its representation theory is the basis of the kinematic theory of relativistic particles.

By using the method of group representation and applying analysis techniques that exploit the symmetries of the system, the form of the decay matrix element can be changed to a new form where the angular-dependent part of the matrix element is expressed by a  $D$ -function, and the energy-dependent part is kept in a reduced matrix element [70, 71, 72]. In this new form, the angular information of the decay matrix element is separated from the energy information. This property is quite useful in partial wave analysis, since the angular-dependence of the decay matrix contains the information of the spin-parity of the decaying particles, and the energy dependence of the decay matrix contains information about the interactions of its constituents, or pole positions of intermediate states. In the PWA technique, both the angular and energy information of the decay matrix are utilized, and the spin-parity and pole position of the resonance can be determined simultaneously.

In this report, we will briefly discuss various kinematic theories of decay processes, such as the helicity formalism, the tensor formalism etc. We then discuss how to apply

---

<sup>9</sup>By Ning Wu, Hanqing Zheng

the PWA technique to sequential decay processes, and how to use PWA to determine the mass, width, spin-parity and branching ratios of a resonance.

### 3.5.2 Decay Amplitude

The helicity formalism is widely used in PWA. Since the helicity formalism is based on first principles of quantum theory, it is considered to be the standard method for determining the spin-parity of a resonance.

The concept of helicity was first proposed by Chou and Shirokov in 1959 [73]. Soon afterwards Jacob, Wick and others systematically proposed the helicity formalism [70, 74, 75]. Subsequently, Chung found a way to express the helicity coupling amplitudes  $F_{\lambda\nu}^J$  that is useful for PWA [76, 77, 78, 79, 80, 81, 82].

The helicity operator is defined as the projection of the spin operator along the direction of motion

$$h = \frac{\vec{J} \cdot \vec{P}}{|\vec{P}|} = \vec{J} \cdot \hat{P}, \quad (3.5.48)$$

where  $\hat{P}$  is the momentum unit vector. The above definition only holds for a moving particle. For particles at rest, the unit vector  $\hat{P}$  generally has no definition, so in this case the helicity operator is defined as the projection of the spin operator along the  $z$ -axis

$$h = J_3. \quad (3.5.49)$$

If a moving particle is obtained by a Lorentz boost, the unit vector  $\hat{P}$  in Eq. (3.5.48) is taken to be along the direction of the motion of the particle before the boost.

One-particle helicity states are taken to be the common eigenstate of the operators  $P_\mu$ ,  $\vec{J}^2$  and  $h$ . These are denoted by

$$|p\lambda\rangle, \quad (3.5.50)$$

and satisfy

$$P_\mu |p\lambda\rangle = p_\mu |p\lambda\rangle, \quad (3.5.51)$$

$$\vec{J}^2 |p\lambda\rangle = s(s+1) |p\lambda\rangle, \quad (3.5.52)$$

$$h |p\lambda\rangle = \lambda |p\lambda\rangle. \quad (3.5.53)$$

A two-particle helicity state is defined as

$$|p; JM\lambda_1\lambda_2\rangle = \frac{N}{2\pi} \int dU D_{M\lambda}^J(\alpha\beta\gamma)^* R(\alpha\beta\gamma) \psi_{p\lambda_1\lambda_2}, \quad (3.5.54)$$

where  $R(\alpha\beta\gamma)$  is the rotation operator,  $D_{M\lambda}^J(\alpha\beta\gamma)$  is the traditional  $D$ -function [83, 84, 85, 86],  $\psi_{p\lambda_1\lambda_2}$  is the two-particle direct product state in the canonical rest frame,  $N = \sqrt{\frac{2J+1}{4\pi}}$  is the normalization factor, and

$$dU = \sin\beta d\alpha d\beta d\gamma; \quad (3.5.55)$$

the integration region is

$$-\pi < \alpha < \pi, \quad 0 < \beta < \pi, \quad -\pi < \gamma < \pi. \quad (3.5.56)$$

We consider a two-body decay process. Suppose that the spin-parity of the parent particle is  $J^{\eta_J}$ , and spin-parities of the two daughter particles are  $s^{\eta_s}$  and  $\sigma^{\eta_\sigma}$ , then, in the center of mass system of the parent particle, the decay amplitude is

$$M_{\lambda\nu}^J(\theta, \varphi, m) \propto D_{m,(\lambda-\nu)}^{J*}(\varphi, \theta, 0) F_{\lambda\nu}^J, \quad (3.5.57)$$

where  $\theta$  and  $\varphi$  are polar and azimuthal angle of one of the daughter particles in the center of mass frame,  $m$  is the magnetic quantum number of the parent particle,  $\lambda$  and  $\nu$  are helicities of the two daughter particles, and  $F_{\lambda\nu}^J$  is called the helicity coupling amplitude. In  $J/\psi$  hadronic or radiative decay processes, parity conservation holds. In this case,  $F_{\lambda\nu}^J$  has the following symmetry property

$$F_{\lambda\nu}^J = \eta_J \eta_s \eta_\sigma (-)^{J-s-\sigma} F_{-\lambda-\nu}^J. \quad (3.5.58)$$

In the helicity formalism, all of the angular dependence of the decay amplitude is contained in the  $D$ -function as shown in Eq. (3.5.57); the helicity coupling amplitudes  $F_{\lambda\nu}^J$  are independent of all angular information and only dependent on the energy of the system. Details on how to calculate  $F_{\lambda\nu}^J$  can be found in the literature [76, 77, 78, 79, 80, 81, 82].

In experimental physics analyses, most decays that are encountered are sequential decays that include some intermediate resonant states. As an example, consider the following sequential decays

$$a \rightarrow b + c, \quad b \rightarrow d + e, \quad (3.5.59)$$

where  $b$  is an intermediate resonant state. The decay amplitude for this sequential decay is

$$M_{\lambda\mu}^{s_a}(\theta_1, \varphi_1, m) \cdot BW(s, M_b, \Gamma_b) \cdot M_{\nu\sigma}^{s_b}(\theta_2, \varphi_2, \mu), \quad (3.5.60)$$

where  $s_a$  and  $s_b$  are the spin quantum numbers of particles  $a$  and  $b$ , respectively,  $\lambda, \mu, \nu$  and  $\sigma$  are the helicities of particles  $b, c, d$  and  $e$ , respectively,  $m$  is the magnetic quantum number of particle  $a$  in its rest frame,  $M_b$  and  $\Gamma_b$  are the mass and width of particle  $b$ ,  $\theta_1$  and  $\phi_1$  are the polar and azimuthal angles of particle  $b$  in the rest frame of particle  $a$ , and  $\theta_2$  and  $\phi_2$  are the polar and azimuthal angles of particle  $d$  in the rest frame of particle  $b$ . In this decay process, the final stable particles are  $c, d$  and  $e$ . Particle  $b$  is a resonant state described by the Breit-Wigner amplitude  $BW(s, M_b, \Gamma_b)$ .

In addition to the helicity formalism, one can sometimes express the decay amplitude in the LS coupling formalism. We again consider the two-body decay process  $a \rightarrow b + c$ , and suppose that two final state particles  $b$  and  $c$  are massive. Then, in the rest frame of parent particle  $a$ , the decay amplitude in the LS coupling formalism is

$$M_{ls}^{s_a}(\theta, \varphi; m_1, m_2, m) \propto \sum_{mm_s} \langle \theta \varphi m_1 m_2 | lmsm_s \rangle \langle lmsm_s | M | s_a m \rangle, \quad (3.5.61)$$

where  $s_a$  and  $m$  are spin quantum number and magnetic quantum number of particle  $a$ ,  $l$  is the relative orbital angular momentum quantum number between particles  $b$  and  $c$ ,  $s$  is the total spin quantum number of particles  $b$  and  $c$ ,  $m_1$  and  $m_2$  are magnetic quantum numbers of particles  $b$  and  $c$ , respectively, and  $m$  is the magnetic quantum number of particle  $a$ . Applying the Wigner-Eckart theorem, we have

$$\langle lmsm_s | M | s_a m \rangle = \langle lmsm_s | s_a m \rangle G_{ls}^J \quad (3.5.62)$$

where  $G_{ls}^J$  is the reduced matrix element. Using the relation

$$\langle \theta \varphi m_1 m_2 | lmsm_s \rangle = \langle s_b m_1 s_c m_2 | sm_s \rangle \cdot Y_m^l(\theta, \varphi), \quad (3.5.63)$$

where  $Y_m^l(\theta, \varphi)$  is a spherical harmonic function, we can convert Eq. (3.5.61) into

$$M_{ls}^{sa}(\theta, \varphi; m_1, m_2, m) \propto G_{ls}^J \langle s_b m_1 s_c m_2 | sm_s \rangle \sum_m \langle lmsm_s | s_a m \rangle Y_m^l(\theta, \varphi). \quad (3.5.64)$$

It can be shown that the LS coupling amplitude  $G_{ls}^J$  and helicity coupling amplitude  $F_{\lambda\nu}^J$  are related as

$$F_{\lambda\nu}^J = \sum_{ls} \sqrt{\frac{2l+1}{2J+1}} \langle l0s\delta | J\delta \rangle \langle s_b \lambda s_c - \nu | s\delta \rangle G_{ls}^J. \quad (3.5.65)$$

Thus, we have

$$\sum_{\lambda\nu} |F_{\lambda\nu}^J|^2 = \sum_{ls} |G_{ls}^J|^2. \quad (3.5.66)$$

Another formalism used for PWA analysis is the so-called tensor formalism, which was first proposed by Zemach in 1965 [87, 88]. The original method proposed by Zemach was non-relativistic, and all tensors were evaluated in their respective rest frames. In this formalism, the decay amplitude and all the angular dependence is expressed directly in terms of the 4-momentum vectors of the initial and final state particles [87, 88, 77, 78, 89, 90, 91]. As an example, consider  $J/\psi$  decay. The general form for the decay amplitude for  $J/\psi$  hadronic decay is

$$A = \psi_\mu(m) A^\mu = \psi_\mu(m) \sum_i \Lambda_i U_i^\mu, \quad (3.5.67)$$

where  $\psi_\mu(m)$  is the polarization vector of the  $J/\psi$ ,  $m$  the magnetic quantum number of the  $J/\psi$  in its rest frame, and  $U_i^\mu$  the  $i^{\text{th}}$  partial wave amplitude with coupling strength determined by a complex parameter  $\Lambda_i$ . For  $J/\psi$  radiative decays, the general form of the decay amplitude is

$$A = \psi_\mu(m) e_\nu^*(m') A^{\mu\nu} = \psi_\mu(m) e_\nu^*(m') \sum_i \Lambda_i U_i^{\mu\nu}, \quad (3.5.68)$$

where  $e_\nu(m')$  is the photon polarization four-vector, and  $m'$  the photon's helicity. In the tensor formalism, the main task is to calculate the partial wave amplitude  $U_i^\mu$  or  $U_i^{\mu\nu}$ . Details on how to calculate them can be found in the literature [87, 88, 90, 91].

### 3.5.3 Partial Wave Analysis

Once the decay amplitude is known, the next task is the calculation of the differential cross-section of the decay. Suppose all decay processes and all respective decay amplitudes are known for a given channel with  $N$  different decay modes, then the total differential cross section is

$$\frac{d\sigma}{d\Phi} = \sum_{m,\lambda} \left| \sum_{i=1}^N \sum_{\mu} A_i(m, \lambda, \mu) \right|^2 + BG, \quad (3.5.69)$$

where  $A_i(m, \lambda, \mu)$  denotes the decay amplitude for the  $i^{\text{th}}$  decay mode,  $m$  is the helicity of the parent particle,  $\lambda = (\lambda_1, \lambda_2, \dots)$  denotes the set of helicities of final state particles,  $\mu = (\mu_1, \mu_2, \dots)$  denotes the set of helicities of intermediate resonances,  $d\Phi$  is the element of phase space, and  $BG$  represents the non-interfering background.

In the tensor formalism, the total differential decay rate is expressed in a different way. For  $J/\psi$  non-radiative decay, it is expressed as

$$\frac{d\sigma}{d\Phi} = \sum_{i,j} P_{ij} \cdot F_{ij}, \quad (3.5.70)$$

where

$$P_{ij} = P_{ji}^* = \Lambda_i \Lambda_j^*, \quad (3.5.71)$$

and

$$F_{ij} = F_{ji}^* = \frac{1}{2} \sum_{\mu=1}^2 U_i^\mu U_j^{\mu*}. \quad (3.5.72)$$

For  $J/\psi$  radiative decay, Eqs. (3.5.70) and (3.5.71) still can be used, but Eq. (3.5.72) changes to

$$F_{ij} = F_{ji}^* = -\frac{1}{2} \sum_{\mu=1}^2 U_i^{\mu\nu} g_{\nu\nu'}^{\perp\perp} U_j^{\mu\nu'*}. \quad (3.5.73)$$

The normalized probability density function (PDF) that is used to describe the decay process is

$$f(x, \alpha) = \frac{d\Gamma/d\Phi}{\Gamma} W(\Phi), \quad (3.5.74)$$

where  $x$  represents a set of quantities that are measured experimentally,  $\alpha$  represents some unknown parameters that have to be determined by the fit, and  $W(\Phi)$  represents effects of detection efficiency. The total decay width,  $\Gamma$ , is given by

$$\Gamma = \int W(\Phi) \frac{d\sigma}{d\Phi} d\Phi. \quad (3.5.75)$$

In PWA, the decay width is determined by Monte Carlo integration,

$$\Gamma = \frac{1}{N_{mc}} \sum_{j=1}^{N_{mc}} \left( \sum_{m,\lambda} \left| \sum_{i=1}^N \sum_{\mu} A_i(m, \lambda, \mu) \right|^2 + BG \right)_j, \quad (3.5.76)$$

where  $N_{mc}$  is the total number of Monte Carlo events, and the subscript  $j$  indicates that the quantity is evaluated for the  $j$ -th Monte Carlo event. It is necessary that these Monte Carlo events are obtained from a complete detector simulation and pass all of the selection conditions applied to the actual data sample.

The maximum likelihood method is utilized in the fit. The likelihood function is given by the adjoint probability density for all the data,

$$\mathcal{L} = \prod_{i=1}^{N_{events}} f(x, \alpha), \quad (3.5.77)$$

where  $N_{events}$  is the total number of events in the channel. In the data analysis, the goal is to find the set of values,  $\alpha$ , that minimize  $S$ , which is defined as

$$S = -\ln \mathcal{L}. \quad (3.5.78)$$

Different spin-parity intermediate resonances have different angular distributions, and different PDFs are used to fit to invariant mass spectra the angular distributions. Because the better fits will have smaller values of  $S$ , we use the information provided by the value of  $S$  to determine the solution that gives the best fit and in this way discriminate between different hypotheses for the spin-parity of a given resonance.

### 3.5.4 Mass, Width and Spin-parity

From the decay amplitude [Eq. (3.5.57)], we know that different spin-parity hypotheses for an intermediate resonance give different angular distributions. Because the helicity coupling amplitude  $F_{\lambda\nu}^J$  is a slowly varying function of energy [see Eq. (3.5.60)], we know that the invariant mass spectrum is mainly dominated by the mass and width of a resonance. Since the PWA fits both the angular distributions and the invariant mass spectrum simultaneously, we can determine the mass, width and spin-parity.

The spin parity of a resonance is determined mainly from the fit to the angular distributions. As an example, we discuss how to determine the spin-parity of the  $\sigma$  particle in  $J/\psi \rightarrow \omega\pi\pi$  decays [92, 93]. We know that the possible spin-parity values for a resonance in the  $\pi\pi$  system produced in  $J/\psi \rightarrow \omega\pi\pi$  decay can only be  $0^{++}$ ,  $2^{++}$ ,  $4^{++}$  etc. Each of these hypothesis is fit to the data and the one with the smallest  $S$  value is selected; the spin-parity of the selected hypothesis will be that of the  $\pi\pi$  resonance.

The mass and width of a resonance is determined in a different way, still using the  $\sigma$  particle as an example. Assuming the spin-parity of the  $\sigma$  particle is known, we first keep the masses and widths of all resonances in this channel fixed except the mass of the  $\sigma$  particle and perform the likelihood fit. The value of the mass of the  $\sigma$  particle is changed step by step and the value of the likelihood function of the corresponding fit is minimized. The mass value corresponding to the minimum value of  $S$  is the measured mass of the  $\sigma$  particle. A similar way is used to determine the width of the  $\sigma$  particle. This technique is called mass and width scanning.

### 3.5.5 Applications

PWA is a powerful tool for the study of hadron spectroscopy, in particular, for the study of the structure in a spectrum of sequential decays. It has been widely in BES physics analyses of  $J/\psi$  and  $\psi'$  decays, and many meaningful results have been obtained. Here, we give a few examples to show how it works.

First, we discuss the  $J/\psi \rightarrow \omega\pi\pi$  channel [92, 93]. As stated above, the possible spin-parities for a resonance in the  $\pi\pi$  spectrum are  $0^{++}$ ,  $2^{++}$ ,  $4^{++}$  etc. For a  $0^{++}$  resonance, there are two independent helicity parameters. For  $2^{++}$  and  $4^{++}$  resonance, there are five independent helicity parameters. Different parameters correspond to different angular distributions, especially for the pion polar angle distribution in the  $\pi\pi$  center of mass frame. Figure 3.15 shows typical pion polar angle distributions in the  $\pi\pi$  center of mass frame. From the figure we can see that the behavior of the angular distribution for different spin-parities are quite different. For a  $0^{++}$  resonance, it is relatively flat; in contrast, for a  $2^{++}$  resonance, it is concave, while for a  $4^{++}$  resonance, it is severely concave with a complex superstructure. Figure 3.16 compares the angular distributions of the  $\sigma$  particle (left panel) with the  $2^{++} f_2(1270)$  meson (right panel) as a comparison. It is clear that the angular distribution of the  $\sigma$  particle is quite similar to  $0^{++}$  expectations, and the angular distribution of  $f_2(1270)$  is that expected for a standard  $2^{++}$  state.

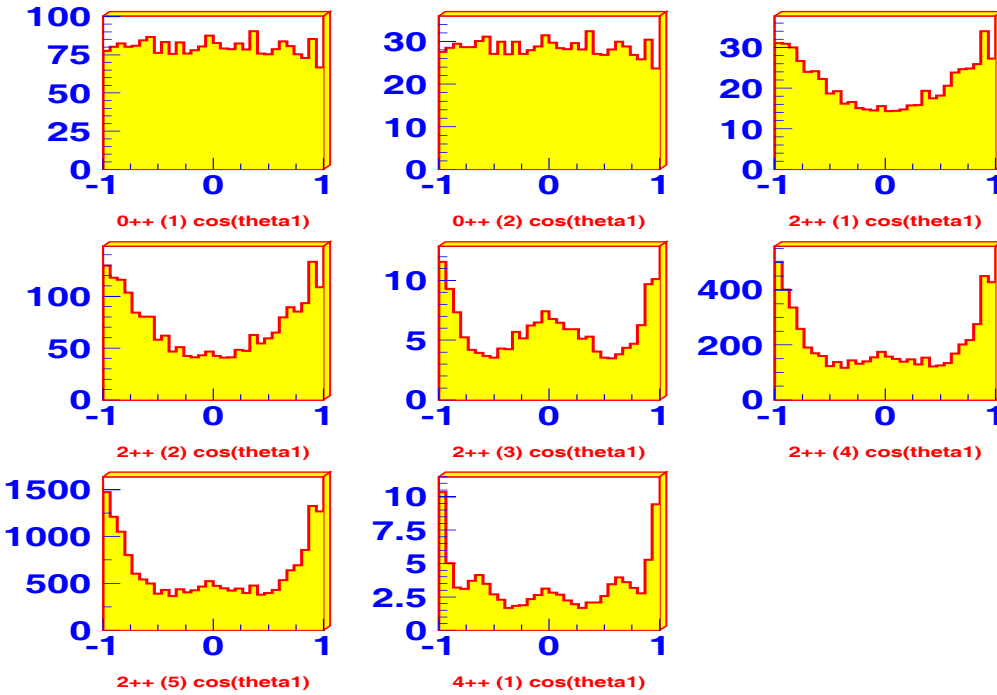


Figure 3.15: Angular distributions for different spin-parity states.

The mass and width of the  $\sigma$  particle is determined by mass and width scans; the corresponding change in  $S$  is shown in Fig. 3.17. In both scan curves, minima are clearly seen, and these correspond to the measured mass and width of the  $\sigma$  particle.

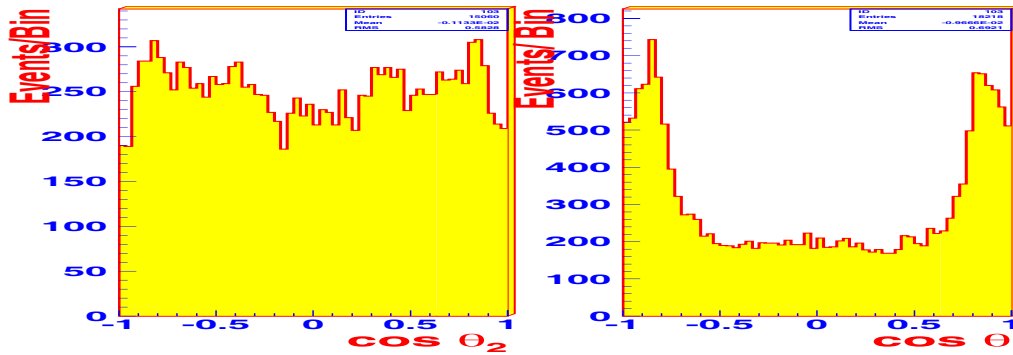


Figure 3.16: LEFT: angular distribution for the  $\sigma$  particle, RIGHT: angular distribution for the  $f_2(1270)$

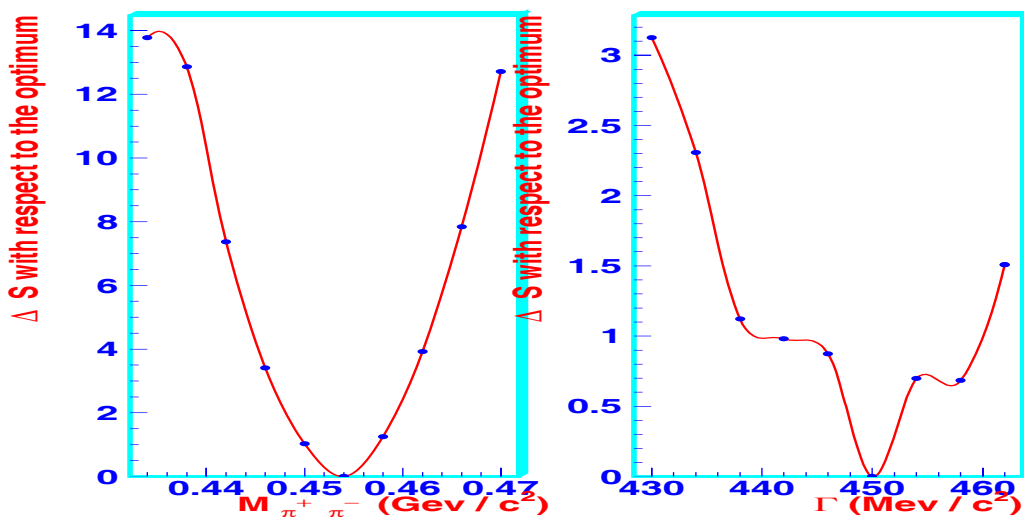


Figure 3.17: Mass and width scans for the  $\sigma$  particle.

### 3. Analysis Tools

Using a similar method, we can determine masses, widths and spin-parities of other resonances.

An interesting example of a PWA is the  $J/\psi \rightarrow \gamma VV$  class of decays, such as  $J/\psi \rightarrow \gamma\rho\rho$ ,  $J/\psi \rightarrow \gamma\omega\omega$ ,  $J/\psi \rightarrow \gamma K^*(892)\bar{K}^*(892)$  etc., where important information is contained in the distribution of the  $\chi$  angle, which is the angle between the decay plans of the two vector mesons. If the resonance is a  $0^{-+}$  meson, the distribution should follow

$$\frac{dN}{d\chi} \sim \sin^2 \chi, \quad (3.5.79)$$

while the expectation for a  $0^{++}$  meson is

$$\frac{dN}{d\chi} \sim 1 + \alpha \cos^2 \chi. \quad (3.5.80)$$

These two distributions are quite different: for a  $0^{-+}$  meson the number of events increases with increasing  $\chi$ , while for a  $0^{++}$  meson the number of events decreases with increasing  $\chi$ .

Sometimes, angular distributions are completely determined by the spin-parity of the resonance. One simple example is  $J/\psi \rightarrow \rho\pi$  with  $\rho \rightarrow \pi\pi$ , where the differential angular distribution is

$$\frac{d\sigma}{d\Omega} \sim \sin^2 \theta_2 [\cos^2 \varphi_2 + \cos^2 \theta_1 \sin^2 \varphi_2], \quad (3.5.81)$$

where  $\theta_2$  and  $\varphi_2$  are the pion polar angle and azimuthal angle distributions in the  $\rho$  center of mass system, and  $\theta_1$  is the polar angle of the  $\rho$  in the  $J/\psi$  center of mass system. In the  $\rho$  center of mass system, the angular distribution for the polar angle  $\theta_2$  is

$$\frac{dN}{d \cos \theta_2} \sim \sin^2 \theta_2, \quad (3.5.82)$$

while that for the azimuthal angle  $\varphi_2$  is

$$\frac{dN}{d\varphi_2} \sim 1 + 2 \cos^2 \varphi_2. \quad (3.5.83)$$

On the right hand side of Eq. (3.5.81), there are no free parameters and, so, the angular distribution is completely specified by the spin-parity of the  $\rho$ . This is a special case; in most cases, the angular distributions are dependent of some unknown parameters, and the magnitude of these parameters effects the behavior of angular distribution.

Relativistic effects also influence the angular distributions of the decay particles. As an example, we discuss the case of  $J/\psi$  decaying into two spin half particles:  $J/\psi \rightarrow \Sigma\bar{\Sigma}$ ,  $J/\psi \rightarrow \Lambda\bar{\Lambda}$ ,  $J/\psi \rightarrow e^+e^-$ , and  $J/\psi \rightarrow \mu^+\mu^-$ . The differential angular distribution for this class of decay processes is

$$\frac{d\sigma}{d\Omega} \sim 1 + \alpha \cos^2 \theta, \quad (3.5.84)$$

where  $\theta$  is the pole angle of a daughter particle in the  $J/\psi$  center of mass system, and

$$\alpha = \frac{|F_{\frac{1}{2}-\frac{1}{2}}^1|^2 - 2|F_{\frac{1}{2}\frac{1}{2}}^1|^2}{|F_{\frac{1}{2}-\frac{1}{2}}^1|^2 + 2|F_{\frac{1}{2}\frac{1}{2}}^1|^2}. \quad (3.5.85)$$

For the case that the  $J/\psi$  decays into a baryon and anti-baryon pair, the velocity of the baryon is non-relativistic, so the parameter  $\alpha$  can take any value between -1 and 1. But for  $J/\psi$  decaying into  $e^+e^-$  or  $\mu^+\mu^-$ , the final state particle is relativistic. In this case, the helicity coupling amplitude  $F_{\frac{1}{2}\frac{1}{2}}^1$  vanishes and  $\alpha = 1$ .

### 3.5.6 Discussions

Partial wave analysis is a powerful tool for the study of hadron spectroscopy: it can simultaneously determine the mass, width, branching ratio and spin-parity of a resonance. However, the theoretical calculation of the formulae used in the PWA analysis can be quite complicated. Moreover, there are many practical difficulties in the application of PWA. For example, a typical PWA requires a enormous amounts of CPU time and lots of memory; at some point, it becomes impractical. New computing methods are needed to facilitate PWA at *BES-III*, where the statistics for many interesting channels will be huge.

For known background sources, Monte Carlo techniques can be used to simulate their behavior and fit the data. Alternatively, one can write out the theoretical formula for the relative decay amplitude and directly fit it as part of the PWA. In other cases, however, the origins of backgrounds are not completely known, which introduces uncertainties into the PDFs used to model them. Often, these are quite similar to phase space and a non-interfering constant amplitude can be used in the fit. However, this is not always the case, and additional free parameters may have to be added to the likelihood, thereby consuming additional memory and CPU time.

A commonly used PWA technique is a bin-by-bin fit. In this case, the parameter space is divided into many small bins. In each bin, if the its size is small enough, one can approximately assume that the amplitude and phase are constant. By analysing the data bin-by-bin, one can obtain the magnitudes of the amplitude and phase of a resonance in each bin, which gives direct measurements of the variation of the amplitude and phase with mass. Thus, a bin-by-bin fit can enable one to determine the phase motion of a resonance. Precise measurements of the phase motion is important for theoretical analyses.

In physics analyses, most intermediate resonances that are encountered are relatively narrow and their mass positions are far from thresholds. Sometimes, however, we have to deal with wide resonances that are close to threshold. In these cases, the traditional Breit-Wigner function, which is an approximate description that is only valid for narrow resonances far away from the threshold, is not applicable. To date, there does not exist a mature description for the shape of a wide near-threshold resonance that is widely accepted. For these cases, when different Breit-Wigner forms are used in the fit, the masses and widths that are determined can be quite different. In fact, in these cases, the masses and widths derived directly from the Breit-Wigner function are not the physical masses and widths of the resonances. The quantity with the most physical significance is the pole position, and the physical mass and width of the resonance should be calculated from it. In analyses of broad, near-threshold resonances, we find that while the masses and widths derived from different Breit-Wigner forms are completely different, the pole positions are approximately the same. Therefore, in these cases, it is best to use pole

positions to describe these resonances.

## 3.6 Dalitz-plot Analysis Formalism<sup>10</sup>

Originally the primary application of Dalitz-plot analyses was to determine the spin and parity of light mesons. Recently Dalitz-plot analyses have emerged as a powerful tool in the study of  $D$  and  $B$  mesons.

Charmed meson decay dynamics have been studied extensively over the last decade. Recent studies of multi-body decays of charmed mesons probe a variety of physics including doubly Cabibbo suppressed decays [94, 95, 96], searches for  $CP$  violation [95, 97, 98, 99, 100],  $T$  violation [101],  $D^0$ – $\bar{D}^0$  mixing [102, 103], the properties of established light mesons [104, 105, 106, 107], the properties of  $\pi\pi$  [94, 106, 108],  $K\pi$  [109, 110], and  $KK$  [111]  $S$ -wave states, and the dynamics of four-body final states [112, 113].

Recently  $B$  meson decay dynamics have been studied. Multi-body decays of  $B$  mesons also probe a variety of physics including, charmless  $B$ -decays [114, 115, 116, 117, 118], measurements of the Cabibbo-Kobayashi-Maskawa (CKM) angle  $\gamma/\phi_3$  [119, 120, 121, 122, 123], searches for direct  $CP$  violation [116, 117, 124], charm spectroscopy [125, 126], the properties of established light mesons [114, 117, 118], the properties of  $KK$  [114, 118] and  $K\pi$  [114, 116, 117]  $S$ -waves, and the three-body production of baryons [115, 127]. Time-dependent Dalitz-plot (TD) analyses have been used to determine the CKM angle  $\alpha/\phi_2$  with  $B \rightarrow \pi^+\pi^-\pi^0$  [128] and to resolve the two-fold ambiguity in the CKM angle  $\beta/\phi_1$  with  $B \rightarrow D\pi^0, D \rightarrow K_S^0\pi^+\pi^-$  [129, 130]. A TD analysis of  $B^0 \rightarrow D^{*\pm}K^0\pi^\mp$  [131] is sensitive  $\gamma/\phi_3$ . Future studies could improve sensitivity to new physics in TD analyses of  $b \rightarrow s$  penguin decays [118].

Additionally, partial wave analyses have been used to study the dynamics of charmonium decays to hadrons, following the formalism presented in Refs. [132, 133], in radiative decays [134, 135, 136, 137] and in decays to all hadronic final states [138, 139, 140, 141]. Multi-body decays of charmonium to all hadronic final states can be analyzed with the Dalitz-plot analysis technique. Studies of the  $\pi\pi$ ,  $K\pi$  and  $KK$   $S$ -wave in charmonium decays probe most of the phase space accessible in  $B$  decays. Thus, Dalitz-plot analyses of charmonia could lead to reduced systematic errors in many  $B$  analyses.

Weak nonleptonic decays of  $B$  and charmed mesons are expected to proceed dominantly through resonant two-body decays in several theoretical models [142]; see Ref. [143] for a review of resonance phenomenology. These amplitudes are typically calculated with the Dalitz plot analysis technique [144], which uses the minimum number of independent observable quantities. For the three-body decay of a spin-0 particle to all pseudo-scalar final states,  $D, B \rightarrow abc$ , the decay rate is

$$\Gamma = \frac{1}{(2\pi)^3 32\sqrt{s}^3} |\mathcal{M}|^2 dm_{ab}^2 dm_{bc}^2, \quad (3.6.86)$$

where  $m_{ij}$  is the invariant mass of  $i - j$  and the coefficient of the amplitude includes all kinematic factors. The scatter plot in  $m_{ab}^2$  versus  $m_{bc}^2$  is called a Dalitz plot. If  $|\mathcal{M}|^2$  is constant the allowed region of the plot will be populated uniformly with events. Any

---

<sup>10</sup>By David Asner

variation in  $|\mathcal{M}|^2$  over the Dalitz plot is due to dynamical rather than kinematical effects. It is straightforward to extend the formalism beyond three-body final states. For  $N$ -body final states, phase space has dimension  $3N - 7$ . Other cases of interest include one vector particle or a fermion/anti-femion pair (e.g.  $B \rightarrow D^* \pi \pi$ ,  $B \rightarrow \Lambda_c p \pi$ ,  $B \rightarrow K \ell \ell$ ) in the final state. For the former case phase space has dimension  $3N - 5$  and for the latter two  $3N - 4$ .

The amplitude of the process,  $R \rightarrow rc, r \rightarrow ab$  where  $R$  is a  $D$ ,  $B$ , or  $q\bar{q}$  meson and  $a, b, c$  are pseudo-scalars, is given by

$$\begin{aligned} \mathcal{M}_r(J, L, l, m_{ab}, m_{bc}) &= \sum_{\lambda} \langle ab | r_{\lambda} \rangle T_r(m_{ab}) \langle cr_{\lambda} | R_J \rangle \\ &= Z(J, L, l, \vec{p}, \vec{q}) B_L^R(|\vec{p}|) B_L^r(|\vec{q}|) T_r(m_{ab}), \end{aligned} \quad (3.6.87)$$

where the sum is over the helicity states  $\lambda$  of the intermediate resonance particle  $r$ ,  $a$  and  $b$  are the daughter particles of the resonance  $r$ ,  $c$  is the spectator particle,  $J$  is the total angular momentum of  $R$ ,  $L$  is the orbital angular momentum between  $r$  and  $c$ ,  $l$  is the orbital angular momentum between  $a$  and  $b$  equivalent to the spin of  $r$ ,  $\vec{p}$  and  $\vec{q}$  are the three-momenta of  $c$  and  $a$ , respectively, in the  $r$  rest frame,  $Z$  describes the angular distribution of final state particles,  $B_L^R$  and  $B_L^r$  are the barrier factors for the production of  $rc$  and  $ab$ , respectively, with angular momentum  $L$ , and  $T_r$  is the dynamical function describing the resonance  $r$ . The amplitude for modeling the Dalitz plot is a phenomenological object. Differences in the parameterizations of  $Z$ ,  $B_L$  and  $T_r$ , as well as the set of resonances  $r$ , complicate the comparison of results from different experiments.

Usually the resonances are modeled with a Breit-Wigner form although some more recent analyses have used the  $K$ -matrix formalism [145, 146, 147] with the  $P$ -vector approximation [148] to describe the  $\pi\pi$   $S$ -wave.

The nonresonant (NR) contribution to  $D \rightarrow abc$  is parameterized as constant ( $S$ -wave) with no variation in magnitude or phase across the Dalitz plot. The available phase space is much greater for  $B$  decay and the nonresonant contribution to  $B \rightarrow abc$  requires a more sophisticated parameterization. Theoretical models of the NR amplitude [149, 150, 151, 152] do not reproduce the distributions observed in the data. Experimentally, several parameterizations have been used [114, 118].

### 3.6.1 Barrier Factor $B_L$

The maximum angular momentum  $L$  in a strong decay is limited by the linear momentum  $\vec{q}$ . Decay particles moving slowly with an impact parameter (meson radius)  $d$  of order 1 fm have difficulty generating sufficient angular momentum to conserve the spin of the resonance. The Blatt-Weisskopf [153, 154] functions  $B_L$ , given in Table 3.8, weight the reaction amplitudes to account for this spin-dependent effect. These functions are normalized to give  $B_L = 1$  for  $z = (|\vec{q}| d)^2 = 1$ . Another common formulation  $B'_L$ , also in Table 3.8, is normalized to give  $B'_L = 1$  for  $z = z_0 = (|\vec{q}_0| d)^2$  where  $q_0$  is the value of  $q$  when  $m_{ab} = m_r$ .

$L$	$B_L(q)$	$B'_L(q, q_0)$
0	1	1
1	$\sqrt{\frac{2z}{1+z}}$	$\sqrt{\frac{1+z_0}{1+z}}$
2	$\sqrt{\frac{13z^2}{(z-3)^2+9z}}$	$\sqrt{\frac{(z_0-3)^2+9z_0}{(z-3)^2+9z}}$

where  $z = (|\vec{q}| d)^2$  and  $z_0 = (|\vec{q}_0| d)^2$

Table 3.8: Blatt-Weisskopf barrier factors.

### 3.6.2 Angular Distributions

The tensor, or Zemach formalism [155, 156] and the helicity formalism [157, 156] yield identical descriptions of the angular distributions for the decay process  $R \rightarrow rc, r \rightarrow ab$  for reactions where  $a, b$  and  $c$  are spin-0 and the initial state is unpolarized. In this scenario, the angular distributions for  $J = 0, 1, 2$  are given in Table 3.9. For polarized initial states, the helicity formalism [157] is used to determine the distinct angular distribution for each helicity state  $|\lambda|$ . The angular distributions for  $J = 1, 2$  for a polarized initial are given in Table 3.10. The sign of the helicity cannot be determined from the Dalitz plot alone when  $a, b$  and  $c$  are spin-0. For final-state particles with non-zero spin (e.g. radiative charmonium decays), the helicity formalism is required.

For the decays of pseudoscalars to three pseudoscalars the formalism simplifies considerably as the angular distribution  $Z$  depends only on the spin  $l$  of resonance  $r$ . Since  $J = 0$  and  $L = l$ , only the first three rows of Table 3.9 are required.

### 3.6.3 The Dynamical Function $T_R$

The dynamical function  $T_r$  is derived from the  $S$ -matrix formalism. In general, the amplitude for a final state  $f$  to couple to an initial state  $i$  is  $S_{fi} = \langle f | S | i \rangle$ , where the scattering operator  $S$  is unitary and satisfies  $SS^\dagger = S^\dagger S = I$ . The transition operator  $\hat{T}$  is defined by separating the probability that  $f = i$  yielding,

$$S = I + 2iT = I + 2i\{\rho\}^{1/2} \hat{T} \{\rho\}^{1/2}, \quad (3.6.88)$$

where  $I$  is the identity operator,  $\hat{T}$  is Lorentz invariant transition operator,  $\rho$  is the diagonal phase space matrix where  $\rho_{ii} = 2q_i/m$  and  $q_i$  is the momentum of  $a$  in the  $r$  rest frame for decay channel  $i$ . In the single channel  $S$ -wave scenario,  $S = e^{2i\delta}$  satisfies unitarity and implies

$$\hat{T} = \frac{1}{\rho} e^{i\delta} \sin \delta. \quad (3.6.89)$$

transition operator.

There are three common formulations of the dynamical function. The Breit-Wigner formalism is the simplest formulation - the first term in a Taylor expansion about a  $T$  matrix pole. The  $K$ -matrix formalism [145] is more general (allowing more than one  $T$

$J \rightarrow l + L$	Angular Distribution
$0 \rightarrow 0+0$	uniform
$0 \rightarrow 1+1$	$(1+\zeta^2) \cos^2 \theta$
$0 \rightarrow 2+2$	$(\zeta^2 + \frac{3}{2})^2 (\cos^2 \theta - 1/3)^2$
$1 \rightarrow 0+1$	uniform
$1 \rightarrow 1+0$	$1 + \zeta^2 \cos^2 \theta$
$1 \rightarrow 1+1$	$\sin^2 \theta$
$1 \rightarrow 1+2$	$1 + (3 + 4\zeta^2) \cos^2 \theta$
$1 \rightarrow 2+1$	$(1 + \zeta^2)[1 + 3 \cos^2 \theta + 9\zeta^2(\cos^2 \theta - 1/3)^2]$
$1 \rightarrow 2+2$	$(1 + \zeta^2) \cos^2 \theta \sin^2 \theta$
$2 \rightarrow 0+2$	uniform
$2 \rightarrow 1+1$	$3 + (1 + 4\zeta^2) \cos^2 \theta$
$2 \rightarrow 1+2$	$\sin^2 \theta$
$2 \rightarrow 2+0$	$1 + \frac{\zeta^2}{3} + \zeta^2 \cos^2 \theta + \zeta^4 (\cos^2 \theta - 1/3)^2$
$2 \rightarrow 2+1$	$1 + \frac{\zeta^2}{9} + (\frac{\zeta^2}{3} - 1) \cos^2 \theta - \zeta^2 (\cos^2 \theta - 1/3)^2$
$2 \rightarrow 2+2$	$1 + \frac{\zeta^2}{9} + (\frac{\zeta^2}{3} - 1) \cos^2 \theta + \frac{(16\zeta^4 + 21\zeta^2 + 9)(\cos^2 \theta - 1/3)^2}{3}$

Table 3.9: Angular distributions for each  $J, L, l$  for *unpolarized* initial states where  $\theta$  is the angle between particles  $a$  and  $c$  in the rest frame of resonance  $r$ ,  $\sqrt{1 + \zeta^2}$  is a relativistic correction with  $\zeta^2 = E_r^2/m_{ab}^2 - 1$ , and  $E_r = (m_R^2 + m_{ab}^2 - m_c^2)/2m_R$ .

$J \rightarrow l + L$	Angular Distribution
$1 \rightarrow 1+0$	$F_0 \gamma^2 \cos^2 \theta + F_1 \sin^2 \theta$
$1 \rightarrow 1+1$	$F_1 \sin^2 \theta$
$1 \rightarrow 1+2$	$F_0 (2\gamma/3)^2 \cos^2 \theta + F_1 (1/9) \sin^2 \theta$
$1 \rightarrow 2+1$	$2F_0 \gamma^4 (\cos^2 \theta - 1/3)^2$ $+ F_1 \gamma^2 [2/9 + 2/3 \cos^2 \theta - 2(\cos^2 \theta - 1/3)^2]$
$1 \rightarrow 2+2$	$F_1 \gamma^2 \cos^2 \theta \sin^2 \theta$
$2 \rightarrow 1+1$	$F_0 (2\gamma^2/3) \cos^2 \theta + F_1 (1/2) \sin^2 \theta$
$2 \rightarrow 1+2$	$F_1 \sin^2 \theta$
$2 \rightarrow 2+0$	$F_0 (4\gamma^4/3 + 4\gamma^2/3 + 1/3) (\cos^2 \theta - 1/3)^2$ $+ F_1 \gamma^2 [4/9 + 4/3 \cos^2 \theta - 4(\cos^2 \theta - 1/3)^2]$ $+ F_2 [8/9 - 4/3 \cos^2 \theta + (\cos^2 \theta - 1/3)^2]$
$2 \rightarrow 2+1$	$F_1 \gamma^2 [1/9 + 1/3 \cos^2 \theta - (\cos^2 \theta - 1/3)^2]$ $+ F_2 [8/9 - 4/3 \cos^2 \theta + (\cos^2 \theta - 1/3)^2]$
$2 \rightarrow 2+2$	$3F_0 (4\gamma^2/9 - 1/9)^2 (\cos^2 \theta - 1/3)^2$ $+ F_1 \gamma^2 [1/9 + 4/3 - (\cos^2 \theta - 1/3)^2]/9$ $+ F_2 [8/9 - 4/3 \cos^2 \theta + (\cos^2 \theta - 1/3)^2]/9$

Table 3.10: Angular distributions for  $J \neq 0, L \neq 0, l$  for *polarized* initial states where  $\cos \theta$  is the angle between particles  $a$  and  $c$  in the rest frame of resonance  $r$ ,  $\gamma = E_r/m_{ab}$ , and  $E_r = (m_R^2 + m_{ab}^2 - m_c^2)/2m_R$ .  $F_\lambda$  denotes the fraction of the initial state in helicity state  $\lambda$ . For unpolarized initial states setting  $F_\lambda = 1$  recovers the angular distributions obtained from the Zemach formalism shown in Table 3.9.

matrix pole and coupled channels while preserving unitarity). The Flatté distribution[158] is used to parameterize resonances near threshold and is equivalent to a one-pole, two-channel  $K$ -matrix.

### 3.6.4 Breit-Wigner Formulation

The common formulation of a Breit-Wigner resonance decaying to spin-0 particles  $a$  and  $b$  is

$$T_r(m_{ab}) = \frac{1}{m_r^2 - m_{ab}^2 - im_r\Gamma_{ab}(q)} \quad (3.6.90)$$

where the “mass dependent” width  $\Gamma$  is

$$\Gamma = \Gamma_r \left( \frac{q}{q_r} \right)^{2L+1} \left( \frac{m_r}{m_{ab}} \right) B'_L(q, q_0)^2 \quad (3.6.91)$$

where  $B'_L(q, q_0)$  is the Blatt-Weisskopf barrier factor from Table 3.8. A Breit-Wigner parameterization best describes isolated, non-overlapping resonances far from the threshold of additional decay channels. For the  $\rho$  and  $\rho(1450)$  a more complex parameterization as suggested by Gounaris-Sakurai [159] is often used [116, 121, 123, 128].

Unitarity can be violated when the dynamical function is parameterized as the sum of two or more overlapping Breit-Wigners. The proximity of a threshold to the resonance shape distorts the line shape from a simple Breit-Wigner. This scenario is described by the Flatté formula and is discussed below.

### 3.6.5 $K$ -matrix Formalism

The  $T$  matrix can be described as

$$\hat{T} = (I - i\hat{K}\rho)^{-1}\hat{K}, \quad (3.6.92)$$

where  $\hat{K}$  is the Lorentz invariant  $K$ -matrix describing the scattering process and  $\rho$  is the phase space factor.

Resonances appear as a sum of poles in the  $K$ -matrix

$$\hat{K}_{ij} = \sum_{\alpha} \frac{\sqrt{m_{\alpha}\Gamma_{\alpha i}(m)m_{\alpha}\Gamma_{\alpha j}(m)}}{(m_{\alpha}^2 - m^2)\sqrt{\rho_i\rho_j}}. \quad (3.6.93)$$

The  $K$ -matrix is real by construction, thus the associated  $T$ -matrix respects unitarity.

For the special case of a single channel, single pole we obtain

$$K = \frac{m_0\Gamma(m)}{m_0^2 - m^2}, \quad (3.6.94)$$

and

$$T = K(1 - iK)^{-1} = \frac{m_0\Gamma(m)}{m_0^2 - m^2 - im_0\Gamma(m)}, \quad (3.6.95)$$

which is the relativistic Breit-Wigner formula. For the special case of a single channel, two poles we have

$$K = \frac{m_{\alpha}\Gamma_{\alpha}(m)}{m_{\alpha}^2 - m^2} + \frac{m_{\beta}\Gamma_{\beta}(m)}{m_{\beta}^2 - m^2}, \quad (3.6.96)$$

and in the limit that  $m_\alpha$  and  $m_\beta$  are far apart relative to the widths we can approximate the  $T$  matrix as the sum of two Breit-Wigners,  $T(K_\alpha + K_\beta) \approx T(K_\alpha) + T(K_\beta)$ ,

$$T \approx \frac{m_\alpha \Gamma_\alpha(m)}{m_\alpha^2 - m^2 - im_\alpha \Gamma_\alpha(m)} + \frac{m_\beta \Gamma_\beta(m)}{m_\beta^2 - m^2 - im_\beta \Gamma_\beta(m)}. \quad (3.6.97)$$

In the case of two nearby resonances Eq. 3.6.97 is not valid and exceeds unity (and hence  $T$  violates unitarity).

This formulation, which applies to  $S$ -channel production in two-body scattering  $ab \rightarrow cd$ , can be generalized to describe the production of resonances in other processes, such as the decay of charmed mesons. The key assumption here is that the two-body system described by the  $K$ -matrix does *not* interact with the rest of the final state [148]. The quality of this assumption varies with the production process and is appropriate for scattering experiments like  $\pi^- p \rightarrow \pi^0 \pi^0 n$ , radiative decays such as  $\phi, J/\psi \rightarrow \gamma \pi \pi$  and semileptonic decays such as  $D \rightarrow K \pi \ell \nu$ . This assumption may be of limited validity for production processes such as  $p\bar{p} \rightarrow \pi \pi \pi$  or  $D \rightarrow \pi \pi \pi$ . In these scenarios the two-body Lorentz invariant amplitude,  $\hat{F}$ , is given as

$$\hat{F}_i = (I - i\hat{K}\rho)^{-1}_{ij} \hat{P}_j = (\hat{T}\hat{K}^{-1})_{ij} \hat{P}_j, \quad (3.6.98)$$

where  $P$  is the production vector that parameterizes the resonance production in the open channels.

For the  $\pi\pi$   $S$ -wave, a common formulation of the  $K$ -matrix [147, 106, 123] is

$$K_{ij}(s) = \left\{ \sum_\alpha \frac{g_i^{(\alpha)} g_j^{(\alpha)}}{m_\alpha^2 - s} + f_{ij}^{sc} \frac{1 - s_0^{sc}}{s - s_0^{sc}} \right\} \times \frac{s - s_A/2m_\pi^2}{(s - s_{A0})(1 - s_{A0})}. \quad (3.6.99)$$

The factor  $g_i^{(\alpha)}$  is the real coupling constant of the  $K$ -matrix pole  $m_\alpha$  to meson channel  $i$ ; the parameters  $f_{ij}^{sc}$  and  $s_0^{sc}$  describe a smooth part of the  $K$ -matrix elements; the multiplicative factor  $\frac{s - s_A/2m_\pi^2}{(s - s_{A0})(1 - s_{A0})}$  suppresses a false kinematical singularity near the  $\pi\pi$  threshold - the Adler zero; and the number 1 has units  $\text{GeV}^2$ .

The production vector, with  $i = 1$  denoting  $\pi\pi$ , is

$$P_j(s) = \left\{ \sum_\alpha \frac{\beta_\alpha g_j^{(\alpha)}}{m_\alpha^2 - s} + f_{1j}^{pr} \frac{1 - s_0^{pr}}{s - s_0^{pr}} \right\} \times \frac{s - s_A/2m_\pi^2}{(s - s_{A0})(1 - s_{A0})}, \quad (3.6.100)$$

where the free parameters of the Dalitz plot fit are the complex production couplings  $\beta_\alpha$ , and the production vector background parameters  $f_{1j}^{pr}$  and  $s_0^{pr}$ . All other parameters are fixed by scattering experiments. Reference [146] describes the  $\pi\pi$  scattering data with a 4 pole, 2 channel ( $\pi\pi, KK$ ) model while Ref. [147] describes the scattering data with 5 pole, 5 channel ( $\pi\pi, KK, \eta\eta, \eta'\eta'$  and  $4\pi$ ) model. The former has been implemented by CLEO [99] and the latter by FOCUS [106] and BaBar [123]. In both cases only the  $\pi\pi$  channel was analyzed. A more complete coupled channel analysis would simultaneously fit all final states accessible by rescattering.

### 3.6.6 Flatté Formalism

The scenario where another channel opens close to the resonance position can be described by the Flatté formulation

$$\hat{T}(m_{ab}) = \frac{1}{m_r^2 - m_{ab}^2 - i(\rho_1 g_1^2 + \rho_2 g_2^2)}, \quad g_1^2 + g_2^2 = m_r \Gamma_r. \quad (3.6.101)$$

This situation occurs in the  $\pi\pi$  S-wave where the  $f_0(980)$  is near the  $K\bar{K}$  threshold and in the  $\pi\eta$  channel where the  $a_0(980)$  also lies near  $K\bar{K}$  threshold. For the  $a_0(980)$  resonance the relevant coupling constants are  $g_1 = g_{\pi\eta}$  and  $g_2 = g_{KK}$  and the phase space terms are  $\rho_1 = \rho_{\pi\eta}$  and  $\rho_2 = \rho_{KK}$ , where

$$\rho_{ab} = \sqrt{\left(1 - \left(\frac{m_a - m_b}{m_{ab}}\right)^2\right) \left(1 + \left(\frac{m_a - m_b}{m_{ab}}\right)^2\right)}. \quad (3.6.102)$$

For the  $f_0(980)$  the relevant coupling constants are  $g_1 = g_{\pi\pi}$  and  $g_2 = g_{KK}$  and the phase space terms are  $\rho_1 = \rho_{\pi\pi}$  and  $\rho_2 = \rho_{KK}$ . The charged and neutral  $K$  channels are usually assumed to have the same coupling constant but separate phase space factors due to  $m_{K^+} \neq m_{K^0}$  resulting in

$$\rho_{KK} = \frac{1}{2} \left( \sqrt{1 - \left(\frac{2m_{K^\pm}}{m_{KK}}\right)^2} + \sqrt{1 - \left(\frac{2m_{K^0}}{m_{KK}}\right)^2} \right). \quad (3.6.103)$$

### 3.6.7 Branching Ratios from Dalitz Fits

The fit to the Dalitz plot distribution using either the Breit-Wigner or the  $K$ -matrix formalism factorizes into a resonant contribution to the amplitude  $\mathcal{M}_j$  and a complex coefficient,  $a_j e^{i\delta_j}$ , where  $a_j$  and  $\delta_j$  are real. The definition of a rate of a single process, given a set of amplitudes  $a_j$  and phases  $\delta_j$  is the square of the relevant matrix element (see Eq. 3.6.86). In this spirit, the fit fraction is usually defined as the integral over the Dalitz plot ( $m_{ab}$  vs  $m_{bc}$ ) of a single amplitude squared divided by the integral over the Dalitz plot of the square of the coherent sum of all amplitudes,

$$\text{Fit Fraction}_j = \frac{\int |a_j e^{i\delta_j} \mathcal{M}_j|^2 dm_{ab}^2 dm_{bc}^2}{\int |\sum_k a_k e^{i\delta_k} \mathcal{M}_k|^2 dm_{ab}^2 dm_{bc}^2}, \quad (3.6.104)$$

where  $\mathcal{M}_j$  is defined by Eq. 3.6.87 and described in Ref. [97]. The sum of the fit fractions for all components will in general not be unity due to interference.

It should be noted that when the  $K$ -matrix description in Eq. 3.6.98 is used to describe a wave (e.g.  $\pi\pi$  S-wave) then  $\mathcal{M}_j$  refers to the entire wave. In these circumstances, it may not be straightforward to separate it into a sum of individual resonances unless these are narrow and well separated, in which case Eq. 3.6.97 can be used.

### Reconstruction Efficiency

The efficiency for reconstructing an event as a function of position on the Dalitz plot is in general non-uniform. Typically, a signal Monte Carlo sample generated with a uniform

distribution in phase space is used to determine the efficiency. The variation in efficiency across the Dalitz plot varies with experiment and decay mode. Most recent analyses utilize a full GEANT [160] detector simulation.

Finite detector resolution can usually be safely neglected as most resonances are comparatively broad. Notable exceptions where detector resolution effects must be modeled are  $\phi \rightarrow K^+K^-$ ,  $\omega \rightarrow \pi^+\pi^-$ , and  $a_0 \rightarrow \eta\pi^0$ . One approach is to convolve the resolution function in the Dalitz-plot variables  $m_{ab}^2$ ,  $m_{bc}^2$  with the function that parameterizes the resonant amplitudes. In high statistics data samples resolution effects near the phase space boundary typically contribute to a poor goodness of fit. The momenta of  $a, b$  and  $c$  can be recalculated with a  $R$  mass constraint. This forces the kinematical boundaries of the Dalitz plot to be strictly respected. If the three-body mass is not constrained, then the efficiency (and the parameterization of background) may also depend on the reconstructed mass. In fits to multi-body decays of charmonia and bottomonia it is not appropriate to constrain the mass due to the finite natural width of the parent.

## Background Parameterization

The contribution of background to the charm and  $B$  samples varies by experiment and final state. The background naturally falls into five categories: (i) purely combinatoric background containing no resonances, (ii) combinatoric background containing intermediate resonances, such as a real  $K^{*-}$  or  $\rho$ , plus additional random particles, (iii) final states containing identical particles as in  $D^0 \rightarrow K_S^0\pi^0$  background to  $D^0 \rightarrow \pi^+\pi^-\pi^0$  and  $B \rightarrow D\pi$  background to  $B \rightarrow K\pi\pi$ , (iv) mistagged decays such as a real  $\overline{D}^0$  or  $\overline{B}^0$  incorrectly identified as  $D^0$  or  $B^0$  and (v) particle misidentification of the decay products such as  $D^+ \rightarrow \pi^-\pi^+\pi^+$  or  $D_s^+ \rightarrow K^-K^+\pi^+$  reconstructed as  $D^+ \rightarrow K^-\pi^+\pi^+$ .

The contribution from combinatoric background with intermediate resonances is distinct from the resonances in the signal because the former do *not* interfere with the latter since they are not from true resonances. Additionally, processes such as  $\psi' \rightarrow \gamma\chi_{c2} \rightarrow \gamma(\gamma J/\psi) \rightarrow \gamma\gamma(\pi\pi)$  and  $\psi' \rightarrow \pi^0 J/\psi, J/\psi \rightarrow \pi\pi$ , do *not* interfere since electromagnetic and hadronic transitions proceed on different time scales. Similarly,  $D^0 \rightarrow \rho\pi$  and  $D^0 \rightarrow K_S^0\pi^0$  do not interfere since strong and weak transitions proceed on different time scales. The usual identification tag of the initial particle as a  $D^0$  or a  $\overline{D}^0$  is the charge of the distinctive slow pion in the decay sequence  $D^{*+} \rightarrow D^0\pi_s^+$  or  $D^{*-} \rightarrow \overline{D}^0\pi_s^-$ . Another possibility is the identification or “tagging” of one of the  $D$  mesons from  $\psi(3770) \rightarrow D^0\overline{D}^0$  as is done for  $B$  mesons from  $\Upsilon(4S)$ . The mistagged background is subtle and may be mistakenly enumerated in the *signal* fraction determined by a  $D^0$  mass fit. Mistagged decays contain true  $\overline{D}^0$ ’s or  $\overline{B}^0$ ’s and so the resonances in the mistagged sample exhibit interference on the Dalitz plot.



# Bibliography

- [1] *BES-III* Collaboration, "The Preliminary Design Report of the *BES-III* Detector", Report No. IHEP-BEPCII-SB-13.
- [2] G. Barrand *et. al.*, Comput. Phys. Commun., 140, 45-55 (2001).
- [3] <http://www.cmtsite.org/>
- [4] <http://cern.ch/geant4>.
- [5] <http://gdml.web.cern.ch/gdml>.
- [6] L. H. Wu, Y. F. Wang, Y. B. Chen, J. B. Liu, R. G. Liu, X. Y. Ma, Chinese Phys. **C** **32**, No. 04, 264-268 (2008).
- [7] <http://docbes3.ihep.ac.cn/DocDB/0000/000018/001/guide.pdf>
- [8] S. Jadach, B.F.L. Ward and Z. Was, Comp. Phys. Commu. 130, 260 (2000);  
S. Jadach, B.F.L. Ward and Z. Was, Phys. Rev. D63, 113009 (2001).
- [9] <http://jadach.web.cern.ch/jadach/>
- [10] S. Jadach, W. Placzek, E. Richter-Was, B.F.L Ward and Z. Was, Comput. Phys. Commun 102, 229 (1997).
- [11] S. Jadach, W. Placzek and B.F.L. Ward, Phys. Lett. B 390, 298 (1997).
- [12] S. Jadach and B. F. L. Ward, Phys. Rev. D40, 3582 (1989).
- [13] W. Beenakker, F.A.Berends, and S.C.van der Marck, Nucl., Phys. B349, 323(1991);  
W. Beenakker, F.A.Berends, and S.C.van der Marck, Nucl. Phys. B355, 281(1991).
- [14] Giovanni Balossini, Carlo M. Carloni calame, Guido Montagna, Oreste Nicrosini and Fulvio Piccinini, Nucl. Phys. B758, 227 (2006).
- [15] The code is available at website <http://www.pv.infn.it/hepcomplex/releases/babayaga.tar.gz>.
- [16] <http://www.thep.lu.se/torbjorn/Pythia.html>.
- [17] J. C. Chen, G. S. Huang, X. R. Qi, D. H. Zhang and Y.S. Zhu, Phys. Rev. D 62, 034003 (2000).

- [18] K. Kasahara, S. Torii, T. Yuda, Proc. 16th ICRC(kyoto) 13, 70 (1979).
- [19] BES Collaboration, J.Z. Bai *et al.*, Phys. Lett. B, 1995, **355**: 374; HEP & NP, 1995, **19**: 673.
- [20] BES Collaboration, J.Z. Bai *et al.*, Phys. Lett. B, 2002, **550**: 24.
- [21] BES Collaboration, M. Ablikim *et al.*, Phys. Rev. Lett. **97**, 121801 (2006).
- [22] BES Collaboration, J.Z. Bai *et al.*, Phys. Rev. Lett., 2000, **84**: 594; Phys. Rev. Lett., 2002, **88**: 101802.
- [23] CLEO Collaboration, G. Crawford *et al.*, CLNS 94/1268 (Jan. 27th, 1994).
- [24] KLOE Collaboration, F. Ambrosino *et al.*, hep-ex/0604048.
- [25] S. Jadach and Z. Was, Comp. Phys. Comm. 36 (1985) 191; S. Jadach and Z. Was, Comp. Phys. Comm. 64 (1991) 267; S. Jadach, J.H. Kuhn and Z. Was, Comp. Phys. Comm. 64 (1991) 275; M. Jezabek, Z. Was, S. Jadach and J.H. Kuhn CERN-TH-6195-91 (Aug. 1991).
- [26] V.M. Budnev *et al.*, Phys. Rep. C15 (1975) 181.
- [27] J. Vermasseren, Nucl. Phys. B299 (1993) 347.
- [28] C.D. Fu, J.H. Zou, X.H. Mo, K.L. He *et al.*, Chinese Physics C (HEP&NP) 32(5), 329-337(2008).
- [29] Y.N. Guo *et al.*, HEP & NP, 1990, **14**: 1057 (in Chinese);  
Z.Q. Yu *et al.*, HEP & NP, 1995, **19**: 1062 (in Chinese).
- [30] G.S. Huang *et al.*, HEP & NP, 2001, **25**: 889.
- [31] F. Berends and R. Kleiss, Nucl.Phys. B228 (1983) 537.
- [32] S. Jadach, B.F.L Ward and Z. Was, hep-ph/9912214; hep-ph/0006359.
- [33] S. Jadach, E. Richter-Was, B.F.L Ward and Z. Was, CERN-TH-6230-91 (Sept. 1991);  
S. Jadach, E. Richter-Was, B.F.L Ward and Z. Was, Phys. Lett. B268 (1991) 253;  
S. Jadach, and B.F.L Ward, Phys. Rev. D40 (1989) 3582; S. Jadach, E. Richter-Was, B.F.L Ward and Z. Was, Phys. Lett. B260 (1991) 438; S. Jadach, E. Richter-Was, B.F.L Ward and Z. Was, Phys. Lett. B253 (1991) 469; Version 1.22 was obtained from B. Ward for the application at CLEOc.
- [34] F. Berends and R. Kleiss, Nucl.Phys. B186 (1981) 22.
- [35] F. Berends, R. Kleiss and S. Jadach, Nucl.Phys. B202 (1982) 63.
- [36] F. Berends and S. van der Mark, Nucl.Phys. B342 (1990) 61.
- [37] C.M. Carloni Calame *et al.*, Nucl. Phys. B **584** (2000) 459.
- [38] C. M. Carloni Calame, Phys. Lett. B **520** (2001) 16.

- [39] E. Drago and G. Venanzoni, ‘A Bhabha generator for DAΦNE including radiative corrections and  $\Phi$  resonance”, report INFN-AE-97-48.
- [40] F. Ambrosino *et al.* [KLOE Coll.], Nucl. Instrum. Meth. A **534** (2004) 403.
- [41] G.V. Fedotovich and A.L. Sibidanov, Nucl. Phys. B(Proc. Suppl.) **131** (2004) 9.
- [42] A. B. Arbuzov *et al.*, JHEP **9710** (1997) 001.
- [43] A. Denig and F. Nguyen, ‘The KLOE luminosity measurement”, KLOE note n.202, July 2005, [www1.infn.it/kloe/pub/knote/kn202.ps](http://www1.infn.it/kloe/pub/knote/kn202.ps).
- [44] Carli T, Koblitz B, Nucl. Instrum. Methods, 2003, **A501**: 576-588; Holmström L, Sain R, Miettinen H E, Comput. Phys. Commun., 1995, **88**: 195.
- [45] Fisher R A, The use of multiple measurements in taxonomic problems Annals of Eugenics **7**, 1936, 179-188.
- [46] Bhat P C (DØ Collaboration), arXiv:hep-ex/9507007, 1995.
- [47] Bishop C M. Neural Networks for Pattern Recognition. Oxford: Clarendon, 1995; Beale R, Jackson T. Neural Computing: An Introduction. New York: Adam Hilger, 1991.
- [48] Roe B. P., Yang H. J. *et. al.*, Nucl. Instrum. Methods, 2005, **A543**: 577–584
- [49] Li Wei-Dong, Liu Huai-Min *et. al.*, The Offline Software for the BESIII Experiment, Proceeding of CHEP06, Mumbai, India, 2006.
- [50] Deng Zi-Yan *et. al.*, HEP & NP, 2006, **30(5)**: 371–377.
- [51] Agostinelli S. *et. al.*, (Geant4 Collaboration), Nucl. Instrum. Methods, 2003, **A506**: 250
- [52] Wang Da-Yong, He Kang-Lin, Li Wei-Guo *et. al.*, Software Developments and Studies of BESIII dE/dx Reconstruction. In: The Publications for the 5th Seminar of Nuclear Instrument and its applications, China, 2005 (in Chinese).
- [53] Hu Ji-Feng, He Kang-Lin, Zhang Zi-Ping *et. al.*, HEP & NP, 2007, **31(10)**: 893–899.
- [54] Edwards C. *et. al.*, Phys. Rev., 1982, **D25**: 3065.
- [55] Sun Sheng-Sen, He Kang-Lin *et. al.*, HEP & NP, 2005, **29(2)**: 162–167(in Chinese).
- [56] Guo Yun-Jun, He Kang-Lin, HEP & NP, 2007, **31(11)**: 1050–1055.
- [57] Gu Jian-Hui, Yu Zhong-Qiang, HEP & NP, 1996, **20(1)**: 26–31 (in Chinese).
- [58] Yao W. M. *et. al.*, Journal of Physics, 2006, **G33**: 1.
- [59] Qin Gang, Lü Jun-Guang, He Kang-Lin, *et. al.*, HEP & NP, 2007, **31(xx)**: xxx–xxx.

- [60] Brun R., Rademakers F. *et. al.*, ROOT Users Guide 5.12. arXiv:<http://root.cern.ch>, 2006. 73–76.
- [61] Brun R., Rademakers F. *et. al.*, An Object-Oriented Data Analysis Framework, arXiv:<http://root.cern.ch>.
- [62] Narsky I, StatPatternRecognition: A C++ Package for Statistical Analysis of High Energy Physics Data, arXiv:[physics/0507143](http://physics/0507143), 2005.
- [63] Paul Avery, Applied Fitting Theory I: General Least Squares Theory, CBX-91-72.
- [64] Y. Z. Sun, K. L. He, *et al.* HEP&NP, 2007, **31(05)** : 423–430.
- [65] M. Xu, K. L. He, *et al.* will appear in Chinese Physics C, 2008.
- [66] R. E. Kalman, A New Approach to Linear Filtering and Prediction Problems, Transaction of the ASME– Journal of Basic Engineering, March 1960: 35–45.
- [67] R. Frühwirth, Nucl. Instrum. Methods, 1987, **A262**: 444–450.
- [68] L. Yan, K. L. He, BESIII internal note-19.
- [69] L. Yan, The recent development in kinematic fitting software, June 2007, BESIII annual meeting.
- [70] M. Jacob and G.C.Wick, Ann. Phys. **7** (1959) 404.
- [71] E.P. Wigner, Group theory and its application to the quantum mechanics of atomic spectra, (Academic Press, New York, 1959).
- [72] S. Weinberg, The Quantum Theory of Fields, (Cambridge University Press, 1992).
- [73] Kuang-Chao Chou, S.Shirkov, JETP (USSR), **36**, (1959) 909.
- [74] A.J. Macfarlane, J. Math. Phys. **4** (1963) 490.
- [75] A. Mckerrell, Nuovo Cimento **34**, (1964) 1298.
- [76] S.U.Chung, Spin Formalism, (CERN Yellow report, No. CERN 71-8, Geneva, Switzerland, 1971).
- [77] S.U.Chung, Phys. Rev. **D48**, (1993) 1225.
- [78] S.U.Chung, Phys. Rev. **D57**, (1998) 431.
- [79] N. Wu, Helicity analysis of relativistic particles, (Ph.D thesis, Univ. of Sci. and Tech. of China, 1997).
- [80] N. Wu, Commun. Theor. Phys. (Beijing, China) **35** (2001) 547.
- [81] N. Wu, Commun. Theor. Phys. (Beijing, China) **35** (2001) 693.
- [82] N. Wu, Commun. Theor. Phys. (Beijing, China) **37** (2002) 309.

- [83] M.E. Rose, Elementary Theory of Angular Momentum, (Wiley, New York, 1957).
- [84] A.R. Edmonds, Angular Momentum in Quantum Mechanics, (Princeton Univ. Press, Princeton, 1957).
- [85] E.U. Condon and G.H. Shortley, The Theory of Atomic Spectra, (Combridge Univ. Press, 1957)
- [86] J.Y. Zeng, Quantum Mechanics, (Science Press, 1986)(in chinese).
- [87] C. Zemach, Phys. Rev. **140**, (1965) B97.
- [88] C. Zemach, Phys. Rev. **140**, (1965) B109.
- [89] C. Fronsdal, Nuovo Cimento suppl. , **9** (1958) 416.
- [90] J.J. Zhu, Helicity Coupling Amplitude in Tensor Formalism, (Ph.D thesis, Univ. of Sci. and Tech. of China, 1997).
- [91] B.S. Zou and D.V. Bugg, Euro. Phys. J. **A16** (2003) 537.
- [92] M. Ablikim, et al., BES Collaboration, Phys. Lett. **B 598** (2004) 149.
- [93] M. Ablikim, et al., BES Collaboration, Phys. Lett. **B 633** (2006) 681.
- [94] H. Muramatsu *et al.* (CLEO Collab.), Phys. Rev. Lett. **89**, 251802 (2002) [Erratum-  
ibid. **90**, 059901 (2003)]
- [95] G. Brandenburg *et al.* (CLEO Collab.), Phys. Rev. Lett. **87**, 071802 (2001)
- [96] J. M. Link *et al.* (FOCUS Collab.), Phys. Lett. B **601**, 10 (2004)
- [97] S. Kopp *et al.* (CLEO Collab.), Phys. Rev. D **63**, 092001 (2001)
- [98] D. M. Asner *et al.* (CLEO Collab.), Phys. Rev. D **70**, 091101 (2004)
- [99] D. Cronin-Hennessy *et al.* (CLEO Collab.), Phys. Rev. D **72**, 031102 (2005)
- [100] B. Aubert *et al.* (BABAR Collab.), Phys. Rev. D **71**, 091101 (2005)
- [101] J. M. Link *et al.* (FOCUS Collab.), Phys. Lett. B **622**, 239 (2005)
- [102] D. M. Asner (CLEO Collab.), Phys. Rev. D **72**, 012001 (2005)
- [103] See the Note on  $D^0$ – $\overline{D}^0$  Mixing by D. Asner in the Review; Dalitz plot analysis of the wrong sign rate  $D^0 \rightarrow K^+ \pi^- \pi^0$ [95] is a candidate processes
- [104] P. L. Frabetti *et al.* (E687 Collab.), Phys. Lett. B **407**, 79 (1997)
- [105] E. M. Aitala *et al.* (E791 Collab.), Phys. Rev. Lett. **86**, 765 (2001)
- [106] J. M. Link *et al.* (FOCUS Collab.), Phys. Lett. B **585**, 200 (2004)
- [107] P. Rubin *et al.* (CLEO Collab.), Phys. Rev. Lett. **93**, 111801 (2004)

- [108] E. M. Aitala *et al.* (E791 Collab.), Phys. Rev. Lett. **86**, 770 (2001)
- [109] E. M. Aitala *et al.* (E791 Collab.), Phys. Rev. Lett. **89**, 121801 (2002)
- [110] E. M. Aitala *et al.* (E791 Collab.), Phys. Rev. **D73**, 032004 (2006); Erratum-*ibid.* **D74**, 059901 (2006).
- [111] B. Aubert *et al.* (BABAR Collab.), Phys. Rev. D **72**, 052008 (2005)
- [112] J. M. Link *et al.* (FOCUS Collab.), Phys. Lett. B **575**, 190 (2003)
- [113] J. M. Link *et al.* (FOCUS Collab.), Phys. Lett. B **610**, 225 (2005)
- [114] A. Garmash *et al.* (Belle Collab.), Phys. Rev. D **71**, 092003 (2005)
- [115] M. Z. Wang *et al.*, Phys. Lett. B **617**, 141 (2005)
- [116] B. Aubert *et al.* (BABAR Collab.), arXiv:hep-ex/0408073.
- [117] B. Aubert *et al.* (BABAR Collab.), Phys. Rev. **D72**, 072003 (2005); Erratum-*ibid.* **D74**, 099903(2006).
- [118] B. Aubert *et al.* (BABAR Collab.), arXiv:hep-ex/0507094.
- [119] A. Poluektov *et al.* (Belle Collab.), Phys. Rev. D **70**, 072003 (2004).  
Haibo
- [120] K. Abe *et al.* (Belle Collab.), arXiv:hep-ex/0411049
- [121] K. Abe *et al.* (Belle Collab.), arXiv:hep-ex/0504013, contributed to Moriond Electroweak 2005 and CKM 2005 Workshop.
- [122] B. Aubert *et al.* (BABAR Collab.), Phys. Rev. Lett. **95**, 121802 (2005)
- [123] B. Aubert *et al.* (BABAR Collab.), arXiv:hep-ex/0507101, contributed to the International Europhysics Conference On High-Energy Physics (HEP 2005), 7/21-7/27/2005, Lisbon, Portugal.
- [124] A. Garmash, arXiv:hep-ex/0505048; A. Garmash, arXiv:hep-ex/0510059;
- [125] K. Abe *et al.* (Belle Collab.), Phys. Rev. D **69**, 112002 (2004)
- [126] K. Abe *et al.* (Belle Collab.), arXiv:hep-ex/0412072, ICHEP04 11-0710, BELLE-CONF-0460
- [127] K. Abe *et al.* (Belle Collab.), Phy. Rev. Lett. **97**, 242001 (2006)[arXiv:hep-ex/0409005].
- [128] B. Aubert *et al.* (BABAR Collab.), arXiv:hep-ex/0408099, contributed to the 32nd International Conference on High-Energy Physics, ICHEP 04, 16-22 August 2004, Beijing, China .

- [129] A. Bondar, T. Gershon and P. Krokovny, Phys. Lett. B **624**, 1 (2005)
- [130] K. Abe *et al.* (Belle Collab.), arXiv:hep-ex/0507065
- [131] B. Aubert *et al.* (BABAR Collab.), Phys. Rev. Lett. **95** (2005) 171802 [arXiv:hep-ex/0412040].
- [132] B. S. Zou and D. V. Bugg, Eur. Phys. J. A **16**, 537 (2003)
- [133] S. Dulat and B. S. Zou, Eur. Phys. J. A **26**, 125 (2005)
- [134] J. Z. Bai *et al.* (BES Collab.), Phys. Rev. D **68**, 052003 (2003)
- [135] J. Z. Bai *et al.* (BES Collab.), Phys. Lett. B **476**, 25 (2000)
- [136] J. Z. Bai *et al.* (BES Collab.), Phys. Lett. B **472**, 207 (2000)
- [137] J. Z. Bai *et al.* (BES Collab.), Phys. Lett. B **472**, 200 (2000)
- [138] M. Ablikim *et al.* (BES Collab.), Phys. Rev. D **72**, 092002 (2005)
- [139] M. Ablikim *et al.* (BES Collab.), Phys. Lett. B **619**, 247 (2005)
- [140] M. Ablikim *et al.* (BES Collab.), Phys. Lett. B **598**, 149 (2004)
- [141] M. Ablikim *et al.* (BES Collab.), Phys. Lett. B **603**, 138 (2004)
- [142] M. Bauer, B. Stech and M. Wirbel, Z. Phys. C **34**, 103 (1987); P. Bedaque, A. Das and V.S. Mathur, Phys. Rev. D **49**, 269 (1994); L.-L. Chau and H.-Y. Cheng, Phys. Rev. D **36**, 137 (1987); K. Terasaki, Int. J. Mod. Phys. A **10**, 3207 (1995); F. Buccella, M. Lusignoli and A. Pugliese, Phys. Lett. B **379**, 249 (1996)
- [143] J. D. Jackson, Nuovo Cim. **34**, 1644 (1964)
- [144] R. H. Dalitz, *Phil. Mag.* **44**, 1068 (1953)
- [145] S.U. Chung *et al.*, Ann. Physik. **4**, 404 (1995)
- [146] K. L. Au, D. Morgan and M. R. Pennington, Phys. Rev. D **35**, 1633 (1987)
- [147] V. V. Anisovich and A. V. Sarantsev, Eur. Phys. J. A **16**, 229 (2003)
- [148] I. J. R. Aitchison, Nucl. Phys. **A 189**, 417 (1972)
- [149] S. Fajfer, R. J. Oakes and T. N. Pham, Phys. Rev. D **60**, 054029 (1999)
- [150] H. Y. Cheng and K. C. Yang, Phys. Rev. D **66**, 054015 (2002)
- [151] S. Fajfer, T. N. Pham and A. Prapotnik, Phys. Rev. D **70**, 034033 (2004)
- [152] H. Y. Cheng, C. K. Chua and A. Soni, arXiv:hep-ph/0506268
- [153] J. Blatt and V. Weisskopf, *Theoretical Nuclear Physics*, New York: John Wiley & Sons (1952)

- [154] F. von Hippel and C. Quigg, Phys. Rev. D **5**, 624, (1972)
- [155] C. Zemach, Phys. Rev. B **133**, 1201 (1964); C. Zemach, Phys. Rev. B **140**, 97 (1965)
- [156] V. Filippini, A. Fontana and A. Rotondi, Phys. Rev. D **51**, 2247 (1995)
- [157] M. Jacob and G. C. Wick, Annals Phys. **7**, 404 (1959) [Annals Phys. **281**, 774 (2000)]; S. U. Chung, Phys. Rev. D **48**, 1225, (1993); J. D. Richman, CALT-68-1148
- [158] S. M. Flatté, Phys. Lett. B **63**, 224 (1976)
- [159] G. J. Gounaris and J. J. Sakurai, Phys. Rev. Lett. **21** 244, (1968)
- [160] R. Brun *et al.*, GEANT 3.15, CERN Report No. DD/EE/84-1 (1987); R. Brun *et al.*, GEANT 3.21, CERN Program Library Long Writeup W5013 (1993), unpublished; S. Agostinelli *et al.* (GEANT4 Collab.), Nucl. Instrum. Meth. A **506**, 250 (2003)

## Part II

**$e^+e^-$  Collision at  $\sqrt{s} = 2 - 5$  GeV**

**Conveners: Yuan-Ning Gao, Xiao-Yuan Li**

### Contributors

**H. M. Hu, X. Y. Li, J. P. Ma, G. Rong, P. Wang,  
D. H. Zhang**



# Chapter 4

## Physics Processes and Radiative Corrections

### 4.1 Physics Processes at BEPC-II <sup>1</sup>

To help make this document self-contained, we list here basic  $e^+e^-$  continuum processes that can be explored at BEPC-II. In addition to their own interest, continuum amplitudes have an important influence in the resonance region, *e.g.* in the  $J/\psi$ ,  $\psi'$  and  $\psi''$  peak regions. A careful understanding of continuum processes is necessary for detailed studies at these resonances. Since the cms energy of BEPC-II is far below the mass of the  $Z$ -boson, weak interactions will not play an important role. Therefore, the basic processes are only QED- and QCD-related.

There are many QED-processes in  $e^+e^-$  collisions. We limit ourself to those that contain only two particles in the final state. These processes are  $e^+e^- \rightarrow \mu^+\mu^-$  or  $\tau^+\tau^-$ ,  $e^+e^- \rightarrow e^+e^-$  and  $e^+e^- \rightarrow \gamma\gamma$ . We first consider the process

$$e^-(p_1) + e^+(p_2) \rightarrow \mu^-(p_3) + \mu^+(p_4), \quad (4.1.1)$$

where the four-momenta are indicated in the brackets. We define the quantities

$$s = (p_1 + p_2)^2, \quad \cos \theta = \frac{\vec{p}_1 \cdot \vec{p}_3}{|\vec{p}_1||\vec{p}_3|}. \quad (4.1.2)$$

Since the mass of the electron is tiny, we neglect it, but we keep terms involving the mass of the  $\mu$ . The differential cross-section for  $e^+e^- \rightarrow \mu^+\mu^-$  is given by:

$$\begin{aligned} \frac{d\sigma}{d\Omega} &= \frac{\alpha^2}{4s} \sqrt{1 - \frac{4m_\mu^2}{s}} \left( 1 + 4\frac{m_\mu^2}{s} + \left( 1 - \frac{4m_\mu^2}{s} \right) \cos^2 \theta \right), \\ \sigma &= \frac{4\pi\alpha^2}{3s} \sqrt{1 - \frac{4m_\mu^2}{s}} \left( 1 + 2\frac{m_\mu^2}{s} \right). \end{aligned} \quad (4.1.3)$$

One gets the result for  $e^+e^- \rightarrow \tau^+\tau^-$  by replacing  $m_\mu$  with  $m_\tau$ .

For the process

$$e^-(p_1) + e^+(p_2) \rightarrow \gamma(p_3) + \gamma(p_4), \quad (4.1.4)$$

---

<sup>1</sup>by J. P. Ma

the differential cross section reads:

$$\frac{d\sigma}{d\Omega} = \frac{\alpha^2}{s} \frac{1 + \cos^2 \theta}{\sin^2 \theta}. \quad (4.1.5)$$

The differential cross-section for Bhabha scattering

$$e^-(p_1) + e^+(p_2) \rightarrow e^-(p_3) + e^+(p_4) \quad (4.1.6)$$

reads:

$$\frac{d\sigma}{d\cos \theta} = \frac{\pi \alpha^2}{2s} \frac{(3 + \cos^2 \theta)^2}{(1 - \cos \theta)^2}. \quad (4.1.7)$$

These formulae summarize all two-body QED processes at BEPC-II. They all can be found in standard text books.

In addition to QED processes, there are also hadronic processes. Because the energy of BEPC-II is rather low, the most interesting continuum process is

$$e^- + e^+ \rightarrow \text{hadrons}. \quad (4.1.8)$$

If  $s$  is sufficiently large, the  $e^-e^+$  pair initially annihilates into quarks and gluons. If we assume that the transmission probability of quarks and gluons into hadrons is unity, the total cross-section can be calculated using perturbative QCD, in the sense that there are no infrared- or collinear divergences. The total cross-section is usually expressed in terms of the famous  $R$ -value, which is defined as:

$$R(s) = \frac{\sigma(e^+e^- \rightarrow \text{hadrons})}{\sigma(e^+e^- \rightarrow \mu^+\mu^-)}. \quad (4.1.9)$$

To the one-loop correction level,  $R$  is given by:

$$R(s) = N_c \sum_q Q_q^2 \left[ 1 + \frac{\alpha_s(\mu)}{\pi} + \mathcal{O}(\alpha_s^2) \right] \theta(s - 4m_q^2). \quad (4.1.10)$$

Here  $\mu$  is the renormalization scale, which is taken to be  $\mu^2 = s$  in order to minimize higher-order corrections. Two-loop level calculations of  $R$  can be found in Ref. [1].

It should be noted that the theoretical basis for the  $R$  calculation is the operator product expansion (OPE). Therefore, there are addition power-corrections to the perturbative prediction given in the above. These power-corrections can be important for *BES-III*. Part of these corrections can be obtained from QCD sum rules, with a result that reads [2]:

$$\begin{aligned} \int_0^\infty ds \exp(-s/M^2) R^{I=1}(s) &= \frac{3}{2} \left[ 1 + \frac{\alpha_s(M)}{\pi} + \mathcal{O}(\alpha_s^2) \right. \\ &\quad \left. + \frac{\pi^2}{3M^4} \langle 0 | \frac{\alpha_s(M)}{\pi} G_{\mu\nu}^a G^{a,\mu\nu} | 0 \rangle - \frac{448\pi^3}{81M^6} |\langle 0 | \bar{q}q | 0 \rangle|^2 + \dots \right], \end{aligned}$$

where the scale parameter  $M$  should be taken as a typical hard scale. In general, these power corrections to  $R$  are expected to be small.

Other QCD processes, such as jet production, inclusive-, and exclusive hadron production have been studied at  $e^+e^-$  colliders with cms energies that are much higher than those of BEPC-II. However, since *BES-III* will primarily concentrate on physics in the resonance regions, these topics may not be heavily pursued.

## 4.2 Radiative corrections<sup>2</sup>

All measurements made by  $e^+e^-$  colliding experiments must apply radiative correction in order to get results that can be compared with results from other types of experiments.

### 4.2.1 First order perturbation and exponentiation

The lowest-order perturbation term takes account of initial state radiation of a single photon. The cross section is expressed by the Bonneau and Martin formula [3]

$$\begin{aligned}\sigma(W) = \sigma_0(W) &\{1 + \frac{2\alpha}{\pi}(\frac{\pi^2}{6} - \frac{17}{36}) + \frac{13}{12}\beta \\ &+ \beta \int_0^E \frac{dk}{k} [(1 - \frac{k}{E} + \frac{k^2}{2E^2}) \frac{\sigma_0(W-k)}{\sigma_0(W)} - 1]\},\end{aligned}\quad (4.2.11)$$

where

$$\beta = \frac{\alpha}{\pi} \log(\frac{s}{m_e^2} - 1). \quad (4.2.12)$$

In Eq. (4.2.11), the upper limit of integration,  $k_{max}$ , has been set to  $E$ , corresponding to the fact that an electron can lose all its energy to radiation. Soft photon emission is contained in the  $dk/k$  factor, which is just the classical result corrected for energy conservation by the cross section  $\sigma_0(W-k)$ . It is convenient to rewrite Eq. (4.2.11) with the soft photon part displayed separately from the “hard” terms

$$\begin{aligned}\sigma(W) = \sigma_0(W) &[1 + \delta] + \beta \int_0^E \frac{dk}{k} [\sigma_0(W-k) - \sigma_0(W)] \\ &- \frac{\beta}{E} \int_0^E dk (1 - \frac{k}{2E}) \sigma_0(W-k);\end{aligned}\quad (4.2.13)$$

where

$$\delta = \frac{2\alpha}{\pi}(\frac{\pi^2}{6} - \frac{17}{36}) + \frac{13}{12}\beta$$

is a small number that changes slowly with energy. (At the  $J/\psi$ ,  $\beta = 0.076$ ,  $\delta = 0.085$ .) The last term in Eq. (4.2.13) is small compared with the first two.

If instead of integrating over the entire photon energy range, we only include photons up to a maximum energy of  $k_{max}$ , and we assume that the variation of  $\sigma_0(s)$  with  $s$  is very slow, we have

$$\sigma(s) \approx \sigma_0(s)(1 + \delta_1 + \beta \ln(\frac{k_{max}}{E})), \quad (4.2.14)$$

where

$$\delta_1 = \frac{3}{4}\beta + \frac{2\alpha}{\pi}(\frac{\pi^2}{6} - \frac{1}{4}).$$

The variable  $k_{max}$  is usually determined by the experimental event selection criteria. However in some experiments there is a natural cut off. For example, in the case of a

---

<sup>2</sup>By Ping Wang

resonance, the width of the resonance  $\Gamma$  provides such a natural cut off. Another example is the  $\tau$ -pair cross section near threshold. Here  $k_{max} = E - 2m_\tau$ .

For a narrow resonance like the  $J/\psi$

$$\beta \ln\left(\frac{\Gamma}{M}\right) \approx -81\%,$$

which is very large for a perturbative expansion. Similarly large values obtain for the  $\psi'$ . For energies near the  $\tau$ -pair threshold,  $\beta \ln\left(\frac{E-2m_\tau}{E}\right)$  can also be large. In these circumstances, the first-order perturbation expansion of Eq. (4.2.14) is not enough, and higher-order terms, including multi-photon emission, must be included. This is done by

$$\begin{aligned} \sigma &= \sigma_0(1 + \delta_1 + \delta_2)(1 + \beta \ln\left(\frac{k_{max}}{E}\right) \\ &\quad + \frac{1}{2!}\beta^2 \ln^2\left(\frac{k_{max}}{E}\right) + \frac{1}{3!}\beta^3 \ln^3\left(\frac{k_{max}}{E}\right) + \dots) \\ &= \exp\left(\beta \ln\left(\frac{k_{max}}{E}\right)\right) = \left(\frac{k_{max}}{E}\right)^\beta. \end{aligned} \quad (4.2.15)$$

That is, the bremsstrahlung spectrum is modified to become

$$\frac{d\sigma}{dk} = \sigma_0(1 + \delta + \dots) \beta k^{(\beta-1)}, \quad (4.2.16)$$

where the  $1/k$  factor is replaced by  $k^\beta(1 + \delta_1 + \dots)/k$ . This is illustrated in Fig. (4.1). The summation can be justified if the emitted photon is collinear with the incoming electron,<sup>3</sup> in which case the electron is almost on the mass shell after the emission. This means that the electron, after emitting the photon, is undisturbed and, so, each successive photon is independent.

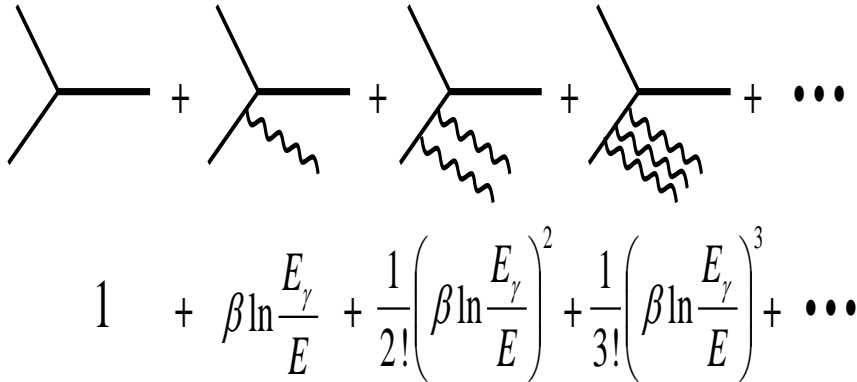


Figure 4.1: The summation of multiphoton emission.

To accommodate the  $s$  dependence of  $\sigma_0(s)$  in multi-photon emission, we introduce a factor

$$\exp[-\beta \ln(E/k)] = (k/E)^\beta$$

<sup>3</sup>In this section we use electron to designate either the incoming electron or positron.

into the integrand in Eq. (4.2.13). The radiatively corrected cross section then becomes

$$\sigma(W) = \beta \int_0^E \frac{dk}{k} \left(\frac{k}{E}\right)^\beta \sigma_0(W - k) + \delta\sigma_0(W). \quad (4.2.17)$$

This is called exponentiation. It was originally conjectured by Schwinger in 1949 [4], and later developed by Yennie, Frautschi and Suura in 1961 [5].

The exponentiation in Eq. (4.2.17) is done after phase space integration over photon momenta, which is appropriate for inclusive distributions. This method is called “inclusive” exponentiation, in contrast to “exclusive exponentiation” in Monte Carlo simulations as discussed below.

### 4.2.2 Structure function approach

A long-standing question in radiative correction methodology was what part of the lowest-order radiative corrections should one exponentiate? This was rigorously solved based on quantum field theory by Kuraev and Fadin [6, 7, 8]. In their approach, single-photon annihilation is regarded as a Drell-Yan process. In the leading logarithmic approximation (*i.e.* when only the terms containing  $\log(\frac{s}{m_e^2})$  are retained), the cross section can be expressed in the form

$$\sigma(s) = \int \int dx_1 dx_2 D(x_1, s) D(x_2, s), \tilde{\sigma}(x_1 x_2 s), \quad (4.2.18)$$

where

$$\tilde{\sigma}(s) = \frac{\sigma_B(s)}{|1 - \Pi(s)|^2}.$$

In the above expression,  $\sigma_B(s)$  is the Born-order cross section, and  $\Pi(s)$  is the vacuum polarization factor. The function  $D(x, s)$  in Eq. (4.2.18) is called the structure function. It satisfies the Lipatov-Altarelli-Parisi equation [9]:

$$D(x, Q^2) = \delta(x - 1) + \int_{m_e^2}^{Q^2} \frac{\alpha(Q'^2)}{2\pi} \frac{dQ'^2}{Q'^2} \int_x^1 \frac{dz}{z} P(z) D\left(\frac{x}{z}, Q'^2\right), \quad (4.2.19)$$

where  $\alpha(Q^2)$  is the running coupling constant given by

$$\alpha(Q^2) = \alpha / \left[1 - \frac{\alpha}{3\pi} \ln \frac{Q^2}{m^2}\right],$$

and  $P(z)$  is the regularized  $e \rightarrow e + \gamma$  splitting function.

$$P(z) = \frac{1 + z^2}{1 - z} - \delta(1 - z) \int_0^1 \frac{dx(1 + x^2)}{1 - x}. \quad (4.2.20)$$

The structure function has a clear and intuitive meaning: it represents the probability density for finding “inside” the parent electron a virtual electron with momentum fraction  $x$  and virtuality  $Q^2$ . ( $Q$  is the four-momentum of the virtual electron.)

By solving Eq. (4.2.19) for  $D(x, s)$  and substituting it into Eq. (4.2.18), the radiatively corrected cross section can be expressed as

$$\sigma(s) = \int_0^{1-s_m/s} dx \tilde{\sigma}(s(1-x))F(x, s), \quad (4.2.21)$$

where  $\sqrt{s}$  is the cms energy of the colliding beam,  $\sqrt{s_m}$  is the cut-off of the invariant mass in the event selection,

$$F(x, s) = \beta x^{\beta-1} \delta^{V+S} + \delta^H, \quad (4.2.22)$$

with  $\beta$  expressed in Eq.(4.2.12), and

$$\delta^{V+S} = 1 + \frac{3}{4}\beta + \frac{\alpha}{\pi} \left( \frac{\pi^2}{3} - \frac{1}{2} \right) + \beta^2 \left( \frac{9}{32} - \frac{\pi^2}{12} \right), \quad (4.2.23)$$

$$\begin{aligned} \delta^H = & -\beta \left( 1 - \frac{x}{2} \right) \\ & + \frac{1}{8}\beta^2 \left[ 4(2-x) \ln \frac{1}{x} - \frac{1+3(1-x)^2}{x} \ln(1-x) - 6+x \right]. \end{aligned} \quad (4.2.24)$$

Here the conversion of bremsstrahlung photons to real  $e^+e^-$  pairs is included in the cross section, which is the usual experimental situation. Thus there is cancellation between the contributions of virtual and real  $e^+e^-$  pairs in the leading term [8].

In quantum field theory, it can be rigorously proved that Eq. (4.2.21) summarizes all of the leading-log (LL) terms such as

$$\left( \frac{\alpha}{\pi} \log \left( \frac{s}{m_e^2} \right) \right)^N$$

for  $N$  from 1 to  $\infty$ . This can be improved to include the next-to-leading-log (NLL) terms [16], such as

$$\left( \frac{\alpha}{\pi} \right)^{(N+1)} \left( \log \left( \frac{s}{m_e^2} \right) \right)^N.$$

Since for the BEPC-II energy scale,  $\frac{s}{m_e^2}$  is large, these leading terms give the main contribution to the initial-state radiative correction. The expression for  $F(x, s)$  in Eq. (4.2.22) also incorporates the non-leading first-order terms from explicit calculation. This method has an accuracy of 0.1%.

The master formula of Eq. (4.2.21) is universally applicable. For example, it can be used for resonances,  $R$ -value measurements, and threshold cross section determinations such as those used for the  $\tau$  mass measurement. One only needs to substitute the Born order cross section for each case.

For resonances,

$$\sigma_B(s) = \frac{12\pi\Gamma_{ee}^0\Gamma_f}{(s-M^2)^2 + \Gamma^2 M^2}, \quad (4.2.25)$$

where  $M$  and  $\Gamma$  are the mass and total width of the resonance;  $\Gamma_{ee}^0$  and  $\Gamma_f$  are the partial widths for the  $e^+e^-$  mode and the detected final state, respectively. Since the decay of a quarkonium  $1^{--}$  state to an  $e^+e^-$  pair is via a virtual photon, there is always vacuum

polarization associated with the process. So, the experimentally measured  $e^+e^-$  partial width, denoted explicitly as  $\Gamma_{ee}^{exp}$ , is related to  $\Gamma_{ee}^0$  by the expression

$$\Gamma_{ee}^{exp} = \frac{\Gamma_{ee}^0}{|1 - \Pi(M^2)|^2}. \quad (4.2.26)$$

The vacuum polarization gets contributions from leptons and hadrons. The latter is treated in Ref. [10]. In order to fit for resonance parameters, the contribution from hadronic resonances to the vacuum polarization should not include the resonance being measured. The Particle Data Group adopts the convention of Refs. [11, 12] that  $\Gamma_{ee}$  means  $\Gamma_{ee}^{exp}$ . So, for the cross section of inclusive hadrons, the vacuum polarization correction should not be applied.

For the near-threshold  $\tau$  mass measurement, the Born-order cross section is

$$\sigma_B(s) = \frac{4\pi\alpha^2}{3s} \frac{v(3-v^2)}{2} F_c(v) F_r(v),$$

with

$$F_c = \frac{\pi\alpha/v}{1 - \exp(-\pi\alpha/v)},$$

and

$$\begin{aligned} F_r = & 1 + (\alpha/\pi v) \{ (1+v^2) [\ln \frac{1+v}{2} \ln \frac{1+v}{1-v} + 2\ell(\frac{1-v}{1+v}) - \frac{\pi^2}{3} + 2\ell(\frac{1+v}{2}) \\ & - 2\ell(\frac{1-v}{2}) - 4\ell(v) + \ell(v^2)] + [\frac{11}{8}(1+v^2) - 3v + \\ & \frac{1}{2} \frac{v^4}{3-v^2}] \ln(\frac{1+v}{1-v}) + 6v \ln(\frac{1+v^2}{2}) - 4v \ln v + \frac{3}{4}v \frac{(5-3v^2)}{(3-v^2)} \} \}, \end{aligned} \quad (4.2.27)$$

where

$$\ell(x) = - \int_0^x \ln(1-t) dt/t,$$

and  $s_m = 4m_\tau^2$  in Eq.(4.2.21). In these equations,  $v = \sqrt{1 - 4m_\tau^2/s}$  is the velocity of  $\tau$ .

Equation (4.2.21) was first derived by Kuraev and Fadin [6], and it has been reproduced and improved by Altarelli and Martinelli, as well as by Nicrosini and Trentadue [7]. Berends and his coworkers have done an explicit second-order calculation to check Kuraev and Fadin's results [8]. As a result of these efforts, Eq. (4.2.21) has been fully checked and is now established as the correct and accurate formula for radiative corrections.

After the publication of Kuraev and Fadin's work, a group of SLAC researchers (G. Alexander, P. Drell, V. Luth *et al.*) used their formula and reanalyzed all  $\psi$  and  $\Upsilon$  family states. They corrected the values of the total widths and leptonic partial widths of these states [12]. The results and the method of this paper have been adopted by the Particle Data Group. Since the mid-1980s, it has been the accepted way to treat radiative corrections by all experiments, including BESI and BESII (*e.g.* the  $J/\psi$  and  $\psi'$  scan, as well as  $\tau$  mass measurement papers) [13, 14, 15]. It has also been used for  $Z$  line-shape fitting in order to extract the parameters of the  $Z$  by the LEP and SLC groups [16].

The correctness and precision of this approach has been fully checked.

### 4.2.3 Initial and final state radiation

Direct calculations show that the vertex correction plus soft bremsstrahlung with photon energy up to  $\Delta E \ll E$  is

$$\frac{3}{4}\beta - \frac{1}{4} + \frac{\pi^2}{6} - \beta \ln\left(\frac{E}{\Delta E}\right), \quad (4.2.28)$$

where  $\beta$  is given by Eq. (4.2.12).

The bremsstrahlung spectrum is

$$\beta \frac{1}{2} [1 + (1 - x)^2] x^{-1} dx, \quad (4.2.29)$$

where  $x = k/E$  with  $k$  the energy of the radiated photon. Here the factor  $\beta$  is due to the radiation of photons along the direction of the incoming electron. It comes from (the square of) the fermion propagator with the emission of a photon by the fermion as shown in Fig. 4.2.

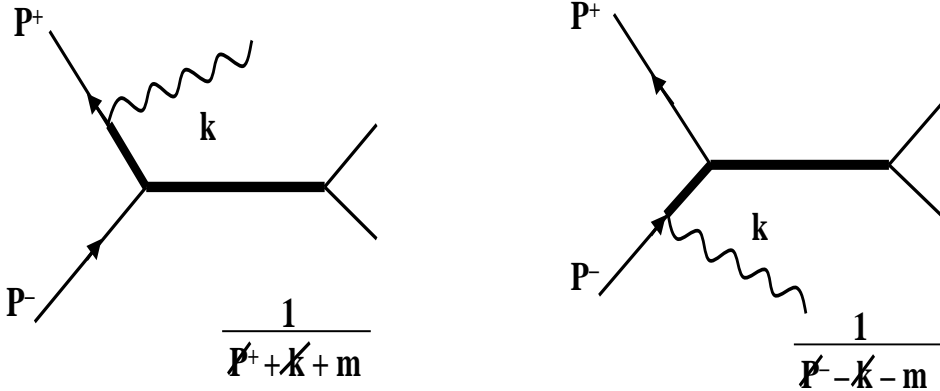


Figure 4.2: The fermion propagator with the emission of a photon by a fermion.

The fermion propagator has the form

$$\begin{aligned} \frac{1}{p - k - m_l} &= \frac{p - k + m_l}{(p - k)^2 - m^2} = \frac{p - k + m_l}{p \cdot k} \\ &= \frac{p - k + m_l}{E_l E_\gamma - |p_l| E_\gamma \cos \theta}. \end{aligned} \quad (4.2.30)$$

For  $E \gg m_e$ ,  $E_l \approx |p_l|$ . So, at  $\theta = 0$ , *i.e.* when the photon is emitted along the direction of the fermion, Eq. (4.2.30) becomes nearly divergent. The term with the factor  $\beta$  comes from the integration of the photon angle relative to the fermion around  $\theta = 0$ . At the GeV mass scale,  $\beta$  is at the order of 0.1, and far greater than the QED fine structure constant  $\alpha$ . The appearance of terms with the factor  $\beta$  is called the collinear divergence (it diverges as  $m_e/E \rightarrow 0$ ), or the mass singularity.

Kinoshita, Lee and Nauenberg observed that if one sums up all the states with the same energy (degenerate states) the mass singularity cancels out to all orders in perturbation

theory. In  $e^+e^-$  experiments, the initial state is preselected by the machine so that both the  $e^+$  and  $e^-$  have a definite energy,  $E_{beam}$ . Thus, the mass singularity due to initial state radiation remains. The final state can be summed and, after doing so, we expect their mass singularity will cancel to all orders in perturbation theory. This can be seen mathematically by integrating the bremsstrahlung spectrum in Eq. (4.2.29) from  $\Delta E \ll E$  to  $E$ , we obtain

$$\begin{aligned} & \int_{\Delta E/E}^1 \beta(x^{-1} - 1 + \frac{1}{2}) dx \\ & \approx \beta \left( \ln \frac{E}{\Delta E} - \frac{3}{4} \right). \end{aligned} \quad (4.2.31)$$

Adding Eq. (4.2.31) to Eq. (4.2.28), the radiative correction becomes

$$\frac{2\alpha}{\pi} \left( -\frac{1}{4} + \frac{\pi^2}{6} \right),$$

which no longer has a mass singularity.

The mass singularity from initial state bremsstrahlung  $\beta$  and the vertex correction do not cancel each other when the photon spectrum is integrated because as the bremsstrahlung is emitted from the initial electron or positron, the virtual photon four-momentum changes from  $s$  to  $s(1 - k/E)$ . Usually the cross section depends on  $s$ . For example, in the point-like coupling  $e^+e^- \rightarrow \mu^+\mu^-$ , the cross section is inversely proportional to  $s$ . In such a case, we have to multiply the integrand of Eq. (4.2.31). by a factor

$$(1 - x)^{-1}.$$

In this case, the mass singularity of the resulting expression does not cancel that from vertex correction. In the language of Lee and Nauenberg we do not expect any cancellation for the initial state because we are not summing over all degenerate initial states. The machine preselects the electron and positron to each have energy  $E_{beam}$ , and no other degenerate state participates in the interaction.

This is very important when dealing with hadronic final states that are usually too complicated to be radiatively corrected. The above indicates that we can ignore the radiative corrections to the final states to an accuracy of  $\frac{\alpha}{\pi}$ .

Nevertheless, in some MC generators with 0.1% precision, final state radiation is included. This is discussed below.

#### 4.2.4 MC generators: inclusive process

The KKMC Montr Carlo program [18] generates radiatively corrected  $e^+e^-$  annihilations to  $\mu^+\mu^-$ ,  $\tau^+\tau^-$  final states as well as inclusive hadronic final states formed from  $u$ ,  $d$ ,  $s$ ,  $c$ ,  $b$  quark pairs.

To realize the Monte Carlo simulation, the authors of KKMC introduce “coherent exclusive exponentiation.” The exclusivity means that the exponentiation procedure is done at the level of the fully differential (multi-photon) cross section, before any phase-space integration over the photon momenta is done. This is in contrast to the “inclusive

exponentiation” of Eq. (4.2.17) where the exponentiation is done after the integration of the photons’ phase space.

In the Monte Carlo event, multiple photons are emitted from the initial state electron; each photon may have a momentum with a finite angle from the incoming electron. The algorithm of coherent exclusive exponentiation treats radiative corrections to infinite order not only including initial-state-radiation, but also interference between initial-final state radiation and narrow resonances. Full scale next-to-leading-log corrections are included. For quarks and  $\tau$  leptons, the simulation of hadronization is done by PYTHIA (in an earlier version JETSET was used). Beam polarization and spin effects in  $\tau$  decays, both longitudinal and transverse, are taken into account.  $\tau$  decays are done by TAUOLA. A precision level of 0.2% is achieved.

The program language is FORTRAN 77, with popular extensions such as long variable names, long source lines, etc. There is a make file that controls the compiling. The program is written with the possible future translation into an object-oriented language such as C++ in mind. The program source code is organized into modules, also called pseudo-classes, which have the structure of the C++ class, as far as this is possible to do in FORTRAN 77.

For most users of KKMC in  $e^+e^-$  experiments, a set of input parameters must be specified. This is done in the file user.input. For most of the parameters, the users are advised to use the default values, or if changed, with special caution, *e.g.* in consultation with the program authors. There are also some parameters which are irrelevant to the  $\tau$ -charm threshold physics, *e.g.* those for beamstrahlung and weak interactions. Only a small subset of the parameters stored in xpar(10000) need to be set by the users.

#### 4.2.5 MC generators: exclusive process

Currently there are two MC generators for exclusive processes: BABAYAGA and MCGPJ.

##### BABAYAGA

BABAYAGA [19] uses the following differential cross section master formula

$$\sigma(s) = \int dx_1 dx_2 dy_1 dy_2 \int d\Omega D(x_1, Q^2) D(x_2, Q^2) D(y_1, Q^2) D(y_2, Q^2) \frac{d\sigma_0(x_1 x_2 s)}{d\Omega}. \quad (4.2.32)$$

Here  $D(x, Q^2)$  is the structure function which satisfies Eq. (4.2.19). Equation (4.2.32) accounts for photon radiation emitted by both initial state and final state fermions. Although this formula allows for the inclusion of the universal virtual photon and real photonic corrections up to all orders of perturbation theory, strictly speaking, the radiation included in Eq. (4.2.32) is collinear with the emitting fermions.

The algorithm employed by BABAYAGA goes beyond the collinear approximation by solving Eq. (4.2.19) by a Monte Carlo algorithm, the so-called Parton-Shower algorithm.

This algorithm exactly solves Eq. (4.2.19) with the iterative solution

$$\begin{aligned}
D(x, Q^2) &= \Pi(Q^2, m^2) \delta(1 - x) \\
&+ \frac{\alpha}{2\pi} \int_{m^2}^s \Pi(Q^2, s') \frac{ds'}{s'} \Pi(s', m^2) \int_0^{x_+} dy P(y) \delta(x - y) \\
&+ \left(\frac{\alpha}{2\pi}\right)^2 \int_{m^2}^{Q^2} \Pi(Q^2, s') \frac{ds'}{s'} \Pi(s', m^2) \\
&\times \int_0^{x_+} dx_1 \int_0^{x_+} dx_2 P(x_1) P(x_2) \delta(x - x_1 x_2) \\
&+ \text{3 photons.}
\end{aligned} \tag{4.2.33}$$

In Eq. (4.2.33),

$$\Pi(s_1, s_2) = \exp\left[-\frac{\alpha}{2}\pi \int_{x_2}^{x_1} \frac{ds'}{s'} \int_0^{x_+} dz P(z)\right]$$

is the Sudakov form factor [20], which represents the probability that the electron evolves from virtuality (virtuality is the squared four-momentum of the off-mass-shell particle)  $s_2$  to virtuality  $s_1$  with no emission of photons of energy fraction greater than (an infrared regulator)  $\epsilon = 1 - x_+$ . The solution in Eq. (4.2.33) accounts for “soft + virtual” and real photons radiation up to all orders of perturbation theory in the leading-logarithmic approximation. The Sudakov form factor exponentiates the leading logarithmic contribution of the  $\mathcal{O}(\alpha)$  “soft + virtual” cross section, as well as the dominant contribution coming from the infrared cancellation between the virtual box and the initial-final state interference of the bremsstrahlung diagrams.

In the implementation of the parton shower algorithm, BABAYAGA simulates a shower of photons emitted by the electron according to Eq. (4.2.33). When the algorithm stops, we are left with the energy fraction  $z_1$  of each photon, distributed according to the splitting function of Eq. (4.2.20), as well as the virtualities of the electron at each branching and the remaining energy fraction  $x$  of the electron after the showering. The  $x$  variable is distributed according to the structure function  $D(x, Q^2)$ . By means of these quantities, an approximate branching kinematics is obtained.

The main advantage of the parton shower algorithm with respect to the collinear treatment of the electron evolution is the possibility of going beyond the strictly collinear approximation and generating transverse momentum  $p_\perp$  of the electrons and photons at each branching. In fact, in BABAYAGA the kinematics of the branching process

$$e(p) \rightarrow e'(p') + \gamma(q)$$

is as

$$p = (E, \vec{0}, p_z),$$

$$p' = (zE, \vec{p}_\perp, P'_z),$$

$$q = ((1 - z)E, -\vec{p}_\perp, q_z). \tag{4.2.34}$$

Once the variables  $p^2$ ,  $p'^2$  and  $z$  are generated by the parton shower algorithm, the on-shell condition  $q^2 = 0$ , together with longitudinal momentum conservation, allows one to obtain an expression for the  $p_\perp$  value:

$$p_\perp^2 = (1 - z)(zp^2 - p'^2).$$

To first order in  $p^2/E^2 \ll 1$ ,  $p_\perp^2 \ll 1$ . All the photons generated by BABAYAGA can have transverse momentum, which is in contrast with the other Monte Carlo generator for exclusive processes, MCGPJ. In the latter only one photon can be emitted at a large angle from one of the fermions, while other photons are emitted within a very small angle from the fermions.

In BABAYAGA, up to 10 photons are emitted from each incoming and outgoing particles in the branching process. Altogether up to 40 photons can be produced in each event. But only the 2 most energetic ones are output.

BABAYAGA is written only for two-body final states. Besides  $e^+e^-$ ,  $\mu^+\mu^-$ ,  $\gamma\gamma$ , hadronic final states include only  $\pi^+\pi^-$ . For this mode, final state radiation is not considered. In the output, there are two final state particles and two photons. The accuracy level is 0.5%. The programming language is FORTRAN.

Unlike KKMC, which stores input parameters in an array xpar with dimension of 10000, the input file of BABAYAGA has only 27 parameters. Their meaning is clearly explained in the file input.txt.

### High precision MC generator for the Bhabha process

BABAYAGA@NLO [21] is a Monte Carlo program that simulates the Bhabha process at flavor factories from the  $\phi$  to the  $\Upsilon$ 's. The calculation is based on the matching of exact next-to-leading-order corrections with a parton shower algorithm.

A corrected differential cross section in the parton shower approach can be written as

$$\begin{aligned} d\sigma^\infty &= \Pi(Q^2, \epsilon) F_{SV} \{ d\sigma_0 + \sum_{n=1}^{\infty} \frac{d\sigma_0}{n!} \\ &\quad \times \prod_{i=1}^n \left[ \frac{\alpha}{2\pi} P(x_i) I(x_i) dx_i \theta(x_i - \epsilon) F_{i,H} \right] \}, \end{aligned} \quad (4.2.35)$$

where  $F_{SV}$  and  $F_{i,H}$  are identical to 1 in the pure parton shower case. To go beyond the leading logarithm approximation and preserve the summation of the higher-order corrections, this program sets

$$\begin{aligned} F_{SV} &= 1 + \frac{d\sigma_{SV}^{\alpha,ex} - d\sigma_{SV}^{\alpha,PS}}{d\sigma_0}, \\ F_{i,H} &= 1 + \frac{d\sigma_{i,H}^{\alpha,ex} - d\sigma_{i,H}^{\alpha,PS}}{d\sigma_{i,H}^{\alpha,PS}}, \end{aligned} \quad (4.2.36)$$

where  $d\sigma_{SV}^{\alpha,ex}$  are the complete expressions for the soft and virtual  $\mathcal{O}(\alpha)$  cross sections and the real one-photon emission cross section;  $d\sigma_{SV}^{\alpha,PS}$   $d\sigma_{i,H}^{\alpha,PS}$  are the parton-shower

approximations for the soft and virtual cross sections and the real one photon emission cross section.

Its accuracy level is 0.1%. Currently, this is the most accurate Monte Carlo program for the Bhabha process. This program is ideally suited for luminosity measurements at *BES-III*.

## MCGPJ

MCGPJ is another Monte Carlo generator for exclusive processes [22]. The current version simulates  $e^+e^-$ ,  $\mu^+\mu^-$ ,  $\pi^+\pi^-$ ,  $K^+K^-$  and  $K_SK_L$  final states.

This program takes higher-order radiative corrections into account by means of the structure function formalism. It involves a convolution of the Born-order cross section with the electron structure function, which describes the leading effects due to emission of photons in the collinear region as well as the radiation of  $e^+e^-$  pairs. The collinear region is defined as a part of the angular phase space inside four narrow cones surrounding the directions of the motion of the initial and final state particles. The emitted photons are inside these cones, which have an opening angle  $2\theta_0$ . The angle  $\theta_0$  has to obey the restriction

$$\frac{m_e}{E_{cm}} \ll \theta_0 \ll 1.$$

This serves as an auxiliary parameter and usually its value is taken to be

$$\theta \sim \sqrt{\frac{2m_e}{E_{cm}}}.$$

Although this program introduces an additional parameter  $\theta_0$ , the physical results are independent of its value. (As is the case for the other auxiliary parameter  $\epsilon$ , —the infrared cutoff (or so-called infrared regulator)— that is used in every Monte Carlo program involving radiative corrections.) The calculation takes into account hard photons emitted in the four narrow cones, which give the main contribution to the radiative correction. In addition, one hard photon is allowed to be emitted at a large angle that is outside the narrow cones. This is included by incorporating an explicit  $\mathcal{O}(\alpha)$  calculation. The accuracy level of the program is 0.2%. It is written in C++.

For the modes other than the Bhabha process, MCGPJ has higher accuracy than BABAYAGA. Unlike BABAYAGA, MCGPJ can be extended to three-body and multi-body final states.

### 4.2.6 MC generators: the radiative return process

The usual way to measure  $R$  values is by energy-scan experiments conducted on  $e^+e^-$  colliders. But an alternative option has been suggested which uses radiative-return at flavor factories [23]. These colliders operate at fixed energies and with enormous luminosities. This peculiar feature of a factory allows the use of the radiative return, *i.e.* the reaction

$$e^+(p_1)e^-(p_2) \rightarrow \gamma(k_1) + \gamma^*(Q) (\rightarrow \text{hadrons})$$

to explore the hadronic cross section in a wide range of  $Q^2$  in a single experiment.

Nominally, invariant masses of hadronic systems everywhere between the production threshold for the respective mode and the operating cms energy of the flavor factory are accessible. In practice, in order to isolate the reaction, it is useful to consider only events with a hard photon, which significantly lowers the accessible mass range.

A dedicated Monte Carlo program PHOKHARA [24] has been developed for such processes. It includes next-to-leading-order corrections from virtual and real photon emission. In the generated events, one or two photons are emitted from the incident  $e^+$  or  $e^-$ , or the final state particles. Two-body and multi-body hadronic final states are included. The present version has nine modes, including  $\mu^+\mu^-$ ,  $\pi^+\pi^-$ ,  $K^+K^-$ , nucleon-anti-nucleon,  $\pi^+\pi^-\pi^0$ ,  $\pi^+\pi^-\pi^+\pi^-$ ,  $\pi^+\pi^-\pi^0\pi^0$  and  $\Lambda\bar{\Lambda}$ . Final-state radiation and interference between initial- and final-state radiation are included for two-body final states.

The programing language is FORTRAN. It is based on the calculation of Feynman diagrams with one or two emitted photons and one-loop corrections.

#### 4.2.7 Summary

In  $e^+e^-$  annihilation experiments, radiative corrections are crucial for achieving precision results in virtually all types of measurements. Sometimes they can change the observed numerical results in a profound way, particularly measurements of resonance properties and cross section determinations near the production threshold. Thanks to steady progress of theoretical techniques, we can now calculate the integrated cross section using formulae derived with the structure function approach. This approach sums up the contributions of leading logarithmic terms to infinite order of  $\alpha$  in the QED perturbative expansion. For differential cross sections, there are different methods to include higher order terms in  $\alpha$ . These schemes are implemented by Monte Carlo programs for both inclusive and exclusive processes. The latest Monte Carlo programs achieve 0.1% precision levels for the Bhabha process (BABAYAGA@NLO), and 0.2% precision levels for other inclusive and exclusive processes (KKMC, MCGPJ and PHOKHARA). They are for general use at flavor factory experiments such as *BES-III*.

# Chapter 5

## Hadronic fragmentation<sup>1</sup>

Quantum Chromodynamics (QCD) is the unique candidate theory for the strong interactions. However, hadronization processes occur in the nonperturbative regime where there are no reliable first principle calculations. Therefore, phenomenological models have been built and are widely used in experiments.

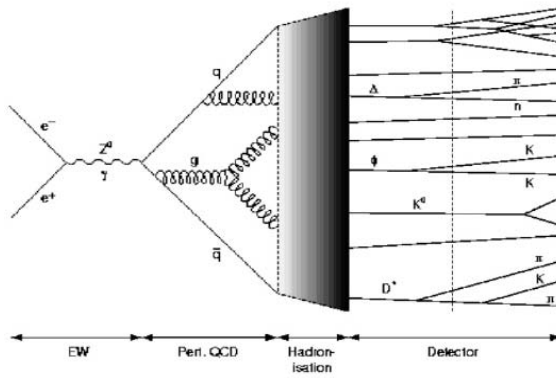


Figure 5.1: Schematic illustration of hadron production in  $e^+e^-$  annihilation.

Hadron production in inclusive  $e^+e^-$  annihilation processes is illustrated in Fig. 5.1. There are two successful hadronization models at high energies: the cluster model (HERWIG) [86, 102] and the Lund string fragmentation model (JETSET) [103, 104]. They agree well with data at the  $Z^0$  energy scale, but were not intended for simulating processes at intermediate and low energy scales. The approximate conditions that are incorporated into these models are not appropriate in the BEPC-II energy region.

---

<sup>1</sup>By Hai-Ming Hu

## 5.1 String fragmentation in the Lund model

The transverse and longitudinal momentum of hadrons relative to directions of the primary partons produced in  $e^+e^-$  annihilations are governed by different mechanisms. In the Lund model [105], the transverse momentum is described as a quantum tunneling effect, and the longitudinal momentum is described as fragmenting string in  $(1+1)$  dimensional (*i.e.* time  $t$  and longitudinal distance  $x$ ) phase space.

The Lund model uses a semi-classical massless relativistic string to model the QCD color field. The foundations of the Lund model are universal, including relativity, causality and quantum mechanics. The picture of the string may be summarized as: the color force field between the  $q\bar{q}$  pair is confined to a narrow tube with potential density  $\kappa$ ; quarks  $q$  and  $\bar{q}$  located at the ends of string; a gluon  $g$  is treated as a transverse excitation of string. The string fragmentation is pictured as: the  $q$  and  $\bar{q}$  stretch field force as they move along in opposite directions in the center-of-mass system; new  $q\bar{q}$  (or  $q\bar{q}q'\bar{q}'$ ) pairs tunnel out from the quantum vacuum, and the string breaks at the production vertex, forming two strings that terminate on the produced quarks. The fragmentation of the string is causally disconnected, and follows a scaling behavior. The produced  $q\bar{q}$  (or  $q\bar{q}q'\bar{q}'$ ) may form mesons and baryons if they carry with the correct flavor quantum numbers, otherwise they just behave as vacuum fluctuations and do not lead to any observable effects.

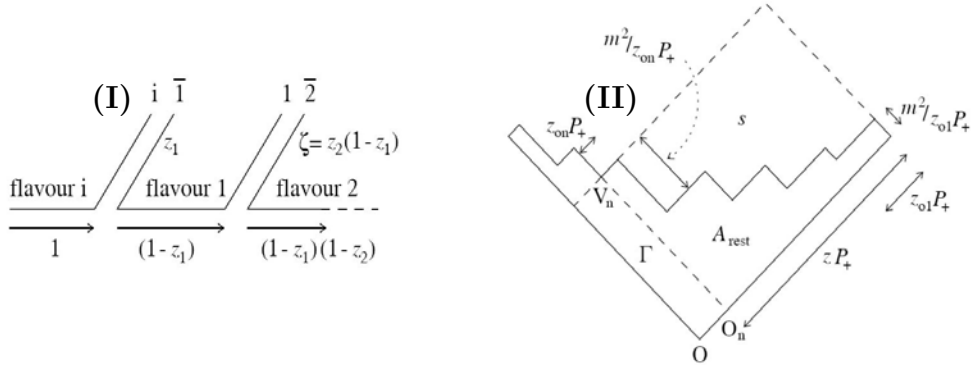


Figure 5.2: (I): an iterative cascade chain, where  $i$  is the flavor of the initial quark, and  $1\bar{1}$ ,  $2\bar{2}$  are the flavors of step-produced quark pairs,  $z_j$  is the light-cone momentum of the  $j$ -th particle; (II): an  $n$ -particle cluster in the infinite iterative processes, where the fragmentation starts from the right end.

In the Lund model,  $n$  hadrons are produced via string fragmentation in an iterative way [105] [see Figure 5.2(I)]. The Lund model based JETSET program is a successful generator for high energies, such as at  $Z^0$  scale, in which the hadron production is simulated according to the fragmentation function in iterative and inclusive ways:

$$f(z) = \frac{N}{z} (1-z)^a \exp(-bm^2/z), \quad (5.1.1)$$

where  $m$  is the mass of hadron,  $z$  is the fraction of light-cone momentum,  $a$  and  $b$  are two dynamical parameters and  $N$  is the normalization constant. In the deduction of  $f(z)$ , right-left symmetry for string fragmentation is assumed (fragmentation starting

from the right end and left end of the string are equal) and the cluster with energy  $\sqrt{s}$  is produced from a total system for which an infinitely large energy is assumed. Thus, the remaining string with area  $\Gamma$  continues to have infinitely large energy after each step of the fragmentation [see Fig. 5.2(II)], which allows the effects of hadronic masses to be ignored. At the  $Z^0$  scale, where the total cms energy is much larger than the sum of the masses of the produced hadrons, the above assumptions are a good approximation. In the BEPC-II energy region, hadronization finishes within a few fragmentation steps; Table 5.1 shows values for  $P(n)$ , the probability for producing  $n$  hadrons. The momentum of the first  $n - 1$  hadrons are determined by  $f(z)$ , while the last one is set by the conservation of the energy-momentum. Thus, at low energies, the momentum of a large fraction of the produced hadrons violate the Lund model assumptions. This problem is avoided by having the string fragment in an exclusive way using the Lund area law.

Table 5.1: The probability  $P(n)$  of the string fragmenting into  $n$  preliminary hadrons.

$E_{ECM}(\text{GeV})$	$P(2)$	$P(3)$	$P(4)$	$P(5)$	$P(6)$
2.200	0.1745	0.6507	0.1593	0.0148	0.0005
2.600	0.1416	0.6435	0.1922	0.0217	0.0010
3.070	0.1125	0.6256	0.2286	0.0316	0.0017
3.650	0.0930	0.6446	0.2925	0.0502	0.0034

## 5.2 The Lund area law

In Lund model, the production of the  $n$ -hadron state takes the following steps

$$e^+e^- \Rightarrow q\bar{q} \Rightarrow \text{string} \Rightarrow m_1 + m_2 + \cdots + m_n.$$

Similar to the expression in quantum field theory, the total matrix element of the hadronization is written as [82, 108]

$$\mathcal{M} \equiv \mathcal{M}_{\text{QED}}(e^+e^- \rightarrow q\bar{q})\mathcal{M}_{\text{LUND}}(q\bar{q} \rightarrow m_1, m_2, \dots, m_n). \quad (5.2.2)$$

The first step is described by the usual QED matrix element  $\mathcal{M}_{\text{QED}}$ . The dynamics of the second step, which governs a string fragmenting into a particular  $n$ -particle state with masses  $m_1, m_2, \dots, m_n$  is factorized as

$$\mathcal{M}_{\text{LUND}}(q\bar{q} \rightarrow m_1, m_2, \dots, m_n) = C_n \mathcal{M}_{\perp} \mathcal{M}_{//}, \quad (5.2.3)$$

where  $\mathcal{M}_{\perp}$  and  $\mathcal{M}_{//}$  describe the transverse and longitudinal momentum distributions (relative to the direction of the initial  $q\bar{q}$  momentum), respectively, and  $C_n$  is a dimensionless normalization constant.

The origin of transverse momentum is from quantum fluctuations in the ground state of the string, which implies a Gaussian distribution,

$$\mathcal{M}_{\perp} = \exp\left(-\sum_{j=1}^n \vec{k}_j^2\right), \quad (5.2.4)$$

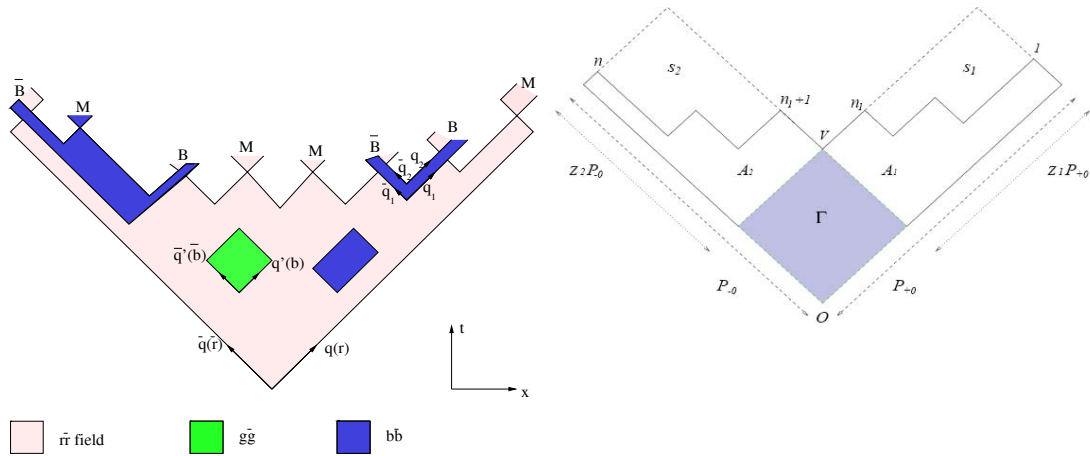


Figure 5.3: (a) String fragmentation in time-longitudinal phase-space by a set of new pairs ( $q\bar{q}$  or  $q\bar{q}q\bar{q}$ ) production, hadrons (mesons  $M$  and baryons  $B$ ) form at the vertices; (b) the vertex  $V$  divides the  $n$ -body string fragmentation into two clusters that contain  $n_1$  and  $n_2$  hadrons with squared invariant masses  $s_1$  and  $s_2$ .

where the relation between transverse momentum  $\vec{p}_\perp$  and the dimensionless vector  $\vec{k}$  is

$$\vec{k}_j \equiv \frac{\vec{p}_{\perp j}}{2\sigma}, \quad (5.2.5)$$

and the variance is  $\sigma^2 \equiv \langle \vec{p}_\perp^2 \rangle$ . The longitudinal matrix is described by the Lund area law

$$\mathcal{M}_{//} = \exp(i\xi \mathcal{A}_n), \quad (5.2.6)$$

where  $\mathcal{A}_n$  is the area enclosed by the quark-antiquark light-cone lines of  $n$ -particles (see Fig. 5.3). The parameter  $\xi$  is given by

$$\xi = \frac{1}{2\kappa} + i\frac{b}{2}, \quad (5.2.7)$$

where  $\kappa$  is the string tension constant and  $b$  is a flavor-independent dynamical parameter. The phase of the hadronic state is given by the real part of  $\xi$ , and the imaginary part corresponds to the production rate of the hadronic state.

### 5.3 Solutions of the Lund area law

In the BEPC-II energy region, the emitted gluons are usually soft, which leads to a small broadening of the two-jet system. The quark and the accompanying gluons behave as a single quark-jet. Gluon emission does not change the topological shapes of the final states and may be neglected.

The probability for the string to fragment into  $n$ -particles state can be written as

$$d\wp_n(m_1, m_2, \dots, m_n) = \delta(1 - \sum_{j=1}^n \frac{m_{\perp j}^2}{s z_j}) \delta(1 - \sum_{j=1}^n z_j) \delta(\sum_{j=1}^n \vec{k}_j) \overline{\sum} |\mathcal{M}_{LUND}|^2 d\Phi_n, \quad (5.3.8)$$

where  $z_j$  is the light-cone momentum  $z_j \equiv (E_j \pm p_{zj})/(E_0 \pm P_{z0})$ ,  $m_{\perp j}$  is the transverse mass

$$m_{\perp j} = \sqrt{m_j^2 + p_{\perp j}^2} = \sqrt{m_j^2 + 4\sigma^2 \vec{k}_j^2}, \quad (j = 1, 2, \dots, n), \quad (5.3.9)$$

and  $d\Phi_n$  is the  $n$ -particle dimensionless phase-space element

$$d\Phi_n = \prod_{j=1}^n d^2 \vec{k}_j \frac{dz_j}{z_j}. \quad (5.3.10)$$

The summation over the fragmentation hadrons gives the following factor

$$\overline{\sum} \Rightarrow B_n \prod_j^n (VPS)_j (SUD)_j, \quad (5.3.11)$$

where  $B_n$  is the combinatorial number of string fragmentations,  $(VSP)$  is the ratio of vector meson to pseudoscalar meson production, which is suppressed from its spin-state counting value 3 : 1, and  $(SUD)$  reflects the suppression of strange meson production relative to that for ordinary mesons.

When integrated over the kinematic variables of the  $n$  hadrons, the Lund area law [Eq. (5.3.8)] has the following solutions for [106, 107]:

- String  $\Rightarrow 2$  hadrons

$$\wp_2 = \frac{C_2}{\sqrt{\lambda(s, m_{\perp 1}^2, m_{\perp 2}^2)}} [\exp(-b\mathcal{A}_2^{(1)}) + \exp(-b\mathcal{A}_2^{(2)})]; \quad (5.3.12)$$

- String  $\Rightarrow 3$  hadrons

$$d\wp_3 = \frac{C_3}{\sqrt{\Lambda}} \exp(-b\mathcal{A}_3) d\mathcal{A}_3; \quad (5.3.13)$$

The area law is Lorentz invariant and factorizes so that the total system may be divided into two subsystems, each of which contains  $n_1$  and  $n_2$  hadrons ( $n_1, n_2 = 2$  or 3) [see Fig. 5.3(b)]. Applying the analytical results for each subsystem, one gets

$$d\wp_n(s; s_1, s_2) = \frac{ds_1 ds_2}{\sqrt{\lambda(s, s_1, s_2)}} [\exp(-b\Gamma^{(1)}) + \exp(-b\Gamma^{(2)})] \wp_{n_1}(s_1) \wp_{n_2}(s_2). \quad (5.3.14)$$

Multi-body fragmentation can be treated in a similar way.

## 5.4 Preliminary multiplicity

The Lund area law can give the multiplicity distribution of the fragmentation hadrons. In fact, the dimensionless  $n$ -particles (neutral and charged) partition function can be defined as [82]

$$Z_n = \int d\Phi_n \exp(-b\mathcal{A}_n). \quad (5.4.15)$$

The relation between  $Z_n$  and the multiplicity distribution is

$$P_n = \frac{Z_n}{\sum Z_n}, \quad (5.4.16)$$

which has the approximate form

$$P_n = \frac{\mu^n}{n!} \exp[c_0 + c_1(n - \mu) + c_2(n - \mu)^2]. \quad (5.4.17)$$

The quantity  $\mu$  can be written in the energy-dependent form

$$\mu = \alpha + \beta \exp(\gamma \sqrt{s}), \quad (5.4.18)$$

where the parameters  $c_0$ ,  $c_1$ ,  $c_2$ ,  $\alpha$ ,  $\beta$  and  $\gamma$  have to be tuned with experimental data.

## 5.5 Parameter tuning

The Lund area law is incorporated into the JETSET program, mainly as the subroutine LUARLW, which contains many phenomenological parameters. Their values are unknown and must be tuned by comparing with data to ensure good agreement for important distributions, such as energy, momentum, multiplicities, polar angle etc. When comparing data distributions with Monte Carlo events, the statistics of all kinds of events (hadronic events, QED backgrounds and beam associated backgrounds) in Monte Carlo sample and data have to be the same, and this requirement can be met by

$$\text{data} \Leftrightarrow \text{MonteCarlo sample} \left\{ \begin{array}{ll} \text{beam} - \text{gas} & BG^* \\ \mu^+ \mu^- & L \cdot \sigma_{\mu\mu} \\ e^+ e^- & L \cdot \sigma_{ee} \\ \tau^+ \tau^- & L \cdot \sigma_{\tau\tau} \\ \gamma\gamma & L \cdot \sigma_{\gamma\gamma} \\ \text{hadrons} & L \cdot \sigma_{had.} \end{array} \right.$$

The beam associated sample,  $BG^*$ , can be obtained from the raw data according to the methods described in Ref. [109].

The distributions to be compared are those that are directly related to the hadronic criteria: multiplicity, space position, momentum, polar-angle, energy deposit, the ratio of  $\pi/K$ , the fractions of the short life-time particle  $K_S$  and  $\Lambda$  (which will influence their secondary vertexes), the time of flight etc. The main parameters to be tuned are:  $PARJ(1-3)$ ,  $PARJ(11-17)$  in JETSET [110] and the parameters in LUARLW [106, 107]. Some comparisons of the sensitive distributions between *BES-III* data and LUARLW at detector level are illustrated in Fig. 5.4.

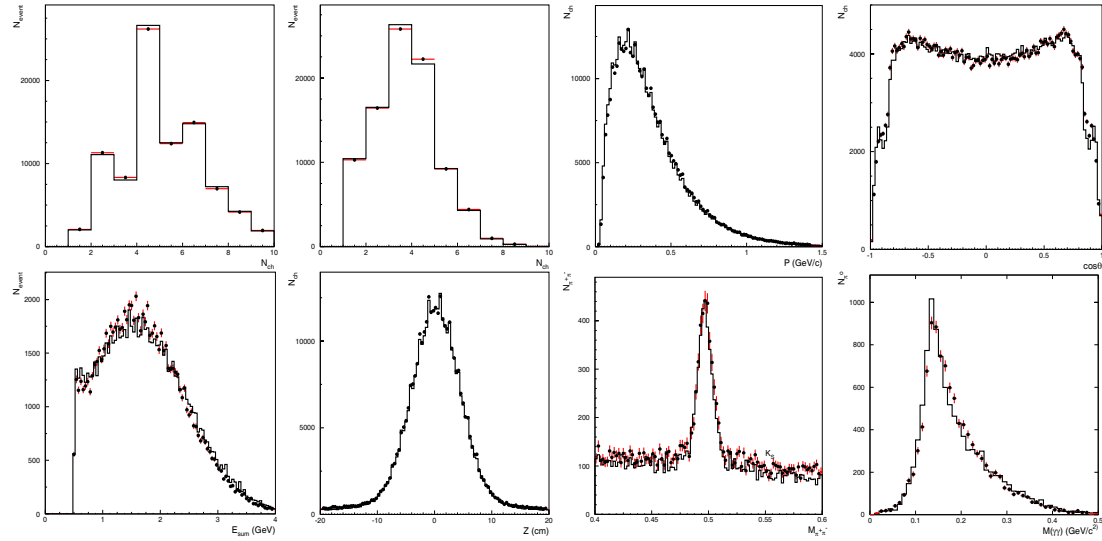


Figure 5.4: Comparisons of data with simulated LUARLW events for distributions of: multiplicity of charged tracks, multiplicity of good tracks, momentum  $p$ , polar-angle  $\cos \theta$ , energy deposited in BSC, vertex position of charged tracks, invariant mass of  $K_S \rightarrow \pi^+\pi^-$  and  $\pi^0 \rightarrow \gamma\gamma$ , at  $\sqrt{s} = 3.65$  GeV.



# Chapter 6

## R values and precise test of the Standard Model <sup>1</sup>

Measurements of the total cross section for  $e^+e^-$ -annihilation into hadrons are indispensable input for the determination of the non-perturbative hadronic contribution to the running of the QED fine structure constant, an essential input parameter in precision electroweak measurements. A number of excellent reviews on this subject are available [25]. Some of the material from these review papers is summarized here. In Sect. 6.1 the definition of  $R_{\text{had}}$ , its experimental determination and the present status of  $R_{\text{had}}$  measurements at low energy are presented. Evaluations of  $\Delta\alpha_{\text{had}}^{(5)}(M_Z^2)$ , the non-perturbative hadronic contribution to the running of the fine structure constant, are given in Sect. 6.2. Section 6.3 contains a discussion of the choice of input parameters for Standard Model tests, in particular, the effective fine structure constant at the scale  $\sqrt{s} = M_Z$ .

### 6.1 $e^+e^- \rightarrow \text{hadrons}$ cross sections and the $R_{\text{had}}$ value

$R_{\text{had}}(s)$ , by the proper definition, is the *ratio of the total cross sections* according to following equation,

$$R_{\text{had}}(s) = \frac{\sigma_{\text{tot}}(e^+e^- \rightarrow \gamma^* \rightarrow \text{hadrons})}{\sigma(e^+e^- \rightarrow \gamma^* \rightarrow \mu^+\mu^-)} . \quad (6.1.1)$$

Usually, however, experiments do not determine  $R_{\text{had}}$  as the ratio of the total cross sections given in Eq. 6.1.1. Rather, the hadronic experimental cross section is first corrected for QED effects [26, 27, 28, 29], which include bremsstrahlung as well as vacuum polarization corrections. The latter account for the running of the fine structure constant  $\alpha(s)$ . After these corrections are applied, the resulting  $\sigma_{\text{tot}}$  is divided by the Born cross section  $\sigma_0(e^+e^- \rightarrow \gamma^* \rightarrow \mu^+\mu^-) = \frac{4\pi\alpha^2}{3s}$ . As a result, the “working” definition of  $R_{\text{had}}(s)$  is:

$$R_{\text{had}}(s) = \frac{\sigma_{\text{tot}}(e^+e^- \rightarrow \gamma^* \rightarrow \text{hadrons})_{\text{exp}}^{\text{corr}}}{\sigma_0(e^+e^- \rightarrow \gamma^* \rightarrow \mu^+\mu^-)} . \quad (6.1.2)$$

---

<sup>1</sup>By Hai-Ming Hu and Xiao-Yuan Li

Note that, the experimental cross section  $\sigma(e^+e^- \rightarrow \gamma^* \rightarrow \mu^+\mu^-)$  never appears here. They are, however, used by some authors to check how good the normalizations are (see *e.g.*, Ref. [30]).

Some general comments concerning the  $R_{\text{had}}$  determination are in order.

- **Exclusive vs Inclusive**

Usually, for energies below  $\sim 2$  GeV exclusive cross sections are measured for individual channels, while at higher energies the hadronic final states are treated inclusively. In exclusive measurements, one directly measures the total and differential cross sections for all exclusive reactions that are kinematically allowed in that energy region. Having measured the exclusive cross sections, one can determine the total cross sections and the value of  $R$  by simply summing them. This is, of course, not at all trivial since one has to be sure that there is neither double counting nor missing final states and that correlations between different channels are properly taken into account [31]. There is, in fact, still a systematic difference between the sum of exclusive channels and the inclusive  $R_{\text{had}}$  measurements in the energy range [1.4–2.1] GeV [32]. In view of the many channels in this energy region, inclusive measurement should be pursued as much as possible [33].

- **Energy scan vs Radiative return**

Measurements of hadronic cross sections have usually been performed via energy scans, *i.e.*, by systematically varying the  $e^+e^-$  beam energies. This traditional way of measuring the hadronic cross section has one disadvantage — it needs dedicated running periods. On the other hand, modern flavor factories, such as the Frascati  $\phi$ -factory DAΦNE or the PEP-II and KEKB  $B$ -factories, are designed for a fixed cms energy  $\sqrt{s}$ . An energy scan for the measurement of hadronic cross sections would, therefore, not be very efficient and an alternative way, the radiative-return method, has been proposed. The radiative-return method (for a brief theoretical review see Ref. [34] and references cited therein) relies on the observation that the cross section of the reaction  $e^+e^- \rightarrow \text{hadrons} + \text{photons}$ , with photons emitted from the initial leptons, factorizes into a function  $H$ , which is fully calculable within QED, and the cross section of the reaction  $e^+e^- \rightarrow \text{hadrons}$

$$d\sigma(e^+e^- \rightarrow \text{hadrons} + \gamma's)(s, Q^2) = H \cdot d\sigma(e^+e^- \rightarrow \text{hadrons})(Q^2), \quad (6.1.3)$$

where  $Q^2$  is the invariant mass of the hadronic system. Thus from the measured  $Q^2$  dependence of the reaction  $e^+e^- \rightarrow \text{hadrons} + \text{photons}$  at fixed  $\sqrt{s}$ , one can evaluate  $\sigma(e^+e^- \rightarrow \text{hadrons})$ , if the function  $H$  is known. As is evident from Eq. (6.1.3), the radiative return method allows for the extraction of the hadronic cross section from the production energy threshold of a given hadronic channel almost to the operating cms energy of a given experiment ( $\sqrt{s}$ ). The smaller cross section for the radiative process in comparison to the corresponding process without photon emission has to be compensated by higher luminosities. This requirement is met by the meson factories (DAPHNE, KEKB and PEPII). These were all built for purposes other than hadronic cross section measurements, but their huge luminosities provide

data samples that are large enough for precise measurements of interesting hadronic channels and give information on rare channels that are not easily accessible in scan experiments.

The radiative-return method has been successfully applied by KLOE to measure the pion form factor below 1 GeV [35] and by BaBar for the timelike proton-antiproton form factor and for several exclusive higher multiplicity final states in the mass range from threshold to 4.5 GeV [36]. The combination of KLOE and BaBar data covers the entire mass range below  $\sim 4.5$  GeV. For an extensive review of the recent radiative-return results from both collaborations see Ref. [37]. This method has the advantage of having the same normalization for each energy point. It requires a good theoretical understanding of the radiative corrections, a precise determination of the angle and energy of the emitted photon, and the full control of backgrounds, especially from events where a photon is emitted in the final state (FSR). The Karlsruhe-Katowice group computed the radiative corrections up to NLO for different exclusive channels, implementing them in the event generator PHOKHARA [38, 39, 40, 41, 42]. The current precision level for the  $\pi^+\pi^-\gamma$  final state is 0.5%.

- **Status of  $R_{had}$  at low energy**

During the last thirty years the  $R_{had}$  ratio has been measured by several experiments. Figure 6.1 gives an updated summary of the  $R_{had}$  measurements by different experiments and the current precision in different  $e^+e^-$  cms energy regions by Burkhardt and Pietrzyk [43].

- **The  $\pi^+\pi^-$  threshold region.**

The experimental data are poor below about 400 MeV because the cross section is suppressed near the threshold. The most effective way to measure the threshold in the time-like region is provided by radiative-radiation events, where the emission of an energetic photon allows one to compensate in part for the experimental difficulties associated with the detection of two pions that are nearly at rest.

- **The  $\rho$  peak region.**

The  $\pi^+\pi^-$  region between 0.5 and 1 GeV has been studied by different experiments. CMD-2 [44] and SND [45] performed an energy scan at the  $e^+e^-$  collider VEPP-2M ( $\sqrt{s} \in [0.4\text{--}1.4]$  GeV) with  $\sim 10^6$  and  $\sim 4.5 \times 10^6$  events, respectively, and with systematic errors that range from 0.6% to 4% in the relative cross-sections, depending on the dipion mass value. The pion form factor has also been measured by KLOE using ISR, and results from BaBar are expected soon. KLOE's published results [35] are based on an integrated luminosity of  $140 \text{ pb}^{-1}$  and has relative errors of 1.3% in the [0.6–0.97] GeV energy region (which are dominated by systematics). KLOE subsequently collected more than  $2 \text{ fb}^{-1}$  at the  $\phi$  meson peak, which corresponds to  $\sim 2 \times 10^7 \pi^+\pi^-\gamma$  events in the  $\rho$  peak region. BaBar [36] has already collected over  $300 \text{ fb}^{-1}$  at the  $\Upsilon(4S)$  peak, and plans to collect about  $1 \text{ ab}^{-1}$  by the end of data taking.

The results of these four experiments (CMD-2, SND, KLOE, BaBar) in the next few years will probably allow us to know the  $\pi^+\pi^-$  cross-section for most of

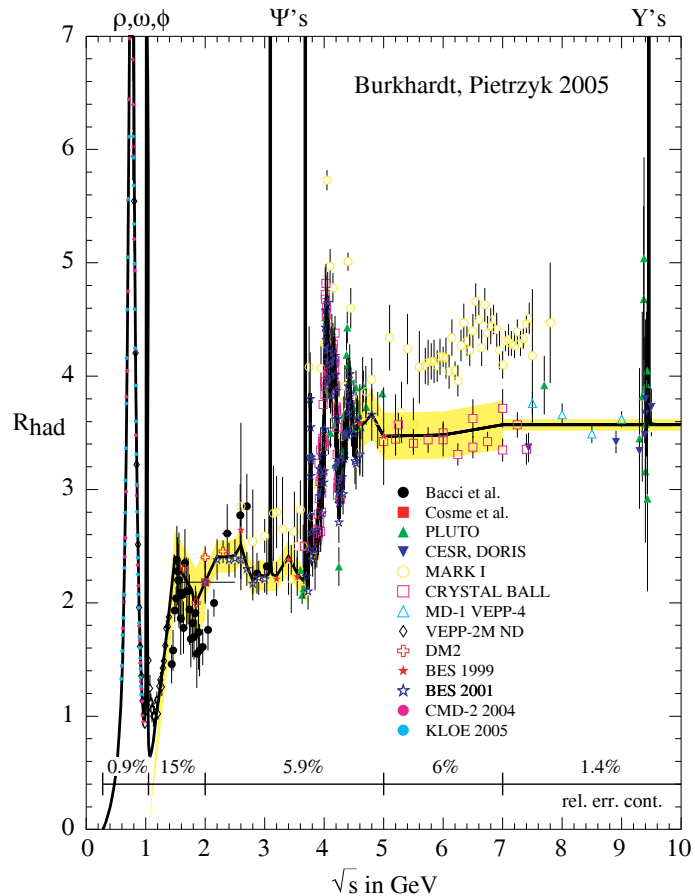


Figure 6.1:  $R_{\text{had}}$  versus cms energy. Measurements are shown with statistical errors. The relative uncertainty assigned to the parameterization is shown as a band and given with numbers at the bottom (from Ref. [43]).

the  $\rho$  region with a relative accuracy that is better than 1% (considering both statistical and systematic errors). In summary [43]:

- \* very minor changes have been introduced by the recent CMD2, KLOE and SND measurements;
  - \* previous measurements in the  $\rho$  region are already quite precise.
- **The 1.05–2.0 GeV energy region.**

The [1.05–2.0 GeV] region is the most poorly known. As can be seen in Fig. 6.2 in Sect. 6.2, the  $R_{had}$  measurements in this energy region contributes about 40% of the uncertainty of the total dispersion integral for  $\Delta_{had}^{(5)}(m_Z^2)$  [43]. It also provides most of the contribution to the uncertainty of  $a_\mu^{\text{HLO}}$  above 1 GeV. New  $R_{had}$  measurements in this energy region will be very valuable.

- **The high energy region**

In the high energy region, we distinguish the  $J/\psi$  and the  $\Upsilon$  resonances and the background inclusive measurements of the total hadronic cross section that are usually presented in terms of  $R_{had}$  values.

For the narrow resonances  $\omega$ ,  $\phi$ , the  $J/\psi$  family (6 states) and the  $\Upsilon$  family (6 states) we can safely use the Breit-Wigner parameterization:

$$\sigma_{BW}(s) = \frac{12\pi}{M_R^2} \frac{\Gamma_{ee}}{\Gamma_R} \frac{M_R^2 \Gamma_R \Gamma(s)}{(s - M_R^2)^2 + M_R^2 \Gamma^2(s)}, \quad (6.1.4)$$

which for zero-width resonances has the form

$$\sigma_{NW}(s) = \frac{12\pi^2}{M_R} \Gamma_{ee} \delta(s - M_R^2). \quad (6.1.5)$$

The masses, widths and the electronic branching fractions for these resonances are listed in the Review of Particle Properties [46].

In the region from the  $J/\psi$  to the  $\Upsilon$  the earlier  $R_{had}$ -measurements are from Mark I [47, 48],  $\gamma\gamma 2$  [49], DASP [50], PLUTO [51], LENA [52], Crystal Ball (CB) [53] and MD-1 [54].

\* **The 2.0 – – 5.0 GeV energy region**

In this energy region the earlier results have a precision of 15%~20% [48, 49, 51]. In 2001, BES-II published the results of  $R_{had}$  measurements at 85 different cms. energies between 2 and 4.8 GeV with an average precision of 6.6% [55], an additional 6 points were published in 1999 [56]. These represent a substantial improvement. The BES-II results were used in the 2001 evaluation of  $\Delta\alpha_{had}^{(5)}(M_Z^2)$  [57, 58] and its uncertainty was reduced to 5.9%.

\* **The 5.0 – – 7.0 GeV energy region**

There is a longstanding annoyance: the values of  $R_{had}$  for the energy region 5.0 – 7.8 GeV from the Mark-I experiment [48] are higher than theoretical expectations, *i.e.*  $4.4 \pm 0.4$  as opposed to  $\sim 3.4$  (see Fig. 6.1). In 1990, the average value of  $R_{had}$  in the  $e^+e^-$  cms energy region between 5 and 7.4 GeV was reported by the Crystal Ball Collaboration [53] to be  $3.44 \pm 0.03 \pm 0.018$

which is much more in line with expectation of perturbation QCD assuming 5 quarks, and in agreement with other experiments PLUTO, LENA and MD-1. These results were used in a 1995 evaluation of  $\Delta\alpha_{\text{had}}^{(5)}(M_Z^2)$  [59, 60]. They, together with the  $R_{\text{had}}$  measurements in the energy region between 2 and 5 GeV from BESII [55, 56], were the two major changes in the history of the determination of  $\Delta\alpha_{\text{had}}^{(5)}(M_Z^2)$ . Although the results of the Crystal Ball are preferred by theorists, these data were never published, leaving some room for doubt. CLEO may have ability to settle this problem [61].

\* **The  $7.0 - 12.0$  GeV energy region**

In this energy region, pQCD calculations are not expected to be very reliable, although the calculations are in good agreement with the existing data. Improved measurements of  $R_{\text{had}}$  are necessary to avoid dependence on pQCD. A CLEO measurement in the  $\Upsilon(4S)$  continuum region at  $\sqrt{s} = 10.52$  GeV,  $R_{\text{had}} = 3.56 \pm 0.01 \pm 0.07$  [62], is one of the most accurate  $R_{\text{had}}$  measurements ever made with both statistical and systematic errors that are quite small. Recently the CLEO collaboration has taken data for  $R$  measurements at energies of 6.96, 7.38, 8.38, 9.4, 10.0, 10.33 and 11.2 GeV. These data are under analysis and results can be expected soon [61].

\* **The energy region above 12.0 GeV** The values of  $R_{\text{had}}$  in this region are described by a parameterization based on third-order QCD [57]

As we discuss below, hadronic cross section measurements are crucial for the precise evaluation of the hadronic contributions to running of the electromagnetic coupling  $\alpha_{QED}$ . This requires a better knowledge of the hadronic cross section over the entire energy range, starting from the  $2m_\pi$  threshold. The optimal exploitation of a high energy linear collider, such as the ILC, for precision physics requires a reduction of the errors on the low energy  $R_{\text{had}}$  measurements by a factor of something like ten.

## 6.2 Hadronic Vacuum Polarization

The running of the electromagnetic coupling with momentum transfer,  $\alpha(0) \rightarrow \alpha(s)$ , caused by fermion-pair loop insertions in the photon propagator, is customarily written as

$$\alpha(s) = \frac{\alpha(0)}{1 - \Delta\alpha(s)} = \frac{\alpha(0)}{1 - \Delta\alpha_{e\mu\tau}(s) - \Delta\alpha_{\text{top}}(s) - \Delta\alpha_{\text{had}}^{(5)}(s)}, \quad (6.2.6)$$

where  $\alpha(0) = 1/137.036$  [63]. The contribution from leptons,  $\alpha_{e\mu\tau}(s)$ , is calculated up to third order:  $\Delta\alpha_{e\mu\tau}(M_Z^2) = 3149.7686 \times 10^{-5}$  with negligible uncertainty [64]. Since heavy particles decouple in QED, the top-quark contribution is small:  $\Delta\alpha_{\text{top}}(M_Z^2) = -0.00007(1)$  as calculated by the TOPAZ0 and ZFITTER programs as a function of the pole mass of the top quark,  $m_t$ . The running electromagnetic coupling is insensitive to new particles with high masses. For light-quark loops, diagrammatic calculations are not viable since at these low energy scales perturbative QCD is not applicable. Therefore, the total contribution from the five light quark flavors to the hadronic vacuum polarization,  $\Delta\alpha_{\text{had}}^{(5)}(M_Z^2)$ , is more accurately obtained from a dispersion integral over the measured hadronic cross-section

in electron-positron annihilations at low center-of-mass energies. The relevant vacuum polarization amplitude satisfies the convergent dispersion relation [58]

$$Re\Pi'_\gamma(s) - \Pi'_\gamma(0) = \frac{s}{\pi} Re \int_{s_0}^{\infty} ds' \frac{Im\Pi'_\gamma(s')}{s'(s' - s - i\varepsilon)},$$

and, using the optical theorem (unitarity), one has

$$Im\Pi'_\gamma(s) = \frac{s}{e^2} \sigma_{tot}(e^+e^- \rightarrow \gamma^* \rightarrow \text{hadrons})(s).$$

In terms of the cross section ratio

$$R_{\text{had}}(s) = \frac{\sigma_{tot}(e^+e^- \rightarrow \gamma^* \rightarrow \text{hadrons})}{\sigma(e^+e^- \rightarrow \gamma^* \rightarrow \mu^+\mu^-)},$$

where  $\sigma(e^+e^- \rightarrow \gamma^* \rightarrow \mu^+\mu^-) = \frac{4\pi\alpha^2}{3s}$  is the tree level value, we obtain

$$\Delta\alpha_{\text{hadrons}}^{(5)}(M_Z^2) = -\frac{\alpha M_Z^2}{3\pi} Re \int_{4m_\pi^2}^{\infty} ds \frac{R(s)}{s(s - M_Z^2 - i\varepsilon)}. \quad (6.2.7)$$

The dispersion integral can be evaluated either by direct integration between measured data points or by using a parameterization of the measured cross section of  $e^+e^- \rightarrow \text{hadrons}$ . In the first approach one tries to rely on the experimental data as much as possible and directly integrates over the experimental cross section measurements, joining adjacent data point with straight lines (the trapezoidal rule). In this approach one can take into account uncertainties of separate measurements in a straightforward manner [59]. In the second approach one fits the experimental points to some model and integrates the resulting parameterization of the data. This procedure inevitably leads to some model-dependence and it is not clear how experimental errors, especially systematic uncertainties, are taken into account [59].

Detailed evaluations of this dispersive integral directly from the experimental data have been carried out by many authors [32, 33, 43, 57, 58, 59, 60, 65, 66, 67]. There are also several evaluations of  $\Delta\alpha_{\text{had}}^{(5)}(M_Z^2)$  that are more theory driven [68].

An important conclusion from studies before 1989, described in Ref. [65], is that the independent programs and parameterization methods gave nearly identical results. Differences in central values obtained from the use of the trapezoidal rule between many data points, partially smoothed functions or broad averages were negligible compared to the experimental uncertainties. The uncertainty in the result obtained from the integration is, therefore, almost entirely due to the experimental errors in the determination of  $R_{\text{had}}(s)$ .

The result of Refs. [59] and [60],

$$\Delta\alpha_{\text{had}}^{(5)} = 2804(65) \times 10^{-5}, \quad (6.2.8)$$

was used by the LEP Collaborations and the LEP Electroweak Working Group as the input parameter to constrain the Standard Model until summer of 2000 [69].

After BES-II published its sequence of substantially improved total cross section measurements between 2 and 5 GeV [56] [55], some of these analyses were updated to include the BES-II as well as measurements from CMD-2 [44], obtaining [57]:

$$\Delta\alpha_{\text{had}}^{(5)} = 2761 (36) \times 10^{-5}, \quad (6.2.9)$$

and [58]:

$$\Delta\alpha_{\text{had}}^{(5)} = 2757 (36) \times 10^{-5}.$$

The factor-of-two reduction in the quoted uncertainty from  $70 \times 10^{-5}$  in Refs. [59, 60] to  $36 \times 10^{-5}$  in Refs. [57, 58] is mainly due to the BES-II data.

The estimates of  $\Delta\alpha_{\text{had}}^{(5)}(M_Z^2)$  from Refs. [57, 58], listed in Eq. 6.2.9, were used as input by the LEP Collaborations and the LEP Electroweak Working Group until the summer of 2004. A more recent update,  $\Delta\alpha_{\text{had}}^{(5)} = 2758 (35) \times 10^{-5}$  [43], includes the KLOE [35] measurements. Figure 6.2 (from Ref. [70]) illustrates the relative contributions from different  $e^+e^-$  cms energy regions to  $\Delta\alpha_{\text{had}}^{(5)}(M_Z^2)$ , both in magnitude (top) and uncertainty (bottom). The region between 1.05 – 2 GeV gives a significant contribution to the uncertainty despite its small contribution to the magnitude. A comparison of estimates of  $\Delta\alpha_{\text{had}}^{(5)}(M_Z^2)$  performed during 90's is shown in Fig. 6.3 (from Ref. [70]).

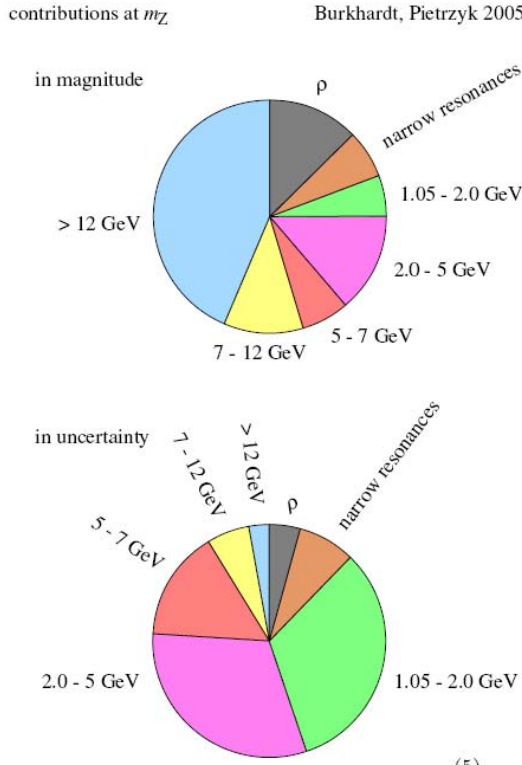


Figure 6.2: Relative contributions to  $\Delta\alpha_{\text{had}}^{(5)}(M_Z^2)$  in magnitude (top) and uncertainty (bottom) (from Ref. [70]).

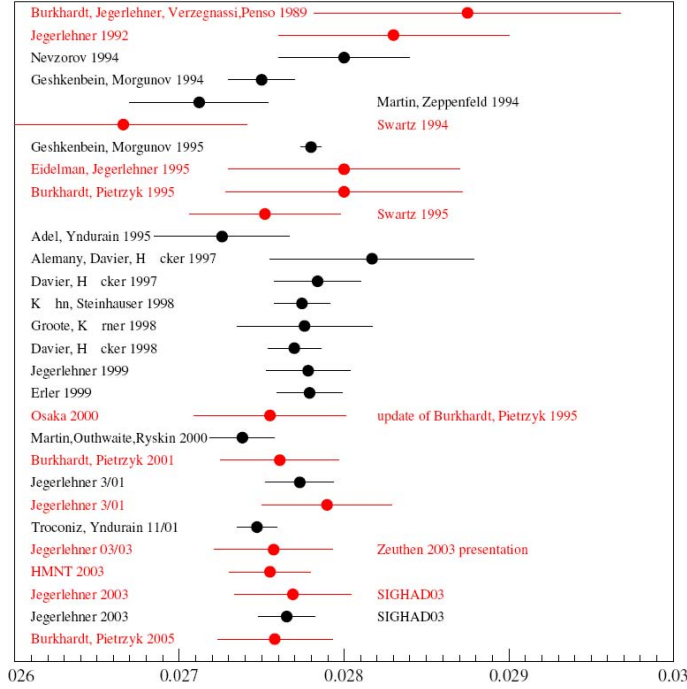


Figure 6.3: Comparison of different estimates of  $\Delta\alpha_{\text{had}}^{(5)}(M_Z^2)$ . Estimates based on dispersion integration of the experimental data are shown with red solid dots and estimates relying on additional theoretical assumptions are shown as black solid dots (from Ref. [70]).

Another recent update [33] based on a compilation of the data shown in Fig. 6.4 (from Ref. [33]), yields  $\Delta\alpha_{\text{had}}^{(5)} = 0.027607 \pm 0.000225$  or  $1/\alpha^{(5)}(m_Z^2) = 128.947 \pm 0.035$ . Contributions from various energy regions and the origin of the errors in this estimate are shown in Fig. 6.5 (from Ref. [33]). More details are given in Table 6.1 (from Ref. [33]).

In summary, to reach higher precision, more experimental effort is required to measure  $\sigma(e^+e^- \rightarrow \text{hadrons})$  precisely both at low and intermediate energies [33].

### 6.3 Input parameters and their uncertainties

In 2005 and 2006, results from “final” fits of electroweak measurements taken at the  $Z$  resonance by the SLC and LEP experiments were reported [71]. The mass and width of the  $Z$  boson,  $M_Z$  and  $\Gamma_Z$ , and its couplings to fermions, for example the  $\rho$  parameter and the effective electroweak mixing angle for leptons, were precisely determined:

$$\begin{aligned}
 M_Z &= 91.1875 \pm 0.0021 \text{ GeV} \\
 \Gamma_Z &= 2.4952 \pm 0.0023 \text{ GeV} \\
 \rho_l &= 1.0050 \pm 0.0010 \\
 \sin^2 \theta_{\text{eff}}^{\text{lept}} &= 0.23153 \pm 0.00016 .
 \end{aligned}$$

Using SM radiative corrections, the large and diverse set of LEP and SLC measurements provide many stringent tests of the Standard Model and tight constraints on its free parameters. The masses of the  $W$  boson and the top quark are predicted to be:  $M_W =$

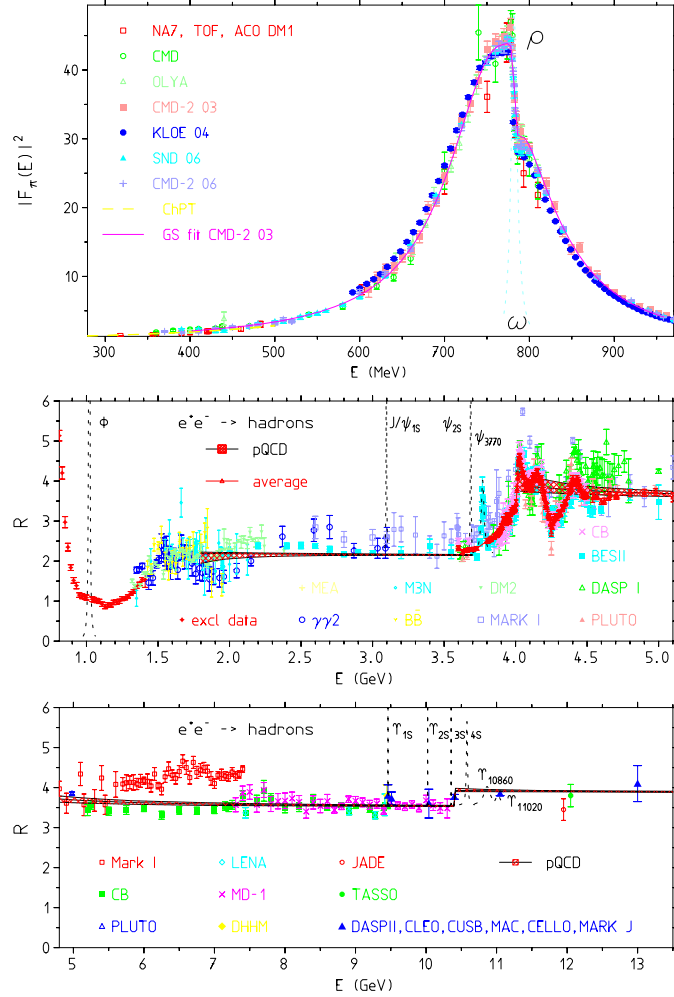


Figure 6.4: A compilation of the presently available experimental hadronic  $e^+e^-$ -annihilation data (from Ref. [33]).

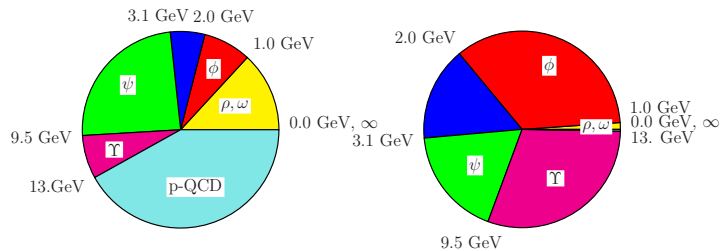


Figure 6.5:  $\Delta\alpha_{\text{had}}^{(5)}(M_Z^2)$ : contributions (left) and squared errors (right) from different  $\sqrt{s}$  regions (from Ref. [33]).

Table 6.1: Contributions for  $\Delta\alpha_{\text{had}}^{(5)}(M_Z^2) \times 10^4$  (direct integration method) with relative (rel) and absolute (abs) error in percent (from Ref. [33]).

Energy range	$\Delta\alpha_{\text{had}}^{(5)}(M_Z^2) \times 10^4$	rel [%]	abs [%]
$\rho, \omega (E < 2M_K)$	36.23 [ 13.1](0.24)	0.7	1.1
$2M_K < E < 2 \text{ GeV}$	21.80 [ 7.9](1.33)	6.1	34.9
$2 \text{ GeV} < E < M_{J/\psi}$	15.73 [ 5.7](0.88)	5.6	15.4
$M_{J/\psi} < E < M_T$	66.95 [ 24.3](0.95)	1.4	18.0
$M_T < E < E_{\text{cut}}$	19.69 [ 7.1](1.24)	6.3	30.4
$E_{\text{cut}} < E \text{ pQCD}$	115.66 [ 41.9](0.11)	0.1	0.3
$E < E_{\text{cut}} \text{ data}$	160.41 [ 58.1](2.24)	1.4	99.7
total	276.07 [100.0](2.25)	0.8	100.0

$80.363 \pm 0.032$  GeV and  $m_t = 173_{-10}^{+13}$  GeV, in good agreement with the subsequent direct measurements of these quantities at LEPII and the TEVATRON [72], thereby successfully testing the Standard Model at the level of its radiative corrections.

Note that the SM perturbation calculations are *approximations* that are obtained by truncation of the perturbation series. The accuracy of the finite-order approximation for each  $Z$ -pole observable depends on the input parameter set that is used in the calculations. A natural choice is the QED-like parameterization in terms of the parameters

$$\alpha, \quad \alpha_s, \quad M_W, \quad M_Z, \quad m_H, \quad \text{and } m_f, \quad (6.3.10)$$

where  $M_W$  and  $M_Z$  are the masses of the  $W$  and  $Z$  bosons,  $m_H$  is the mass of the Higgs boson,  $m_f$  are the masses of all known fundamental fermions  $f$ , in particular  $m_t$  is the top quark mass, and  $\alpha$  and  $\alpha_s$  just are the coupling constants of the electromagnetic and strong interactions. Loop corrections induce a running of the coupling constants with increasing momentum transfer (or  $s$ ). The running of the strong coupling,  $\alpha_s(s)$ , is even larger than that for the QED coupling  $\alpha$ . Since the  $Z^0$  resonance is sufficiently dominant for  $Z$ -pole observables, the relevant coupling constants become simply  $\alpha(m_Z^2)$  and  $\alpha_s(m_Z^2)$ .

Within the SM, the mass of the  $W$  that is directly measured at the TEVATRON and LEPII, is related to  $M_Z$  and the Fermi constant  $G_\mu$  through radiative corrections. A very precise value for the latter,  $G_\mu = 1.16637(1) \cdot 10^{-5} \text{ GeV}^{-2}$ , is derived from measurements of the muon lifetime plus two-loop corrections. The 9 ppm precision on  $G_\mu$  greatly exceeds the relative precision with which  $M_W$  will be measured at any time in the foreseeable future. This motivates our substitution of  $G_\mu$  for  $M_W$  as an input parameter for SM calculations.

Therefore, the fine-structure constant  $\alpha$ , the Fermi coupling constant  $G_\mu$ , and the mass of  $Z$  boson  $M_Z$  are the preferred choice for input parameters for precise calculations of SM radiative corrections, since these are the most precisely measured:

- the fine-structure constant in the Thomson limit determined from the  $e^\pm$  anomalous magnetic moment, the quantum Hall effect, and other measurements is [63]

$$\begin{aligned} \alpha^{-1}(0) &= 137.03599911(46), \\ \frac{\delta\alpha}{\alpha} &= 3.6 \times 10^{-9}; \end{aligned} \quad (6.3.11)$$

- the Fermi constant determined from the muon lifetime formula is [74, 75]

$$\begin{aligned} G_\mu &= 1.16637(1), \\ \frac{\delta G_\mu}{G_\mu} &= 8.6 \times 10^{-6}; \end{aligned} \quad (6.3.12)$$

- the  $Z$  boson mass determined from the  $Z$ -lineshape scan at LEP I is [71]

$$\begin{aligned} M_Z &= 91.1875(21), \\ \frac{\delta M_Z}{M_Z} &= 2.4 \times 10^{-5}; \end{aligned} \quad (6.3.13)$$

- the effective fine-structure constant at the  $M_Z$  scale is [43]

$$\begin{aligned} \alpha^{-1}(M_Z) &= 128.940(48), \\ \frac{\delta \alpha(M_Z)}{\alpha(M_Z)} &= (1.6 \sim 6.8) \times 10^{-4}. \end{aligned} \quad (6.3.14)$$

The relative uncertainty of  $\alpha(M_Z)$  is roughly one order of magnitude worse than that of  $M_Z$ , making it one of the limiting factors in the calculation of precise SM predictions.

Note that  $\Delta\alpha$  enters in electroweak precision physics typically when calculating the weak mixing parameter  $\sin^2 \Theta_i$  from  $\alpha$ ,  $G_\mu$  and  $M_Z$  via [76]

$$\sin^2 \Theta_i \cos^2 \Theta_i = \frac{\pi \alpha}{\sqrt{2} G_\mu M_Z^2} \frac{1}{1 - \Delta r_i}, \quad (6.3.15)$$

where

$$\Delta r_i = \Delta r_i(\alpha, G_\mu, M_Z, m_H, m_{f \neq t}, m_t) \quad (6.3.16)$$

includes higher-order corrections that can be calculated in the SM or in alternative models.

The value of  $\Delta r_i$  depends on the definition of  $\sin^2 \Theta_i$ . The various definitions coincide at tree level and only differ by quantum-loop induced effects. From the weak gauge boson masses, the electroweak gauge couplings and the neutral current couplings of the charged fermions we obtain

$$\sin^2 \Theta_W = 1 - \frac{M_W^2}{M_Z^2}, \quad (6.3.17)$$

$$\sin^2 \Theta_g = e^2/g^2 = \frac{\pi \alpha}{\sqrt{2} G_\mu M_W^2}, \quad (6.3.18)$$

$$\sin^2 \Theta_f = \frac{1}{4|Q_f|} \left( 1 - \frac{v_f}{a_f} \right), \quad f \neq \nu, \quad (6.3.19)$$

respectively. For the most important cases the general form of  $\Delta r_i$  reads

$$\Delta r_i = \Delta\alpha - f_i(\sin^2 \Theta_i) \Delta\rho + \Delta r_{i \text{ remainder}}, \quad (6.3.20)$$

where:

- The large term  $\Delta\alpha$  is due to the photon vacuum polarization

$$\Delta\alpha = \Pi_1^{\gamma\gamma}(0) - \Pi_1^{\gamma\gamma}(M_Z^2). \quad (6.3.21)$$

This is a universal term that influences predictions for  $M_W$ ,  $A_{LR}$ ,  $A_{FB}^f$ ,  $\Gamma_f$ , etc. These terms can be calculated safely in perturbation theory.

- $\Delta\rho$  is the famous correction to the  $\rho$ -parameter that is defined as the neutral to charged current ratio

$$\Delta\rho = \rho - 1 = \frac{G_{NC}}{G_\mu} = \frac{\Pi_1^{ZZ}(0)}{M_Z^2} - \frac{\Pi_1^{WW}(0)}{M_W^2}. \quad (6.3.22)$$

$\Delta\rho$  exhibits the leading top mass correction

$$\Delta\rho \simeq \frac{\sqrt{2}G_\mu}{16\pi^2} 3m_t^2 ; \quad m_t \gg m_b, \quad (6.3.23)$$

that allowed LEP experiments to obtain a rather good indirect estimate of the top quark mass prior to its discovery at the TEVATRON.

Note that in Eq. (6.3.20)  $f_W = c_W^2/s_W^2 \simeq 3.35$  is substantially enhanced relative to  $f_f = 1$ .

- The “remainder” term, although sub-leading, is very important for the interpretation of the precision experiments at LEP and includes part of the leading Higgs mass dependence. For a heavy Higgs particle we obtain the simple expression

$$\Delta r_i^{\text{Higgs}} \simeq \frac{\sqrt{2}G_\mu M_W^2}{16\pi^2} \left\{ c_i^H \left( \ln \frac{m_H^2}{M_W^2} - \frac{5}{6} \right) \right\} \quad m_M \gg M_W, \quad (6.3.24)$$

where, for example,  $c_f^H = (1 + 9 \sin^2 \Theta_f) / (3 \sin^2 \Theta_f)$  and  $c_W^H = 11/3$ .

The uncertainty  $\delta\Delta\alpha$  implies uncertainties  $\delta M_W$ ,  $\delta \sin^2 \Theta_f$  that are given by

$$\frac{\delta M_W}{M_W} \sim \frac{1}{2} \frac{\sin^2 \Theta_W}{\cos^2 \Theta_W - \sin^2 \Theta_W} \delta\Delta\alpha \sim 0.23 \delta\Delta\alpha, \quad (6.3.25)$$

$$\frac{\delta \sin^2 \Theta_f}{\sin^2 \Theta_f} \sim \frac{\cos^2 \Theta_f}{\cos^2 \Theta_f - \sin^2 \Theta_f} \delta\Delta\alpha \sim 1.54 \delta\Delta\alpha. \quad (6.3.26)$$

The effects of the uncertainty due to  $\Delta\alpha_{\text{had}}^{(5)}(M_Z^2)$  on the SM prediction for the  $\rho$  parameter and  $\sin^2 \theta_{\text{eff}}^{\text{lept}}$  can be seen in Fig 6.6. While the SM prediction for the  $\rho$  parameter is not effected by the uncertainty in  $\Delta\alpha_{\text{had}}^{(5)}(M_Z^2)$ , the uncertainty on the prediction of  $\sin^2 \theta_{\text{eff}}^{\text{lept}}$  within the SM due to the uncertainty on  $\Delta\alpha_{\text{had}}^{(5)}(M_Z^2)$  is nearly as large as the

accuracy of the experimental measurement of  $\sin^2 \theta_{\text{eff}}^{\text{lept}}$ . The present error in the effective electromagnetic coupling constant,  $\delta \Delta \alpha(M_Z^2) = 35 \times 10^{-5}$  [43], dominates the uncertainty of the theoretical prediction of  $\sin^2 \theta_{\text{eff}}^{\text{lept}}$ , inducing an error  $\delta(\sin^2 \theta_{\text{eff}}^{\text{lept}}) \sim 12 \times 10^{-5}$ , which is not much smaller than the experimental value  $\delta(\sin^2 \theta_{\text{eff}}^{\text{lept}})^{\text{EXP}} = 16 \times 10^{-5}$  determined by LEP-I and SLD [71]. This observation underlines the importance of a precise cross-section measurement of electron-positron annihilation into hadrons at low cms energies.

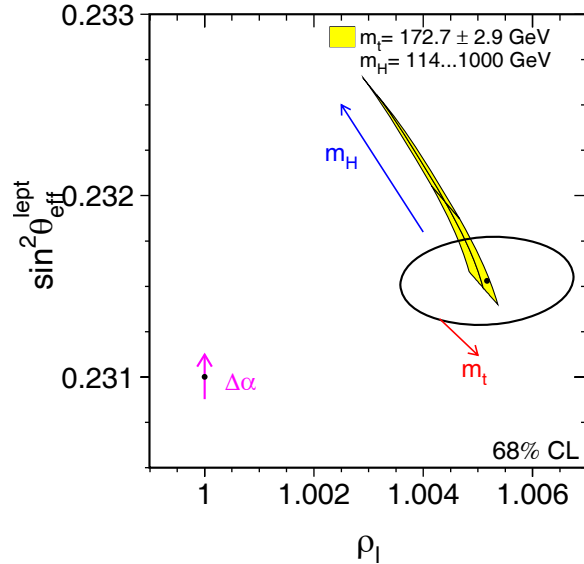


Figure 6.6: Contour curve of 68% probability in the  $(\rho_l, \sin^2 \theta_{\text{eff}}^{\text{lept}})$  plane. The prediction of a theory based on electroweak Born-level formulae and QED with running  $\alpha$  is shown as the dot, with the arrow representing the uncertainty due to the hadronic vacuum polarization  $\Delta \alpha_{\text{had}}^{(5)}(M_Z^2)$ . The same uncertainty also affects the SM prediction, shown as the shaded region drawn for fixed  $\Delta \alpha_{\text{had}}^{(5)}(M_Z^2)$  while  $m_t$  and  $m_H$  are varied in the ranges indicated (from Ref. [71]).

Moreover, since measurements of the effective EW mixing angle at a future linear collider will improve the precision by about an order of magnitude [77], a much smaller value of  $\delta \Delta \alpha(M_Z^2)$  will be required. It is therefore crucial to assess all viable options to further reduce this uncertainty.

Table 6.2 (from Ref. [58, 78]) shows that an uncertainty  $\delta \Delta \alpha_{\text{had}}^{(5)} \sim 5 \times 10^{-5}$ , needed for precision physics at a future linear collider, requires the measurement of the hadronic cross section with a precision of  $O(1\%)$  from threshold up to the  $\Upsilon$  region.

In the SM, the Higgs mass  $m_H$  is the only relevant unknown parameter and by confronting the calculated with the experimentally determined value of  $\sin^2 \Theta_i$  one obtains important indirect constraint on the Higgs mass. The uncertainty  $\delta \Delta \alpha$  thus obscures the indirect bounds on the Higgs mass obtained from electroweak precision measurements. As is mentioned in Sect. 6.2, the current uncertainty in the  $1.05 \sim 2.0$  GeV energy region is 15%. Improving the precision from 15% (see Fig. 6.1) to 5% would change the total uncertainty on  $\Delta \alpha_{\text{had}}^{(5)}(M_Z^2)$  from 0.00035 to 0.00027. The change in the fitted value of

$\delta\Delta\alpha_{\text{had}}^{(5)} \times 10^5$	$\delta(\sin^2\theta_{\text{eff}}^{\text{lept}}) \times 10^5$	Request on $R$
35	12.5	Present
7	2.5	$\delta R/R \sim 1\% \text{ for } \sqrt{s} \leq M_{J/\psi}$
5	1.8	$\delta R/R \sim 1\% \text{ for } \sqrt{s} \leq M_T$

Table 6.2: Values of the uncertainties  $\delta\Delta\alpha_{\text{had}}^{(5)}$  (first column) and the errors induced by these uncertainties on the theoretical SM prediction for  $\sin^2\theta_{\text{eff}}^{\text{lept}}$  (second column). The third column indicates the corresponding requirements on the  $R$  measurement.

the Higgs mass would be small; however changing  $R_{\text{had}}$  by  $\pm 1\sigma$  in this cms energy region would shift the central value of the fitted Higgs mass by  $^{+16}_{-9}$  GeV. Therefore more precise measurements in this cms energy region are important.

The importance of the external  $\Delta\alpha_{\text{had}}^{(5)}(M_Z^2) = 0.02758 \pm 0.00035$ [43] determination for the constraint on  $m_H$  is shown in Fig. 6.7. Without the external  $\Delta\alpha_{\text{had}}^{(5)}(M_Z^2)$  constraint, the fit results are  $\Delta\alpha_{\text{had}}^{(5)}(M_Z^2) = 0.0298^{+0.0010}_{-0.0017}$  and  $m_H = 29^{+77}_{-15}$  GeV, with a correlation of  $-0.88$  between these two fit results.

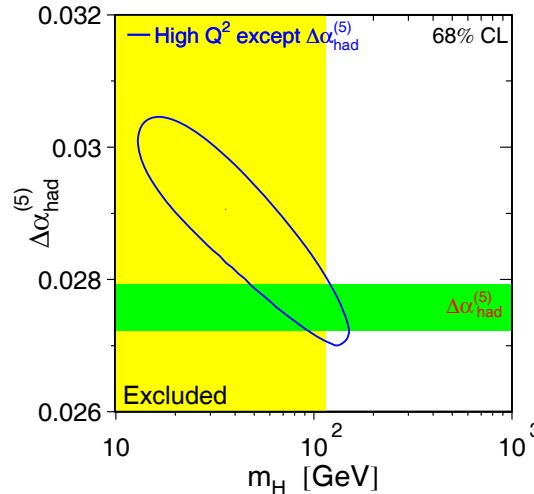


Figure 6.7: Contour curve of 68% probability in the  $(\Delta\alpha_{\text{had}}^{(5)}(M_Z^2), m_H)$  plane, based on all measurements other than that of  $\Delta\alpha_{\text{had}}^{(5)}(M_Z^2)$ . The direct measurements of the excluded observable is shown as the horizontal bands of width  $\pm 1$  standard deviation. The vertical band shows the 95% confidence level exclusion limit on  $m_H$  of 114.4 GeV derived from the direct search at LEPII [73].

The latest global fit of the LEP Electroweak Working Group, which employs the complete set of EW observables, leads to the predicted value  $m_H = 91^{+45}_{-32}$  GeV, with a 95% confidence level upper limit of 186 GeV [73] (see Fig. 6.8). This upper limit increases to 219 GeV when the LEP-II direct search lower limit of 114 GeV is included.

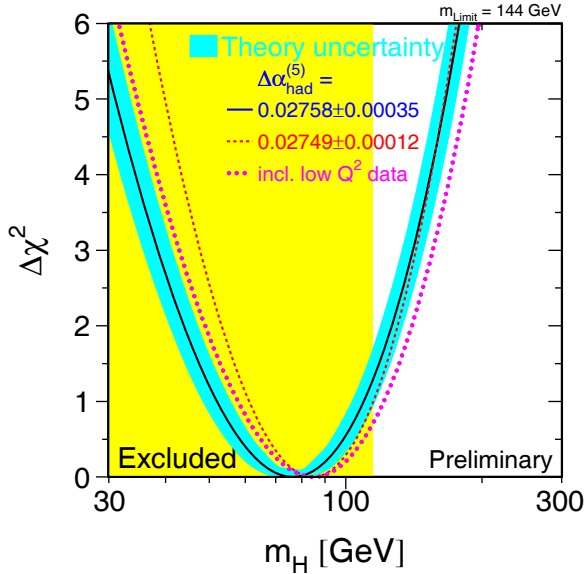


Figure 6.8: The black line is the result of the Electroweak Working Group fit using all data [73]; the band represents an estimate of the theoretical error due to missing higher-order corrections. The vertical band shows the 95% CL exclusion limit on  $m_H$  from the direct search.

## 6.4 Measurement of $R$ value at **BES-III**

The  $R$  value is defined in Eq. 6.1.1. Experimentally, it is determined from [79, 80, 81]

$$R_{exp} = \frac{N_{had}^{obs} - N_{bg}}{\sigma_{\mu\mu}^0 L \epsilon_{trg} \bar{\epsilon}_{had} (1 + \delta)}, \quad (6.4.27)$$

where  $N_{had}^{obs}$  is the number of observed hadronic events,  $N_{bg}$  is the number of the residual backgrounds,  $L$  is the integrated luminosity,  $\bar{\epsilon}_{had}$  is the average detection efficiency for hadronic events [82],  $\epsilon_{trg}$  is the trigger efficiency [83],  $(1 + \delta)$  is the correction factor of the initial state radiation (ISR), and  $\sigma_{\mu\mu}^0$  is the theoretical Born cross section for  $e^+e^- \rightarrow \mu^+\mu^-$ . Figure 6.9 shows the measured  $R$  values below 5 GeV and the higher charmonium resonance structures measured by BES-II.

### 6.4.1 Hadronic event selection and background subtraction

In the BEPC energy region, the event types in the raw data are the QED processes ( $e^+e^- \rightarrow e^+e^-$ ,  $\mu^+\mu^-$ ,  $\tau^+\tau^-$ ,  $\gamma\gamma$ , etc.), hadronic processes (including continuum and resonance states) and beam-associated backgrounds. The observed final-state particles are  $e$ ,  $\mu$ ,  $\pi$ ,  $K$ ,  $p$  and  $\gamma$ .

Different types of final states can be identified with specialized selection criteria. At high energies ( $E_{cm} > 2$  GeV), there are many unknown and unobservable hadronic production channels, one cannot measure  $R$  by summing up all of the exclusive cross sections.

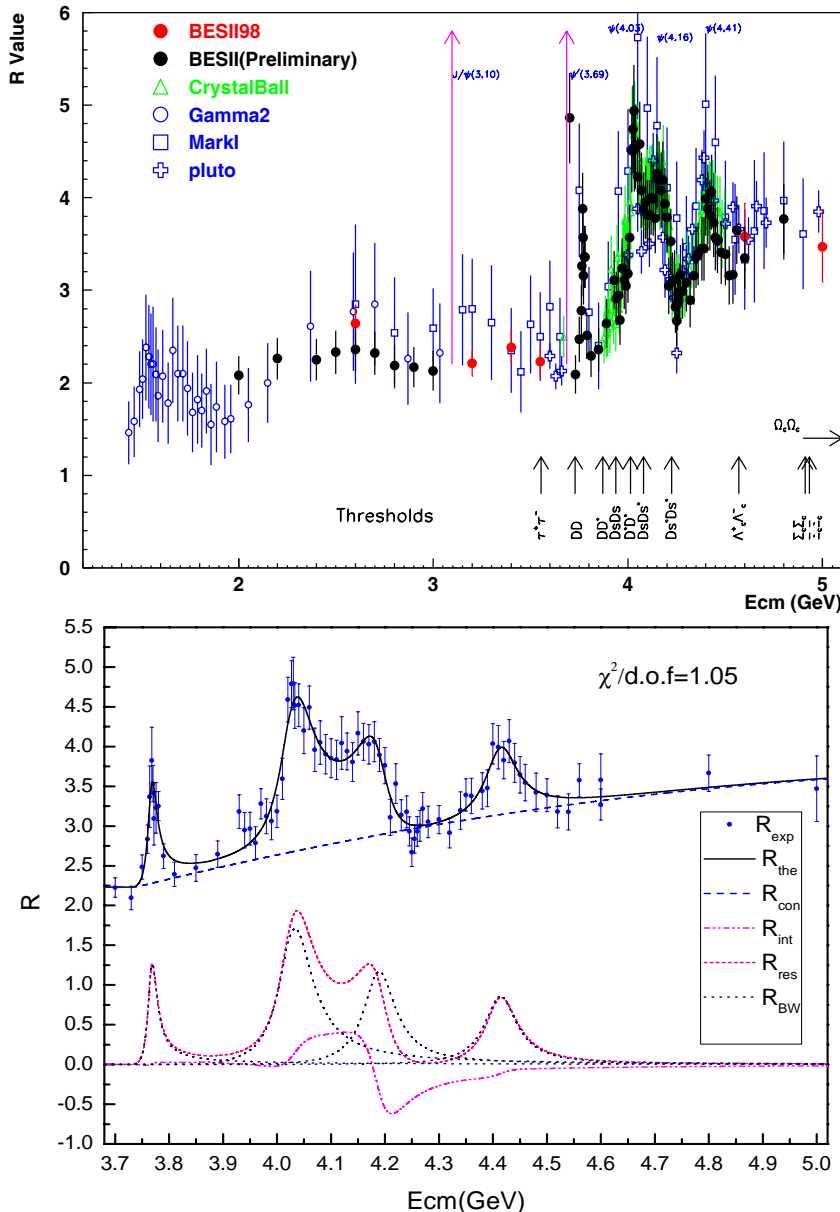


Figure 6.9: Upper:  $R$  values measured between 2-5 GeV. Lower: the charmonium resonance structures measured with BESII.

The strategy for selecting an inclusive sample of hadronic events is to first subtract the backgrounds, and then judge the remaining events by specific criteria [84]: (1) if an event is classified as  $e^+e^-$  or  $\gamma\gamma$  or  $\mu^+\mu^-$ , it is rejected; (2) the residual backgrounds are further removed by the hadronic criteria; (3) an energy deposit cut is used to remove most of the beam-associated backgrounds.

In the data analysis, the hadronic events are classified by the number of their charged tracks and the hadronic criteria may be divided into track level and event level. Hadronic events with two or more good charged tracks ( $n_{gd} \geq 2$ ) are selected by the criteria described in Refs. [80] and [81]. For events with a single good charged track ( $n_{gd} = 1$ ), one or more  $\pi^0$ 's are required [84].

The number of observed hadronic events,  $N_{had}^{obs}$ , is obtained by fitting the  $z$ -vertex distribution of the selected events with a Gaussian signal function and a polynomial background [81]. The number of the residual QED backgrounds  $N_{bg}$  is estimated statistically from

$$N_{bg} = L \sum_{QED} \epsilon_{QED} \cdot \sigma_{QED}, \quad (6.4.28)$$

where  $\sigma_{QED}$  is the theoretical cross section of the QED process and  $\epsilon_{QED}$  is the corresponding residual efficiency [79].

The fraction of the hadronic events lost in the reconstruction and data analysis is compensated by the Monte Carlo-determined hadronic event efficiency

$$\bar{\epsilon}_{had} = \frac{N_{gen}^{MC}}{N_{obs}^{MC}}, \quad (6.4.29)$$

where  $N_{gen}^{MC}$  is the number of the inclusive hadronic events produced by the generator, and  $N_{obs}^{MC}$  is the observed number of events passing the detector simulations and the event selection requirements.

### 6.4.2 Scan of the continuum and resonances

The measured  $R$  values for the 2-5 GeV energy region are shown in Fig. 6.9. The region between 2.0 and 3.73 GeV is called the continuum region (except for the two narrow resonances  $J/\psi$  and  $\psi'$ ). The  $R$  values in this region are approximately smooth and change very slowly with energy, as predicted by QCD. The energy range above the open-charmed meson pair-production threshold (3.73 GeV), is called the resonance region. There, previously observed resonances are the  $\psi(3773)$ ,  $\psi(4040)$ ,  $\psi(4190)$  and  $\psi(4415)$  [87][88]; the  $Y(4260)$  resonance was only recently observed [89] and only in its  $\pi^+\pi^-J/\psi$  decay mode;  $Y(4260)$  decays to open-charmed mesons have yet to be seen. They might be observed at *BES-III* in a scan with small energy steps and large statistics at each point.

The measured  $R$  value have to be corrected by the ISR factor  $(1 + \delta)$ , which depends on the  $R$  value and the resonance parameters. In general, the measurement of  $R$  value in the resonance region has to be an iterative procedure [88] and the following issues should be taken into account:

- Breit-Wigner amplitude: The relativistic Breit-Wigner amplitude for  $e^+e^- \rightarrow$  resonance  $\rightarrow$  final state  $f$  is

$$\mathcal{T}_r^f(W) = \frac{M_r \sqrt{\Gamma_r^{ee} \Gamma_r^f}}{W^2 - M_r^2 + i M_r \Gamma_r} e^{i\delta_r}, \quad (6.4.30)$$

where  $W \equiv E_{cm} \equiv \sqrt{s}$  is the cms energy, the index  $r$  represents the resonance being considered,  $M_r$  is the nominal resonance mass,  $\Gamma_r$  is the full width,  $\Gamma_r^{ee}$  is the electron width,  $\Gamma_r^f$  is the hadronic width for the decay channel  $f$ , and  $\delta_r$  is the phase.

High mass charmonium states can decay into several two-body final states  $f$ . According to the Eichten model [91] and existing experimental data [92], the allowed decay channels (including their conjugate states) are:

$$\begin{aligned} \psi(3770) &\Rightarrow D\bar{D}; \\ \psi(4040) &\Rightarrow D\bar{D}, D^*\bar{D}^*, D\bar{D}^*, D_s\bar{D}_s; \\ \psi(4140) &\Rightarrow D\bar{D}, D^*\bar{D}^*, D\bar{D}^*, D_s\bar{D}_s, D_s\bar{D}_s^*; \\ \psi(4415) &\Rightarrow D\bar{D}, D^*\bar{D}^*, D\bar{D}^*, D_s\bar{D}_s, D_s\bar{D}_s^*, D_s^*\bar{D}_s^*, D\bar{D}_1, D\bar{D}_2^*. \end{aligned}$$

The total squared inclusive amplitude of the resonances is the incoherent sum over all different decay channels  $f$ ,

$$|\mathcal{T}_{res}|^2 = \sum_f |\sum_r \mathcal{T}_r^f(W)|^2. \quad (6.4.31)$$

The resonance cross section can be expressed in terms of  $R$  as

$$R_{res} = \frac{12\pi}{s} \{ |\mathcal{T}_{\psi(2S)}|^2 + |\mathcal{T}_{res}|^2 \}, \quad (6.4.32)$$

where the contribution from the high-mass tail of  $\psi(2S)$  is included.

- Hadronic width: The hadronic width of a broad resonance depends on the energy. The calculation of  $\Gamma_r^f(W)$  involves strong interactions, and phenomenological models have to be used. The decay of a resonance can be viewed as quantum mechanical barrier penetration [93], and this predicts the energy-dependence of the hadronic width to be [94, 95]

$$\Gamma_r^f(W) = \hat{\Gamma}_r \sum_L \frac{Z_f^{2L+1}}{B_L}, \quad (6.4.33)$$

where  $L$  is the orbital angular momentum of the decaying final state,  $\hat{\Gamma}_r$  is a parameter to be determined by fitting experimental data,  $Z_f \equiv \rho P_f$ ,  $\rho$  is the radius of the interaction (of the order of a few fermis) and  $P_f$  is the decay momentum. The energy-dependent functions  $B_L$  are given in Ref. [94].

- Continuum backgrounds: Contributions from continuum backgrounds that originate from initial light-quark pairs ( $u\bar{u}$ ,  $d\bar{d}$  and  $s\bar{s}$ ) are well described by pQCD for cms energies above 2 GeV. Because of the proximity of the production threshold, open- $c\bar{c}$  continuum backgrounds can only be described by phenomenological models or experimental expressions. The DASP group assumes that the continuum charm backgrounds are the two-body

states  $D\bar{D}$ ,  $D\bar{D}^*$ ,  $D^*\bar{D}^*$ ,  $D_s\bar{D}_s$ ,  $D_s\bar{D}_s^*$  and  $D_s^*\bar{D}_s^*$ . The cross sections for these continuum backgrounds are given in Ref. [97]. One can assume that there are many possible continuum states above the open-charm threshold, and the inclusive cross section is expected to vary smoothly with energy. For simplicity, it is parameterized as a second-order polynomial [88]. The shape of the continuum backgrounds can be calculated using the LUND area law [Eq. (5.3.8)], but the normalization constants have to be determined from data. Note that both the DASP-form and the polynomial provide smooth backgrounds shapes, while the LUND area law can be used to describe more complex threshold behaviors.

- Fitting function: The iterative fits can be done with a least squares method using MINUIT [98] with a  $\chi^2$  is defined as

$$\chi^2 = \sum_i \frac{[f_c \tilde{R}_{exp}(W_i) - \tilde{R}_{the}(W_i)]^2}{[f_c \Delta \tilde{R}_{exp}^{(i)}]^2} + \frac{(f_c - 1)^2}{\sigma_c^2}, \quad (6.4.34)$$

where the experimental and the corresponding theoretical quantities are

$$\tilde{R}_{exp} = \frac{N_{had}^{obs} - N_{bg}}{\sigma_{\mu\mu}^0 L \epsilon_{trg} \bar{\epsilon}_{had}} \quad \text{and} \quad \tilde{R}_{the} = (1 + \delta) R_{the}. \quad (6.4.35)$$

Here  $\Delta \tilde{R}_{exp}^{(i)}$  is the statistical and non-common systematic errors of  $\tilde{R}_{exp}(W_i)$ ,  $\sigma_c$  is the common error, and the scale factor  $f_c$  reflects the influence of the common error. If interference between the continuum and resonance states is ignored,  $R_{the}$  is given by

$$R_{the} = R_{con} + R_{res}. \quad (6.4.36)$$

The measurement of the resonance parameters and  $R$  is performed iteratively: the initial values of the parameters are used as the inputs to calculate the radiative correction factors  $(1 + \delta)$  at all energy-points; then these values are updated in the next iteration; the fitting continues until  $\chi^2$  satisfies the convergence conditions and the correct error matrix is given, and the measured  $R$  values and resonance parameters are obtained.

### 6.4.3 *R* values from radiative return

Energy scans were used to collect data at different cms energies to measure  $R$  values at BEPC/BESII, and the effects of ISR are corrected by the factor  $(1 + \delta)$ . The luminosity of BEPC-II will be 100 times higher than that at BEPC, and the photon resolution at *BES-III* is significantly improved. This will make it possible to measure  $R$  values with the ISR (radiative return) events:

$$e^+ e^- \rightarrow \gamma^{hrd} + \gamma^{sft} + \text{hadrons},$$

where  $\gamma^{hrd}$  indicates an observed hard radiated photon with large momentum from the initial  $e^+$  or  $e^-$ , and  $\gamma^{sft}$  indicates possible observed or unobserved soft photons. In terms of  $x$ , the fraction of the beam particle's energy that is transferred to the ISR photon, the effective energy for producing the final-state hadrons is  $s' = s(1 - x)$ . The cross section for the ISR process  $e^+ e^- \rightarrow \gamma^{hrd} + f$  with a particular final state  $f$  is related to the cross section  $\sigma_f(s)$  for the direct annihilation as [99]

$$\frac{d\sigma_f(s, x)}{dx} = W(s, x) \sigma_f[s(1 - x)], \quad (6.4.37)$$

where  $x = 2E_\gamma^*/\sqrt{s}$ ,  $E_\gamma^*$  is the radiated photon fractional energy in the  $e^+e^-$  frame (laboratory system) and  $\sqrt{s}$  the nominal center-of-mass energy of the collider. The radiator function  $W(s, x)$  has been computed including radiative correction to an accuracy that is better than 1% [100, 101]

$$W(s, x) = \beta[(1 + \delta)x^{\beta-1} - 1 + \frac{x}{2}], \quad (6.4.38)$$

where  $\beta = 2\alpha/\pi(\ln(s/m_e^2) - 1)$  and  $\delta$  takes into account vertex and self-energy corrections.

The production of ISR photons is strongly concentrated along the incident beam direction, which means that most of the ISR events can not be identified and lost in data analysis. In order to accumulate a data sample within a small window of lower effective energy  $\Delta s'$  and with large enough statistics for a particular channel  $f$ , it is necessary to run BEPCII at a fixed nominal energy  $\sqrt{s}$  (such as a resonance peak) for a long period, as was done with PEP-II at SLAC.

Typically, many photons are observed in an event, most of which are produced either via hadronic processes (*e.g.*  $\pi^0 \rightarrow \gamma\gamma$  etc.), by interactions between produced hadrons and the material of the detector or by soft ISR. In order to be able to distinguish the hard ISR photon from soft ISR photons and hadronically produced photons, the measured energy region  $s'$  must be substantially lower than  $s$ . For example, PEP-II runs at nominal energy  $\sqrt{s} = 10.5$  GeV, while the the energy region for the BaBar  $R$  measurements is below 5 GeV.

The main focus of radiative-return  $R$  measurements has been the study of exclusive hadronic channels. The interesting channels at low energies are:  $\pi^+\pi^-$ ,  $K^+K^-$ ,  $p\bar{p}$ ,  $\pi^+\pi^-\pi^0$ ,  $4\pi$ ,  $5\pi$ ,  $6\pi$ ,  $\pi\pi\eta$ ,  $K\bar{K}\pi$ ,  $K\bar{K}\pi\pi$ ,  $2K2\bar{K}$ ,  $K\bar{K}\eta$ . Measurements of the leptonic process  $e^+e^- \rightarrow \gamma\mu^+\mu^-$  provides the ISR luminosity. Thus the Born cross section  $\sigma_s(s')$  is obtained from [99]

$$\sigma_f(s') = \frac{\Delta N_{\gamma f} \epsilon_{\mu\mu} (1 + \delta_{FSR}^{\mu\mu})}{\Delta N_{\gamma\mu\mu} \epsilon_f (1 + \delta_{FSR}^f)} \sigma_{\mu\mu}(s'), \quad (6.4.39)$$

where  $\Delta N_{\gamma f}$  is the number of detected  $\gamma f$  events in the bin of width  $\Delta s'$  centered at  $s'$ ,  $\epsilon_f$  is the detected efficiency for the final state  $f$ , and  $\delta_{FSR}^f$  is the fraction of times the photon is emitted by one of the final state particles. The quantities for  $\gamma\mu^+\mu^-$  have similar meanings. It is important to correctly compute the  $s'$  value for each event as it has to be obtained from the momenta of the produced particles, since the photon energy is rather insensitive to  $s'$  in the low-energy regime of interest.

The  $R$  measurement for the inclusive hadronic cross section with ISR data needs more detailed study. One of the main difficulties, based on BaBar's experience, is that the resolution deteriorates rapidly for low recoil masses [99].

Assuming that the luminosity of BEPC-II is  $10^{33} \text{cm}^2 \text{s}^{-1}$  at 4 GeV, one can collect about  $10^8$  hadronic events in a one-year run ( $\sim 10^7$ s). Table 6.3 shows the estimated number of the produced hadronic events in a series of effective energy intervals  $\Delta\sqrt{s'}$ . The hadronic efficiency depends on  $\sqrt{s'}$ , it was typically about 0.50–0.68 for  $N_{gd} \geq 1$ -prong events in the solid angle  $|\cos\theta| < 0.86$  for BESII, but the efficiency will fall rapidly with decreasing  $\sqrt{s'}$ .

Table 6.3: Estimated numbers of the produced hadronic events in a series of effective energy intervals in a one year ( $10^7$  seconds) BEPC-II run at  $\sqrt{s} = 4\text{GeV}$ .

$\sqrt{s'}$	$\Delta N_{had}^{gen}$	$\sqrt{s'}$	$\Delta N_{had}^{gen}$	$\sqrt{s'}$	$\Delta N_{had}^{gen}$
0.4–0.5	$4.8 \times 10^5$	1.3–1.4	$3.0 \times 10^5$	2.2–2.3	$3.6 \times 10^5$
0.5–0.6	$5.3 \times 10^5$	1.4–1.5	$3.0 \times 10^5$	2.3–2.4	$3.6 \times 10^5$
0.6–0.7	$12.1 \times 10^5$	1.5–1.6	$2.7 \times 10^5$	2.4–2.5	$3.7 \times 10^5$
0.7–0.8	$31.8 \times 10^5$	1.6–1.7	$3.3 \times 10^5$	2.5–2.6	$3.7 \times 10^5$
0.8–0.9	$10.7 \times 10^5$	1.7–1.8	$3.2 \times 10^5$	2.6–2.7	$3.8 \times 10^5$
0.9–1.0	$3.2 \times 10^5$	1.8–1.9	$2.8 \times 10^5$	2.7–2.8	$3.8 \times 10^5$
1.0–1.1	$7.5 \times 10^5$	1.9–2.0	$2.5 \times 10^5$	2.8–2.9	$3.9 \times 10^5$
1.1–1.2	$2.4 \times 10^5$	2.0–2.1	$3.3 \times 10^5$	2.9–3.0	$4.2 \times 10^5$
1.2–1.3	$2.2 \times 10^5$	2.1–2.2	$3.4 \times 10^5$		

#### 6.4.4 Systematic errors

The two largest error sources for the  $R$  measurement are the error on the number of observed hadronic events  $N_{had}^{obs}$  and the error associated with hadronic event detection efficiency  $\bar{\epsilon}_{had}$ . Since the systematic errors of these two terms are estimated by comparing the difference between data and MC, the equivalent number of hadronic events can be defined as

$$\tilde{N}_{had}^{obs} = \frac{N_{had}}{\bar{\epsilon}_{had}} = N_{had}^{MC} \frac{N_{had}}{N_{had}^{MC}}. \quad (6.4.40)$$

In Eq. (6.4.27), the main systematic error for the  $R$  value measurement is estimated as

$$\frac{\Delta R}{R} \cong \sqrt{\left(\frac{\Delta \tilde{N}_{had}}{\tilde{N}_{had}}\right)^2 + \left(\frac{\Delta L}{L}\right)^2 + \left(\frac{\Delta \epsilon_{trg}}{\epsilon_{trg}}\right)^2 + \left(\frac{\Delta(1+\delta)}{1+\delta}\right)^2}. \quad (6.4.41)$$

In addition, the error of the tracking efficiency  $\sigma_{trk}$ , which reflects the difference of the track reconstruction between data and MC, will cause an additional error  $\Delta \epsilon_{trk}$ . The probability that  $n_{er}$  charged tracks are incorrectly reconstructed in an  $n_{gd}$ -prong event ( $n_{er} \leq n_{ch}$ ) can be considered to roughly obey a binomial distribution  $B(n_{er}; n_{gd}, \sigma_{trk})$ . With a multiplicity distribution of the form  $P(n_{gd})$ ,  $\Delta \epsilon_{trk}$  is estimated to be [84]

$$\Delta \epsilon_{trk} = \sum_{n_{gd}} P(n_{gd}) B(n_{er}; n_{gd}, \sigma_{trk}). \quad (6.4.42)$$

For measurements of the inclusive cross section, only those cases where *all*  $n_{gd}$  tracks in an event are incorrectly reconstructed ( $n_{er} = n_{gd}$ ) will contribute to the error on  $R$ .

# Chapter 7

## Experimental tests of QCD<sup>1</sup>

Quantum Chromodynamics (QCD) provides a means to apply perturbative techniques to quark-gluon evolution processes with large momentum transfer [122, 123]. However, the treatment of hadronization (the transition from quarks and gluons to hadrons at nonperturbative scales) has not been solved mathematically. At present, some assumptions about hadronization are commonly made. Local parton-hadron duality (LPHD) [124] predicts that the parton distributions are simply renormalized in the hadronization process without any shape changes. The modified leading-logarithmic approximation (MLLA) takes into account the soft partons and strict transverse momentum ordering in subsequent perturbative series. All distributions derived from LPHD/MLLA contain a few free parameters that have to be determined from experiment, and LPHD/MLLA itself still has to be experimentally tested. Some distributions that have not yet been predicted by LPHD/MLLA can be measured in experiments. Experimental tests of QCD-motivated models are very helpful for providing understanding of the strong interaction and for giving guidance to the development of nonperturbative QCD techniques.

### 7.1 Inclusive distributions

The different types of hadronic production measurements can be classified as total cross sections, and exclusive, inclusive, semi-inclusive and single-particle distributions according to how many and what kinds of the final particles are measured [131]. Note that the meanings of these terms may not be exactly the same in different references. In the following, some possible measurements are listed.

In general, inclusive distributions are measured as a function of the kinematic variables  $(s, p_{\parallel}, p_{\perp})$ . Two questions are addressed: (1) how do the distributions change with the cms energy  $\sqrt{s}$ ? and (2) how do these distributions change with momentum  $(p_{\parallel}, p_{\perp})$  when  $\sqrt{s}$  is fixed? The answer to the second question depends on the type of the initial state and the properties of measured particles in the final state.

Feynman hypothesized that at sufficiently high energies, where quark and hadron masses can be neglected, quark fragmentation depends only on the quark flavor and a dimensionless scaling variable  $x = 2p/E_{cm}$ . This scaling property means that the distributions are functions only of the scaling variable  $x$  and transverse momentum  $p_{\perp}$  at large

---

<sup>1</sup>By Hai-Ming Hu

energies. Thus, the cross section  $s d\sigma/dx$  averaged over  $p_\perp$  should be  $s$ -independent [111]. The scaling assumption is found to be a good approximation in high energy reactions. It has also been tested at BES-II, but further tests are needed to understand where and how scaling fails. This should provide some insight into pQCD and non-pQCD.

Commonly, inclusive distributions are measured as a function of Feynman  $x$  or  $\xi = -\ln x$ , rapidity  $y$  or  $\eta$ , and  $p_\perp$ .

•  $x$  distribution

Inclusive differential cross sections can be expressed in terms of the structure functions  $F_1$  and  $F_2$  [121],

$$\frac{d^2\sigma}{dxd\cos\theta} = \frac{3}{4}\sigma_0 x\beta[2F_1(x, s) + \frac{x\beta}{2}F_2(x, s)\sin^2\theta], \quad (7.1.1)$$

where  $\sigma_0$  is the zeroth-order QED cross section. The relationships between  $F_1$  &  $F_2$  and the longitudinal and transverse structure functions  $F_T$  &  $F_L$  are

$$F_T(x, s) = 2F_1(x, s), \quad (7.1.2)$$

$$F_L(x, s) = 2F_1(x, s) + xF_2(x, s). \quad (7.1.3)$$

•  $\xi$  distribution

The inclusive  $\xi$  distribution can be derived from MLLA/LPHD [132, 133, 134]

$$\frac{1}{\sigma} \frac{d\sigma^h}{d\xi} = 2K_{LPHD} \times f_{MLLA}(\xi, Q_0, \Lambda_{eff}), \quad (7.1.4)$$

where  $f_{MLLA}(\xi, Q_0, \Lambda_{eff})$  is the  $\xi$  distribution at the parton level and  $K_{LPHD}$  is a factor that connects the parton level and hadron level in the context of LPHD. The  $\xi$  range for Eq. (7.1.4) is  $0 \leq \xi \leq Y \equiv \ln(\sqrt{s}/2\Lambda_{eff})$ . In the neighborhood of the peak value  $\xi^*$ , the  $\xi$  distribution can be replaced with a distorted Gaussian form [112, 113]:

$$DG(\xi; N, \bar{\xi}, \sigma, s_k, k) = \frac{N}{\sigma\sqrt{2\pi}} \exp\left[\frac{1}{8}k - \frac{1}{2}s_k k\delta - \frac{1}{4}(2+k)\delta^2 + \frac{1}{6}s_k k\delta^3 + \frac{1}{24}k\delta^4\right], \quad (7.1.5)$$

where  $\delta = (\xi - \bar{\xi})/\sigma$ ,  $\bar{\xi}$  is the average value of  $\xi$ ,  $\sigma$  is the width of the  $\xi$  distribution, and  $s_k$  and  $k$  are the skewness and kurtosis, respectively. For a normal Gaussian function, both  $s_k$  and  $k$  are zero. MLLA/LPHD predicts that the peak position of  $\xi$  depends on the energy as

$$\xi^* = 0.5Y + \sqrt{cY} + c + \mathcal{O}(1/\sqrt{Y}), \quad (7.1.6)$$

where  $c$  is a function of the number of colors  $N_c$  and the number of the active quarks  $n_f$ . The energy dependence of  $\xi^*$  may be described as [117]

$$\xi^* = A \ln s + B, \quad (7.1.7)$$

where  $A$  and  $B$  are free parameters that are determined from experiment.

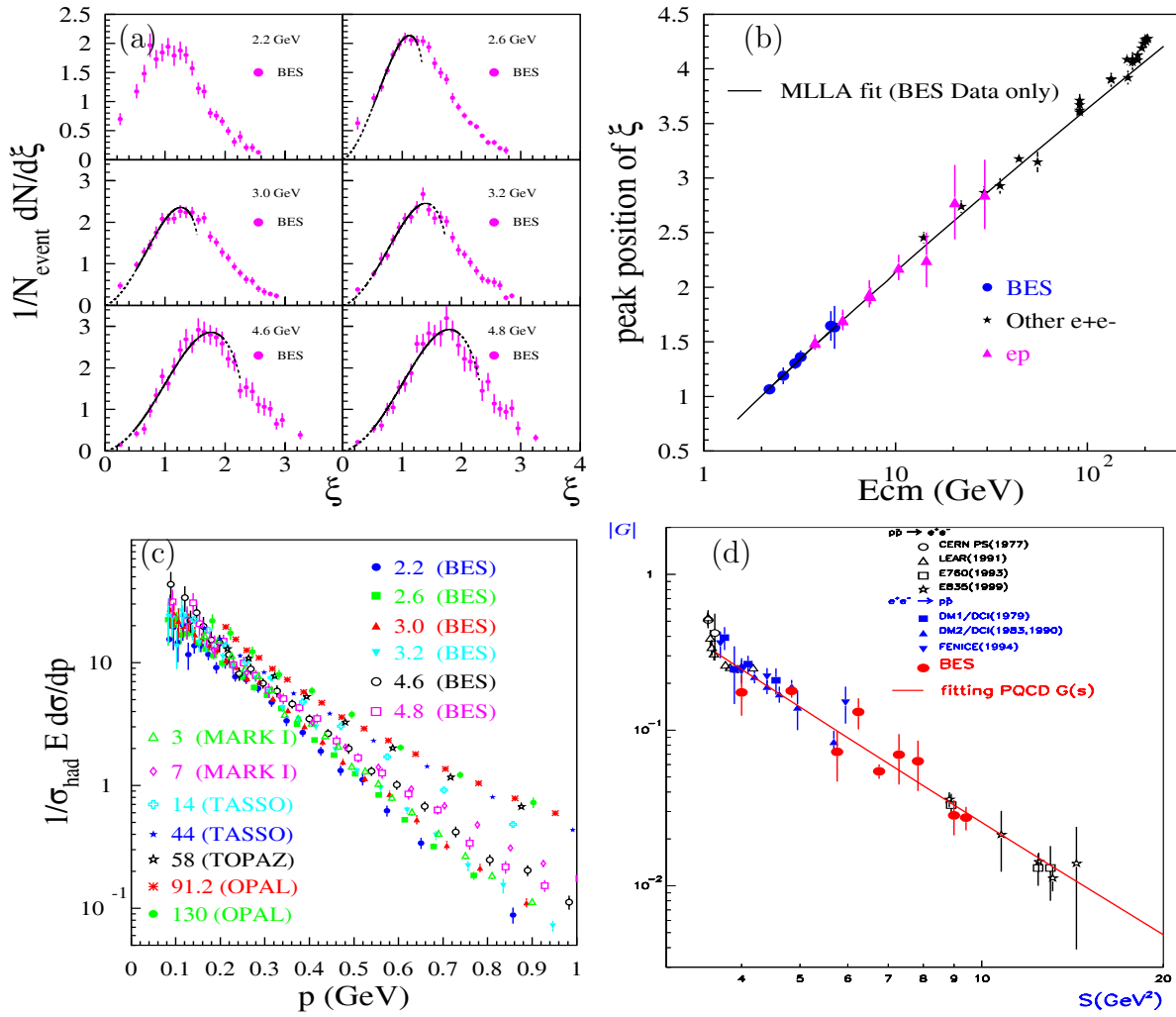


Figure 7.1: (a) Distributions of  $\xi$ ; (b) energy dependence of the peak position of  $\xi$ ; (c) distribution of momentum  $p$ ; (d)  $p\bar{p}$  form factors.

## 7.2 Exclusive cross sections and form factors

Exclusive cross sections can be written as functions of form factors that embody the influence of the strong interaction on the properties of electro-magnetic interaction vertices. Precise measurements of hadronic form factors helps promote the understanding to the strong interaction. In particular, in the BEPC energy region,  $e^+e^- \rightarrow \pi^+\pi^-$ ,  $\pi^+\pi^-\pi^0$ ,  $\pi^+\pi^-\pi^+\pi^-$ ,  $\pi^+\pi^-\pi^0\pi^0$ ,  $\pi^+\pi^-K^+K^-$ ,  $p\bar{p}$ ,  $\Lambda\bar{\Lambda}$  etc. have large production cross sections and it is important that they are properly modeled by the Monte Carlo generators.

- $e^+e^- \rightarrow N\bar{N}$

Nucleons, the proton  $p$  and neutron  $n$ , are the two most common components of matter. Their electromagnetic form factors describe their internal structure and dynamics.

In the process  $e^+e^- \rightarrow p\bar{p}$ , a pair of spin-1/2 baryons with internal structure are produced. The current contains two independent form factors, the Dirac  $F_1(q^2)$  and Pauli

$F_2(q^2)$  form factors [115], defined as

$$\langle N(p') | J^\mu(0) | N(p) \rangle = e\bar{u}(p')[F_1(q^2)\gamma^\mu + \frac{i}{2M}F_2(q^2)\sigma_{\mu\nu}q_\nu]u(p), \quad (7.2.8)$$

where  $M$  is the mass of nucleon and  $q^2 = (p - p')^2 = s$  is the squared momentum transfer at the photon-nucleon vertex.  $F_1(q^2)$  and  $F_2(q^2)$  are normalized so that for the proton  $F_1^p(0) = 1$  and  $F_2^p(0) = \kappa_p = \mu_p - 1$ , and for neutron  $F_1^n(0) = 0$  and  $F_2^n(0) = \kappa_n = \mu_n$ , where  $\kappa_p$  and  $\kappa_n$  are the anomalous part of proton and neutron magnetic moments. The electric  $G_E(s)$  and magnetic  $G_M(s)$  form factors are defined by the combinations

$$G_E = F_1 + \tau F_2, \quad G_M = F_1 + F_2. \quad (7.2.9)$$

The differential and total cross sections are given by [114, 116]

$$\frac{d\sigma}{d\Omega} = \frac{\alpha^2\beta}{4s}C[|G_M(s)|^2(1 + \cos^2\theta) + \frac{1}{\tau}|G_E(s)|^2\sin^2\theta] \quad (7.2.10)$$

$$\sigma = \frac{4\alpha^2\pi\beta}{3s}[|G_M(s)|^2 + \frac{1}{2\tau}|G_E(s)|^2], \quad (7.2.11)$$

where  $\tau = s/4M^2$ ,  $\theta$  is the scattering angle,  $\beta = \sqrt{1 - 1/\tau}$  is the velocity and  $C$  is the Coulomb correction factor. For the neutron  $C = 1$ , and for the proton

$$C = \frac{y}{1 - \exp(-y)}, \quad y = \pi\alpha M/\beta\sqrt{s}. \quad (7.2.12)$$

The electronic  $G_E(s)$  and magnetic  $G_M(s)$  are two independent form factors with normalizations  $G_E(0) = 1$  and  $G_M(0) = \mu_p$ . Figure 7.1(d) shows the measured form factor of the proton under the assumption that  $G_E(s) = G_M(s)$ . The measurement of the angular distribution of Eq. (7.2.10) determines  $G_E(s)$  and  $G_M(s)$  simultaneously, provided the data sample is sufficiently large.

- $e^+e^- \rightarrow \pi$  mesons

In 1988, the  $\rho(1600)$  entry in the PDG tables was replaced by two new resonances: the  $\rho(1450)$  and  $\rho(1700)$ . It has been suggested that this assignment can be validated by a theoretical analysis on the consistency of the  $2\pi$  and  $4\pi$  electromagnetic form factors. In any case, detailed experimental data on the cross section for  $e^+e^- \rightarrow \pi^+\pi^-\pi^+\pi^-$  will make possible the accurate determination of the parameters of the  $\rho$ -meson and its radial recurrences.

The venerable vector-meson-dominance model (VMD) has been modified to expand the contributions of the lowest-lying vector-mesons to include their high-mass recurrences [136, 137]. Previous analyses [136] used different decay channels to obtain the relevant parameters. Reference [135] uses the cross section for  $e^+e^- \rightarrow \pi^+\pi^-\pi^+\pi^-$  derived from the extended VMD model to fit BaBar experimental data. Cross sections for the processes  $e^+e^- \rightarrow \pi^+\pi^-$ ,  $\omega\pi^0$ ,  $\eta\pi^+\pi^-$ ,  $\pi^+\pi^-\pi^+\pi^-$  and  $\pi^+\pi^-\pi^0\pi^0$  can be found in Refs. [136, 137].

- Higher order corrections for  $e^+e^- \rightarrow \pi^+\pi^-(\gamma)$

More precision measurements of the pion form factor will require a careful consideration of the radiative corrections, including the initial state (IS) and the final state (FS) contributions. Reference [143] presents field-theory-based calculations for  $e^+e^- \rightarrow \pi^+\pi^-(\gamma)$  production with higher order radiative corrections. The Born cross section for  $e^+e^- \rightarrow \pi^+\pi^-$

can be written as

$$\frac{d\sigma_0}{d\Omega} = \frac{\alpha^2 \beta_\pi^3}{8s} \sin^2 \theta |F_\pi(s)|^2, \quad \text{or} \quad \sigma_0(s) = \frac{3\pi \alpha^2 \beta_\pi^3}{3s} |F_\pi(s)|^2, \quad (7.2.13)$$

where  $\theta$  is the angle between  $\vec{p}_{\pi^-}$  and  $\vec{p}_{e^-}$  and  $\beta_\pi = \sqrt{1 - 4m_\pi^2/s}$ . The form factor  $F_\pi(s)$  encodes the substructure of the pion with the charge normalization constraint  $F_\pi(0) = 1$  (classical limit). For real radiation  $e^+e^- \rightarrow \pi^+\pi^-\gamma$ , the invariant mass square of the pion pair is  $s' = (p_{\pi^+} + p_{\pi^-})^2$ . Reference [143] presents the differential cross section, the total cross section and the pion form factor with higher-order corrections. Discussions for  $e^+e^- \rightarrow K_SK_L(\gamma)$  and  $K^+K^-(\gamma)$  can be found in Ref. [149]. The Monte Carlo generator MCGPJ [144] simulates events with two-body final states, including  $e^+e^- \rightarrow \pi^+\pi^-(\gamma)$ ,  $K^+K^-(\gamma)$ ,  $\mu^+\mu^-(\gamma)$  and  $e^+e^-(\gamma)$ .

## 7.3 Multiplicity distribution

The charged particle multiplicity distribution is a basic quantity for any reaction. Precise measurements need reliable Monte Carlo and efficiency matrices to translate from measured to physical (theoretical) quantities. Experiments often measure the multiplicity distribution of the charged particles with the definition:

$$P(n_c) = \frac{\sigma_{n_c}}{\sum \sigma_{n_c}}, \quad (7.3.14)$$

where  $\sigma_n$  is the topological cross section for  $n$ -particle production; the average multiplicity is given by

$$\langle n_c \rangle = \sum n_c P(n_c). \quad (7.3.15)$$

The observed multiplicity distribution  $P_{obs}(n_c)$  is not the physical distribution  $P_{true}(n_c)$ . They are related by the migration matrix  $M(n'_c, n_c)$  [150, 151],

$$P_{obs}(n'_c) = \sum_{n_c} M(n'_c, n_c) P_{true}(n_c). \quad (7.3.16)$$

The matrix element  $M(n'_c, n_c)$  corresponds to the probability for events with  $n_c$  produced charged particles to end up with  $n'_c$  detected charged tracks. This can be determined from MC as

$$M(n'_c, n_c) = \frac{N_{MC}(n'_c, n_c)}{\sum_{n_c} N_{MC}(n'_c, n_c)}, \quad (7.3.17)$$

where  $N_{MC}(n'_c, n_c)$  is the number of events with  $n_c$  generated and  $n'_c$  observed charged particles. Equation (7.3.16) can be rewritten in matrix notation as

$$P_{obs} = M P_{true}, \quad \text{or} \quad P_{true} = M^{-1} P_{obs}, \quad (7.3.18)$$

where  $P_{true}$  and  $P_{obs}$  are vectors whose elements are  $P_{true}(n_c)$  and  $P_{obs}(n'_c)$ .

QCD-motivated models interpret the jet evolution as a branching process, and predict mean multiplicities to increase with energy as

$$\langle n_c \rangle = a + b \cdot \exp\{c[\ln(s/Q_0^2)]^{1/2}\}. \quad (7.3.19)$$

The NLO-based QCD evolution relation for fragmentation predicts [118]

$$\langle n_c \rangle = a[\alpha_s(s)]^b \exp[c/\sqrt{\alpha_s(s)}][1 + d\sqrt{\alpha_s(s)}], \quad (7.3.20)$$

where

$$b = \frac{1}{4} + \frac{10n_f}{27\beta_0}, \quad c = \frac{\sqrt{96\pi}}{\beta_0}, \quad (7.3.21)$$

with  $n_f$  the number of the active quarks,  $\beta_0 = 11 - (2/3)n_f$ ;  $a$  and  $d$  free parameters. NLO predicts the second-order moment to be

$$R_2 \equiv \frac{\langle n_c(n_c - 1) \rangle}{\langle n_c \rangle^2} = \frac{11}{8}[1 - c\sqrt{\alpha_s(s)}], \quad (7.3.22)$$

where

$$c = \frac{1}{\sqrt{6\pi}} \frac{4455 - 40n_f}{1782}. \quad (7.3.23)$$

The average multiplicity derived from MLLA/LPHD can be written as [119]

$$\langle n_c \rangle = c_1 \frac{4}{9} N_{LA} + c_2, \quad (7.3.24)$$

where

$$N_{LA} = \Gamma(B) \left(\frac{z}{2}\right)^{(1-B)} I_{1+B}(z), \quad (7.3.25)$$

and  $z = \sqrt{48Y/\beta_0}$ ,  $Y = \ln(\sqrt{s}/2Q_0)$ ,  $B = a/\beta_0$ ,  $a = 11 + 2n_f/27$ . Here  $\Gamma$  is the Gamma function and  $I_x$  is the modified Bessel function of order  $x$ . The factor  $Q_0$  is the energy scale parameter, its value is taken to be 0.27 GeV in Ref. [119].

A commonly used expression for the average multiplicity is [120]

$$\langle n_c \rangle = a + b \ln s + c \ln^2 s, \quad (7.3.26)$$

where  $a$ ,  $b$  and  $c$  are free parameters. The energy variation of the multiplicity distribution can be studied by measuring its variance

$$D_c = \sqrt{\langle n_c^2 \rangle - \langle n_c \rangle}. \quad (7.3.27)$$

In hadron production experiments, the forward and backward correlations

$$\langle n_B \rangle = a + b n_F \quad \text{or} \quad \langle n_F \rangle = c + d n_B \quad (7.3.28)$$

can give some useful information.

Feynman scaling predicts that the hadronic cross section  $\sigma_{n_c}(s)$  satisfy a scaling law for large  $\langle n_c \rangle$  [130]:

$$\langle n_c \rangle \frac{\sigma_{n_c}(s)}{\sum_{n_c} \sigma_{n_c}(s)} = \langle n_c \rangle P(n_c) \rightarrow \Psi(z), \quad (7.3.29)$$

which means  $\langle n_c \rangle P(n_c)$  depends on  $n_c$  through  $z \equiv n_c/\langle n_c \rangle$ . Here,  $\Psi(z)$  is a energy independent function. The scaling law has been tested at high energies [120], but the approximation of the scaling assumption has not been tested in BEPC energies with high precision.

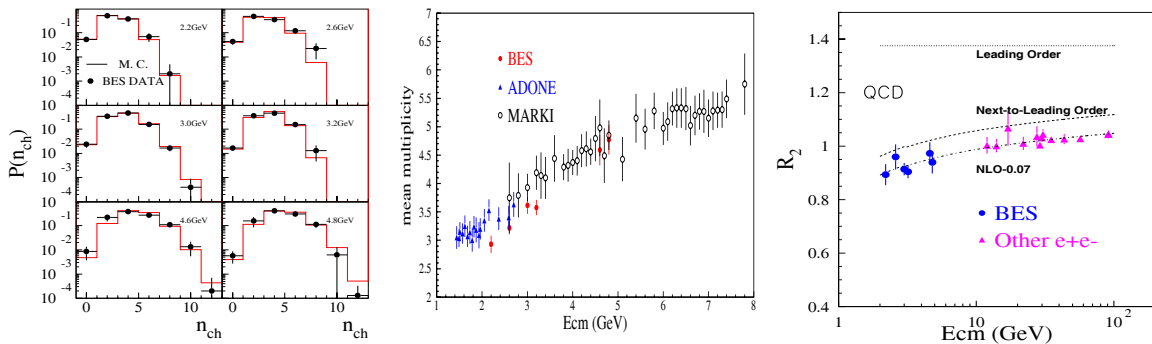


Figure 7.2: Left: multiplicity distributions; middle: the energy dependence of average multiplicity; right: a comparison of data and QCD predictions for  $R_2$ .

## 7.4 Kinematical and dynamical correlations

In inclusive measurements, only the kinematics of one particle are measured; the kinematics of all the others are averaged. Thus, a great amount of information is lost in the summation. Measurements of correlation effects is a more valid way to extract dynamical information from experimental data and test hadronization models.

The simplest correlation function is the two-particle correlation. In order to separate pseudo-correlations from the true one, experiments measure the inclusive correlation function [138]

$$C_2(x_1, x_2) = C_S(x_1, x_2) + C_L(x_1, x_2), \quad (7.4.30)$$

where

$$\begin{aligned} C_S(x_1, x_2) &= \sum_{n_c} P(n_c) C_2^{(2)}(x_1, x_2), \\ C_L(x_1, x_2) &= \sum_{n_c} P(n_c) \Delta \rho^{(n_c)}(x_1) \Delta \rho^{(n_c)}(x_2). \end{aligned} \quad (7.4.31)$$

Here  $x$  can be any kinematical observable.  $C_S$  is the average of the semi-inclusive correlation functions and is more sensitive to the dynamical correlations.  $C_L$  arises from mixing different topological particle densities. Related distributions are defined as

$$\rho_1^{(n_c)}(x) = \frac{1}{\sigma_{n_c}} \frac{d\sigma}{dx}, \quad (7.4.32)$$

$$\rho_2^{(n_c)}(x_1, x_2) = \frac{1}{\sigma_{n_c}} \frac{d^2\sigma}{dx_1 dx_2}, \quad (7.4.33)$$

$$C_2^{(n_c)}(x_1, x_2) = \rho_2^{(n_c)}(x_1, x_2) - \rho_1^{(n_c)}(x_1) \rho_1^{(n_c)}(x_2), \quad (7.4.34)$$

$$\Delta \rho^{(n_c)}(x) = \rho_1^{(n_c)}(x) - \rho_1(x). \quad (7.4.35)$$

Discussions about distribution and correlation functions can be found in Refs. [146, 147, 148].

## 7.5 Topological event shapes

A typical event produced in a collision process has several final-state particles and kinematical parameters are needed to summarize global correlations among these particles. To describe the complicated topologies encountered in multihadronic events, a number of event measures have been introduced, including the event-shape parameters sphericity and thrust. These quantities are intended to provide a global view of the properties of a given process, wherein the full information content of the event is condensed into one or two measured numbers. QCD-motivated models give quantitative predictions for sphericity and thrust that agree with high energy measurements; these have not yet been studied at intermediate energies.

The SPEAR Group introduced a method based on the inertia tensor in classical dynamics to make the first studies of jet structure in  $e^+e^-$  annihilation events [139, 104].

- Sphericity  $S$

Sphericity is a geometrical parameter reflecting the degree of isotropy in configurations of final-state hadrons. The sphericity tensor is defined as [140]

$$S^{\alpha\beta} \equiv \frac{\sum_i p_i^\alpha p_i^\beta}{\sum_i |\vec{p}_i|^2}, \quad \alpha, \beta = 1, 2, 3, \quad (7.5.36)$$

where  $\vec{p}_i$  is the momentum of final state hadron  $i$  and the summation runs over all observed hadrons in an event. The three eigenvalues of  $S^{\alpha\beta}$  are ordered as  $\lambda_1 \geq \lambda_2 \geq \lambda_3$  with  $\lambda_1 + \lambda_2 + \lambda_3 = 1$ . “Sphericity” is defined as

$$S = \frac{3}{2}(\lambda_1 + \lambda_2), \quad (7.5.37)$$

so that  $0 < S < 1$ . Sphericity is essentially a measure of the summed  $p_\perp$  with respect to the event axis. A severe two-jet event corresponds to  $S \approx 0$  and an isotropic event to  $S \approx 1$ . In practice, the special direction  $\vec{n}_S$ , which minimizes the value of  $S$ , is found:

$$S = \min \frac{3 \sum_i |\vec{n}_S \cdot \vec{p}_i|^2}{2 \sum_i \vec{p}_i^2}. \quad (7.5.38)$$

- Trust  $T$

Trust is a parameter that reflects the degree of anisotropy of the three-momenta of final state particles and is defined as

$$T = \max \frac{\sum_i |\vec{n}_T \cdot \vec{p}_i|}{\sum_i |\vec{p}_i|}. \quad (7.5.39)$$

where the vector  $\vec{n}_T$  defines the “thrust axis”, *i.e.* the direction that maximizes the value of  $T$ . It is often useful to divide an event into two hemispheres by a plane through the origin and perpendicular to the trust axis. The allowed range of  $T$  is  $0.5 < T < 1$ ; a severe two-jet event corresponds to  $T \approx 1$  and an isotropic event to  $T \approx 0.5$ . The quantity  $\tau = 1 - T$  is often used to replace  $T$ .

pQCD predicts that average trust values can be expressed as [141]

$$\langle \tau \rangle = \langle \tau^{pert} \rangle + \langle \tau^{pow} \rangle, \quad (7.5.40)$$

where  $\langle \tau^{pert} \rangle$  is the value calculated by pQCD, and  $\langle \tau^{pow} \rangle$  is the contribution from power corrections.  $\langle \tau^{pert} \rangle$  has been calculated based on NLO to be

$$\langle \tau^{pert} \rangle = A\tilde{\alpha}_s + (B - 2A)\tilde{\alpha}_s^2, \quad (7.5.41)$$

where  $\tilde{\alpha}_s = \alpha_s/2\pi$ , and the coefficients  $A$  and  $B$  are obtained from the integral of the NLO matrix element to be  $A = 2.103$  and  $B = 40.99$  [142].

## 7.6 Bose-Einstein correlations (BEC)

In quantum mechanics, the wave function of identical bosons is symmetric under the exchange of any two identical bosons. This property leads to a special statistical correlation, *i.e.* the so-called Bose-Einstein correlation, which exists in boson system even in the absence of any interactions. This symmetry leads an interference term that contains information on the space-time extent of hadronic sources.

### Correlation function

The manifestation of BEC is that the possibility of finding two identical bosons in a small phase-space volume element is larger than that for two different particles. The space-time properties of hadronic source can be inferred from measurements of Bose-Einstein correlation functions [152]. Suppose that a particle can be emitted at the space-time point  $x = (\vec{r}, t)$  from an extended hadronic source with the probability amplitude  $f_c(x)$ , and the wave function of the particle is a plane wave  $\psi(x) \sim \exp(ipx)$ . If the hadronic source is coherent, the probability for observing a stable and free particle with 4-momentum  $p = (\vec{p}, E)$  reads

$$P_c(p) = \left| \int \psi(x) f_c(x) d^4x \right|^2. \quad (7.6.42)$$

The joint probability for observing two identical bosons with momenta  $p_1$  and  $p_2$  can be written as

$$P_c(p_1, p_2) = \frac{1}{2} \left| \int d^4x_1 d^4x_2 \psi(x_1, x_2) f_c(x_1) f_c(x_2) \right|^2. \quad (7.6.43)$$

The spatial distribution of the hadronic source and the momentum distribution are related by a Fourier transformation and, so, the spatial distribution can be derived from the measured momentum distribution.

In experiments, correlation functions with slightly different definitions are used, such as [152]

$$R_2(p_1, p_2) = \frac{P_c(p_1, p_2)}{P_c(p_1)P_c(p_2)} - 1, \quad (7.6.44)$$

where one can see that  $R_2 = 0$  if there is no correlation between the two particles. Another form that is commonly used is [153]

$$C_2(Q^2) = \frac{N_2(p_i, p_j)}{N_1(p_i)N(p_j)}, \quad (7.6.45)$$

which is the ratio of the two-identical-boson distribution to the product of two single boson distributions. Following a suggestion in Ref. [154], Bose-Einstein correlation up to 5<sup>th</sup> order can be used in experimental studies. The correlation function of order  $q$ :

$$R_q(Q_{q\pi}^2) = \frac{N_q(Q_{q\pi}^2)}{N_q^{BG}(Q_{q\pi}^2)}, \quad (7.6.46)$$

is defined as the ratio of the distribution of like-charged  $q$ -tuplets ( $q = 2, 3, 4, 5$ )  $N_q(Q_{q\pi}^2)$  and a reference distribution (background)  $q$ -tuplets  $N_q^{BG}(Q_{q\pi}^2)$  obtained from random event-mixing. The variable  $Q_{q\pi}^2$  is defined as the sum over all permutations:

$$Q_{q\pi}^2 = Q_{12}^2 + Q_{13}^2 + Q_{23}^2 + \cdots + Q_{(q-1)q}^2, \quad (7.6.47)$$

of the squared 4-momentum difference  $Q_{ij}^2 = (p_i - p_j)^2$  of particle  $i$  and  $j$ .

Gyulassy suggests a simple procedure for incorporating the Coulomb final-state interaction between two charged pions [157]:

$$[R(\vec{p}_1, \vec{p}_2) + 1]_{theory+Coulomb} = W(\vec{p}_1, \vec{p}_2)[R(\vec{p}_1, \vec{p}_2) + 1]_{theory}, \quad (7.6.48)$$

where the Gamov factor  $W(\vec{p}_1, \vec{p}_2)$  is the square modulus of the relativistic Coulomb wave function at the origin [158]

$$W(\vec{p}_1, \vec{p}_2) = \frac{2\pi\eta}{\exp(2\pi\eta) - 1}, \quad (7.6.49)$$

with  $\eta = \alpha m_\pi / |\vec{p}_1 - \vec{p}_2|$ . The Gamov factor suppresses the correlation function at small relative momentum.

### Parametrization of the source distribution

Measurements of the BEC have two aims: the study the quantum effects of the particles and the space-time distribution of hadronic sources. For the latter, some models for the sources have been suggested [152].

- Gaussian source:

The most extensively used parametrization is a static hadronic source with a Gaussian form

$$\rho(\vec{r}) = \frac{1}{\sqrt{a_x^2 a_y^2 a_z^2 \pi^3 R^6}} \exp\{-(x/a_x)^2 - (y/a_y)^2 - (z/a_z)^2\}/R^2, \quad (7.6.50)$$

where  $(a_x, a_y, a_z)$  are dimensionless constants that allow for a nonspherical source, and  $R$  represents the scale of the source.

- Source with finite lifetime:

If one considers a source with a finite lifetime  $\tau$  and space dimension  $r_0$ , its distribution can be written as [155, 156]

$$\rho(\vec{r}, t) = \frac{1}{\pi^2 r_0^3 \tau} \exp(-r^2/r_0^2 - t^2/\tau^2). \quad (7.6.51)$$

The free parameters in the models can be determined by fitting the data, and the possible space-time distributions of the hadronic sources can be deduced. It is expected that the following subjects may be done for charged bosons: (1) two-body correlations: the inflections of multi-body correlation and the final-state electromagnetic and strong interactions; (2) the multiplicity dependence of BE correlations; (3) the space-time form of hadronic sources; and (4) BE correlations in resonance decays. This latter measurement requires large hadronic samples and excellent particle identification.

## 7.7 Possible fractal structure of final state phase-space

There has been a flaw in the study of the spectrum of the final state particles, *i.e.* one usually pays attention to averaged distributions only and attributes fluctuations to the statistical effects associated with having a finite number of particles. Events with abnormally high particle density condensed in small phase-space volumes have been observed in several types of high energy reactions [159, 160, 161, 162, 163, 164, 165, 166, 167].

Bialas and Peschanski [168, 169] suggested that spikes observed in experimental distributions could be the manifestation of “intermittency” in hadron physics. They argue that if intermittency occurs in particle production, large fluctuations are not only expected, they should also exhibit self-similarity with respect to the size of the phase-space volume. Various efforts [170, 171] have been undertaken to understand the physics behind these experimental findings.

The important questions to address are: do the anomalous fluctuations have intrinsic dynamical origins? is the phase-space of the final state isotropic or not? is the phase-space continuous or fractal? does the approximate intermittency observed at very high energies also exist at intermediate energies? can intermittency be explained theoretically (such as by cascading, BEC, etc.)?

The study of these phenomena has two aspects: (1) Experimentally, one measures fractal moments and the Hurst index. In a one-dimension case, phase-space variables can be chosen as the rapidity, or the transverse momentum, or azimuthal angle. Combinations of any two of these can be used for two-dimensional analyses. (2) A theoretical question is whether or not the asymptotic fractal behavior in the perturbative evolution of partons persists after hadronization processes?



# Chapter 8

## Lineshapes of charmonium resonances<sup>1</sup>

### 8.1 Resonance production and $1^{--}$ charmonium states

In  $e^+e^-$  annihilation,  $1^{--}$  resonances of the quarkonium family can be formed directly in the  $s$ -channel. Each of these can have a number of different decay modes. The total width of a resonance  $\Gamma_{\text{tot}}$  is the sum of its partial widths for each decay mode, *i.e.*  $\Gamma_{\text{tot}} = \sum_i \Gamma_i$ . For a resonance  $R$  decaying to a final state  $F$ , the cross section for the  $R \rightarrow F$  production is given by the relativistic Breit-Wigner formula [192]

$$\sigma_{(e^+e^- \rightarrow R \rightarrow F)}(E) = \frac{12\pi\Gamma_{ee}\Gamma_F}{(E^2 - M_R^2)^2 + \Gamma_{\text{tot}}^2 M_R^2},$$

where  $\Gamma_{ee}$  is the leptonic width,  $\Gamma_F$  is the partial width for the decay  $R \rightarrow F$ ,  $M_R$  is the mass of the resonance  $R$ , and  $E$  is the center-of-mass energy. The corresponding non-relativistic Breit-Wigner formula is given by

$$\sigma_{(e^+e^- \rightarrow R \rightarrow F)}(E) = \frac{3\pi}{M_R^2} \frac{\Gamma_{ee}\Gamma_F}{(E - M_R)^2 + \Gamma_{\text{tot}}^2/4}.$$

The  $1^{--}$  quarkonium resonances are generally described by the parameters  $M_R$ ,  $\Gamma_{\text{tot}}$ , the hadronic width  $\Gamma_h$  for the decay  $R \rightarrow$  hadrons, and their leptonic width  $\Gamma_{ee}$ .

There are six established  $1^{--}$  charmonium resonances, the  $J/\psi$ ,  $\psi(2S)$ ,  $\psi(3770)$ ,  $\psi(4040)$ ,  $\psi(4160)$  and  $\psi(4415)$ . These are generally classified as the  $1^3S_1$ ,  $2^3S_1$ ,  $1^3D_1$ -dominant,  $3^3S_1$ ,  $4^3S_1$ -dominant, and  $5^3S_1$   $c\bar{c}$  charmonium states [193], respectively. They are directly produced in  $e^+e^-$  annihilation in the energy region between 3.0 and 4.5 GeV. Using the well measured resonance parameters of the  $J/\psi$  and  $\psi(2S)$  as input, charmonium models predict the masses, total widths and leptonic widths of these other  $1^{--}$  charmonium states.

In addition to the above-listed charmonium resonances, a  $1^{--}$  resonance called the  $Y(4260)$  was discovered by the BaBar experiment in the  $e^+e^-$  radiative-return production of  $\pi^+\pi^-J/\psi$  final states. In addition to uncertainties in the interpretation of the  $Y(4260)$ , there are on-going debates about the classifications of some of the other  $1^{--}$  states.

---

<sup>1</sup>By Gang Rong and Da-Hua Zhang

For example, Close and Page [194] suggest that the  $\psi(4040)$  and  $\psi(4160)$  are strong mixtures of a ground-state hybrid-charmonium state with mass  $M \sim 4.1$  GeV and the conventional  $\psi(3S)$  charmonium meson.

Theoretical classifications of the charmonium states are based on the measured resonance parameters and their decay products. To help clarify the situation, more precise measurements of these resonance parameters, and studies their decay final states are needed.

More precisely measured resonance parameters of the  $\psi(3770)$  are needed for a better understanding of the nature of this state too. At present, the  $\psi(3770)$  is considered to be a mixture of the  $1^3D_1$  and  $2^3S_1$  charmonium states, an interpretation that is based on the measured leptonic width. However, there are still open questions about  $\psi(3770)$  production and decay. According to QCD-based models, more than 97% of the  $\psi(3770)$  decays should proceed into  $D\bar{D}$  ( $D^0\bar{D}^0$  and  $D^+\bar{D}^-$ ) final states. However, the BES Collaboration recently measured the branching fraction for  $\psi(3770) \rightarrow \text{non-}D\bar{D}$  to be  $B[\psi(3770) \rightarrow \text{non-}D\bar{D}] = (16.4 \pm 7.3 \pm 4.2)\%$  [195] and  $B[\psi(3770) \rightarrow \text{non-}D\bar{D}] = (14.5 \pm 1.7 \pm 5.8)\%$  [196]. These two independent results were obtained from two different data samples with different analysis methods. Both of the measurements indicate a branching fraction that is larger than the 3% QCD expectation. If the branching fraction is really significantly larger than 3%, there may be some new process involved. To resolve this puzzle, more accurate measurements of the  $\psi(3770)$  resonance parameters are needed. This will require more careful studies of the line-shapes for the formation and for subsequent inclusive hadronic decays, inclusive  $J/\psi$  decays, and other specific exclusive decays.

In addition to the conventional charmonium states, there may be other  $1^{--}$  states in the energy region between 3.0 and 4.5 GeV, such as hybrid charmonia, glueballs, and/or 4-quark states. To understand better the nature of the charmonium states and to search for other types of  $1^{--}$  mesons, more precise measurements of the resonance parameters and careful analysis of the line-shapes of the resonances for different decay modes are essential.

## 8.2 Key points for precision measurements

Parameters of  $1^{--}$  resonances can be directly determined from the energy dependence of the cross sections for production via  $e^+e^-$  annihilation. These parameters can also be measured in other production experiments such as  $p\bar{p}$  annihilation [197].

The MARK-I [198, 199], FRAG [200], FRAM [201], DASP [202], MARK-II [203], DELCO [204], BES [205] and BES-II [206, 195] experiments previously measured these parameters using  $e^+e^-$  annihilation; E760 [197] measured the masses and the total widths of the  $J/\psi$  and  $\psi(2S)$  in  $p\bar{p}$  annihilation by analyzing cross section scan data.

An examination of the analyses of the cross section scan data from previous experiments shows some potential problems with the way the resonance parameters have been extracted. First, other than BES-II measurements of the resonance parameters of the  $\psi(2S)$  and  $\psi(3770)$  [195], none of the previous  $e^+e^-$  experiments considered the effects of photon vacuum polarization corrections to continuum hadron production on the total and leptonic widths. If BES-II had not considered these effects, their measured total

width of the  $\psi(2S)$  resonance would be reduced by about 40 keV [195], while the leptonic width would be larger by about 4%. Moreover, most previous experiments assumed that the detection efficiency for the observation of inclusive hadronic events is an almost linear function of the  $e^+e^-$  cms energy. This assumption systematically increases the inferred leptonic width of a resonance. In addition, none of the previous experiments considered the effect of possible interference between the amplitude for continuum hadron production and the resonance amplitude. This effect can also systematically shift the measured resonance parameters by a significant amount.

To measure the resonance parameters more precisely, one has to determine accurately the detection efficiencies for inclusive hadronic events at different cms energies. In addition, photon vacuum polarization corrections for continuum hadron production in the resonance region have to be applied and the possible interference between the amplitude for continuum hadron production and the amplitude for the electromagnetic decays of the resonance has to be considered. Moreover, better methods for dealing with initial state radiative (ISR) and photon vacuum polarization corrections should be employed.

To determine detection efficiencies precisely at different cms energies, Monte Carlo generators that include both ISR and photon vacuum polarization corrections have to be used. The generator should not only include charmonium production and decays, but also all relevant sub-processes. It should also allow for the possibility of interference between the continuum and resonance amplitudes and simulate the line-shapes of the narrow resonances exactly. Recently, Zhang *et al.* [207] developed a generator with these properties for use in the measurement of the  $\psi(3770)$  and  $\psi(2S)$  resonance parameters and branching fractions for  $\psi(3770) \rightarrow D^0\bar{D}^0$ ,  $D^+\bar{D}^-$  and  $\psi(3770) \rightarrow \text{non-}D\bar{D}$  [195, 196]. This generator was developed with the aim of making precise measurements of the resonance parameters and search for new  $1^{--}$  states with the *BES-III* detector at the BEPC-II collider.

### 8.3 An example for measuring $\psi(2S)$ and $\psi(3770)$ parameters

Among the six resonances that are seen via direct production in  $e^+e^-$  annihilation between 3.0 and 4.5 GeV, the  $\psi(2S)$  and  $\psi(3770)$  are closest in mass to each other. To get reliably measured parameters for these two resonances, simultaneous measurements with a common data set are necessary. In this section, we take the  $\psi(2S)$  and  $\psi(3770)$  measurements performed with BES-II as an example to illustrate how the simultaneous determination of the two resonances' parameter values can be done. The method for measuring the parameters of the  $1^{--}$  resonances in more complicated cases is similar. The data sets used for these measurements were taken in March, 2003. The total integrated luminosity of the data sets is  $\sim 5 \text{ pb}^{-1}$  collected over the 3.66 to 3.88 GeV energy range.

The  $\psi(3770)$  and  $\psi(3686)$  resonance parameters can be extracted from a fit to the observed hadronic cross sections or from a fit to both the observed hadronic cross sections and the observed  $D\bar{D}$  ( $D^0\bar{D}^0$  and  $D^+\bar{D}^-$ ) cross sections. The observed hadronic cross sections are determined from

$$\sigma_{\text{had}}^{\text{obs}} = \frac{N_{\text{had}}^{\text{obs}}}{L \epsilon_{\text{had}} \epsilon_{\text{had}}^{\text{trig}}}, \quad (8.3.1)$$

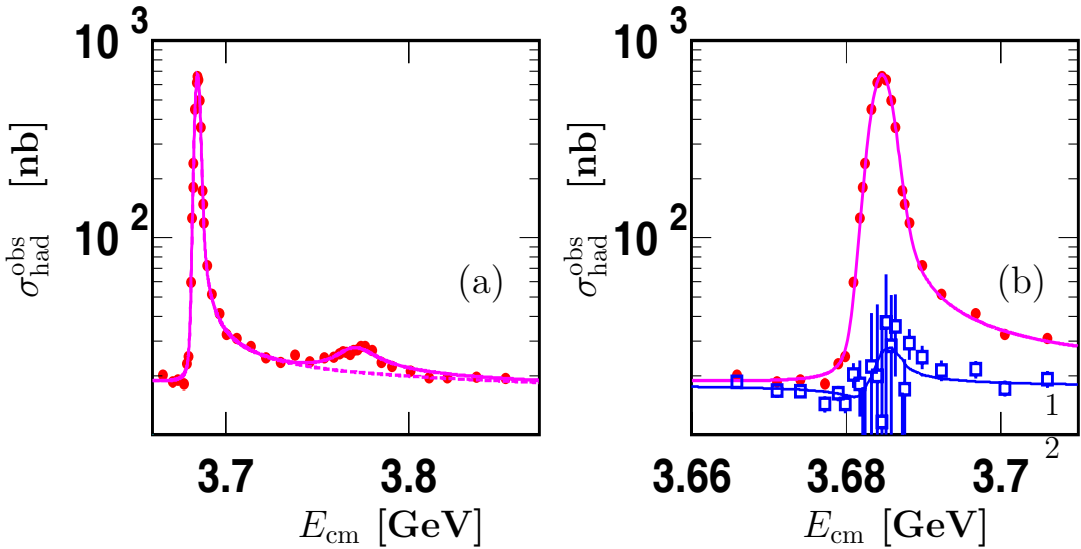


Figure 8.1: The hadronic cross sections versus the CMS energy (see text).

where  $N_{\text{had}}^{\text{obs}}$  is the number of the observed hadronic events,  $L$  is the integrated luminosity,  $\epsilon_{\text{had}}$  is the efficiency for the detection of inclusive hadronic events and  $\epsilon_{\text{had}}^{\text{trig}}$  is the trigger efficiency for recording hadronic events in the online data acquisition system. The observed cross sections for  $D^0\bar{D}^0$  (or  $D^+D^-$ ) production are determined from

$$\sigma_{D^0\bar{D}^0(\text{or } D^+D^-)}^{\text{obs}} = \frac{N_{D_{\text{tag}}^0}^{\text{obs}} (\text{or } N_{D_{\text{tag}}^+}^{\text{obs}})}{2 \times L \times B \times \epsilon}, \quad (8.3.2)$$

where  $N_{D_{\text{tag}}^0}$  ( $N_{D_{\text{tag}}^+}$ ) is the number of reconstructed  $D^0$  ( $D^+$ ) events obtained from an analysis of the  $K^\mp\pi^\pm$  and  $K^\mp\pi^\pm\pi^\pm\pi^\mp$  (or  $K^\mp\pi^\pm\pi^\pm$ ) invariant mass spectra as discussed in detail in Ref. [209];  $B$  is the branching fraction for the relevant decay mode, and  $\epsilon$  is its detection and trigger efficiency. Figure 8.1 shows the observed cross sections (points with errors) for inclusive hadronic event production, while Figs. 8.2(b) and (c), respectively, display the observed cross sections (circles with errors) for  $D^0\bar{D}^0$  and  $D^+D^-$  production.

The determination of the resonance parameters is accomplished by simultaneously fitting the observed cross sections for  $\psi(2S)$ ,  $\psi(3770)$ ,  $D^0\bar{D}^0$  and  $D^+D^-$  to functions that describe the combined  $\psi(2S)$ ,  $\psi(3770)$  resonance shapes, the tail of the  $J/\psi$  resonance and the non-resonant hadronic background, as well as the partial  $\psi(3770)$  resonance shapes for  $\psi(3770) \rightarrow D^0\bar{D}^0$  and  $\psi(3770) \rightarrow D^+D^-$ . Assuming that there are no additional structures and effects, we use a pure  $P$ -wave Born-order Breit-Wigner function with energy-dependent total widths to describe  $\psi(3770)$  and  $D\bar{D}$  ( $D^0\bar{D}^0$  and  $D^+D^-$ ) production via  $\psi(3770)$  decay. The  $\psi(3770)$  resonance shape is taken to be

$$\sigma_{\psi(3770)}^B(s') = \frac{12\pi\Gamma_{ee}^{\psi(3770)}\Gamma_{\text{tot}}^{\psi(3770)}(s')}{(s' - M^{\psi(3770)}{}^2)^2 + [M^{\psi(3770)}\Gamma_{\text{tot}}^{\psi(3770)}(s')]^2}, \quad (8.3.3)$$

while the  $D\bar{D}$  resonance shapes are taken as

$$\sigma_{D\bar{D}}^B(s') = \frac{12\pi\Gamma_{ee}^{\psi(3770)}\Gamma_{D\bar{D}}(s')}{(s' - M^{\psi(3770)}{}^2)^2 + [M^{\psi(3770)}\Gamma_{\text{tot}}^{\psi(3770)}(s')]^2}, \quad (8.3.4)$$

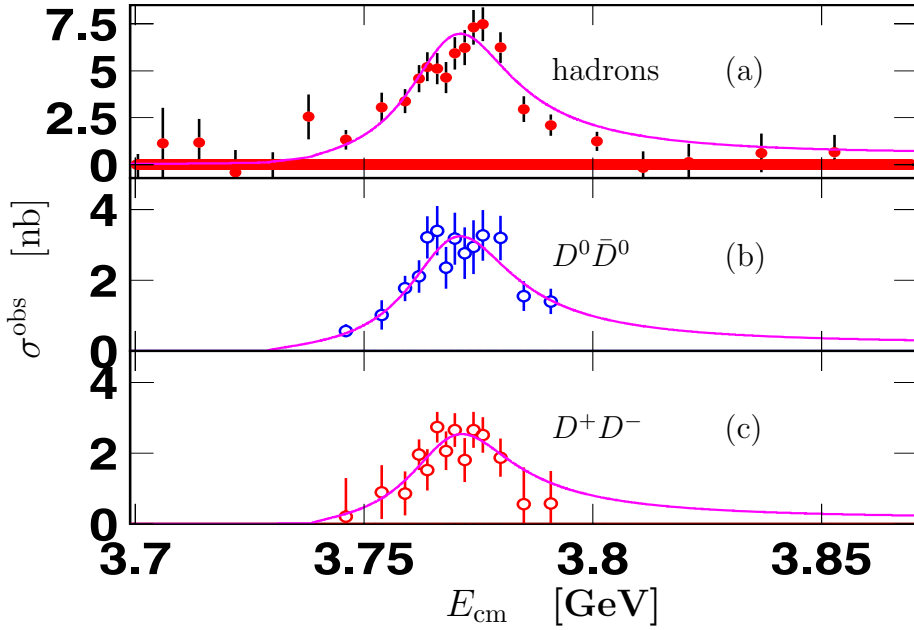


Figure 8.2: The observed cross sections versus the cms energy.

where  $M^{\psi(3770)}$  and  $\Gamma_{ee}^{\psi(3770)}$  are the mass and leptonic width of the  $\psi(3770)$  resonance, respectively;  $\Gamma_{D\bar{D}}$  is the partial width of  $\psi(3770)$  decay into  $D\bar{D}$ ;  $\Gamma_{\text{tot}}^{\psi(3770)}(s')$  and  $\Gamma_{D\bar{D}}(s')$  have energy dependence defined as

$$\Gamma_{\text{tot}}^{\psi(3770)}(s') = \Gamma_{D^0\bar{D}^0}(s') + \Gamma_{D^+D^-}(s') + \Gamma_{\text{non-}D\bar{D}}(s'), \quad (8.3.5)$$

where

$$\Gamma_{D^0\bar{D}^0}(s') = \Gamma_0 \theta_{00} \frac{(p_{D^0})^3}{(p_{D^0}^0)^3} \frac{1 + (rp_{D^0}^0)^2}{1 + (rp_{D^0})^2} B_{00}, \quad (8.3.6)$$

$$\Gamma_{D^+D^-}(s') = \Gamma_0 \theta_{+-} \frac{(p_{D^+})^3}{(p_{D^+}^0)^3} \frac{1 + (rp_{D^+}^0)^2}{1 + (rp_{D^+})^2} B_{+-}, \quad (8.3.7)$$

and

$$\Gamma_{\text{non-}D\bar{D}}(s') = \Gamma_0 [1 - B_{00} - B_{+-}]. \quad (8.3.8)$$

Here  $p_D^0$  and  $p_D$  are the momenta of the  $D$  mesons produced at the peak of the  $\psi(3770)$  and at the actual cms energy  $\sqrt{s'}$ , respectively;  $\Gamma_0$  is the total width of the  $\psi(3770)$  at its peak,  $B_{00} = B(\psi(3770) \rightarrow D^0\bar{D}^0)$  and  $B_{+-} = B(\psi(3770) \rightarrow D^+D^-)$  are the branching fractions for  $\psi(3770) \rightarrow D^0\bar{D}^0$  and  $\psi(3770) \rightarrow D^+D^-$ , respectively,  $r$  is the interaction radius of the  $c\bar{c}$ , and  $\theta_{00}$  and  $\theta_{+-}$  are step functions that account for the thresholds of  $D^0\bar{D}^0$  and  $D^+D^-$  production, respectively. In the fit we take  $\Gamma_0$ ,  $B_{00}$ ,  $B_{+-}$  and  $r$  as free parameters.

The non-resonant background shape is taken as

$$\begin{aligned} \sigma_h^{nrsnt}(s) &= \int_0^\infty ds'' G(s, s'') \int_0^1 dx \frac{R_{uds}(s') \sigma_{\mu^+\mu^-}^B(s')}{|1 - \Pi(s')|^2} F(x, s) \\ &+ f_{D\bar{D}} \left[ \left( \frac{p_{D^0}}{E_{D^0}} \right)^3 \theta_{00} + \left( \frac{p_{D^+}}{E_{D^+}} \right)^3 \theta_{+-} \right] \sigma_{\mu^+\mu^-}^B(s), \end{aligned} \quad (8.3.9)$$

Table 8.1: The measured  $\psi(3770)$  and  $\psi(2S)$  parameters, where  $M$  is the mass,  $\Gamma_{\text{tot}}$  the total width [ $\Gamma_{\text{tot}} = \Gamma_0$  for  $\psi(3770)$ ],  $\Gamma_{ee}$  the partial leptonic width and  $\Delta M$  the measured mass difference of the  $\psi(3770)$  and the  $\psi(2S)$ .

Res.	$M$ (MeV)	$\Gamma_{\text{tot}}$ (MeV)	$\Gamma_{ee}$ (eV)	$\Delta M$ (MeV)
$\psi(3770)$	$3772.2 \pm 0.7 \pm 0.3$	$26.9 \pm 2.4 \pm 0.3$	$251 \pm 26 \pm 11$	
$\psi(2S)$	$3685.5 \pm 0.0 \pm 0.3$	$0.331 \pm 0.058 \pm 0.002$	$2330 \pm 36 \pm 110$	$86.7 \pm 0.7$

where  $G(s, s'')$  is a Gaussian function that describes the beam-energy spread,  $F(x, s)$  is the sampling function [210],  $1/|1 - \Pi(s(1 - x))|^2$  is the vacuum polarization correction function [211] including the contributions from all  $1^{--}$  resonances, the QED continuum hadron spectrum as well as the contributions from the lepton pairs ( $e^+e^-$ ,  $\mu^+\mu^-$  and  $\tau^+\tau^-$ ) [207];  $\sigma_{\mu^+\mu^-}^B(s)$  is the Born cross section for  $e^+e^- \rightarrow \mu^+\mu^-$ ,  $E_{D^0}$  and  $E_{D^+}$  are the energies of  $D^0$  and  $D^+$  mesons produced at the nominal energy  $\sqrt{s}$ ,  $f_{D\bar{D}}$  is a parameter to be fitted, and  $R_{uds}(s')$  is the  $R$  value for light hadron production via direct one-photon  $e^+e^-$  annihilation.

In the fit we leave  $R_{uds}(s')$  as a free parameter, assuming that its value is independent of the energy, and fix the  $J/\psi$  resonance parameters at their PDG values [213]. Figure 8.1(a) shows the observed cross sections and the results of the fit, where the solid line shows the fit to the data and the dashed line represents the contributions from the  $J/\psi$ ,  $\psi(2S)$  and continuum hadron production. To examine directly the contribution from the vacuum polarization corrections to the Born hadronic cross section due to one photon annihilation, we subtract the contributions of the  $\psi(2S)$  and  $\psi(3770)$  as well as the  $J/\psi$  from the observed cross sections to get the expected cross sections for continuum hadron production corrected for radiative effects given by Eq.(8.3.9). The squares with errors in Fig. 8.1(b) show the extracted cross sections, where the errors are the original absolute errors of the total observed cross sections shown in Fig. 8.1(a). The blue curve (lower curve) in Fig. 8.1(b) shows the fit to the expected cross sections for continuum hadron production corrected for the radiative effects as given in Eq. (8.3.9). Figure 8.2(a) shows the observed cross sections for inclusive hadronic event production, where the contributions from the  $J/\psi$  and  $\psi(2S)$  radiative tails as well as continuum hadron production are removed. Figures 8.2(b) and (c) display the observed cross sections for  $D^0\bar{D}^0$  and  $D^+D^-$  production together with the fits to the data, respectively.

The results from the fit are summarized in Table 8.1, where the first error is statistical and second systematic. From the fit we obtain  $R_{uds}$  in the region between 3.660 and 3.872 GeV to be

$$R_{uds} = 2.262 \pm 0.054 \pm 0.109,$$

where the errors are, respectively, statistical and the systematic. The fit yields a non- $D\bar{D}$  branching fraction for the  $\psi(3770)$  of

$$B(\psi(3770) \rightarrow \text{non-}D\bar{D}) = (16.4 \pm 7.3 \pm 4.2)\%.$$

The fit has  $\chi^2/\text{d.o.f} = 65.4/64 = 1.02$ .

The continuum background shape effects the measured total and leptonic widths of

the resonances from the line-shape analysis. If we use

$$\begin{aligned}\sigma_h^{nrsnt}(s) &= h \sigma_{\mu^+\mu^-}^B(s) + f_{D\bar{D}} \times \\ &\left[ \left( \frac{p_{D^0}}{E_{D^0}} \right)^3 \theta_{00} + \left( \frac{p_{D^+}}{E_{D^+}} \right)^3 \theta_{+-} \right] \sigma_{\mu^+\mu^-}^B(s),\end{aligned}\quad (8.3.10)$$

in the fit to the data (where  $h$  is a free parameter), we obtain  $\Gamma_{\psi(2S)}^{\text{tot}} = 290 \pm 59 \pm 5$  keV,  $\Gamma_{\psi(2S)}^{ee} = 2.378 \pm 0.036 \pm 0.103$  keV,  $\Gamma_{\psi(3770)}^{\text{tot}} = 27.3 \pm 2.5 \pm 1.1$  MeV and  $\Gamma_{\psi(3770)}^{ee} = 256 \pm 27 \pm 13$  eV, with almost unchanged measurements of the resonance masses. This fit has  $\chi^2/\text{d.o.f} = 75.3/64 = 1.18$ . This indicates that the vacuum polarization corrections to the Born order cross sections for the continuum hadron production cannot be ignored in precision measurements of the resonance parameters of the narrow resonances like  $J/\psi$  and  $\psi(2S)$  (and also the  $\Upsilon(1S)$  etc.) in  $e^+e^-$  cross section scan experiments. Ignoring the effects of the vacuum polarization corrections on continuum hadron production in the analysis of the cross section scan data taken in the  $\psi(2S)$  resonance region would decrease the  $\psi(2S)$  total width by about 40 keV.

## 8.4 Resonance measurements at *BES-III*

As mentioned above, precise measurements of the  $1^{--}$  charmonium resonance parameters are important for the understanding of the dynamics of charmonium resonance production in  $e^+e^-$  annihilation. Before clarifying the situation of the understanding the exact natures of  $\psi(4040)$  and  $\psi(4160)$ , one has to measure precisely and accurately their resonance parameters. At present, one still does not understand why the  $\psi(3770)$  decays to non- $D\bar{D}$  with a such large branching fraction. To resolve this “puzzle,” one has to measure the parameters of the  $\psi(3770)$  and  $\psi(2S)$  more precisely. In this section, we discuss how well the branching fractions and parameters of the  $\psi(3770)$  can be measured at *BES-III*.

According to our experience with the measurement the  $\psi(3770)$  and  $\psi(2S)$  parameters, the branching fraction for  $\psi(3770) \rightarrow \text{non-}D\bar{D}$ , and the  $R$  value for the range from 3.65 to 3.88 GeV [195, 214, 196, 215], we expect that the total systematic uncertainty on the observed cross section for inclusive hadronic event production can be reduced to the level of  $\sim 2.5\%$  at *BES-III*. In light of this, one should consider collecting cross section scan data with a statistical precision of  $\sim 1.5\%$ .

Assuming that the  $\psi(2S)$  and  $\psi(3770)$  are the only two resonances in the 3.65 to 3.88 GeV energy range, we did a Monte Carlo study to determine how well we can measure their resonance parameters and the branching fraction for  $\psi(3770) \rightarrow \text{non-}D\bar{D}$ . The events were generated at the same 49 energy points where we collected cross section scan data with the BES-II detector in March, 2003. The total integrated luminosity is about  $60 \text{ pb}^{-1}$ . Following the same procedure that was used to deal with the cross section scan data discussed above, we obtain  $\psi(2S)$  and  $\psi(3770)$  resonance oparameters and the branching fraction for  $\psi(3770) \rightarrow \text{non-}D\bar{D}$ . Figure 8.3 shows the observed cross section as a function of cms energy, where the dots with errors show the cross section for inclusive hadronic event production; the circles with errors represent the cross section for continuum hadron production with ISR and photon vacuum polarization corrections applied; the red (green) solid line gives the best fit to the observed cross sections for inclusive hadronic

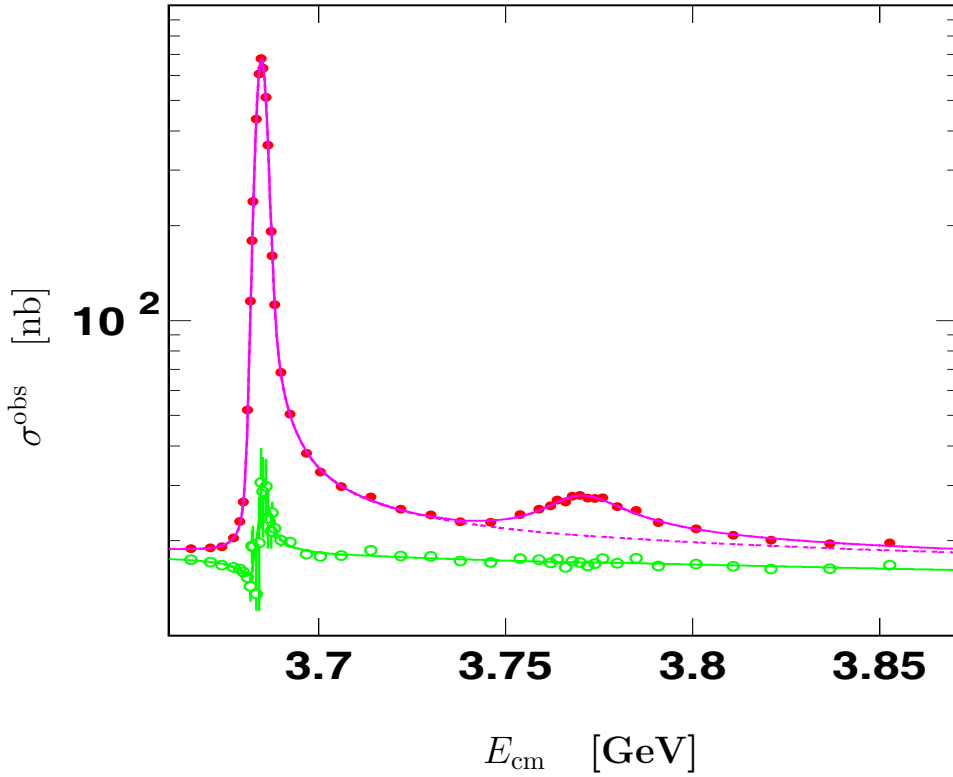


Figure 8.3: The observed cross sections versus the cms energy.

event production (continuum hadronic event production); while the red dashed line shows the total contributions from continuum hadronic event production,  $\psi(2S)$  production and  $J/\psi$  production. Tables 8.2 and 8.3 summarize, respectively, the results of the simulated measurements of the  $\psi(2S)$  and the  $\psi(3770)$  resonance parameters, where the errors are statistical and systematic, respectively. As a comparison, we also list the values of the parameters input to the Monte Carlo simulation. The measured  $R_{uds}$  value (“measured”) along with the input  $R_{uds}$  value (“input”) are listed in Table 8.4, where the errors are statistical and systematic errors, respectively.

In Table 8.2, the “non-rsnc BCK shape” entry indicates which non-resonant background shape, as given in Eqs. (8.3.9) and (8.3.10), is used in the data reduction. From the Monte Carlo simulation, we find that the total width of the  $\psi(2S)$  resonance is reduced by  $\sim 20\%$  and the partial leptonic width is increased by  $\sim 4\%$  if we do not consider the effect of the photon vacuum polarization corrections on continuum hadron production in the data reduction.

Figures 8.4(b) and (c) show the observed cross sections for  $D^0\bar{D}^0$  and  $D^+D^-$  production with the best fits to the data, respectively. The observed cross sections for the decays  $\psi(3770) \rightarrow$  hadrons is displayed in Fig. 8.4(a). The fit yields the branching fractions for  $\psi(3770) \rightarrow D\bar{D}$  and  $\psi(3770) \rightarrow$  non- $D\bar{D}$  summarized in Table 8.5 along with the branching fractions used in the Monte Carlo simulation. The errors listed in the table are the statistical and systematic, respectively. The fit also gives the measured branching

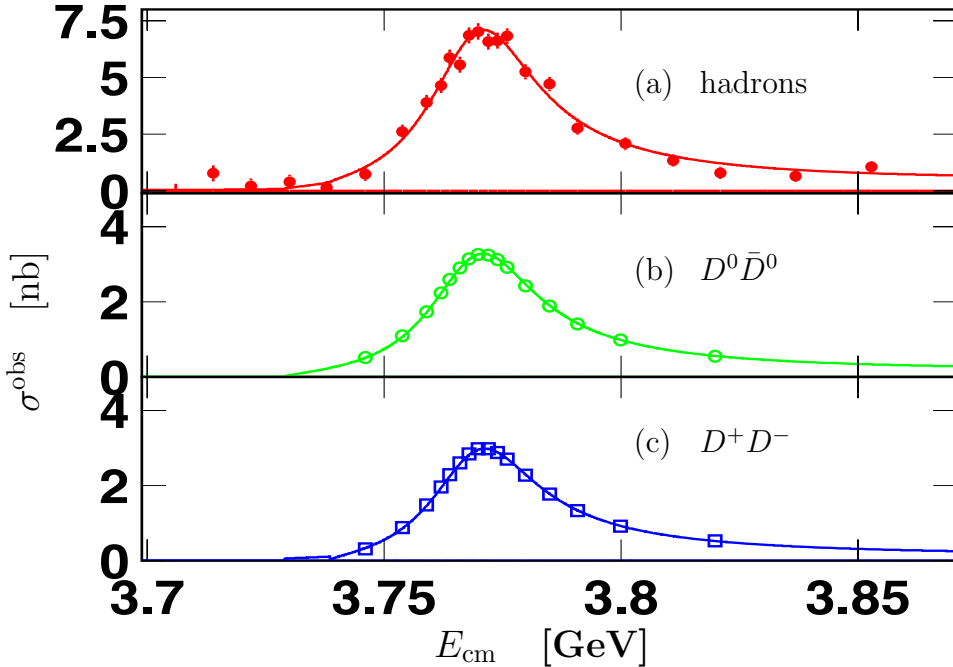


Figure 8.4: The observed cross sections versus the cms energy.

Table 8.2: The input and measured  $\psi(2S)$  parameters, where  $M$  is the mass,  $\Gamma_{\text{tot}}$  the total width and  $\Gamma_{ee}$  the partial leptonic width, where “input” means the value of the parameter used in the Monte Carlo simulation and “measured” means its measured values.

input or measured	$M$ (MeV)	$\Gamma_{\text{tot}}$ (keV)	$\Gamma_{ee}$ (keV)	non-rsnc BCK shape
input	3686.09	337	2.33	–
measured	$3686.08 \pm 0.01 \pm 0.1$	$349.6 \pm 13.0 \pm 2$	$2.33 \pm 0.01 \pm 0.05$	Eq. (8.3.9)
measured	$3686.06 \pm 0.01 \pm 0.1$	$289.1 \pm 11.0 \pm 2$	$2.42 \pm 0.01 \pm 0.05$	Eq. (8.3.10)

Table 8.3: The input and measured  $\psi(3770)$  parameters, where  $M$  is the mass,  $\Gamma_{\text{tot}}$  the total width [ $\Gamma_{\text{tot}} = \Gamma_0$  for  $\psi(3770)$ ] and  $\Gamma_{ee}$  the partial leptonic width, where “input” means the value of the parameter used in the Monte Carlo simulation and “measured” means its measured value.

input/measured	$M$ (MeV)	$\Gamma_{\text{tot}}$ (MeV)	$\Gamma_{ee}$ (eV)
input	3772.3	26.9	251
measured	$3772.1 \pm 0.2 \pm 0.1$	$26.8 \pm 0.5 \pm 0.1$	$255 \pm 7 \pm 6$

Table 8.4: The input and measured  $R_{uds}$  values in the resonance region from 3.65 to 3.88 GeV.

$R_{uds}$ [measured]	$R_{uds}$ [input]
$2.254 \pm 0.012 \pm 0.056$	2.260

Table 8.5: The input and measured branching fraction for  $\psi(3770) \rightarrow \text{non-}D\bar{D}$ , where "input" means the value of the parameter used in the Monte Carlo simulation and "measured" means its measured value.

input/measured	$B(\psi(3770) \rightarrow D\bar{D}) [\%]$	$B(\psi(3770) \rightarrow \text{non-}D\bar{D}) [\%]$
input	90%	10%
measured	$88.8 \pm 2.4 \pm 2.0$	$11.2 \pm 2.4 \pm 2.0$

fractions for  $\psi(3770) \rightarrow D^0\bar{D}^0$  and  $\psi(3770) \rightarrow D^+D^-$  to be

$$B[\psi(3770) \rightarrow D^0\bar{D}^0] = (46.3 \pm 1.3 \pm 1.0)\%,$$

and

$$B[\psi(3770) \rightarrow D^+D^-] = (42.5 \pm 1.2 \pm 0.9)\%;$$

the corresponding MC input values are  $B[\psi(3770) \rightarrow D^0\bar{D}^0] = 46.8\%$  and  $B[\psi(3770) \rightarrow D^+D^-] = 43.2\%$ , respectively.

From analyzing the Monte Carlo sample generated at the 49 energy points, we notice that the line-shape of the observed cross sections are smooth. However, if there are states other than the  $\psi(2S)$  and  $\psi(3770)$  in this energy region, the observed cross sections would deviate from these expectations (as shown by the lines in Fig. 8.3 and Fig. 8.4). This provides a method to search for new  $1^{--}$  states in the energy region from 3.0 to 4.5 GeV.

For measurements of the parameters of the other resonances in the energy region from 3.87 to 4.50 GeV, the method used for the measurements of the  $\psi(2S)$  and  $\psi(3770)$  parameters can be used. However, since the  $\psi(4040)$ ,  $\psi(4160)$  and  $Y(4260)$  resonances overlap each other, the possibility of interference between them has to be included.<sup>2</sup> To get reliable resonance parameters, point-to-point detection efficiencies should be used to extract the observed cross sections, not the almost straight line detection efficiency curves used in most of the previous  $e^+e^-$  experiments. An improved formalism for dealing with the ISR correction should be used. In this way precise and accurate measurements of the resonance parameters can be made. These considerations are also important for  $J/\psi$  resonance parameter determinations.

## 8.5 Summary

For a better understanding of the dynamics of charmonium resonance production in  $e^+e^-$  annihilation, precise measurements of the parameters of the charmonium resonances in the energy region from 3.0 to 4.5 GeV are needed. At present, most available measurements of the parameters of the  $1^{--}$  charmonium resonances may be biased since most previous  $e^+e^-$  experiments did not consider the effects of the photon vacuum polarization corrections on continuum hadron production, did not consider the possible interference between the continuum hadron amplitude and the resonance amplitude, and used almost linear detection efficiency curves to extract the observed cross sections. For these reasons, the parameters of the resonances should be remeasured with the *BES-III* detector. Such

<sup>2</sup>At present, the leptonic width of the  $Y(4260)$  resonance is not measured.

measurements could provide useful input into the debate about the interpretation of the  $\psi(4040)$  and  $\psi(4160)$  states.

Precision measurements of the parameters of the  $\psi(2S)$  and  $\psi(3770)$  would address the question of non- $D\bar{D}$  decays of  $\psi(3770)$ . A careful analysis of the line-shape of the observed cross sections for inclusive hadronic event production,  $D\bar{D}$  (including  $D^*$  and  $D_S^+$ ) production, other exclusive final states (such as  $J/\psi\pi\pi$ ,  $J/\psi\eta$ ,  $J/\psi\eta'$ ,  $J/\psi\omega$ ,  $\phi K^+K^-$ ,  $\phi\pi^+\pi^-$ ,  $\chi_{cJ}\rho$ ,  $\chi_{cJ}\omega$  ...) and inclusive final states (  $J/\psi X$ ,  $\eta X$ ,  $\eta' X$  ...) at different energies in the range from 3.7 to 4.5 GeV will provide the opportunity to search for new, non-conventional resonances. These can be done well with the *BES-III* detector.



# Bibliography

- [1] W.A. Bardeen, A.J. Buras, D.W. Duke and T. Muta, Phys. Rev. **D 18**, 3998 (1978).
- [2] M.A. Shifman, A.I. Vainshtein and V.I. Zakharov, Nucl. Phys. **B147**, 385, 448, 519 (1979).
- [3] G. Bonneau and F. Martin, Nucl.Phys. **B27** (1971) 381.
- [4] J. Schwinger, Phys.Rev. **76** (1949) 700.
- [5] D. R. Yennie, S. C. Frantschi and H. Suura, Ann Phys. **13** (1961) 379.
- [6] E. A. Kuraev and V. S. Fadin, Yad. Fiz. **41** (1985) 733 [Sov. J. Nucl. Phys. **41** (1985) 466].
- [7] G. Altarelli and G. Martinelli, CERN **86-02** (1986) 47; O. Nicrosini and L. Trentadue, Phys. Lett. **B196** (1987) 551.
- [8] F. A. Berends, G. Burgers and W. L. Neerven, Nucl. Phys. **B297** (1988) 429; *ibid.* **304** (1988) 921.
- [9] V. N. Gribov and L. N. Lipatov, Sov. J. Nucl. Phys. **15** (1972) 298; G. Altarelli and G. Parisi, Nucl. Phys. **B126** (1977) 298; Y. L. Dokshitzer, Sov. Phys. JETP **46** (1977) 641.
- [10] F. A. Berends and G. L. Komen, Phys. Lett. **B63** (1976) 432.
- [11] Y. S. Tsai, SLAC-PUB-3129 (1983).
- [12] P. Alexander *et al.*, Nucl. Phys. **B320** (1989) 45; P. Alexander *et al.*, Phys. Rev. **D37** (1987) 56.
- [13] J. Z. Bai *et al.* Phy. Lett. **B335** (1995) 374.
- [14] J. Z. Bai *et al.* Phy. Lett. **B550** (2002) 24.
- [15] J. Z. Bai *et al.* Phys. Rev. Lett. **21** (1992) 3021.
- [16] F. A. Berends *et al.*, in Proceedings of the Workshop on Z Physics at LEP, v.1, (1989) page 89, edited by G. Altarelli, R. Kleiss and C. Verzegnassi; P. Alexander *et al.*, Phys. Rev. **D37** (1988) 56.
- [17] S. Jadach, B. F. L. Ward and Z. Was, Phys. Rev. **D63** (2001) 113009.

- [18] S. Jadach, B. F. L. Ward and Z. Was, *Comput. Phys. Commun.* **130** (2000) 260.
- [19] C. M. Carloni *et al.*, *Nucl. Phys.* **B584** (2000) 459;  
C. M. Carloni *et al.*, *Phys. Lett.* **B520** (2001) 16.
- [20] V. V. Sudakov, *Sov. Phys. JETP* **3** (1956) 65.
- [21] C. M. Carloni *et al.*, *Nucl. Phys.* **B758** (2006) 227.
- [22] A. B. Arbuzov *et al.*, *Eur. Phys. J.* **C46** (2006) 689.
- [23] S. Binner, J. H. Kuhn and K. Melnikov, *Phys. Lett.* **B527** (2002) 161;  
K. Melnikov, F. Nguyen, B. Valeriani and G. Venanzoni, *Phys. Lett.* **B477** (2000) 114;  
H. Czyz and J. H. Kuhn, *Eur. Phys. J.* **C18** (2001) 497;  
S. Spagnolo, *Eur. Phys. J.* **C6** (1999) 637.
- [24] G. Rodrigo, A. Gehrann-De Ridder, M. Guilleaume, J. H. Kuhn, *Eur. Phys. J.* **C22** (2001) 81;  
G. Rodrigo, H. Czyz, J. H. Kuehn and M. Szopa, *Eur. Phys. J.* **C24** (2002) 71;  
H. Czyz, A. Grzelinska, J. H. Kuhn and G. Rodrigo, *Eur. Phys. J.* **C25** (2003) 563.
- [25] For most recent reviews see, for example,  
B. Pietrzyk, *Nucl. Phys. B(Proc. Suppl.)* **162** 18 (2006);  
F. Jegerlehner, *Nucl. Phys. B(Proc. Suppl.)* **162** 22 (2006)(hep-ph/0608329);  
F. Ambrosino *et al.*, hep-ex/0603056, and reference therein.
- [26] G. Bonneau and F. Martin, *Nucl. Phys.* **B27** 381 (1971);  
D.R. Yennie, *Phys. Rev. Lett.* **34** 239 (1975);  
J.D. Jackson and D.L. Scharre, *Nucl. Instrum. Methods* **128** 13 (1975);  
M. Greco, G. Pancheri-Srivastava and Y. Srivastava, *Nucl. Phys.* **B101** 234 (1975);  
**B202** 118 (1980).
- [27] Y.S. Tsai, SLAC-PUB-1515 (1975); SLAC-PUB-3129 (1983).
- [28] F.A. Berends *et al.*, *Nucl. Phys.* **B57** 381 (1973); *ibid.* **B68** 541 (1974);  
F.A. Berends and R. Kleiss, *Nucl. Phys.* **B178** 141 (1981);  
F.A. Berends, R. Kleiss and S. Jadach, *Nucl. Phys.* **B202** 63 (1982);  
F.A. Berends and R. Kleiss, *Nucl. Phys.* **B228** 537 (1983).
- [29] S.I. Eidelman and E.A. Kuraev, *Phys. Lett.* **B80** 94 (1978);  
V.N. Baier, V.S. Fadin, V.A. Khoze and E.A. Kuraev, *Phys. Rep.* **C78** 293 (1981);  
E.A. Kuraev and V.S. Fadin, *Sov. J. Nucl. Phys.* **41** 466 (1985).
- [30] F.A. Berends and A. Böhm, in “High Energy Electron-Positron Physics”,  
eds. A. Ali and P. Söding, World Scientific, Singapore, 1988, p. 27-140 (see Fig. 8.5).
- [31] S. Eidelman, *Nucl. Phys. B(Proc. Suppl.)* **162** 323 (2006)
- [32] K. Hagiwara, A. D. Martin, D. Nomura, and T. Teubner, *Phys. Lett.* **B557**, 69 (2003) (hep-ph/0209187); *Phys. Rev.* **D69**, 093003 (2004) (hep-ph/0312250).

- [33] F. Jegerlehner, Nucl. Phys. B(Proc. Suppl.) **162** 22 (2006)(hep-ph/0608329).
- [34] H. Czyż, Nucl. Phys. B (Proc. Suppl.) **162** 76(2006) (hep-ph/0606227).
- [35] A. Aloisio *et al.*, [KLOE Collaboration] Phys. Lett. **B606** 12 (2005)(hep-ex/ 0407048).
- [36] B. Aubert *et al.*, [BaBar Collaboration] Phys. Rev. D **D70** 072004 (2004); Phys. Rev. D **D71** 052001 (2005).
- [37] A. Denig, Nucl. Phys. B(Proc. Suppl.) **162** 81(2006) (hep-ex/0611024).
- [38] G. Rodrigo, A. Gehrmann-De Ridder, M. Guilleaume and J. H. Kühn, Eur. Phys. J. **C22** 81 (2001) (hep-ph/0106132).
- [39] J. H. Kühn and G. Rodrigo, Eur. Phys. J. **C25** 215 (2002) (hep-ph/0204283).
- [40] G. Rodrigo, H. Czyż, J.H. Kühn and M. Szopa, Eur. Phys. J. **C24** 71 (2002)(hep-ph/0112184).
- [41] H. Czyż, A. Grzelińska, J. H. Kühn and G. Rodrigo, Eur. Phys. J. **C27** 563 (2003) (hep-ph/0212225).
- [42] H. Czyż, A. Grzelińska, J. H. Kühn and G. Rodrigo, Eur. Phys. J. **C33** 333 (2004) (hep-ph/0308312).
- [43] H. Burkhardt and B. Pietrzyk, Phys. Rev. **D72**, 057501 (2005) (hep-ph/0506323).
- [44] R. R. Akhmetshin *et al.*, Phys. Lett. **B578** 285 (2004).
- [45] M.N. Achasov *et al.*, J. Exp. Theor. Phys. **101** 1053 (2005) (hep-ex/ 0506076).
- [46] W.-M. Yao *et al.*, J. Phys. **G33** 1 (2006).
- [47] P.A. Rapidis *et al.* (Mark I/Lead Glass Wall), Phys. Rev. Lett **39** 526 (1977);  
W. Bacino *et al.* (Mark I/Lead Glass Wall), Phys. Rev. Lett. **40** 671 (1978).
- [48] J. L. Siegrist *et al.* (Mark I), Phys. Rev. **D26** 969 (1982).
- [49] C. Bacciet *et al.* (  $\gamma\gamma$ 2 Collaboration), Phys. Lett. **B86** 234 (1979).
- [50] R. Brandelik *et al.* (DASP), Phys. Lett. **B76** 361 (1978);  
H. Albrecht *et al.* (DASP), Phys. Lett. **B116** 383 (1982).
- [51] J. Burmeister *et al.* (PLUTO), Phys. Lett. **B66** 395 (1977);  
Ch. Berger *et al.* (PLUTO), Phys. Lett. **B81** 410 (1979);  
L. Criegee and G. Knies (PLUTO), Phys. Rep. **83** 151 (1982).
- [52] B. Niczyporuk, *et al.* (LENA), Z. Phys. **C15** 299 (1982).
- [53] Z. Jakubowsky *et al.* (Crystal Ball), Z. Phys. **C40** 49 (1988);  
C. Edwards *et al.* (Crystal Ball), SLAC-PUB-5160, 1990.

- [54] A.E. Blinov *et al.* (MD-1), Z. Phys. **C49** 239 (1991);  
A.E. Blinov *et al.* (MD-1), Preprint BudkerINP 93-54, Novosibirsk, 1993.
- [55] J. Z. Bai *et al.* ( BES Collaboration), Phys. Rev. lett. **88**, 101802 (2002) (hep-ex/0102003).
- [56] J. Z. Bai *et al.* ( BES Collaboration), Phys. Rev. lett. **84**, 594 (2000) (hep-ex/9908046).
- [57] H. Burkhardt and B. Pietrzyk, Phys. Lett. **B513**, 46 (2001).
- [58] F. Jegerlehner, J. Phys. **G29**, 101 (2003) (hep-ph/0104304).
- [59] S. Eidelman and F. Jegerlehner, Z. Phys. **C67** 585 (1995)(hep-ph/9502228).
- [60] H. Burkhardt and B. Pietrzyk, Phys. Lett. **B356** 398 (1995).
- [61] S. A. Dytman( CLEO Collaboration), Nucl. Phys. Proc. Suppl. **131** 32(2004).
- [62] R. Ammar *et al.*, [CLEO collaboration], Phys. Rev. **D57** 1350 (1998).
- [63] P. J. Mohr and B. N. Taylor, Rev. Mod. Phys. **72** 351 (2000); *ibid* **77** 1 (2005).
- [64] M. Steinhauser, Phys. Lett. **B429** 158 (1998).
- [65] H. Burkhardt, F. Jegerlehner, G. Penso and Verzegnassi, Z. Phys. **C43** 497 (1989).
- [66] M.L. Swartz, Phys. Rev. **D53** 5268 (1996) (hep-ph/9411353) ;  
M.L. Swartz, Phys. Rev. **D53** 5268 (1996) (hep-ph/9509248) ;
- [67] F. Jegerlehner, hep-ph/0105283;  
F. Jegerlehner, hep-ph/0308117;  
F. Jegerlehner, hep-ph/0310234;  
F. Jegerlehner, hep-ph/0312372.
- [68] R. B. Nevezorov, A. V. Novikov and M. I. Vysotsky, JETP Lett. **60** 399 (1994);  
B. V. Geshkenbein and V. L. Morganov, Phys. Lett. **B340** 185 (1994), *ibid* **B352** 456 (1995);  
A.D. Martin and D. Zeppenfeld, Phys. Lett. **B345** 558(1995) (hep-ph/9411377);  
K. Adel and F. J. Yuduráin, hep-ph/9509378;  
R. Alemany, M. Davier and A. Höcker, Eur. Phys. J. **C2** 123 (1998) (hep-ph/9703220).  
M. Davier and A. Höcker, Phys. Lett. **B419** 419 (1998) (hep-ph/9711308); *ibid.* **B435** 427 (1998) (hep-ph/9805470).  
J. H. Kühn and M. Steinhauser, Phys. Lett. **B437** 425 (1998) (hep-ph/9802241);  
Nucl. Phys. **B619** 588 (2001) (hep-ph/0109084); *ibid* **B640** 415 (2002)(E).  
S. Groote *et al.*, Phys. Lett. **B440** 375 (1998) (hep-ph/9802374);  
J. Erler, Phys. Rev. **D59** 054008 (1999) (hep-ph/9803453);  
A.D. Martin, J. Outhwaite and M.G. Ryskin, Phys. Lett. **B492** 69 (2000) (hep-ph/0008078); Euro. Phys. J. **C19** 681 (2001)(hep-ph/0012231).

- J. F. de Trocóniz and F. J. Yuduráin, Phys. Rev. **D65** 093002 (2002) (hep-ph /0107318); Phys. Rev. **D71** 073008 (2005) (hep-ph /0402285).
- [69] The LEP Collaborations, the LEP Electroweak Working Group, and the SLD Heavy Flavor and Electroweak Group, CERN-EP/2001-021 (hep-ex/0103048).
- [70] B. Pietrzyk, Nucl. Phys. B(Proc. Suppl.) **162** 18 (2006).
- [71] The LEP Collaborations, the LEP Electroweak Working Group, and the SLD Heavy Flavor and Electroweak Group, Phys. Rep. **427** 257 (2006) (hep-ex/0509008).
- [72] The LEP Collaborations, the LEP Electroweak Working Group, hep-ex/0511027.
- [73] The LEP Collaborations, the LEP Electroweak Working Group, hep-ex/0612054.
- [74] W. J. Marciano and A. Sirlin, Phys. Rev. Lett. **61** 1815 (1988).
- [75] T. van Ritbergen and R. G. Stuart, Phys. Rev. Lett. **82** 488 (1999).
- [76] F. Jegerlehner, in Testing the Standard Model, eds. by M. Cvetič and P. Langacker, World Scientific, Singapore, 1991, p.476.
- [77] G. Weiglein *et al.* [LHC/LC Study Group], hep-ph/0410364.
- [78] F.Ambrosino *et al.*, hep-ex/0603056.
- [79] Crystal Ball Collaboration, A. Osterfeld *et al.*, Report No. SLAC-PUB-4160 (1986) (unpublished).
- [80] BES Collaboration, J.Z.Bai *et al.*, Phys. Rev. Lett. **84**, 594 (2000).
- [81] BES Collaboration, J. Z. Bai *et al.*, Phys. Rev. Lett. **88**, 101802(2002).
- [82] H. M. Hu *et al.*, High Energy Physics and Nuclear Physics, **25**, 1035(2001) (in Chinese).
- [83] G. S. Huang *et al.*, High Energy Physics and Nuclear Physics, **25**, 889(2001) (in Chinese).
- [84] H.M. Hu *et al.*, High Energy Phys. and Nucl. Phys. **31**, 797(2007).
- [85] S.Jadach *et al.*, hep-ph/9912214.
- [86] G.Marchesini, B.R.Webber, Nucl. Phys. **B310** (1988) 461.
- [87] K.K.Seth, arXiv:hep-xp/0405007.
- [88] BES Collaboration, M.Ablikim *et al.*, arXiv:0705.4500[hep-ex].
- [89] BaBar Collaboration, B.Aubert *et al.*, Phys. Rev. Lett. **95**, (2005)142001.
- [90] BaBar Collaboration, B.Aubert *et al.*, arXiv:hep-ex/0502025.

- [91] E. Eichten *et al.*, Phys. Rev. D **21**, (1980) 203.
- [92] T. Barnes *et al.*, Phys. Rev. D **72**, (2005) 054026.
- [93] C. S. Gao, Lectures on Particle Physics and Nuclear Physics. Beijing: Higher Education Press, 1990. 101.
- [94] J. M. Blatt and V. F. Weisskopf, Theoretical Nuclear Physics, Wiley, New York, (1952) 361.
- [95] A. Barbaro-Galtieri, Advances in Particle Physics (Volume 2) P197, editrd by Cool and Marshak.
- [96] Gao C.S, The Group Theory and Its Application in Particle Physics, Higher Education Press, Beijing, 1992.
- [97] R. Brandelik *et al.*, Physics Letters B 76, 361 (1978).
- [98] CERN Program Library entry D **506**.
- [99] M. Davier, arXiv:hep-ex/0312063.
- [100] B.Aubert *et al.*, arXiv:hep-ex/0502025.
- [101] B.Aubert *et al.*, arXiv:hep-ex/0512023.
- [102] I.G.Knowles, Nucl. Phys. **B310**(1988)571
- [103] T.Sjöstrand, Computer Physics Commun. **39** (1986) 347.
- [104] T.Sjöstrand, Computer Physics Commun. **43** (1987) 367.
- [105] Bo Andersson, The Lund Model, pp.142.
- [106] B.Andersson and H.Hu, hep-ph/9810285.
- [107] H.M. Hu *et al.*, Applications of LUND Area Law Generator in R Measurement, High Energy Phys. and Nucl. Phys. (in Chinese).
- [108] H.M. HU *et al.* Nucl. Phys. (Proc. Suppl)**B31** (2004)25.
- [109] Y. Weng *et al.*, High Energy Phys. and Nucl. Phys. **31**, 703(2007).
- [110] Torbjorn Sjostrand, CERN-TH.7112/93.
- [111] J.F. Patrick *et al.* Phys. Rev. Lett. **49** (1982)1232.
- [112] Yu.L. Dokshitzer *et al.*, Int. J. Mod. Phys. **A7** (1992)1875.
- [113] C.P. Fong and B.R.Webber, Phys. Lett. **B229** (1989) 289.
- [114] A.A. Botov *et al.*, Nucl. Phys. (Proc. Suppl)**B162** (2006) 41.

- [115] S.D.Drell and F.Zachariasen, Electromagnetic structure of the nucleons, Oxford University Press (1961).
- [116] See Letter of Intent (working version) on Measurement of the Nucleon Form Factors in Time-Like Region at DAΦNE , October, 2005.
- [117] OPAL Collaboration, M.Z.Akrawy *et al.*, Phys. Lett. **B247** (1990)617.
- [118] E.D.Malaza and B.R.Webber, Phys. Lett. **B149** (1984)501; Phys. Lett. **B267** (1986)702.
- [119] S.Lupia and W.Ochs, Phys. Lett. **B143** (1984)501.
- [120] P.Mattic, Phys. Rept. **177** (1984)141.
- [121] S.D.Drell *et al.*, Phys. Rev. **187** (1969)187; Phys. Rev. **D1**, (1970)1617.
- [122] F.J.Yndurain, Quantum Chromodynamics (N.-Y.-Berlin-Heidelberg-Tokyo, Springer Verlag, 1983).
- [123] Yu.L.Dokshitzer *et al.*, Basics of perturbative QCD (Gif-sur Yvette, Editions Frontieres, 1991).
- [124] Y.I.Azimov *et al.*, Z. Phys. **C27** (1985)65.
- [125] S.J.Bethke, J.Phys. **G26**, (2000)R27.
- [126] K.G. Chetykin *et al.*, Phys. Rev. Lett. **79**, (1997)2184.
- [127] S.G. Kataev *et al.*, Phys. Lett. **B259**, (1991)144.
- [128] P.A.Chetyrkin *et al.*, Phys. Lett. **B559**, (2003)245.
- [129] J.H. Hu *et al.*, High Energy Phys. and Nucl. Phys. **31**, (2007)518.
- [130] Z.Koba, H.B.Nielsen and P.Oleson, Nucl. Phys. **B40** (1972)317.
- [131] S.Humble, Introduction to Particle Production in Hadron Physics, Academic Press, London and New York, (1974).
- [132] M.Schmelling, Phys. Scripta **51**, 683 (1995).
- [133] C.P.Fong and B.R.Webber, Phys. Lett. **B229**, 289 (1989).
- [134] C.P.Fong and B.R.Webber, Nucl. Phys. **B355**, 54 (1991).
- [135] H.H.Hu *et al.*, Nucl. Phys. **B162**(Proc. Suppl.) (2006)5.
- [136] N.N.Achasov and A.A.Kozhevnikov, Phys. Rev. D **55** 2663 (1997).
- [137] N.N.Achasov and A.A.Kozhevnikov, hep-ph/9904326.
- [138] P.Carruther, Phys. Rev **A43**, (1991)2632.

- [139] G. Hanson *et al.*, Phys. Rev. Lett. **35**, 1609 (1975).
- [140] J.D.Bjorken and S.J.Brosky, Phys. Rev. **D1** (1970) 1416.
- [141] R.K. Ellis, D.A. Ross and A.E. Terrano, Nucl. Phys. **B718**, 421 (1981).
- [142] M. Seymour, URL: <http://hepwww.rl.ac.uk/theory/seymour/nlo>.
- [143] A.Hoefer *et al.*, hep-ph/0107154.
- [144] G.V.Fedotovich and A.L.Sibidanov, Nucl. Phys. **B162**(Proc. Suppl.) (2006)63; Nucl. Phys. **B131**(Proc. Suppl.) (2004)9.
- [145] G.Atarelli *et al.*, Z Physics at LEP1, Volume 3: Event Generators and Software, CERN 89-08 V3.
- [146] A.H.Mueller, Phys. Rev. **D4** (1971)150.
- [147] M.G.Kendall and A.Stuart, The advanced Theory of Statistics, Vol.1, C.Griffin and Co., London (1969).
- [148] P.Carruthers, Phys. Rev. **A43** (1991)2632.
- [149] A.B.Abuzov, hep-ph/9703456.
- [150] Dominique Jean-Marie Jacques Mangeol, Doctoral Dissertation, (2002).
- [151] J.L.Siegrist *et. al.* Phys. Rev. **D26** (1982)969.
- [152] D.H.Boal, Rev. Mod. Phys. **62**, (1990)553.
- [153] O.V.Utyuzh and G.Wilk, hep-ph/0205087.
- [154] M.Biyajima and A.Bartl, Theor. Phys. **84** (1990)931.
- [155] S.E.Koonin, Phys. Lett. **B70**, (1977)43.
- [156] F.B.Yano and S.E.Koonin, Phys. Lett. **B78**, (1978)556.
- [157] M.Gyulassy *et al.* Phys. Rev. **C20**, (1979)2267.
- [158] L.I.Schiff, Quantum Mechanics (McGraw-Hill, New York)1955.
- [159] T.H.Burnett *et al.* (JACEE), Phys. Rev. Lett. **50** (1983)2062.
- [160] M.Adamus *et al.* (NA22), Phys. Lett. **B185**, (1987)200.
- [161] G.J.Alner *et al.* (UA5), Phys. Rep. **154** (1987)247.
- [162] M.I.Adamovich *et al.* (EMU01), Phys. Lett. **201** (1988)397.
- [163] W.Braunschweig *et al.* (TASSO), Phys. Lett. **B231** (1989)548.
- [164] H.J.Behrend *et al.* (CELLO), Phys. Lett. **256** (1991)97.

- [165] P. Abreu *et al.* (DELPHI), Phys. Lett. **B247** (1990)137; A. De Angelis, Mod. Phys. Lett. **A5** (1990)2395; P. Abreu *et al.* (DELPHI), Nucl. Phys. **B386** (1992)471
- [166] M. Z. Akrawy *et al.* (OPAL), Phys. Lett. **B262** (1991)351
- [167] D. Decamp *et al.* (ALEPH), Z. Physik C-Particles and Fields **53** (1992)21.
- [168] A. Bialas and R. Peschanski, Nucl. Phys. **B273** (1986)703.
- [169] A. Bialas and R. Peschanski, Nucl. Phys. **B308** (1988)857.
- [170] P. Carruthers *et al.*, Phys. Lett. **B222** (1989)487.
- [171] Y. Wu and L. Liu, Phys. Rev. Lett. **21** (1993)3197; Phys. Rev. **D51** (1995) 6567.
- [172] T. Barnes, S. Godfrey and E. S. Swanson, arXiv:hep-ph/0505002.
- [173] see reference [46].
- [174] R. Poling, arXiv:hep-ex/0606016.
- [175] E. Eichten, *et al.* Phys. Rev. D, 1980, **21**: 203.
- [176] J. Adler *et al.* Phys. Rev. Lett., 1988, **60**: 89
- [177] Q. He *et al.* Phys. Rev. Lett., 2005, **95**: 121801
- [178] J. Z. Bai *et al.* Phys. Rev. D, 1995, **52**: 3781
- [179] H. W. Zhao, PhD. thesis(in Chinese); K. L. He, PhD. thesis (in chinese)
- [180] M. W. Coles *et al.* Phys. Rev. D, 1982, **26**: 2190
- [181] J. Adler *et al.* Phys. Lett. B, 1988, **208**: 152
- [182] G. Blaylock *et al.* Phys. Rev. Lett., 1987, **58**: 2171
- [183] N. Cahn, B. Kayser, Phys. Rev. D, 1980, **22**: 2752
- [184] T. Barnes, S. Godfrey and E. S. Swanson, Phys. Rev. D, 2005, **72**: 054026
- [185] E. J. Eichten, K. Lane and C. Quigg, Phys. Rev. D, 2006, **73**: 014014, Phys. Rev. D, 2006, **73**: 079903
- [186] S. Jadach, B. F. L. Ward, Z. Was, Phys. Rev. D, 2001, **63**: 113009
- [187] David Lange and Anders Ryd, proceeding of CHEP98, 1998, <http://www.slac.stanford.edu/~lange/EvtGen>.
- [188] E. A. Kuraev and V. S. Fadin, Sov. J. Nucl. Phys. 41, 466(1985).
- [189] G. Altarelli and G. Martinelli, CERN Yellow Report 86-02(1986)47; O. Niclosini and L. Trentadue, Phys. Lett. B, 1987, **196**: 551.

- [190] F. A. Berends, G. Burgers and W. L. van Neeren, Nucl. Phys. B, 1988, **297**: 429; Nucl. Phys. B, 1986, **304**: 921.
- [191] T. Kinoshita, J. Math. Phys. **3**, 650(1962); T. D. Lee and M. Nauenberg, Phys. Rev. **B133**, 1549(1964).
- [192] B. Dewit and J. Smith, Field theory in particle physics, Volume 1, Elsevier Science Publishing Company, Inc.
- [193] Yi-Bing Ding, Kuang-Ta Zhao and Dan-Hua Qin, Phys Rev. D **51** (1995) 5064.
- [194] F.E. Close and P.R. Page, Phys. Lett. B **366** (1996) 323.
- [195] BES Collaboration, M. Ablikim *et al.*, Phys. Rev. Lett., 97, 121801 (2006).
- [196] BES Collaboration, M. Ablikim *et al.*, Phys. Lett., B641, 145 (2006).
- [197] E760 Collaboration, T.A. Armstrong *et al.*, Phys Rev. D **47** (1993) 772.
- [198] M. Boyaski et al., Phys. Rev. Lett., 34, 1357(1975).
- [199] MARK-I Collaboration, P.A. Rapidis *et al.*, Phys. Rev. Lett. **39**, 526, 1977, Erratum-ibid. **39**, 974,1977.
- [200] R. Baldini Celio et al., Phys. Lett. B58, 471(1975).
- [201] B. Esposito et al., Lett. Nuovo Cim., 14 73(1975).
- [202] R. Brandelik et al., Z. Phys., Cl, 233(1997).
- [203] MARK-II Collaboration, R.H. Schindler *et al.*, Phys Rev. D **21** (1980) 2716.
- [204] DELCO Collaboration, W. Bacino *et al.*, Phys. Rev. Letts. **40** 671 (1978).
- [205] BES Collaboration, J.Z. Bai *et al.*, Phys. Lett. **B 355** 374 (1995).
- [206] BES Collaboration, J.Z. Bai *et al.*, Phys. Lett. **B 550** 24 (2002).
- [207] D.H. Zhang, G. Rong, and J.C. Chen, Phys Rev. D **74** (2006) 054012.
- [208] M. Ablikim *et al.* (BES Collaboration), physics/0503001, submitted to Nucl. Instr. and Meth. A.
- [209] J.Z. Bai *et al.* (BES Collaboration), Phys. Lett. **B 603** 130 (2004).
- [210] See reference [6].
- [211] Andrej B. Arbuzov, Eduard A. Kuraev *et al.*, JHEP10 006 (1997).
- [212] M. Ablikim *et al.* (BES Collaboration), Nucl. Phys. **B 727** 395 (2005).
- [213] S. Eidelman *et al.* (Particle Data Group), Phys. Lett. **B 592** 1(2004).
- [214] BES Collaboration, M. Ablikim *et al.*, hep-ex/0612056.
- [215] BES Collaboration, M. Ablikim *et al.*, Phys. Rev. Lett., 97, 262001 (2006).

# Part III

## Light Hadron Physics

Conveners  
Xiao-Yan Shen, Bing-Song Zou

Contributors  
Jian-Ming Bian, Vladimir Bytev, Ying Chen,  
Hong-Ying Jin, Shan Jin, Hu Qin, Xiao-Yan Shen,  
Ning Wu, Guo-Fa Xu, Zhen-Xia Zhang, Qiang Zhao,  
Alexey Zhemchugov, Han-Qing Zheng, Shi-Lin Zhu,  
Bing-Song Zou



Our knowledge about the structure of matter and the nature of the interactions between its constituent components follows a hierarchy that closely tracks the evolution of experimental measurements from low to higher and higher energies. For example, with an electron beam of a given energy, one can access the microscopic structure of matter at length scales corresponding to the de-Broglie wave length of the electrons that are being used:  $\lambda = 2\pi \times 197.3 \text{ MeV}\cdot\text{fm}/E_\gamma$ , where  $E_\gamma$  is the energy of the photon that is exchanged in the experimentally observed process. As the energy of the beams that are available get higher and higher, the sizes of objects that can be probed get smaller and smaller.

Using this relation, theoretical prescriptions for phenomena observed at different microscopic scales can be classified in terms of the corresponding energy scales. At momentum transfers of several MeV, which is much below  $\Lambda_{QCD} \sim 200 \text{ MeV}$  the fundamental scale of Quantum Chromodynamics (QCD), explicit chiral-symmetry breaking is revealed by the pattern of pseudoscalar meson masses and the  $\pi N \sigma$ -terms. Chiral perturbation theory can, in principle, provide a rigorous solution for physics that involve soft (*i.e.* low-energy) pions. At the very high energy (short distance) extreme (*i.e.* energies much greater than  $\Lambda_{QCD}$ ), partonic and gluonic degrees of freedom are revealed in deep inelastic scattering measurements. In this energy region perturbative expansions of QCD are valid and rigorous solutions can be pursued. However, in the intermediate region between these two energy extremes, excitations of meson and baryon resonances reveal effective constituent degrees of freedom. These, together with their mutual strong interactions, give rise to the complex spectroscopy of hadrons. Since neither perturbative expansions of QCD nor chiral perturbation theory is valid at these length scales, it remains a great challenge to physicists to describe the underlying physics on the basis of first principles. This challenge is the focus of a large amount of recent experimental and theoretical effort.

Hadron spectroscopy has been the major platform for probing many of the dynamical aspects of strong interactions in the non-perturbative regime. It also connects fundamental approaches such as lattice QCD calculations to phenomenological tools such as the quark model, QCD sum rules, etc., and provide insights into non-perturbative properties of QCD.

Quarks, the basic building blocks of hadrons, are bound together by the color force mediated by the exchanges of gluons to form color-singlet hadrons. The underlying dynamics are described by the widely tested QCD Lagrangian [1]:

$$\begin{aligned} \mathcal{L} = & i \sum_i \bar{q}_i(x) [\partial_\mu - ig_s \sum_a \frac{1}{2} \lambda^a A_\mu^a(x)] \gamma^\mu q_i(x) \\ & - \frac{1}{4} \sum_a F_{\mu\nu}^a(x) F^{\mu\nu a}(x) - \sum_i \bar{q}_i(x) m_i q_i(x) , \end{aligned} \quad (8.5.11)$$

where  $g_s$  is the strong coupling constant,  $i$  is the index for quark-flavor of the  $q_i(x)$  Dirac spinor in three-dimensional color space and  $\lambda^a$  denote the  $3 \times 3$  Gell-Mann matrices with  $a = 1, \dots, 8$ . Here, a  $q\bar{q}$  pair is the minimal configuration of quarks and antiquarks that can form a color-singlet meson, while  $qqq$  is the minimal configuration that can form a color-singlet baryon.

Note that the QCD quark-gluon interaction conserves flavor, and the interaction strength is flavor-independent. The only dependence on flavor in the QCD Lagrangian is through the quark-mass terms.

In the  $u$ ,  $d$  &  $s$  light quark sector, the mass differences are relatively small:  $m_d - m_u \simeq 3$  MeV and  $m_s - m_d = 150$  MeV. Therefore, the strong interactions have an approximate global  $SU(3)$  flavor symmetry, where quarks (antiquarks) are assigned to a triplet representation  $\mathbf{3}$  ( $\bar{\mathbf{3}}$ ). Mesons made of  $q\bar{q}$  are then irreducible representations given by the following product decomposition:

$$\mathbf{3} \otimes \bar{\mathbf{3}} = \mathbf{1} + \mathbf{8} , \quad (8.5.12)$$

and baryons are:

$$\mathbf{3} \otimes \mathbf{3} \otimes \mathbf{3} = \mathbf{1}_a + \mathbf{8}_\lambda + \mathbf{8}_\rho + \mathbf{10}_s , \quad (8.5.13)$$

where the subscripts  $a$ ,  $s$ ,  $\lambda$  and  $\rho$  denote antisymmetric, symmetric, and the two mixed symmetries for the two-body substates within the three-quark system.

$SU(3)$ -flavor symmetry implies the existence of flavor nonets with the same  $J^P$  but different charges in the meson spectrum. For example, there are eight pseudoscalars with masses below  $\sim 500$  MeV:  $\pi^0$ ,  $\pi^\pm$ ,  $K^0$ ,  $\bar{K}^0$ ,  $K^\pm$  and  $\eta$ , and one at about 1 GeV:  $\eta'$ . These states are collectively identified as the  $0^-$  flavor nonet of the meson spectrum.

Similarly, for the lowest-mass baryons, one expects the existence of flavor singlets, octets and decuplets. In the spectrum of the lowest-lying baryon states, one identifies eight baryons that correspond to an octet with  $J^P = 1/2^+$ :  $p(uud)$ ,  $n(udd)$ ,  $\Sigma^+(uus)$ ,  $\Sigma^0(uds)$ ,  $\Sigma^-(dds)$ ,  $\Lambda(uds)$ ,  $\Xi^0(uss)$  and  $\Xi^-(dss)$ , with masses in the  $0.9 \sim 1.3$  GeV range, and ten states of a decuplet with  $J^P = 3/2^+$ :  $\Delta^{++}(uuu)$ ,  $\Delta^+(uud)$ ,  $\Delta^0(udd)$ ,  $\Delta^-(ddd)$ ,  $\Sigma^+(uus)$ ,  $\Sigma^0(uds)$ ,  $\Sigma^-(dds)$ ,  $\Xi^0(uss)$ ,  $\Xi^-(dss)$ , and  $\Omega^-(sss)$ , with masses in the  $1.2 \sim 1.7$  GeV range. The flavor-singlet baryon with  $J^P = 1/2^+$  has a higher mass that is produced by the spatial and spin degrees of freedom.

By relating the breaking of  $SU(3)$ -flavor symmetry to the mass term in the QCD Lagrangian, an early successful prediction of the quark model was that the hadrons within an  $SU(3)$ -flavor multiplet will differ in mass linearly with the number of  $s$ -quarks that they contained. Namely, one has

$$\begin{aligned} \Omega^-(1672) - \Xi(1530) &\simeq \Xi(1530) - \Sigma(1385) \\ &\simeq \Sigma(1385) - \Delta(1232) \\ \phi(1020) - K^*(890) &\simeq K^*(890) - \rho(770) . \end{aligned} \quad (8.5.14)$$

A compact expression is given by the Gell-Mann-Okubo mass relation:

$$\Sigma + 3\Lambda = 2(N + \Xi) . \quad (8.5.15)$$

The main hypotheses of the QCD-motivated naive quark model [2, 3] are:

- i) Spontaneous breaking of chiral symmetry leads to the presence of massive constituent quarks within a hadron as effective degrees of freedom.
- ii) Hadrons can be viewed as a quark system in which the gluon fields generate effective potentials that depend on the relative positions and spins of the massive quarks.

These two hypotheses inspire a non-relativistic treatment as a leading-order approach. Meanwhile, for quarks that have constituent masses that are comparable to the QCD scale, the creation of constituent quark pairs will be suppressed. Thus, the lowest-lying

meson states are  $q\bar{q}$  and lowest-lying baryon states are  $qqq$ . By treating the gluon fields as effective potentials, the hadron wavefunctions only depend on quark variables.

By incorporating these simple hypotheses in a framework that accommodates the color, flavor, spin, and spatial degrees of freedom in the wavefunction solutions for bound quark systems, the quark model provides an efficient and evidently successful classification for a large number of hadrons that are observed experimentally [4].

In the light hadron sector, the nonrelativistic approach of the naive quark model unavoidably suffers the problem that the excitation energies of the excited hadron states (*i.e.* resonances) are comparable to the constituent masses, thereby making the nonrelativistic approach questionable. Although it is still unclear why such a nonrelativistic model works so well for the light flavor  $u$ -,  $d$ - and  $s$ -quark systems, there is no doubt about its extensive range of empirical successes. Various investigations are making progress on providing a firmer basis for the quark model phenomenology. For instance, recent progress in lattice QCD is providing evidence for effective degrees of freedom that can be identified as constituent quarks inside the nucleon.

Another tantalizing aspect of the low-energy properties of QCD that needs understanding is the possible existence of hadrons with structures that are more complex than the traditional  $q\bar{q}$  or  $qqq$  configurations of the quark model. QCD is a non-Abelian theory that does not appear to forbid formations of so-called ‘exotics’, *i.e.* color-singlet constituent arrangements that are more complex than the conventional  $q\bar{q}$  or  $qqq$  hadrons. These include, for example: glueballs, made only of gluons; hybrids, made of both quarks and gluons as effective constituents; multiquark states; *etc.* These forms of hadrons have still evaded any explicit confirmations from experiment or theory. This reflects poorly on what we know about the fundamental strong force in the nonperturbative regime. Such states, if they exist, will enrich the population of states in the spectroscopy of hadrons, and deepen our understanding of the properties of QCD. As a result, they have received a tremendous amount of experimental and theoretical effort.

Applications of various types of QCD-motivated phenomenological models to the study of hadron spectroscopy can be found in the literature. These include: the semirelativistic flux-tube model [5, 6]; the instanton model [7]; the Goldstone boson exchange model [8]; the diquark model [9]; *etc.* Masses of the non-strange  $P$ -wave baryons have also been examined by means of a mass operator analysis in large  $N_c$  QCD [10]. Moreover, there continue to be attempts at formulating relativistic versions of the quark model [11]. QCD-inspired approaches for understanding the dynamics of hadron EM and strong decays and hadron-hadron interactions have also been extensively described in the literature. Generally speaking, those approaches take into account different specific ingredients of the quark interactions and shed new light on corresponding aspects of non-perturbative QCD. (See Ref. [12] for a recent review.) The ultimate prescription for understanding non-perturbative QCD dynamics in the light quark sector may come from future lattice QCD studies.

The study of light hadron spectroscopy is a major activity at many hadron facilities. The primary focus of the CLAS collaboration at Hall B at Jefferson Laboratory are the properties of baryons, including those of the ground states and a nearly complete set of excited baryon resonances. It has the capability to do polarized-beam asymmetry measurements and, eventually, experiments with polarized targets will also be performed. With its primary electron energy upgraded to 12 GeV, measurements of the baryon reso-

nance form-factors from low to high momentum-transfers will be carried out. One of the most important physics goals of CLAS is to look for the “missing baryon resonances”, *i.e.* states that are predicted by the quark model, but which have so far not been seen in the  $\pi$ - $N$  scattering data. Similar projects are also underway at ELSA, ESRF, MAMI and SPring-8, via nucleon photo- and/or electro-excitations. In contrast to these, the study of baryon resonances in charmonium decays at *BES-III* will have the advantages of reduced non-resonant background and the ability to disentangle individual resonances thanks to the natural isospin filter provided by the initial charmonia. We discuss experiments on light meson spectroscopy at other experimental facilities such as BaBar, Belle, BNL, Fermilab, CLEO-c/Cornell, FAIR, *etc.*, below.

# Chapter 9

## Meson spectroscopy

### 9.1 Introduction

The ultimate goal of the study of hadron spectroscopy is to understand the dynamics of the constituent interactions. For light hadron systems, perturbative QCD is not applicable, and the path towards this ultimate goal has to be via phenomenological methods or lattice QCD (LQCD) calculations. In the past decade, LQCD has experienced drastic improvements aided in part by the continued rapid development of computing resources. But a lot of technical difficulties persist in the simulation of fully non-perturbative QCD processes; *e.g.*, unquenched calculations are still unavailable. In contrast, the development of phenomenological methods has made progress over the whole range of modern sciences, and especially in the study of hadron spectroscopy (see Ref. [13] and references therein). For these approaches, experimental data is required to provide necessary constraints on the various parameters introduced by the theory.

In this Chapter, we will discuss how a  $q\bar{q}$  meson can be constructed in the quark model [4, 13]. In addition to “conventional”  $q\bar{q}$  mesons, it is known that the non-Abelian property of QCD also suggests the possible existence of bound states that are made completely of gluons, *i.e.* so-called “glueballs”, and/or a gluon continuum. Furthermore, it may also be possible to form multiquark mesons, such as  $qq\bar{q}\bar{q}$ , and so-called “hybrid” mesons, which contain both  $q\bar{q}$  and a gluon ( $g$ ) as constituents,  $q\bar{q}g$ . Such unconventional states, if they exist, will enrich greatly the meson spectrum and shed light on the dynamics of strong QCD. Thus, searching for those unconventional mesons in experiment is a topical subject for modern intermediate- and high-energy physics [302, 14].

### 9.2 Conventional meson spectrum

For conventional  $q\bar{q}$  mesons, the goal of phenomenological studies is, on the one hand, to find an empirically efficient way to describe the meson spectrum, and on the other hand maintain the general properties of QCD. In the quark model framework, the starting point for the study of the meson spectrum is the construction of the Hamiltonian for color-singlet

$q\bar{q}$  systems:

$$H = \int d\mathbf{x} \sum_i q_i^\dagger(\mathbf{x}) \beta \left( m_i - \frac{\Delta}{2m_i} \right) q_i(\mathbf{x}) + \frac{1}{2} \int d\mathbf{x} d\mathbf{y} V_0(\mathbf{x} - \mathbf{y}) \sum_{ija} q_i^\dagger(\mathbf{x}) \frac{\lambda^a}{2} q_i(\mathbf{x}) q_j^\dagger(\mathbf{y}) \frac{\lambda^a}{2} q_j(\mathbf{y}) , \quad (9.2.1)$$

where  $i$  and  $j$  are flavor indices,  $\lambda^a$  are the Gell-Mann Matrices for the SU(3)-color interactions, and  $V_0(\mathbf{x} - \mathbf{y})$  is a central potential, *i.e.* it only depends on  $|(\mathbf{x} - \mathbf{y})|$ . Note that this Hamiltonian is independent of flavor, as required by QCD. Also, one can see that a particular assumption for the form of the potential  $V_0$  can reflect properties of QCD, such as in one-gluon-exchange Coulomb approximation  $V_0(\mathbf{x}) = \alpha_s/|\mathbf{x}|$  at short separation distances, with an increasing confinement behavior at larger distances.

The potential part of the Hamiltonian operating on a color-singlet  $q\bar{q}$ ,  $|(q\bar{q})_1\rangle$ , gives

$$\langle (q\bar{q})_1 | \hat{V} | (q\bar{q})_1 \rangle = -\frac{4}{3} V_0 , \quad (9.2.2)$$

where  $\hat{V}$  denotes the second term of Eq. (9.2.1). Therefore, one can simplify the Hamiltonian for a color-singlet  $q_i\bar{q}_j$  system to be:

$$H = \frac{\mathbf{p}_x^2}{2m_i} + \frac{\mathbf{p}_y^2}{2m_j} - \frac{4}{3} V_0(\mathbf{x} - \mathbf{y}) , \quad (9.2.3)$$

where  $\mathbf{p}_x$  ( $\mathbf{p}_y$ ) and  $\mathbf{x}$  ( $\mathbf{y}$ ) are the momentum and position of quark  $i$  ( $j$ ), respectively.

In the center-of-mass frame, the Hamiltonian can be written as

$$H = \frac{\mathbf{P}^2}{2M} + \frac{\mathbf{p}^2}{2m} + V(\mathbf{r}) , \quad (9.2.4)$$

where  $\mathbf{P} = \mathbf{p}_x + \mathbf{p}_y$  is the c.m. momentum of the  $q\bar{q}$  system,  $\mathbf{r} = \mathbf{x} - \mathbf{y}$  and  $\mathbf{p} = (\mathbf{p}_x - \mathbf{p}_y)/2$  are the relative distance and momentum between these two quarks, and  $M \equiv m_i + m_j$  &  $m \equiv m_i m_j / M$  are the total and reduced masses. Since  $V(\mathbf{r})$  is assumed to be spin-independent, Eq. (9.2.3) is invariant under separate orbital and spin rotations. By defining the radial quantum number  $N$ , the orbital angular momentum  $L$ , and the total spin  $S = 0, 1$ , one can classify the eigenstates of Eq. (9.2.3) (including the spin wavefunctions) as  $N^{2S+1} L_J$  with the total angular momentum  $J = L$  for  $S = 0$  or  $J = |L - 1|, L, L + 1$  for  $S = 1$ . Given an explicit form for  $V(\mathbf{r})$ , one in principle is able to produce a  $q\bar{q}$  spectrum to compare with experimental data. For instance, the ground state will correspond to  $N = 1, L = 0$  with  $S = 0$  or  $1$ , *i.e.* a spin singlet  $1^1S_0$  and a spin triplet  $1^3S_0$ . In the charmonium spectrum – a suitable example for spin-independent potential quark model – one can identify these as the  $\eta_c(2980)$  and  $J/\psi(3097)$ . Table 9.2 lists a classification based on this scheme for some of the low-lying mesons in the light quark sector [259].

There are also spin-dependent forces between the quarks that result in fine and hyperfine structures in the hadron spectrum. In fact, without spin-dependent forces, the spectrum obtained from the Hamiltonian of Eq. (9.2.3) cannot match the pattern observed in experiment. On the other hand, relativistic effects will break the invariance of Hamiltonian under separate orbital and spin rotations. Therefore, it is natural to introduce spin-dependent forces that are phenomenologically analogous to those in the hydrogen atom.

Table 9.1: Quark model classification for some of those low-lying  $q\bar{q}$  states.  $f'$  and  $f$  denote the octet-singlet mixings. It should be noted that the nature of the  $f_0(1710)$  and  $f_0(1370)$  is still subject to debate.

$N^{2S+1}L_J$	$J^{PC}$	$I = 1$ $u\bar{d}, d\bar{u}, (d\bar{d} - u\bar{u})/\sqrt{2}$	$I = 1/2$ $u\bar{s}, s\bar{u}, d\bar{s}, s\bar{d}$	$I = 0$ $f'$	$I = 0$ $f$
$1^1S_0$	$0^{-+}$	$\pi$	$K$	$\eta$	$\eta'$
$1^3S_1$	$1^{--}$	$\rho(770)$	$K^*(892)$	$\phi(1020)$	$\omega(782)$
$1^1P_1$	$1^{+-}$	$b_1(1235)$	$K_{1B}$	$h_1(1380)$	$h_1(1170)$
$1^3P_0$	$0^{++}$	$a_0(1450)$	$K_0^*(1430)$	$f_0(1710)$	$f_0(1370)$
$\dots$					

De Rujula, Georgi and Glashow first illustrated that the spin-dependent forces in the quark potential originate from the short-range QCD one-gluon-exchange (OGE) [1]. In a nonrelativistic expansion, in addition to a colored Coulomb-type potential, the OGE generates a Breit-Fermi interaction:

$$H_{BF} = k\alpha_s \sum_{i < j} S_{ij} , \quad (9.2.5)$$

where  $k = -4/3$  and  $-2/3$  for a  $q\bar{q}$  singlet and  $qq$  in a  $\bar{\mathbf{3}}$ , respectively, and

$$\begin{aligned} S_{ij} = & \frac{1}{|\mathbf{r}|} - \frac{1}{2m_i m_j} \left( \frac{\mathbf{p}_i \cdot \mathbf{p}_j}{|\mathbf{r}|} + \frac{\mathbf{r} \cdot (\mathbf{r} \cdot \mathbf{p}_i) \mathbf{p}_j}{|\mathbf{r}|^3} \right) - \frac{\pi}{2} \delta(\mathbf{r}) \left( \frac{1}{m_i^2} + \frac{1}{m_j^2} + \frac{16\mathbf{S}_i \cdot \mathbf{S}_j}{3m_i m_j} \right) \\ & - \frac{1}{2|\mathbf{r}|^3} \left\{ \frac{1}{m_i^2} (\mathbf{r} \times \mathbf{p}_i) \cdot \mathbf{S}_i - \frac{1}{m_j^2} (\mathbf{r} \times \mathbf{p}_j) \cdot \mathbf{S}_j \right. \\ & \left. + \frac{1}{m_i m_j} \left[ 2(\mathbf{r} \times \mathbf{p}_i) \cdot \mathbf{S}_j - 2(\mathbf{r} \times \mathbf{p}_j) \cdot \mathbf{S}_i - 2\mathbf{S}_i \cdot \mathbf{S}_j + 6 \frac{(\mathbf{S}_i \cdot \mathbf{r})(\mathbf{S}_j \cdot \mathbf{r})}{|\mathbf{r}|^2} \right] \right\} + \dots \end{aligned} \quad (9.2.6)$$

Although it is still questionable as to whether or not one can apply the OGE picture to the hadron spectrum, these results turn out to be in good agreement with experimental observations.

We do not review the Goldstone boson exchange model developed in the past decade, but refer readers to recent reviews [8] for details. A review of constituent quark model approaches for  $q\bar{q}$  system can be found in Ref. [13].

According to the constituent quark model (CQM), mesons and baryons are composed of  $q\bar{q}$  and  $qqq$  respectively. The CQM provides a convenient framework for the classification of hadrons and most of the experimentally observed hadron states fit into this scheme quite neatly. Any states beyond the CQM are labelled as “non-conventional” hadrons.

However, the CQM is only a phenomenological model. It is not derived from the underlying theory of the strong interaction—*i.e.* Quantum Chromodynamics (QCD). Hence the CQM spectrum is not necessarily the same as the physical spectrum of QCD, which remains ambiguous and elusive after decades of intensive theoretical and experimental exploration. No one has been able to either prove or exclude the existence of

non-conventional states rigorously, since no one has yet been able to solve the confinement issue in QCD.

Hadron physicists generally take a modest and practical attitude. If one supposes that these non-conventional states exist, then the important issues are: (1) How to determine their characteristic quantum numbers and estimate their masses, production cross-sections and decay widths reliably? (2) How and in which channels can we distinguish their signals from background and identify them unambiguously?

There are three classes of non-conventional hadrons. The first class are mesons with "exotic"  $J^{PC}$  quantum numbers. The possible angular momentum, parity and charge conjugation parity of a neutral  $q\bar{q}$  meson can only be  $J^{PC} = 0^{++}, 0^{-+}, 1^{++}, 1^{--}, 1^{+-}, \dots$ ;  $q\bar{q}$  mesons cannot have  $J^{PC} = 0^{--}, 0^{+-}, 1^{-+}, 2^{+-}, 3^{-+}, \dots$ . Any state with these "exotic" quantum numbers will clearly be beyond the CQM. We want to emphasize that these would be "exotic" only in the context of the CQM. One can construct color-singlet local operators to verify that these quantum numbers are allowed in QCD. "Exotic" quantum numbers provide a powerful signatures for experimental searches for non-conventional meson states. In contrast, the  $qqq$  baryons of the CQM exhaust all possible  $J^P$ , i.e.,  $J^P = \frac{1}{2}^{\pm}, \frac{3}{2}^{\pm}, \frac{5}{2}^{\pm}, \dots$ .

The second class of unconventional hadrons are those with exotic flavor content. One example of this would be the purported  $\Theta^+$  pentaquark. This was studied in the  $K^+n$  channel with the quark content  $uudd\bar{s}$ . Such a state, should it exist, would clearly be beyond the CQM. Exotic flavor content is thus an important aspect of experimental searches for non-QPM states.

The third class are hadrons that have non-exotic quantum numbers but do not fit into the CQM spectrum. Take, for example, the  $J^{PC} = 0^{++}$  scalar mesons. Below 2 GeV there exists the  $\sigma, f_0(980), f_0(1370), f_0(1500), f_0(1710), f_0(1790)$  and the  $f_0(1810)$  candidate scalar meson states. Within the CQM, only two scalars are expected in this mass range, at least if we ignore radial excitations. Including radial excitations, the CQM could accommodate no more than four scalars. Clearly there is a serious overpopulation of the scalar meson spectrum. If all of the states listed above are genuine and distinct, the content of some of them cannot be simply  $q\bar{q}$ . The overpopulation of the spectrum provides another useful tool for the experimental search for non-conventional states.

Glueballs are hadrons comprised of gluons. Quenched lattice QCD simulations suggest that the scalar glueball is the lightest of these states, with a mass in the  $1.5 \sim 1.7$  GeV range. Glueballs with other quantum numbers are expected to have higher masses. In the large  $N_c$  limit, glueballs decouple from the conventional  $q\bar{q}$  mesons [15]. In the real world with  $N_c = 3$ , glueballs can mix with any nearby  $q\bar{q}$  mesons that have the same quantum numbers, which renders the experimental identification of scalar glueballs very difficult. In the following we discuss all of the non-conventional hadrons according to their underlying quark gluon structure.

## 9.3 Glueball spectrum

Glueballs are bound states of at least 2 or 3 gluons in a color singlet due to the non-Abelian property of QCD:

$$\begin{aligned} gg : \quad \mathbf{8} \otimes \mathbf{8} &= \mathbf{1} + \mathbf{8} + \dots \\ ggg : \quad \mathbf{8} \otimes \mathbf{8} \otimes \mathbf{8} &= (\mathbf{8} \otimes \mathbf{8})_{\mathbf{8}} \otimes \mathbf{8} = \mathbf{1} + \dots, \end{aligned} \quad (9.3.7)$$

where the charge conjugation is  $C = +$  for  $gg$  states and  $C = -$  for  $ggg$  states. Assuming that gluons inside glueballs are massive, for  $gg$  with orbital angular momentum  $L = 0$ , states of  $0^{++}$  and  $2^{++}$  can be formed, with  $0^{++}$  being the ground state. For  $ggg$ , the lowest states are  $0^{-+}$ ,  $1^{--}$  and  $3^{--}$ .

Both  $gg$  and  $ggg$  can form states with quantum numbers that cannot be produced by  $q\bar{q}$  quark model states. Such states, called “oddballs,” would be “smoking guns” in searching for glueball candidates. (Experimental evidence for such a state is still unavailable.) Possible quantum numbers for oddballs are:  $0^{--}$ ,  $0^{+-}$ ,  $1^{-+}$ ,  $2^{+-}$ ,  $3^{-+}$ .... However, for  $gg$  states, if the gluons inside are massless,  $J = \text{odd}$  states would be forbidden by Yang’s theorem [16] though they could exist in  $ggg$  sector.

There is no explicit correlation between the  $gg$  and  $ggg$  ground state masses, although the  $0^{++}$  is expected to be lighter than the  $0^{-+}$ . Theoretical predictions for the glueball masses vary significantly among different approaches. Early phenomenological models find rather light masses for the scalar glueball, *e.g.*,  $M(0^{++}) = 0.65 \sim 1.21$  GeV in the bag model [17, 18, 19], and  $M(0^{++}) = 1.15$  GeV in a potential model [20]. Other QCD-motivated approaches produce larger masses for the scalar such as  $M(0^{++}) = 1.52$  GeV in a flux-tube model [21], and  $M(0^{++}) \simeq 1.5$  GeV in QCD sum rule calculations [22, 23, 24, 25, 26, 27, 28].

Over the past twenty years, extensive numerical studies have been carried out aimed at calculating the glueball spectrum in LQCD. Although the earliest LQCD predictions [29, 30] for the glueball masses varied significantly, the more recent predictions for several lightest glueballs have converged to a similar mass region despite the use of different approaches [31, 32, 33, 34]. The lowest glueball state in these calculations is the  $J^{PC} = 0^{++}$  state (scalar) with a mass of about  $1.5 \sim 1.7$  GeV, and the mass ratios of the tensor and pseudoscalar to the scalar are about 1.4 and 1.5, respectively. The latest results [34] on the glueball spectrum from a larger and finer lattice are listed in Table 9.3 and shown in Fig. 9.1.

The calculations of the glueball spectrum are mostly from quenched lattice QCD. Therefore, an open question remains: *How large is the systematic uncertainty associated with the use of the quenched approximation?* A recent preliminary analysis of the scalar glueball mass based on the MILC dynamical gauge configuration indicates that the scalar glueball mass of the dynamic lattice simulation is not much effected by this approximation [35].

### 9.3.1 Glueball signatures

Using the spectrum of the  $q\bar{q}$  nonet of pseudoscalar ( $0^-$ ) and vector ( $1^-$ ) mesons as a reference, one expects the scalar nonet to lie in the  $1 \sim 2$  GeV mass window [13,

Table 9.2: The predicted glueball spectrum in physical units. In column 2, the first error is the statistical uncertainty coming from the continuum extrapolation, the second one is the 1% uncertainty resulting from the approximate anisotropy. In column 3, the first error comes from the combined uncertainty of  $r_0 M_G$ , the second from the uncertainty of  $r_0^{-1} = 410(20)$  MeV

$J^{PC}$	$r_0 M_G$	$M_G$ (MeV)
$0^{++}$	4.16(11)(4)	1710(50)(80)
$2^{++}$	5.83(5)(6)	2390(30)(120)
$0^{-+}$	6.25(6)(6)	2560(35)(120)
$1^{+-}$	7.27(4)(7)	2980(30)(140)
$2^{-+}$	7.42(7)(7)	3040(40)(150)
$3^{+-}$	8.79(3)(9)	3600(40)(170)
$3^{++}$	8.94(6)(9)	3670(50)(180)
$1^{--}$	9.34(4)(9)	3830(40)(190)
$2^{--}$	9.77(4)(10)	4010(45)(200)
$3^{--}$	10.25(4)(10)	4200(45)(200)
$2^{+-}$	10.32(7)(10)	4230(50)(200)
$0^{+-}$	11.66(7)(12)	4780(60)(230)

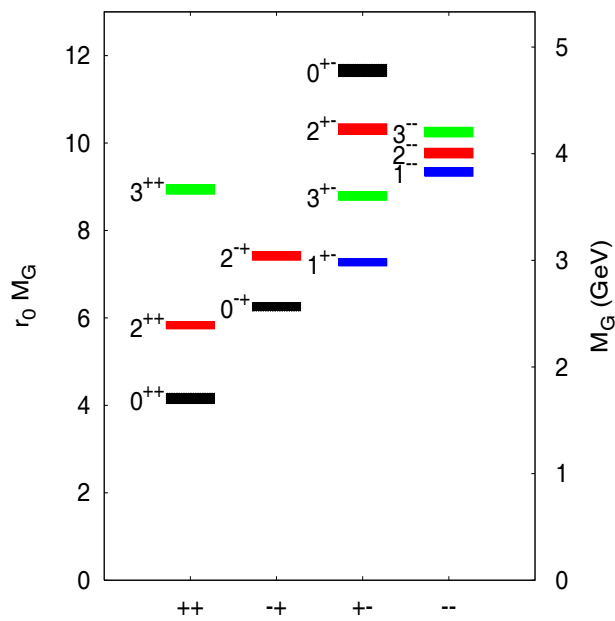


Figure 9.1: The mass spectrum of glueballs in pure  $SU(3)$  gauge theory. The masses are given both in terms of  $r_0$  ( $r_0^{-1} = 410$  MeV) and in GeV. The thickness of each colored box indicates the statistical uncertainty of the mass.

302, 14]. The established  $a_0(1450)$  and  $K_0^*(1430)$  scalar states in this mass region are rather naturally assigned as the  $I = 1$  and  $I = 1/2$  members, respectively, leaving at issue the identification of the  $I = 0$  members of the nonet. For  $I = 0$ , there are a number of candidate states reported in the literature [36, 37, 38, 39, 40], namely, the  $f_0(1370)$ ,  $f_0(1500)$ ,  $f_0(1710)$ , and recent observations of  $f_0(1790)$  and  $f_0(1810)$  at BES-II. As mentioned above, this over-population may already be a signal for the existence of scalars beyond the conventional quark model classification.

There also exists a scalar nonet with masses below 1 GeV, *i.e.* the  $f_0(980)$ ,  $a_0(980)$ ,  $\sigma(600)$ , and  $\kappa(800)$ , which are candidates for multiquark or molecule states [41, 42]. This nonet is discussed in detail in Chapter 11.

Recent LQCD results [32, 33, 34] indicate that the mass region between 1 and 2 GeV is extremely interesting for the ground state scalar glueball ( $J^{PC} = 0^{++}$ ) search, especially in light of the observation of a number of  $f_0$  states with similar masses ( $f_0(1370)$ ,  $f_0(1500)$  and  $f_0(1710)$ ) [43]. However, since glueball properties are not expected to be drastically different from those of conventional  $q\bar{q}$  mesons, one is faced with the difficulty of distinguishing the scalar glueball from conventional  $q\bar{q}$  states. Nonetheless, more than two  $f_0$  states with similar masses implies that mixing of a pure gluonic scalar (glueball) with  $I = 0$  members of the nearby  $q\bar{q}$  nonet can be occurring [44, 45, 46, 47, 48, 49, 50, 27]. This greatly complicates the task of identifying the scalar glueball both experimentally and theoretically. In contrast, signals for oddballs would be decisive evidence for the existence of glueballs. Unfortunately, to date concrete experimental identification of an oddball is still unavailable.

Theoretical expectations for a glueball with conventional quantum numbers have been widely discussed in the literature [302]. Although these are not sufficient in most cases for distinguishing a glueball candidate from a conventional  $q\bar{q}$  state, they are still useful for providing guidance for further efforts. In the following we briefly review some of these expectations.

### 1). Flavor-blindness of glueball decays

The predicted ratios for flavor-singlet glueball decay branching fractions are:

$$\frac{1}{P.S.} \Gamma(G \rightarrow \pi\pi : K\bar{K} : \eta_8\eta_8 : \eta_1\eta_8 : \eta_1\eta_1) = 3 : 4 : 1 : 0 : 1 , \quad (9.3.8)$$

where P.S. denotes the phase space factor, and  $\eta_1$  and  $\eta_8$  are the  $I = 0$  flavor-singlet and flavor-octet members of the SU(3) nonet. It can be shown that this relation holds for  $\pi\pi : K\bar{K} : \eta\eta : \eta\eta' : \eta'\eta'$  after taking into account the singlet-octet mixing:

$$\begin{aligned} \eta &= \eta_8 \cos \theta - \eta_1 \sin \theta \\ \eta' &= \eta_8 \sin \theta + \eta_1 \cos \theta . \end{aligned} \quad (9.3.9)$$

The most significant feature for a pure glueball decays to  $PP$  is the vanishing branching ratio for  $G \rightarrow \eta\eta'$ . However, the observation of a vanishing rate for  $X \rightarrow \eta\eta'$  does not necessarily allow one to conclude unambiguously that  $X = G$ , since interference between different components in a  $q\bar{q}$  state could also lead to a vanishing  $\eta\eta'$  branching ratio [44, 45, 46].

## 2). Glueball couplings to $\gamma\gamma$

Since gluons are electrically neutral, glueball production in  $\gamma\gamma$  collisions and glueball decays into  $\gamma\gamma$  final states are suppressed. However, a small branching fraction for  $X \rightarrow \gamma\gamma$  does not necessarily prove that  $X$  is a glueball because of effects of possible interference with mixed components. For instance, in Ref. [51], the branching fractions for  $f_0 \rightarrow \gamma\gamma$  are found to be  $f_0(1710) : f_0(1500) : f_0(1370) \simeq 3 : 1 : 12$ , which indicates smaller  $\gamma\gamma$  couplings for  $f_0(1500)$  and  $f_0(1710)$  than that for  $f_0(1370)$ .

Alternatively, the scalar's  $q\bar{q}$  component can be probed in  $e^+e^-$  annihilation via two virtual photon intermediate states. VEPP and DAΦNE have access to the production of scalars in the  $1 \sim 2$  GeV mass range, while BEPCII will be able to access heavier scalars, up to about 3 GeV [52].

## 3). Glueball production in heavy quarkonium radiative decays

The  $J/\psi$  radiative decay process is gluon rich and ideal for searches of glueballs as intermediate hadronic resonances in the  $J/\psi \rightarrow \gamma G \rightarrow \gamma + \text{hadrons}$  process. This will provide access to all isoscalar states with charge conjugation  $C = +$  and forbids all  $C = -$  states. These allowed quantum numbers include the low-lying glueballs and hybrids for which the production phase space is generally large. Thus, a systematic study of  $J/\psi$  radiative decays with high statistics at *BES-III* will be extremely important for clarifying some long-standing puzzles.

Information about intermediate resonances can be obtained by measuring their hadronic and/or radiative decays. Two measures are proposed in the literature to quantify the gluonic contents of the resonances. One is called “Stickiness”, and defined as

$$S = \frac{\Gamma(J/\psi \rightarrow \gamma X) \times P.S.(X \rightarrow \gamma\gamma)}{\Gamma(X \rightarrow \gamma\gamma) \times P.S.(J/\psi \rightarrow \gamma X)}, \quad (9.3.10)$$

by Chanowitz [53]. This is intended to measure the color-to-electric-charge ratio with phase space factored out, and maximize the effects from the glue dominance inside a glueball. If  $X$  is a glueball, one would expect that its production is favored in  $J/\psi$  radiative decays, while its decays into  $\gamma\gamma$  are strongly suppressed. Therefore, a glueball should have large stickiness in comparison to a conventional  $q\bar{q}$  state.

Cakir and Farrar [54] propose another quantitative measure of the gluonic content of a resonance by calculating its branching ratio to gluons, *i.e.*  $b_{R \rightarrow gg}$ . This quantity can be related to the production branching ratio of a resonance  $R$  in heavy quarkonium radiative decays. Its value is expected to be in the range of  $b_{R \rightarrow gg} = O(\alpha_s^2) \simeq 0.1 - 0.2$  for a  $q\bar{q}$  state, and  $\sim 1$  for a glueball. Interestingly, for most of the well established  $q\bar{q}$  states,  $b_{R \rightarrow gg}$  is found to be rather small, while for the scalar glueball candidates  $f_0(1500)$  and  $f_0(1710)$  the value is rather large, in particular for the  $f_0(1710)$  [51].

These two measures, however, still cannot provide unambiguous evidence for glueballs. “Stickiness” works in a world where there is no glueball and  $q\bar{q}$  mixing (quenched approximation in LQCD), *i.e.* for pure glueballs. In the event that glueball- $q\bar{q}$  mixing occurs (unquenched), interference between glueball and  $q\bar{q}$  components can violate the expectation of large stickiness for glueball states. In this sense, the scheme of Ref. [54, 51] seems to be more applicable because it directly measures the coupling of a resonance to

gluons.

#### 4). Chiral suppression

A criterion first pointed out by Carlson [55] and recently developed by Chanowitz [56] is the chiral suppression mechanism for  $J = 0$  glueballs. Due to the fact that in pQCD the amplitude is proportional to the current quark mass in the final state,  $J = 0$  glueballs should have larger couplings to *e.g.*  $K\bar{K}$  than to  $\pi\pi$ . For  $J \neq 0$ , the decay amplitude is flavor symmetric. Combined with the quenched LQCD prediction, this suggests that the  $f_0(1710)$  is a gluon-dominant state while the  $f_0(1500)$  is dominated by  $s\bar{s}$  [47]. However, because of the complexity of the gluon hadronization and the unclear extent of  $G - q\bar{q}$  mixing, the observation of a relatively large branching ratio to  $K\bar{K}$  for a candidate does not conclusively establish it as being a glueball [57, 58].

#### 5). Charmonium hadronic decays

Decays of charmonium states to light hadrons have great advantages for systematic analyses for both light mesons and baryons. For instance,  $SU(3)$ -flavor symmetry breaking can be investigated in the decays  $J/\psi \rightarrow VP, VS, VT; \chi_{cJ} \rightarrow VV, PP, SS; \eta_c \rightarrow VV, PP$ , etc. The decays  $J/\psi \rightarrow Vf_1$  also provide access to the axial vectors  $f_1(1285)$  and  $f_1(1420)$ . An important issue here is the study of the properties of the final state mesons and the search for evidence for nonconventional states, such as: the  $f_0(980)$  and  $a_0(980)$  as either four-quark states [41] or  $K\bar{K}$  molecules; a scalar glueball component of the  $f_0(1370)$ ,  $f_0(1500)$  &  $f_0(1710)$ ; and hybrids. Specifically, for states  $X$  recoiling from an  $\omega$  or  $\phi$  in  $J/\psi \rightarrow \omega X$  and  $\phi X$ , one can gain information about the flavor components of the resonance  $X$ . Since the  $\omega$  and  $\phi$  are ideally mixed, i.e.  $|\omega\rangle = |u\bar{u} + d\bar{d}\rangle/\sqrt{2}$  and  $|\phi\rangle = |s\bar{s}\rangle$ , the flavor content of a resonance  $X$  can be probed based on the OZI rule [59]. However, it should be cautioned that so far at least the role played by the empirical OZI rule has not been fully understood in the charmonium energy region. For systems that are recoiling from light mesons, large OZI-violations have been found in some QCD-inspired calculations [60, 61, 62]. Dynamical studies of possible OZI rule violations should be carried out; these may be of essential importance for understanding the production of various final state mesons [46, 63, 64, 65].

#### 6). Other glueball-favored processes

Glueball signals have also been searched for in other reactions, such as  $p\bar{p}$  annihilation, and central collisions of the type  $pp \rightarrow ppG$ . In  $p\bar{p}$  reactions, because of the competition of  $q\bar{q}$  meson formation via quark and antiquark rearrangement, identification of glueball signals will be contaminated. Similarly, competition from  $q\bar{q}$  production in  $pp$  central collisions will mix with possible glueball signals.

It is proposed by Close and Kirk [66] that in  $pp$  central collisions, the production of  $S$ -wave resonances (*e.g.*  $0^{++}$  and  $2^{++}$  glueballs, or  $S$ -wave tetraquark states, or  $K\bar{K}$  molecules) will be favored due to the small recoil transverse momentum difference ( $dP_T$ ) of the final state protons, while  $q\bar{q}$  production will be favored in the larger  $dP_T$  region ( $dP_T \geq O(\Lambda_{QCD})$ ). Therefore, different kinematic regions serve as a production filter for

$S$ -wave resonances. Following this, an experimental analysis by WA102 [67] revealed a clear azimuthal dependence as a function of  $J^{PC}$  and  $P_T$  at the proton vertices, and the scalars appeared to divide into two classes:  $f_0(980)$ ,  $f_0(1500)$  and  $f_0(1710)$  strongly peak at small  $\phi$  angle (corresponding to small  $dP_T$ ) and  $f_0(1370)$  at large  $\phi$ .

The above criteria cannot individually provide indisputable evidence for glueball candidates with conventional quantum numbers, especially in the case of a scalar glueball. However, the combined effect of all of the above expectations and criteria might be useful for placing bounds on the glueball and  $q\bar{q}$  contents of a state and, thereby, provide some insight into the complex issue of strong QCD. In fact, because of the limitations imposed by the use of the quenched approximation in present LQCD calculations, the effects arising from an unquenched approach need to be investigated in detail. Phenomenological progress along this direction was proposed by Tornqvist [68] who emphasized the difference between bare states (quark model bound states that do not decay) and dressed ones (physical states that decay to hadrons). For the case of scalars, Boglione and Pennington [69] showed that a pure glue or  $q\bar{q}$  state (e.g. unquenched bare state studied by LQCD) is so different from the dressed hadrons that reliable calculations of the hadron properties are crucial for extracting the scalars and for making sense of the experimental measurements.

### 9.3.2 Glueball candidates

#### Scalar glueball candidates

The abundance of isoscalar scalars in the  $1 \sim 2$  GeV, mass region, *i.e.* the  $f_0(1370)$ ,  $f_0(1500)$ , and  $f_0(1710)$  (the  $f_0(1790)$  and  $f_0(1810)$  should be confirmed in further experiments), makes them natural scalar glueball candidates. In the following, we briefly review the available experimental information about these states and examine the theoretical expectations of their nature. Controversies will be identified.

##### 1). $f_0(1370)$

The  $f_0(1370)$  is broader than the  $f_0(1500)$  and  $f_0(1710)$ , and is strongly coupled to  $\pi\pi$ . Its decays into  $K\bar{K}$  were also observed by the Crystal Barrel  $p\bar{p}$  annihilation experiment [36], and confirmed by the WA102  $pp$  scattering experiment [37] in the  $\pi\pi$ ,  $K\bar{K}$  and  $\eta\eta'$  decay channels. Its absence in  $\eta\eta'$  can be mainly due to the limited phase space and does not necessarily mean that it has a large glueball component. In light of the large value of the ratio  $BR_{f_0(1370) \rightarrow \pi\pi}/BR_{f_0(1370) \rightarrow K\bar{K}} = 2.17 \pm 0.9$  [37], the  $f_0(1370)$  seems to be a likely candidate for a  $n\bar{n}$  scalar meson ( $n = u$  or  $d$ ).

Recent data from BESII also show a strong  $f_0(1370)$  signal in  $J/\psi \rightarrow \phi\pi^+\pi^-$  [38]. Figure 9.2(a) shows the  $K^+K^-$  invariant mass distribution for  $J/\psi \rightarrow K^+K^-\pi^+\pi^-$ , where a strong  $\phi$  signal is evident. The spectrum of  $\pi^+\pi^-$  invariant masses recoiling against the  $\phi$  is shown in Fig. 9.2(b), where, in addition to a strong  $f_0(980)$  peak, there is a broad enhancement around 1370 MeV.

No significant  $f_0(1370)$  signal is observed in  $J/\psi \rightarrow \phi K^+K^-$  [38],  $\omega K^+K^-$  [39] or  $\omega\pi^+\pi^-$  [70]. Figures 9.3(a) and (b) show the  $\phi$  signal and  $K^+K^-$  invariant mass recoiling against a  $\phi$  for  $J/\psi \rightarrow K^+K^-K^+K^-$  decays.

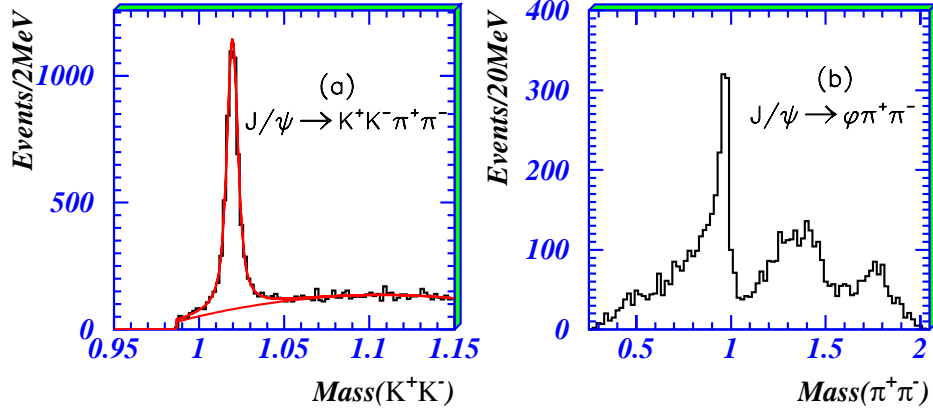


Figure 9.2: (a) The  $K^+K^-$  invariant mass distribution for  $J/\psi \rightarrow K^+K^-\pi^+\pi^-$ . (b) The  $\pi^+\pi^-$  invariant mass for events selected within  $\pm 15$  MeV of the  $\phi$ .

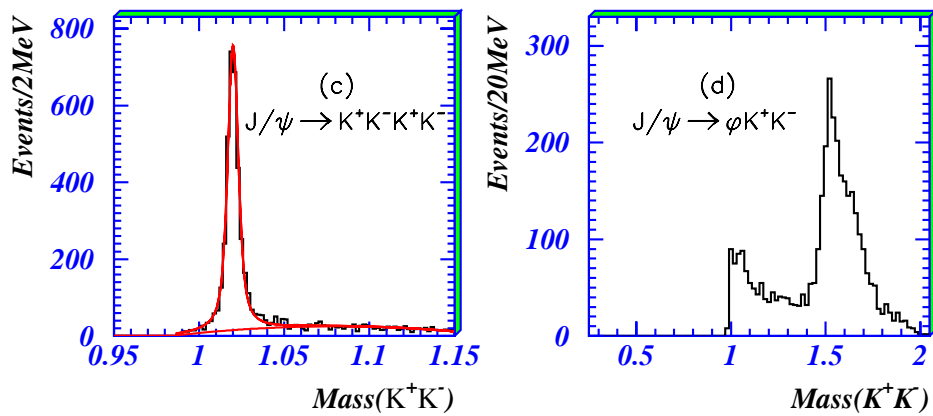


Figure 9.3: (a) The  $K^+K^-$  invariant mass distribution for  $J/\psi \rightarrow K^+K^-K^+K^-$ . (b) The  $K^+K^-$  invariant mass for events selected within  $\pm 15$  MeV of the  $\phi$ .

A partial wave analysis (PWA) was performed to  $J/\psi \rightarrow \phi\pi^+\pi^-$  and  $\phi K^+K^-$  using relativistic tensor expressions for the amplitudes as documented in Ref. [71]. The full angular dependence of the decays of the  $\phi$  and  $\pi^+\pi^-$  or  $K^+K^-$  resonances is fitted, including correlations between them. The line-shape of the  $\phi$  is not fitted, because the  $\phi$  is much narrower than the experimental resolution. The  $\phi\pi^+\pi^-$  and  $\phi K^+K^-$  data are fitted simultaneously, and resonance masses and widths are constrained to be the same for both sets of data. The PWA results show that the peak around 1370 MeV in the  $\pi^+\pi^-$  invariant mass spectrum in Fig. 9.2(b) comes from a dominant  $f_0(1370)$  term that interferes with an  $f_2(1270)$  and a smaller  $f_0(1500)$ . The  $\phi K\bar{K}$  data contains a strong peak due to  $f'_2(1525)$ , with a shoulder on its upper side that can be fitted by interference between  $f_0(1500)$  and  $f_0(1710)$ . The mass and width of the  $f_0(1370)$  are determined to be:  $M = 1350 \pm 50$  MeV and  $\Gamma = 265 \pm 40$  MeV.

The absence of an  $f_0(1370)$  signal in  $J/\psi \rightarrow \omega\pi\pi$  indicates that the branching ratio for  $J/\psi \rightarrow \phi f_0(1370)$  is larger than that for  $J/\psi \rightarrow \omega f_0(1370)$ . This certainly raises concerns about the  $f_0(1370)$  interpretation as an  $n\bar{n}$  ( $n = u$  or  $d$ ) meson since, in the context of the OZI rule, one would expect that an  $n\bar{n}$  meson would more likely recoil against an  $\omega$  than against a  $\phi$ .

## 2). $f_0(1500)$

The  $f_0(1500)$  was observed in many experiments, such as pion induced interactions  $\pi^-p$ ,  $p\bar{p}$  annihilation [72, 73],  $pp$  central collisions [74, 75] and  $J/\psi$  radiative decays [76, 77]. Most of the data on the  $f_0(1500)$  comes from the Crystal Barrel collaboration, which resolved two scalar states in this mass region, and determined their decay branching ratios to a number of final states, including  $\pi^0\pi^0$ ,  $\eta\eta$ ,  $\eta\eta'$ ,  $K_LK_L$  and  $4\pi^0$ . It has also been noted that it is absent in the glueball-suppressed processes  $\gamma\gamma \rightarrow K_sK_s$  and  $\pi^+\pi^-$ . All of these features favor the interpretation of the  $f_0(1500)$  as a non- $q\bar{q}$  state.

If the  $f_0(1500)$  is a scalar glueball, it should be copiously produced in  $J/\psi$  radiative decays. The  $J/\psi \rightarrow \gamma\pi^+\pi^-$  process was analyzed previously by the Mark III [78], DM2 [79] and BESI [80] experiments, where there was evidence for the  $f_2(1270)$  and an additional  $f_2(1720)$ . In addition, a high mass shoulder to the  $f_2(1270)$ , at about 1.45 GeV, was seen. A revised amplitude analysis of the Mark III data found this shoulder to be a scalar at  $\sim 1.43$  GeV, and, in addition, found that the peak at  $\sim 1.7$  GeV to be scalar rather than tensor [81]. The  $J/\psi \rightarrow \gamma\pi^0\pi^0$  process was also studied by the Crystal Ball [82] and BESI experiments [83], but no partial wave analyses were performed on this channel.

Recently, BES reported the results on  $J/\psi$  radiative decays to  $\pi^+\pi^-$  and  $\pi^0\pi^0$  based on a sample of 58M  $J/\psi$  events taken with the BES II detector [84]. Figure 9.4 shows the  $\pi^+\pi^-$  mass spectrum for the selected events, together with the corresponding background distributions and Dalitz plot. There is a strong  $\rho^0(770)$  peak mainly due to background from  $J/\psi \rightarrow \rho^0\pi^0$ . A strong  $f_2(1270)$  signal, a shoulder on the high mass side of  $f_2(1270)$ , an enhancement at  $\sim 1.7$  GeV, and a peak at  $\sim 2.1$  GeV are clearly visible. The lightly shaded histogram in Fig. 9.4 corresponds to the dominant background  $J/\psi \rightarrow \pi^+\pi^-\pi^0$ . Other backgrounds are shown as the dark shaded histogram in Fig. 9.4. Figure 9.5 shows the  $\pi^0\pi^0$  mass spectrum and Dalitz plot. The shaded histogram corresponds to the sum of estimated backgrounds determined using branching ratios from Ref. [259]. In general, the  $\pi^+\pi^-$  and  $\pi^0\pi^0$  mass spectra exhibit similar structures above 1.0 GeV.

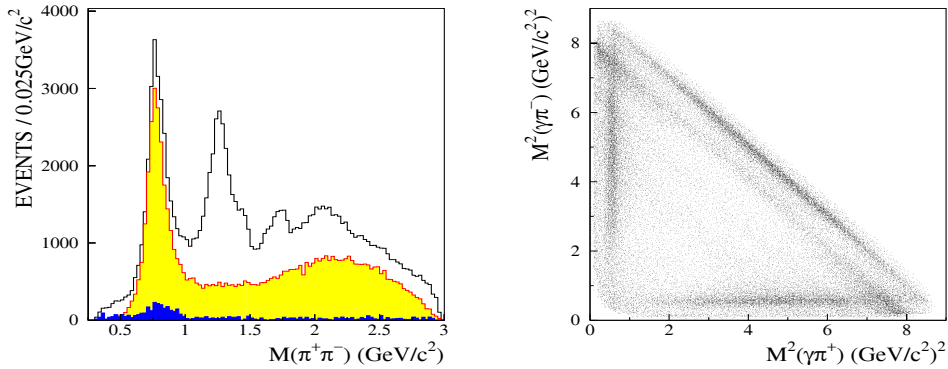


Figure 9.4: Invariant mass spectrum of  $\pi^+ \pi^-$  and the Dalitz plot for  $J/\psi \rightarrow \gamma \pi^+ \pi^-$ , where the lightly and dark shaded histograms in the upper panel correspond to  $J/\psi \rightarrow \pi^+ \pi^- \pi^0$  and other estimated backgrounds, respectively.

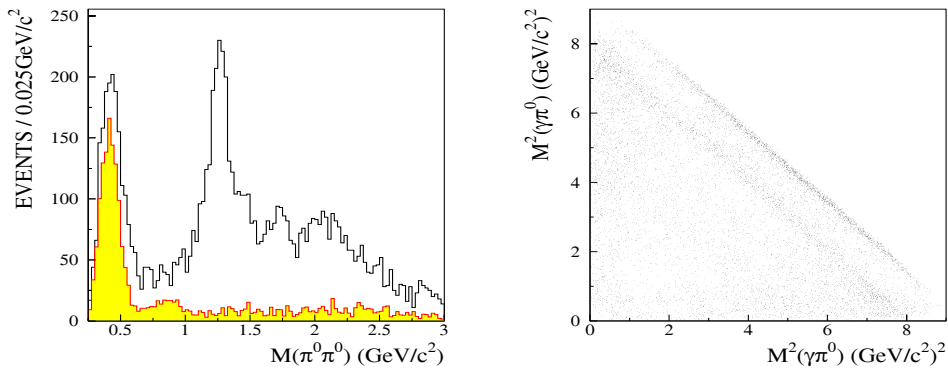


Figure 9.5: Invariant mass spectrum of  $\pi^0 \pi^0$  and the Dalitz plot for  $J/\psi \rightarrow \gamma \pi^0 \pi^0$ , where the shaded histogram in the upper panel corresponds to the estimated backgrounds.

Partial wave analyses (PWA) of the 1.0 to 2.3 GeV  $\pi\pi$  mass range were carried out using the relativistic covariant tensor amplitude method. There are conspicuous peaks due to  $f_2(1270)$  and two  $0^{++}$  states in the 1.45 and 1.75 GeV mass regions. The first  $0^{++}$  state, which is considered to be the  $f_0(1500)$ , has a mass of  $1466 \pm 6 \pm 20$  MeV, a width of  $108_{-11}^{+14} \pm 25$  MeV, and a branching fraction  $\mathcal{B}(J/\psi \rightarrow \gamma f_0(1500) \rightarrow \gamma\pi^+\pi^-) = (0.67 \pm 0.02 \pm 0.30) \times 10^{-4}$ . Spin 0 is strongly preferred over spin 2. Figure 9.6 shows the  $\pi^+\pi^-$  and  $\pi^0\pi^0$  invariant mass distributions for  $J/\psi \rightarrow \gamma\pi^+\pi^-$  and  $\gamma\pi^0\pi^0$ , where the PWA fit projection is shown as a histogram.

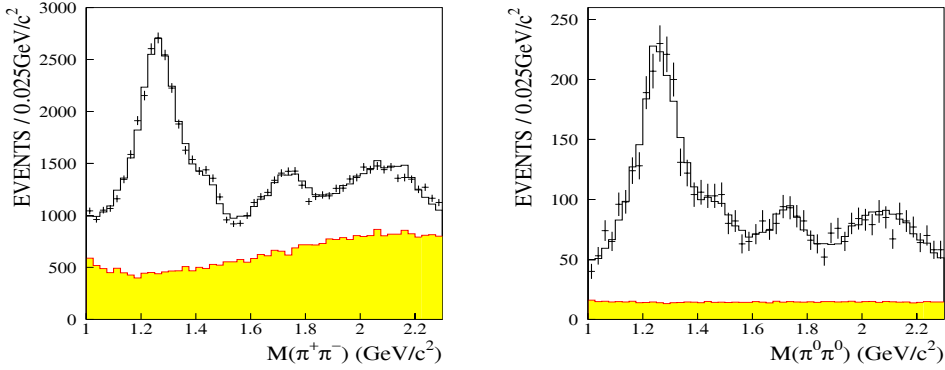


Figure 9.6: The  $\pi^+\pi^-$  invariant mass distribution from  $J/\psi \rightarrow \gamma\pi^+\pi^-$ . The crosses are data, the full histogram shows the PWA fit projection, and the shaded histogram corresponds to the background.

In contrast to the  $f_0(1370)$ , the  $f_0(1500)$  is not directly observed in  $J/\psi$  hadronic decays, such as  $J/\psi \rightarrow \phi K\bar{K}$ ,  $\omega K\bar{K}$ ,  $\phi\pi\pi$ ,  $\omega\pi\pi$  at BES [38, 39]. In most of the above production channels, the  $f_0(1500)$  turns to have a larger branching fraction to  $\pi\pi$  than  $K\bar{K}$ . However, recent Belle data on  $B^+ \rightarrow K^+ K\bar{K}$  and  $K^+\pi\pi$  [85] suggest the existence of a  $0^{++}$  scalar at 1.5 GeV with a larger branching fraction to  $K\bar{K}$  than to  $\pi\pi$ .

Searching for the  $f_0(1500)$  in more decay modes and studying its spin-parity will be crucial for clarifying its nature.

### 3). $f_0(1710)$

The  $f_0(1710)$  is a main competitor of the  $f_0(1500)$  for the lightest  $0^{++}$  glueball assignment, primarily due to its large production rate in gluon rich processes such as  $J/\psi$  radiative decays,  $pp$  central production etc., as well as the predictions of lattice QCD. However, there has been a long history of uncertainty about the properties of the  $f_0(1710)$ . Table 9.3.2 [259] lists results on the  $f_0(1710)$  from different experiments before the BESII era. Apparently, different experiments give different masses, widths and spin-parities. The latest analysis of the MarkIII  $J/\psi \rightarrow \gamma K\bar{K}$  data by Dunwoodie [81] favors  $J^P = 0^+$  over an earlier assignment of  $2^+$ . The latest central production data of WA76 and WA102 ( $pp \rightarrow p(K\bar{K})p$ ) also favor  $0^+$  [86, 87] as does the BESI  $J/\psi \rightarrow \gamma 4\pi$  data [77]. The spin-parity of  $f_0(1710)$  in these observed processes is crucial for clarifying whether the  $f_0(1710)$  is a  $q\bar{q}$  or a non- $q\bar{q}$  state. If  $J = 0$ , the  $f_0(1710)$  and  $f_0(1500)$  might represent the glueball and the  $q\bar{q}$  state, or more likely each is a mixture of both. However, if  $J = 2$ ,

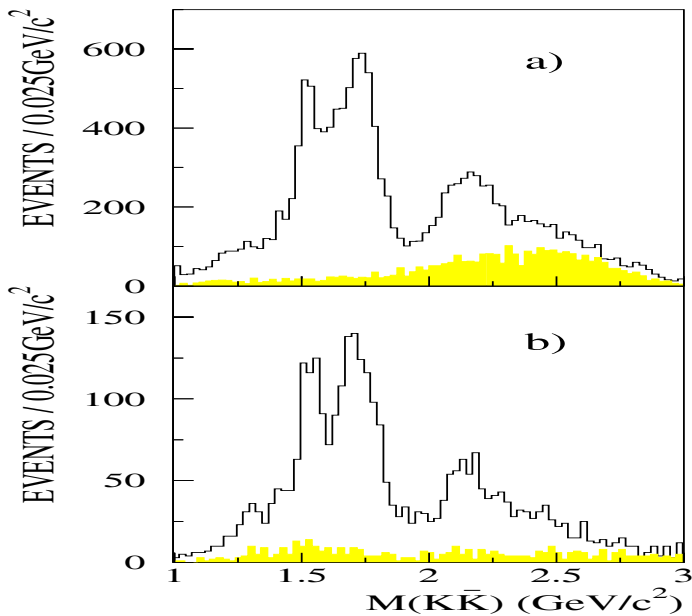


Figure 9.7: Invariant mass spectra of a)  $K^+K^-$ , b)  $K_S^0K_S^0$  for  $J/\psi \rightarrow \gamma K\bar{K}$  events, where the shaded histograms correspond to the estimated background contributions.

it will be difficult to assign a glueball status to an  $f_2(1710)$ , since this mass would be at odds with all current lattice gauge calculations.

To study the structure around 1.7 GeV, partial wave analyses (PWA) of  $J/\psi \rightarrow \gamma K\bar{K}$ ,  $\gamma\pi\pi$ ,  $\omega\pi^+\pi^-$ ,  $\omega K^+K^-$ ,  $\phi\pi^+\pi^-$  and  $\phi K^+K^-$  were carried out using the  $5.8 \times 10^7 J/\psi$  events collected at BESII.

Figure 9.7 shows the  $K^+K^-$  and  $K_S^0K_S^0$  mass spectra for selected  $J/\psi \rightarrow \gamma K\bar{K}$  events, together with the corresponding background distributions. These two mass spectra agree closely below 2.0 GeV. The resonant structure in the 1.7 GeV mass region is clearly visible in both decay modes, in addition there is a strong signal for the  $f'_2(1525)$ .

A partial wave analyses, using relativistic covariant tensor amplitudes constructed from Lorentz-invariant combinations of the 4-vectors and the photon polarization for  $J/\psi$  initial states with helicity  $\pm 1$ , was carried out for  $K\bar{K}$  masses below 2.0 GeV. Both bin-by-bin and global fits were performed and consistent results were obtained. The analyses show that spin 0 is strongly preferred over spin 2 for the resonance around 1.7 GeV. The  $f_0(1710)$  peak mass is  $1740 \pm 4^{+10}_{-25}$  MeV and the width is  $166^{+5+15}_{-8-10}$  MeV.

In  $J/\psi \rightarrow \omega K^+K^-$  decays, the  $K^+K^-$  invariant mass shows a conspicuous signal for the  $f_0(1710)$ , as is shown in Fig. 9.8. A partial wave analysis determines its mass and width to be:  $M = 1738 \pm 30$  MeV and  $\Gamma = 125 \pm 20$  MeV.

In the spectrum of  $\pi^+\pi^-$  invariant masses recoiling against the  $\phi$  in  $J/\psi \rightarrow \phi\pi^+\pi^-$  decays, shown in Fig. 9.2, a peak at around 1.79 GeV is evident. No peak in this region is seen in the  $K^+K^-$  spectrum for the  $J/\psi \rightarrow \phi K^+K^-$  channel. A simultaneous PWA fit to  $J/\psi \rightarrow \phi K^+K^-$  and  $\phi\pi^+\pi^-$  shows that this peak has a mass and width of  $M = 1790^{+40}_{-30}$  MeV and  $\Gamma = 270^{+60}_{-30}$  MeV, and spin 0 is preferred over spin 2. This state, the  $f_0(1790)$ , is distinct from the  $f_0(1710)$ , seen in the  $J/\psi \rightarrow \gamma K^+K^-$  and  $\omega K^+K^-$  channels, because of its different mass, width and decay or production branching fractions to  $\pi\pi$  and  $KK$ .

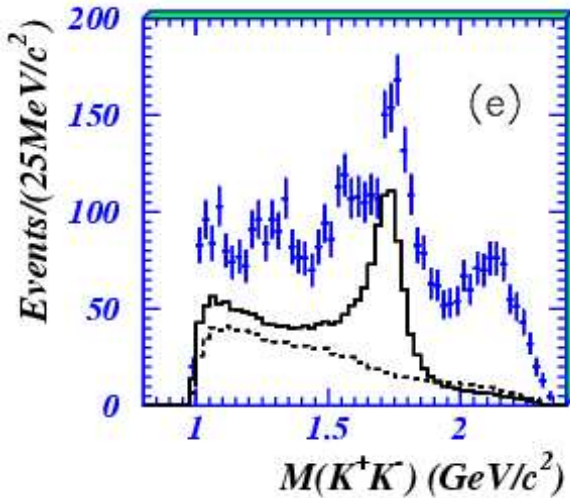


Figure 9.8:  $K^+K^-$  invariant mass spectrum in  $J/\psi \rightarrow \omega K^+K^-$ . The crosses are data and the histogram is PWA fit projection for the  $0^{++}$  amplitude.

For  $J/\psi \rightarrow \gamma\pi\pi$ , the production of a  $0^{++}$  state is also observed in the 1.7 GeV mass region. Its mass and width are  $1765^{+4}_{-3} \pm 13$  MeV and  $145 \pm 8 \pm 69$  MeV. This  $0^{++}$  state may be the  $f_0(1710)$  that is observed in  $J/\psi \rightarrow \gamma K\bar{K}$  and  $\omega K^+K^-$ , it may be the  $f_0(1790)$  which is seen in  $J/\psi \rightarrow \phi\pi^+\pi^-$ , or it may be a superposition of these two states.

More recently, BESII reported the observation of a near-threshold enhancement in the  $\omega\phi$  invariant mass spectrum from the OZI suppressed decays of  $J/\psi \rightarrow \gamma\omega\phi$  [88]. Figure 9.9(a) shows the  $K^+K^-\pi^+\pi^-\pi^0$  invariant mass distribution for events with  $K^+K^-$  invariant mass within the  $\phi$  mass range ( $|m_{K^+K^-} - m_\phi| < 15$  MeV) and the  $\pi^+\pi^-\pi^0$  mass within the  $\omega$  mass range ( $|m_{\pi^+\pi^-\pi^0} - m_\omega| < 30$  MeV); a structure peaked near the  $\omega\phi$  mass threshold is observed. The peak is also evident as a band along the upper right-hand edge of the Dalitz plot in Fig. 9.9(b). No evidence of an enhancement near the  $\omega\phi$  threshold is observed for events from either the  $\omega$  or  $\phi$  sidebands. Moreover, studies using inclusive and exclusive Monte-Carlo samples show that the  $\omega\phi$  threshold enhancement is not due to background.

The significance of the  $\omega\phi$  threshold enhancement is more than  $10\sigma$ . From a partial wave analysis with covariant helicity coupling amplitudes, a spin-parity of  $0^{++}$  with the  $\omega\phi$  system in an  $S$ -wave, is favored. The mass and width of the enhancement are determined to be  $M = 1812^{+19}_{-26}$  (stat)  $\pm 18$  (syst) MeV and  $\Gamma = 105 \pm 20$  (stat)  $\pm 28$  (syst) MeV, and the product branching fraction is  $\mathcal{B}(J/\psi \rightarrow \gamma X) \cdot \mathcal{B}(X \rightarrow \omega\phi) = (2.61 \pm 0.27 \text{ (stat)} \pm 0.65 \text{ (syst)}) \times 10^{-4}$ . The mass and width of this state are not compatible with any known scalars listed in the Particle Data Book [259].

These states have attracted considerable interest and stimulated much speculation about their underlying nature [89, 90, 91, 92, 93, 94]. They raise essential questions about their production mechanisms in  $J/\psi$  hadronic and radiative decays [94].

In addition to the above, recent analyses suggest the existence of a broad scalar  $f_0(1200-1600)$  with a half width 500-900 GeV [95, 96]. The existence of such a broad state would lead to a rearrangement of the assignments of particles to the scalar nonets, where

Table 9.3: Results of  $f_0(1710)$  from different experiments before the BESII era.

Process	Collaboration	$M(\text{MeV})$	$\Gamma(\text{MeV})$	$J^{PC}$
$J/\psi \rightarrow \gamma \eta \eta$	C. B.(82)	$1640 \pm 50$	$200_{-70}^{+100}$	$2^{++}$
$\pi^- p \rightarrow K_S^0 K_S^0 n$	BNL(82)	$1771_{-53}^{+77}$	$200_{-9}^{+156}$	$0^{++}$
$\pi^- N \rightarrow K_S^0 K_S^0 n$	FNAL(84)	$1742 \pm 15$	$57 \pm 38$	—
$\pi^- p \rightarrow \eta \eta N$	GAMS(86)	$1755 \pm 8$	$< 50$	$0^{++}$
$J/\psi \rightarrow \gamma K^+ K^-$	MARK3(87)	$1720 \pm 14$	$130 \pm 20$	$2^{++}$
$J/\psi \rightarrow \gamma K^+ K^-$	DM2(88)	$1707 \pm 10$	$166 \pm 33$	—
$pp \rightarrow p(K^+ K^-)p$ $\rightarrow p(K_S^0 K_S^0)p$	WA76(89)	$1713 \pm 10$	$181 \pm 30$	$2^{++}$
		$1706 \pm 10$	$104 \pm 30$	
$J/\psi \rightarrow \gamma K \bar{K}$	MARK3(91)	$1710 \pm 20$	$186 \pm 30$	$0^{++}$
$p\bar{p} \rightarrow \pi^0 \eta \eta$	E760(93)	$1748 \pm 10$	$264 \pm 25$	<i>even</i> $^{++}$
$J/\psi \rightarrow \gamma 4\pi$	MARK3 data D. Bugg(95)	$1750 \pm 15$	$160 \pm 40$	$0^{++}$
$J/\psi \rightarrow \gamma K \bar{K}$	MARK3 data Dunwoodie	$1704_{-23}^{+16}$	$124_{-44}^{+52}$	$0^{++}$
$pp \rightarrow p(K \bar{K})p$	WA102(99)	$1730 \pm 15$	$100 \pm 25$	$0^{++}$
$J/\psi \rightarrow \gamma 4\pi$	BES(2000)	$1740_{-25}^{+20}$	$135_{-25}^{+40}$	$0^{++}$

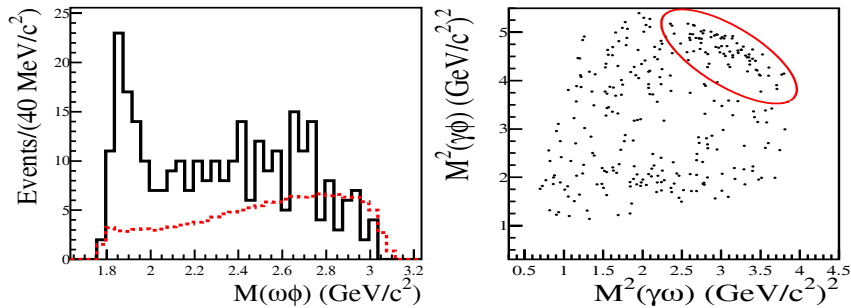


Figure 9.9: (a) The  $K^+K^-\pi^+\pi^-\pi^0$  invariant mass distribution for the  $J/\psi \rightarrow \gamma\omega\phi$  candidate events. The dashed curve indicates the acceptance varying with the  $\omega\phi$  invariant mass. (b) Dalitz plot.

$\sigma(600)$  and  $\kappa(800)$  are no longer physical states. In contrast to two nonets, one above and one below 1 GeV, the new arrangement might be: i)  $f_0(980)$ ,  $f_0(1300)$ ,  $a_0(980)$ ,  $K_0(1415)$  for the  $q\bar{q}$  with radial quantum number  $n = 1$ ; and ii)  $f_0(1500)$ ,  $f_0(1750)$ ,  $a_0(1520)$ ,  $K_0(1820)$  for  $n = 2$ . The broad  $f_0(1200 - 1600)$  is then regarded as a descendant of the scalar glueball.

The light-meson spectroscopy of scalar states in the mass range of 1~2 GeV/, which has long been a source of controversy, remains very complicated. Overlapping states interfere with each other differently in different production and decay channels. Therefore, high statistics and high precision experimental data that includes many production and decay channels are needed to sort out the properties of these scalar states.

In brief, in the 1~2 GeV mass region, there are at least three isoscalar scalars, the  $f_0(1370)$ ,  $f_0(1500)$  and  $f_0(1710)$ , that are well established experimentally. However, the behaviour of these states in different processes has a number of unexpected features, which raise questions about their nature. These include: What are the constituent structures of these scalars? Are any one of these scalars a glueball state? Is the glueball a pure and/or mixed state? What and how does the present experimental information tell us about scalar production and decay mechanisms? . . .

### Pseudoscalar glueball candidates

The Particle Data Book [259] lists five  $0^{-+}$  states above 1 GeV: the  $\eta(1295)$ ,  $\eta(1405)$ ,  $\eta(1475)$ ,  $\eta(1760)$ , and  $\eta(2225)$ . The former three are well established in a variety of experimental observations (see review by Amsler and Masoni [259]), while the latter two states need further confirmation.

Signals for the  $\eta(1295)$  were observed in  $\pi^-p$  [97, 98, 99],  $\bar{p}p$  annihilation [100, 101, 102], and  $J/\psi$  radiative decays [103] in the  $\eta\pi\pi$  spectrum either via  $a_0(980)\pi$  or directly coupled to  $\eta\pi\pi$ . There is no clear signal for the  $\eta(1295)$  in  $K\bar{K}\pi$ , which could be a hint for its non-strange  $q\bar{q}$  nature.

Historically, there was only one pseudoscalar, the so-called  $E/\iota(1440)$ , observed in  $p\bar{p}$  annihilation [104] and  $J/\psi$  radiative decays [105, 106, 107]. After about 1990, more and more observations revealed the existence of two resonance structures around 1.45 GeV in the  $a_0(980)\pi$ ,  $K\bar{K}\pi$  and  $K^*\bar{K}$  spectra [108, 97, 109, 103, 110, 111, 112]. The lower-mass

state, the  $\eta(1405)$ , has large couplings to  $a_0(980)\pi$  and  $K\bar{K}\pi$ , while the higher-mass state, the  $\eta(1475)$ , favors  $K^*\bar{K}$ .

The  $\eta(1405)$  was confirmed by MARKIII [113], Crystal Barrel [114] and DM2 [107] in its decays into  $\eta\pi\pi$ ; its production has been seen in both  $J/\psi$  radiative decays and  $\bar{p}p$  annihilations. In contrast, although the  $\eta(1475)$  has been observed in  $K\bar{K}\pi$  ( $K^*\bar{K}$ ) [108, 97, 109, 103, 110, 111, 112], signals for it are not seen in  $\eta\pi\pi$ . A study of  $K\bar{K}\pi$  and  $\eta\pi\pi$  production in  $\gamma\gamma$  collisions [115] showed that the  $\eta(1475)$  appeared in  $K\bar{K}\pi$ , but not in  $\eta\pi\pi$ , while the  $\eta(1405)$  was not seen in either channel.

A reasonable assignment for these three states, the  $\eta(1295)$ ,  $\eta(1405)$  and  $\eta(1475)$ , was proposed by Close and Kirk [116], and Barnes *et al.* [117], who suggested that the  $\eta(1295)$  is the radial excitation of the  $\eta'$ . Because of its degeneracy with the  $\pi(1300)$ , the  $\eta(1295)$  should be dominantly  $n\bar{n}$  and hence strongly coupled to  $\eta\pi\pi$  (it has not been seen in  $K\bar{K}\pi$ ). As a result, its  $I = 0$  partner should be mainly  $s\bar{s}$  due to ideal mixing. Notice that the  $\eta(1405)$  is not seen in  $\gamma\gamma$  while the  $\eta(1475)$  appears in  $K\bar{K}\pi$  but not  $\eta\pi\pi$ . This observation leads to the identification of the  $\eta(1475)$  as a  $s\bar{s}$  state and the  $\eta(1405)$  as a  $0^{-+}$  glueball candidate [116, 117, 51].

The above classification was questioned by Klempert who pointed out that the absence of  $\eta(1295)$  production in  $\gamma\gamma$  collisions made it hard to assign it to a  $q\bar{q}$  state [118]. Applying a quark model approach by Barnes *et al.* [117], Klempert showed that the three  $\eta$  resonances could be due to a single state. The wavefunction overlap between the initial and final states can give rise to different invariant mass distributions for  $\eta^* \rightarrow a_0(980)\pi$ ,  $\sigma\eta$  and  $K^*\bar{K}$  and, thus, result in the different peak positions that have been interpreted as signals for different states. In this scheme, the  $\eta(1440)$  exists as the radial excitation of the  $\eta$  in the range from 1.3 to 1.5 GeV, while that for the  $\eta'$  is identified as the  $\eta(1760)$ .

To clarify the nature of these  $\eta$  resonances, higher-statistics searches in  $\gamma\gamma$  collisions and  $J/\psi$  radiative decays have been strongly urged. In a recent analysis by the BESII experiment [119], the  $\eta(1295)$  is observed in  $J/\psi \rightarrow \gamma\eta(1295) \rightarrow \gamma(\gamma\rho)$ , but absent in  $J/\psi \rightarrow \gamma(\gamma\phi)$ . Meanwhile, another state, the  $\eta(1424)$ , is seen in  $J/\psi \rightarrow \gamma X$  with  $X \rightarrow \gamma\rho$ , but is absent in its decays into  $\gamma\phi$ . This seems to favor the interpretation by Klempert, but is still not conclusive.

The  $\eta(1760)$  was reported by the MARK III collaboration in  $J/\psi$  radiative decays and was found to decay to  $\omega\omega$  [120] and  $\rho\rho$  [121]. It was also observed by the DM2 collaboration in  $J/\psi$  radiative decays in the  $\rho\rho$  decay mode with a mass of  $M = 1760 \pm 11$  MeV and a width of  $\Gamma = 60 \pm 16$  MeV [122] and in the  $\omega\omega$  decay mode [123]. The BESI experiment reported its  $\eta\pi^+\pi^-$  decay with a mass of  $M = 1760 \pm 35$  MeV, but without a determination of its width [124]. Also, the possible production of a pseudoscalar  $\phi\phi$  threshold enhancement in  $\pi^-p$  scattering has been reported [125]. The  $\eta(1760)$  was suggested to be a  $3^1S_0$  pseudoscalar  $q\bar{q}$  meson, but some authors suggest a mixture of glueball and  $q\bar{q}$  or a hybrid [126, 127]. Recently, in Ref. [128], it was argued that the pseudoscalar glueball may be in the 1.5 to 1.9 GeV mass region, and that it would also have Vector Vector decay modes.

The decay channel  $J/\psi \rightarrow \gamma\omega\omega$ ,  $\omega \rightarrow \pi^+\pi^-\pi^0$  was analyzed by BESII, using a sample of  $5.8 \times 10^7$   $J/\psi$  events [129]. The histogram in Fig. 9.10(a) shows the  $2(\pi^+\pi^-\pi^0)$  invariant mass distribution of events when both  $\pi^+\pi^-\pi^0$  masses are within the  $\omega$  range ( $|m_{\pi^+\pi^-\pi^0} - m_\omega| < 40$  MeV). The  $\omega\omega$  invariant mass distribution peaks at 1.76 GeV, just above the  $\omega\omega$  mass threshold. The phase space distribution and the acceptance versus

$\omega\omega$  invariant mass are also shown in the figure. The corresponding Dalitz plot is shown in Fig. 9.10(b). The shaded histogram in Fig. 9.10(c) indicates the background.

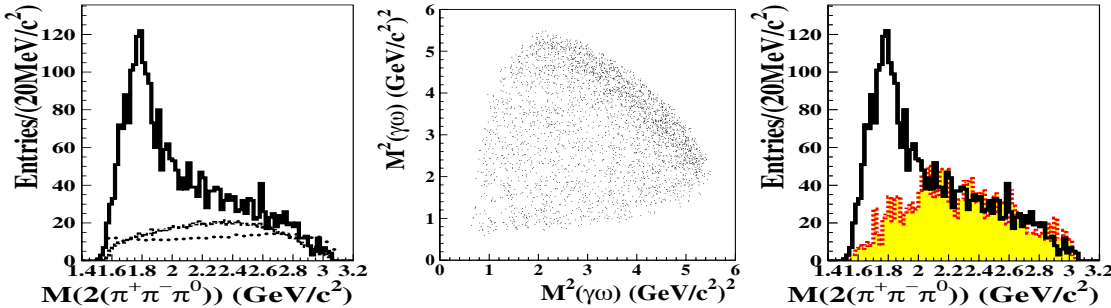


Figure 9.10: (a) The  $2(\pi^+\pi^-\pi^0)$  invariant mass distribution for candidate events. The dashed curve is the phase space invariant mass distribution, and the dotted curve shows the acceptance versus the  $\omega\omega$  invariant mass. (b) The Dalitz plot. (c) The shaded histogram is the background.

Analysis of angular correlations indicates that the  $\omega\omega$  system below 2 GeV is predominantly pseudoscalar. A partial wave analysis confirms the predominant pseudoscalar nature, together with small  $0^{++}$  and  $2^{++}$  contributions, and yields a pseudoscalar mass  $M = 1744 \pm 10$  (stat)  $\pm 15$  (syst) MeV, a width  $\Gamma = 244^{+24}_{-21}$  (stat)  $\pm 25$  (syst) MeV, and a product branching fraction  $\text{Br}(J/\psi \rightarrow \gamma\eta(1760)) \cdot \text{Br}(\eta(1760) \rightarrow \omega\omega) = (1.98 \pm 0.08 \text{ (stat)} \pm 0.32 \text{ (syst)}) \times 10^{-3}$ . The  $\eta(1760)$  observed here is broader than the one listed in the PDG [259].

To identify the pseudoscalar glueball and clarify the pseudoscalar spectrum, further studies of the  $\eta(1295)$ ,  $\eta(1405)$ ,  $\eta(1475)$ ,  $\eta(1760)$  and other high mass  $0^{-+}$  states are needed with a high statistics data sample.

### Tensor glueball candidates

Lattice QCD predicted the  $2^{++}$  tensor glueball to be the second lowest-mass glueball state with a mass around 2.3 GeV, which makes it interesting to search for it in experiments.

Mark III first presented signals for a narrow state ( $\Gamma \sim 20$  MeV), the so-called  $\xi(2230)$  or  $f_J(2220)$ , at 2.2 GeV in  $J/\psi \rightarrow \gamma K^+ K^-$  [130], and later in  $\gamma K_s^0 K_s^0$  [131]. However, there was no clear signal seen at DM2 in the same decay channels [132]. In hadron scattering experiments, the GAMS Collaboration found a structure in the  $\eta\eta'$  invariant mass spectrum at  $m = 2220 \pm 10$  MeV with a width of  $\Gamma \sim 80$  MeV in  $\pi^- p \rightarrow \eta\eta' n$  interactions at 38 GeV and 100 GeV [133], while the LASS group reported a structure at 2.2 GeV in the  $K_s^0 K_s^0$  invariant mass spectrum for  $K^- p \rightarrow K_s^0 K_s^0 \Lambda$  [134].

Further evidence for this state was reported by BESI based on a  $\sim 8 \times 10^6$   $J/\psi$  event sample. Structures near 2220 MeV were reported in  $\pi^+\pi^-$ ,  $K^+K^-$ ,  $K_s^0 K_s^0$ ,  $p\bar{p}$ , and  $\pi^0\pi^0$  [135, 136]. In addition, stringent limits were placed on the two-photon coupling of the  $\xi(2230)$  ( $f_J(2220)$ ) by CLEO collaboration studies of the reactions  $\gamma\gamma \rightarrow K_s K_s$  [137] and  $\gamma\gamma \rightarrow \pi^+\pi^-$  [138]. The copious production of  $\xi(2230)$  in  $J/\psi$  radiative decays, its narrow width and small two-photon coupling suggested it be the lightest tensor glueball

candidate. However, the  $\xi(2230)$  was neither seen in the inclusive  $\gamma$  spectrum by the Crystal Ball collaboration [139] nor in  $p\bar{p}$  annihilations to  $K_s^0 K_s^0$  [140],  $\eta\eta$  and  $\pi^0\pi^0$  [141].

The  $\xi(2230)$  ( $f_J(2220)$ ) was not observed in the mass spectrum of  $K^+K^-$ ,  $\pi^+\pi^-$  or  $p\bar{p}$  in the higher-statistics  $5.8 \times 10^7$   $J/\psi$  event sample at BESII. However, preliminary results from a partial wave analysis (PWA) of  $J/\psi \rightarrow \gamma K^+K^-$  at BESII showed that it is difficult to exclude the existence of the  $\xi(2230)$ ; a  $4.5\sigma$  significance signal with mass, width and product branching fraction consistent with the BESI results was found [142]. More careful studies are needed to draw firm conclusions on the  $\xi(2230)$  at *BES-III*.

No other tensor glueball candidates have been observed in radiative  $J/\psi$  decays in the mass range favored by LQCD. If the  $\xi(2230)$  ( $f_J(2220)$ ) does indeed not exist, one of the following must be true: 1) The LQCD prediction on the tensor glueball mass is unreliable; 2) The tensor glueball production rate in an particular exclusive mode is very low; 3) The glueball width is wide. Thus, in order to confirm whether or not a tensor glueball exists, more experimental and theoretical efforts are needed. Reliable theoretical predictions on the production rates of glueballs in  $J/\psi$  radiative decays and their decay properties would be useful.

### 9.3.3 Hunting for glueballs at *BES-III*

The peak luminosity of BEPCII is designed to be  $10^{33} \text{ cm}^{-2}\text{s}^{-1}$  at the center-of-mass energy around the  $\psi(3770)$  peak; scaling from this we determine an expectation for the luminosity at the  $J/\psi$  peak that is about 60% of the peak design value. If the average luminosity is assumed to be half of the peak luminosity and the effective running time for data accumulation is  $10^7$  s/year, the 3400 nb peak cross section for  $J/\psi$  production translates into about 10 billion  $J/\psi$  events accumulated in a one year data run. Compared to previous exposures, this data sample is huge. (This is nearly 200 times as large as the BESII 58 million  $J/\psi$  event sample.) Moreover, the new *BES-III* detector has much better performance characteristics than those of previous  $e^+e^-$  detectors that operated at the  $J/\psi$  peak. The large data sample and excellent detector performance will make possible studies of light hadron spectroscopy and searches for new hadron states with sensitivities that far exceed those of previous measurements.

Glueballs are expected to be copiously produced in radiative  $J/\psi$  decays. The inclusive photon spectrum from radiative  $J/\psi$  decays can be used to search for new states, *e.g.*, glueballs, especially when these states have a relatively large production rate in radiative  $J/\psi$  decays.

The study of exclusive  $J/\psi$  radiative and hadronic decays, as well as two-photon processes will also provide important information for the identification of the glueballs. As suggested by Close, the decays of  $J/\psi \rightarrow \gamma\gamma\rho$  and  $\gamma\gamma\phi$  can act as flavor filters that can be used to tag the flavor content of mesons that decay to  $\gamma\gamma$ .

As briefly summarized in Section 9.3.2, the existence of at least three  $I = 0$  scalar mesons in the  $1 \sim 2$  GeV mass range — the  $f_0(1370)$ ,  $f_0(1500)$  and  $f_0(1710)$  — is well established. However the nature of these states remains a mystery. Recently, two additional scalar meson candidates, the  $f_0(1790)$  and  $f_0(1810)$ , were reported by BESII and require confirmation.

With a high statistics  $J/\psi$  data sample taken with a high performance detector, the confirmation of these new states and the determination of their quantum numbers via

PWA, their masses, widths and decay branching ratios, as well as systematic studies of the  $f_0(1370)$ ,  $f_0(1500)$  and  $f_0(1710)$  produced in both radiative and hadronic decays to  $PP$  ( $P$  denotes a pseudoscalar meson),  $VV$  ( $V$  denotes a vector meson), *etc* is necessary and possible. This will help clarify the scalar situation. In addition, studies of these states in high statistics two-photon data samples will be crucial for determining their gluonic content through the determination of their two-photon couplings.

Five pseudoscalar states above 1 GeV: the  $\eta(1295)$ ,  $\eta(1405)$ ,  $\eta(1475)$ ,  $\eta(1760)$ , and  $\eta(2225)$ , are listed in the PDG [259]. Of these, some are well established, while others need further confirmation. The nature of these states is still controversial, as is discussed above in Sect. 9.3.2. With *BES-III* data, the decays  $J/\psi \rightarrow \gamma\eta\pi\pi$ ,  $\gamma\eta'\pi\pi$ ,  $\gamma K\bar{K}\pi$ ,  $\gamma VV$  *etc.*, and their corresponding hadronic decays can be investigated, which will help identify the pseudoscalar glueballs and eventually understand the pseudoscalar spectrum.

### The tensor glueball candidate in $J/\psi \rightarrow \gamma\eta\eta$ and $\gamma\eta\eta'$

In order to investigate the *BES-III* sensitivity for searching for the  $2^{++}$  glueball candidate  $f_J(2220)$ , we did a simulation study of  $J/\psi \rightarrow \gamma\eta\eta$  and  $\gamma\eta\eta'$  decays where the  $\eta$  decays to  $\gamma\gamma$  or  $\pi^+\pi^-\pi^0$  and the  $\eta'$  to  $\eta\pi^+\pi^-$ . A full Monte-Carlo simulation, based on a *BES-III* detector model in the GEANT4 MC framework, is used.

The final states of the examined channels include five photons or five photons plus multi-prong charged pions. In the event selection, all of the candidate events are required to satisfy the following common criteria for charged tracks and photons: 1) all charged tracks are required to be within the polar angle region of  $|\cos\theta| < 0.93$ , have points of closest approach that are within 1 cm of the beam axis and 5 cm of the center of the interaction point; 2) a total net charge is zero; 3) each candidate photon is required to have an energy deposit in the electromagnetic calorimeter that is greater than 40 MeV, to be isolated from charged tracks by more than  $20^\circ$  in both the  $x-y$  and  $r-z$  planes and an angle between any other photon in the event that is greater than  $7^\circ$ . Candidate  $\eta$  mesons are reconstructed via their decays to  $\gamma\gamma$  or  $\pi^+\pi^-\pi^0$ , and  $\eta'$  mesons are reconstructed from the decay chain  $\eta' \rightarrow \eta\pi^+\pi^-$ ,  $\eta \rightarrow \gamma\gamma$ . A four-constraint (4C) energy-momentum conservation kinematic fit is applied using the hypothesis of each decay mode. When the number of photons in an event exceeds the minimum, all combinations are tried, and the combination with the smallest  $\chi^2$  is retained.

#### a). $J/\psi \rightarrow \gamma\eta\eta$

In the simulation of  $J/\psi \rightarrow \gamma\eta\eta$ , we include the processes:  $J/\psi \rightarrow \gamma f_0(1500)$ ,  $\gamma f_0(1710)$ ,  $\gamma f_2(1910)$ ,  $\gamma f_0(2100)$ ,  $\gamma f_2(2100)$  and  $\gamma f_J(2220)$ . The input masses and widths of the resonances are taken from ref. [259] and listed in Table 9.4.

In ref. [259], the following branching fractions are reported:

$$Br(J/\psi \rightarrow \gamma f_0(1500))Br(f_0(1500) \rightarrow \eta\eta) = 1.84 \times 10^{-5}$$

$$Br(J/\psi \rightarrow \gamma f_0(1710))Br(f_0(1710) \rightarrow \eta\eta) = 2.88 \times 10^{-5}.$$

Branching ratios not listed in ref. [259] are taken to be:

$$Br(J/\psi \rightarrow \gamma f_2(1910))Br(f_2(1910) \rightarrow \eta\eta) \sim 1 \times 10^{-5}$$

Table 9.4: The masses and widths of the input resonances

	$f_0(1500)$	$f_0(1710)$	$f_2(1910)$	$f_0(2100)$	$f_2(2150)$	$f_J(2220)$
Mass(MeV)	1507.0	1714.0	1915.0	2103.0	2156.0	2231.0
Width((MeV)	109.0	140.0	163.0	206.0	167.0	23.0

$$Br(J/\psi \rightarrow \gamma f_0(2100))Br(f_0(2100) \rightarrow \eta\eta) \sim 1 \times 10^{-5}$$

$$Br(J/\psi \rightarrow \gamma f_2(2150))Br(f_2(2150) \rightarrow \eta\eta) \sim 1 \times 10^{-5}$$

$$Br(J/\psi \rightarrow \gamma f_J(2220))Br(f_J(2220) \rightarrow \eta\eta) \sim 1 \times 10^{-5}.$$

The further requirements  $|M_{\gamma\gamma} - M_\eta| < 0.035$  GeV or  $|M_{\pi^+\pi^-\pi^0} - M_\eta| < 0.030$  GeV are applied for  $J/\psi \rightarrow \gamma\eta\eta$ ,  $\eta \rightarrow \gamma\gamma$  or  $\eta \rightarrow \pi^+\pi^-\pi^0$ , respectively. Table 9.5 lists the mass resolutions and efficiencies for each resonance region for both of the  $\eta$  decay modes after the application of the above-listed selection criteria. For the case of  $\eta \rightarrow \pi^+\pi^-\pi^0$ , there are charged pions in the final states and, therefore, the mass resolution is better than that for the  $\eta \rightarrow \gamma\gamma$  case where there are only neutral tracks. However, the selection efficiency for this mode is very low.

Table 9.5: Mass resolutions and efficiencies for  $J/\psi \rightarrow \gamma\eta\eta$ 

process	$\eta$ decay mode	mass resolution (MeV)	efficiency(%)
$J/\psi \rightarrow \gamma f_0(1500) \rightarrow \gamma\eta\eta$	$\eta \rightarrow \gamma\gamma$	$18.4 \pm 0.2$	25.7
	$\eta \rightarrow \pi^+\pi^-\pi^0$	$10.9 \pm 0.4$	1.56
$J/\psi \rightarrow \gamma f_0(1710) \rightarrow \gamma\eta\eta$	$\eta \rightarrow \gamma\gamma$	$20.1 \pm 0.2$	25.9
	$\eta \rightarrow \pi^+\pi^-\pi^0$	$9.7 \pm 0.6$	1.71
$J/\psi \rightarrow \gamma f_2(1910) \rightarrow \gamma\eta\eta$	$\eta \rightarrow \gamma\gamma$	$21.3 \pm 0.3$	25.9
	$\eta \rightarrow \pi^+\pi^-\pi^0$	$10.7 \pm 0.5$	1.73
$J/\psi \rightarrow \gamma f_0(2100) \rightarrow \gamma\eta\eta$	$\eta \rightarrow \gamma\gamma$	$22.0 \pm 0.2$	26.5
	$\eta \rightarrow \pi^+\pi^-\pi^0$	$10.5 \pm 0.4$	1.37
$J/\psi \rightarrow \gamma f_2(2150) \rightarrow \gamma\eta\eta$	$\eta \rightarrow \gamma\gamma$	$22.2 \pm 0.2$	26.5
	$\eta \rightarrow \pi^+\pi^-\pi^0$	$9.8 \pm 0.4$	1.44
$J/\psi \rightarrow \gamma f_J(2230) \rightarrow \gamma\eta\eta$	$\eta \rightarrow \gamma\gamma$	$22.8 \pm 0.3$	26.7
	$\eta \rightarrow \pi^+\pi^-\pi^0$	$11.0 \pm 0.3$	2.09

The main backgrounds for  $J/\psi \rightarrow \gamma\eta\eta \rightarrow 5\gamma$  come from  $J/\psi \rightarrow \omega\eta, \omega \rightarrow \gamma\pi^0$  and  $J/\psi \rightarrow \gamma\eta, \eta \rightarrow \pi^0\pi^0\pi^0$ . However, these tend to accumulate in the high mass region of the  $\eta\eta$  invariant mass spectrum.

Figure 9.11 shows the  $\eta\eta$  invariant mass spectrum for the incoherent sum of the generated signals and backgrounds when both  $\eta$  candidates decay into  $\gamma\gamma$ . The generated signal and background events are normalized to a  $10^{10}$   $J/\psi$  event sample.

For  $J/\psi \rightarrow \gamma\eta\eta \rightarrow 5\gamma 2(\pi^+\pi^-)$ , the main contamination to the  $\eta\eta$  spectrum is from  $J/\psi \rightarrow 2(\pi^+\pi^-)3\pi^0$ . The  $\eta\eta$  invariant mass spectrum for the incoherent sum of the generated signals and backgrounds with  $\eta$  decaying into  $\pi^+\pi^-\pi^0$  is shown in Fig. 9.12. The generated signal and background events are normalized to  $10^{10}$  total  $J/\psi$  events.

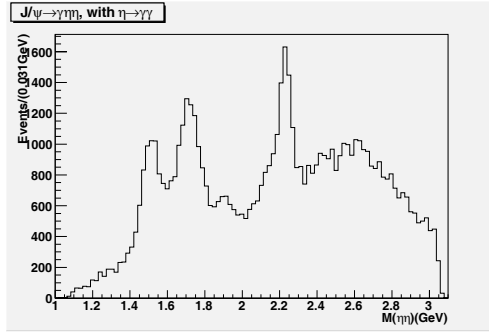


Figure 9.11: The  $\eta\eta$  invariant mass spectrum in  $J/\psi \rightarrow \gamma\eta\eta \rightarrow 5\gamma$ . The generated signals and backgrounds are normalized to  $10^{10} J/\psi$  decays and are added incoherently.

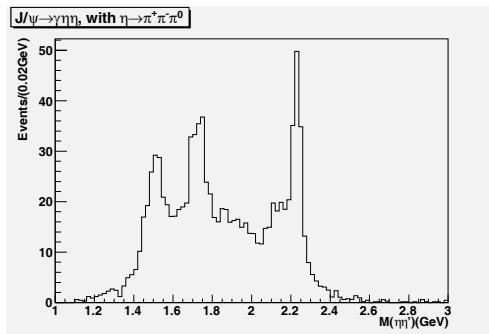


Figure 9.12: The  $\eta\eta$  invariant mass spectrum in  $J/\psi \rightarrow \gamma\eta\eta \rightarrow 5\gamma 2(\pi^+ \pi^-)$ . The generated signals and backgrounds are normalized to  $10^{10} J/\psi$  events and are added incoherently.

A significant  $f_J(2220)$  signal is seen in both the  $\eta \rightarrow \gamma\gamma$  and  $\pi^+\pi^-\pi^0$  modes. The Breit-Wigner fit to the  $\eta\eta$  invariant mass spectra yields a statistical significance for the  $f_J(2220)$  signal that is larger than  $7\sigma$  in both cases.

If we take the product branching fraction for  $J/\psi \rightarrow \gamma f_J(2220)$ ,  $f_J(2220) \rightarrow \eta\eta$  to be  $0.5 \times 10^{-5}$  and that for  $J/\psi \rightarrow \gamma f_J(2150)$ ,  $f_J(2150) \rightarrow \eta\eta$  to be  $1 \times 10^{-5}$ , the statistical significance of the  $f_J(2220)$  is found to be larger than  $7\sigma$  for the both the  $\eta \rightarrow 2\gamma$  and  $\eta \rightarrow \pi^+\pi^-\pi^0$  modes. The  $\eta\eta$  invariant mass spectra are shown in Fig. 9.13 for  $\eta \rightarrow 2\gamma$  and Fig. 9.14 for  $\eta \rightarrow \pi^+\pi^-\pi^0$ , respectively. If we assume the product branching fraction for  $J/\psi \rightarrow \gamma f_J(2220)$ ,  $f_J(2220) \rightarrow \eta\eta$  is  $0.5 \times 10^{-6}$  and that for  $J/\psi \rightarrow \gamma f_2(2150)$ ,  $f_2(2150) \rightarrow \eta\eta$  is  $3 \times 10^{-5}$ , the statistical significance of the  $f_J(2220)$  signal is larger than  $7\sigma$  for the  $\eta \rightarrow 2\gamma$  and  $4.3\sigma$  for  $\eta \rightarrow \pi^+\pi^-\pi^0$  modes.

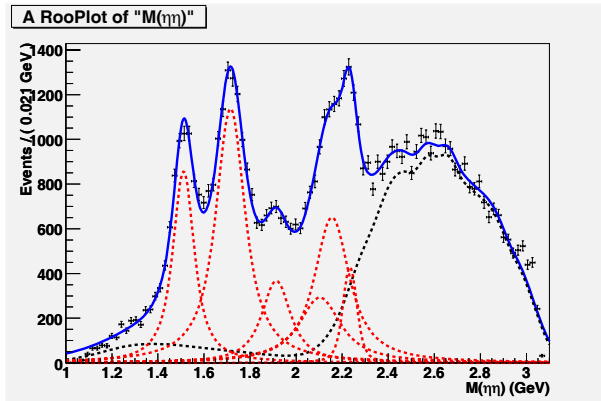


Figure 9.13: Fit result after adding all resonances together. ( $J/\psi \rightarrow \gamma\eta\eta$ ,  $\eta \rightarrow \gamma\gamma$ ,  $\eta \rightarrow \gamma\gamma$  channel).

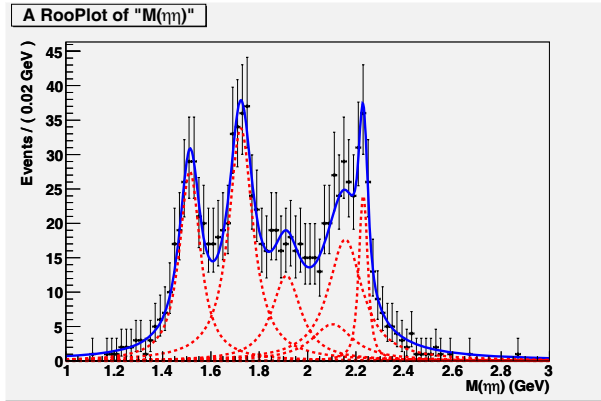


Figure 9.14: Fit result after adding all resonances together ( $J/\psi \rightarrow \gamma\eta\eta$ ,  $\eta \rightarrow \pi^+\pi^-\pi^0$ ,  $\eta \rightarrow \pi^+\pi^-\pi^0$  channel).

Table 9.6 shows a comparison of the input resonances' masses, widths and branching ratios with those obtained from the fit, when the product branching fraction for  $J/\psi \rightarrow \gamma f_J(2220)$ ,  $f_J(2220) \rightarrow \eta\eta$  is taken to be  $0.5 \times 10^{-5}$  and  $J/\psi \rightarrow \gamma f_2(2150)$ ,  $f_2(2150) \rightarrow \eta\eta$  to be  $1 \times 10^{-5}$ . The fitted results are consistent with the input values.

From the simulation, one can see that if the branching ratio of  $f_J(2220)$  is large enough compared with that for the nearby resonance, *e.g.* the  $f_2(2150)$ , the  $f_J(2220)$  can be clearly seen in the mass spectrum. If  $f_J(2220) \rightarrow \eta\eta$  is  $0.5 \times 10^{-6}$  and  $J/\psi \rightarrow \gamma f_2(2150)$ ,  $f_2(2150) \rightarrow \eta\eta$  is  $3 \times 10^{-5}$ , then the broad  $f_2(2150)$  may interfere with the observation of the  $f_J(2220)$ . In this case, a partial wave analysis (PWA) that determines the contribution of each spin-parity component will be needed to distinguish the  $f_J(2220)$  and  $f_2(2150)$ .

	Mass(MeV)		Width(MeV)		Branching ratio( $\times 10^{-7}$ )	
	input	fit	input	fit	input	fit
$f_0(1500)$	1507.0	$1512.8 \pm 3.8$	109.0	$97.4 \pm 8.2$	14.43	$14.67 \pm 0.94$
$f_0(1710)$	1714.0	$1723.8 \pm 3.5$	140.0	$117.2 \pm 10.4$	22.58	$22.75 \pm 1.47$
$f_2(1910)$	1915.0	$1912.2 \pm 1.1$	163.0	$143.8 \pm 8.2$	7.8	$7.98 \pm 0.93$
$f_0(2100)$	2103.0	fixed	206.0	fixed	7.8	$6.59 \pm 2.62$
$f_2(2150)$	2156.0	fixed	167.0	fixed	7.8	$7.98 \pm 2.72$
$f_J(2220)$	2231.1	$2230.8 \pm 2.7$	23.0	$27.6 \pm 7.2$	3.9	$4.57 \pm 0.71$

Table 9.6: Input and output comparison of mass, width and branching ratio in the simulation. Here, the masses and widths of  $f_0(2100)$  and  $f_2(2150)$  are fixed. ( $J/\psi \rightarrow \gamma\eta\eta$ ,  $\eta \rightarrow \pi^+\pi^-\pi^0$ ,  $\eta \rightarrow \pi^+\pi^-\pi^0$  channel).

b).  $J/\psi \rightarrow \gamma\eta\eta'$

According to some theoretical calculations, the  $f_J(2220)$  may have a large decay branching fraction to  $\eta\eta'$ . Therefore we performed a full Monte-Carlo simulation to investigate the sensitivity of the observation of  $f_J(2220)$  in this decay channel. Here, only the case where the  $\eta'$  is reconstructed through  $\eta' \rightarrow \eta\pi^+\pi^-$  and the  $\eta$  through  $\eta \rightarrow \gamma\gamma$  is considered, corresponding to a final state with five photons and one  $\pi^+\pi^-$  pair. To select the  $\eta$  and  $\eta'$ ,  $|M_{\gamma\gamma} - M_\eta| < 0.035$  GeV and  $|M_{\pi^+\pi^-\eta} - M_{\eta'}| < 0.040$  GeV are required. The resonances included in the simulation are the same as those used in the  $J/\psi \rightarrow \gamma\eta\eta$  simulation. Table 9.7 lists the mass resolutions and efficiencies in each resonance region for  $J/\psi \rightarrow \gamma\eta\eta'$ .

Table 9.7: Mass resolutions and efficiencies for  $J/\psi \rightarrow \gamma\eta\eta'$ .

process	mass resolution (MeV)	efficiency(%)
$J/\psi \rightarrow \gamma f_0(1500) \rightarrow \gamma\eta\eta'$	$14.2 \pm 0.4$	4.5
$J/\psi \rightarrow \gamma f_0(1710) \rightarrow \gamma\eta\eta'$	$16.7 \pm 0.5$	4.8
$J/\psi \rightarrow \gamma f_2(1910) \rightarrow \gamma\eta\eta'$	$17.2 \pm 0.4$	4.9
$J/\psi \rightarrow \gamma f_0(2100) \rightarrow \gamma\eta\eta'$	$18.6 \pm 0.4$	5.6
$J/\psi \rightarrow \gamma f_2(2150) \rightarrow \gamma\eta\eta'$	$18.1 \pm 0.4$	5.7
$J/\psi \rightarrow \gamma f_J(2220) \rightarrow \gamma\eta\eta'$	$19.0 \pm 0.5$	6.1

The main backgrounds for  $J/\psi \rightarrow \gamma\eta\eta' \rightarrow 5\gamma\pi^+\pi^-$  come from  $J/\psi \rightarrow \omega\eta$ ,  $\omega \rightarrow \pi^+\pi^-\pi^0$ ,  $\eta \rightarrow \gamma\gamma$ ,  $J/\psi \rightarrow \omega\pi^0$ ,  $\omega \rightarrow \pi^+\pi^-\pi^0$  and  $J/\psi \rightarrow \omega\eta'$ ,  $\omega \rightarrow \pi^+\pi^-\pi^0$ ,  $\eta \rightarrow \gamma\gamma$ .

According to the Particle Data Book [259],

$$Br(J/\psi \rightarrow \gamma f_0(1500))Br(f_0(1500) \rightarrow \eta\eta') \sim 1.8 \times 10^{-5}$$

$$Br(J/\psi \rightarrow \gamma f_0(1710))Br(f_0(1710) \rightarrow \eta\eta') \sim 1.8 \times 10^{-5}.$$

Other branching fractions not listed in [259] are taken to be:

$$Br(J/\psi \rightarrow \gamma f_2(1910))Br(f_2(1910) \rightarrow \eta\eta') \sim 1 \times 10^{-5}$$

$$Br(J/\psi \rightarrow \gamma f_0(2100))Br(f_0(2100) \rightarrow \eta\eta') \sim 1 \times 10^{-5}$$

$$Br(J/\psi \rightarrow \gamma f_2(2150))Br(f_2(2150) \rightarrow \eta\eta') \sim 1 \times 10^{-5}$$

$$Br(J/\psi \rightarrow \gamma f_J(2220))Br(f_J(2220) \rightarrow \eta\eta') \sim 1 \times 10^{-5}.$$

Figure 9.15 shows the  $\eta\eta'$  invariant mass spectrum for the incoherent sum of the generated signals and backgrounds, with the branching fraction assumptions listed above. The generated signal and background events are normalized to  $10^{10} J/\psi$  events. The background level in the 2220 MeV region is very low and the  $f_J(2220)$  signal can be clearly seen.

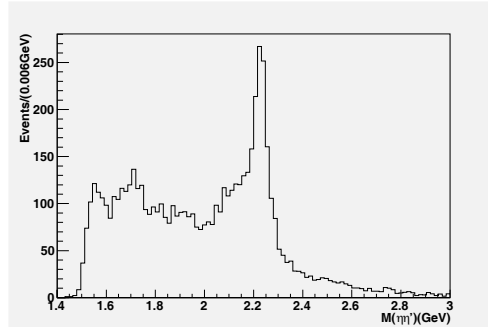


Figure 9.15: The  $\eta\eta'$  invariant mass spectrum in  $J/\psi \rightarrow \gamma\eta\eta' \rightarrow 5\gamma\pi^+\pi^-$ . The generated signals and backgrounds are normalized to  $10^{10} J/\psi$  events and are added incoherently.

If a different branching fraction is assumed for the  $f_2(2150)$ , say

$$Br(J/\psi \rightarrow \gamma f_2(2150))Br(f_2(2150) \rightarrow \eta\eta') \sim 3 \times 10^{-5},$$

the resulting  $\eta\eta'$  invariant mass spectrum for the incoherent sum of the generated signals and backgrounds looks like that shown in Fig. 9.16.

In summary, the decays of  $J/\psi \rightarrow \gamma\eta\eta$  and  $\gamma\eta\eta'$  are studied based on a full Monte-Carlo simulation of *BES-III*. From the simulation, we determine that the sensitivity of searches for the tensor glueball  $f_J(2220)$  at *BES-III* not only depends on the production rate of  $f_J(2220)$  in  $J/\psi$  radiative decays and its decay branching ratios to the examined final states, but also on the production and decays of nearby resonances. In some cases, a partial wave analysis will be needed to resolve ambiguities.

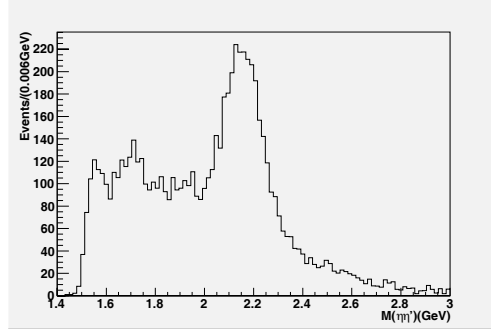


Figure 9.16: The  $\eta\eta$  invariant mass spectrum in  $J/\psi \rightarrow \gamma\eta\eta' \rightarrow 5\gamma\pi^+\pi^-$ . The generated signals and backgrounds are normalized to  $10^{10} J/\psi$  events and are added incoherently.

### Inclusive photon spectrum

The inclusive photon spectrum from radiative  $J/\psi$  decays can be used to search for new states, especially when these states have a relatively large production rate in radiative  $J/\psi$  decays, as is expected for glueballs.

The Crystal Ball experiment presented an inclusive photon spectrum for radiative  $J/\psi$  decays, where the  $\eta$ ,  $\eta'$  and a peak corresponding to a recoil mass of around 1440 MeV are clearly seen [139]. However no clear signal for  $J/\psi \rightarrow \gamma f_J(2220)$  is observed and no numerical upper limit on inclusive  $f_J(2220)$  production in radiative  $J/\psi$  decays is set because of the uncertainties in the photon efficiency as a function of energy.

A Monte-Carlo study of inclusive radiative  $J/\psi$  decays at *BES-III* has been performed. For the selected events, the charged tracks are required to be within the polar angle region of  $|\cos\theta| < 0.93$  and to come from the interaction point. The total net charge of the charged tracks is required to be zero. The candidate photon is required to have an energy deposit in the electromagnetic calorimeter that is greater than 40 MeV and have polar and azimuthal opening angles between it and any charged track that are greater than  $20^\circ$ . In order to reject photons from  $\pi^0$  decays, it is required that the invariant mass of it and any other photon in the event should be greater than 0.2 GeV. A pairing with an invariant mass between 0.5 and 0.7 GeV is considered to be an  $\eta$  candidate and is also removed.

Figure 9.17 shows the results of a Monte-Carlo study of inclusive radiative  $J/\psi$  decays at *BES-III*. Here, the branching ratio of  $J/\psi \rightarrow \gamma f_J(2220)$  is assumed to be  $Br(J/\psi \rightarrow \gamma f_J(2220)) = 2.5 \times 10^{-3}$ .

## 9.4 Hybrid Mesons

### 9.4.1 Theoretical models for hybrid mesons

#### Large $N_C$ expansion

Hybrid mesons are hypothesized to be formed from a  $q\bar{q}$  pair plus one explicit gluon field  $G$ . In the large  $N_c$  limit, the amplitude for creating a hybrid meson from the vacuum has the same  $N_c$ -order as that for creating a  $q\bar{q}$  meson [143]. If kinematics and other

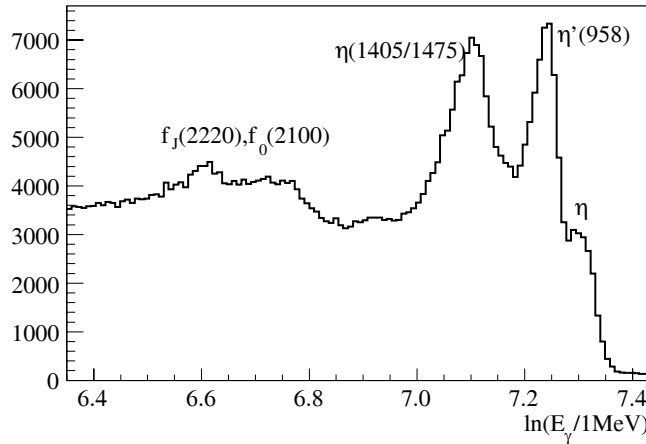


Figure 9.17: The inclusive photon spectrum for  $J/\psi$  radiative decays.

conservation laws allow, the production cross section for hybrid mesons is expected to be roughly the same as that of ordinary mesons. At least it is not suppressed in the large  $N_c$  limit. In the same limit, hybrid mesons and ordinary mesons with the same quantum numbers can mix freely. Thus, the identification of hybrid mesons can be very difficult unless they have exotic quantum numbers. That is why considerable efforts have been devoted to the search for  $1^{-+}$  hybrid mesons.

### Flux tube model

The flux tube model is based on intuition gained from the strong-coupling limit of lattice QCD [144, 145]. In this picture, a meson is described as a quark-antiquark pair linked by a color flux tube. The quarks move adiabatically in an effective potential generated by the dynamics of the flux tube. The flux tube can rotate along its axis, but the orbital angular momentum along the flux tube is zero. When the flux tube is in its ground state, the excitations of the quark-antiquark pair yields the conventional meson spectrum.

Hybrid mesons are defined as excitations of the color flux tube. The lowest-lying exotic hybrid meson is predicted to have quantum numbers  $J^{PC} = 1^{-+}$  and a mass around 1.9 GeV [145], consistent with predictions from lattice QCD. In the flux tube model, the decay of a hybrid is triggered by the breaking the flux tube [144]. In this breaking process, a quark-antiquark pair is created with spin  $S_{q\bar{q}} = 1$ , orbital angular momentum  $L_{q\bar{q}} = 1$  and total angular momentum  $J_{q\bar{q}} = 0$ , a process called ‘ ${}^3P_0$  pair creation’. In this picture, a state with spin  $S = 0$  can not decay into two  $S = 0$  states [146]. In the flux tube model, the quark-antiquark pair of the lowest-lying  $1^{-+}$  hybrid is in a spin singlet and, thus, cannot decay into a pair of spin zero mesons, such as  $\pi\pi$  and  $\pi\eta$ . In addition, when a single flux tube breaks into two flux tubes (two mesons), the relative coordinate of the two final flux tubes (the line that connects the centers of the two flux tubes) is parallel to the original one (denoted as  $\mathbf{r}$ ). As a result, the two final-state mesons that materialize

Table 9.8: Decay widths of the  $1^{-+}$  hybrid meson from the two flux tube model.

	$b_1\pi$	$\rho\pi$	$f_1\pi$	$\eta(1295)\pi$	$K^*K$
PSS(MeV)	24	9	5	2	0.8
IKP(MeV)	59	8	14	1	0.4

from the two tubes cannot absorb the unit of string angular momentum about the  $\mathbf{r}$  axis [144, 146] as relative orbital angular momentum. Therefore a  $1^{-+}$  hybrid (with one excited phonon polarized along the flux tube) cannot decay into two ground states, such as  $\pi\pi$ ,  $\pi\eta$  and  $\pi\rho\cdots$ . The preferential decay modes are those with one excited meson, such as  $b_1\pi$ ,  $f_1\pi\cdots$ . This selection rule can be violated when the two final ground states have different spatial wave functions (*i.e.*, different spatial size). One calculation shows that the partial width for  $1^{-+} \rightarrow \rho\pi$  can be large and compatible with  $\pi_1(1600)$  being a hybrid if the  $\pi$  shrinks to a point [147].

The original flux tube model (the IKP model) was modified by the introduction of a new decay vertex that is constructed using the heavy quark expansion of the Coulomb-gauge QCD Hamiltonian to identify relevant operators [148, 149]. This new model (the PSS model), which is an extension of IKP, states that the decay amplitude for a hybrid meson vanishes when the daughter mesons are identical. This means that not only  $S$ - plus  $S$ -wave final states are forbidden but also  $P$ - plus  $P$ -wave final states, and the preferred decay channels are  $S$ - plus  $P$ -wave pairs. The predicted partial widths for  $1^{-+}$  hybrid meson to each channel differ as shown in Table 9.8 [149], where the mass of the  $1^{-+}$  hybrid is taken to be 1.6 GeV. It should be noted that in PSS the width to  $\rho\pi$  is larger than that for  $f_1\pi$ . An extensive study of the decay patterns of hybrid mesons with other quantum numbers in the flux tube model have been performed by Page, Swanson and Szczepaniak [149].

In Tables 9.9 through 9.24, collected from ref. [149], the dominant widths for hybrid decays  $H \rightarrow AB$  for various  $J^{PC}$  hybrids in a partial wave  $L$  are presented. In each table, column 1 indicates the  $J^{PC}$  of the hybrid, column 2 the decay mode and column 3,  $L$ . In columns 4, 5, 6 and 8, the predictions of this model are indicated. Column 6 uses the ‘standard parameters’ used throughout ref. [149] and are defined in the Appendix of ref. [149]. Column 5 uses the same parameters, except that all hybrids are assumed to be 0.2 GeV heavier (and the  $c\bar{c}$  hybrids 0.3 GeV heavier to put them above the  $D^{**}D$  thresholds at approximately 4.3 GeV). Column 4 uses so-called ‘alternative parameters.’ Comparisons of columns 4 and 6 can, therefore, be used to estimate the parameter sensitivity of the predictions. For hybrid decays to two ground state  $S$ -wave mesons, the ‘reduced width’ is indicated in column 8. This is the width divided by the dimensionless ratio  $(\beta_A^2 - \beta_B^2)^2 / (\beta_A^2 + \beta_B^2)^2$ , where  $\beta$  is the inverse radius of the SHO wave function [150]. This gives a measure of how strong the decay is with the wave function dependence explicitly removed. In column 7, the IKP model predictions for the ‘standard parameters’ are given. Thus, columns 6 and 7 should be compared to see differences between the PSS and IKP model predictions.

Table 9.9:  $2^{-+}$  Isovector Hybrid Decay Modes from Ref. [149].

		alt	2.0 GeV hybrid	standard	IKP	reduced
$2^{-+}$						
$\rho\pi$	P	9	16	13	12	57
$K^*K$	P	1	5	2	1	17
$\rho\omega$	P	0	0	0	0	20
$f_2(1270)\pi$	S	19	10	9	14	
	D	.1	.2	.05	11	
$f_1(1285)\pi$	D	.1	.3	.06	$\emptyset$	
$f_0(1370)\pi$	D	.02	.08	.01	.6	
$b_1(1235)\pi$	D	$\emptyset$	$\emptyset$	$\emptyset$	20	
$a_2(1320)\eta$	S	—	7	—	—	
	D	—	.01	—	—	
$a_1(1260)\eta$	D	0	.05	0	0	
$a_0(1450)\eta$	D	—	0	—	—	
$K_2^*(1430)K$	S	—	11	—	—	
	D	—	0	—	—	
$K_1(1270)K$	D	0	.01	0	.02	
$K_0^*(1430)K$	D	—	0	—	—	
$K_1(1410)K$	D	—	0	—	—	
$\rho_1(450)\pi$	P	.8	12	3	2	
$K^*(1410)K$	P	—	1	—	—	
$\Gamma$		30	63	27	59	

### QCD sum rules

The mass and decay width of the  $1^{-+}$  hybrid meson has been studied using QCD sum rules. Within this framework, one considers a two-point correlator

$$\Pi_{\mu\nu}(q^2) = i \int d^4x e^{iqx} \langle 0 | T\{j_\mu(x), j_\nu^+(0)\} | 0 \rangle, \quad (9.4.11)$$

where  $j_\mu(x) = \bar{q}(x)T^a\gamma_\nu igG_{\mu\nu}^a q(x)$  is the interpolating current for the  $1^{-+}$  isospin vector hybrid meson.

The spectral density  $\rho_v(s) = \frac{1}{\pi} \text{Im} \Pi_v(s)$  can be expressed in terms of the hybrid meson observables such as its mass etc:

$$\frac{1}{\pi} \text{Im} \Pi_v(s) = \sum_R M_R^6 f_R^2 \delta(s - M_R^2) + \text{QCD continuum.} \quad (9.4.12)$$

It can also be related to the correlator  $\Pi_v(q^2)$  at the scale  $-q^2$  via the dispersion relation

$$\Pi_{v,s}(q^2) = (q^2)^n \int_0^\infty ds \frac{\rho_v(s)}{s^n(s - q^2)} + \sum_{k=0}^{n-1} a_k(q^2)^k, \quad (9.4.13)$$

where the  $a_k$  are appropriate subtraction constants.

After invoking a Borel transformation to enhance the lowest-lying resonance in the spectral density, we have the QCD sum rules

$$R_k(\tau, s_0) = \int^{s_0} s^k e^{-s\tau} \rho_v(s) ds ; \quad k = 0, 1, 2, \dots, \quad (9.4.14)$$

Table 9.10:  $1^{-+}$  Isovector Hybrid Decay Modes from Ref. [149].

		alt	high mass	standard	IKP	reduced
$1^{-+}$						
	$\eta\pi$	P	0	.02	.02	99
	$\eta'\pi$	P	0	.01	.01	30
	$\rho\pi$	P	9	16	13	57
	$K^*K$	P	1	5	2	17
	$\rho\omega$	P	0	0	0	13
	$f_2(1270)\pi$	D	.2	.5	.1	$\emptyset$
	$f_1(1285)\pi$	S	18	10	9	14
		D	.06	.2	.04	7
	$b_1(1235)\pi$	S	78	40	37	51
		D	2	3	1	11
	$a_2(1320)\eta$	D	—	.02	—	—
	$a_1(1260)\eta$	S	5	7	3	8
		D	0	.01	0	.01
	$K_2^*(1430)K$	D	—	0	—	—
	$K_1(1270)K$	S	4	7	2	6
		D	0	.2	0	.04
	$K_1(1410)K$	S	—	33	—	—
		D	—	0	—	—
	$\pi(1300)\eta$	P	—	5	—	—
	$\eta_u(1295)\pi$	P	3	27	11	8
	$K(1460)K$	P	—	.8	—	—
	$\rho(1450)\pi$	P	.8	12	3	2
	$K^*(1410)K$	P	—	1	—	—
	$\Gamma$		121	168	81	117

Table 9.11:  $1^{--}$  Isovector Hybrid Decay Modes from Ref. [149].

		alt	2.0 GeV hybrid	standard	IKP	reduced
$1^{--}$	$\omega\pi$	P	9	16	13	12
	$\rho\eta$	P	4	9	6	4
	$\rho\eta'$	P	.1	1	.2	.1
	$K^*K$	P	3	9	5	3
	$a_2(1320)\pi$	D	.5	2	.3	16
	$a_1(1260)\pi$	S	78	41	37	51
		D	.4	.8	.2	11
	$h_1(1170)\pi$	S			$\emptyset$	
		D			$\emptyset$	
	$b_1(1235)\eta$	S			$\emptyset$	
		D			$\emptyset$	
	$K_2^*(1430)K$	D	—	0	—	—
	$K_1(1270)K$	S	6	12	4	11
		D	0	.01	0	0
	$K_1(1400)K$	S	—	17	—	—
		D	—	0	—	—
	$\omega(1420)\pi$	P	1	14	4	4
	$K^*(1410)K$	P	—	3	—	—
	$\Gamma$		103	121	70	112

where the quantity  $R_k$  represents the QCD prediction, and  $s_0$  is the threshold parameter.

The sum rules for a  $1^{-+}$  hybrid meson have been obtained by various authors. The prediction for the hybrid mass is sensitive to the threshold  $s_0$ , and the sum rule in the leading order of  $\alpha_s$  expansion is unstable. When the next-to-leading-order correction is included, the sum rule becomes more stable. An upper bound on the  $1^{-+}$  hybrid mass is predicted to be 2.0 GeV [151].

The decay widths of the  $1^{-+}$  hybrid can be obtained by a three-point correlator

$$\Pi(p, q) = i \int d^4x d^4y e^{ipx+iqy} \langle 0 | T\{j_A(x)j_B(y)j_\mu(0)\} | 0 \rangle, \quad (9.4.15)$$

where  $j_A(x)$  and  $j_B(y)$  are operators that annihilate the final states  $A$  and  $B$  respectively.

When  $A$  and  $B$  are two pseudoscalars,  $\Pi(p, q) = F_1(p+q)_\mu + F_2(p-q)_\mu$ . Only  $F_2$  is relevant to the process  $1^{-+} \rightarrow AB$  and vanishes at the leading order [152]. At the next leading order, it was estimated [153] to be:  $\Gamma(1^{-+} \rightarrow \pi\eta') \sim 3\text{MeV}$ ,  $\Gamma(1^{-+} \rightarrow \pi\eta) \sim 0.3\text{MeV}$ , which is quite consistent with flux tube model predictions.

However, the channel  $\pi\rho$  is not narrow in the QCD sum rules approach. By using the three-point function at the symmetric point, the width of  $1^{-+} \rightarrow \pi\rho$  was predicted to be in the 250-600 MeV range [153, 154]. Later, it was pointed out that the calculation at the symmetric point receives large contamination from higher resonances and the continuum [155]. By using the light-cone QCD sum rules and a double Borel transformation, the width is reduced to be  $40 \pm 20$  MeV [155]. The similar channel,  $K^*K$ , is suppressed by the kinematic phase space. The  $f_1\pi$  channel is very broad ( $\sim 100$  MeV) in the QCD sum rule approach.

Table 9.12:  $2^{+-}$  Isovector Hybrid Decay Modes from Ref. [149].

		alt	2.0 GeV hybrid	standard	IKP	reduced
$2^{+-}$	$\omega\pi$	D	.5	1	1	4
	$\rho\eta$	D	.1	.6	.2	.1
	$\rho\eta'$	D	0	.02	0	0
	$K^*K$	D	.04	.2	.08	.04
	$a_2(1320)\pi$	P	.7	.9	.4	130
		F	0	.02	0	.2
	$a_1(1260)\pi$	P	3	4	2	45
		F	.01	.02	0	.3
	$h_1(1170)\pi$	P	2	2	1	69
		F	.01	.03	.01	.5
	$b_1(1235)\eta$	P	.02	.5	.01	.8
		F	0	0	0	0
	$K_2^*(1430)K$	P	—	.04	—	—
		F	—	0	—	—
	$K_1(1270)K$	P	0	.03	0	.6
		F	0	0	0	0
	$K_1(1400)K$	P	—	.3	—	—
		F	—	0	—	—
	$\pi(1300)\pi$	D	.08	1	.2	.2
	$\omega(1420)\pi$	D	.02	.4	.04	.04
	$K^*(1410)K$	D	—	.01	—	—
	$\Gamma$		7	11	5	248

Table 9.13:  $0^{-+}$  Isovector Hybrid Decay Modes from Ref. [149].

		alt	2.0 GeV hybrid	standard	IKP	reduced
$0^{-+}$	$\rho\pi$	P	37	63	51	47
	$K^*K$	P	5	18	10	5
	$\rho\omega$	P			$\emptyset$	
	$f_2(1270)\pi$	D	1	3	.6	8
	$f_0(1370)\pi$	S	62	40	30	62
	$a_2(1320)\eta$	D	—	.1	—	—
	$a_0(1450)\eta$	S	—	4	—	—
	$K_2^*(1430)K$	D	—	.02	—	—
	$K_0^*(1430)K$	S	—	44	—	—
	$\rho(1450)\pi$	P	3	47	10	10
	$K^*(1410)K$	P	—	5	—	—
	$\Gamma$		108	224	102	132

Table 9.14:  $1^{+-}$  Isovector Hybrid Decay Modes from Ref. [149].

		alt	2.0 GeV hybrid	standard	IKP	reduced
1 <sup>+-</sup>	$\omega\pi$	S 23	19	26	38	118
		D .3	.8	.4	.3	2
	$\rho\eta$	S 15	21	25	22	118
		D .07	.3	.1	.06	.6
	$\rho\eta'$	S 3	8	5	4	25
		D 0	.01	0	0	0
	$K^*K$	S 27	52	47	36	339
		D .02	.1	.04	.02	.3
	$a_2(1320)\pi$	P 19	26	10	49	
		F 0	.02	0	.1	
	$a_1(1260)\pi$	P 9	10	5	29	
	$a_0(1450)\pi$	P 3	6	1	26	
	$h_1(1170)\pi$	P $\emptyset$	$\emptyset$	$\emptyset$	95	
	$b_1(1235)\eta$	P $\emptyset$	$\emptyset$	$\emptyset$	1	
	$K_2^*(1430)K$	P —	1	—	—	
		F —	0	—	—	
	$K_1(1270)K$	P .04	.6	.02	5	
	$K_0^*(1430)K$	P —	.4	—	—	
	$K_1(1400)K$	P —	.4	—	—	
	$\omega(1420)\pi$	S 16	82	58	79	
		D .01	.2	.02	.02	
	$K^*(1410)K$	S —	110	—	—	
		D —	.01	—	—	
	$\Gamma$	115	338	177	384	

Table 9.15:  $0^{+-}$  Isovector Hybrid Decay Modes from Ref. [149].

		alt	2.0 GeV hybrid	standard	IKP	reduced
0 <sup>+-</sup>	$a_1(1260)\pi$	P $\emptyset$	$\emptyset$	$\emptyset$	309	
	$h_1(1170)\pi$	P 47	45	24	37	
	$b_1(1235)\eta$	P .6	12	.4	.3	
	$K_1(1270)K$	P .7	10	.4	7	
	$K_1(1400)K$	P —	1	—	—	
	$\pi(1300)\pi$	S 60	246	222	312	
	$K(1460)K$	S —	115	—	—	
	$\Gamma$	108	429	247	665	

Table 9.16:  $1^{++}$  Isovector Hybrid Decay Modes from Ref. [149].

$1^{++}$			alt	2.0 GeV hybrid	standard	IKP	reduced
$\rho\pi$	S	23		19	26	38	116
	D	1		3	2	1	8
$K^*K$	S	14		26	24	18	170
	D	.04		.3	.09	.04	.6
$\rho\omega$	S	0		0	0	0	47
	D	0		0	0	0	.03
$f_2(1270)\pi$	P	4		5	2	75	
	F	.01		.03	0	.3	
$f_1(1285)\pi$	P	7		9	4	62	
$f_0(1370)\pi$	P	$\emptyset$		$\emptyset$	$\emptyset$	4	
$b_1(1235)\pi$	P	$\emptyset$		$\emptyset$	$\emptyset$		
$a_2(1320)\eta$	P	—		.9	—	—	
	F	—		0	—	—	
$a_1(1260)\eta$	P	.2		3	.09	1	
$a_0(1450)\eta$	P	—		$\emptyset$	—	—	
$K_2^*(1430)K$	P	—		.4	—	—	
	F	—		0	—	—	
$K_1(1270)K$	P	.07		1	.05	1	
$K_0^*(1430)K$	P	—		0	—	—	
$K_1(1400)K$	P	—		.7	—	—	
$\rho(1450)\pi$	S	14		80	50	66	
	D	.02		.6	.05	.04	
$K^*(1410)K$	S	—		55	—	—	
	D	—		.01	—	—	
$\Gamma$		63		204	108	269	

Table 9.17: Isoscalar Hybrid Decay Modes from Ref. [149].

		alt	2.0 GeV hybrid	standard	IKP	reduced
2 <sup>-+</sup>	$K^*K$	P	1	5	2	1
	$a_2(1320)\pi$	S	52	31	25	45
		D	.2	.6	.1	22
	$a_1(1260)\pi$	D	.5	1	.3	$\emptyset$
	$a_0(1450)\pi$	D	.02	.1	.01	.6
	$f_2(1270)\eta$	S	—	8	—	—
		D	—	.02	—	—
	$f_1(1285)\eta$	D	—	.02	—	—
	$f_0(1370)\eta$	D	—	0	—	—
	$K_2^*(1430)K$	S	—	11	—	—
		D	—	0	—	—
		G	—	0	—	—
	$K_1(1270)K$	D	0	.01	0	0
	$K_0^*(1430)K$	D	—	0	—	—
	$K_1(1400)K$	D	—	0	—	—
	$K^*(1410)K$	P	—	1	—	—
	$\Gamma$		54	58	27	69
1 <sup>-+</sup>	$\eta'\eta$	P	0	0	0	0
	$K^*K$	P	1	5	2	1
	$a_2(1320)\pi$	D	.4	1	.2	$\emptyset$
	$a_1(1260)\pi$	S	59	30	28	38
		D	.3	.6	.2	34
	$f_2(1270)\eta$	D	—	.05	—	—
	$f_1(1285)\eta$	S	—	8	—	—
		D	—	.01	—	—
	$K_2^*(1430)K$	D	—	0	—	—
	$K_1(1270)K$	S	4	7	2	7
		D	0	.2	0	0
	$K_1(1400)K$	S	—	33	—	—
		D	—	0	—	—
	$\pi(1300)\pi$	P	8	65	27	27
	$\eta_u(1295)\eta$	P	—	6	—	—
	$K(1460)K$	P	—	.8	—	—
	$K^*(1410)K$	P	—	1	—	—
	$\Gamma$		73	158	59	107

Table 9.18: Isoscalar Hybrid Decay Modes from Ref. [149].

		alt	2.0 GeV hybrid	standard	IKP	reduced
0 <sup>+</sup>	$K^*K$	P	5	18	10	5
	$a_2(1320)\pi$	D	2	6	1	16
	$a_0(1450)\pi$	S	145	114	70	175
	$f_2(1270)\eta$	D	—	.2	—	—
	$f_0(1370)\eta$	S	—	23	—	—
	$K_2^*(1430)K$	D	—	.02	—	—
	$K_0^*(1430)K$	S	—	44	—	—
	$K^*(1410)K$	P		5		
	$\Gamma$		152	210	81	196
1 <sup>--</sup>	$\rho\pi$	P	28	47	38	35
	$\omega\eta$	P	3	9	6	4
	$\omega\eta'$	P	.1	1	.2	.3
	$K^*K$	P	3	9	5	3
	$b_1(1235)\pi$	S	$\emptyset$	$\emptyset$	$\emptyset$	$\emptyset$
		D			$\emptyset$	$\emptyset$
	$h_1(1170)\eta$	S				$\emptyset$
	$K_2^*(1430)K$	D	—	0	—	—
	$K_1(1270)K$	S	6	12	4	11
		D	0	.01	0	0
	$K_1(1400)K$	S	—	17	—	—
		D	—	0	—	—
	$\rho(1450)\pi$	P	2	35	8	7
	$\omega(1420)\eta$	P	—	.6	—	—
	$K^*(1410)K$	P	—	3	—	—
	$\Gamma$		42	134	61	60

Table 9.19: Isoscalar Hybrid Decay Modes from Ref. [149].

		alt	2.0 GeV hybrid	standard	IKP	reduced
2 <sup>+-</sup>	$\rho\pi$	D	1	4	2	2
	$\omega\eta$	D	.1	.5	.2	.1
	$\omega\eta'$	D	0	.03	0	0
	$K^*K$	D	.04	.2	.08	.04
	$b_1(1235)\pi$	P	4	5	2	164
		F	.02	.07	.01	.8
	$h_1(1170)\eta$	P	.2	.7	.1	6
	$K_2^*(1430)K$	P	—	.04	—	—
		F	—	0	—	—
	$K_1(1270)K$	P	0	.03	0	.6
		F	0	0	0	0
	$K_1(1400)K$	P	—	.3	—	—
		F	—	0	—	—
	$\rho(1450)\pi$	D	.02	.8	.06	.05
	$\omega(1420)\eta$	D	—	0	—	—
	$K^*(1410)K$	D	—	.01	—	—
	$\Gamma$		5	12	4	166
1 <sup>+-</sup>	$\rho\pi$	S	70	57	77	114
		D	.8	2	1	1
	$\omega\eta$	S	15	22	25	22
		D	.07	.3	.1	.06
	$\omega\eta'$	S	4	8	5	15
		D	0	.02	0	0
	$K^*K$	S	27	52	47	36
		D	.02	.1	.04	.02
	$b_1(1235)\pi$	P	Ø	Ø	Ø	231
	$h_1(1170)\eta$	P	Ø	Ø	Ø	9
	$K_2^*(1430)K$	P	—	1	—	—
		F	—	0	—	—
	$K_1(1270)K$	P	.04	.6	.02	5
	$K_0^*(1430)K$	P	—	.4	—	—
	$K_1(1400)K$	P	—	.4	—	—
	$\rho(1450)\pi$	S	42	240	150	199
		D	.01	.4	.04	.03
	$\omega(1420)\eta$	S	—	38	—	—
		D	—	0	—	—
	$K^*(1410)K$	S	—	110	—	—
		D	—	.01	—	—
	$\Gamma$		158	529	305	632

Table 9.20: Isoscalar Hybrid Decay Modes from Ref. [149].

			alt	2.0 GeV hybrid	standard	IKP	reduced
0 <sup>+-</sup>	$b_1(1235)\pi$	P	110	119	56	85	
	$h_1(1170)\eta$	P	4	17	3	2	
	$K_1(1270)K$	P	.7	10	.4	7	
	$K_1(1400)K$	P	—	1	—	—	
	$K(1460)K$	S	—	115	—	—	
	$\Gamma$		115	262	59	94	
1 <sup>++</sup>	$K^*K$	S	17	26	24	18	170
		D	.04	.3	.09	.04	.6
	$a_2(1320)\pi$	P	10	14	5	179	
		F	.01	.06	.01	.4	
	$a_1(1260)\pi$	P	28	30	14	232	
	$a_0(1450)\pi$	P	Ø	Ø	Ø	6	
	$f_2(1270)\eta$	P	—	1	—	—	
		F	—	0	—	—	
	$f_1(1285)\eta$	P	—	2	—	—	
	$f_0(1370)\eta$	P	Ø	Ø	Ø	—	
	$K_2^*(1430)K$	P	—	.4	—	—	
		F	—	0	—	—	
	$K_1(1270)K$	P	.07	1	.05	1	
	$K_0^*(1430)K$	P	—	0	—	—	
	$K_1(1400)K$	P	—	.7	—	—	
	$K^*(1410)K$	S	—	55	—	—	
		D	—	.01	—	—	
	$\Gamma$		55	130	43	436	

Table 9.21:  $s\bar{s}$  Hybrid Decay Modes from Ref. [149].

		alt	high mass	standard	IKP	reduced
$2^{-+}$	$K^*K$	P	6	13	11	8
	$K_2^*(1430)K$	S	28	29	21	44
		D	.03	.5	.02	1
	$K_1(1270)K$	D	.2	.5	.1	10
	$K_0^*(1430)K$	D	.02	.3	.01	.2
	$K_1(1400)K$	D	.06	.5	.03	.6
	$f_2'(1525)\eta$	S	—	20	—	—
		D	—	.2	—	—
	$f_1(1510)\eta$	D	—	.03	—	—
	$f_0(1370)\eta$	D	.01	.08	0	.1
	$K^*(1410)K$	P	2	27	6	5
	$\Gamma$		36	91	38	69
$1^{-+}$	$\eta'\eta$	P	0	0	0	44
	$K^*K$	P	6	13	11	8
	$K_2^*(1430)K$	D	.07	1	.04	$\emptyset$
	$K_1(1270)K$	S	14	10	11	14
		D	3	8	2	21
	$K_1(1400)K$	D	83	76	61	121
		D	.03	.2	.02	.4
	$f_2'(1525)\eta$	D	—	.04	—	—
	$f_1(1510)\eta$	S	—	21	—	—
		D	—	.02	—	—
	$K(1460)K$	P	1	45	4	3
	$\eta_s(1490)\eta$	P	—	15	—	—
	$K^*(1410)K$	P	2	27	6	5
	$\Gamma$		109	216	95	172
$0^{-+}$	$K^*K$	P	26	52	46	33
	$K_2^*(1430)K$	D	.4	6	.2	1
	$K_0^*(1430)K$	S	113	117	83	174
	$f_2'(1525)\eta$	D	—	.2	—	—
	$f_0(1370)\eta$	S	72	105	64	109
	$K^*(1410)K$	P	7	110	22	18
	$\Gamma$		218	390	215	335
$1^{--}$	$K^*K$	P	13	26	23	16
	$\phi\eta$	P	2	19	11	3
	$\phi\eta'$	P	.01	2	.1	.02
	$K_2^*(1430)K$	D	.1	2	.07	2
	$K_1(1270)K$	S	23	16	18	24
		D	.2	.6	.1	2
	$K_1(1400)K$	S	43	40	32	63
		D	.1	.6	.04	.7
	$h_1(1380)\eta$	S	—	—	$\emptyset$	—
		D	—	—	$\emptyset$	—
		D	.07	.6	.04	.3
	$K^*(1410)K$	P	3	55	11	9
	$\Gamma$		84	155	95	120

Table 9.22:  $s\bar{s}$  Hybrid Decay Modes from Ref. [149].

		alt	high mass	standard	IKP	reduced
2 <sup>+-</sup>	$K^*K$	D	1	3	2	1
	$\phi\eta$	D	.06	.8	.3	.08
	$\phi\eta'$	D	0	0	0	0
	$K_2^*(1430)K$	P	.3	1	.2	32
		F	0	.03	0	.01
	$K_1(1270)K$	P	.2	.3	.1	17
		F	.04	.2	.02	.6
	$K_1(1400)K$	P	3	8	2	28
		F	0	0	0	0
	$h_1(1380)\eta$	P	.3	2	.2	9
		F	0	0	0	0
	$K^*(1410)K$	D	.04	2	.1	.08
	$\Gamma$		5	18	5	79
1 <sup>+-</sup>	$K^*K$	S	20	19	34	42
		D	.6	2	1	.6
	$\phi\eta$	S	11	63	66	28
		D	.03	.5	.2	.04
	$\phi\eta'$	S	2	19	8	3
		D	0	.02	0	0
	$K_2^*(1430)K$	P	8	35	5	10
		F	0	.02	0	.01
	$K_1(1270)K$	P	4	5	2	122
	$K_0^*(1430)K$	P	3	14	2	18
	$K_1(1400)K$	P	3	8	2	4
	$h_1(1380)\eta$	P	$\emptyset$	$\emptyset$	$\emptyset$	14
	$K^*(1410)K$	S	39	206	181	201
		D	.02	1	.06	.04
	$\Gamma$		91	373	301	443
0 <sup>+-</sup>	$K_1(1270)K$	P	66	95	43	165
	$K_1(1400)K$	P	10	30	6	36
	$h_1(1380)\eta$	P	8	42	5	4
	$K(1460)K$	S	46	323	205	221
	$\Gamma$		130	490	259	426
1 <sup>++</sup>	$K^*K$	S	10	9	17	21
		D	1	4	2	1
	$K_2^*(1430)K$	P	3	13	2	27
		F	0	.05	0	.01
	$K_1(1270)K$	P	7	11	5	37
	$K_0^*(1430)K$	P	$\emptyset$	$\emptyset$	$\emptyset$	2
	$K_1(1400)K$	P	6	16	3	29
	$f_2'(1525)\eta$	P	—	2	—	—
		F	—	0	—	—
	$f_1(1510)\eta$	P	—	4	—	—
	$f_0(1370)\eta$	P	$\emptyset$	$\emptyset$	$\emptyset$	2
	$K^*(1410)K$	S	19	103	90	100
		D	.05	2	.1	.08
	$\Gamma$		46	164	119	219

Table 9.23:  $c\bar{c}$  Hybrid Decay Modes from Ref. [149].

			alt	high mass	standard	IKP	reduced
$2^{-+}$	$D^*D$	P	.5	.1	.8	4	19
	$D^{**}(2^+)D$	S	—	9	—	—	
		D	—	.2	—	—	
	$D^{**}(1_L^+)D$	D	—	.2	—	—	
	$D^{**}(0^+)D$	D	—	.2	—	—	
	$D^{**}(1_H^+)D$	D	—	.2	—	—	
	$\Gamma$		.5	10	.8	4	
$1^{-+}$	$D^*D$	P	.5	.1	.8	4	19
	$D^{**}(2^+)D$	D	—	.5	—	—	
	$D^{**}(1_L^+)D$	S	—	1.2	—	—	
		D	—	2.5	—	—	
	$D^{**}(1_H^+)D$	S	—	25	—	—	
		D	—	0	—	—	
	$\Gamma$		.5	29	.8	4	
$0^{-+}$	$D^*D$	P	2	.3	3	16	76
	$D^{**}(2^+)D$	D	—	2.5	—	—	
	$D^{**}(0^+)D$	S	—	25	—	—	
	$\Gamma$		2	28	3	16	
$1^{--}$	$D^*D$	P	1	.2	1.5	8	38
	$D^{**}(2^+)D$	D	—	1	—	—	
	$D^{**}(1_L^+)D$	S	—	7	—	—	
		D	—	.3	—	—	
	$D^{**}(1_H^+)D$	S	—	10	—	—	
		D	—	.2	—	—	
	$\Gamma$		1	19	1.5	8	
$2^{+-}$	$D^*D$	D	.2	.2	.3	1	7
	$D^{**}(2^+)D$	P	—	.5	—	—	
		F	—	.02	—	—	
	$D^{**}(1_L^+)D$	P	—	0	—	—	
		F	—	0	—	—	
	$D^{**}(1_H^+)D$	P	—	3	—	—	
		F	—	0	—	—	
	$\Gamma$		.2	4	.3	1	
$1^{+-}$	$D^*D$	S	.3	.1	.5	8	12
		D	.1	.1	.1	.5	4
	$D^{**}(2^+)D$	P	—	13	—	—	
		F	—	.01	—	—	
	$D^{**}(1_L^+)D$	P	—	2	—	—	
	$D^{**}(0^+)D$	P	—	8	—	—	
	$D^{**}(1_H^+)D$	P	—	2.5	—	—	
	$\Gamma$		.4	26	.6	8.5	

Table 9.24:  $c\bar{c}$  Hybrid Decay Modes from Ref. [149].

		alt	high mass	standard	IKP	reduced
0 <sup>+-</sup>	$D^{**}(1_L^+)D$	P	—	25	—	—
	$D^{**}(1_H^+)D$	P	—	15	—	—
	$\Gamma$	—	40	—	—	—
1 <sup>++</sup>	$D^*D$	S	.2	.1	.3	1
		D	.2	.2	.3	.3
	$D^{**}(2^+)D$	P	—	5	—	—
		F	—	.03	—	—
	$D^{**}(1_L^+)D$	P	—	5	—	—
	$D^{**}(0^+)D$	P	—	$\emptyset$	—	—
	$D^{**}(1_H^+)D$	P	—	5	—	—
	$\Gamma$	—	.4	15	.6	1.3

Table 9.25: Comparison of the decay widths of the 1<sup>+-</sup> hybrid meson for the flux tube model and QCD sum rule approaches.

	QCDSR	Flux Tube Model	PDG ( $\pi_1(1600)$ )
$b_1\pi$ (MeV)	unstable	$40 \pm 20$	seen
$f_1\pi$ (MeV)	100	$10 \pm 5$	seen
$\rho\pi$ (MeV)	$40 \pm 20$	9	seen
$K^*K$ (MeV)	8	0.6	no
$\eta'\pi$ (MeV)	3	small	seen
$\eta\pi$ (MeV)	0.3	small	no

It is interesting to compare QCD sum rule predictions with those of the flux tube model, since the bases of these two approaches are contradictory. The former is based on an  $\alpha_s$  expansion while the latter is based on the strong coupling expansion. From Table 9.25, the decay patterns from these two approaches are seen to be very similar although the partial decay widths for each channel are quite different:

$$\Gamma(f_1\pi) > \Gamma(\rho\pi) > \Gamma(K^*K) > \Gamma(\eta'\pi) > \Gamma(\eta\pi). \quad (9.4.16)$$

### Comments

It is important to note that the gluon inside the hybrid meson can easily split into a  $q\bar{q}$  pair. Therefore, tetraquarks can always have the same quantum numbers as hybrid mesons, including exotic ones. The discovery of a candidate hadron with  $J^{PC} = 1^{-+}$  does not ensure that it is an exotic hybrid meson. One has to exclude the tetraquark possibility based on its mass, decay width, decay patterns *etc.* This argument holds for the  $\pi_1(1400)$  and  $\pi_1(1600)$  hybrid candidates.

The flux tube model predicts that hybrid mesons prefer to decay into a pair of mesons with  $L = 1$  and  $L = 0$ . Heavy hybrid mesons tend to decay into one  $P$ -wave heavy meson and one pseudoscalar meson according to a light-cone QCD sum rule calculation [156]. A

lattice QCD simulation suggests the string breaking mechanism may play an important role for the decays of heavy quarkonium hybrids [157]. When the string between the heavy quark and antiquark breaks, light mesons are created. As a result, the preferred final states are a heavy quarkonium plus light mesons. However, readers should exercise caution with these so-called “selection rules.” None of them have been tested experimentally because no  $1^{-+}$  hybrid candidates have yet been established unambiguously.

### 9.4.2 Signatures of the hybrid mesons

Hybrid mesons are color-singlet composites of constituent quarks and gluons, such as  $q\bar{q}g$  bound states. Evidence for the existence of hybrid mesons would be direct proof of the existence of the gluonic degree of freedom and the validity of QCD. The conventional wisdom is that it would be more fruitful to search for low-lying hybrid mesons with exotic quantum numbers than to search for glueballs. Hybrids have the additional attraction that, unlike glueballs, they span complete flavor nonets and, thus, provide many possibilities for experimental detection. In addition, the lightest hybrid multiplet includes at least one  $J^{PC}$  exotic state.

In searches for hybrids, there are two primary methods to distinguish them from conventional states. One is to look for an excess of observed states over the number predicted by the quark model. The drawback to this method is that it depends on a good understanding of the hadron spectrum in a mass region where it is still rather murky. At present, phenomenological models have not been tested experimentally to the extent to where a given state can be reliably ruled out as a conventional meson. The situation is further muddled by the expectation of mixing between conventional  $q\bar{q}$  states and hybrids with the same  $J^{PC}$  quantum numbers. The other approach is to search for the states with quantum numbers that cannot be accommodated in the quark model. The discovery of exotic quantum numbers would be definite evidence of something new.

Some experimental searches for an isovector  $1^{-+}$  hybrid have claimed positive evidence for the existence of such a state. Evidence for an exotic  $\pi\eta$  resonance in the charge exchange reaction  $\pi^-p \rightarrow \eta\pi^0n$  was claimed by the GAMS collaboration [158]. These findings were, however, found to be ambiguous in later analyses [159]. Evidence for an exotic  $P$ -wave  $\pi\eta$  state was also reported by the VES experiment [160]. The observation of a  $\pi\eta$  resonance, with a mass and width that coincide with those of the  $a_2(1320)$ , was claimed by a KEK group [161]. However, here feedthrough from the dominant  $D$ -wave into the  $P$ -wave cannot be excluded. E852 at BNL reported the observation of an isovector  $1^{-+}$  state with a mass and width of  $(1370 \pm 16^{+50}_{-30})$  MeV and  $(385 \pm 40^{+65}_{-105})$  MeV, respectively, produced in  $\pi^-p \rightarrow \eta\pi^-p$  at 18 GeV/c [162]. In these studies, the  $\pi\eta$   $P$ -wave is seen to have a forward-backward asymmetry, which is evidence for interference between even and odd  $\pi\eta$  partial waves. Subsequently, the Crystal Barrel Collaboration found evidence for an  $I^G(J^{PC}) = 1^-(1^{-+})$  exotic state [163] with mass and width of  $(1400 \pm 20 \pm 20)$  MeV and  $(310 \pm 50^{+50}_{-30})$  MeV, respectively, in the reaction  $\bar{p}n \rightarrow \pi^-\pi^0\eta$  produced by stopping antiprotons in liquid deuterium. The partial wave analysis of data on  $p\bar{p}$  annihilation at rest in liquid hydrogen ( $\text{LH}_2$ ) into  $\pi^0\pi^0\eta$  by the Crystal Barrel shows that the inclusion of a  $\pi\eta$   $P$ -wave in the fit gives supporting evidence for an  $1^{-+}$  exotic state with parameters compatible with the previous findings [164]. Another isovector  $1^{-+}$  meson, the  $\pi_1(1600)$ , was observed in  $\rho\pi$  [165],  $\eta'\pi$  [166], and  $f_1\pi$  [167] final states.

The latter experiment also revealed a higher state,  $\pi_1(2000)$  [167], and  $f_1\pi$  decays of the  $\pi_1(1600)$  and the  $\pi_1(2000)$  are measured. Such a rich spectrum of exotic mesons is somewhat puzzling, since lattice QCD [168] and flux-tube model [169, 170] calculations predict only one low-mass  $\pi_1$  meson.

In the flux-tube model, the lightest  $1^{-+}$  isovector hybrid is predicted to decay primarily into  $b_1\pi$  [169]. The  $f_1\pi$  branch is also expected to be large and many other decay modes are suppressed. However, few experiments have addressed the  $b_1\pi$  and  $f_1\pi$  decay channels. The VES collaboration reported a broad  $1^{-+}$  peak in  $b_1\pi$  decay [171], and Lee, *et al.* [172] observed significant  $1^{-+}$  strength in  $f_1\pi$  decay. In neither case, however, was a definitive resonance interpretation of the  $1^{-+}$  wave possible. Preliminary results from a later VES analysis show the excitation of the  $\pi_1(1600)$  [173]. The E852 experiment at BNL reported the observation of a strong excitation of the exotic  $\pi_1(1600)$  in the  $(b_1\pi)^-$  decay channel, and confirmed the exotic  $\pi_1(2000)$  in the reaction  $\pi^-p \rightarrow \pi^+\pi^-\pi^-\pi^0\pi^0p$  [174].

### 9.4.3 Monte-Carlo simulation of $1^{-+}$ exotic state $\pi_1(1400)$

From simple counting of the powers of the electromagnetic and strong coupling constants, one obtains:

$$\Gamma(J/\psi \rightarrow MH) > \Gamma(J/\psi \rightarrow MM') \approx \Gamma(J/\psi \rightarrow MG), \quad (9.4.17)$$

where  $M$  stands for an ordinary  $q\bar{q}$  meson,  $G$  for a glueball and  $H$  for a hybrid state. Therefore, hadronic  $J/\psi$  decays provide a good place to search for hybrid states. A full Monte-Carlo simulation of the decays  $J/\psi \rightarrow \rho\eta\pi^0$ , with  $\rho \rightarrow \pi^+\pi^-$  and  $\eta \rightarrow \gamma\gamma$ , was done, and a partial wave analysis was carried out to study the *BES-III* sensitivity to an  $1^{-+}$  exotic state in the  $\eta\pi^0$  final state. The simulation is based on GEANT4 and the *BES-III* detector design.

For  $J/\psi \rightarrow \rho\eta\pi^0$ , we generated  $\rho\pi_1(1400)$  as well as the expected non-exotic processes  $J/\psi \rightarrow \rho a_0(980)$ ,  $\rho a_2(1320)$  and  $\rho a_2(1700)$ , with the decay branching fractions:

$$\begin{aligned} Br(J/\psi \rightarrow \rho a_0(980)) &\sim 4.38\% \\ Br(J/\psi \rightarrow \rho\pi_1(1400)) &\sim 14.57\% \\ Br(J/\psi \rightarrow \rho a_2(1320)) &\sim 21.39\% \\ Br(J/\psi \rightarrow \rho a_2(1700)) &\sim 41.64\%, \end{aligned}$$

and considered the angular distributions of different spin-parities and the interference between them. The main background to  $J/\psi \rightarrow \rho\eta\pi^0$  comes from  $J/\psi \rightarrow \gamma\rho^+\rho^-$ , which were also generated.

To select candidate events, we require two good charged tracks with zero net charge and at least four good photons. A good charged track is one that is within the polar angle region  $|\cos\theta| < 0.93$  and has points of closest approach that are within 1 cm of the beam axis and within 5 cm of the center of the interaction region. The two charged tracks are required to consist of an unambiguously identified  $\pi^+\pi^-$  pair. Candidate photons are required to have an energy deposit in the electromagnetic calorimeter that is greater than 50 MeV and to be isolated from charged tracks by more than  $20^\circ$  in both the

Table 9.26: Input and output comparison of masses, widths and branching fractions. Here the masses and widths of  $a_0(980)$  and  $a_2(1700)$  are fixed to PDG values.

		$a_0(980)$	$a_2(1320)$	$\pi_1(1400)$	$a_2(1700)$
Mass (MeV)	input	0.985	1.318	1.376	1.732
	output	fixed	$1.320 \pm 0.002$	$1.380 \pm 0.008$	fixed
Width (MeV)	input	0.08	107	360	0.194
	output	fixed	$112 \pm 4$	$376 \pm 16$	fixed
Fraction	input	4.38	21.39	14.57	43.36
	output	$4.55 \pm 0.30$	$19.50 \pm$	$14.53 \pm$	$41.64 \pm$

x-y and r-z planes; at least four photons are required. A four-constraint (4C) energy-momentum conservation kinematic fit is performed to the  $\pi^+\pi^-\gamma\gamma\gamma\gamma$  hypothesis and the  $\chi^2_{4C}$  is required to be less than 15. For events with more than four selected photons, the combination with the smallest  $\chi^2$  is chosen. The photons from the decays of  $\pi^0$  and  $\eta$  are selected based on the combination with the smallest  $\delta$ , where

$$\delta = \sqrt{(M_\eta - M\gamma_i\gamma_j)^2 + (M_{\pi^0} - M\gamma_k\gamma_l)^2}. \quad (9.4.18)$$

All of the generated  $J/\psi \rightarrow \rho\eta\pi^0$  events are subjected to the selection criteria described above. The points with error bars in Fig. 9.18(a) show the  $\eta\pi^0$  invariant mass spectrum for the surviving events and the shaded area shows the background. The signal and background events are normalized to  $1.5 \times 10^8 J/\psi$  events. The mass resolutions and efficiencies in the 1.4 GeV mass region are about 10 MeV and 27.2% respectively.

All of the signal events are added by taking into account possible interference between them, and the backgrounds are added incoherently. A partial wave analyses is applied to these events using the covariant helicity coupling amplitude method to construct the amplitudes. The relative magnitudes and phases of the amplitudes are determined by a maximum likelihood fit. Each resonance is represented by a constant-width Breit-Wigner functions of the form

$$BW_X = \frac{m\Gamma}{s - m^2 + im\Gamma},$$

where  $s$  is the square of the two-particle invariant mass,  $m$  and  $\Gamma$  are the mass and width of intermediate resonance  $X$ , respectively. The background events from  $J/\psi \rightarrow \gamma\rho^+\rho^-$  are given the opposite log likelihood in the fit to cancel the background events in the data. In this analysis, the masses and widths of  $a_0(980)$  and  $a_2(1700)$  are fixed to PDG values and those for  $a_2(1320)$  and  $\pi_1(1400)$  are allowed to float.

Figure 9.18 (a) shows a comparison of the  $\eta\pi^0$  invariant mass spectrum for the generated events and that from PWA projections. The consistency is reasonable. Figure 9.18 (b) indicates the contributions from each component. The angular distributions for the generated events and that from the PWA are shown in Figs. 9.19.

A comparison of the input and output values for the masses, widths and branching fractions is shown in Table 9.26, where the output masses, widths and branching fractions that are obtained from the PWA analysis agree with the input values reasonably well.

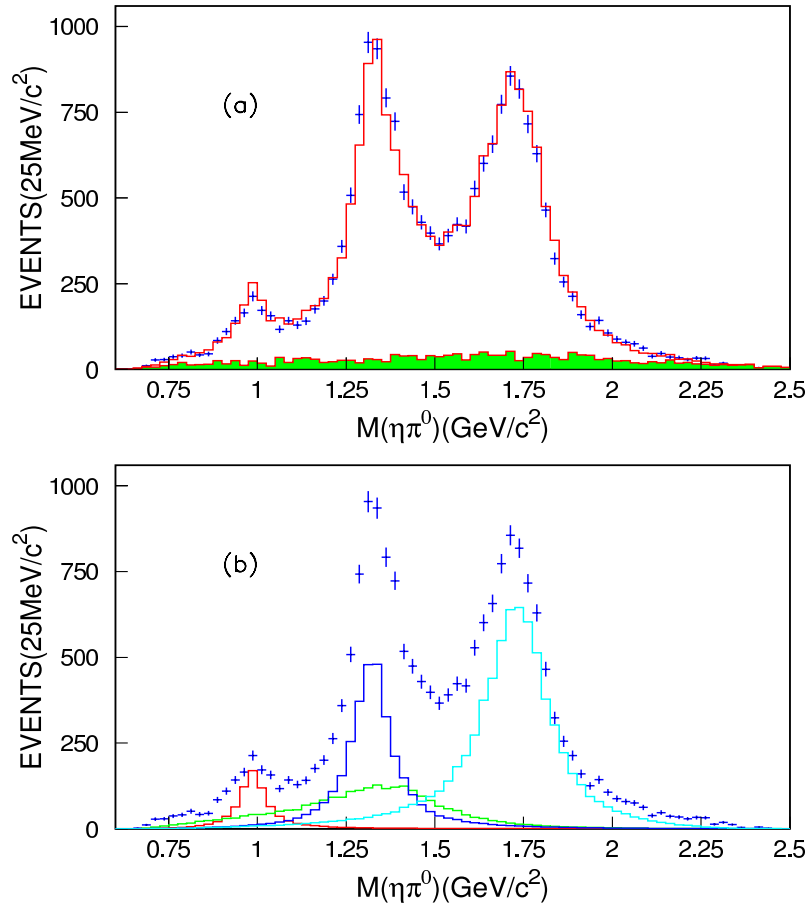


Figure 9.18: The  $\eta\pi^0$  invariant mass spectrum for  $J/\psi \rightarrow \rho\eta\pi^0$ . The signals are Monte-Carlo events generated by taking into account the angular distributions of each resonance and the interference between them, as described in the text; the backgrounds are added to the signals incoherently. The sum of the signals and backgrounds are shown as the point with error bars. (a). The comparison of the generated mass spectrum and PWA projection from all contributions. The background is shown as the shaded region. (b). The contribution to the PWA projections of the different resonant components.

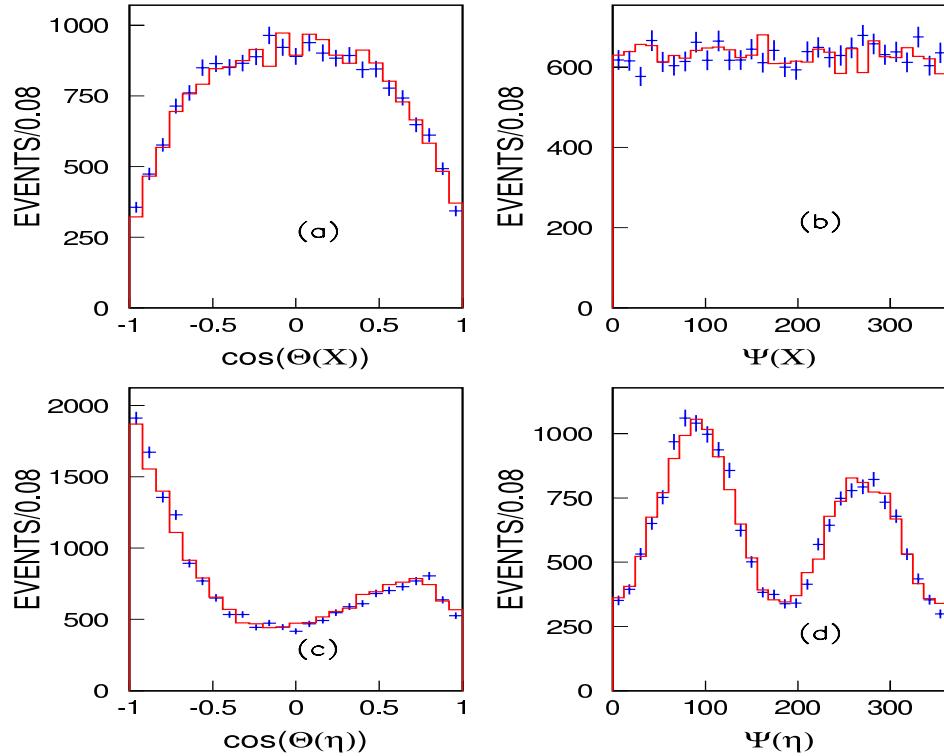


Figure 9.19: Angular distributions for  $J/\psi \rightarrow \rho\eta\pi^0$ . The points with error bars indicate the distributions for signal and background events and the histograms show the PWA results.

The Monte-Carlo simulation indicates that the partial wave analysis is able to separate components with similar masses but with different spin-parities (*i.e.*,  $a_2(1320)$  and  $\pi_1(1400)$ ), when the statistics are large and the detector performance is good. With a large statistics sample, it will also be possible to measure the phase motion, which would give additional convincing evidence for the existence of a resonance.

## 9.5 Multiquarks

### 9.5.1 Multiquark candidates

When  $N$  ( $N \geq 4$ ) quarks-antiquarks are confined within a single MIT bag, a *multiquark* state is formed. The color structure within a multiquark state is complicated and not unique. It always has a component that is the product of two (or more) color-singlet hadrons. A special mechanism is needed to prevent the multiquark from falling apart easily and thereby becoming extremely broad when it lies above threshold for decay into conventional hadrons.

There are several well known multiquark candidates. The first one is the  $H$  dibaryon suggested by Jaffe decades ago [175]. On-going doubly strange hypernuclei search experiments have pushed its binding energy to be less than several MeV, about to the point where the existence of the  $H$  existence is now rather dubious. Jaffe also suggested that the low-lying scalar nonet are tetraquarks because of their low and inverted mass pattern [176]. The third one is the rapidly fading  $\Theta^+$  pentaquark. Interested readers may consult a recent review [177].

In general, a multiquark state is expected to have a broad width since it can easily fall apart into mesons and/or baryons when its mass is above the mass threshold for producing these hadrons. Multiquark states may only be experimentally observable when their masses are near these mass thresholds — either below or just above them — otherwise the widths of the multiquark states might be too wide to be experimentally distinguishable from non-resonant background. The  $J/\psi$  meson serves a unique role for searches of new hadrons and studies of light hadron spectroscopy. Recently, a number of new structures have been observed in  $J/\psi$  decays, including a strong near-threshold mass enhancement in the  $p\bar{p}$  invariant mass spectrum from  $J/\psi \rightarrow \gamma p\bar{p}$  decays [178], the  $p\bar{\Lambda}$  and the  $K^-\bar{\Lambda}$  mass spectra in  $J/\psi \rightarrow pK^-\bar{\Lambda}$  decays [179], the  $\omega\phi$  mass spectrum in the double-OZI suppressed decay  $J/\psi \rightarrow \gamma\omega\phi$  [88], and two new resonances, the  $X(1835)$ , in  $J/\psi \rightarrow \gamma\pi^+\pi^-\eta'$  decays [180] as well as a very broad  $1^{--}$  resonant structure in the  $K^+K^-$  invariant mass spectrum from  $J/\psi \rightarrow K^+K^-\pi^0$  decays. All of these new structures are possibly multiquark states.

#### Observation of a strong near-threshold mass enhancement in the $p\bar{p}$ invariant mass spectrum

The BES Collaboration observed an anomalous strong  $p\bar{p}$  mass enhancement near the  $m_p + m_{\bar{p}}$  mass threshold in  $J/\psi \rightarrow \gamma p\bar{p}$  decays [178]. It can be fit with an  $S$ - or  $P$ - wave Breit-Wigner resonance function; in the case of the  $S$ -wave fit, the mass is below  $m_p + m_{\bar{p}}$

at  $1859^{+3}_{-10-0.5}$  MeV and the width is smaller than 30 MeV at the 90% C.L. (see Fig. 9.20).

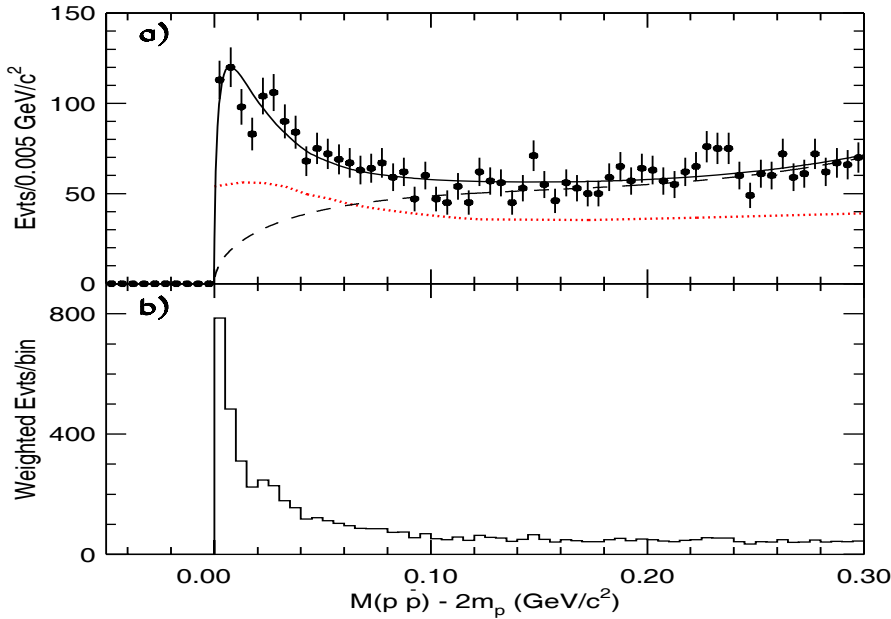


Figure 9.20: (a) The near-threshold  $M_{p\bar{p}} - 2m_p$  distribution for the  $J/\psi \rightarrow \gamma p\bar{p}$  events. The dashed curve is the background from  $\pi^0 p\bar{p}$  final states. The dotted curve indicates how the acceptance varies with  $p\bar{p}$  invariant mass. (b) The  $M_{p\bar{p}} - 2m_p$  distribution with events weighted by  $q_0/q$ .

It is interesting to note that such a strong mass threshold enhancement is not observed in  $p\bar{p}$  cross section measurements, also not in  $B$  decays [181], nor in radiative  $\psi(2S)$  or  $\Upsilon(1S) \rightarrow \gamma p\bar{p}$  decays [182, 183], and not in  $J/\psi \rightarrow \omega p\bar{p}$  [184]. These non-observations disfavor a purely  $p\bar{p}$  FSI interpretation of the strong mass threshold enhancement which is, as of now, uniquely observed in the  $J/\psi \rightarrow \gamma p\bar{p}$  decay process.

This surprising experimental observation has stimulated a number of theoretical speculations [185, 186, 187, 188, 189, 190]. Among these, the most intriguing is that it is an example of a  $p\bar{p}$  bound state, sometimes called *baryonium* [185, 191, 188], which has been the subject of many experimental searches [192].

It is worth noting that if the observed  $p\bar{p}$  mass enhancement is due to a resonance, the decay branching fraction (BF) to  $p\bar{p}$  is larger than expected for a conventional  $q\bar{q}$  meson. From Ref. [178],  $B(J/\psi \rightarrow \gamma X) \cdot B(X \rightarrow p\bar{p}) = (7.0 \pm 0.4(\text{stat})^{+1.9}_{-0.8}(\text{syst})) \times 10^{-5}$ . Measurements of the inclusive photon spectrum in  $J/\psi$  decays by the Crystal Ball group limit the branching fraction for radiative production of a narrow resonance around 1.85 GeV to be below  $2 \times 10^{-3}$  (an estimate that is based on data reported in Ref. [139]). Thus, if a resonance is responsible for producing the observed enhancement, it would have a branching fraction to  $p\bar{p}$  that is larger than 4%, which would be the *largest*  $p\bar{p}$  branching fraction of all known mesons [259]. Since decays to  $p\bar{p}$  are kinematically possible only for

a small portion of the high-mass tail of the resonance and have very limited phase space, a large  $p\bar{p}$  branching fraction implies an unusually strong coupling to  $p\bar{p}$ , as expected for a  $p\bar{p}$  bound state.

### Observation of $X(1835)$ in $J/\psi \rightarrow \gamma\pi^+\pi^-\eta'$

The baryonium interpretation of the  $p\bar{p}$  mass enhancement requires a new resonance with a mass around 1.85 GeV, which would be supported by the observation of a resonance in other decay channels. Possible strong decay channels for a  $p\bar{p}$  bound state, suggested in Ref. [187, 188], include  $\pi^+\pi^-\eta'$ .

An analysis of  $J/\psi \rightarrow \gamma\pi^+\pi^-\eta'$  with  $\eta' \rightarrow \eta\pi^+\pi^-$  and  $\eta' \rightarrow \gamma\rho$  is reported in Ref. [180]. For both the  $\eta' \rightarrow \eta\pi^+\pi^-$  and  $\eta' \rightarrow \gamma\rho$  data samples, the  $\pi^+\pi^-\eta'$  invariant mass spectra for the selected events exhibit peaks at a mass around 1835 MeV. Figure 9.21 is the  $\eta'\pi^+\pi^-$  mass spectrum for both  $\eta'$  decay modes combined, where a distinct peak near 1835 MeV is observed. The combined spectrum is fitted with a Breit-Wigner (BW) function convolved with a Gaussian mass resolution function (with  $\sigma = 13$  MeV) to represent the  $X(1835)$  signal plus a smooth polynomial background. The mass and width obtained from the fit are  $M = 1833.7 \pm 6.1$  MeV and  $\Gamma = 67.7 \pm 20.3$  MeV, respectively. The signal yield from the fit is  $264 \pm 54$  events with a confidence level of 45.5% ( $\chi^2/d.o.f. = 57.6/57$ ) and  $-2\ln L = 58.4$ . A fit to the mass spectrum without a BW signal function returns  $-2\ln L = 126.5$ . The change in  $-2\ln L$  with  $\Delta(d.o.f.) = 3$  corresponds to a statistical significance of  $7.7\sigma$  for the signal.

Using MC-determined selection efficiencies of 3.72% and 4.85% for the  $\eta' \rightarrow \pi^+\pi^-\eta$  and  $\eta' \rightarrow \gamma\rho$  modes, respectively, we determine a product branching fraction of

$$B(J/\psi \rightarrow \gamma X(1835)) \cdot B(X(1835) \rightarrow \pi^+\pi^-\eta') = (2.2 \pm 0.4) \times 10^{-4}.$$

The mass and width of the  $X(1835)$  are not compatible with any known meson resonance [259]. We examined the possibility that the  $X(1835)$  is responsible for the  $p\bar{p}$  mass threshold enhancement observed in radiative  $J/\psi \rightarrow \gamma p\bar{p}$  decays [178]. Subsequent to the publication of Ref. [178], it was pointed out that the  $S$ -wave BW function used for the fit should be modified to include the effect of final-state-interactions (FSI) on the shape of the  $p\bar{p}$  mass spectrum [189, 190]. Redoing the  $S$ -wave BW fit to the  $p\bar{p}$  invariant mass spectrum of Ref. [178] with the zero Isospin and  $S$ -wave FSI factor of Ref. [190] included, yields a mass  $M = 1831 \pm 7$  MeV and a width  $\Gamma < 153$  MeV (at the 90% C.L.); values that are in good agreement with the mass and width of  $X(1835)$  seen in  $\pi\pi\eta'$ . Moreover, according to Ref. [188], the  $\pi\pi\eta'$  decay mode is expected to be a strong sub-threshold decay channel for a  $p\bar{p}$  bound state. Thus, the  $X(1835)$  resonance is a prime candidate for the source of the  $p\bar{p}$  mass threshold enhancement in  $J/\psi \rightarrow \gamma p\bar{p}$  process. In this case, the  $J^{PC}$  and  $I^G$  of the  $X(1835)$  could only be  $0^{-+}$  and  $0^+$ , which can be tested in future experiments. Also in this context, the relative  $p\bar{p}$  decay strength is quite strong:  $B(X \rightarrow p\bar{p})/B(X \rightarrow \pi^+\pi^-\eta') \sim 1/3$  (The product BF determined from the fit that includes FSI effects on the  $p\bar{p}$  mass spectrum is within the systematic errors of the result reported in Ref. [178].) Since decays to  $p\bar{p}$  are kinematically allowed only for a small portion of the high-mass tail of the resonance and have very limited phase space, the large  $p\bar{p}$  branching fraction implies an unusually strong coupling to  $p\bar{p}$ , as expected

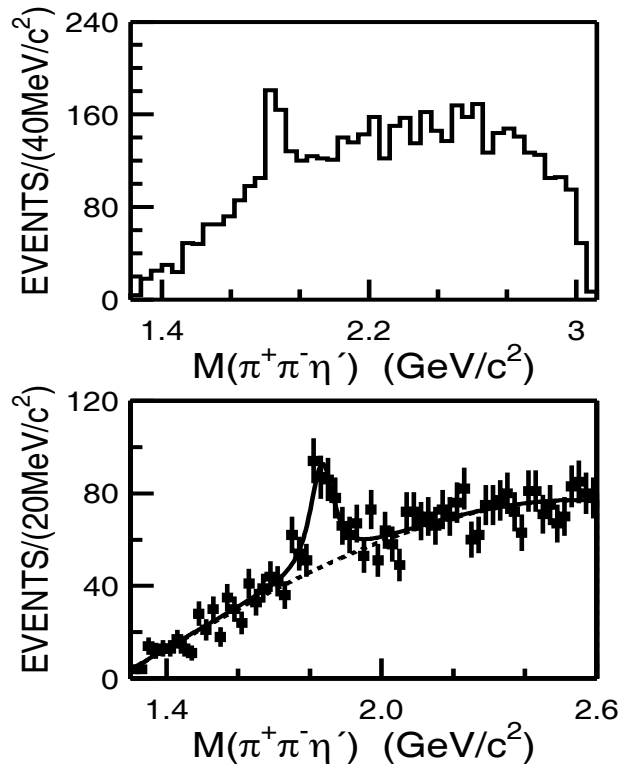


Figure 9.21: The  $\pi^+\pi^-\eta'$  invariant mass distribution for selected events from both the  $J/\psi \rightarrow \gamma\pi^+\pi^-\eta'(\eta' \rightarrow \pi^+\pi^-\eta, \eta \rightarrow \gamma\gamma)$  and  $J/\psi \rightarrow \gamma\pi^+\pi^-\eta'(\eta' \rightarrow \gamma\rho)$  analyses. The bottom panel shows the fit (solid curve) to the data (points with error bars); the dashed curve indicates the background function.

for a  $p\bar{p}$  bound state [191, 193]. However, other possible interpretations of the  $X(1835)$  that have no relation to the  $p\bar{p}$  mass threshold enhancement are not excluded.

### Observation of $p\bar{\Lambda}$ mass threshold enhancement in $J/\psi \rightarrow pK^-\bar{\Lambda}$

An analysis of  $J/\psi \rightarrow pK^-\bar{\Lambda}$  is described in detail in Ref. [179]. The  $p\bar{\Lambda}$  invariant mass spectrum for selected events is shown in Fig. 9.22(a), where an enhancement is evident near the  $m_\Lambda + m_p$  mass threshold. No corresponding structure is seen in a sample of  $J/\psi \rightarrow pK^-\bar{\Lambda}$  Monte-Carlo events generated with a uniform phase space distribution. The  $pK^-\bar{\Lambda}$  Dalitz plot is shown in Fig. 9.22(b), where, in addition to bands for the well established  $\Lambda^*(1520)$  and  $\Lambda^*(1690)$ , a significant  $N^*$  band near the  $K^-\bar{\Lambda}$  mass threshold, and a  $p\bar{\Lambda}$  mass enhancement in the right-upper part of the Dalitz plot, isolated from both the  $\Lambda^*$  and  $N^*$  bands, are evident.

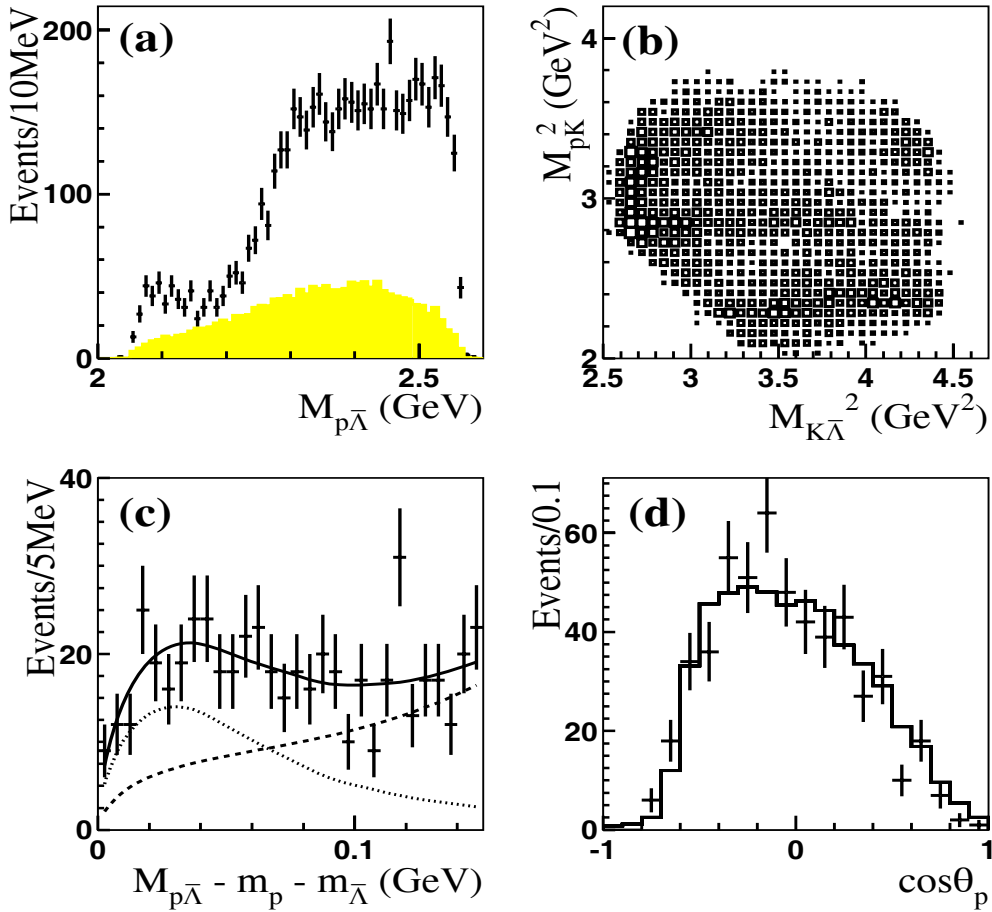


Figure 9.22: (a) The points with error bars indicate the measured  $p\bar{\Lambda}$  mass spectrum from  $/\psi \rightarrow K^+\bar{p}\Lambda$  decays; the shaded histogram indicates phase space MC events (arbitrary normalization). (b) The Dalitz plot for the selected event sample. (c) A fit (solid line) to the data. The dotted curve indicates the Breit-Wigner signal and the dashed curve the phase space ‘background’. (d) The  $\cos\theta_p$  distribution under the enhancement, the points are data and the histogram is the MC (normalized to the data).

The  $p\bar{\Lambda}$  invariant mass enhancement is fitted with an acceptance-weighted  $S$ -wave Breit-Wigner function, together with a function describing the phase space contribution, as shown in Fig. 9.22(c). The fit gives a peak mass of  $m = 2075 \pm 12$  MeV and a width  $\Gamma = 90 \pm 35$  MeV. The enhancement deviates from the shape of the phase space contribution with a statistical significance of about  $7\sigma$ .

The fit yields  $N_{res} = 238 \pm 57$  signal events, corresponding to a product branching fraction

$$BR(J/\psi \rightarrow K^- X)BR(X \rightarrow p\bar{\Lambda}) = (5.9 \pm 1.4) \times 10^{-5}.$$

Searches for the same enhancement in  $K\pi$  and  $K\pi\pi$  modes in the  $J/\psi, \psi' \rightarrow KK\pi, KK\pi\pi$  decays would help to confirm the presence of this anomalous peak and understand its nature, and in particular distinguish whether or not it is due to a conventional  $K^*$  meson, a multiquark state, or a baryon-antibaryon resonance. If its decay widths to  $K\pi$  and  $K\pi\pi$  modes are much smaller than to  $p\bar{\Lambda}$ , its interpretation as a conventional  $K^*$  meson would be disfavored.

### Observation of $K^-\bar{\Lambda}$ mass threshold enhancement in $J/\psi \rightarrow pK^-\bar{\Lambda}$

In the Dalitz plot of Fig. 9.22(b), a clear band is also observed near the  $K^-\bar{\Lambda}$  mass threshold. We have performed a preliminary partial wave analysis (PWA) of these data and determined that the mass of this threshold structure (dubbed  $N_X^*$ ) is in the range between 1500 to 1650 MeV, with a width between 70 and 110 MeV and a favored spin-parity of  $1/2^-$ . It has a product branching fraction  $B(J/\psi \rightarrow \bar{p}N_X^*)B(N_X^* \rightarrow K^-\bar{\Lambda})$  that is larger than  $2 \times 10^{-4}$ .

Considering the fact that the  $N_X^*$  mass is below or very close to the  $K^-\bar{\Lambda}$  mass threshold, the phase space available to the  $K^-\bar{\Lambda}$  final state is very small. Thus, the large branching fraction to  $K^-\bar{\Lambda}$  indicates that the  $N_X^*$  has very strong coupling to  $K^-\bar{\Lambda}$ , suggesting that it could be the  $K^-\bar{\Lambda}$  resonant state predicted by the chiral- $SU(3)$  quark model [194].

### Observation of a broad $1^{--}$ resonant structure in the $K^+K^-$ mass spectrum in $J/\psi \rightarrow K^+K^-\pi^0$

A broad peak is observed at low  $K^+K^-$  invariant masses in  $J/\psi \rightarrow K^+K^-\pi^0$  decays; the analysis is described in detail in Ref. [195]. The Dalitz plot for the selected  $K^+K^-\pi^0$  events is shown in Fig. 9.23(b), where there is a broad  $K^+K^-$  (diagonal) band in addition to prominent  $K^*(892)$  and  $K^*(1410)$  signals. This band corresponds to the broad low-mass peak observed around 1.5 GeV in the  $K^+K^-$  invariant mass projection shown in Fig. 9.23(c).

A partial wave analysis shows that the  $J^{PC}$  of this structure is  $1^{--}$ . Its pole position is determined to be  $(1576^{+49+98}_{-55-91})$  MeV -  $i(409^{+11+32}_{-12-67})$  MeV, and the product branching fraction is  $B(J/\psi \rightarrow X\pi^0) \cdot B(X \rightarrow K^+K^-) = (8.5 \pm 0.6^{+2.7}_{-3.6}) \times 10^{-4}$ , where the first errors are statistical and the second are systematic. These parameters are not compatible with any known meson resonances [259].

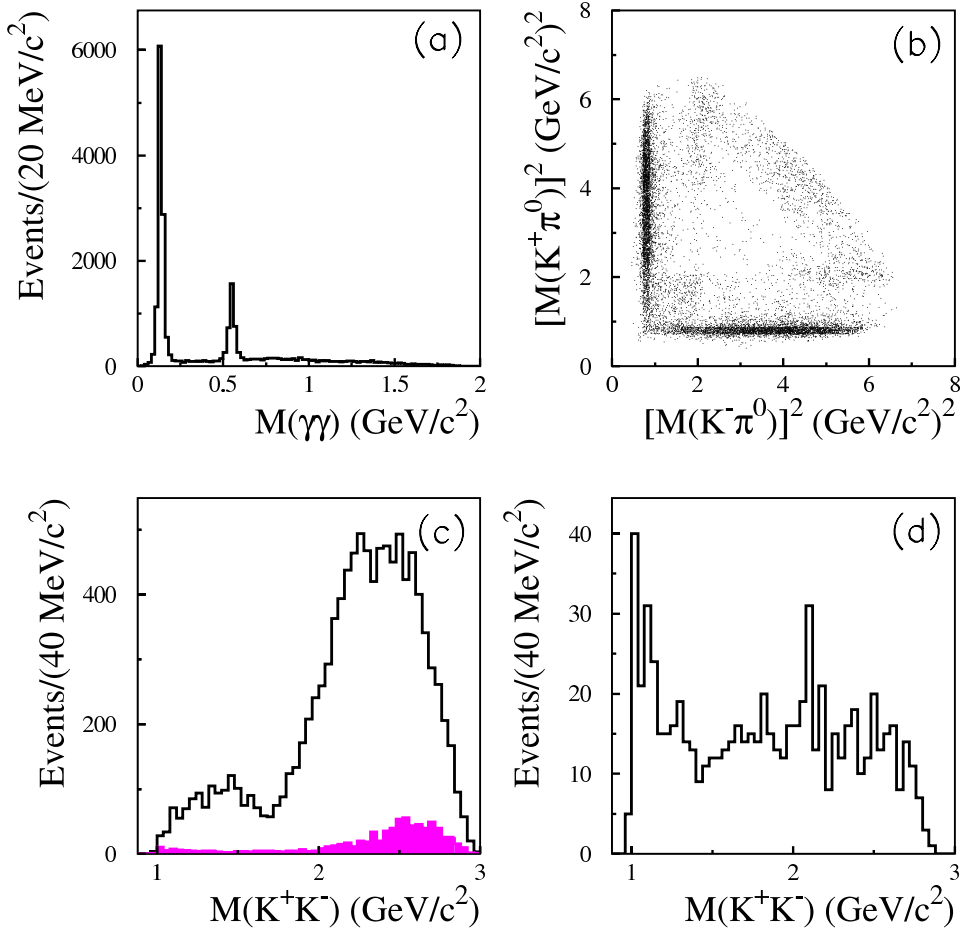


Figure 9.23: (a) The  $\gamma\gamma$  invariant mass distribution for  $J/\psi \rightarrow \gamma\gamma K^+K^-$  events. (b) The Dalitz plot for  $K^+K^-\pi^0$  candidate events. (c) The  $K^+K^-$  invariant mass distribution for the  $K^+K^-\pi^0$  candidate events; the solid histogram is data and the shaded histogram is the background (normalized to the data). (d) The  $K^+K^-$  invariant mass distribution for the  $\pi^0$  mass sideband events (not normalized).

To understand the nature of this broad  $1^{--}$  peak, it is important to search for a similar structure in  $J/\psi \rightarrow K_S K^\pm \pi^\mp$  decays to determine its isospin. It would also be intriguing to search for it in  $K^* K$ ,  $K K \pi$  decay modes. In the mass region covered by the  $X$ , there are several other  $1^{--}$  states, such as the  $\rho(1450)$  and  $\rho(1700)$ , but the width of the  $X$  is much broader than the widths of any of these other meson states. This may be an indication that the  $X$  has a different nature than these other mesons. For example, the very broad width is suggestive of a multiquark state.

### 9.5.2 Simulation of the $X(1835)$ in $J/\psi$ decays at *BES-III/BEPCII*

The numerous near-threshold enhancements observed at BESII motivated us to simulate the production of  $X(1835)$  in  $J/\psi \rightarrow \gamma X(1835)$ ,  $J/\psi \rightarrow \omega X(1835)$  and  $J/\psi \rightarrow \phi X(1835)$ , with  $X(1835) \rightarrow \eta' \pi^+ \pi^-$ , at *BES-III*.

#### $J/\psi \rightarrow \gamma X(1835)$

In the simulation, we only focused on the decay mode of  $X(1835) \rightarrow \eta' \pi^+ \pi^-$  with  $\eta' \rightarrow \eta \pi^+ \pi^-$  and  $\eta \rightarrow \gamma \gamma$ . Therefore, the final-state composition is  $3\gamma 2(\pi^+ \pi^-)$ . The main backgrounds come from  $J/\psi \rightarrow \eta' \pi^+ \pi^- \pi^0$ ,  $\omega \eta'$ ,  $b_1 \pi$  and  $\phi f_2'$ , of which  $J/\psi \rightarrow \eta' \pi^+ \pi^- \pi^0$  is dominant.

Charged tracks are selected by requiring that they are within the polar angle region  $|\cos \theta| < 0.93$  and within the vertex region of  $r_{xy} < 1$  cm and  $|z| < 5$  cm. Four good charged tracks with zero net charge are required. Candidate photons are required to have an energy deposit in the EMC that is greater than 40 MeV, to be isolated from charged tracks by more than  $20^\circ$  in both the  $x - y$  and  $r - z$  planes and the opening angle with any other photon in the event that is greater than  $7^\circ$ . Finally, the four charged tracks and photons in the event are kinematically fitted using four energy and momentum conservation constraints (4C) to the  $J/\psi \rightarrow 3\gamma 2(\pi^+ \pi^-)$  hypothesis. The fit is repeated using all permutations and the combination with the best fit to  $3\gamma 2(\pi^+ \pi^-)$  is retained. In order to further suppress the backgrounds and improve the mass resolution, a 5C kinematic fit is imposed to constrain the invariant mass of two of the photons to the  $\eta$  mass. The  $\eta'$  is selected by requiring  $|m_{\eta\pi^+\pi^-} - m'_{\eta}| < 0.04$  GeV.

About 11,000  $J/\psi \rightarrow \gamma X(1835)$ ,  $X(1835) \rightarrow \eta' \pi^+ \pi^-$ ,  $\eta' \rightarrow \eta \pi^+ \pi^-$  and  $\eta \rightarrow \gamma \gamma$  simulated events pass the above-listed selection criteria. According to the product branching fraction reported in Ref. [180], this number of events is equivalent to a  $3 \times 10^9$   $J/\psi$  event sample. We also generated and selected events from the background channels mentioned above and normalized these to the same number of  $J/\psi$  events.

The *BES-III*  $\eta' \pi^+ \pi^-$  mass resolution near the resonance mass of 1835 MeV is about 3 MeV and the selection efficiency for the above-listed selection criteria is about 10%.

Figure 9.24 shows the  $\eta' \pi^+ \pi^-$  invariant mass spectrum for the selected  $J/\psi \rightarrow \gamma X(1835)$ ,  $X(1835) \rightarrow \eta' \pi^+ \pi^-$  signal and background events. Compared with the BESII results ((Fig. 9.21), the background level at *BES-III* is much lower and the  $X(1835)$  signal more distinct due to much better energy and momentum resolutions.

A fit with a Breit-Wigner signal and a second order polynomial background function yields mass, width and branching fractions for the  $X(1835)$  that are consistent with the

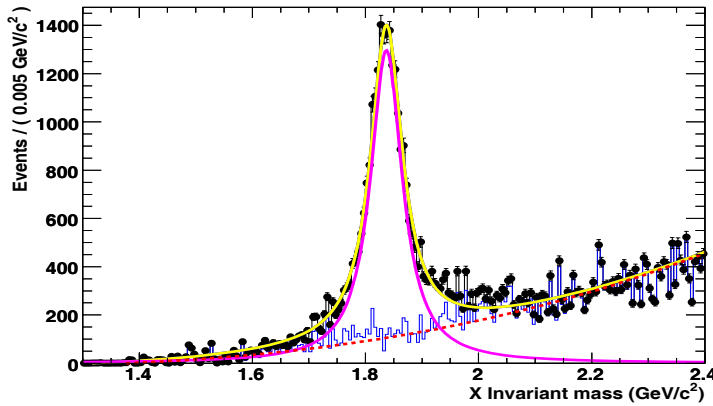


Figure 9.24: The  $\eta'\pi^+\pi^-$  invariant mass for  $J/\psi \rightarrow \gamma\eta'\pi^+\pi^-$ . The generated signals and backgrounds are normalized to  $3 \times 10^9 J/\psi$  events and are added incoherently.

MC-input parameters.

### $J/\psi \rightarrow \omega X(1835)$

A sample of  $J/\psi \rightarrow \omega X(1835)$  events was generated with  $\omega$  decaying into  $\pi^+\pi^-\pi^0$  and  $X(1835)$  to  $\eta'\pi^+\pi^-$ . The final states contain four  $\gamma$ 's and three  $(\pi^+\pi^-)$  pairs. Potential background channels are  $J/\psi \rightarrow \omega K_s K\pi$ ,  $KK4\pi$ ,  $\phi 4\pi$ ,  $\phi K^* K$ ,  $\omega K^* K$ , and  $\pi^0 6\pi$ .

The selection of the good charged tracks and photons are similar to those for the  $J/\psi \rightarrow \gamma X(1835)$  analysis described above. Events with six good charged tracks and at least four good photons are retained. The 4C kinematic fit is applied using the  $J/\psi \rightarrow 4\gamma 3(\pi^+\pi^-)$  hypothesis.

After the final selection, the efficiency for  $J/\psi \rightarrow \omega X(1835)$ ,  $\omega \rightarrow \pi^+\pi^-\pi^0$ ,  $X(1835) \rightarrow \eta'\pi^+\pi^-$ , and  $\eta' \rightarrow \eta\pi^+\pi^-$  is about 2.4% and the mass resolution at 1835 MeV is 3 MeV.

Figure 9.25 shows the invariant mass spectrum of  $\eta'\pi^+\pi^-$  for the  $J/\psi \rightarrow \omega X(1835)$ ,  $\omega \rightarrow \pi^+\pi^-\pi^0$ ,  $X(1835) \rightarrow \eta'\pi^+\pi^-$  signal and background events.

### $J/\psi \rightarrow \phi X(1835)$

For  $J/\psi \rightarrow \phi X(1835)$ ,  $\phi \rightarrow K^+K^-$  and  $\eta' \rightarrow \eta\pi^+\pi^-$ , the final states include two photons, two charged kaons and four charged pions. The numbers of generated signal events and background events that pass the event selection criteria, are listed in Table 9.27, where one can see that the background level is very low. The invariant mass spectrum of  $\eta'\pi^+\pi^-$  for the  $J/\psi \rightarrow \phi X(1835)$ ,  $\phi \rightarrow K^+K^-$ ,  $X(1835) \rightarrow \eta'\pi^+\pi^-$  for signal and background events are shown in Fig. 9.26, where the  $X(1835)$  is almost free of the backgrounds. The selection efficiency for this channel is about 2.6% and the  $\pi^+\pi^-\eta'$  invariant mass resolution near 1835 MeV is about 3 MeV.

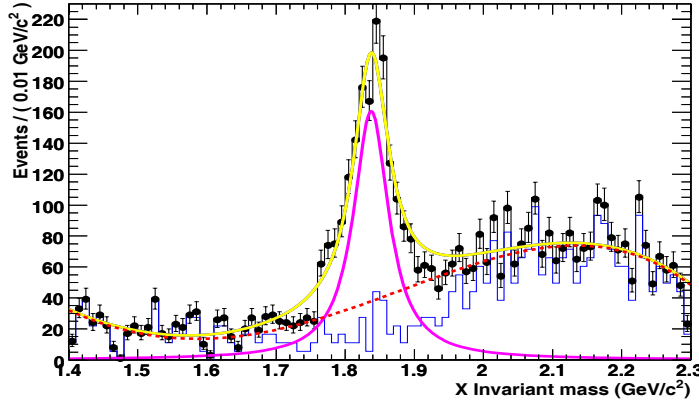


Figure 9.25: The  $\eta'\pi^+\pi^-$  invariant mass for  $J/\psi \rightarrow \omega\eta'\pi^+\pi^-$ . The generated signals and backgrounds are normalized to  $3 \times 10^9 J/\psi$  events and are added incoherently.

Table 9.27:  $J/\psi \rightarrow \phi X$  and its background channels

	$\phi X(1835)$	$KK4\pi$	$\omega K_s K\pi$	$\phi f'_2$	$\phi 4\pi$	$\omega K^* K$	$\pi^0 6\pi$
Entries	169318	54798	89891	79874	45959	90866	127540
$N_{ch} = 6$	21272	15611	15025	1254	11405	26310	48359
$N_{\pi^+} = 2$							
$N_{\pi^-} = 2$	18024	13021	1036	1063	9266	2224	516
$N_{K^+} = 1$							
$N_{K^-} = 1$	17492	12409	184	1031	8972	175	9
Vertex	5434	3816	18	464	2671	91	8
4C-fit	2369	206	2	42	156	0	0
5C-fit	1914	0	0	3	1	0	0
Scale	1914	0	0	8	86	0	0

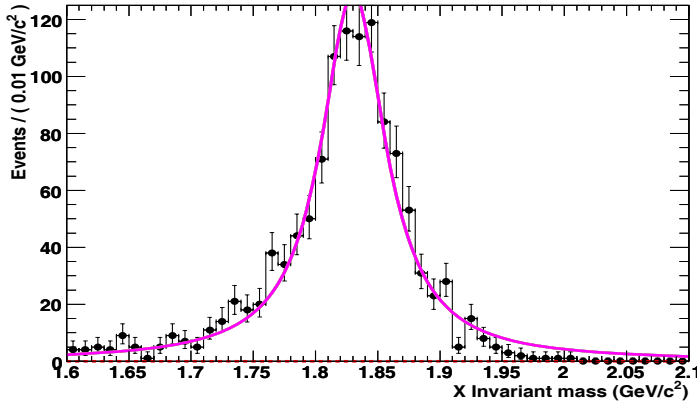


Figure 9.26: The  $\eta'\pi^+\pi^-$  invariant mass for  $J/\psi \rightarrow \phi\eta'\pi^+\pi^-$ . The generated signals and backgrounds are normalized to  $3 \times 10^9 J/\psi$  events and are added incoherently.

## 9.6 Molecular states

Molecular states are bound states of two (or more) color-singlet hadrons. In other words, there are two (or more) MIT bags. Color-singlet hadrons — usually  $\pi$ -mesons — are exchanged between these bags to produce the attractive force. There have been speculations that the  $f_0(980)$  and  $a_0(980)$  are  $K\bar{K}$  molecules since they are only 10 MeV below  $K\bar{K}$  threshold [196]. The  $\Lambda(1405)$  is sometimes postulated as a  $KN$  molecule. More recently, the  $X(3872)$  meson, which has a mass that is very nearly equal to  $m_{D^0} + m_{D^{*0}}$ , has been hypothesized to be a  $D^0\bar{D}^{*0}$  molecular state [197].

# Chapter 10

## Baryon spectrum

### 10.1 Baryons as $qqq$ states

The classical picture for baryons is that each baryon is comprised of three quarks. Based on this picture, the non-relativistic constituent quark model (NRCQM) provides an explicit classification for light baryons in terms of group symmetry. Until now, all established baryons listed in the PDG tables [259]. can be ascribed to three-quark ( $qqq$ ) configurations.

Here we briefly review the main ingredients of the model and indicate how the many deviations that have been observed in experiment might be exposing complicated aspects of strong QCD dynamics. The understanding of these deviations and searches for new non-NRCQM states and phenomena is the main motivation for further studies of baryon spectroscopy.

In the light quark (*i.e.*  $u$ ,  $d$ , and  $s$ ) sector, the total wavefunction of a baryon consists of four parts: i) the spatial wavefunction  $\psi$ ; ii) the flavor wavefunction  $\phi$ ; iii) the spin wavefunction  $\chi$ ; and iv) the color wavefunction  $\phi_c$ . For such systems of fermions, the Pauli principle requires that the total wavefunction is antisymmetric under exchange of any two quarks. Therefore, the total wavefunction must be anti-symmetrized. Note that the color wavefunction of a normal baryon state is a color singlet state and, thus, the color wavefunction is always anti-symmetric under exchange of any two quarks. As a consequence, one needs to *symmetrize* the rest part of the total wavefunction, *i.e.* spatial, spin and isospin, to obtain an overall antisymmetric baryon wavefunction. Since the representations of the permutation group  $S_3$  are also representations of the  $SU(2)$ ,  $SU(3)$  and  $SU(6)$  groups, it is convenient to construct the baryon wavefunctions on the basis of  $S_3$  group symmetry.

In general, there are four representations of  $S_3$ : the totally symmetric basis  $e^s$ , the totally antisymmetric basis  $e^a$ , and the two mixed-symmetry bases  $e^\lambda$  and  $e^\rho$ , which are defined under the permutation transformations:

$$P_{12} \begin{pmatrix} e^\lambda \\ e^\rho \end{pmatrix} = \begin{pmatrix} 1 & 0 \\ 0 & -1 \end{pmatrix} \begin{pmatrix} e^\lambda \\ e^\rho \end{pmatrix}, \quad (10.1.1)$$

and

$$P_{13} \begin{pmatrix} e^\lambda \\ e^\rho \end{pmatrix} = \begin{pmatrix} -\frac{1}{2} & -\frac{\sqrt{3}}{2} \\ -\frac{\sqrt{3}}{2} & \frac{1}{2} \end{pmatrix} \begin{pmatrix} e^\lambda \\ e^\rho \end{pmatrix}, \quad (10.1.2)$$

where  $P_{12}$  and  $P_{13}$  are permutation operators for exchange of  $1 \leftrightarrow 2$  and  $1 \leftrightarrow 3$ , respectively.

The wavefunctions of spin ( $SU(2)$ ), flavor ( $SU(3)$ ) and combined spin-flavor ( $SU(6)$ ) are also representations of the  $S_3$  group, and can be expressed as:

$$SU(2) \quad \mathbf{2} \otimes \mathbf{2} \otimes \mathbf{2} = \mathbf{4}_s + \mathbf{2}_\rho + \mathbf{2}_\lambda, \quad (10.1.3)$$

$$SU(3) \quad \mathbf{3} \otimes \mathbf{3} \otimes \mathbf{3} = \mathbf{10}_s + \mathbf{8}_\rho + \mathbf{8}_\lambda + \mathbf{1}_a, \quad (10.1.4)$$

$$SU(6) \quad \mathbf{6} \otimes \mathbf{6} \otimes \mathbf{6} = \mathbf{56}_s + \mathbf{70}_\rho + \mathbf{70}_\lambda + \mathbf{20}_a, \quad (10.1.5)$$

where the subscripts denote the corresponding  $S_3$  basis for each representation, and the bold numbers denote the dimension of the corresponding representation. Note that we cannot construct an antisymmetric spin state with identical spin 1/2 fermions.

Thus, the spin-flavor wavefunctions can be expressed as  $|\mathbf{N}_6, {}^{2S+1}\mathbf{N}_3\rangle$ , where  $\mathbf{N}_6$  and  $\mathbf{N}_3$  denote the  $SU(6)$  and  $SU(3)$  representation and  $S$  stands for the total spin of the wavefunction. For example, the spatial ground states with a spatial part that is trivially symmetric necessarily have a spin-flavor ( $\chi\phi$ ) part that is also symmetric, which can be made up of either  $\phi^s\chi^s$  or  $(\phi^\rho\chi^\rho + \rho^\lambda\chi^\lambda)/\sqrt{2}$ ; *i.e.*,  $|\mathbf{56}, {}^4\mathbf{10}\rangle^s$  or  $|\mathbf{56}, {}^2\mathbf{8}\rangle^s$ . These are, respectively, the  $J^P = 3/2^+$  decuplet that contains the  $\Delta(1232)$  and the  $J^P = 1/2^+$  octet that contains the nucleon.

In the NRCQM, it is assumed that the total orbital angular momentum of the three-quark system is conserved, which means that the spatial wavefunction is also a representation of the  $S_3$  group. Combining the spatial wavefunctions, baryons can be constructed in the  $SU(6) \otimes O(3)$  symmetry limit. A useful classification, one used by the PDG [259], is to assign the baryons into harmonic oscillator bands that have the same number of quanta of excitation  $N$ . Each band consists of a number of supermultiplets, specified by  $(\mathbf{N}_6, L_N^P)$  with  $L$  the total quark orbital angular momentum and  $P$  the total parity. The  $N = 0$  bands consists of the spatial ground state 56-plet ( $56, 0_0^+$ ). The  $N = 1$  band contains the  $L = 1$  negative-parity baryons with masses below 1.9 GeV and consists of the  $(70, 1_1^-)$  multiplet, which, with a total of  $70 \times 3$  spin-flavor states, is composed of two decuplets with  $J^P = 1/2^-$  and  $3/2^-$ , two nonets with  $J^P = 1/2^-$  and  $3/2^-$ , and three octets with  $J^P = 1/2^-$ ,  $3/2^-$  and  $5/2^-$ . The  $N = 2$  band contains five supermultiplets:  $(56, 0_2^+)$ ,  $(70, 0_2^+)$ ,  $(56, 2_2^+)$ ,  $(70, 2_2^+)$ , and  $(20, 1_2^+)$ . The PDG [259] gives quark-model assignments for some of the known baryons in terms of the flavor-spin  $SU(6)$  basis listed in Table 10.1. Here for simplicity the  $SU(6) \otimes O(3)$  configurations are assumed unmixed. In reality, not only do the  $\Lambda$  singlet and octet states mix, states with same  $J^P$  but different  $L$ - $S$  combinations can mix as well [198, 199].

All members of the spatial ground state 56-plet ( $56, 0_0^+$ ) are experimentally well-established. Their static properties, such as masses, magnetic moments etc., are well reproduced by the most basic versions of the quark model with either harmonic-oscillator or linear confinement terms, which are generally spin-independent, plus a spin-spin interaction that produces the octet-decuplet mass splitting.

The situation for excited states is much more complicated. In order to reproduce the properties of the excited baryon states, various quark models with different dynamical ingredients have been proposed and developed. See Ref. [199] for a recent review. Among these models, two of the most detailed and most quoted ones are the one gluon exchange model (OGE) and the Goldstone boson exchange model (GBE).

Table 10.1: Quark-model assignments for some of the known baryons in terms of the flavor-spin  $SU(6)$  basis. Only the dominant representation is listed. (Copied from the PDG, (Ref [259])

$J^P$	$(D, L_N^P)$	$S$	Octet members			Singlets
$1/2^+$	$(56, 0_0^+)$	$1/2$	$N(938)$	$\Lambda(1116)$	$\Sigma(1193)$	$\Xi(1318)$
$1/2^+$	$(56, 0_2^+)$	$1/2$	$N(1440)$	$\Lambda(1600)$	$\Sigma(1660)$	$\Xi(?)$
$1/2^-$	$(70, 1_1^-)$	$1/2$	$N(1535)$	$\Lambda(1670)$	$\Sigma(1620)$	$\Xi(?)$
$3/2^-$	$(70, 1_1^-)$	$1/2$	$N(1520)$	$\Lambda(1690)$	$\Sigma(1670)$	$\Xi(1820)$
$1/2^-$	$(70, 1_1^-)$	$3/2$	$N(1650)$	$\Lambda(1800)$	$\Sigma(1750)$	$\Xi(?)$
$3/2^-$	$(70, 1_1^-)$	$3/2$	$N(1700)$	$\Lambda(?)$	$\Sigma(?)$	$\Xi(?)$
$5/2^-$	$(70, 1_1^-)$	$3/2$	$N(1675)$	$\Lambda(1830)$	$\Sigma(1775)$	$\Xi(?)$
$1/2^+$	$(70, 0_2^+)$	$1/2$	$N(1710)$	$\Lambda(1810)$	$\Sigma(1880)$	$\Xi(?)$
$3/2^+$	$(56, 2_2^+)$	$1/2$	$N(1720)$	$\Lambda(1890)$	$\Sigma(?)$	$\Xi(?)$
$5/2^+$	$(56, 2_2^+)$	$1/2$	$N(1680)$	$\Lambda(1820)$	$\Sigma(1915)$	$\Xi(2030)$
$7/2^-$	$(70, 3_3^-)$	$1/2$	$N(2190)$	$\Lambda(?)$	$\Sigma(?)$	$\Xi(?)$
$9/2^-$	$(70, 3_3^-)$	$3/2$	$N(2250)$	$\Lambda(?)$	$\Sigma(?)$	$\Xi(?)$
$9/2^+$	$(56, 4_4^+)$	$1/2$	$N(2220)$	$\Lambda(2350)$	$\Sigma(?)$	$\Xi(?)$
Decuplet members						
$3/2^+$	$(56, 0_0^+)$	$3/2$	$\Delta(1232)$	$\Sigma(1385)$	$\Xi(1530)$	$\Omega(1672)$
$3/2^+$	$(56, 0_2^+)$	$3/2$	$\Delta(1600)$	$\Sigma(?)$	$\Xi(?)$	$\Omega(?)$
$1/2^-$	$(70, 1_1^-)$	$1/2$	$\Delta(1620)$	$\Sigma(?)$	$\Xi(?)$	$\Omega(?)$
$3/2^-$	$(70, 1_1^-)$	$1/2$	$\Delta(1700)$	$\Sigma(?)$	$\Xi(?)$	$\Omega(?)$
$5/2^+$	$(56, 2_2^+)$	$3/2$	$\Delta(1905)$	$\Sigma(?)$	$\Xi(?)$	$\Omega(?)$
$7/2^+$	$(56, 2_2^+)$	$3/2$	$\Delta(1950)$	$\Sigma(2030)$	$\Xi(?)$	$\Omega(?)$
$11/2^+$	$(56, 4_4^+)$	$3/2$	$\Delta(2420)$	$\Sigma(?)$	$\Xi(?)$	$\Omega(?)$

The OGE models originated from the renowned 1975 paper of De Rujula, Georgi and Glashow (DGG) [200]. In addition to the confinement potential, the basic ingredient of the DGG model is a flavor-independent but spin-dependent interaction that is modeled on the short-range, one-gluon-exchange (OGE) of QCD. In a non-relativistic approximation, the OGE leads to a potential :

$$V^{OGE}(\mathbf{r}_{ij}) = V_{cen}^{OGE}(\mathbf{r}_{ij}) + V_{ten}^{OGE}(\mathbf{r}_{ij}) + V_{LS}^{OGE}(\mathbf{r}_{ij}), \quad (10.1.6)$$

where  $V_{cen}^{OGE}(\mathbf{r}_{ij})$ ,  $V_{ten}^{OGE}(\mathbf{r}_{ij})$  and  $V_{LS}^{OGE}(\mathbf{r}_{ij})$  are central, tensor and spin-orbit forces, respectively. These have the forms

$$V_{cen}^{OGE}(\mathbf{r}_{ij}) = \frac{\alpha_S}{4}(\lambda_i^c \cdot \lambda_j^c) \left\{ \frac{1}{r_{ij}} - \frac{\pi}{2} \delta(\mathbf{r}_{ij}) \left[ \frac{1}{m_i^2} + \frac{1}{m_j^2} + \frac{4}{3m_i m_j} (\sigma_i \cdot \sigma_j) \right] \right\}, \quad (10.1.7)$$

$$V_{ten}^{OGE}(\mathbf{r}_{ij}) = -\frac{\alpha_S}{4}(\lambda_i^c \cdot \lambda_j^c) \frac{1}{4m_i m_j} \frac{1}{3r_{ij}^3} (3\sigma_i \cdot \hat{\mathbf{r}}_{ij} \sigma_j \cdot \hat{\mathbf{r}}_{ij} - \sigma_i \cdot \sigma_j), \quad (10.1.8)$$

$$V_{LS}^{OGE}(\mathbf{r}_{ij}) = -\frac{\alpha_S}{4}(\lambda_i^c \cdot \lambda_j^c) \frac{m_i^2 + m_j^2 + 4m_i m_j}{8m_i^2 m_j^2} \frac{1}{3r_{ij}^3} [\mathbf{L} \cdot (\sigma_i + \sigma_j)], \quad (10.1.9)$$

where  $\lambda_i^c$  ( $i = 1, \dots, 8$ ) are the color- $SU(3)$  unitary spin matrices. The most detailed and phenomenologically successful extension of the DGG model was made by Isgur and his collaborators, first non-relativistically [198, 199], and subsequently in a relativized formulation [199, 201]. In their model calculations, the  $V_{LS}^{OGE}(\mathbf{r}_{ij})$  term is neglected based on the argument that it is cancelled by an inevitable Thomas precession term that is generated by confinement [202]. Otherwise, the inclusion of this term would spoil the agreement with the observed spectrum. Results from a recent OGE quark model calculation [201] for the excitation spectrum of the nucleon is shown in Fig. 10.1, where it is compared with experimental observations. Many baryon electromagnetic couplings and strong decay couplings have also been calculated within the context of this model [199].

The GBE models originated from the 1984 work of Manohar and Georgi [203]. The basic idea here is that constituent quarks with internal structure are a consequence of the spontaneous breaking of the approximate chiral symmetry of QCD and, thus, couple to the chiral meson fields. Glozman and Riska [204] have popularized this idea by making an extensive analysis of the baryon spectrum using a model based on a hyperfine interaction arising solely from the exchange of a pseudoscalar octet instead of the gluons of the OGE model. In their model, the spin-dependent hyperfine interaction is flavor-dependent:

$$H_{HF} \propto \sum_{i < j} V(\vec{r}_{ij}) \lambda_i^F \cdot \lambda_j^F \vec{\sigma}_i \cdot \vec{\sigma}_j, \quad (10.1.10)$$

where the  $\lambda_i^F$  are flavor  $SU(3)$  Gell-Mann matrices. It is the flavor-dependent factor  $\lambda_i^F \cdot \lambda_j^F$  of the GBE interaction that produces parity orderings for the  $N^*$ ,  $\Delta^*$  and  $\Lambda^*$  spectra that are different than those of the OGE models, and in agreement with observation. After further extending this model to include the exchange of a nonet of vector mesons and a scalar meson [205], the low-lying  $N^*$ ,  $\Delta^*$  and  $\Lambda^*$  spectra can be well reproduced as shown in Fig. 10.2. A problem for the model is whether or not the large number of parameters introduced to fit the spectra can also reproduce the relevant strong decays of the excited baryons and baryon-baryon interactions.

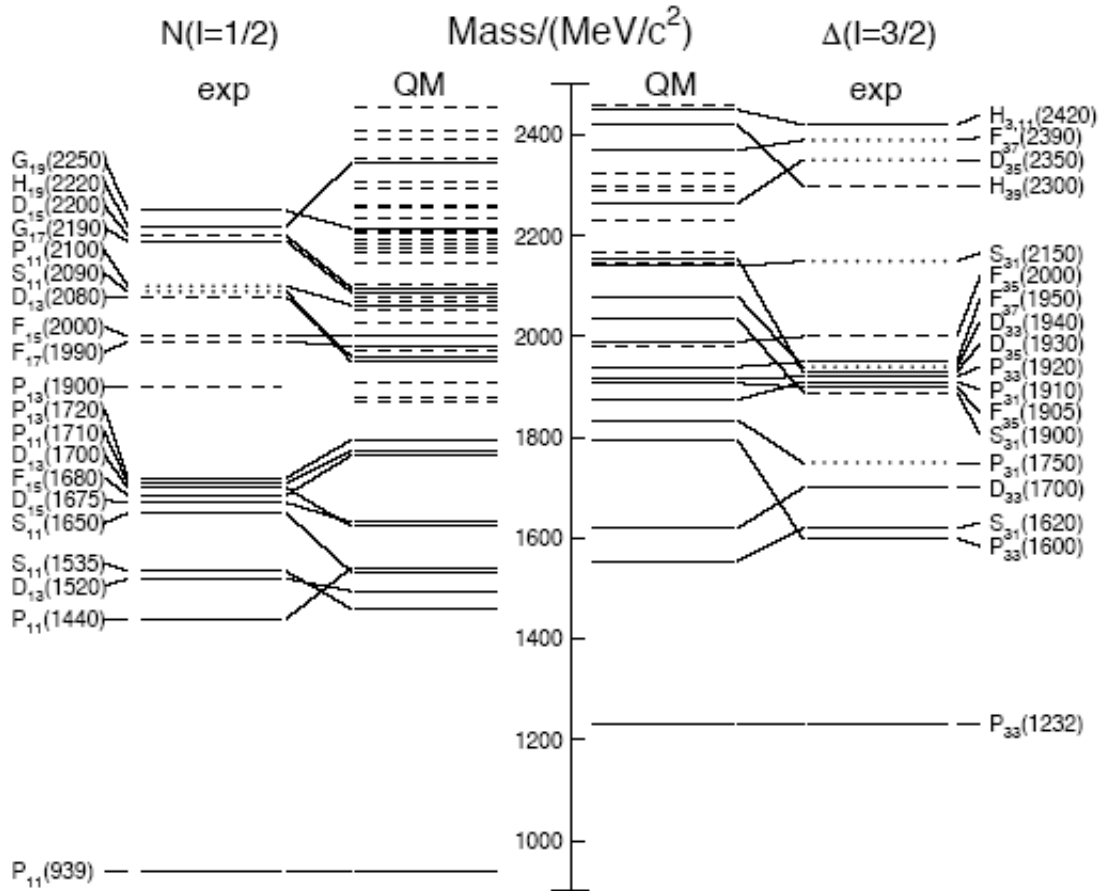


Figure 10.1: The nucleon excitation spectrum. The positions of the excited state identified in experiment are compared to those predicted by a modern quark model calculation. Left hand side: isospin  $I = 1/2$  N-states, right hand side: isospin  $I = 3/2$   $\Delta$ -states. Experimental: (columns labelled 'exp'), three and four star states are indicated by full lines (two-star dashed lines, one-star dotted lines). At the very left and right of the figure the spectroscopic notation of these states is given. Quark model [201]: (columns labelled 'QM'), all states for the  $N=1,2$  bands, low lying states for  $N=3,4,5$  bands. Full lines: at least tentative assignment to observed states, dashed lines: so far no observed counterparts. (Copied from PDG [259])

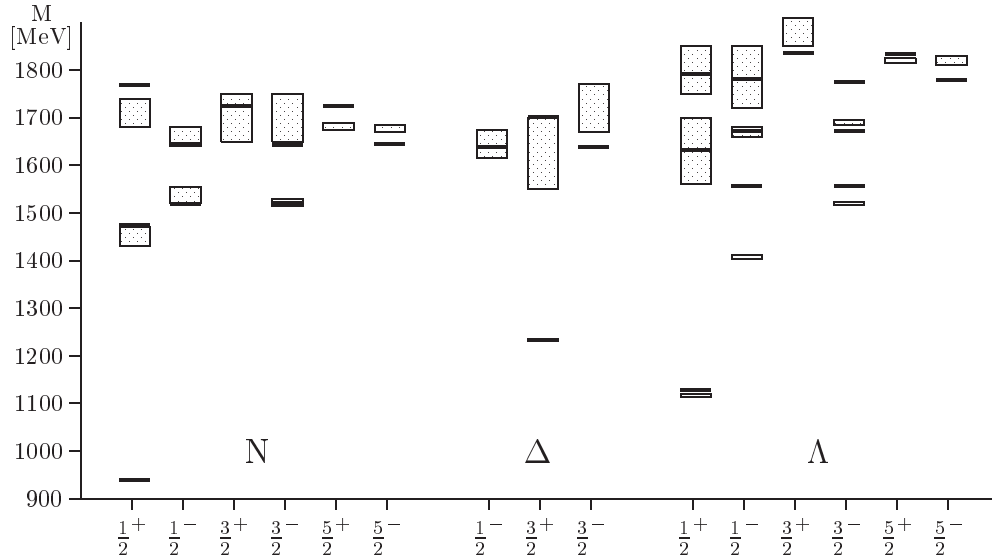


Figure 10.2: Energy levels of low-lying  $N^*$ ,  $\Delta^*$  and  $\Lambda^*$  baryons from Ref.[205], compared to the range of central values for resonances masses from the PDG [259].

In order to describe simultaneously the baryon spectrum, baryon decays and baryon-baryon interactions, some hybrid models that include both OGE and GBE interactions have been developed [206]. Until now, these hybrid models have been mainly applied to studies of dibaryon systems using parameters determined from fits to ground state baryon masses, the deuteron binding energy, etc.

Besides the OGE and GBE interactions, an alternative flavor-spin-dependent hyperfine interaction that derives from instanton effects was proposed [207]. This interaction acts only on scalar, isoscalar pairs of quarks in relative  $S$ -wave states:

$$\langle q^2; S, L, I | H_{HF} | q^2; S, L, I \rangle \propto \mathcal{W} \delta_{S,0} \delta_{L,0} \delta_{I,0}, \quad (10.1.11)$$

where  $\mathcal{W}$  is the radial matrix element of the contact interaction. In this approach, baryons are described by the homogeneous Bethe-Salpeter equation with three- and two-particle instantaneous interaction kernels, which implement confinement and the flavor-spin-dependent interaction from instanton effects to account for the major mass splittings. Its predictions for the baryon spectrum are of similar quality as OGE models. But it can give a description of the mass spectrum while implementing relativistic covariance both in the quark dynamics and in the calculation of currents needed for decay observables.

Other quite well known models based on the three-quark picture for baryons include the MIT bag model [208], the cloudy bag model [209] and the algebraic model [210]. The MIT bag model is relativistic and confines three valence quarks to the interior of baryons by a bag pressure term with a parameter  $B$  that is used to set the scale of the baryon masses. The cloudy bag model incorporates chiral invariance by allowing a cloud of pion fields to couple to the confined quarks only at the surface of the MIT bag. The algebraic model is also called the collective model. Its approach to the dynamics is not the usual solution of some Schrödinger-like equation, but rather bosonic quantization of the spatial degree of freedom that has a  $Y$ -shaped string-like configuration with possible vibrations and rotations. For more details of these models, we refer readers to the corresponding

original papers [208, 209, 210] or Ref. [199] for a recent review.

In the following sections, we review some of the outstanding problems in baryon spectroscopy in the context of the  $qqq$  picture for baryons and introduce new pictures of baryons that go beyond this simplest three-quark configuration. We then summarize the accomplishments of BESI and BESII in the area of baryon spectroscopy and discuss the prospects for *BES-III*.

## 10.2 Outstanding problems in baryon spectroscopy

Although the quark model has achieved a number of significant successes in the interpretation of many of the static properties of nucleons and excited resonances, our present knowledge on baryon spectroscopy is still in its infancy [259]. Many very fundamental issues in baryon spectroscopy are still not well understood [199].

On the theoretical side, an unsolved fundamental problem that still persists is: *What are the proper effective degrees of freedom for describing the internal structure of baryons?* Several pictures based on various effective degrees of freedom are shown in Fig. 10.3.

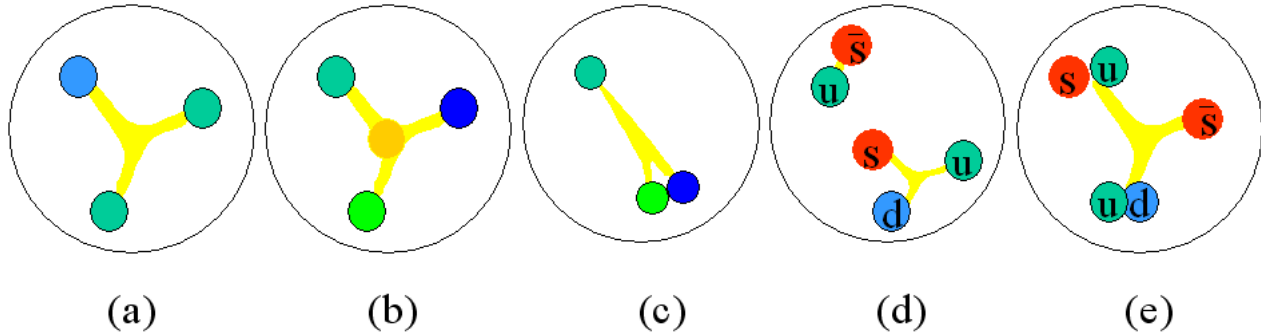


Figure 10.3: Various pictures for internal quark-gluon structure of baryons: (a)  $qqq$ , (b)  $qqgg$  hybrid, (c) diquark, (d) meson-baryon state, (e) pentaquark with diquark clusters.

The classical and simple  $qqq$  configuration of the constituent quark model, shown in Fig. 10.3(a), has been very successful at explaining the static properties such as masses and magnetic moments of the spatial ground states of the flavor  $SU(3)$  octet and decuplet baryons. It predicted the  $\Omega^-$  baryon to have a mass around 1670 MeV, as was subsequently discovered experimentally. However, its predictions for the spatially excited baryons have not been as successful, as illustrated in Fig. 10.1. In the simple  $qqq$  constituent quark model, the lowest spatially excited baryon is expected to be a  $(uud)$   $N^*$  state with one quark in orbital angular momentum  $L = 1$  state, and, hence, with negative parity. Experimentally [259], the lowest negative parity  $N^*$  resonance is found to be the  $N^*(1535)$ , which is heavier than two other spatially excited baryons: the  $\Lambda^*(1405)$  and  $N^*(1440)$ . In the classical  $qqq$  constituent quark model, the  $\Lambda^*(1405)$  with spin-parity  $1/2^-$  is supposed to be a  $(uds)$  baryon with one quark in orbital angular momentum  $L = 1$  state and about 130 MeV heavier than its  $N^*$  partner, the  $N^*(1535)$ ; the  $N^*(1440)$  with spin-parity  $1/2^+$  is supposed to be a  $(uud)$  state with one quark in radial  $n = 1$  excited state and should be heavier than the  $L = 1$  excited  $(uud)$  state  $N^*(1535)$  (based on the result that for a simple harmonic oscillator potential the state energy is  $(2n + L + 3/2)\hbar\omega$ ).

Thus, for the three lowest spatially excited baryons, the classical quark model picture has already failed.

The second outstanding problem for the classical  $qqq$  model is that in many of its forms it predicts a substantial number of ‘missing  $N^*$  states’ around 2 GeV, which have so far not been observed [199]. Since the predicted number of excited states decreases with the number of the effective degrees of freedom, it is argued that the missing  $N^*$  states problem favors the diquark picture as shown in Fig. 10.3(c), which has fewer degree of freedom and predicts fewer  $N^*$  states [211]. For example, in diquark models, the two quarks forming the diquark are constrained to be in the relative  $S$ -wave, and, thus, cannot combine with the third quark to form  $(20,1_2^+)$ -multiplet baryons. Experimentally, not a single  $(20,1_2^+)$ -multiplet baryon has yet to be identified [259]. However, the non-observation of these missing  $N^*$  states does not necessarily mean that they do not exist. In the limit that the  $\gamma$  or  $\pi$  couples to only one quark in the nucleon in  $\gamma N$  or  $\pi N$  reactions, the  $(20,1_2^+)$ -multiplet baryon cannot be produced [212]. As for higher-order effects, they can have couplings to  $\pi N$  and  $\gamma N$ , but maybe these are too weak to be seen in presently available  $\pi N$  and  $\gamma N$  experiments [199, 212]. Other production processes should be explored. Moreover, the diquark models have been successful in only a few, very limited areas.

The third outstanding problem for the classical  $qqq$  quark model is that in deep inelastic scattering and Drell-Yan experiments the number of  $\bar{d}$  quarks in the proton is found to be more than the number of  $\bar{u}$  quarks by about 12% [213]. It is argued that this favors a mixture of meson-baryon states as shown in Fig. 10.3(d). In this picture, the  $\bar{d}$  over  $\bar{u}$  excess in the proton is explained by a mixture of  $n\pi^+$  with the  $\pi^+$  composed of  $u\bar{d}$  [214]; the  $N^*(1535)$  and  $\Lambda^*(1405)$  are identified as quasi-bound  $K\Sigma$  and  $\bar{K}N$  states, respectively [215]. The extreme of this picture is that only the ground state baryon-octet  $1/2^+$  and baryon-decuplet  $3/2^+$  are dominated by  $qqq$ , while all excited baryons are generated by meson-baryon coupled channel dynamics [216, 217]. However, a mixture of pentaquark components with diquark clusters, as shown in Fig. 10.3(e), could also explain these properties [218, 219, 220, 221].

Another unsolved fundamental question is: *Even if we know the effective degrees of freedom in the baryon, how do we deal with the interactions between them?* In general, in most fields of physics, two-body forces dominate and three-body forces are treated as a residual interaction. In QCD, however, the three-body force between three quarks is expected to be the “primary” force that reflects the  $SU(3)_c$  gauge symmetry; a point of view that is strongly supported by a recent lattice calculation [222]. An earlier constituent quark model calculation [223] also suggested that the three-quark potential is directly responsible for the structure and properties of baryons. It is much more complicated to deal with a three-body force than the usual two-body force. Furthermore, the center of the Y-shaped gluon field could act as an additional, vibrational degree of freedom that makes the baryon behave as a  $qqq$ -gluon hybrid as shown by Fig. 10.3(b). Fortunately, the gluonic excitation energy is found to be about 1 GeV for a typical hadronic scale, which is substantially larger than typical quark excitation energies [224]. This large gluonic excitation energy explains the great success of the simple  $qqq$  quark model for the spatial ground state baryons. On the other hand, the three-body Y-shaped gluon field interaction is obtained in the quenched approximation [222]; some people believe that the effective interaction field between the constituent quarks should be a meson field rather than a gluon field [203, 204]. Thus, the three-body force may also be generated by various

couplings of meson fields.

There are also various phenomenological models for hybrid baryons [225]. The earliest one is the bag model which places relativistic quarks and gluons in a spherical cavity and allows them to interact via QCD forces such as one-gluon exchange, the color Compton effect, etc. [226]. The lightest hybrid baryon was predicted to be an “extra”  $1/2^+ N^* P11$  state with a mass of about  $1.5 \sim 1.6$  GeV, which is suggestive of the  $N^*(1440)$  Roper resonance. This is supported by QCD sum rule calculations [227] that also predict the lightest  $1/2^+$  hybrid to be around 1.5 GeV and conclude that the Roper is largely a hybrid. However, more recent flux tube model calculations [228] predict a larger mass for the lightest hybrid baryons, about 1.9 GeV, with a twofold degenerate pair of  $1/2^+$  and  $3/2^+ N^*$  hybrids. This is closer to lattice QCD predictions [224].

In reality, a baryon state around 2 GeV could be a mixture of all five of the configurations shown in Fig. 10.3. As for the existence or non-existence of genuine pentaquark states, we refer the reader to recent reviews [229].

On the experimental side, our present knowledge of baryon spectroscopy has come almost entirely from partial-wave analyses of  $\pi N$  total, elastic, and charge-exchange scattering data from more than twenty years ago [259]. However, recently a new generation of experiments on  $N^*$  physics with electromagnetic probes has been started at new facilities such as CEBAF at JLAB, ELSA at Bonn, GRAAL at Grenoble and SPRING8 at JASRI. Some nice results have already been produced [230, 231, 232, 233]. However, a problem for these experiments is that above 1.8 GeV there are many broad resonances with various possible quantum numbers that overlap each other and are very difficult to disentangle. Moreover resonances with weak couplings to  $\pi N$  and  $\gamma N$  will not show up in these experiments.

### 10.3 Baryon Spectroscopy at BESI and BESII

In 2000, BESII started a baryon resonance research program that has been focused on the study of excited  $N^*$  baryons [234]. This takes advantage of the fact that  $J/\psi$  and  $\psi'$  decays provide excellent opportunities for studying excited nucleon ( $N^*$ ) and hyperon ( $\Lambda^*$ ,  $\Sigma^*$  &  $\Xi^*$ ) resonances [235]. The Feynman graph for the production of excited nucleons and hyperons in  $\psi$  decays is shown in Fig. 10.4, ( $\psi = J/\psi$  or  $\psi'$ ).

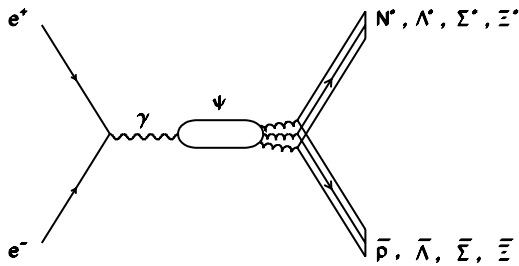


Figure 10.4:  $\bar{p}N^*$ ,  $\bar{\Lambda}\Lambda^*$ ,  $\bar{\Sigma}\Sigma^*$  and  $\bar{\Xi}\Xi^*$  production from  $e^+e^-$  collision through  $\psi$  meson.

In comparison to other facilities, the BES baryon program has advantages in at least three important aspects:

(1) isospin conservation ensures that the  $J/\psi \rightarrow \bar{N}N\pi$  ( $\bar{N}N\pi\pi$ ) decay processes produce pure isospin=1/2  $\pi N$  ( $\pi\pi N$ ) systems. In contrast, such systems produced in  $\pi N$  and  $\gamma N$

experiments are mixture of isospin=1/2 and 3/2, and analyses of these final states suffer from the complications of the isospin decomposition;

(2) decays of  $\psi$  mesons to final states containing baryons proceed via three or more virtual gluons, which is a favorable environment for producing hybrid ( $qqq$ -gluon) baryons, and for looking for “missing”  $N^*$  resonances, such as members of a possible  $(20,1_2^+)$ -multiplet baryons, that have weak couplings to both  $\pi N$  and  $\gamma N$ , but a strong coupling to  $g^3 N$ ;

(3) In addition to  $N^*$   $\Lambda^*$  &  $\Sigma^*$  baryons,  $\psi$  decays can access doubly strange  $\Xi^*$  baryons. Many QCD-inspired models [201, 204] are expected to be more reliable for baryons containing two strange quarks because of the heavier quark mass. More than thirty  $\Xi^*$  resonances are predicted to exist, while currently only two such states are experimentally well established. The theory for these states is left essentially unchallenged because of this paucity of data.

BESI started data-taking in 1989 and was upgraded in 1998 to BESII. BESI collected 7.8 million  $J/\psi$  events and 3.7 million  $\psi'$  events. BESII collected 58 million  $J/\psi$  events and 14 million  $\psi'$  events.

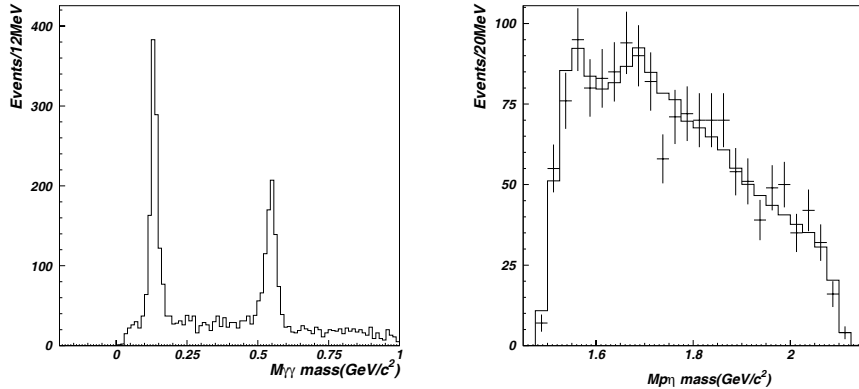


Figure 10.5: left:  $\gamma\gamma$  invariant mass for  $J/\psi \rightarrow \bar{p}p\gamma\gamma$ ; right:  $p\eta$  invariant mass spectrum for  $J/\psi \rightarrow \bar{p}p\eta$ . BESI data

From the 7.8 million  $J/\psi$  event sample collected at BESI between 1990 and 1991, events of the type  $J/\psi \rightarrow \bar{p}p\pi^0$  and  $\bar{p}p\eta$  were selected and reconstructed with the  $\pi^0$  and  $\eta$  detected via their  $\gamma\gamma$  decay mode [234]. The  $\gamma\gamma$  invariant mass, shown in Fig. 10.5 (left), exhibits two distinct peaks corresponding to the  $\pi^0$  and  $\eta$ . The  $p\eta$  invariant mass spectrum, shown in Fig. 10.5 (right), has two peaks: one at 1540 MeV and another at 1650 MeV. A partial wave analysis was applied to the  $J/\psi \rightarrow \bar{p}p\eta$  channel [234], using the effective Lagrangian approach [236, 237] with the Rarita-Schwinger formalism [238, 239, 240, 241] and the extended automatic Feynman Diagram Calculation (FDC) package [242]. The results indicate a definite signal for a  $J^P = \frac{1}{2}^-$  component at  $M = 1530 \pm 10$  MeV with  $\Gamma = 95 \pm 25$  MeV, which is very close to the  $\eta N$  threshold. In addition, there is a distinct resonance at  $M = 1647 \pm 20$  MeV with  $\Gamma = 145^{+80}_{-45}$  MeV and a preferred  $J^P$  value of  $\frac{1}{2}^-$ . These two  $N^*$  resonances are probably the well established  $S_{11}(1535)$  and  $S_{11}(1650)$  states. In the higher  $p\eta(\bar{p}\eta)$  mass region, there is evidence for a structure around 1800 MeV; however, with the limited statistical precision of BESI, a determination of its quantum numbers was not possible. The  $p\pi^0$  invariant mass spec-

trum from  $J/\psi \rightarrow p\bar{p}\pi^0$ , shown in Fig. 10.6 (left), has clear peaks around 1500 MeV and 1670 MeV, and some weak structure around 2 GeV.

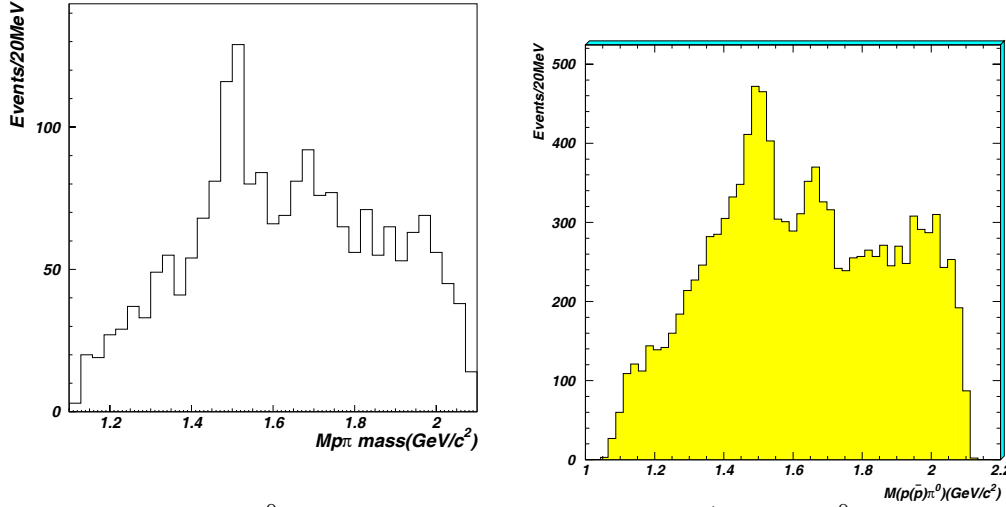


Figure 10.6:  $p\pi^0$  invariant mass spectrum for  $J/\psi \rightarrow \bar{p}p\pi^0$  from BESI (left) and preliminary BESII data (right)

With the 58 million  $J/\psi$  event sample collected in the more efficient BESII detector, an order-of-magnitude increase in the number of reconstructed events for each channel is obtained. Results for  $J/\psi$  decays to  $p\bar{p}\pi^0$ ,  $p\bar{n}\pi^- + c.c.$ ,  $pK^-\bar{\Lambda} + c.c.$  and  $\bar{\Lambda}\bar{\Sigma}\pi + c.c.$  are shown in Figs. 10.6, 10.7, 10.8 & 10.9, respectively. These are useful channels for studies of  $N^*$ ,  $\Lambda^*$  and  $\Sigma^*$  resonances.

For the  $J/\psi \rightarrow p\bar{p}\pi^0$  channel, the  $N\pi$  invariant mass spectrum from the BESII sample, shown in Fig. 10.6 (right), looks similar to that of the BESI data shown in Fig. 10.6 (left), but with much higher statistics.

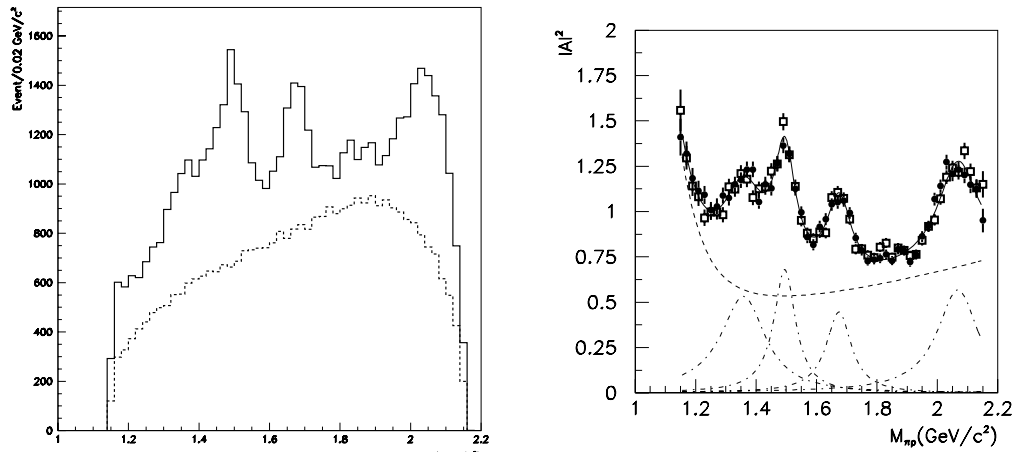


Figure 10.7: The  $p\pi^-$  and  $\bar{p}\pi^+$  invariant mass spectra for  $J/\psi \rightarrow p\pi^- \bar{n}$  (left) and  $\bar{p}\pi^+ n$  (right), compared with phase space distribution and data divided by Monte Carlo phase space vs  $p\pi$  invariant mass for  $J/\psi \rightarrow \bar{p}\pi^- \bar{n}$  (solid circle) and  $J/\psi \rightarrow \bar{p}\pi^+ n$  (open square).

In the analysis of the  $J/\psi \rightarrow p\bar{n}\pi^-$  channel, only the proton and  $\pi^-$  are detected. After the application of some selection requirements to reduce backgrounds, the missing mass spectrum shows a very clean peak corresponding to the missing antineutron. In the  $p\pi^-$  invariant mass spectrum, shown in Fig. 10.7 (left), in addition to the two well known  $N^*$  peaks at 1500 MeV and 1670 MeV,  $N^*$  peaks around 1360 MeV and 2030 MeV are evident. The charge-conjugate channel  $\bar{p}\pi^+n$  gives results that are very similar, as shown in Fig. 10.7 (right).

To investigate the behavior of the amplitude squared, the invariant mass distribution has to be corrected for phase-space and efficiency effects. The corrected results are shown in Fig. 10.7 (right). At low  $p\pi$  invariant mass, the tail from the nucleon pole term, predicted from theoretical considerations [243, 244], is clearly seen. In addition, four peaks, around 1360 MeV, 1500 MeV, 1670 MeV and 2065 MeV, are evident. Note that the well known lowest-mass nucleon resonance, the  $\Delta(1232)$ , which dominates the low mass  $\pi N$  and  $\gamma N$  scattering data, does not show up here because of the isospin filtering effects of  $J/\psi$  decay. While the peaks around 1500 MeV and 1670 MeV correspond to the well known second and third resonance peaks observed in  $\pi N$  and  $\gamma N$  scattering data, the two peaks around 1360 MeV and 2065 MeV have not been previously observed in  $\pi N$  invariant mass spectra. The 1360 MeV peak could be from the  $N^*(1440)$ , which has a pole position near 1360 MeV [259, 245, 246] and is usually buried under a huge  $\Delta(1232)$  peak in  $\pi N$  and  $\gamma N$  experiments; The peak near 2065 MeV may be one (or more) of the long-sought-for “missing”  $N^*$  resonance(s). For the decay  $J/\psi \rightarrow \bar{N}N^*(2065)$ , the orbital angular momentum of  $L = 0$  is much preferred due to the centrifugal barrier suppression factor for  $L \geq 1$ . For  $L = 0$ , the spin-parity of the  $N^*(2065)$  would be limited to be  $1/2^+$  and  $3/2^+$ . This could be the reason that the  $N^*(2065)$  shows up as a peak in  $J/\psi$  decays and not in  $\pi N$  and  $\gamma N$  production experiments, where all  $1/2^\pm$ ,  $3/2^\pm$ ,  $5/2^\pm$  and  $7/2^\pm$   $N^*$  resonances around 2.05 GeV are allowed and can overlap and interfere with each other. A simple Breit-Wigner fit [247] gives a mass and width for the  $N^*(1440)$  peak of  $1358 \pm 6 \pm 16$  MeV and  $179 \pm 26 \pm 50$  MeV; for the new  $N^*(2065)$  the fitted mass and width are  $2068 \pm 3^{+15}_{-40}$  MeV and  $165 \pm 14 \pm 40$  MeV. A partial wave analysis indicates that the  $N^*(2065)$  peak contains both spin-parity  $1/2^+$  and  $3/2^+$  components [247].

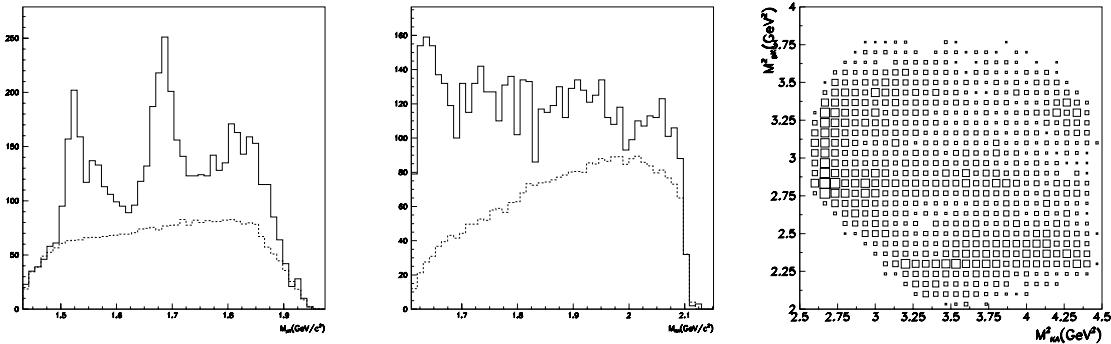


Figure 10.8:  $pK$  (left) and  $K\Lambda$  (middle) invariant mass spectra for  $J/\psi \rightarrow pK^-\bar{\Lambda}+\text{c.c.}$ , compared with phase space distribution; right: the Dalitz plot for  $J/\psi \rightarrow pK^-\bar{\Lambda}+\text{c.c.}$

In the BESII  $J/\psi \rightarrow pK^-\bar{\Lambda}$  and  $\bar{p}K^+\Lambda$  data [248], there are clear  $\Lambda^*$  peaks at 1.52 GeV, 1.69 GeV and 1.8 GeV in the  $pK$  invariant mass spectrum shown in Fig. 10.8 (left),

and  $N^* \rightarrow K\Lambda$  peaks near the  $K\Lambda$  threshold at 1.9 GeV and another near 2.05 GeV (Fig. 10.8 (center)). The  $N^*$  peak near the  $K\Lambda$  threshold is most probably due to the  $N^*(1535)$ , which is known to have large coupling to  $K\Lambda$  [217, 220]. The SAPHIR experiment at ELSA [231] also observed an  $N^*$  peak around 1.9 GeV in the  $K\Lambda$  invariant mass spectrum from photo-production, and a fit [249] to the data reveals a large  $1/2^-$  near-threshold enhancement that is mainly due to the  $N^*(1535)$ . The  $N^*$  peak at 2.05 GeV is compatible with the  $\pi N$  peak observed in  $J/\psi \rightarrow N\bar{N}\pi$  decays. Fits to the Dalitz plot distribution (Fig. 10.8 (right)) prefer a spin-parity for the  $N^*(2050)$  of  $3/2^+$ .

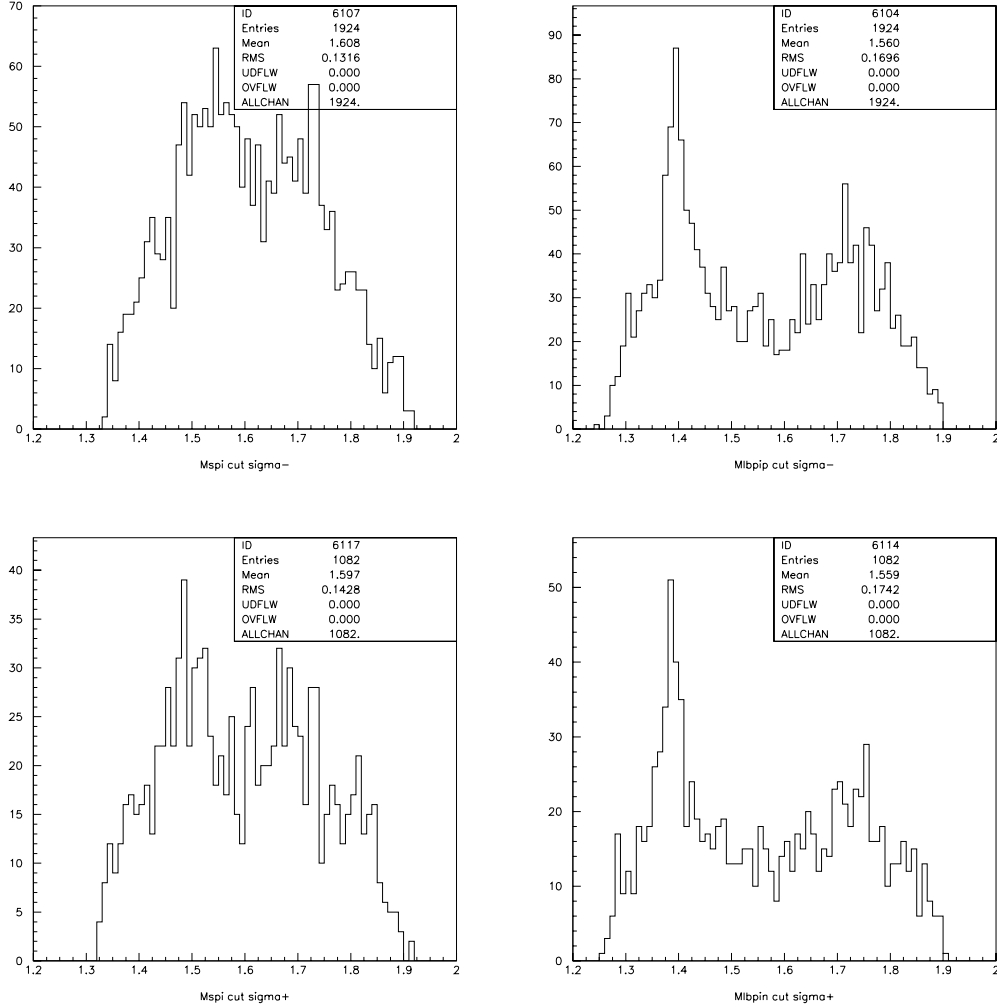


Figure 10.9:  $\bar{\Sigma}\pi$  (left) and  $\Lambda\pi$  (right) invariant mass spectrum for  $J/\psi \rightarrow \Lambda\bar{\Sigma}^+\pi^-$  (up) and  $J/\psi \rightarrow \Lambda\Sigma^-\pi^+$  (down), respectively. These are preliminary data from BESII [250].

In  $J/\psi \rightarrow \Lambda\Sigma\pi$  decays [250],  $\Lambda^*$  peaks in the  $\Sigma\pi$  invariant mass spectra (Fig. 10.9 (left)) are seen at 1.52 GeV, 1.69 GeV and 1.8 GeV. These are similar to the  $\Lambda^*$  peaks seen in the  $pK\Lambda$  channel, although less distinct. In the  $\Lambda\pi$  invariant mass spectra from  $J/\psi \rightarrow \Lambda\Sigma\pi$ , shown in Fig. 10.9 (right), there is a very clear peak around 1.385 GeV corresponding to the well established  $\Sigma(1385)$  resonance and there is an additional  $\Sigma^*$  peak around

1.72 GeV.

### 10.3.1 Partial Wave Analysis for Baryon Resonances

In order to get more useful information about the properties of the baryon resonances that are being produced, such as their  $J^P$  quantum numbers, masses, widths, production and decay rates, etc., partial wave analyses (PWA) are necessary. A brief introduction to PWA is given below with specific emphasis on baryonic final states; a more generalized description on PWA can be found in section 3.5.

The basic procedure for partial wave analysis uses the standard maximum likelihood method and consists of three main steps:

- (1) construct amplitudes  $A_i$  for each allowed partial wave  $i$ ;
- (2) form the total transition probability for each event from linear combinations of the individual partial wave amplitudes:  $w = |\sum_i c_i A_i|^2$ , where  $c_i$  are free parameters to be determined from the fit;
- (3) determine the  $c_i$  parameters as well as resonance mass and width parameters by maximizing the likelihood function  $L$ :

$$L = \prod_{n=1}^N \frac{w_{data}}{\int w_{MC}}, \quad (10.3.12)$$

where  $N$  is the number of reconstructed data events and  $w_{data}$ ,  $w_{MC}$  are evaluated for data and Monte Carlo events, respectively.

For the form of the partial wave amplitudes, we use the effective Lagrangian approach [236, 237] with the Rarita-Schwinger formalism [238, 239, 240]. In this approach, there are three basic elements for constructing amplitudes: particle spin wave functions, propagators and the effective vertex couplings; the amplitude can be written out using Feynman rules for tree diagrams.

For example, for  $J/\psi \rightarrow \bar{N}N^*(3/2+) \rightarrow \bar{N}(k_1, s_1)N(k_2, s_2)\pi(k_3)$ , the amplitude can be expressed as

$$A_{3/2+} = \bar{u}(k_2, s_2)k_{2\mu}P_{3/2}^{\mu\nu}(c_1g_{\nu\lambda} + c_2k_{1\nu}\gamma_\lambda + c_3k_{1\nu}k_{1\lambda})\gamma_5v(k_1, s_1)\psi^\lambda, \quad (10.3.13)$$

where  $u(k_2, s_2)$  and  $v(k_1, s_1)$  are 1/2-spinor wave functions for the  $N$  and  $\bar{N}$ , respectively, and  $\psi^\lambda$  is the spin-1 wave function (*i.e.* the polarization vector) for the  $J/\psi$ . The  $c_1$ ,  $c_2$  and  $c_3$  terms correspond to three possible couplings of the  $J/\psi \rightarrow \bar{N}N^*(3/2^+)$  vertex. The  $c_1$ ,  $c_2$  and  $c_3$  can be taken as constant parameters or some smooth vertex form-factor modulation can be included if necessary. The spin 3/2 propagator  $P_{3/2}^{\mu\nu}$  for  $N^*(3/2^+)$  resonances is

$$P_{3/2}^{\mu\nu} = \frac{\gamma \cdot p + M_{N^*}}{M_{N^*}^2 - p^2 - iM_{N^*}\Gamma_{N^*}} \left[ g^{\mu\nu} - \frac{1}{3}\gamma^\mu\gamma^\nu - \frac{2p^\mu p^\nu}{3M_{N^*}^2} + \frac{p^\mu\gamma^\nu - p^\nu\gamma^\mu}{3M_{N^*}} \right], \quad (10.3.14)$$

with  $p = k_2 + k_3$ . Other partial wave amplitudes can be constructed similarly [238, 241].

## 10.4 Prospects for baryon spectroscopy at BESIII

Recent empirical indications of a positive strangeness magnetic moment and positive strangeness radius of the proton suggest that the five-quark components in baryons may be largely in colored diquark cluster configurations rather than in “meson cloud” configurations or in the form of a sea of quark-antiquark pairs [218, 219]. The diquark cluster picture also gives a natural explanation that the excess of  $\bar{d}$  over  $\bar{u}$  in the proton is due to the presence of a  $[ud][ud]\bar{d}$  component. More precise measurements and analyses of the strange form factors are needed to examine the relative importance of the meson-cloud components and  $q^2q^2\bar{q}$  components in the proton.

For baryons, the spatial excitation energy could be larger than that needed to pull a  $q\bar{q}$  pair from the gluon field around a quark to form diquark clusters that contain a valence quark. As a result, five-quark components could be dominant for some excited baryon states.

The diquark cluster picture for the five-quark components in baryons also gives a natural explanation for the long-standing mass-reversal problem of the  $N^*(1535)$ ,  $N^*(1440)$  and  $\Lambda^*(1405)$  resonances, as well as the unusual decay pattern of the  $N^*(1535)$  resonance, *i.e.* the large coupling to  $K\Lambda$ . These could be the consequence of a large  $|[ud][us]\bar{s}\rangle$  component [218, 220].

The diquark cluster picture predicts the existence of  $SU(3)$  nonet partners of the  $N^*(1535)$  and  $\Lambda^*(1405)$ , *i.e.*, an additional  $\Lambda^* 1/2^-$  around 1570 MeV, a triplet  $\Sigma^* 1/2^-$  around 1360 MeV and a doublet  $\Xi^* 1/2^-$  around 1520 MeV [221]. There is, in fact, some evidence for all of these in BES  $J/\psi$  data. Figure 10.8 (left) shows the  $pK$  invariant mass spectrum for  $J/\psi \rightarrow pK^-\bar{\Lambda}+c.c.$  and Fig. 10.9 (right) shows the  $\Lambda\pi$  invariant mass spectrum for  $J/\psi \rightarrow \Lambda\bar{\Sigma}^+\pi^-$  [250]. In the  $pK$  invariant mass spectrum, beneath the narrow  $\Lambda^*(1520) 3/2^-$  peak is a quite obvious broader peak around 1570 MeV. A preliminary partial wave analysis [251] indicates its spin-parity to be  $1/2^-$ . Such a  $\Lambda^*(1570) 1/2^-$  resonance would fit neatly into the new scheme for a  $1/2^-$   $SU(3)$  baryon nonet. In the  $\Lambda\pi$  invariant mass spectrum of Fig. 10.9 (right), there are signs of a broad structure under the  $\Sigma^*(1385) 3/2^+$  peak. No partial wave analysis has yet been performed for this channel, but there is good reason to expect that there may be  $1/2^-$  component underneath the  $\Sigma^*(1385) 3/2^+$  peak.

According to the PDG [259], the branching fractions for  $J/\psi \rightarrow \bar{\Sigma}^-\Sigma^*(1385)^+$  and  $J/\psi \rightarrow \bar{\Xi}^+\Xi^*(1530)^-$  are  $(3.1 \pm 0.5) \times 10^{-4}$  and  $(5.9 \pm 1.5) \times 10^{-4}$ , respectively. These two processes are  $SU(3)$ -violating decays since the  $\Sigma$  and  $\Xi$  belong to an  $SU(3) 1/2^+$  octet while  $\Sigma^*(1385)$  and  $\Xi^*(1530)$  belong to an  $SU(3) 3/2^+$  decuplet. For comparison, the  $SU(3)$ -violating decay  $J/\psi \rightarrow \bar{p}\Delta^+$  has a branching fraction that is less than  $1 \times 10^{-4}$ , while the  $SU(3)$ -allowed decay  $J/\psi \rightarrow \bar{p}N^*(1535)^+$  has a branching fraction of  $(10 \pm 3) \times 10^{-4}$ . Thus the branching fractions for  $J/\psi \rightarrow \bar{\Sigma}^-\Sigma^*(1385)^+$  and  $J/\psi \rightarrow \bar{\Xi}^+\Xi^*(1530)^-$  are anomalously large. A possible explanation for this anomaly is that there are substantial  $1/2^-$  components under the  $3/2^+$  peaks and the two branching ratios were obtained assuming a pure  $3/2^+$  contribution. This possibility could be easily checked with the high statistics *BES-III* data in near future.

With two orders-of-magnitude higher statistics expected at *BES-III*, numerous important baryon spectroscopy issues can be studied with both  $J/\psi$  and  $\psi'$  decays. Data from the  $\psi'$  will significantly extend the mass range for the study of baryon spectroscopy.

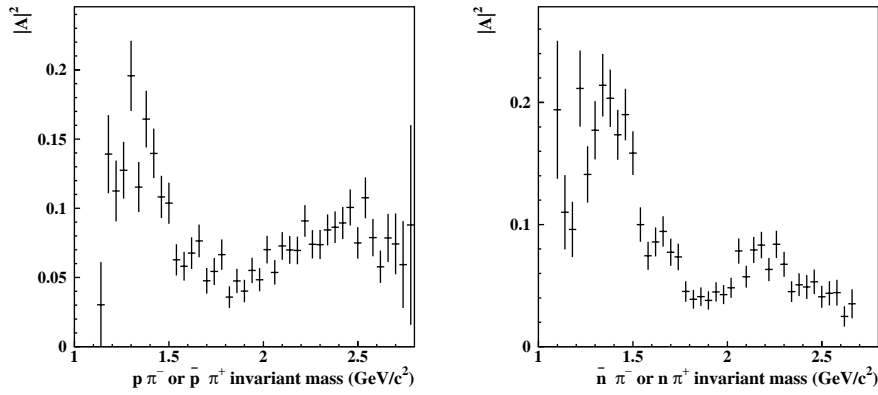


Figure 10.10: Data corrected by MC simulated efficiency and phase space versus  $p\pi^-$  (or  $\bar{p}\pi^+$ ) and  $\bar{n}\pi^-$  (or  $n\pi^+$ ) invariant mass for  $\psi' \rightarrow p\bar{n}\pi^- + c.c.$  candidate events [252].

For example, in a sample of  $\psi' \rightarrow p\bar{n}\pi^- + c.c.$  events collected at BESII [252], obvious structures at  $M_{N\pi} > 2$  GeV in the  $N\pi$  invariant mass spectra are evident (Fig. 10.10). However, the statistics are insufficient for drawing any conclusions about high mass  $N^*$  resonances [252, 253]. Determinations of the properties of these high mass  $N^*$  resonances can be done with the huge *BES-III* data samples. More importantly, many of the “missing”  $\Lambda^*, \Sigma^*$  and  $\Xi^*$  hyperon resonances are expected to be produced and observable in the high statistics *BES-III*  $J/\psi$  and  $\psi'$  data samples. Figure 10.11 shows the  $\Lambda^*, \Sigma^*, \Xi^*$  mass spectra (solid line) predicted by the classical  $qqq$  quark model [254, 199] and the predicted lowest  $1/2^-$   $\Lambda^*, \Sigma^*, \Xi^*$  states (dashed line) with pentaquark configurations [221], compared with observed states (indicated by boxes). The classical  $qqq$  quark model [254] predicts more than 30  $\Xi^*$  resonant states between 1.78 and 2.35 GeV as shown in Fig. 10.11. None of these have yet been established. These  $\Xi^*$  states cannot be produced in  $J/\psi$  decays because of the limited phase space, but all of them can be produced in  $\psi'$  decays. *BES-III*  $\psi'$  data will enable us to complete the  $\Lambda^*, \Sigma^*$  and  $\Xi^*$  spectrum and distinguish between various models for their internal structure, such as the simple  $qqq$  quark structure and more complicated structures in which pentaquark components dominate.

Table 10.2: Measured  $J/\psi$  decay branching ratios ( $\text{BR} \times 10^3$ ) for channels involving baryon anti-baryon and meson(s) [259, 247]

$p\bar{n}\pi^-$	$p\bar{p}\pi^0$	$p\bar{p}\pi^+\pi^-$	$p\bar{p}\eta$	$p\bar{p}\eta'$	$p\bar{p}\omega$
$2.4 \pm 0.2$	$1.1 \pm 0.1$	$6.0 \pm 0.5$	$2.1 \pm 0.2$	$0.9 \pm 0.4$	$1.3 \pm 0.3$
$\Lambda\bar{\Sigma}^-\pi^+$	$pK^-\bar{\Lambda}$	$pK^-\bar{\Sigma}^0$	$\bar{p}p\phi$	$\Delta(1232)^{++}\bar{p}\pi^-$	$pK^-\bar{\Sigma}(1385)^0$
$1.1 \pm 0.1$	$0.9 \pm 0.2$	$0.3 \pm 0.1$	$0.045 \pm 0.015$	$1.6 \pm 0.5$	$0.51 \pm 0.32$

The measured  $J/\psi$  decay branching ratios for channels involving baryon anti-baryon plus meson(s) are listed in Table 10.2. With  $10^{10}$   $J/\psi$  events, all of these channels will have large enough event samples to support partial wave analyses. Among these channels, the  $\Sigma\bar{\Lambda}\pi + c.c.$  channels will be given high priority in order to pin down the lowest  $1/2^-$   $\Sigma^*$  and  $\Lambda^*$  resonances as well as other, higher excited  $\Sigma^*$  and  $\Lambda^*$  states. Another very

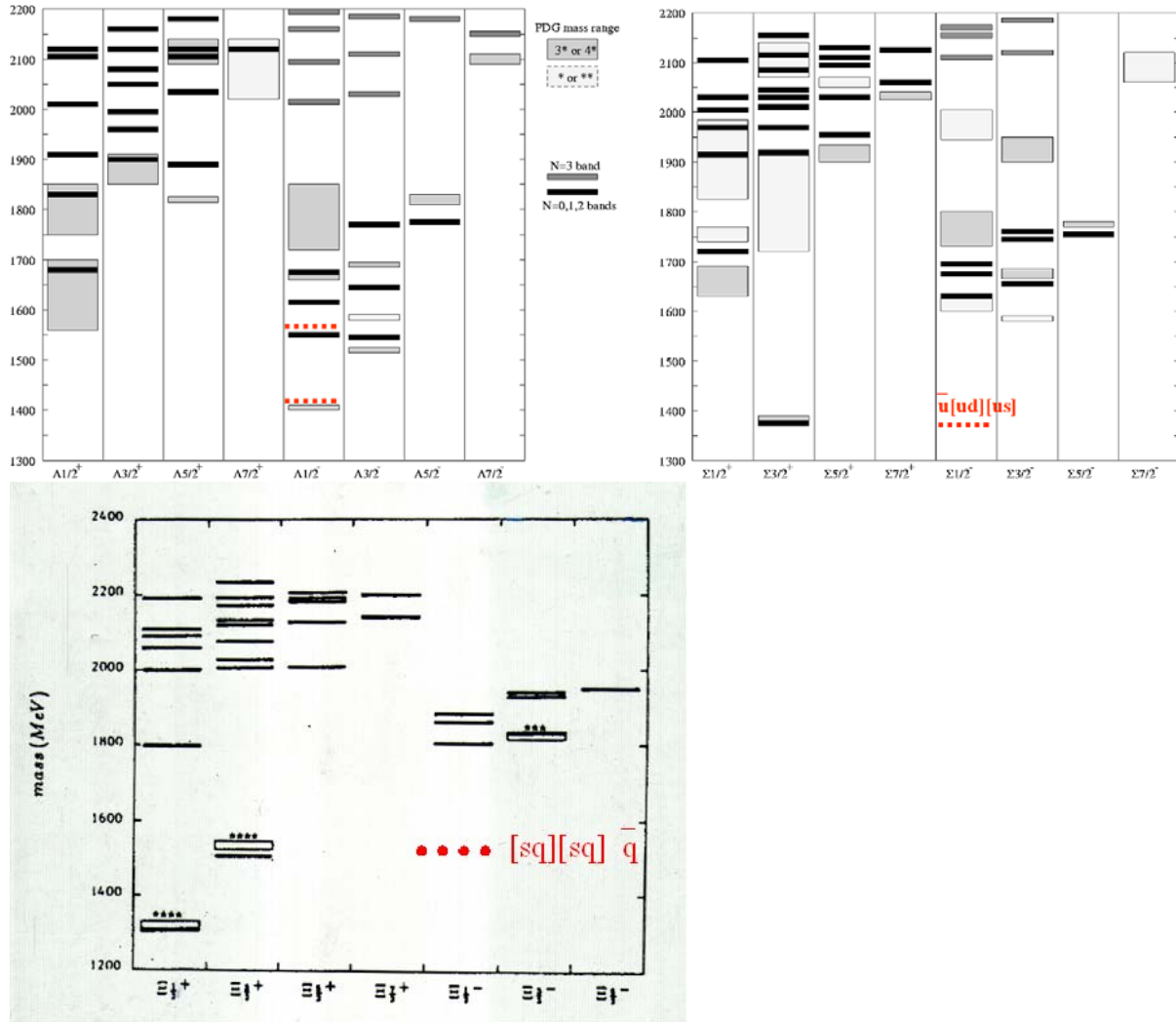


Figure 10.11: Predicted  $\Lambda^*, \Sigma^*, \Xi^*$  mass spectra (solid line) by the classical 3q quark model [254, 199] and the predicted lowest  $1/2^-$   $\Lambda^*, \Sigma^*, \Xi^*$  states (dashed line) with pentaquark configuration [221], compared with observed states (indicated by boxes).

important channel is  $K^-\Lambda\bar{\Xi}^+ + c.c.$  which will be the best channel for finding the lowest  $1/2^- \Xi^*$  resonance and other “missing”  $\Xi^*$  states that decay via  $\Xi^* \rightarrow K\Lambda$ . This channel should be rather easily reconstructed in *BES-III*. One can select events containing a  $K^-$  and a  $\Lambda$  with  $\Lambda \rightarrow p\pi^-$  and then use the narrow peak in the  $K^-\Lambda$  recoil mass spectrum to identify the undetected  $\bar{\Xi}^+$ .

For  $10^9 \psi'$  events, the  $K^-\Lambda\bar{\Xi}^+ + c.c.$  and  $p\bar{p}\phi$  final states, which have very limited phase space in  $J/\psi$  decays, will be given high priority. The  $K^-\Lambda\bar{\Xi}^+ + c.c.$  channel will provide opportunities to discover many of the “missing”  $\Xi^*$  resonances, while the  $p\bar{p}\phi$  channel should allow us to find  $N^*$  resonances that have a large coupling to  $N\phi$  [255] and, thus, large five-quark components.

After analyzing the easier three-body final states, four-body and even five-body channels could also be investigated. Among these,  $\Delta(1232)^{++}\bar{p}\pi^-$  in  $p\bar{p}\pi^+\pi^-$  and  $\Delta(1232)^{++}\bar{\Sigma}^-K^-$  in  $p\bar{\Sigma}^-\pi^+K^-$  are very good channels for finding “missing”  $\bar{\Delta}^{*--}$  states decaying to  $\bar{p}\pi^-$  and  $\bar{\Sigma}^-K^-$ . The spectrum of isospin  $3/2$   $\Delta^{++*}$  resonances is of special interest since it is the most experimentally accessible system that is comprised of three identical valence quarks. It has recently been proposed that the lowest  $1/2^-$  baryon decuplet contains large vector-meson-baryon molecular components [256]. In this new scheme, the  $\Xi^*(1950)$  is predicted to be a  $1/2^-$  resonance with a large coupling to  $\Lambda K^*$ . The  $\psi' \rightarrow \bar{\Xi}\Lambda K^*$  process will provide a very good place to look for a “missing”  $\Xi^*$  with a large  $\Lambda K^*$  coupling.

In summary, *BES-III* data can play a very important role in the study of excited nucleons and hyperons, *i.e.*, the very poorly understood  $N^*$ ,  $\Lambda^*$ ,  $\Sigma^*$ ,  $\Xi^*$  and  $\Delta^{*++}$  resonances.

# Chapter 11

## Physics of soft pions and the lightest scalars at *BES-III*

A brief introduction to the physics related to soft pions, light scalar mesons and the final state interaction theorem for *BES-III* experiments is given.

### 11.1 Partially conserved vector current (PCAC) and soft pions

#### 11.1.1 PCAC

Strong interaction physics is described by Quantum Chromodynamics (QCD), where  $\bar{\psi}\psi$  has vacuum quantum numbers and a non-vanishing vacuum expectation value:  $\langle\bar{\psi}\psi\rangle \neq 0$ . As a consequence, the pseudo-Goldstone bosons,  $\pi^a$ , couple to the axial-vector current,  $\langle 0|A_\mu^a|\pi^a \rangle \neq 0$ . If isospin is a good quantum number then,

$$\langle 0|A_\mu^a|\pi^b \rangle = f_\pi \delta^{ab} p_\mu , \quad (11.1.1)$$

where  $f_\pi = 93\text{MeV}$  is the  $\pi$  decay constant as determined from  $\pi \rightarrow l\nu$  decay. For an on-shell pion Eq. (11.1.1) becomes

$$\langle 0|\partial^\mu A_\mu^a|\pi^b \rangle = f_\pi \delta^{ab} m_\pi^2 , \quad \text{or} \quad \langle 0|\partial^\mu A_\mu^a|\pi^b \rangle = f_\pi m_\pi^2 \langle 0|\phi^a|\pi^b \rangle . \quad (11.1.2)$$

Generalizing to the operator form, we have

$$\partial^\mu A_\mu^a = f_\pi m_\pi^2 \phi^a . \quad (11.1.3)$$

This is the celebrated Partial Conservation of Axial Current (PCAC) relation [257]. The most important applications of PCAC are the derivations of various soft pion theorems. In the following we briefly discuss a few of them.

#### 11.1.2 Adler's theorem with one soft pion

Adler's theorem states that: *In order to calculate the matrix element for a strong interaction process involving one soft pion:  $i \rightarrow f + \pi$ , one only needs to consider the*

process without the pion,  $i \rightarrow f$ , and then insert the pion into any of the external lines, using derivative coupling theory. A diagrammatic explanation to the Adler's theorem is given in Fig. 11.1.

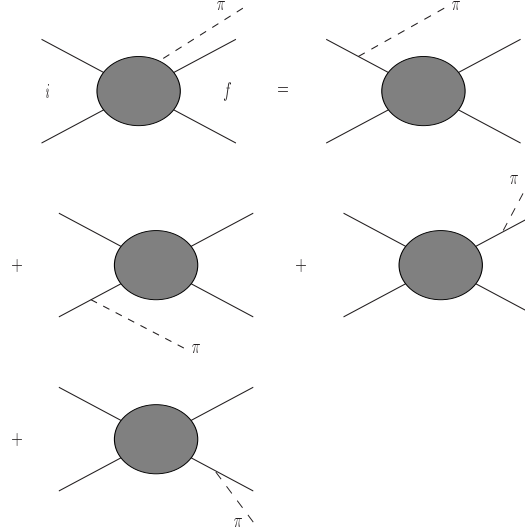


Figure 11.1: Diagrammatic explanation of the Adler's theorem.

Notice that the theorem as stated above is only exact when all four components of the pion momentum  $k_\pi^\mu \rightarrow 0$  simultaneously ( $\pi$  off-shell). In practice it means that any quantity  $k \cdot p$ , where  $p$  is any momentum involved in the process  $i \rightarrow f + \pi$ , can be considered to be small. A simple proof of the theorem can be found in Ref. [258].

An important application of the soft pion theorem is to  $\pi\pi \rightarrow \pi\pi$  scatterings. Where, since there is no  $3\pi$  coupling,

$$T(p_1, p_2, p_3 \rightarrow 0, p_4) = 0 . \quad (11.1.4)$$

In terms of the Mandelstam variables, when  $p_3 \rightarrow 0$ , one has  $s = (p_1 + p_2)^2 = m_\pi^2$ ,  $t = (p_1 - p_3)^2 = m_\pi^2$ ,  $u = (p_1 - p_4)^2 = m_\pi^2$ , and we find that the Adler zero for  $\pi\pi$  scattering corresponds to  $s = t = u = m_\pi^2$ . This zero is not far from  $\pi\pi$  scattering threshold. Hence the threshold parameters for  $\pi\pi$  scatterings are suppressed due to the existence of this  $T$ -matrix zero.

An important process in  $J/\psi$  physics where the soft pion theorem can be applied is  $\psi' \rightarrow J/\psi\pi\pi$  decay. The decay branching ratio of  $\psi'(3685)$  into  $J/\psi$  and light hadrons is  $(55.7 \pm 2.6)\%$  [259], including  $\text{Br}(\psi' \rightarrow J/\psi \pi^+ \pi^-) = (30.5 \pm 1.6)\%$  and  $\text{Br}(\psi' \rightarrow J/\Psi \pi^0 \pi^0) = (18.2 \pm 1.2)\%$ . Therefore the  $\psi' \rightarrow J/\psi\pi\pi$  process is a dominant  $\psi'$  decay channel. The transition amplitude for  $\psi' \rightarrow J/\psi\pi\pi$  is

$$M = \langle \psi\pi\pi | \psi' \rangle = \langle P, \epsilon; p_{1a}, p_{2b} | P', \epsilon' \rangle . \quad (11.1.5)$$

Using PCAC one can obtain, after some algebraic manipulation [260],

$$\begin{aligned} \langle \psi\pi\pi | \psi' \rangle &= -(p_1^2 - m_\pi^2)(p_2^2 - m_\pi^2)(\phi^a \phi^b) \\ &= f_\pi^{-2} p_1^\mu p_2^\nu (\overline{A}_\mu^a \overline{A}_\nu^b) - i f_\pi^{-1} (p_1^2 + p_2^2 - m_\pi^2) \langle \psi | \tilde{\Sigma}^{ab} | \psi' \rangle , \end{aligned} \quad (11.1.6)$$

where  $\overline{A}$  indicates that the pion pole part of the axial vector current,  $A$ , has been subtracted. Both the term in the parentheses, and the inner product term (*i.e.* the Sigma term) are regular functions when  $p_\mu \rightarrow 0$  [260]. It is evident from the formula that when  $p_1^\mu \rightarrow 0$  and  $p_2$  is on-shell or vice versa,  $M \rightarrow 0$ . This is the Adler zero condition.

### 11.1.3 The linear $\sigma$ model and chiral shielding

Historically, the  $\sigma$  meson was first introduced in association with the  $SU(2) \times SU(2)$  linear  $\sigma$  model in an attempt to describe the spontaneous breaking of chiral symmetry. The model has the advantage of a natural realization of PCAC and current algebra. In the linear sigma model lagrangian there are iso-triplet ( $\pi_1, \pi_2, \pi_3$ ) fields and a scalar iso-singlet  $\sigma$  field [261]:

$$\begin{aligned}\mathcal{L} &= \mathcal{L}_s + c\sigma , \\ \mathcal{L}_s &= \frac{1}{2}[(\partial_\mu\sigma)^2 + (\partial_\mu\pi)^2] - \frac{m^2}{2}[\sigma^2 + \pi^2] - \frac{\lambda}{4}[\sigma^2 + \pi^2]^2 .\end{aligned}\quad (11.1.7)$$

The last term in the first equation indicates that chiral symmetry is not exact,  $c = f_\pi m_\pi^2$  is a small quantity. If  $c = 0$ , the lagrangian is invariant under the  $SU_L(2) \times SU_R(2)$  chiral rotations:

$$\begin{aligned}\vec{\pi} &\rightarrow \vec{\pi} + \vec{\alpha} \times \vec{\pi} - \vec{\beta}\sigma , \\ \sigma &\rightarrow \sigma + \vec{\beta} \cdot \vec{\pi} .\end{aligned}\quad (11.1.8)$$

When  $m^2 < 0$ , chiral symmetry is spontaneously broken; the minimum of the effective potential is taken at  $\langle \sigma \rangle = f_\pi$  and we can redefine another scalar field with vanishing vacuum expectation value  $s$  as,

$$\sigma = s + f_\pi , \quad \langle s \rangle = 0 . \quad (11.1.9)$$

The new lagrangian expressed in terms of the shifted field is

$$\mathcal{L} = \frac{1}{2}[(\partial_\mu\pi)^2 - m_\pi^2\pi^2] + \frac{1}{2}[(\partial_\mu s)^2 - m_\sigma^2 s^2] - \lambda f_\pi s(s^2 + \pi^2) - \frac{\lambda}{4}[s^2 + \pi^2]^2 . \quad (11.1.10)$$

From the above we find

$$m_\sigma^2 = m_\pi^2 + 2\lambda f_\pi^2 . \quad (11.1.11)$$

In addition we determine the  $\sigma\pi\pi$  coupling constant,

$$g_{\sigma\pi\pi} = \frac{m_\sigma^2 - m_\pi^2}{f_\pi} = 2\lambda f_\pi . \quad (11.1.12)$$

Here the coupling constant  $g_{\sigma\pi\pi}$  is proportional to the mass square of the  $\sigma$  meson and, thus, the interaction becomes very strong in the large  $m_\sigma$  limit. As a result, there does not exist a trivial decoupling limit when  $m_\sigma \rightarrow \infty$ . As a consequence, the decay width of  $\sigma \rightarrow \pi\pi$  (in the chiral limit) at tree level is proportional to the  $m_\sigma^3$ :

$$\Gamma(\sigma \rightarrow \pi\pi) = \frac{3m_\sigma^3}{32\pi f_\pi^2} \sqrt{1 - \frac{4m_\pi^2}{m_\sigma^2}} . \quad (11.1.13)$$

From this formula one sees that when  $m_\sigma = 600\text{MeV}$ ,  $\Gamma_\sigma \simeq 660\text{MeV}$ , *i.e.*, its large width already exceeds its mass. The appearance of a large width indicates the failure of perturbation calculations and also the Breit–Wigner description of the resonance, since the latter is only a narrow width approximation [262]. The  $\pi\pi$  scattering amplitudes can be calculated at tree level using the linear sigma model, as shown in Fig. 11.2.

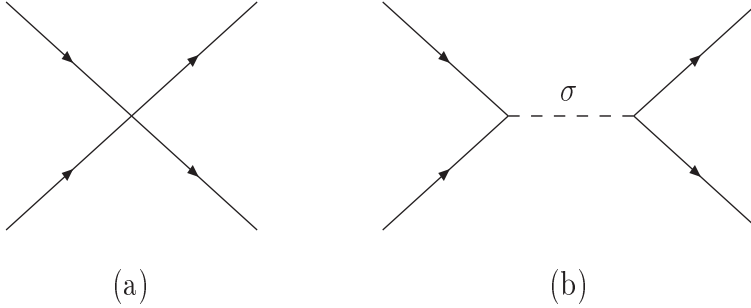


Figure 11.2: First-order Feynman graphs for  $\pi\pi$  scatterings in the linear  $\sigma$  model. The crossed channel diagrams are not shown.

There are only two types of diagrams: the  $4\pi$  contact interaction (Fig. 11.2(a)), and the  $\sigma$  exchange diagram (Fig. 11.2(b)). One has,

$$\begin{aligned} T^{I=0}(s, t, u) &= 3A(s, t, u) + A(t, u, s) + A(u, s, t) , \\ T^{I=1}(s, t, u) &= A(t, u, s) - A(u, s, t) , \\ T^{I=2}(s, t, u) &= A(t, u, s) + A(u, s, t) , \end{aligned} \quad (11.1.14)$$

where

$$A(s, t, u) = -2\lambda\left(1 + \frac{2\lambda v^2}{s - m_\sigma^2}\right) = -\frac{m_\sigma^2 - m_\pi^2}{s - m_\sigma^2} \frac{s - m_\pi^2}{f_\pi^2} . \quad (11.1.15)$$

In the above, the first term on the *r.h.s.* of the first equality corresponds to the background contact  $\lambda\phi^4$  interaction. To preserve the boundedness of the vacuum energy from below,  $\lambda$  must be positive and, thus, the  $\lambda\phi^4$  contact interaction is repulsive. The second term is from the  $\sigma$  pole and provides an attractive force at low energies. The explicit calculation described at the conclusion of Sec. 11.1.2 confirms this; the two terms in Eq. (11.1.15) cancel almost exactly at threshold, which is as expected from the low energy soft pion theorem.

The partial wave projection of the full amplitude is,

$$T_J^I(s) = \frac{1}{32\pi(s - 4m_\pi^2)} \int_{4m_\pi^2 - s}^0 dt P_J\left(1 + \frac{2t}{s - 4m_\pi^2}\right) T^I(s, t, u) . \quad (11.1.16)$$

From Eq. (11.1.15) one gets partial wave amplitudes  $T_J^I$  as follows:

$$\begin{aligned} T_0^0 &= \frac{\lambda}{16\pi} \left( \frac{3(m_\sigma^2 - m_\pi^2)}{m_\sigma^2 - s} + \frac{2(m_\sigma^2 - m_\pi^2) \log[\frac{m_\sigma^2 + s - 4m_\pi^2}{m_\sigma^2}]}{s - 4m_\pi^2} - 5 \right) , \\ T_0^2 &= -\frac{\lambda}{8\pi} \left( 1 - \frac{2\lambda v^2}{s - 4m_\pi^2} \log[\frac{m_\sigma^2 + s - 4m_\pi^2}{m_\sigma^2}] \right) , \\ T_1^1 &= \frac{\lambda^2 v^2 (16m_\pi^2 - 4s - 2(4m_\pi^2 - 2m_\sigma^2 - s) \log[\frac{m_\sigma^2 + s - 4m_\pi^2}{m_\sigma^2}])}{8\pi(s - 4m_\pi^2)^2} . \end{aligned} \quad (11.1.17)$$

It is not very easy to recognize the  $T$ -matrix zero from the above partial wave amplitudes. Taking the limit of  $m_\sigma \rightarrow \infty$  while keeping  $\lambda$  fixed, we find that the zeros are located at  $s = m_\pi^2/2$ ,  $4m_\pi^2$  and  $2m_\pi^2$  for  $IJ = 00, 11$  and  $20$ , respectively. The positions of these zeros also receive small corrections from higher orders. In the limit of  $m_\sigma \rightarrow \infty$  and  $f_\pi$  fixed, the partial wave amplitudes from Eq. (11.1.17) become

$$T_0^0 = \frac{2s - m_\pi^2}{32\pi f_\pi^2}, \quad T_0^2 = \frac{2m_\pi^2 - s}{32\pi f_\pi^2}, \quad T_1^1 = \frac{s - 4m_\pi^2}{96\pi f_\pi^2}, \quad (11.1.18)$$

which agree with the lowest order results from chiral perturbation theory, and are, in fact, predictions from current algebra.

The lesson we learn from the above is that it is very difficult to identify the  $\sigma$  pole (if there is one) in experiments, since the background contribution cancels that from the  $\sigma$  near threshold, as dictated by the soft pion theorem. In the language of Ref. [263], this is called ‘chiral shielding’. Furthermore, the  $\sigma$  meson has a large width which makes it difficult to distinguish from backgrounds.

#### 11.1.4 Why should there be a $\sigma$ resonance?

The chiral shielding of the  $\sigma$  has probably been known since the invention of the linear  $\sigma$  model. It implies, on one hand, the cancelation between a positive  $\sigma$  contribution and a negative background contribution to the  $\pi\pi$  scattering phase shift, a fact that has led many physicists to argue for the possible existence of the  $\sigma$  resonance [264, 265]. On the other hand, since no firm evidences for the  $\sigma$  meson had been found experimentally, it was thought that the  $\sigma$  meson is not necessary for describing chiral symmetry breaking and this, in turn, led to the invention of the non-linear realization of chiral symmetry, from which chiral perturbation theory was constructed [266]. The latter has been very successful at describing low energy strong interaction physics without referring to a  $\sigma$  meson. Indeed the chiral cancelation mechanism in the linear realization only provides at most a self-consistent description to the data and is insufficient to provide solid proof for the existence of the  $\sigma$  pole. However, the background contribution from the nearby left-hand cut can be estimated using chiral perturbation theory, and the background contribution to the  $\pi\pi$  scattering phase shift is found to be negative. This proves that the  $\sigma$  pole is essential for the application of chiral perturbation theory to experimental data [267].

The existence of the  $\sigma$  pole has been reported in production experiments, such as in  $D$ -meson decays in E791 [268] and  $J/\psi$  and  $\psi(2S)$  decays at BES [269, 271]. In Ref. [268], a sample of  $1172 \pm 61$   $D^- \rightarrow \pi^-\pi^+\pi^+$  decays (the ratio  $\Gamma(D^+ \rightarrow \pi^-\pi^+\pi^+)/\Gamma(D^+ \rightarrow K^-\pi^+\pi^+)$  is about 3%), is used to provide evidence for the existence of a scalar resonance with mass and width  $M = 478_{-23}^{+24} \pm 17$  MeV,  $\Gamma = 324_{-40}^{+42} \pm 21$  MeV, with a corresponding pole position of  $M = 489$  MeV,  $\Gamma = 346$  MeV. As is mentioned in the following section, BES data also show a strong broad scalar  $\pi\pi$  resonance in  $J/\psi$  and  $\psi(2S)$  decays.

Furthermore, it is found that the broad scalar resonance accounts for approximately half of all decays. However, the results from the BES collaboration [269] and the E791 collaboration [268] look somewhat different, reflecting the uncertainties in parameterization of a light and broad resonance.

## 11.2 Beyond the Breit–Wigner description of a broad resonance

In production experiments, different processes have shown evidence for the  $\sigma$  meson. However, since the  $\sigma$  pole has a large width, it is difficult to separate it unambiguously from background contributions. It has been pointed out that in phase shift analyses, crossing symmetry plays a very important role and, thus, is useful for determining the pole location [272]. The mass and width are found to be  $m_\sigma = 470 \pm 50$  MeV and  $\Gamma_\sigma = 570 \pm 50$  MeV, respectively, which is in good agreement with the Roy equation determination of the  $\sigma$  pole:  $m_\sigma = 441^{+16}_{-8}$  MeV and  $\Gamma_\sigma = 544^{+18}_{-25}$  MeV [273]. The evidence for such a light and broad resonance requires careful attention to the issue on how to parameterize it.

### 11.2.1 How to describe a light and broad resonance

For a resonance as broad as the  $\sigma$  meson, its lineshape's peak mass value can be drastically different from its pole mass location [274]. The simple form for a resonance propagator is

$$\Delta(s) = \frac{1}{s - M^2 + iM\Gamma(s)} , \quad (11.2.19)$$

where  $\Gamma(s)$  is the momentum dependent width, which is proportional to the square of the coupling constant,  $g^2$  and also proportional to the phase space factor,  $\rho$ . In Eq. (11.2.19),  $M$  is a mass parameter (the lineshape mass), when  $\sqrt{s} = M$  the real part of the propagator vanishes. The pole mass of the resonance, denoted as  $m_{pole}$ , however, is defined as the zero of the denominator of  $\Delta(s)$ :

$$m_{pole}^2 - M^2 + iM\Gamma(m_{pole}^2) = 0 . \quad (11.2.20)$$

The complex root of this equation is located on the un-physical sheet<sup>1</sup> as dictated by the requirement of micro-causality. Apparently,  $m_{pole}$  is usually complex. It may be further written as  $m_{pole} \equiv m - i\Gamma/2$ . When the coupling constant  $g$  is large,  $m$  and  $\Gamma$  can be totally different from  $M$  and  $\Gamma(M^2)$ . Taking the  $\sigma$  resonance as an example, one estimate gives  $m_{pole} \simeq 450$  MeV, but with a lineshape mass as large as 1 GeV. The latter in general is not a good definition of a broad resonance, because when the coupling strength becomes strong, the real part of the self-energy may contain a non-negligible  $s$  dependence [264]. One of the frequently used simple parametrization forms for the  $\sigma$  meson is

$$\Delta(s) = \frac{1}{s - M^2 + i\rho(s)G} , \quad (11.2.21)$$

where  $G$  is a constant to be fixed by the fit. However, as pointed out in Ref. [275], Eq. (11.2.21) does not describe a single pole. Instead, it contains in addition a virtual pole for equal-mass scattering, or an additional resonance pole for unequal-mass scattering. These additional poles are located in the small  $|s|$  region and should not, in fact, exist if we trust chiral perturbation theory predictions for small  $|s|$ . The spurious pole(s) hidden

<sup>1</sup>The kinematic factor,  $\rho$  is of square root cut structure where the resonance couples to two massive particles. The un-physical sheet is reached by changing the sign of  $\rho$ .

in Eq. (11.2.21) can be simply subtracted out in which case Eq. (11.2.21) can be rewritten as

$$\Delta(s) = \frac{1}{s - M^2 + i\rho(s)sG} . \quad (11.2.22)$$

This equation, called the "Red Dragon" by Minkowski and Ochs [276], depicts very well the smooth but steady rise of the low energy  $\pi\pi$  phase shift in the  $IJ = 00$  channel.

A parametrization frequently found in the literature introduces an exponential form-factor aimed at suppressing the resonance contribution at large momentum separations (see, for example, Ref. [277, 264]). This has the form,

$$\Gamma(s) = \alpha(2s - m_\pi^2) \frac{\sqrt{s - 4m_\pi^2}}{\sqrt{s}} e^{-(s - M_r^2)/4\beta^2} , \quad (11.2.23)$$

where  $\alpha$  and  $\beta$  are free parameters and  $M_r$  is the resonance mass. Other parametrization forms can also be found in the literature [278]. The BES experiment [269] tested both Eq. (11.2.22) and Eq. (11.2.23). Despite the very different parameterizations, they were not able, at their level of experimental precision, to distinguish between them based on the quality of fit. On the other hand, there exist ambiguities associated with the description of a broad resonance. There are only a few general rules that govern the form of the propagator: first, chiral suppression of the  $\sigma$  coupling to pion fields at low energies has to be taken into account; second, spurious singularities hidden in the propagator, if any, have to lie very far from the physical region where they can be considered as purely background contributions; third, the propagator must obey real analyticity. The latter means  $\Delta(s - i\epsilon) = \Delta(s + i\epsilon)^*$ . Aside from these basic rules, it is not known how to separate clearly background contributions from a broad pole contribution. There exist some freedom to absorb part of the background contributions into the  $\sigma$  propagator and vice versa. Hence the differences between two parameterizations only reflect the different definition of background contributions. Nevertheless, the  $\sigma$  pole location itself is a physical quantity and should not, in principle, depend on the parameterization form that is used.

### 11.2.2 The $\sigma$ pole in the BESII experiment

In an analysis of the  $J/\psi \rightarrow \omega\pi^+\pi^-$  [269] process, the BESII collaboration found strong evidence for the existence of the  $\sigma$ , as shown in Figs. 11.3 and 11.4. The pole mass and width are found to be  $m_\sigma = 541 \pm 39$  MeV and  $\Gamma_\sigma = 504 \pm 84$  MeV, respectively. Different parameterizations were tested in the analysis. Nevertheless, within the current experimental precision and the lack of the knowledge of the production vertex, it is difficult to distinguish between different parametrization forms.

In an early study of the  $\psi' \rightarrow J/\psi\pi^+\pi^-$  process by the BES collaboration, it is found that the data can be well described without assuming the existence of the  $\sigma$  [270]. However, the  $\sigma$  pole, if it exists in  $J/\psi \rightarrow \omega\pi\pi$  process, has to be present in  $\psi' \rightarrow J/\psi\pi^+\pi^-$  as well. In Ref. [271], this process is re-investigated and the data are described by the cancelation between the sigma pole and a negative background, in agreement with the picture given in Section 11.1.3. More importantly, the sigma pole location, although with large uncertainties, is found to be stable and consistent with the result given in Ref. [269], in agreement with the concept of pole universality discussed below. Figure 11.5 shows the experimental results.

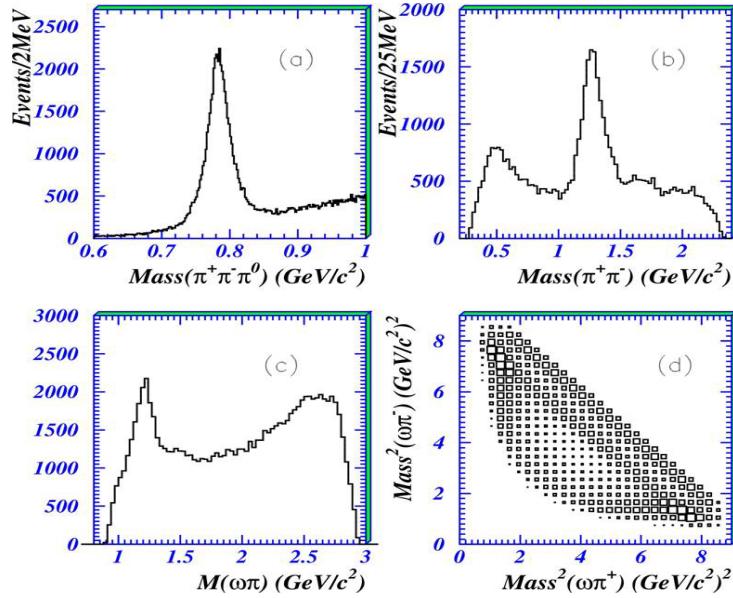


Figure 11.3: (a.) Distribution of  $\pi^+\pi^-\pi^0$  mass. (b.) Distribution of the  $\pi^+\pi^-$  invariant mass recoiling against the  $\omega$ . (c.) Distribution of  $\omega\pi$  invariant mass. (d.) Dalitz plot.

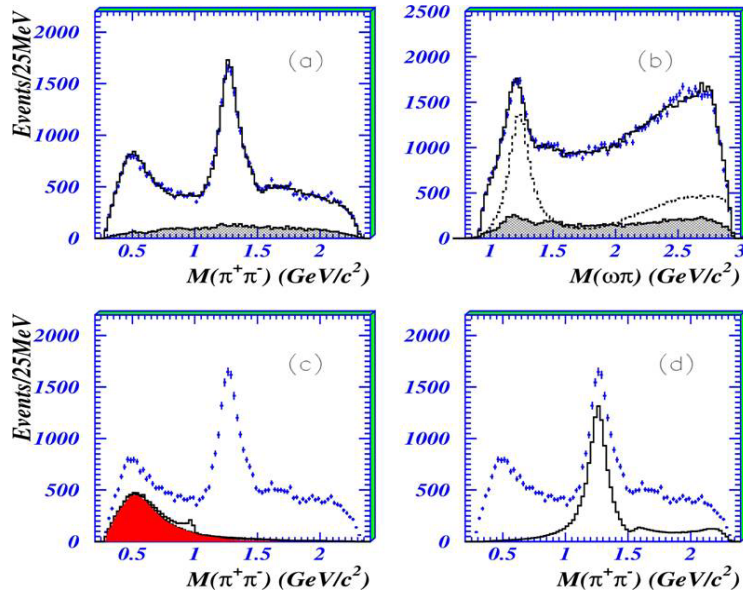


Figure 11.4: Mass projections of data compared with the fit (histograms); the shaded region shows background estimated from sidebands. (a) and (b):  $\pi\pi$  and  $\omega\pi$  mass; the dashed curve in (b) shows the fitted  $b_1(1235)$  signal (two charge combinations). (c) and (d): mass projections of  $0^{++}$  and  $2^{++}$  contributions to  $\pi^+\pi^-$  from the fit; in (c), the shaded area shows the  $\sigma$  contribution alone, and the full histogram shows the coherent sum of  $\sigma$  and  $f_0(980)$ .

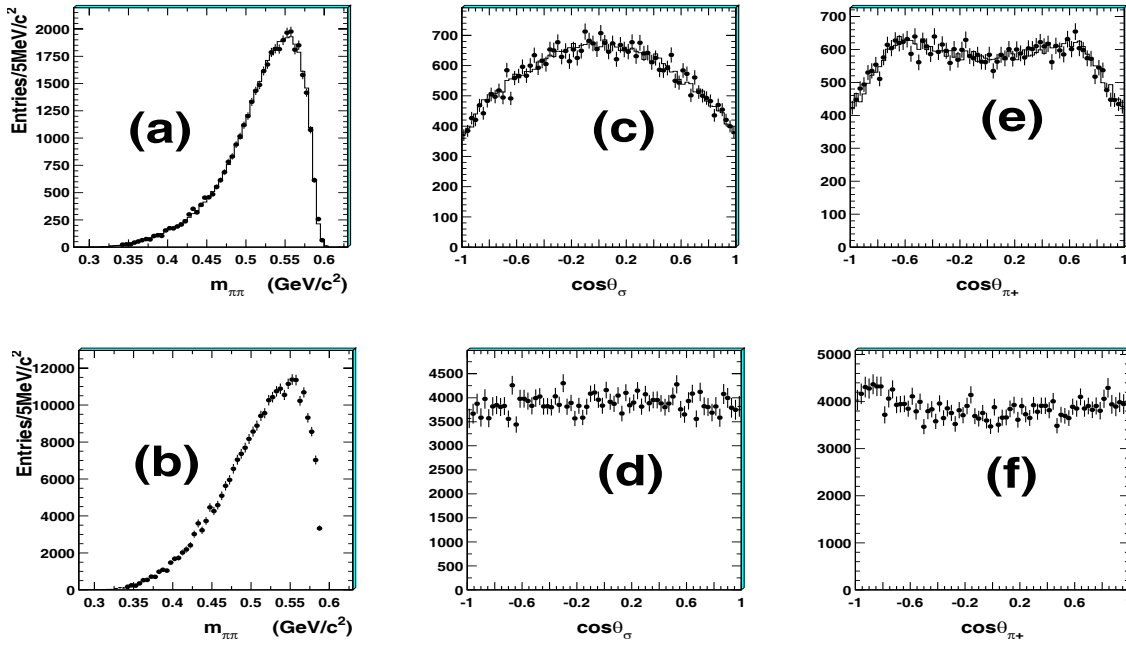


Figure 11.5: Fit results of  $\psi(2S) \rightarrow \pi^+\pi^-J/\psi$  (P.K.U. ansatz). Dots with error bars are data and the histograms are the fit results. (a) and (b) are the  $\pi^+\pi^-$  invariant mass, (c) and (d) the cosine of the  $\sigma$  polar angle in the lab frame, and (e) and (f) the cosine of the  $\pi^+$  polar angle in the  $\sigma$  rest frame. (From Ref. [271])

It is generally expected that for a certain resonance, its pole location should be unique, no matter what process it appears in. Although resonance parameters, such as mass and width, obtained using different parametrizations as described in Sec. 11.2.1 can be very different, their pole positions are the same. This is demonstrated by experimental results obtained by the BES experiment [269, 271, 292].

## 11.3 Final state interaction theorem and Omn  s solution

### 11.3.1 The final state interaction theorem

Assuming there exist a group of eigenstates of the strong interaction and total angular momentum  $J$  ( $J$  is a good quantum number),  $|1\rangle, |2\rangle, \dots, |n\rangle$ , the strong interaction  $S$  matrix has the diagonal form  $S_0 = \text{diag}(e^{2i\delta_1}, \dots, e^{2i\delta_n})$ . After introducing the “weak” interaction, the  $S$  matrix elements are no longer diagonal. The non-diagonal elements are assumed weak,  $i\Sigma \propto O(\epsilon)$ . In the zero-th order approximation,  $S = S_0$ . In the first-order approximation

$$S = S_0 + i\Sigma . \quad (11.3.24)$$

Unitarity requires  $SS^+ = S^+S = 1$ , or

$$1 \simeq S_0^+ S_0 + i(\Sigma S_0^+ - S_0 \Sigma^+) + O(\epsilon^2) . \quad (11.3.25)$$

This leads to  $\Sigma S_0^+ = S_0 \Sigma^+$ . From time reversal invariance  $\Sigma_{mn} = \Sigma_{nm}$  we get

$$\Sigma_{mn} = |\Sigma_{mn}| e^{i(\delta_n + \delta_m)} . \quad (11.3.26)$$

For a “weak” two body final state amplitude, we have  $A_{i \rightarrow f} = |A_{i \rightarrow f}| e^{i\delta_f}$  where  $\delta_f$  is the phase shift of the two body final-state interaction. This is called Watson’s theorem for final state interactions [279]. Examples are  $\gamma\gamma \rightarrow 2\pi$ ,  $K_s \rightarrow 2\pi$ ,  $\Sigma^- \rightarrow n\pi^-$  and  $\Lambda^0 \rightarrow \pi N$ , etc..

### 11.3.2 $D^+ \rightarrow K^-\pi^+l\nu_l$ decays

An important process for future *BES-III* experimentation, for which the final state interaction theorem applies, is  $D^+ \rightarrow K^-\pi^+l\nu_l$ . Since the leptons are spectators to the strong interactions, the strong phase is generated from  $\pi K$  rescattering, when the invariant mass of the  $\pi K$  system is less than the  $\pi\eta'$  threshold, are exactly the same as the one that appears in  $\pi K$  elastic scattering, according to the final state interaction theorem. The  $D^+ \rightarrow K^-\pi^+l\nu_l$  process should be *P*-wave dominant (via  $D^+ \rightarrow \bar{K}^{*0}l\nu_l$ ), but the FOCUS Collaboration found evidence for a small, even-spin  $K\pi$  amplitude that interferes with the dominant  $\bar{K}^{*0}$  component [280]. The data can be described by  $\bar{K}^{*0}$  interference with either a constant amplitude or a broad spin 0 resonance. Thus, a careful reanalysis at *BES-III* that extracts the *S*-wave component and the phase is very important for further investigation of the  $\kappa$  pole problem. The final state interaction theorem is also confirmed in Ref. [281]. Edera and Pennington give a review on the related experimental analyses in Ref. [282].

### 11.3.3 $D^+ \rightarrow K^-\pi^+\pi^+$ decays

In Ref. [283], an isobar model is used to parameterize the partial wave amplitude. In this model, the decay amplitude  $\mathcal{A}$  is described by a sum of quasi two-body terms  $D \rightarrow R + k$ ,  $R \rightarrow i + j$ , in each of the three channels  $k = 1, 2, 3$ :

$$\mathcal{A} = d_0 e^{i\delta_0} + \sum_{n=1}^N d_n e^{i\delta_n} \frac{F_R(p, r_R, J)}{m_{R_n}^2 - s_{ij} - im_{R_n} \Gamma_{R_n}(s_{ij})} \times F_D(q, r_D, J) M_J(p, q) ,$$

where  $s_{ij}$  is the squared invariant mass of the  $ij$  system,  $J$  is the spin,  $m_{R_n}$  the mass and  $\Gamma_{R_n}(s_{ij})$  the width of the  $n$ th resonance,  $F_R$  and  $F_D$  are form factors, with effective radius parameters  $r_R$  and  $r_D$ , for all  $R_n$  and for the parent  $D$  meson, respectively,  $p$  and  $q$  are momenta of  $i$  and  $k$ , respectively, in the  $ij$  rest frame, and  $M_J(p, q)$  is a factor introduced to describe spin conservation in the decay. For more detailed discussions on this expression see Ref. [268].

The complex coefficients  $d_n e^{i\delta_n}$  ( $n = 0, N$ ) are determined by the  $D$  decay dynamics and are parameters estimated by a fit to the data. The first, the non-resonant (*NR*) term describes direct decay to  $i + j + k$  with no intermediate resonance, and  $d_0$  and  $\delta_0$  are assumed to be independent of  $s_{ij}$ . For  $D^+ \rightarrow K^-\pi_a^+\pi_b^+$  decays,  $\mathcal{A}$  is Bose-symmetrized with respect to interchange of  $\pi_a^+$  and  $\pi_b^+$ . In Ref. [283] it is noticed that the *NR* term is small, and that a further term, parameterized as a new  $J = 0$  resonance  $\kappa(800)$ , with

$m_R = (797 \pm 19 \pm 43)\text{MeV}$  and  $\Gamma_R = (410 \pm 43 \pm 87)\text{MeV}$ , gives a much better description of the data.

Apparently the above parametrization forms are not satisfactory for the purpose of searching for broad resonances and for testing final state phases. In Ref. [284], an improved approach to the above analysis is presented that uses a generalized isobar picture of two body interactions. While higher  $K\pi$  waves are described by sums of known resonances, the  $s$ -wave amplitude and phase are determined bin-by-bin in  $K\pi$  mass. The phase variation is found to be not that of the  $K^-\pi^+$  elastic scattering obtained by the LASS Collaboration [285]. The applicability of the Watson theorem in three-body hadronic decays is examined in Ref. [284]. In three-body  $D^+ \rightarrow K^-\pi^+\pi^+$  decays, the  $K^-\pi^+$  pairs form both isospin  $1/2$  and  $3/2$  components. It is not clear, however, how to estimate the  $I = \frac{3}{2}$   $S$ -wave component. In the literature it is often assumed, based on a simple spectator-quark model for  $D$  decay to  $K\pi\pi$ , that the  $K\pi$  system has only  $I = 1/2$ . However, it is found that if  $I = \frac{1}{2}$  dominates, the Watson theorem does not describe these data very well. This question is re-examined in Ref. [282]. It is suggested that in  $D \rightarrow K\pi\pi$  decays there exists a different mixture of  $I = 1/2$  and  $I = 3/2$   $S$ -wave interactions than in elastic scattering. Applying Watson's theorem to this generalized isobar model allows one to estimate the  $I = 3/2$   $K\pi$   $S$ -wave component, and it is found to be larger than in either hadronic scattering or semi-leptonic processes.

Another very interesting process for future *BES-III* experimentation is  $\psi' \rightarrow J/\psi\pi\pi$ . This is a three body final state. But due to color transparency arguments, one can, to a very good approximation, neglect the final state interactions between the  $J/\psi$  and the pions. In this case, the problem is reduced to a two-body final state. The kinematics constrains the  $\pi\pi$  system to be solely elastic and, thus, the  $\psi' \rightarrow J/\psi\pi\pi$  channel provides another good opportunity to extract the final state phase of  $S$ -wave  $\pi\pi$  interactions. However, in this channel the phase is obtained by interference between  $S$ - and  $D$ -waves and the latter is very small. So, high statistics are needed, which will be available at *BES-III*. The measured phase shift difference  $\delta_0^0 - \delta_0^2$  will be important complementary information to other determinations, since it covers the energy region around 500 MeV, which is not covered by previous experiments.

Precision experiments also require more theoretical investigations into three-body final state interactions, such as, for example, in the  $D \rightarrow K\pi\pi$  process. Corrections to the Watson theorem for three-body decays are discussed theoretically in Ref. [286].

### 11.3.4 More on final state interactions in the $J/\psi \rightarrow \omega\pi\pi$ process

The final state phases in  $J/\psi \rightarrow \omega\pi\pi$  process is also discussed in Ref. [287]. The final state is three body and a complicated pattern of final state interactions is involved. Nevertheless the  $\omega\pi$  two-body interaction may be subtracted using a suitable parametrization (*i.e.*, the generalized isobar model). In the low  $\pi\pi$  invariant mass region, the  $\pi\pi \rightarrow 4\pi$  final state interaction is negligible. Hence the remaining part of the decay amplitude characterizing the  $\pi\pi$  final state interactions, denoted as  $A_0$ , may be related to the Watson theorem by fixing the final state phase:

$$A_0(s) = |A_0(s)|e^{i\delta_\pi}, \quad (11.3.27)$$

which is similar to the scalar form factor

$$F_0(s) = |F_0(s)|e^{i\delta_\pi}. \quad (11.3.28)$$

That means the ratio  $R(s) = A_0(s)/F_0(s)$  is real when  $s < 4M_K^2$ . Furthermore, since the  $\sigma$  pole both in  $A_0$  and  $F_0$  cancel each other and the cut in  $R$  is distant (starting from  $4M_K^2$ ),  $R$  has to be a slowly varying function, at least at low energies (*i.e.*, when  $s \ll 4M_K^2$ ). This can be seen immediately if one writes down a dispersion relation of  $R$  with one subtraction,

$$R(s) = R_0 + R_1 s + \frac{(s - 4M_K^2)^2}{\pi} \int_{4M_K^2} \frac{\text{Im}R(t)}{(t - 4M_K^2)^2(t - s)}. \quad (11.3.29)$$

The scalar form factor can be determined from theory [288]. The ratio  $R$  is plotted in Fig. 11.6 where one sees that  $R$  does not show any curvature-like structure, hence the integral in Eq. (11.3.29) is small and  $R \simeq R_0 + R_1 s$ . Furthermore, the scalar amplitude may be parameterized as  $A_0(s) = R_0(1 - s/s_0)F_0(s)$  and  $s_0 \simeq 1.65 \text{ GeV}^2$  [289]. On the other hand,  $J/\psi$  decays to  $\omega\pi\pi$ ,  $\omega K\bar{K}$ ,  $\phi\pi\pi$  and  $\phi K\bar{K}$  are studied in Ref. [290], using the assumption that  $A_0/F_0 \simeq \text{const}$ . The observed energy dependence, shown in Fig. 11.6, seems to suggest that the final-state interaction between the  $\omega$  and  $\pi$  and also the three-body final state interaction can be safely removed. This conclusion seems to disagree with the conclusion reported by E791 based on their analysis of  $D \rightarrow K\pi\pi$  decays (bear in mind that the processes are different). Hence it would be interesting for future *BES-III* experiments and related theoretical studies to improve the understanding of three body final state interactions.

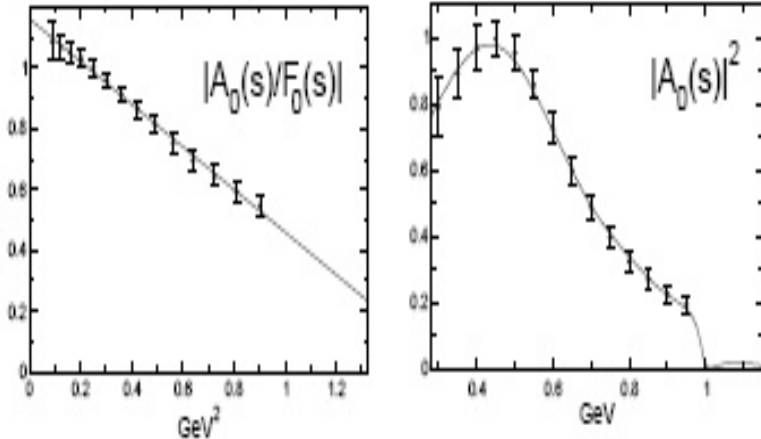


Figure 11.6: The comparison between the scalar form factor and the scalar amplitude extracted from BES  $J/\Psi \rightarrow \omega\pi\pi$  process. Data are from Ref. [287].

### 11.3.5 The Omn s solution

Consider a pion form factor, or a form-factor-like quantity,  $A(s)$ , which is an analytic function on the entire cut  $s$  plane. Neglecting inelasticity effects and assuming that the

single channel unitarity relation holds over the entire physical region:  $4m_\pi^2 < s < \infty$ , the spectral function of the form-factor satisfies

$$\text{Im}A = \rho AT^* , \quad (11.3.30)$$

where  $T$  is the  $\pi\pi$  (partial wave) scattering amplitude. Equation (11.3.30) has a simple solution, called the Omn s solution:

$$A(s + i\epsilon) = P_n(s) \exp\left\{\frac{s}{\pi} \int_{4m_\pi^2}^{\infty} \frac{\delta_\pi(s')ds'}{s'(s' - s - i\epsilon)}\right\} , \quad (11.3.31)$$

where  $P_n(s)$  is a (real analytic) polynomial, representing the possible zeros of  $A(s)$  on the complex  $s$  plane, and  $\delta_\pi$  is the  $\pi\pi$  scattering phase shift.

## 11.4 On the nature of the lightest scalar resonances

Issues related to the lightest scalar resonances,  $\sigma$ ,  $\kappa$ ,  $f_0(980)$  and  $a_0(980)$  have attracted much interest. Important among these is the  $\kappa$ , the other (*i.e.* in addition to the  $\sigma$ ) broad resonance among these states.

The E791 experiment at Fermilab reported the evidence for the  $\kappa$  in the  $D^+ \rightarrow K^+\pi^+\pi^-$  [291], with a mass and width of  $797 \pm 19 \pm 43$  MeV/c<sup>2</sup> and  $410 \pm 43 \pm 87$  MeV/c<sup>2</sup>. The  $\bar{K}^*(892)^0 K^+\pi^-$  channel in  $J/\psi \rightarrow K^+K^-\pi^+\pi^-$  was studied at BES [292] and a clear low mass enhancement in the invariant mass spectrum of  $K^+\pi^-$  is observed. Two independent partial wave analyses were performed and different parametrizations of  $\kappa$  tried. Both analyses favor the interpretation of the low mass enhancement as the  $\kappa$ . The average mass and width of the  $\kappa$  in the two analyses are  $878 \pm 23^{+64}_{-55}$  MeV/c<sup>2</sup> and  $499 \pm 52^{+55}_{-87}$  MeV/c<sup>2</sup>, respectively, corresponding to a pole at  $(841 \pm 30^{+81}_{-73}) - i(309 \pm 45^{+48}_{-72})$  MeV/c<sup>2</sup>. Figure 11.7 shows the  $K\pi$  invariant mass spectrum that recoils against a  $K^*(892)$ . The crosses are data and histograms represent the PWA fit projection. The shaded area shows the  $\kappa$  contribution.

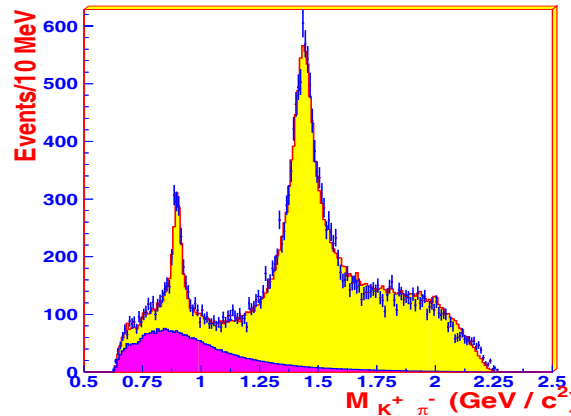


Figure 11.7: The  $K\pi$  invariant mass recoiling against a  $K^*$ . The crosses are data and histograms represent the PWA fit projection. The shaded area shows the  $\kappa$  contribution.

These results should be compared with a recent phase shift analysis based on LASS [285] data:  $M_\kappa = 694 \pm 53$  MeV,  $\Gamma_\kappa = 606 \pm 59$  MeV [293], and the Roy–Steiner equation analysis [294]:  $M_\kappa = 658 \pm 13$  MeV,  $\Gamma_\kappa = 557 \pm 24$  MeV.

An immediate question of interest concerning these scalars is whether or not they comprise the lowest scalar octet, and, if the answer is yes, how to explain the large difference between their masses and widths. A widely accepted understanding to such question has not yet emerged, but the key must be related to a proper treatment to the strong interaction dynamics especially with respect to unitarity. Large  $SU_f(3)$ -breaking effects must also be taken into account. First of all, it should be stressed that a naive quark model description of the lightest scalar meson cannot be successful. As emphasized by Törnqvist [295], this is simply because in naive quark models, chiral symmetry, which is crucial for scalars, is absent. Indeed, if the ‘ $\sigma$ ’ resonance really has something to do with the  $\sigma$  particle in the linear  $\sigma$  model Eq. (11.1.10), then from (Eq. 11.1.8) it is realized that the  $\sigma$  is the chiral partner of the pion field. The latter is a collective excitation – that would be a Goldstone boson. Hence the  $\sigma$  must share many properties of the pion field, and it is well known that it is very difficult to understand the pion field in terms of simple quark models.

The  $\kappa$  meson contains an  $s$ -quark component, while the  $a_0$  does not. In the naive  $q\bar{q}$  picture this would indicate a heavier  $\kappa$  than  $a_0$ . In a phenomenological approach, Jaffe relates the unusual properties of the light scalar mesons to the assumption that the lightest scalar mesons are mainly composed of  $(qq)(\bar{q}\bar{q})$  [296]. With this, he observes that the spectrum of the flavor nonet is inverted as compared to a standard  $q\bar{q}$  nonet, and contains a light isospin singlet, a strange doublet, and a heavy triplet plus singlet with hidden strangeness. This picture agrees well with the observed spectrum of a light  $\sigma$ , a strange  $\kappa$ , and the heavier  $a_0(980)$  and  $f_0(980)$ . It also explains why the  $a_0(980)$  and  $f_0(980)$  strongly couple to  $K\bar{K}$  and  $\pi\eta$ . However, the large width of the  $\sigma$  and  $\kappa$  are still waiting for an explanation in this approach. On the other hand, the mass splitting between the  $\sigma$  and  $a_0(980)$  may also be explained by instanton effects [297] and are investigated in the literature [298].

The  $\gamma\gamma \rightarrow \pi^+\pi^-$ ,  $\pi^0\pi^0$  process has been studied in Ref. [299] using a dispersive calculation and the decay width  $\Gamma(\sigma \rightarrow 2\gamma)$  is extracted. The result is compared to quark model calculations with different assumptions about the content of the sigma meson and it indicates that the extracted  $\sigma$  coupling to two photons is very different from that for gluonium or even tetraquark descriptions to the  $\sigma$  resonance.

In Ref. [300], QCD spectral sum rules (QSSR) calculations based on different proposals ( $q\bar{q}$ ,  $qq\bar{q}\bar{q}$  and gluonium) are performed and discussed. It is found that, in the  $I=1$  and  $I=1/2$  channel the unusual wrong splitting between the mass of  $a_0(980)$  and  $\kappa$  and also the width of  $a_0(980)$  can be understood from QSSR within a  $q\bar{q}$  assignment. However the large width of  $\kappa$  can not be explained either in  $q\bar{q}$  or  $qq\bar{q}\bar{q}$  pictures. In the  $I = 0$  channel, the important role of QCD trace anomaly was emphasized, and based on this the observed masses of the  $\sigma$  and  $f_0(980)$  can be explained as a maximal mixing between a low lying gluonium and a conventional  $q\bar{q}$  state, based on analysis of BES results on  $J/\psi \rightarrow \phi\pi\pi$ ,  $\omega\pi\pi$ ,  $f_0K^+K^-$  and other experimental information. Furthermore, with the aid of experimental information on OZI-violating  $J/\psi \rightarrow \phi\pi\pi$ ,  $D_s \rightarrow 3\pi$  decays and especially  $J/\psi \rightarrow \gamma S$ , it is found that most of the vacuum scalars below 2 GeV, other than the  $f_0(1370)$ , contain a large gluonium component.

A lattice study of the vacuum scalars has also been performed, and it suggests the existence of a low-lying sigma [301]. It is pointed out that the physics content of the  $\sigma$ , i.e., a tetraquark, a hybrid with a glue ball or a  $q\bar{q}$  collective state, is obscure: the disconnected diagram gives the dominant contribution [301]. Investigations have also been made based on Lagrangian models at the meson or quark levels. In Ref. [302], the lightest scalars are depicted as a nonet with a complicated structure. Near the center they are  $(qq)_{\bar{3}}(\bar{q}\bar{q})_3$  in an  $S$ -wave, with some  $q\bar{q}$  in a  $P$ -wave, but further out they rearrange as  $(q\bar{q})_1(q\bar{q})_1$  and finally as meson-meson states. In Ref. [303] a review is given of studies on lightest scalars based on a coupled-channel model of potential scattering. The potential contains a confining part of harmonic oscillator type as well as a  ${}^3P_0$  transition potential characterizing the phase transition from a  $q\bar{q}$  pair to a meson pair. In such a model calculation,  $T$  matrix zeros are found to be close to those predicted by current algebra. Reasonable fit results are found for phase shifts, using only a small set of parameters and the  $\sigma$  and  $\kappa$  resonances are predicted dynamically. Variations of Padé approximations to  $\chi$ PT amplitudes are also studied in the literature to explore the nature of the lightest scalars that are generated dynamically [304].

The substructure of the  $f_0(980)$  resonance is also a long standing issue. Even its small peak width may be explained as the Flatté effect, which means that although it manifests itself as a narrow peak, the  $f_0(980)$  may have a large decay width [305]. One interpretation of the quark content of the  $f_0(980)$  is that it mainly has an  $s\bar{s}$  component, while another explanation is that it is a  $K\bar{K}$  molecule. The latter would require

$$\frac{\Gamma(\phi \rightarrow f_0\gamma)}{\Gamma(\phi \rightarrow a_0\gamma)} \sim 1. \quad (11.4.32)$$

However, recent KLOE results indicate [306]

$$\frac{\Gamma(\phi \rightarrow f_0\gamma)}{\Gamma(\phi \rightarrow a_0\gamma)} = 6.1 \pm 0.6. \quad (11.4.33)$$

If, on the other hand, it is explained as a  $q\bar{q}$  state, it cannot explain the large branching ratio ( $\geq 10^{-4}$ ). Another interpretation of the lightest scalar resonances is that they are  $qq\bar{q}\bar{q}$  states. In such a scheme the mass relations are explained [307] without considering the large widths and strong interaction corrections. In Ref. [308] some decay modes of these resonances are estimated using both  $q\bar{q}$  and  $qq\bar{q}\bar{q}$  picture and it was found that neither picture can give the correct branching ratio.

To conclude, the nature of the lightest scalars remains mysterious. Future *BES-III* experimentation in this area will be highly prized since it could provide information helpful for understanding strong interaction physics at low energies.



# Chapter 12

## Two-photon physics

### 12.1 Introduction

Two-photon processes have always held a special fascination for physicists because of the opportunity they provide to study the conversion of pure photons into matter (leptons and hadrons). The original calculation for these processes is reported in Ref. [309], and the first detailed consideration of possible applications of these processes was first presented independently by two groups [310, 311].

Two-photon collisions can be accessed in electron-positron or electron-electron colliders via the process

$$e^\pm + e^- \rightarrow e^\pm + e^- + \gamma + \gamma \rightarrow e^\pm + e^- + X,$$

where  $X$  describes any final state. Note that intermediate photons can be virtual or almost real. In the case of almost real photons, one has the possibility of studying processes of type  $\gamma\gamma \rightarrow X$ . Not all final states can be accessed in two-photon processes; since each photon has odd  $C$  parity, only final states  $X$  with even  $C$  parity are produced.

An interesting feature of this process is that its cross-section rises slowly with the energy and becomes comparable with the  $e^+e^-$  annihilation channel at  $\sqrt{s}/2 \approx 1$  GeV, (see Fig. 12.1) [312]. For example, the cross section for  $e^+e^- \rightarrow \pi^+\pi^-$  pair in the single-photon annihilation channel is proportional to  $\alpha^2/q^2$ , where  $q$  is the virtuality of the intermediate photon. Although the two-photon process has an additional factor of  $\alpha^2$  it has a logarithmic reinforcement that increases with the energies of initial-state particles [316]:

$$\sigma_{e^\pm e^- \rightarrow e^\pm e^- h} = \frac{\alpha^4}{18\pi^2 m_\pi^2} \ln \frac{sm_\rho^2}{m_e^2 m_\pi^2} \ln \frac{sm_\rho^6}{m_e^6 m_\pi^2} \left( \ln \frac{s}{m_\pi^2} \right)^2.$$

This is because the two-photon cross-section is enhanced when the virtualities of interacting photons go to zero (see Fig. 12.2). In this case, they are almost real and, from kinematic restrictions, are emitted along initial particle directions as illustrated in Fig. 12.3.

Keeping this enhancement in mind and taking into account only leading terms (the so-called Equivalent Photon Approximation (EPA)) the cross section has the form

$$\frac{d\sigma^{(0)}}{ds d\Gamma} = 2 \left( \frac{\alpha}{\pi} \right)^2 \frac{1}{s} \ln^2 \frac{E}{m_e} f\left(\frac{\sqrt{s}}{2E}\right) \frac{d\sigma_{\gamma\gamma \rightarrow X(s)}}{d\Gamma},$$

$$f(\gamma) = -(2 + \gamma^2)^2 \ln \gamma - (1 - \gamma^2)(3 + \gamma^2),$$

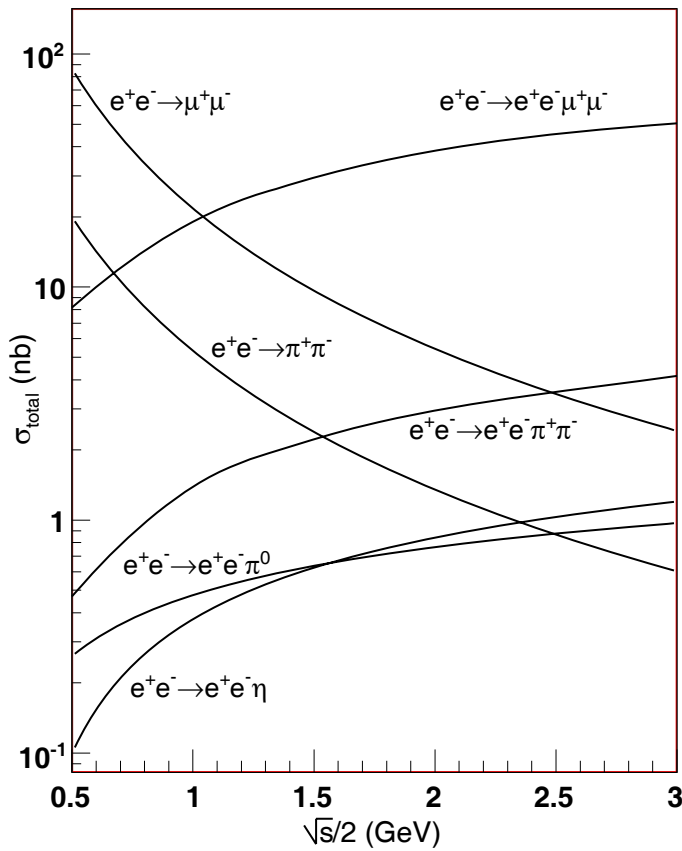


Figure 12.1: Cross sections for two-photon production of lepton and hadron pairs.

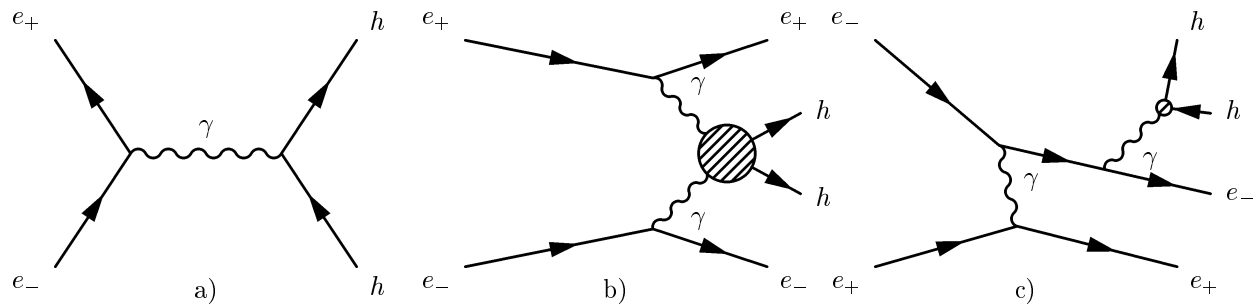


Figure 12.2: Feynman diagrams for hadron pair production in  $e^+e^-$  collisions. The contribution from diagram b) is enhanced by the intermediate photon poles.

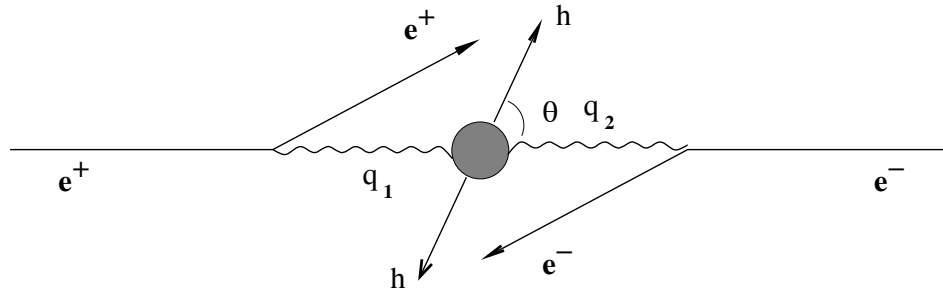


Figure 12.3: Kinematics of the two-photon process.

where  $E$  is the energy of initial electron. We can see that the cross-section for the two-photon process splits into two different parts: one part is connected with emission of the two real photons by the incoming beam particles and the other part is final state production by the two photons. This formula contains the essence of two-photon physics.

The cost of this simplicity is the underestimation of the cross-section in some specific kinematic regions, and loss of information about the scattered particle's angular dependence, and deep-virtual scattering, when one of the photons has a large  $|q^2|$ . On the other hand, events with highly virtual intermediate photons are quite rare, since for these there is no  $q^2$  pole enhancement. These are called "single-tag" events (*i.e.*, events where one photon has a nonzero virtuality  $q^2$ ) and are useful for studying resonance production by off-shell photons.

The main research object in two-photon physics is the determination of the amplitudes for  $\gamma\gamma \rightarrow X$  processes, both for off-mass-shell and for almost-real photons. Another way to describe two-photon cross sections is in terms of five structure functions. Three of them can represent the cross section  $\sigma_{a,b}$  for scalar ( $a, b = S$ ) and transverse photons ( $a, b = T$ ). The other structure functions  $\tau_{TT}$  and  $\tau_{TS}$  correspond to transitions where each of the photons flip their spin while conserving the total helicity [312]:

$$\begin{aligned} d\sigma = & \frac{\alpha^2}{16\pi^4 q_1^2 q_2^2} \sqrt{\frac{(q_1 q_2)^2 - q_1^2 q_2^2}{(p_1 p_2)^2 - m_1^2 m_2^2}} \left( 4\rho_1^{++} \rho_2^{++} \sigma_{TT} + 2|\rho_1^{+-} \rho_2^{+-}| \tau_{TT} \cos(2\tilde{\phi}) \right. \\ & \left. + 2\rho_1^{++} \rho_2^{00} \sigma_{TS} + 2\rho_1^{00} \rho_2^{++} \sigma_{ST} + \rho_1^{00} \rho_2^{00} \sigma_{SS} - 8|\rho_1^{+0} \rho_2^{+0}| \tau_{TS} \cos(\tilde{\phi}) \right) \frac{d^3 p'_1 d^3 p'_2}{E_1 E_2}. \end{aligned}$$

Here  $\rho_i^{ab}$  are the density matrices of the virtual photon in the  $\gamma\gamma$ -helicity basis.

At large  $q_1$  or  $q_2$  the two-gamma cross-section  $\sigma_{ab}$  can be calculated in the context of perturbative QCD. For small virtualities of the intermediate photons (*i.e.*,  $q_i^2 \ll W^2$ , where  $W$  is the invariant mass of the state  $X$ ), the situation is not so simple. However, it is possible to use different low-energy models. For example, when it is assumed that the  $W$  and  $q_i$  dependence factorize [315], one has the form:

$$\sigma_{ab}(W, q_i^2) = h_a(q_1^2) h_b(q_2^2) \sigma_{\gamma\gamma}(W^2);$$

this approximation is called the "improved EPA". For more details, see the original papers of Refs. [313, 312]; a recent review can be found in Ref. [317]. A summary of recent experimental work can be found in Ref. [318]. A very interesting review of two-photon event generators (for LEP1 energies) can be found in Ref. [314].

## 12.2 Experimental status of two-photon processes

Lepton pair production in two-photon processes can be calculated in the framework of QED. While di-lepton production does not have much bearing on new physics searches, measurements at large cm energies, where radiative corrections are essential, can provide precise tests of QED. At *BES-III* energies, di-lepton production by two photons is not particularly interesting, although it has to be taken into account as a possible background source for some channels.

Of more interest is two-photon production of hadronic final states. During the past few years a number of experiments using single-tag photons were carried out, primarily to measure the photon structure function  $F_2^\gamma$ . These were done at cm energies well above the *BES-III* range. Also, high energy  $\gamma\gamma \rightarrow jet$  or  $\gamma\gamma \rightarrow 2jet$  processes have been studied, and measurements of the  $p_T$  distributions for inclusive  $\pi$  production and cross-sections for charm and beauty production reported.

In the energy range accessible at *BES-III*, hadron production via two photon collisions has been studied by several experiments. At the MARK-II experiment [319] the  $\gamma\gamma \rightarrow \pi^+\pi^-$  cross section was measured for invariant masss from 0.35 to 1.6 GeV, and  $f_2(1270)$  and  $f_0(1010)$  production was observed. In addition, the decay width of the  $\eta'(958)$  to two photons was measured [320].

The CLEO-II collaboration detected two-photon production of pairs of charged pions and kaons with invariant masses in the range between 1.5 and 5.0 GeV. The data show a  $\sim 40\%$  discrepancy from leading-order (LO) QCD predictions [321].

The CELLO Collaboration measured  $\gamma\gamma \rightarrow \pi^+\pi^-$  production over the energy range 0.75 – 1.9 GeV [322].

The Belle collaboration reported the observation of  $f_0(980)$  production in the  $\gamma\gamma \rightarrow \pi^+\pi^-$  reaction [323]. They find a line-shape for the resonance that differs from the standard Breit-Wigner form and a total  $f_0(980)$  width that is much narrower than the PDG value. The authors of Ref. [325] argue that this effect can be explained by destructive interference between the  $f_0(980)$  and coherent non-resonant  $\pi^+\pi^-$  background.

Neutral pion pair production by two photons has been measured by the Crystal Ball collaboration [324]. The  $\gamma\gamma \rightarrow \pi^0\pi^0$  process provides a very crucial test of Chiral Perturbation Theory (ChPT) [326]. A key feature is that this process appears only in one-loop calculations in ChPT and some theoretical predictions conflict with the Crystal Ball data. This can be used to estimate the two-loop contribution and determine constraints of higher-order renormalization constants. Because of the very high luminosity of BEPCII it should be possible to obtain new and more precise data of neutral pion pair production with *BES-III*.

In the photon-photon center of mass energy  $0.5 < W < 2$  GeV one can measure resonant structures in the hadron spectrum. In the  $\pi\pi$  final state there are many, perhaps too many, scalar resonances:  $f_0(400 - 1200)$ ,  $f_0(980)$ ,  $f_0(1370)$ ,  $f_0(1500)$ ,  $f_0(1710)$ , etc. Some are not well established and some authors doubt their existence [327]. In the *BES-III* experiment, higher statistics can be obtained over the same angular acceptance than at (for example) the Belle experiment. By combining data from different channels, such as  $\pi^0\pi^0$  and  $\pi^+\pi^-$ , it will be possible to separate the contributions to the cross sections of states with definite spin. Accurate measurements of this channel can provide the possibility of determining whether or not any of the above-noted candidate scalar states

are glueballs, based on non-observation at a high level of sensitivity.

Searches for events with higher hadron multiplicity in the final state are also of interest. As an example, one can search for three pion final states with invariant mass below 2 GeV. The ARGUS collaboration presented a clear  $a_2(1370)$  signal resonance but did not observe the pseudoscalar resonance  $\pi_2(1300)$  or any significant enhancements near the  $\pi_2(1670)$  [328]. However, this measurement contradicts results from the Crystal Ball [329] and CELLO [330] experiments. *BES-III* can shed light on this puzzle.

Single-tag data (when one of the photons is considerably off-shell) might possibly be measured with *BES-III*, although here the cross section is much lower than for two-photon processes with real photons. Such measurements can be used to determine the photon structure function at small  $q^2$ .

The total hadronic cross-section can be measured by *BES-III* as well. In this case corrections for the angular acceptance of the detector will be necessary.

## 12.3 Measurement of two-photon processes at *BES-III*

The combination of the very high luminosity of the BEPCII accelerator together with the excellent *BES-III* detector performance offers opportunities for precision measurements of hadron production by two photons.

To study the *BES-III* potential for  $\gamma\gamma$  physics, the Monte-Carlo program GALUGA 2.0 [331] was used with small modification. Since the production of charged and neutral pion pairs in two-photon reactions is an important topic for *BES-III*, relevant models based on the point-like pion approximation and on ChPT [312, 334] were implemented in the program.

The luminosity function has been calculated for several working energies of the BEPCII machine (see Fig. 12.4). Given that the integrated luminosity of BEPCII will be of order  $5 \text{ fb}^{-1}/\text{year}$ , one can see that relatively high statistics two-photon event samples are expected at *BES-III*, especially at low energies ( $m_\pi < W < m_{f_0}$ ).

One can, in principle at least, tag two-photon events by the detection of one or both of scattered electrons (single tag or double tag mode). Tagging allows one to suppress backgrounds significantly, but at the cost of a dramatic reduction in experimental statistics. In addition, the requirement of the detection of a scattered electron into a specific energy and angular range can distort the measurement results.

The main source of background in the *BES-III* experiment will be hadronic decays of charmonium with one or more particles undetected. To suppress this background, at least single tagging is needed. Studies using the no-tag mode are probably only possible at  $E_{cm} = 3.77 \text{ GeV}$ , or at other non-narrow resonances. Background contributions from  $D$  and  $\Psi(3770)$  decays are small and, probably, easily suppressed. However this has yet to be confirmed by a detailed background study. Since no special tagging system is available in the *BES-III* detector, only scattered electrons at the angular range  $|\cos(\Theta)| < 0.93$  can be used.

The number of two-photon-produced hadronic final states has been estimated for  $E_{cm}=3.77 \text{ GeV}$  and an integrated luminosity  $L_{int} = 5 \text{ fb}^{-1}$  ( $\approx 1$  year of data taking). Results of the calculation are provided in Table 12.1.

The relative increase in the number of heavier mesons, like  $\eta, \eta'$ , in the tagged modes

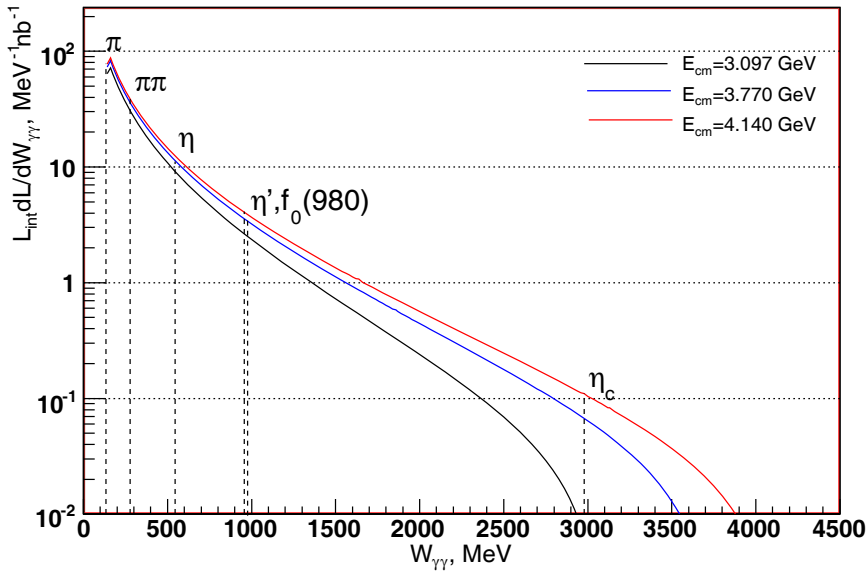


Figure 12.4: The photon-photon flux at *BES-III* for several beam energies, for an integrated luminosity of  $1 \text{ fb}^{-1}$ .

Mode	Total cross-section [nb]	No tag $\times 10^6$	Single tag $\times 10^3$	Double tag
$\pi^+ \pi^-$	2.38	11.9	236.5	5860
$\pi^0 \pi^0$	0.062	0.31	25.5	885
$\pi^0$	0.67	3.35	7.85	90
$\eta$	0.24	1.20	32.8	490
$\eta'$	0.37	1.85	113.0	2255
$a_0(980)$	0.33	1.65	7.87	990
$f_0(980)$	0.046	0.23	9.5	140
$\eta_c$	0.0016	0.008	1.9	225

Table 12.1: The total number of two-photon-produced events for an integrated luminosity of  $5 \text{ fb}^{-1}$  at  $E_{cm}=3.77 \text{ GeV}$ .

with respect to the decreasing total cross sections is due to the increase of the production cross section with increasing  $W$  (see Fig. 12.5). As a result, the scattering angle of electrons and, consequently, the number of double-tag events for these mesons will likely be larger than those for  $\pi^0$  production.

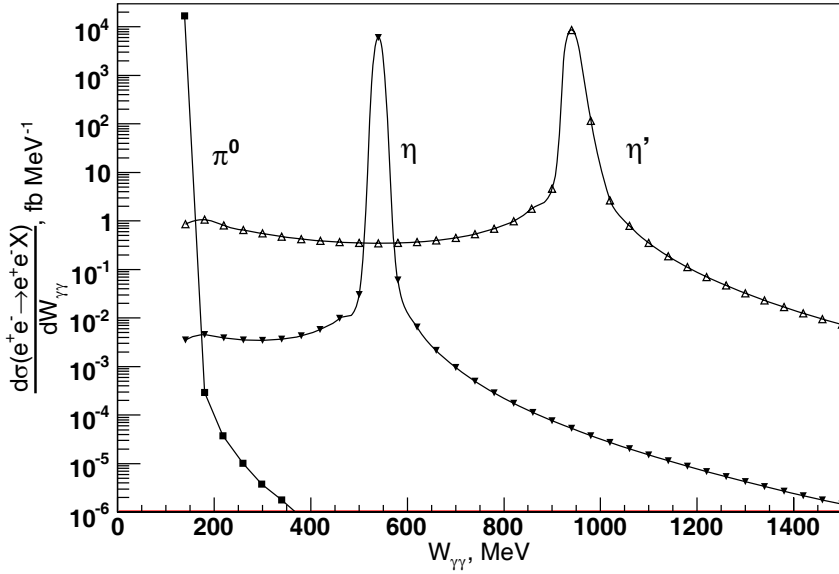


Figure 12.5: Differential cross section  $\frac{d\sigma}{dW}$  of meson formation in two photon reactions  $e^+e^- \rightarrow e^+e^-X$  ( $E_{cm} = 3.77\text{GeV}$ ).

The production of  $\pi^+\pi^-$  and  $\pi^0\pi^0$  pairs in two photon processes at *BES-III* has been studied in detail for  $E_{cm}=3.77\text{ GeV}$ . In Figs. 12.6, 12.7, & 12.8 one can see the momentum distribution of the produced pions. Only events where both pions are within the *BES-III* angular acceptance ( $|\cos(\Theta)| < 0.93$ ) are selected. The plots are normalized by the total number of events. The no-tag-mode events are indicated by solid line, the dotted line corresponds to double-tag-mode events.

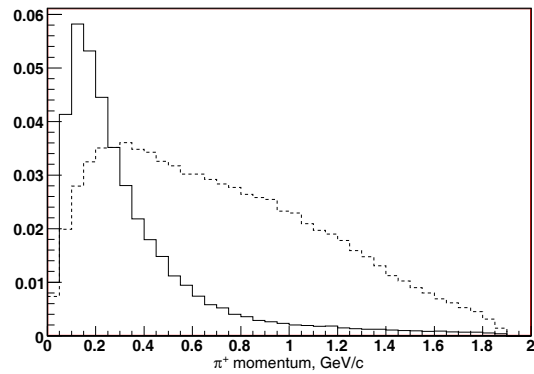


Figure 12.6: Momentum distribution of  $\pi^+$  mesons from  $e^+e^- \rightarrow e^+e^-\pi^+\pi^-$ .

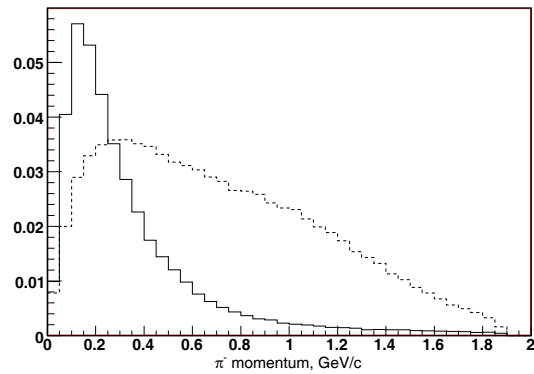


Figure 12.7: Momentum distribution of  $\pi^-$  mesons from  $e^+e^- \rightarrow e^+e^-\pi^+\pi^-$ .

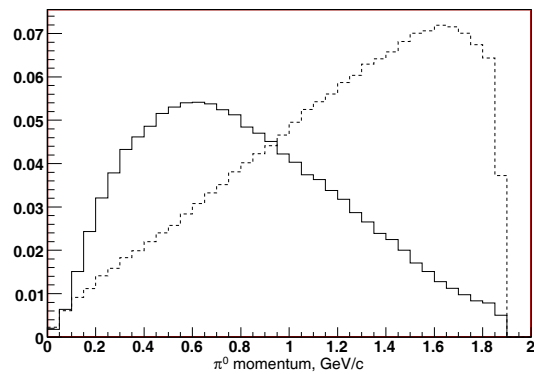


Figure 12.8: Momentum distribution of  $\pi^0$  mesons from  $e^+e^- \rightarrow e^+e^-\pi^0\pi^0$ .

## 12.4 Summary

A feasibility study for measurements of hadron production in two-photon reactions at *BES-III* has been carried out. The two-photon invariant mass region accessible at the *BES-III* energies extends up to 3 GeV. For data-taking at the  $J/\psi$  and  $\psi'$  resonances, electron tagging of two-photon events will be necessary for reducing backgrounds from hadronic charmonium decays. At  $E_{cm} = 3.77$  GeV, however, where backgrounds from  $\Psi(3770)$  and  $D$  decays is expected to be small, no-tag data will be useful. The double-tag requirement will provide the most effective background suppression, however the data yield would be too small except for a few channels (production of  $\pi^+\pi^-$ ,  $\eta'$ ). Single-tag measurements are more promising: for example, the estimated numbers of events should be sufficient for precision measurements of neutral-pion pair production. In general, *BES-III* offers some good opportunities for precision measurements of the production of low-mass hadronic systems in two-photon collisions.



# Bibliography

- [1] A. De Rujula, H. Georgi and S.L. Glashow, Phys. Rev. D **12**, 147 (1975).
- [2] N. Isgur and G. Karl, Phys. Lett. **72B**, 109 (1977); N. Isgur and G. Karl, Phys. Rev. D **18**, 4187 (1978); *ibid* D **19**, 2653 (1979); Erratum **23**, 817 (1981); *ibid* D **20**, 1191 (1979).
- [3] K.-T. Chao, N. Isgur and G. Karl, Phys. Rev. D **23**, 155 (1981).
- [4] F.E. Close, *Introduction to quarks and partons* (Academic Press 1978).
- [5] J. Carlson, J.B. Kogut and V.B. Pandharipande, Phys. Rev. D **28**, 2807 (1983).
- [6] R. Sartor and F. Stancu, Phys. Rev. D **31**, 128 (1985); *ibid* **33**, 727 (1986); F. Stancu and Stassart, Phys. Rev. D **41**, 916 (1990); Phys. Lett. B **269**, 243 (1991).
- [7] W.H. Blask *et al.*, Z. Phys. A **337**, 327 (1990); E.V. Shuryak and J.L. Rosner, Phys. Lett. B **218**, 72 (1989); A. Dorokhov and N.I. Kochelev, Sov. J. Nucl. Phys. **52**, 135 (1990); D. Klabucar, Phys. Rev. D **49**, 1506 (1994).
- [8] L. Y. Glozman and D. O. Riska, Phys. Rept. **268**, 263 (1996).
- [9] M. Anselmino, E. Predazzi, S. Ekelin, S. Fredriksson, and D.B. Lichtenberg, Rev. Mod. Phys. **65**, 1199 (1993).
- [10] C.E. Carlson *et al.*, Phys. Lett. B **438**, 327 (1998); Phys. Rev. D **59**, 114008 (1999).
- [11] R.P. Feynman, M. Kislinger, and F. Ravndal, Phys. Rev. D **3**, 2706 (1971); F. Ravndal, Phys. Rev. D **4**, 1466 (1971); L.A. Copley, G. Karl, and E. Obryk, Phys. Rev. D **4**, 2844 (1971); R.G. Lipes, Phys. Rev. D **5**, 2849 (1972); S. Godfrey and N. Isgur, Phys. Rev. D **32**, 189 (1985); S. Capstick and N. Isgur, Phys. Rev. D **34**, 2809 (1986); F.E. Close and Z.-P. Li, Phys. Rev. D **42**, 2194 (1990); Z.-P. Li and F.E. Close, Phys. Rev. D **42**, 2207 (1990); S. Capstick and B.D. Keister, Phys. Rev. D **51**, 3598 (1995).
- [12] S. Capstick and W. Roberts, Prog. Part. Nucl. Phys. **45**, 5241 (2000).
- [13] S. Godfrey and J. Napolitano, Rev. Mod. Phys. **71**, 1411 (1999).
- [14] C. Amsler and N.A. Törnqvist, Phys. Rep. **389**, 61 (2004).
- [15] E. Witten, Nucl. Phys. B 169 (1979) 57.

- [16] C.N. Yang, Phys. Rev. **77**, 242 (1950).
- [17] C.E. Carlson, T.H. Hansson and C. Peterson, Phys. Rev. D **30**, 1594 (1984).
- [18] J.F. Donoghue, K. Johnson and B. Li, Phys. Lett. B **99**, 416 (1981).
- [19] M. Chanowitz and S. Sharpe, Nucl. Phys. B **222**, 211 (1983).
- [20] J.M. Cornwall and A. Soni, Phys. Lett. B **120**, 431 (1983).
- [21] N. Isgur and J. Paton, Phys. Lett. **124B**, 247 (1983); Phys. Rev. D **31**, 2910 (1985).
- [22] V.A. Novikov, M.A. Shifman, and V.I. Zakharov, Nucl. Phys. B **165**, 67 (1980).
- [23] M.A. Shifman, A.I. Vainshtein, and V.I. Zakharov, Nucl. Phys. B **147**, 385 (1979)
- [24] J.L. Latorre *et al.*, Phys. Lett. **147B**, 169 (1984).
- [25] S. Narison, Phys. Lett. B **509**, 312 (1998).
- [26] L. S. Kisslinger, J. Gardner and C. Vanderstraeten, Phys. Lett. B **410**, 1 (1997).
- [27] F. Giacosa, T. Gutsche, V. E. Lyubovitskij and A. Faessler, Phys. Rev. D **72**, 094006 (2005) [arXiv:hep-ph/0509247].
- [28] T. Huang, H. Jin, and A. Zhang, Phys. Rev. D **59**, 034026 (1999).
- [29] K. Ishikawa, M. Teper and G. Schierholz, Phys. Lett. **116B**, 429 (1982); C. Michael and I. Teasdale, Nucl. Phys. B **215**, 433 (1983); H.W. Hamber and V.M. Heller, Phys. Rev. D **29**, 928 (1984).
- [30] P. De Forcrand *et al.*, Phys. Lett. **B152**, 107 (1985); A. Patel *et al.*, Phys. Rev. Lett. **57**, 1288 (1986).
- [31] C. Michael and M. Teper, Nucl. Phys. **B314**, 347 (1989).
- [32] C. Morningstar and M. Peardon, Phys. Rev. D **56**, 4043 (1997); Phys. Rev. **D60**, 034509 (1999).
- [33] G. Bali *et al.*, UKQCD Collaboration, Phys. Lett. B **309**, 378 (1993).
- [34] Y. Chen *et al.*, Phys. Rev. D **73**, 014516 (2006).
- [35] A. Irving *et al.*, PoS(Lat2005)027
- [36] A. Abele *et al.*, [Crystal Barrel Collaboration], Phys. Lett. B **385**, 425 (1996).
- [37] D. Barberis *et al.*, [WA102 Collaboration], Phys. Lett. B **479**, 59 (2000).
- [38] M. Ablikim *et al.* [BES Collaboration], Phys. Lett. B **607**, 243 (2005) [arXiv:hep-ex/0411001].
- [39] M. Ablikim *et al.* [BES Collaboration], Phys. Lett. B **603**, 138 (2004) [arXiv:hep-ex/0409007].

- [40] M. Ablikim *et al.* [BES Collaboration], Phys. Rev. Lett., **96**, 162002 (2006) [arXiv:hep-ex/0602031].
- [41] R.L. Jaffe, Phys. Rev. D**15**, 267 (1977); *ibid*, D**15**, 281 (1977).
- [42] R.L. Jaffe and F.E. Low, Phys. Rev. D**19**, 2105 (1979).
- [43] D.V. Bugg, Phys. Rept. **397**, 257 (2004).
- [44] F.E. Close and C. Amsler, Phys. Lett. B **353**, 385 (1995); Phys. Rev. D**53**, 295 (1996).
- [45] F.E. Close and A. Kirk, Phys. Lett. B **483**, 345 (2000).
- [46] F.E. Close and Q. Zhao, Phys. Rev. D **71**, 094022 (2005).
- [47] W. Lee and D. Weingarten, Nucl. Phys. B, Proc. Suppl. **53**, 236 (1997); Phys. Rev. D **61**, 014015 (1999).
- [48] H. Y. Cheng, C. K. Chua and K. F. Liu, Phys. Rev. D **74**, 094005 (2006) [arXiv:hep-ph/0607206].
- [49] D. M. Li, H. Yu and Q. X. Shen, Commun. Theor. Phys. **34**, 507 (2000); Eur. Phys. J. C **19**, 529 (2001).
- [50] X. G. He, X. Q. Li, X. Liu and X. Q. Zeng, Phys. Rev. D **73**, 114026 (2006)
- [51] F.E. Close, G.R. Farrar, and Z. Li, Phys. Rev. D **55**, 5749 (1997).
- [52] S.J. Brodsky, A.S. Goldhaber and J. Lee, Phys. Rev. Lett. **91**, 112001 (2003).
- [53] M. Chanowitz, in *Proceeding of the VI International Workshop on Photon-Photon Collisions, 1984*, edited by R. Lander (World Scientific, Singapore, 1985), pp4.
- [54] M.B. Cakir and G.R. Farrar, Phys. Rev. D **50**, 3268 (1994).
- [55] C. E. Carlson, J. J. Coyne, P. M. Fishbane, F. Gross and S. Meshkov, Phys. Lett. B **99**, 353 (1981).
- [56] M. Chanowitz, Phys. Rev. Lett. **95**, 172001 (2005) [arXiv:hep-ph/0506125].
- [57] K. T. Chao, X. G. He and J. P. Ma, arXiv:hep-ph/0512327; Phys. Rev. Lett. **98**, 149103(2007).
- [58] Z. F. Zhang and H. Y. Jin, arXiv:hep-ph/0511252.
- [59] S. Okubo, Phys. Lett. **5**, 1975 (1963); G. Zweig, in *Development in the Quark Theory of Hadrons*, edited by D.B. Lichtenberg and S.P. Rosen (Hadronic Press, Massachusetts, 1980); J. Iizuka, Prog. Theor. Phys. Suppl. **37**, 38 (1966).
- [60] P. Geiger and N. Isgur, Phys. Rev. D **47**, 5050 (1993).
- [61] H.J. Lipkin and B.S. Zou, Phys. Rev. D **53**, 6693 (1996).

- [62] X.Q. Li, D.V. Bugg, and B.S. Zou, Phys. Rev. D **55**, 1421 (1997).
- [63] Q. Zhao, B. S. Zou and Z. B. Ma, Phys. Lett. B **631**, 22 (2005) [arXiv:hep-ph/0508088].
- [64] Q. Zhao, Phys. Rev. D **72**, 074001 (2005) [arXiv:hep-ph/0508086].
- [65] Q. Zhao, Phys. Lett. B **636**, 197 (2006) [arXiv:hep-ph/0602216].
- [66] F.E. Close and A. Kirk, Phys. Lett. B 397, 333 (1997).
- [67] D. Barberis *et al.* [WA102 Collaboration], Phys. Lett. B **397**, 339 (1997).
- [68] N.A. Tornqvist, Acta Phys. Pol. **B** **16**, 503 (1985); Z. Phys. C **68**, 647 (1995).
- [69] M. Boglione and M.R. Pennington, Phys. Rev. Lett. **79**, 1998 (1997); M.R. Pennington, hep-ph/9811276.
- [70] M. Ablikim *et al.* [BES Collaboration], Phys. Lett. B **598**, 149 (2004) [arXiv:hep-ex/0406038].
- [71] B. S. Zou and D. V. Bugg, Euro. Phys. J. **A16** (2003) 537
- [72] Amsler, C., et al., [CBR collaboration], Phys. Lett. **B340** (1994) 259, Phys. Lett., B355 (1995) 425
- [73] Abele, A., et al., [CBR collaboration], Phys. Lett. **B380** (1996) 453, Phys. Lett. B385 (1996) 425, Nucl. Phys. **A609** (1996) 562
- [74] Antinori, F., et al., [WA91 collaboration], Phys. Lett. **B353** (1995) 589
- [75] Arberis, D., et al., [WA102 collaboration], Phys. Lett. **B413** (1997) 217
- [76] Bugg, D., et al., Phys. Lett. **B353** (1995) 378
- [77] Bai, J. Z., et al., [BES collaboration], Phys. Lett. **B472** (2000) 207
- [78] R. M. Baltrusaitis et al., [MARKIII Collaboration], Phys. Rev. D **35**, 2077 (1987)
- [79] J. E. Augustin et at., [DM2 Collaboration], Zeit. Phys. C **36**, 369 (1987).
- [80] J. Z. Bai et at., [BES Collaboration], Phys. Rev. Lett. **76** 3502 (1996).
- [81] W. Dunwoodie, *Hadron Spectroscopy*, AIP Conf. Proc. No. 432 (AIP. Melville, NY, 1997), p. 753.
- [82] L. Köpke, N. Wermes, Phys. Rep. **174**, 67 (1989).
- [83] J. Z. Bai et al., [BES Collaboration], Phys. Rev. Lett. **81**, 1179 (1998).
- [84] M. Ablikim et al., [BES Collaboration], Phys. Lett. **B 642**, 441 (2006).
- [85] A. Garmash et al., Belle Collaboration, Phys. Rev. **D 71**, 092003 (2005).

- [86] B. French *et al.*, [WA76 Collaboration], Phys. Lett. **B214** (1999) 213.
- [87] D. Barberis *et al.*, [WA102 Collaboration], Phys. Lett. **B453** (1999) 305 and 316;
- [88] M. Ablikim et al., [BES Collaboration], Phys. Rev. Lett. **96**, 162002 (2006)
- [89] P. Bicudo, S.R. Cotanch, F.J. Llanes-Estrada, and D.G. Robertson, hep-ph/0602172.
- [90] D.V. Bugg, hep-ph/0603018.
- [91] K.T. Chao, hep-ph/0602190.
- [92] X. G. He, X. Q. Li, X. Liu and X. Q. Zeng, Phys. Rev. **D73**, 114026 (2006); [arXiv:hep-ph/0604141].
- [93] B.A. Li, Phys. Rev. **D74**, 054017 (2006); [hep-ph/0602072].
- [94] Q. Zhao and B.S. Zou, Phys. Rev. **D74**, 114025 (2006); [hep-ph/0606196].
- [95] V.V. Anisovich, Int. J. Mod. Phys. **A21**, 3615-3640 (2006); [hep-ph/0510409].
- [96] P. Minkowsky and W. Ochs, Eur. Phys. J. C **9**, 283 (1999).
- [97] T. Adams *et al.*, Phys. Rev. Lett. **87**, 041801 (2001).
- [98] S. Fukui *et al.*, Phys. Lett. B **267**, 293 (1991).
- [99] J.J. Manak *et al.*, Phys. Rev. D **62**, 012003 (2000).
- [100] A. Abele *et al.*, Phys. Rev. D **57**, 3860 (1998).
- [101] A.V. Anisovich, Nucl. Phys. A **690**, 567 (2001).
- [102] C. Amsler *et al.*, Euro. Phys. J. C **33**, 23 (2004).
- [103] J.E. Augustin *et al.*, Phys. Rev. D **46**, 1951 (1992).
- [104] P.H. Baillon *et al.*, NC 50A, 393(1967).
- [105] D.L. Scharre *et al.*, Phys. Lett. **97B**, 329 (1980).
- [106] C. Edwards *et al.*, Phys. Rev. Lett. **49**, 259 (1982); *ibid*, **50**, 219 (1982).
- [107] J.E. Augustin *et al.*, Phys. Rev. D **42**, 10(1990).
- [108] M.G. Rath *et al.*, Phys. Rev. D **40**, 693 (1989).
- [109] Z. Bai *et al.*, Phys. Rev. Lett. **65**, 2507 (1990).
- [110] A. Bertin *et al.*, Phys. Lett. **B361**, 187 (1997); *ibid* **400**, 226 (1997).
- [111] C. Cicalo *et al.*, Phys. Lett. **B462**, 453 (1999).
- [112] F. Nichitiu *et al.*, Phys. Lett. B **545**, 261 (2002).

- [113] T. Bolton *et al.*, Phys. Rev. Lett. **69**, 1328 (1992).
- [114] C. Amsler *et al.*, Phys. Lett. B **358**, 389 (1995).
- [115] M. Acciarri *et al.*, Phys. Lett. B **501**, 1 (2001).
- [116] F.E. Close and A. Kirk, Phys. Lett. B **397**, 333 (1997).
- [117] T. Barnes, F.E. Close, P.R. Page and E.E. Swanson, Phys. Rev D. 4157 (1997).
- [118] E. Klempt, Contributed to 32nd International Conference on High-Energy Physics (ICHEP 04), Beijing, China, 16-22 Aug 2004; [hep-ph/0409148].
- [119] J.Z. Bai *et al.* [BES Collaboration], Phys. Lett. B **594**, 47 (2004).
- [120] R. M. Baltrusaitis et al. (MARKIII Collaboration), Phys. Rev. Lett. **55**, 1723 (1985).
- [121] R. M. Baltrusaitis et al. (MARKIII Collaboration), Phys. Rev. D **33**, 1222 (1986).
- [122] D. Bisello et al. (DM2 Collaboration), Phys. Rev. D **39**, 701 (1989).
- [123] D. Bisello et al. (DM2 Collaboration), Phys. Lett. B **192**, 239 (1987).
- [124] J. Z. Bai et al. (BES Collaboration), Phys. Lett. B **446**, 356 (1999).
- [125] A. Etkin et al., Phys. Rev. Lett. **40**, 422 (1978).
- [126] P. R. Page, X. Q. Li, Eur. Phys. J. C1, **579** (1998).
- [127] N. Wu et al, Chin. Phys. **10**, 611 (2001); [hep-ph/0011338].
- [128] B. A. Li, Phys. Rev. **D74**, 034019 (2006); [hep-ph/0510093].
- [129] M. Ablikim et at., BES Collaboration, Phys. Rev. **D 73**, 112007 (2006).
- [130] K. Einsweiler, SLAC-PUB-4279 (1983).
- [131] R.M. Baltrusaitis *et al.*, Phys. Rev. Lett. **56**, 107 (1985).
- [132] J.E. Augustin *et al.*, Phys. Rev. Lett. **60**, 2238 (1988).
- [133] D. Alde *et al.*, Phys. Lett. **177B**, 120 (1986).
- [134] D. Aston *et al.*, Phys. Lett. B **201**, 169 (1988).
- [135] J.Z. Bai *et al.* [BES Collaboration], Phys. Rev. Lett. **76**, 3502 (1996).
- [136] J.Z. Bai *et al.* [BES Collaboration], Phys. Rev. Lett. **81**, 1179 (1998).
- [137] Godang R., et at., CLEO collaboration, Phys. Rev. Lett., 79, 3829 (1997)
- [138] Alam M. S., et at., CLEO collaboration, Phys. Rev. Lett., 81, 3328 (1998)

- [139] L. Kopke and N. Wermes, Phys. Rep. 174 (1989) 67
- [140] C. Evangelista *et al.* [JETSET Collaboration], Phys. Rev. D **56**, 3803 (1997).
- [141] K.K. Seth, Proceedings of XXXI Rencontres de Moriond, Les Arcs, 1997, edited by J. Tren Thanh Van (Editions Frontieres, Paris), p599.
- [142] H.B. Liao, PhD thesis, Huazhong Normal Univ. (2005)
- [143] T. D. Cohen, Phys. Lett. B 427 (1998) 348.
- [144] N. Isgur, R. Kokoski and J. Paton, Phys. Rev. Lett. 54 (1985) 869.
- [145] N. Isgur and J. Paton, Phys. Rev. **D31** (1985) 2910.
- [146] F. E. Close and P. R. Page, Nucl. Phys. **B443** (1995) 233.
- [147] F. E. Close, J. J. Dudek, Phys. Rev. **D70** (2004) 094015.
- [148] E. S. Swanson and A. P. Szczepaniak. Phys. Rev. **D56** (1997) 5692.
- [149] P. R. Page, E. S. Swanson and A. P. Szczepaniak. Phys. Rev. **D59** (1999) 034016.
- [150] F.E. Close and P.R. Page, *Nucl. Phys.* **B443** (1995) 233; *Phys. Rev.* **D52** (1995) 1706.
- [151] H. Y. Jin, J. G. Korner and T. G. Steele, Phys. Rev. **D67** (2003) 014025.
- [152] J. Govaerts *et al.*, Phys. Rev. Lett **53** (1984) 2207.
- [153] J. I. Latorre, P. Pascual and S. Narison, Z. Phys. **C37**(1987) 347.
- [154] S. Narison, QCD Spectral Sum Rules, Lecture Notes in Physics, Vol. 26, P368.
- [155] S.-L. Zhu, Phys. Rev. **D60** (1999) 097502.
- [156] S.-L. Zhu, Phys. Rev. **D60** (1999) 014008.
- [157] G. S. Bali, Phys. Rev. **D71** (2005) 114513.
- [158] D. Alde, Phys. Lett. **B 205** (1988) 397.
- [159] Yu.D. Prokoshkin, S. A. Sadovski, Phys. Atom. Nucl., 58 (1995) 606.
- [160] G. M. Beladidze, Phys. Lett. **B 313** (1993) 276.
- [161] K. Aoyagi, Phys. Lett. **B 314** (1993) 246.
- [162] D. R. Thompson Phys. Rev. Lett., 79 (1997) 1630
- [163] A. Abele, Phys. Lett. **B 423** (1998) 175.
- [164] A. Abele, Phys. Lett. **B 446** (1999) 349.

- [165] G. Adams, *et al.*, Phys. Rev. Lett., 81 (1998) 5760
- [166] E.I. Ivanov, *et al.*, Phys. Rev. Lett. **86**, 3977 (2001).
- [167] J. Kuhn, *et al.*, Phys. Lett. **B 595** (2004) 109
- [168] C. Bernard, *et al.*, Nucl. Phys. B(Proc. Suppl.)**73**, 264 (1999); P. Lacock and K. Schilling, Nucl. Phys. B(Proc. Suppl.)**73**, 261 (1999).
- [169] N. Isgur and J. Paton, Phys. Rev. D**31**, 2910 (1985); F.E. Close and P.R. Page, Nucl. Phys. B**443**, 233 (1995); Philip R. Page, Eric S. Swanson, and Adam P. Szczepaniak, Phys. Rev. D**59**, 034016-1 (1999).
- [170] T. Barnes, F.E. Close, and E.S. Swanson, Phys. Rev. D**52**, 5242 (1995)
- [171] D.V. Amelin, *et al.*, Yad. Fiz. **62**, 487 (1999); *ibid*, Phys. Atom. Nucl. **62**, 445 (1999).
- [172] J.H. Lee, *et al.*, Phys. Lett. B**323**, 227 (1994).
- [173] Valery Dorofeev, *et al.*, AIP Conf. Proc. **619**, 143 (2002).
- [174] M. Lu., *et al.*, Phys. Rev. Lett., 94 (2005) 032002
- [175] R. L. Jaffe, Phys. Rev. Lett. 38 (1977) 195.
- [176] R. L. Jaffe, Phys. Rev. D 15 (1977) 267.
- [177] S.-L. Zhu, Int. J. Mod. Phys. A 19 (2004) 3439.
- [178] BES Collaboration, J.Z. Bai *et al.*, Phys. Rev. Lett. **91**, 022001 (2003).
- [179] BES Collaboration, M. Ablikim *et al.*, Phys. Rev. Lett. **93**, 112002 (2004).
- [180] BES Collaboration, M. Ablikim *et al.*, Phys. Rev. Lett. **95**, 262001 (2005).
- [181] M. Z. Wang *et al.*, Phys. Rev. Lett. **92**, 131801 (2004).
- [182] BES Collaboration (M. Ablikim *et al.*), Phys. Rev. Lett. **99**, 011802, 2007
- [183] S. B. Athar et al., Phys. Rev. D **73**, 032001 (2006).
- [184] BES Collaboration (M. Ablikim *et al.*), Eur. Phys. J. **C53**, 15-20, 2008
- [185] A. Datta, P.J. O'Donnell, Phys. Lett. **B567**, 273 (2003); M.L. Yan *et al.*, hep-ph/0405087; B. Loiseau, S. Wycech, Phys. Rev. **C72**, 011001(2005).
- [186] J. Ellis, Y. Frishman and M. Karliner, Phys. Lett. **B566**, 201 (2003); J.L. Rosner, Phys. Rev. D **68**, 014004 (2003).
- [187] C.S. Gao and S.L. Zhu, Commun. Theor. Phys. 42, 844 (2004), hep-ph/0308205.
- [188] G.J. Ding and M.L. Yan, Phys. Rev. C **72**, 015208 (2005).
- [189] B.S. Zou and H.C. Chiang, Phys. Rev. D **69**, 034004 (2003).

- [190] A. Sibirtsev *et al.*, Phys. Rev. D **71**, 054010 (2005).
- [191] I.S. Shapiro, Phys. Rept. **35**, 129 (1978); C.B. Dover, M. Goldhaber, Phys. Rev. D **15**, 1997 (1977).
- [192] For recent reviews of this subject, see E. Klempt *et al.*, Phys. Rep. **368**, 119 (2002) and J-M. Richard, Nucl. Phys. Proc. Suppl. **86**, 361 (2000).
- [193] S.L. Zhu and C.S. Gao, Commun. Theor. Phys. **46**, 291 (2006); [hep-ph/0507050].
- [194] F. Huang and Z.Y. Zhang, Phys. Rev. C **72**, 024003 (2005), nucl-th/0507025.
- [195] BES Collaboration, M. Ablikim *et al.*, Phys. Rev. Lett. **97**, 142002 (2006).
- [196] J. Weinstein, N. Isgur, Phys. Rev. D **41**, 2236 (1990).
- [197] N. A. Tornqvist, Phys. Lett. **B590**, 2009 (2004).
- [198] N.Isgur and G.Karl, Phys. Rev. **D18**, 4187 (1978); ibid. **D19**, 2653 (1979); ibid. **D20**, 1191 (1979); K.T.Chao, N.Isgur and G.Karl, Phys. Rev. **D23** (1981) 155.
- [199] S.Capstick and W.Robert, *Prog. Part. Nucl. Phys.* **45**, S241 (2000), and references therein.
- [200] A. De Rujula, H. Georgi, S.I.Glashow, Phys. Rev. **D12**, 147 (1975).
- [201] S. Capstick and W. Roberts, Phys. Rev. **D49**, 4570 (1994); ibid. **D57**, 4301 (1998); ibid. **58**, 074011 (1998).
- [202] N.Isgur, Phys. Rev. **D62**, 014025 (2000).
- [203] A. Manohar and H. Georgi, Nucl. Phys. **B234**, 189 (1984).
- [204] L.Y.Glozman and D.O.Riska, *Phys. Rep.* **268**, 1 (1996); L.Glozman, W.Plessas, K.Varga and R.Wagenbrunn, Phys. Rev. **D58**, 094030 (1998).
- [205] L.Y.Glozman, Nucl. Phys. **A663**, 103 (2000).
- [206] F.Fermamdez, A.Valcarce, U.Straub, A.Fässler, J. Phys. **G19**, 2013 (1993); Z.Y.Zhang, Y.W.Yu, P.N.Shen *et al.*, Nucl. Phys. **A625**, 59 (1997); P.N.Shen, Y.B.Dong, Z.Y.Zhang *et al.*, Phys. Rev. **C55**, 2024 (1997); Y.B.Dong, K.Shimizu, A.Fässler and A.J.Buchmann, Phys. Rev. **C60**, 35203 (1999).
- [207] U.Löring, K.Kretschmar, B.C.Metsch, H.R.Petry, Euro. Phys. J. **A10**, 309 (2001); U.Löring, B.C.Metsch, H.R.Petry, Euro. Phys. J. **A10**, 395 (2001); ibid. **A10**, 447 (2001).
- [208] A.Chodos, R.L.Jaffe, K.Johnson, C.B.Thorn and V.F.Weisskopf, Phys. Rev. **D9**, 3471 (1974); T.A.DeGrand, R.L.Jaffe, K.Johnson and J.Kiskis, Phys. Rev. **D12**, 2060 (1975); T.A.DeGrand and R.L.Jaffe, Ann. Phys. **100**, 425 (1976).
- [209] S.Theberge, A.W.Thomas and G.A.Miller, Phys. Rev. **D22**, 2838 (1980); A.W.Thomas, S.Theberge and G.A.Miller, Phys. Rev. **D24**, 216 (1981).

- [210] R.Bijker, F.Iachello and A.Levitan, Ann. Phys. **236**, 69 (1994); ibid. **284**, 89 (2000).
- [211] K.F.Liu and C.W.Wong, *Phys. Rev.* **D28** (1983) 170; M.Anselmino et al., *Rev. Mod. Phys.* **65**, 1199 (1993).
- [212] Q.Zhao and F.E.Close, *Phys. Rev.* **D74**, 094014 (2006).
- [213] G.T.Garvey, J.C.Peng, *Prog. Part. Nucl. Phys.* 47 (2001) 203, and references therein.
- [214] J.P.Speth and A.W.Thomas, *Adv. Nucl. Phys.* 24 (1997) 93, and references therein.
- [215] N.Kaiser, P.B.Siegel and W.Weise, *Phys. Lett.* **B362**, 23 (1995); N.Kaiser, T.Waas and W.Weise, *Nucl. Phys.* **A612**, 297 (1997).
- [216] M.F.M.Lutz and E.E.Kolomeitsev, *Nucl. Phys.* **A700**, 193 (2002); ibid. **A730**, 392 (2004); E.E.Kolomeitsev and M.F.M.Lutz, *Phys. Lett.* **B585**, 243 (2004).
- [217] E.Oset et al., *Int. J. Mod. Phys.* **A18**, 387 (2003); E.Oset, A.Ramos, C.Bennhold, *Phys. Lett.* **B527**, 99 (2002); L.Roca, S.Sarkar, V.K. Magas, E.Oset, *Phys. Rev.* **C73**, 045 (2006); S.Sarkar, E.Oset, M.J. Vicente Vacas, *Nucl. Phys.* **A755**, 503 (2005).
- [218] B.S.Zou, nucl-th/0610062, *Nucl. Phys. A* (in press) and reference therein.
- [219] B. S. Zou and D. O. Riska, *Phys. Rev. Lett.* 95 (2005) 072001; C. S. An, B. S. Zou and D. O. Riska, *Phys. Rev. C73* (2006) 035207.
- [220] B.C. Liu and B.S. Zou, *Phys. Rev. Lett.* **96**, 042002 (2006); ibid. **98**, 039102 (2007).
- [221] A.Zhang et al., hep-ph/0403210, *High Energy Phys. Nucl. Phys.* **29**, 250 (2005).
- [222] T.T.Takahashi et al., *Phys. Rev. Lett.* **86**, 18 (2001); *Phys. Rev.* **D65**, 114509 (2002).
- [223] S.Capstick and N.Isgur, *Phys. Rev.* **D34**, 2809 (1986).
- [224] T.T.Takahashi et al., *Nucl. Phys.* **A721**, 926 (2003).
- [225] T.Barnes, nucl-th/0009011, Published in \*Juelich 2000, Baryon excitations\* 121-131, and reference therein; P.Page, *Int. J. Mod. Phys.* **A20**, 1791 (2005).
- [226] T.Barnes and F.E.Close, *Phys. Lett.* **B123**, 89 (1983); E.Golowich, E.Haqq and G.Karl, *Phys. Rev.* **D28**, 160 (1983); C.E.Carlson and T.H.Hansson, *Phys. Lett.* **B128**, 95 (1983).
- [227] L.S.Kisslinger and Z.Li, *Phys. Rev.* **D51**, R5986 (1995); *Phys. Lett.* **B445**, 271 (1999); L.S.Kisslinger, *Nucl. Phys.* **A629**, 30c (1998).
- [228] S.Capstick and P.Page, *Phys. Rev.* **D60**, 111501 (1999); *Phys. Rev.* **C66**, 065204 (2002).
- [229] E.Klempt, *AIP Conf. Proc.* **814**, 723 (2006); S.L.Zhu, *Int. J. Mod. Phys.* **A19**, 3439 (2004); ibid. **A20** 1548 (2005).

- [230] M. Ripani et al., *Phys. Rev. Lett.* **91**, 022002 (2003); M. Dugger et al., *Phys. Rev. Lett.* **96**, 062001 (2006); R.Bradford et al., *Phys. Rev. C*73, 035202(2006); H.Egiyan et al., *Phys. Rev. C*73, 025204 (2006).
- [231] M.Q.Tran *et al.*, *Phys. Lett.* **B445**, 20 (1998); T.Mart and C.Bennhold, *Phys. Rev. C*61, 012201 (2000); K.H.Glander et al., *Euro. Phys. J. A*19, 251 (2004); R.Lawall et al., *Euro. Phys. J. A*24, 275 (2005).
- [232] Y. Assafiri et al., *Phys. Rev. Lett.* **90**, 222001 (2003); J.Ajaka et al., *Phys. Rev. Lett.* **96**, 132003 (2006).
- [233] A.V.Sarantsev et al., *Eur. Phys. J. A*25, 441 (2005).
- [234] BES Collaboration, J.Z.Bai et al., *Phys. Lett.* **B510**, 75 (2001); BES Collaboration, H.B.Li et al., *Nucl. Phys.* **A675**, 189c (2000); BES Collaboration, B.S.Zou et al., *Excited Nucleons and Hadronic Structure, Proc. of NSTAR2000 Conf. at JLab, Feb 2000*. Eds. V.Burkert et al., World Scientific (2001) p.155.
- [235] B.S.Zou, *Nucl. Phys.* **A684**, 330 (2001); *Nucl. Phys.* **A675**, 167 (2000).
- [236] M.Benmerrouche, N.C.Mukhopadhyay and J.F.Zhang, *Phys. Rev. Lett.* **77**, 4716 (1996); *Phys. Rev. D*51, 3237 (1995).
- [237] M.G.Olsson and E.T.Osypowski, *Nucl. Phys.* **B87**, 399 (1975); *Phys. Rev. D*17, 174 (1978); M.G.Olsson et al., *ibid.* **17**, 2938 (1978).
- [238] W.Rarita and J.Schwinger, *Phys. Rev.* **60**, 61 (1941).
- [239] C.Fronsdal, *Nuovo Cimento Suppl.* **9**, 416 (1958); R.E.Behrends and C.Fronsdal, *Phys. Rev.* **106**, 345 (1957).
- [240] S.U.Chung, *Spin Formalisms*, CERN Yellow Report 71-8 (1971); *Phys. Rev. D*48, 1225 (1993); J.J.Zhu and T.N.Ruan, *Communi. Theor. Phys.* **32**, 293, 435 (1999).
- [241] W.H.Liang, P.N.Shen, J.X.Wang and B.S.Zou, *J. Phys. G*28 (2002) 333.
- [242] J.X.Wang, *Comput. Phys. Commun.* **77**, 263 (1993).
- [243] R. Sinha and S. Okubo, *Phys. Rev. D*30 (1984) 2333.
- [244] W.H.Liang, P.N.Shen, B.S.Zou and A.Faessler, *Euro. Phys. J. A*21 (2004) 487.
- [245] R.A. Arndt et al., *Phys.Rev.C*69, 035213 (2004); M.Manley, talk at NSTAR2004, Grenoble, March 2004.
- [246] T.P.Vrana, S.A.Dytman and T.S.H.Lee, *Phys. Rep.* 328 (2000) 181.
- [247] BES Collaboration, *Phys. Rev. Lett.* **97** (2006) 062001.
- [248] H.X.Yang et al., (BES Collaboration), *Int. J. Mod. Phys. A*20 (2005) 1985; BES Collaboration, *Phys. Rev. Lett.* **93** (2004) 112002.

- [249] G.Penner and U.Mosel, Phys. Rev. **C66**, 055211 (2002); ibid. **C66**, 055212 (2002); V.Shklyar, H.Lenske and U.Mosel, Phys. Rev. **C72**, 015210 (2005); B.Julia-Diaz, B.Saghai, T.S.H.Lee and F.Tabakin, Phys. Rev. **C73**, 055204 (2006).
- [250] B.S.Zou (for BES Collaboration), *Proc. of the Workshop on the Physics of Excited Nucleons (NSTAR2004)*, Grenoble, France, March 2004. Eds. J.P.Bocquet et al., World Scientific (2004) p.271.
- [251] H.X.Yang, IHEP Ph.D thesis (2001).
- [252] BES Collaboration, Phys.Rev. D74 (2006) 012004.
- [253] BES Collaboration, Phys.Rev. D71 (2005) 072006.
- [254] S. Capstick and N. Isgur, Phys. Rev. D34 (1986) 2809.
- [255] F.Huang, Z.Y.Zhang and Y.W.Yu, Phys. Rev. **C73**, 025207 (2006).
- [256] J.J.Xie and B.S.Zou, Phys. Lett. **B** (2007); [nucl-th/0701021].
- [257] Y. Nambu and G. Jona-Lasinio, Phys. Rev. **122**(1961)345; K. C. Chou, JETP 12(1961)492.
- [258] S. Coleman, *Aspects of Symmetry*, Cambridge University Press 1985.
- [259] W.-M. Yao *et al.* (Particle Data Group), J. Phys. G: Nucl. Part. Phys. **33**, 1(2006).
- [260] L. S. Brown and R. N. Cahn, Phys. Rev. Lett. **35** (1975)1.
- [261] A theoretical review on linear  $\sigma$  model can be found in, B. W. Lee, *Chiral Dynamics*.
- [262] See for example, C. S. Gao and J. Y. Zeng, *Lectures on Particle Physics and Nuclear Physics*, High Education Press, Beijing, 1990(in chines).
- [263] N. N. Achasov, A. V. Kiselev and G. N. Shestakov, Talk given at  $e^+e^-$  Collisions from  $\phi$  to  $\psi$ , Novosibirsk, Russia, 27 Feb - 2 Mar 2006; [hep-ph/0605126].
- [264] N. A. Törnqvist, Zeit. Phys. **C68**(1995)647.
- [265] R. Kaminski, L. Leśniak and J.-P. Maillet, Phys. Rev. **D50**(1994)3154; N. N. Achasov and G. N. Shestakov, Phys. Rev. **D49**(1994)5779; M. Ishida, S. Ishida and T. Ishida, Prog. Theor. Phys. **99**(1998)1031.
- [266] J. Gasser and H. Leutwyler, Annals Phys.158:142,1984.
- [267] Z. G. Xiao and H. Q. Zheng, Nucl. Phys. **A695**(2001)273.
- [268] E. M. Aitala *et al.*, Phys. Rev. Lett. **86**(2001)770.
- [269] M. Ablikim *et al.* (The BES Collaboration), Phys. Lett. **B598**(2004)149; J. Z. Bai *et al.*, High Energy Phys. Nucl. Phys. **28**(2004)215.
- [270] M. Ablikim *et al.* (The BES Collaboration), Phys. Lett. **B 645**, 19-25 (2007).

- [271] M. Ablikim et al. (The BES Collaboration), Phys. Lett. **B 645** (2007) 19
- [272] Z. Y. Zhou et. al., JHEP0502(2005)43.
- [273] I. Caprini, G. Colangelo and H. Leutwyler, Phys. Rev. Lett. **96**(2006)132001.
- [274] L. Y. Xiao, H. Q. Zheng, Z. Y. Zhou, *Lightest scalars as chiral partners of the Nambu-Goldstone bosons* Invited talk given at 13th International Conference in QCD (QCD 06), Montpellier, France, 3-7 Jul 2006. hep-ph/0609009.
- [275] H. Q. Zheng *et al.*, Nucl. Phys. **A733**(2004)235.
- [276] P. Minkowski, W. Ochs, *Talk given at Workshop on Hadron Spectroscopy (WHS 99), Rome, Italy, 8-12 Mar 1999. In \*Frascati 1999, Hadron spectroscopy\* 245-255*; hep-ph/9905250.
- [277] B.S. Zou and D.V. Bugg, Phys. Rev. D48 (1993) R3948.
- [278] See for example, N. N. Achasov and A. V. Kiselev, Phys. Rev. **D73**(2006)054029; L. O. Arantes and M. R. Robilotta, Phys. Rev. **D73**(2006)034028.
- [279] K. M. Watson, Phys. Rev. **88** (1952) 1163.
- [280] J. M. Link *et al.*, (The FOCUS Collaboration), Phys. Lett. **B535** (2002)43.
- [281] J. M. Link *et al.*, (The FOCUS Collaboration), Phys.Lett. B621 (2005)72.
- [282] L. Edera, M. R. Pennington Phys. Lett. **B623**(2005)55.
- [283] E. M. Aitala et al., Phys. Rev. Lett. **89**(2002)121801.
- [284] B. Meadows, hep-ex/0506040; Invited talk in the Moriond QCD 2005, La Thuile, March 2005.
- [285] D. Aston et al. (LASS Collaboration), Nucl. Phys. **B296**(1988)493.
- [286] I. Caprini, Phys. Lett. **B638**(2006)468 and reference therein; A. V. Anisovich and V. V. Anisovich, Phys. Lett. **B345**(1995)321.
- [287] D. V. Bugg, J. Phys. **G34**, 151(2007); [hep-ph/0608081].
- [288] B. Ananthanarayan, I. Caprini, G. Colangelo, J. Gasser, H. Leutwyler, Phys. Lett. **B602**(2004)218.
- [289] H. Leutwyler, talk given at QCHS VII, Ponta Delgada, Azores, Portugal, September 2 - 7, 2006.
- [290] T. A. Lahde, Ulf-G. Meissner, Phys. Rev. **D74**(2006)034021.
- [291] E. M. Aitala et al. (E791 Collaboration), Phys. Rev. Lett. **89**, 121801(2002).
- [292] M. Ablikim et al. (The BES Collaboration), Phys. Lett. **B 633** (2006) 681

- [293] Z. Y. Zhou and H. Q. Zheng, Nucl. Phys. **A755**(2006)212.
- [294] S. Descotes-Genon, B. Moussallam, hep-ph/0607133.
- [295] N. A. Törnqvist, Talk given at International Europhysics Conference on High-Energy Physics (EPS-HEP 99), Tampere, Finland, 15-21 Jul 1999; hep-ph/9910443.
- [296] R. L. Jaffe, Phys. Rev. **D15**(1977)267;  
M. G. Alford and R. L. Jaffe, Nucl. Phys. **B578**(2000)367.
- [297] G. 't Hooft, Phys. Rep. **142**(1986)357.
- [298] N. A. Tornqvist, hep-ph/0606041;  
Y. B. Dai and Y. L. Wu, Eur. Phys. J. **C39**(2005)S1;  
T. Schafer, Phys. Rev. D68(2003)114017;  
M. Napsuciale, S. Rodriguez, Int. J. Mod. Phys. **A16**(2001)3011.
- [299] M. R. Pennington, Phys. Rev. Lett. 97, 011601 (2006).
- [300] S. Narison, Phys. Rev. **D73**(2006)114024.
- [301] T. Kunihiro, talk given at “New Forntiers in QCD: exotic hadrons and hadronic matter”, November 20 – December 8, 2006, Kyoto, Japan. <http://www2.yukawa.kyoto-u.ac.jp/ykis06/>
- [302] F. E. Close and N. A. Tornqvist, J. Phys. G28(2002)R249.
- [303] E. van Beveren, D. V. Bugg, F. Kleefeld and G. Rupp, Phys. Lett. **B641**, 265-271 (2006); [hep-ph/0606022].
- [304] J. A. Oller, E. Oset, J. R. Pelaez, Phys. Rev. **D59**(1999)074001, Erratum-ibid. **D60**(1999)099906; J. Peláez, Phys. Rev. Lett. **92**(2004)102001.
- [305] V. V. Anisovich, D. Bugg, A. V. Sarentsev and B. S. Zou, Phys. Rev. **D50**(1994)972.
- [306] A. Aloisio et al., Phys. Lett. **B537**(2002)21; A. Aloisio et al., Phys. Lett. **B536**(2002)209.
- [307] L. Maiani, F. Piccinini, A. D. Polosa and V. Riquer, Phys. Rev. Lett. **93**(2004)212002.
- [308] D. V. Bugg, Eur. Phys. J. **C47**(2006)57.
- [309] F. Calogero and C. Zemach, Phys. Rev. 120 (1960) 1860
- [310] V. E. Balakin, V. M. Budnev and I. F. Ginzburg, Pisma Zh. Eksp. Teor. Fiz. **11** (1970) 559.
- [311] S. J. Brodsky, T. Kinoshita and H. Terazawa, Phys. Rev. Lett. **25** (1970) 972.
- [312] V. M. Budnev, I. F. Ginzburg, G. V. Meledin and V. G. Serbo, Phys. Rept. **15** (1974) 181.

- [313] S. J. Brodsky, T. Kinoshita and H. Terazawa, Phys. Rev. D **4** (1971) 1532.
- [314] L. Lonnblad *et al.*, Presented at 2nd General Meeting LEP2 Physics Workshop, Geneva, Switzerland, 15-16 Jun 1995; [arXiv:hep-ph/9512371].
- [315] G. A. Schuler, arXiv:hep-ph/9610406.
- [316] V. M. Budnev, I. F. Ginzburg, Phys. Lett. **37B** (1971) 320.
- [317] M. R. Pennington, Invited talk at Workshop on  $e^+e^-$  in the 1-GeV to 2-GeV Range: Physics and Accelerator Prospects - ICFA Mini-workshop - Working Group on High Luminosity  $e^+e^-$  Colliders, Alghero, Sardinia, Italy, 10-13 Sep (2003) [hep-ph/0311299]; Acta Phys. Polon. **B37**, 857-866 (2006) [hep-ph/0511146].
- [318] M. R. Whalley, J. Phys. G: Nucl. Part. Phys. **27** (2001) A1-121
- [319] J. Boyer *et al.* (Mark-II Collaboration), Phys. Rev. D **42**, 1350 (1990).
- [320] F. Butler *et al.* (Mark-II Collaboration), Phys. Rev. D **42**, 1368 (1990).
- [321] J. Dominick *et al.* (CLEO-II Collaboration), Phys. Rev. D **50**, 3027 (1994).
- [322] H. J. Behrend *et al.* (CELLO Collaboration), Z. Phys. **C56**, 381 (1992).
- [323] T. Mori *et al.* (Belle Collaboration), Jour. Phys. Soc. of Japan **A 76**, 074102 (2007) and Phys. Rev. D **75**, 051101(R) (2007).
- [324] H. Marsiske *et al.* (Crystal Ball Collaboration), Phys. Rev. D **41**, 3324 (1990).
- [325] N.N. Achasov, G.N. Shestakov, Yadernaya Fizika, 2006, Vol. 69, No. 9, pp. 15451556,hep-ph/0506046
- [326] L. Maiani, Proc. Workshop on Physics and Detectors for DAFNE (1991) 719
- [327] M.R. Pennington, Int. J. Mod. Phys. **A21**, 747-756 (2006)[hep-ph/0509265]; P. Minkowski, W. Ochs, Eur. Phys. J. C9 (1999) 283 [hep-ph/9811518]; W. Ochs, AIP Conf.Proc. 717 295-306 (2004) [hep-ph/0311144].
- [328] H. Albrecht *et al.* (ARGUS Collaboration), Z. Phys. **C74**, 469 (1997).
- [329] D. Antreasyan *et al.* (Crystal Ball Collaboration), Z. Phys. **C48**, 561 (1990).
- [330] H. J. Behrend *et al.* (CELLO Collaboration), Z. Phys. **C46**, 583 (1990).
- [331] G. Schuler, Comput. Phys. Commun. **108**, 279-303(1998)[hep-ph/9710506].
- [332] F.A. Berends, P.H. Daverveld, R. Kleiss, Nucl. Phys. B253 (1985) 421, Comput. Phys. Commun. 40 (1986) 271,285,309
- [333] F.L. Kinde, "Charm production in two-photon physics", RX-1224 (LEIDEN) (1988) thesis
- [334] J. Bijnens, F. Cornet, Nucl.Phys.B296 (1988)



# Part IV

## Charmonium Physics

Conveners  
Cong-Feng Qiao, Changzheng Yuan.

Contributors  
T. Barnes, N. Brambilla, H. X. Chen, Y. Q. Chen,  
X. Garcia i Tormo, Z. G. He, Y. Jia, Y. P. Kuang,  
H. B. Li, J. L. Li, H. L. Ma, J. P. Ma, X. H. Mo,  
S. L. Olsen, A. Pineda, R. G. Ping, C. F. Qiao,  
G. Rong, J. Soto, A. Vairo, P. Wang, C. Z. Yuan,  
D. H. Zhang, X. M. Zhang and Y. J. Zhang



# Chapter 13

## Theoretical Frameworks of Charmonium Physics

The discovery of the  $J/\psi$  in 1974 had a huge impact on the development of the theory of strong interactions and the Standard Model. Still today, mesons made from two heavy quarks, *i.e.* heavy quarkonia, play a prominent role in investigations of QCD dynamics both within and beyond the Standard Model [1]. These are multi-scale systems that probe all of the energy regimes of QCD: from the hard region, where expansions in the coupling constant are legitimate, to the low-energy region, where nonperturbative effects dominate. Heavy quark-antiquark states are thus an ideal, and to some extent unique, laboratory where our understanding of nonperturbative QCD and its interplay with perturbative QCD can be tested in a controlled framework. In correspondence with the hierarchy of energy scales in quarkonia, a hierarchy of nonrelativistic effective field theories (NR EFT) may be constructed, each one with fewer degrees of freedom that are left dynamical and thus simpler. Some of these physical scales are large and may be treated with perturbation theory. These features make mesons that are made from two heavy quarks accessible inside QCD.

### 13.1 Non-Relativistic QCD effective theory<sup>1</sup>

Charmonia are bound states of the  $c\bar{c}$  pair by the strong interaction. The charm quark mass  $m_c$  is so large that the motion of the charm quark inside the bound state is slow and charmonium can be approximately regarded as a non-relativistic bound state.  $v^2 \sim 0.3$  for charmonia and 0.1 for bottomonia by potential model calculations or by Lattice simulation, where  $v$  is the relative velocity between the  $c$  and  $\bar{c}$ . For a small value of  $v$ , there are several distinct energy scales in charmonium. The 3-momentum is order  $m_c v$ . The binding energy is order  $m_c v^2$ . Numerically, they are around 800 MeV and 500 MeV, respectively. In the limit of  $v^2 \ll 1$ , those energy scales satisfy a hierarchy relation  $m_c \gg m_c v \gg m_c v^2$ , with which the effects at energy scale  $m_c$  can be integrated out explicitly. The resultant theory, being expressed as a Pauli two-component field theory, is just the *nonrelativistic QCD* (NRQCD) effective theory [2, 3, 4]. NRQCD is equivalent to the full QCD but it simplifies QCD by taking a nonrelativistic expansion and by reducing the number of the

---

<sup>1</sup>By Yu-Qi Chen

energy scales. Essentially, NRQCD can be regarded as an effective theory which expands the full QCD in powers of  $v$ . It turns out to be very useful in dealing with charmonium relevant processes such as spectroscopies, annihilation decays, and inclusive productions. Starting from NRQCD, one may integrate out further the effects at energy scale  $m_c v$  and obtain an effective theory contains only energy scale  $m_c v^2$ , called as *potential NRQCD* (pNRQCD) [5, 6, 7], which will be reviewed in the next subsection.

### 13.1.1 NRQCD effective theory

QCD fully describes the strong interactions of the quarks and gluons. QCD lagrangian for heavy quark is given by:

$$\mathcal{L} = \bar{\Psi}(x) (i \not{D} - m_c) \Psi(x), \quad (13.1.1)$$

where  $iD^\mu = i\partial^\mu + gA^{a\mu}T^a$  is the covariant derivative. It looks simple but it turns out to be complicated. As a relativistic quantum field theory, it describes heavy quark and antiquark together and quantum effects from all energy scales. It can be simplified in the nonrelativistic limit  $v \ll 1$ . First, in this limit, the heavy quark pair creation and annihilation effects is suppressed. The quark and the antiquark are decouple. All relativistic effects can be expanded as power series of  $v$ . Second, those quantum effects arising from high energy scales  $m$  or above are perturbatively calculable since QCD is a theory with asymptotical freedom. This can be done by taking the hard cut-off energy scale  $\Lambda$  less than  $m_c$ . Quantum effects above  $\Lambda$  can be expressed as contributions from a sum of certain local operators in powers of  $v$  since in this region the internal particles are far off-shell and can only propagate in a short distance which is less than  $1/m_c$ . Consequently, taking  $\Lambda < m_c$ , adding certain local operators in the lagrangian, and making expansion in terms of  $v$ , one obtains an effective theory, which reproduces the results of the full QCD at low energy scale. The coefficients of those local operators are called as the Wilson short distance coefficients which can be calculated by matching the QCD full theory and that of the effective theory.

In NRQCD effective theory, the quark and the antiquark fields are described by the two component Pauli field instead of the Dirac four component field in QCD. Up to order  $v^4$ , the NRQCD effective lagrangian reads [2, 3, 4]

$$\mathcal{L}_{\text{NRQCD}} = \mathcal{L}_l + \mathcal{L}_0 + \delta\mathcal{L}, \quad (13.1.2)$$

where  $\mathcal{L}_l$  is the usual lagrangian that describes gluons and light quarks;

$$\mathcal{L}_0 = \psi^\dagger \left( iD_0 + \frac{\mathbf{D}^2}{2m_c} \right) \psi + \chi^\dagger \left( iD_0 + \frac{\mathbf{D}^2}{2m_c} \right) \chi \quad (13.1.3)$$

is the leading order NRQCD effective lagrangian; and

$$\begin{aligned} \delta\mathcal{L} = & \frac{c_1}{8m_c^3} \psi^\dagger (\mathbf{D}^2)^2 \psi + \frac{c_2}{8m_c^2} \psi^\dagger g(\mathbf{D} \cdot \mathbf{E} - \mathbf{E} \cdot \mathbf{D}) \psi + \frac{c_3}{2m_c} \psi^\dagger g\boldsymbol{\sigma} \cdot \mathbf{B} \psi \\ & + i \frac{c_4}{8m_c^2} \psi^\dagger g\boldsymbol{\sigma} \cdot (\mathbf{D} \times \mathbf{E} - \mathbf{E} \times \mathbf{D}) \psi + \text{charge conjugate terms} \end{aligned} \quad (13.1.4)$$

are  $v^2$  correction terms to  $\mathcal{L}_0$ . Here  $\psi$  and  $\chi$  are the Pauli spinor fields of quark and antiquark, respectively. Gauge invariance implies that gluon field appears in the lagrangian

always only through the gauge-covariant derivatives  $iD_0$ ,  $i\mathbf{D}$  and the QCD field strength  $\mathbf{E}$ ,  $\mathbf{B}$ .

In  $\mathcal{L}_0$ , both the  $iD_0$  term and the  $\mathbf{D}^2/2m_c$  term contribute to the same order of the quarkonium energy in Coulomb gauge. In QED, neglecting  $\mathbf{A}$  field, variation to the  $\mathcal{L}_0$  gives to the Schrödinger equation of the hydrogen atom. No Pauli matrix  $\sigma^i$  in  $\mathcal{L}_0$  implies a symmetry of the heavy quark spin. It means that spin-flip of the heavy quark does not change the energy of the system at leading order and the spin-dependent effects are suppressed. Consequently, at leading order the states  $J/\psi$  and  $\eta_c$  are degenerate and the states  $\chi_{c0}, \chi_{c1}, \chi_{c2}$ , and  $h_c$  are also degenerate. This symmetry is violated after including the next leading order corrections since the spin dependent term with  $\sigma^i$  appearing in  $\delta\mathcal{L}$ . The velocity scaling rule [2, 3, 4] can be used to count the relative importance of each term in  $\delta\mathcal{L}$ . Those Wilson short-distance coefficients  $c_i$ 's has been calculated in pQCD. They can be expanded as power series of  $\alpha_s$  at energy scale  $m_c$ . Other coefficients can be determined by matching the full QCD and the NRQCD effective theory. Some relationships between these coefficients follows from the reparameterization invariance [8, 9, 10, 11, 12, 13]. Especially, the coefficient of the kinetic energy term in  $\mathcal{L}_0$  is not renormalization.

### 13.1.2 Inclusive Charmonium Annihilation Decays

An important decay mode of charmonium is the annihilation decay, in which the  $c\bar{c}$  pair annihilates into a light quark antiquark pairs or gluons, or photon(s). Those light partons eventually form light hadrons by hadronization. The inclusive process that  $c\bar{c}$  annihilates into all light hadrons is infrared safety and hence perturbatively calculable although the hadronization process is infrared sensitive. When a  $c\bar{c}$  pair annihilates, the total energy  $2m_c$  is released. Thus it occurs at distance of  $1/(2m_c)$ . The typical size of a charmonium state is order of  $1/(m_c v)$ . Thus in the limit of  $v \ll 1$ , the effects happened at these two distinct distance scales are separated well. NRQCD factorization formula [4] provide a systematic framework to analyze the annihilation decay rates. In the formula, the annihilation decay rate is factorized into a sum of the products of the short-distance coefficients and the long-distance matrix elements [4]:

$$\Gamma(H) = \frac{1}{2M_H} \sum_{mn} \frac{C_{mn}(\mu)}{m_c^{d_{mn}-N-1}} \langle H | \mathcal{O}_{mn} | H \rangle^{(\mu)}, \quad (13.1.5)$$

where  $M_H$  is the mass of the charmonium state  $H$  and  $d_{mn}$  is the mass dimension of the operator  $\mathcal{O}_{mn}$ . The matrix elements  $\langle H | \mathcal{O}_{mn} | H \rangle$  are expectation values in the quarkonium state  $H$  of local 4-fermion operators that have the structure

$$\mathcal{O}_{mn} = \psi^\dagger \mathcal{K}'_m^\dagger \chi \chi^\dagger \mathcal{K}_n \psi, \quad (13.1.6)$$

where  $\mathcal{K}_n$  and  $\mathcal{K}'_m^\dagger$  are products of a color matrix (1 or  $T^a$ ), a spin matrix, and a polynomial in the gauge covariant derivative  $\mathbf{D}$ . The color singlet dimension 6 and 8 operators are:

$$\begin{aligned} \mathcal{O}_1(^3S_1) &= \psi^\dagger \boldsymbol{\sigma} \chi \chi^\dagger \boldsymbol{\sigma} \psi, \\ \mathcal{O}_1(^1S_0) &= \psi^\dagger \chi \chi^\dagger \psi, \end{aligned}$$

$$\mathcal{O}_1(^3P_0) = \psi^\dagger \mathbf{D} \cdot \boldsymbol{\sigma} \chi \chi^\dagger \mathbf{D} \cdot \boldsymbol{\sigma} \psi,$$

$$\begin{aligned}
\mathcal{O}_1(^3P_1) &= \psi^\dagger \mathbf{D} \times \boldsymbol{\sigma} \chi \chi^\dagger \mathbf{D} \times \boldsymbol{\sigma} \psi, \\
\mathcal{O}_1(^3P_2) &= \psi^\dagger \sigma^{(i} D^{j)} \chi \chi^\dagger \sigma^{(i} D^{j)} \psi, \\
\mathcal{O}_1(^1P_1) &= \psi^\dagger \mathbf{D} \chi \chi^\dagger \mathbf{D} \psi,
\end{aligned} \tag{13.1.7}$$

The corresponding color octet operators could be obtained by inserting  $T^a$  between  $\psi^\dagger$  and  $\chi$  and between  $\chi^\dagger$  and  $\psi$ . In NRQCD factorization formula, the quantum number of the state  $H$  is not necessarily the same with that of the operator  $O$ . When  $H$  and  $Q$  hold the same quantum number,  $H$  decays via the leading Fock space. Otherwise,  $H$  decays via the higher Fock space with electric or magnetic transition. It differs from the conventional color-singlet model in which the  $H$  decays only via the leading Fock space. The relative importance of each matrix element can be estimated by the velocity scaling rule [4]. Suppose  $E$  and  $M$  be the total number of the electric and magnetic transitions;  $D$  the derivative number contain in the operator  $O$ , then the matrix element  $\langle H | \mathcal{O}_{mn} | H \rangle$  scales like  $v^{3+D+E+3M/2}$ . This rule can be used to estimate the order of magnitude of the NRQCD matrix elements.

To reduce the number of the NRQCD matrix elements, some comments can be given below:

(1) In the electromagnetic annihilation decay mode, the  $c\bar{c}$  pair annihilates to the vacuum. Thus one needs to insert a vacuum state  $|0\rangle\langle 0|$  between those two two-fermion operators. It corresponds to take the vacuum saturation approximation, in which the NRQCD matrix elements are proportional to the square of the wavefunctions at the origin for  $S$ -wave and its derivative for  $P$ -wave and so on. The approximation validates up to order  $v^4$  [4] for a  $S$ -wave NRQCD matrix elements.

(2) In annihilation processes of charmonium decay and production, the relativistic correction is typically large. The Gramm-Kapustin relation [14] relates the leading order matrix elements to the relativistic correction ones. However, the pole mass enter into the relation so that some ambiguities are involved.

(3) With pNRQCD, the color-octet matrix elements are related to the corresponding color-singlet one by some universal factor which are state and flavor independent [5, 6, 7]. This will be reviewed in detail in the next subsection.

Thus up to certain orders of  $v$ , there are only a few independent long-distance matrix elements, which are nonperturbative in nature. They may be determined by fitting experimental data, by Lattice simulation, or by pNRQCD. This feature makes NRQCD factorization formula be useful in analyzing the inclusive or electromagnetic charmonium annihilation decays.

The short-distance coefficients for annihilation decay rates  $C_{mn}(\mu)$  can be expanded as a power series of  $\alpha_s(\mu)$ . They can be determined by matching perturbative calculations of  $c\bar{c}$  scattering amplitudes. For annihilation decays,  $\mu \sim m$ . The  $\mu$  dependence in the short-distance coefficients cancels that in the matrix elements. A general matching prescription is the threshold expansion method [15].

In sections 18.1 and 18.2, we will discuss the light hadron decays of the  $J/\psi$ ,  $\psi'$ ,  $\eta_c$ ,  $\chi_{cJ}$  and  $h_c$  in framework of NRQCD factorization method.

## 13.2 *p*NRQCD and its applications<sup>2</sup>

### 13.2.1 *p*NRQCD

*p*NRQCD [5, 6, 7] is the EFT for two heavy quark systems that follows from NRQCD by integrating out the soft scale  $mv$ . Here the role of the potentials and the quantum mechanical nature of the problem are realized in the fact that the Schrödinger equation appears as zero order problem for the two quark states. We may distinguish two situations: 1) weakly coupled *p*NRQCD when  $mv \gg \Lambda_{\text{QCD}}$ , where the matching from NRQCD to *p*NRQCD may be performed in perturbation theory; 2) strongly coupled *p*NRQCD when  $mv \sim \Lambda_{\text{QCD}}$ , where the matching has to be nonperturbative. Recalling that  $r^{-1} \sim mv$ , these two situations correspond to systems with inverse typical radius smaller than or of the same order as  $\Lambda_{\text{QCD}}$ .

#### Weakly coupled *p*NRQCD

The effective degrees of freedom that remain dynamical are: low energy  $Q\bar{Q}$  states (that can be decomposed into a singlet and an octet field under colour transformations) with energy of order  $\Lambda_{\text{QCD}}$ ,  $mv^2$  and momentum  $\mathbf{p}$  of order  $mv$ , plus low energy (ultrasoft) gluons with energy and momentum of order  $\Lambda_{\text{QCD}}$ ,  $mv^2$ . All the gluon fields are multipole expanded (i.e. expanded in the quark-antiquark distance  $r$ ). The Lagrangian is then given by terms of the type

$$\frac{c_k(m, \mu)}{m^k} \times V_n(r\mu', r\mu) \times O_n(\mu', mv^2, \Lambda_{\text{QCD}}) r^n. \quad (13.2.8)$$

where the matching coefficients  $c_k$  are inherited from NRQCD and contain the logs in the quark masses, while the *p*NRQCD potential matching coefficients  $V_n$  encode the non-analytic behaviour in  $r$ . At leading order in the multipole expansion, the singlet sector of the Lagrangian gives rise to equations of motion of the Schrödinger type. Each term in the *p*NRQCD Lagrangian has a definite power counting. The bulk of the interaction is carried by potential-like terms, but non-potential interactions, associated with the propagation of low energy degrees of freedom are present as well. These retardation (or non-potential) effects start at the next-to-leading order (NLO) in the multipole expansion and are systematically encoded in the theory and typically related to nonperturbative effects [6]. There is a systematic procedure to calculate corrections in  $v$  to physical observables: higher order perturbative (bound state) calculations in this framework become viable. In particular the EFT can be used for a very efficient resummation of large logs (typically logs of the ratio of energy and momentum scales) using the renormalization group (RG) adapted to the case of correlated scales [16, 17]; Poincaré invariance is not lost, but shows up in some exact relations among the matching coefficients [13].

#### Strongly coupled *p*NRQCD

In this case the matching to *p*NRQCD is nonperturbative. Away from threshold (precisely when heavy-light meson pair and heavy hybrids develop a mass gap of order

---

<sup>2</sup>By Nora Brambilla, Yu Jia, and Antonio Vairo

$\Lambda_{\text{QCD}}$  with respect to the energy of the  $Q\bar{Q}$  pair), the quarkonium singlet field  $S$  remains as the only low energy dynamical degree of freedom in the pNRQCD Lagrangian (if no ultrasoft pions are considered), which reads [18, 19, 7]:

$$L_{\text{pNRQCD}} = \text{Tr} \left\{ S^\dagger \left( i\partial_0 - \frac{\mathbf{p}^2}{2m} - V_S(r) \right) S \right\}. \quad (13.2.9)$$

The matching potential  $V_S(r)$  is a series in the expansion in the inverse of the quark masses: static,  $1/m$  and  $1/m^2$  terms have been calculated, see [18, 19]. They involve NRQCD matching coefficients and low energy nonperturbative parts given in terms of Wilson loops and field strengths insertions in the Wilson loop. In this regime we recover the quark potential singlet model from pNRQCD. However the potentials are calculated from QCD in the formal nonperturbative matching procedure. An actual evaluation of the low energy part requires lattice evaluation [20] or QCD vacuum models calculations [21].

### 13.2.2 Applications

It is important to establish when  $\Lambda_{\text{QCD}}$  sets in, i.e. when we have to resort to non-perturbative methods. For low-lying resonances, it is reasonable, although not proved, to assume  $mv^2 \gtrsim \Lambda_{\text{QCD}}$ . The system is weakly coupled and we may rely on perturbation theory, for instance, to calculate the potential. The theoretical challenge here is performing higher-order calculations and the goal is precision physics. For high-lying resonances, we assume  $mv \sim \Lambda_{\text{QCD}}$ . The system is strongly coupled and the potential must be determined non-perturbatively, for instance, on the lattice. The theoretical challenge here is providing a consistent framework where to perform lattice calculations and the progress is measured by the advance in lattice computations.

For what concerns systems close or above the open flavor threshold, a complete and satisfactory understanding of the dynamics has not been achieved so far. Hence, the study of these systems is on a less secure ground than the study of states below threshold. Although in some cases one may develop an EFT owing to special dynamical conditions (as for the  $X(3872)$  interpreted as a loosely bound  $D^0 \bar{D}^{*0} + \bar{D}^0 D^{*0}$  molecule), the study of these systems largely relies on phenomenological models. The major theoretical challenge here is to interpret the new states in the charmonium region discovered at the B-factories in the last years.

### 13.2.3 QCD potentials

pNRQCD allows us to properly define the QCD potentials and give a well defined procedure to properly calculate them. In this modern description the potentials are matching coefficients of the EFT and as such depend on the scale of the matching. In weakly coupled pNRQCD the soft scale is bigger than  $\Lambda_{\text{QCD}}$  and so the singlet and octet potentials have to be calculated in the perturbative matching. In [22] a determination of the singlet potential at three loops leading log has been obtained inside the EFT which gives the way to deal with the well known infrared singularity arising in the potential at this order. From this,  $\alpha_s$  in the  $V$  regularization can be obtained, showing at this order and for this regularization a dependence on the infrared behaviour of the theory.

The finite terms in the singlet static potential at three loops are not yet known but has been estimated [23]. Recently also the logarithmic contribution at four loops has been calculated [24]. The three loop renormalization group improved calculation of the static singlet potential has been compared to the lattice calculation and found in good agreement up to about 0.25 fm [25]. The static octet potential is known at two loops [26] and again agrees well with the lattice data [27].

At a scale  $\mu$  such that  $mv \sim \Lambda_{\text{QCD}} \gg \mu \gg mv^2$ , confinement sets in and the potentials become admixture of perturbative terms, inherited from NRQCD, which encode high-energy contributions, and non-perturbative objects. Strongly coupled pNRQCD gives us the general form of the potentials obtained in the nonperturbative matching to QCD in the form of Wilson loops and Wilson loop chromoelectric and chromomagnetic field strengths insertions [18, 19], very well suited for lattice calculations. These will be in general a complex valued functions. The real part controls the spectrum and the imaginary part controls the decays.

The real part of the potential has been one of the first quantities to be calculated on the lattice (for a review see [20]). In the last year, there has been some remarkable progress. In [28], the  $1/m$  potential has been calculated for the first time. The existence of this potential was first pointed out in the pNRQCD framework [18]. A  $1/m$  potential is typically missing in potential model calculations. The lattice result shows that the potential has a  $1/r$  behaviour, which, in the charmonium case, is of the same size as the  $1/r$  Coulomb tail of the static potential and, in the bottomonium one, is about 25%. Therefore, if the  $1/m$  potential has to be considered part of the leading-order quarkonium potential together with the static one, as the pNRQCD power counting suggests and the lattice seems to show, then the leading-order quarkonium potential would be, somewhat surprisingly, a flavor-dependent function. In [29], spin-dependent potentials have been calculated with unprecedented precision. In the long range, they show, for the first time, deviations from the flux-tube picture of chromoelectric confinement [30]. The knowledge of the potentials in pNRQCD could provide an alternative to the direct determination of the spectrum in NRQCD lattice simulations: the quarkonium masses would be determined by solving the Schrödinger equation with the lattice potentials. The approach may present some advantages: the leading-order pNRQCD Lagrangian, differently from the NRQCD one, is renormalizable, the potentials are determined once for ever for all quarkonia, and the solution of the Schrödinger equation provides also the quarkonium wave functions, which enter in many quarkonium observables: decay widths, transitions, production cross-sections. The existence of a power counting inside the EFT selects the leading and the subleading terms in quantum-mechanical perturbation theory. Moreover, the quantum mechanical divergences (typically encountered in perturbative calculations involving iterations of the potentials, as in the case of the iterations of spin delta potentials) are absorbed by NRQCD matching coefficients. Since a factorization between the hard (in the NRQCD matching coefficients) and soft scales (in the Wilson loops or nonlocal gluon correlators) is realized and since the low energy objects are only glue dependent, confinement investigations, on the lattice and in QCD vacuum models become feasible [21, 30].

The potentials evaluated on the lattice once used in the Schrödinger equation produce the spectrum. The calculations involve only QCD parameters (at some scale and in some scheme).

### 13.2.4 Precision determination of Standard Model parameters

#### *c* and *b* mass extraction

The lowest heavy quarkonium states are suitable systems to extract a precise determination of the mass of the heavy quarks  $b$  and  $c$ . Perturbative determinations of the  $\Upsilon(1S)$  and  $J/\psi$  masses have been used to extract the  $b$  and  $c$  masses. The main uncertainty in these determinations comes from nonperturbative nonpotential contributions (local and nonlocal condensates) together with possible effects due to subleading renormalons. These determinations are competitive with those coming from different systems and different approaches (for the  $b$  mass see e.g. [31]). We report some recent determinations in Table 13.1.

Table 13.1: Different recent determinations of  $\overline{m}_b(\overline{m}_b)$  and  $\overline{m}_c(\overline{m}_c)$  in the  $\overline{\text{MS}}$  scheme from the bottomonium and the charmonium systems. The displayed results either use direct determinations or non-relativistic sum rules. Here and in the text, the \* indicates that the theoretical input is only partially complete at that order.

reference	order	$\overline{m}_b(\overline{m}_b)$ (GeV)
[32]	NNNLO*	$4.210 \pm 0.090 \pm 0.025$
[33]	NNLO +charm	$4.190 \pm 0.020 \pm 0.025$
[34]	NNLO	$4.24 \pm 0.10$
[35]	NNNLO*	$4.346 \pm 0.070$
[36]	NNNLO*	$4.20 \pm 0.04$
[37]	NNNLO*	$4.241 \pm 0.070$
[38]	NNLL*	$4.19 \pm 0.06$
reference	order	$\overline{m}_c(\overline{m}_c)$ (GeV)
[39]	NNLO	$1.24 \pm 0.020$
[34]	NNLO	$1.19 \pm 0.11$

A recent analysis performed by the QWG [1] and based on all the previous determinations indicates that at the moment the mass extraction from heavy quarkonium involves an error of about 50 MeV both for the bottom (1% error) and in the charm (4% error) mass. It would be very important to be able to further reduce the error on the heavy quark masses.

#### Determinations of $\alpha_s$ .

Heavy quarkonia leptonic and non-leptonic inclusive and radiative decays may provide means to extract  $\alpha_s$ . The present PDG determination of  $\alpha_s$  from bottomonium pulls down the global  $\alpha_s$  average noticeably [1]. Recently, using the most recent CLEO data on radiative  $\Upsilon(1S)$  decays and dealing with the octet contributions within weakly coupled pNRQCD, a new determination of  $\alpha_s(M_{\Upsilon(1S)}) = 0.184^{+0.014}_{-0.013}$  has been obtained [40], which corresponds to  $\alpha_s(M_Z) = 0.119^{+0.006}_{-0.005}$  in agreement with the central value of the PDG and with competitive errors. A similar extraction of  $\alpha_s$  from the inclusive photon spectrum

for radiative  $J/\psi$  decays may be possible (cf. the contribution by X. Garcia i Tormo and J. Soto in this Book in section 17.1).

### Top-antitop production near threshold at ILC.

In [38, 41] the total cross section for top quark pair production close to threshold in  $e+e-$  annihilation is investigated at NNLL in the weakly coupled EFT. Here we see how the summation of the large logarithms in the ratio of the energy scales significantly reduces the scale dependence. Studies like these will make feasible a precise extractions of the strong coupling, the top mass and the top width at a future ILC.

### 13.2.5 Gluelump Spectrum and exotic states

The gluelumps are states formed by a gluon and two heavy quarks in a octet configuration at small interquark distance [42]. The mass of such nonperturbative objects are typically measured on the lattice. The tower of hybrids static energies [43] reduces to the gluelump masses for small interquark distances. In pNRQCD [6, 27] the full structure of the gluelump spectrum has been studied, obtaining model independent predictions on the shape, the pattern, the degeneracy and the multiplet structure of the hybrid static energies for small  $Q\bar{Q}$  distances that well match and interpret the existing lattice data. These studies may be important both to elucidate the confinement mechanism (the gluelump masses control the behaviour of the nonperturbative glue correlators appearing in the spectrum and in the decays) and in relation to the exotic states recently observed at the B-factories. The  $Y(4260)$  in the charmonium sector may be identified with an hybrid state inside such picture [44].

### 13.2.6 Outlook

pNRQCD makes possible to investigate a wide range of heavy quarkonium observables in a controlled and systematic fashion and therefore it makes possible to learn about one of the most elusive sectors of the Standard Model: low-energy QCD. Among the most interesting and open theory challenges there are: the construction of an EFT close to threshold to understand the new exotic states, the taming of quarkonium production and the development of an EFT approach to quarkonium suppression in media and quarkonium-nuclei interaction.

The many new data coming in the last few years from B-Factories, CLEO, BES, HERA and the Tevatron experiment have given us glimpses of interesting physics to be explored. With the new theory tools discussed here and with the impressive number of produced and detected charmonium states, BES-III will make the difference in this field allowing to carry on important investigation inside the Standard Model and beyond the Standard Model (see [1] Chapter Beyond the Standard Model and [45]).



# Chapter 14

## Charmonium Spectroscopy

### 14.1 Introduction<sup>1</sup>

Historically [46, 47, 48, 49, 50, 51] charmonium has played an important rôle in the study of the strong interaction, including the search for exotica, and in the development of our understanding of the forces between quarks. The spectrum of relatively narrow charmonium states that cannot decay into open-charm modes is experimentally very clear; this has made it possible to precisely measure the masses of states that in the quark model are identified with N,L multiplets, and in addition the effects of the weaker spin-dependent forces (spin-spin, spin-orbit and tensor) in splitting these multiplets into states of definite S and J can also be quantified. Not only are the effects of the Breit-Fermi Hamiltonian (which is due to one gluon exchange, “OGE”) evident in the spectrum, but the Lorentz nature of the confining interaction itself has also been established (as scalar rather than timelike vector).

In future studies of charmonium spectroscopy at *BES-IIIS* it should be possible to discover many charmonium states that are expected theoretically but have not yet been observed. Some of the as yet unknown states are expected to be very narrow resonances. In addition one can presumably identify novel exotica that are currently unknown or poorly understood, such as charm molecules and charmonium hybrids. Our understanding of the known charmonium states can be greatly improved through more precise measurements of transitions involving these states, including both radiative and strong couplings. These studies have the potential to greatly improve our understanding of strong decays in particular. In this section we will review the current status of our understanding of charmonium and closely related systems, and will discuss some ways in which *BES-III* can contribute to our understanding of QCD through future experimental studies of charmonium.

### 14.2 Conventional charmonium states

The spectrum of the known “conventional” charmonium states, by which we mean states that appear to be in relatively good agreement with the predictions of simple  $c\bar{c}$  potential models, is summarized in Table 14.1. The table, which is abstracted from the

---

<sup>1</sup>By T. Barnes

2006 PDG [52], gives the usual quark model N,L multiplet assignment, the quark model spectroscopic assignment, the PDG name, and the mass and width of each state.

Table 14.1: Experimental spectrum of reasonably well established “conventional”  $c\bar{c}$  states. This table gives the usual quark model multiplet and spectroscopic assignment for each state and the PDG label for the state, followed by their masses and widths. Partner states that are expected theoretically but not yet identified experimentally are indicated by a dash.

Mult.	Spec.	Expt. state	Mass [MeV]	Width [MeV]
1S	$1^3S_1$	$J/\psi(1S)$	$3096.916 \pm 0.011$	$0.0934 \pm 0.0021$
	$1^1S_0$	$\eta_c(1S)$	$2980.4 \pm 1.2$	$25.5 \pm 3.4$
1P	$1^3P_2$	$\chi_{c2}(1P)$	$3556.20 \pm 0.09$	$2.06 \pm 0.12$
	$1^3P_1$	$\chi_{c1}(1P)$	$3510.66 \pm 0.07$	$0.89 \pm 0.05$
	$1^3P_0$	$\chi_{c0}(1P)$	$3414.76 \pm 0.35$	$10.4 \pm 0.7$
	$1^1P_1$	$h_c(1P)$	$3525.93 \pm 0.27$	$< 1$
2S	$2^3S_1$	$\psi(2S)$	$3686.093 \pm 0.034$	$0.337 \pm 0.013$
	$2^1S_0$	$\eta_c(2S)$	$3638 \pm 4$	$14 \pm 7$
1D	$1^3D_3$	-		
	$1^3D_2$	-		
	$1^3D_1$	$\psi(3770)$	$3771.1 \pm 2.4$	$23.0 \pm 2.7$
	$1^1D_2$	-		
2P	$2^3P_2$	$\chi_{c2}(2P)$	$3929 \pm 5 \pm 2$	$29 \pm 10 \pm 2$
	$2^3P_1$	-		
	$2^3P_0$	-		
	$2^1P_1$	-		
3S	$3^3S_1$	$\psi(4040)$	$4039 \pm 1$	$80 \pm 10$
	$3^1S_0$	-		
2D	$2^3D_3$	-		
	$2^3D_2$	-		
	$2^3D_1$	$\psi(4160)$	$4153 \pm 3$	$103 \pm 8$
	$2^1D_2$	-		
4S	$4^3S_1$	$\psi(4415)$	$4421 \pm 4$	$62 \pm 20$
	$4^1S_0$	-		

This spectrum of states can be described surprisingly well using a simple  $c\bar{c}$  potential model. In these models one typically assumes a zeroth-order (spin-independent) potential that combines a OGE color Coulomb term and a linear confining interaction,

$$V_0^{(c\bar{c})}(r) = -\frac{4}{3} \frac{\alpha_s}{r} + br. \quad (14.2.1)$$

This is augmented by the spin-dependent Breit-Fermi Hamiltonian due to OGE, and an inverted spin-orbit term that arises from the (assumed) scalar nature of the confining

Table 14.2: Theoretical predictions for the spectrum of  $c\bar{c}$  states in a nonrelativistic potential model (NR) and the Godfrey-Isgur relativized potential model (GI). (This table is abstracted from Ref.[54].)

Mult.	State	Input mass (NR model)	Theor. mass	
			NR	GI
1S	$J/\psi(1^3S_1)$	3097	3090	3098
	$\eta_c(1^1S_0)$	2979	2982	2975
2S	$\psi'(2^3S_1)$	3686	3672	3676
	$\eta'_c(2^1S_0)$	3638	3630	3623
3S	$\psi(3^3S_1)$	4040	4072	4100
	$\eta_c(3^1S_0)$		4043	4064
4S	$\psi(4^3S_1)$	4415	4406	4450
	$\eta_c(4^1S_0)$		4384	4425
1P	$\chi_2(1^3P_2)$	3556	3556	3550
	$\chi_1(1^3P_1)$	3511	3505	3510
	$\chi_0(1^3P_0)$	3415	3424	3445
	$h_c(1^1P_1)$		3516	3517
2P	$\chi_2(2^3P_2)$		3972	3979
	$\chi_1(2^3P_1)$		3925	3953
	$\chi_0(2^3P_0)$		3852	3916
	$h_c(2^1P_1)$		3934	3956
3P	$\chi_2(3^3P_2)$		4317	4337
	$\chi_1(3^3P_1)$		4271	4317
	$\chi_0(3^3P_0)$		4202	4292
	$h_c(3^1P_1)$		4279	4318
1D	$\psi_3(1^3D_3)$		3806	3849
	$\psi_2(1^3D_2)$		3800	3838
	$\psi(1^3D_1)$	3770	3785	3819
	$\eta_{c2}(1^1D_2)$		3799	3837
2D	$\psi_3(2^3D_3)$		4167	4217
	$\psi_2(2^3D_2)$		4158	4208
	$\psi(2^3D_1)$	4159	4142	4194
	$\eta_{c2}(2^1D_2)$		4158	4208
1F	$\chi_4(1^3F_4)$		4021	4095
	$\chi_3(1^3F_3)$		4029	4097
	$\chi_2(1^3F_2)$		4029	4092
	$h_{c3}(1^1F_3)$		4026	4094
2F	$\chi_4(2^3F_4)$		4348	4425
	$\chi_3(2^3F_3)$		4352	4426
	$\chi_2(2^3F_2)$		4351	4422
	$h_{c3}(2^1F_3)$		4350	4424
1G	$\psi_5(1^3G_5)$		4214	4312
	$\psi_4(1^3G_4)$		4228	4320
	$\psi_3(1^3G_3)$		4237	4323
	$\eta_{c4}(1^1G_4)$		4225	4317

interaction,

$$V_{spin-dep} = \frac{32\pi\alpha_s}{9m_c^2} \vec{S}_c \cdot \vec{S}_{\bar{c}} \delta(\vec{x}) + \frac{1}{m_c^2} \left[ \left( \frac{2\alpha_s}{r^3} - \frac{b}{2r} \right) \vec{L} \cdot \vec{S} + \frac{4\alpha_s}{r^3} T \right]. \quad (14.2.2)$$

Two examples of the spectra predicted by this type of model, a fully nonrelativistic potential model “NR” and the relativized Godfrey-Isgur model [53] “GI” are shown in Fig.14.1. (Here and in much of our discussion of charmonia we will refer to the  $c\bar{c}$  potential model of Ref.[54], since potential models give predictions for many of the observed properties of charmonium resonances. Much of the original literature is also cited in this reference, and should be reviewed for a more complete discussion. We also note that several excellent and very extensive reviews of charmonia have appeared [55, 56, 57, 58, 59, 60, 61] which discuss recent developments in the field in detail.)

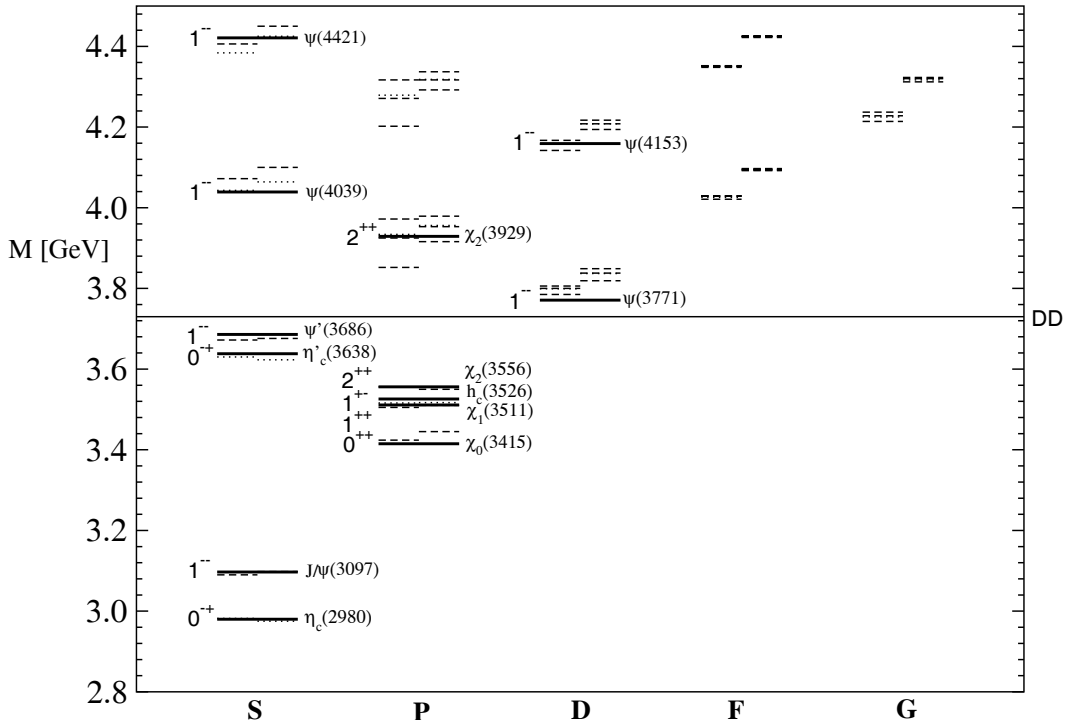


Figure 14.1: Predicted and observed spectrum of charmonium states (Table 14.2). The solid lines are experiment for reasonably well-established charmonium states, and the particle labels give the actual 2006 PDG masses in MeV rather than the usual rounded PDG mass labels. The broken lines are theory (NR model left, GI right). In the theoretical spectra, spin triplet levels are dashed and spin singlets are dotted. The DD open-charm threshold at 3.73 GeV is also shown.

The experimental and theoretical masses (in the two models of Table 14.2) are shown in Fig. 14.1. Evidently there is reasonably good agreement between the current experimental spectrum and the potential model predictions. Comparison between the nonrelativistic and relativized models shows some discrepancies, notably in the scales of 2P and 3P multiplet splittings and in the positions of the higher-L multiplets. The immediate experimental tasks suggested by this spectrum are the identification of the remaining 2P states, the 3P states and the higher-L levels. Identification of the remaining 2P states

(those with  $C=(+)$ ) can be carried out at *BES-III* using E1 radiative transitions from the higher  $1^{--}$  levels  $\psi(4040)$  and  $\psi(4160)$ ). Identification of the 3P levels will be more complicated because hybrid charmonia are expected at similar masses; we shall see that this may be possible using  $\psi(4415)$  radiative transitions. Finally, the important problem of the identification of the higher-L states is a difficult problem. It may be possible to identify one such state, the  $^3F_2 c\bar{c}$ , in radiative transitions from the  $\psi(4160)$ . Experimentally accessing the other higher-L  $c\bar{c}$  states is an unsolved problem.

It is also possible to predict the spectrum of charmonia, especially the lowest-lying states in each sector of state space, using lattice gauge theory (LGT); for some recent references see Refs.[62, 63, 64, 65]. This approach is very attractive in that it does not require the assumptions of potential models, and can in addition be applied to the study of novel states such as the  $J^{PC}$ -exotic charmonium hybrids, where potential models are of unknown accuracy. To date the results of LGT for the charmonium spectrum are very similar to the predictions of potential models for the lighter states, which are experimentally well established. Current LGT predictions for the more controversial higher-mass states unfortunately have rather large errors (100 MeV is typical at present), so they cannot yet usefully be compared to experimental candidates or potential model calculations. Future LGT calculations of the charmonium spectrum should be very interesting in this regard. One very interesting question that LGT can hopefully address will be the importance of quenching (the effect of closed  $q\bar{q}$  loops on the spectrum and couplings of charmonia). The closely related question of the importance of closed virtual continuum channels on the properties of heavy quarkonia and hadrons more generally is a very important and controversial issue.

### 14.2.1 Particle widths

Charmonium states that are below their open-charm decay threshold (all states below  $2m_D = 3.73$  GeV, and in addition the lightest  $2^{-+}$  and  $2^{--}$  1D states) must decay through annihilation of the  $c\bar{c}$  pair. The total widths in these decays have traditionally been described as annihilation into gluons, using the corresponding formulas for positronium annihilation into photons but with  $\alpha_s$  vertices and combinatoric color factors.

These calculations are dubious for several reasons. First, the assumption of free gluons final states and pQCD dynamics is presumably a bad approximation, since the actual glueball spectrum has widely spaced discrete levels and a mass gap that is about half as large as charmonium itself. Second, when higher-order pQCD radiative corrections are incorporated, it is often found that they are so large as to make the numerical predictions clearly unreliable. Finally, the use of positronium formulas is a nonrelativistic approximation, which is not well justified for the charmonium system.

Despite these many caveats these pQCD predictions for charmonium annihilation total widths remain interesting as rough guidelines, and some of the qualitative predictions do seem to be satisfied. For example, since  $\alpha_s$  is not large at the  $c\bar{c}$  mass scale one expects that the annihilation decay widths of negative C-parity charmonia (which must decay into at least three gluons) should be rather smaller than the decay widths of similar positive C-parity charmonia (which can decay into two gluons). Inspection of the total widths of well established  $c\bar{c}$  states below 3.73 GeV in Table 14.1 shows that this guideline is indeed well satisfied.

Similar positronium annihilation rate formulas for other states can be adapted to give strong (gluonic and  $q\bar{q}g$ ) total annihilation width estimates for other heavy quarkonia. These lead to the expectation that the two as yet unknown D-wave  $c\bar{c}$  states  $h_{c2}$  ( $2^{++} {}^1D_2$ ) and  $\psi_2$  ( $2^{--} {}^3D_2$ ) should be quite narrow, with strong annihilation widths of perhaps  $\sim 1$  MeV [69]. These predictions of very narrow widths make the discovery of the  $h_{c2}$  and  $\psi_2$  two of the most important outstanding experimental goals of charmonium spectroscopy. We note in passing that their 1D partner state  $\psi_3$  ( $3^{--} {}^3D_3$ ) should have a comparably small total width; it can decay to  $DD$ , but the  $L=3$  angular momentum barrier should make this a narrow state as well.

Discovery of these narrow states may be feasible at *BES-III*. Production of the three narrow 1D  $c\bar{c}$  states may be possible using E1 radiative transitions from the appropriate 2P  $c\bar{c}$  states; once formed, these narrow 1D states may then be detected through their large E1 branching fractions to the 1P  $c\bar{c}$  multiplet. (Ref.[54] gives E1 radiative partial width estimates for all these transitions.)

## 14.3 Issues for *BES-III*<sup>2</sup>

*BES-III* is well suited to address the remaining experimental questions that are related to the low-mass (*i.e.* below open-charm threshold) charmonium spectrum. These include precise determinations of the masses and widths of the  $\eta_c$  and  $\eta'_c$ , and the relation of the  $h_c$  mass relative to the center-of-gravity mass of the  $\chi_{cJ}$  states. In addition, we advocate a precision measurement of the partial width  $\Gamma(J/\psi \rightarrow \gamma\eta_c)$ .

### 14.3.1 Measurements related to the $\eta_c$

Although the  $\eta_c$  is the ground state  $c\bar{c}$  meson and, in some sense, the most fundamental of the charmonium mesons, its properties are very poorly understood, both theoretically and experimentally.

#### Mass of the $\eta_c$

In spite of the fact that the PDG lists more than 20 measurements of the  $\eta_c$  mass [52], the world average value,  $2979.8 \pm 1.2$  MeV has a precision that is poorer, by an order-of-magnitude or more than the listed mass values for the  $J/\psi$ ,  $\psi'$ ,  $h_c$ ,  $\chi_{c1}$  or  $\chi_{c2}$ . The agreement between different measurements is poor; the PDG group's fit to the measured values has a confidence level of 0.6% (see Fig. 14.2). Moreover, the mass value itself is somewhat mysterious. From Eqn. 14.2.2, the potential model expectation for the  $J/\psi$ - $\eta_c$  mass splitting is

$$M(J/\psi) - M(\eta_c) = \frac{32\pi\alpha_s(m_c)}{9m_c^2} |\Psi(0)|^2, \quad (14.3.3)$$

where  $|\Psi(0)|$ , the wave function at the origin, can be determined from the  $J/\psi \rightarrow e^+e^-$  partial width via

$$\Gamma(J/\psi \rightarrow e^+e^-) = \frac{16\pi\alpha^2 q_c^2 |\Psi(0)|^2}{M_{J/\psi}^2} \left(1 - \frac{16\alpha_s}{3\pi} + \dots\right). \quad (14.3.4)$$

---

<sup>2</sup>By S.L. Olsen

Using the world average value  $\Gamma(J/\psi \rightarrow e^+e^-) = 5.55 \pm 0.14$  keV,  $\alpha_s(M_{J/\psi}^2) \simeq 0.33$ , and  $m_c \simeq M_{J/\psi}/2$ , we find a prediction for the mass splitting of  $M(J/\psi) - M(\eta_c) \sim 60$  MeV, which is about half the measured value of  $116.5 \pm 1.2$  MeV. This discrepancy is also seen in lattice QCD calculations [70].

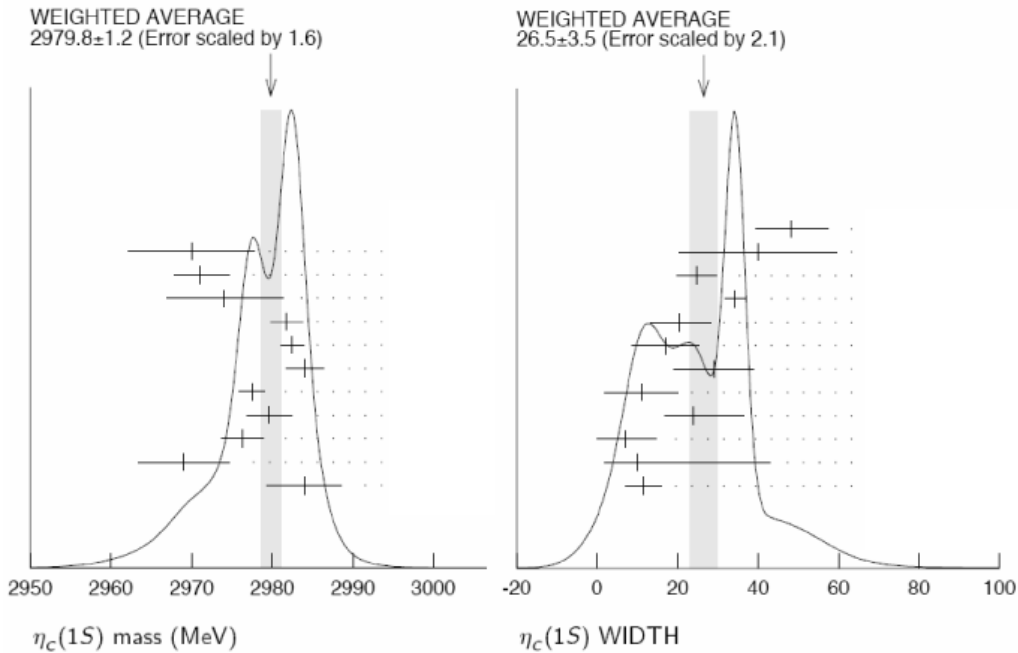


Figure 14.2: The distribution of measurements of the  $\eta_c$  mass (left) and width (right) from PDG-2006.

### Width of the $\eta_c$

The experimental situation on the  $\eta_c$  total width is even more confused. The right panel of Fig. 14.2 shows the range of  $\eta_c$  total width measurements listed in the PDG tables. The PDG fit for a world average value of  $\Gamma = 26.5 \pm 3.5$  MeV has a confidence level of only 0.1%, and, so, the errors on the measurements going into the averaging process are scaled by a factor of 2.1. Here there is a notable discrepancy between measurements using  $\eta_c$  mesons produced from the radiative decay  $J/\psi \rightarrow \gamma\eta_c$ , which tend to give low values, and those where the  $\eta_c$  is produced directly by two-photons, *i.e.*  $\gamma\gamma \rightarrow \eta_c$ , or in  $B$  mesons decays via  $B \rightarrow K\eta_c$ , which give higher values.

### The $\Gamma(\psi \rightarrow \gamma\eta_c)$ partial width

In the potential model, radiative decays of the  $J/\psi$  and  $\psi'$  to the  $\eta_c$  states, *i.e.*,  $\psi(nS) \rightarrow \gamma\eta_c(n'S)$ , proceed primarily via magnetic dipole (M1) transitions, with an amplitude given by

$$\Gamma(\psi(nS) \rightarrow \gamma\eta_c(n'S)) = \frac{4}{3}\alpha q_c^2 \frac{k_\gamma^3}{m_c^2} \left| \int dr r^2 R_{n'0}(r) R_{n0}(r) j_0\left(\frac{k_\gamma r}{2}\right) \right|^2. \quad (14.3.5)$$

Here  $q_c$  and  $m_c$  are the charge and mass of the  $c$ -quark and  $k_\gamma$  is the transition photon energy. For  $J/\psi \rightarrow \gamma\eta_c$ ,  $n = n' = 1$  and, in the limit of zero recoil momentum, *i.e.*  $k_\gamma r \simeq 0$ , the overlap integral is unity and the  $\eta_c$  line shape is modulated by a factor of  $k_\gamma^3$ .

Taking  $m_c = M_{J/\psi}/2$  and using the PDG world average values for the  $\eta_c$  mass and  $J/\psi$  mass and total width, we determine the predicted partial width value from Eqn. 14.3.5 to be

$$\Gamma(J/\psi \rightarrow \gamma\eta_c) = 2.90 \text{ keV} \quad \text{Prediction,} \quad (14.3.6)$$

which would correspond to the branching fraction  $\mathcal{B}(\Gamma(J/\psi \rightarrow \gamma\eta_c)) = 3.1\%$ . The PDG value for this branching fraction is based solely on a single measurement from the Crystal Ball group [71] and is  $\mathcal{B}(\Gamma(J/\psi \rightarrow \gamma\eta_c)) = 1.3 \pm 0.4\%$ . The corresponding partial width is

$$\Gamma(J/\psi \rightarrow \gamma\eta_c) = 1.2 \pm 0.4 \text{ keV} \quad \text{Crystal Ball measurement,} \quad (14.3.7)$$

which is far below the predicted value.

This very dramatic discrepancy between potential model predictions and the measured value of the  $J/\psi \rightarrow \gamma\eta_c$  partial width makes it urgent that *BES-III* remeasure this quantity reliably and with high precision. In addition to its obvious theoretical significance, such a measurement has important engineering consequences. The extraction of all  $\eta_c$  branching fraction determinations that use  $\eta_c$  mesons produced by the  $J/\psi \rightarrow \gamma\eta_c$  process (as is the case for most of the  $\eta_c$  branching fraction measurements listed in the PDG) rely on this measurement.

## Experimental considerations

With a sample of  $\sim 10^9$   $J/\psi$  events accumulated at the resonance peak, we can expect many thousands of detected  $\gamma\eta_c$  events for each of the dominant  $\eta_c$  decay modes. This will provide the opportunity to measure the mass and width in each mode with a statistical precision that is about and order-of-magnitude better than the current world averages. Since the effects of interference between the  $\eta_c$  amplitude and that for possible coherent continuum production of the same final state will be an important source of systematic error, the measurements should be done using as many different  $\eta_c$  decay modes as possible.

Additional data accumulated at the peak of the  $\psi'$  would be very useful. The transition gamma-ray energies for the  $E1$  decays  $\psi' \rightarrow \gamma\chi_{c2}$  and  $\psi' \rightarrow \gamma\chi_{c1}$ , namely  $127.60 \pm 0.09$  MeV and  $166.07 \pm 0.08$  MeV, respectively, are very similar to that of the gamma in  $J/\psi \rightarrow \gamma\eta_c$  and, thanks to precision measurements from Fermilab experiment E835 [72], these energy values are very well known. Moreover, the  $\chi_{c1,2}$  and the  $\eta_c$  have many decay final states in common and with similar branching fractions. Therefore, since the  $\chi_{c1,2}$  states are narrow and the branching fractions for  $\psi' \rightarrow \gamma\chi_{c1,2}$  are larger than that for  $J/\psi \rightarrow \gamma\eta_c$ , a sample of  $\sim 10^8$  events taken at the  $\psi'$  peak will allow for measurements of these two calibration channels that would have precision levels comparable to those of the  $\eta_c$  measurements with the same final state, made with  $\sim 10^9$   $J/\psi$  events. Such complementary measurements would be useful for controlling the experimental systematic effects to levels that are smaller than the statistical errors.

For the  $\psi' \rightarrow \gamma\eta_c$  transition,  $n = 2$  and  $n' = 1$ , the radial wave functions in Eqn. 14.3.5 are different and the  $\eta_c$  recoil momentum is not small. In this case, the the line shape is

modulated by an *additional*, model-dependent factor that the CLEO group estimated to be  $\sim k_\gamma^4$  [73]. Therefore, although  $\psi'$  data will provide checks and calibrations for measurements done with  $J/\psi$  data, this strong, model-dependent modulation of the line shape probably precludes using the  $\psi' \rightarrow \gamma\eta_c$  data itself to make precise model-independent measurements of the mass and width of the  $\eta_c$ .

The  $\mathcal{B}(J/\psi \rightarrow \gamma\eta_c)$  measurement has to be done inclusively, *i.e.*, the  $\eta_c$  signal has to be measured from the  $E_\gamma \simeq 114$  MeV peak in the inclusive photon spectrum, independently (as much as possible) of any specific  $\eta_c$  decay mode. Since the Crystal Ball group was able to identify and measure such a peak, this should be doable in *BES-III*, where the electromagnetic calorimeter has better granularity and a factor-of-two better gamma-ray energy resolution. A difficulty here is that the low energy of the transition gamma makes it not useful as an event trigger. For  $J/\psi$  running, trigger conditions have to be established that insure all significant  $\eta_c$  decay modes satisfy them with high efficiency.

Trigger biases can be avoided by using tagged  $J/\psi$  events from the  $\pi^+\pi^- J/\psi$  decays of the  $\psi'$  that are triggered only by the tracks of the transition  $\pi^+\pi^-$  pair. With a  $\sim 10^8$  event sample taken at the peak of the  $\psi'$  resonance, we can expect about  $\sim 10^7$  tagged  $J/\psi$  decays, including nearly  $10^5$  with monochromatic gammas from the  $J/\psi \rightarrow \gamma\eta_c$  transition detected in the electromagnetic calorimeter.

### 14.3.2 Mass and width of the $\eta'_c$

Among the below-threshold charmonium states, the  $\eta'_c$  meson has the most poorly measured mass and width. The PDG average for the mass,  $3637 \pm 4$  MeV, has a fit confidence level of 2.1%. The average width value, based on two measurements, is  $14 \pm 7$  MeV.

At *BES-III*,  $\eta'_c$  mesons will be produced during  $\psi'$  running via the radiative M1 decay  $\psi' \rightarrow \gamma\eta'_c$ . According to the relation given in Eqn. 14.3.5, the partial width  $\Gamma(\psi' \rightarrow \gamma\eta'_c)$  can be estimated by scaling the measured the measured partial width for  $J/\psi \rightarrow \gamma\eta_c$  ( $1.19 \pm 0.34$  keV by  $k'_\gamma/k_\gamma^3$ , where  $k'_\gamma = 48 \pm 4$  MeV ( $k_\gamma = 114.3 \pm 1.2$  MeV) is gamma energy for the  $\psi'\gamma\eta'_c$  ( $J/\psi\gamma\eta_c$ ) transition. This gives an expected partial width  $\Gamma(\psi' \rightarrow \gamma\eta'_c) = 87 \pm 25$  eV, and branching fraction  $\mathcal{B}(\psi' \rightarrow \gamma\eta'_c) = (2.6 \pm 0.7) \times 10^{-4}$ . Thus, the expected  $\eta'$  mesons production rate in *BES-III* will be low and, because of the low energy of the transition gamma ray, detection will be difficult. Precise  $\eta'_c$  mass and width measurements will be a challenge for *BES-III*.

### 14.3.3 The $h_c$ mass

The  $h_c$  meson was observed by CLEO in both inclusive and exclusive processes. In the inclusive process  $\psi' \rightarrow \pi^0 h_c$  the  $h_c$  decay products are not detected and the signal is a distinct peak in the  $\pi^0$  recoil mass distribution. Figure 14.3 shows the very clean signal seen by CLEO for the exclusive process  $\psi' \rightarrow \pi^0 h_c$  with  $h_c \rightarrow \gamma\eta_c$  [74]. Evidence for the  $h_c$  was also reported by Fermilab experiment E835 in the process  $\bar{p}p \rightarrow h_c \rightarrow \gamma\eta_c \rightarrow \gamma\gamma\gamma$  [75]. CLEO measures  $M(h_c) = 3525.35 \pm 0.27 \pm 0.2$  MeV; E835 reports  $3525.8 \pm 0.2 \pm 0.2$  MeV.

Naively, if the radial dependence of the  $\vec{S}_c \cdot \vec{S}_{\bar{c}}$  term in Eq. 14.2.2 is truly a  $\delta$ -function, one would expect the mass of the  $h_c$  to be equal to the center-of-gravity mass of the  $\chi_{cJ}$

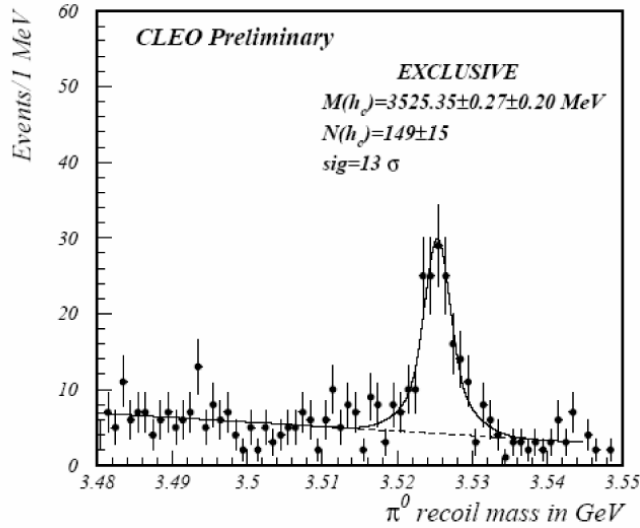


Figure 14.3: The exclusive signal for  $\psi' \rightarrow \pi^0 h_c$ ;  $h_c \rightarrow \gamma \eta_c$  from CLEO.

states:

$$M_{c.o.g.}(\chi_c) = \frac{1}{9}(M(\chi_{c0}) + 3M(\chi_{c1}) + 5M(\chi_{c2})) = 3525.30 \pm 0.08 \text{ MeV}, \quad (14.3.8)$$

where PDG masses for the  $\chi_{cJ}$  states are used. A more detailed calculation [76], discussed below in Sect. 15.1.4, predicts the mass to be a few MeV below  $M_{c.o.g.}(\chi_c)$ . The  $M(h_c)$  measurements seem to prefer the naive expectations. However, the current precision leaves room for at least a factor of two improvement from *BES-III*. The cleanliness of the CLEOc  $h_c$  signal in the exclusive decay channel (see Fig. 14.3) indicates that improved statistics afforded by the large  $\psi'$  sample expected for *BES-III* will result in a commensurate improvement in the precision of the  $h_c$  mass measurement.

## 14.4 Novel states incorporating a $c\bar{c}$ subsystem<sup>3</sup>

### 14.4.1 Charm Molecules

Molecules are weakly bound states of more than one hadron, of which by far the best known examples are nuclei and hypernuclei. There are also speculations that certain unusual hadrons may also be similar weakly bound states of mesons, such as the  $f_0(980)$  and  $a_0(980)$  “KKbar-molecule” candidates. One of the earliest suggestions for a mesonic molecule in the charm sector pertains to the  $\psi(4040)$ ; it was suggested by Voloshin *et al.* [77] that this state might be a  $D^*D^*$  molecule, because the mass is close to the mass of two  $D^*$  mesons, and this state couples very strongly to  $D^*D^*$  final states. (See also Refs.[78, 79].) It has since been realized that this  $D^*D^*$  dominance is also expected for a conventional  $3^3S_1$   $c\bar{c}$  charmonium state [541, 54].

The obvious characteristics of molecules are that they should have masses just below the sum of the masses of their constituent hadrons (to within a nuclear physics scale

<sup>3</sup>By T. Barnes

binding energy of perhaps *ca.* 10 MeV, and that they should decay strongly to their constituents (if allowed by width effects) or to final states that those constituents would naturally couple strongly to. Their most plausible quantum numbers are those of an S-wave constituent pair, since the residual binding forces between color-singlet hadrons are relatively weak and short relative to forces between quarks and gluons. (This argues against the  $\psi(4040)$  being a  $D^*D^*$  molecule, since the binding forces would be competing against a P-wave angular momentum barrier.)

Rather remarkably, a very strong candidate for a charmed meson molecule was identified in recent years in B-meson decays, the  $X(3872)$ . This state was originally identified by Belle [80] in the final state  $J/\psi\pi^+\pi^-$ , where the mass distribution of the  $\pi^+\pi^-$  system is consistent with, and believed to be dominantly due to, a  $\rho^0$ .

The mass and width (still only known as an upper limit) for this state are

$$M(X(3872)) = 3871.2 \pm 0.5 \text{ MeV}, \quad (14.4.9)$$

$$\Gamma(X(3872)) < 2.3 \text{ MeV, 90\% c.l.} \quad (14.4.10)$$

There is now clear evidence from the decay angular distribution that the  $J^{PC}$  quantum numbers are  $1^{++}$  [81]. Comparison with the spectrum of expected  $c\bar{c}$  states in Fig.14.1 shows that no  $1^{++} c\bar{c}$  state is expected near this mass, although one could clearly consider a low-mass  $2^3P_1 \chi'_1$  state as a possibility. This and other  $c\bar{c}$  possibilities were initially considered, and the combined mass and narrow width of the  $X(3872)$  were found to be inconsistent with any  $c\bar{c}$  assignment [69].

The proximity of the  $X(3872)$  to the mass of a (neutral)  $D^0D^{*0}$  pair (at an almost identical  $3871.2 \pm 0.6$  MeV) immediately suggested that this state might be a weakly bound  $D^0D^{*0}$  molecule (see for example Refs.[82, 83, 84]). (A binding energy of *ca.* 1 MeV is allowed by the current experimental mass errors.) Note that this  $DD^*$  molecule would have a much smaller charged  $D^+D^{*-}$ ,  $D^-D^{*+}$  component, since this basis state has a mass of  $3879.3 \pm 0.6$  MeV, and hence is at a much higher mass on the scale of a bound state with only 1 MeV binding.

Although the residual “nuclear” forces that can lead to the formation of hadronic molecules are usually not well understood, in this case there is less ambiguity; the longest-ranged force, which should be the most important for a weakly bound system, is one pion exchange. Since the strength of the required  $D^*D\pi$  coupling can be inferred from the partial width for  $D^* \rightarrow D\pi$ , it is straightforward to calculate the effective  $DD^*$  interaction due to one pion exchange. (There is however some ambiguity in the treatment of the short-range truncation of this force.) Studies of one pion exchange forces in the  $DD^*$  system by Tornqvist [82] and Swanson [84] showed that the  $1^{++}$  state experienced the strongest binding forces from one pion exchange, and that they were numerically just strong enough to (perhaps) form a  $DD^*$  bound state.

One especially striking prediction of the (neutral D)  $D^0D^{*0}$  molecule model is that one should observe comparable strength  $J/\psi\omega$  and  $J/\psi\rho^0$  decay modes [84] (see also Ref.[85]), due to the maximal isospin breaking present in the initial state. This prediction appears to have been confirmed by the evidence from Belle for the  $\omega$  in the  $3\pi$  mode  $X(3872) \rightarrow J/\psi\pi^+\pi^-\pi^0$  [86]. The  $3\pi$  invariant mass peaks at the highest mass, as expected for a virtual  $\omega$ , and the ratio of  $2\pi$  to  $3\pi$  branching fractions is close to unity,

$$\frac{\Gamma(X(3872) \rightarrow J/\psi\pi^+\pi^-\pi^0)}{\Gamma(X(3872) \rightarrow J/\psi\pi^+\pi^-)} = 1.0 \pm 0.4 \pm 0.3, \quad (14.4.11)$$

as predicted by Swanson in the DD\* model.

There is also evidence from Belle for the radiative transition  $X(3872) \rightarrow \gamma J/\psi$  [86], with the width ratio

$$\frac{\Gamma(X(3872) \rightarrow \gamma J/\psi)}{\Gamma(X(3872) \rightarrow J/\psi\pi^+\pi^-)} = 0.14 \pm 0.05, \quad (14.4.12)$$

which should be useful in testing the details of different models of the X(3872).

There are several interesting studies of charm molecules that might be possible at BES. Detection of this  $1^{++}$  state at all at an  $e^+e^-$  facility is nontrivial, but may be feasible through E1 decays of the  $\psi(4040)$  and  $\psi(4160)$ . (Both will couple to the X(3872) through its  $c\bar{c}$  component.) If the X(3872) can be studied, a measurement of the total width of the X(3872) would be very interesting, since the current upper limit is not far above the estimate Swanson gives in the DD\* molecule model [84, 59]. Measurements of the branching fractions of the X(3872) into the various final states predicted by the molecule model would then be very interesting, especially the ratios of different isospin modes such as  $J/\psi\omega$  versus  $J/\psi\rho^0$ .

Given that the X(3872) does appear likely as a DD\* molecule, it is of interest to search for other molecules that are predicted assuming similar interactions between charmed mesons. Swanson [59] notes that one attractive possibility is a  $0^{++}$   $D^*D^*$  molecule, which could be produced in  $\psi(4160)$  E1 decays and observed in the  $J/\psi\omega$  final state.

#### 14.4.2 Charmonium Hybrids

The discovery of charmonium hybrids may be the most exciting goal of the current and near future studies of the charmonium system. These states should be accessible at BES.

Hybrids are hadrons in which the gluonic degree of freedom has been excited. The nature of this gluonic excitation is not well understood at present, and has been described by various models, including valence gluon models such as the bag model and nonperturbative systems such as the flux tube model. To date most theoretical studies have considered hybrid mesons ( $q\bar{q}$  with a gluonic excitation) and hybrid baryons ( $qqq$  with a gluonic excitation). Although the models differ in detail regarding their predictions for the spectrum of hybrids, there is general agreement that hybrid mesons have the very attractive feature of including states with  $J^{PC}$ -exotic quantum numbers. These are the quantum numbers  $J^{PC} = 0^{--}$  and the series  $0^{+-}, 1^{+-}, 2^{+-}, 3^{+-}, \dots$ , which are forbidden to conventional  $q\bar{q}$  systems, but can all be formed from hybrid basis states. The search for resonances with exotic quantum numbers is therefore a principal goal of searches for hybrid mesons. Hybrid basis states also span all the conventional  $q\bar{q}$   $J^{PC}$  quantum numbers, and should give rise to a rich overpopulation of the experimental spectrum relative to the expectations of the naive  $q\bar{q}$  quark model.

In view of the current uncertainty regarding the nature of hybrids in models, the predictions of LGT studies are correspondingly very important. The most recent studies of charmonium hybrids suggest a mass scale for the lightest exotic charmonium hybrid, which probably has  $J^{PC} = 1^{-+}$ , of approximately 4.4 GeV (see for example Refs.[87, 88, 89, 90, 91, 92]). In the flux tube model, which in comparison anticipates the lightest charmonium hybrid multiplet near 4.2 GeV [93], this lightest hybrid multiplet is predicted

to contain three exotic and five nonexotic hybrid states, including both a  $1^{-+}$  exotic and a  $1^{--}$  nonexotic.

The prediction of hybrids in this approximate mass region, including a nonexotic  $1^{--}$  state, is especially interesting in view of the recent discovery of the Y(4260). This remarkable new state was reported by BaBar in initial state radiation (ISR) in the reaction  $e^+e^- \rightarrow \gamma_{ISR} J/\psi \pi^+ \pi^-$  [94], and has been confirmed by CLEO-c [95] and Belle [96] in the same process. There may also be evidence for an enhancement in  $J/\psi \pi^+ \pi^-$  near 4.26 GeV in the decay  $B \rightarrow K J/\psi \pi^+ \pi^-$  (in both neutral and negative B/K charge states) [97]. The mass and width reported for the Y(4260) by BaBar [94] are

$$M = 4259 \pm 8 \begin{array}{l} +2 \\ -6 \end{array} \text{ MeV}, \quad (14.4.13)$$

$$\Gamma = 88 \pm 23 \begin{array}{l} +6 \\ -4 \end{array} \text{ MeV}, \quad (14.4.14)$$

with consistent results from CLEO-c, but a somewhat higher mass and larger width from Belle.

The ISR production mechanism tells us that this state must be  $1^{--}$ , but it cannot be a conventional  $c\bar{c}$  state because the  $1^{--}$  states in this mass region are well established from earlier  $e^+e^-$  annihilation experiments. (The Y(4260) is bracketed by the  $2^3D_1 \psi(4160)$  and the  $4^3S_1 \psi(4415)$ , which have masses that are in excellent agreement with the expectations of  $c\bar{c}$  potential models.)

The Y(4260) (if a real resonance) evidently represents “overpopulation” of the expected quark potential model spectrum of  $1^{--} c\bar{c}$  states. In addition, as most models of hybrids have a vanishing  $c\bar{c}$  wavefunction at contact, it has long been speculated that they would have small  $e^+e^-$  widths, and thus make rather weak contributions to  $R$ . This overpopulation of the spectrum and the fact that there is no enhancement visible in  $R$  near this mass has led to suggestions that this state may be a charmonium hybrid [98].

Another indication that the Y(4260) may be a charmonium hybrid follows from a LGT study by the UKQCD group [99] of the strong decay couplings of exotic  $b\bar{b}$  hybrids. This LGT study found strikingly large couplings of  $b\bar{b}$  hybrids to closed flavor modes (specifically to  $\chi_b S$ , where  $S$  is a light scalar isoscalar meson that would decay to  $\pi\pi$ ). This is sufficiently similar to the BaBar observation of the Y(4260) in the single closed-charm mode  $J/\psi \pi^+ \pi^-$  to be cited as additional possible evidence for a hybrid interpretation.

The unusual  $J/\psi \pi^+ \pi^-$  mode and the UKQCD study suggest searches of any other accessible closed-charm modes with  $1^{--}$  quantum numbers, such as  $J/\psi \eta$ ,  $J/\psi \eta'$ ,  $\chi_J \omega$  and so forth. Ideally the light system should have quantum numbers thought to couple strongly to pure glue, such as  $0^{++}$  and  $0^{-+}$ .

In specific decay models, notably the flux-tube decay model [547], theorists have long anticipated that the dominant open-flavor decay modes of hybrids would be a meson pair with one internal S-wave (for charmonium hybrids,  $D$ ,  $D^*$ ,  $D_s$ ,  $D_s^*$ ) and one internal P-wave (such as  $D_J$  and  $D_{sJ}$ ). In the case of the Y(4260) this suggests dominance of the decay mode  $DD_1(2430)$ . This broad  $D_1$  has a width of *ca.* 400 MeV, and decays to  $D^* \pi$ , so this suggests a search for evidence of the Y(4260) in  $DD^* \pi$ . Since this is a prediction of a decay model in an untested regime (hybrids), one should be cautious and search the more familiar two-body modes  $DD$ ,  $DD^*$ ,  $D^*D^*$ ,  $D_s D_s$ ,  $D_s D_s^*$  and  $D_s^* D_s^*$  for evidence of the Y(4260) as well. If there is evidence of a large  $DD_1(2430)$  signal, the Y(4260) would then

be quite convincing as a hybrid having properties predicted by the flux tube model. If it appears in some of these open charm modes such as  $DD^*$  and  $D_sD_s^*$  at rates comparable to or larger than  $J/\psi\pi^+\pi^-$ , one might claim a hybrid but speculate that the flux tube decay model was inaccurate in predicting hybrid decay modes. Finally, if the  $Y(4260)$  does not appear in any other mode, one might be skeptical about whether the  $J/\psi\pi^+\pi^-$  signal is due to a resonance at all; there are nonresonant possibilities, such as production of  $DD_1$  in  $e^+e^- \rightarrow DD_1$  followed by an inelastic FSI that produces a broad  $J/\psi\pi^+\pi^-$  enhancement due to the (very broadened) onset of  $DD_1(2430)$  threshold events (which would appear near 4.3 GeV).

In any case since it is clear from the reported mass that the  $Y(4260)$  is not a conventional  $c\bar{c}$  state, it will be very important to establish the properties of this signal through the accumulation of better statistics. This applies even more strongly to the more recently reported states discussed in the following section.

## 14.5 The $XYZ$ mesons, recent experimental developments<sup>4</sup>

In this section we briefly discuss some of the other so-called  $XYZ$  mesons, concentrating mainly on recent experimental developments.

### 14.5.1 The $X(3940)$ (and $X(4160)$ )

Belle observed the  $X(3940)$  recoiling from the  $J/\psi$  in double-charmonium production in the reaction  $e^+e^- \rightarrow J/\psi + X$  at  $E_{cm} \simeq 10.58$  GeV [100]. In addition to the  $X(3940)$ , Belle observed the well known  $J = 0$  charmonium states  $\eta_c$ ,  $\chi_{c0}$ , and  $\eta_c(2S)$  with properties consistent with PDG values.

While a distinct signal for  $X(3940) \rightarrow D\bar{D}^*$  is also seen, there is no evidence for the  $X(3940)$  in either the  $D\bar{D}$  or  $\omega J/\psi$  decay channels. If the  $X(3940)$  has  $J = 0$ , as seems to be the case for mesons produced via this production mechanism, the absence of a substantial  $D\bar{D}$  decay mode strongly favors  $J^P = 0^-$ , for which the most likely charmonium assignment is the  $\eta_c''$ , the  $3^1S_1$  charmonium state. The fact that the lower mass  $\eta_c(1S)$  and  $\eta_c(2S)$  are also produced in double charm production seems to support this assignment. The predicted width for a  $3^1S_0$  state with a mass of 3943 MeV is  $\sim 50$  MeV [101], which is in acceptable agreement with the measured  $X(3940)$  width.

However, there are problems with this assignment, the first being that the measured mass of the  $X(3940)$ , recently updated by Belle to be  $3942 \pm 8$  MeV/ $c^2$  [102], is below potential model estimates of  $\sim 4050$  MeV/ $c^2$  or higher [54]. A further complication is the recent observation by Belle of a mass peak in the  $D^*\bar{D}^*$  system  $m = 4156 \pm 29$  MeV/ $c^2$  and total width of  $\Gamma = 139_{-65}^{+113}$  MeV/ $c^2$ , recoiling from a  $J/\psi$  in the process  $e^+e^- \rightarrow J/\psi D^*\bar{D}^*$  [102]. Using similar arguments, this latter state, called the  $X(4160)$  could also be attributed to the  $3^1S_0$  state. But the  $X(4160)$  mass is well above expectations for the  $3^1S_0$  and well below those for the  $4^1S_0$ , which is predicted to be near 4400 MeV/ $c^2$  [54].

---

<sup>4</sup>By S.L. Olsen

Although the  $X(3940)$  or the  $X(4160)$  might conceivably fit a charmonium assignment, it seems very unlikely that both of them could be accommodated as  $c\bar{c}$  states.

### 14.5.2 The $Y(3940)$

Belle observed the  $Y(3940)$  via its  $Y(3940) \rightarrow \omega J/\psi$  decay in  $B \rightarrow K\omega J/\psi$  decays [103]. This observation has recently been confirmed by BaBar [104]. Belle reports a mass and width of  $M = 3943 \pm 17 \text{ MeV}/c^2$  and  $\Gamma = 87 \pm 34 \text{ MeV}/c^2$  while BaBar reports the preliminary values of  $M = 3914.3^{+3.8}_{-3.4} \pm 1.6 \text{ MeV}$  and  $\Gamma = 33^{+12}_{-8} \pm 0.6 \text{ MeV}$  which are somewhat different from Belle's.

The measured product branching fractions agree:  $\mathcal{B}(B \rightarrow KY(3940))\mathcal{B}(X(3940) \rightarrow \omega J/\psi) = (7.1 \pm 3.4) \times 10^{-5}$  (Belle), and  $\mathcal{B}(B \rightarrow KY(3940))\mathcal{B}(X(3940) \rightarrow \omega J/\psi) = (4.9 \pm 1.1) \times 10^{-5}$  (BaBar). These values together with an assumption that the branching fraction  $\mathcal{B}(B \rightarrow KY(3940))$  is less than or equal to  $1 \times 10^{-3}$ , the value that is typical for allowed  $B \rightarrow K + \text{charmonium}$  decays, implies a partial width  $\Gamma(Y(3940) \rightarrow \omega J/\psi) > 1 \text{ MeV}/c^2$ , which is at least an order-of-magnitude higher than those for hadronic transitions between any of the established charmonium states. The Belle group's 90% confidence level limit on  $\mathcal{B}(X(3940) \rightarrow \omega J/\psi) < 26\%$  [100] is not stringent enough to rule out the possibility that the  $X(3940)$  and the  $Y(3940)$  are the same state.

### 14.5.3 The $Z(3930)$

The  $Z(3930)$  is a peak reported by Belle in the spectrum of  $D\bar{D}$  mesons produced in  $\gamma\gamma$  collisions, with mass and width  $M = 3929 \pm 6 \text{ MeV}/c^2$  and  $\Gamma = 29 \pm 10 \text{ MeV}/c^2$  [106]. The  $D\bar{D}$  decay mode makes it impossible for the  $Z(3930)$  to be the  $\eta_c(3S)$  state. The two-photon production process can only produce  $D\bar{D}$  in a  $0^{++}$  or  $2^{++}$  state and for these, the  $dN/d\cos\theta^*$  distribution, where  $\theta^*$  is the angle between the  $D$  meson and the incoming photon in the  $\gamma\gamma$  cm, are quite distinct: flat for  $0^{++}$  and  $\propto \sin^4\theta^*$  for  $2^{++}$ . The Belle measurement strongly favors the  $2^{++}$  hypothesis (see Fig. 14.4), making the  $Z(3930)$  a prime candidate for the  $\chi'_{c2}$ , the  $2^3P_2$  charmonium state. The predicted mass of the  $\chi_{c2}(2P)$  is  $3972 \text{ MeV}/c^2$  and the predicted total width assuming the observed mass value is  $\Gamma_{\text{total}}(\chi_{c2}(2P)) = 28.6 \text{ MeV}/c^2$  [107, 54, 101], in good agreement with the experimental measurement. Furthermore, the two-photon production rate for the  $Z(3930)$  is also consistent with expectations for the  $\chi'_{c2}$  [105].

### 14.5.4 $\pi^+\pi^-\psi'$ resonances at $4360 \text{ MeV}/c^2$ and $4660 \text{ MeV}/c^2$

In addition to the  $Y(4260)$ , which is discussed at length in Sect. 14.4.2 above, BaBar also found a broad peak in the cross section for  $e^+e^- \rightarrow \pi^+\pi^-\psi'$  that is distinct from the  $Y(4260)$ ; its peak position and width are not consistent with those of the  $Y(4260)$  [108]. The BaBar observation was subsequently confirmed by a Belle group study that used a larger data sample [109]. The Belle group was able to determine that the  $\pi^+\pi^-\psi'$  mass enhancement is produced by two distinct peaks, one, the  $Y(4360)$  with  $M = 4361 \pm 13 \text{ MeV}/c^2$  and  $\Gamma = 74 \pm 18 \text{ MeV}/c^2$  and a second, the  $Y(4660)$  with  $M = 4664 \pm 12 \text{ MeV}/c^2$  and  $\Gamma = 48 \pm 15 \text{ MeV}/c^2$  [109]. These masses and widths are not consistent with any of the established  $1^{--}$  charmonium states, and no sign of a peak at either of these

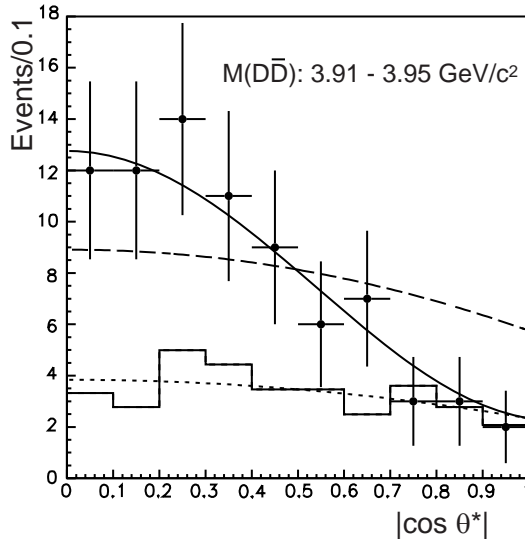


Figure 14.4: Belle's  $\chi_{c2}(2P)$  candidate [106]:  $\cos \theta^*$ , the angle of the  $D$  meson relative to the beam axis in the  $\gamma\gamma$  center-of-mass frame for events with  $3.91 < m(D\bar{D}) < 3.95 \text{ GeV}$ ; the data (circles) are compared with predictions for  $J = 2$  (solid) and  $J = 0$  (dashed). The background level can be judged from the solid histogram or the interpolated smooth dotted curve.

masses is evident in the  $e^+e^-$  total annihilation cross section [110] or in the exclusive cross sections  $e^+e^- \rightarrow D\bar{D}$  [111],  $D\bar{D}^*$  or  $D^*\bar{D}^*$  [112], or  $D\bar{D}\pi$  (non- $D^*$ ) [113], which indicates that the  $\pi^+\pi^-\psi'$  partial width for these states is unusually large (at least by charmonium standards). Moreover, as is evident in Fig. 14.5, which shows the recent Belle results [114] for  $\pi^+\pi^-J/\psi$  (top) and  $\pi^+\pi^-\psi'$  (bottom) with the same horizontal mass scales, there is no sign of either the  $Y(4360)$  or  $Y(4660)$  in the  $\pi^+\pi^-J/\psi$  channel; nor is there any sign of the  $Y(4260)$  peak in the  $\pi^+\pi^-\psi'$  mass spectrum.

### 14.5.5 The $Z^\pm(4430) \rightarrow \pi^\pm\psi'$

In Summer 2007, the Belle group reported observed the relatively narrow enhancement in the  $\pi^+\psi'$  invariant mass distribution in the  $B \rightarrow K\pi^\pm\psi'$  decay process shown in Fig. 14.6 [115]. The fitted peak mass and width values are  $M = (4433 \pm 5) \text{ MeV}/c^2$  and  $\Gamma = (45^{+35}_{-18}) \text{ MeV}/c^2$ , which is too narrow to be caused by interference effects in the  $K\pi$  channel. The  $B$  meson decay rate to this state, which is called  $Z^\pm(4430)$ , is similar to that for decays to the  $X(3872)$  and  $Y(3940)$ , which implies that the  $Z^\pm(4430)$  has a substantial branching fraction (*i.e.* greater than a few percent) to  $\pi^\pm\psi'$  and, thus, a partial decay width for this mode that is on the MeV scale. There are no reports of a  $Z^\pm(4430)$  signal in the  $\pi^+J/\psi$  decay channel.

Among the  $XYZ$  exotic meson candidates, the  $Z^\pm(4430)$  is unique in that it has a non-zero electric charge, a feature that cannot occur for  $c\bar{c}$  charmonium states or  $c\bar{c}$ -gluon hybrid mesons. It is, therefore, a prime candidate for a multiquark meson.

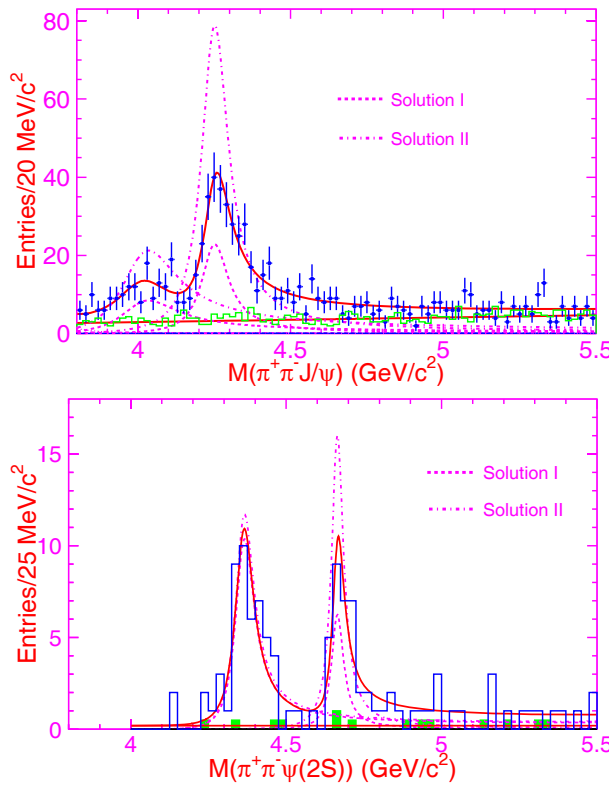


Figure 14.5: The  $\pi^+\pi^-J/\psi$  (Top) and  $\pi^+\pi^-\psi'$  (Bottom) invariant mass distributions for the ISR processes  $e^+e^- \rightarrow \gamma\pi^+\pi^-J/\psi(\psi')$ , from Refs. [114, 109]. The curves indicate the results of fits of interfering Breit Wigner resonances to the data.

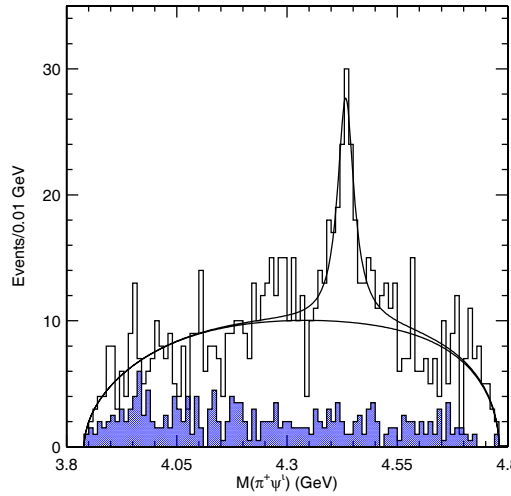


Figure 14.6: The  $\pi^\pm\psi'$  invariant mass distribution for  $B \rightarrow K\pi^\pm\psi'$  decays [115]. The shaded histogram is the estimated background. The curve is the result of a fit to a relativistic  $S$ -wave Breit Wigner signal function plus a phase-space-like continuum term.

### 14.5.6 Evidence for corresponding states in the $s$ - and $b$ -quark sectors?

The proliferation of meson candidates that are strongly coupled to  $c\bar{c}$  quark pairs but not compatible with a conventional charmonium assignment leads one naturally to question whether or not similar states exist that are strongly coupled to  $s\bar{s}$  or  $b\bar{b}$  quark pairs. There is some evidence that this, in fact, may be the case.

#### The $Y(2175)$

In 2006, the BaBar group reported a resonance-like structure in the  $f_0(980)\phi$  invariant mass distribution produced in  $e^+e^- \rightarrow \gamma_{ISR}f_0(980)\phi$  radiative-return events [116]. They report resonance parameters of  $M = (2170 \pm 10 \pm 15)$  MeV &  $\Gamma = (58 \pm 16 \pm 20)$  MeV. They see no signal for this peak in a sample of  $K^*(892)K\pi$  events that has little kinematic overlap with  $f_0(980)\phi$ , and conclude that this structure, which they call the  $Y(2175)$ , has a relatively large branching fraction for  $f_0(980)\phi$ .

The similarities with the  $Y(4260)$ , both in production and decay properties, leads naturally to the speculation that the  $Y(2175)$  might be an  $s\bar{s}$  analogue of the  $Y(4260)$ , *i.e.* it is the “ $Y_s(2175)$ ”. On the other hand, there is no compelling evidence against it being a conventional  $3^3S_1$  or  $2^3D_1$   $s\bar{s}$  “strangeonium” state. The study of the  $Y(2175)$  in other production and decay modes would be useful for distinguishing between different possibilities [117].

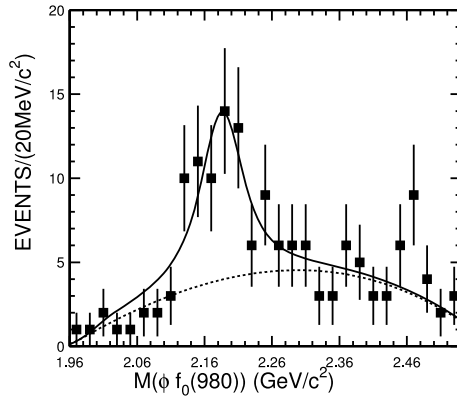


Figure 14.7: The  $M(f_0(980)\phi)$  distribution for  $J/\psi \rightarrow \eta f_0(980)\phi$  decays in BESII.

The BESII group made a first step in this program by finding an  $f_0(980)\phi$  mass peak with similar parameters produced in  $J/\psi \rightarrow \eta f_0(980)\phi$  decays (see Fig. 14.7) [118]. The BESII fit yields a mass and width of  $M = (2186 \pm 10 \pm 6)$  MeV &  $\Gamma = (65 \pm 23 \pm 17)$  MeV, which are in good agreement with BaBar’s measurements.

The next steps will be finding it in other decay modes and searching for counterpart states with quantum numbers other than  $1^{--}$  that, perhaps, decay into final states containing an  $\eta'$ . This will be an important task for *BES-III*, and is discussed in some detail elsewhere in this report.

### Anomalous $\pi^+\pi^-\Upsilon(nS)$ production at the $\Upsilon(5S)$

Using a sample of 236 million  $\Upsilon(4S)$  mesons, BaBar [119] observed  $167 \pm 19$  and  $97 \pm 15$  event signals for  $\Upsilon(4S) \rightarrow \pi^+\pi^-\Upsilon(1S)$  and  $\pi^+\pi^-\Upsilon(2S)$ , respectively, from which they infer partial widths  $\Gamma(\Upsilon(4S) \rightarrow \pi^+\pi^-\Upsilon(1S)) = (1.8 \pm 0.4)$  keV.  $\Gamma(\Upsilon(4S) \rightarrow \pi^+\pi^-\Upsilon(2S)) = (2.7 \pm 0.8)$  keV. Belle [120], with a sample of 464 million  $\Upsilon(4S)$  events reported a  $44 \pm 8$  event signal for the transition  $\Upsilon(4S) \rightarrow \pi^+\pi^-\Upsilon(1S)$ , from which they infer a partial width  $\Gamma(\Upsilon(4S) \rightarrow \pi^+\pi^-\Upsilon(1S)) = (3.65 \pm 0.67 \pm 0.65)$  keV. These partial widths are comparable in magnitude to those measured for  $\pi^+\pi^-$  transitions between the  $\Upsilon(3S)$ ,  $\Upsilon(2S)$  and  $\Upsilon(1S)$ , as discussed below in Sect. 15.1.

In 2006, Belle had a one-month-long run at  $e^+e^-$  cm energy of 10.87 GeV, which corresponds to the peak mass of the  $\Upsilon(5S)$ . The total data sample collected was  $21.7 \text{ fb}^{-1}$  and the number of  $\Upsilon(5S)$  events collected was 6.3 million. Scaling from the  $\Upsilon(4S)$  observations, they did not expect to see any significant evidence for  $\Upsilon(5S) \rightarrow \pi^+\pi^-\Upsilon(nS)$  transitions in this data set. Contrary to expectations based on the  $\Upsilon(4S)$  measurements, the Belle group found large numbers of  $\pi^+\pi^-\Upsilon(nS)$  events in this data sample:  $325 \pm 20$   $\pi^+\pi^-\Upsilon(1S)$  events and  $186 \pm 15$   $\pi^+\pi^-\Upsilon(2S)$  events (see Figs. 14.8(a) and (b)) [121]. (The  $\Upsilon(2,3S) \rightarrow \pi^+\pi^-\Upsilon(1S)$  signals in Fig. 14.8(a) are produced by radiative-return transitions  $e^+e^-\gamma_{ISR}\Upsilon(2,3S)$ .)

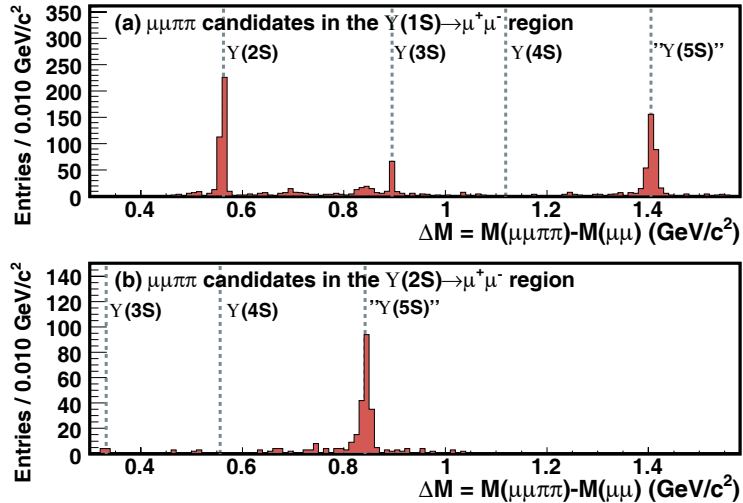


Figure 14.8: Belle's  $M(\mu^+\mu^-\pi^+\pi^-) - M(\mu^+\mu^-)$  mass difference distributions for events with (a)  $M(\mu^+\mu^-) = \Upsilon(1S)$  and (b)  $M(\mu^+\mu^-) = \Upsilon(2S)$ . Vertical dashed lines show the expected locations for  $\Upsilon(nS) \rightarrow \pi^+\pi^-\Upsilon(1,2S)$  transitions.

If one assumes that these events are coming from  $\Upsilon(5S) \rightarrow \pi^+\pi^-\Upsilon(nS)$  transitions, the inferred partial widths are huge:  $\Gamma(\Upsilon(5S) \rightarrow \pi^+\pi^-\Upsilon(1S)) = (590 \pm 40 \pm 90)$  keV.  $\Gamma(\Upsilon(5S) \rightarrow \pi^+\pi^-\Upsilon(2S)) = (850 \pm 70 \pm 160)$  keV, more than two orders-of-magnitude higher than corresponding transitions from the  $\Upsilon(4S)$ .

A likely explanation for these unexpectedly large partial widths (and, in fact, the motivation for Belle's pursuit of this subject) is that there is a “ $Y_b$ ”, *i.e.* a  $b\bar{b}$  counterpart of the  $\Upsilon(4260)$ , that is overlapping the  $\Upsilon(5S)$  [122] and this state is producing the  $\pi^+\pi^-\Upsilon(1,2S)$  events that are seen.

### 14.5.7 Summary

There is a large (and growing) number of candidate charmonium-like meson states that have been observed that do not seem to fit into the quark-antiquark classification scheme of the constituent quark model.

These states exhibit a number of peculiar features:

- Many of them have partial widths for decays to charmonium + light hadrons that are at the  $\sim$ MeV scale, which is much larger than is typical for established  $c\bar{c}$  meson states.
- They are relatively narrow although many of them are well above relevant open-charm thresholds.
- There seems to be some selectivity: states seen to decay to final states with a  $\psi'$  are not seen in the corresponding  $J/\psi$  channel, and *vice versa*.
- The new  $1^{--}$  charmonium states are not apparent in the  $e^+e^- \rightarrow$  charmed-meson-pair or the total hadronic cross sections.
- There are no evident changes in the properties of these states at the  $D^*D^{**}$  mass threshold.
- Although some states are near mass thresholds for pairs of open charmed mesons, this is not a universal feature.
- There is some evidence that similar states exist in the  $s$ - and  $b$ -quark sectors.

Attempts to explain these states theoretically have usually been confined to subsets of the observed states. For example, the  $X(3872)$  and  $Z(4430)$  have been attributed to bound molecular states of  $D\bar{D}^*$  and  $D^*\bar{D}^{**}$  mesons, or as diquark-antidiquark tetraquark states, the  $Y(4260)$  as a  $c\bar{c}$ -gluon hybrid, etc. However, no single model seems able to deal with the whole system and their properties in a compelling way. In general, the predictions of the various models have had limited success.

### 14.5.8 Implications for *BES-III*

This continues to be a data-driven field, with an increasingly large number of new results continuing to come out from BaBar, Belle and BESII. Many of the observed states in the  $c\bar{c}$  sector states can be accessed at *BES-III*; examples of how this might be done are discussed above in Sects. 14.4.1 and 14.4.2. If there is a corresponding spectroscopy for the  $s\bar{s}$  sector, which seem likely to be the case, all of the low-lying versions of those states should be accessible at *BES-III* either in decays of  $\psi$  resonances and/or by continuum  $e^+e^-$  production.

For the latter, dedicated energy scans might not be the best strategy. Thanks to BEPCII's high luminosity, continuum  $e^+e^-$  processes in the  $2 \sim 3$  GeV c.m. energy region can be accessed via initial-state-radiation while running at the  $\psi(3770)$  resonance, or higher. It is expected that *BES-III* will collect about  $5 \text{ fb}^{-1}/\text{yr}$  at the  $\psi(3770)$ , where many years will be invested. Figure 14.9 shows the energy dependence of the luminosity

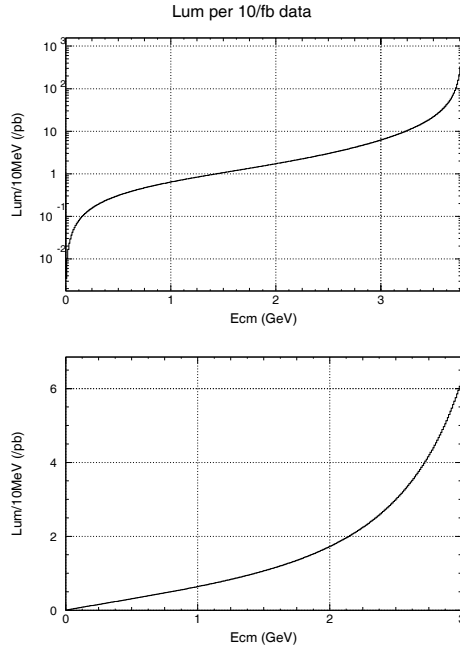


Figure 14.9: The energy dependence of the luminosity associated with the initial state radiation collected by *BES-III* in a  $10 \text{ fb}^{-1}$  data sample accumulated at the peak of the  $\psi(3770)$  resonance. The top has a semi-log scale, the bottom one has a linear scale.

associated with the initial state radiation collected by *BES-III* in a  $10 \text{ fb}^{-1}$  data sample accumulated at the peak of the  $\psi(3770)$  resonance [123]. Since the total cross section for  $e^+e^-$  annihilation into hadrons near  $E_{cm} = 2.5 \text{ GeV}$  is  $\sim 30 \text{ nb}$ , thousands of hadronic events per  $10 \text{ MeV}$  c.m. energy bin will be collected in this energy region during a multiyear run at the  $\psi(3770)$ .



# Chapter 15

## Charmonium transitions

### 15.1 Hadronic transitions<sup>1</sup>

#### 15.1.1 QCD Multipole Expansion

Hadronic transitions are important decay modes of heavy quarkonia (bound states of heavy quarks  $Q$  and  $\bar{Q}$ ). For instance, the branching ratio for  $\psi' \rightarrow J/\psi + \pi + \pi$  is approximately 50%. In general, let us consider the hadronic transitions

$$\Phi_I \rightarrow \Phi_F + h \quad (15.1.1)$$

in which  $\Phi_I$ ,  $\Phi_F$  and  $h$  stand for the initial state quarkonium, the final state quarkonium, and the emitted light hadron(s), respectively.

In the  $c\bar{c}$  and  $b\bar{b}$  systems, the typical mass difference  $M_{\Phi_I} - M_{\Phi_F}$  is around a few hundred MeV, so that the typical momentum of the light hadron(s)  $h$  is low. In this section, we consider only the single-channel approach (For a coupled-channel approach, see Refs. [124, 125] and references therein). In this picture, the light hadron(s)  $h$  are produced from gluons emitted by the  $Q$  and/or  $\bar{Q}$  in the transition. The typical momentum of the emitted gluons is also low, and, thus, perturbative QCD does not work in these processes. Certain nonperturbative approaches are needed for studying hadronic transitions. The *QCD multipole expansion* (QCDME) is a feasible approach to hadronic transitions.

Due to the nonrelativistic nature of the process, the heavy quarkonia  $n^\sigma L_J$  [labelled by the principal quantum number  $n$ , the orbital angular momentum  $L$ , the total angular momentum  $J$ , and the spin multiplicity  $\sigma$  ( $\sigma = 1$  or  $3$ )], can be considered as solutions of the Schrödinger equation within a given potential model. The typical radius  $a = \sqrt{\langle r^2 \rangle}$  of the  $c\bar{c}$  and  $b\bar{b}$  quarkonia obtained in this way is of the order of  $10^{-1}$  fm. For soft gluon emission with gluon momenta  $k$  satisfying  $ak < 1$ ,  $ak$  can be a good expansion parameter. In classical electrodynamics, the coefficient of the  $(ak)^l$  term in the multipole expansion contains a factor  $\frac{1}{(2l+1)!}$ . Hence such a multipole expansion actually works better than

expected simply from consideration of the magnitude of  $(ak)^l$ . Note that the convergence of QCDME does not depend on the value of the QCD coupling constant  $g_s$ . Therefore QCDME is a feasible approach to the soft gluon emission in hadronic transitions (15.1.1).

---

<sup>1</sup>By Yu-Ping Kuang

QCDME has been studied by many authors [126, 127, 128, 129, 130, 131]. The gauge invariant formulation is given in Ref. [130]. For a systematic review of this type of the theory and its applications to hadronic transitions, see Ref. [125]. In this expansion, the general formula for the  $S$  matrix element between the initial state  $|I\rangle$  and the final state  $|F\rangle$  in the single-channel approach has been given in Ref. [131]. Explicit evaluation of the  $S$  matrix elements in various cases will be presented in the following sections.

### 15.1.2 Hadronic Transitions Between $S$ -Wave Quarkonia

In the single-channel approach, the amplitude for hadronic transitions (15.1.1) is diagrammatically shown in Fig. 15.1. In the figure, there are two complicated vertices: the vertex of *multipole gluon emissions* (**MGE**) from the heavy quarks and the vertex of *hadronization* (**H**) describing the conversion of the emitted gluons into light hadron(s). The **MGE** vertex is at the scale of the heavy quarkonium, and depends on the properties of the heavy quarkonia. The **H** vertex is at the scale of the light hadron(s) and is independent of the heavy quarkonia. In the following, we shall treat them separately. To illustrate, we take the  $\pi\pi$  and  $\eta$  transitions between  $S$ -wave quarkonia as examples.

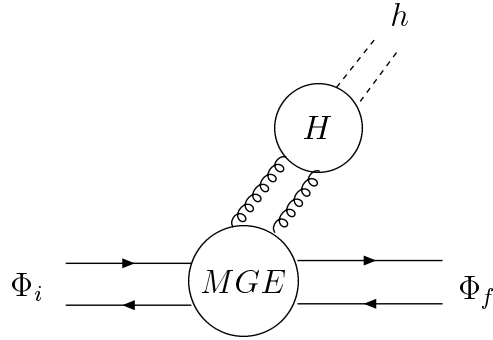


Figure 15.1: Diagram for a typical hadronic transition in the single-channel approach.

#### $\pi\pi$ Transitions

Consider the transition  $n_I^3S_1 \rightarrow n_F^3S_1 + \pi + \pi$ . These processes are dominated by double electric-dipole transitions (E1E1), whose transition amplitude can be obtained from Refs. [131, 130, 132]. The  $n_I^3S_1 \rightarrow n_F^3S_1 + \pi + \pi$  transition rate can be expressed as [132]

$$\Gamma(n_I^3S_1 \rightarrow n_F^3S_1 \pi \pi) = |C_1|^2 G |f_{n_I 0 n_F 0}^{111}|^2, \quad (15.1.2)$$

where

$$f_{n_I l_I n_F l_F}^{LP_I P_F} \equiv \sum_K \frac{\int R_F(r) r^{P_F} R_{KL}^*(r) r^2 dr \int R_{KL}^*(r') r'^{P_I} R_I(r') r'^2 dr'}{M_I - E_{KL}}, \quad (15.1.3)$$

and the phase-space factor  $G$  is given by [132]

$$G \equiv \frac{3}{4} \frac{M_{\Phi_F}}{M_{\Phi_I}} \pi^3 \int K \sqrt{1 - \frac{4m_\pi^2}{M_{\pi\pi}^2}} (M_{\pi\pi}^2 - 2m_\pi^2)^2 dM_{\pi\pi}^2, \quad (15.1.4)$$

$$K \equiv \frac{\sqrt{(M_{\Phi_I} + M_{\Phi_F})^2 - M_{\pi\pi}^2} \sqrt{(M_{\Phi_I} - M_{\Phi_F})^2 - M_{\pi\pi}^2}}{2M_{\Phi_I}}.$$

In (15.1.3),  $R_I$ ,  $R_F$ , and  $R_{KL}$  are the radial wave functions of the initial, final, and intermediate vibrational states, and they can be calculated from the Schrödinger equation within a given potential model.

There is only one overall unknown constant  $C_1$  left in this transition amplitude, and it can be determined by taking one well measured hadronic transition rate as an input. So far, the best-measured  $S$ -state to  $S$ -state  $\pi\pi$  transition rate is  $\Gamma(\psi' \rightarrow J/\psi \pi\pi)$ . The updated experimental value is [52]

$$\begin{aligned}\Gamma_{\text{tot}}(\psi') &= 277 \pm 22 \text{ keV}, \\ B(\psi' \rightarrow J/\psi \pi^+ \pi^-) &= (31.8 \pm 0.6)\%, \\ B(\psi' \rightarrow J/\psi \pi^0 \pi^0) &= (16.46 \pm 0.35)\%. \end{aligned}\quad (15.1.5)$$

Table 15.1: The value of  $|C_1|^2$  and the predicted rates  $\Gamma(\Upsilon' \rightarrow \Upsilon \pi\pi)$ ,  $\Gamma(\Upsilon'' \rightarrow \Upsilon \pi\pi)$ , and  $\Gamma(\Upsilon'' \rightarrow \Upsilon' \pi\pi)$  (in keV) in the Cornell model and the BGT model. The corresponding updated experimental values of the transition rates are taken from Ref. [52] and listed for comparison.

	Cornell	BGT	Expt.
$ C_1 ^2$	$83.4 \times 10^{-6}$	$67.8 \times 10^{-6}$	
$\Gamma(\Upsilon' \rightarrow \Upsilon \pi\pi)$ (keV)	8.6	7.8	$8.89 \pm 1.17$
$\Gamma(\Upsilon'' \rightarrow \Upsilon \pi\pi)$ (keV)	0.44	1.2	$1.33 \pm 0.22$
$\Gamma(\Upsilon'' \rightarrow \Upsilon' \pi\pi)$ (keV)	0.78	0.53	$0.98 \pm 0.28$

Using (15.1.5) as an input to determine  $C_1$ , we can predict all of the  $S$ -state to  $S$ -state  $\pi\pi$  transition rates in the  $\Upsilon$  system. Since the amplitude (15.1.3) depends on the potential model, the determined value of  $|C_1|$  is model dependent. Here we take the Cornell Coulomb plus linear potential model [133] and the Buchmüller-Grunberg-Tye (BGT) potential model [134] as examples to show the determined  $|C_1|$  and the predicted rates of  $\Upsilon' \rightarrow \Upsilon \pi\pi$ ,  $\Upsilon'' \rightarrow \Upsilon \pi\pi$ , and  $\Upsilon'' \rightarrow \Upsilon' \pi\pi$ . The results are listed in Table 15.1. We see that the predicted rates for the BGT model are close to the experimental values.

Note that the phase space factor  $G$  for  $\Upsilon'' \rightarrow \Upsilon \pi\pi$  is much larger than that for  $\Upsilon' \rightarrow \Upsilon \pi\pi$ :  $G(\Upsilon'' \rightarrow \Upsilon \pi\pi)/G(\Upsilon' \rightarrow \Upsilon \pi\pi) = 33$ . Thus, one might naively expect that  $\Gamma(\Upsilon'' \rightarrow \Upsilon \pi\pi) > \Gamma(\Upsilon' \rightarrow \Upsilon \pi\pi)$ . However, as we see from the experimental values in Table 15.1,  $\Gamma(\Upsilon'' \rightarrow \Upsilon \pi\pi)/\Gamma(\Upsilon' \rightarrow \Upsilon \pi\pi) \approx 1.33/8.89 = 0.15$ . The reason why the predictions for this ratio are close to the experimental value is that the contributions from various intermediate states to the overlap integrals in the summation in  $f_{3010}^{111}$  [cf. Eq. (15.1.3)] *drastically cancel* each other due to the fact that the  $\Upsilon''$  wave function contains two nodes. This is a *characteristic* of this type of intermediate state model (QCS or bag model).

Improved theoretical studies of these processes in a systematic relativistic coupled-channel theory are needed since the  $\psi'$  and  $\Upsilon''$  are close to the open flavor thresholds.

Recently, the  $\eta'_c$  state was found experimentally with a mass  $M_{\eta'_c} = 3.638 \pm 0.004$  GeV [52]. It will be interesting to measure the hadronic transition  $\eta'_c \rightarrow \eta_c \pi\pi$  at *BES-III*.

A very crude estimate of the transition rate was made in Ref. [135] by only estimating the phase space in the single-channel approach. Since the  $\eta'_c$  lies very close to the  $c\bar{c}$  threshold, a more sophisticated theoretical study of this transition that takes into account the coupled-channel and relativistic corrections is needed.

## $\eta$ Transitions

The transitions  $n_I^3S_1 \rightarrow n_F^3S_1 + \eta$  have contributions from E1M2 and M1M1 transitions, and is dominated by an E1M2 transition. Similar to  $\pi\pi$  transitions, using the data [52]

$$\Gamma_{\text{tot}}(\psi') = 277 \pm 22 \text{ keV}, \quad B(\psi' \rightarrow J/\psi \eta) = (3.09 \pm 0.08)\% \quad (15.1.6)$$

as inputs, we can predict the rates for  $\Upsilon' \rightarrow \Upsilon \eta$  and  $\Upsilon'' \rightarrow \Upsilon \eta$  to be

$$\Gamma(\Upsilon(n_I^3S_1) \rightarrow \Upsilon \eta) = \frac{\left| \frac{f_{n_I 010}^{111}(b\bar{b})}{m_b} \right|^2}{\left| \frac{f_{2010}^{111}(c\bar{c})}{m_c} \right|^2} \frac{|\mathbf{q}(b\bar{b})|^3}{|\mathbf{q}(c\bar{c})|^3} \Gamma(\psi' \rightarrow J/\psi \eta). \quad (15.1.7)$$

where  $\mathbf{q}(b\bar{b})$  and  $\mathbf{q}(c\bar{c})$  are the momenta of  $\eta$  in  $\Upsilon(n_I^3S_1) \rightarrow \Upsilon \eta$  and  $\psi' \rightarrow J/\psi \eta$ , respectively. Taking the BGT model as an example to calculate the ratio of transition amplitudes in (15.1.7), we obtain

$$\Gamma(\Upsilon' \rightarrow \Upsilon \eta) = 0.022 \text{ keV}, \quad \Gamma(\Upsilon'' \rightarrow \Upsilon \eta) = 0.011 \text{ keV}, \quad (15.1.8)$$

which are consistent with the present experimental bounds [52]

$$\Gamma(\Upsilon' \rightarrow \Upsilon \eta) < 0.064 \text{ keV}, \quad \Gamma(\Upsilon'' \rightarrow \Upsilon \eta) < 0.045 \text{ keV}. \quad (15.1.9)$$

We can also compare the ratios  $R' \equiv \Gamma(\Upsilon' \rightarrow \Upsilon \eta)/\Gamma(\psi' \rightarrow J/\psi \eta)$  and  $R'' \equiv \Gamma(\Upsilon'' \rightarrow \Upsilon \eta)/\Gamma(\psi' \rightarrow J/\psi \eta)$  with recent experimental measurements. Recently BESII has reported accurate measurements of  $\Gamma(\psi' \rightarrow J/\psi \eta)$  and  $\Gamma(\psi' \rightarrow J/\psi \pi^0)$  [136]. With the new BESII values and the bounds on  $\Gamma(\Upsilon' \rightarrow \Upsilon \eta)$  and  $\Gamma(\Upsilon'' \rightarrow \Upsilon \eta)$  [52], the experimental bounds on  $R'$  and  $R''$  are [136]

$$R'|_{\text{expt}} < 0.0061, \quad R''|_{\text{expt}} < 0.0043. \quad (15.1.10)$$

Using the BGT model to calculate the ratios  $R'$  and  $R''$ , we obtain

$$R'|_{\text{BGT}} = 0.0025, \quad R''|_{\text{BGT}} = 0.0013, \quad (15.1.11)$$

which are consistent with the experimental bounds (15.1.10). *BES-III* can further improve the measurements of  $\Gamma(\psi' \rightarrow J/\psi \eta)$  and  $\Gamma(\psi' \rightarrow J/\psi \pi^0)$ .

### 15.1.3 $\pi\pi$ Transitions of $D$ -Wave Charmonium

The  $\psi(3770)$  (or  $\psi''$ ) is primarily the  $1D$  state of the charmonium. The measured leptonic width of the  $\psi(3770)$  is  $(0.24 \pm 0.06)$  keV [52]. If we simply regard the  $\psi(3770)$  as a pure  $1D$  state of charmonium, the predicted leptonic width is smaller than the experimental value by an order of magnitude. Therefore it is generally considered that the  $\psi(3770)$  is a mixture of charmonium states, i.e., the observed  $\psi'$  and  $\psi(3770)$  states are [137, 138, 139].

$$\begin{aligned}\psi' &= \psi(2S) \cos \theta + \psi(1D) \sin \theta, \\ \psi(3770) &= -\psi(2S) \sin \theta + \psi(1D) \cos \theta.\end{aligned}\quad (15.1.12)$$

The mixing angle  $\theta$  can be determined phenomenologically by fitting the ratio of the leptonic widths of the  $\psi'$  and  $\psi(3770)$ . The leptonic widths of the  $\psi(2S)$  and  $\psi(1D)$  are proportional to the wave function at the origin  $\psi_{2S}(0)$  and the second derivative of the wave function at the origin  $\frac{5}{\sqrt{2}} \frac{d^2\psi_{1D}(0)/dr^2}{2m_c^2}$ , respectively. Therefore the determination of  $\theta$  depends on the potential model. Here we take two potential models as examples, namely the Cornell model [133] and an improved QCD-motivated potential model by Chen and Kuang (CK) [140] that produces more successful phenomenological results. The determined values of  $\theta$  are

$$\begin{aligned}\text{Cornell : } \theta &= -10^\circ, \\ \text{CK : } \theta &= -12^\circ.\end{aligned}\quad (15.1.13)$$

Since the  $\psi(3770)$  lies above the  $D\bar{D}$  threshold, it is usually believed that the  $\psi(3770)$  mainly decays into the open channel  $D\bar{D}$ . However, the measured cross section  $\sigma(e^+e^- \rightarrow \psi(3770) \rightarrow D\bar{D}) = 5.0 \pm 0.5$  nb [141] is smaller than the measured direct production cross section  $\sigma(e^+e^- \rightarrow \psi(3770)) = 7.5 \pm 0.8$  nb [142, 143]. Experiments have been searching for non- $D\bar{D}$  decays of the  $\psi(3770)$  that might account for this discrepancy for a long time. In 2005, BESII detected the hadronic transition  $\psi(3770) \rightarrow J/\psi \pi\pi$  [144], which was later confirmed by CLEO-c [145]. This was the first experimentally observed non- $D\bar{D}$  decay mode of the  $\psi(3770)$ . More non- $D\bar{D}$  decay channels have been searched for.

Theoretical studies of the  $\psi(3770) \rightarrow J/\psi \pi\pi$  transition were reported much earlier [137, 138]. This transition is dominated by E1E1 gluon emission and its rate is given by [137]

$$\begin{aligned}\Gamma(\psi(3770) \rightarrow J/\psi \pi\pi) &= |C_1|^2 \left[ \sin^2 \theta \, G(\psi') \, |f_{2010}^{111}(\psi')|^2 + \right. \\ &\quad \left. \frac{4}{15} \left| \frac{C_2}{C_1} \right|^2 \cos^2 \theta \, H(\psi'') \, |f_{1210}^{111}(\psi'')|^2 \right].\end{aligned}\quad (15.1.14)$$

This rate depends both on the value of  $C_2/C_1$  and the potential model (through the amplitudes  $f_{2010}^{111}$ ,  $f_{1210}^{111}$ ). We use the Cornell model [133] and the CK model [140] as examples. Taking the possible parameter range of [137]

$$1 \leq C_2/C_1 \leq 3,\quad (15.1.15)$$

Table 15.2: The predicted transition rate  $\Gamma(\psi(3770) \rightarrow J/\psi + \pi^+ + \pi^-)$  (in keV) in the Cornell model and the CK model with the updated input data (15.1.5).

Model	$\Gamma(\psi(3770) \rightarrow J/\psi + \pi^+ + \pi^-)$ (keV)
Cornell	26 – 139
CK	32 – 147

we obtain the values of  $\Gamma(\psi(3770) \rightarrow J/\psi + \pi^+ + \pi^-)$  listed in Table 15.2. Note that  $S$ - $D$  mixing only affects the rate at the few percent level and, so, the rate is essentially that for  $\Gamma(\psi(1D) \rightarrow J/\psi + \pi^+ + \pi^-)$ .

The BESII-measured branching ratio  $\mathcal{B}(\psi(3770) \rightarrow J/\psi + \pi^+ + \pi^-)$ , based on 27.7  $\text{pb}^{-1}$  data at the  $\psi(3770)$ , is [144]

$$B(\psi(3770) \rightarrow J/\psi + \pi^+ + \pi^-) = (0.34 \pm 0.14 \pm 0.09)\%, \quad (15.1.16)$$

which, using the  $\psi(3770)$  total width of[52]

$$\Gamma_{tot}(\psi(3770)) = 23.0 \pm 2.7 \text{ MeV}, \quad (15.1.17)$$

gives the partial width value [144]

$$\Gamma_{BES}(\psi(3770) \rightarrow J/\psi + \pi^+ + \pi^-) = 80 \pm 32 \pm 21 \text{ keV}. \quad (15.1.18)$$

This is in agreement with the theoretical predictions in Table 15.2. Using the BESII data (15.1.18) and Eq. (15.1.14) to determine  $C_2/C_1$ , we obtain

$$C_2/C_1 = 2_{-1.3}^{+0.7}. \quad (15.1.19)$$

This shows that  $C_2/C_1$  is, in fact, within the estimated range (15.1.15).

The CLEO-c measurement of the branching ratio is [145]

$$B(\psi(3770) \rightarrow J/\psi + \pi^+ + \pi^-) = (0.214 \pm 0.025 \pm 0.022)\%, \quad (15.1.20)$$

which corresponds to a partial width of

$$\Gamma(\psi(3770) \rightarrow J/\psi + \pi^+ + \pi^-) = 50.5 \pm 16.9 \text{ keV}. \quad (15.1.21)$$

Considering the experimental errors, this is consistent with the BESII result (15.1.18). We can also determine  $C_2/C_1$  from (15.1.21) and (15.1.14), and the result is

$$C_2/C_1 = 1.52_{-0.45}^{+0.35}. \quad (15.1.22)$$

This is consistent with the value (15.1.19) determined from the BESII data, but with better precision.

Further improvement of the measurement of the transition rate of  $\psi(3770) \rightarrow J/\psi + \pi^+ + \pi^-$  at *BES-III* is needed to determine the fundamental parameter  $C_2/C_1$  that occurs in other hadronic transitions.

### 15.1.4 Studying the $h_c$ State

The spin-singlet  $P$ -wave state  $h_c$  (or  $\psi(1^1P_1)$ ) is of special interest since the difference between its mass  $M_{h_c}$  and the center-of-gravity of the  $\chi_{cJ}$  states,  $M_{\text{c.o.g.}}(\chi_c) = (5M_{\chi_{c2}} + 3M_{\chi_{c1}} + M_{\chi_{c0}})/9 = 3525.30 \pm 0.08$  MeV, gives useful information about the spin-dependent interactions between the heavy quark and antiquark. If the spin-dependent interaction is perturbative, it is shown in Ref. [76] that  $M_{h_c}$  will be a few MeV smaller than  $M_{\text{c.o.g.}}(\chi_c)$ . There have been a number of experiments that searched for the  $h_c$  state.

In  $\bar{p}p$  collisions,  $h_c$  can be directly produced. The E835 experiment recently found the  $h_c$  state via the decay channel  $\bar{p}p \rightarrow h_c \rightarrow \eta_c \gamma$ , and the measured resonance mass is  $M_{h_c} = 3525.8 \pm 0.2 \pm 0.2$  MeV with a width  $\Gamma_{\text{tot}}(h_c) \lesssim 1$  MeV [75]. The measured production rate is consistent with the theoretical range given in Ref. [146] (see, in addition, Ref. [75]).

At  $e^+e^-$  colliders, the  $h_c$  state cannot be produced directly in the  $s$ -channel due to its  $C$  and  $P$  quantum numbers. Because of the limited phase space, the best way to search for the  $h_c$  state at CLEO-c or *BES-III* is through the isospin-violating hadronic transition [147, 146, 138]

$$\psi' \rightarrow h_c + \pi^0. \quad (15.1.23)$$

Recently, CLEO-c has found the  $h_c$  state via the process  $\psi' \rightarrow h_c \pi^0 \rightarrow \eta_c \gamma \gamma \gamma$  [74]. The measured resonance mass is  $M_{h_c} = 3525.35 \pm 0.27 \pm 0.2$  MeV [74], which is consistent with the E835 result at about the  $1\sigma$  level.

Theoretical studies were given much earlier in Refs. [146, 138, 148]. The process  $\psi' \rightarrow h_c + \pi^0$  is dominated by E1M1 transitions. Taking account of the  $S$ - $D$  mixing (15.1.12) in the  $\psi'$ , the transition rate is [138]

$$\begin{aligned} \Gamma(\psi' \rightarrow h_c \pi^0) &= \frac{\pi^3}{143m_c^2} \left( \frac{\alpha_M}{\alpha_E} \right) \left| \cos \theta \left( f_{2011}^{110} + f_{2011}^{001} \right) - \sqrt{2} \sin \theta \left( f_{1211}^{110} + f_{1211}^{201} \right) \right|^2 \\ &\times \frac{E_{h_c}}{M_{\psi'}} \left[ \frac{m_d - m_u}{m_d + m_u} f_\pi m_\pi^2 \right]^2 |\mathbf{q}_\pi|. \end{aligned} \quad (15.1.24)$$

Numerical results based on the CK potential model are [138]

$$\begin{aligned} \Gamma(\psi' \rightarrow h_c \pi^0) &= 0.06 \left( \frac{\alpha_M}{\alpha_E} \right) \text{ keV}, \\ B(\psi' \rightarrow h_c \pi^0) &= (2.2 \pm 0.2) \left( \frac{\alpha_M}{\alpha_E} \right) \times 10^{-4}. \end{aligned} \quad (15.1.25)$$

Calculations show that the dependence of the transition rate on the potential model is mild [138, 146].

We know that the  $\pi^0$  decays 99% into two photons. Thus the signal in (15.1.23) is  $\psi' \rightarrow h_c \gamma \gamma$  with  $M_{\gamma \gamma} = m_{\pi^0}$ . If the momenta of the two photons can be measured with sufficient accuracy, one can look for monochromatic  $\pi^0$ 's as the signal. From the branching ratio in Eq. (15.1.25), we see that, taking account of a  $\sim 10\%$  detection efficiency, hundreds of signal events can be observed in a data sample of 10 millions of  $\psi'$ 's. The backgrounds are shown to be either small or can be clearly excluded [138]. Once

the two photon energies  $\omega_1$  and  $\omega_2$  are measured, the  $h_c$  mass can be extracted from the relation  $M_{h_c}^2 = M_{\psi'}^2 + m_{\pi^0}^2 - 2M_{\psi'}(\omega_1 + \omega_2)$ .

To have a clearer signal, one can further look at the decay products of the  $h_c$ . It has been shown that the main decay channel for the  $h_c$  is  $h_c \rightarrow \eta_c \gamma$  [138]. So, the cleanest signal would be  $\psi' \rightarrow h_c \pi^0 \rightarrow \eta_c \gamma \gamma \gamma$ . The branching ratio  $B(h_c \rightarrow \eta_c \gamma)$  depends on the hadronic width of the  $h_c$ . In Ref. [138], the hadronic width of  $h_c$  was studied both in the conventional perturbative QCD (PQCD) and in the nonrelativistic QCD (NRQCD) approaches. The predictions are [138]

$$\text{PQCD : } B(h_c \rightarrow \eta_c \gamma) = (88 \pm 2)\%, \quad (15.1.26)$$

$$\text{NRQCD : } B(h_c \rightarrow \eta_c \gamma) = (41 \pm 3)\%. \quad (15.1.27)$$

These lead to the predictions

$$\begin{aligned} \text{PQCD : } B(\psi' \rightarrow h_c \pi^0) \times B(h_c \rightarrow \eta_c \gamma) &= 1.9 \left( \frac{\alpha_M}{\alpha_E} \right) \times 10^{-4} \\ &= (1.9 - 5.8) \times 10^{-4}, \end{aligned} \quad (15.1.28)$$

$$\begin{aligned} \text{NRQCD : } B(\psi' \rightarrow h_c \pi^0) \times B(h_c \rightarrow \eta_c \gamma) &= 0.9 \left( \frac{\alpha_M}{\alpha_E} \right) \times 10^{-4} \\ &= (0.9 - 2.7) \times 10^{-4}. \end{aligned} \quad (15.1.29)$$

CLEO-c measured [74]

$$B(\psi' \rightarrow h_c \pi^0) \times B(h_c \rightarrow \eta_c \gamma) = (3.5 \pm 1.0 \pm 0.7) \times 10^{-4} \quad (15.1.30)$$

which is within the theoretically predicted range (15.1.28) for the PQCD approach. However, considering the large measurement errors in (15.1.30), the present CLEO-c value is also consistent with the NRQCD prediction (15.1.29). Future improved measurements at *BES-III* and CLEO-c can distinguish between these two different approaches to hadronic decays.

CLEO-c has also studied the branching ratios for some exclusive hadronic decay channels of  $\eta_c$  [74]. More accurate measurement of the branching ratios of these exclusive hadronic channels at *BES-III* and CLEO-c can also be used to compare the corresponding predictions in Ref. [138] and test the PQCD and NRQCD approaches.

In summary, there are many aspects that need improved experimental studies of the  $h_c$  state at *BES-III* and CLEO-c.

- i) Because of the errors in the E835 and CLEO-c experiments, we still cannot judge whether  $M_{h_c}$  is larger or smaller than  $M_{c.o.g.}(\chi_c)$ . Improved measurements of  $M_{h_c}$ , e.g. including exclusive channel measurements, can clarify this issue.
- ii) In order to determine the fundamental parameter  $\alpha_M/\alpha_E$  and to test the PQCD and NRQCD approaches to the hadronic decays of  $h_c$ , improved measurements of  $B(\psi' \rightarrow h_c \pi^0) \times B(h_c \rightarrow \eta_c \gamma)$  are needed.

- iii) Branching ratios for various exclusive channels have been calculated in Ref. [138] and found to be different in the PQCD and the NRQCD approaches. Improved measurements of the exclusive channel branching ratios can distinguish between these two approaches.
- iv) Some other decay modes of the  $h_c$  state have been discussed in Ref. [146]. For instance,  $\Gamma(h_c \rightarrow J/\psi \pi\pi) = 4.12 \left( \frac{\alpha_M}{\alpha_E} \right)$  keV, etc [146]. After the accumulation of a large enough  $\psi'$  sample, other decay modes of  $h_c$  may also be measured and the properties of the  $h_c$  state better understood.

### 15.1.5 $\pi\pi$ Transitions of $P$ -Wave Quarkonia

Theoretical studies of the hadronic transitions  $\chi_b(2^3P_{J_I}) \rightarrow \chi_b(1^3P_{J_F})\pi\pi$  have been reported in Ref. [132]. Recently, CLEO measured the transition rate of  $\Gamma(\chi_b(2^3P_{J_I}) \rightarrow \chi_b(1^3P_{J_F})\pi\pi)$  [149], and the results are consistent with the theoretical predictions [125].

So far, no hadronic transitions of the  $\chi_{cJ}$  states have yet been observed. The  $\chi_{cJ}$  decays that have been observed are mainly decays into light hadrons, and the hadronic widths of the three  $\chi_{cJ}$  states are rather different. The  $\chi_{c1}$  has the smallest hadronic decay rate [52], and is, thus, the most promising of the three  $\chi_{cJ}$  states for studying hadronic transitions. The main hadronic transition process for  $\chi_{c1}$  is expected to be  $\chi_{c1} \rightarrow \eta_c\pi\pi$  which is dominated by the E1-M1 transition. Its transition rate has been computed in Ref. [150], and the obtained rate in the two-gluon approximation is

$$\Gamma(\chi_{c1} \rightarrow \eta_c\pi\pi) = \frac{4\alpha_E\alpha_M}{8505\pi m_c^2} |f_{1110}^{010} + |f_{1110}^{101}|^2 (M_{\chi_{c1}} - M_{\eta_c})^7, \quad (15.1.31)$$

where

$$f_{n_I l_I n_F l_F}^{LP_I P_F} = \sum_K f_{n_I l_I n_F l_F}^{LP_I P_F}(K),$$

$$f_{n_I l_I n_F l_F}^{LP_I P_F}(K) \equiv \frac{\int R_F^*(r') r'^{P_F} R_{KL}(r') r'^2 dr' \int R_{KL}^*(r) r^{P_I} R_I(r) r^2 dr}{E_I - E_{KL}}. \quad (15.1.32)$$

We use the CK potential model [140] as an example to calculate the radial wave functions in (15.1.32). To determine  $\alpha_E$ , we take the same approximation for  $\Gamma(\psi' \rightarrow J/\psi \pi\pi)$  which is

$$\Gamma(\psi' \rightarrow J/\psi \pi\pi) = \frac{8\alpha_E^2}{8505\pi} |f_{2010}^{111}|^2 (M_{\psi'} - M_{J/\psi})^7, \quad (15.1.33)$$

and determine  $\alpha_E$  by taking Eqn. (15.1.5) as input. This gives  $\alpha_E = 0.46$ . In this case the predicted partial width is

$$\Gamma(\chi_{c1} \rightarrow \eta_c\pi\pi) = 9.0 \left( \frac{\alpha_M}{\alpha_E} \right) \text{ keV} = 16.3 \pm 8.1 \text{ keV}. \quad (15.1.34)$$

The result in the Cornell potential model is smaller than the value in (15.1.34) by 14% [150], so that the model dependence of the prediction is not significant. The total width of  $\chi_{c1}$  is  $\Gamma(\chi_{c1}) = 0.89 \pm 0.05$  MeV [52]. So that the predicted branching fraction is

$$B(\chi_{c1} \rightarrow \eta_c\pi\pi) = (1.82 \pm 1.02)\%. \quad (15.1.35)$$

At  $e^+e^-$  colliders, the  $\chi_{c1}$  state can be produced at the  $\psi'$  peak via  $\psi' \rightarrow \gamma\chi_{c1}$  decay. In the rest frame of the  $\psi'$ , the momentum of the  $\chi_{c1}$  is 171 MeV which is only 5% of its mass  $M_{\chi_{c1}} = 3510.66$  MeV. Therefore we can neglect the motion of  $\chi_{c1}$ , and simply take the branching fraction (15.1.35) to estimate the event numbers in the experiments.

The detection of the process

$$\psi' \rightarrow \gamma\chi_{c1} \rightarrow \gamma\eta_c\pi\pi \quad (15.1.36)$$

can be performed in two ways, namely the *inclusive* and the *exclusive* detections [151]. In the inclusive detection, only the photon and the two pions are detected, while the  $\eta_c$  is inferred from the missing energy and momentum. In the exclusive detection, the photon, the two pions, and the decay products of the  $\eta_c$  are all detected. Reconstruction of the  $\eta_c$  and  $\chi_{c1}$  from the measured final state tagging particles can suppress backgrounds.

The inclusive detection requires measuring the momenta of the photon and the pions to certain precision. It is difficult to do this kind of analysis with the BESII data because the BESII photon resolution is not good enough. At *BES-III* and CLEO-c, this kind of detection may be possible.

For *BES-III*, it is not expected to be difficult to accumulate a data sample of  $\sim 10^8$   $\psi'$  events. CLEO-c is now running at the  $\psi'$  peak again, and will soon accumulate  $\sim 3 \times 10^7$   $\psi'$  events. The branching ratio of  $\psi' \rightarrow \gamma\chi_{c1}$  is  $B(\psi' \rightarrow \gamma\chi_{c1}) = (8.7 \pm 0.4)\%$  [52]. Taking account of a 15% detection efficiency, we obtain the number of events of type (15.1.36) at *BES-III* and CLEO-c

$$BES-III : \quad N_{incl}(\psi' \rightarrow \gamma\chi_{c1} \rightarrow \gamma\eta_c\pi\pi) = (2.38 \pm 1.43) \times 10^4; \quad (15.1.37)$$

$$CLEO-c : \quad N_{incl}(\psi' \rightarrow \gamma\chi_{c1} \rightarrow \gamma\eta_c\pi\pi) = (7.15 \pm 4.27) \times 10^3. \quad (15.1.38)$$

These numbers are so large that it seems the transition (15.1.36) should be clearly identified.

For the exclusive detection, suitable decay modes of the  $\eta_c$  should be used for identifying the  $\eta_c$  in the process (15.1.36). Some feasible decay modes that have reasonable branching fractions are [52, 74]

$$\eta_c \rightarrow \rho\rho : \quad B(\eta_c \rightarrow \rho\rho) = (2.0 \pm 0.7)\%, \quad (15.1.39)$$

$$\eta_c \rightarrow K^*\bar{K}^* : \quad B(\eta_c \rightarrow K^*\bar{K}^*) = (1.03 \pm 0.26)\%, \quad (15.1.40)$$

$$\eta_c \rightarrow \phi\phi : \quad B(\eta_c \rightarrow \phi\phi) = (0.27 \pm 0.09)\%, \quad (15.1.41)$$

$$\eta_c \rightarrow K^*(892)^0 K^- \pi^+ : \quad B(\eta_c \rightarrow K^*(892)^0 K^- \pi^+) = (2.0 \pm 0.7)\%, \quad (15.1.42)$$

$$\eta_c \rightarrow K^+ K^- \pi^+ \pi^- : \quad B(\eta_c \rightarrow K^+ K^- \pi^+ \pi^-) = (1.5 \pm 0.6)\%, \quad (15.1.43)$$

$$\eta_c \rightarrow 2(\pi^+ \pi^-) : \quad B(\eta_c \rightarrow 2(\pi^+ \pi^-)) = (1.20 \pm 0.30)\%, \quad (15.1.44)$$

$$\eta_c \rightarrow \eta\pi\pi \rightarrow \gamma\gamma\pi\pi : \quad B(\eta_c \rightarrow \eta\pi\pi \rightarrow \gamma\gamma\pi\pi) = (1.9 \pm 0.7)\%, \quad (15.1.45)$$

$$\eta_c \rightarrow K_S K^\pm \pi^\mp : \quad B(\eta_c \rightarrow K_S K^\pm \pi^\mp) = (1.9 \pm 0.5)\%, \quad (15.1.46)$$

$$\eta_c \rightarrow K_L K^\pm \pi^\mp : \quad B(\eta_c \rightarrow K_L K^\pm \pi^\mp) = (1.9 \pm 0.5)\%. \quad (15.1.47)$$

The modes (15.1.46) and (15.1.47) have been used by CLEO-c in the search for the  $h_c$  state [74].

For the exclusive detection, the requirement of the precision of the photon momentum measurement in (15.1.36) is not as strict. So it is possible to do this kind of analysis

Table 15.3: Predictions for the numbers of events in the exclusive detection of the process (15.1.36) in the CK potential model using the  $\eta_c$  decay modes shown in (15.1.39)–(15.1.47) at BESII, *BES-III*, and CLEO-c. The accumulated numbers of the  $\psi'$  events are taken to be  $1.4 \times 10^7$  for BESII,  $10^8$  for *BES-III*, and  $3 \times 10^7$  for CLEO-c. The detection efficiency is taken to be 10% for BES II, and 15% for *BES-III* and CLEO-c.

modes	BESII	<i>BES-III</i>	CLEO-c
$\rho\rho$	$44 \pm 42$	$476 \pm 454$	$143 \pm 136$
$K^* \bar{K}^*$	$23 \pm 20$	$245 \pm 210$	$74 \pm 62$
$\phi\phi$	$6 \pm 6$	$64 \pm 60$	$19 \pm 18$
$K^*(892)^0 K^- \pi^+$	$44 \pm 42$	$476 \pm 454$	$143 \pm 136$
$K^+ K^- \pi^+ \pi^-$	$34 \pm 34$	$358 \pm 358$	$107 \pm 107$
$2(\pi^+ \pi^-)$	$26 \pm 23$	$286 \pm 243$	$85 \pm 73$
$\eta \pi\pi \rightarrow \gamma\gamma \pi\pi$	$42 \pm 41$	$452 \pm 439$	$136 \pm 132$
$K_S K^\pm \pi^\mp$	$42 \pm 36$	$452 \pm 391$	$136 \pm 118$
$K_L K^\pm \pi^\mp$	$42 \pm 36$	$452 \pm 391$	$136 \pm 118$

with the BESII data except for those  $\eta_c$  decay modes that have photons. Therefore we also estimate the event numbers in BESII. The BESII data sample contains  $1.4 \times 10^7$   $\psi'$  events. Considering the ability of the BESII detector, we take a detection efficiency of  $\sim 10\%$ . The predicted numbers of events for BESII, *BES-III*, and CLEO-c are listed in Table 15.3. We see that the exclusive detection of the process (15.1.36) can be well studied at *BES-III* and CLEO-c. Considering the theoretical uncertainties, the number of events at BESII may be marginal.

As we have mentioned in the last subsection, improved measurements of  $B(\psi' \rightarrow h_c \pi^0) \times B(h_c \rightarrow \eta_c \gamma)$  at *BES-III* and CLEO-c will determine  $\alpha_M/\alpha_E$  more accurately. In this case, the predictions for the numbers of events of process (15.1.36) will be more reliable.

### 15.1.6 Summary

We have seen that the theory of hadronic transitions based on QCDME is quite successful (For details see Ref. [125]). Future studies will include hadronic transitions involving excited states that are close to or above the open-flavor threshold. Therefore, the development of a systematic theory for hadronic transitions that includes relativistic and coupled-channel effects is needed.

Soon, the *BES-III* group will have a high-quality detector plus the highest luminosity ever enjoyed by an  $e^+e^-$  experiment in the charm threshold region. Thus, even transitions with small rates could be detected and studied by them.

## 15.2 Radiative transition<sup>2</sup>

### 15.2.1 E1 radiative transitions

Radiative transitions are a very interesting feature of charmonium physics. They are quite straightforward to evaluate in  $c\bar{c}$  potential models, and (with sufficient statistics) provide a route from the initial  $1^{--}$  states produced in  $e^+e^-$  annihilation to  $C = (+)$  charmonia.

The largest rates are for E1 (electric dipole) transitions, which in the nonrelativistic quark model involve a simple matrix element of  $\vec{x}$ . The results we will quote here use the expression

$$\Gamma_{E1}(n^{2S+1}L_J \rightarrow n'^{2S'+1}L'_{J'} + \gamma) = \frac{4}{3} e_c^2 \alpha E_\gamma^3 \frac{E_f^{(c\bar{c})}}{M_i^{(c\bar{c})}} C_{fi} \delta_{SS'} |\langle n'^{2S'+1}L'_{J'} | r | n^{2S+1}L_J \rangle|^2 \quad (15.2.48)$$

where  $e_c = 2/3$  is the  $c$ -quark charge in units of  $|e|$ ,  $\alpha$  is the fine-structure constant,  $E_\gamma$  is the photon's energy, and the angular matrix element  $C_{fi}$  is

$$C_{fi} = \max(L, L') (2J' + 1) \begin{Bmatrix} L' & J' & S \\ J & L & 1 \end{Bmatrix}^2. \quad (15.2.49)$$

This is the formula quoted by Ref.[152], except for our inclusion of a relativistic phase space factor. (We note in passing that it is also possible to evaluate these E1 transition rates using LGT; preliminary results of this work have been presented by Dudek [87].) We evaluate the matrix elements  $\langle n'^{2S'+1}L'_{J'} | r | n^{2S+1}L_J \rangle$  using the nonrelativistic Schrödinger wavefunctions obtained in the model described in the previous section.

Several very interesting features of E1 radiative transitions are evident in Tables 15.4 and 15.5. First, the  $1P \rightarrow 1S$  (Table 15.4) transitions are in very reasonable agreement with experiment. It is notable that the predicted radiative partial width for  $h_c \rightarrow \gamma\eta_c$  is especially large, which would be an interesting measurement provided that an entry channel for the  $h_c$  can be identified at BES.

The theoretical rates for the  $2S \rightarrow 1P$  transitions (Table 15.4) appear too large by about a factor of two, although the relativized model of Godfrey and Isgur [53] does not share this difficulty. We note in passing that apparent good agreement between a pure- $c\bar{c}$  charmonium potential model and experiment may actually be spurious; decay loop effects will contribute two-meson continuum components to all these charmonium resonances, which may significantly modify the predicted radiative transition rates.

E1 radiative transitions from the higher-mass charmonium states are especially interesting. The  $1^3D_1$  candidate  $\psi(3770)$  (Table 15.4) is predicted to have large partial widths to  $\gamma\chi_1$  and  $\gamma\chi_0$  (with branching fractions of 0.5% and 1.7% respectively), but the branching fraction to  $\gamma\chi_2$  is predicted to be only about  $2 \cdot 10^{-4}$ . This small number however follows from the assumption that the  $\psi(3770)$  is a pure  $^3D_1$  state; if there is a significant admixture of S-wave basis states in the  $\psi(3770)$ ,

$$|\psi(3770)\rangle = \cos(\theta) |^3D_1\rangle + \sin(\theta) |^2S_1\rangle \quad (15.2.50)$$

---

<sup>2</sup>By Ted Barnes

Table 15.4: E1 radiative transitions of the low-lying narrow  $c\bar{c}$  states in the NR and GI potential models, abstracted from Ref.[54]. The masses are taken from Table 14.2; experimental masses were used (rounded “input” column) if known, otherwise, theoretical values were assumed.

Initial meson	Multiplets	Final meson	$E_\gamma$ (MeV)		$\Gamma_{\text{thy}}$ (keV)		$\Gamma_{\text{expt}}$ (keV)
			NR	GI	NR	GI	
$\chi_2$	1P → 1S	$J/\psi$	429.	429.	424.	313.	426. ± 51.
$\chi_1$	1P → 1S	$J/\psi$	390.	389.	314.	239.	291. ± 48.
$\chi_0$	1P → 1S	$J/\psi$	303.	303.	152.	114.	119. ± 19.
$h_c$	1P → 1S	$\eta_c$	504.	496.	498.	352.	
$\psi'$	2S → 1P	$\chi_2$	128.	128.	38.	24.	27. ± 4.
		$\chi_1$	171.	171.	54.	29.	27. ± 3.
		$\chi_0$	261.	261.	63.	26.	27. ± 3.
$\eta'_c$	2S → 1P	$h_c$	111.	119.	49.	36.	
$\psi_3(1^3D_3)$	1D → 1P	$\chi_2$	242.	282.	272.	296.	
$\psi_2(1^3D_2)$		$\chi_2$	236.	272.	64.	66.	
		$\chi_1$	278.	314.	307.	268.	
$\psi(3770)$		$\chi_2$	208.	208.	4.9	3.3	< 21 (90% <i>c.l.</i> ) [153]
		$\chi_1$	250.	251.	125.	77.	70 ± 17 [153]
		$\chi_0$	338.	338.	403.	213.	172 ± 30 [153]
$h_{c2}(1^1D_2)$		$h_c$	264.	307.	339.	344.	

Table 15.5: E1 radiative transitions of the broader  $1^{--}$  charmonium states above 4 GeV in the NR and GI quark models (evaluated as in Table 15.4).

Initial meson	Transition	Final meson	E <sub><math>\gamma</math></sub> (MeV)		$\Gamma_{\text{thy}}$ (keV)		$\Gamma_{\text{expt}}$ (keV)
			NR	GI	NR	GI	
$\psi(4040)$	3S $\rightarrow$ 2P	$\chi'_2$	67.	119.	14.	48.	
		$\chi'_1$	113.	145.	39.	43.	
		$\chi'_0$	184.	180.	54.	22.	
	$\rightarrow$ 1P	$\chi_2$	455.	508.	0.70	12.7	
		$\chi_1$	494.	547.	0.53	0.85	
		$\chi_0$	577.	628.	0.27	0.63	
$\psi(4160)$	2D $\rightarrow$ 2P	$\chi'_2$	183.	210.	5.9	6.3	
		$\chi'_1$	227.	234.	168.	114.	
		$\chi'_0$	296.	269.	483.	191.	
	$\rightarrow$ 1P	$\chi_2$	559.	590.	0.79	0.027	
		$\chi_1$	598.	628.	14.	3.4	
		$\chi_0$	677.	707.	27.	35.	
		$\chi_2(1^3F_2)$	128.	101.	51.	17.	
$\psi(4415)$	4S $\rightarrow$ 3P	$\chi_2(3^3P_2)$	97.	112.	68.	66.	
		$\chi_1(3^3P_1)$	142.	131.	126.	54.	
		$\chi_0(3^3P_0)$	208.	155.	0.003	25.	
	$\rightarrow$ 2P	$\chi'_2$	421.	446.	0.62	15.	
		$\chi'_1$	423.	469.	0.49	0.92	
		$\chi'_0$	527.	502.	0.24	0.39	
	$\rightarrow$ 1P	$\chi_2$	775.	804.	0.61	5.2	
		$\chi_1$	811.	841.	0.41	0.53	
		$\chi_0$	887.	915.	0.18	0.13	

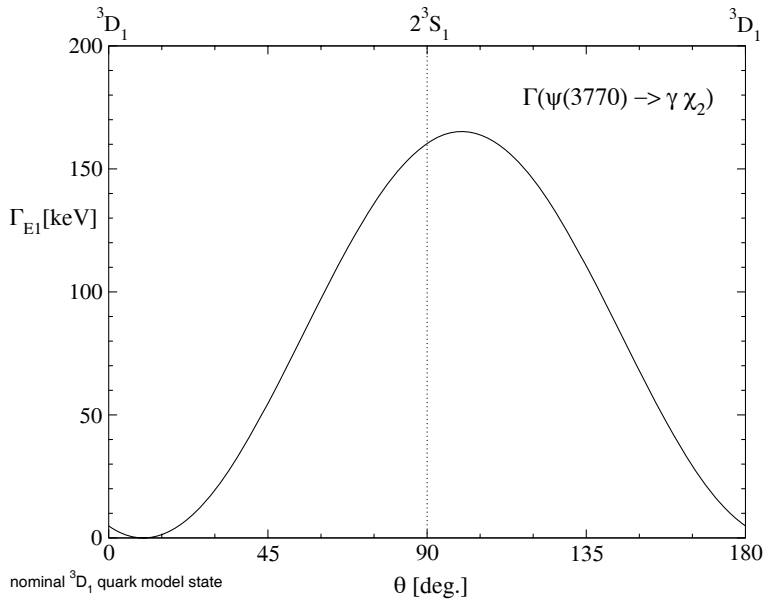


Figure 15.2: Predicted radiative partial width for the E1 transition  $\psi(3770) \rightarrow \gamma\chi_2$  as a function of the  $2^3S_1$ - $^3D_1$  mixing angle  $\theta$ .

one typically finds a much larger radiative width to  $\gamma\chi_2$  [154, 166, 183]. (See Fig. 15.2. The sign of the mixing angle  $\theta$  depends on the convention for the normalization of the  $^3D_1$  and  $2^3S_1$  basis states; note for example in Fig.1 of Ref.[183] that a zero  $\psi(3770) \rightarrow \gamma\chi_2$  width requires a small negative mixing angle, whereas with our conventions it would be positive.) Since the coupling of the  $\psi(3770)$  to  $e^+e^-$  suggests a significant  $2^3S_1$  component, a measurement of this radiative partial width at BES will be especially useful as an independent test of the presence of this amplitude in the  $\psi(3770)$  wavefunction.

We note in passing that if the dominant mechanism of  $^3D_1$  -  $2^3S_1$  basis state mixing in the  $\psi(3686)$  and  $\psi(3770)$  is through virtual charm meson decay loops such as  $DD$ ,  $DD^*$  and  $D^*D^*$ , the assumption of a  $2 \otimes 2$  orthogonal mixing matrix as in Eq.15.2.50 is incorrect. In this case the  $\langle ^3D_1|\psi(3686)\rangle$  and  $\langle 2^3S_1|\psi(3770)\rangle$  overlaps will no longer be simply related, and radiative transition amplitudes will also receive contributions due to photon emission from the two-meson continua.

Next we consider radiative decays of the higher-mass vectors  $\psi(4040)$  and  $\psi(4160)$ . As is evident in Table 15.5, if the  $\psi(4040)$  is dominantly a  $3^3S_1$  state as we assume here, it should have very small E1 radiative widths to the triplet members of the 1P multiplet, with branching fractions of at most about  $10^{-6}$ . Since other components of the  $\psi(4040)$  state vector (for example  $^3D_1$  or charmed meson continua) may lead to significant radiative couplings to 1P states, it will be very interesting for BES to search for these radiative modes. The radiative widths of the  $\psi(4040)$  to the controversial 2P triplet states are predicted to be much larger, with branching fractions of up to  $\sim 10^{-3}$ . Since the 2P states should have large strong branching fractions to  $DD$  ( $\chi_0$  and  $\chi_2$ ) and  $DD^*$  ( $\chi_1$  and  $\chi_2$ ) [54], it may be possible to identify these states in the  $DD$  and  $DD^*$  invariant mass distributions of the decays  $\psi(4040) \rightarrow \gamma DD$  and  $\gamma DD^*$ .

Radiative decays of the  $\psi(4160)$  share certain features with the decays of both the  $\psi(3770)$  and the  $\psi(4040)$ . First, the coupling to the 2P multiplet is again predicted to be

much stronger than to the 1P multiplet, so radiative decays of the  $\psi(4160)$  can be used to search for 2P states. The branching fraction to the  $2^3P_0 \chi_0$  state in particular may be as large as  $\sim 0.5\%$  if it is at  $\approx 3850$  MeV. Second, just as for the  $\psi(3770)$  a strong suppression of decays to all  $^3P_2$  “ $\chi_2$ ” states is predicted, but this follows from the assumption that the  $\psi(4160)$  is a pure D-wave  $c\bar{c}$  state; with an S-wave  $\psi(4160)$  admixture, which is required to explain the  $\psi(4160)$  leptonic width, the coupling to  $^3P_2$  states may be much larger; this should be searched for at BES. Finally, an interesting feature of D-wave  $c\bar{c}$  E1 decays is that one may reach the currently unknown 1F  $c\bar{c}$  multiplet (specifically the state  $^3F_2$ );  $\psi(4160)$  decays to  $\gamma DD$  should be appropriate for this. Unfortunately, the  $^3F_2$  state is expected to be rather broad [54].

### 15.2.2 Accessing the new states near 3.9 GeV through E1 transitions

Table 15.6: Theoretical E1 radiative partial widths of the  $\psi(4040)$  and  $\psi(4160)$  into  $C = (+)$  2P  $c\bar{c}$  states, recalculated in the NR model with masses suggested by the new XYZ states.

Initial State	Final State	E1 Width (keV)	E1 B.F.
$\psi(4040)$	$\chi'_2(3929)$	56.	$0.7 \cdot 10^{-3}$
	$\chi'_1(3940)$	25.	$0.3 \cdot 10^{-3}$
	$\chi'_0(3940)$	8.3	$0.1 \cdot 10^{-3}$
$\psi(4160)$	$\chi'_2(3929)$	9.9	$0.1 \cdot 10^{-3}$
	$\chi'_1(3940)$	129.	$1.3 \cdot 10^{-3}$
	$\chi'_0(3940)$	172.	$1.7 \cdot 10^{-3}$

The  $\psi(4040)$  and  $\psi(4160)$  can be used as  $1^{--}$  entry states for the study of the new XYZ states near 3.9 GeV. As shown in Table 15.6, both these states are expected to have relatively large E1 branching fractions into the 2P  $c\bar{c}$  multiplet,  $\psi(4040, 4160) \rightarrow \gamma \chi'_J$ . (These E1 partial widths were calculated as in Table 15.5 and Ref.[54], but the final masses were lowered to 3929 MeV and 3940 MeV to accommodate the new XYZ resonances as 2P candidates.) Note that these lower masses give significantly larger E1 partial widths than in Table 15.5. Evidently, studies of E1 transitions from the  $\psi(4040)$  and  $\psi(4160)$  at BES should allow the identification of the 2P resonances through their hadronic decays. In this approach one would study the invariant mass and angular distributions of the final charmed mesons in the processes  $e^+e^- \rightarrow \psi(4040, 4160) \rightarrow \gamma DD$  and  $\gamma DD^*$ .

### 15.2.3 M1 radiative transitions

M1 transitions between charmonium states in pure  $c\bar{c}$  models result from photon emission through the  $H_I = -\vec{\mu} \cdot \vec{B}$  magnetic moment interaction of the  $c$  quark (and antiquark), and as such are suppressed relative to E1 transitions by the small factor of  $1/m_c$  in the magnetic moment operator. The M1 transition amplitude is proportional to the matrix element of the spin operator, with a spatial factor that (without recoil corrections) is simply the matrix element of unity. M1 transitions are therefore nonzero only between states with the same  $L_{c\bar{c}}$  (and different  $S_{c\bar{c}}$ , since the C-parity must change). If we assumed a spin-independent zeroth-order potential and neglect recoil effects, M1 transitions between different radial multiplets would vanish because the  $n^3S_1$  and  $n'1S_0$  states have orthogonal spatial wavefunctions. One such transition is actually observed in charmonium,  $\psi' \rightarrow \gamma\eta_c$ , which must be due in part to the nonorthogonal  $\psi'$  and  $\eta_c$  spatial wavefunctions and final meson recoil effects.

The formula for M1 decay rates analogous to the E1 formula used in the previous section is

$$\Gamma_{M1}(n^{2S+1}L_J \rightarrow n'^{2S'+1}L'_{J'} + \gamma) = \frac{4}{3} e_c^2 \frac{\alpha}{m_c^2} E_\gamma^3 \frac{E_f^{(c\bar{c})}}{M_i^{(c\bar{c})}} \frac{2J'+1}{2L+1} \delta_{LL'} \delta_{S,S'\pm 1} \cdot |\langle n'^{2S'+1}L'_{J'} | n^{2S+1}L_J \rangle|^2. \quad (15.2.51)$$

Evaluating this formula for transitions from the  $\psi$  and  $\psi'$  gives the results shown in Table 15.7. A more detailed study of M1 radiative decay rates, incorporating recoil corrections (which are numerically important for transitions between multiplets such as  $2S \rightarrow 1S$ ) appears in Ref.[54].

An even larger discrepancy between experiment and theory is evident in the “hindered” M1 transition  $\psi' \rightarrow \gamma\eta_c$ . Since this rate is only nonzero due to recoil effects (not included here) and corrections to the naively orthogonal  $1S$  and  $2S$   $c\bar{c}$  wavefunctions, the discrepancy is perhaps less surprising than that found in the allowed  $1S \rightarrow 1S \psi \rightarrow \gamma\eta_c$  transition rate. In any case this is another example of an M1 transition rate in charmonium in which experiment and theory are clearly in disagreement. Since the experimental rate is again only about  $4\sigma$  from zero, it would be very useful to improve the accuracy of this measurement at BES.

Table 15.7: Theoretical and experimental M1 radiative partial widths of the  $\psi$  and  $\psi'$ , neglecting recoil effects.

Initial meson	Final meson	$\Gamma_{thy.}$ (keV)	$\Gamma_{expt.}$ (keV)
$J/\psi$	$\eta_c$	2.9	$1.2 \pm 0.3$
$\psi'$	$\eta_c'$	0.21	
$\psi'$	$\eta_c$	4.6	$0.8 \pm 0.2$
$\eta_c'$	$J/\psi$	7.9	

A well-known problem is evident in the decay rate  $J/\psi \rightarrow \gamma\eta_c$ , which is that the predicted rate in the nonrelativistic potential model is about a factor of 2-3 larger than

experiment. Since this rate only involves the charm quark magnetic moment, and hence only its mass, this discrepancy is a surprise. The relativized Godfrey-Isgur model [53] predicts a somewhat smaller rate of 2.4 keV, which is still about a factor of two larger than experiment. Since the errors are rather large, it would clearly be very interesting to improve the experimental accuracy of this surprising partial width. If this discrepancy is confirmed, it may be an indication that pure- $c\bar{c}$  models are a rather inaccurate description of charmonium, and that other components of the state vector such as two-meson continua make comparable important contributions to the M1 transition amplitudes. In view of the inaccuracy of the theoretical 1S M1 transition rate, it would also be interesting to test the 2S transition rate  $\psi' \rightarrow \gamma\eta_c'$  experimentally. Unfortunately, this rate is predicted to be a rather small 0.21 keV in the nonrelativistic  $c\bar{c}$  model.

An even larger discrepancy between experiment and theory is evident in the “hindered” M1 transition  $\psi' \rightarrow \gamma\eta_c$ . Since this rate is only nonzero due to recoil effects (not included here) and corrections to the naively orthogonal 1S and 2S  $c\bar{c}$  wavefunctions, the discrepancy is perhaps less surprising than that found in the allowed 1S  $\rightarrow$  1S  $\psi \rightarrow \gamma\eta_c$  transition rate. In any case this is another example of an M1 transition rate in charmonium in which experiment and theory are clearly in disagreement. Since the experimental rate is again only about  $4\sigma$  from zero, it would be very useful to improve the accuracy of this measurement and to search for the other M1 transitions at BES.

M1 decays between charmonium resonances have only been observed between S-wave states. The rates between orbitally excited states are typically predicted to be quite small, due to the small splittings within excited-L multiplets. They are large enough however to be observable given narrow initial states and large event samples. For example, a hypothetical  $^1D_2$   $c\bar{c}$  assignment for the X(3872) could be tested through a search for its M1 decay to  $\gamma\psi(3770)$ , which would have a partial width of about 1.2 keV in the nonrelativistic potential model. The  $h_c$  decay  $h_c \rightarrow \gamma\chi_0$  has similar phase space, and is predicted to have a partial width of 0.8 keV. In contrast, the smaller phase space of the M1 transition from the higher-mass  $\chi_2$  state leads to an expected partial width for  $\chi_2 \rightarrow \gamma h_c$  of only about 60 eV.

## 15.3 Channels for measurement at *BES-III*<sup>3</sup>

### 15.3.1 Introduction

The BEPCII design peak luminosity is  $10^{33} \text{ cm}^{-2}\text{s}^{-1}$  for center-of-mass energies near the  $\psi''$  peak. Thus, the peak luminosity at the  $\psi'$ , which is less than 100 MeV below the  $\psi''$  peak, should be about the same. Since the beam energy spread of BEPCII will be around 1.4 MeV, the peak cross section for  $\psi'$  production will be around 600 nb. Assuming that the average luminosity is half of the peak luminosity and the effective running time each year is around  $10^7$  s, one can expect as many as 3 billion  $\psi'$  events in a one year run [155]. This data sample would be huge compared to those used by previous experiments, and the detector performance will also be much better. The combined effect will be to make high precision measurements of  $\psi'$  decays possible, and make searches for the modes with very small branching fractions feasible.

---

<sup>3</sup>By Changzheng Yuan

The spectrum of charmonium states below the open-charm threshold is shown in Fig. 15.3. Since the mass of  $\psi'$  is higher than those of all of the other  $n = 1$   $S$ - and  $P$ -wave charmonium states, all these lower-mass charmonia can, in principle, be accessed by radiative and/or hadronic decays of  $\psi'$ . In the past, such processes have been fruitful for both our theoretical and experimental understanding of charmonium physics [156, 52]. However, because of the limited statistics of the old generation experiments, and the poorer detector performance, not all of the possible transition have been measured. Some that are crucial for the further development of phenomenological models of charmonium physics have still not been observed.

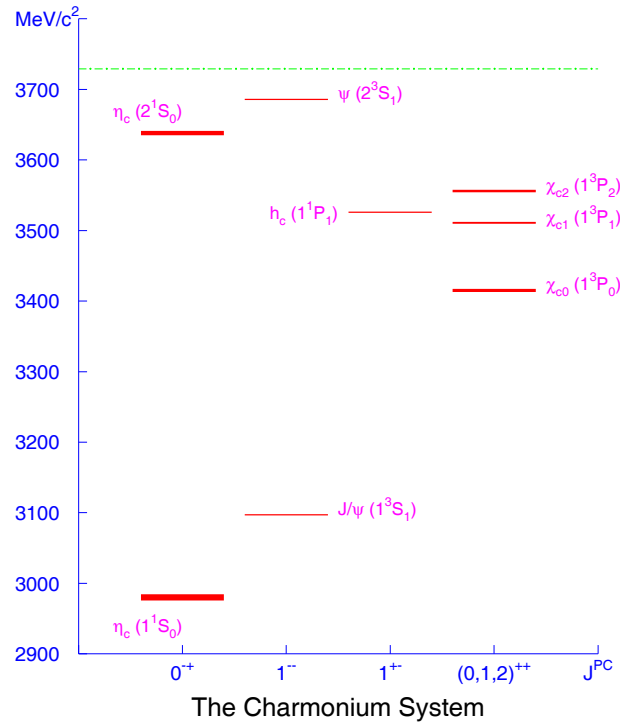


Figure 15.3: Charmonium spectroscopy below the open charm threshold.

In this section, we list all the allowed radiative transitions and hadronic transitions that can be studied with the large  $\psi'$  data sample that will be collected by *BES-III*. In addition, we give an overview of the status of our studies and point out some topics where additional theoretical effort is called for.

### 15.3.2 Radiative transitions

Since the  $J^{PC}$  of the photon is  $1^{--}$ , single photon transitions can only occur between two states of different  $C$ -parity. The transitions are either electric- or magnetic-multipole processes, depending on the spins and parities of the initial and final states. In those cases where the spins of the initial and final states are  $S_i$  and  $S_f$ , respectively, the total angular momentum carried by the photon ( $J_\gamma$ ) can be any integer between  $|S_i - S_f|$  and  $S_i + S_f$ . If the product of the parities of the initial state ( $\pi_i$ ) and final state ( $\pi_f$ ) is equal to  $(-1)^{J_\gamma}$ , the transition is an  $EJ_\gamma$  transition; otherwise, if  $\pi_i \cdot \pi_f = (-1)^{J_\gamma+1}$ , it is an  $MJ_\gamma$  transition. It is apparent that the electric multipole transitions preserve the initial

quark spin directions, while the magnetic multipole transitions are accompanied by spin flip of one of the quarks.

In general, when more than one multipole transitions are allowed, only the lowest one is important. Nevertheless, for some charmonium transitions, contributions of higher multipoles have been studied both theoretically and experimentally.

Radiative transitions between charmonium states have been studied extensively by many authors both theoretically and experimentally [157, 158, 159, 160, 161, 162, 163, 164]. The partial widths for some of the transitions have also been calculated with lattice QCD [165].

### $\psi'$ decays

- $\psi' \rightarrow \gamma \chi_{cJ}, J = 0, 1, 2$

These are the transitions between  $S$ -wave and  $P$ -wave spin triplets. For  $\psi' \rightarrow \gamma \chi_{c0}$  there is only an  $E1$  transition, while for  $\psi' \rightarrow \gamma \chi_{c1}$  there can be  $E1$  and  $M2$  transitions, and in  $\psi' \rightarrow \gamma \chi_{c2}$  there can be  $E1, M2$ , as well as  $E3$  transitions.

In general, it is believed that  $\psi' \rightarrow \gamma \chi_{cJ}$  is dominated by the  $E1$  transition, but with some  $M2$  (for  $\chi_{c1}$  and  $\chi_{c2}$ ) and  $E3$  (for  $\chi_{c2}$ ) contributions due to relativistic corrections. These contributions have been used to explain the big differences between the calculated pure  $E1$  transition rates and the experimental results [158]. They will also affect the angular distribution of the radiative photon. Thus, measurements of the photon angular distribution can be used to determine the contributions of the higher multipoles in the transition.

Moreover, for  $\psi' \rightarrow \gamma \chi_{c2}$ , the  $E3$  amplitude is directly connected with  $D$ -state mixing in the  $\psi'$ , which has been regarded as a possible explanation of the large leptonic annihilation rate of  $\psi''$  [162]. Since recent studies [166, 167, 168] also suggest the  $S$ - and  $D$ -wave mixing of  $\psi'$  and  $\psi''$  may be the key to solve the longstanding “ $\rho\pi$  puzzle” and to explain  $\psi''$  non- $D\bar{D}$  decays, more experimental information on multipole amplitudes gains additional importance.

Decay angular distributions in  $\psi' \rightarrow \gamma \chi_{c2}$  were studied by the Crystal Ball experiment using  $\psi' \rightarrow \gamma \gamma J/\psi$  events [169]; no significant contributions from higher multipoles were found, but the errors were large due to the limited statistics. In a recent analysis at BESII [170],  $\psi' \rightarrow \gamma \chi_{c2} \rightarrow \gamma \pi^+ \pi^-$  and  $\gamma K^+ K^-$  decays were used for a similar study. The analysis gave a magnetic quadrupole amplitude  $a'_2 = -0.051^{+0.054}_{-0.036}$  and an electric octupole amplitude  $a'_3 = -0.027^{+0.043}_{-0.029}$  [171], neither of which differs significantly from zero. The results are in good agreement with what is expected for a pure  $E1$  transition. As for the  $D$ -state mixing of  $\psi'$ , the results do not contradict previous theoretical calculations by more than one standard deviation [172].

The contribution of these higher multipoles are of theoretical interest, so further studies at *BES-III*, where a much higher sensitivity for probing the higher multipoles contribution would be possible, are anticipated.

- $\psi' \rightarrow \gamma \eta_c$

This is a hindered  $M1$  transition, as it occurs between  $n = 2$  and  $n = 1$  states.

- $\psi' \rightarrow \gamma\eta'_c$

This is an *M1* transition, and analogous to the similar transition between  $J/\psi$  and  $\eta_c$ . However, the transition rate, which is proportional to  $E_\gamma^3$ , is very small since the mass difference between the  $\psi'$  and  $\eta'_c$  is not very large.

The study of the  $\eta'_c$  in  $\psi'$  decays at *BES-III* will challenge the ability of the experimentalists and the capabilities of the detector.

### $\eta'_c$ decays

The observation of these transitions will be very helpful for understanding the  $\eta'_c$  properties. From the experimental point of view, these final states are observationally clean, but the rates are small.

- $\eta'_c \rightarrow \gamma J/\psi$

This is an *M1* transition. It has been calculated in Ref. [172].

- $\eta'_c \rightarrow \gamma h_c(^1P_1)$

This is an *E1* transition. It was calculated some time ago [161] to have a partial width of 16 keV.

### $\chi_{cJ}$ decays

- $\chi_{cJ} \rightarrow \gamma J/\psi$

These are the transitions between the *P*-wave and *S*-wave spin triplets. For  $\chi_{c0} \rightarrow \gamma J/\psi$ , there is only an *E1* transition, while for  $\chi_{c1} \rightarrow \gamma J/\psi$ , there are *E1* and *M2* transitions, and for  $\chi_{c2} \rightarrow \gamma J/\psi$ , there could be *E1*, *M2*, as well as *E3* transitions.

Decay angular distributions for  $\psi' \rightarrow \gamma\chi_{c2}$  were studied by the Crystal Ball experiment using  $\psi' \rightarrow \gamma\gamma J/\psi$  events [169]; the no significant contribution from higher multipoles was found, but the errors were large due to the limited statistics. The  $\chi_{c2} \rightarrow \gamma J/\psi$  decay was also studied by E835 in  $p\bar{p}$  annihilation.

- $\chi_{c2} \rightarrow \gamma h_c(^1P_1)$

This can be an *M1*, *E2* and/or *M3* transition. There are no published calculations for this process.

### $h_c(^1P_1)$ decays

- $h_c(^1P_1) \rightarrow \gamma\eta_c$

This *E1* transition was the discovery mode for the  $h_c(^1P_1)$  state that was used by CLEO [173]. The transition branching fraction is expected to be large (more than 50% of all  $h_c(^1P_1)$  decays), which was confirmed by the CLEOc measurement. This should be measured with higher precision at *BES-III*.

- $h_c(^1P_1) \rightarrow \gamma\chi_{c0}, \gamma\chi_{c1}$

$h_c(^1P_1) \rightarrow \gamma\chi_{c0}$  is an  $M1$  transition, and  $h_c(^1P_1) \rightarrow \gamma\chi_{c1}$  is an  $M1$  and/or  $E2$  transition. There are no calculations of this transition in the literature.

Measurements of these transitions as well as  $\chi_{c2} \rightarrow \gamma h_c(^1P_1)$  will be difficult, since the rates may be small, and the photons are very low energy.

### $J/\psi$ decays

- $J/\psi \rightarrow \gamma\eta_c$

This is an  $M1$  transition and a better measurement is needed to clarify the difference between the existing Crystal Ball measurement, which is smaller than theoretical predictions. Also, there are some discrepancies between  $\eta_c$  properties measured using  $J/\psi$  decays and those derived from experiments using other production modes, such as  $\gamma^*\gamma^*$  fusion,  $B$  decays etc., that have to be investigated and clarified.

This mode can be studied using either  $\psi'$  data sample, via  $\psi' \rightarrow J/\psi\pi^+\pi^-$ , or using the  $J/\psi$  data sample collected at the  $J/\psi$  resonance peak.

All the radiative transitions between the charmonium states listed above are indicated by arrows in Fig. 15.4.

#### 15.3.3 Hadronic transitions

There are strong and electromagnetic transitions between two charmonium states if the mass difference is large enough to produce one or more  $\pi$ 's, and/or an  $\eta$ .  $C$ -parity conservation and Parity conservation may forbid some of the transitions, and these are pointed out below. The study of their usefulness for searches for rare decays and potential signals for new physics is beyond the scope of this section.

Only the hadronic transitions of the  $\psi'$  have been well studied experimentally. These include the  $\pi^+\pi^-J/\psi$ ,  $\pi^0\pi^0J/\psi$ ,  $\eta J/\psi$  and  $\pi^0J/\psi$  decay modes of the  $\psi'$ . Extensive theoretical calculations have been for these transitions as well. The other possible transitions have not been well studied. Below we indicate those where results are available.

It should be noted that, since the mass differences between the charmonium states are not large, the light hadrons are generally produced at very low momentum, this may provide some unique opportunities to studying the physics of this energy domain.

### $\psi'$ decays

Since the mass difference between the  $\psi'$  and many of the charmonium states are much larger than one  $\pi$  mass, there are a number of possible transitions. All the kinematically allowed transitions are indicated in Fig. 15.5 and discussed below.

1.  $\psi' \rightarrow \eta_c + X$

The mass difference between the  $\psi'$  and  $\eta_c$  is  $706$  MeV/ $c^2$ , which is greater than  $5m_\pi$  and  $m_\eta + m_\pi$ ; all of the possible combinations are listed below. There are no reported measurements for any of the channels listed here, and only a very few theoretical considerations.

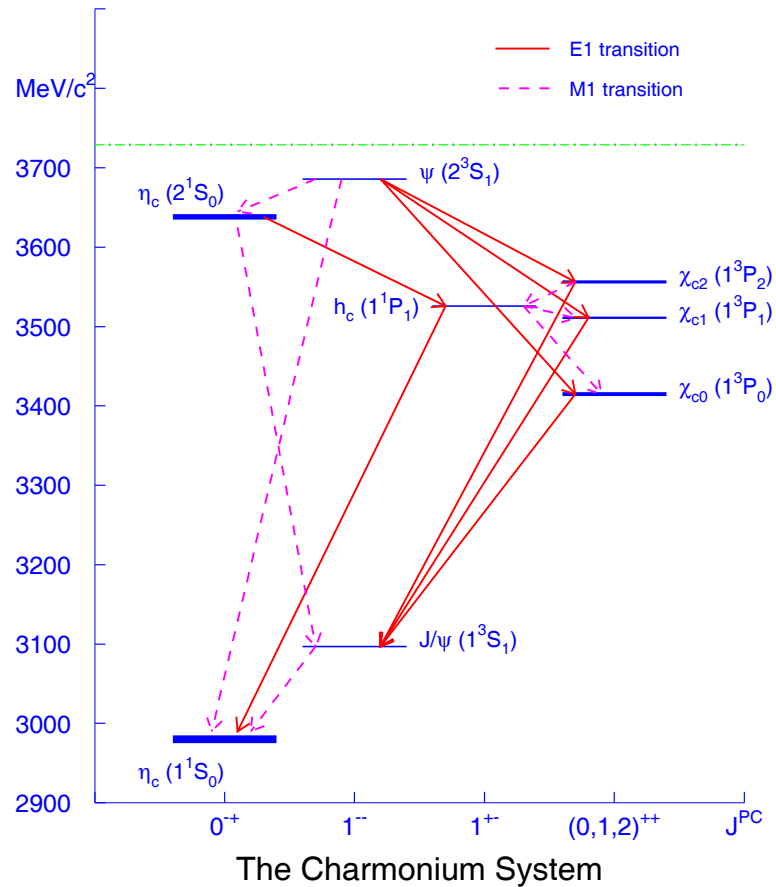


Figure 15.4: Radiative transitions between charmonium states below the open charm threshold.

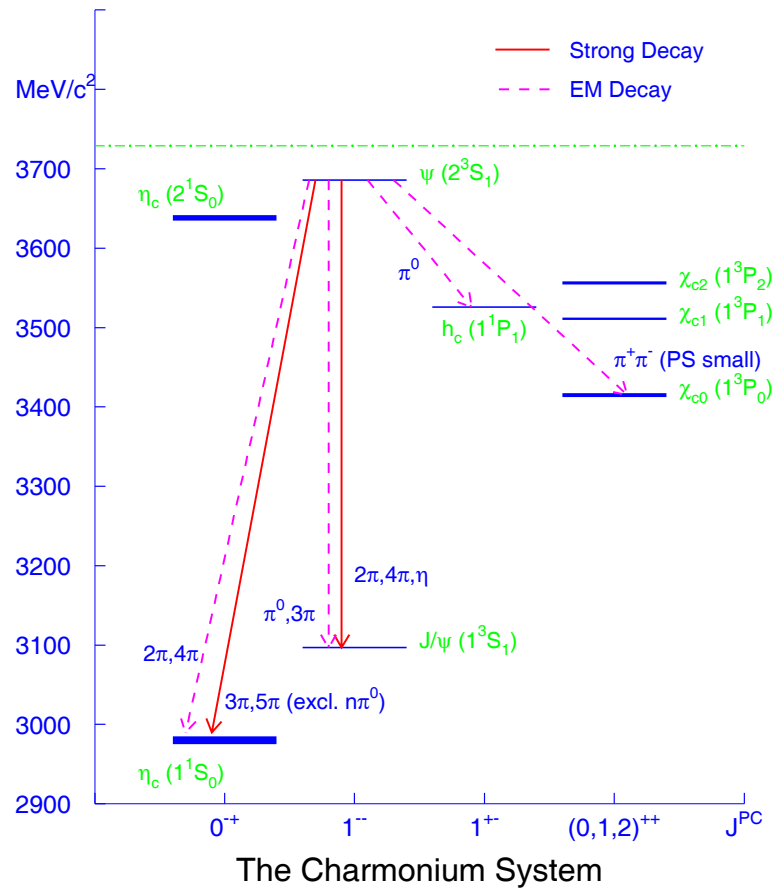


Figure 15.5: Hadronic transitions of  $\psi'$  to other charmonium states.

- $\psi' \rightarrow n\pi^0\eta_c$ ,  $n = 1, 2, 3, 4, 5$ :  $C$ -violating, not allowed
- $\psi' \rightarrow \pi^+\pi^-\eta_c$ :  $G$ -parity violating, EM decays only, via  $\rho^*$
- $\psi' \rightarrow \pi^+\pi^-\pi^0\eta_c$ : strong decays, via  $\omega^*$

It was predicted that this mode would have a branching fraction at the 1% level [174] in a model that was developed to explain the “ $\rho\pi$  puzzle” between  $\psi'$  and  $J/\psi$  hadronic decays. Using a 3 million  $\psi'$  data sample, CLEOc [175] established an upper limit on the branching fraction of less than  $1.0 \times 10^{-3}$  at 90% C.L.

- $\psi' \rightarrow 2(\pi^+\pi^-)\eta_c$ :  $G$ -parity violating, EM decays only
- $\psi' \rightarrow \pi^+\pi^-2\pi^0\eta_c$ :  $G$ -parity violating, EM decays only
- $\psi' \rightarrow 2(\pi^+\pi^-)\pi^0\eta_c$ : strong decays
- $\psi' \rightarrow \pi^+\pi^-3\pi^0\eta_c$ : strong decays
- $\psi' \rightarrow \eta\eta_c$ :  $C$ -violating, not allowed
- $\psi' \rightarrow \eta\pi^0\eta_c$ :  $C$ -violating, not allowed

## 2. $\psi' \rightarrow J/\psi + X$

The mass difference between the  $\psi'$  and  $J/\psi$  is 589 MeV/ $c^2$ , which is greater than  $4m_\pi$  and  $m_\eta$ , all the possible combinations are listed below. The channels in this category have been studied well both experimentally and theoretically, thanks to the large decay branching fractions and the distinct signature of the leptonic decays of the  $J/\psi$ .

- $\psi' \rightarrow \pi^0J/\psi$ :  $G$ -parity violating, EM decays

This transition has been observed (via  $\pi^0 \rightarrow \gamma\gamma$  and  $J/\psi \rightarrow \ell^+\ell^-$ ) by many experiments, most recently BESII and CLEO.

- $\psi' \rightarrow \pi^+\pi^-J/\psi$ : strong decays

This is one of the main transition modes of the  $\psi'$  with a branching fraction that corresponds to about one third of all decays. The  $\pi^+\pi^-$  mass shows the interesting feature of events clustering at high  $\pi^+\pi^-$  masses, which has been a hot topic of theoretical discussion that dates from the time of the discovery of this decay mode and persisting until now.

The  $\pi\pi$  are produced mainly in an  $S$ -wave, with the same  $0^{++}$  quantum number as the  $\sigma$ , the  $D$ -wave component was found to be small by a BESI analysis based on a 4 million  $\psi'$  event sample.

The process has been analyzed in various models by many authors [125, 176, 177, 178, 179]; all the models fit the data well.

- $\psi' \rightarrow \pi^0\pi^0J/\psi$ : strong decays

This is similar to  $\pi^+\pi^-J/\psi$  mode. Isospin symmetry predicts that its production rate should be half of that of  $\pi^+\pi^-J/\psi$ . This was tested with high precision by CLEOc using a 3 million  $\psi'$  event sample.

An isospin violation may exist, but it should be small, as indicated by the  $\pi^0J/\psi$  and  $\eta J/\psi$  rate difference. This may be tested with more and higher precision data.

- $\psi' \rightarrow \pi^+ \pi^- \pi^0 J/\psi$ :  $G$ -parity violating, EM decays only  
This rate can be roughly estimated from the  $\pi^0 J/\psi$  decay rate.
- $\psi' \rightarrow 3\pi^0 J/\psi$ :  $G$ -parity violating, EM decays only
- $\psi' \rightarrow 2(\pi^+ \pi^-) J/\psi$ : strong decays  
Here the phase space is small, however the rate may not be small since it is a strong decay. The experimental detection is difficult, since the  $\pi^\pm$  momenta are low.
- $\psi' \rightarrow \pi^+ \pi^- 2\pi^0 J/\psi$ : strong decays  
This is similar to  $\psi' \rightarrow 2(\pi^+ \pi^-) J/\psi$ , *i.e.* hard to detect.
- $\psi' \rightarrow 4\pi^0 J/\psi$ : strong decays  
This is similar to  $\psi' \rightarrow 2(\pi^+ \pi^-) J/\psi$ . The detection of eight photons with energy near half of the  $\pi^0$  mass will challenge the Electromagnetic Calorimeter.
- $\psi' \rightarrow \eta J/\psi$ : strong decays  
There are many measurements of this mode. The ratio between the rate of this mode and the isospin-violating  $\pi^0 J/\psi$  mode is used to measure the mass difference of the  $u$ - and  $d$ -quarks, and the strength of electromagnetic contributions to  $\psi'$  hadronic transitions.

### 3. $\psi' \rightarrow \chi_{cJ} + X$

The mass difference between the  $\psi'$  and  $\chi_{c0}$  is 271 MeV/ $c^2$ , only slightly greater than  $2m_{\pi^0}$  and lower than  $m_{\pi^+} + m_{\pi^-}$ . Since the width of the  $\chi_{c0}$  is around 10 MeV/ $c^2$ , the decay  $\psi' \rightarrow \pi^+ \pi^- \chi_{c0}$  could, in principle, be accessed via the low-mass tail of the  $\chi_{c0}$ .

The mass difference between the  $\psi'$  and  $\chi_{c1}$  is 176 MeV/ $c^2$ , slightly greater than  $m_{\pi^0}$ ; the mass difference between the  $\psi'$  and  $\chi_{c2}$  is 130 MeV/ $c^2$ , lower than  $m_{\pi^0}$ . All the possible transitions are listed below.

- $\psi' \rightarrow n\pi^0 \chi_{cJ}$ ,  $n = 1, 2$ :  $C$ -violating, not allowed
- $\psi' \rightarrow \pi^+ \pi^- \chi_{c0}$ :  $G$ -parity violating, EM decays only, via  $\rho^*$ . However the available phase space is very small and only the low-mass tail of  $\chi_{c0}$  can be produced. There are no measurements and no theoretical calculations.

### 4. $\psi' \rightarrow h_c(^1P_1) + X$

The mass difference between the  $\psi'$  and  $h_c(^1P_1)$  is 160 MeV/ $c^2$ , slightly greater than  $m_{\pi^0}$ . The only kinematically allowed hadronic transition is  $\psi' \rightarrow \pi^0 h_c(^1P_1)$ .

- $\psi' \rightarrow \pi^0 h_c(^1P_1)$ :  $G$ -parity violating, EM decays only  
This is the  $h_c(^1P_1)$  discovery mode that was exploited by CLEO [173]. The product of the branching fraction and that of  $h_c(^1P_1) \rightarrow \gamma \eta_c$  was determined in the same experiment.

More experimental effort is needed to understand this transition, as well as to study better the properties of the  $h_c(^1P_1)$ .

### $\eta'_c$ decays

Since the mass of  $\eta'_c$  is only slightly below than that of  $\psi'$ , the mass difference between the  $\eta'_c$  and many of the charmonium states is also larger than one  $\pi$  mass. As a result, there are many possible transitions. All of the kinematically allowed hadronic transitions are indicated in Fig. 15.6 and discussed below.

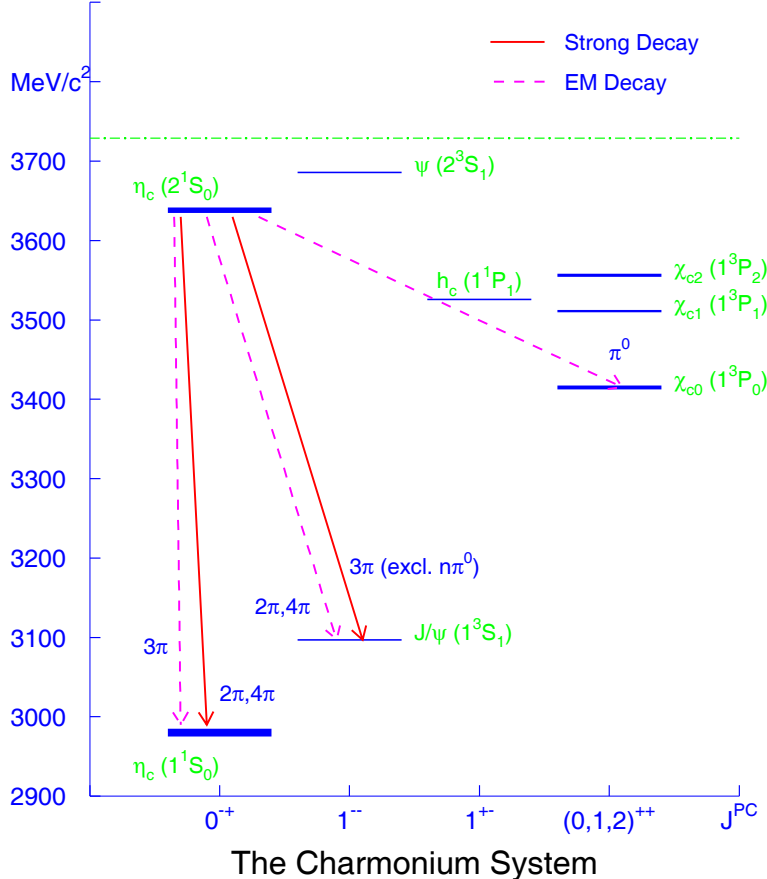


Figure 15.6: Hadronic transitions of  $\eta'_c$  to other charmonium states.

1.  $\eta'_c \rightarrow \eta_c + X$

The mass difference between  $\eta'_c$  and  $\eta_c$  is  $658 \text{ MeV}/c^2$ , which is greater than  $4m_\pi$  and  $m_\eta$ . The possible hadronic transitions are listed below.

- $\eta'_c \rightarrow \pi^0 \eta_c$ :  $P$ -violating, not allowed
- $\eta'_c \rightarrow \pi^+ \pi^- \eta_c$ : strong decays, via  $\sigma$

Voloshin [180] pointed out that this decay is related to the well studied  $\psi' \rightarrow \pi^+ \pi^- J/\psi$  transition, and estimated that the branching fraction could be around 5-10%, including the neutral  $\pi^0 \pi^0$  mode. No experimental information is currently available.

The study of this transition will very hard to do with  $\eta'_c$  mesons produced from radiative  $\psi'$  decays, since in this process the  $\eta'_c$  is produced with a very small

branching fraction and the photon energy is quite low, which makes it hard to distinguish from background.

- $\eta'_c \rightarrow \pi^0 \pi^0 \eta_c$ : strong decays, via  $\sigma$

This is similar to, but harder than, the detection of  $\eta'_c \rightarrow \pi^+ \pi^- \eta_c$  decays. Its observation will require the identification of multi-photons in the event.

- $\eta'_c \rightarrow \pi^+ \pi^- \pi^0 \eta_c$ :  $G$ -parity violating, EM decays only, also high orbital angular momentum

This probably will not be detectable at *BES-III*.

- $\eta'_c \rightarrow 3\pi^0 \eta_c$ :  $G$ -parity violating, EM decays only, high orbital angular momentum

This will also be unlikely to be detected at *BES-III*.

- $\eta'_c \rightarrow 2(\pi^+ \pi^-) \eta_c$ : strong decays

Here the phase space small and this may not be detected at *BES-III*.

- $\eta'_c \rightarrow \pi^+ \pi^- 2\pi^0 \eta_c$ : strong decays

This process has very small phase space and multiple low momentum charged and neutral pions. It is unlikely that it will be detected at *BES-III*.

- $\eta'_c \rightarrow 4\pi^0 \eta_c$ : strong decays

Here the phase space is small and there are numerous low-energy photons. It will not be detectable at *BES-III*.

- $\eta'_c \rightarrow \eta \eta_c$ :  $P$ -violating, not allowed

## 2. $\eta'_c \rightarrow J/\psi + X$

The mass difference between the  $\eta'_c$  and  $J/\psi$  is 541 MeV/ $c^2$ , which is slightly greater than  $4m_{\pi^0}$  and smaller than  $2(m_{\pi^+} + m_{\pi^-})$ . Considering the uncertainty of the  $\eta'_c$  mass is large and the width of  $\eta'_c$  is probably at the  $\sim 10$  MeV/ $c^2$  level, the high mass tail of the  $\eta'_c$  could, in principle, decay into  $2(\pi^+ \pi^-)J/\psi$ . All the possible combinations are listed below.

- $\eta'_c \rightarrow n\pi^0 J/\psi$ ,  $n = 1, 2, 3, 4$ :  $C$ -violating, not allowed
- $\eta'_c \rightarrow \pi^+ \pi^- J/\psi$ :  $G$ -parity violating, EM decays only, via  $\rho^*$
- $\eta'_c \rightarrow \pi^+ \pi^- \pi^0 J/\psi$ : strong decays, via  $\omega^*$
- $\eta'_c \rightarrow 2(\pi^+ \pi^-)J/\psi$ :  $G$ -parity violating, EM decays only, with very small phase space
- $\eta'_c \rightarrow \pi^+ \pi^- 2\pi^0 J/\psi$ :  $G$ -parity violating, EM decays only, with very small phase space

The detection of the above modes maybe a bit easier than the corresponding  $\eta'_c \rightarrow \eta_c$  transition modes since the  $J/\psi$  tag is much simpler, very narrow and quite distinct.

A naive estimate indicates that the rates for the  $\eta'_c \rightarrow J/\psi$  transition should be smaller than the  $\eta'_c \rightarrow \eta_c$  transitions, since the former requires a quark spin flip. There has been no serious theoretical effort expended on these estimations.

3.  $\eta'_c \rightarrow \chi_{cJ} + X$ 

The mass difference between the  $\eta'_c$  and  $\chi_{c0}$  is 223 MeV/ $c^2$ , slightly greater than  $m_{\pi^0}$ ; the mass difference between  $\eta'_c$  and  $\chi_{c1}$  is 128 MeV/ $c^2$ , and that between  $\eta'_c$  and  $\chi_{c2}$  is 82 MeV/ $c^2$ , smaller than  $m_{\pi^0}$ . The only possible transition is  $\eta'_c \rightarrow \pi^0 \chi_{c0}$ .

- $\eta'_c \rightarrow \pi^0 \chi_{c0}$ :  $G$ -parity violating, EM decays only

4.  $\eta'_c \rightarrow h_c(^1P_1) + X$ 

The mass difference between the  $\eta'_c$  and  $h_c(^1P_1)$  is 112 MeV/ $c^2$ , smaller than  $m_{\pi^0}$ . No hadronic transitions are allowed.

 $h_c(^1P_1)$  decays

The mass difference between the  $h_c(^1P_1)$  and many of the charmonium states are also much larger than one  $\pi$  mass, thus there are many possible transitions. All the allowed hadronic transitions are indicated in Fig. 15.7 and discussed below.

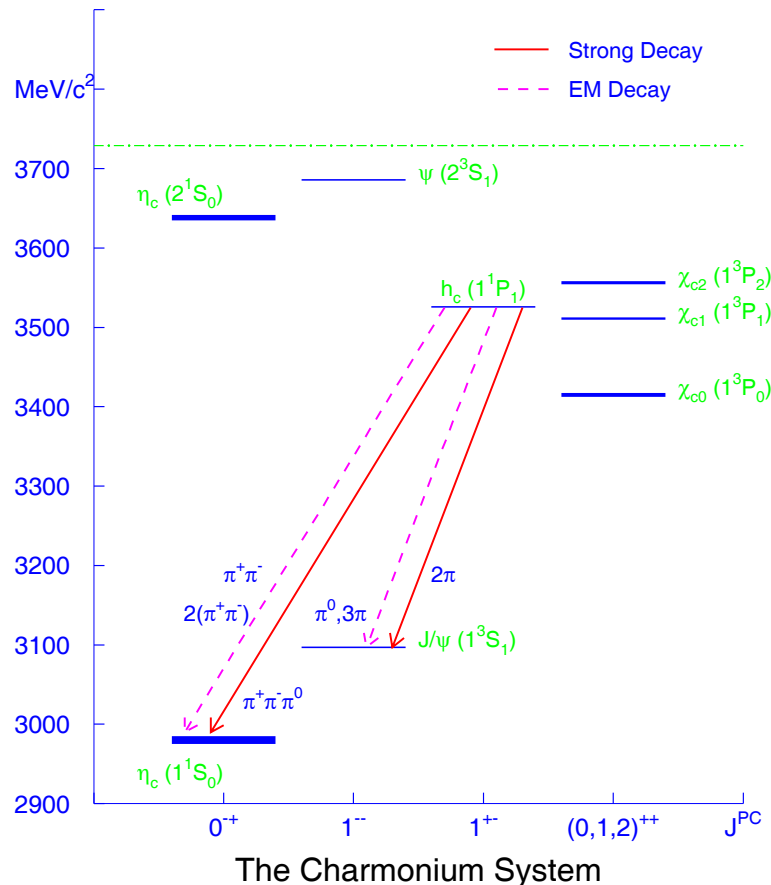


Figure 15.7: Hadronic transitions of  $h_c(^1P_1)$  to other charmonium states.

1.  $h_c(^1P_1) \rightarrow \eta_c + X$

The mass difference between the  $h_c(^1P_1)$  and  $\eta_c$  is  $546$  MeV/ $c^2$ , which is greater than  $4m_\pi$  and about the same as  $m_\eta$ . All possible hadronic transitions are listed below.

- $h_c(^1P_1) \rightarrow n\pi^0\eta_c$ ,  $n = 1, 2, 3, 4$ :  $C$ -violating, not allowed
- $h_c(^1P_1) \rightarrow \pi^+\pi^-\eta_c$ :  $G$ -parity violating, EM decays only, via  $\rho^*$
- $h_c(^1P_1) \rightarrow \pi^+\pi^-\pi^0\eta_c$ : strong decays, via  $\omega^*$
- $h_c(^1P_1) \rightarrow 2(\pi^+\pi^-)\eta_c$ :  $G$ -parity violating, EM decays only
- $h_c(^1P_1) \rightarrow \eta\eta_c$ :  $C$ -violating, not allowed

$h_c(^1P_1) \rightarrow \pi^+\pi^-\eta_c$  and  $h_c(^1P_1) \rightarrow \pi^+\pi^-\pi^0\eta_c$  should be looked for experimentally,  $h_c(^1P_1) \rightarrow 2(\pi^+\pi^-)\eta_c$  rate may be too small to be detectable at *BES-III*.

### 2. $h_c(^1P_1) \rightarrow J/\psi + X$

The mass difference between the  $h_c(^1P_1)$  and  $J/\psi$  is  $429$  MeV/ $c^2$ , greater than  $3m_{\pi^0}$ . All possible hadronic transitions are listed below.

There is no experimental information currently available, neither are there any theoretical calculations.

- $h_c(^1P_1) \rightarrow \pi^0J/\psi$ :  $G$ -parity violating, EM decays only
- $h_c(^1P_1) \rightarrow \pi^+\pi^-J/\psi$ : strong decays, via  $\sigma$
- $h_c(^1P_1) \rightarrow \pi^0\pi^0J/\psi$ : strong decays, via  $\sigma$
- $h_c(^1P_1) \rightarrow \pi^+\pi^-\pi^0J/\psi$ :  $G$ -parity violating, EM decays only
- $h_c(^1P_1) \rightarrow 3\pi^0J/\psi$ :  $G$ -parity violating, EM decays only

### 3. $h_c(^1P_1) \rightarrow \chi_{c0} + X$

The mass difference between the  $h_c(^1P_1)$  and  $\chi_{c0}$  is  $111$  MeV/ $c^2$ , smaller than  $m_{\pi^0}$ . There are no kinematically allowed hadronic transitions.

## $\chi_{c2}$ decays

The mass difference between the  $\chi_{c2}$  and many of the charmonium states are also much larger than one  $\pi$  mass. Thus there are many possible hadronic transitions. All of the possible transitions are indicated in Fig. 15.8 and discussed below.

### 1. $\chi_{c2} \rightarrow \eta_c + X$

The mass difference between the  $\chi_{c2}$  and  $\eta_c$  is  $576$  MeV/ $c^2$ , greater than  $4m_\pi$  and  $m_\eta$ , all the possible hadronic transitions are listed below.

- $\chi_{c2} \rightarrow \pi^0\eta_c$ :  $G$ -parity violating, EM decays only
- $\chi_{c2} \rightarrow \pi^+\pi^-\eta_c$ : Strong decays, high orbital angular momentum
- $\chi_{c2} \rightarrow \pi^0\pi^0\eta_c$ : Strong decays, high orbital angular momentum
- $\chi_{c2} \rightarrow \pi^+\pi^-\pi^0\eta_c$ :  $G$ -parity violating, EM decays only

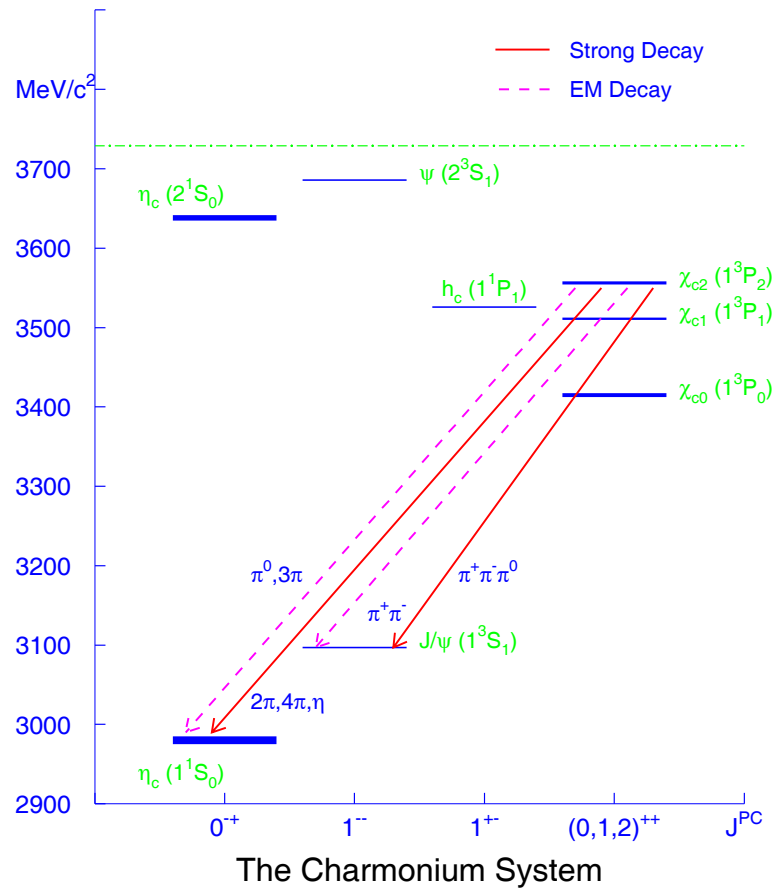


Figure 15.8: Hadronic transitions of  $\chi_{c2}$  to other charmonium states.

- $\chi_{c2} \rightarrow 3\pi^0\eta_c$ :  $G$ -parity violating, EM decays only
- $\chi_{c2} \rightarrow 2(\pi^+\pi^-)\eta_c$ : strong decays, but the phase space is very small and orbital angular momentum very high
- $\chi_{c2} \rightarrow \pi^+\pi^-2\pi^0\eta_c$ : strong decays, phase space very small, orbital angular momentum very high
- $\chi_{c2} \rightarrow 4\pi^0\eta_c$ : strong decays, with small phase space and high orbital angular momentum
- $\chi_{c2} \rightarrow \eta\eta_c$ : strong decays, but with small phase space

### 2. $\chi_{c2} \rightarrow J/\psi + X$

The mass difference between the  $\chi_{c2}$  and  $J/\psi$  is  $459 \text{ MeV}/c^2$ , slightly greater than  $3m_\pi$ . All possible hadronic transitions are listed below.

- $\chi_{c2} \rightarrow n\pi^0J/\psi$ ,  $n = 1, 2, 3$ :  $C$ -violating, not allowed
- $\chi_{c2} \rightarrow \pi^+\pi^-J/\psi$ :  $G$ -parity violating, EM decays only, via  $\rho^*$
- $\chi_{c2} \rightarrow \pi^+\pi^-\pi^0J/\psi$ : strong decays, via  $\omega^*$

### 3. $\chi_{c2} \rightarrow \chi_{c0} + X$ , $\chi_{c1} + X$

The mass difference between the  $\chi_{c2}$  and  $\chi_{c0}$  is  $141 \text{ MeV}/c^2$ , slightly greater than  $m_{\pi^0}$ ; the mass difference between  $\chi_{c2}$  and  $\chi_{c1}$  is  $46 \text{ MeV}/c^2$ , smaller than  $m_{\pi^0}$ . The only possible hadronic transition is  $\chi_{c2} \rightarrow \pi^0\chi_{c0}$ .

- $\chi_{c2} \rightarrow \pi^0\chi_{c0}$ :  $P$ -violating, not allowed

### 4. $\chi_{c2} \rightarrow h_c(^1P_1) + X$

The mass difference between the  $\chi_{c2}$  and  $h_c(^1P_1)$  is  $30 \text{ MeV}/c^2$ , smaller than  $m_{\pi^0}$ . There are no kinematically allowed hadronic transitions.

## $\chi_{c1}$ decays

The mass difference between the  $\chi_{c1}$  and many of the charmonium states are also much larger than one  $\pi$  mass. Thus, there are many possible transitions. All the allowed transitions are indicated in Fig. 15.9 and discussed below.

### 1. $\chi_{c1} \rightarrow \eta_c + X$

The mass difference between the  $\chi_{c1}$  and  $\eta_c$  is  $531 \text{ MeV}/c^2$ , greater than  $3m_\pi$ , all the possible transitions are listed below.

- $\chi_{c1} \rightarrow \pi^0\eta_c$ :  $P$ -violating, not allowed
  - $\chi_{c1} \rightarrow \pi^+\pi^-\eta_c$ : strong decays, via  $\sigma$
- A very rough measurement at BESII showed that it was not observable using the BESII data sample.
- $\chi_{c1} \rightarrow \pi^0\pi^0\eta_c$ : strong decays, via  $\sigma$

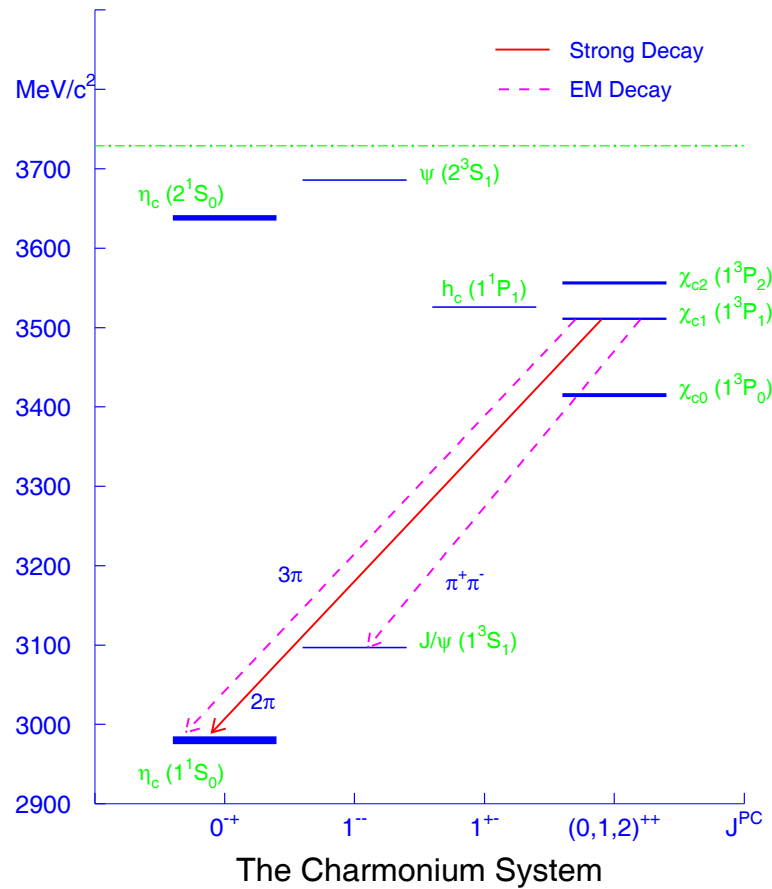


Figure 15.9: Hadronic transitions of  $\chi_{c1}$  to other charmonium states.

- $\chi_{c1} \rightarrow \pi^+ \pi^- \pi^0 \eta_c$ :  $G$ -parity violating, EM decays only
- $\chi_{c1} \rightarrow 3\pi^0 \eta_c$ :  $G$ -parity violating, EM decays only

### 2. $\chi_{c1} \rightarrow J/\psi + X$

The mass difference between the  $\chi_{c1}$  and  $J/\psi$  is  $413 \text{ MeV}/c^2$ , slightly greater than  $3m_{\pi^0}$  and smaller than  $m_{\pi^+} + m_{\pi^-} + m_{\pi^0}$  by  $2 \text{ MeV}/c^2$ . All the possible transitions are listed below.

- $\chi_{c1} \rightarrow n\pi^0 J/\psi$ ,  $n = 1, 2, 3$ :  $C$ -violating, not allowed
- $\chi_{c1} \rightarrow \pi^+ \pi^- J/\psi$ :  $G$ -parity violating, EM decays only, via  $\rho^*$
- $\chi_{c1} \rightarrow \pi^+ \pi^- \pi^0 J/\psi$ : no phase space

### 3. $\chi_{c1} \rightarrow \chi_{c0} + X$

The mass difference between the  $\chi_{c1}$  and  $\chi_{c0}$  is  $95 \text{ MeV}/c^2$ , smaller than  $m_{\pi^0}$ . There are no kinematically allowed hadronic transitions.

## $\chi_{c0}$ decays

The mass difference between the  $\chi_{c0}$  and many of the charmonium states are also much larger than one  $\pi$  mass, thus there are many possible transitions. All the allowed transitions are indicated in Fig. 15.10 and discussed below.

### 1. $\chi_{c0} \rightarrow \eta_c + X$

The mass difference between the  $\chi_{c0}$  and  $\eta_c$  is  $435 \text{ MeV}/c^2$ , greater than  $3m_\pi$ , all the possible hadronic transitions are listed below.

- $\chi_{c0} \rightarrow \pi^0 \eta_c$ :  $G$ -parity violating, EM decays only
- $\chi_{c0} \rightarrow \pi^+ \pi^- \eta_c$ :  $P$ -violating, not allowed
- $\chi_{c0} \rightarrow \pi^0 \pi^0 \eta_c$ :  $P$ -violating, not allowed
- $\chi_{c0} \rightarrow \pi^+ \pi^- \pi^0 \eta_c$ :  $G$ -parity violating, EM decays only
- $\chi_{c0} \rightarrow 3\pi^0 \eta_c$ :  $G$ -parity violating, EM decays only

### 2. $\chi_{c0} \rightarrow J/\psi + X$

The mass difference between the  $\chi_{c0}$  and  $J/\psi$  is  $318 \text{ MeV}/c^2$ , slightly greater than  $2m_\pi$ . All the possible hadronic transitions are listed below.

- $\chi_{c0} \rightarrow n\pi^0 J/\psi$ ,  $n = 1, 2$ :  $C$ -violating, not allowed
- $\chi_{c0} \rightarrow \pi^+ \pi^- J/\psi$ :  $G$ -parity violating, EM decays only, via  $\rho^*$

### 15.3.4 Summary

In this section, we listed all the kinematically allowed transitions between the known charmonium states below the charm threshold, more studies are needed for a better understanding of these transitions.

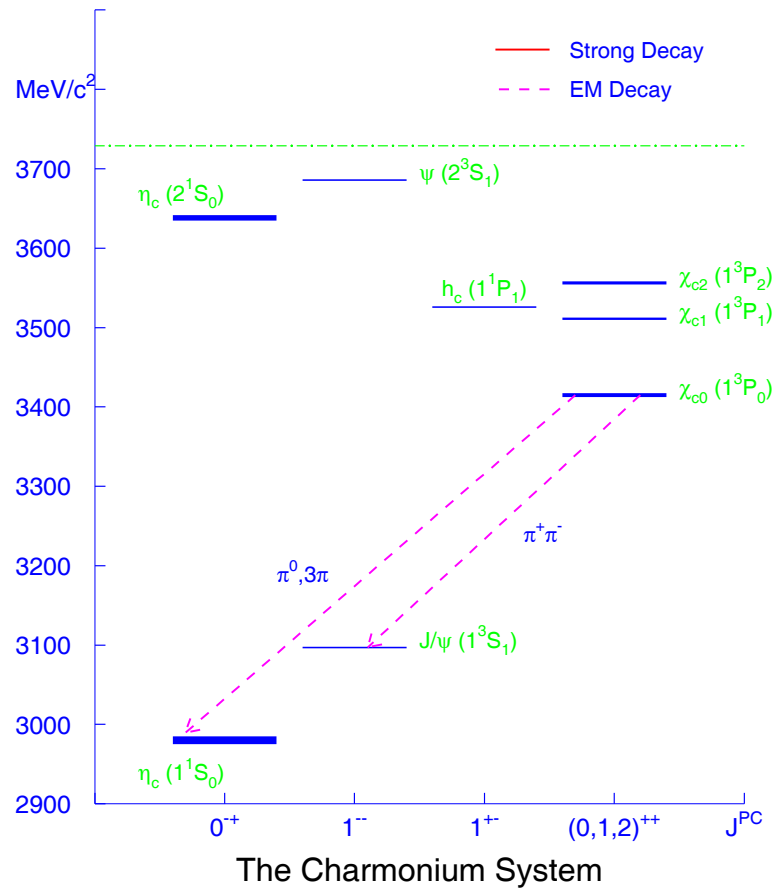


Figure 15.10: Hadronic transitions of  $\chi_{c0}$  to other charmonium states.

## 15.4 Monte Carlo simulation of spin-singlet charmonium states<sup>4</sup>

### 15.4.1 $\psi' \rightarrow \gamma\eta_c, \eta_c \rightarrow K_S^0 K\pi$

Using the BESIII Offline Software System (BOSS), a data sample of about 150,000 Monte Carlo simulated  $\psi' \rightarrow \gamma\eta_c, \eta_c \rightarrow K_S^0 K^\pm \pi^\mp$  events has been analyzed. In order to extract the  $\eta_c$  signal, two charged tracks with net charge zero and originating from the interaction region plus a  $K_S \rightarrow \pi^+\pi^-$  decay with a reconstructed secondary vertex are required. The photon candidate with highest energy is regarded as the radiative photon from the  $\psi'$ . The  $K_S$  selection includes the requirements  $m_{K_S} \in [0.44, 0.56] \text{ GeV}/c^2$  and  $\cos\theta > 0.9$ , where  $\theta$  is the angle between the radiative photon and the PMISS direction of the  $\eta_c \rightarrow K_S^0 K\pi$  candidate. Figure 15.4.1 shows the  $K_S K\pi$  invariant mass distribution, where the  $\eta_c$  signal is evident; a fit gives a mass resolution value of  $(6.78 \pm 0.05) \text{ MeV}/c^2$ . The output value of  $m_{\eta_c}$  from the fit to the reconstructed  $M_{K_S K\pi}$  peak is  $2979.94 \pm 0.06 \text{ MeV}/c^2$ . The difference from the input mass is  $\Delta m_{\eta_c} = (0.14 \pm 0.06) \text{ MeV}/c^2$ , thereby demonstrating that  $m_{\eta_c}$  can be correctly reconstructed in this channel. The detection efficiency based on these event selection requirements is  $(14.60 \pm 0.07)\%$ , where uniform angular distributions are assumed. The detection efficiency is presumed to be smaller if more realistic angular distributions are considered. Using the branching fractions of  $\psi' \rightarrow \gamma\eta_c$  and  $\eta_c \rightarrow K_S^0 K^\pm \pi^\mp$  [52], and assuming a detection efficiency of 10%, 1800  $\eta_c$  signal signal events are expected to be observed in a  $3 \times 10^8 \psi'$  event sample (which could be collected within about 0.1 year of BESIII operation).

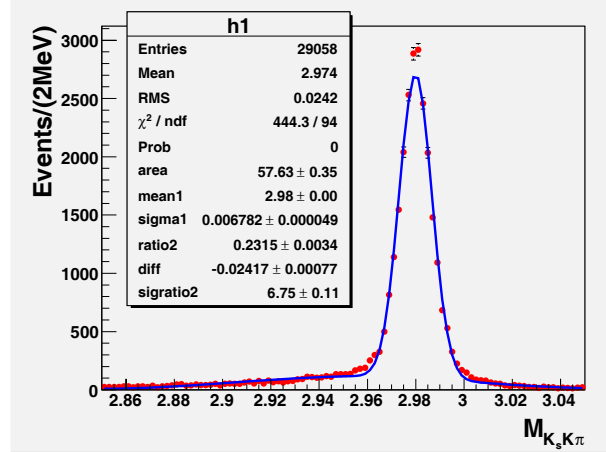


Figure 15.11: The  $K_S K\pi$  invariant mass distribution in the  $\eta_c$  mass region. The distribution is fitted using a double Gaussian function.

### 15.4.2 $\psi' \rightarrow \gamma\eta'_c, \eta'_c \rightarrow K_S^0 K\pi$

About 150,000 Monte Carlo simulated  $\psi' \rightarrow \gamma\eta'_c, \eta'_c \rightarrow K_S^0 K^\pm \pi^\mp$  events are analyzed. The same selection criteria as those used in analysis of  $\psi' \rightarrow \gamma\eta_c$  are applied to the recon-

<sup>4</sup>By Haixuan Chen

structed data and the resulting  $K_SK\pi$  invariant mass distribution is shown in Fig. 15.4.2. An  $\eta'_c$  signal with a mass resolution of  $(9.64 \pm 0.11)$  MeV/ $c^2$  is evident. The output value of  $m_{\eta'_c}$  from a fit is  $3628.41 \pm 0.11$  MeV/ $c^2$ , which corresponds to an input-output mass difference of  $\Delta m_{\eta'_c} = (0.41 \pm 0.11)$  MeV/ $c^2$ . This means that  $m_{\eta'_c}$  can also be reconstructed correctly. The detection efficiency based on these event selection criteria is  $(8.03 \pm 0.11)\%$  where uniform angular distributions are assumed. The detection efficiency is expected to be smaller for more realistic angular distributions. Assuming a detection efficiency of 5%, about 900  $\eta'_c \rightarrow K_SK\pi$  signal events are expected to be observed in a  $3 \times 10^9 \psi'$  event sample.

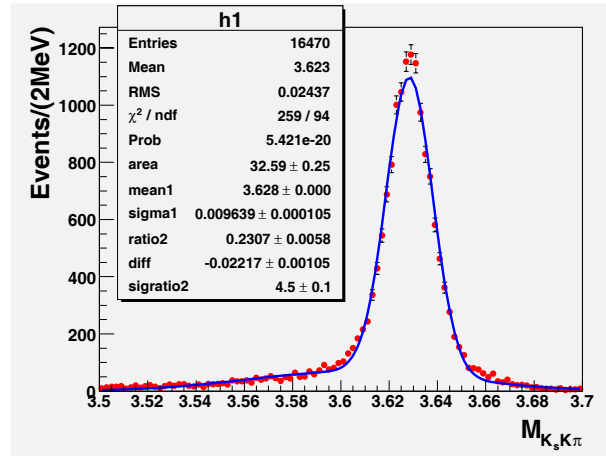


Figure 15.12: The  $K_SK\pi$  invariant mass distribution in the  $\eta'_c$  mass region. The distribution is fitted with a double Gaussian.

### 15.4.3 $\psi' \rightarrow \pi^0 h_c, h_c \rightarrow \gamma\eta_c, \eta_c \rightarrow K_S^0 K\pi$

About 50,000 Monte Carlo simulated events of the type  $\psi' \rightarrow \pi^0 h_c, h_c \rightarrow \gamma\eta_c, \eta_c \rightarrow K_S^0 K\pi^\pm$  are analyzed. For the event selection, two charged tracks with net charge zero and originating from the interaction region plus a  $K_S \rightarrow \pi^+\pi^-$  candidate with a reconstructed secondary vertex are required. At least three photon candidates are required in each event and the photon candidate with highest energy is regarded as the radiative photon from the  $h_c \rightarrow \eta_c$  transition. The two-photon combination with smallest  $|m_{\gamma\gamma} - m_{\pi^0}|$  value are regarded as the candidate  $\pi^0$ . The  $K_S$  selection includes the requirement  $m_{K_S} \in [0.44, 0.56]$  GeV/ $c^2$ . The  $\eta_c \rightarrow K_SK\pi$  signal requirements are  $m_{K_SK\pi} \in [2.6, 3.4]$  GeV/ $c^2$  and  $\cos\theta > 0.95$ , where  $\theta$  is the angle between the radiative photon from the  $h_c \rightarrow \gamma\eta_c$  decay and the PMISS direction of the candidate  $\eta_c \rightarrow K_S^0 K\pi$  track combination. The resulting invariant mass distribution of  $\gamma K_SK\pi$  is shown in Fig. 15.4.3. An  $h_c$  signal is observed with a resolution of  $(11.3 \pm 0.6)$  MeV/ $c^2$ . The output value of  $m_{h_c}$  from the fit to the peak is  $3528.1 \pm 0.7$  MeV/ $c^2$ , which corresponds to an input-output difference of  $\Delta m_{h_c} = (2.0 \pm 0.7)$  MeV/ $c^2$ . This indicates that  $m_{h_c}$  is not reconstructed perfectly in this mode, presumably because of the presence of three relatively low energy photons. A possible reason is that the current version of BOSS's modeling and reconstruction of the photon energy is not very accurate and this results in a systematic error in the final result. The detection efficiency for these event selection

criteria is  $(8.71 \pm 0.33)\%$ , where uniform angular distributions are assumed. The detection efficiency is expected to be smaller for more realistic angular distributions. Assuming a detection efficiency of 5%, an  $h_c \rightarrow \gamma\eta_c$ ,  $\eta_c \rightarrow K_SK\pi$  signal of about 450 detected events is expected in a  $3 \times 10^9 \psi'$  event sample.

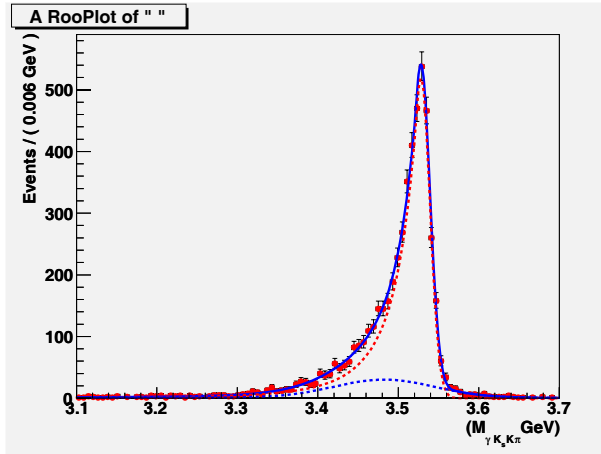


Figure 15.13: Invariant mass distribution of  $M_{\gamma K_SK\pi}$  in the  $h_c$  mass region. The distribution is fitted using a CB function plus double Gaussian.

# Chapter 16

## Charmonium Leptonic and EM Decays

### 16.1 Leptonic and EM Decays in Potential Models<sup>1</sup>

#### 16.1.1 $e^+e^-$ widths of $1^{--}$ states

Leptonic partial widths are immediately accessible at  $e^+e^-$  machines, and they provide interesting (and currently rather puzzling) information regarding the wavefunctions of  $1^{--}$  charmonium states. In the nonrelativistic limit of an S-wave quarkonium system the coupling to  $e^+e^-$  through a virtual photon involves the wavefunction at contact (the van Royen - Weisskopf formula); for an S-wave  $c\bar{c}$  system this partial width is given by [181],

$$\Gamma_{c\bar{c}}^{e^+e^-}(^3S_1) = \frac{16}{9} \alpha^2 \frac{|\psi(0)|^2}{M_{c\bar{c}}^2} \quad (16.1.1)$$

where the radial wavefunction is normalized to  $\int_0^\infty r^2 dr |\psi(r)|^2 = 1$ . For relativistic bound states the annihilation is nonlocal, so a nonvanishing  $e^+e^-$  coupling of D-wave (and higher-L  $1^{--}$  states) is also predicted. This width at leading nonrelativistic order is proportional to the  $L$ th derivative of the  $Q\bar{Q}$  wavefunction at contact, and for D-wave  $c\bar{c}$  states is given by

$$\Gamma_{c\bar{c}}^{e^+e^-}(^3D_1) = \frac{50}{9} \alpha^2 \frac{|\psi''(0)|^2}{M_{c\bar{c}}^2 m_c^4}. \quad (16.1.2)$$

This is typically much smaller than the leptonic widths of  $^3S_1$  states. Evaluating these widths using the nonrelativistic quark model wavefunctions described here gives the results quoted in Table 16.1.

Note that the agreement between the model and experiment is not especially good. This overestimate of the  $J/\psi$  leptonic width by roughly a factor of two seems to be a common difficulty in naive potential models, and may in part be due to the use of the nonrelativistic “wavefunction at contact” approximation for this decay rate. Non-valence components in the charmonium states, such as  $c\bar{c}g$  or D meson pairs from decay loops, may also contribute to this inaccuracy. Concerns have also been expressed that the leading-order QCD radiative corrections may be large [182], which could significantly reduce the

---

<sup>1</sup>By T. Barnes

Table 16.1: Predictions of a nonrelativistic  $c\bar{c}$  potential model for  $e^+e^-$  partial widths, together with current (2006) PDG experimental values [52].

State	Asst.	$\Gamma_{thy.}^{e^+e^-}$ (keV)	$\Gamma_{expt.}^{e^+e^-}$ (keV)
$J/\psi$	$1^3S_1$	12.13	$5.55 \pm 0.14 \pm 0.02$
$\psi'$	$2^3S_1$	5.03	$2.48 \pm 0.06$
$\psi(3770)$	$1^3D_1$	0.056	$0.242^{+0.027}_{-0.024}$
$\psi(4040)$	$3^3S_1$	3.48	$0.86 \pm 0.07$
$\psi(4160)$	$2^3D_1$	0.096	$0.83 \pm 0.07$
$\psi(4415)$	$4^3S_1$	2.63	$0.58 \pm 0.07$

overall scale of the leptonic widths. Of course the leading-order pQCD corrections are prescription-dependent, so it is not clear that this claim is reliable. In any case it is evident that a simple change of scale alone will not resolve the discrepancies in Table 16.1, since the nominally D-wave states  $\psi(3770)$  and  $\psi(4160)$  both have much larger couplings that would be expected for pure D-wave states.

The large experimental leptonic widths of the  $\psi(3770)$  and  $\psi(4160)$  relative to predictions for pure D-wave  $c\bar{c}$  states (see Table 16.1) may be due to admixtures of S-wave  $c\bar{c}$  components [166, 183]. As we shall discuss in the next section, these mixing angles can be estimated through measurements of the E1 radiative decay rates  $\psi(3770) \rightarrow \gamma\chi_2$  and (with more difficulty)  $\psi(4160) \rightarrow \gamma\chi_2$  and  $\gamma\chi_2'$ , since these transitions are very sensitive to the presence of S-wave  $c\bar{c}$  components. Radiative width ratios such as  $\Gamma(\psi(3770) \rightarrow \gamma\chi_2)/\Gamma(\psi(3770) \rightarrow \gamma\chi_1)$  and the leptonic width ratio  $\Gamma(\psi(3770) \rightarrow e^+e^-)/\Gamma(\psi' \rightarrow e^+e^-)$  provide two independent tests of S-D mixing.

At BES, in addition to testing the existing measurements of the leptonic widths of the vector states cited in Table 16.1, it will also be very important to determine the leptonic widths of new  $1^{--}$  hybrid candidates such as the  $Y(4260)$  (to be discussed in the section on hybrid charmonia). It has widely been anticipated that  $1^{--}$  hybrids should have suppressed leptonic widths relative to conventional S-wave  $1^{--}$  vector quarkonia; this may indeed be the case for the  $Y(4260)$ , since it is not apparent in the existing R measurements.

### 16.1.2 Two-photon couplings

Although BES will not have adequate  $\sqrt{s}$  to usefully exploit two-photon production of charmonium resonances, this has been a useful technique at higher-energy  $e^+e^-$  facilities, which we briefly mention here in the interest of completeness. This subject has been

reviewed elsewhere [105].

Two-photon resonance production involves the reaction  $e^+e^- \rightarrow e^+e^-R, R \rightarrow f$ , where  $R$  is a  $C = (+)$  meson resonance and  $f$  is the exclusive final state observed. This process proceeds dominantly through the two-photon coupling of the resonance,  $e^+e^- \rightarrow e^+e^-\gamma\gamma$ ,  $\gamma\gamma \rightarrow R$ , and hence implicitly gives the two-photon partial width  $\Gamma_{\gamma\gamma}(R)$  times the branching fraction  $B(R \rightarrow f)$ . One may also consider the case of one or both photons significantly off mass shell  $q_\gamma^2 \neq 0$ , which gives the generalized widths  $\Gamma_{\gamma^*\gamma}(R)$  and  $\Gamma_{\gamma^*\gamma^*}(R)$ . The interesting question for off-shell widths is whether they are given by a vector dominance formula with the mass of the relevant vector, in this case the  $J/\psi$ .

In the limit of large quark mass (and hence a zero-range charm quark propagator) the two-photon width of an S-wave charmonium state is proportional to the wavefunction at contact squared. In this approximation, higher-L states are produced with amplitudes proportional to the  $L^{th}$  derivative of the wavefunction at contact [66, 67]. (In practice the attractively simple contact approximation appears marginal at best at the  $c\bar{c}$  mass scale.) Both the  $\eta_c$  and  $\eta_c'$  have been seen in two-photon collisions; the  $\gamma\gamma$  width of the  $\eta_c$  is approximately 7 keV, comparable to quark model expectations. Two-photon production of the  $\eta_c'$  has been observed by CLEO-c [68], but the  $\eta_c' \rightarrow \gamma\gamma$  partial width is not known because experimentally one measures the  $\gamma\gamma$  width times the branching fraction to an exclusive final state, and the  $\eta_c'$  absolute branching fractions are not known.

Higher-L  $c\bar{c}$  two-photon widths are suppressed by the mass of the charm quark, and therefore are not very well established; only the P-wave  $\chi_0$  and  $\chi_2$  states and the  $2^3P_2$  candidate  $\chi_2(3929)$  have been observed. The theoretical ratio of P-wave  $\gamma\gamma$  widths within a multiplet (such as 1P or 2P) in the large quark mass limit is  $\Gamma_{\gamma\gamma}(^3P_0)/\Gamma_{\gamma\gamma}(^3P_2) = 15/4$ , however this may be modified significantly by QCD radiative corrections and finite quark mass effects. Nonrelativistically the  $\gamma\gamma$  state produced by the  $^3P_2$  should be pure helicity two; relativistic corrections are expected to give rise to a small helicity-zero  $\gamma\gamma$  component as well. Although one can in principle produce higher-L  $c\bar{c}$  states in  $\gamma\gamma$  collisions, in practice these rates fall rapidly with increasing L for  $c\bar{c}$  and heavier  $Q\bar{Q}$  systems. As an example, the two-photon width of a hypothetical  $^1D_2(3840)$   $c\bar{c}$  state is predicted to be only 20 eV [105].

### 16.1.3 QCD radiative and relativistic corrections to EM decays<sup>2</sup>

Table 16.2: Present PDG [184] values for the leptonic widths of the  $J/\psi$ ,  $\psi(2S)$ , and  $\psi(3770)$  states.

Resonance	$\Gamma_{\text{tot}}$ (keV)	$\Gamma_{ee}$ (keV)	$\mathcal{B}_{\mu\mu}(\%)$	$\mathcal{B}_{\tau\tau}(\%)$
$J/\psi$	$93.4 \pm 2.1$	$5.55 \pm 0.14 \pm 0.02$	$5.93 \pm 0.06$	—
$\psi(2S)$	$337 \pm 13$	$2.48 \pm 0.06$	$0.73 \pm 0.08$	$0.28 \pm 0.07$
$\psi(3770)$	$(23.0 \pm 2.7) \times 10^3$	$0.242^{+0.027}_{-0.024}$	—	—

<sup>2</sup>By Y.J. Zhang

Beyond the tree level result, QCD radiative and relativistic corrections in the electromagnetic decay of charmonium have been considered. The one-loop QCD radiative correction to the leptonic width of  $^3S_1$  states has been calculated in Refs.[185, 186]

$$\Gamma_{Q\bar{Q}}^{e^+e^-}(^3S_1) = e_Q^2 \alpha^2 \frac{|\psi(0)|^2}{m_Q^2} \left( 1 - \frac{16\alpha_s}{3\pi} \right). \quad (16.1.3)$$

where  $|\psi(0)|$  is the radial wavefunction at the origin, and it is normalized by  $\int r^2 |\psi(r)|^2 = 1$ . For  $m_e \ll m_c$  and  $m_\mu \ll m_c$ , the masses of leptons are ignored here.

The two-loop QCD correction has been given in Ref. [187], and these contributions lead to

$$\begin{aligned} \Gamma_{Q\bar{Q}}^{e^+e^-}(^3S_1) = & e_Q^2 \alpha^2 \frac{|\psi(0)|^2}{m_Q^2} \left\{ 1 - 4C_F \frac{\alpha_s(m)}{\pi} + \right. \\ & \left. \left[ -117.46 + 0.82n_f + \frac{140\pi^2}{27} \ln\left(\frac{2m}{\mu_\Lambda}\right) \right] \left(\frac{\alpha_s}{\pi}\right)^2 \right\}, \end{aligned} \quad (16.1.4)$$

where  $\alpha_s(m_c) \approx 0.35$  and  $\alpha_s(m_b) \approx 0.21$ .

Relativistic corrections to the leptonic width of  $^3S_1$  states have also been considered to  $\mathcal{O}(v^4)$ , and given in Ref.[188]:

$$\begin{aligned} \Gamma_{Q\bar{Q}}^{e^+e^-}(^3S_1) = & \frac{F_{ee}(^3S_1)}{m_Q^2} \left| \langle 0 | \chi^\dagger \boldsymbol{\sigma} \psi | ^3S_1 \rangle \right|^2 \\ & + \frac{G_{ee}(^3S_1)}{m_Q^4} \text{Re} \left[ \langle ^3S_1 | \psi^\dagger \boldsymbol{\sigma} \chi | 0 \rangle \cdot \langle 0 | \chi^\dagger \boldsymbol{\sigma} \left(-\frac{i}{2} \overleftrightarrow{\mathbf{D}}\right)^2 \psi | ^3S_1 \rangle \right] \\ & + \frac{H_{ee}^1(^3S_1)}{m_Q^6} \langle ^3S_1 | \psi^\dagger \boldsymbol{\sigma} \left(-\frac{i}{2} \overleftrightarrow{\mathbf{D}}\right)^2 \chi | 0 \rangle \cdot \langle 0 | \chi^\dagger \boldsymbol{\sigma} \left(-\frac{i}{2} \overleftrightarrow{\mathbf{D}}\right)^2 \psi | ^3S_1 \rangle \\ & + \frac{H_{ee}^2(^3S_1)}{m_Q^6} \text{Re} \left[ \langle ^3S_1 | \psi^\dagger \boldsymbol{\sigma} \chi | 0 \rangle \cdot \langle 0 | \chi^\dagger \boldsymbol{\sigma} \left(-\frac{i}{2} \overleftrightarrow{\mathbf{D}}\right)^4 \psi | ^3S_1 \rangle \right], \end{aligned} \quad (16.1.5)$$

where the short-distance coefficients at leading order in  $\alpha_s$  are

$$F_{ee}(^3S_1) = \frac{2\pi}{3} e_Q^2 \alpha^2, \quad (16.1.6)$$

$$G_{ee}(^3S_1) = -\frac{8\pi}{9} e_Q^2 \alpha^2, \quad (16.1.7)$$

$$H_{ee}^1(^3S_1) + H_{ee}^2(^3S_1) = \frac{58\pi}{54} e_Q^2 \alpha^2. \quad (16.1.8)$$

The relativistic leading-order matrix element  $\left| \langle 0 | \chi^\dagger \boldsymbol{\sigma} \psi | ^3S_1 \rangle \right|^2$  is related to the radial wavefunction at the origin by

$$\left| \langle 0 | \chi^\dagger \boldsymbol{\sigma} \psi | ^3S_1 \rangle \right|^2 = \frac{N_c}{2\pi} |\psi(0)|^2. \quad (16.1.9)$$

Relations of higher order matrix elements to leading-order matrix element  $\left| \langle 0 | \chi^\dagger \boldsymbol{\sigma} \psi | ^3S_1 \rangle \right|^2$  are

$$\mathcal{O}(v^2) \left| \langle 0 | \chi^\dagger \boldsymbol{\sigma} \psi | ^3S_1 \rangle \right|^2 \sim \langle ^3S_1 | \psi^\dagger \boldsymbol{\sigma} \chi | 0 \rangle \cdot \langle 0 | \chi^\dagger \boldsymbol{\sigma} \left(-\frac{i}{2} \overleftrightarrow{\mathbf{D}}\right)^2 \psi | ^3S_1 \rangle$$

$$\mathcal{O}(v^4) \left| \langle 0 | \chi^\dagger \boldsymbol{\sigma} \psi | {}^3S_1 \rangle \right|^2 \sim \langle {}^3S_1 | \psi^\dagger \boldsymbol{\sigma} \left( -\frac{i}{2} \overleftrightarrow{\mathbf{D}} \right)^2 \chi | 0 \rangle \cdot \langle 0 | \chi^\dagger \boldsymbol{\sigma} \left( -\frac{i}{2} \overleftrightarrow{\mathbf{D}} \right)^2 \psi | {}^3S_1 \rangle \\ \sim \langle {}^3S_1 | \psi^\dagger \boldsymbol{\sigma} \chi | 0 \rangle \cdot \langle 0 | \chi^\dagger \boldsymbol{\sigma} \left( -\frac{i}{2} \overleftrightarrow{\mathbf{D}} \right)^4 \psi | {}^3S_1 \rangle \quad (16.1.10)$$

Table 16.3: Present PDG [184] values for the two-photon widths of the  $\eta_c$ ,  $\chi_{c0}$ ,  $\chi_{c2}$ , and  $\eta'_c$  states.

Resonance	$\Gamma_{\text{tot}}$ (MeV)	$\Gamma_{\gamma\gamma}$ (keV)	$\mathcal{B}_{\gamma\gamma} \times 10^4$
$\eta_c$	$25.5 \pm 3.4$	$7.2 \pm 0.7 \pm 2.0$	$2.8 \pm 0.9$
$\chi_{c0}$	$10.4 \pm 0.7$	$2.87 \pm 0.39$	$2.76 \pm 0.33$
$\chi_{c2}$	$2.06 \pm 0.12$	$0.53 \pm 0.05$	$2.59 \pm 0.19$
$\eta'_c$	$14 \pm 4$	seen	seen

For the decay of  ${}^1S_0$  states into two photons, the one-loop QCD radiative correction is given in Refs. [189, 190]:

$$\Gamma_{Q\bar{Q}}^{\gamma\gamma}({}^1S_0) = 2\pi e_Q^4 \alpha^2 \left[ 1 + \left( \frac{\pi^2}{4} - 5 \right) C_F \frac{\alpha_s}{\pi} \right] \frac{\left| \langle 0 | \chi^\dagger \psi | {}^1S_0 \rangle \right|^2}{m_Q^2}. \quad (16.1.11)$$

And the relativistic leading-order matrix element  $\left| \langle 0 | \chi^\dagger \psi | {}^1S_0 \rangle \right|^2$  is related to the radial wavefunction at origin by

$$\left| \langle 0 | \chi^\dagger \psi | {}^1S_0 \rangle \right|^2 = \frac{N_c}{2\pi} |\psi(0)|^2. \quad (16.1.12)$$

The two-loop QCD radiative corrections are given in Ref. [191]:

$$\frac{\Gamma_{Q\bar{Q}}^{e^+e^-}({}^3S_1)}{\Gamma_{Q\bar{Q}}^{\gamma\gamma}({}^1S_0)} = \frac{1}{3e_Q^2} \left[ 1 - 0.62\alpha_s(m_Q) + \alpha_s(m_Q)^2 (2.37 \ln \alpha_s(m_Q) - 1.8) \right]. \quad (16.1.13)$$

Relativistic corrections to the two-photon width of  ${}^1S_0$  states have also been considered to  $\mathcal{O}(v^4)$ , and given in Ref.[188]:

$$\Gamma_{Q\bar{Q}}^{\gamma\gamma}({}^1S_0) = \frac{F_{\gamma\gamma}({}^1S_0)}{m_Q^2} \left| \langle 0 | \chi^\dagger \psi | {}^1S_0 \rangle \right|^2 \\ + \frac{G_{\gamma\gamma}({}^1S_0)}{m_Q^4} \text{Re} \left[ \langle {}^1S_0 | \psi^\dagger \chi | 0 \rangle \langle 0 | \chi^\dagger \left( -\frac{i}{2} \overleftrightarrow{\mathbf{D}} \right)^2 \psi | {}^1S_0 \rangle \right] \\ + \frac{H_{\gamma\gamma}^1({}^1S_0)}{m_Q^6} \langle {}^1S_0 | \psi^\dagger \left( -\frac{i}{2} \overleftrightarrow{\mathbf{D}} \right)^2 \chi | 0 \rangle \langle 0 | \chi^\dagger \left( -\frac{i}{2} \overleftrightarrow{\mathbf{D}} \right)^2 \psi | {}^1S_0 \rangle \\ + \frac{H_{\gamma\gamma}^2({}^1S_0)}{m_Q^6} \text{Re} \left[ \langle {}^1S_0 | \psi^\dagger \chi | 0 \rangle \langle 0 | \chi^\dagger \left( -\frac{i}{2} \overleftrightarrow{\mathbf{D}} \right)^4 \psi | {}^1S_0 \rangle \right], \quad (16.1.14)$$

where the short-distance coefficients at leading order in  $\alpha_s$  are

$$F_{\gamma\gamma}(^1S_0) = 2\pi e_Q^4 \alpha^2, \quad (16.1.15)$$

$$G_{\gamma\gamma}(^1S_0) = -\frac{8\pi e_Q^4}{3} \alpha^2, \quad (16.1.16)$$

$$H_{\gamma\gamma}^1(^1S_0) + H_{\gamma\gamma}^2(^1S_0) = \frac{136\pi}{45} e_Q^4 \alpha^2. \quad (16.1.17)$$

The relative orders of the matrix elements are similar to that for the  $^3S_1$  states.

The two-photon decay of the spin one state  $\chi_{c1}$  is forbidden by the Landau-Yang theorem [192, 193]. The one-loop QCD radiative corrections to the decays of  $^3P_0$  and  $^3P_2$  states into two photons are given in Refs. [194, 195, 196, 197, 198]:

$$\begin{aligned} \Gamma_{\chi_{c0}}^{\gamma\gamma} &= \frac{27e_Q^4 \alpha^2}{m^4} |R'_{\chi_{c0}}(0)|^2 \left[ 1 + \frac{\alpha_s}{\pi} \left( \frac{\pi^2}{3} - \frac{28}{9} \right) \right], \\ \Gamma_{\chi_{c2}}^{\gamma\gamma} &= \frac{36e_Q^4 \alpha^2}{5m^4} |R'_{\chi_{c2}}(0)|^2 \left( 1 - \frac{\alpha_s}{\pi} \frac{16}{3} \right). \end{aligned} \quad (16.1.18)$$

The current PDG values are [184]  $\Gamma_{\chi_{c0}}^{\gamma\gamma} = (2.87 \pm 0.39)$  keV,  $\Gamma_{\chi_{c2}}^{\gamma\gamma} = (0.53 \pm 0.05)$  keV, then we can get  $\mathcal{R} \equiv \Gamma_{\chi_{c2}}^{\gamma\gamma}/\Gamma_{\chi_{c0}}^{\gamma\gamma} = 0.186 \pm 0.02$ . Recently it is given by the CLEO Collaboration that  $\Gamma_{\chi_{c0}}^{\gamma\gamma} = (2.53 \pm 0.37 \pm 0.26)$  keV,  $\Gamma_{\chi_{c2}}^{\gamma\gamma} = (0.60 \pm 0.06 \pm 0.06)$  keV, and then  $\mathcal{R} = 0.237 \pm 0.043 \pm 0.034$ . [199]. From Eq.(16.1.18),  $\mathcal{R} = 4/15 \sim 0.267$  at leading-order in  $\alpha_s$  and  $4/15(1 - 1.76\alpha_s) \sim 0.149$  at next to leading-order in  $\alpha_s$  can be obtained.

The value of  $|R'_{\chi_{c2}}(0)|^2$  may be calculated using potential models, and then the two-photon widths and  $\mathcal{R}$  can be estimated with Eq.(16.1.18). The theoretical predictions for two-photon widths of  $\chi_{c2}$  and  $\chi_{c0}$  and the ratio  $\mathcal{R}$  derived from them are listed in Table.16.4.

Table 16.4: Potential model predictions for the two-photon widths of  $\chi_{c2}$  and  $\chi_{c0}$  and the ratio  $\mathcal{R}$  derived from them. They are cited from Ref. [199]

Reference	$\Gamma_{\gamma\gamma}(\chi_{c2})$ (eV)	$\Gamma_{\gamma\gamma}(\chi_{c0})$ (eV)	$\mathcal{R}$
Barbieri [200]	930	3500	0.27
Godfrey [201]	459	1290	0.36
Barnes [202]	560	1560	0.36
Bodwin [203]	$820 \pm 230$	$6700 \pm 2800$	$0.12_{-0.06}^{+0.15}$
Gupta [204]	570	6380	0.09
Münz [205]	$440 \pm 140$	$1390 \pm 160$	$0.32_{-0.12}^{+0.16}$
Huang [195]	$490 \pm 150$	$3720 \pm 1100$	$0.13_{-0.06}^{+0.11}$
Ebert [206]	500	2900	0.17
Schuler [207]	280	2500	0.11

## 16.2 Leptonic and EM Decays in Effective Field Theories<sup>3</sup>

### 16.2.1 Introduction

The use of effective field theories allows one to tackle the computation of heavy quarkonium observables directly from QCD. The effective field theories available for the study of these systems are NRQCD [2, 4] and pNRQCD [5, 6, 18]. They profit from the fact that a dimensionless variable (the relative velocity between the quark and antiquark),  $v \ll 1$ , appears and that the mass,  $m_Q$ , of the heavy quark is much larger than  $\Lambda_{\text{QCD}}$ . Therefore, a bunch of inequalities between the different physical scales appearing in the system show up and effective field theories are specially suitable to take profit of them. The most obvious inequalities we have are  $m_Q \gg m_Q v \gg m_Q v^2$  and  $m_Q \gg \Lambda_{\text{QCD}}$ , though some others may arise in some specific cases as we will discuss next.

Trying to get a further understanding on the dynamics of the heavy quarkonium one can distinguish between the weak and strong coupling regime. In short, we will denote by weak coupling regime the situation where the soft scale,  $m_Q v$ , is much larger than  $\Lambda_{\text{QCD}}$  and the strong coupling regime the situation when  $m_Q v \sim \Lambda_{\text{QCD}}$ . To discern to which regime each bottomonium and charmonium state belongs to is one of main open questions in heavy quarkonium physics. Whereas there is certain consensus that the bottomonium ground state belongs to the weak coupling regime [39, 32, 33, 36, 208, 209]. The situation is not that clear for higher excitations of bottomonium and for charmonium. There are different claims by different groups. To illustrate the point, we can find the evaluations in Refs. [39, 33] where they perform a weak coupling analysis for the first two states of charmonium and for the first three states of bottomonium claiming that a reasonable description can be obtained with perturbation theory. On the other hand there is the analysis of Ref. [209], where they claim that no convergence is found in the perturbative series for these states. It should be mentioned that different renormalon subtraction schemes has been used in both approaches. It would be welcome to see how things work out in other schemes. Another point that should be stressed is that these analysis mainly focussed on the determination of the heavy quarkonium spectrum. However, if a given state belongs to the weak or strong coupling regime should also be reflected in other observables of these states. In particular this should happen for the inclusive electromagnetic decays, being among the cleanest observables one can think of. However, the situation for the inclusive electromagnetic decays is quite less clear. The convergence of the perturbative series is much worse than in the spectrum (actually this has some side effects in finite order computation of heavy quarkonium sum rules). A detailed discussion can be found in Ref. [210]. Note that this bad convergence also affects to the bottomonium ground state, not to mention higher excitations or charmonium. Therefore, before making clear cut statements upon whether one state belongs to the weak or strong coupling regime the situation of the inclusive electromagnetic decay widths should be clarified.

Another aspect that should be mentioned is that finite order theoretical evaluations of the inclusive electromagnetic decay widths appear to be very scale dependent. At this respect the use of renormalization group techniques [211] have shown itself to be a conve-

---

<sup>3</sup>By A. Pineda

nient tool to reduce the scale dependence of bottomonium and charmonium observables [212, 213, 38, 210].

In the next section we elaborate in somewhat more detail upon the above discussion.

### 16.2.2 Weak coupling regime

In the weak coupling regime the inclusive electromagnetic decay widths read

$$\Gamma(\Upsilon(nS) \rightarrow e^+ e^-) = 16\pi \frac{C_A}{3} \left[ \frac{\alpha_{EM} e_Q}{M_{\Upsilon(nS)}} \right]^2 \left| \phi_n^{(s=1)}(\mathbf{0}) \right|^2 \left\{ c_1 - d_1 \frac{M_{\Upsilon(nS)} - 2m_Q}{6m_Q} \right\}^2 \quad (16.2.19)$$

$$\Gamma(\eta_b(nS) \rightarrow \gamma\gamma) = 16\pi C_A \left[ \frac{\alpha_{EM} e_Q^2}{M_{\eta_b(nS)}} \right]^2 \left| \phi_n^{(s=0)}(\mathbf{0}) \right|^2 \left\{ c_0 - d_0 \frac{M_{\eta_b(nS)} - 2m_Q}{6m_Q} \right\}^2 \quad (16.2.20)$$

The coefficients  $c_{0,1}$  are known with two loop accuracy [214, 215, 216, 217, 218].  $d_0 = d_1 = 1$  at lowest order. The wave function corrections are also known with two-loop accuracy. The corrections to the wave function at the origin are obtained by taking the residue of the Green function at the position of the poles

$$\left| \phi_n^{(s)}(\mathbf{0}) \right|^2 = \left| \phi_n^{(0)}(\mathbf{0}) \right|^2 (1 + \delta\phi_n^{(s)}) = \underset{E=E_n}{\text{Res}} G_s(\mathbf{0}, \mathbf{0}; E), \quad (16.2.21)$$

where the LO wave function is given by

$$\left| \phi_n^{(0)}(\mathbf{0}) \right|^2 = \frac{1}{\pi} \left( \frac{m_Q C_F \alpha_s}{2n} \right)^3. \quad (16.2.22)$$

The corrections to  $\delta\phi_n^{(s)}$  produced by  $\delta V$  have been calculated with NNLO accuracy [219, 220] in the direct matching scheme. One can also obtain them in the dimensional regularized  $\overline{\text{MS}}$  scheme with NNLL accuracy by incorporating the renormalization group improved matching coefficients [210]. Also a partial evaluation of the matching coefficients at NNLL is available [38, 210], see also [221, 211, 222]. Therefore, the complete NNLO result for the decay is at present available as well as a partial evaluation with NNLL accuracy. One may try then to apply these results to charmonium and bottomonium decay widths.

The results for the vector and pseudoscalar bottomonium ground state decay can be found in Figs. 16.1 and 16.2 respectively. One problem is the large magnitude of the two loop correction to the matching coefficient of the electromagnetic current. This is puzzling from the theoretical point of view, since the hard scale should be perturbative in nature. On the other hand one may argue that the result for the matching coefficient is scheme dependent and that a better convergence is expected for the full result where the scheme dependence disappears. This is actually not so as we show in Figs. 16.1 and 16.2, which we take from Ref. [210]. One can discuss whether the charm quark mass is large enough but the convergence problem also appears in the case of bottomonium. This may point out to the fact that this convergence problem is fake. One may try to introduce renormalization group techniques. This significantly diminishes the scale dependence of the theoretical prediction and improves the convergence of the series, yet, the absolute

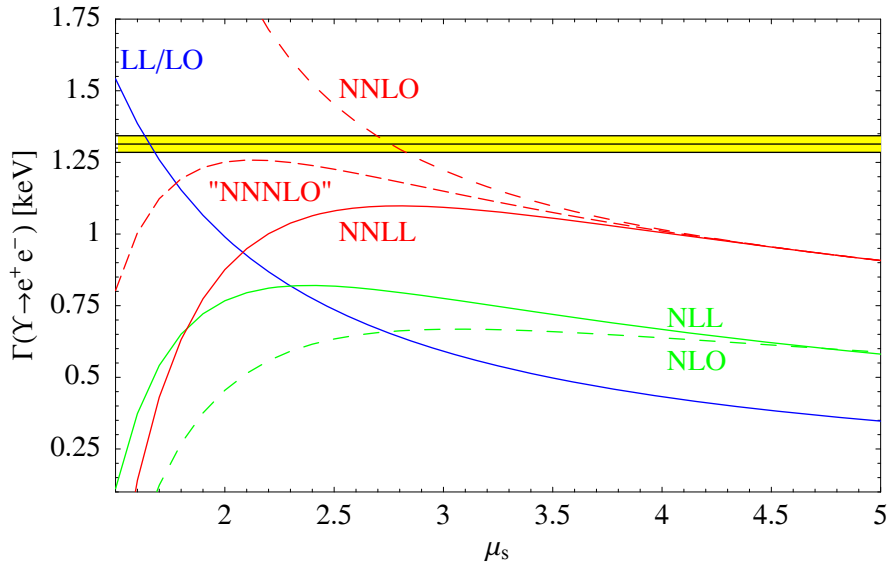


Figure 16.1: Prediction for the  $\Upsilon(1S)$  decay rate to  $e^+e^-$ . We work in the RS' scheme. Figure from Ref. [210].

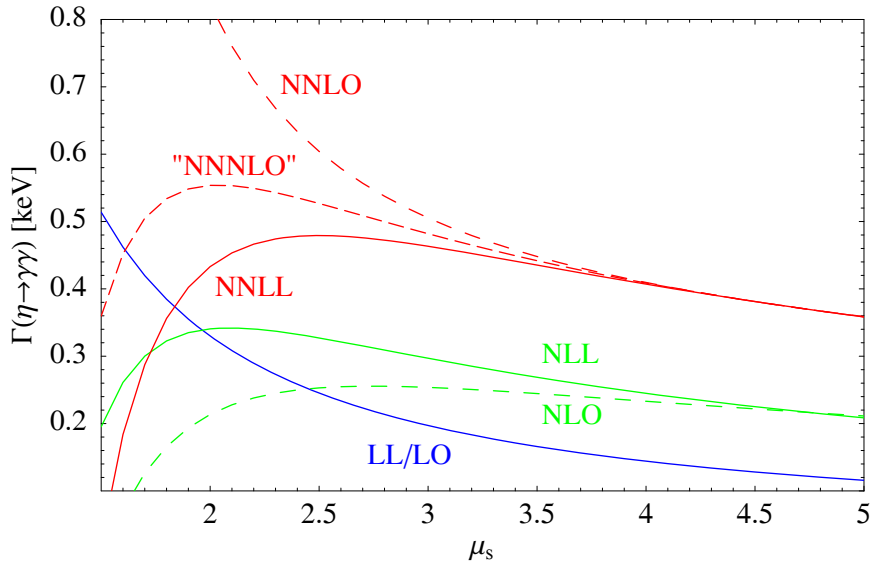


Figure 16.2: Prediction for the  $\eta_b(1S)$  decay rate to two photons. We work in the RS' scheme. Figure from Ref. [210].

magnitude of the correction is large. From the numerical analysis, we find that the NNLL corrections are huge, especially for the  $\eta_b(1S) \rightarrow \gamma\gamma$  decay. The result we obtain for this decay is compatible with the number obtained in Ref. [213]. This is somewhat reassuring, since in that reference the ratio of the spin-one spin-zero decay was considered, which was much more scale independent, as well as more convergent (yet still large) than for each of the decays themselves. This agreement can be traced back to the fact that, for the spin-one decay, for which we can compare with experiment, we find that the NNLL result

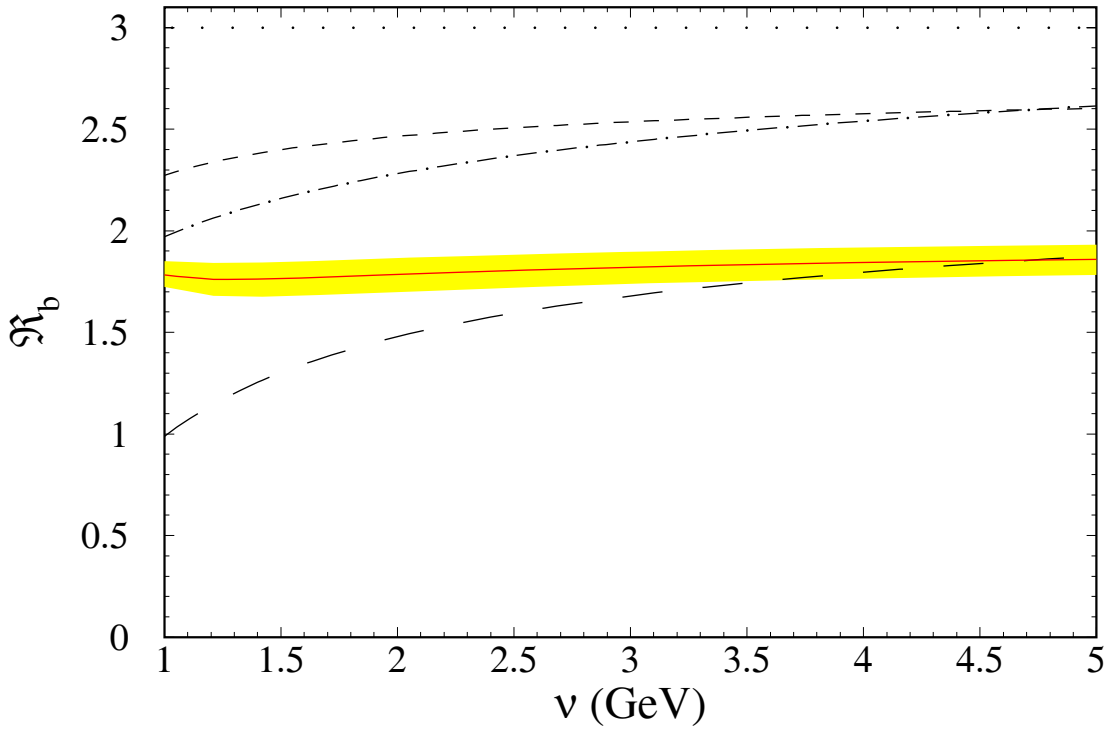


Figure 16.3: The spin ratio as the function of the renormalization scale  $\nu$  in  $\text{LO} \equiv \text{LL}$  (dotted line), NLO (short-dashed line), NNLO (long-dashed line), NLL (dot-dashed line), and NNLL (solid line) approximation for the bottomonium ground state with  $\nu_h = m_b$ . For the NNLL result the band reflects the errors due to  $\alpha_s(M_Z) = 0.118 \pm 0.003$ . Figure from Ref. [213].

improves the agreement with the data. Overall, the resummation of logarithms always significantly improves over the NNLO result, the scale dependence greatly improves, as well as the convergence of the series. On the other hand the problem of lack of convergence of the perturbative series is not really solved by the resummation of logarithms and it remains as an open issue. Due to the lack of convergence no numbers or errors are given. In this respect we can not avoid to mention that, whereas the perturbative series in non-relativistic sum rules is sign-alternating, is not sign-alternating for the electromagnetic decays. Finally, we would also like to remark the strong scale dependence that we observe at low scales, which we believe to have the same origin than the one observed in  $t\bar{t}$  production near threshold in Ref. [210].

One may argue that maybe considering the ratio between spin one and spin zero decays one may get a better convergence (moreover for the renormalization group result we do not have the complete expression at NNLL but we do for the ratio [213]). Actually this is so as we can see for the bottomonium but for charmonium physics the magnitude of the corrections is still very large. One may wonder whether there are renormalon effects

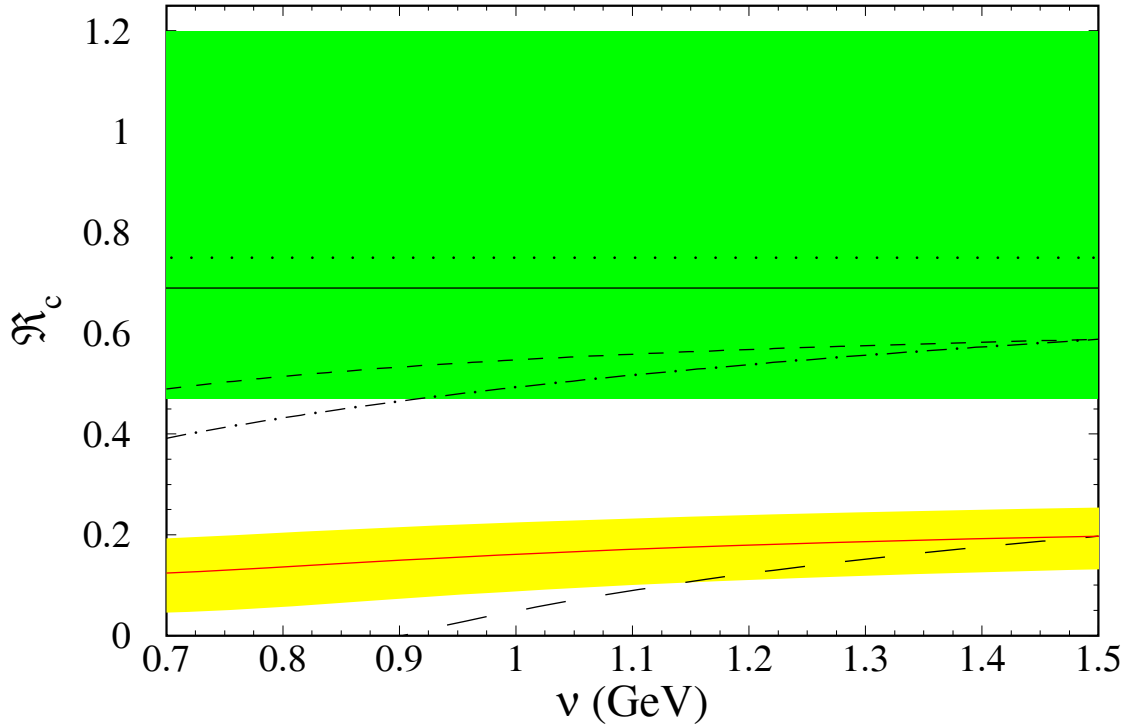


Figure 16.4: The spin ratio as the function of the renormalization scale  $\nu$  in LO $\equiv$ LL (dotted line), NLO (short-dashed line), NNLO (long-dashed line), NLL (dot-dashed line), and NNLL (solid line) approximation for the charmonium ground state with  $\nu_h = m_c$ . For the NNLL result the lower (yellow) band reflects the errors due to  $\alpha_s(M_Z) = 0.118 \pm 0.003$ . The upper (green) band represents the experimental error of the ratio where the central value is given by the horizontal solid line. Figure from Ref. [213].

here [223].

For bottomonium, the logarithmic expansion shows nice convergence and stability (c.f. Fig. 16.3) despite the presence of ultrasoft contributions with  $\alpha_s$  normalized at a rather low scale  $\nu^2/m_b$ . At the same time, the perturbative corrections are important and reduce the leading order result by approximately 41%. For illustration, at the scale of minimal sensitivity,  $\nu = 1.295$  GeV, we have the following series:

$$\mathcal{R}_b = \frac{\Gamma(\Upsilon(1S) \rightarrow e^+e^-)}{\Gamma(\eta_b(1S) \rightarrow \gamma\gamma)} = \frac{1}{3Q_b^2} (1 - 0.302 - 0.111) . \quad (16.2.23)$$

In contrast, the fixed-order expansion blows up at the scale of the inverse Bohr radius.

For the charmonium, the NNLO approximation becomes negative at an intermediate scale between  $\alpha_s m_c$  and  $m_c$  (c.f. Fig. 16.4) and the use of the NRG is mandatory to get a sensible perturbative approximation. The NNLL approximation has good stability against the scale variation but the logarithmic expansion does not converge well. This is the main factor that limits the theoretical accuracy since the nonperturbative contribution is expected to be under control. For illustration, at the scale of minimal sensitivity,  $\nu = 0.645$  GeV, we obtain

$$\mathcal{R}_c = \frac{\Gamma(J/\Psi(1S) \rightarrow e^+e^-)}{\Gamma(\eta_c(1S) \rightarrow \gamma\gamma)} = \frac{1}{3Q_c^2} (1 - 0.513 - 0.326) . \quad (16.2.24)$$

The central value of our NNLL result is  $2\sigma$  below the experimental value. The discrepancy may be explained by the large higher order contributions. This should not be surprising because of the rather large value of  $\alpha_s$  at the inverse Bohr radius of charmonium. For the charmonium hyperfine splitting, however, the logarithmic expansion converges well and the prediction of the renormalization group is in perfect agreement with the experimental data [212]. Thus one can try to improve the convergence of the series for the production/annihilation rates by accurately taking into account the renormalon-related contributions. One point to note is that with a potential model evaluation of the wave function correction, the sign of the NNLO term is reversed in the charmonium case [218]. This is very interesting since, actually, one can also see that the main effects of higher order effects in the static potential is to make it to agree with the lattice potential and therefore with the standard parameterizations of the non-perturbative potential like Cornell, etc... At the same time the subtraction of the pole mass renormalon from the perturbative static potential makes explicit that the potential is steeper and closer to lattice and phenomenological potential models [224]. Therefore, the incorporation of higher order effects from the static potential may improve the agreement with experiment, and it may look foreseeable to obtain a description of the ground state charmonium with mainly perturbative ingredients. However, how to match the hard coefficient with the perturbative potential is challenging since the logs of the potential get entangled with those of the hard matching coefficient. In any case, if we estimate the theoretical uncertainty as the difference of the NNLL and the NLL result at the soft scale  $\alpha_s m_c$ , the theoretical and experimental values agree within the error bars.

### 16.2.3 Final discussion

In order to determine unambiguously which bottomonium and charmonium states belong to the weak or strong coupling regime it is necessary to understand the lack of

convergence of the perturbative series for the inclusive electromagnetic decays. At this respect understanding the following points would be of great help:

- A complete NNLL computation would be most welcome in order to have a better estimate of the theoretical uncertainties.
- A complete NNNLO computation would be most welcome in that it would provide a better estimate of the theoretical uncertainties. Moreover it would help to asses the importance of the resummation of logarithms.
- Estimates of the non-perturbative corrections are needed. They also depend on the same chromoelectric gluonic correlator than the  $\Upsilon(1S)$  mass.
- The rearrangement (renormalon-based?) of the perturbative series needs better a understanding.

Finally, we also note that a renormalization group analysis for non-relativistic charmonium sum rules remains to be done. In this respect, there are new R measurements in the sub-charmonium region with BES at BEPC and just above the charm threshold with CLEO at CESR. These provide important input to the determinations of the charm quark mass.



# Chapter 17

## Radiative decays

### 17.1 Inclusive Radiative Decays<sup>1</sup>

#### 17.1.1 Introduction

Inclusive radiative decays of heavy quarkonium systems to light hadrons have been a subject of investigation since the early days of QCD [225, 226]. It was thought for some time that a reliable extraction of  $\alpha_s$  was possible from the inclusive  $\gamma gg$  decay normalized to the inclusive  $ggg$  decay. However, when the experimental data became available for  $J/\psi$  [227], it turned out that the photon spectrum, and in particular the upper end-point region of it, appeared to be poorly described by the theory. The situation was slightly better for the  $\Upsilon(1S)$  [228], where, at least, good agreement with QCD was found in the central region [229]. In fact, the whole photon spectrum for the  $\Upsilon(1S)$  is now well understood thanks to a number of theoretical advances which have taken place in recent years (see [230] and references therein). Here we will mainly translate in a critical way these advances to the case of the  $J/\psi$ .

We will stay in the effective theory framework of Non-relativistic QCD (NRQCD) [2, 4] and Potential NRQCD (pNRQCD) [5, 6], and our terminology will follows that of [7]. Let us remind the reader that heavy quarkonium systems enjoy the hierarchies of scales  $m \gg mv \gg mv^2$  and  $m \gg \Lambda_{\text{QCD}}$ , where  $m$  is the heavy quark mass,  $v \ll 1$  the relative velocity of the heavy quarks and  $\Lambda_{\text{QCD}}$  a typical hadronic scale. States fulfilling  $\Lambda_{\text{QCD}} \lesssim mv^2$  are said to be in the weak coupling regime (the binding is essentially due to a Coulomb-like potential) whereas states fulfilling  $\Lambda_{\text{QCD}} \gg mv^2$  are said to be in the strong Coupling regime (the binding is due to a confining potential). States below the open flavor threshold and not too deep are expected to be in the strong coupling regime whereas deep states are expected to be in the weak coupling one. States above (or very close to) the open flavor threshold are not expected to be in either regime.

#### 17.1.2 The photon spectrum

The contributions to the decay width can be split into direct ( ${}^{dir}$ ) and fragmentation ( ${}^{frag}$ )

---

<sup>1</sup>By Xavier Garcia i Tormo and Joan Soto

$$\frac{d\Gamma}{dz} = \frac{d\Gamma^{dir}}{dz} + \frac{d\Gamma^{frag}}{dz} \quad (17.1.1)$$

We will call direct contributions to those in which the observed photon is emitted from the heavy quarks and fragmentation contributions to those in which it is emitted from the decay products (light quarks). This splitting is correct at the order we are working but should be refined at higher orders.  $z \in [0, 1]$  is defined as  $z = 2E_\gamma/M$ ,  $M$  being the heavy quarkonium mass.

### Direct Contributions

The starting point is the QCD formula [231]

$$\begin{aligned} \frac{d\Gamma}{dz} &= z \frac{M}{16\pi^2} \text{Im}T(z) \\ T(z) &= -i \int d^4x e^{-iq\cdot x} \langle V_Q(nS) | T\{J_\mu(x)J_\nu(0)\} | V_Q(nS) \rangle \eta_\perp^{\mu\nu} \end{aligned} \quad (17.1.2)$$

where  $J_\mu(x)$  is the electromagnetic current for heavy quarks in QCD and we have restricted ourselves to  ${}^3S_1$  states.  $q$  is the photon momentum, which in the rest frame of the heavy quarkonium is  $q = (q_+, q_-, q_\perp) = (zM, 0, 0)$ ,  $q_\pm = q^0 \pm q^3$ . Different approximations to this formula are necessary for the central ( $z \sim 0.5$ ), lower end-point ( $z \rightarrow 0$ ) and upper end-point ( $z \rightarrow 1$ ) regions.

#### 1. The central region

For  $z$  away from the lower and upper end-points (0 and 1 respectively), no further scale is introduced beyond those inherent of the non-relativistic system. The integration of the scale  $m$  in the time ordered product of currents in (17.1.2) leads to local NRQCD operators with matching coefficients which depend on  $m$  and  $z$ . At leading order one obtains

$$\frac{1}{\Gamma_0} \frac{d\Gamma_{\text{LO}}}{dz} = \frac{2-z}{z} + \frac{z(1-z)}{(2-z)^2} + 2\frac{1-z}{z^2} \ln(1-z) - 2\frac{(1-z)^2}{(2-z)^3} \ln(1-z), \quad (17.1.3)$$

where

$$\Gamma_0 = \frac{32}{27} \alpha \alpha_s^2 e_Q^2 \frac{\langle V_Q(nS) | \mathcal{O}_1({}^3S_1) | V_Q(nS) \rangle}{m^2}, \quad (17.1.4)$$

and  $e_Q$  is the charge of the heavy quark. The  $\alpha_s$  correction to this rate was calculated numerically in Ref. [232] for the bottomonium case. A reasonable estimate for charmonium maybe obtained by multiplying it by  $\alpha_s(2m_c)/\alpha_s(2m_b)$ . The expression corresponding to (17.1.4) in pNRQCD is obtained at lowest order by just making the substitution

$$\langle V_Q(nS) | \mathcal{O}_1({}^3S_1) | V_Q(nS) \rangle = \frac{N_c}{2\pi} |R_{n0}(0)|^2, \quad (17.1.5)$$

where  $R_{n0}(0)$  is the radial wave function at the origin. The final result coincides with the one of the early QCD calculations [225, 226]. The NLO contribution in the weak coupling regime reads [4],

$$\frac{d\Gamma_{\text{NLO}}}{dz} = C'_1 ({}^3S_1) \frac{\langle V_Q(nS) | \mathcal{P}_1({}^3S_1) | V_Q(nS) \rangle}{m^4} \quad (17.1.6)$$

ant it is  $v^2$  suppressed with respect to (17.1.3). The new matrix element above can be written in terms of the original one [233]

$$\frac{\langle V_Q(nS) | \mathcal{P}_1({}^3S_1) | V_Q(nS) \rangle}{m^4} = \left( \frac{M - 2m - \mathcal{E}_1/m}{m} \right) \frac{\langle V_Q(nS) | \mathcal{O}_1({}^3S_1) | V_Q(nS) \rangle}{m^2} (1 + \mathcal{O}(v^2)) \quad (17.1.7)$$

In the weak coupling regime  $\mathcal{E}_1/m$  is absent [234], but in the strong coupling regime it must be kept ( $\mathcal{E}_1 \sim \Lambda_{\text{QCD}}^2$  is a bound state independent non-perturbative parameter). The matching coefficient can be extracted from an early calculation [235] (see also [236]). It reads

$$C'_1 ({}^3S_1) = -\frac{16}{27} \alpha \alpha_s^2 e_Q^2 \left( \left( F_B(z) + \frac{1}{2} F_W(z) \right) \frac{1}{2} + \frac{1}{\Gamma_0} \frac{d\Gamma_{\text{LO}}}{dz} \right) \quad (17.1.8)$$

where  $F_B(z)$  and  $F_W(z)$  are defined in Ref. [236]<sup>2</sup>.

In the weak coupling regime the contributions of color octet operators start at order  $v^4$ . Furthermore, away of the upper end-point region, the lowest order color octet contribution identically vanishes [238]. Hence there is no  $1/\alpha_s$  enhancement in the central region and we can safely neglect these contributions in this case. However, in the strong coupling regime the color octet contributions may become order  $v^2$  and should be kept at NLO.

Then in the weak coupling regime (if we use the counting  $\alpha_s(m) \sim v^2$ ,  $\alpha_s(m\alpha_s) \sim v$ ) the complete NLO ( $v^2$  suppressed) contribution consists of the  $\alpha_s$  correction to (17.1.3), the relativistic corrections in (17.1.6) and the corrections to the wave function at the origin up to order  $\alpha_s^2(m\alpha_s)$  [239, 240]. Using  $m = m_c = 1.6 \text{ GeV}$ ,  $M = 3.1 \text{ GeV}$ ,  $\alpha_s(2m_c) = 0.23$  and  $\alpha_s(m\alpha_s) = 0.4$  we obtain the solid green curve in Fig. 17.1.

## 2. The lower end-point region

For  $z \rightarrow 0$ , the emitted low energy photon can only produce transitions within the non-relativistic bound state without destroying it. Hence the direct low energy photon emission takes place in two steps: (i) the photon is emitted (dominantly by dipole electric and magnetic transitions) and (ii) the remaining (off-shell) bound state is annihilated into light hadrons. For  $z$  very close to zero it has a suppression  $\sim z^3$  with respect to  $\Gamma_0$  (see [241, 242] for a recent analysis of this region in QED). Hence, at some point the direct photon emission is overtaken by the fragmentation contributions  $\bar{Q}Q \rightarrow ggg \rightarrow gg\bar{q}q\gamma$  [243, 238]. In practise this is expected to happen somewhere between  $0.2 \lesssim z \lesssim 0.4$ , namely much before than the  $z^3$  behavior of the very low energy direct photon emission can be observed, and hence we shall neglect the latter in the following.

<sup>2</sup>The last term in (17.1.8) was missing in [230], see footnote 4 of [237].

### 3. The upper end-point region

In this region the standard NRQCD factorization is not applicable [231]. This is due to the fact that small scales induced by the kinematics enter the problem and have an interplay with the bound state dynamics. In order to study this region, one has to take into account collinear degrees of freedom in addition to those of NRQCD. This can be done using Soft-Collinear Effective Theory (SCET) [244, 245] as it has been described in [246, 247]. This region has only been considered in the weak coupling regime, which we will restrict our discussion to. The color octet contributions are only suppressed by  $v^2$  or by  $1 - z$ . Since their matching coefficients are enhanced by  $1/\alpha_s(m)$ , they become as important as the color singlet contributions if we count  $\alpha_s(m) \sim v^2 \sim 1 - z$ . The formula one may use for the semi-inclusive width in the end-point region, which was successful for the bottomonium case, reads

$$\frac{d\Gamma^e}{dz} = \frac{d\Gamma_{CS}^e}{dz} + \frac{d\Gamma_{CO}^e}{dz} \quad (17.1.9)$$

where  $CS$  and  $CO$  stand for color singlet and color octet contributions respectively. For the color singlet contribution one may use the expression with the Sudakov resummed coefficient in Ref. [248]

$$\begin{aligned} \frac{1}{\Gamma_0} \frac{d\Gamma_{CS}^e}{dz} = \Theta(M - 2mz) \frac{8z}{9} \sum_{n \text{ odd}} \left\{ \frac{1}{f_{5/2}^{(n)}} \left[ \gamma_+^{(n)} r(\mu_c)^{2\lambda_+^{(n)}/\beta_0} - \gamma_-^{(n)} r(\mu_c)^{2\lambda_-^{(n)}/\beta_0} \right]^2 + \right. \\ \left. + \frac{3f_{3/2}^{(n)}}{8[f_{5/2}^{(n)}]^2} \frac{\gamma_{gq}^{(n)2}}{\Delta^2} \left[ r(\mu_c)^{2\lambda_+^{(n)}/\beta_0} - r(\mu_c)^{2\lambda_-^{(n)}/\beta_0} \right]^2 \right\} \end{aligned} \quad (17.1.10)$$

where the definitions for the different functions appearing in (17.1.10) can be found in [248, 230].

For the color octet contributions we use

$$\frac{d\Gamma_{CO}^e}{dz} = \alpha_s(\mu_u) \alpha_s(\mu_h) e_Q^2 \left( \frac{16M\alpha}{9m^4} \right) \int_z^{\frac{M}{2m}} C(x - z) S_{S+P}(x) dx \quad (17.1.11)$$

$\mu_u \sim mv^2$  and  $\mu_h \sim m$  are the ultrasoft and hard scales respectively.  $C(x - z)$  contains the Sudakov resummations of Ref. [246]. The (tree level) matching coefficients (up to a global factor) and the various shape functions are encoded in  $S_{S+P}(x)$ . See [230] for a precise definition of these objects.

We would like to comment on the validity of the formulas above. This is limited by the perturbative treatment of the collinear and ultrasoft gluons. For the collinear gluons, entering in the jet functions, we have  $1\text{GeV} \lesssim M\sqrt{1-z}$ , which for  $J/\psi$  implies  $z \lesssim 0.9$ . The formalism is not reliable beyond that point. For the ultrasoft gluons, entering in the shape functions ( $S_{S+P}(x)$ ), we have  $1\text{GeV} \lesssim M(1-z)$ , which implies  $z \lesssim 0.7$ . Hence, due to the latter, we do not really have a reliable QCD description of the upper end-point region for charmonium. However, for the bottomonium system, the shape function above turns out to describe very well the data even in the far end-point region, where it is not supposed to be reliable either.

In view of this, we believe that the formulas above may provide a reasonable model for the description of the region  $0.7 \lesssim z \lesssim 0.9$ . The outcome is the blue dot-dashed curve of Fig. 17.1 (the flattening of the curve for  $z > 0.85$  is an artifact, see footnote 2 of Ref. [230])

#### 4. Merging the central and upper end-point regions

As we have seen, different approximations are necessary in the central and upper end-point regions. It is then not obvious how the results for the central and for the upper end-point regions must be combined in order to get a reliable description of the whole spectrum. When the results of the central region are used in the upper end-point region, one misses certain Sudakov and Coulomb resummations which are necessary because the softer scales  $M\sqrt{1-z}$  and  $M(1-z)$  become relevant. Conversely, when results for the end-point region are used in the central region, one misses non-trivial functions of  $z$ , which are approximated by their end-point ( $z \sim 1$ ) behavior. In [230] the following merging formula was proposed, which works reasonably well for bottomonium,

$$\frac{1}{\Gamma_0} \frac{d\Gamma^{dir}}{dz} = \frac{1}{\Gamma_0} \frac{d\Gamma^c}{dz} + \left( \frac{1}{\Gamma_0} \frac{d\Gamma^e}{dz} - \frac{1}{\Gamma_0} \frac{d\Gamma^e}{dz} \Big|_c \right) \quad (17.1.12)$$

$|_c$  means the expansion of the end-point formulas when  $z$  approaches the central region. This expansion must be carried out at the same level of accuracy as the one we use for the formulas in the central region.

Putting all the ingredients together in formula (17.1.12) we obtain the red dashed line in Fig. 17.1 for the direct contributions to the photon spectrum. Note that a deep is generated for  $0.8 \lesssim z \lesssim 0.9$  which makes the decay width negative. This happens in the region  $0.7 \lesssim z$  where the calculation of the shape function is not reliable. A deep was also generated in the  $\Upsilon(1S)$  case, but the effect was not so dramatic there [230]. We conclude that, unlike in the  $\Upsilon(1S)$  case, the limitations in the theoretical description of the end point region make the merging procedure deliver an unsatisfactory description of this end point region for  $J/\psi$ . Clearly, further work is required to understand better the end-point region, in particular a description assuming  $J/\psi$  in the strong coupling regime would be desirable. For the present analysis, one should only use the outcome of the merging procedure for  $z < 0.7$ , if at all. Indeed, an alternative way to proceed would be to ignore the end-point region and only try to describe data in the central region with the QCD formulas for this region given above.

#### Fragmentation contributions

The fragmentation contributions can be written as

$$\frac{d\Gamma^{\text{frag}}}{dz} = \sum_{a=q,\bar{q},g} \int_z^1 \frac{dx}{x} C_a(x) D_{a\gamma} \left( \frac{z}{x}, M \right), \quad (17.1.13)$$

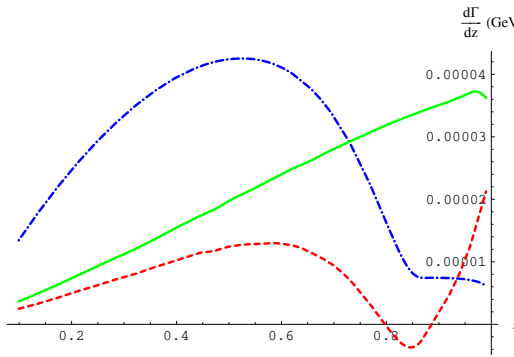


Figure 17.1: Direct contributions in the weak coupling regime. The solid green line corresponds to the calculation for the central region at NLO, which should be reliable up to  $z \lesssim 0.7$ . The blue dot-dashed line corresponds to the calculation for the upper end-point region, which is expected to provide a reasonable model for  $0.7 \lesssim z \lesssim 0.9$ . The red dashed line is the curve obtained by merging.

where  $C_a$  represents the partonic kernels and  $D_{a\gamma}$  represents the fragmentation functions. The partonic kernels can again be expanded in powers of  $v$  [238]

$$C_a = \sum_{\mathcal{Q}} \hat{C}_a[\mathcal{Q}] \frac{\langle J/\psi | \mathcal{Q} | J/\psi \rangle}{m^{d_{\mathcal{Q}}-1}} \quad (17.1.14)$$

where  $\mathcal{Q}$  stands for NRQCD operators,  $\hat{C}_a[\mathcal{Q}]$  for their matching coefficients, and  $d_{\mathcal{Q}}$  for their dimension. The leading order term in  $v$  is the color singlet rate to produce three gluons ( $\mathcal{Q} = \mathcal{O}_1(^3S_1)$ ). The color octet contributions have a  $1/\alpha_s$  enhancement. In the weak coupling regime, which we will assume in the following, they are  $v^4$  suppressed, but one should keep in mind that in the strong coupling regime they may become order  $v^2$ . Then the color singlet fragmentation contribution is of order  $\alpha_s^3 D_{g \rightarrow \gamma}$  and the color octet fragmentation are of order  $v^4 \alpha_s^2 D_{g \rightarrow \gamma}$  ( $\mathcal{Q} = \mathcal{O}_8(^1S_0)$ ,  $\mathcal{O}_8(^3P_J)$ ) or  $v^4 \alpha_s^2 D_{q \rightarrow \gamma}$  ( $\mathcal{Q} = \mathcal{O}_8(^3S_1)$ ). We can use, as before, the counting  $v^2 \sim \alpha_s$  to compare the relative importance of the different contributions. The existing models for the fragmentation functions [249] show us that  $D_{q \rightarrow \gamma}$  is much larger than  $D_{g \rightarrow \gamma}$ . This causes the  $v^4 \alpha_s^2 D_{q \rightarrow \gamma}$  of the  $\mathcal{O}_8(^3S_1)$  contribution to dominate in front of the singlet  $\alpha_s^3 D_{g \rightarrow \gamma}$  and the octet  $v^4 \alpha_s^2 D_{g \rightarrow \gamma}$  contributions. Moreover, the  $\alpha_s$  corrections to the singlet rate will produce terms of order  $\alpha_s^4 D_{q \rightarrow \gamma}$ , that is of the same order as the octet  $\mathcal{O}_8(^3S_1)$  contribution, which are unknown. This results in a large theoretical uncertainty in the fragmentation contributions, which would be greatly reduced if the leading order calculation of  $\hat{C}_q[\mathcal{O}_1(^3S_1)]$  (this requires a tree level four body decay calculation plus a three body phase space integral) was known.

For the quark fragmentation function we will use the LEP measurement [250] and for the gluon fragmentation function the model [251]. These are the same choices as in [247]. For the  $\mathcal{O}_8(^1S_0)$  and  $\mathcal{O}_8(^3P_0)$  matrix elements we will use our estimates in [252]

$$\langle J/\psi | \mathcal{O}_8(^1S_0) | J/\psi \rangle \Big|_{\mu=M} \sim 0.0012 \text{ GeV}^3 \quad (17.1.15)$$

$$\langle J/\psi | \mathcal{O}_8(^3P_0) | J/\psi \rangle \Big|_{\mu=M} \sim 0.0028 \text{ GeV}^5 \quad (17.1.16)$$

The estimate for  $\langle J/\psi | \mathcal{O}_8(^1S_0) | J/\psi \rangle$  is compatible with the lattice results [253] (nrqcd and Coulomb algorithms). For the  $\mathcal{O}_8(^3S_1)$  matrix element the same lattice calculation

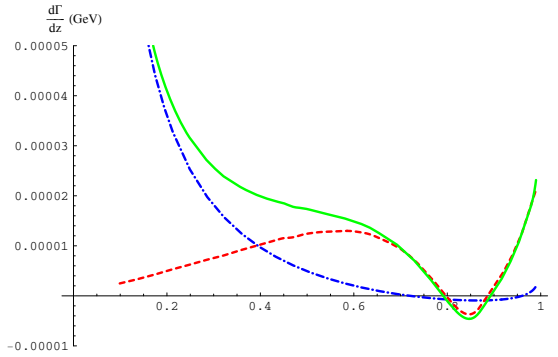


Figure 17.2: The red dashed line corresponds to the direct contributions (merging), the blue dot-dashed line to the fragmentation contributions ( $v$  scaling for  $O_8(^3S_1)$ ) and the solid green line is the total.

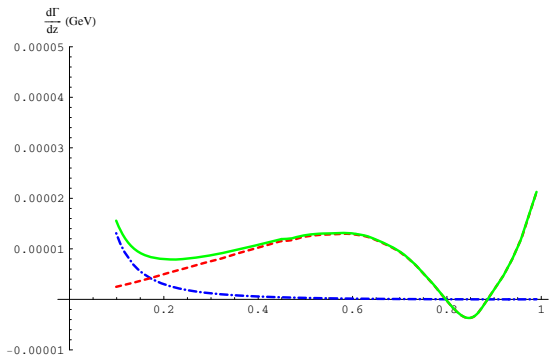


Figure 17.3: The red dashed line corresponds to the direct contributions (merging), the blue dot-dashed line to the fragmentation contributions (lattice, nrqcd algorithm, for  $O_8(^3S_1)$ ) and the solid green line is the total.

gives

$$\begin{aligned} \langle J/\psi | O_8(^3S_1) | J/\psi \rangle_{\text{nrqcd}} &= 0.0005 \text{ GeV}^3 \\ \langle J/\psi | O_8(^3S_1) | J/\psi \rangle_{\text{coulomb}} &= 0.0002 \text{ GeV}^3 \end{aligned} \quad (17.1.17)$$

which is much smaller than using the NRQCD  $v$  scaling

$$\langle J/\psi | O_8(^3S_1) | J/\psi \rangle \sim v^4 \langle J/\psi | O_1(^3S_1) | J/\psi \rangle \sim 0.05 \text{ GeV}^3 \quad (17.1.18)$$

with  $v^2 \sim 0.3$ . With the choices above we obtain the blue dot-dashed curves in Fig. 17.2 ( $v$  scaling) and Fig. 17.3 (lattice, nrqcd algorithm) for the fragmentation contributions. These curves turns out to be very sensitive to the value assigned to  $\langle J/\psi | O_8(^3S_1) | J/\psi \rangle$ . When we put together direct (red dashed curve in Figs. 17.2 and 17.3) and fragmentation contributions we obtain the solid green curves in Figs. 17.2 and 17.3, if the merging formula is used, and Figs. 17.4 and 17.5, if only the central region is taken into account. The shape of this curve in Fig. 17.2 is in qualitative agreement with the early Mark II results for  $0.4 \lesssim z \lesssim 0.7$  [227].

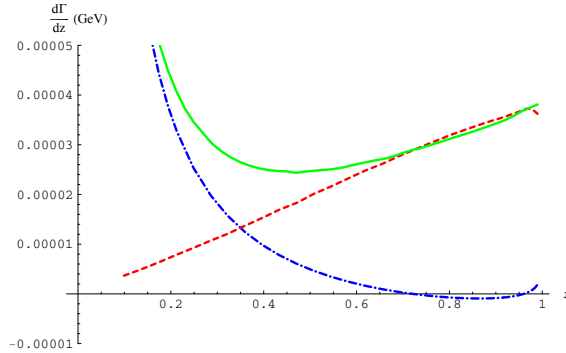


Figure 17.4: The red dashed line corresponds to the direct contributions (central region), the blue dot-dashed line to the fragmentation contributions ( $v$  scaling for  $O_8(^3S_1)$ ) and the solid green line is the total.

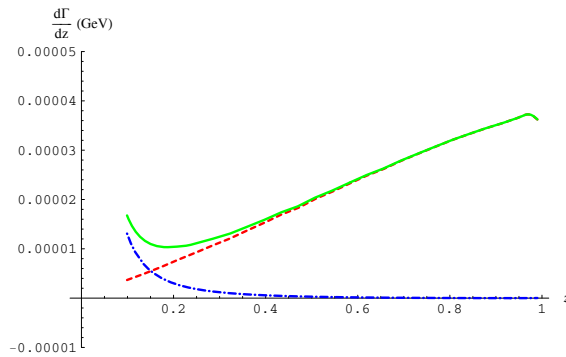


Figure 17.5: The red dashed line corresponds to the direct contributions (central region), the blue dot-dashed line to the fragmentation contributions (lattice, nrqcd algorithm, for  $O_8(^3S_1)$ ) and the solid green line is the total.

### 17.1.3 Extraction of $\alpha_s(M_{J/\psi})$

As mentioned in the introduction,  $\alpha_s(M_{J/\psi})$  can in principle be extracted from the ratio  $\Gamma(J/\psi \rightarrow \gamma_{\text{direct}} X)$  over  $\Gamma_{\text{strong}}(J/\psi \rightarrow X)$ ,  $X$  stands for light hadrons,  $\gamma_{\text{direct}}$  for photons produced from the heavy quarks and  $\Gamma_{\text{strong}}$  for subtracting from  $\Gamma$  the decays mediated by a virtual photon. This maybe done in an analogous way as it has been recently carried out for bottomonia in [254]. In order to obtain  $\Gamma(J/\psi \rightarrow \gamma_{\text{direct}} X)$  it is important to have a good QCD description of the photon spectrum since one should be able to disentangle fragmentation contributions from direct ones. This may be done by restricting the fit to data of the QCD expression for direct contributions to the upper end-point region and the part of the central region where fragmentation contributions are negligible. As we have seen in the previous section, we do not have at the moment a good QCD description of the upper end point region for  $J/\psi$  and hence a model, like the one in [255](see also [256]), might be unavoidable. This expression is then used to interpolate data to small  $z$  and hence to be able to obtain the full inclusive width for direct photons. Then  $\alpha_s(M_{J/\psi})$  may be extracted from

$$R_\gamma \equiv \frac{\Gamma(J/\psi \rightarrow \gamma_{\text{direct}} X)}{\Gamma_{\text{strong}}(J/\psi \rightarrow X)} = \frac{36}{5} \frac{e_c^2 \alpha}{\alpha_s} \left( 1 + \mathcal{O}(\alpha_s) + \mathcal{O}\left(\frac{v^4}{\alpha_s(m)}\right) + \dots \right) \quad (17.1.19)$$

where  $e_c^2 = 4/9$ , the  $\mathcal{O}(v^2)$  cancel in the ratio, and  $\dots$  stand for higher order contributions. In the extraction of  $\alpha_s$  from bottomonium of [254],  $\mathcal{O}(\alpha_s(m))$  corrections were taken into account but not  $\mathcal{O}\left(\frac{v^4}{\alpha_s}\right)$  which are of the same order if  $\alpha_s(m) \sim v^2$  and in practise turn out to be very important. These have been included in [257].

### 17.1.4 Learning about the nature of $J/\psi$ and $\psi(2S)$

It has recently been shown that if two heavy quarkonium states are in the strong coupling regime then the ratio of their total photon spectrum in the central region is predictable from QCD at NLO [258]. If the spectrum of both  $J/\psi$  and  $\psi(2S)$  is measured and fits well with the strong coupling regime formula, it would indicate that both  $J/\psi$  and  $\psi(2S)$  are in the strong coupling regime. Unfortunately, if it does not, we will not be able to learn much, because it may be due to the fact that  $J/\psi$  is in the weak coupling regime or to the fact that  $\psi(2S)$  is too close to the open flavor threshold for the strong coupling regime to hold for it (or to both).

### 17.1.5 Conclusions

A new measurement of the inclusive photon spectrum for radiative  $J/\psi$  decays would be of great interest since it has only been measured before by the Mark II collaboration more than 25 years ago. The theoretical progress which has occurred since may allow, among other things, for a sensible extraction of  $\alpha_s(M_{J/\psi})$ . The additional measurement of the photon spectrum for  $\psi(2S)$  might shed some light on the nature of these states. No theoretical analysis are available for other states like  $\eta_c s$  or  $\chi_c s$ . Experimental measurements would definitively trigger them.

## 17.2 Exclusive Radiative Decays <sup>3</sup>

### 17.2.1 Introduction

At *BES-III*, there will be huge data samples of vector charmonium states, such as  $J/\psi$ ,  $\psi'$ , and  $\psi''$ , and possibly not small samples for  $\psi(4040)$ ,  $\psi(4160)$ ,  $\psi(4415)$ . The non-vector charmonium states, including pseudoscalars,  $\eta_c$  and  $\eta'_c$ , and the  $P$ -wave states  $\chi_{cJ}$ , can be produced via radiative transition of the vector states, considering the large transition rates (except for  $\psi' \rightarrow \gamma\eta'_c$ ), the data samples of these states will also be large. These will make detailed studies of the radiative decays of charmonium into light hadrons possible. A discussion on inclusive radiative decays can be found in Sect. 17.1.

The radiative decays of vector charmonia have been used extensively for the study of the light hadron spectroscopy, especially in  $J/\psi$  decays, this is reviewed in the hadron spectroscopy part of this report. The study of the other charmonium states is rather limited. In the following sections, we will review the studies of radiative decays of the states other than  $J/\psi$ , and the prospects for what can be expected at *BES-III*.

### 17.2.2 Radiative decays of vector charmonia

The dominant radiative decays of vector charmonia proceed via the diagram shown in Fig. 17.6. The rate of the photon radiation from the *final state* quarks is expected to be very small, as has been shown to be the case by the experimental measurements of final-state-radiation dominant processes like  $J/\psi \rightarrow \gamma\pi^0$  [156, 52]. In pQCD, assuming the emission of hard gluons, the inclusive radiative decay rate of the  $J/\psi$  is around 6%, while that for  $\psi'$  decays is around 1% [259]. There are no estimates for other vector charmonia, such as the  $\psi''$ ,  $\psi(4040)$ , etc., but it is expected that the rates are very small, since all these states are above the open charm threshold and the dominant decay modes are OZI-allowed.

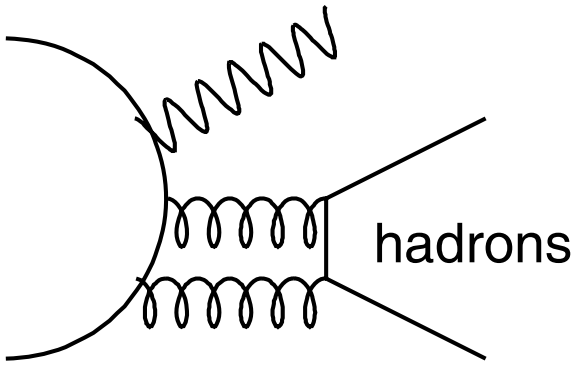


Figure 17.6: Radiative decays of vector charmonium state into light hadrons.

Although radiative  $\psi'$  decays are expected to be about 1% of all decays, existing

---

<sup>3</sup>By Changzheng Yuan

Table 17.1: Branching fractions of  $\psi'$  radiative decays, only modes that have been observed are listed, for a complete list of all measurements, refer to PDG [52].

Mode	Branching Fraction ( $\times 10^{-5}$ )	Experiment	Comment
$\gamma\eta'(958)$	$15.4 \pm 3.1 \pm 2.0$	BESI [260]	
	$12.4 \pm 2.7 \pm 1.5$	BESII [262]	
$\gamma\eta\pi^+\pi^-$	$36.0 \pm 14.2 \pm 18.3$	BESII [262]	
$\gamma f_2(1270)$	$21.2 \pm 1.9 \pm 3.2$	BESI [261]	
$\gamma f_0(1710) \rightarrow \gamma\pi\pi$	$3.01 \pm 0.41 \pm 1.24$	BESI [261]	
$\gamma f_0(1710) \rightarrow \gamma K\bar{K}$	$6.04 \pm 0.90 \pm 1.32$	BESI [261]	
$\gamma p\bar{p}$	$2.9 \pm 0.4 \pm 0.4$	BESII [263]	mass $< 2.9 \text{ GeV}/c^2$
$\gamma 2(\pi^+\pi^-)$	$39.6 \pm 2.8 \pm 5.0$	BESII [263]	mass $< 2.9 \text{ GeV}/c^2$
$\gamma K_S^0 K^+\pi^- + c.c.$	$25.6 \pm 3.6 \pm 3.6$	BESII [263]	mass $< 2.9 \text{ GeV}/c^2$
$\gamma\pi^+\pi^- K^+ K^-$	$19.1 \pm 2.7 \pm 4.3$	BESII [263]	mass $< 2.9 \text{ GeV}/c^2$
$\gamma\pi^+\pi^- p\bar{p}$	$2.8 \pm 1.2 \pm 0.7$	BESII [263]	mass $< 2.9 \text{ GeV}/c^2$

measurements are very limited. The only observation so far is  $\psi' \rightarrow \gamma\eta'$  [260],  $\gamma\pi\pi$  and  $\gamma K\bar{K}$  [261], with a total branching fraction about 0.05%. Final states with three pseudoscalars have been measured by BESII, and no significant structures in the  $\eta\pi^+\pi^-$  and  $K\bar{K}\pi$  mass spectra are seen; the upper limits for the production of the pseudoscalar states  $\eta(1405)$  or  $\eta(1475)$  are set at the 90% C.L [262].

The most recent study of  $\psi'$  radiative decays was performed by BESII [263], where the total and differential branching fractions of  $\psi' \rightarrow \gamma p\bar{p}$ ,  $\gamma 2(\pi^+\pi^-)$ ,  $\gamma K_S^0 K^+\pi^- + c.c.$ ,  $\gamma\pi^+\pi^- K^+ K^-$ , and  $\gamma\pi^+\pi^- p\bar{p}$  have been measured. For invariant masses of the charged particle system less than  $2.9 \text{ GeV}/c^2$ , the total branching fraction of all these modes is about 0.1%, which is about 10% of the total radiative decays of the  $\psi'$ . Unfortunately, due to the low statistics, production of intermediate states could not be studied. The observed modes are listed in Table 17.1, together with their measured branching fractions.

Since the dominant decay dynamics of  $\psi'$  or  $J/\psi$  radiative decay is the  $c\bar{c}$  emission of a real photon and subsequent annihilation into two gluons, it is expected that glueball states, if they exist, should be copiously produced. This has been a widely circulated argument in favor of careful studies of  $J/\psi$  radiative decays. The same argument also holds for  $\psi'$  radiative decays, in spite of the obvious disadvantage of a lower production rate. However, this disadvantage may no longer be an issue at *BES-III*, which should have a very large (or even huge)  $\psi'$  data sample, with the obvious advantage that the allowed mass range for investigation is larger than that for  $J/\psi$  decays.

Lattice QCD (LQCD) [264] calculations indicate that—except for the  $J^{PC} = 0^{++}$  glueball, which is expected at about  $1.7 \text{ GeV}/c^2$ , and the  $J^{PC} = 2^{++}$  glueball, expected at about  $2.3 \text{ GeV}/c^2$ —most glueball states (*i.e.* those with other  $J^{PC}$  values) have rather large masses: above  $2.5 \text{ GeV}/c^2$  for  $J^{PC} = 0^{-+}$  and around  $3 \text{ GeV}/c^2$  for  $J^{PC} = 2^{-+}$ . Since these states are expected to have broad widths, their study in  $J/\psi$  decays would be somewhat cumbersome. All things being equal, it would be more suitable to search for them in  $\psi'$  decays.

Contrary to initial naive expectations, many  $\psi'$  hadronic decay channels are observed

to be dramatically different. Likewise, it may very well be that the notion that  $\psi'$  radiative decays have similar properties as those for the  $J/\psi$  may be incorrect;  $\psi'$  and  $J/\psi$  radiative decays may turn out to be very different. For example, in the decays to  $\gamma\pi\pi$ , the relative strengths of the  $\pi\pi$  resonances could be very different, in which case the two decays would supply very different information, and this might provide some helpful insights into meson spectroscopy. Another possible advantage of using the  $\psi'$  data is that the backgrounds are very different. For example, in  $\gamma\pi^+\pi^-$  channels, there is almost no background from  $\rho\pi$  in  $\psi'$  decays, while this is the dominant background for  $J/\psi$  decays, since  $J/\psi \rightarrow \rho\pi$  is the largest two-body hadronic mode in  $J/\psi$  decays.

While the  $J^{PC} = 0^{++}$  and  $2^{++}$  states can be well studied in their decays into a pair of pseudoscalars, such as  $\pi\pi$ ,  $K\bar{K}$ ,  $\eta\eta$ ,  $\eta'\eta'$ , or  $\eta\eta'$ , the  $J^{PC} = 0^{-+}$  and  $2^{-+}$  states have to be studied in their decays into three pseudoscalars, such as  $\eta\pi\pi$ ,  $K\bar{K}\pi$ ,  $\eta K\bar{K}$ ,  $\eta'\pi\pi$ , etc. Final states like  $\gamma p\bar{p}$  and  $\gamma\Lambda\bar{\Lambda}$  can be used to search for the glueball with any quantum numbers, so long as the mass is above the baryon-antibaryon mass threshold.

The dominant decay modes of the glueballs are expected to be to multi-hadron final states. However, the spin-parity analysis of multi-hadron final states can be very complicated, due to the contributions of many mesons with different spin-parity, and many different intermediate states. In the case of many parameters, partial wave analyses (PWA) might give meaningless results.

### 17.2.3 Radiative decays of pseudoscalar charmonia

So far there are no measurements of radiative decays of the  $\eta_c$ , let alone its excited state, the  $\eta_c(2S)$ .

The decay rates of  $\eta_c$  to a  $\gamma$  and a vector meson (like  $\rho$ ,  $\omega$  and  $\phi$ ) is of great interest to probe the wave function of the  $\eta_c$ , where it is suspected that the mixing from  $\eta$  and  $\eta'$  may exist to explain for example the decay rates of  $J/\psi \rightarrow \gamma\eta$  and  $\gamma\eta'$  [156]. The decays of a pure  $c\bar{c}$  states into  $\gamma V$  may be very weak, however, if the mixing from the  $\eta$  and  $\eta'$  exists, the decay rate may be enhanced to a much higher level. So far there is no theoretical estimation of the rates yet, either with or without the mixing from light quarks.

If the photon is emitted from the  $c\bar{c}$  quark pair in the  $\eta_c$ , the decay will be quite similar to  $\eta_c \rightarrow \gamma\gamma$ , with one real photon replaced by a virtual one and further coupled to a vector meson. Since  $\mathcal{B}(\eta_c \rightarrow \gamma\gamma) = (2.8 \pm 0.9) \times 10^{-4}$  [52], the decay rates of  $\eta_c \rightarrow \gamma V$  should not be very different from that if estimated from Vector Meson Dominance model.

### 17.2.4 Radiative decays of P-wave charmonia

There is no experimental information on the radiative decays of the  $P$ -wave charmonia, including  $\chi_{c0}$ ,  $\chi_{c1}$ , and  $\chi_{c2}$ .

A recent theoretical calculation of  $\chi_{cJ} \rightarrow \gamma V$ ,  $V = \rho$ ,  $\omega$ , or  $\phi$ , was given in Ref. [265] based on nonrelativistic quantum chromodynamics, the results are shown in Table 17.2. The branching fractions are at a level which can be searched for, or be observed, using the  $\psi'$  data sample at *BES-III*.

Table 17.2: calculated branching fractions of  $\chi_{cJ} \rightarrow \gamma V$  from Ref. [265], in unit of  $\times 10^{-6}$ .

Mode	$\chi_{c0}$	$\chi_{c1}$	$\chi_{c2}$
$\gamma\rho$	1.2	14	4.4
$\gamma\omega$	0.13	1.6	0.50
$\gamma\phi$	0.46	3.6	1.1

### 17.2.5 Discussions and conclusions

From the above analysis, we conclude the radiative decays of the vector charmonium states, especially of  $J/\psi$  and  $\psi'$ , should be studied with great care for the understanding of light hadron spectroscopy, as well as for a better understanding of the charmonium decay dynamics. While the decays of  $J/\psi$  are much rich, the study of the  $\psi'$  is rather limited, more effort should be made to find possible new phenomena in  $\psi'$  decays.

The search for the decays into  $\gamma$ +Vector allows a probe for the wave functions of  $\eta_c$  and  $\chi_{cJ}$  states, to test whether there is mixture from the light quark mesons.



# Chapter 18

## Hadronic decays

### 18.1 Light hadron decay <sup>1</sup>

In charmonium annihilation decay, the basic process is the annihilation of the  $c\bar{c}$  inside the charmonium to light quarks, gluons, or leptons. The energy release in the process is  $2m_c$ , which means that space-time distance of the annihilation process is of order  $1/(2m_c)$ . In QCD, processes happened at such high energy scale is perturbatively calculable. In the non-relativistic limit  $v \rightarrow 0$ , the annihilation space-time region is much smaller than the radius of charmonium at order  $1/(m_c v)$ , where  $v$  is the relative velocity between  $c$  and  $\bar{c}$ . Thus the annihilation decay rate is expected to be proportional to the probability of the  $c\bar{c}$  pair appearing at the same point in space-time and the probability in which a point-like  $c\bar{c}$  pair annihilates into light partons. The former one is a long-distance effect depending on the dynamics of the charmonium, while the later one is a short-distance effect. In this way, the long-distance effects and the short-distance one are separated.

The old-fashion factorization formula to calculate the annihilation decay rates is the so-called “color singlet model” (CSM), in which the charmonium is treated as a pure color-singlet  $c\bar{c}$  pair. The annihilation decay amplitude is then factored into the wavefunction at the origin of the  $c\bar{c}$ , which accounts for the long-distance effects and the amplitude of the  $c\bar{c}$  annihilation process, which gives the short-distance contributions. Drawbacks of this model are obvious. When some of the annihilated partons are soft, the whole annihilation process is no longer purely short distance, and this naive factorization of the CSM fails, especially for processes with essential contributions to the decay rate from these regions. Some typical examples appear in the P-wave [266, 267, 268, 269] and D-wave [270, 271] decay, whose rates at  $\alpha_s^3$  by CSM are infrared sensitive.

A modern-fashion factorization scheme to calculate the charmonium annihilation decay rate is the NRQCD factorization formula[272]. It improves CSM by absorbing the contribution from the annihilated soft partons into the long-distance effects. The short-distance effects is that the  $c\bar{c}$  pair annihilates into hard partons. The  $c\bar{c}$  pair in the short-distance annihilation is not necessarily color-singlet and not necessary with the same quantum number as the charmonium state. The charmonium state is treated as superposition state of  $|Q\bar{Q}\rangle$ ,  $|Q\bar{Q}g\rangle$ ,  $|Q\bar{Q}gg\rangle$  and other higher Fock states, rather than only the  $|Q\bar{Q}\rangle$  color-singlet state as in CSM. The contribution of each Fock state, organized in powers

---

<sup>1</sup>Yu-Qi Chen and Zhi-Guo He

of  $v^2$ , could be written as a product of long matrix element and short distance coefficient accordingly. The short distance coefficients are calculated perturbatively, while the non-perturbative long distance matrix elements could be studied in lattice simulations, or determined phenomenologically, or estimated through velocity scaling rules.

Below  $D\bar{D}$  open flavor threshold, one expects to have ten charmonium states by potential model calculation. They are 4 S-wave states ( $\eta_c(nS)$  and  $\psi(nS)$  with  $n=1,2$ ), 4 P-wave states ( $h_c$  and  $\chi_{cJ}$  with  $J=0,1,2$ ) and 2 D-wave states ( $^1D_2$  and  $^3D_2$ ). Many works have been done to study the light hadron decay of S-wave and P-wave in framework of NRQCD factorization method while for D-wave states decay into light hadron the numerical prediction is still given by potential model until now. In the following, we will briefly review the knowledge of both the short distance coefficients and long distance matrix elements for the LH decay of S-wave and P-wave states  $J/\psi$ ,  $\psi(2S)$ ,  $\eta_c$   $\eta_c(2S)$ ,  $\chi_{cJ}$  and  $h_c$ .

### 18.1.1 $J/\psi$ , $\psi'$ decay

The  $J/\psi$  and  $\psi'$  can decay to light hadrons via the annihilation of the  $c$  and  $\bar{c}$ . The annihilation decay dominates the  $J/\psi$  decay rate, while it accounts for 14% of the  $\psi'$  decay rate since hadron and the electro-magnetic transitions govern  $\psi'$  decays. The  $J/\psi$  and  $\psi'$  annihilation decay rates are small since at leading order, they can decay only through three-gluon annihilations. Both the matrix element and the phase-space constraint the rate. In the NRQCD factorization formula[272], the expressions for inclusive decay rate of  $J/\psi$  have been known at relative  $v^4$  order:[273]

$$\begin{aligned} \Gamma(J/\psi \rightarrow l.h.) = & \frac{2\text{Im}f_1(^3S_1)}{m_c^2} \langle \psi | \mathcal{O}_1(^3S_1) | \psi \rangle + \frac{2\text{Im}g_1(^3S_1)}{m_c^4} \langle \psi | \mathcal{P}_1(^3S_1) | \psi \rangle \\ & + \frac{2\text{Im}f_8(^1S_0)}{m_c^2} \langle \psi | \mathcal{O}_8(^1S_0) | \psi \rangle + \frac{2\text{Im}f_8(^3S_1)}{m_c^2} \langle \psi | \mathcal{O}_8(^3S_1) | \psi \rangle \\ & + \sum_{J=0,1,2} \frac{2\text{Im}f_8(^3P_J)}{m_c^4} \langle \psi | \mathcal{O}_8(^3P_J) | \psi \rangle + \frac{2\text{Im}h_1^1(^3S_1)}{m_c^6} \langle \psi | \mathcal{Q}_1^1(^3S_1) | \psi \rangle \\ & + \frac{2\text{Im}h_1^2(^3S_1)}{m_c^6} \langle \psi | \mathcal{Q}_1^2(^3S_1) | \psi \rangle. \end{aligned} \quad (18.1.1)$$

where the definitions of those operators  $\mathcal{O}$ ,  $\mathcal{P}$  and  $\mathcal{Q}$  could be found in Ref.[272, 273]. From the velocity scaling rule in Ref.[272], it could be find that the matrix element of  $\mathcal{O}_1(^3S_1)$  is at relative  $v^0$  order, the matrix element of  $\mathcal{P}_1(^3S_1)$  is at relative  $v^2$  order, the matrix element of  $\mathcal{O}_8(^1S_0)$  is at relative  $v^3$  order and the matrix elements of  $\mathcal{O}_8(^3S_1)$ ,  $\mathcal{O}_8(^3P_J)$ ,  $\mathcal{Q}_1^1(^3S_1)$ ,  $\mathcal{Q}_1^2(^3S_1)$  is at relative order  $v^4$ .

The short distance coefficients have been calculated by many groups to different order of  $\alpha_s$ .  $2\text{Im}f_1(^3S_1)$  were computed at  $\mathcal{O}(\alpha_s^3)$  and  $\mathcal{O}(\alpha_s^4)$  by Mackenzie and Lapage[274]:

$$2\text{Im}f_1(^3S_1) = \frac{20(\pi^2 - 9)\alpha_s^3(m_c)}{243} \left\{ 1 + [-9.46(2)C_F + 4.13(17)C_A - 1.161(2)n_f] \frac{\alpha_s}{\pi} \right\}^2 \quad (18.1.2)$$

<sup>2</sup>We have drop the contribution of electromagetic annihilation process  $J/\psi \rightarrow \gamma^* \rightarrow q\bar{q}$

where  $C_F = \frac{4}{3}$ ,  $C_A = 3$  and  $n_f$  is the flavors of light quarks and equals to 3 in charmonium systems. The coefficient of relative order  $v^2$  operator  $\mathcal{P}(^3S_1)$  was calculated in Ref.[275]:

$$2\text{Im}g_1(^3S_1) = -\frac{5(19\pi^2 - 132)}{729}\alpha_s^3, \quad (18.1.3)$$

which is about 5.33 times larger than  $2\text{Im}f_1(^3S_1)$  at  $\alpha_s$  leading order. This indicates that the relativistic corrections to  $J/\psi$  decay into *l.h.* is important. The coefficients of those color octet coefficients were computed up to  $\mathcal{O}(\alpha_s^3)$  in Ref.[276]. Some of them are about two orders of magnitude larger than  $2\text{Im}f_1(^3S_1)$ , which suggests that the higher Fock states may play a more important role in annihilation decays than is commonly believed. The combination  $2\text{Im}h_1(^3S_1) + 2\text{Im}h_1^2(^3S_1)$  were compute in Ref.[273], which is also about an order of magnitude larger than  $2\text{Im}f_1(^3S_1)$ .

The matrix elements are expectation values in the  $J/\psi$  of local gauge-invariant NRQCD operators that measure the inclusive probability of finding a  $c\bar{c}$  in the  $J/\psi$  at the same point and in the color and angular-momentum state specified. They could be studied in lattice simulations, or determined by fitting the experiment decay data, or estimated through the operator evolution equations. The vacuum-saturation approximation relates the matrix element of  $\mathcal{O}_1(^3S_1)$  in (18.1.1) with the square of the non-relativistic shördinger wave function at the origin with errors up to  $\mathcal{O}(v^4)$ . In pNRQCD effective theory the matrix elements of  $\mathcal{P}_1(^3S_1)$ ,  $\mathcal{O}_8(^1S_0)$ ,  $\mathcal{O}_8(^3S_1)$ , and  $\mathcal{O}_8(^3P_J)$  could be related with the leading order matrix element  $\langle\psi|\mathcal{O}_1(^3S_1)|\psi\rangle$  (For details see [277] and reference therein). And the knowledge of the the dimension 10 operators  $\mathcal{Q}$  is poor. The same expression of the decay rate hold for  $\psi'$  once the state  $J/\psi$  is substituted by the  $\psi'$ . Since a large number of  $J/\psi$  and  $\psi'$  could be directly produced at BES, then the BES III project provide a good way to determinate those non-perturbative parameters.

### 18.1.2 $\eta_c$ decay

The  $\eta_c$  is the ground state of the charmonium states that could be produced through the  $\gamma\eta_c$  decay channel of  $J/\psi$ . It can decay only via annihilation of the  $c\bar{c}$ . NRQCD factorization formula for  $\eta_c$  decay into light hadron at  $\mathcal{O}(v^4)$  are:

$$\begin{aligned} \Gamma(\eta_c \rightarrow \text{l.h.}) = & \frac{2\text{Im}f_1(^1S_0)}{m_c^2}\langle\eta_c|\mathcal{O}_1(^1S_0)|\eta_c\rangle + \frac{2\text{Im}g_1(^1S_0)}{m_c^4}\langle\eta_c|\mathcal{P}_1(^1S_0)|\eta_c\rangle \\ & + \frac{2\text{Im}f_8(^3S_1)}{m_c^2}\langle\eta_c|\mathcal{O}_8(^3S_1)|\eta_c\rangle + \frac{2\text{Im}f_8(^1S_0)}{m_c^2}\langle\eta_c|\mathcal{O}_8(^1S_0)|\eta_c\rangle \\ & + \frac{2\text{Im}f_8(^1P_1)}{m_c^4}\langle\eta_c|\mathcal{O}_8(^1P_1)|\eta_c\rangle + \frac{2\text{Im}h_1(^1S_0)}{m_c^6}\langle\eta_c|\mathcal{Q}_1^1(^1S_0)|\eta_c\rangle \\ & + \frac{2\text{Im}h_1^2(^1S_0)}{m_c^6}\langle\eta_c|\mathcal{Q}_1^2(^1S_0)|\eta_c\rangle, \end{aligned} \quad (18.1.4)$$

Where the definitions of those operators  $\mathcal{O}$ ,  $\mathcal{P}$  and  $\mathcal{Q}$  could also be found in Ref.[272, 273]. The coefficients  $2\text{Im}f_1(^1S_0)$  were given up to  $\mathcal{O}(\alpha_s^3)$  in Ref.[278, 279]:

$$2\text{Im}f_1(^1S_0) = \frac{4\pi\alpha_s^2(2m_c)}{9}\{1 + [(\frac{\pi^2}{4} - 5)C_F$$

$$+ \left( \frac{199}{18} - \frac{13\pi^2}{24} \right) C_A - \frac{8}{9} n_f \right] \frac{\alpha_s}{\pi} \} \quad (18.1.5)$$

The coefficient of the relative order  $v^2$  operator  $\mathcal{P}(^1S_0)$  is computed in Ref.[275]. It is

$$2\text{Img}(^1S_0) = -\frac{4C_F}{3N_c}\alpha_s^2 \quad (18.1.6)$$

At leading order in  $\alpha_s$   $\frac{\text{Img}(^1S_0)}{\text{Im}f(^1S_0)} = -\frac{4}{3}$ , which means the leading order relativistic corrections is sizable in  $\eta_c$  decay into light hadrons. The coefficients  $2\text{Im}f_8(^3S_1)$  and  $2\text{Im}f_8(^1S_0)$  have been computed in Ref.[276], which are in the same order of magnitude as  $\text{Im}f(^1S_0)$ . The coefficient  $2\text{Im}f_8(^1P_1)$  could be found in the Appendix of Ref.[272] at  $\mathcal{O}(\alpha_s^2)$ :

$$2\text{Im}f_8(^1P_1) = \frac{\pi N_c}{6}\alpha_s^2. \quad (18.1.7)$$

The combination  $2\text{Im}h_1^1(^1S_0) + 2\text{Im}h_1^2(^1S_0)$  were compute in Ref.[273], which is also at the same order of magnitude as  $2\text{Im}f_1(^1S_0)$ .

In heavy quark limit, the matrix elements of  $\mathcal{O}_1(^1S_0)$ ,  $\mathcal{P}_1(^1S_0)$ ,  $\mathcal{O}_8(^3S_1)/3$ ,  $\mathcal{O}_8(^1S_0)$ ,  $\mathcal{O}_8(^1P_1)/9$ ,  $\mathcal{Q}_1^1(^1S_0)$ ,  $\mathcal{Q}_1^2(^1S_0)$  in  $\eta_c$  state are equal to the matrix elements of  $\mathcal{O}_1(^3S_1)$ ,  $\mathcal{P}_1(^3P_1)$ ,  $\mathcal{O}_8(^1S_0)$ ,  $\mathcal{O}_8(^3S_1)$ ,  $\mathcal{O}_8(^3P_J)/(2J+1)$ ,  $\mathcal{Q}_1^1(^3S_1)$ ,  $\mathcal{Q}_1^2(^3S_1)$  in  $J/\psi$  state, respectively, with errors up to relative  $\mathcal{O}(v^2)$ . In Ref.[280],  $\langle \eta_c | \mathcal{O}_1(^1S_0) | \eta_c \rangle$  was calculated in quenched lattice simulation, and their result in  $\overline{MS}$  scheme and at the factorization scale of 1.3GeV is about 0.33GeV<sup>3</sup>.

Comparing with the  $J/\psi$ , the decay width of  $\eta_c$  is much larger because  $c\bar{c}$  can annihilate into two gluons and the short distance coefficients is order  $\alpha_s^2$  at the leading order. Also in the case of  $J/\psi$ , there is an additional suppression factor  $\pi^2 - 9$  in the short distance coefficient of  $c\bar{c} \rightarrow ggg$

The  $\eta_c$  have also electromagnetic decay  $\eta_c \rightarrow \gamma\gamma$ . NRQCD factorization formula can also apply for  $\eta_c \rightarrow \gamma\gamma$ . An interesting quantity is the ratio of the decay rate for  $\eta_c \rightarrow$  light hadrons to that for the  $\eta_c \rightarrow \gamma\gamma$ , the inverse branching fraction, denoted by  $R$ . It is relatively easy to be measured in experiments. In  $R$ , the NRQCD matrix element cancel up to order  $v^4$ , the relativistic corrections also cancel at the leading order of  $\alpha_s$ . This leaves  $R$  almost a pure short-distance number. In principle,  $R$  may be calculated precisely in pQCD. However, one find that the radiative correction to  $R$  is quite large and  $R$  is sensitive to the choice of the renormalization scale  $\mu$ . *e.g.*, when  $\mu$  varies from  $2m_c$  to  $0.5m_c$ ,  $R$  varies by factor 5 for the next leading order result. Bodwin and Chen show that the most important corrections arise from the bubble diagram. After the bubble diagrams are resummed, a result which is insensitive to  $\mu$  is obtained, which is in agreement with the experimental results. This quantity is expected to be measured accurately at BES III.

### 18.1.3 $P$ -wave $\chi_{cJ}$ decay

An interesting application of the NRQCD factorization formula is the charmonium  $P$ -wave annihilation decay. The decay rate was calculated by Barbieri *et al.*[268, 269] to the next-leading order of  $\alpha_s$  in the color-singlet model. It was found that in  $\chi_{cJ} \rightarrow ggg$  ( $J = 0, 2$ ) processes the infrared divergence cancels when combined with the virtual corrections, while there were infrared divergences, which arise from the kinematic region where the emitted gluon is soft in the process  $\chi_{cJ} \rightarrow q\bar{q}g$ . This indicates that the long-distance

effects enter into the short-distance coefficients and the factorization in the conventional color-singlet model fails. The problem was nicely solved in the NRQCD factorization framework[281]. According to it, the soft gluon emitting process is absorbed into the long distance matrix elements while the short-distance process is the color-octet  $c\bar{c}$  annihilation into a light quark pair. The corresponding long-distance matrix element is NRQCD S-wave color-octet matrix element. Its contribution to the annihilation decay rates of the  $P$ -wave charmonia is significant since the short distance process is the same order as the leading order color singlet process for  $\chi_{c0}$  and  $\chi_{c2}$  but enhanced by order  $\alpha_s(m_c)$  for  $\chi_{c1}$  compared with the leading order color-single process. The color-octet matrix elements are at the same order of  $v^2$  as that of the color-singlet one. In the NRQCD factorization formula, the  $P$ -wave annihilation decay rates at  $v^2$  leading order are expressed as:

$$\begin{aligned}\Gamma(\chi_{cJ} \rightarrow l.h.) &= \frac{2\text{Im}f_1(^3P_J)}{m_c^4} \langle \chi_{cJ} | \mathcal{O}_1(^3P_J) | \chi_{cJ} \rangle \\ &+ \frac{2\text{Im}f_8(^3S_1)}{m_c^2} \langle \chi_{cJ} | \mathcal{O}_8(^3S_1) | \chi_{cJ} \rangle,\end{aligned}\quad (18.1.8)$$

A full list of those short-distance coefficients is summarized in Ref.[276]<sup>3</sup>.

$$\begin{aligned}2\text{Im}f_1(^3S_1) &= n_f \frac{\alpha_s^2 \pi}{3} \left\{ 1 + \frac{\alpha_s}{\pi} \left[ -C_F \frac{13}{4} + C_A \left( \frac{133}{18} + \frac{2}{3} \ln 2 - \frac{\pi^2}{4} \right) \right. \right. \\ &\quad \left. \left. - \frac{5}{9} n_f + 2b_0 \log \frac{\mu}{2m_c} \right] \right\} + \frac{5}{3} \alpha_s^3 \left( -\frac{73}{4} + \frac{67}{36} \pi^2 \right)\end{aligned}\quad (18.1.9)$$

$$\begin{aligned}2\text{Im}f_1(^3P_0) &= C_F \alpha_s^2 \pi \left\{ 1 + \frac{\alpha_s}{\pi} \left[ C_F \left( -\frac{7}{3} + \frac{\pi^2}{4} \right) + C_A \left( \frac{427}{81} - \frac{1}{144} \pi^2 \right) \right. \right. \\ &\quad \left. \left. + 2b_0 \log \frac{\mu}{2m_c} \right] \right\} + n_f \alpha_s^3 \frac{4}{27} C_F \left( -\frac{29}{6} - \log \frac{\mu_\Lambda}{2m_c} \right)\end{aligned}\quad (18.1.10)$$

$$2\text{Im}f_1(^3P_1) = \frac{C_F \alpha_s^3}{2} \left( \frac{587}{27} - \frac{317}{144} \pi^2 \right) + n_f \alpha_s^3 \frac{4}{27} C_F \left( -\frac{4}{3} - \log \frac{\mu_\Lambda}{2m_c} \right)\quad (18.1.11)$$

$$\begin{aligned}2\text{Im}f_1(^3P_2) &= \frac{4C_F \alpha_s^2 \pi}{15} \left\{ 1 + \frac{\alpha_s}{\pi} \left[ -4C_F + C_A \left( \frac{2185}{216} - \frac{337}{384} \pi^2 + \frac{5}{3} \log 2 \right) \right. \right. \\ &\quad \left. \left. + 2b_0 \log \frac{\mu}{2m_c} \right] \right\} + n_f \alpha_s^3 \frac{4}{27} C_F \left( -\frac{29}{15} - \log \frac{\mu_\Lambda}{2m_c} \right)\end{aligned}\quad (18.1.12)$$

At  $\mathcal{O}(v^0)$ , both the color singlet matrix elements  $\langle \chi_{cJ} | \mathcal{O}_1(^3P_J) | \chi_{cJ} \rangle$  and color octet ones  $\langle \chi_{cJ} | \mathcal{O}_8(^3S_1) | \chi_{cJ} \rangle$  are the same for different  $J$ , then there are only two non-perturbative parameters in three independent processes  $\chi_{cJ} \rightarrow l.h.$ . This provides a good way to test the validity of NRQCD factorization method. In [282], Huang and Chao use  $\Gamma(\chi_{c1,c2} \rightarrow l.h.)$  as inputs to predict  $\Gamma(\chi_{c0} \rightarrow l.h.)$ , and their result is consistent with the experimental data.<sup>4</sup> As pointed out in chapter 4 of Ref.[283], the ratios of the differences of  $\chi_{cJ} \rightarrow l.h.$  are not dependent on any non-perturbative parameters, and there they give the experimental results of the considered ratios determined from PDG 2000 [284] and PDG

<sup>3</sup>The normalization of the color singlet operators in Ref.[276] is different from those given in Ref.[272]

<sup>4</sup>There is an error in their original expression, but it has only a little effect on the numerical result.

2004 [285] respectively, and the theory predictions at LO and NLO are also given. Here in Table 18.1, we give the PDG 2006 [286] results of these ratios, and also list experimental results of PDG 2004 and the theoretical LO and NLO results in Table 4.8 of Ref.[283] for comparison. The values in Table 18.1 show that the discrepancy between experimental and NLO theoretical results becomes a little larger, but still consistent with NLO theoretical results and the errors are reduced. In Ref.[287], the BES Collaboration only reports their measurements of  $\Gamma(\chi_{c0})$  and  $\Gamma(\chi_{c1})$  in the  $\psi(2S) \rightarrow \gamma\chi_{cJ}$  processes. With more data accumulated at BES III,  $\Gamma(\chi_{c2})$  could be measured and then the experimental results of the considered ratios will be more accurate, and this is helpful for our understanding of the light hadron decay of  $\chi_{cJ}$ . Another usage of the experimental data of  $\Gamma(\chi_{cJ} \rightarrow l.h.)$

Table 18.1: Comparison of the ratios of the differences between  $\chi_{cJ} \rightarrow l.h.$ . The experimental values PDG 2006 are obtained from Ref.[286] with the inputs  $\Gamma(\chi_{c0} \rightarrow l.h.) \approx \Gamma(\chi_{c0}) = 10.5 \pm 0.9$  MeV,  $\Gamma(\chi_{c1} \rightarrow l.h.) \approx \Gamma(\chi_{c1})[1 - \mathcal{B}(\chi_{c1} \rightarrow \gamma J/\psi)] = 0.57 \pm 0.04$  MeV,  $\Gamma(\chi_{c2} \rightarrow l.h.) \approx \Gamma(\chi_{c2})[1 - \mathcal{B}(\chi_{c2} \rightarrow \gamma J/\psi)] = 1.56 \pm 0.10$  MeV. The PDG 2004 experimental values and LO and NLO theoretical results are the same as those in Table 4.8 of Ref.[283].

Ratio	PDG 2006	PDG 2004	LO	NLO
$\frac{\Gamma(\chi_{c0} \rightarrow l.h.) - \Gamma(\chi_{c1} \rightarrow l.h.)}{\Gamma(\chi_{c2} \rightarrow l.h.) - \Gamma(\chi_{c1} \rightarrow l.h.)}$	$10.0 \pm 0.9$	$8.9 \pm 1.1$	3.75	$\approx 7.63$
$\frac{\Gamma(\chi_{c0} \rightarrow l.h.) - \Gamma(\chi_{c2} \rightarrow l.h.)}{\Gamma(\chi_{c2} \rightarrow l.h.) - \Gamma(\chi_{c1} \rightarrow l.h.)}$	$9.0 \pm 0.9$	$7.9 \pm 1.5$	2.75	$\approx 6.63$

is to determine the long distance matrix elements in  $\chi_{cJ}$  production processes, since in NRQCD factorization method the long distance matrix elements are universal and the differences between the decay matrix elements and production matrix elements are at relative  $v^4$  order. With the obtained production matrix elements from decay processes, it is certainly helpful for us to understand the production mechanism of  $\chi_{cJ}$ . In Ref.[288], the color singlet matrix elements are obtained by fitting experiment data and the best value result at  $m_c=1.5$  GeV is  $\langle \chi_{cJ} | \mathcal{O}_1(^3P_J) | \chi_{cJ} \rangle / m_c^2 = 3.2 \pm 0.4 \times 10^{-2}$  GeV<sup>3</sup>, and the ratio of color singlet matrix element to color octet matrix element is also given there. In Table 18.2 we give the average values of  $\langle \chi_{cJ} | \mathcal{O}_1(^3P_J) | \chi_{cJ} \rangle$ <sup>5</sup> and  $\langle \chi_{cJ} | \mathcal{O}_8(^3S_1) | \chi_{cJ} \rangle$  obtained from PDG 2006 [286] at different renormalization scales.

## 18.2 P-wave $h_c$ decay

P-wave  $h_c$  decay<sup>6</sup> Because of C-parity conservation,  $h_c$  can not decay into  $gg$  final

<sup>5</sup>There is a factor  $1/(2N_c)$  difference between our singlet operators and those in the original paper.

<sup>6</sup>Yu-Qi Chen and Zhi-Guo He

Table 18.2: Results of the long distance matrix elements at different renormalization scales by fitting PDG 2006 [286]. The numerical inputs are  $\Gamma(\chi_{c0} \rightarrow l.h.) \approx \Gamma(\chi_{c0}) = 10.5 \pm 0.9$  MeV,  $\Gamma(\chi_{c1} \rightarrow l.h.) \approx \Gamma(\chi_{c1})[1 - \mathcal{B}(\chi_{c1} \rightarrow \gamma J/\psi)] = 0.57 \pm 0.04$  MeV,  $\Gamma(\chi_{c2} \rightarrow l.h.) \approx \Gamma(\chi_{c2})[1 - \mathcal{B}(\chi_{c2} \rightarrow \gamma J/\psi)] = 1.56 \pm 0.10$  MeV,  $m_c = 1.5$  GeV,  $\alpha_s = \alpha_s(\mu)$  and  $\alpha_s(2m_c) = 0.249$ .

	$\mu = 1.0m_c$	$\mu = \sqrt{2}m_c$	$\mu = 2.0m_c$
$\langle \chi_{cJ}   \mathcal{O}_1(^3P_J)   \chi_{cJ} \rangle (10^{-2} \text{GeV}^5)$	0.97	1.1	1.4
$\langle \chi_{cJ}   \mathcal{O}_1(^3P_J)   \chi_{cJ} \rangle (10^{-2} \text{GeV}^3)$	0.40	0.38	0.39

state. And there is also infrared divergence problem[266] in  $h_c \rightarrow ggg$  process in the color-singlet model. This problem was solved in the framework of NRQCD factorization method in Ref.[289], and summarized in [276]. At leading order in  $v^2$  the expression of  $h_c$  decay into light hadron is:

$$\begin{aligned} \Gamma(h_c \rightarrow l.h.) &= \frac{2\text{Im}f_1(^1P_1)}{m_c^4} \langle h_c | \mathcal{O}_1(^1P_1) | h_c \rangle \\ &+ \frac{2\text{Im}f_8(^1S_0)}{m_c^2} \langle h_c | \mathcal{O}_8(^1S_0) | h_c \rangle, \end{aligned} \quad (18.2.13)$$

And at  $\mathcal{O}(\alpha_s^3)$  the expression of the short distance coefficients are:

$$2\text{Im}f_1(^1P_1) = \frac{40\alpha_s^3}{81} \left( -\frac{7}{3} + \frac{7\pi^2}{48} - \ln \frac{\mu_\Lambda}{2m_c} \right) \quad (18.2.14)$$

$$\begin{aligned} 2\text{Im}f_8(^1S_0) &= \frac{5C_F\alpha_s^2\pi}{6} \left\{ 1 + \frac{\alpha_s}{\pi} \left[ C_F \left( -5 + \frac{\pi^2}{4} \right) \right. \right. \\ &\quad \left. \left. + C_A \left( \frac{122}{9} - \frac{17}{24}\pi^2 \right) - \frac{8}{9}n_f + 2b_0 \log \frac{\mu}{2m_c} \right] \right\} \end{aligned} \quad (18.2.15)$$

The matrix elements of both color singlet and color octet operators are studied in quenched lattice simulations[280]. The numerical result is  $\langle h_c | \mathcal{O}_1(^1P_1) | h_c \rangle \approx 8.0 \times 10^{-2} \text{GeV}^5$  and  $\langle h_c | \mathcal{O}_8(^1S_0) | h_c \rangle \approx 4.7 \times 10^{-3} \text{GeV}^3$  in the  $\overline{MS}$  scheme with the factorization scale equaling to 1.3GeV. In Ref.[288], the matrix elements of  $h_c$  are estimated through the experimental data of  $\chi_{cJ}$  owing to heavy quark spin symmetry, and the light hadron decay width is also predicted to be  $\Gamma(h_c \rightarrow l.h.) = 0.72 \pm 0.32$  MeV. At present the uncertainty of  $h_c$  decay into light hadrons is not small on both experimental side and theoretical side. With more  $h_c$  are accumulated at BES III from  $\psi' \rightarrow \pi^0 h_c$  process, the light hadron decay width of  $h_c$  will be measured more precisely.

## 18.3 $\rho - \pi$ puzzle<sup>7</sup>

### 18.3.1 Introduction

Crisply defined experimental puzzles in high-energy physics frequently have the prospect for leading to new discoveries. Therefore puzzles in physics often draw considerable attention from theorists. The ratios of hadronic decays of the  $\psi(3686)$  (also known as  $\psi'$ ) to the same decay modes of the  $J/\psi$  is a puzzle that has been studied in some depth since 1983.

The OZI suppressed decays of  $J/\psi$  and  $\psi'$  to hadrons are via three gluons or a photon. In both cases, perturbative QCD (pQCD) provides the relation [290]

$$Q_h = \frac{\mathcal{B}_{\psi' \rightarrow h}}{\mathcal{B}_{J/\psi \rightarrow h}} = \frac{\mathcal{B}_{\psi' \rightarrow e^+ e^-}}{\mathcal{B}_{J/\psi \rightarrow e^+ e^-}} \approx 12.7\%. \quad (18.3.16)$$

This relation is referred to as the “12% rule” and it is expected to hold to a reasonably good degree for both inclusive and exclusive decays. The so-called “ $\rho\pi$  puzzle” is the observation that the Eq. (18.3.16) prediction is severely violated for the  $\rho\pi$  and several other decay channels. The first evidence for this effect was reported by the Mark-II Collaboration in 1983 [291]. Since then, many theoretical explanations have been put forth in attempts to decipher this puzzle.

With the recent BESII and CLEOc experimental results on  $J/\psi$  and  $\psi'$  two-body decays to vector-pseudoscalar ( $VP$ ), vector-tensor ( $VT$ ), pseudoscalar-pseudoscalar ( $PP$ ), and baryon-antibaryon ( $B\bar{B}$ ) pairs, plus results on multi-body decays of the  $J/\psi$ , the  $\psi'$  and even the  $\psi(3770)$  (also known as  $\psi''$ ) [292]-[312], a variety of explanations have been proposed for this puzzle that can be tested with higher accuracy data. Here we survey theoretical work on the  $\rho\pi$  puzzle and compare them with available experimental data. From the theoretical point of view, since the  $Q$ -value for  $\rho\pi$  is smaller than 12%, it may be caused either by an enhanced  $J/\psi$  or suppressed  $\psi'$  decay rate, or by a combination of the two. Thus, we classify the various theoretical speculations into three categories:

1.  $J/\psi$ -enhancement hypothesis, which attributes the small  $Q$ -value to an enhanced branching fraction for  $J/\psi$  decays.
2.  $\psi'$ -suppression hypothesis, which attributes the small  $Q$ -value to a suppression of branching fractions for  $\psi'$  decays.
3. Other hypotheses, *i.e.* those not included in the above two categories.

### 18.3.2 Review of theoretical work on the $\rho\pi$ puzzle

#### $J/\psi$ -enhancement models

In the earlier days of the  $\rho\pi$  puzzle, it was noticed that the decay of  $1^{--}$  charmonium into  $\rho\pi$  final state violates the Hadronic Helicity Conservation (HHC) theorem (this is discussed below) [313], and, so, such decays should be suppressed. Therefore, there is some speculation on possible mechanisms that enhance  $J/\psi \rightarrow \rho\pi$  decays. Two schemes were proposed that follow this line of reasoning.

---

<sup>7</sup>Xiaohu Mo, Ping Wang, and Changzheng Yuan

### 1. $J/\psi$ -glueball admixture scheme

The idea that  $J/\psi$  hadronic decays proceed via glueball emission was first proposed by Freund and Nambu [314] (FN hereafter) soon after the discovery of the  $J/\psi$  to explain the breaking of Okubo-Zweig-Iizuka (OZI) rule [315]. In this mechanism, the breaking results from the mixing of the  $\omega$ ,  $\phi$ , and  $J/\psi$  mesons with an  $SU(4)$ -singlet vector meson  $\mathcal{O}$ . They predicted that this  $\mathcal{O}$  meson would lie in the 1.4-1.8  $\text{GeV}/c^2$  mass range with a width that is greater than  $40 \text{ MeV}/c^2$ , and that it would decay copiously into  $\rho\pi$  and  $K^*\overline{K}$ , while decays into  $K\overline{K}$ ,  $e^+e^-$  and  $\mu^+\mu^-$  final states would be severely suppressed. These authors presented several quantitative predictions for experimental investigation. Two of them are:

$$R_1 = \frac{\Gamma_{J/\psi \rightarrow \rho\pi}}{\Gamma_{\phi \rightarrow \rho\pi}} = 0.0115 - 0.087 ,$$

$$R_2 = \frac{\Gamma_{J/\psi \rightarrow K\overline{K}}}{\Gamma_{J/\psi \rightarrow \rho\pi}} < 8 \times 10^{-5} .$$

With currently available data and using the three pion final state as a substitute for  $\rho\pi$  in both  $\phi$  [52] and  $J/\psi$  [292, 293] decays, we obtain  $R_1 \approx 0.003$  for the first ratio, which is almost an order-of-magnitude smaller than the prediction. For the second ratio, using the PDG [52] value for  $K^+K^-$  and a new experiment result for  $K_S^0 K_L^0$  [295], we estimate that  $\mathcal{B}(J/\psi \rightarrow K\overline{K}) \sim 10^{-4}$ , which, taken together with the results for  $\rho\pi$  [292, 293], gives  $R_2 \sim 10^{-2}$  which is much larger than the prediction.

The first attempt to explain the  $\rho\pi$  puzzle in terms of a glueball with mass near that of the  $J/\psi$  was proposed by Hou and Soni [316] (HS hereafter). They attributed the enhancement of  $J/\psi \rightarrow K^*\overline{K}$  and  $J/\psi \rightarrow \rho\pi$  decay modes to the mixing of the  $J/\psi$  with a near-by  $J^{PC} = 1^{--}$  vector gluonium, also designated by  $\mathcal{O}$ . The differences between FN's and HS's pictures lie in the following aspects:

- Based on the potential model applied to glueballs, the mass of a low-lying three-gluon state is estimated to be around  $2.4 \text{ GeV}/c^2$  [317], rather than the 1.4 to  $1.8 \text{ GeV}/c^2$  value of Ref. [314].
- Mixing of  $\mathcal{O}$  with  $\psi'$  is also taken into account; this was ignored in the previous work.
- Since the gauge coupling constant in QCD is momentum dependent, the mixing parameter is taken to be a function of the invariant mass  $q^2$ , and, therefore, decreases rather sharply with increasing  $q^2$ . Such a propagator effect gives rise to suppression of the  $\psi'$  decay rates to  $\rho\pi$  and  $K^*\overline{K}$  channels relative to those of the  $J/\psi$ .

By virtue of these assumptions, HS suggested a search for the vector gluonium state in certain hadronic decays of the  $\psi'$ , such as  $\psi' \rightarrow \pi\pi + X$ ,  $\eta + X$ ,  $\eta' + X$ , where  $X$  decays into VP final states [316].

Based on HS's idea, Brodsky, Lepage, and Tuan [318] (BLT) refined the glueball hypothesis for the  $\rho\pi$  puzzle. They assumed the general validity of the pQCD theorem that the total hadron helicity is conserved in high-momentum-transfer exclusive

processes, in which case the decays to  $\rho\pi$  and  $K^*\overline{K}$  are forbidden for both the  $J/\psi$  and  $\psi'$ . This pQCD theorem is often referred to as the rule of Hadronic Helicity Conservation (HHC) [313], and is based on the assumption of the short-range “pointlike” interactions among the constituent quarks. For instance,  $J/\psi(c\bar{c}) \rightarrow 3g$  has a short range  $\simeq 1/m_c$  and a correspondingly short time-scale for the interaction. Nevertheless, if the three gluons subsequently resonate, thereby forming an intermediate gluonium state  $\mathcal{O}$  with a large transverse size and a correspondingly extended time scale, HHC would cease to be valid. In essence, the HS mechanism takes over at this latter stage.

Decays to final states  $h$  that proceed only through the intermediate gluonium state are expected to satisfy the ratio

$$Q_h = \frac{\mathcal{B}(\psi' \rightarrow e^+e^-)}{\mathcal{B}(J/\psi \rightarrow e^+e^-)} \frac{(M_{J/\psi} - M_{\mathcal{O}})^2 + \Gamma_{\mathcal{O}}^2/4}{(M_{\psi'} - M_{\mathcal{O}})^2 + \Gamma_{\mathcal{O}}^2/4}. \quad (18.3.17)$$

The  $Q_h$  value is small when the  $\mathcal{O}$  mass is close to the mass of the  $J/\psi$ . Experimental limits at the time [319, 291, 318] implied that the  $\mathcal{O}$  mass was within  $80 \text{ MeV}/c^2$  of the mass of the  $J/\psi$  and its total width was less than  $160 \text{ MeV}/c^2$ . Brodsky *et al.* recommended direct searches for the  $\mathcal{O}$  by scan measurements of the  $e^+e^- \rightarrow VP$  cross section across the  $J/\psi$  resonance.

A related work by Chan and Hou [320] studied the  $J/\psi$  and vector glueball  $\mathcal{O}$  mixing angle  $\theta_{\mathcal{O}\psi}$  and amplitude  $f_{\mathcal{O}\psi}$  in the framework of potential models of heavy quarks and constituent gluons. They obtained  $|\tan \theta_{\mathcal{O}\psi}| = 0.015$  and  $f_{\mathcal{O}\psi}(m_{\mathcal{O}\psi}^2) = 0.008 \text{ GeV}^2$ .

On the experimental side, BES searched for this hypothetical particle in a  $\rho\pi$  scan across the  $J/\psi$  mass region in  $e^+e^-$  annihilations as well as in the decays of  $\psi' \rightarrow \pi\pi\mathcal{O}$ ,  $\mathcal{O} \rightarrow \rho\pi$ , and found no evidence for its existence [297, 321]. The data constrained the mass and width of the  $\mathcal{O}$  to be in the ranges  $|M_{\mathcal{O}} - M_{J/\psi}| < 80 \text{ MeV}/c^2$  and  $4 < \Gamma_{\mathcal{O}} < 50 \text{ MeV}/c^2$  [322]. Although the absence of any distortion to the  $J/\psi \rightarrow \rho\pi$  line-shape in the BES energy scan does not rule out  $M_{\mathcal{O}} \simeq M_{J/\psi}$ , it puts a lower bound on  $\Gamma_{\mathcal{O}}$ . However, as indicated in Ref. [323], the experimentally constrained mass is several hundred  $\text{MeV}/c^2$  lower than the mass of the lightest vector glueball calculated in lattice simulations of QCD without dynamical quarks [324].

Recent experimental data from BES and CLEOc are unfavorable to this glueball hypothesis. Among these results is the observed large branching fraction for the isospin-violating VP mode  $\psi' \rightarrow \omega\pi^0$  [298, 299, 305]. This contradicts the assertion that the pattern of suppression depends on the spin-parity of the final state mesons. In addition, according to BLT’s analysis, one obtains the prediction [325]

$$\frac{\mathcal{B}(J/\psi \rightarrow \omega\pi^0)}{\mathcal{B}(J/\psi \rightarrow \rho^0\pi^0)} < 0.0037$$

which is much smaller than the PDG06 value 0.08 [52]. Another experimental result that is unfavorable to this hypothesis is the suppression of  $\psi'$  decays into vector-tensor (VT) final states [307, 308]. Since hadronic VT decays, unlike the VP decays,

conserve HHC, some other mechanism(s) must be responsible for this suppression. Furthermore, it has been argued that the  $\mathcal{O}$  may also explain the decay of  $J/\psi$  into  $\phi f_0$  (previously named  $S^*$ ) but not to  $\rho a_0(980)$  (previously named  $\delta$ ), since the  $\mathcal{O}$  mixes with the  $\phi$  and enhances a mode that would otherwise be suppressed [318]. However, the decay  $\psi' \rightarrow \phi f_0$  [322] is not suppressed experimentally, which implies the absence of an anomalous enhancement in  $J/\psi \rightarrow \phi f_0$ , thus contradicting this explanation. Anselmino *et al.* extended the idea of  $J/\psi$ - $\mathcal{O}$  mixing to the case of  $\eta_c \rightarrow VV$  and  $p\bar{p}$  [326]. They suggested that the enhancement of these decays can be attributed to the presence of a tri-gluonium pseudoscalar state with a mass close to the  $\eta_c$  mass. So far there is no experimental evidence for such a state.

## 2. Intrinsic-charm-component scheme

Brodsky and Karliner (BK) put forth an explanation for the puzzle based on the hypothesized existence of intrinsic charm  $|q\bar{q}c\bar{c}\rangle$  Fock components in the light vector mesons [327]. They noticed that quantum fluctuations in a QCD bound state wave function will inevitably produce Fock states containing heavy quark pairs. The intrinsic heavy quark pairs are multiconnected to the valence quarks of the light hadrons, and the wave functions describing these configurations will have maximal amplitude at minimal off-shellness and minimal invariant mass. In the case of the  $\rho$  meson, the light-cone Fock representation becomes:

$$\rho^+ = \psi_{u\bar{d}}^\rho |u\bar{d}\rangle + \psi_{u\bar{d}c\bar{c}}^\rho |u\bar{d}c\bar{c}\rangle + \dots$$

Here we expect the wave function of the  $c\bar{c}$  quarks to be in an  $S$ -wave configuration with no radial nodes, in order to minimize the kinetic energy of the charm quarks and, thus, also minimize the total invariant mass.

The presence of such a  $|u\bar{d}c\bar{c}\rangle$  Fock state in the  $\rho$  would allow the  $J/\psi \rightarrow \rho\pi$  decay to proceed through rearrangement of the incoming and outgoing quark lines; in fact, the  $|u\bar{d}c\bar{c}\rangle$  Fock state wave function has a good overlap with the radial and spin  $|c\bar{c}\rangle$  and  $|u\bar{d}\rangle$  wave functions of the  $J/\psi$  and pion. On the other hand, the overlap with the  $\psi'$  would be suppressed, since the radial wave function of the  $n = 2$  quarkonium state is orthogonal to the nodeless  $c\bar{c}$  in the  $|u\bar{d}c\bar{c}\rangle$  state of the  $\rho\pi$ . Similarly, the  $|u\bar{s}c\bar{c}\rangle$  Fock component of the  $K^*$  favors the  $J/\psi K$  configuration, allowing the  $J/\psi \rightarrow K^* \bar{K}$  decay to also proceed by quark line rearrangement, rather than by  $c\bar{c}$  annihilation.

These authors also suggested comparing branching fractions for the  $\eta_c$  and  $\eta'_c$  decays as clues to the importance of  $\eta_c$  intrinsic charm excitations in the wavefunctions of light hadrons.

## $\psi'$ -suppressed models

The hypothesis of the existence of a glueball to explain the  $\rho\pi$  was brought into question soon after it was proposed. In addition, it is also pointed out [328] that helicity suppression is not a strong constraint at the charmonium energy scale. In such a case, one comes naturally to the idea that it is not  $J/\psi \rightarrow \rho\pi$  that is enhanced, but rather  $\psi' \rightarrow \rho\pi$  that is suppressed. Seven explanations or models along these lines were put forth.

## 1. Sequential-fragmentation Model

Karl and Roberts suggested explaining the  $\rho\pi$  puzzle based on the mechanism of sequential quark pair creation [329]. The idea is that the quark-antiquark pairs are produced sequentially, as a result the amplitude to produce two mesons in their ground state is an oscillatory function of the total energy of the system. They argue that the oscillatory fragmentation probability could have a minimum near the mass of  $\psi'$ , which provides a mechanism for suppressing  $\psi'$  decays. Even though their evaluations could generally accommodate the data for decays of  $J/\psi$  and  $\psi'$  to  $\rho\pi$  and  $K^*\bar{K}$ , it runs into difficulties when it is extrapolated to  $\Upsilon$  decays. According to their calculation, the oscillations of probability amplitude are damped out in the region of the  $\Upsilon$  resonances, so the  $\rho\pi$  channel is present in the decay of all  $\Upsilon$ ,  $\Upsilon'$ ,  $\Upsilon''$ ,  $\dots$  resonances with a common rate. This leads to a prediction  $\Gamma(\Upsilon \rightarrow \rho\pi) = 0.05$  keV, or, equivalently,  $\mathcal{B}(\Upsilon \rightarrow \rho\pi) = 9.4 \times 10^{-4}$ , which is above the current upper limit  $\mathcal{B}(\Upsilon \rightarrow \rho\pi) < 2 \times 10^{-4}$  [52]. Moreover, their model has difficulty explaining the large branching fraction for  $\phi$  decays to  $\rho\pi$  [52] due to the fact that their fragmentation probability tends to zero as the mass of the  $\rho\pi$  decaying system approaches  $1 \text{ GeV}/c^2$ .

In a further analysis [330], Karl and Tuan pointed out that if a suppression is observed in three-meson channels the explanation based on sequential pair creation would be undermined. Recently such a suppressed channel, viz.  $\phi KK$ , was found by CLEOc [310].

## 2. Exponential-form-factor model

Guided by the suppressed ratios of  $\psi'$  to  $J/\psi$  decays to two-body hadronic modes, Chaichian and Törnqvist suggested [331] that the hadronic form factors fall exponentially as described by the overlap of wave functions within a nonrelativistic quark model. This behavior explains the drastically suppressed two-body decay rates of the  $\psi'$  compared with those of the  $J/\psi$ . Recently reported observations of a number of VP channels in  $\psi'$  decays [298, 299, 305] such as  $\omega\eta'$ ,  $\phi\eta'$ ,  $\rho\eta'$  indicate that the predicted decay fractions are overestimated. Moreover, the branching fraction for  $\omega\pi^0$  [52], is well below the prediction of this model, which is  $1.04 \times 10^{-4}$ .

## 3. Generalized hindered M1 transition model

A so-called generalized hindered M1 transition model was proposed by Pinsky as a solution for the puzzle [332]. It is argued that because  $J/\psi \rightarrow \gamma\eta$  is an allowed M1 transition while  $\psi' \rightarrow \gamma\eta'$  is hindered (in the nonrelativistic limit), using the vector-dominance model to relate  $\psi' \rightarrow \gamma\eta'$  to  $\psi' \rightarrow \psi\eta'$  one could find the coupling  $G_{\psi'\psi\eta_c}$  is much smaller than  $G_{\psi\psi\eta_c}$ , and then, by analogy, the coupling  $G_{\omega'\rho\pi}$  would be much smaller than  $G_{\omega\rho\pi}$ . Here  $G_{\omega\rho\pi}$  can be extracted from data by virtue of the analysis using the vector-dominance model and a standard parameterization of the OZI process [333]. Then, assuming  $\psi' \rightarrow \rho\pi$  proceeds via  $\psi'\text{-}\omega'$  mixing, while  $J/\psi \rightarrow \rho\pi$  proceeds via  $J/\psi\text{-}\omega$  mixing, one finds that  $\psi' \rightarrow \rho\pi$  is much more severely suppressed than  $J/\psi \rightarrow \rho\pi$ . A similar estimate could be performed for  $K^*\bar{K}$  and

other VP final states, and one could expect a reduced value for  $Q$ :

$$\frac{\mathcal{B}(\psi' \rightarrow VP)}{\mathcal{B}(\psi \rightarrow VP)} = 1.47 \frac{\Gamma_{tot}(\psi)}{\Gamma_{tot}(\psi')} \left( \frac{G_{V'VP}}{G_{VVP}} \right)^2 \frac{F_{V'}}{F_V} = 0.06\% , \quad (18.3.18)$$

where  $F_{V'}/F_V = 0.3$ ,  $G_{\omega'\rho\pi}/G_{\omega\rho\pi} = 0.066$  according to Ref. [332]. This  $Q$  is much smaller than the present experimental results [298, 299, 305].

Moreover, in this model, the coupling  $G_{\omega'\omega f_2}$  for  $\omega' \rightarrow \omega f_2$  should not be suppressed because, by analogy, the coupling  $G_{\psi'\psi\chi_{c2}}$  is not small due to the fact that the E1 transition  $\psi' \rightarrow \gamma\chi_{c2}$  is not hindered [334]. Therefore, since it proceeds via  $\psi'\text{-}\omega'$  mixing, the  $\psi' \rightarrow \omega' \rightarrow \omega f_2$  decay is not expected to be suppressed, which contradicts the BES result [308].

#### 4. Higher-Fock-state scheme

Chen and Braaten (CB) proposed an explanation [323] for the  $\rho\pi$  puzzle, where they argue that the decay  $J/\psi \rightarrow \rho\pi$  is dominated by a Fock state in which the  $c\bar{c}$  pair is in a color-octet  ${}^3S_1$  state which decays via  $c\bar{c} \rightarrow q\bar{q}$ , while the suppression of this decay mode for the  $\psi'$  is attributed to a dynamical effect due to the small energy gap between the mass of the  $\psi'$  and the  $D\bar{D}$  threshold. Using the BES data on the branching fractions into  $\rho\pi$  and  $K^*\bar{K}$  as input, they predicted branching fractions for many other VP decay modes of the  $\psi'$ , as listed in Table 18.3. For these we see that most measured values fall within the ranges of the predictions, but we also note that for the  $\omega\pi$  mode, a deviation far from the prediction is evident. Here it should be noticed that the values deduced in Table 18.3 are calculated based on the strength of the measured branching fractions determined from earlier experiments; the new measurements on the branching fractions for  $\rho\pi$  and  $K^{*0}\bar{K}^0 + c.c.$  from BES [300, 303] and CLEOc [305] may have impact on the corresponding evaluations.

Table 18.3: Predictions and measurements for  $Q_{VP}$  in unit of 1% for all VP final states. The value for  $\rho\pi$  and  $K^{*0}\bar{K}^0 + c.c.$  from Ref. [335] were used as input. The theoretical parameter  $x = 0.64$  is from Ref. [336] and the experimental results come from Refs. [298, 299, 300, 337].

VP	$x = 0.64$	Exp.
$\rho\pi$	$0 - 0.25$	$0.13 \pm 0.03$
$K^{*0}\bar{K}^0 + c.c.$	$1.2 - 3.0$	$3.2 \pm 0.08$
$K^{*+}K^- + c.c.$	$0 - 0.36$	$0.59^{+0.27}_{-0.36}$
$\omega\eta$	$0 - 1.6$	$< 2.0$
$\omega\eta'$	$12 - 55$	$19^{+15}_{-13}$
$\phi\eta$	$0.4 - 3.0$	$5.1 \pm 1.9$
$\phi\eta'$	$0.5 - 2.2$	$9.4 \pm 4.8$
$\rho\eta$	$14 - 22$	$9.2^{+3.6}_{-3.3}$
$\rho\eta'$	$12 - 20$	$17.8^{+15.9}_{-11.1}$
$\omega\pi$	$11 - 17$	$4.4^{+1.9}_{-1.6}$

## 5. Survival-chamonia-amplitude explanation

A model put forward by Gérard and Weyers entertains the assumption that the three-gluon annihilation amplitude and the QED amplitude add incoherently in all channels in  $J/\psi$  decays into light hadrons, while in the case of  $\psi'$  decays the dominant QCD annihilation amplitude is not into three gluons, but into a specific configuration of five gluons [338]. More precisely, they suggest that the strong annihilation of the  $\psi'$  into light hadrons is a two step process: in the first step the  $\psi'$  goes into two gluons in a  $0^{++}$  or  $0^{-+}$  state and an off-shell  $h_c(3526)$ ; in the second step the off-shell  $h_c$  annihilate into three gluons to produce light hadrons. Their argument implies: (a) to leading order there is no strong decay amplitude for the processes  $\psi' \rightarrow \rho\pi$  and  $\psi' \rightarrow K^*\bar{K}$ ; (b) the 12 % rule should hold for hadronic processes which take place via the QED amplitude only. As far as the second implication is concerned, the present data give different ratios between  $\psi'$  and  $J/\psi$  decay for  $\omega\pi^0$  and  $\pi^+\pi^-$  final states, both of which are electromagnetic processes. Here even when form factor effects are taken into account [339], the difference between the two types of processes is still obvious. Besides providing a potential explanation for the  $\rho\pi$  puzzle, this model predicts sizable  $\psi' \rightarrow (\pi^+\pi^- \text{ or } \eta) h_1(1170)$  branching fractions.

In a recent paper [340], Artoisenet, Gérard and Weyers (AGW) update and sharpen the above idea, which leads to a somewhat unconventional point of view: all non-electromagnetic hadronic decays of the  $\psi'$  proceed via a transition amplitude that contains a  $c\bar{c}$  pair. AGW provide two patterns for these two-step decays, the first is

$$\psi' \rightarrow (2\text{NP}g) + (3g) . \quad (18.3.19)$$

The physics picture is as follows: the excited  $c\bar{c}$  pair in the  $\psi'$  does not annihilate directly. Instead, it spits out two non-perturbative gluons (2NPg) and survives in a lower  $c\bar{c}$  configuration ( $1^{--}$  or  $1^{-+}$ ) which then eventually annihilate into 3g. The decays  $\psi' \rightarrow (2\pi)J/\psi$  and  $\psi' \rightarrow \eta J/\psi$  follow this pattern. The second pattern is

$$\psi' \rightarrow (3\text{NP}g) + (2g) , \quad (18.3.20)$$

where the lower  $c\bar{c}$  configuration ( $0^{-+}$  or  $0^{++}$ ) annihilates into 2g. The only on-shell channel for this type of decay is  $\psi' \rightarrow (3\pi)\eta_c$ , whose branching fraction is estimated as ( $1 \sim 2$ )% level. A recent measurement from CLEOc [309] provides an upper limit on this decay that is one order of magnitude below this theoretical prediction. Furthermore, the substitution of one photon for one gluon in Eqs. (18.3.19) and (18.3.20) allows

$$\psi' \rightarrow (2\text{NP}g) + (2g) + \gamma . \quad (18.3.21)$$

This pattern corresponds to on-shell radiative decays such as  $\psi' \rightarrow (\pi^+\pi^-)\eta_c\gamma$  and  $\psi' \rightarrow \eta\eta_c\gamma$ , which could be larger than the observed  $\psi' \rightarrow \eta_c\gamma$  mode.

In addition to the above predication, AGW also estimate

$$\mathcal{B}(\psi' \rightarrow b_1\eta) = (1.3 \pm 0.3) \times 10^{-3} , \quad (18.3.22)$$

$$\mathcal{B}(\psi' \rightarrow h_1\pi^0) = (1.9 \pm 0.4) \times 10^{-3} , \quad (18.3.23)$$

$$\mathcal{B}(J/\psi \rightarrow b_1\eta) \approx \mathcal{B}(\psi' \rightarrow b_1\eta) \approx 1\% . \quad (18.3.24)$$

All these can be tested by experiment.

## 6. Nonvalence component explanation

Since the  $\psi'$  is a highly excited state and close to the  $D\bar{D}$  threshold, it is suggested [341] that unlike the  $J/\psi$ , the  $\psi'$  may be an admixture of large nonvalence components in its wave function. The so-called nonvalence components includes those with an additional gluon or a light quark-antiquark pair (as in Ref. [341], a  $c\bar{c}g$  component and a quasi-molecular  $D\bar{D}$  state), which make  $\psi'$  decays quite distinctive from those of the  $J/\psi$ . The nonvalence component of the  $J/\psi$  is expected to be less significant because it is the lowest state. In a following paper [328], Chernyak uses this picture to explain the  $\rho\pi$  puzzle. He suggests that the valence and nonvalence strong contributions interfere destructively in  $\rho\pi$  channel and consequently cancel to a large extent in the total  $\psi' \rightarrow \rho\pi$  strong amplitude, while the role of nonvalence contributions is much less significant in  $J/\psi \rightarrow \rho\pi$ . From this viewpoint, there is no deep reason for the experimentally observed very strong suppression of  $\psi' \rightarrow \rho\pi$ , rather this is the result of an accidental cancellation.

Chernyak also tries to use the above idea to explain qualitatively other decay modes, such as  $VT$ ,  $AP$ ,  $PP$ ,  $VV$  and  $B\bar{B}$  decay. However, such ideas remain pure speculation, and no concrete calculations have been performed as of yet.

## 7. $S$ - $D$ wave mixing scheme

The  $\psi''$  is generally considered to be a  $D$ -wave charmomium state. Although it is primarily  $c\bar{c}(1^3D_1)$ , its leptonic width indicates some mixing with  $S$ -wave states, mainly the nearby  $\psi(2^3S_1)$ . This led Rosner to propose that the small  $\rho\pi$  branching fraction for the  $\psi'$  is due to the cancellation of the  $2S$  and  $1D$  matrix elements. In his scheme

$$\begin{aligned}\langle \rho\pi | \psi' \rangle &= \langle \rho\pi | 2^3S_1 \rangle \cos \theta - \langle \rho\pi | 1^3D_1 \rangle \sin \theta, \\ \langle \rho\pi | \psi'' \rangle &= \langle \rho\pi | 2^3S_1 \rangle \sin \theta + \langle \rho\pi | 1^3D_1 \rangle \cos \theta,\end{aligned}\quad (18.3.25)$$

where  $\theta$  is the mixing angle between pure  $\psi(2^3S_1)$  and  $\psi(1^3D_1)$  states [342] and is fitted from the leptonic widths of the  $\psi''$  and the  $\psi'$  to be  $(12 \pm 2)^\circ$  [166]; this is consistent with the coupled channel estimates [343, 344] and with the ratio of  $\psi'$  and  $\psi''$  partial widths to  $J/\psi\pi^+\pi^-$  [137]. If the mixing and coupling of the  $\psi'$  and  $\psi''$  lead to complete cancellation of  $\psi' \rightarrow \rho\pi$  decay ( $\langle \rho\pi | \psi' \rangle = 0$ ), the missing  $\rho\pi$  decay mode of the  $\psi'$  should show up, instead, in the decays of the  $\psi''$ , enhanced by the factor  $1/\sin^2 \theta$ . A concrete estimate gives [166]

$$\mathcal{B}_{\psi'' \rightarrow \rho\pi} = (4.1 \pm 1.4) \times 10^{-4}. \quad (18.3.26)$$

To test this scenario with data collected at the  $\psi''$  in  $e^+e^-$  experiments, it has been pointed out [345, 346] that the continuum contribution must be considered carefully. Specifically speaking, by Rosner's estimation, the Born-order cross section for  $\psi'' \rightarrow \rho\pi$  is

$$\sigma_{\psi'' \rightarrow \rho\pi}^{Born} = (4.8 \pm 1.9) \text{ pb}, \quad (18.3.27)$$

which is comparable in magnitude to that of the continuum cross section, viz.

$$\sigma_{e^+e^- \rightarrow \rho\pi}^{Born} = 4.4 \text{ pb}. \quad (18.3.28)$$

So, what is observed is the coherent interference of these two amplitudes. Based on the analysis of experimental data, it has been suggested that there be an universal phase between strong and electromagnetic amplitudes in charmonium decays. With this assumption, the strong decay amplitude interferes with the continuum amplitude either maximally destructively, e.g. for  $\rho\pi$ ,  $\omega\eta$  and  $K^{*+}K^-$  or maximally constructively, e.g. for  $K^{*0}\bar{K}^0$ . The destructive interference case leads to the phenomena that the measured cross section on top of the resonance could be smaller than that off the resonance. Recent experimental results [311, 302] on  $\rho\pi$ ,  $\omega\eta$  and  $K^{*+}K^-$  have demonstrated such an interference pattern. This provides support to the prediction of Eq.(18.3.26). However, to determine  $\mathcal{B}_{\psi'' \rightarrow \rho\pi}$  unambiguously, currently available experimental data are insufficient; the  $\psi''$  resonance must be scanned [347]. So, a quantitative test of Rosner's scenario remains as a task of the future experiments at *BES-III*.

In a subsequent study [348], Wang, Yuan and Mo (WYM) extend the *S-D* wave-mixing scenario to *PP* final state, and give a constraint for  $\psi'' \rightarrow K_S^0 K_L^0$  decay,

$$0.12 \pm 0.07 \leq 10^5 \times \mathcal{B}(\psi'' \rightarrow K_S^0 K_L^0) \leq 3.8 \pm 1.1 , \quad (18.3.29)$$

which is compatible with both the BESII result  $\mathcal{B}(\psi'' \rightarrow K_S^0 K_L^0) < 2.1 \times 10^{-4}$  at 90% C.L. [301] and the CLEOc result  $\mathcal{B}(\psi'' \rightarrow K_S^0 K_L^0) < 1.17 \times 10^{-5}$  at 90% C.L. [312]. Extrapolating these ideas to all charmless decays [349], WYM found that this scenario could accommodate large non- $D\bar{D}$  decay of the  $\psi''$ . Although recent experimental measurements from CLEOc favor a nearly zero non- $D\bar{D}$  cross section at  $\psi''$  [350], the large errors prevent them from ruling out the existence of non- $D\bar{D}$  decays with a branching fraction at the 10% level.

## Other Explanations

Besides the aforementioned models, more speculations involving the  $\rho\pi$  puzzle are described below.

### 1. Final-state-interaction scheme

Li, Bugg and Zou [351] (LBZ) pointed out that final state interactions (FSI) in  $J/\psi$  and  $\psi'$  decays give rise to effects that are of the same order as the tree level amplitudes. They argue that  $J/\psi \rightarrow \rho\pi$  is strongly enhanced by the  $a_2\rho$  loop diagram, while the direct tree-production for  $\rho\pi$  may be suppressed by the HHC mechanism [313]. The contribution of the  $a_1\rho$  loop diagram is much smaller than that of  $a_2\rho$  loop for the  $J/\psi \rightarrow \rho\pi$ , but they have similar strength for the  $\psi' \rightarrow \rho\pi$  and may cancel each other by interfering destructively. A similar apparent suppression for  $\psi' \rightarrow K^*\bar{K}$  and  $f_2\omega$  may also be explained by the  $K^*\bar{K}_{2,1}^*$  and  $b_1\pi$  loop, respectively. Therefore, LBZ expect that FSI might provide a coherent explanation for all the observed suppressed modes of  $\psi'$  decays. However, as remarked in Ref. [352], this interference model appears to have more assumptions than predictions. The only qualitative prediction by LBZ is that the  $a_1\rho$  and  $K_1^*\bar{K}^*$  production rates should be large for the  $\psi'$ . So far, no measurements of these modes have been reported.

## 2. Large phase scheme

Suzuki gave another FSI-based explanation for  $J/\psi$  decays [325]. He performed a detailed amplitude analysis for  $J/\psi \rightarrow 1^-0^-$  decay to test whether or not the short-distance FSI dominates over the long-distance FSI in  $J/\psi$  decay. His result indicates that there is a large phase between the three-gluon and one-photon amplitudes. Since the large phase cannot be produced by a perturbative QCD interaction, its source must be in the long-distance part of the strong interaction, namely, rescattering among hadrons in their inelastic energy region. Suzuki then performed a similar analysis for  $J/\psi \rightarrow 0^-0^-$  decay, and obtained a similar conclusion about the existence of a large phase [353]. His analysis also shows that the exclusive decay ratio at the  $J/\psi$  is in line with that of the inclusive decay. This fact led him to conclude that the origin of the relative suppression of  $\psi' \rightarrow 1^-0^-$  to  $J/\psi \rightarrow 1^-0^-$  is not in the  $J/\psi$  but in the  $\psi'$ .

As more  $\psi'$  decays were analyzed, the experimental data at first seemed to favor a phase close to  $180^\circ$  [354], contrary to the expectation that the decays of the  $J/\psi$  and  $\psi'$  should not be very different. However, it was pointed out by Wang *et al.* that the previously published data did not take the continuum one-photon process into account. Their reanalysis of the experimental data showed that a phase with a value around  $-90^\circ$  could fit  $\psi' \rightarrow 1^-0^-$  data [346] and  $\pm 90^\circ$  could fit  $\psi' \rightarrow 0^-0^-$  data [355]. The latter is confirmed by more recent results from CLEOc [294]. Furthermore, this large phase also shows up in the OZI-suppressed decay modes of the  $\psi''$ . In many decays modes of the  $\psi''$ , the strong decay amplitudes have comparable strength to the non-resonance continuum amplitude, and a large phase around  $-90^\circ$  leads to destructive or constructive interference. In the case of destructive interference, the observed cross sections for some modes are smaller at the peak of the  $\psi''$  than the cross section that is measured off-resonance [345]. This is demonstrated by data from CLEOc [311].

## 3. Mass reduction explanation

In a study [356] of radiative decays of  $1^{--}$  quarkonium into  $\eta$  and  $\eta'$ , Ma presented a QCD-factorization approach, with which he obtained theoretical predictions that are consistent with CLEOc measurements. The largest possible uncertainties in the analysis are from relativistic corrections involving the value of the charm quark mass. Ma argued that the effect of these uncertainties can be reduced by using quarkonium masses instead of the quark mass. As an example of such a reduction, he provides a modified version of the original 12% rule

$$Q_{\rho\pi} = \frac{\mathcal{B}(J/\psi \rightarrow \rho\pi)}{\mathcal{B}(\psi' \rightarrow \rho\pi)} = \frac{M_{J/\psi}^8}{M_{\psi'}^8} \frac{\mathcal{B}(J/\psi \rightarrow e^+e^-)}{\mathcal{B}(\psi' \rightarrow e^+e^-)} \\ = (3.6 \pm 0.6)\% .$$

However, this reduced value is still much larger than the experimental result given above in Table 18.3.

## 4. Vector-meson-mixing model

With the intention of providing a comprehensive description of  $J/\psi$  two-body decays, Clavelli and Intemann (CI) proposed a vector-meson-mixing model in which the vector mesons ( $\rho$ ,  $\omega$ ,  $\phi$ ,  $J/\psi$ ) are regarded as being admixtures of light-quark-antiquark states and charmed-quark-antiquark states [357]. The coupling of the  $J/\psi$  to any state of light quarks is then related to the corresponding coupling of the  $\rho$ ,  $\omega$ , and  $\phi$  to the same state. With a few experiment inputs to determine the mixing parameters, CI calculate VP, PP, and BB decay rates for the  $J/\psi$  as a function of the pseudoscalar mixing angle. Most of the predictions agree with experimental results at the order of magnitude level, but discrepancies are obvious for some channels, such as the  $K_S^0 K_L^0$  final state [295]. CI also extended their model to hadronic decays of the  $\psi'$ . However, their evaluations for  $\mathcal{B}(J/\psi \rightarrow \omega\pi^0) = 3 \times 10^{-5}$  and  $\mathcal{B}(\psi' \rightarrow \omega\pi^0) = 3 \times 10^{-3}$  contradict the present experimental values  $(4.5 \pm 0.5) \times 10^{-4}$  and  $(2.1 \pm 0.6) \times 10^{-4}$  [52], respectively.

Starting from an effective Lagrangian wherein nonet-symmetry breaking and pseudoscalar-meson mixing can be studied, Haber and Perrier parametrized the decay modes of  $J/\psi \rightarrow PP$  (also for  $J/\psi \rightarrow VV$  or  $\eta_c \rightarrow VP$ ),  $J/\psi \rightarrow VP$  (also for  $J/\psi \rightarrow VT$  or  $\eta_c \rightarrow VV$ ),  $J/\psi \rightarrow PPP$  (also for  $J/\psi \rightarrow VVP$  or  $\eta_c \rightarrow PPV$ ), and  $\eta_c \rightarrow PPP$  (also for  $J/\psi \rightarrow PPV$  or  $\eta_c \rightarrow VVP$ ) [358]. Experimental data were used to determine their phenomenological parameters. In a follow-on work, Seiden, Sadrozinski and Haber took the doubly Okubo-Zweig-Iizuka suppression (DOZI) effect into consideration, and presented a more general parameterization of amplitudes for  $J/\psi \rightarrow PP$  decays [359]. With this form, one could easily derive the relative decay strengths between different final states. However, for the most general cases of symmetry breaking, too many parameters are introduced for a general analysis to be useful. In order to reduce the number of new parameters considerably and make the analysis manageable, only special cases have to be considered.

Table 18.4: Comparison of predictions [360] and measurements [52] for the branching ratios ( $10^{-5}$ ) for  $\psi'$  decays. The upper limits are presented at 90% C.L.

VP	Prediction	Measurement
$\rho\pi$	1.3	$3.2 \pm 1.2$
$K^{*0}\bar{K}^0 + c.c.$	5.1	$10.9 \pm 2.0$
$K^{*+}K^- + c.c.$	1.3	$1.7^{+0.8}_{-0.7}$
$\omega\eta$	1.2	$< 1.1$
$\omega\eta'$	6.3	$3.2^{+2.5}_{-2.1}$
$\phi\eta$	1.6	$2.8^{+1.0}_{-0.8}$
$\phi\eta'$	4.6	$3.1 \pm 1.6$
$\rho\eta$	2.1	$2.2 \pm 0.6$
$\rho\eta'$	1.2	$1.9^{+1.7}_{-1.6}$
$\omega\pi^0$	3.8	$2.1 \pm 0.6$
$\phi\pi^0$	0.01	$< 0.40$

A similar parameterization of mixing-induced strong interaction mechanisms was proposed by Feldmann and Kroll (FK) [360] for the hadron-helicity non-conserving

$J/\psi$  and  $\psi'$  decays, but with a different interpretation from those put forth in Refs. [323, 336, 359, 352]. FK assume that, with a small probability, charmonium states have Fock components built from light quarks only. Through these Fock components the charmonium state decays by a soft mechanism that is modeled by  $J/\psi$ - $\omega$ - $\phi$  mixing and the subsequent  $\omega$  (or  $\phi$ ) decays into the  $VP$  final state. In absence of a leading-twist perturbative QCD contribution, the dominant mechanism is supplemented by electromagnetic and DOZI-violating contributions. FK argue that this mechanism can probe the charmonium wave function at all quark-antiquark separations and thereby experiences the differences between the  $1S$  and  $2S$  radial wave functions. The node in the latter is supposed to lead to a strong suppression mechanism for  $\psi'$  decays. With a few parameters adjusted to the experimental data, FK obtain a numerical description of the branching fractions for many  $VP$  decay modes of the  $J/\psi$  and  $\psi'$ , and these agree with the measured branching fractions at the order of magnitude level, as shown in Table 18.4. Moreover, FK have extended their mixing approach to  $\eta_c \rightarrow VV$  decays and obtain a reasonable description of the branching fractions for these decays, with the  $\eta'_c \rightarrow VV$  decays expected to be strongly suppressed.

### 18.3.3 Summary

Here we have presented a general review on the subject of the  $\rho\pi$  puzzle. Although there is still no satisfactory explanation for all existing experimental results, some enlightening ideas have been put forth.

As we know, physics in the charm threshold region is in the boundary domain between perturbative and nonperturbative QCD. Recently observed hadronic decays of charmonium may give new challenges to the present theoretical understanding of the extant decay mechanisms. Many of the new charmonium states observed by Belle and BaBar, which have difficulty being accommodated by potential models, have led to new theoretical speculations about charmonium spectroscopy and novel production mechanisms [361].

Experimentally, the expected large data sample from CLEOc in the near future, and even larger data samples from *BES-III* will open a new era for charmonium dynamics study, even though we may not obtain a thoroughly revolutionary theory, we may acquire a more profound understanding of the existing theory. At the same time we can hope for some new enlightenment on the  $\rho\pi$  puzzle.

## 18.4 Open-flavor decays<sup>8</sup>

It is well known from the phenomenology of even the lightest hadrons that the dominant strong decays of mesons are those that do not involve the annihilation of the valence  $q\bar{q}$  pair. It was this observation, in the context of the decays of the  $\phi(1020)$ , that led Zweig to the suggestion of strange quarks. (Specifically, he suggested that the dominance of the  $\phi(1020)$  decay mode  $KK$  over  $\rho\pi$  could be understood if the  $\phi(1020)$  contained a valence  $s\bar{s}$  pair that could not easily annihilate, which is now known as the OZI rule. This assumption would explain why the  $KK$  transition  $(s\bar{s} \rightarrow (s\bar{n})(n\bar{s}))$ , where  $n = u, d$ )

---

<sup>8</sup>T. Barnes

dominates the transition to  $\rho\pi$  ( $s\bar{s} \rightarrow (n\bar{n}')(n'\bar{n})$ ), although  $KK$  has very little phase space.

Although these open-flavor decay modes are usually the dominant strong decay amplitudes when allowed by phase space, they remain surprisingly poorly understood. The approach normally used by theorists to model these decays is to assume pair production of a  $q\bar{q}$  pair from the vacuum with  $0^{++}$  (vacuum) quantum numbers, with a dimensionless amplitude  $\gamma$  that is independent of the initial state and the flavor of the  $q\bar{q}$  pair. This is now known as the  ${}^3P_0$  model, and originally suggested by Micu in 1968 [537] (pre-QCD), and was subsequently developed for explicit quark model wavefunctions by the Orsay group of LeYaouanc *et al.* [538]. The well-known flux-tube decay model of Kokoski and Isgur [539] is actually a variant of this model with some spatial modulation assumed for the  $q\bar{q}$  pair production amplitude. A description in terms of Feynman diagrams and a comparison with OGE and other pair production amplitudes was given by Ackleh *et al.* [540]. This  ${}^3P_0$  model has now been applied very extensively to most sectors of hadron Hilbert space, including charmonia [541, 542, 69, 54]. Ref.[54] gives numerical predictions for the decay amplitudes and strong branching fractions of all charmonia expected to the mass of the  $\psi(4415)$ . These predictions are especially interesting because the  ${}^3P_0$  model is only a simple phenomenological description, and may be inaccurate in practice. Since the many theoretical predictions of the preferred strong decay modes of many hadrons, including light and strange mesons [53, 543, 544], baryons, including suggestions for finding the “missing” baryons [545, 546], and hybrid mesons [547, 548] all rely on this specific decay model, it is evidently very important to test its accuracy in describing strong decays in an experimentally relatively clear sector such as charmonium.

Of course one can easily construct other models for strong decay amplitudes, and it is interesting that in their early studies of charmonium the Cornell group [549] used such an alternative model. In particular they assumed that these strong decays were a result of the linear confining interaction, which gave rise to  $q\bar{q}$  pair production from the initial  $c\bar{c}$  system with a  $\gamma_0 \otimes \gamma_0$  nonlocal interaction and a linear  $br$  kernel between the vertices. (This choice of  $\gamma_0 \otimes \gamma_0$  was motivated by the belief current in the 1970s that confinement acted as a timelike vector interaction rather than a Lorentz scalar, which is the more usual assumption at present.) Several recent charmonium papers also assume this timelike vector decay model [550, 551]. An alternative model with an  $I \otimes I$  linear scalar confining interaction was developed and applied to light quarks by Ackleh *et al.* [540], but has not yet been applied to charmonium.

It will be very interesting to use charmonium decays at *BES-III* to test these strong decay models. The most sensitive tests involve the determination of amplitude *ratios*, which require studies of open-flavor decays into final states that have more than one amplitude. These relative amplitude phases are typically very sensitive to the assumed quantum numbers of the  $q\bar{q}$  pair produced during the decay, whereas simple branching fractions and partial widths are affected by common features such as the available phase space.

For the decays of the most easily accessible  $1^{--}$  charmonia, studies of relative decay amplitude phases requires final states consisting of a pair of open-charm vectors, the “VV modes”, since the PsPs and PsV modes involve single amplitudes (respectively  ${}^1P_1$  and  ${}^3P_1$ ). Thus PsPs and PsV final states do not allow measurements of the relative phases of strong decay amplitudes, whereas in the decay  $1^{--} \rightarrow VV$  there are three amplitudes

Table 18.5: Theoretical ( ${}^3P_0$  model) open-flavor strong decay amplitudes and widths of the four  $1^{--}$  charmonium states above 3.73 GeV most easily accessible at *BES-III* (abstracted from Ref.[54]). Multiamplitude decay channels are indicated by boldface.

Meson	State	Mode	$\Gamma_{thy}$ [ $\Gamma_{expt}$ ] (MeV)	Amps. ( $\text{GeV}^{-1/2}$ )
$\psi(3770)$	$1^3D_1$	DD	43 [23.0 $\pm$ 2.7]	${}^1P_1 = +0.1668$
$\psi(4040)$	$3^3S_1$	DD	0.1	${}^1P_1 = -0.0052$
		$DD^*$	33	${}^3P_1 = -0.0954$
		$D^*D^*$	33	${}^1P_1 = +0.0338$ ${}^5P_1 = -0.1510$ ${}^5F_1 = 0$
	$D_sD_s$		7.8	${}^1P_1 = +0.0518$
	<i>total</i>		74 [80 $\pm$ 10]	
$\psi(4160)$	$2^3D_1$	DD	16	${}^1P_1 = -0.0522$
		$DD^*$	0.4	${}^3P_1 = +0.0085$
		$D^*D^*$	35	${}^1P_1 = +0.0489$ ${}^5P_1 = -0.0219$ ${}^5F_1 = -0.0845$
	$D_sD_s$		8.0	${}^1P_1 = -0.0427$
	$D_sD_s^*$		14	${}^3P_1 = +0.0733$
	<i>total</i>		74 [103 $\pm$ 8]	
$\psi(4415)$	$4^3S_1$	DD	0.4	${}^1P_1 = +0.0066$
		$DD^*$	2.3	${}^3P_1 = +0.0177$
		$D^*D^*$	16	${}^1P_1 = -0.0109$ ${}^5P_1 = +0.0487$ ${}^5F_1 = 0$
	$DD_1$		31	${}^3S_1 = 0$ ${}^3D_1 = +0.0933$
	$DD'_1$		1.0	${}^3S_1 = +0.0168$ ${}^3D_1 = 0$
	$DD_2^*$		23	${}^5D_1 = -0.0881$
	$D^*D_0^*$		0.0	${}^3S_1 = -8.7 \cdot 10^{-4}$
			0	${}^3D_1 = 0$
	$D_sD_s$		1.3	${}^1P_1 = -0.0135$
	$D_sD_s^*$		2.6	${}^3P_1 = +0.0212$
	$D_s^*D_s^*$		0.7	${}^1P_1 = +0.0027$ ${}^5P_1 = -0.0119$ ${}^5F_1 = 0$
	<i>total</i>		78 [62 $\pm$ 20]	

present,  ${}^1\text{P}_1$ ,  ${}^5\text{P}_1$  and  ${}^5\text{F}_1$ . The  ${}^3\text{P}_0$  model predicts very characteristic ratios for these decay amplitudes, depending on whether the initial  $1^{--} c\bar{c}$  is an S-wave ( ${}^3\text{S}_1$ ) or a D-wave ( ${}^3\text{D}_1$ ) state. For an S-wave one finds  ${}^5\text{P}_1/{}^1\text{P}_1 = -2\sqrt{5}$  and  ${}^5\text{F}_1 = 0$ , whereas for a D-wave one finds  ${}^5\text{P}_1/{}^1\text{P}_1 = -1/\sqrt{5}$  and  ${}^5\text{F}_1 \neq 0$  (both sets of results are independent of the radial wavefunction). Results from a recent calculation [54] are listed in Table 18.5. There is some evidence that the physical states  $\psi(4040)$  and  $\psi(4160)$  may be strongly mixed linear combinations of S- and D-wave basis states, which will instead give a weighted set of decay amplitudes.

The highest-mass  $c\bar{c}$  state known at present is the  $1^{--} \psi(4415)$ , which is usually given a  $4{}^3\text{S}_1$  assignment. Calculations of the decay branching fractions of a  $4{}^3\text{S}_1 c\bar{c} \psi(4415)$  in the  ${}^3\text{P}_0$  model [54] predict that the largest mode should be the unusual  $\text{DD}_1$  (the narrow  $\text{D}_1$ ), and in pure D-wave rather than S-wave! It would clearly be a very interesting test of strong decay models to measure the strong decay amplitudes and branching fractions of this state. There is also an “industrial” application of the  $\psi(4415)$  [54, 552]; by running on the high mass tail of this resonance, one can expect a relatively large branching fraction into the enigmatic  $\text{D}_{s0}(2317)$ , which is otherwise difficult to produce with useful statistics. A study of interesting decays such as the radiative branching fraction of the  $\text{D}_{s0}(2317)$  into  $\gamma\text{D}_s^*$  could then be carried out at *BES-III*; this would be valuable in determining the relative size of the  $c\bar{s}$  and DK components of the  $\text{D}_{s0}(2317)$ .

Unfortunately, the corresponding predictions for the open-flavor decay amplitudes of these charmonium states using other strong decay models, such as the timelike vector model assumed by the Cornell group [549], have not yet been published. It will be a very important exercise for theorists to evaluate the strong decay predictions of this model for comparison both with future *BES-III* data and with the predictions of the  ${}^3\text{P}_0$  model shown here.

An experimental study of the decays of these vector states should begin with a simple scan in energy of the exclusive cross sections for  $e^+e^-$  into the various open-charm final states, to establish whether the individual resonances contributions can be clearly separated. Such measurements of exclusive open-charm cross sections have recently been carried out by Belle [111, 113, 112].

## 18.5 $\psi(3770)$ non- $D\bar{D}$ decays<sup>9</sup>

### 18.5.1 Introduction

Potential Models based on QCD predict charmonium and charmed meson properties quite well. Until now, most of the states predicted by the charmonium model have been observed, and many of their decay channels have been observed and their branching fractions have been well measured.

Based on the conventional charmonium potential model, the  $\psi(3770)$  resonance is identified as a mixture of the  $1{}^3\text{D}_1$  and  $2{}^3\text{S}_1$  angular momentum states, and is expected to decay into the OZI-allowed  $D\bar{D}$  ( $D^0\bar{D}^0$  and  $D^+\bar{D}^-$ ) final states with a branching fraction  $B(\psi(3770) \rightarrow D\bar{D}) \geq 97\%$ . However, there is a long-standing puzzle in the understanding of the  $\psi(3770)$  production and decays. Previously published results [362]

---

<sup>9</sup>G. Rong, D.H. Zhang, and H.L. Ma

indicated about a 38% discrepancy between the measured  $D\bar{D}$  production cross section  $\sigma_{D\bar{D}}^{\text{obs}}$  and the observed  $\psi(3770)$  production cross section  $\sigma_{\psi(3770)}^{\text{obs}}$ . Recently, the BESII Collaboration measured the total branching fraction for non- $D\bar{D}$  decays of the  $\psi(3770)$  to be  $B(\psi(3770) \rightarrow \text{non-}D\bar{D}) = (16.4 \pm 7.3 \pm 4.2)\%$  [363], based on measurements of the continuum light hadron cross section below the  $D\bar{D}$  threshold, the observed cross section for  $D\bar{D}$  production and the observed cross section for inclusive hadron production at the peak of  $\psi(3770)$ , and  $B(\psi(3770) \rightarrow \text{non-}D\bar{D}) = (16.4 \pm 7.3 \pm 4.2)\%$  [364] obtained from an analysis of the line-shapes of inclusive hadron and  $D\bar{D}$  ( $D^0\bar{D}^0$  and  $D^+\bar{D}^-$ ) production. These results indicate that either, contrary to what is generally expected, the  $\psi(3770)$  has a substantial decay rate into non- $D\bar{D}$  final states, or the measured cross sections for  $D\bar{D}$  and  $\psi(3770)$  production suffer from large systematic shifts, even in the latest BESII measurements. Another possibility is that there may be some other effect or new phenomena that is responsible for this discrepancy.

To clarify this situation one needs to measure more precisely  $\sigma_{D\bar{D}}^{\text{obs}}$ ,  $\sigma_{\psi(3770)}^{\text{obs}}$ , the parameters of  $\psi(3770)$  and  $\psi(2S)$  resonances, the branching fractions for  $\psi(3770) \rightarrow D^0\bar{D}^0$ ,  $D^+\bar{D}^-$ , non- $D\bar{D}$ , and extensively search for and study exclusive non- $D\bar{D}$  decay modes of the  $\psi(3770)$  with a high statistics data sample. These can be done with the *BES-III* detector at the BEPC-II collider. In this section we summarize the status of the experimental studies of non- $D\bar{D}$  decays of  $\psi(3770)$  resonance and propose an extensive study the light hadron decays of the  $\psi(3770)$  with the *BES-III* detector at the BEPC-II collider.

### 18.5.2 S-D mixing and mixing angle $\theta_{\text{mix}}$

The charmonium model predicts the leptonic width of the  $1^3D_1$   $c\bar{c}$  state to be 70 eV [365], while early experiments measured a leptonic width of about 250 eV. To explain the large leptonic width, the  $\psi(3770)$  is assumed to be a mixture of the  $1^3D_1$  and  $2^3S_1$  states plus some other  $1^{--}$  states near the  $D\bar{D}$  thresholds, caused by some dynamic mechanism [366, 367]. The simplest scheme, where the  $1^3D_1$  mixes with only the  $2^3S_1$  state, which is the dominant component of the mixed part of the  $1^3D_1$  state, is characterized by the mixing angle  $\theta_{\text{mix}}$ , and the corresponding physical states  $\psi(3686)$  and  $\psi(3770)$  are described as,

$$|\psi(3770)\rangle = |1^3D_1\rangle \cos\theta_{\text{mix}} + |2^3S_1\rangle \sin\theta_{\text{mix}}, \quad (18.5.30)$$

$$|\psi(3686)\rangle = -|1^3D_1\rangle \sin\theta_{\text{mix}} + |2^3S_1\rangle \cos\theta_{\text{mix}}. \quad (18.5.31)$$

This is enough to settle some important issues in charmonium physics. With this simple model, the leptonic widths of  $\psi(3770)$  and  $\psi(3686)$  resonances are then calculated as a function of  $\theta_{\text{mix}}$  to be [166, 368]

$$\Gamma(\psi(3770) \rightarrow e^+e^-) = \frac{4\alpha^2 e_c^2}{M_{\psi(3770)}^2} \left| \sin\theta_{\text{mix}} R_{2S}(0) + \frac{5}{2\sqrt{2}m_c^2} \cos\theta_{\text{mix}} R_{1D}''(0) \right|^2, \quad (18.5.32)$$

$$\Gamma(\psi(3686) \rightarrow e^+e^-) = \frac{4\alpha^2 e_c^2}{M_{\psi(3686)}^2} \left| \cos\theta_{\text{mix}} R_{2S}(0) - \frac{5}{2\sqrt{2}m_c^2} \sin\theta_{\text{mix}} R_{1D}''(0) \right|^2, \quad (18.5.33)$$

where  $e_c = 2/3$ ,  $R_{2S}(0) = \sqrt{4\pi}\Psi_{2S}(0)$  is the radial  $2S$  wave function at  $r = 0$ , and  $R_{1D}''(0)$  is the second derivative of the radial  $1D$  wave function at the origin. Experimentally, using

the measured values of  $\Gamma(\psi(3686) \rightarrow e^+e^-)$  and  $\Gamma(\psi(3770) \rightarrow e^+e^-)$  one can determine the mixing angle  $\theta_{\text{mix}}$ .

Taking the ratio of Eq. 18.5.32 and Eq. 18.5.33, we derive the relation

$$R_{\psi(3770)/\psi(3686)} = \frac{M_{\psi(3773)}^2 \Gamma(\psi(3773) \rightarrow e^+e^-)}{M_{\psi(3686)}^2 \Gamma(\psi(3686) \rightarrow e^+e^-)} = \left| \frac{0.734 \sin \theta_{\text{mix}} + 0.095 \cos \theta_{\text{mix}}}{0.734 \cos \theta_{\text{mix}} - 0.095 \sin \theta_{\text{mix}}} \right|^2. \quad (18.5.34)$$

Using the parameters of  $\psi(3770)$  and  $\psi(3686)$  resonances recently measured by the BESII Collaboration [369], we can determine the ratio of the partial leptonic widths of the  $\psi(3770)$  and the  $\psi(3686)$

$$R_{\psi(3770)/\psi(3686)}^{BES} = 0.105 \pm 0.015. \quad (18.5.35)$$

From the relations given in the Eqs. 18.5.34 and 18.5.35, we can extract a value for the mixing angle,  $\theta_{\text{mix}}$ . The relation of  $R_{\psi(3770)/\psi(3686)}$  to  $\theta_{\text{mix}}$  is plotted as the parabolic curve in Fig. 18.1, where the horizontal lines give the measured value of  $R_{\psi(3770)/\psi(3686)}$  and the  $\pm 1\sigma$  interval of the value; the vertical lines give  $\pm 1\sigma$  intervals of the measured values of the mixing angle  $\theta_{\text{mix}}$ . There are two solutions as shown in the figure. One is  $\theta_{\text{mix}} = (10.6 \pm 1.3)^\circ$  and the another is  $\theta_{\text{mix}} = (-25.3 \pm 1.3)^\circ$ . However, the solution  $\theta_{\text{mix}} = (10.6 \pm 1.3)^\circ$  is favored by the relative decay rates for  $\psi(3770) \rightarrow J/\psi \pi^+ \pi^-$  and  $\psi(3686) \rightarrow J/\psi \pi^+ \pi^-$ . If the mixing angle is  $\theta_{\text{mix}} = (-25.3 \pm 1.3)^\circ$ , the partial width for  $\psi(3770) \rightarrow J/\psi \pi^+ \pi^-$  would be larger than that for  $\psi(3686) \rightarrow J/\psi \pi^+ \pi^-$ , which is in conflict with measurements, as discussed below.

Measurements of  $\theta_{\text{mix}}$  and the rates of charmonium decays and transitions in experiments are essential for testing the theoretical predictions and in the understanding of the nature of the  $\psi(3770)$ .

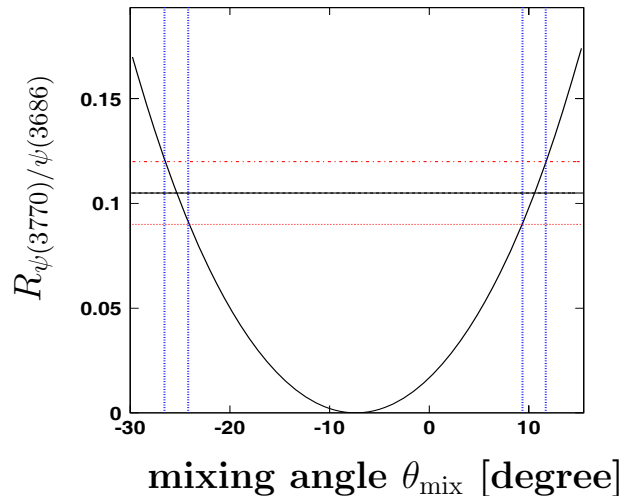


Figure 18.1: The ratio  $R_{\psi(3770)/\psi(3686)}$  of the scaled leptonic widths as a function of mixing angle  $\theta_{\text{mix}}$ , where the dashed lines show the  $\pm 1\sigma$  intervals of the measured quantities.

### 18.5.3 Electromagnetic transitions

#### Predictions for $\psi(3770)$ electromagnetic transitions

Charmonium states that are above the ground state can have significant decays into the states with the lower mass that proceed via electromagnetic transitions. For the  $\psi(3770)$  resonance, although it predominantly decays to  $D\bar{D}$  final states, there are, in addition, electromagnetic transitions between the  $\psi(3770)$  and lower mass states. According to selection rules, the  $\psi(3770)$  can decay into  $\chi_{cJ}$  ( $J = 0, 1, 2$ ) through radiating an E1 photon.

The measurements of the rates of the EM transition of  $\psi(3770)$  to  $\chi_{cJ}$  ( $J = 0, 1, 2$ ) has a special advantage. In the  $1D$  to  $1P$  system the radial integrals are relatively model-independent because of the absence of the wave function nodes in both states. In addition, the relativistic corrections and long distance effects might be small. So, by directly comparing the measured gamma transition rates from  $\psi(3770)$  to  $\chi_{cJ(J=0,1,2)}$  to the non-relativistic estimates based on the potential model, one can get credible information about the transition mechanism. A non-relativistic calculation for the EM transitions of  $\psi(3770) \rightarrow \gamma\chi_{cJ}$  ( $J = 0, 1, 2$ ) gives the partial width [166, 370] as a function of  $\theta_{mix}$ :

$$\Gamma(\psi(3770) \rightarrow \gamma\chi_{c0}) = 145 \cos^2\theta_{mix}(1.73 + \tan\theta_{mix})^2 \text{ keV}, \quad (18.5.36)$$

$$\Gamma(\psi(3770) \rightarrow \gamma\chi_{c1}) = 176 \cos^2\theta_{mix}(-0.87 + \tan\theta_{mix})^2 \text{ keV}. \quad (18.5.37)$$

$$\Gamma(\psi(3770) \rightarrow \gamma\chi_{c2}) = 167 \cos^2\theta_{mix}(0.17 + \tan\theta_{mix})^2 \text{ keV}, \quad (18.5.38)$$

Inserting the mixing angle  $\theta_{mix} = (10.6 \pm 1.3)^\circ$  determined with the parameters of the  $\psi(2S)$  and  $\psi(3770)$  measured by BESII [369] in the Eqs. 18.5.36 -18.5.38 yields the partial widths

$$\Gamma(\psi(3770) \rightarrow \gamma\chi_{c0}) = 515 \pm 17 \text{ keV}$$

$$\Gamma(\psi(3770) \rightarrow \gamma\chi_{c1}) = 79 \pm 6 \text{ keV}$$

$$\Gamma(\psi(3770) \rightarrow \gamma\chi_{c2}) = 21 \pm 3 \text{ keV}.$$

These partial widths are sensitive to the mixing schemes. Coupled-channel effects and more general mixing schemes than the one given in the Eqs. 18.5.30 and 18.5.31 would affect their values. A more complex mixing scheme [371], where the  $\psi(3770)$  is composed of only 52% pure  $c\bar{c}$  components, and where, in addition to the  $2^3S_1$  and  $1^3D_1$  states, there are other  $S$ - and  $D$ -wave  $1^{--}$  charmonium states included, with the remainder of the wave function containing additional virtual or real charmed meson pairs, predicts partial widths of:

$$\Gamma(\psi(3770) \rightarrow \gamma\chi_{c0}) = 225 \text{ or } 254 \text{ keV}$$

$$\Gamma(\psi(3770) \rightarrow \gamma\chi_{c1}) = 59 \text{ or } 183 \text{ keV}$$

$$\Gamma(\psi(3770) \rightarrow \gamma\chi_{c2}) = 3.9 \text{ or } 3.2 \text{ keV},$$

where the values in italics are the results when the influence of the open-charm channels is not included. In contrast, if the  $\psi(3770)$  is a pure  $1^3D_1$  state, the partial widths would be

$$\Gamma(\psi(3770) \rightarrow \gamma\chi_{c0}) = 434 \text{ keV},$$

$$\Gamma(\psi(3770) \rightarrow \gamma\chi_{c1}) = 133 \text{ keV},$$

$$\Gamma(\psi(3770) \rightarrow \gamma\chi_{c2}) = 4.8 \text{ keV.}$$

Thus, measurements of the partial widths for the EM transitions can provide useful information about the nature of  $\psi(3770)$  resonance and potential model dynamics.

### Measurements at *BES-III*

Measuring these branching fractions are experimentally challenging. It requires a good electromagnetic calorimeter to detect the low energy photons. The CLEO Collaboration measured the partial width for  $\psi(3770) \rightarrow \gamma\chi_{c1}$  to be  $\Gamma(\psi(3770) \rightarrow \gamma\chi_{c1}) = 75 \pm 18$  keV, which agrees well with most of the theoretical predictions [166, 371, 372]. *BES-III* has a good electromagnetic calorimeter with an energy resolution of  $\sim 3\%$ . With *BES-III*, we will be able to measure the branching fractions for these transitions quite well.

To study how well we can measure the transition rates with the *BES-III* detector, we generated Monte Carlo events of the type  $\psi(3770) \rightarrow \gamma\chi_{cJ}$  ( $J = 0, 1, 2$ ), where we make the  $\chi_{cJ}$  ( $J = 0, 1, 2$ ) decay to  $\pi^+\pi^-\pi^+\pi^-$ ,  $K^+K^-\pi^+\pi^-$ ,  $p\bar{p}\pi^+\pi^-$  and  $\pi^+\pi^-\pi^+\pi^-\pi^+\pi^-$  final states. Figure 18.2 shows the distributions of the invariant masses of the combinations for the different charged particle final states. We find that the  $\chi_{cJ}$  ( $J = 0, 1, 2$ ) states can be well reconstructed with the *BES-III* detector.

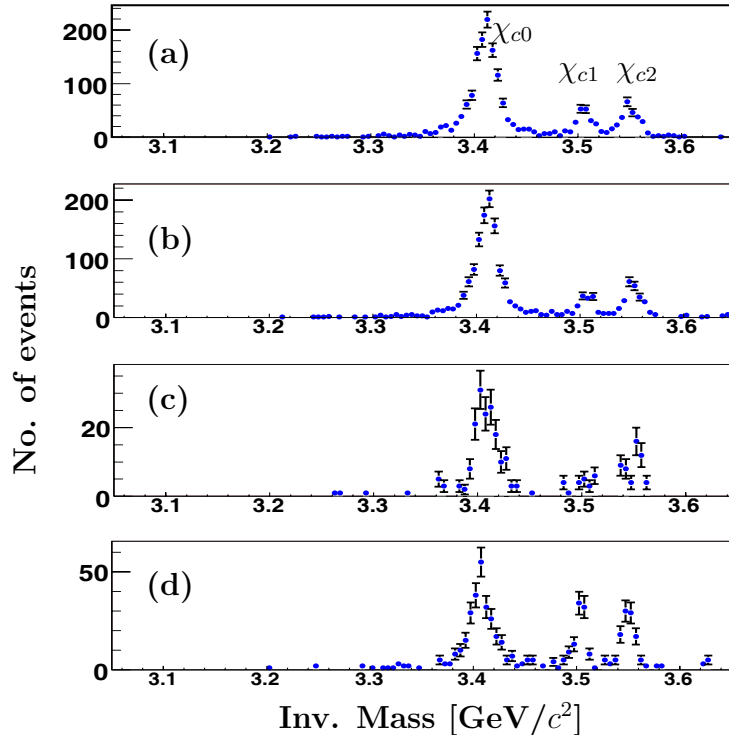


Figure 18.2: The distributions of the invariant masses of (a)  $\pi^+\pi^-\pi^+\pi^-$ , (b)  $K^+K^-\pi^+\pi^-$ , (c)  $p\bar{p}\pi^+\pi^-$  and (d)  $\pi^+\pi^-\pi^+\pi^-\pi^+\pi^-$  combinations, where the charged particles are coming from the  $\chi_{cJ}(J=0,1,2)$  decays.

### 18.5.4 Hadronic transitions

#### Predictions for $\psi(3770)$ hadronic transition

Measurements of the hadronic transitions of  $\psi(3770) \rightarrow J/\psi$  hadron(s) are important for consideration of non- $D\bar{D}$  decays of the  $\psi(3770)$  and to check the hadronic transition mechanism in the potential model. Like the case for the  $\psi(3686)$ , the emitted light hadron(s) can be  $\pi^+\pi^-$ ,  $\pi^0$  and  $\eta$  mesons that have hadronized from radiated gluons. Other hadronic transitions that emit different light hadrons are kinematically forbidden. Generally, the transition rates, as described in Refs. [373, 374, 137], are

$$\Gamma(2S \rightarrow 1S) = |c_1|^2 G |f_{2S,1S}|^2, \quad (18.5.39)$$

$$\Gamma(1D \rightarrow 1S) = 4/15 |c_2|^2 H |f_{1D,1S}|^2, \quad (18.5.40)$$

where  $G$  and  $H$  denote the phase space integrals for the two processes,  $f_{A,B}$  represents the radial matrix element between the states  $A$  and  $B$ , and  $c_1$  &  $c_2$  denote the strengths that appear in the soft pion matrix elements of the gluon operators for  $S$ - and  $D$ -waves respectively. In the  $S$ - $D$  mixing scheme, the partial widths for the hadronic  $\pi^+\pi^-$  transitions of the two charmonium states are given by [137]:

$$\Gamma(\psi(3770) \rightarrow J/\psi \pi^+ \pi^-) = |c_1|^2 \left[ \sin^2 \theta_{mix} U + \frac{4}{15} \left| \frac{c_2}{c_1} \right|^2 \cos^2 \theta_{mix} V \right], \quad (18.5.41)$$

$$\Gamma(\psi(3686) \rightarrow J/\psi \pi^+ \pi^-) = |c_1|^2 \left[ \cos^2 \theta_{mix} W + \frac{4}{15} \left| \frac{c_2}{c_1} \right|^2 \sin^2 \theta_{mix} X \right], \quad (18.5.42)$$

where  $U = G_{\psi(3770)} |f_{2S,1S}(M_{\psi(3770)})|^2$ ,  $V = H_{\psi(3770)} |f_{1D,1S}(M_{\psi(3770)})|^2$ ,  $W = G_{\psi(3686)} |f_{2S,1S}(M_{\psi(3686)})|^2$  and  $X = H_{\psi(3686)} |f_{1D,1S}(M_{\psi(3686)})|^2$ . In Eqs. (18.5.41) and (18.5.42) the values for the quantities  $G$ ,  $H$  and  $f_{A,B}$  ( $A = 2S$  &  $1D$ , and  $B = 1S$ ), can be calculated using different models, which all give similar results. For example, Ref. [137] gives

$$f_{2S,1S}(M_{\psi(3686)}) = 7.018 \text{ GeV}^{-3}, \quad (18.5.43)$$

$$f_{1D,1S}(M_{\psi(3686)}) = -8.796 \text{ GeV}^{-3}, \quad (18.5.44)$$

$$f_{2S,1S}(M_{\psi(3770)}) = 8.172 \text{ GeV}^{-3}, \quad (18.5.45)$$

$$f_{1D,1S}(M_{\psi(3770)}) = 10.266 \text{ GeV}^{-3}, \quad (18.5.46)$$

$$G_{\psi(3686)} = 0.0353 \text{ GeV}^7, \quad (18.5.47)$$

$$H_{\psi(3686)} = 0.00291 \text{ GeV}^7, \quad (18.5.48)$$

$$G_{\psi(3770)} = 0.102 \text{ GeV}^7, \quad (18.5.49)$$

$$H_{\psi(3770)} = 0.00943 \text{ GeV}^7. \quad (18.5.50)$$

However, the ratios  $c_1/c_2$  are quite different for the different models [373, 374, 137]. From the decay rates for the two hadronic transitions given in Eqs. 18.5.41 and 18.5.42, we have the ratio

$$R_{\psi(3770)/\psi(3686)}(J/\psi\pi^+\pi^-) = \frac{\left[ \sin^2\theta_{mix}U + \frac{4}{15} \left| \frac{c_2}{c_1} \right|^2 \cos^2\theta_{mix}V \right]}{\left[ \cos^2\theta_{mix}W + \frac{4}{15} \left| \frac{c_2}{c_1} \right|^2 \sin^2\theta_{mix}X \right]}, \quad (18.5.51)$$

which can be measured experimentally. From the ratio  $R_{\psi(3770)/\psi(3686)}(J/\psi\pi^+\pi^-)$  we can extract the ratio  $c_1/c_2$ .

The BESII Collaboration observed the hadronic transition process  $\psi(3770) \rightarrow J/\psi\pi^+\pi^-$  and measured the partial width to be  $\Gamma(\psi(3770) \rightarrow J/\psi\pi^+\pi^-) = 80 \pm 33 \pm 23$  keV [375]. Recently, CLEO confirmed the BESII observation for this transition process and measured the branching fraction for  $\psi(3770) \rightarrow J/\psi\pi^+\pi^-$  to be  $(0.189 \pm 0.020 \pm 0.020)\%$  [376]. These give a weighted average partial width of  $\Gamma(\psi(3770) \rightarrow J/\psi\pi^+\pi^-) = 49.0 \pm 8.4$  keV, where the uncertainty is the combined statistical and systematic errors. The world averaged partial width for  $\psi(3686) \rightarrow J/\psi\pi^+\pi^-$  process is  $\Gamma(\psi(3686) \rightarrow J/\psi\pi^+\pi^-) = 89.1 \pm 6.2$  keV. These give the ratio of partial widths

$$R_{\psi(3770)/\psi(3686)}(J/\psi\pi^+\pi^-) = 0.55 \pm 0.10. \quad (18.5.52)$$

Inserting  $\theta_{mix}$  in Eq. 18.5.51 combined with the ratio of the partial widths yields a first measurement of the parameters of  $c_1$  and  $c_2$ . The relation of the  $R_{\psi(3770)/\psi(3686)}(J/\psi\pi^+\pi^-)$  to the ratio  $c_2/c_1$  is plotted in Fig. 18.3, where the horizontal lines give the measured value of  $R_{\psi(3770)/\psi(3686)}(J/\psi\pi^+\pi^-)$  and its  $\pm 1\sigma$  interval; the vertical lines give  $\pm 1\sigma$  interval of the measured values of the ratio  $c_2/c_1$ . We find that the value of the ratio is

$$\frac{c_2}{c_1} = 2.08^{+0.31}_{-0.38}. \quad (18.5.53)$$

Inserting this solution for the ratio and the partial width  $\Gamma(\psi(3770) \rightarrow J/\psi\pi^+\pi^-) = 49.0 \pm 8.4$  keV into Eq. 18.5.41, we obtain

$$c_1 = (7.25 \pm \Delta_{\text{err}}) \times 10^{-3}. \quad (18.5.54)$$

## Measurements of hadronic transitions

From an experimental point of view, since the mass difference between  $\psi(3770)$  and  $J/\psi$  is 0.675 GeV, the typical momentum of the light hadron(s) system is low. This gives a clear kinematic signature that can be used to cleanly separate these decays from most other processes. The difficulty in selecting these decays will be separating  $\psi(3770)$  hadronic transitions from the same  $\psi(3686)$  hadronic transition when the  $\psi(3686)$  is produced either by ISR return to the  $\psi(3686)$  peak or is produced in its high energy tail. To separate the  $\psi(3770)$  hadronic transitions, including  $\psi(3770) \rightarrow J/\psi\pi^+\pi^-$ ,  $J/\psi\pi^0\pi^0$ ,  $J/\psi\eta$ , one needs a precision Monte Carlo event generator to simulate these processes including the effects of ISR, and must correctly subtract the backgrounds due to the  $\psi(3686)$  hadronic transitions from the candidates for the  $\psi(3770)$  hadronic

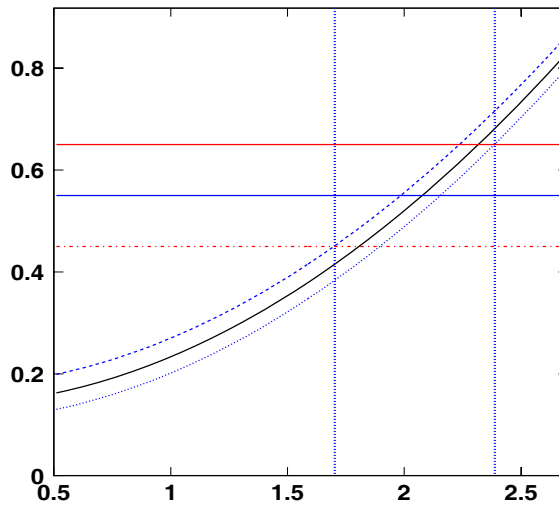


Figure 18.3: The ratio  $R_{\psi(3770)/\psi(3686)}(J/\psi\pi^+\pi^-)$  of the partial widths as a function of the ratio  $|c_2/c_1|$ , where the dashed lines show the  $\pm 1\sigma$  intervals of the measured quantities.

transitions observed in experiments. This technique of subtracting the  $\psi(3686)$  background in the selected sample for  $\psi(3770) \rightarrow J/\psi\pi^+\pi^-$  has been developed for the BESII measurement of the partial width for  $\psi(3770) \rightarrow J/\psi\pi^+\pi^-$  [375]. The generator used in the analysis of the decay is being developed for use in the analysis of *BES-III* data.

### 18.5.5 Light hadron decays

According to theory, the branching fractions for  $\psi(3770) \rightarrow$  light hadrons are expected to be small. However, there are some models [377, 378] that contain mechanisms that can enhance non- $D\bar{D}$  decays. For example, the re-annihilation amplitude of charmed meson pairs into the states containing light quarks can interfere with the corresponding amplitude for continuum light quark production of the same state. This re-annihilation effect may result in a significant enhancement of the production of light hadron final states at the  $\psi(3770)$  [379]. Such re-annihilation mechanisms are also relevant for non- $K\bar{K}$  decays of the  $\phi$  meson [379]. If this re-annihilation effect is really responsible for the non- $D\bar{D}$  decays of  $\psi(3770)$ , the enhanced penguin amplitudes in  $B$  decays can be explained by similar re-annihilation effects. So the experimental study of the exclusive non- $D\bar{D}$  decays of  $\psi(3770)$  is important for the understanding of a variety of puzzles in hadronic physics.

#### Light-hadron final states

Because of the large total width of the  $\psi(3770)$ , the decay amplitudes for any exclusive channels cannot result in branching fractions as large as those in the narrow resonance cases, *i.e.*, the  $J/\psi$  and  $\psi(3686)$ . As a result, the corresponding amplitudes from continuum production may compete with them. On the experimental side, the most difficult

item that has to be considered is the possible interference between the continuum amplitude and the  $\psi(3770)$  resonance decay amplitude. Because of the interference effects between these two amplitudes, it is not possible to measure the branching fractions for the exclusive light hadron decays of  $\psi(3770)$  by simply considering the difference of yields observed far off the  $\psi(3770)$  resonance and at the peak of  $\psi(3770)$  [380]. For example, the light hadron decays of  $\psi(3770)$  were extensively studied by both the BES and CLEO Collaborations with data taken at  $\sqrt{s} = 3.773$  GeV and at  $\sqrt{s}$  around 3.66 GeV. However, if one only considers the observed cross sections for the light hadron final states at the two energies, for some decay modes the observed cross sections at  $\sqrt{s} = 3.773$  GeV are less than those observed at  $\sqrt{s}$  around 3.66 GeV, while, for some other decay modes, the observed cross sections at  $\sqrt{s} = 3.773$  GeV are larger than those observed at  $\sqrt{s}$  around 3.66 GeV. These are probably due to interference effects between the two amplitudes. Owing to these effects, one cannot simply determine the branching fractions of  $\psi(3770)$  light hadron decays just based on the measured cross sections at two energy points.

To measure the branching fractions of  $\psi(3770)$  light hadron decays, one should measure the cross sections for exclusive decay modes at different center-of-mass energies and fit these cross sections to theoretical formulae that take interference effects into account. This is probably the best method to measure the branching fractions for  $\psi(3770) \rightarrow$  light hadrons, as well as determine the phase difference between the continuum light hadron production and the  $\psi(3770) \rightarrow$  light hadrons [381] amplitudes.

For families of decay modes that have some special symmetry, for example  $SU_3$  octets, the symmetry constrains the couplings in different ways for the different channels. In this case, one could fit the different couplings belong to various processes, e.g. the EM coupling and the strong decay strength, using the observed cross sections for these channels.

### The PV decays of $\psi(3770)$

Studies of the PV decay channels of  $\psi(3770)$  are interesting and very important for understanding the enhancement of  $\psi(3770)$  non- $D\bar{D}$  decays and the origin of the  $\rho - \pi$  puzzle seen in  $\psi(3686)$  decays. The most important PV channel is the  $\psi(3770) \rightarrow (0^{++} \text{ octet}) (1^{--} \text{ octet})$ . CLEO has measured the production cross sections for  $e^+e^- \rightarrow \rho\pi$ ,  $K^*(892)\bar{K}$ ,  $\omega\eta$ ,  $\omega\eta'$ ,  $\phi\eta$ ,  $\phi\eta'$ ,  $\rho\eta$ ,  $\rho\eta'$ ,  $\omega\pi^0$  and  $\phi\pi^0$  [382] at two center-of-mass energies of 3.671 and 3.773 GeV. They claimed that there is no evidence for significant  $\psi(3770)$  decays into PV channels.

#### A. $\psi(3770) \rightarrow K^{*0}\bar{K}^0, K^{*\pm}K^\mp, +\text{c.c.}$

From the observed decay channel  $\psi(3770) \rightarrow K^-\pi^+\pi^-\pi^+ + \text{c.c.}$ , one can analyze two correlated modes with different charge states, i.e.  $\psi(3770) \rightarrow K^{*0}\bar{K}^0 + \text{c.c.}$  with  $\bar{K}^{*0} \rightarrow K^-\pi^+$  and  $K_S^0 \rightarrow \pi^+\pi^-$ , and  $\psi(3770) \rightarrow K^{*\pm}K^\mp$  with  $K^{*\pm} \rightarrow K^0\pi^\pm$  and  $K_S^0 \rightarrow \pi^+\pi^-$  by tagging the different charge combinations of the  $K^*(892)$ . In this special example one can determine the EM coupling and the strong decay strength in this channel using measurements of the two charge modes at two energy points, say at  $\sqrt{s} = 3.650$  GeV which is far away from resonance and at  $\sqrt{s} = 3.773$  GeV which is the peak of the  $\psi(3770)$  resonance, without the need from measurements of any other PV channel at all. Unlike the measurements of the most other PV channels, the observations can provide us with four (not just two, as is the case for other channels) observed numbers, which are the numbers

of  $K^*(892)^\pm K^\mp$  and  $K^{*0}\bar{K}^0 + \text{c.c.}$  observed at the two energy points. The four observed numbers give us four equations to use to extract three unknown parameters, the coupling of  $K^*\bar{K} + \text{c.c.}$  with  $\gamma^*$ , the coupling of  $K^*\bar{K} + \text{c.c.}$  with  $\psi(3770)$  and the phase difference between them, and, finally, the branching fraction for  $\psi(3770) \rightarrow K^*(892)\bar{K} + \text{c.c.}$  and the EM coupling for PV channel in continuum production.

With this method, the BESII Collaboration measured the branching fraction for the decay  $\psi(3770) \rightarrow K^{*0}\bar{K}^0 + \text{c.c.}$  to be [383]

$$B(\psi(3770) \rightarrow K^{*0}\bar{K}^0 + \text{c.c.}) = (4.3^{+5.4}_{-3.4} \pm 1.3) \times 10^{-4},$$

which corresponds an upper limit on the branching fraction of

$$B(\psi(3770) \rightarrow K^{*0}\bar{K}^0 + \text{c.c.}) < 0.12\% \quad \text{at 90\% C.L.},$$

corresponding to a limit on the partial width of

$$\Gamma(\psi(3770) \rightarrow K^{*0}\bar{K}^0 + \text{c.c.}) < 29 \text{ keV} \quad \text{at 90\% C.L.}.$$

For these two decay modes, the CLEO Collaboration observed the number of signal events at the two energy points ( $\sqrt{s} = 3.671$  GeV and  $\sqrt{s} = 3.773$  GeV) and measured the observed cross sections to be [382]

$$\begin{aligned} N_{3.773\text{GeV}}^0 &= 438 & \sigma_{3.773\text{GeV}}^0 &= 19.1 \text{ pb}, \\ N_{3.671\text{GeV}}^0 &= 38 & \sigma_{3.671\text{GeV}}^0 &= 19.2 \text{ pb}, \\ N_{3.773\text{GeV}}^{\text{ch}} &= 4 & \sigma_{3.773\text{GeV}}^{\text{ch}} &= 0.09 \text{ pb}, \\ N_{3.671\text{GeV}}^{\text{ch}} &= 4 & \sigma_{3.671\text{GeV}}^{\text{ch}} &= 1.14 \text{ pb}, \end{aligned}$$

where the upper script 0 and ch mean the neutral and charged decay modes, respectively. When first looking at the numbers of the observed signal events and the values of the observed cross sections, it seems that there is no room for the existence of strong decays  $\psi(3770) \rightarrow K^*(892)\bar{K} + \text{c.c.}$  due to the tiny differences between the observed cross sections at the resonance peak and off the resonance. However, the larger differences of the cross sections observed for the two different modes at each of the two energy points may indicate that there is something else going on. This difference cannot be explained only by the EM coupling.

### B. $\psi(3770) \rightarrow \rho\pi$

The partial width of the PV channel  $\psi(3770) \rightarrow \rho\pi$  decay might have a measurable value like that for the  $\psi(3770) \rightarrow K^*(892)\bar{K}$  decay mode mentioned above. However, BESII [384] did not observe positive signals of  $\psi(3770) \rightarrow \rho\pi$  or  $e^+e^- \rightarrow \rho\pi$  at either of the two energy points. This might be due to the lack of sufficient statistics. Like the case for  $K^{*\pm}K^\mp$ , there might exist a cancellation between the amplitudes for the EM coupling and the strong decay in the decay of  $\psi(3770) \rightarrow \rho\pi$  [385].

### C. Fits to PV decays of the $\psi(3770)$

Like the treatments of the PV decay channels for  $J/\psi$  and  $\psi(3686)$ , an important task is the measurement of all of the PV modes at the same time, such as  $\psi(3770) \rightarrow$

$\rho\pi$ ,  $K^*(892)\bar{K}$ ,  $\omega\eta$ ,  $\omega\eta'$ ,  $\phi\eta$ ,  $\phi\eta'$ ,  $\rho\eta$ ,  $\rho\eta'$ ,  $\omega\pi^0$  and  $\phi\pi^0$ , etc., and to fit all of these measured cross sections to get the information about the strong and electro-magnetic couplings, the strength of  $SU_3$  breaking, and the mixing of  $\eta - \eta'$ . These types of measurements are important for understanding the strength of  $\psi(3770)$  non- $D\bar{D}$  decays and can perhaps help in the understanding of the origin of the ' $\rho\pi$ ' puzzle.

#### D. EM PV decays of the $\psi(3770)$

BESII has measured the production cross sections for  $e^+e^- \rightarrow \omega\pi^0$ ,  $\rho\eta$  and  $\rho\eta'$  [386]. Due to isospin conservation, a  $1^{--}$  quarkonium state is only allowed to decay into  $\omega\pi^0$ ,  $\rho\eta$  and  $\rho\eta'$  through its electro-magnetic coupling. However, the small leptonic decay width of the  $\psi(3770)$  makes the observation of the decays  $\psi(3770) \rightarrow \omega\pi^0$ ,  $\rho\eta$  and  $\rho\eta'$  very difficult (the branching fraction is at the level of  $\leq 10^{-9}$ ), even with *BES-III* detector at the BEPC-II collider. However, the measured cross sections for  $e^+e^- \rightarrow \omega\pi^0$  etc. are meaningful and give form factor values for these modes. These indicate the common  $\gamma^*$ -PV coupling of continuum hadron production in this energy region.

#### Monte Carlo simulation

For measurements of the branching fractions for  $\psi(3770) \rightarrow$  light hadrons, we need to reconstruct  $\psi(3770)$  decay final states. To understand how well we can do this with the *BES-III* detector, we generated the two different types of  $\psi(3770) \rightarrow$  light hadrons decays. The first type contains only stable or long-life-time charged particles ( $K^\pm$ ,  $\pi^\pm$  and  $p$  or  $\bar{p}$ ), and the second type contains a promptly decaying particle, such as a  $\pi^0$ . To reconstruct the final states for the first type, we calculate the total measured energy  $E_{\text{measure}}$  of the final state containing all of the charged particles. Then we calculate the ratio of the  $E_{\text{measure}}$  over the  $E_{\text{cm}}$ . The most probable ratio  $R = E_{\text{measure}}/E_{\text{cm}}$  should be around 1 for the light hadron decays of  $\psi(3770)$ . For the second type of decay mode, we simply reconstructed the  $\pi^0$  from the decay mode under study. Figures 18.4 (a), (b), (c) and (d) show the reconstructed ratio  $R$  for the final states of  $\pi^+\pi^-\pi^+\pi^-$ ,  $K^+K^-\pi^+\pi^-$ ,  $p\bar{p}\pi^+\pi^-$  and  $3(\pi^+\pi^-)$ , respectively; while Figs. 18.4(e), (f), (g) and (h) show the distributions of the invariant masses of the  $\gamma\gamma$  combinations from the final states of  $2(\pi^+\pi^-)\pi^0$ ,  $K^+K^-\pi^+\pi^-\pi^0$ ,  $p\bar{p}\pi^+\pi^-\pi^0$  and  $3(\pi^+\pi^-)\pi^0$ , respectively.

Monte Carlo studies of light hadron decays and PV decays of the  $\psi(3770)$  are still in progress.

#### 18.5.6 Studies of inclusive decays

##### Measurement of branching fractions for $\psi(3770) \rightarrow D^0\bar{D}^0$ , $D^+D^-$ , $D\bar{D}$ and $\psi(3770) \rightarrow$ non- $D\bar{D}$

Recently, the BESII Collaboration reported measurements of the branching fractions for  $\psi(3770) \rightarrow D^0\bar{D}^0$ ,  $D^+D^-$  and the branching fraction for  $\psi(3770) \rightarrow$  non- $D\bar{D}$ . Based on analysis of two different kinds of data samples collected at  $\sqrt{s} = 3.773$  GeV and at  $\sqrt{s}$  around 3.66 GeV, and collected in the range from 3.65 to 3.872 GeV, BESII obtained the non- $D\bar{D}$  branching fraction  $B(\psi(3770) \rightarrow \text{non-}D\bar{D}) = (16.4 \pm 7.3 \pm 4.2)\%$  [363] and  $B(\psi(3770) \rightarrow \text{non-}D\bar{D}) = (16.4 \pm 7.3 \pm 4.2)\%$  [364]. A better way to measure

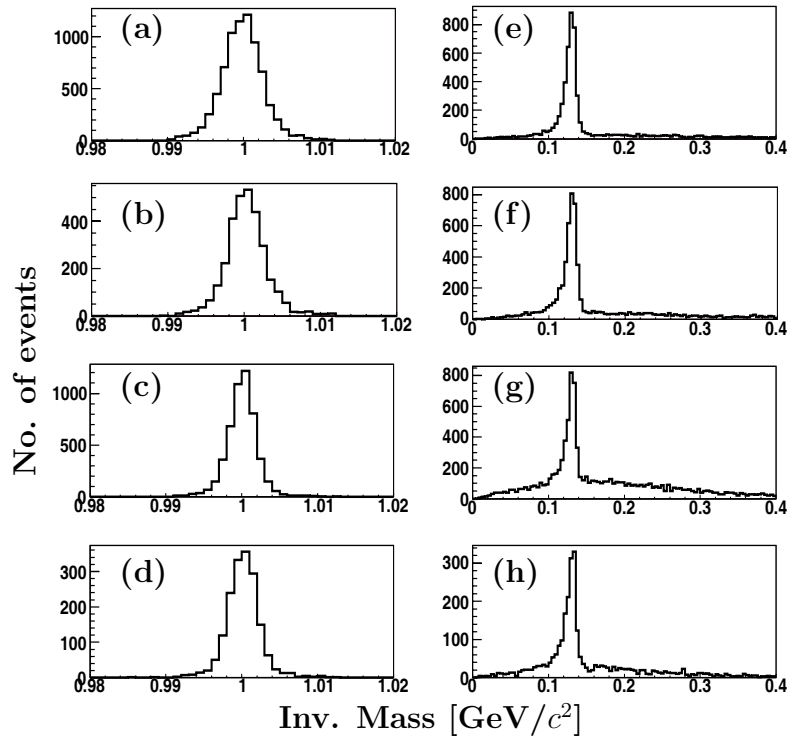


Figure 18.4: The distributions of the ratio  $R = E_{\text{measure}}/E_{\text{cm}}$  and the invariant masses of  $\gamma\gamma$  combinations, where the (a), (b), (c) and (d) show the  $R$  for the combinations of  $\pi^+\pi^-\pi^+\pi^-$ ,  $K^+K^-\pi^+\pi^-$ ,  $p\bar{p}\pi^+\pi^-$  and  $3(\pi^+\pi^-)$ , respectively; while the (e), (f), (g) and (h) show the invariant masses of  $\gamma\gamma$  combinations for the final states of  $2(\pi^+\pi^-)\pi^0$ ,  $K^+K^-\pi^+\pi^-\pi^0$ ,  $p\bar{p}\pi^+\pi^-\pi^0$  and  $3(\pi^+\pi^-)\pi^0$ , respectively.

the branching fraction for  $\psi(3770) \rightarrow \text{non-}D\bar{D}$  is to analyze the energy dependent cross sections for inclusive hadron,  $D^0\bar{D}^0$  and  $D^+D^-$  event production in the energy range covering both the  $\psi(2S)$  and  $\psi(3770)$  resonances, in a single scan. In this way one can also more accurately measure the parameters of the two resonances, since they are correlated to each other in the analysis of the cross section scan data.

Using the same method as that used in the measurements of the branching fractions for  $\psi(3770) \rightarrow D^0\bar{D}^0$ ,  $D^+D^-$ , and non- $D\bar{D}$  [363], we study by Monte Carlo simulation how well we can measure the branching fractions with the *BES-III* detector at BEPC-II collider. We generated a total of  $60 \text{ pb}^{-1}$  of data at 49 energy points from 3.66 to 3.88 GeV. By analyzing these Monte Carlo events, we obtain the branching fractions for  $\psi(3770) \rightarrow D\bar{D}$  and  $\psi(3770) \rightarrow \text{non-}D\bar{D}$ . Table 18.6 summarizes the measured branching fractions from the Monte Carlo simulation along with the branching fractions input into the Monte Carlo simulation. The errors listed in the table are the statistical and systematic, respectively. From the Monte Carlo simulation, we also obtain the measured branching fractions for the decays  $\psi(3770) \rightarrow D^0\bar{D}^0$  and  $\psi(3770) \rightarrow D^+D^-$  to be

$$B[\psi(3770) \rightarrow D^0\bar{D}^0] = (46.3 \pm 1.3 \pm 1.0)\%,$$

and

$$B[\psi(3770) \rightarrow D^+D^-] = (42.5 \pm 1.2 \pm 0.9)\%,$$

Table 18.6: The input and measured branching fraction for  $\psi(3770) \rightarrow \text{non-}D\bar{D}$ , where the "input" means the value of the parameter set in the Monte Carlo simulation and the "measured" means the measured value of the parameters from the Monte Carlo simulation.

input/measured	$B(\psi(3770) \rightarrow D\bar{D}) [\%]$	$B(\psi(3770) \rightarrow \text{non-}D\bar{D}) [\%]$
input	90%	10%
measured	$88.8 \pm 2.4 \pm 2.0$	$11.2 \pm 2.4 \pm 2.0$

which correspond to the set values of the branching fractions of  $B[\psi(3770) \rightarrow D^0\bar{D}^0] = 46.8\%$  and  $B[\psi(3770) \rightarrow D^+D^-] = 43.2\%$  in the Monte Carlo simulation, respectively.

Figure 18.5 shows the observed cross sections for inclusive hadron and  $D\bar{D}$  production from  $\psi(3770)$  decays, where the dots with errors are the observed cross section for the inclusive hadronic events from  $\psi(3770)$  decays, the triangles with errors are the observed cross sections for  $D^+D^-$  from  $\psi(3770)$  decays, and the inverted triangles with errors are the observed cross sections for  $D^0\bar{D}^0$  from  $\psi(3770)$  decays, and the squares with errors are the totally observed cross sections over the neutral and the charged  $D\bar{D}$  production from  $\psi(3770)$  decays. The lines show the best fits to the observed cross sections.

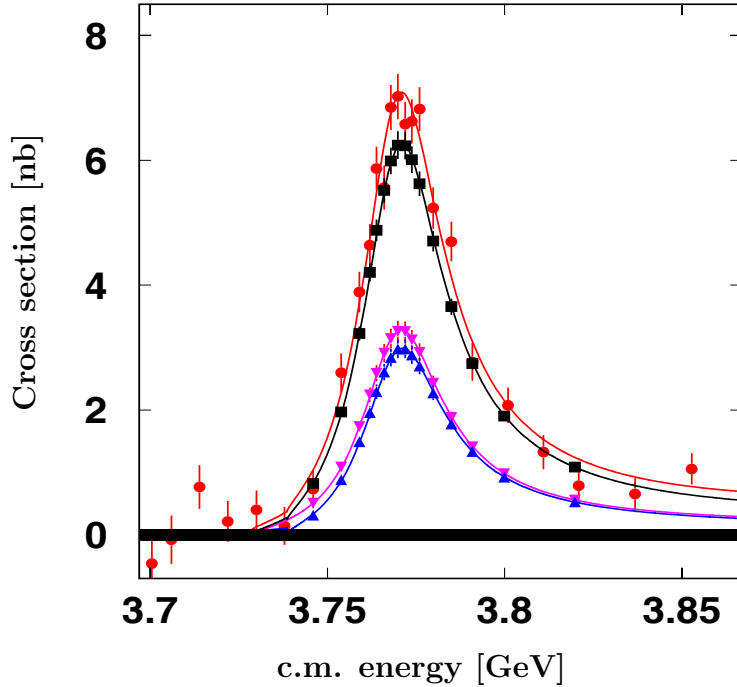


Figure 18.5: The observed cross sections versus the nominal c.m. energies.

### Measurements of branching fractions for inclusive decay modes

By fitting the cross sections for the inclusive  $J/\psi$ ,  $\eta$ ,  $\eta'$  ... observed at different center-of-mass energies to a theoretical formula to describe the production of the inclusive final states, we can measure the branching fractions for  $\psi(3770)$  decay into these final

states. These branching fractions might prove useful for understanding of the nature of the  $\psi(3770)$ .

Monte Carlo studies of these decays are still in progress.

### Measurements of cross sections for $e^+e^- \rightarrow \text{hadrons}_{\text{non-}D\bar{D}}$

Another way to search directly for the non- $D\bar{D}$  decays of  $\psi(3770)$  is to measure the cross section for  $e^+e^- \rightarrow \text{hadrons}_{\text{non-}D\bar{D}}$ , where the  $\text{hadrons}_{\text{non-}D\bar{D}}$  means that the final state hadrons are not coming from the  $D\bar{D}$  decays. In analysis of the cross section scan data, if we find an enhancement in the observed cross sections for the processes  $e^+e^- \rightarrow \text{hadrons}_{\text{non-}D\bar{D}}$  around  $\psi(3770)$  resonance, we directly observe the non- $D\bar{D}$  decays of the  $\psi(3770)$  resonance. Actually, we can also examine the observed cross sections for inclusive  $K_S^0$ ,  $K^{*0}$ ,  $K^{*+}$  and  $\phi$ . For these analyses, we need more data samples taken at different center-of-mass energies.

In order to verify and calibrate the cross sections of the non- $D\bar{D}$  event production in  $\psi(3770)$  resonance region, it is necessary to have data taken over the whole energy region covered by the  $\psi(3686)$  resonance.

#### 18.5.7 Summary

In studies of the  $\psi(3770)$  production in  $e^+e^-$  annihilation and its decays, there are still "puzzles" in understanding the physical  $\psi(3770)$  state and its decays. What does the  $\psi(3770)$  consist of and how do the components of the  $\psi(3770)$  effect its various non- $D\bar{D}$  decays, the  $\gamma$ -transitions, the hadronic transitions, and the different exclusive non- $D\bar{D}$  decays? It is not understood how  $\psi(3770)$  can decay into non- $D\bar{D}$  final states with such a large branching fraction. On one hand, the newest BESII measurements on the branching fraction may still suffer from a large systematic shift; on the other hand, there may exist some other effects or new phenomena that are responsible for the large discrepancy in the measured cross sections  $\sigma_{D\bar{D}}^{\text{obs}}$  and  $\sigma_{\psi(3770)}^{\text{obs}}$ , and this results in the large non- $D\bar{D}$  branching fraction. With the *BES-III* detector at BEPC-II collider, we can measure the branching fraction for  $\psi(3770) \rightarrow \text{non-}D\bar{D}$  well. With about  $60 \text{ pb}^{-1}$  of data collected in the range from 3.65 to 3.88 GeV, we can measure the branching fraction with an accuracy level of 2.5%. With more data taken across the  $\psi(3770)$  resonance region covering  $\psi(3686)$  resonance, we can extensively study the exclusive light hadron final states of  $\psi(3770)$  decays and may shed light on the "puzzles" mentioned above.

## 18.6 Baryonic decays<sup>10</sup>

### 18.6.1 Introduction

The discovery of the  $J/\psi$  particle [387] opened a new epoch of hadronic physics. Many theoretical concepts and tools have been put forth to describe features of charmonium decays (see Ref. [388] for a general review). However, since the structure of baryons is comparatively more complicated than that for mesons, theoretical research in the area of

---

<sup>10</sup>Xiaohu Mo, Ronggang Ping, and Changzheng Yuan

baryonic decays are at present relatively limited, and scattered in a variety of references. Here we collect various discussions and descriptions that are pertinent to baryonic decays, so that we can identify what is known about mechanisms for baryonic decays, what remains unclear, and what needs further exploration.

### 18.6.2 Theoretical Framework

#### Fock expansion

Exclusive  $J/\psi$  decays into baryon anti-baryon ( $B\bar{B}$ ) pairs have been investigated by a number of authors in the framework of perturbative QCD (pQCD) [389, 390, 391, 392]; for a recent review see Ref. [393]. The dominant dynamical mechanism is  $c\bar{c}$  annihilation into the minimum number of gluons allowed by symmetries and the subsequent creation of light quark-antiquark pairs that form the final state baryons. The decay amplitude is expressed as a convolution of a hard scattering amplitude and a factor that involves the initial-state charmonium wave function and the final-state baryonic wave function. As shown in Ref. [394], the charmonium wave function can be organized into a hierarchy of scales associated with powers of the velocity of the  $c$  quark in the charmonium meson. The Fock expansions for the charmonium states start as:

$$\begin{aligned}
 |J/\psi\rangle &= \underbrace{|c\bar{c}_1(^3S_1)\rangle}_{\mathcal{O}(1)} + \underbrace{|c\bar{c}_8(^3P_J)g\rangle}_{\mathcal{O}(v)} + \underbrace{|c\bar{c}_8(^3S_1)gg\rangle}_{\mathcal{O}(v^2)} + \dots, \\
 |\eta_c\rangle &= \underbrace{|c\bar{c}_1(^1S_0)\rangle}_{\mathcal{O}(1)} + \underbrace{|c\bar{c}_8(^1P_1)g\rangle}_{\mathcal{O}(v)} + \underbrace{|c\bar{c}_8(^1S_0)gg\rangle}_{\mathcal{O}(v^2)} + \dots, \\
 |\chi_{cJ}\rangle &= \underbrace{|c\bar{c}_1(^3P_J)\rangle}_{\mathcal{O}(1)} + \underbrace{|c\bar{c}_8(^3S_1)g\rangle}_{\mathcal{O}(v)} + \dots,
 \end{aligned} \tag{18.6.55}$$

where the subscripts to the  $c\bar{c}$  pair specify whether it is in a colour-singlet (1) or colour-octet (8) state;  $\mathcal{O}(1)$ ,  $\mathcal{O}(v)$  and  $\mathcal{O}(v^2)$  are the orders to which the corresponding Fock states contribute, once evaluated in a matrix element.

As shown in Ref. [395], decays of  $P$ -wave charmonium into baryon anti-baryon pairs are suppressed by a factor of  $1/M$  relative to those for  $S$ -wave charmonium. For charmonium decays into  $B\bar{B}$ , the decay amplitude can be expressed as:

$$\mathcal{M} \sim f_c \phi_c(x) \otimes f_N \phi_N(x) \otimes f_{\bar{N}} \phi_{\bar{N}} \otimes T_H(x), \tag{18.6.56}$$

where  $T_H$  is the hard perturbative part, and  $f_i$  and  $\phi_i$  are the decay constant and the hadronic wave function for charmonium and baryon/anti-baryon, respectively. It is easy to use power counting in Eq.(18.6.56) to compare  $S$ -wave and  $P$ -wave charmonium, as well as the color-singlet and octet contributions to the decay width. For vector charmonia decays into  $B\bar{B}$ , the decay amplitude dependence on  $M$  goes as:

$$\mathcal{M}_S^{(1)} \sim M \frac{f_c^{(1)}}{M} \left( \frac{f_N}{M^2} \right)^2 \sim \frac{1}{M^4},$$

$$\mathcal{M}_S^{(8)} \sim M \frac{f_c^{(8)}}{M^2} \left( \frac{f_N}{M^2} \right)^2 \sim \frac{1}{M^5}. \quad (18.6.57)$$

For example, in the case of  $J/\psi$  decays to  $B\bar{B}$ , the color-octet contribution is suppressed by the energy scale  $1/M$ . Therefore, the color octet contribution can be neglected in  $S$ -wave decays. However, for  $P$ -wave charmonium decays, the color-octet contribution cannot be neglected. For example, the amplitudes of  $\chi_{cJ} \rightarrow B\bar{B}$  depend on the energy scale as:

$$\begin{aligned} \mathcal{M}_P^{(1)} &\sim M \frac{f_c^{(1)}}{M^2} \left( \frac{f_N}{M^2} \right)^2 \sim \frac{1}{M^5}, \\ \mathcal{M}_P^{(8)} &\sim M \frac{f_c^{(8)}}{M^2} \left( \frac{f_N}{M^2} \right)^2 \sim \frac{1}{M^5}. \end{aligned} \quad (18.6.58)$$

To evaluate the decay widths, information on decay constants of charmonium can be determined from the leptonic decay width. For example:

$$\Gamma(J/\psi \rightarrow e^+e^-) = \frac{4\pi}{3} \frac{e_c^2 \alpha_{em}^2 f_{J/\psi}^2}{M_{J/\psi}}. \quad (18.6.59)$$

One gets  $f_{J/\psi} = 409\text{MeV}$ ,  $f_{\psi(2S)} = 282\text{MeV}$ . The other soft physics information required is the leading-twist baryon distribution amplitude [396, 397].

### Hadronic helicity conservation

The leading-twist formation for the light hadrons in the final state has implications for their helicity configurations. As a consequence of the vector nature of QCD (and QED), time-like virtual gluons (or photons) create light, (almost) massless quarks and antiquarks in opposite helicity states. To leading-twist accuracy, such partons form the valence quarks of the light hadrons and transfer their helicities to them. Hence, the total hadronic helicity is zero

$$\lambda_1 + \lambda_2 = 0. \quad (18.6.60)$$

The conservation of hadronic helicities is a dynamical consequence of QCD (and QED) that holds to leading-twist order. The violation of helicity conservation in a decay process signals the presence of higher-twist, higher Fock states and/or soft, non-factorizable contributions.

We note that hadronic helicity conservation does not hold either in  $\eta_c$  or  $\chi_{c0}$  decays into baryon–antibaryon pairs where, in the charmonium rest frame, angular momentum conservation requires  $\lambda_B = \lambda_{\bar{B}}$ . A systematic investigation of higher-twist contributions to these processes is still lacking despite some attempts at estimating them. For a review see Ref. [398]. Recent progress in classifying higher-twist distribution amplitudes and understanding their properties [399, 400] now permits such analyses. The most important question to be answered is whether or not factorization holds for these decays to higher-twist order. It goes without saying that besides higher-twist effects, the leading-twist forbidden channels might be under control of other dynamical mechanisms such as higher Fock state contributions or soft power corrections.

There is no reliable theoretical interpretation of these decays as yet. One proposition [401] is the use of a diquark model, a variant of the leading-twist approach in which baryons are viewed as being composed of quarks and quasi-elementary diquarks. With vector diquarks as constituents, one may overcome the helicity sum rule (18.6.60). The diquark model in its present form, however, has some difficulties. Large momentum transfer data on the Pauli form factor of the proton, as well as a helicity correlation parameter for Compton scattering off protons are in severe conflict with predictions from the diquark model. Other phenomenological models argue that  $\chi_{cJ}$  helicity violation decays might proceed via uncommon mechanisms, such as quark pair creation in  $\chi_{cJ} \rightarrow B\bar{B}$  decays [402] and the exchange of an intermediate state in  $\chi_{cJ}$  decays [403].

### Analysis based on $SU(3)$ symmetry

In  $SU(3)_{\text{flavour}}$  representations, the baryons are arranged in singlet, octet, and decuplets:

$$\mathbf{3} \otimes \mathbf{3} \otimes \mathbf{3} = \mathbf{1}_A \oplus \mathbf{8}_{M_1} \oplus \mathbf{8}_{M_2} \oplus \mathbf{10}_S .$$

The subscripts indicate antisymmetric, mixed-symmetric or symmetric multiplets under interchange of flavor labels of any two quarks. Each multiplet corresponds to a unique baryon number, spin, parity and its members are classified by  $I$ ,  $I_3$ , and  $S$ . The lowest lying singlet, octet, and decuplet states, denoted  $B_1$ ,  $B_8$ , and  $B_{10}$ , correspond to  $J^P = \frac{1}{2}^-, \frac{1}{2}^+, \frac{3}{2}^+$ , respectively.

In an  $SU(3)$ -symmetric world, only the decays into final states  $B_1\bar{B}_1$ ,  $B_8\bar{B}_8$ , and  $B_{10}\bar{B}_{10}$  are allowed, with the same decay amplitudes within a given decay family if electromagnetic contributions are neglected. Nevertheless,  $SU(3)$  symmetry can be broken in several ways [404], so in phenomenological analyses both symmetric and symmetry-breaking terms have to be included.

As a specific example, the parameterization forms for octet-baryon-pair final state are worked out and presented in Table 18.7.

Table 18.7: Amplitude parameterization forms [404, 405] for decays of the  $J/\psi$  into a pair of octet baryons (phase space is not included). General expressions in terms of singlet  $A$ , as well as symmetric and antisymmetric charge-breaking ( $D, F$ ) and mass-breaking terms ( $D', F'$ ) are given..

Final state	Amplitude parameterization form
$p\bar{p}$	$A + D + F - D' + F'$
$n\bar{n}$	$A - 2D - D' + F'$
$\Sigma^+\bar{\Sigma}^-$	$A + D + F + 2D'$
$\Sigma^0\bar{\Sigma}^0$	$A + D + 2D'$
$\Sigma^-\bar{\Sigma}^+$	$A + D - F + 2D'$
$\Xi^0\bar{\Xi}^0$	$A - 2D - D' - F'$
$\Xi^-\bar{\Xi}^+$	$A + D - F - D' - F'$
$\Lambda\bar{\Lambda}$	$A - D - 2D'$
$\Sigma^0\bar{\Lambda} + \bar{\Sigma}^0\Lambda$	$\sqrt{3}D$

Here, we add a remark concerning the treatment of charge-conjugated final states. Applying the operator for charge conjugation to a baryon-antibaryon system,

$$C|B_n \bar{B}_m\rangle = |\bar{B}_n B_m\rangle \begin{cases} = |B_n \bar{B}_m\rangle & \text{for } n = m \\ \neq |B_n \bar{B}_m\rangle & \text{for } n \neq m \end{cases}, \quad (18.6.61)$$

generally leads to a different state. Charge conjugated states will nevertheless be produced with the **same** branching ratio if **isospin** is conserved in the decay of the final state particles. We therefore adopt the convention that charge conjugated states are implicitly included in the measurement of branching ratios. In fact, the parameterization in Table 18.7 has followed such a convention.

### 12% rule and decay ratio

The ratio derived based on the perturbative QCD:

$$Q_h = \frac{\mathcal{B}_{\psi' \rightarrow h}}{\mathcal{B}_{J/\psi \rightarrow h}} = \frac{\mathcal{B}_{\psi' \rightarrow \ell^+ \ell^-}}{\mathcal{B}_{J/\psi \rightarrow \ell^+ \ell^-}} \approx (12.4 \pm 0.4)\%, \quad (18.6.62)$$

appears to be valid for a number of hadronic final states, but is violated severely in the  $\rho\pi$  and several other decay channels. This is the so-called “ $\rho\pi$  puzzle.” However, the naive prediction for  $Q_h$  suffers from several apparently simplistic approximations. More detailed and quantitative analyses are needed to refine the estimate. One such refinement was put forth by Chernyak [406]. Based on the investigation of the asymptotic behaviour of hadronic exclusive processes within the framework of QCD [398], Chernyak suggested the adoption of the ratio of “reduced” decay amplitudes instead of branching fractions to describe the relation between the  $J/\psi$  and  $\psi'$  decays:

$$\kappa_h \equiv \left| \frac{A'}{A} \right| = \left\{ \frac{1}{f_\kappa} \cdot \frac{\mathcal{B}_{\psi' \rightarrow h}}{\mathcal{B}_{J/\psi \rightarrow h}} \right\}^{1/2}, \quad (18.6.63)$$

where  $A'$  and  $A$  are the “reduced” decay amplitudes of the  $J/\psi$  and  $\psi' \rightarrow h$  decays and  $f_\kappa$  is a scaling factor:

$$f_\kappa = \frac{\mathcal{B}_{\psi' \rightarrow \ell^+ \ell^-}}{\mathcal{B}_{J/\psi \rightarrow \ell^+ \ell^-}} \cdot \left( \frac{M_{J/\psi}}{M_{\psi'}} \right)^{n_{\text{eff}}} \cdot \left( \frac{\xi'}{\xi} \right)^k. \quad (18.6.64)$$

Here  $n_{\text{eff}}$  is the effective index obtained by asymptotic dynamic analysis of component quarks and contains the corresponding helicity information [406],  $k$  is a kinetic index for  $\xi$  and  $\xi'$ , which are phase space factors for the  $J/\psi$  and  $\psi'$  decays. For a two-body decay,  $\xi$  or  $\xi'$  can be written explicitly as

$$\xi = \frac{|\mathbf{p}|}{M} = \frac{\sqrt{[M^2 - (m_1 + m_2)^2][M^2 - (m_1 - m_2)^2]}}{2M^2},$$

where  $\mathbf{p}$  is the center-of-mass momentum of one of decay particles;  $M$  and  $(m_1, m_2)$  correspond to the masses of the parent and two decay particles, respectively. For some special decay modes, the values of  $n_{\text{eff}}$  and  $k$  are given in Ref. [406] (see Table 18.8).

Although from a theoretical point of view  $\kappa_h$  seems more reasonable than  $Q_h$ , as discussed in Ref. [407], from an experimental point of view the estimation of  $Q_h$  value affords us some clues concerning the exploration of charmonium decay dynamics. Therefore, in the following discussions  $Q_h$  and/or  $\kappa_h$  will be used.

Table 18.8: The values of  $n_{eff}$  and  $k$  for some kinds of the  $J/\psi$  and  $\psi'$  decay modes .

Mode	$VP$	$VT, AP$	$BB$	$PP, VV$	$\gamma T$	$\gamma P$
$n_{eff}$	6	6	8	4	2	$4\dagger$
$k$	3	1	1	2	1	3

$\dagger$ : the value only for  $\gamma\eta$  and  $\gamma\eta'$ .

### 18.6.3 Two body decays

In this section, experimental data for baryonic decays are collected as much as possible and compared with various kinds of theoretical predictions and suggestions. For the  $\chi_{cJ}$ ,  $J/\psi$ , and  $\psi'$ , only the results on two-body decays are presented and discussed while for the  $\eta_c$ ,  $\eta'_c$ ,  $\psi''$ , and other higher-charmonium states, all results involving baryonic pairs are mentioned since available measurements are rather limited.

#### $\eta_c$ and $\eta'_c$

All experimental results up to now relevant to  $\eta_c$  decays into final-states containing baryons are summarized in Table 18.9; results involving baryon-pair for  $\eta'_c$  decays are still not available. Inclusive decays of the  $\eta_c$  and  $\eta'_c$  are discussed in section 18.6.5. For the  $\eta_c$  and  $\eta'_c$  decays, more work is needed both theoretically and experimentally.

Table 18.9: Experimental results for  $\eta_c$  decays into baryon-containing final states. The upper limits are at the 90% confidence level.  $\mathcal{B}_{\eta_c \rightarrow X} = \mathcal{B}_{J/\psi, \psi' \rightarrow \gamma\eta_c, \eta_c \rightarrow X} / \mathcal{B}_{J/\psi, \psi' \rightarrow \gamma\eta_c}$  and the values of  $\mathcal{B}_{J/\psi, \psi' \rightarrow \gamma\eta_c}$  are from PDG06 [408]; the values with  $\star$  are for  $\psi' \rightarrow \gamma\eta_c$  while the others are for  $J/\psi \rightarrow \gamma\eta_c$ .

Mode	Number of events	$\mathcal{B}_{J/\psi, \psi' \rightarrow \gamma\eta_c, \eta_c \rightarrow X}$ ( $\times 10^{-4}$ )	$\mathcal{B}_{\eta_c \rightarrow X}$ ( $\times 10^{-3}$ )	$\mathcal{B}_{J/\psi, \psi' \rightarrow \gamma\eta_c}$ ( $\times 10^{-2}$ )	Reference
$p\bar{p}$	$213 \pm 33$	$0.19 \pm 0.03 \pm 0.03$	$1.5 \pm 0.6$	$1.27 \pm 0.36$	[409]
	$18 \pm 6$	$0.13 \pm 0.04 \pm 0.03$	$1.0 \pm 0.3 \pm 0.4$	$1.27 \pm 0.36$	[410]
	$23 \pm 1$	$0.14 \pm 0.07$	$1.1 \pm 0.6$	$1.27 \pm 0.36$	[411]
		$0.08^{+0.08}_{-0.04}$	$2.9^{+2.9}_{-1.5}$	$0.28 \pm 0.06\star$	[412]
[average]			$1.3 \pm 0.4$		[408]
$\Lambda\bar{\Lambda}$	$< 6$	$< 0.25$	$< 2$	$1.27 \pm 0.36$	[410]
			$0.87^{+0.38}_{-0.37}$		[413]
$p\bar{p}\pi^+\pi^-$		$< 0.05$	$< 12$	$0.28 \pm 0.06\star$	[412]

#### $\chi_{cJ}$

The colour-singlet contribution to the decays  $\chi_{cJ} \rightarrow p\bar{p}$  ( $J = 1, 2$ ) has been investigated by a number of authors [391, 398, 414, 415]. Employing the proton distribution amplitude (Ref. [397]) or a similar one, one again finds results that are clearly below experiment, which again signals the importance of colour-octet contributions. An analysis of  $\chi_{c1(2)}$

decays into the octet and decuplet baryons along the same lines as for the pseudoscalar meson channels [394] has been carried out by Wong [395]. The branching ratios have been evaluated from the baryon wave functions and the same colour-octet  $\chi_{cJ}$  wave function as in Ref. [394]. Some of the results obtained in Ref. [395] are shown and compared to experiment in Table 18.10. As can be seen from the table, the results for the  $p\bar{p}$  channels are in good agreement with experiment while the branching ratios for  $\Lambda\bar{\Lambda}$  channels are much smaller than experiment [416] although the errors are large. A peculiar fact should be noted: the experimental  $\Lambda\bar{\Lambda}$  branching ratios are larger than the proton–antiproton ones although the difference is only at the two standard deviation level.

Table 18.10: Comparison of theoretical and experimental branching ratios for various  $\chi_{cJ}$  decays into pairs of light hadrons. The theoretical values have been computed within the modified perturbative approach, colour-singlet and -octet contributions are taken into account. The branching ratios are quoted in units  $10^{-5}$ . The data are taken from ref. [408]. The values listed for the  $p\bar{p}$  branching ratios do not include the most recent values  $(27.4_{-4.0}^{+4.2} \pm 4.5) \cdot 10^{-5}$ ,  $(5.7_{-1.5}^{+1.7} \pm 0.9) \cdot 10^{-5}$  and  $(6.9_{-2.2}^{+2.5} \pm 1.1) \cdot 10^{-5}$  measured by BES [421] for  $\chi_{c0}$ ,  $\chi_{c1}$  and  $\chi_{c2}$  respectively.

process	theory	experiment
$\mathcal{B}(\chi_{c0} \rightarrow p\bar{p})$	–	$22.4 \pm 2.7$
$\mathcal{B}(\chi_{c1} \rightarrow p\bar{p})$	$6.4$ [395]	$7.2 \pm 1.3$
$\mathcal{B}(\chi_{c2} \rightarrow p\bar{p})$	$7.7$ [395]	$6.8 \pm 0.7$
$\mathcal{B}(\chi_{c0} \rightarrow \Lambda\bar{\Lambda})$	–	$47 \pm 16$
$\mathcal{B}(\chi_{c1} \rightarrow \Lambda\bar{\Lambda})$	$3.8$ [395]	$26 \pm 12$
$\mathcal{B}(\chi_{c2} \rightarrow \Lambda\bar{\Lambda})$	$3.5$ [395]	$34 \pm 17$

The present analyses of baryonic  $\chi_{cJ}$  decays suffer from the rough treatment of the colour-octet charmonium wave function. As mentioned above, a reanalysis of the decays into the  $PP$  and  $B\bar{B}$  channels, as well as an extension to  $VV$  decays is required. Our knowledge of the colour-octet wave function has been improved recently due to the intense analyses of inclusive processes involving charmonia (see Ref. [417]). This new information may be used to ameliorate the analysis of the  $\chi_{cJ} \rightarrow PP, B\bar{B}$  decays and, perhaps, to reach a satisfactory quantitative understanding of these processes. We finally remark that the colour-octet contribution not only plays an important role in the  $\chi_{cJ}$  decays into  $PP$  and  $B\bar{B}$  pairs but is potentially important for their two-photon decays as well [418, 419, 420].

The leading-twist-forbidden  $\chi_{c0} \rightarrow B\bar{B}$  decays have sizeable experimental branching ratios; see Table 18.10. As of now, there is no reliable theoretical interpretation for these decays. One phenomenological model argues that the quark-pair creation mechanism makes a large contribution to these helicity violating decays [402]. It is assumed that the  $c\bar{c}$  quarks annihilate into two gluons, and then the two gluons materialize into two quark-antiquark pairs. Due to the quark-gluon coupling, another quark pair is allowed to be created from the QCD vacuum with quantum numbers  $J^{PC} = 0^{++}$ , thereafter the three (anti)quarks hadronize into the outgoing (anti)baryon. It is found that the quark pair

creation mechanism, together with the  $SU(3)_f$  symmetry breaking effect, give calculated branching fractions for  $\chi_{cJ} \rightarrow \Lambda\bar{\Lambda}$  that are comparable with the measured values.

Experimentally, tests for the colour-octet contribution involve comparisons between reliable theoretical width calculations, or other observables, such as helicity amplitudes and angular distributions etc., with measurements. More experiments on charmonium decays to baryon-antibaryon pair will be useful for determining the color-octet wave function.

### $J/\psi$ and $\psi'$

The experimental data for two-body baryonic decays of the  $J/\psi$  and  $\psi'$  are summarized in Table 18.11. Values of  $Q_h$  and  $\kappa_h$ , as defined in Eqns. (18.6.62) and (18.6.63), are also presented. From Table 18.11, we see that for baryonic decays,  $Q_h$  is fairly consistent with the 12% rule, within experimental errors. The scaling factor defined in Eq. (18.6.64), ranges from 3.3 to 4.6, and the corresponding  $\kappa_h$  value is almost a constant around 2. All this indicates that the dynamics of baryonic decays of the  $J/\psi$  and  $\psi'$  are fairly well described by pQCD. This point is further confirmed by the amplitude analyses discussed below.

As discussed in section 18.6.2, two-body octet baryon decays can be parameterized by five quantities:  $A$  (the strong amplitude in the limit of exact  $SU(3)$ ),  $D, F$  (the symmetric and antisymmetric charge-breaking amplitudes), and  $D', F'$  (the symmetric and antisymmetric mass-breaking amplitudes). Specific expressions for the different decay modes are listed in Table 18.7. These five amplitudes could, in principle, be complex, each with a magnitude and a phase, giving a total of ten parameters, which are too many for the nine baryonic decay modes. Thus, we adopt the following assumptions to make our fit practical:

1. The isospin-violating decay  $J/\psi \rightarrow \Sigma^0\bar{\Lambda} + \bar{\Sigma}^0\Lambda$  is proportional to  $D$ . As indicated in Table 18.11, the branching fraction for this channel is at least one order-of-magnitude smaller than the others. Accordingly, we set  $D = 0$ .<sup>11</sup>
2. There are no relative phases between the amplitudes  $A, D',$  and  $F'$ .

In the context of these assumptions, the parameterization forms are given in Table 18.12, where  $A, D, F, D'$ , and  $F'$  are now real numbers. In addition, another point should be noted. The parameterization forms in Table 18.7 and 18.12 do not include phase space effects. This could be corrected for by the use of so-called “reduced” branching fractions, defined as

$$\tilde{\mathcal{B}} = \mathcal{B}/PSF_2 ,$$

where  $PSF_2$  is the phase space factor for two-body decay. These are tabulated in Table 18.12. With this information and the corresponding parameterization forms, we do the fit and present the results in the Table 18.13.

From Table 18.13, we notice the following points

- The absolute values of  $D', F',$  and  $F$  are much smaller than that for  $A$ , which means the  $SU(3)$ -breaking effects, both charge-breaking ( $D, F$ ) and mass-breaking

---

<sup>11</sup>As a result, it is important to measure the  $\Sigma^0\bar{\Lambda} + \bar{\Sigma}^0\Lambda$  final state; even a determination of an upper limit would be very useful for phenomenological or theoretical analysis.

Table 18.11: Experimental data [408] on two-body baryonic decays of the  $J/\psi$  and  $\psi'$ . The  $Q_h$  and  $\kappa_h$  defined in Eq. (18.6.62) and (18.6.63) respectively, are also listed. The upper limits are given at 90% C.L.

Mode	$\mathcal{B}_{J/\psi \rightarrow B\bar{B}}$ ( $10^{-3}$ )	$\mathcal{B}_{\psi' \rightarrow B\bar{B}}$ ( $10^{-4}$ )	$Q_h$ (%)	$\kappa_h$ (%)
$p\bar{p}$	$2.17 \pm 0.08$	$2.65 \pm 0.22$	$12.2 \pm 1.1$	$1.91 \pm 0.09$
$n\bar{n}$	$2.2 \pm 0.4$	—	—	—
$\Sigma^+ \bar{\Sigma}^-$	—	$2.6 \pm 0.8$	—	—
$\Sigma^0 \bar{\Sigma}^0$	$1.31 \pm 0.10$	$2.1 \pm 0.7$	$16.0 \pm 5.5$	$2.09 \pm 0.36$
$\Sigma^- \bar{\Sigma}^+$	—	—	—	—
$\Xi^0 \bar{\Xi}^0$	—	$2.8 \pm 0.9$	—	—
$\Xi^- \bar{\Xi}^+$	$0.9 \pm 0.2$	$1.5 \pm 0.7$	$16.7 \pm 8.2$	$2.01 \pm 0.52$
$\Lambda \bar{\Lambda}$	$1.54 \pm 0.19$	$2.5 \pm 0.7$	$16.2 \pm 5.0$	$2.14 \pm 0.33$
$\Sigma^0 \bar{\Lambda} + \bar{\Sigma}^0 \Lambda$	$< 0.15$	—	—	—
$\Delta(1232)^{++} \bar{\Delta}(1232)^{--}$	$1.10 \pm 0.29$	$1.28 \pm 0.35$	$11.6 \pm 4.5$	$1.76 \pm 0.34$
$\Delta(1232)^+ \bar{p}$	$< 0.1$	—	—	—
$\Sigma(1385)^- \bar{\Sigma}(1385)^+ \text{ (or c.c.)}$	$1.03 \pm 0.13$	$1.1 \pm 0.4$	$10.7 \pm 4.2$	$1.53 \pm 0.30$
$\Sigma(1385)^- \bar{\Sigma}^+ \text{ (or c.c.)}$	$0.31 \pm 0.05$	—	—	—
$\Sigma(1385)^0 \bar{\Lambda}$	$< 0.2$	—	—	—
$\Xi(1530)^0 \bar{\Xi}(1530)^0$	—	$< 0.81$	—	—
$\Xi(1530)^0 \bar{\Xi}^0$	$0.32 \pm 0.14$	—	—	—
$\Xi(1530)^- \bar{\Xi}^+$	$0.59 \pm 0.15$	—	—	—
$\Omega^- \bar{\Omega}^+$		$< 0.73$		

Table 18.12: Reduced branching ratios  $\tilde{\mathcal{B}}$  for two-body octet baryonic final states compared with the parameterization of the squared amplitude described in the text. The numbers in the parentheses are the calculated results with the fitted parameters given in Table 18.13 for  $\phi = -90^\circ$ .

Final state	Parameterization	$\tilde{\mathcal{B}}_{J/\psi}$	$\tilde{\mathcal{B}}_{\psi'}(10^{-1})$
$p\bar{p}$	$ A + e^{i\phi}(D + F) - D' + F' ^2$	$1.29 \pm 0.05(1.30)$	$1.46 \pm 0.13(1.47)$
$n\bar{n}$	$ A - e^{i\phi}(2D) - D' + F' ^2$	$1.31 \pm 0.24(1.31)$	— (1.11)
$\Sigma^+ \bar{\Sigma}^-$	$ A + e^{i\phi}(D + F) + 2D' ^2$	— (0.96)	$1.61 \pm 0.50(1.62)$
$\Sigma^0 \bar{\Sigma}^0$	$ A + e^{i\phi}(D) + 2D' ^2$	$0.97 \pm 0.07(0.97)$	$1.31 \pm 0.46(1.25)$
$\Sigma^- \bar{\Sigma}^+$	$ A + e^{i\phi}(D - F) + 2D' ^2$	— (0.99)	— (1.04)
$\Xi^0 \bar{\Xi}^0$	$ A - e^{i\phi}(2D) - D' - F' ^2$	— (0.79)	$1.89 \pm 0.61(1.58)$
$\Xi^- \bar{\Xi}^+$	$ A + e^{i\phi}(D - F) - D' - F' ^2$	$0.82 \pm 0.18(0.81)$	$1.02 \pm 0.48(1.34)$
$\Lambda \bar{\Lambda}$	$ A - e^{i\phi}(D) - 2D' ^2$	$1.05 \pm 0.13(1.06)$	$1.49 \pm 0.42(1.36)$
$\Sigma^0 \bar{\Lambda} + \bar{\Sigma}^0 \Lambda$	$ \sqrt{3}D ^2$	— (0.00)	— (0.00)

Table 18.13: Fit results for two-body baryonic decay. The parameterization forms and data are given in Table 18.12. The  $\star$  indicates the phase value is fixed in the fit.

Paramter	$J/\psi$ decay		$\psi'$ decay	
$A$	$1.008 \pm 0.029$	$1.008 \pm 0.029$	$1.132 \pm 0.096$	$1.143 \pm 0.105$
$D'$	$-0.010 \pm 0.016$	$-0.010 \pm 0.016$	$-0.023 \pm 0.053$	$-0.013 \pm 0.051$
$F'$	$0.127 \pm 0.110$	$0.127 \pm 0.114$	$-0.167 \pm 0.181$	$-0.103 \pm 0.157$
$F$	$0.008 \pm 0.107$	$0.020 \pm 0.249$	$-0.221 \pm 0.207$	$-0.290 \pm 0.316$
$\phi$	$-91.12 \pm 3.675$	$-90 \star$	$-91.11 \pm 2.505$	$-90 \star$
$\chi^2$	$4.3^{-3}$	$4.0^{-3}$	0.4	0.4

$(D', F')$ , are weak for  $J/\psi$  and  $\psi'$  baryonic decays. In addition, the antisymmetric breaking term is about one order of magnitude stronger than the symmetric term.

- The phase between the strong and electromagnetic amplitudes is almost  $-90^\circ$  from the free parameter fit for both the  $J/\psi$  and  $\psi'$  decays. This large phase is consistent with a previous analysis [422], and also consistent with results from the analyses for two-body mesonic decays, such  $1^+0^- (90^\circ)$  [423],  $1^-0^- (106 \pm 10)^\circ$  [424, 425],  $1^-1^- (138 \pm 37)^\circ$  [404, 425, 426],  $0^-0^- (89.6 \pm 9.9)^\circ$  [404, 425, 426] and so on. Moreover, the fit results also support the idea of a universal phase proposed in Ref. [427].
- Electromagnetic-breaking (due to value  $F$ ) is much stronger for the  $\psi'$  than for the  $J/\psi$ . This phenomenon has been noticed in an analysis of  $\psi' \rightarrow K^*(892)\bar{K} + c.c.$  decays [428].

Using the fit parameters, the reduced branching fractions are calculated and results are given in Table 18.12. Since there are many parameters to adjust, the calculated branching fractions agree with experiment fairly well, as might be expected. Moreover, some branching fractions that have not be measured are also calculated to provide predictions for further experimental work.

Table 18.14: Comparison between theoretical evaluation [396] and experimental data [408] (or refer to Table 18.11). Here the branching fractions are transformed into decay widths by using  $\Gamma_{J/\psi} = (93.4 \pm 2.1)$  keV [408].  $\mathcal{R} \equiv \Gamma_{B\bar{B}}/\Gamma_{p\bar{p}}$ .

Mode	$\Gamma_{the.}$ (eV)		$\Gamma_{exp.}$ (eV)	$\mathcal{R}_{the.}$	$\mathcal{R}_{exp.}$
	$m_s = 150$ MeV	$m_s = 350$ MeV			
$p\bar{p}$	174	174	$203 \pm 9$	1	1
$\Sigma^0\bar{\Sigma}^0$	128	113	$122 \pm 10$	0.649	$0.604 \pm 0.052$
$\Lambda\bar{\Lambda}$	133	117	$144 \pm 19$	0.672	$0.710 \pm 0.092$
$\Xi^-\bar{\Xi}^+$	92.8	62.5	$84 \pm 19$	0.359	$0.415 \pm 0.094$
$\Delta^{++}\bar{\Delta}^{--}$		105	$103 \pm 28$	0.603	$0.507 \pm 0.135$
$\Sigma^{*-}\bar{\Sigma}^{*+}$		66.1	$96 \pm 13$	0.380	$0.475 \pm 0.065$

Now we turn to another aspect of comparison between theoretical predictions and experimental measurements. As mentioned in section 18.6.2, the decay width of the  $J/\psi$  (or  $\psi'$ ) can be calculated with information about hadronic distribution amplitudes. In Ref. [396], a modified perturbative approach is adopted, where quark transverse momenta are retained and Sudakov suppressions, comprising those gluonic radiative corrections not included in the evolution of the distribution amplitude, are taken into account. The advantage of this modified perturbative approach is the strong suppression of the soft end-point regions where the pQCD can not be applied.

An evaluation of  $J/\psi \rightarrow B\bar{B}$  via the hard process  $c\bar{c} \rightarrow 3g^* \rightarrow 3(q\bar{q})$  is described in Ref. [396] and listed in Table 18.14. The theoretical values are in good agreement with the measured values within errors.<sup>12</sup> Predictions for the absolute value of a decay width are subject to many uncertainties [396] while the ratios of any two  $B\bar{B}$  decay widths are robust since many uncertainties cancel to a large extent. For this reason the ratios of branching fractions (normalized to the  $p\bar{p}$  final state) are also presented in Table 18.14. Although good agreement can be seen for both absolute decay widths and relative ratios, there still exist a 10% to 20% difference between the theoretical and experimental values. Here the results from the amplitude analysis should be noted, particularly electromagnetic breaking effects which are at the level of 10% to 20%. Moreover, the relative phase between the strong and electromagnetic interaction is around  $-90^\circ$  and is a crucial piece of information for the improvement of the calculation in Ref. [396].

Table 18.15: Angular distribution parameter  $\alpha$  for  $J/\psi \rightarrow B\bar{B}$  decays. They are assumed to be the form of  $dN/d\cos\theta \propto 1 + \alpha \cos^2\theta$ .

Decay mode	Measured value of $\alpha$	Calculated value of $\alpha$	
		Ref. [390]	Ref. [429]
$J/\psi \rightarrow p\bar{p}$	$0.68 \pm 0.06$ [430]	1	0.69
$J/\psi \rightarrow \Lambda\bar{\Lambda}$	$0.65 \pm 0.11$ [431]	1	0.51
$J/\psi \rightarrow \Sigma\bar{\Sigma}$	$-0.24 \pm 0.20$ [431]	1	0.43
$J/\psi \rightarrow \Xi^-\bar{\Xi}^+$	$-0.13 \pm 0.59$ [432]	1	0.27
$\psi' \rightarrow p\bar{p}$	$0.67 \pm 0.16$ [433]	1	0.80

Last, but not least, are measurements of the angular distributions for the processes  $e^+e^- \rightarrow (J/\psi \text{ or } \psi') \rightarrow B_8\bar{B}_8$ . This has the form :

$$\frac{d\Gamma}{d\cos\theta} \propto 1 + \alpha \cos^2\theta, \quad (18.6.65)$$

where  $\theta$  is the angle between the out-going baryon and the  $e^+e^-$  beam. Table 18.15 summarizes the measured angular distribution parameters and provides comparisons with theoretical predictions. In the limit of the helicity conservation,  $\alpha = +1$ . This is prominently violated for the  $J/\psi \rightarrow \Sigma\bar{\Sigma}$  and  $\Xi^-\bar{\Xi}^+$  modes, where not only the magnitude is smaller than expected, but also the sign contradicts the prediction. This violation has been attributed to a constituent quark [429, 434] and/or hadron mass effect [435] or final

<sup>12</sup>In Ref. [396], the decay widths for  $\psi' \rightarrow B\bar{B}$  are also presented, which are actually scaled results assuming the 12% rule. Thus, the consistency between theoretical evaluations and experimental measurements for  $\psi'$  decay depends only on those of the  $J/\psi$  and the validity of 12% rule.

state interactions [436], both of these effects are part of the  $\mathcal{O}(v^2)$  and high-twist/power corrections. Also electromagnetic effects on the value of  $\alpha$  have been investigated.

### $\psi''$ and other higher charmonium states

Charmless decays of the  $\psi''$  can shed light on  $S$ - $D$  mixing, missing  $\psi'$  decays such as  $\psi' \rightarrow \rho\pi$ , the discrepancy between the total and  $D\bar{D}$  cross section at the  $\psi''$ , and rescattering effects contributing to an enhanced  $b \rightarrow s$  penguin amplitude in  $B$  meson decays [437]. A phenomenological analysis [438] also indicates the possibility of a large charmless branching fraction for the  $\psi''$ . Stimulated by theoretical suggestions and based on observations with data samples of  $55.8 \text{ pb}^{-1}$  on the peak of the  $\psi''$  and  $20.70 \text{ pb}^{-1}$  at the continuum ( $\sqrt{s}=3.67 \text{ GeV}$ ) (which is used for background subtraction), CLEOc reported results of searches for a wide variety of non- $D\bar{D}$  modes [439], among which the results involving baryonic pairs are reproduced in Table 18.16. However, no signals are reported and only the upper limits are given, which indicates that the charmless fraction is rather small. This seems also consistent with CLEOc's inclusive results [440].

Table 18.16: Experiment results for exclusive baryonic decays of the  $\psi''$  [439]. Listed are cross section upper limits that include systematic errors (90% C.L.), and the branching ratio upper limit (90% C.L.).

mode	$\sigma$ U.L. (pb)	$\mathcal{B}$ U.L. ( $10^{-4}$ )
$p\bar{p}\pi^+\pi^-$	4.5	5.8
$p\bar{p}\pi^+\pi^-\pi^0$	14.4	18.5
$\eta p\bar{p}$	4.2	5.4
$\omega p\bar{p}$	2.2	2.9
$p\bar{p}K^+K^-$	2.5	3.2
$\phi p\bar{p}$	1.1	1.3
$\Lambda\bar{\Lambda}$	1.0	1.2
$\Lambda\bar{\Lambda}\pi^+\pi^-$	2.0	2.5
$\Lambda\bar{p}K^+$	2.2	2.8
$\Lambda\bar{p}K^+\pi^+\pi^-$	4.9	6.3

Since the masses of higher charmonium states (i.e. the  $\psi$ -family members with mass above  $\psi''$ ) are above the threshold for open charm production, the  $B\bar{B}$  branching fractions are likely to be very small and it is unlikely that they will be measured. Therefore, up to now, no attempts have been made nor have reports been forthcoming for higher charmonium state decays into baryon-pair-containing final states.<sup>13</sup>

### 18.6.4 Three body decays

Compared with two-body decays, the theoretical analysis relevant to three-body decays is more difficult and only special final states have been discussed phenomenologically [441].

<sup>13</sup>The only exception is for  $Y(4260)$ , the upper limit at 90% C.L. is reported:  $\mathcal{B}(Y \rightarrow p\bar{p})/\mathcal{B}(Y \rightarrow \pi^+\pi^-J/\psi) < 13\%$ .

Recently, theoretical interest in baryon-containing final states has been revived thanks to recent experimental discoveries, especially the phenomena of baryon-antibaryon invariant mass enhancements near thresholds.

### Baryon-antibaryon enhancements

In charmonium decays, the BESII collaboration observed  $p\bar{p}$  and  $p\bar{\Lambda}$  enhancements in  $J/\psi \rightarrow \gamma p\bar{p}$  [442],  $\psi' \rightarrow \pi^0 p\bar{p}$ ,  $\eta p\bar{p}$  [443], and  $J/\psi \rightarrow p\bar{\Lambda}K^- + c.c.$  [444], as well as in  $\psi' \rightarrow p\bar{\Lambda}K^- + c.c.$  decays [444]. In  $B$  decays, many baryon-antibaryon-pair-containing final states have been measured by the CLEO, Belle, and BABAR collaborations, such as  $B^\pm \rightarrow p\bar{p}K^\pm$  [445],  $B^0 \rightarrow p\bar{\Lambda}\pi^-$  [446],  $B^+ \rightarrow \Lambda\bar{\Lambda}K^+$  [447],  $B^0 \rightarrow D^{*-}p\bar{n}$  [448],  $\bar{B}^0 \rightarrow D^{*0}p\bar{p}$ ,  $D^0p\bar{p}$  [449],  $B^+ \rightarrow p\bar{p}\pi^+$ ,  $p\bar{p}K^{*+}$ ,  $B^0 \rightarrow p\bar{p}K^0$  [450],  $B^0 \rightarrow \bar{D}^{*0}p\bar{p}$ ,  $\bar{D}^0p\bar{p}$  [451], and so on, with enhancements observed in  $p\bar{p}$ ,  $p\bar{\Lambda}$ , and  $\Lambda\bar{\Lambda}$  mass spectra. Other than the enhancement in  $J/\psi \rightarrow \gamma p\bar{p}$ , which is claimed to be very narrow and below the  $p\bar{p}$  mass threshold, all the other enhancements are slightly above the baryon antibaryon mass threshold and have widths that range from a few tens of  $\text{MeV}/c^2$  to less than  $200 \text{ MeV}/c^2$ .

To interpret these various enhancements in a uniform framework, Yuan, Mo and Wang (YMW), motivated by the Fermi-Yang-Sakata (FYS) model [452, 453], suggested a nonet scheme to accommodate the baryon-antibaryon enhancements observed in charmonium and  $B$  decays [454]. In the YMW approach, the baryon and antibaryon are presumed to be bound together by residual forces that originate from the strong interaction between the quarks and gluons inside the baryon or antibaryon. On one hand, the masses of the three-quark systems (the baryon and the antibaryon) increase by a small amount due to the residual forces required to form the bound state; on the other hand, the binding energy between the two three-quark systems reduces the mass of the baryon-antibaryon system to lower than the sum of the masses of the three-quark systems, but very close to the baryon-antibaryon mass threshold. This supplies a phenomenological surmise, based on which the further analysis suggests many experimental consequences.

First, because of the large phase space,  $B$ -meson decays play important roles in the study of the baryon-antibaryon resonances. A detailed discussion can be found in Ref. [454].

Second, charmonium provides another domain to study baryon-antibaryon states. Unlike  $B$  decays, conservation laws limit the possible decay modes. Some possible modes are listed in Table 18.17. The production of a  $0^-$  baryon-antibaryon bound states in  $J/\psi$  (or  $\psi'$ ) decays can be accompanied by a vector meson. For the iso-vector bound states, one may look at  $\rho N\bar{N}$  (nucleon antinucleon) final states, including  $\rho^+ n\bar{p}$ ,  $\rho^0 p\bar{p}$  and  $\rho^- p\bar{n}$ ; for the iso-scalar bound state, one may look at the  $\omega p\bar{p}$  final state; while for the strange states, one may look at  $K^{*+}\Lambda\bar{p} + c.c.$  and  $K^{*0}\Lambda\bar{n} + c.c.$  final states. The neutron or anti-neutron, which is not detected, may be reconstructed by a kinematic fit to the rest of the tracks in the event. An  $SU(3)$  singlet state can be searched for in the  $\phi\Lambda\bar{\Lambda}$  final state. The measurement of the  $0^-$  baryon-antibaryon bound states produced together with an axial-vector meson is less promising since almost all of the axial-vector mesons are resonances.

The production of  $1^-$  baryon-antibaryon bound states can be accompanied by a pseudoscalar ( $\pi$ ,  $\eta$ ,  $\eta'$ ,  $K$ ), scalar, tensor or axial-vector meson. The most promising way to look for them is in the decays with a pseudoscalar meson: *i.e.* analyze  $\pi N\bar{N}$  for the

Table 18.17: Decay modes containing baryon-antibaryon nonets in charmonium decays. The first  $J^P$  is for the accompanying particle while the second for the baryon-antibaryon resonance.

	decay mode	Note
$1^- \& 0^-$	$\rho^0(p\bar{p})$ , $\rho^+(n\bar{p})$ , $\rho^-(p\bar{n})$ $K^{*+}(\bar{p}\Lambda)$ , $K^{*-}(p\bar{\Lambda})$ $K^{*0}(\bar{n}\Lambda)$ , $\bar{K}^{*0}(n\bar{\Lambda})$ $\omega(p\bar{p})$ $\phi(\Lambda\bar{\Lambda})$	*
$1^+ \& 0^-$	$b_1^0(1235)(p\bar{p})$ $b_1^+(1235)(n\bar{p})$ , $b_1^-(1235)(p\bar{n})$ $h_1(1170)(p\bar{p})$ , $h_1(1170)(\Lambda\bar{\Lambda})$ $K_1^+(1270)(\bar{p}\Lambda)$ , $K_1^-(1270)(p\bar{\Lambda})$ $K_1^0(1270)(\bar{n}\Lambda)$ , $\bar{K}_1^0(1270)(n\bar{\Lambda})$ $K_1^+(1400)(\bar{p}\Lambda)$ , $K_1^-(1400)(p\bar{\Lambda})$ $K_1^0(1400)(\bar{n}\Lambda)$ , $\bar{K}_1^0(1400)(n\bar{\Lambda})$	*
$0^- \& 1^-$	$\pi^0(p\bar{p})$ , $\pi^+(n\bar{p})$ , $\pi^-(p\bar{n})$ $K^+(\bar{p}\Lambda)$ , $K^0(\bar{n}\Lambda)$ $K^-(p\bar{\Lambda})$ , $\bar{K}^0(n\bar{\Lambda})$ $\eta(p\bar{p})$ , $\eta(\Lambda\bar{\Lambda})$ $\eta'(p\bar{p})$ , $\eta'(\Lambda\bar{\Lambda})$	*
$0^+ \& 1^-$	$a_0^0(980)(p\bar{p})$ $a_0^+(980)(n\bar{p})$ , $a_0^-(980)(p\bar{n})$ $a_0^0(1450)(p\bar{p})$ $a_0^+(1450)(n\bar{p})$ , $a_0^-(1450)(p\bar{n})$ $f_0(980)(p\bar{p})$ , $f_0(980)(\Lambda\bar{\Lambda})$ $f_0(1370)(p\bar{p})$ , $f_0(1370)(\Lambda\bar{\Lambda})$ $K_0^{*+}(1430)(\bar{p}\Lambda)$ , $K_0^{*-}(1430)(p\bar{\Lambda})$ $K_0^{*0}(1430)(\bar{n}\Lambda)$ , $\bar{K}_0^{*0}(1430)(n\bar{\Lambda})$	*
$1^+ \& 1^-$	$a_1^0(1260)(p\bar{p})$ $a_1^+(1260)(n\bar{p})$ , $a_1^-(1260)(p\bar{n})$ $f_1(1285)(p\bar{p})$ , $f_1(1420)(\Lambda\bar{\Lambda})$ $K_1^+(1270)(\bar{p}\Lambda)$ , $K_1^-(1270)(p\bar{\Lambda})$ $K_1^0(1270)(\bar{n}\Lambda)$ , $\bar{K}_1^0(1270)(n\bar{\Lambda})$ $K_1^+(1400)(\bar{p}\Lambda)$ , $K_1^-(1400)(p\bar{\Lambda})$ $K_1^0(1400)(\bar{n}\Lambda)$ , $\bar{K}_1^0(1400)(n\bar{\Lambda})$	*
$2^+ \& 1^-$	$a_2^0(1320)(p\bar{p})$ $a_2^+(1320)(n\bar{p})$ , $a_2^-(1320)(p\bar{n})$ $f_2(1270)(p\bar{p})$ $K_2^{*+}(1430)(\bar{p}\Lambda)$ , $K_2^{*-}(1430)(p\bar{\Lambda})$ $K_2^{*0}(1430)(\bar{n}\Lambda)$ , $\bar{K}_2^{*0}(1430)(n\bar{\Lambda})$	*

\*: not allowed in  $J/\psi$  decays.

iso-vector bound states;  $\eta p\bar{p}$  for iso-scalar bound state;  $K^+\Lambda\bar{p} + c.c.$  and  $K^0\Lambda\bar{n} + c.c.$  for the strange bound states. An  $SU(3)$  singlet bound state can be searched for in the  $\eta'\Lambda\bar{\Lambda}$  channel.

It should be noted that neutral non-strange  $0^-$  baryon-antibaryon bound states can also be produced via radiative decays of the  $J/\psi$  (or  $\psi'$ );  $1^-$  baryon-antibaryon bound states can not be produced this way because of spin-parity conservation.

Although among various charmonium decays, the  $J/\psi$  provides a good source of the baryon-antibaryon bound states because of the large data samples, it has some disadvantages: the phase space is small and there are many  $N^*$ 's near the nucleon-meson mass threshold, and these affect the identification of the states [455].  $\psi'$  decays have larger phase space, however the data samples are smaller, and there is a large fraction of charmonium transitions. CLEOc and *BES-III* will study these decays with higher statistics, and partial wave analyses will be required to account for the  $N^*$  contributions correctly.

At last, it is worthwile to mention that another meticulous and mathematical study of baryon-antibaryon enhancements is described in Ref. [456], where the group theory technique employed in the Jaffe's studies on the  $q^2\bar{q}^2$  system [457] is extended to the  $q^3\bar{q}^3$  system.

## Experiment results

Some experimental results on three body decays involving baryon and antibaryon pairs are summarized in Table 18.18. In fact, the available results for three body baryonic decay are at present rather limited. For  $J/\psi$  decays, all quoted results are experimental measurements before 1990; for  $\psi'$  decays, the results are mainly due to BES [458, 459] and CLEOc [460]; for  $\psi''$  and  $\chi_{cJ}$  decays, the results are solely from CLEOc [461]. As to the energy region above the  $\psi''$ , results are still unavailable as mentioned above in section 18.6.3.

However, even with these limited results, we can see some interesting phenomena. One interesting fact, as pointed out in Ref. [458], is that for the  $\pi^0 p\bar{p}$  final state,  $Q_{\pi^0 p\bar{p}} = 12.2 \pm 1.9$ , in agreement with the 12% rule. In contrast, for the  $\eta p\bar{p}$  final state,  $Q_{\eta p\bar{p}} = 2.8 \pm 0.6$ , which seems to be suppressed significantly. Another suppression seems in effect for the  $\omega p\bar{p}$  final state, while for  $K^+\bar{p}\Lambda$  final state, there is no suppression. Here more accurate data are needed for further study.

### 18.6.5 Multi-body and Semi-inclusive decay

#### Multi-body decay

By multi-body decays, we mean charmonium decays into a state with at least four particles, including one pair of baryons. Since baryon pair masses are around  $2 \text{ GeV}/c^2$  or larger, the number of allowed decay modes is not large, especially for the low lying charmonium states like the  $\eta_c$  and  $J/\psi$ . Since the kaon mass is around  $0.5 \text{ GeV}/c^2$ , modes with kaons are further suppressed.

So far, only the  $\pi^+\pi^- p\bar{p}$  mode has been measured in the decays of most of the charmonium states below open charm threshold, with observations for  $J/\psi$ ,  $\psi'$ , and  $\chi_{cJ}$  decay;  $\pi^+\pi^-\pi^0 p\bar{p}$  is observed in  $J/\psi$  and  $\psi'$  decays; while  $J/\psi \rightarrow \pi^+\pi^- N\bar{N}$  was measured with 100% uncertainty.

Table 18.18: Branching ratios for three-body decays involving baryons for charmonium states. Most results are from PDG06 [408], except for  $\chi_{cJ}$  decays, which are from CLEOc [461]. The upper limits are given at 90% C.L. and  $Q_h = \mathcal{B}_{\psi' \rightarrow h} / \mathcal{B}_{J/\psi \rightarrow h}$  is also given for possible final states. The numbers in parentheses are the “reduced” branching fractions, defined as  $\tilde{\mathcal{B}} = \mathcal{B} / PSF_3$ , where  $PSF_3$  is the phase space factor for the three-body decay. The units of  $PSF_3$  are  $10^1$  and  $10^{-1}$  for the  $J/\psi$  and  $\psi'$  decays respectively.

Final State	$J/\psi$ ( $10^{-4}$ )	$\psi'$ ( $10^{-5}$ )	$Q_h$ (%)	$\chi_{cJ}$ ( $J = 0, 1, 2$ ) ( $10^{-3}$ )
$\pi^0 p\bar{p}$	$10.9 \pm 0.9(1.84)$	$13.3 \pm 1.7(6.83)$	$12.2 \pm 1.9$	$0.59 \pm 0.13$
				$0.12 \pm 0.06$
				$0.44 \pm 0.10$
$\pi^- p\bar{n}$	$20.0 \pm 1.0(3.40)$			
$\eta pp$	$20.9 \pm 1.0(7.23)$	$6.0 \pm 1.2(4.48)$	$2.8 \pm 0.6$	$0.39 \pm 0.12$
				$< 0.16$
				$0.19 \pm 0.08$
$\rho^0 p\bar{p}$	$< 3.7$	$5.0 \pm 2.2(5.24)$	$> 5.9$	
$\omega p\bar{p}$	$13.0 \pm 2.5(9.91)$	$6.9 \pm 2.1(7.31)$	$5.3 \pm 1.9$	
$\phi p\bar{p}$	$4.5 \pm 1.5(15.6)$	$< 2.4$	$< 9.3$	
$\pi^0 \Lambda\bar{\Lambda}$	$2.2 \pm 0.6(0.84)$			
$K^+ \bar{p}\Lambda$	$8.9 \pm 1.6(4.65)$	$10.0 \pm 1.4(9.18)$	$11.2 \pm 2.5$	$1.07 \pm 0.21$
				$0.33 \pm 0.10$
				$0.85 \pm 0.18$
$K^- p\bar{\Sigma}^0$	$2.9 \pm 0.8(2.05)$			
$K^- p\bar{\Sigma}(1385)^0$	$5.1 \pm 3.2(10.2)$			
$\pi^- \bar{p}\Delta^{++}(1231)$	$1.6 \pm 0.5(0.52)$			
$\eta'(958)p\bar{p}$	$9 \pm 4 (18.4)$			

For final states with strangeness,  $\pi^+ \pi^- \Lambda\bar{\Lambda}$  has only been observed in  $\psi'$  decays. Although it has been searched for in  $\chi_{cJ}$  decays, no signal has been seen. An observed five-body decay is  $\psi' \rightarrow \bar{p}K^+ \Lambda\pi^+ \pi^-$ .  $K_S^0 K_S^0 p\bar{p}$  has been searched for in  $\chi_{cJ}$  and  $\psi'$  decays, but with no signal. As a byproduct of a search for the penta-quark state candidate ( $\Theta(1540)$ ), upper limits for  $J/\psi$  and  $\psi' \rightarrow K_S^0 p K^- \bar{n}$  branching fractions have been determined.

Generally speaking, except for the fact that the selection efficiency will not be high because of the high multiplicity and low track momentum, the identification of final states with four or more final particles including a baryon pair is quite easy and the purity is relatively high. This makes it possible to study the interaction between baryon and mesons, such as  $N\pi\pi$ ,  $N\pi\pi\pi$ ,  $NK$ ,  $NK\pi$ ,  $N\rho$ ,  $N\omega$ , those with the nucleon replaced by a  $\Lambda$  etc. However, as these excited Baryon states are generally broad, and the mass difference between states is small, the successful identifications of the states or the decay mode require partial wave analyses, as has been performed for  $J/\psi \rightarrow p\bar{n}\pi^- + c.c.$  As one can imagine, when there are more final states particles, the PWA will be correspondingly more difficult, more model-dependent, and, sometimes, more unreliable [462].

## Semi-inclusive decays

### 1. Semi-inclusive $\eta_c$ and $\eta'_c$ decays

In an earlier study of  $\eta_c$  and  $\eta'_c$  hadronic decays, Lee, Quigg, and Rosner advanced [463] a statistical model appropriate to particle decay according to which the mean multiplicity of decay products is

$$\begin{aligned}\langle n \rangle &= n_0 + \left(\frac{4}{\pi}\right)^{1/4} \frac{\zeta(3)}{[3\zeta(4)]^{3/4}} \left(\frac{E}{E_0}\right)^{3/4} \\ &= n_0 + 0.528(E/E_0)^{3/4}.\end{aligned}\quad (18.6.66)$$

Here  $\zeta(x) \equiv \sum_{i=1}^{\infty} 1/i^x$ , is the Riemann Zeta function and  $E$  is the energy available in excess of the rest mass of the lowest-multiplicity ( $n_0$ ) decay channel. For the decay like  $\eta_c \rightarrow N\bar{N} + (m \text{ pions})^0$ ,  $E = (M_{\eta_c} - M_N - M_{\bar{N}})c^2$  and  $n_0 = 2$ . The scale  $E_0$  is given by the hadronic radius  $R_0$ :

$$E_0 \equiv \hbar c/R_0. \quad (18.6.67)$$

For a radius of 1 fm (typical for bag models of hadrons [464]),  $E_0 \simeq 0.2$  GeV. As for the  $\eta_c$  and  $\eta'_c$  decay calculation, the value  $E_0 \simeq 0.17$  GeV is suggested in Ref. [465]. A Poisson distribution is assumed for the variable ( $\langle n \rangle - n_0$ ) with neutral decay particles incorporated by means of statistical isospin weights. The calculated results for  $\eta_c, \eta'_c \rightarrow N\bar{N} + (m \text{ pions})$  can be found in Ref. [465, 466], where it is noted that the  $p\bar{p}$  mode accounts for about 5% of all decays  $\eta_c \rightarrow N\bar{N} + \text{ pions}$ . In the statistical model [465], the semi-inclusive rates as fractions of the total baryonic decay rate of  $\eta_c$  are estimated to be

$\Gamma(N\bar{N} + \text{ pions})$	44%
$\Gamma(\Lambda\bar{\Lambda} + \text{ pions})$	7%
$\Gamma(\Lambda\bar{\Sigma} \text{ or } \bar{\Lambda}\Sigma + \text{ pions})$	24%
$\Gamma(\Sigma\bar{\Sigma} + \text{ pions})$	20%
$\Gamma(\Xi\bar{\Xi} + \text{ pions})$	6%.

On this basis, the  $p\bar{p}$  mode is approximately 2% of all the baryonic decays. For  $J/\psi$ , the  $p\bar{p}$  mode makes up about 0.2% of the direct hadronic decays [408]. This suggests that the semi-inclusive baryonic decays of  $\eta_c$  makes up about 10% of its hadronic width.

### 2. The Lund model and general inclusive decays

JETSET and PYTHIA are well-known Monte Carlo packages used for simulating inclusive (multihadron) final states at fairly high energies (*i.e.* around or above the  $Z_0$  mass). The generation of inclusive final states in JETSET or PYTHIA is based on the famous Lund model [467], which adopts and synthesizes many physics models, such as the massless relativistic string model, the dipole cascade model, the linked dipole chain model, the Feynman parton model, the string fragmentation model, etc. The simulated results work fairly well at high energies.

Recently, by virtue of the basic Lund-model “area law,” a theoretical formalism has been developed for simulation of inclusive hadronic final state at comparatively low

energies, including the charmonium region [468]. This formalism has been used to generate hadronic final state for  $R$ -value measurement studies and the simulated results agree fairly well with data [469].

We will not go into further discussion about the Lund model, the area law, and the details involving Monte Carlo simulation here. It is only necessary to note that the Lund model is a fairly sucessful model for the generation of general inclusive decays. Moreover, it provides an intuitive, visualized and calculable decay model for hadronization processes and, in fact, provides us with many ideas for dynamics exploration. However, studies of inclusive final states in the charmonium region are still rather limited, due to a dearth of data; much is left to be done with *BES-III*.

### 18.6.6 Summary and discussion

Herein we have collected and summarized some theoretical ideas concerning the charmonium dynamics and some phenomenological models commonly used in high energy physics.

Experimental measurements are used to the extent possible to test these theoretical predictions and provide clues for further advances in understanding charmonium decay dynamics.

From the previous review, we notice that on one hand most of the theoretical explanations are still qualitative and on the other hand the experiment data are rather limited and with fairly large uncertainties. Anyway, with the unprecedently large data samples forthcoming from *BES-III*, we could make systematic experimental investigations of hadronic decays of charmonium, from the  $\eta_c$  to to the  $\psi''$  or even higher, both on resonances and off resonances, for strong interactions and electromagnetic interactions, covering phenomenology and dynamics, and hopefully finding some empirical rules and establishing a universal model, or, even better, come across an unexpected discovery.

## 18.7 $\psi(3770)$ and $\psi(4415)$ decays to $p\bar{p}$ <sup>14</sup>

Another very interesting question that can be addressed using the  $\psi(3770)$  is the strength of the coupling of orbitally excited  $c\bar{c}$  states to  $p\bar{p}$ . This is a very important question for the future PANDA experiment [470] at GSI, which plans to use  $p\bar{p}$  annihilation to produce excited  $c\bar{c}$  and charmonium hybrids. At present we have the intriguing experimental observation that the  $L=1$   $c\bar{c} \chi_J$  states couple much more strongly to  $p\bar{p}$  than the  $L=0$   $J/\psi$ , but whether this trend continues to  $L=2$  is an open question. BES can easily answer this question through a high-statistics search for  $\psi(3770) \rightarrow p\bar{p}$ . Charmonium decays to final states including a  $p\bar{p}$  pair, such as  $\Psi \rightarrow p\bar{p}$  and  $\Psi \rightarrow p\bar{p}m$  (where  $\Psi$  is a generic charmonium or charmonium hybrid resonance and  $m$  is a light meson) are also very interesting in this regard, and can be used to estimate the associated production cross section for  $p\bar{p} \rightarrow m\Psi$  (see Refs.[471, 472]); this reaction in particular will be used by PANDA to search for  $J^{PC}$ -exotic charmonium hybrids.

---

<sup>14</sup>T. Barnes

# Chapter 19

## Rare and forbidden charmonium decays<sup>1</sup>

At present, two general trends can be distinguished in accelerator particle physics. On one hand, very high energy accelerators, for example the LHC, provide the ability to explore physics at high energy frontier. On the other hand, smaller experiments at lower energies but with very high intensities and low backgrounds, for example the  $B$  factories and *BES-III*, provide capabilities for performing precise tests and accurate determinations of many parameters of the Standard Model (SM). Moreover, the close scrutiny of rare processes may illuminate new physics in a complementary fashion to high-energy colliders.

With huge  $J/\psi$  and  $\psi(2S)$  data samples, the *BES-III* experiment will approach a precision level where rare  $\psi$  decays can be used to provide important tests of the Standard Model, with the accompanying possibility for uncovering new-physics induced deviations.

### 19.1 Weak Decays of Charmonium

The low-lying charmonium states, *i.e.* those below the open-charm threshold, usually decay through intermediate photons or gluons produced by the annihilation of the parent  $c\bar{c}$  quark pair. These OZI-violating but flavor-conserving decays result in narrow natural widths of the  $J/\psi$  and  $\psi(2S)$  states. In the SM framework, flavor-changing weak decays of these states are also possible, although they are expected to have rather low branching fractions. The huge  $J/\psi$  data samples at *BES-III* will provide opportunities to search for such rare decay processes, which in some cases may be detectable, even at SM levels. The observation of an anomalous production rate for single charmed mesons in  $J/\psi$  or  $\psi(2S)$  decays at *BES-III* would be a hint of possible new physics, either in underlying continuum processes via flavor-changing-neutral-currents [473] or in the decays of the  $\psi$  resonances due to unexpected effects of quark dynamics [474].

#### 19.1.1 Semileptonic Decays of Charmonium

The inclusive branching fraction for  $J/\psi$  weak decays via a single quark (either the  $c$  or the  $\bar{c}$ ) has been estimated to be  $(2 \sim 4) \times 10^{-8}$  by simply using the  $D^0$  lifetime [475]. Such

---

<sup>1</sup>By Haibo Li, Jianping Ma and Xinmin Zhang

a small branching fraction makes the observation of weak decays of the  $J/\psi$  or  $\psi(2S)$  quite challenging, despite the expected cleanliness of the events. However, BEPC-II, running at design luminosity, will produce of order  $10^{10}$   $J/\psi$  events per year of data taking, leading to  $\cong 400$  weak decays for the predicted SM branching fraction. The semi-leptonic decay of a  $c\bar{c}$  ( $1^{--}$ ) vector charmonium state below the open-charm threshold is induced by the weak quark-level transition  $c \rightarrow qW^*$ , where  $W^*$  is a virtual intermediate boson. Hence, the accessible exclusive semi-leptonic channels are:

$$\psi(nS) \rightarrow D_q l \nu, \quad (19.1.1)$$

$$\psi(nS) \rightarrow D_q^* l \nu, \quad (19.1.2)$$

where  $n = 1$  or  $2$ , and  $q$  can be either a  $d$ - or  $s$ -quark, which corresponds to a  $D^\pm$  (Cabibbo-suppressed mode) or  $D_s$  (Cabibbo-allowed mode) meson. Semi-leptonic weak decays of the  $J/\psi$  will offer several advantages over the purely hadronic ones from both the experimental and theoretical points of view: the prompt charged lepton  $l = e, \mu$  can be used to tag the events, removing a large fraction of conventional  $\psi(nS)$  hadronic decays. In addition, the missing energy due to the escaping neutrino can be also exploited to remove backgrounds. The identification of the charm meson in the final state would provide an unambiguous signature of the semi-leptonic weak decays of  $\psi(nS)$ . Meanwhile, decays of the excited mesons  $D_s^*$  and  $D^{*\pm}$  produced in reaction (19.1.2) would provide useful additional experimental handles. In the lab system, the detectable photons from the  $D_s^{*\pm} \rightarrow D_s^\pm \gamma$ , radiative transition are in the  $90\sim200$  MeV energy interval. These, and the soft pion produced from  $D^{*\pm}$  in  $D^{*\pm} \rightarrow D^0 \pi^\pm$  decay, can provide powerful constraints to help identify a  $D_s$  or  $D^0$  meson produced in the weak decay of a charmonium state.

A specific calculation based on Heavy Quark Spin Symmetry (HQSS) [476, 477], gives branching fractions for the Cabibbo-allowed mode of [475]:

$$\begin{aligned} BR(J/\psi \rightarrow D_s l \nu) &\cong 0.26 \times 10^{-8}, \\ BR(J/\psi \rightarrow D_s^* l \nu) &\cong 0.42 \times 10^{-8}. \end{aligned} \quad (19.1.3)$$

Summing over both modes, one gets a total  $BR \cong 0.7 \times 10^{-8}$ , which is about 20% of the expected total rate for weak decays ( $4 \times 10^{-8}$ ) estimated in Ref. [475]. Taking into account the overall theoretical uncertainty ( $\cong 40\%$ ), the expected branching ratios are within the range  $(0.4 \sim 1.0) \times 10^{-8}$ . For the Cabibbo-suppressed decay modes, one can obtain the following ratio:

$$\frac{BR(J/\psi \rightarrow D_s l \nu)}{BR(J/\psi \rightarrow D^\pm l \bar{\nu})} = \frac{BR(J/\psi \rightarrow D_s^* l \nu)}{BR(J/\psi \rightarrow D^{*\pm} l \bar{\nu})} \cong \frac{|V_{cs}|^2}{|V_{cd}|^2} \cong 20, \quad (19.1.4)$$

where  $V_{cs} (\cong 1.0)$  and  $V_{cd} (\cong 0.22)$  denote the relevant Cabibbo-Kobayashi-Mashkawa (CKM) mixing matrix elements.

### 19.1.2 Two-body Weak Hadronic Decays of Charmonium

Non-leptonic, two-body weak hadronic decays of the  $J/\psi$  and  $\psi(2S)$  are addressed in the context of the factorization scheme for both the Cabibbo-allowed ( $c \rightarrow s$ ) and

Cabibbo-suppressed ( $c \rightarrow d$ ) quark-level transitions in Ref. [478]. There, expressions for branching fractions for  $\psi \rightarrow PP/PV$  decays (where  $P$  and  $V$  represent pseudoscalar mesons and vector mesons, respectively) are given. Using the decay rate formula (5) in Ref. [478], the  $\psi \rightarrow PP$  branching ratio values listed in Table 19.1 are computed. Among the Cabibbo-allowed decays, one finds that the dominant mode is  $\psi \rightarrow D_s^+ \pi^-$ , with a branching ratio

$$BR(\psi \rightarrow D_s^+ \pi^-) = 0.87 \times 10^{-9}; \quad (19.1.5)$$

the next strongest is  $\psi \rightarrow D^0 K^0$ , with a branching ratio

$$BR(\psi \rightarrow D^0 K^0) = 0.28 \times 10^{-9}. \quad (19.1.6)$$

The branching ratios of  $\psi \rightarrow PV$  decays in Cabibbo-allowed and Cabibbo-suppressed channels are listed in Table 19.2. For the color enhanced modes of the Cabibbo-allowed channels, one finds

$$BR(\psi \rightarrow D_s^+ \rho^-) = 0.36 \times 10^{-8}, \quad (19.1.7)$$

which is higher than the  $\psi \rightarrow D_s^+ \pi^-$  branching ratio. The following relative ratio is used in the discussions below [478]

$$\frac{BR(\psi \rightarrow D_s^+ \rho^-)}{BR(\psi \rightarrow D_s^+ \pi^-)} = 4.2. \quad (19.1.8)$$

The  $\psi \rightarrow D_s^+ \rho^-$  mode may be measurable at the SM level at *BES-III*.

Table 19.1: SM branching fractions for  $\psi \rightarrow PP$  from Ref. [478]. The transition mode,  $\Delta C = \Delta S = +1$ , corresponds to Cabibbo-allowed decay modes, while  $\Delta C = +1, \Delta S = 0$  corresponds to Cabibbo-suppressed decay modes.

Transition Mode	Decay Modes	Branching ratio( $\times 10^{-10}$ )
$\Delta C = \Delta S = +1$	$\psi \rightarrow D_s^+ \pi^-$	8.74
	$\psi \rightarrow D^0 K^0$	2.80
$\Delta C = +1, \Delta S = 0$	$\psi \rightarrow D_s^+ K^-$	0.55
	$\psi \rightarrow D^+ \pi^-$	0.55
	$\psi \rightarrow D^0 \eta$	0.016
	$\psi \rightarrow D^0 \eta'$	0.003
	$\psi \rightarrow D^0 \pi^0$	0.055

The  $\psi(nS)$  semi-leptonic decay modes can be related to the two-body hadron decay modes by applying both spin symmetry and the non-recoil approximation to the semi-leptonic decay rates [475]. For  $J/\psi \rightarrow D_s^+(D_s^{*+})\pi^-$  decay modes,  $q^2 = (p_\psi - p_D)^2 = m_\pi^2$  (here  $p_\psi$  and  $p_D$  are the four momenta of the initial and final state heavy mesons) and, assuming factorization as suggested by Bjorken [479] for  $B$  decays, and in the non-recoil approximation for the hadronic transition amplitudes [480], equations (7) and (8) in Ref. [475] give the relation between relative branching ratios:

$$r = \frac{BR(J/\psi \rightarrow D_s^{*+} \pi^-)}{BR(J/\psi \rightarrow D_s^+ \pi^-)} \cong \left[ \frac{d\Gamma(J/\psi \rightarrow D_s^{*+} l^- \nu) / dq^2}{d\Gamma(J/\psi \rightarrow D_s^+ l^- \nu) / dq^2} \right]_{q^2=m_\pi^2} \cong 3.5. \quad (19.1.9)$$

Table 19.2: SM branching fractions for  $\psi \rightarrow PV$  from Ref. [478]. The transition mode,  $\Delta C = \Delta S = +1$ , corresponds to Cabibbo-allowed decay modes, while  $\Delta C = +1, \Delta S = 0$  corresponds to Cabibbo-suppressed decay modes.

Transition Mode	Decay Modes	Branching ratio( $\times 10^{-10}$ )
$\Delta C = \Delta S = +1$	$\psi \rightarrow D_s^+ \rho^-$	36.30
	$\psi \rightarrow D^0 K^{*0}$	10.27
$\Delta C = +1, \Delta S = 0$	$\psi \rightarrow D_s^+ K^{*-}$	2.12
	$\psi \rightarrow D^+ \rho^-$	2.20
	$\psi \rightarrow D^0 \rho^0$	0.22
	$\psi \rightarrow D^0 \omega$	0.18
	$\psi \rightarrow D^0 \phi$	0.65

If a  $\rho$  is substituted for the  $\pi$  one gets  $r \cong 1.4$ . In this way, the estimated branching ratios in Table 19.1 for  $\psi(nS) \rightarrow PP$  channels can be related to  $\psi(nS) \rightarrow VP$  channels with the pseudoscalar charm mesons replaced by vector charm mesons.

All of the above estimates show an overall enhancement of final-state vector charm mesons with respect to the pseudoscalar ones. This suggests the use of  $D_s^*$  or  $D^{*\pm}$  as signals in searches for weak decays of the  $\psi(nS)$  in non-leptonic decay channels as well.

### 19.1.3 Searches at *BES-III*

At *BES-III*, assuming a  $10^{10}$   $J/\psi$  event sample, the central value  $BR \cong 0.7 \times 10^8$  translates into about 70 semi-leptonic decay events of the type  $J/\psi \rightarrow D_s(D_s^*) l \bar{\nu}$ . The following event selection criteria would be useful for searches for such exclusive semi-leptonic channels :

- The prompt charged lepton can be used to tag the weak decay: in order to suppress cascade decay backgrounds from  $J/\psi$  strong decays, the tagging lepton momentum could be required to be between 0.5 GeV and 1.0 GeV, close to the upper kinematic limit for the decay under consideration. High quality lepton discrimination from charged pions or kaons is needed for the measurement.
- The missing mass of the reconstructed candidates must be consistent with the (nearly) zero mass of the undetected neutrino.
- The reconstruction of a  $D_s$  or  $D^\pm$  meson would provide an unambiguous signature for a weak decay of a below-open-charm threshold  $\psi(nS)$ . Good invariant mass resolution of the  $D_s$  decay products will be important for reducing combinatorial backgrounds.
- Soft photons in the energy interval (90~200) MeV from the  $D_s^* \rightarrow \gamma D_s$  transition and soft charged pions from  $D^{*\pm} \rightarrow \pi^\pm D$  decay can provide further suppression of combinatorial backgrounds: the additional constraint of an intermediate  $D_s^*$  state would reconfirm the  $D_s$  signal.

In general, exclusive hadronic decays are probably too tiny to look for in any specific fully reconstructed decay channel. Therefore, it seems that an inclusive search for  $J/\psi \rightarrow D_s^* + X$  at *BES-III* may be more fruitful. The  $\gamma$  from the decay of a  $D_s^*$  meson should be useful as a kinematic constraint to clean up any  $D_s$  meson signal, as discussed in [475].

Finally, in the Standard Model, weak flavor-changing-neutral-current (FCNC)  $J/\psi$  decays are predicted to be unobservably small [474] and, thus, any observation of such would provide a signal for new physics. In Ref. [474] the predictions of various models, such as TopColor models, minimal supersymmetric standard model (MSSM) with R-parity violation and a general two-Higgs-doublet model, are discussed. These authors find that the branching fraction for  $J/\psi \rightarrow D/\bar{D}X_u$ , which is mediated by the weak  $c \rightarrow u$  transition, could be as large as  $10^{-6} \sim 10^{-5}$  in some new physics scenarios.

At *BES-III* it will be difficult to isolate pure,  $c \rightarrow u$  mediated, hadronic  $J/\psi \rightarrow D/\bar{D}X_u$  decays. On the other hand the decays  $J/\psi \rightarrow D^0/\bar{D}^0 l^+ l^-$  ( $l = e, \mu$ ) and  $J/\psi \rightarrow D^0/\bar{D}^0 \gamma$  decays, which are also dominated by FCNC processes, would be quite distinct.

## 19.2 Search for the invisible decays of Quarkonium

Invisible decays of quarkonium states such as the  $J/\psi$  and the  $\Upsilon$  etc., offer a window into what may lie beyond the Standard Model [481, 482]. The reason is that other than neutrinos, the SM includes no other invisible final particles that these states can decay into. *BESII* explored such a window by establishing the first experimental limits on invisible decays of the  $\eta$  and  $\eta'$ , which complemented the limit of  $2.7 \cdot 10^{-7}$  that was previously established for invisible decays of the  $\pi^0$  [483].

Some theories of beyond the SM physics predict new particles with masses that are accessible at *BES-III*, such as the light dark matter (LDM) particles discussed in Ref. [484]. These can have the right relic abundance to constitute the nonbaryonic dark matter of the Universe, if they are coupled to the SM via a new light gauge boson  $U$  [485], or exchanges of heavy fermions. A light neutralino with a coupling to the SM that is mediated by a light scalar singlet in the next-to-minimal supersymmetric standard model has also been considered [486].

These considerations have received a boost in interest by the recent observation of a bright 511 keV  $\gamma$ -ray line from the galactic bulge reported by the SPI spectrometer on the INTEGRAL satellite [487]. The corresponding galactic positron flux, as well as the smooth symmetric morphology of the 511 keV  $\gamma$  emission, could be interpreted as originating from the annihilation of LDM particles into  $e^+e^-$  pairs [484, 488]. It would be very interesting to see evidence for such light invisible particles in collider experiments. CLEO gave an upper bound on  $\Upsilon(1S) \rightarrow \gamma + \text{invisible}$ , which is sensitive to dark matter candidates lighter than about  $3 \text{ GeV}/c^2$  [489], and also provided an upper limit on the axial coupling of any new  $U$  boson to the  $b$  quark. It is important, in addition, to search for the invisible decays of other light quarkonium states ( $q\bar{q}$ ,  $q = u, d$ , or  $s$  quark), since these can be used to constrain the masses of LDM particles and the couplings of a  $U$  boson to the light quarks [482].

It has been shown that measurements of the  $J/\psi$  invisible decay widths can be used to constrain new physics models [490]. It is straightforward for one to calculate the SM ratio of branching fractions for  $J/\psi$  invisible decays and its measured branching fraction

for decays into electron-positron pairs [490]. Within the SM, the invisible mode consists solely of decays into the three types of neutrino-antineutrino pairs. Neglecting polarization effects and taking into account  $e^+e^-$  production through a photon only, one gets [490]:

$$\frac{\Gamma(J/\psi \rightarrow \nu\bar{\nu})}{\Gamma(J/\psi \rightarrow e^+e^-)} = \frac{27G^2 M_{J/\psi}^4}{256\pi^2 \alpha^2} \left(1 - \frac{8}{3} \sin^2(\theta_W)\right)^2 = 4.54 \times 10^{-7}, \quad (19.2.10)$$

where  $G$  and  $\alpha$  are the Fermi and fine-structure constants, respectively, and  $M_{J/\psi}$  is the  $J/\psi$  mass. The uncertainty of the above relation is about 2~3% and comes mainly from corrections to the  $J/\psi$  wave function,  $e^+e^-$  production via the  $Z$  boson and electroweak radiative corrections [490].

At *BES-III*, one can tag charmonium states that decay invisibly by looking for a particular cascade transition, such as  $\psi(2S) \rightarrow \pi^+\pi^- J/\psi$ ,  $\psi(2S) \rightarrow \gamma\chi_c$  and so on, where the soft  $\pi^+\pi^-$  pairs or the monoenergetic  $\gamma$  serves as a tag for the invisibly decaying  $J/\psi$  or  $\chi_c$  state. A list of potentially useful decay chains is provided in Table 19.3.

Table 19.3:  $\psi(2S)$  and  $J/\psi$  decay modes that can be used to search for invisible decays of the  $J/\psi$ ,  $\chi_{c0}$ ,  $\chi_{c1}$ ,  $\chi_{c2}$ ,  $\eta_c(1S)$  and  $\eta_c(2S)$ . The branching fractions are taken from the PDG [491]. For each mode, a “tagging topology” is given, which is the set of visible particles that are seen within the detector’s acceptance. In each case the tagging topology has well defined kinematics. The number of events are the expected event yield in a 3 billion  $\psi(2S)$  (10 billion  $J/\psi$ ) data set, in which we did not consider the decay probabilities of the tagging particles.

$\psi(2S)$ decay mode	Branching fraction ( $10^{-2}$ )	Number of events /3 billion $\psi(2S)$ s	Invisible decay mode	Tagging topology
$\psi(2S) \rightarrow \pi^+\pi^- J/\psi$	$31.7 \pm 1.1$	$9.3 \times 10^8$	$J/\psi \rightarrow$ invisible	$\pi^+\pi^-$
$\psi(2S) \rightarrow \pi^0\pi^0 J/\psi$	$18.6 \pm 0.8$	$5.6 \times 10^8$	$J/\psi \rightarrow$ invisible	$\pi^0\pi^0$
$\psi(2S) \rightarrow \eta J/\psi$	$3.08 \pm 0.17$	$9.3 \times 10^7$	$J/\psi \rightarrow$ invisible	$\eta$
$\psi(2S) \rightarrow \pi^0 J/\psi$	$0.123 \pm 0.018$	$3.7 \times 10^6$	$J/\psi \rightarrow$ invisible	$\pi^0$
$\psi(2S) \rightarrow \gamma\chi_{c0}$	$9.0 \pm 0.4$	$2.7 \times 10^8$	$\chi_{c0} \rightarrow$ invisible	$\gamma$
$\psi(2S) \rightarrow \gamma\chi_{c1}$	$8.7 \pm 0.5$	$2.6 \times 10^8$	$\chi_{c1} \rightarrow$ invisible	$\gamma$
$\psi(2S) \rightarrow \gamma\chi_{c2}$	$8.2 \pm 0.3$	$2.5 \times 10^8$	$\chi_{c2} \rightarrow$ invisible	$\gamma$
$\psi(2S) \rightarrow \gamma\eta_c(1S)$	$0.26 \pm 0.04$	$7.8 \times 10^6$	$\eta_c(1S) \rightarrow$ invisible	$\gamma$
$J/\psi \rightarrow \gamma\eta_c(1S)$	$1.3 \pm 0.4$	$1.3 \times 10^8$	$\eta_c(1S) \rightarrow$ invisible	$\gamma$

It is also interesting to search for invisible decays of the  $\eta$ ,  $\eta'$ ,  $\rho$ ,  $\omega$  and  $\phi$  light mesons, using two-body decay modes of the  $J/\psi$ . For example, the two-body decay modes  $J/\psi \rightarrow \phi\eta$  or  $\phi\eta'$  can be selected using only the very clean and distinct  $\phi \rightarrow K^+K^-$  decays, which then tag the presence of an  $\eta$  or  $\eta'$  meson that has decayed into an invisible final state, as illustrated in Fig. 19.1. Since both the  $\phi$  and  $\eta$  ( $\eta'$ ) have natural widths that are negligible compared with the detector resolution, the shape of the momentum distribution of the  $\phi$  is approximately Gaussian. The mean value of the  $\phi$  momentum distribution is  $1.320 \text{ GeV}/c$  for  $J/\psi \rightarrow \phi\eta$  and  $1.192 \text{ GeV}/c$  for  $J/\psi \rightarrow \phi\eta'$ . The missing momentum,  $P_{\text{miss}} = |\vec{P}_{\text{miss}}|$ , is a powerful discriminating variable to separate signal events from possible backgrounds in which the missing side is not from an  $\eta$  ( $\eta'$ ). Here,  $\vec{P}_{\text{miss}} = -\vec{P}_\phi$ . In addition, the

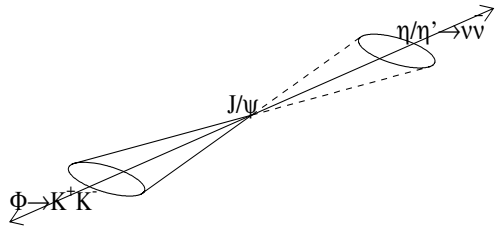


Figure 19.1: The demonstration of  $J/\psi \rightarrow \phi\eta$  or  $\phi\eta'$ , the  $\phi$ , which is reconstructed in the  $K^+K^-$  decay mode, and can be used to tag the invisible decays of the missing particles.

regions of the detector where the  $\eta$  and  $\eta'$  decay products are expected to go are easily defined thanks to the strong boost from the  $J/\psi$  decay, as illustrated in Fig. 19.1.

Using  $\phi \rightarrow K^+K^-$ -tagged  $J/\psi \rightarrow \phi\eta$  and  $\phi\eta'$  decays in a 58 million  $J/\psi$  event sample, BES II searched for invisible decays of the  $\eta$  and  $\eta'$  mesons [492]. Candidate events are those where the only charged tracks seen in the detector are the  $K^+K^-$  pair from the  $\phi$  decay. In addition, events with any neutral energy clusters within a  $30^0$  cone around the axis of the charged tracks (see Fig. 19.1) are rejected. The  $M(K^+K^-)$  distribution for selected events is shown in Fig. 19.2(a), where a  $\phi \rightarrow K^+K^-$  peak is evident at the  $\phi$  mass ( $1.02 \text{ GeV}/c^2$ ). The  $P_{miss}$  distribution for events in the  $\phi$  signal region (indicated by the arrows in Fig. 19.2(a)) is shown in Fig. 19.2(b). No evidence is seen for either  $\eta$  or  $\eta'$  invisible decays.

An unbinned extended maximum likelihood (ML) fit was used to extract the event yield for  $J/\psi \rightarrow \phi\eta(\eta')$  [ $\phi \rightarrow K^+K^-$  and  $\eta(\eta') \rightarrow \text{invisible}$ ]. In the ML fit,  $P_{miss}$  was used as the discriminating variable and the signal region was defined as  $1.00 < P_{miss} < 1.45 \text{ GeV}/c$ , shown in Fig. 19.2(b), over which the background shape was well understood. Probability density functions (PDFs) for the  $P_{miss}$  distributions for ( $\mathcal{F}_{sig}^\eta$  and  $\mathcal{F}_{sig}^{\eta'}$ ) signals and background ( $\mathcal{F}_{bkgd}$ ) were constructed using detailed MC simulations of signal and background. The PDFs for the signals were parameterized by double Gaussian distributions with common means, one relative fraction and two distinct widths, which are all fixed to the MC simulation. The PDF for the background was a bifurcated Gaussian plus a first-order polynomial ( $P_1$ ). All parameters related to the background shape were floated in the fit to data. The PDFs for signals and background were combined in a likelihood function  $\mathcal{L}$ , defined as a function of the free parameters  $N_{sig}^\eta$ ,  $N_{sig}^{\eta'}$ , and  $N_{bkgd}$ ,

$$\mathcal{L}(N_{sig}^\eta, N_{sig}^{\eta'}, N_{bkgd}) = \frac{e^{-(N_{sig}^\eta + N_{sig}^{\eta'} + N_{bkgd})}}{N!} \times \prod_{i=1}^N [N_{sig}^\eta \mathcal{F}_{sig}^\eta(P_{miss}^i) + N_{sig}^{\eta'} \mathcal{F}_{sig}^{\eta'}(P_{miss}^i) + N_{bkgd} \mathcal{F}_{bkgd}(P_{miss}^i)], \quad (19.2.11)$$

where  $N_{sig}^\eta$  and  $N_{sig}^{\eta'}$  are the number of  $J/\psi \rightarrow \phi(\rightarrow K^+K^-)\eta(\rightarrow \text{invisible})$  and  $J/\psi \rightarrow \phi(\rightarrow K^+K^-)\eta'(\rightarrow \text{invisible})$  signal events;  $N_{bkgd}$  is the number of background events. The fixed parameter  $N$  is the total number of selected events in the fit region, and  $P_{miss}^i$  is the value of  $P_{miss}$  for the  $i$ th event. The negative log-likelihood ( $-\ln \mathcal{L}$ ) was minimized with

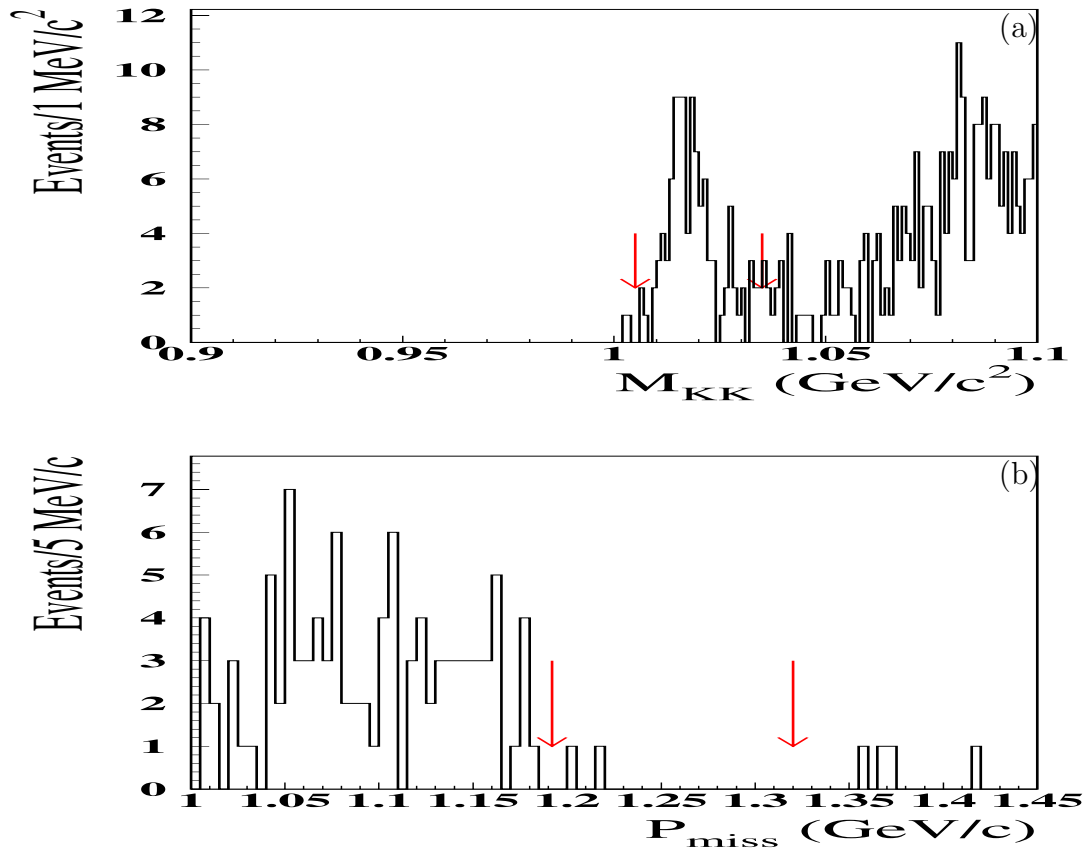


Figure 19.2: (a) The  $m_{KK}$  distribution for candidate events. The arrows on the plot indicate the signal region of  $\phi$  candidates. (b)  $P_{miss}$  distribution for the events with  $1.005 < m_{KK} < 1.035 \text{ GeV}/c^2$  in (a). The mean values of the missing momenta for  $J/\psi \rightarrow \phi\eta$  and  $J/\psi \rightarrow \phi\eta'$  are located around  $1.32$  and  $1.20 \text{ GeV}/c$ , respectively, as indicated by the two arrows.

respect to  $N_{sig}^\eta$ ,  $N_{sig}^{\eta'}$ , and  $N_{bkgd}$  in the data sample. A total of 105 events were used in the fit, and the resulting fitted values of  $N_{sig}^\eta$ ,  $N_{sig}^{\eta'}$ , and  $N_{bkgd}$  were  $-2.8 \pm 1.4$ ,  $2.2 \pm 3.4$ , and  $106 \pm 11$ , where the errors are statistical. Figure 19.3 shows the  $P_{miss}$  distribution and fitted result superimposed. No significant signal is observed for the invisible decay of either the  $\eta$  or the  $\eta'$ . Upper limits were obtained by integrating the normalized likelihood distribution over the positive values of the number of signal events. The upper limits at the 90% confidence level were 3.56 events for the  $\eta$  and 5.72 events for the  $\eta'$ , respectively.

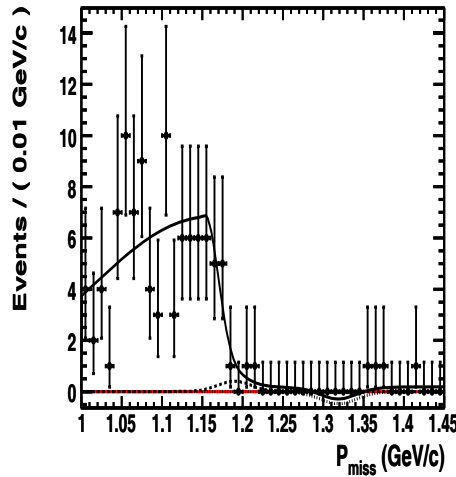


Figure 19.3: The  $P_{miss}$  distribution for candidate events. The data (black crosses) are compared to the total fit results. The dotted curve is the projection of  $\eta$  signal component, and the dashed curve is the projection of  $\eta'$  signal component, and the solid curve is the total likelihood fit result.

The branching fraction of  $\eta(\eta') \rightarrow \gamma\gamma$  was also determined in  $J/\psi \rightarrow \phi\eta(\eta')$  decays, in order to provide the ratio  $\mathcal{B}(\eta(\eta') \rightarrow \text{invisible})$  to  $\mathcal{B}(\eta(\eta') \rightarrow \gamma\gamma)$ . The advantage of measuring  $\frac{\mathcal{B}(\eta(\eta') \rightarrow \text{invisible})}{\mathcal{B}(\eta(\eta') \rightarrow \gamma\gamma)}$  is that the uncertainties due to the total number of  $J/\psi$  events, tracking efficiency, PID, the number of the charged tracks, the cut on  $M(KK)$ , and residual noise in the BSC all cancel.

For these  $\eta(\eta') \rightarrow \gamma\gamma$  measurements, two good photons with energy greater than 50 MeV were required to be within the  $30^0$  cone. A 4C kinematic fit was applied to the selected  $K^+K^-\gamma\gamma$  combination and the  $\eta(\eta')\gamma\gamma$  signal yields of  $\eta$  and  $\eta'$  events were determined from fits to peaks seen in the  $\gamma\gamma$  invariant mass distribution.

The upper limit on the ratio of the  $\mathcal{B}(\eta \rightarrow \text{invisible})$  to  $\mathcal{B}(\eta \rightarrow \gamma\gamma)$  was calculated with

$$\frac{\mathcal{B}(\eta \rightarrow \text{invisible})}{\mathcal{B}(\eta \rightarrow \gamma\gamma)} < \frac{n_{UL}^\eta / \epsilon_\eta}{n_{\gamma\gamma}^\eta / \epsilon_{\gamma\gamma}^\eta} \cdot \frac{1}{(1 - \sigma_\eta)}, \quad (19.2.12)$$

where  $n_{UL}^\eta$  is the 90% upper limit of the number of observed events for  $J/\psi \rightarrow \phi\eta$ ,  $\phi \rightarrow K^+K^-$ ,  $\eta \rightarrow \text{invisible}$  decay,  $\epsilon_\eta$  is the MC determined efficiency for the signal channel,

$n_{\gamma\gamma}^\eta$  is the number of events for the  $J/\psi \rightarrow \phi\eta$ ,  $\phi \rightarrow K^+K^-$ ,  $\eta \rightarrow \gamma\gamma$  decay,  $\epsilon_{\gamma\gamma}^\eta$  is the MC determined efficiency for the decay mode, and  $\sigma_\eta$  is  $\sqrt{(\sigma_\eta^{sys})^2 + (\sigma_\eta^{stat})^2} = 8.1\%$ , where  $\sigma_\eta^{sys}$  and  $\sigma_\eta^{stat}$  are the total relative systematical error for the  $\eta$  case from Table 19.4 and the relative statistical error of  $n_{\gamma\gamma}^\eta$ , respectively. For  $\eta'$ ,  $\sigma_{\eta'}$  is  $\sqrt{(\sigma_{\eta'}^{sys})^2 + (\sigma_{\eta'}^{stat})^2} = 21.6\%$ . The relative statistical error of the fitted yield for  $J/\psi \rightarrow \phi\eta(\eta')$ ,  $\eta(\eta') \rightarrow \gamma\gamma$ , is 2.8% (18.5%) according to the results from the fit to the invariant mass of  $\gamma\gamma$ . The upper limit on the ratio of the  $\mathcal{B}(\eta' \rightarrow \text{invisible})$  to  $\mathcal{B}(\eta' \rightarrow \gamma\gamma)$  was determined by replacing  $\eta$  with  $\eta'$  in Eq. (19.2.12).

Table 19.4: The numbers used in the calculations of the ratios in Eq. (19.2.12), where  $n_{UL}^\eta$  ( $n_{UL}^{\eta'}$ ) is the upper limit of the signal events at the 90% confidence level,  $\epsilon_\eta$  ( $\epsilon_{\eta'}$ ) is the selection efficiency,  $n_{\gamma\gamma}^\eta$  ( $n_{\gamma\gamma}^{\eta'}$ ) is the number of the events of  $J/\psi \rightarrow \phi\eta(\eta')$ ,  $\phi \rightarrow K^+K^-$ ,  $\eta(\eta') \rightarrow \gamma\gamma$ ,  $\epsilon_{\gamma\gamma}^\eta$  ( $\epsilon_{\gamma\gamma}^{\eta'}$ ) is its selection efficiency.  $\sigma_\eta^{stat}$  ( $\sigma_{\eta'}^{stat}$ ) is the relative statistical error and  $\sigma_\eta^{sys}$  ( $\sigma_{\eta'}^{sys}$ ) is the relative statistical error of  $n_{\gamma\gamma}^\eta$  ( $n_{\gamma\gamma}^{\eta'}$ ),  $\sigma_\eta$  ( $\sigma_{\eta'}$ ) is the total relative error.

quantity	value	
	$\eta$	$\eta'$
$n_{UL}^\eta$ ( $n_{UL}^{\eta'}$ )	3.56	5.72
$\epsilon_\eta$ ( $\epsilon_{\eta'}$ )	23.5%	23.2%
$n_{\gamma\gamma}^\eta$ ( $n_{\gamma\gamma}^{\eta'}$ )	$1760.2 \pm 49.3$	$71.6 \pm 13.2$
$\epsilon_{\gamma\gamma}^\eta$ ( $\epsilon_{\gamma\gamma}^{\eta'}$ )	17.6%	15.2%
$\sigma_\eta^{stat}$ ( $\sigma_{\eta'}^{stat}$ )	2.8%	18.5%
$\sigma_\eta^{sys}$ ( $\sigma_{\eta'}^{sys}$ )	7.7	11.1
$\sigma_\eta$ ( $\sigma_{\eta'}$ )	8.1%	21.6%

Using the numbers in Table 19.4, the upper limit on the ratio of  $\mathcal{B}(\eta(\eta') \rightarrow \text{invisible})$  and  $\mathcal{B}(\eta(\eta') \rightarrow \gamma\gamma)$  was obtained at the 90% confidence level of  $1.65 \times 10^{-3}$  ( $6.69 \times 10^{-2}$ ).

Table 19.5 lists possible two-body  $J/\psi$  decay modes that can be used to study the invisible decays of the  $\eta$ ,  $\eta'$ ,  $\rho$ ,  $\omega$  and  $\phi$  mesons at *BES-III*.

### 19.3 Search for $C$ or $P$ violating processes in $J/\psi$ decays

With its huge  $J/\psi$  and  $\psi(2S)$  data samples, the *BES-III* experiment will be approaching the statistics regime where studies of rare  $\psi$  decays can provide important tests of the SM and possibly uncover deviations. Among the interesting examples are  $C$ ,  $P$  or  $CP$  violating processes in  $J/\psi$  decays. An example of such modes would be  $\psi(nS) \rightarrow V^0V^0$ , where  $V^0$  is used to denote  $J^{PC} = 1^{--}$  vector mesons ( $\phi$ ,  $\omega$ ,  $\rho^0$  and  $\gamma$ ). A distinct signal for this class of event would be  $\psi(nS) \rightarrow \phi\phi$  detected in  $\psi(nS) \rightarrow K^+K^-K^+K^-$  final states. Because of the  $C$  violation,  $\psi(nS) \rightarrow V^0V^0$  decays can only occur in the SM via  $c\bar{c}$  annihilation via a  $Z^0$  or  $W$ -exchange decays as discussed in Ref. [493]. The rate for this type of weak decay can provide a measurement of the charmonium wave function at the origin [493].

Table 19.5:  $J/\psi$  decay modes that can be used to study invisible decays of  $\eta$ ,  $\eta'$ ,  $\rho$ ,  $\omega$  and  $\phi$  mesons. The branching fractions are from the PDG [491]. For each mode, a “tagging topology” is given, which is the set of visible tracks in the detector’s acceptance. In each case the tagging topology has well defined kinematics. The produced number of events are the expected events in 10 billion  $J/\psi$  event data set at *BES-III*, with the decay probabilities of the tagging particles included.

$J/\psi$ decay mode	Branching fraction ( $10^{-4}$ )	Invisible decay mode	Tagging topology	Number of events /10 billion $J/\psi$ s
$J/\psi \rightarrow \phi\eta$	$6.5 \pm 0.7$	$\eta \rightarrow$ invisible	$\phi \rightarrow K^+K^-$	$(31.4 \pm 3.4) \times 10^5$
	$6.5 \pm 0.7$	$\phi \rightarrow$ invisible	$\eta \rightarrow \gamma\gamma$	$(25.7 \pm 2.8) \times 10^5$
$J/\psi \rightarrow \phi\eta'$	$3.3 \pm 0.4$	$\eta' \rightarrow$ invisible	$\phi \rightarrow K^+K^-$	$(16.2 \pm 1.9) \times 10^5$
	$3.3 \pm 0.4$	$\phi \rightarrow$ invisible	$\eta' \rightarrow \gamma\rho^0$	$(9.6 \pm 1.2) \times 10^5$
$J/\psi \rightarrow \omega\eta$	$15.8 \pm 1.6$	$\eta \rightarrow$ invisible	$\omega \rightarrow \pi^+\pi^-\pi^0$	$(13.9 \pm 1.4) \times 10^6$
	$15.8 \pm 1.6$	$\omega \rightarrow$ invisible	$\eta \rightarrow \gamma\gamma$	$(6.2 \pm 0.6) \times 10^6$
$J/\psi \rightarrow \omega\eta'$	$1.67 \pm 0.25$	$\eta' \rightarrow$ invisible	$\omega \rightarrow \pi^+\pi^-\pi^0$	$(1.5 \pm 0.2) \times 10^6$
	$1.67 \pm 0.25$	$\omega \rightarrow$ invisible	$\eta' \rightarrow \gamma\rho^0$	$(0.7 \pm 0.1) \times 10^6$
$J/\psi \rightarrow \rho^0\eta$	$1.93 \pm 0.23$	$\eta \rightarrow$ invisible	$\rho^0 \rightarrow \pi^+\pi^-$	$(1.9 \pm 0.2) \times 10^6$
	$1.93 \pm 0.23$	$\rho^0 \rightarrow$ invisible	$\eta \rightarrow \gamma\gamma$	$(0.8 \pm 0.09) \times 10^6$
$J/\psi \rightarrow \rho^0\pi^0$	$56 \pm 7$	$\rho^0 \rightarrow$ invisible	$\pi^0 \rightarrow \gamma\gamma$	$(55.3 \pm 5.8) \times 10^6$

In order to make a rough estimate for the rate, we first consider just the rate due to the  $W$ -exchange contribution, which is straightforward to compute [494]

$$\frac{\Gamma(J/\psi \rightarrow s\bar{s})^{weak}}{\Gamma(J/\psi \rightarrow e^+e^-)} \cong \frac{1}{2} \left( \frac{m_{J/\psi}}{m_W} \right)^4, \quad (19.3.13)$$

where  $m_{J/\psi}$  and  $m_W$  are the masses of  $J/\psi$  and  $W$  boson, respectively. This leads to  $BR(J/\psi \rightarrow s\bar{s})^{weak} \cong 10^{-7}$  for this weak contribution. To form the  $\phi\phi$  final state, another  $s\bar{s}$  pair must be produced from the vacuum and these  $s$ -quarks have to bind with the outgoing  $s\bar{s}$  from the  $c\bar{c}$  decay to produce the  $\phi\phi$  final state [493]. When this is considered, it seems that one can expect that the SM exclusive  $BR(\psi(nS) \rightarrow \phi\phi)$  rate should be below the level of  $10^{-8}$  and probably out of reach of the *BES-III* experiment.

Experimentally, there are some possible backgrounds that will dilute the signal for  $J/\psi \rightarrow \phi\phi$  decays. One major background is  $J/\psi \rightarrow \gamma\phi\phi$ , which is mainly from  $J/\psi \rightarrow \gamma\eta_c(1S)$ ,  $\eta_c(1S) \rightarrow \phi\phi$ . This background can be removed by doing a constrained kinematic fit. A detailed calculation had been done to estimate the background from  $J/\psi \rightarrow \gamma\phi\phi$  [493]. Another background appears if one studies only  $2(K\bar{K})$  invariant pair mass distributions. It arises from the  $C$  and  $P$ -conserving reaction  $J/\psi \rightarrow \phi(K\bar{K})_{S-wave}$ , due to the fact that the  $\phi$  mass is only two  $S$ -wave-widths away from the  $K\bar{K}$   $S$ -wave resonance mass, for example,  $f_0(980) \rightarrow K\bar{K}$ . Although it may be difficult to subtract in a small statistical sample, one can, in principle, remove this kind of background by either a spin-parity analysis of the  $K\bar{K}$  pairs in a narrow window about  $\phi$  mass, or by a subtraction normalized to an observed  $S$ -wave mass peak. To avoid the  $S$ -wave contribution, one can reconstruct one  $\phi$  from  $K^+K^-$  and another  $\phi$  from the  $K_SK_L$  mode, which is not allowed to form an  $S$ -wave. It will be easy to look for the missing mass of one  $\phi$  reconstructed from  $K^+K^-$ , to see if there is any peak under the  $\phi$  mass region by also requiring  $K_S$  and  $K_L$  information in the final states.

It is noted that there is possible continuum background produced via a two-photon annihilation process. It is a peaking background that cannot be removed without considering detail angular distributions in a high statistics sample. It is very hard to deal with this kind of peaking source with a small sample of signal events. One way is to use off-peak data which are taken below the  $J/\psi$  mass peak. The  $e^+e^- \rightarrow \gamma\gamma$  process has been investigated before [495], and it has a unique production angle ( $\theta^*$ ) distribution, which is defined as the angle between  $\phi$  and  $e^-$  beam direction in the Center-of-Mass (CM) frame. The production angle distribution for the two real photon annihilation process has the form of

$$\sigma(\cos\theta^*)_{e^+e^- \rightarrow \gamma\gamma} = \frac{1 + \cos\theta^{*2}}{1 - \cos\theta^{*2}}, \quad (19.3.14)$$

while, in the process of two virtual photon into  $V^0V^0$  pairs, the distribution is (to first order) [496]:

$$\sigma(\cos\theta^*)_{e^+e^- \rightarrow \gamma^*\gamma^* \rightarrow V^0V^0} = \frac{1 + \cos\theta^{*2}}{k^2 - \cos\theta^{*2}}, \quad (19.3.15)$$

where factor  $k$  is:

$$k = \frac{2m_{V^0}^2 - S}{\sqrt{S^2 - 4Sm_{V^0}^2}}, \quad (19.3.16)$$

where  $S$  is the square of CM energy. In principle, by using an angular analysis, one can remove the peaking background with high statistic data sample. To avoid the peaking background from the continuum,  $\psi(2S) \rightarrow \pi\pi J/\psi$  could be used to study this kind of rare  $J/\psi$  decays with 3 billion  $\psi(2S)$  sample, but the statistics will be substantially reduced.

## 19.4 Lepton flavor violating processes in decays of $J/\psi$

Standard Model lepton-flavor-violating (LFV) processes are suppressed by powers of the very small neutrino masses [497]. Therefore, such decays can be used as a probe for possible new physics. At present, there are many stringent bounds for  $\mu$ ,  $\tau$  and  $Z$  boson decays, such as  $BR(\mu \rightarrow 3e) \leq 10^{-12}$ ,  $BR(\mu \rightarrow e\gamma\gamma) \leq 10^{-10}$  and somewhat weaker  $O(10^{-6})$  bounds on LFV  $\tau$  decays [52]. There have been a lot of studies, both theoretically and experimentally, on testing the lepton flavor conservation law [497, 498]. With a huge  $J/\psi$  event sample, the *BES-III* experiment will be able to make high sensitivity experimental searches for lepton flavor violating processes of the type  $J/\psi \rightarrow ll'$  ( $l$  and  $l' = \tau, \mu, e$ ,  $l \neq l'$ ).

To estimate the branching ratio for the lepton flavor violating  $J/\psi$  decays that are allowed by the current experimental data, Peccei, Wang and Zhang used a model-independent approach to new physics and introduced an effective four-fermion contact interaction [497, 499, 500]:

$$\frac{4\pi}{\Lambda^2} \bar{c}\gamma^\mu c \bar{l}\gamma^\mu l', \quad (19.4.17)$$

where  $\Lambda$  is the new physics cutoff. This effective operator is forbidden in the standard model, however, it will be generated in theories where lepton flavor is not conserved, such as the MSSM with and/or without R parity, and models with large extra dimension [501]. Any observed signal would be direct evidence for non-standard physics and improve our understanding of flavor dynamics, especially in the lepton sector.

There is no direct experimental limit on the  $\Lambda$  cutoff in eqn. 19.4.17. However, at the one-loop level, attaching a neutral gauge boson  $Z$  to the charm quark loop generates an effective coupling of  $Z$  to  $\bar{l}l'$ . From the limits given in the PDG on  $BR(Z \rightarrow \bar{l}l')$  [52], one obtains upper bounds on the branching fractions of  $J/\psi$  decay into leptons [500]:

$$BR(J/\psi \rightarrow \tau^+ e^-) < 2.7 \times 10^{-5}; \quad (19.4.18)$$

$$BR(J/\psi \rightarrow \tau^+ \mu^-) < 4.9 \times 10^{-5}; \quad (19.4.19)$$

$$BR(J/\psi \rightarrow \mu^+ e^-) < 8.3 \times 10^{-6}. \quad (19.4.20)$$

Recently, Nussinov, Peccei and Zhang [497] have also examined “unitarity inspired” relations between two- and three-body lepton flavor violating decays and found that the existing strong bounds on  $\mu \rightarrow 3e$  and  $\mu \rightarrow e\gamma\gamma$  severely constrain two-body lepton flavor violating decays of vector mesons, such as the  $J/\psi$ ,  $\Upsilon(1S)$  and  $\phi$ , into  $\mu^\pm e^\mp$  final states. In Ref. [497], using  $BR(\mu \rightarrow 3e) \leq 10^{-12}$  and data pertaining to the  $e^+e^-$  widths of the  $J/\psi$ , the bound on the branching ratio for the two-body LFV decay  $J/\psi \rightarrow \mu^\pm e^\mp$  decay is

$$BR(J/\psi \rightarrow \mu^\pm e^\mp) < 4 \times 10^{-13}. \quad (19.4.21)$$

Likewise, the generic upper bounds on LPV  $\tau$  decays  $BR(\tau \rightarrow ll'\bar{l}\bar{l}) \leq 10^{-6}$  yields

$$BR(J/\psi \rightarrow \tau^\pm l^\mp) < 6 \times 10^{-7}. \quad (19.4.22)$$

with  $l/l' = e/\mu$ . These inferred bounds are unlikely to be improved by future experimental data on two-body decays, especially at *BES-III*. However, all the bounds derived in Ref. [497, 500] can be evaded if there is a kinematical suppression or some cancellations [497]. Searching for lepton flavor violating decays of  $J/\psi$  with a huge sample a *BES-III* remains a worthwhile experimental challenge [500].

With a 58 M  $J/\psi$  event sample at BESII, the following upper limits have been established [502]:

$$BR(J/\psi \rightarrow \tau^\pm e^\mp) < 8.3 \times 10^{-6}; \quad (19.4.23)$$

$$BR(J/\psi \rightarrow \tau^\pm \mu^\mp) < 2.0 \times 10^{-6}; \quad (19.4.24)$$

$$BR(J/\psi \rightarrow \mu^\pm e^\mp) < 1.1 \times 10^{-6}. \quad (19.4.25)$$

The limits on the two-body lepton flavor violating decays of the  $J/\psi$  could be reduced to the  $10^{-8} \sim 10^{-9}$  level at *BES-III* with a one year full-luminosity run at the  $J/\psi$  peak. This would be a significant improvement.



# Chapter 20

## Miscellaneous

### 20.1 Bell inequalities in high energy physics<sup>1</sup>

In 1935, Einstein, Podolsky, and Rosen (EPR) [503] demonstrated that quantum mechanics (QM) could not provide a complete description of the “physical reality” for two spatially separated but quantum mechanically correlated particle systems. Alternatively, local hidden variable theories (LHVTs) have been developed to restore the completeness of QM. In 1964, Bell [504] showed that in realistic LHVTs two-particle correlation functions satisfy a set of Bell inequalities (BI), whereas the corresponding QM predictions can violate such inequalities in some region of parameter space. This leads to the possibility of experimental testing of the validity of LHVTs in comparison with QM.

The definition of correlations for LHVTs and QM read respectively as:

$$E(\mathbf{a}, \mathbf{b}) = \int d\lambda \rho(\lambda) A(\mathbf{a}, \lambda) B(\mathbf{b}, \lambda) , \quad (20.1.1)$$

$$E(\mathbf{a}, \mathbf{b}) = \langle \psi | \sigma \cdot \mathbf{a} \otimes \sigma \cdot \mathbf{b} | \psi \rangle = -\mathbf{a} \cdot \mathbf{b} . \quad (20.1.2)$$

Here,  $\rho(\lambda)$  is the distribution of a hidden variable regardless of whether  $\lambda$  is a single variable or a set, or even a set of functions. These variables can be either discrete or continuous.  $\mathbf{a}$  and  $\mathbf{b}$  indicate spin directions. One of the Bell inequalities, the CHSH inequality, takes the form [505]

$$S = |E(\mathbf{a}, \mathbf{b}) - E(\mathbf{a}, \mathbf{b}')| + |E(\mathbf{a}', \mathbf{b}) + E(\mathbf{a}', \mathbf{b}')| \leq 2 . \quad (20.1.3)$$

The correlation function  $E$  above can be calculated by

$$E(\mathbf{a}, \mathbf{b}) = P_{++}(\mathbf{a}, \mathbf{b}) - P_{+-}(\mathbf{a}, \mathbf{b}) - P_{-+}(\mathbf{a}, \mathbf{b}) + P_{--}(\mathbf{a}, \mathbf{b}) , \quad (20.1.4)$$

where  $P_{\pm\pm} = N_{\pm\pm}(\mathbf{a}, \mathbf{b})/N$ ,  $N$  is the total number of particle pairs, and  $N_{++(+-)}$  means that two particle has the same (opposite) spin directions.

In 1992, Hardy proved without using inequalities, a kind of definite conflict that can occur for any non-maximally entangled state composed of two two-level subsystems [506]. Later, Hardy’s argument was expanded on by Jordan [507], who demonstrated that there exist four projection operators satisfying

$$\langle FG \rangle = 0 , \quad \langle D(1 - G) \rangle = 0 , \quad (20.1.5)$$

---

<sup>1</sup>Junli Li and Cong-Feng Qiao

$$\langle (1 - F)E \rangle = 0, \quad \langle DE \rangle > 0, \quad (20.1.6)$$

which are in contradiction with LHVTs. Jordan also demonstrated in a converse way that for any choice of four different measurements, there exists a state satisfying Hardy's argument [507]. In 1995, Garuccio [508] found that the contradiction between QM and LHVT can be embedded in Clauser-Horne (CH) inequalities [509], *i.e.*,

$$\langle DE \rangle \leq \langle FG \rangle + \langle D(1 - G) \rangle + \langle (1 - F)E \rangle. \quad (20.1.7)$$

Many experiments in regard of the Bell inequalities have been carried out by using the entangled photons. In the optical experiment the correlation of polarizers in orientations  $\mathbf{a}$  and  $\mathbf{b}$  is defined as follows:

$$E(\mathbf{a}, \mathbf{b}) = \frac{N_{++}(\mathbf{a}, \mathbf{b}) + N_{--}(\mathbf{a}, \mathbf{b}) - N_{+-}(\mathbf{a}, \mathbf{b}) - N_{-+}(\mathbf{a}, \mathbf{b})}{N_{++}(\mathbf{a}, \mathbf{b}) + N_{+-}(\mathbf{a}, \mathbf{b}) + N_{-+}(\mathbf{a}, \mathbf{b}) + N_{--}(\mathbf{a}, \mathbf{b})}, \quad (20.1.8)$$

where  $N_{+-}$  is the coincidence rate of photon polarizations; + for parallel and - for perpendicular to the chosen direction. Of the various optical experiments, one of the important ones was carried out by Aspect *et al.* [510]. Their measurement gave

$$S_{exp} = 2.697 \pm 0.015. \quad (20.1.9)$$

This result is in excellent agreement with the predictions of quantum mechanics, which, for their polarizer efficiencies and lens apertures, gives  $S_{QM} = 2.7 \pm 0.05$ .

It has been noted that the experiments testing the completeness of QM are mainly limited to the electromagnetic interaction regime, *i.e.*, by employing entangled photons, no matter whether the photons are generated from atomic cascades or the PDC method. Considering the fundamental importance of the questions involved, experimental tests of LHVT with massive quanta and with other kinds of interactions are necessary [511].

As early as the 1960s, the EPR-like features of the  $K^0\bar{K}^0$  pair in decays of the  $J^{PC} = 1^{--}$  vector particles was noticed by Lipkin [512]. Other early attempts at testing LHVTs through the Bell inequality in high energy physics focused on exploiting the nature of particle spin correlations [511, 513, 514]. In Ref. [513] Törnqvist suggested measuring the BI via the

$$e^+e^- \rightarrow \Lambda\bar{\Lambda} \rightarrow \pi^- p \pi^+ \bar{p} \quad (20.1.10)$$

process. A similar process was suggested by Privitera [514], *i.e.*,

$$e^+e^- \rightarrow \tau^+\tau^- \rightarrow \pi^+\bar{\nu}_\tau \pi^- \nu_\tau. \quad (20.1.11)$$

The DM2 Collaboration [515] observed  $7.7 \times 10^6$   $J/\psi$  events with about  $10^3$  of them identified as being from the process  $J/\psi \rightarrow \Lambda\bar{\Lambda} \rightarrow \pi^- p \pi^+ \bar{p}$ . The experimental measurement unfortunately does not give a very significant result [516] due to insufficient statistics.

However, it was subsequently realized that these proposals have controversial assumptions [517]. It was found that for testing the LHVTs in high energy physics, using the "quasi-spin" to mimic the photon polarization in the construction of entangled states is a more practical approach. A typical process that produces an entangled  $K^0\bar{K}^0$  state is

$e^+e^- \rightarrow \phi \rightarrow K^0\bar{K}^0$ . The wave function of the  $J^{PC} = 1^{--}$  particles, like the  $\phi$  which decays into  $K^0\bar{K}^0$ , can be formally configured as [518]:

$$|\phi\rangle = \frac{1}{\sqrt{2}}\{|K^0\rangle|\bar{K}^0\rangle - |\bar{K}^0\rangle|K^0\rangle\}. \quad (20.1.12)$$

Similar expressions apply to  $\Upsilon(4S) \rightarrow B^0\bar{B}^0$ ,  $\Upsilon(5S) \rightarrow B_s^0\bar{B}_s^0$ , and  $\psi(3770) \rightarrow D^0\bar{D}^0$  cases. There are two different methods in this “quasi-spin” scheme. In the first method, one fixes the quasi-spin, but leaves the time free. The second method is to leave the quasi-spin free but fix the time.

Consider the first case: we can choose different times to measure the final states, the kaons, on each side. We choose the quantum number of strangeness as the quasi-spin in our consideration, but neglect  $CP$  violation effects, which in some sense is a good approximation. With the time evolution, the initial entangled state, like in (20.1.12), becomes:

$$|\Psi(t_l, t_r)\rangle = \frac{1}{\sqrt{2}}\{e^{-i(m_L t_l + m_S t_r)}e^{-\frac{\Gamma_L}{2}t_l - \frac{\Gamma_S}{2}t_r}|K_L\rangle|K_S\rangle - e^{-i(m_S t_l + m_L t_r)}e^{-\frac{\Gamma_S}{2}t_l - \frac{\Gamma_L}{2}t_r}|K_S\rangle|K_L\rangle\}. \quad (20.1.13)$$

In the above, the small letters  $l$  and  $r$  denote left side and right side; we name the two entangled particles to be left and right without lose generality. Choosing different measurement times for the two sides, the expectation value of correlation is [519]:

$$E(t_l, t_r) = -\cos(\Delta m \Delta t) e^{-\frac{\Gamma_L + \Gamma_S}{2}(t_l + t_r)}. \quad (20.1.14)$$

Inserting this correlation directly into the CHSH inequality, one finds that the violation of the inequality depends on the ratio of  $x = \Delta m / \Gamma$  [520], where  $\Delta m$  characterizes the strangeness oscillation and  $\Gamma$  characterizes the weak decay lifetime. Among the known neutral mesons, the  $B_s^0\bar{B}_s^0$  system has the largest value of  $x$ , and hence the violation of inequalities might be found there.

The EPR-type strangeness correlation in the process  $p\bar{p} \rightarrow K^0\bar{K}^0$  has been tested at the CPLEAR detector [521] at CERN. In the experiment the  $K^0\bar{K}^0$  pairs were created in  $J^{PC} = 1^{--}$  configuration. The wave function at proper time  $t_l = t_r = 0$  is

$$|\Psi(0, 0)\rangle = \frac{1}{\sqrt{2}}[|K^0\rangle_l|\bar{K}^0\rangle_r - |\bar{K}^0\rangle_l|K^0\rangle_r]. \quad (20.1.15)$$

The strangeness was tagged via strong interaction with absorbers away from the creation point. From Fig.20.1 one notices that the non-separability hypothesis of QM is strongly favoured by experiment.

The  $B^0\bar{B}^0$  entangled system produced at the  $\Upsilon(4S)$  resonance has also been measured in the KEKB  $B$ -factory [522]. The wave function for  $\Upsilon(4S) \rightarrow B^0\bar{B}^0$  has the same form as the spin singlet:

$$|\Upsilon\rangle = \frac{1}{\sqrt{2}}\{|B^0\rangle_l|\bar{B}^0\rangle_r - |\bar{B}^0\rangle_l|B^0\rangle_r\}. \quad (20.1.16)$$

Here, the  $b$ -flavor quantum number plays the role of spin polarization in the spin

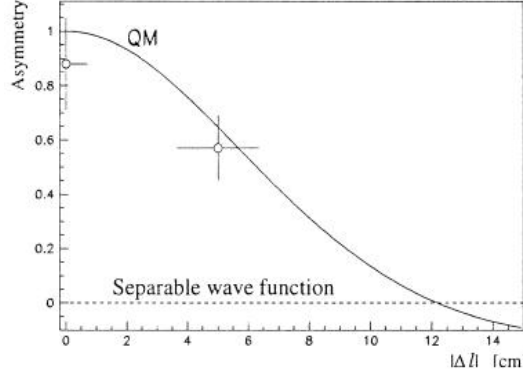


Figure 20.1: The best fit to the experimental measurement [521]. The two points with error bars correspond to time difference  $\Delta t = 0$  and  $\Delta t = 1.2\tau_s$ . The solid line represents the QM prediction.

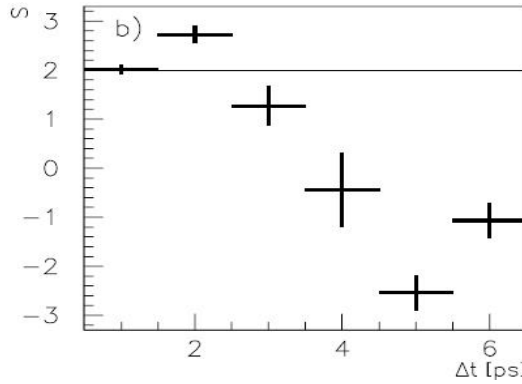


Figure 20.2: The experimental result on the violation of the inequality [522]. The horizontal axis refers to  $\Delta t$  and the vertical axis to the  $S$ . The LHVTs limit of 2 is shown by the solid line.

correlation system. The experiment, which is based on a data sample of  $80 \times 10^6$   $\Upsilon(4S) \rightarrow B\bar{B}$  decays at Belle detector at the KEKB asymmetric collider in Japan, gives  $S = 2.725 \pm 0.167_{stat}$ . It is obviously a result that violate the Bell inequality, as shown in Fig.20.2. However, debates on whether this was genuine test of LHVTs or not is still ongoing [523].

Recently, expanding on Hardy's approach, Bramon and Garbarino proposed a new scheme to test the local realism by virtue of entangled neutral kaons [524, 525]. After neglecting the small  $CP$ -violation effect, the initial  $K_SK_L$  pair from  $\phi$  decay, or proton-antiproton annihilation has the form:

$$|\phi(T=0)\rangle = \frac{1}{\sqrt{2}}[K_SK_L - K_LK_S] , \quad (20.1.17)$$

where  $K_S = (K^0 + \bar{K}^0)/\sqrt{2}$  and  $K_L = (K^0 - \bar{K}^0)/\sqrt{2}$  are the mass eigenstates of the  $K$  mesons. One of the key points of the scheme is to test the LHVTs by generating a

nonmaximally entangled (asymmetric) state. That is

$$|\phi(T)\rangle = \frac{1}{\sqrt{2 + |R|^2}} [K_S K_L - K_L K_S - r e^{-i(m_L - m_S)T + [(\Gamma_S - \Gamma_L)/2]T} K_L K_L] . \quad (20.1.18)$$

Here,  $r$  is the regeneration parameter of the order of magnitude  $10^{-3}$  [525],  $\Gamma_L$  and  $\Gamma_S$  are the  $K_L$  and  $K_S$  decay widths, respectively, and  $T$  is the evolution time of kaons after their production. Technically, this asymmetric state can be achieved by placing a thin regenerator close to the  $\phi$  decay point.

Four specific transition probabilities for joint measurements from QM take the following forms:

$$\begin{aligned} P_{QM}(K^0, \bar{K}^0) &\equiv |\langle K^0 \bar{K}^0 | \phi(T) \rangle|^2 \\ &= \frac{|2 + \text{Re}^{i\varphi}|^2}{4(2 + |R|^2)} , \end{aligned} \quad (20.1.19)$$

$$\begin{aligned} P_{QM}(K^0, K_L) &\equiv |\langle K^0 K_L | \phi(T) \rangle|^2 \\ &= \frac{|1 + \text{Re}^{i\varphi}|^2}{2(2 + |R|^2)} , \end{aligned} \quad (20.1.20)$$

$$\begin{aligned} P_{QM}(K_L, \bar{K}^0) &\equiv |\langle K_L \bar{K}^0 | \phi(T) \rangle|^2 \\ &= \frac{|1 + \text{Re}^{i\varphi}|^2}{2(2 + |R|^2)} , \end{aligned} \quad (20.1.21)$$

$$P_{QM}(K_S K_S) \equiv |\langle K_S K_S | \phi(T) \rangle|^2 = 0 , \quad (20.1.22)$$

where  $R = -|R| = -|r|e^{[(\Gamma_S - \Gamma_L)/2]T}$  and  $\varphi$  is the phase of  $R$ . In Ref. [525] the special case of  $R = -1$  was considered, in which

$$P_{QM}(K^0, \bar{K}^0) = 1/12 , \quad (20.1.23)$$

$$P_{QM}(K^0, K_L) = 0 , \quad (20.1.24)$$

$$P_{QM}(K_L, \bar{K}^0) = 0 , \quad (20.1.25)$$

$$P_{QM}(K_S, K_S) = 0 . \quad (20.1.26)$$

These equations has the same form as (20.1.6), and are in conflict with QM.

For simplicity we consider an ideal case, in which the detection efficiency for the kaon decays is 100 percent. Then the Eberhard inequality (EI) for the kaon system takes the similar form as Eq.(20.1.7) [526, 508]. It reads

$$P_{LR}(K^0, \bar{K}^0) \leq P_{LR}(K^0, K_L) + P_{LR}(K_S, K_S) + P_{LR}(K_L, \bar{K}^0) . \quad (20.1.27)$$

For the case of QM, substituting equations (20.1.19) - (20.1.22) into the inequality (20.1.27) and assuming  $\varphi = 0$ , we have

$$\frac{(2 + R)^2}{4(2 + R^2)} \leq \frac{(1 + R)^2}{2(2 + R^2)} + 0 + \frac{(1 + R)^2}{2(2 + R^2)} . \quad (20.1.28)$$

The above inequality is apparently violated by QM while  $R = -1$ . In Ref. [527] we generalized the method used in [525] to heavy quarkonium. This straightforward generalization however leads to some new observations of a nonlocal property. Upon further

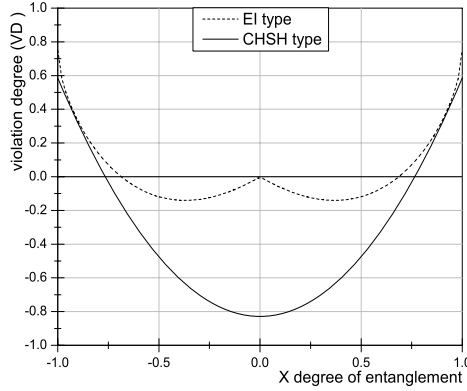


Figure 20.3: The violation degree of the Bell inequalities (the dashed line for EI type and the solid line for CHSH type) in terms of the entanglement. Here, for the sake of transparency, we make the coordinate transformation  $C = 1 - x^2$ . Magnitudes of  $VD$  less than zero indicate the breaking of the BIs.

analyzing the  $R$  value when it produces a violation of Eq.(20.1.28), we find out that there exists a period of time during which the violation becomes larger via its time evolution. In quantum information theory the entanglement property of two pure state qubits is well understood and can be characterized by the concurrence  $C$  [528]. We can also see how the degree of entanglement evolves with time. According to the definition of concurrence we have:

$$C(J/\psi) = |\langle J/\psi | \widetilde{J/\psi} \rangle| = \frac{2}{2 + |R|^2} = \frac{2}{2 + |r|^2 e^{(\Gamma_S - \Gamma_L)T}}, \quad (20.1.29)$$

where  $|\widetilde{J/\psi}\rangle = \sigma_y^1 \sigma_y^2 |(J/\psi)^*\rangle$  and  $\sigma^1, \sigma^2$  are Pauli matrices.  $C$  ranges from null to unity for no entanglement and full entanglement. Equation (20.1.29) shows that the state becomes less entangled as time evolves. So, considering Ref. 20.1.28 we realize that the violation does not decrease monotonically with the degree of entanglement. To clarify this phenomenon we express the degree of violation ( $VD$ ) of the inequalities (left side minus the right side) in terms of  $C$  and compare it with the usual CHSH inequality [505]. In Fig. 20.3, the differing  $VD$  behavior of CHSH's and EI's inequalities are presented. For the CHSH case, the  $VD_{CHSH}$  is obtained by the same condition since the maximal violation happens at full entanglement, *i.e.*  $C = 1$ . We have:

$$VD_{CHSH} = \sqrt{2}(1 + C) - 2. \quad (20.1.30)$$

In fact, the above  $VD_{CHSH}$  can be deduced from the results given in Refs. [529, 530, 531]. For the EI case,

$$VD_{EI} = \frac{-3(1 - C) + 2\sqrt{2}\sqrt{C - C^2}}{4}. \quad (20.1.31)$$

Here, in EI the counterintuitive quantum effect shows up, *i.e.* less entanglement corresponds to a larger  $VD$  in some regions (see Fig.20.3). It is worth noting that with the

time evolution, when  $R$  becomes less than  $-\frac{4}{3}$ , both QM and LHVTs satisfy the inequality (20.1.27). Thus given a certain asymmetrically entangled state, the Hardy state [506], in the region of  $R \in [-4/3, 0]$  QM and LHVTs can be distinguished from EI.

In a recent work [532], an improved measurement of branching ratio  $B(J/\psi \rightarrow K_S^0 K_L^0) = (1.80 \pm 0.04 \pm 0.13) \times 10^{-4}$  is reported, which is significant larger than previous ones. Entangled kaon pairs from heavy quarkonium decays can be easily space-like separated. Thus, a little evolution time  $T$  will guarantee the locality condition [527], and enable us to test the full range of  $R$  and the peculiar quantum effects. It is promising and worthwhile to implement such tests in future tau-charm factories, because of both the experimental feasibility and their theoretical importance.

## 20.2 Special topics in $B\bar{B}$ final states<sup>2</sup>

In this section we discuss the study of  $SU(3)$  flavor symmetry breaking effects, searches for  $CP$  violation, exotic states, bound states, tests of the Bell inequality and other special topics in hadronic decays of charmonium states.

### 20.2.1 $SU(3)$ flavor symmetry breaking effects

At the level of  $SU(3)$  symmetry, only  $J/\psi$  baryonic decays of the type

$$J/\psi \rightarrow B_1 \bar{B}_1, B_8 \bar{B}_8, B_{10} \bar{B}_{10}$$

are allowed, with a single decay amplitude for each given decay family if electromagnetic contributions are neglected. However, the MarkII collaboration first published experimental results showing that a large  $SU(3)$  flavor symmetry breaking takes place in the  $J/\psi$  decays into baryon pairs [533], especially, into octet-decuplet baryon pairs. This was confirmed by the DM2 [534] and MarkIII [535] collaborations. Table 20.1 summarizes the DM2 results on the  $J/\psi$  SU(2) or SU(3) forbidden decays. For the  $J/\psi \rightarrow \Lambda \bar{\Lambda} \pi^0$ , it seems that a large contamination from  $J/\psi \rightarrow \Sigma \bar{\Lambda} \pi^0$  would lead to a small branching fraction. These  $SU(3)$  flavor symmetry decays will be studied at *BES-III*.

As discussed in the literature,  $SU(3)$ -flavor symmetry can be broken in several ways:

- One photon processes, i.e.  $c\bar{c} \rightarrow \gamma \rightarrow B_{10} \bar{B}_8$ . Because the direct product  $8 \otimes \bar{10}$  contains an octet contribution, this is possible via the octet component of the photon. It also occurs via the processes  $c\bar{c} \rightarrow gg\gamma \rightarrow B_{10} \bar{B}_8$ , which represent a direct electromagnetic decay. As calculated in the framework of pQCD, the ratio  $R$  for this decay amplitude to that for the three-gluon decay is a few percent,  $R_{QCD} = -4\alpha/(5\alpha_s)$  [536]; in the framework of vector meson dominance,  $R_{VMD} = 24\alpha/(5\alpha_s)$ .
- A second  $SU(3)$  breaking mechanism arises from the mass difference of light and strange quarks. The decay chain  $c\bar{c} \rightarrow (u\bar{u} + d\bar{d} + s\bar{s})_1 \rightarrow \alpha(u\bar{u} + d\bar{d})_{1\oplus 8} + \beta(s\bar{s})_{1\oplus 8} \rightarrow B_{10} \bar{B}_8$  can occur if the coupling  $\alpha$  and  $\beta$  differ. The mass breaking can equivalently be described by an octet [553] or 27-plet representation to the  $J/\psi$  wave function [534].

<sup>2</sup>Xiaohu Mo, Ronggang Ping and Changzheng Yuan

Table 20.1: Summary of  $J/\psi$  SU(2) and SU(3) forbidden decay mode measurements.

Decay Mode	Number of events	Branching fraction ( $\times 10^{-4}$ )
SU(3) forbidden decay modes		
$J/\psi \rightarrow \Sigma(1385)^-\bar{\Sigma}^+$	$74 \pm 8$	$3.0 \pm 0.3 \pm 0.8$
$J/\psi \rightarrow \Sigma(1385)^+\bar{\Sigma}^-$	$77 \pm 9$	$3.4 \pm 0.4 \pm 0.8$
$J/\psi \rightarrow \Xi(1530)^-\bar{\Xi}^+$	$80 \pm 9$	$5.9 \pm 0.7 \pm 1.5$
$J/\psi \rightarrow \Xi(1530)^0\bar{\Xi}^0$	$24 \pm 5$	$3.2 \pm 0.7 \pm 1.5$
SU(2) forbidden decay modes		
$J/\psi \rightarrow \Lambda\Lambda\pi^0$	$19 \pm 4$	$2.2 \pm 0.5 \pm 0.5$
$J/\psi \rightarrow \Sigma(1385)^0\bar{\Lambda}$	13	$< 2.0(90\% CL)$
$J/\psi \rightarrow \Sigma^0\bar{\Lambda}$	11	$< 0.9(90\% CL)$
$J/\psi \rightarrow \Delta^+\bar{p}$	50	$< 1.0(90\% CL)$

- The third possible mechanism can come from intermediate states. As pointed by Genz *et al.* [554], an intermediate  $q\bar{q}$  state could lead to an apparent  $SU(3)$  violation. A generalization to multi-quark intermediate states would also make the contribution of a 27-plet possible. If the decay amplitudes are decomposed into the contributions from one-photon ( $D$ ), octet SU(3) breaking ( $D'$ ), and 27-plet terms ( $D''$ ), the ratios of branching fractions for  $J/\psi$  decays into octet-decuplet baryon pairs are given by

$$\begin{aligned}
 R_1 &= \frac{B(\Xi(1530)^0\bar{\Xi}^0)}{B(\Sigma(1385)^+\bar{\Sigma}^-)} \propto \left| \frac{2D + D' + \frac{3}{2}D''}{2D + D' - D''} \right|^2, \\
 R_2 &= \frac{B(\Xi(1530)^-\bar{\Xi}^+)}{B(\Sigma(1385)^-\bar{\Sigma}^+)} \propto \left| \frac{D' + \frac{3}{2}D''}{D' - D''} \right|^2, \\
 R_3 &= \frac{B(\Sigma(1385)^+\bar{\Sigma}^-) - B(\Sigma(1385)^-\bar{\Sigma}^+)}{B(\Xi(1530)^0\bar{\Xi}^0) - B(\Xi(1530)^-\bar{\Xi}^+)} \propto \frac{|2D + D' - D''|^2 - |D' - D''|^2}{|2D + D' + \frac{3}{2}D''|^2 - |D' + \frac{3}{2}D''|^2}.
 \end{aligned} \tag{20.2.32}$$

Octet dominance ( $D' \gg D''$ ) predicts that  $R_1 = R_2 = R_3 = 1$ , in contradiction with the measured values  $R_1 = 1.3 \pm 0.6$ ,  $R_2 = 2.8 \pm 1.0$  and  $R_3 = -0.1 \pm 0.3$ . The more sophisticated model of Körner [555], which allows for strong mass breaking effects and final state dependent electromagnetic amplitudes but neglects a 27-plet contribution, runs into similar problems. While a model allowing electromagnetic contributions is ruled out, some electromagnetic component seems to be required, since  $B(J/\psi \rightarrow \Xi^0(1530)\bar{\Xi}^0) \neq B(J/\psi \rightarrow \Xi(1530)^-\bar{\Xi}^+)$ . In the framework of the given model, the data can be well described if both electromagnetic and strong isospin breaking effects are taken into account.

### 20.2.2 $CP$ violation

The decays of  $J/\psi$  (or  $\psi(2S)$ )  $\rightarrow B_8 B_8$  ( $B_8$ : octet baryon) can be used to search for an electric dipole momentum (EDM) of baryons. A non-zero value of EDM would indicate

that  $CP$  symmetry is violated. As shown in Ref. [556], for  $J/\psi \rightarrow B(p_1)\bar{B}(p_2)$  the decay amplitudes can be parameterized as

$$\mathcal{M} = \epsilon^\mu \bar{u}(p_1) [\gamma_\mu (a + b\gamma_5) + (p_{1\mu} - p_{2\mu})(c + id\gamma_5)] v(p_2) \equiv \epsilon^\mu A_\mu, \quad (20.2.33)$$

where  $\epsilon^\mu$  is the polarization of the  $J/\psi$ . If  $CP$  is violated,  $d \neq 0$ .

From an experimental point of view, the decay  $J/\psi \rightarrow \Lambda\bar{\Lambda}$  is a good laboratory to search for an EDM of the  $\Lambda$ , since this channel has a large branching fraction ( $B(J/\psi \rightarrow \Lambda\bar{\Lambda}) = (1.54 \pm 0.19) \times 10^{-3}$ ) and can be well reconstructed with almost no background. The polarization of the  $\Lambda$  ( $\bar{\Lambda}$ ) particles are measured by analyzing the subsequent  $\Lambda(\mathbf{s}_1) \rightarrow p(\mathbf{q}_1)\pi^-$ ,  $\bar{\Lambda}(\mathbf{s}_2) \rightarrow \bar{p}(\mathbf{q}_2)\pi^+$  decays with density matrices  $\rho_\Lambda = 1 + \alpha_+ \mathbf{s}_1 \cdot \mathbf{q}_1 / |\mathbf{q}_1|$  and  $\rho_{\bar{\Lambda}} = 1 - \alpha_- \mathbf{s}_2 \cdot \mathbf{q}_2 / |\mathbf{q}_2|$ . Experimental observables  $O$  can be constructed from  $\mathbf{p}, \mathbf{q}_i$  and the electron beam direction  $\mathbf{k}$ . Their expectation values are given by

$$\langle O \rangle = \frac{\sqrt{1 - 4m^2/M^2}}{2M\Gamma(J/\psi \rightarrow \Lambda\bar{\Lambda})8\pi} \frac{1}{(4\pi)^3} \int d\Omega_p d\Omega_{q_1} d\Omega_{q_2} O \text{Tr}\{R_{ij}\rho_{ji}\rho_\Lambda\rho_{\bar{\Lambda}}\}, \quad (20.2.34)$$

where  $R_{ij} = A_i A_j^*$  and  $\rho_{ij}$  are the density matrices for  $J/\psi$  decays into  $\Lambda\bar{\Lambda}$  and  $J/\psi$  production from  $e^+e^-$ , respectively. The  $CP$ -odd observable  $A$  and  $CPT$ -even observable  $B$  are constructed as:

$$\begin{aligned} A &= \theta(\hat{p} \cdot (\hat{q}_1 \times \hat{q}_2)) - \theta(-\hat{p} \cdot (\hat{q}_1 \times \hat{q}_2)) \\ B &= \hat{p} \cdot (\hat{q}_1 \times \hat{q}_2), \end{aligned} \quad (20.2.35)$$

where  $\theta(x)$  is 1 if  $x > 0$  and 0 if  $x < 0$ . The expectation values can be expressed as:

$$\begin{aligned} \langle A \rangle &= -\frac{\alpha_-^2 \beta^2}{96M\Gamma(J/\psi \rightarrow \Lambda\bar{\Lambda})} M^2 [2m\text{Re}(da^*) + (M^2 - 4m^2)\text{Re}(dc^*)] \\ \langle B \rangle &= -\frac{48}{27\pi} \langle A \rangle. \end{aligned} \quad (20.2.36)$$

The quantity  $\langle A \rangle$  is equal to

$$\langle A \rangle = \frac{N^+ - N^-}{N^+ + N^-}, \quad (20.2.37)$$

where  $N^\pm$  indicate events with  $\text{sgn}[\mathbf{p} \cdot (\mathbf{q}_1 \times \mathbf{q}_2)] = \pm$ , respectively.

The EDM  $d_\Lambda$  of  $\Lambda$  is related to the quantity  $\langle A \rangle$  by the Lagrangian:

$$L_{\text{dipole}} = i \frac{d_\Lambda}{2} \bar{\Lambda} \sigma_{\mu\nu} \gamma_5 \Lambda F^{\mu\nu},$$

where  $F^{\mu\nu}$  is the field strength of the electromagnetic field. Exchanging a photon between the  $\Lambda$  and a  $c$  quark, the  $CP$  violating  $c - \Lambda$  interaction is expressed by

$$L_{c-\Lambda} = -\frac{2}{3M^2} ed_\Lambda (p_1^\mu - p_2^\mu) \bar{c} \gamma_\mu c \bar{\Lambda} i \gamma_5 \Lambda$$

From these relations one has  $d = -\frac{2.5}{3M^2} ed_\Lambda$ , and

$$|\langle A \rangle| = \begin{cases} 5.6 \times 10^{-3} d_\Lambda / (10^{-16} e \text{ cm}), & \text{if the } a \text{ term dominates} \\ 1.25 \times 10^{-2} d_\Lambda / (10^{-16} e \text{ cm}), & \text{if the } c \text{ term dominates.} \end{cases} \quad (20.2.38)$$

The current experimental upper bound on  $d_\Lambda$  is  $1.5 \times 10^{-16} e \text{ cm}$  [408]. If  $d_\Lambda$  indeed has a value close to its experimental upper bound, the asymmetry  $|\langle A \rangle|$  can be as large as  $10^{-2}$ . So  $\langle A \rangle$  can be used to improve the bound on  $d_\Lambda$ . If  $10^{10} J/\psi$  events are produced, one can improve the upper bound on  $d_\Lambda$  by more than an order of magnitude. The same analysis can be easily extended to  $J/\psi$  to  $\Sigma$ ,  $\Xi$ , etc.

Quantitative predictions for  $CP$  violation in hyperon decays indicate that  $A = \frac{\alpha_\Lambda + \alpha_{\bar{\Lambda}}}{\alpha_\Lambda - \alpha_{\bar{\Lambda}}}$  should be in the range  $(-2 \times 10^{-5} \sim -1 \times 10^{-4})$ . Present experimental results do not have sufficient sensitivity to observe such a small effect, but *BES-III* will have an opportunity to measure this quality. As shown by DM2 collaboration, the decay of  $J/\psi \rightarrow \Lambda\bar{\Lambda}$  can be used to look for  $CP$  violation by studies of the correlations between the  $p$  and  $\bar{p}$  momenta in the mother system frame [557]. The differential cross-section for the  $J/\psi \rightarrow \Lambda\bar{\Lambda} \rightarrow p\pi^- \bar{p}\pi^+$  decay chain can be expressed as:

$$\frac{d\Gamma}{d\cos\theta d\Omega' d\Omega''} \propto 2 \left| \frac{A_{++}}{A_{--}} \right| \sin^2\theta [1 - \alpha_\Lambda\alpha_{\bar{\Lambda}}(\cos\theta' \cos\theta'' - \sin\theta' \sin\theta'' \cos(\phi' - \phi'')] + (1 + \cos^2\theta)(1 + \alpha_\Lambda\alpha_{\bar{\Lambda}} \cos\theta' \cos\theta''), \quad (20.2.39)$$

where  $\alpha_\Lambda$  ( $\alpha_{\bar{\Lambda}}$ ) is the  $\Lambda$  ( $\bar{\Lambda}$ ) decay constant and  $A_{\lambda_1\lambda_2}$  and  $\theta$  are the helicity amplitude and polar angle of the out-going  $\Lambda$  for the  $J/\psi \rightarrow \Lambda\bar{\Lambda}$ , respectively. The angular variables  $\Omega'$  and  $\Omega''$  are defined as shown in Fig. 20.4. Using this equation, the quantity  $\alpha_\Lambda\alpha_{\bar{\Lambda}}$  can be obtained experimentally.

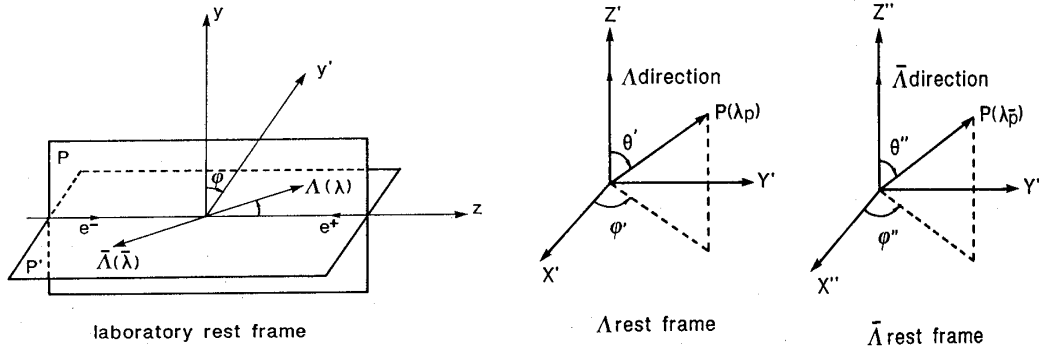


Figure 20.4: The definition of helicity system for  $J/\psi \rightarrow \Lambda\bar{\Lambda}$ ,  $\Lambda(\bar{\Lambda}) \rightarrow p\pi^- (\bar{p}\pi^+)$ .

As Törnqvist [558] first demonstrated, the decays  $\eta_c$  and  $J/\psi \rightarrow \Lambda\bar{\Lambda}$  are experimental realizations of Bell's conceptual proposition for testing Quantum Mechanics versus local hidden variable theories. The initial state is well known and due to parity symmetry breaking, the decay of the  $\Lambda$  serves as a spin analyser. The proton direction plays the same part that the direction of external polarimeter in classical experiments with photons [559]. The important quantity is the scalar product of  $p$  and  $\bar{p}$  3-momentum vectors in the  $\Lambda$  and  $\bar{\Lambda}$  rest frames. The differential cross-section of the  $\eta_c \rightarrow \Lambda\bar{\Lambda}$  decay is directly proportional to  $\vec{a} \cdot \vec{b}$ . So it is the most sensitive test of Quantum Mechanics since this scalar product can be compared to Bell's inequality. The decay  $\eta_c \rightarrow \Lambda\bar{\Lambda}$  was recently observed by the Belle Collaboration [560] with a branching fraction of  $(8.7 \pm 3.7) \times 10^{-4}$ . This would correspond to a  $\eta_c \rightarrow \Lambda\bar{\Lambda}$  sample of about 100,000 events in a 10 billion  $J/\psi$  data sample, it will be a

very suitable sample for this study. For the  $J/\psi \rightarrow \Lambda\bar{\Lambda}$  case, Tornqvist reformulated the differential cross-section as:

$$\frac{d\Gamma}{d\cos\theta d\Omega' d\Omega''} \propto 2(1 - \frac{p_\Lambda^2}{E_\Lambda^2} \sin^2\theta)(1 - \alpha_\Lambda^2 a_n b_n) + \frac{p_\Lambda^2}{E_\Lambda^2} \sin^2\theta[1 - \alpha_\Lambda^2(\vec{a} \cdot \vec{b} - 2a_x b_x)], \quad (20.2.40)$$

where  $\vec{a}$  and  $\vec{b}$  are the proton and antiproton momentum, respectively in the  $\Lambda$  ( $\bar{\Lambda}$ ) rest frame,  $x$  is the direction orthogonal to the  $\Lambda\bar{\Lambda}$  direction and to the  $e^+e^-$  beam axis and  $\vec{n}$  is an axis defined to take into account the suppression of 0-spin projection in the  $J/\psi$  decays. The terms containing  $a_n b_n$  or  $a_x b_x$  only reduce the sensitivity of the test since they do not depend on the nature of the theory, and they play the same role as hidden parameters [558]. The contribution of the  $\vec{a} \cdot \vec{b}$  term is important for the test of Quantum Mechanics. Unfortunately  $p_\Lambda^2/E_\Lambda^2$  from  $J/\psi$  decay is only equal to 0.48 and  $\alpha_\Lambda^2$  is 0.412; this reduces the contribution of the  $\vec{a} \cdot \vec{b}$  term to the experimental measurement.

The DM2 collaboration [557] measured the  $\Lambda\bar{\Lambda}$  decay parameter asymmetry to be:

$$A = \frac{\alpha_\Lambda + \alpha_{\bar{\Lambda}}}{\alpha_\Lambda - \alpha_{\bar{\Lambda}}} = 0.01 \pm 0.10$$

with 1077 observed  $J/\psi \rightarrow \Lambda\bar{\Lambda}$  events. The precision of this measurement does not permit one to conclude anything about  $CP$  violation; with  $10^{10}$   $J/\psi$  events, the sensitivity is expected to improve to  $8 \times 10^{-4}$ .

The measurement of the correlation between the proton and antiproton in  $J/\psi \rightarrow \Lambda\bar{\Lambda}$  decay is associated with the test of Bell's inequality. For example, in the  $\eta_c \rightarrow \Lambda\bar{\Lambda} \rightarrow p\bar{p}\pi^+\pi^-$  decay, the spin correction between the two nucleon predicted by Quantum Mechanics can be expressed by [558]:

$$I(\vec{a}, \vec{b}) \propto 1 + \alpha^2 \vec{a} \cdot \vec{b}, \quad (20.2.41)$$

while a hidden measurement of  $\Lambda$  polarization before the decay would reduce the slope to  $\alpha^2/3$ , *i.e.*

$$I(\vec{a}, \vec{b}) \propto 1 + \frac{\alpha^2}{3} \vec{a} \cdot \vec{b}. \quad (20.2.42)$$

Using invariance under rotations and reflections, one can derive a special bound for Bell's inequality:

$$|E(\theta)| \leq 1 - \frac{2}{\pi} \theta, \quad 0 \leq \theta \leq \pi.$$

Figure 20.5 shows the distribution in the angle  $\theta$  between two pions as predicted by Quantum Mechanics and the area bounded by Bell's inequality.

### 20.2.3 Exotic states

As is well known, in addition to conventional  $q\bar{q}$  mesons and  $qqq$  baryons, QCD theory also predicts the existence of multiquark states, hybrid states and other exotic states. Searching for such exotic states has been attempted for a long time, but none are established experimentally. One of the difficulties in identifying exotic states is the need to find signature properties that distinguish them from the common states or get information about their mixing. For this it is important for experimentalists to collaborate

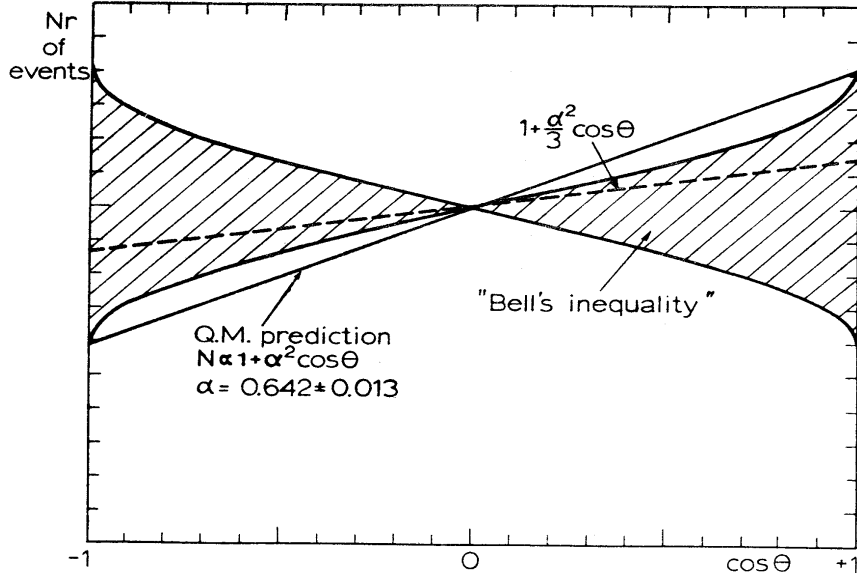


Figure 20.5: The distribution in the angle  $\theta$  between the  $\pi^+$  and the  $\pi^-$  as predicted by Quantum Mechanics (solid line), and if a "hidden"  $\Lambda$  polarization measurement is done before the decay (dashed line). The shaded area gives the domain where the inequality is satisfied.

closely with theoretical physicists. Hadronic spectroscopy will continue to be a key tool to search for  $N^*$  states (see the section of "Baryon spectroscopy") and exotic states. Various models and methods have been used to predict the spectrum of hybrid mesons/baryons, such as the bag model, QCD sum rule, the flux tube model, and so on. Though each model assumes a particular description of excited glue, fortunately they often reach similar conclusions regarding the quantum numbers and approximate masses of these states. For instance, the predictions on the light hybrid mesons are in good agreement with each other, with the so-called exotic number  $J^{PC} = 1^{-+}$  states having masses about 1.5-2.0 GeV. In the baryon sector, the Roper resonance, *i.e.* the  $N^*(1440)$  has been suggested as a potential candidate for a hybrid baryon for a long time.

As shown in Ref. [561],  $J/\psi$  decays provide an excellent place for studying the Roper resonance. Using  $58 \times 10^6$   $J/\psi$  decays, the  $N^*(1440)$  is clearly seen with a statistical significance of  $11\sigma$ . For the identification of the Roper resonance as a hybrid state, information on transition amplitudes from partial wave analyses will play an important role at *BES-III*. As demonstrated in Ref. [562], if the Roper resonance is assigned as a pure hybrid state, numerical results show that the ratios  $\Gamma(J/\psi^{(\Lambda)} \rightarrow \bar{p}N^*)/\Gamma(J/\psi^{(\Lambda)} \rightarrow \bar{p}p) < 2\%$ , and  $\Gamma(J/\psi^{(\Lambda)} \rightarrow \bar{N}^*N^*)/\Gamma(J/\psi^{(\Lambda)} \rightarrow \bar{p}p) < 0.2\%$ , and their angular distribution parameters are  $\alpha_* = 0.42 \sim 0.57$  and  $\alpha_{**} = (-0.1) - (-0.9)$ , respectively. However, when the Roper resonance is assumed to be a common  $2S$  state, the results are quite different, with  $\Gamma(J/\psi^{(\Lambda)} \rightarrow \bar{p}N^*)/\Gamma(J/\psi^{(\Lambda)} \rightarrow \bar{p}p) = 2.0 \sim 4.5$ , and  $\Gamma(J/\psi^{(\Lambda)} \rightarrow \bar{N}^*N^*)/\Gamma(J/\psi^{(\Lambda)} \rightarrow \bar{p}p) = 3.2 \sim 22.0$ , and with the angular distribution parameter  $\alpha_* = 0.22 \sim 0.70$ ,  $\alpha_{**} = 0.06 \sim 0.08$ . This implies that, not only the dynamics of three gluons and created quarks, but also the structure of the final cluster state, *i.e.*  $|qqq\rangle$  or  $|qqgg\rangle$ , play important roles in the evaluation of the amplitudes in these decay processes.

So it is suggestive that an accurate measurement of the decay widths and angular distributions of these channels may provide a novel tool to probe the structure of the Roper resonance. If the Roper resonance is assumed to be a mixture of a pure quark state  $|qqq\rangle$  with a hybrid state  $|qqg\rangle$  with a mixing parameter  $\delta$ , the results show that the hybrid constituent makes a large contribution to the decay width of the  $J/\psi$  into  $\bar{p}N^*(1440)$  and  $\bar{N}^*(1440)N^*(1440)$ .

In a search for the pentaquark state  $\Theta(1540)^+$  in  $J/\psi$  and  $\psi(2S)$  decays into  $p\bar{n}K_S^0K^-$  and  $\bar{p}nK_S^0K^+$  with 14 million  $\psi(2S)$  and 58 million  $J/\psi$  events accumulated at the BESII detector, no  $\Theta(1540)$  signal events are observed, and upper limits are set for  $\mathcal{B}(\psi(2S) \rightarrow \Theta\bar{\Theta} \rightarrow K_S^0 p K^- \bar{n} + K_S^0 \bar{p} K^+ n) < 0.84 \times 10^{-5}$  and  $\mathcal{B}(J/\psi \rightarrow \Theta\bar{\Theta} \rightarrow K_S^0 p K^- \bar{n} + K_S^0 \bar{p} K^+ n) < 1.1 \times 10^{-5}$  at the 90% confidence level [563]. So far there have been a number of other high statistics experiments, none of which have found any evidence for the  $\Theta^+$ ; all attempts to confirm the two other claimed pentaquark states have led to negative results. As reviewed by Particle Data Group 2006, *"The conclusion that Pentaquarks in general, and the  $\Theta^+$ , in particular, do not exist, appears compelling."*

### 20.2.4 Meson-nucleon bound states

Searching for nucleon-nucleon and meson-nucleon bound states is an intriguing problem in studies of the nuclear interaction. The recent discoveries of near-threshold baryon-anitbaryon enhancements, as discussed above, motivates searches for other possible bound states. In this section, we first introduce some ideas on such possible bound states from the point view of nuclear physics, then turn to ways to search for them at *BES-III*.

The idea of explaining the interaction between nucleons at the quark level was put forth three decades ago [564]. Resorting to the quark and gluon theory, the nucleon interaction at short distances which had been credited to vector-meson exchanges could then be interpreted as a manifestation of diquark-diquark and quark-quark interactions. Along these lines, a QCD van der Waals force was introduced to describe a special kind of bound states – charmonium-nucleon bound states [565], say an  $\eta_c$ - $N$  or a  $J/\psi$ - $N$  bound state. In the QCD picture, the nuclear forces are identified with the residual strong color interactions due to quark interchange and multiple-gluon exchange. The peculiar feature of charmonium-nucleon bound state lies in the fact that because of the distinct flavors of the quarks involved in the charmonium-nucleon interaction there is no quark exchange to first order in the elastic processes and, therefore, no single-meson-exchange potential from which to build a usual nuclear potential. The nuclear interaction in this case is purely gluonic and, thus, of a distinctive nature from the ordinary nuclear forces. The production of a charmonium-nucleon bound state would be the first realization of a hadronic nucleus with exotic components bound by a purely gluonic potential. In Ref. [565], a nonrelativistic Yukawa-type attractive potential  $V_{(Q\bar{Q})A} = -\alpha e^{-\mu r}/r$  was utilized to characterize the QCD van der Waals interaction. Estimates indicated that the QCD van der Waals interaction due to multiple-gluon exchange can provide a kind of attractive nuclear force capable of binding heavy quarkonia to nuclei.

Following the above idea, the possibility of a  $\phi$ - $N$  bound state was studied in Ref. [566]. Similar to the charmonium state, here the  $\phi$  meson is almost a pure  $s\bar{s}$  state, so one could expect that the attractive QCD van der Waals force dominates the  $\phi$ - $N$  interaction. Using a variational method and following Ref. [565] to assume  $V_{(Q\bar{Q})N} = -\alpha e^{-\mu r}/r$ , it was

found [566] that a  $\phi$ - $N$  bound state is possible, with a binding energy of around 1.8 MeV.

Recently, a  $\phi$ - $N$  bound state structure with spin-parity  $J^P = 3/2^-$  and  $J^P = 1/2^-$  were dynamically studied in both the chiral  $SU(3)$  quark model and the extended chiral  $SU(3)$  quark model [567]. In the chiral  $SU(3)$  quark model, the quark-quark interaction containing confinement, one gluon exchange (OGE) and boson exchange stemming from scalar and pseudoscalar nonets, and short range quark-quark interactions provided by OGE and quark exchange effects are included. It remains a controversial problem for low-energy hadron physics whether gluons or Goldstone bosons are the proper effective degree of freedom in addition to the constituent quarks. Thus the  $SU(3)$  quark model has been extended to include the coupling of the quark and vector chiral fields, and the role of OGE in the short range quark-quark interaction is then nearly replaced by the vector meson exchanges. This so-called extended chiral  $SU(3)$  quark model can successfully reproduce as many physics features as does of the chiral  $SU(3)$  quark model. Therefore, both models are adopted to study  $\phi$ - $N$  bound state, where  $N$  and  $\phi$  are treated as two clusters and the corresponding resonating group method (RGM) equation are solved. The calculation results indicate the mechanisms of the quark-quark short-range interaction are quite different for the two chiral models. Moreover, one result from the extended chiral  $SU(3)$  quark model indicates the existence of a  $\phi$ - $N$  bound state.

Next we turn to experiment aspects of searching for a  $\phi$ - $N$  bound state in *BES-III*. The calculation [568] gives  $M_{\phi N} \simeq 1950 \sim 1957$  MeV and  $\Gamma_{\phi N} \simeq 4.4$  MeV, the intrinsic width of the  $\phi$  meson. The invariant mass of the  $\phi$  reconstructed from two kaons will be less than that of free  $\phi$  due to the existence of some bounding energy. This mass deficit can be understood as a result of the fact that the  $\phi$  decays off its energy shell when bound to the nucleus.

Since the total mass of the  $\phi N$  system and a  $\bar{N}$  is close to 3.0 GeV, the production of such state in  $J/\psi$  decays will be suppressed due to small phase space, however, it could be produced in  $\psi'$  decays, or from  $\chi_{cJ}$  decays with much larger phase space, although with fewer statistics.

The decays of the  $\phi N$  bound state could be  $K\bar{K}N$ , with a  $K\bar{K}$  mass that is below the  $\phi$  resonance. Experimentally, one expects to see a shoulder on the low-mass side of the  $\phi$  meson peak or another narrow peak below the  $\phi$  resonance. In principle, there could be interference between  $\phi \rightarrow K\bar{K}$  and the  $K\bar{K}$  from  $\phi N$  bound state decays, this may make the identification of the bound state difficult.

The annihilation of the  $s\bar{s}$  quark inside the  $\phi$  meson is not small, so another way of searching for the  $\phi N$  bound state is through its decay into  $\pi^+\pi^-\pi^0 + N$ , considering the large branching fraction of  $\phi \rightarrow \pi^+\pi^-\pi^0$ , with even smaller phase space to  $K\bar{K}N$ , the decay rate for the  $\phi N$  bound state to  $\pi^+\pi^-\pi^0 + N$  could even be larger. However, the background may be more serious in the  $\pi^+\pi^-\pi^0 + N$  mode.

# Bibliography

- [1] N. Brambilla *et al.*, *Heavy quarkonium physics*, CERN-2005-005, (CERN, Geneva, 2005) [arXiv:hep-ph/0412158]; See also the talks at the last QWG meeting at BNL available at <http://www.qwg.to.infn.it/>.
- [2] W. E. Caswell and G. P. Lepage, Phys. Lett. B **167**, 437 (1986).
- [3] G. P. Lepage, L. Magnea, C. Nakhleh, U. Magnea and K. Hornbostel, Phys. Rev. D **46**, 4052 (1992) [arXiv:hep-lat/9205007].
- [4] G. T. Bodwin, E. Braaten and G. P. Lepage, Phys. Rev. D **51**, 1125 (1995) [Erratum-ibid. D **55**, 5853 (1997)] [arXiv:hep-ph/9407339].
- [5] A. Pineda and J. Soto, Nucl. Phys. Proc. Suppl. **64**, 428 (1998) [arXiv:hep-ph/9707481].
- [6] N. Brambilla, A. Pineda, J. Soto and A. Vairo, Nucl. Phys. B **566**, 275 (2000) [arXiv:hep-ph/9907240].
- [7] N. Brambilla, A. Pineda, J. Soto and A. Vairo, Rev. Mod. Phys. **77**, 1423 (2005) [arXiv:hep-ph/0410047].
- [8] M. E. Luke and A. V. Manohar, Phys. Lett. B **286**, 348 (1992) [arXiv:hep-ph/9205228].
- [9] Y. Q. Chen, Phys. Lett. B **317**, 421 (1993).
- [10] R. Sundrum, Phys. Rev. D **57**, 331 (1998) [arXiv:hep-ph/9704256].
- [11] M. Finkemeier, H. Georgi and M. McIrvin, Phys. Rev. D **55**, 6933 (1997) [arXiv:hep-ph/9701243].
- [12] Y. Q. Chen, Phys. Rev. D **69**, 096001 (2004) [arXiv:hep-ph/0207333].
- [13] N. Brambilla, D. Gromes and A. Vairo, Phys. Lett. B **576**, 314 (2003) [arXiv:hep-ph/0306107].
- [14] M. Gremm and A. Kapustin, Phys. Lett. B **407**, 323 (1997) [arXiv:hep-ph/9701353].
- [15] E. Braaten and Y. Q. Chen, Phys. Rev. D **54**, 3216 (1996) [arXiv:hep-ph/9604237].
- [16] A. Pineda, Phys. Rev. D **65**, 074007 (2002); A. Pineda and J. Soto, Phys. Lett. B **495**, 323 (2000).

- [17] M. E. Luke, A. V. Manohar and I. Z. Rothstein, Phys. Rev. D **61**, 074025 (2000) [arXiv:hep-ph/9910209]; A. H. Hoang and I. W. Stewart, Phys. Rev. D **67**, 114020 (2003) [arXiv:hep-ph/0209340]. A. V. Manohar and I. W. Stewart, Phys. Rev. D **62**, 014033 (2000) [arXiv:hep-ph/9912226].
- [18] N. Brambilla, A. Pineda, J. Soto and A. Vairo, Phys. Rev. D **63**, 014023 (2001) [arXiv:hep-ph/0002250].
- [19] A. Pineda and A. Vairo, Phys. Rev. D **63**, 054007 (2001) [Erratum-ibid. D **64**, 039902 (2001)] [arXiv:hep-ph/0009145].
- [20] G. S. Bali, Phys. Rept. **343**, 1 (2001) [arXiv:hep-ph/0001312].
- [21] N. Brambilla and A. Vairo, arXiv:hep-ph/9904330.
- [22] N. Brambilla, A. Pineda, J. Soto and A. Vairo, Phys. Rev. D **60**, 091502 (1999) [arXiv:hep-ph/9903355].
- [23] F. A. Chishtie and V. Elias, Phys. Lett. B **521**, 434 (2001) [arXiv:hep-ph/0107052].
- [24] N. Brambilla, X. Garcia i Tormo, J. Soto and A. Vairo, arXiv:hep-ph/0610143.
- [25] A. Pineda, J. Phys. G **29**, 371 (2003) [arXiv:hep-ph/0208031].
- [26] B. A. Kniehl, A. A. Penin, Y. Schroder, V. A. Smirnov and M. Steinhauser, Phys. Lett. B **607**, 96 (2005) [arXiv:hep-ph/0412083].
- [27] G. S. Bali and A. Pineda, Phys. Rev. D **69**, 094001 (2004) [arXiv:hep-ph/0310130].
- [28] Y. Koma, M. Koma and H. Wittig, Phys. Rev. Lett. **97**, 122003 (2006) [arXiv:hep-lat/0607009].
- [29] Y. Koma and M. Koma, arXiv:hep-lat/0609078.
- [30] N. Brambilla, arXiv:hep-ph/9809263; M. Baker, N. Brambilla, H. G. Dosch and A. Vairo, Phys. Rev. D **58**, 034010 (1998) [arXiv:hep-ph/9802273]. N. Brambilla and A. Vairo, Phys. Rev. D **55**, 3974 (1997) [arXiv:hep-ph/9606344]. N. Brambilla, P. Consoli and G. M. Prosperi, Phys. Rev. D **50**, 5878 (1994) [arXiv:hep-th/9401051].
- [31] A. X. El-Khadra and M. Luke, Ann. Rev. Nucl. Part. Sci. **52**, 201 (2002) [arXiv:hep-ph/0208114].
- [32] A. Pineda, JHEP **0106**, 022 (2001) [arXiv:hep-ph/0105008].
- [33] N. Brambilla, Y. Sumino and A. Vairo, Phys. Rev. D **65**, 034001 (2002) [arXiv:hep-ph/0108084].
- [34] M. Eidemüller, Phys. Rev. D **67**, 113002 (2003) [arXiv:hep-ph/0207237].
- [35] A. A. Penin and M. Steinhauser, Phys. Lett. B **538**, 335 (2002) [arXiv:hep-ph/0204290].

- [36] T. Lee, JHEP **0310**, 044 (2003) [arXiv:hep-ph/0304185].
- [37] C. Contreras, G. Cvetic and P. Gaete, Phys. Rev. D **70**, 034008 (2004) [arXiv:hep-ph/0311202].
- [38] A. Pineda and A. Signer, Phys. Rev. D **73**, 111501 (2006) [arXiv:hep-ph/0601185].
- [39] N. Brambilla, Y. Sumino and A. Vairo, Phys. Lett. B **513**, 381 (2001) [arXiv:hep-ph/0101305].
- [40] N. Brambilla, X. Garcia i Tormo, J. Soto and A. Vairo “Extraction of  $\alpha_s$  from radiative  $Y(1S)$  decays” IFUM-886-FT
- [41] A. H. Hoang, A. V. Manohar, I. W. Stewart and T. Teubner, Phys. Rev. D **65**, 014014 (2002) [arXiv:hep-ph/0107144].
- [42] M. Foster and C. Michael [UKQCD Collaboration], Phys. Rev. D **59**, 094509 (1999) [arXiv:hep-lat/9811010].
- [43] K. J. Juge, J. Kuti and C. Morningstar, Phys. Rev. Lett. **90**, 161601 (2003) [arXiv:hep-lat/0207004].
- [44] A. Vairo, arXiv:hep-ph/0611310.
- [45] M. A. Sanchis-Lozano, arXiv:hep-ph/0503266.
- [46] J. J. Aubert *et al.* [E598 Collaboration], Phys. Rev. Lett. **33**, 1404 (1974).
- [47] J. E. Augustin *et al.* [SLAC-SP-017 Collaboration], Phys. Rev. Lett. **33**, 1406 (1974).
- [48] T. Appelquist and H. D. Politzer, Phys. Rev. Lett. **34**, 43 (1975).
- [49] A. De Rujula and S. L. Glashow, Phys. Rev. Lett. **34**, 46 (1975).
- [50] T. Appelquist, A. De Rujula, H. D. Politzer and S. L. Glashow, Phys. Rev. Lett. **34**, 365 (1975).
- [51] E. Eichten, K. Gottfried, T. Kinoshita, J. B. Kogut, K. D. Lane and T. M. Yan, Phys. Rev. Lett. **34**, 369 (1975) [Erratum-ibid. **36**, 1276 (1976)].
- [52] W.-M. Yao *et al.* (Particle Data Group), J. Phys. G **33**, 1 (2006)
- [53] S. Godfrey and N. Isgur, Phys. Rev. D **32**, 189 (1985).
- [54] T. Barnes, S. Godfrey and E. S. Swanson, Phys. Rev. D **72**, 054026 (2005) [arXiv:hep-ph/0505002].
- [55] C. Quigg, arXiv:hep-ph/0403187.
- [56] R. S. Galik, arXiv:hep-ph/0408190.
- [57] N. Brambilla *et al.*, arXiv:hep-ph/0412158.

- [58] K. K. Seth, arXiv:hep-ex/0504052.
- [59] E. S. Swanson, Phys. Rept. **429**, 243 (2006) [arXiv:hep-ph/0601110].
- [60] J. L. Rosner, arXiv:hep-ph/0612332.
- [61] K. K. Seth, arXiv:hep-ex/0611035.
- [62] M. Okamoto *et al.* [CP-PACS Collaboration], Phys. Rev. D **65**, 094508 (2002) [arXiv:hep-lat/0112020].
- [63] M. di Pierro *et al.*, Nucl. Phys. Proc. Suppl. **129**, 340 (2004) [arXiv:hep-lat/0310042].
- [64] T. Umeda, Prog. Theor. Phys. Suppl. **151**, 149 (2003).
- [65] J. Dudek, R. Edwards, N. Mathur and D. Richards, arXiv:hep-lat/0611006.
- [66] E. S. Ackleh, T. Barnes and F. E. Close, Phys. Rev. D **46**, 2257 (1992).
- [67] E. S. Ackleh and T. Barnes, Phys. Rev. D **45**, 232 (1992).
- [68] D.M. Asner *et al.* (CLEO Collaboration), Phys. Rev. Lett. **92**, 142001 (2004) [arXiv:hep-ex/0312058].
- [69] T. Barnes and S. Godfrey, Phys. Rev. D **69**, 054008 (2004) [arXiv:hep-ph/0311162].
- [70] S. Choe *et al.* (QCD-TARO Collaboration), hep-lat/0307004.
- [71] J. Gaiser *et al.* (Crystal Ball Collaboration), Phys. Rev. D **34**, (1986) 711.
- [72] M. Andreotti *et al.* (E835 Collaboration), Nucl. Phys. B **717**, (2005) 34.
- [73] Ryan Mitchell (CLEOc Collaboration), Plenary talk at QWG 2007, Oct17-20, DESY, Hamburg, Germany.
- [74] P. Rubin *et al* (CLEO Collaboration), Phys. Rev. D **72** (2005) 092004; J.L. Rosner *et al.* (CLEO Collaboration), Phys. Rev. Lett. **95** (2005) 102003. Preliminary results from a larger data sample were reported by K. Seth at QWG 2007, Oct17-20, DESY, Hamburg, Germany.
- [75] C. Patrignani *et al.*, (E835 Collaboration) Nucl. Phys. Proc. Suppl., **142** (2005) 98.
- [76] Y.-Q. Chen and R.J. Oakes, Phys. Rev. D **53** (1996) 5051.
- [77] M.B. Voloshin and L.B. Okun, JETP Lett. **23**, 333 (1976) [Pisma Zh. Eksp. Teor. Fiz. **3**, 369 (1976)].
- [78] A. De Rújula, H. Georgi and S.L. Glashow, Phys. Rev. Lett. **38**, 317 (1977).
- [79] S. Iwao, Lett. Nuovo Cim. **28**, 305 (1980).

- [80] S. K. Choi *et al.* [Belle Collaboration], Phys. Rev. Lett. **91**, 262001 (2003) [arXiv:hep-ex/0309032].
- [81] K. Abe *et al.* [Belle Collaboration], arXiv:hep-ex/0505038.
- [82] N. A. Tornqvist, arXiv:hep-ph/0308277.
- [83] F. E. Close and P. R. Page, Phys. Lett. B **578**, 119 (2004) [arXiv:hep-ph/0309253].
- [84] E. S. Swanson, Phys. Lett. B **588**, 189 (2004) [arXiv:hep-ph/0311229].
- [85] N. A. Tornqvist, Phys. Lett. B **590**, 209 (2004) [arXiv:hep-ph/0402237].
- [86] K. Abe *et al.* [Belle Collaboration], arXiv:hep-ex/0505037.
- [87] J. J. Dudek, R. G. Edwards and D. G. Richards, Phys. Rev. D **73**, 074507 (2006) [arXiv:hep-ph/0601137].
- [88] C. W. Bernard *et al.* [MILC Collaboration], Phys. Rev. D **56**, 7039 (1997) [arXiv:hep-lat/9707008].
- [89] Z. H. Mei and X. Q. Luo, Int. J. Mod. Phys. A **18**, 5713 (2003) [arXiv:hep-lat/0206012].
- [90] X. Liao and T. Manke, arXiv:hep-lat/0210030.
- [91] G. S. Bali, Eur. Phys. J. A **19**, 1 (2004) [arXiv:hep-lat/0308015].
- [92] X. Q. Luo and Y. Liu, Phys. Rev. D **74**, 034502 (2006) [Erratum-ibid. D **74**, 039902 (2006)] [arXiv:hep-lat/0512044].
- [93] T. Barnes, F. E. Close and E. S. Swanson, Phys. Rev. D **52**, 5242 (1995) [arXiv:hep-ph/9501405].
- [94] B. Aubert *et al.* [BABAR Collaboration], Phys. Rev. Lett. **95**, 142001 (2005) [arXiv:hep-ex/0506081].
- [95] Q. He *et al.* [CLEO Collaboration], Phys. Rev. D **74**, 091104 (2006) [arXiv:hep-ex/0611021].
- [96] K. Abe *et al.* [Belle Collaboration], arXiv:hep-ex/0612006.
- [97] B. Aubert *et al.* [BABAR Collaboration], Phys. Rev. D **73**, 011101 (2006) [arXiv:hep-ex/0507090].
- [98] F. E. Close and P. R. Page, Phys. Lett. B **628**, 215 (2005) [arXiv:hep-ph/0507199].
- [99] UKQCD Collab. (C. McNeile, C. Michael and P. Pennanen), Phys. Rev. D **65**, 094505 (2002) [arXiv:hep-lat/0201006].
- [100] K. Abe *et al.* (Belle Collaboration), Phys. Rev. Lett. **98**, 082001 (2007)

- [101] E.J. Eichten, K. Lane and C. Quigg New states above charm threshold. *Phys. Rev. D* **73**, 014014 (2006) Erratum: *Phys. Rev. D* **73**, 079903 (2006).
- [102] P. Pakhlov *et al.* (Belle Collaboration), arXiv:0708.3812v2 [hep-ex].
- [103] S.-K. Choi *et al.*, (Belle Collaboration) *Phys. Rev. Lett.* **94**, 18200 (2005).
- [104] B. Aubert (BaBar Collaboration), arXiv:0711.2047 [hep-ex]
- [105] T. Barnes Two photon couplings of quarkonia with arbitrary  $J(P)$ . Invited paper at *Int. Workshop on Photon-Photon Collisions, La Jolla, CA, March 22 – 26, 1992*. Oak Ridge National Laboratory Report No. ORNL-CCIP-92-05.
- [106] S. Uehara *et al.* (Belle Collaboration) *Phys. Rev. Lett.* **96**, 082003 (2006).6
- [107] E. Swanson *Int. J. Mod. Phys. A* **21**, 733 (2006).
- [108] B. Aubert *et al.* (BaBar Collaboration), *Phys. Rev. Lett.* **98** 212001 (2007).
- [109] X.L. Wang *et al.* (Belle Collaboration), *Phys. Rev. Lett.* **99**, 142002 (2007).
- [110] J.Z. Bai *et al.* (BES Collaboration), *Phys. Rev. Lett.* **88**, 101802 (2002).
- [111] Belle Collaboration, G. Pakhlova *et al.*, *Phys. Rev. D* **77**, 011103 (2008).
- [112] Belle Collaboration, G. Pakhlova *et al.*, *Phys. Rev. Lett.* **98**, 092001 (2007).
- [113] Belle Collaboration, G. Pakhlova *et al.*, arXiv 0708.3313 [hep-ex].
- [114] C.Z. Yuan *et al.* (Belle Collaboration), *Phys. Rev. Lett.* **99**, 182004 (2007).
- [115] S.-K. Choi *et al.* (Belle Collaboration), arXiv:0708.1790v2 [hep-ex].
- [116] B. Aubert *et al.* (BaBar Collaboration), *Phys. Rev. D* **74**, 091103 (2006)
- [117] G.J. Ding and M.L. Yan, *Phys. Lett. B* **650**, 390 (2007) and *Phys. Lett. B* **657**, 49 (2007)
- [118] M. Ablikim *et al.* (BESII Collaboration), arXiv:0712.1143 [hep-ex].
- [119] B. Aubert *et al.* (BaBar Collaboration), *Phys. Rev. Lett.* **96**, 232001 (2006).
- [120] A. Sokolov *et al.* (Belle Collaboration), *Phys. Rev. D* **75**, 0710013 (2007).
- [121] K.F. Chen *et al.* (Belle Collaboration), arXiv:0710.2577 [hep-ex].
- [122] W.-S. Hou *Phys. Rev. D* **74**, 017504 (2006).
- [123] C.-Z. Yuan, private communication.
- [124] H.-Y. Zhou and Y.-P. Kuang, *Phys. Rev. D* **44** (1991) 756.
- [125] Y.-P. Kuang, *Front. Phys. China* **1** (2006) 19 [hep-ph/0601044]; N. Brambilla *et al.*, CERN Yellow Report, CERN-2005-005 [hep-ph/0412158].

- [126] K. Gottfried, in *Proc. 1977 International Symposium on Lepton and Photon Interactions at High Energies*, edited by F. Gutbrod, DESY, Hamburg, 1977, p. 667; *Phys. Rev. Lett.* **40** (1978) 598.
- [127] G. Bhanot, W. Fischler and S. Rudas, *Nucl. Phys. B* **155** (1979) 208.
- [128] M.E. Peskin, *Nucl. Phys. B* **156** (1979) 365; G. Bhanot and M.E. Peskin, *ibid.* **156** (1979) 391.
- [129] M.B. Voloshin, *Nucl. Phys. B* **154** (1979) 365; M.B. Voloshin and V.I. Zakharov, *Phys. Rev. Lett.* **45** (1980) 688; V.A. Novikov and m.A. Shifman, *Z. Phys. C* **8** (1981) 43.
- [130] T.M. Yan, *Phys. Rev. D* **22** (1980) 1652.
- [131] Y.-P. Kuang, Y.-P. Yi and B. Fu, *Phys. Rev. D* **42** (1990) 2300.
- [132] Y.-P. Kuang and T.-M. Yan, *Phys. Rev. D* **24** (1981) 2874.
- [133] E. Eichten, K. Gottfried, T. Kinoshita, K.D. Lane, and T.-M. Yan, *Phys. Rev. D* **17** (1978) 3090; *ibid.*, **D 21** (1980) 203.
- [134] W. Buchmüller, G. Grunberg, and S.-H. H. Tye, *Phys. Rev. Lett.* **45** (1980) 103; W. Buchmüller and S.-H. H. Tye, *Phys. Rev. D* **24** (1981) 132.
- [135] M.B. Voloshin, *Mod. Phys. Lett.A* **17** (2002) 1533.
- [136] J.Z. Bai *et al.* (BES Collaboration), *Phys. Rev. D* **70** (2004) 012006.
- [137] Y.-P. Kuang and T.-M. Yan, *Phys. Rev. D* **41** (1990) 155.
- [138] Y.-P. Kuang, *Phys. Rev. D* **65** (2002) 094024.
- [139] S. Godfrey, *Z. Phys. C* **31** (1986) 77.
- [140] Y.-Q. Chen and Y.-P. Kuang, *Phys. Rev. D* **46** (1992) 1165; **47** (1993) 350E.
- [141] J. Adler, *et al.*, *Phys. Rev. Lett.* **60** (1988) 89.
- [142] R.H. Schindler, Ph.D. thesis, Report No. SLAC-219, UC-34d(T/E), 1979.
- [143] R.A. Partridge, Ph.D. thesis, Report No. CALT-68-1150, 1984.
- [144] J.Z. Bai *et al.* (BES Collaboration), *Phys. Lett. B* **605** (2005) 63.
- [145] N.E. Adam *et al.* (CLEO Collaboration), *Phys. Rev. Lett.* **96** (2006) 082004.
- [146] Y.-P. Kuang, S.F. Tuan, and T.-M. Yan, *Phys. Rev. D* **37** (1998) 1210.
- [147] Crystal Ball Group, *Annu. Rev. Nucl. Part. Sci.* **33** (1983) 143.
- [148] S. Godfrey and J.L. Rosner, *Phys. Rev. D* **66** (2002) 014012.

- [149] C. Cawlfield *et al.* (CLEO Collaboration), Phys. Rev. D **73** (2006) 012003.
- [150] Q. Lu and Y.-P. Kuang, Phys. Rev. D **75** (2007) 054019 [hep-ph/0609091].
- [151] See for example, J. Green *et al.*, Phys. Rev. Lett. **49**, 617 (1982); T. Bowcock *et al.*, *ibid.* **58**, 307 (1987).
- [152] W. Kwong and J. L. Rosner, Phys. Rev. D **38**, 279 (1988).
- [153] R. A. Briere *et al.* [CLEO Collaboration], arXiv:hep-ex/0605070.
- [154] Y. B. Ding, D. H. Qin and K. T. Chao, Phys. Rev. D **44**, 3562 (1991).
- [155] C. Z. Yuan, Q. Qin, and B. Y. Zhang, HEP&NP **26**, 1201 (2002).
- [156] QWG group, CERN Yellow Report, CERN-2005-005, hep-ph/0412158.
- [157] M. A. Doncheski *et al.*, Phys. Rev. D **42**, 2293 (1990).
- [158] E. Eichten *et al.*, Phys. Rev. D **21**, 203 (1980).
- [159] K. J. Sebastian, Phys. Rev. D **26**, 2295 (1982).
- [160] G. Hardekopf and J. Sucher, Phys. Rev. D **25**, 2938 (1982).
- [161] R. McClary and N. Byers, Phys. Rev. D **28**, 1692 (1983).
- [162] P. Moxhay and J. L. Rosner, Phys. Rev. D **28**, 1132 (1983).
- [163] J. Z. Bai *et al.* (BES Collab.), Phys. Rev. D **70**, 012006 (2004).
- [164] N. E. Adam *et al.* [CLEO Collaboration], Phys. Rev. Lett. **94**, 232002 (2005) [arXiv:hep-ex/0503028].
- [165] J. J. Dudek, R. G. Edwards, and D. G. Richards, hep-ph/0601137.
- [166] J. L. Rosner, Phys. Rev. D **64**, 094002 (2001).
- [167] P. Wang, X. H. Mo and C. Z. Yuan, Phys. Lett. B **574**, 41 (2003).
- [168] P. Wang, X. H. Mo and C. Z. Yuan, Phys. Rev. D **70**, 077505 (2004).
- [169] M. Oreglia *et al.*, Phys. Rev. D **25**, 2259 (1982).
- [170] M. Ablikim *et al.* [BES Collaboration], Phys. Rev. D **70**, 092004 (2004) [arXiv:hep-ex/0409034].
- [171] For the amplitude calculation formulas, see G. Karl, S. Meshkov and J. L. Rosner, Phys. Rev. D **13**, 1203 (1976).
- [172] H. Grotch *et al.*, Phys. Rev. D **30**, 1924 (1984).
- [173] J. L. Rosner *et al.* [CLEO Collaboration], Phys. Rev. Lett. **95** (2005) 102003; P. Rubin *et al* (CLEO Collaboration), Phys. Rev. D **72** (2005) 092004.

- [174] P. Artoisenet, J. M. Gérard and J. Weyers, Phys. Lett. B **628**, 211 (2005).
- [175] T. Pedlar *et al.* (CLEO Collab.), Phys. Rev. D **75**, 011102 (2007).
- [176] M. B. Voloshin, Nucl. Phys. B **154** (1979) 365; M. B. Voloshin and V. I. Zakharov, Phys. Rev. Lett. **45** (1980) 688; V.A. Novikov and M. A. Shifman, Z. Phys. C **8** (1981) 43.
- [177] M. L. Yan *et al.*, Eur. Phys. J. C. **7** (1999) 61.
- [178] M. Ablikim *et al.* [BES Collab.], Phys. Lett. B **645**, 19 (2007).
- [179] F. K. Guo *et al.*, Phys. Rev. D **74**, 014011 (2006).
- [180] M. B. Voloshin, hep-ph/0206240.
- [181] R. Van Royen and V. F. Weisskopf, Nuovo Cim. A **50**, 617 (1967) [Erratum-ibid. A **51**, 583 (1967)].
- [182] R. Barbieri, R. Gatto, R. Kogerler and Z. Kunszt, Phys. Lett. B **57**, 455 (1975).
- [183] J. L. Rosner, arXiv:hep-ph/0405196.
- [184] W. M. Yao *et al.* [Particle Data Group], J. Phys. G **33**, 1 (2006).
- [185] See reference [182].
- [186] W. Celmaster, Phys. Rev. D **19**, 1517 (1979).
- [187] M. Beneke, A. Signer and V. A. Smirnov, Phys. Rev. Lett. **80**, 2535 (1998) [arXiv:hep-ph/9712302].
- [188] G. T. Bodwin and A. Petrelli, Phys. Rev. D **66**, 094011 (2002) [arXiv:hep-ph/0205210].
- [189] R. Barbieri, E. d'Emilio, G. Curci, and E. Remiddi, Nucl. Phys. **B154**, 535 (1979).
- [190] K. Hagiwara, C. B. Kim, and T. Yoshino, Nucl. Phys. **B177**, 461 (1981).
- [191] A. Czarnecki and K. Melnikov, Phys. Lett. B **519**, 212 (2001) [arXiv:hep-ph/0109054].
- [192] L. Landau, Phys. Abstracts A **52**, 125 (1949);
- [193] C. N. Yang, Phys. Rev. **77**, 242 (1950).
- [194] H. W. Huang, C. F. Qiao and K. T. Chao, Phys. Rev. D **54**, 2123 (1996) [arXiv:hep-ph/9601380].
- [195] H. W. Huang and K. T. Chao, Phys. Rev. D **54**, 6850 (1996) [Erratum-ibid. D **56**, 1821 (1997)] [arXiv:hep-ph/9606220].

- [196] A. Petrelli, M. Cacciari, M. Greco, F. Maltoni and M. L. Mangano, Nucl. Phys. B **514**, 245 (1998) [arXiv:hep-ph/9707223].
- [197] R. Barbieri, M. Caffo, R. Gatto and E. Remiddi, Nucl. Phys. B **192** (1981) 61.
- [198] R. Barbieri, M. Caffo, R. Gatto and E. Remiddi, Phys. Lett. B **95** (1980) 93.
- [199] K. M. Ecklund *et al.* [CLEO Collaboration], arXiv:0803.2869 [hep-ex].
- [200] R. Barbieri, R. Gatto and R. Kogerler, Phys. Lett. B **60**, 183 (1976).
- [201] See reference[53].
- [202] T. Barnes, *Proceedings of the IX International Workshop on Photon-Photon Collisions*, edited by D.O. Caldwell and H.P. Paar (World Scientific, Singapore, 1992), p. 263.
- [203] G. T. Bodwin, E. Braaten and G. P. Lepage, Phys. Rev. D **46**, 1914 (1992) [arXiv:hep-lat/9205006].
- [204] S. N. Gupta, J. M. Johnson and W. W. Repko, Phys. Rev. D **54**, 2075 (1996) [arXiv:hep-ph/9606349].
- [205] C. R. Munz, Nucl. Phys. A **609**, 364 (1996) [arXiv:hep-ph/9601206].
- [206] D. Ebert, R. N. Faustov and V. O. Galkin, Mod. Phys. Lett. A **18**, 601 (2003) [arXiv:hep-ph/0302044].
- [207] G. A. Schuler, F. A. Berends and R. van Gulik, Nucl. Phys. B **523**, 423 (1998) [arXiv:hep-ph/9710462].
- [208] A. A. Penin, V. A. Smirnov and M. Steinhauser, Nucl. Phys. B **716**, 303 (2005) [arXiv:hep-ph/0501042].
- [209] M. Beneke, Y. Kiyo and K. Schuller, Nucl. Phys. B **714**, 67 (2005) [arXiv:hep-ph/0501289].
- [210] A. Pineda and A. Signer, Nucl. Phys. B **762**, 67 (2007) [arXiv:hep-ph/0607239].
- [211] A. Pineda, Phys. Rev. D **65** (2002) 074007; Phys. Rev. D **66** (2002) 054022.
- [212] B. A. Kniehl, A. A. Penin, A. Pineda, V. A. Smirnov and M. Steinhauser, Phys. Rev. Lett. **92**, 242001 (2004) [arXiv:hep-ph/0312086].
- [213] A. A. Penin, A. Pineda, V. A. Smirnov and M. Steinhauser, Nucl. Phys. B **699**, 183 (2004) [arXiv:hep-ph/0406175].
- [214] G. Källen and A. Sarby, K. Dan. Vidensk. Selsk. Mat.-Fis. Medd. **29**, N17 (1955) 1.
- [215] I. Harris and L.M. Brown, Phys. Rev. **105** (1957) 1656.
- [216] A. Czarnecki and K. Melnikov, Phys. Rev. Lett. **80** (1998) 2531.

- [217] M. Beneke, A. Signer, and V.A. Smirnov, Phys. Rev. Lett. **80** (1998) 2535.
- [218] A. Czarnecki and K. Melnikov, Phys. Rev. D **65** (2002) 051501; Phys. Lett. B **519** (2001) 212.
- [219] K. Melnikov and A. Yelkhovsky, Phys. Rev. D **59** 114009 (1999).
- [220] A. A. Penin and A. A. Pivovarov, Nucl. Phys. B **549**, 217 (1999) [arXiv:hep-ph/9807421].
- [221] A. Pineda and J. Soto, Phys. Lett. B **495**, 323 (2000) [arXiv:hep-ph/0007197].
- [222] A. H. Hoang and I. W. Stewart, Phys. Rev. D **67**, 114020 (2003) [arXiv:hep-ph/0209340].
- [223] E. Braaten and Y.Q. Chen, Phys. Rev. D **57** (1998) 4236; Erratum *ibid.* D **59** (1999) 079901.
- [224] Y. Sumino, Phys. Rev. D **65** (2002) 054003; S. Recksiegel and Y. Sumino Phys. Rev. D **65** (2002) 054018; A. Pineda, J. Phys. G **29** (2003) 371; T. Lee, Phys. Rev. D **67** (2003) 014020.
- [225] S. J. Brodsky, D. G. Coyne, T. A. DeGrand and R. R. Horgan, Phys. Lett. B **73** (1978) 203.
- [226] K. Koller and T. Walsh, Nucl. Phys. B **140** (1978) 449.
- [227] D. L. Scharre *et al.*, Phys. Rev. D **23** (1981) 43.
- [228] B. Nemati *et al.* [CLEO Collaboration], Phys. Rev. D **55** (1997) 5273 [arXiv:hep-ex/9611020].
- [229] S. Wolf, Phys. Rev. D **63** (2001) 074020 [arXiv:hep-ph/0010217].
- [230] X. Garcia i Tormo and J. Soto, Phys. Rev. D **72** (2005) 054014 [arXiv:hep-ph/0507107].
- [231] I. Z. Rothstein and M. B. Wise, Phys. Lett. B **402** (1997) 346 [arXiv:hep-ph/9701404].
- [232] M. Kramer, Phys. Rev. D **60** (1999) 111503 [arXiv:hep-ph/9904416].
- [233] N. Brambilla, D. Eiras, A. Pineda, J. Soto and A. Vairo, Phys. Rev. D **67** (2003) 034018 [arXiv:hep-ph/0208019].
- [234] M. Gremm and A. Kapustin, Phys. Lett. B **407** (1997) 323 [arXiv:hep-ph/9701353].
- [235] W. Y. Keung and I. J. Muzinich, Phys. Rev. D **27** (1983) 1518.
- [236] M. A. Yusuf and P. Hoodbhoy, Phys. Rev. D **54** (1996) 3345 [arXiv:hep-ph/9608244].
- [237] X. Garcia i Tormo, arXiv:hep-ph/0610145.

- [238] F. Maltoni and A. Petrelli, Phys. Rev. D **59** (1999) 074006 [arXiv:hep-ph/9806455].
- [239] A. A. Penin and A. A. Pivovarov, Nucl. Phys. B **549** (1999) 217 [arXiv:hep-ph/9807421].
- [240] K. Melnikov and A. Yelkhovsky, Phys. Rev. D **59** (1999) 114009 [arXiv:hep-ph/9805270].
- [241] A. V. Manohar and P. Ruiz-Femenia, Phys. Rev. D **69** (2004) 053003 [arXiv:hep-ph/0311002].
- [242] M. B. Voloshin, Mod. Phys. Lett. A **19** (2004) 181 [arXiv:hep-ph/0311204].
- [243] S. Catani and F. Hautmann, Nucl. Phys. Proc. Suppl. **39BC** (1995) 359 [arXiv:hep-ph/9410394].
- [244] C. W. Bauer, S. Fleming and M. E. Luke, Phys. Rev. D **63** (2001) 014006 [arXiv:hep-ph/0005275].
- [245] C. W. Bauer, S. Fleming, D. Pirjol and I. W. Stewart, Phys. Rev. D **63** (2001) 114020 [arXiv:hep-ph/0011336].
- [246] C. W. Bauer, C. W. Chiang, S. Fleming, A. K. Leibovich and I. Low, Phys. Rev. D **64** (2001) 114014 [arXiv:hep-ph/0106316].
- [247] S. Fleming and A. K. Leibovich, Phys. Rev. D **67** (2003) 074035 [arXiv:hep-ph/0212094].
- [248] S. Fleming and A. K. Leibovich, Phys. Rev. D **70** (2004) 094016 [arXiv:hep-ph/0407259].
- [249] P. Aurenche, P. Chiappetta, M. Fontannaz, J. P. Guillet and E. Pilon, Nucl. Phys. B **399** (1993) 34.
- [250] D. Buskulic *et al.* [ALEPH Collaboration], Z. Phys. C **69** (1996) 365.
- [251] J. F. Owens, Rev. Mod. Phys. **59** (1987) 465.
- [252] X. Garcia i Tormo and J. Soto, Phys. Rev. D **69** (2004) 114006 [arXiv:hep-ph/0401233].
- [253] G. T. Bodwin, J. Lee and D. K. Sinclair, Phys. Rev. D **72** (2005) 014009 [arXiv:hep-lat/0503032].
- [254] D. Besson *et al.* [CLEO Collaboration], Phys. Rev. D **74** (2006) 012003 [arXiv:hep-ex/0512061].
- [255] R. D. Field, Phys. Lett. B **133** (1983) 248.
- [256] J. H. Field, Phys. Rev. D **66** (2002) 013013 [arXiv:hep-ph/0101158].
- [257] N. Brambilla, X. Garcia i Tormo, J. Soto and A. Vairo, in preparation.

- [258] X. Garcia i Tormo and J. Soto, Phys. Rev. Lett. **96** (2006) 111801 [arXiv:hep-ph/0511167].
- [259] P. Wang, C. Z. Yuan and X. H. Mo, Phys. Rev. D **70**, 114014 (2004) [arXiv:hep-ph/0410300], and references therein.
- [260] J. Z. Bai *et al.* [BES Collaboration], Phys. Rev. D **58**, 097101 (1998) [arXiv:hep-ex/9806002].
- [261] J. Z. Bai *et al.* [BES Collaboration], Phys. Rev. D **67**, 032004 (2003).
- [262] M. Ablikim *et al.* [BES Collaboration], Phys. Rev. D **74**, 072001 (2006) [arXiv:hep-ex/0607023].
- [263] M. Ablikim *et al.* [BES Collaboration], Phys. Rev. Lett. **99**, 011802 (2007) [arXiv:hep-ex/0612016].
- [264] Y. Chen *et al.*, Phys. Rev. D **73**, 014516 (2006).
- [265] Y. J. Gao, Y. J. Zhang, and K. T. Chao, Chin. Phys. Lett. **23**, 2376 (2006), hep-ph/0607278.
- [266] R. Barbieri, R. Gatto and E. Remiddi, Phys. Lett. B **61**, 465 (1976).
- [267] R. Barbieri, M. Caffo and E. Remiddi, Nucl. Phys. B **162**, 220 (1980).
- [268] See reference [198].
- [269] See reference[197].
- [270] G. Belanger and P. Moxhay, Phys. Lett. B **199**, 575 (1987).
- [271] L. Bergstrom and P. Ernstrom, Phys. Lett. B **267**, 111 (1991).
- [272] See reference [4].
- [273] See reference[188].
- [274] P. B. Mackenzie and G. P. Lepage, Phys. Rev. Lett. **47**, 1244 (1981).
- [275] See reference[235].
- [276] See reference [196].
- [277] See reference[233].
- [278] See reference[189].
- [279] See reference[190].
- [280] G. T. Bodwin, D. K. Sinclair and S. Kim, Phys. Rev. Lett. **77**, 2376 (1996)
- [281] A. Petrelli, Phys. Lett. B **380**, 159 (1996) [arXiv:hep-ph/9603439].

- [282] See reference[195].
- [283] See reference[1]
- [284] D. E. Groom *et al.* [Particle Data Group], Eur. Phys. J. C **15**, 1 (2000).
- [285] S. Eidelman *et al.* [Particle Data Group], Phys. Lett. B **592** (2004) 1.
- [286] See reference[184]
- [287] M. Ablikim *et al.* [BES Collaboration], Phys. Rev. D **71**, 092002 (2005) [arXiv:hep-ex/0502031].
- [288] F. Maltoni, [arXiv:hep-ph/0007003].
- [289] H. W. Huang and K. T. Chao, Phys. Rev. D **54**, 3065 (1996) [Erratum-ibid. D **56**, 7472 (1997); D **60**, 079901 (1999)] [arXiv:hep-ph/9601283].
- [290] T. Appelquist and H. D. Politzer, Phys. Rev. Lett. **34**, 43 (1975); A. De Rújula and S. L. Glashow, Phys. Rev. Lett. **34**, 46 (1975).
- [291] Mark-II Collaboration, M. E. B. Franklin *et al.*, Phys. Rev. Lett. **51**, 963 (1983).
- [292] BES Collaboration, J. Z. Bai, *et al.*, Phys. Rev. D **70**, 012005 (2004).
- [293] Babar Collaboration, B. Aubert, *et al.*, Phys. Rev. D **70**, 072004 (2004).
- [294] CLEO Collaboration, S. Dobbs *et al.*, Phys. Rev. Lett. **74**, 011150 (2006).
- [295] BES Collaboration, J. Z. Bai *et al.*, Phys. Rev. D **69**, 012003 (2004).
- [296] BES Collaboration, J. Z. Bai *et al.*, Phys. Rev. Lett. **91**, 052001 (2004).
- [297] BES Collaboration, J. Z. Bai, *et al.*, Phys. Rev. D **54**, 1221 (1996); Erratum: ibid. **57**, 3187 (1998).
- [298] BES Collaboration, M. Ablikim *et al.*, Phys. Rev. D **70**, 112003 (2004).
- [299] BES Collaboration, M. Ablikim *et al.*, Phys. Rev. D **70**, 112007 (2004).
- [300] BES Collaboration, M. Ablikim *et al.*, Phys. Lett. B **614**, 37 (2005).
- [301] BES Collaboration, M. Ablikim *et al.*, Phys. Rev. D **70**, 077101 (2004).
- [302] BES Collaboration, M. Ablikim *et al.*, Phys. Rev. D **72**, 072007 (2005).
- [303] BES Collaboration, M. Ablikim *et al.*, Phys. Lett. B **619**, 247 (2005).
- [304] BES Collaboration, M. Ablikim *et al.*, Phys. Rev. D **71**, 072006 (2005).
- [305] CLEO Collaboration, N. E. Adam *et al.*, Phys. Rev. Lett. **94**, 012005 (2005).
- [306] BES Collaboration, J. Z. Bai *et al.*, Phys. Rev. Lett. **81**, 5080 (1998).

- [307] BES Collaboration, J. Z. Bai *et al.*, Phys. Rev. D **67**, 052002 (2003).
- [308] BES Collaboration, J. Z. Bai *et al.*, Phys. Rev. D **69**, 072001 (2004).
- [309] Z. Metreveli (for CLEO Collaboration), “Recent  $\psi(2S)$  results from CLEOc”, talk at Charm2006, Beijing, China, June 5-7, 2006.
- [310] CLEO Collaboration, R. A. Briere *et al.*, Phys. Rev. Lett. **95**, 062001 (2005).
- [311] CLEO Collaboration, G. S. Adams *et al.*, Phys. Rev. D **73**, 012002 (2006).
- [312] CLEO Collaboration, D. Cronin-Hennessy *et al.*, hep-ex/0603026.
- [313] S. J. Brodsky, G. P. Lepage, Phys. Rev. D **24**, 2848 (1981).
- [314] P.G.O. Freund and Y. Nambu, Phys. Rev. Lett. **34**, 569 (1983).
- [315] S. Okubo, Phys. Lett. **5**, 165 (1963); G. Zweig, CERN-preprint CERN-TH-401, 402, 412 (1964); Iizuka, Prog. Theor. Phys. Suppl. **37-38**, 21 (1996).
- [316] W. S. Hou and A. Soni, Phys. Rev. Lett. **50**, 569 (1983).
- [317] W. S. Hou and A. Soni, Phys. Rev. D **29**, 101 (1984).
- [318] S. J. Brodsky, G. P. Lepage and S. F. Tuan, Phys. Rev. Lett. **59**, 621 (1987).
- [319] Particle Data Group, M. Aguilar-Benitez *et al.*, Phys. Lett. B **170**, 1 (1986).
- [320] C. T. Chan and W. S. Hou, Nucl. Phys. A **675**, 367c (2000).
- [321] Y. H. Xie, Ph.D. thesis, IHEP, Chinese Academy of Sciences, 1998 (unpublished).
- [322] F. A. Harris, hep-ex/9903036 (unpublished).
- [323] Y. Q. Chen and E. Braaten, Phys. Rev. Lett. **80**, 5060 (1998).
- [324] See, for example, M. Peardon, Nucl. Phys. Proc. Suppl. **63**, 22-27, (1998).
- [325] M. Suzuki, Phys. Rev. D **57**, 5171 (1998).
- [326] M. Anselmino, M. Genovese, and E. Predazzi, Phys. Rev. D **44**, 1597 (1991); M. Anselmino, M. Genovese, and D. E. Kharzeev, *ibid.* **50**, 595 (1994).
- [327] S. J. Brodsky and M. Karliner, Phys. Rev. Lett. **78**, 4682 (1997).
- [328] V. L. Chernyak, hep-ph/9906387.
- [329] G. Karl and W. Roberts, Phys. Lett. B **144**, 263 (1984).
- [330] G. Karl and S-F. Tuan, Phys. Rev. D **34**, 1692 (1986).
- [331] M. Chaichian and N. A. Törnqvist, Phys. Lett. B **323**, 75 (1989).
- [332] S. S. Pinsky, Phys. Lett. B **236**, 479 (1990).

- [333] S. S. Pinsky, Phys. Rev. D **31**, 1753 (1985).
- [334] K.-T. Chao, Proc. 17th Intern. Symp. on Lepton-Photon Interactions at high Energies, Beijing, China, 1995, ed. Z. P. Zheng and H. S. Chen (World Scientific, Singapore, 1996) p. 106.
- [335] Y. S. Zhu, in *Proceedings of the 28th International Conference on High Energy Physics*, edited by Z. Adjuk and A. K. Wroblewski (World Scientific, Singapore, 1997).
- [336] A. Bramon, R. Escribano, and M. D. Scadron, Phys. Lett. B **403**, 339 (1997).
- [337] C. Z. Yuan, HEP & NP **30**, 488 (2006).
- [338] J. M. Gérard and J. Weyers, Phys. Lett. B **462**, 324 (1999).
- [339] P. Wang, X. H. Mo and C. Z. Yuan, Phys. Lett. B **557**, 197 (2003).
- [340] P. Artoisenet, J. M. Gérard and J. Weyers, Phys. Lett. B **628**, 211 (2005).
- [341] V. L. Chernyak and A. R. Zhitnitsky, Phys. Rep. **112**, 173 (1984).
- [342] We did not consider the possible different mixing angle extracted from the Belle results by K. Y. Liu and K. T. Chao, hep-ph/0405126.
- [343] E. Eichten, K. Gottfried, T. Kinoshita, K. D. Lane and T. M. Yan, Phys. Rev. **D17** (1978) 3090; **D21** (1980) 313(E); **D21** (1980) 203(E).
- [344] K. Heikkilä, N. A. Törnqvist and S. Ono, Phys. Rev. D **29**, 110 (1984); *ibid.* D **29**, 2136(E) (1984).
- [345] P. Wang, C. Z. Yuan and X. H. Mo, Phys. Lett. B **574**, 41 (2004).
- [346] P. Wang, C. Z. Yuan and X. H. Mo, Phys. Rev. D **69**, 057502 (2004).
- [347] P. Wang, X. H. Mo and C. Z. Yuan, Int. J. Mod. Phys. A **21**, 5163 (2006).
- [348] P. Wang, X. H. Mo and C. Z. Yuan, Phys. Rev. D **70**, 077505 (2004).
- [349] P. Wang, C. Z. Yuan and X. H. Mo, Phys. Rev. D **70**, 114014 (2004).
- [350] CLEO Collaboration, D. Besson *et al.*, CLEO 05-27 (2005).
- [351] X. Q. Li, D. V. Bugg and B. S. Zou, Phys. Rev. D **55**, 1421 (1997).
- [352] S. F. Tuan, Commun. Theor. Phys. **33**, 285 (2000).
- [353] M. Suzuki, Phys. Rev. D **60**, 051501 (1999).
- [354] M. Suzuki, Phys. Rev. D **63**, 054021 (2001).
- [355] C. Z. Yuan, P. Wang and X. H. Mo, Phys. Lett. B **567**, 73 (2003).

- [356] J. P. Ma, Phys. Rev. D **65**, 097506 (2002).
- [357] L. J. Clavelli and G. W. Intemann, Phys. Rev. D **28**, 2767 (1983).
- [358] H. E. Haber and J. Perrier, Phys. Rev. D **32**, 2961 (1985).
- [359] A. Seiden, H. F-W. Sadrozinski, and H. E. Haber Phys. Rev. D **38**, 824 (1988).
- [360] T. Feldmann and P. Kroll, Phys. Rev. D **62**, 074006 (2000).
- [361] E.S. Swanson, Phys. Rep. **429**, 243 (2006).
- [362] G. Rong, D.H. Zhang, and J.C. Chen, hep-ex/0506051.
- [363] M. Ablikim *et al.* (BES Collaboration) Phys. Rev. Lett. **97**, 121801 (2006).
- [364] M. Ablikim *et al.* (BES Collaboration) Phys. Lett. B **141**, 145 (2006)
- [365] E. Eichten *et al.*, Phys. Rev. D **21**, 203 (1980).
- [366] E. Eichten, Phys. Rev. D **22**, 1819 (1980).
- [367] P. Moxhay and J.L. Rosner, Phys. Rev. D **28**, 1132 (1983)
- [368] Y.P. Kuang, Phys. Rev. D **65**, 094024 (2002).
- [369] BES Collaboration, M. Ablikim *et al.*, Phys. Rev. Lett. **97**, 121801 (2006).
- [370] Y. Yamamoto, A. Nishimura and Y. Yamaguchi, Prog. Theor. Phys. **58**, 347 (1977);  
Y. Yamamoto and A. Nishimura, Prog. Theor. Phys. **59**, 2151 (1978).
- [371] E.J. Eichten, K. Lane, C. Quigg, Phys. Rev. D **69**, 094019 (2004).
- [372] T. Barnes, S. Godfrey, E.S. Swanson, Phys. Rev. D **72**, 054026 (2005).
- [373] P. Maxhay, Phys. Rev. D **37**, 2557 (1988).
- [374] A. Billoir *et al.*, Nucl. Phys. B **155**, 493.
- [375] BES Collaboration, J.Z. Bai *et al.*, Phys. Lett. B **605**, 63 (2005).
- [376] N. E. Adam *et al.* [CLEO Collaboration], Phys. Rev. Lett. **96**, 082004 (2006)  
[arXiv:hep-ex/0508023].
- [377] J.L. Rosner, Anal. Phys. **319**, 1 (2005).
- [378] P. Wang, C. Z. Yuan and X. H. Mo, Phys. Rev. D **70**, 114014 (2004) [arXiv:hep-ph/0410300], and references therein.
- [379] H.J. Lipkin, Phys. Lett. B **179**, 278 (1986).
- [380] P. Wang, X. H. Mo, and C. Z. Yuan, Int. J. Mod. Phys. A **21**, 5163 (2006).

- [381] K. L. He, X. H. Mo, P. Wang, and C. Z. Yuan, High Energy Phys. and Nucl. Phys. **31**, 125 (2007).
- [382] CLEO Collaboration, N. E. Adam *et al.*, Phys. Rev. Lett. **94**, 012005 (2005).
- [383] G. Rong, in proceedings of the 32nd International Conference on High Energy Physics, Beijing, China 16–22 August 2004, p1200.
- [384] M. Ablikim *et.al.* Phys. Rev. D **72**, 072007 (2005)
- [385] C. Z. Yuan, High Energy Phys. and Nucl. Phys. **30**, 488 (2006).
- [386] M. Ablikim *et.al.* Physi. Rev. D **70**, 112007 (2004)
- [387] J.J. Aubert *et al.*, Phys. Rev. Lett. **33**, 1404 (1974); J.E. Augustin *et al.*, Phys. Rev. Lett. **33**, 1406 (1974).
- [388] S. Bianco, F. L. Fabbri, D. Benson and I. Bigi, Riv. Nuovo Cim. **26N7**, 1 (2003) [arXiv:hep-ex/0309021].
- [389] A. Duncan and A. H. Mueller, Phys. Lett. B **93**, 119 (1980).
- [390] S. J. Brodsky and G. P. Lepage, Phys. Rev. D **24**, 2848 (1981).
- [391] V. L. Chernyak and A. R. Zhitnitsky, Nucl. Phys. B **201**, 492 (1982) [Erratum-ibid. B **214**, 547 (1983)].
- [392] V. N. Baier and A. G. Grozin, Z. Phys. C **29**, 161 (1985).
- [393] QWG group, CERN Yellow Report, CERN-2005-005, Geneva: CERN, 2005. -487. hep-ph/0412158.
- [394] J. Bolz, P. Kroll and G. A. Schuler, Phys. Lett. B **392**, 198 (1997) [arXiv:hep-ph/9610265] and Eur. Phys. J. C **2**, 705 (1998) [arXiv:hep-ph/9704378].
- [395] S. M. Wong, Nucl. Phys. A **674**, 185 (2000) [arXiv:hep-ph/9903221]; Eur. Phys. J. C **14**, 643 (2000) [arXiv:hep-ph/9903236].
- [396] J. Bolz and P. Kroll, Eur. Phys. J. C **2**, 545 (1998) [arXiv:hep-ph/9703252].
- [397] J. Bolz and P. Kroll, Z. Phys. A **356**, 327 (1996) [arXiv:hep-ph/9603289].
- [398] V. L. Chernyak and A. R. Zhitnitsky, Phys. Rept. **112**, 173 (1984).
- [399] V. M. Braun and I. E. Filyanov, Z. Phys. C **48**, 239 (1990) [Sov. J. Nucl. Phys. **52**, 126 (1990 YAFIA,52,199-213.1990)]; P. Ball, V. M. Braun, Y. Koike and K. Tanaka, Nucl. Phys. B **529**, 323 (1998) [arXiv:hep-ph/9802299]; M. Beneke and T. Feldmann, Nucl. Phys. B **592**, 3 (2001) [arXiv:hep-ph/0008255].
- [400] V. Braun, R. J. Fries, N. Mahnke and E. Stein, Nucl. Phys. B **589**, 381 (2000) [Erratum-ibid. B **607**, 433 (2001)] [arXiv:hep-ph/0007279].
- [401] M. Anselmino, R. Cancelliere and F. Murgia, Phys. Rev. D **46**, 5049 (1992).

- [402] R. G. Ping, B. S. Zou and H. Q. Chiang, Eur. Phys. J. A 23, 129-133 (2005).
- [403] H. Q. Zhou, R. G. Ping and B. S. Zou, Physics Letters B 611 123-128 (2005).
- [404] L. Köpke and N. Wermes, Phys. Rep. **174**, 67 (1989).
- [405] H. Kowalski and T. F. Walsh, Phys. Rev. D **14**, 852 (1976).
- [406] V. Chernyak, arXiv:hep-ph/9906387.
- [407] X. H. Mo, C. Z. Yuan and P. Wang, arXiv:hep-ph/0611214.
- [408] Partical Data Group, J. Phys. G, **33**, 1 (2006).
- [409] J. Z. Bai *et al.* [BES Collaboration], Phys. Lett. B **578**, 16 (2004) [arXiv:hep-ex/0308073].
- [410] D. Bisello *et al.* [DM2 collaboration], Nucl. Phys. B **350**, 1 (1991).
- [411] R. M. Baltrusaitis *et al.* [Mark-III Collaboration], Phys. Rev. D **33**, 629 (1986).
- [412] T. Himmel *et al.*, Phys. Rev. Lett. **45**, 1146 (1980).
- [413] C. H. Wu *et al.*, Phys. Rev. Lett. **97**, 162003 (2006) [arXiv:hep-ex/0606022].
- [414] N. G. Stefanis and M. Bergmann, Phys. Rev. D **47**, 3685 (1993) [arXiv:hep-ph/9211250]; V. L. Chernyak, A. A. Ogloblin and I. R. Zhitnitsky, Z. Phys. C **42**, 583 (1989) [Yad. Fiz. **48**, 1398 (1988 SJNCA,48,889-895.1988)];
- [415] A. Andrikopoulou, Z. Phys. C **22**, 63 (1984); P. H. Damgaard, K. Tsokos and E. L. Berger, Nucl. Phys. B **259**, 285 (1985).
- [416] J. Z. Bai *et al.* [BES Collaboration], Phys. Rev. D **67**, 112001 (2003) [arXiv:hep-ex/0304012].
- [417] E. Braaten and J. Lee, Phys. Rev. D **67**, 054007 (2003) [arXiv:hep-ph/0211085].
- [418] M. L. Mangano and A. Petrelli, Phys. Lett. B **352**, 445 (1995) [arXiv:hep-ph/9503465].
- [419] H. W. Huang, C. F. Qiao and K. T. Chao, Phys. Rev. D **54**, 2123 (1996) [arXiv:hep-ph/9601380].
- [420] J. P. Ma and Q. Wang, Phys. Lett. B **537**, 233 (2002) [arXiv:hep-ph/0203082].
- [421] J. Z. Bai *et al.* [BES Collaboration], Phys. Rev. D **69**, 092001 (2004) [arXiv:hep-ex/0401011].
- [422] R. Baldini, *et al.* Phys. Lett. B **444**, 111 (1998).
- [423] M. Suzuki, Phys. Rev. D **63**, 054021 (2001).

- [424] J. Jousset *et al.*, Phys. Rev. D **41**, 138 (1990); D. Coffman *et al.*, Phys. Rev. D **38**, 2695 (1988); A. Bramon, R. Escribano and M.D. Scadron, Phys. Lett. B **403**, 339 (1997); M. Suzuki, Phys. Rev. D **58**, 111504 (1998); N.N. Achasov, Relative Phase between the Three Gluon and One Photon Amplitudes of the  $J/\psi$  Decays, in Proc. ninth International Conference on Hadron Spectroscopy (Protvino, Russia, August 2001), AIP Conf. Proc. **619** 649 (AIP, New York, 2002).
- [425] G. López Castro *et al.*, Tests of Flavor Symmetry in  $J/\psi$  Decays, in: Proc. CAM-94 (ed. A. Zepeda, Cancum, Mexico, 1994), AIP Conf. Proc. **342**, 441 (AIP, New York, 1995).
- [426] M. Suzuki, Phys. Rev. D **60**, 051501 (1999).
- [427] P. Wang, C. Z. Yuan and X. H. Mo, Phys. Lett. B **574**, 41 (2004).
- [428] BES Collaboration, M. Ablikim *et al.*, Phys. Lett. B **614**, 37 (2005).
- [429] C. Carimalo, Int. J. Mod. Phys. A2 (1987) 249.
- [430] BES Collaboration, J.Z. Bai, *et al.*, Phys. Lett. B 591, 42 (2004) .
- [431] BES Collaboration, M. Ablikim, *et al.*, Phys. Lett. B 632, 181 (2006) .
- [432] M. W. Eaton, *et al.* Phys. Rev. D 29, 804 (1984) .
- [433] Fermilab E835 Collaboration, A. Buzzo,
- [434] F. Murgia and M. Melis, distribution amplitudes," Phys. Rev. D **51**, 3487 (1995) [arXiv:hep-ph/9412205]; R. G. Ping, H. C. Chiang and B. S. Zou, Phys. Rev. D **66**, 054020 (2002).
- [435] M. Claudson, S. L. Glashow and M. B. Wise, Phys. Rev. D **25**, 1345 (1982).
- [436] Hong Cheng, Rong-Gang Ping hep-ph/0601202.
- [437] J. L. Rosner, arXiv:hep-ph/0405196.
- [438] P. Wang, C. Z. Yuan and X. H. Mo, Phys. Rev. D **70**, 114014 (2004) [ArXiv:hep-ph/0410300].
- [439] G. S. Huang *et al.* [CLEO Collaboration], Phys. Rev. Lett. **96**, 032003 (2006) [arXiv:hep-ex/0509046].
- [440] D. Besson *et al.* [CLEO Collaboration], Phys. Rev. Lett. **96**, 092002 (2006) [arXiv:hep-ex/0512038].
- [441] R. Sinha and S. Okubo, Phys. Rev. D **30**, 2333 (1984).
- [442] BES Collaboration, J. Z. Bai *et al.*, Phys. Rev. Lett. **91**, 022001 (2003).
- [443] BES Collaboration, M. Ablikim *et al.*, Phys. Rev. D **71**, 072006 (2005).
- [444] BES Collaboration, M. Ablikim *et al.*, Phys. Rev. Lett. **93**, 112002 (2004).

- [445] Belle Collaboration, K. Abe *et al.*, Phys. Rev. Lett. **88**, 181803 (2002).
- [446] Belle Collaboration, M.-Z. Wang *et al.*, Phys. Rev. Lett. **90**, 201802 (2003).
- [447] Belle Collaboration, Y.-J. Lee *et al.*, Phys. Rev. Lett. **93**, 211801 (2004).
- [448] CLEO Collaboration, S. Anderson *et al.*, Phys. Rev. Lett. **86**, 2732 (2001).
- [449] Belle Collaboration, K. Abe *et al.*, Phys. Rev. Lett. **89**, 151802 (2002).
- [450] Belle Collaboration, M.-Z. Wang *et al.*, Phys. Rev. Lett. **92**, 131801 (2004).
- [451] BABAR Collaboration, B. Aubert *et al.*, hep-ex/0408035.
- [452] E. Fermi and C. N. Yang, Phys. Rep. **76**, 1739 (1949).
- [453] S. Sakata, Prog. Theor. Phys. **16**, 686 (1956).
- [454] C.Z. Yuan, X.H. Mo and P. Wang, Phys. Rev. Lett. **626**, 95 (2005).
- [455] For example, compare the Dalitz plots in Ref. [443] and hep-ex/0405030.
- [456] G. J. Ding, J. l. Ping and M. L. Yan, Phys. Rev. D **74**, 014029 (2006) [arXiv:hep-ph/0510013].
- [457] R. Jaffe, Phys. Rev. D **72**, 074508 (2005) [arXiv:hep-ph/0507149].
- [458] BES Collaboration, M. Ablikim *et al.*, Phys. Rev. D **71**, 072006 (2005).
- [459] BES Collaboration, J. Z. Bai *et al.*, Phys. Rev. D **67**, 052002 (2003).
- [460] CLEO Collaboration, R. A. Briere *et al.*, Phys. Rev. Lett. **95**, 062001 (2005).
- [461] CLEO Collaboration, S. B. Athar *et al.*, hep-ex/0611032.
- [462] C.Z. Yuan, HEP & NP **30** (2006) 488-496.
- [463] B.W. Lee, C. Quigg, and J.L. Rosner, Phys. Rev. D **15**, 157 (1977).
- [464] A. Chodos *et al.*, Phys. Rev. D **9**, 3471 (1974); W. Bardeen *et al.*, Phys. Rev. D **11**, 1094 (1975).
- [465] C. Quigg and J.L. Rosner, Phys. Rev. D **16**, 1497 (1977).
- [466] M.K. Gaillard, B.W. Lee, and J.L. Rosner, Phys. Rev. D **47**, 277 (1975).
- [467] B. Andersson, *The Lund Model*, Cambridge Universaty Press, 1998.
- [468] B. Andersson and H.M. Hu, arXiv:hep-ph/9910285.
- [469] H.M. Hu *et al.*, HEP & NP **25** (2001) 1045-1043.
- [470] Technical Progress Report for PANDA. Strong Interaction Studies with Antiprotons. (PANDA Collaboration, Feb.2005).

- [471] A. Lundborg, T. Barnes and U. Wiedner, Phys. Rev. D **73**, 096003 (2006) [arXiv:hep-ph/0507166].
- [472] T. Barnes and X. Li, arXiv:hep-ph/0611340.
- [473] M. A. Sanchis, Phys. Lett. B **280**, 299 (1992); Phys. Lett. B **312**, 333 (1993).
- [474] A. Datta, P. O'Donnell, S. Pakvasa, X. Zhang, Phys. Rev. D **60**, 014011 (1999).
- [475] M. A. Sanchis-Lozano, Z. Phys. C **62**, 271 (1994).
- [476] F. Hussain, J. G. Korner and G. Thompson, Ann. Phys. **206**, 334 (1991).
- [477] A. F. Falk, Nucl. Phys. B **378**, 79 (1992).
- [478] K. K. Sharma and R. C. Verma, Int. J. Mod. Phys. A **14**, 937 (1999).
- [479] J. D. Bjorken, Nucl. Phys. B **11**, 325 (1989); D. Bortoletto and S. Stone, Phys. Rev. Lett. **65**, 2951 (1990).
- [480] M. B. Voloshin and M. A. Shifman, Sov. J. Nucl. Phys. **47**, 511 (1988).
- [481] P. Fayet, Phys. Lett. B **84**, 421 (1979); D. Besson *et. al.* (CLEO Collaboration), Phys. Rev. D **30**, 1433 (1984); P. Fayet and J. Kaplan, Phys. Lett. B **269**, 213 (1991); B. McElrath, Phys. Rev. D **72**, 103508 (2005).
- [482] P. Fayet, Phys. Rev. D **74**, 054034 (2006).
- [483] A. V. Artamonov, *et al.* (E949 Collaboration), Phys. Rev. D **72**, 091102 (2005).
- [484] C. Boehm and P. Fayet, Nucl. Phys. B **683**, 219 (2004); C. Boehm, D. Hooper, J. Silk, M. Casse and J. Paul, Phys. Rev. Lett. **92**, 101301 (2004); P. Fayet, Phys. Rev. D **70**, 023514 (2004).
- [485] P. Fayet, Phys. Lett. B **95**, 285 (1980); P. Fayet, Nucl. Phys. B **187**, 184 (1981).
- [486] J. Ellis, J. F. Gunion, H. E. Haber, L. Roszkowski, and F. Zwirner, Phys. Rev. D **39**, 844 (1989); J. F. Gunion, D. Hooper, and B. McElrath, Phys. Rev. D **73**, 015011 (2006); G. Bertone, D. Hooper and J. Silk, Phys. Rept. **405**, 279 (2005) [arXiv:hep-ph/0404175].
- [487] P. Jean *et al.*, Astron. Astrophys. **407**, L55 (2003).
- [488] J. F. Beacom, N. F. Bell, and G. Bertone, Phys. Rev. Lett. **94**, 171301 (2005); P. Fayet, D. Hooper, and G. Sigl, Phys. Rev. Lett. **96**, 211302 (2006).
- [489] R. Balest, *et al.* (CLEO Collaboration), Phys. Rev. D **51**, 2053 (1995).
- [490] L. N. Chang, O. Lebedev and J. N. Ng, Phys. Lett. B **44**, 419 (1998).
- [491] S. Eidelman *et al.*, Phys. Lett. B **592**, 1 (2004)

- [492] M. Ablikim *et al.* [BES Collaboration], Phys. Rev. Lett. **97**, 202002 (2006) [arXiv:hep-ex/0607006].
- [493] T. Goldman, H. E. Haber, Los Alamos preprint LA-UR-83-2323, (1983).
- [494] G. Goggi and G. Penso, Nucl. Phys. B **165**, 249 (1980).
- [495] Jade Collaboration, Phys. Lett. B **92**, 806 (1980); TASSO Collaboration, Phys. Lett. B **92**, 199 (1980); PLUTO Collaboration, Phys. Lett. B **94**, 87 (1980).
- [496] Stan Brodsky, private communication.
- [497] S. Nussinov, R. D. Peccei and X. M. Zhang, Phys. Rev. D **63**, 016003 (2000).
- [498] W. Hou, C. Yue and T. Feng, Phys. Rev. D **67**, 114001 (2003).
- [499] "Probing for lepton flavor violation in decays of Charmonium and bottomonium systems", R. D. Peccei, J-X. Wang and X. Zhang, May 1998 Note (unpublished); X. Zhang, invited talk given at the national conference on high energy physics, Chengde, China, in April 1998.
- [500] Xin-min Zhang, hep-ph/0010105.
- [501] Z. K. Silagadze, hep-ph/9907328; T .Huang, Z. Lin and X. Zhang, hep-ph/0009353; H-M. Chan *et al.*, hep-ph/0006338; hep-ph/0007004.
- [502] J. Z. Bai *et al.*, [BES Collaboration], Phys. Lett. B **561**, 49 (2003); M. Ablikim *et al.*, [BES Collaboration], Phys. Lett. B **598**, 172 (2004).
- [503] A. Einstein, B. Podolsky, and N. Rosen, Phys. Rev. **47**, 777 (1935).
- [504] J.S. Bell, Physics **1**, 195 (1964).
- [505] J.F. Clauser, M.A. Horne, A. Shimony, and R.A. Holt, Phys. Rev. Lett. **23**, 880 (1969).
- [506] L. Hardy, Phys. Rev. Lett. **71**, 1665 (1993).
- [507] Thomas F. Jordan, Phys. Rev. A **50**, 62 (1994).
- [508] A. Garuccio, Phys. Rev. A **52**, 2535 (1995).
- [509] J.F. Clauser, M.A. Horne, Phys. Rev. D **10**, 526 (1974).
- [510] A. Aspect, P. Grangier, and G. Roger, Phys. Rev. Lett. **49**, 91 (1982).
- [511] S.A. Abel, M. Dittmar, and H. Dreiner, Phys. Lett. B **280**, 304 (1992).
- [512] H.J. Lipkin, Phys. rev. **176**, 1715 (1968).
- [513] N.A. Törnqvist, Found. Phys. **11**, 171 (1981).
- [514] P. Privitera, Phys. lett. B **275**, 172 (1992).

- [515] M.H. Tixier *et al.* (the DM2 Collaboration, LAL Orsay, LPC, Clermont, Padova, Frascati), Presentation at: Conference on Microphysical Reality and Quantum Formalism, Urbino, Italy (1985).
- [516] N.A. Törnqvist, in: */Quantum Mechanics Versus Local Realism.* (F.Selleri, ed.), Plenum Press, New York, 1988, pp.115-132.
- [517] A. Afriat, F. Selleri, */The Einstein Podolsky and Rosen Paradox in atomic nuclear and particle physics.* (Plenum Press, New York, 1999).
- [518] J. Bernabéu, N.E. Mavromatos, and J. Papavassiliou, *Phys. Rev. Lett.* **92**, 131601 (2004).
- [519] A. Bramon, R. Escribano, and G. Garbarino, *Found. Phys.* **36** 563 (2006).
- [520] Reinhold A. Bertlmann, *quant-ph/0410028*.
- [521] CPLEAR Collaboration, *Phys. Lett. B* **422**, 339 (1998).
- [522] Apollo. Go, *Journal of Modern Optics* **51**, 991 (2004).
- [523] R.A. Bertlmann, A. Bramon, G. Garbarino, and B.C. Hiesmayr, *Phys. lett. A* **332**, 355 (2004).
- [524] A. Bramon and G. Garbarino, *Phys. Rev. Lett.* **88**, 040403 (2002).
- [525] A. Bramon and G. Garbarino, *Phys. Rev. Lett.* **89**, 160401 (2002).
- [526] P. Eberhard, *Phys. Rev. A* **47**, R747 (1993).
- [527] Junli Li, Cong-Feng Qiao, *Phys. Rev. D* **74**, 076003 (2006).
- [528] William K. Wootters, *Phys. Rev. Lett.* **80**, 2245 (1998).
- [529] N. Gisin, *Phys. Lett. A* **154**, 201 (1991).
- [530] G. Kar, *Phys. Lett. A* **204**, 99 (1995).
- [531] Ayman F. Abouraddy, Bahaa E.A. Saleh, Alexander V. Sergienko, and Malvin C. Teich, *Phys. Rev. A* **64**, 050101 (2001).
- [532] BES Collaboration, *Phys. Rev. D* **69**, 012003 (2004).
- [533] M. W. Eaton et al., *Phys. Rev. D* **29**(1984)804.
- [534] P. Henrard et al., *Nucl. Phys. B* **292**(1987) 670.
- [535] L. Kopke, Talk given at XXIIrd Intern Conf. on High Energy Physics (Berkeley, CA, 1986).
- [536] J. -G. Korner, *Z. Phys. C* **33** (1987) 529.
- [537] L. Micu, *Nucl. Phys. B* **10**, 521 (1969).

- [538] A. LeYaouanc, L. Oliver, O. Pène and J.-C. Raynal, Phys. Rev. D **8**, (1973) 2223.
- [539] R. Kokoski and N. Isgur, Phys. Rev. D **35**, 907 (1987).
- [540] E. S. Ackleh, T. Barnes and E. S. Swanson, Phys. Rev. D **54**, 6811 (1996). [arXiv:hep-ph/9604355].
- [541] A. Le Yaouanc, L. Oliver, O. Pène and J.-C. Raynal, Phys. Lett. B **71**, 397 (1977).
- [542] A. Le Yaouanc, L. Oliver, O. Pène and J.-C. Raynal, Phys. Lett. B **72**, 57 (1977).
- [543] T. Barnes, F. E. Close, P. R. Page and E. S. Swanson, Phys. Rev. D **55**, 4157 (1997) [arXiv:hep-ph/9609339].
- [544] T. Barnes, N. Black and P. R. Page, Phys. Rev. D **68**, 054014 (2003) [arXiv:nucl-th/0208072].
- [545] S. Capstick and N. Isgur, Phys. Rev. D **34**, 2809 (1986).
- [546] S. Capstick and W. Roberts, Phys. Rev. D **49**, 4570 (1994) [arXiv:nucl-th/9310030].
- [547] N. Isgur, R. Kokoski and J. Paton, Phys. Rev. Lett. **54**, 869 (1985).
- [548] F. E. Close and P. R. Page, Nucl. Phys. B **443**, 233 (1995) [arXiv:hep-ph/9411301].
- [549] E. Eichten, K. Gottfried, T. Kinoshita, K. D. Lane and T. M. Yan, Phys. Rev. D **17**, 3090 (1978) [Erratum-ibid. D **21**, 313 (1980)].
- [550] E. J. Eichten, K. Lane and C. Quigg, Phys. Rev. Lett. **89**, 162002 (2002) [arXiv:hep-ph/0206018].
- [551] E. J. Eichten, K. Lane and C. Quigg, Phys. Rev. D **69**, 094019 (2004) [arXiv:hep-ph/0401210].
- [552] X. H. Guo, H. W. Ke, X. Q. Li, X. Liu and S. M. Zhao, arXiv:hep-ph/0510146.
- [553] H. E. Haber and J. Perrier, Phys. Rev. D **31** (1985) 1751.
- [554] H. Genz, M. Malvetti and S. Tatur, Phys. Rev. D **31** (1985) 1751.
- [555] J. -G. Korner, Z. Phys. C **33** (1987) 529.
- [556] Xiao-Gang He , J. P. Ma, and Bruce McKellar, Phys. Rev. D**47**(1993) 1744; Xiao-Gang He , J. P. Ma, and Bruce McKellar, Phys. Rev. D**49**(1994) 4548;
- [557] M. H. Tixier et al. DM2 Collaboration, Phys. Lett. B **212** 523.
- [558] N. A. Tornqvist, Found. of Phys., 11 (1981) 171; N. A. Tornqvist, Phys. Lett. A **117** (1986) 1.
- [559] A. Aspect, Phys. Rev. Lett., **49**(1982) 91.
- [560] Belle Collaboration, C.H. Wu *et al.*, Phys. Rev. Lett. **97**, 162003 (2006).

- [561] BES Collaboration, M. Ablikim, *et al.*, Phys. Rev. Lett. **97** (2006) 62001.
- [562] R.G. Ping, H.C. Chiang and B.S. Zou, Nucl. Phys. A**743** 149.
- [563] BES Collaboration, Phys. Rev. D**70** (2004) 012004.
- [564] D.A. Liberman, Phys. Rev. D **16**, 1542 (1977);  
G.W. Barry, Phys. Rev. D **16**, 2886 (1977).
- [565] S.J. Brodsky, I. Schimidt, and G.F. de Téramond, Phys. Rev. Lett. **64**, 1011 (1990).
- [566] H. Gao, T.-S.H. Lee, and V. Marinov, Phys. Rev. C **63**, 022201 (2001).
- [567] F. Huang, Z.Y. Zhang, and Y.W. Yu, Phys. Rev. C **73**, 025207 (2006).
- [568] Z.Y. Zhang, private communication.

# Part V

## Charm Physics

### Conveners

Hai-Bo Li, Zhi-Zhong Xing

### Contributors

D. M. Asner, I. I. Bigi, J. Charles, J. C. Chen,  
H. Y. Cheng, S. Descotes-Genon, K. L. He, H. B. Li,  
J. Liu, H. H. Liu, H. L. Ma, G. Rong, L. Roos, S. S.  
Sun, S. T'Jampens, Y. L. Wu, Z. Z. Xing, M. Yang,  
M. Z. Yang, Y. D. Yang, D. Y. Zhang, M. Zhong and  
Jia-Heng Zou



Nobody doubts that the discovery of hadrons with charm of the hidden and open variety – *i.e.* charmonium as well as  $D$  mesons – was instrumental in the acceptance of the Standard Model (SM) in general, and of quarks as *physical* degrees of freedom, rather than objects of mere *mathematical* convenience, in particular. Yet charm is all too often viewed as a quantum number with a great past and with no particularly interesting future. This is due to SM predictions of a rather dull electroweak phenomenology of CKM parameters, a low frequency for  $D^0 - \bar{D}^0$  oscillations, tiny (at best)  $CP$  asymmetries, and extremely rare flavor changing neutral currents which, in any case, are swamped by huge backgrounds from long-distance dynamics.

However, this pessimistic view focuses merely on the surface. A more profound perspective starts from the observation that charmed quark dynamics is full of challenges and promises. There is actually a three-fold motivation for *further dedicated and comprehensive* studies of charmed-quark physics:

1. Because the SM weak forces are well known, charmed particle decays provide an excellent laboratory for studying the impact of nonperturbative-QCD dynamics and for testing the validity of theoretical methods for dealing with them.
2. This, in turn, provides a calibration of the theoretical tools that are available for dealing with  $B$  decays.
3. Charm decays provide a novel window on New Physics in the weak sector, precisely because there is so little SM Background, in particular in  $CP$  violating processes.

None of the novel successes that the SM has scored since the turn of the millenium in the heavy flavour sector invalidates at all the case for the incompleteness of the SM. However, they strongly suggest that we *cannot* count on a numerically massive impact of New Physics on heavy flavour transitions. Thus, high accuracy and reliability – on the experimental as well as theoretical side – are *essential* for the exploitation of the indirect probes of New Physics that are accessible in heavy flavor decays, as is also the need to search in unusual places. Items (2) and (3) above can be expanded as follows:

- In order to saturate the discovery potential provided by  $B$  and  $D$  meson decays, we have to bring them under as precise theoretical control as possible. This requires much more than simply obtaining “engineering” input such as absolute branching ratios or the spectrum and quantum numbers of charmed hadrons. In addition we have to map out and understand in detail the Dalitz plots of many three-body  $D^0$ ,  $D^+$  and  $D_s^+$  decay channels, and extend such analyses to four-body final states.
- As mentioned above, the SM predicts at best small  $CP$ -violating asymmetries in charmed particle decays (basically in singly Cabibbo suppressed modes only) – a domain we are just now starting to probe in a quantitatively meaning way. While we cannot count on New Physics inducing large  $CP$  violation in charmed particle decays, the SM Background is either absent or very small. In this sense, the NP signal-to-noise ratio is favorable for  $CP$  studies in charm transitions. On the other hand, large data samples are required, and complex final states have to be analyzed with good control over the systematics.

In the following, these issues are addressed in considerable detail. While there are already several very good reviews in the recent literature [1], we have striven to make this exposition as self-contained as reasonably possible.

# Chapter 21

## Charm production and $D$ tagging <sup>1</sup>

### 21.1 Charmed particle production cross sections

#### 21.1.1 Introduction

Evidence for the onset of charmed particle production is clearly seen in the energy-dependence of the  $R$  values for  $e^+e^- \rightarrow \text{hadrons}$  shown in Fig. 21.1. Below the open charm  $D\bar{D}$  threshold, the strikingly narrow  $J/\psi$  and  $\psi'$  peaks have been assigned to the  $1S$  and  $2S$   $c\bar{c}$  bound states predicted by potential models that incorporate a color Coulomb term at short distances and a linear scalar confining term at large distances. Above the  $D\bar{D}$  threshold, there are several broad resonance peaks that decay predominantly into pairs of open-flavor charmed meson final states and, thus, have the potential of serving as “factories” for the production of charmed mesons. In the strong decays of these above-threshold resonances, the initial  $c\bar{c}$  meson decays via the production of a light  $q\bar{q}$  quark-antiquark pair ( $q = u, d, s$ ), forming  $c\bar{q}-\bar{c}q$  systems that subsequently separate into two charmed mesons. The mechanism of this open-charm decay process of the charmonium resonances is still poorly understood. In quark-model calculations, the process is modeled by a simple phenomenological  $q\bar{q}$  pair production amplitude, where the  $q\bar{q}$  pair is usually assumed to be produced with vacuum ( $0^{++}$ ) quantum numbers; variants of this decay model make different assumptions regarding the spatial dependence of the pair production amplitude relative to the initial  $c\bar{c}$  pair.

A detailed study of the charmed particle production cross section above the  $D\bar{D}$  mass threshold may provide a wealth of information about the strong dynamics of heavy and light quarks. Experimentally, charmed cross sections ( $\sigma_{\text{charm}}$ ) are determined from:

$$\sigma_{\text{charm}} = \frac{N_{\text{charm}}}{\mathcal{L}} \quad (21.1.1)$$

where  $\mathcal{L}$  is the integrated luminosity, and  $N_{\text{charm}}$  is the number of produced charmed meson pairs.  $N_{\text{charm}}$  can be obtained using a tagging technique that measures the number of charmed mesons that decay via a certain “tag” decay mode, and relating this to  $N_{\text{charm}}$  via

$$\mathcal{S} = N_{\text{charm}} \cdot \epsilon \cdot B,$$

---

<sup>1</sup>By Kang-Lin He, Sheng-Sen Sun, Ming Yang and Da-Yong Zhang

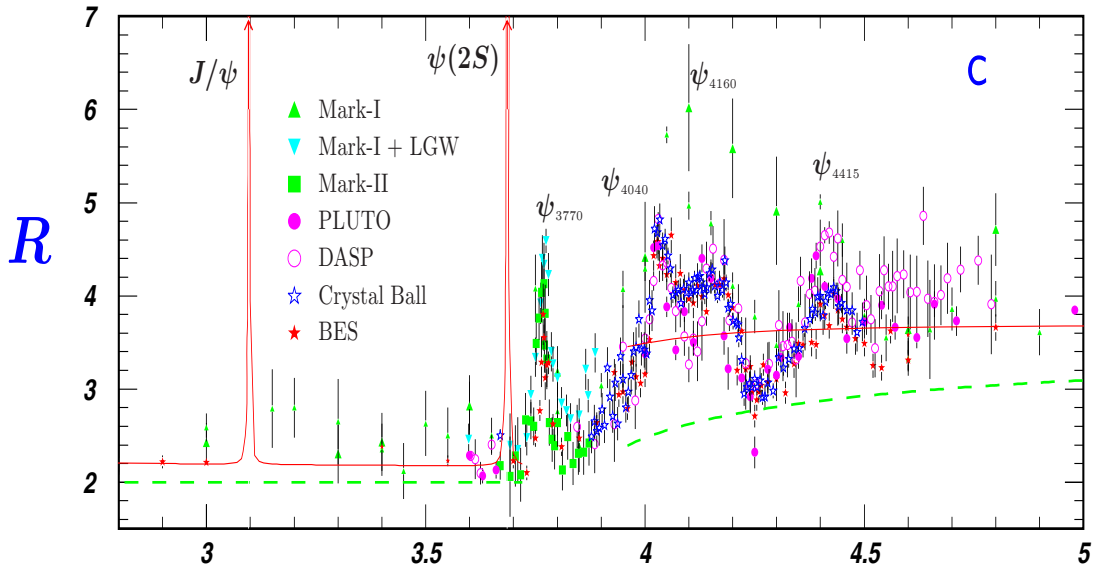


Figure 21.1: Measured  $R$  values in the region of the open charmed particle threshold.

where  $\mathcal{S}$  is the number of observed tags,  $\epsilon$  is the detection efficiency, and  $B$  is the branching fraction for the tag mode. Accurate measurements of charm production cross sections require both a large amount of integrated luminosity and high efficiency ( $\epsilon \cdot B$ ). The high statistics charm data obtained at *BES-III* will provide precision charm production cross section measurements above the  $D\bar{D}$  threshold.

In the early fall of 2005 and in the summer of 2006, the CLEO-c experiment spent two months of data-taking time scanning the 3.97–4.26 GeV center-of-mass (c.m.) energy range in order to determine the optimal c.m. energy value for studying  $D_s$  decays. They measured cross sections at twelve c.m. energies with a total luminosity of about  $60 \text{ pb}^{-1}$ . At each energy point, three, five and eight tag decay modes were used for  $D^0$ ,  $D^+$  and  $D_s^+$  meson production measurements, respectively. The different production channels can be distinguished based on the kinematics of the reconstructed tags using the kinematic variables  $M_{\text{inv}}$  and  $p_D$  (*i.e.* the invariant mass and c.m. momentum of the tagged  $D$ 's). Preliminary cross section results (with partially evaluated systematic uncertainties, no correction for multi-body contributions and not radiatively corrected) [4] are shown in Figure 21.2. The CLEO-c results agree well with previous measurements [9, 10, 11, 12, 13].

As shown in Figure 21.2, there is very little  $D\bar{D}$  production at any energy covered by the scan. Instead there is a sharply peaked  $D^*\bar{D}$  structure near the  $D^*\bar{D}^*$  threshold and a broad  $D^*\bar{D}^*$  peak or plateau that sets in just above threshold. The total charmed-particle production cross section throughout this region is considerable, and comparable to that for  $D\bar{D}$  production at the  $\psi(3770)$  ( $\sim 6 \text{ nb}$ ). There is a visible, but disappointingly small, peak in  $D_s\bar{D}_s$  production near the  $D^*\bar{D}^*$  threshold ( $\sim 0.3 \text{ nb}$ ), but a more impressive broad peak near 4.17 GeV, where there is about 1 nb of  $D_s^*\bar{D}_s$  production.

The CLEO-c scan data suggest the existence of “multi-body” production such as  $e^+e^- \rightarrow D^*\bar{D}\pi$ , which is reflected in the fact that the sum of the two-body modes that are measured does not account for all of charmed-meson production as determined from inclusive measurements. This is a very interesting possibility that can be studied at *BES-III*.

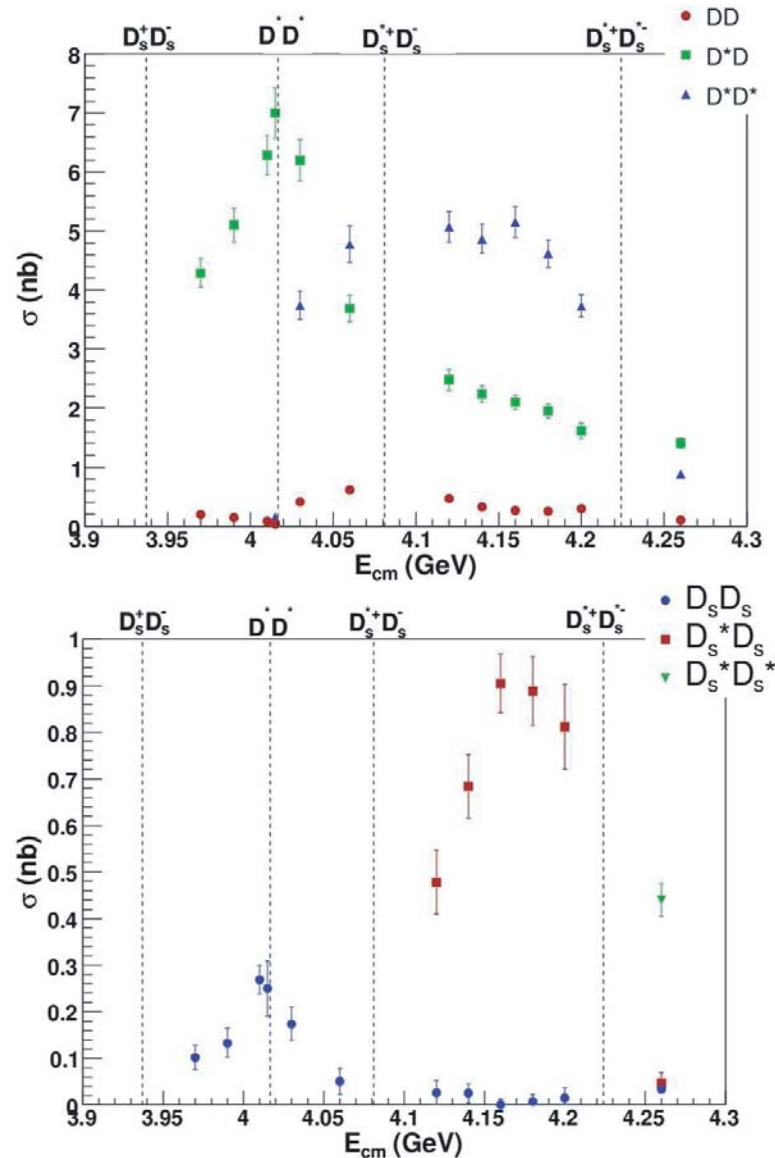


Figure 21.2: Cross sections for  $D\bar{D}$ ,  $D^*\bar{D}$ ,  $D^*\bar{D}^*$ ,  $D_s\bar{D}_s$ ,  $D_s^*\bar{D}_s$  and  $D_s^{*\pm}D_s^{*\mp}$  from CLEO-c.

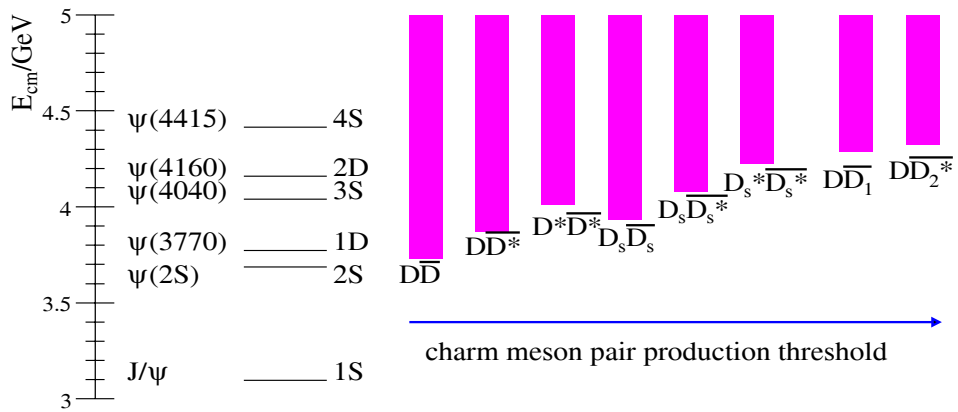


Figure 21.3: The  $c\bar{c}$  spectrum above the  $D\bar{D}$  threshold, and the thresholds for the lowest-lying charmed-meson decay channels. A comparison of the masses with potential model predictions indicate  $\psi(3770)$ ,  $\psi(4040)$ ,  $\psi(4160)$  and  $\psi(4415)$  assignments as the  $1^3D_1$ ,  $3^3S_1$ ,  $2D^3D_1$  and  $4^3S_1$   $c\bar{c}$  states, respectively.

### 21.1.2 The $1^{--}$ resonances around 4.0 GeV

The four known  $1^{--}$   $c\bar{c}$  states above the  $D\bar{D}$  threshold, *i.e.* the  $\psi(3770)$ ,  $\psi(4040)$ ,  $\psi(4160)$  and  $\psi(4415)$ , are of special interest because they are easily produced at an  $e^+e^-$  collider. The cross section in the region around 4.0 GeV can be understood as the successive onset of specific charmed meson channels:  $D\bar{D}$ ,  $D^*\bar{D}$ ,  $D_s\bar{D}_s$ , etc. Figure 21.3 shows the  $c\bar{c}$  spectrum above the  $D\bar{D}$  threshold, with the thresholds of the lowest-lying charmed-meson decay channels indicated at the right. Table 21.1 lists Ref. [2]’s predicted decay widths for these four  $1^{--}$   $c\bar{c}$  states.

#### $\psi(3770)$

The  $\psi(3770)$  lies below the  $D\bar{D}^*$  threshold and decays predominately into  $D\bar{D}$  pairs, making it an ideal “ $D$ -meson factory.” The  $\psi(3770)$  is generally considered to be the  $1^3D_1$   $c\bar{c}$  state. Some theoretical models predict  $\Gamma(\psi(3770) \rightarrow D\bar{D}) = 43$  MeV [2] for a pure  $^3D_1$  state, which is much wider than its measured value of  $23.6 \pm 2.7$  MeV[3]. This can be explained by the influence of an admixture of a  $2^3S_1$  component:

$$|\psi(3770)\rangle = \cos \theta |1^3D_1\rangle + \sin \theta |2^3S_1\rangle, \quad (21.1.2)$$

in this case the experimental  $\psi(3770)$  width can be accommodated with a mixing angle of  $\theta = -17.4^\circ \pm 2.5^\circ$ .

On the basis of isospin conservation and phase space considerations alone, one expects

$$\frac{\sigma(\psi(3770) \rightarrow D^0\bar{D}^0)}{\sigma(\psi(3770) \rightarrow D^+\bar{D}^-)} = \left( \frac{p_{D^0}}{p_{D^+}} \right)^3 = 1.45. \quad (21.1.3)$$

Mode	$\psi(3770)$	$\psi(4040)$	$\psi(4160)$	$\psi(4415)$
$D\bar{D}$	43	0.1	16	0.4
$D^*\bar{D}$		33	0.4	23
$D^*\bar{D}^*$		33	35	16
$D_s\bar{D}_s$		7.8	8.0	1.3
$D_s^*\bar{D}_s$			14	2.6
$D_s^*\bar{D}_s^*$				0.7
$D_1\bar{D}$				32
$D_2^*\bar{D}$				23
total	43	74	74	78
experiment[3]	$(23.6 \pm 2.7)$	$(52 \pm 10)$	$(78 \pm 20)$	$(43 \pm 15)$

Table 21.1: Open-charm strong decays widths for the  $\psi(3770)$ ,  $\psi(4040)$ ,  $\psi(4160)$  and  $\psi(4415)$ , as predicted by Ref. [2] (in MeV).

	$\sqrt{s}$	$\sigma(D^0\bar{D}^0)$	$\sigma(D^+\bar{D}^-)$
Mark-III[6]	3.768	$2.9 \pm 0.25 \pm 0.2$	$2.1 \pm 0.3 \pm 0.15$
BES-II[7]	3.773	$3.36 \pm 0.29 \pm 0.18$	$2.34 \pm 0.28 \pm 0.12$
CLEO-c[8]	3.773	$3.60 \pm 0.07^{+0.07}_{-0.04}$	$2.79 \pm 0.07^{+0.10}_{-0.05}$

Table 21.2: Charmed meson cross sections at the  $\psi(3770)$  (in nb).

However, in the calculation of Ref. [5], the ratio of  $D^0$  to  $D^+$  produced at  $\psi(3770)$  peak is predicted to be lower, namely 1.36, because of the influence of a  $^3D_1$  form-factor suppression. Precise determinations of the  $D^0$  and  $D^+$  cross sections near  $\psi(3770)$  will make it possible to measure this momentum-dependent form factor.

Charmed meson cross sections at the  $\psi(3770)$  have been measured by Mark-III [6], BES-II [7] and CLEO-c [8]. The results are listed in Table 21.2.

### $\psi(4040)$

The  $\psi(4040)$  is generally considered to be the  $^3S_1$  charmonium state. Studies of its strong decays are interesting because there are four kinematically allowed open-charm modes:  $D\bar{D}$ ,  $D^*\bar{D}$ ,  $D^*\bar{D}^*$  and  $D_s\bar{D}_s$ . Experimental results for the three non-strange modes as well as the  $D_s\bar{D}_s$  mode from BES-I and CLEO-c, are listed in Table 21.3. Here  $\sigma_{D\bar{D}}$  is pretty low, about 0.3 nb, while the cross sections for  $D^*\bar{D}$  and  $D^*\bar{D}^*$  are approximately equal, even though  $D^*\bar{D}^*$  has very little phase space. The reported relative branching fractions (scaled by  $p^{-3}$ , where  $p$  is the c.m. frame momentum) show a very strong preference for  $D^*$  final states:  $D^{*0}\bar{D}^{*0} \gg D^{*0}\bar{D}^0 \gg D^0\bar{D}^0$ . This motivated suggestions that the  $\psi(4040)$  might be a  $D^*\bar{D}^*$  molecule.

The cross sections reported by BES-I and CLEO-c for  $D_s\bar{D}_s$  production at  $E_{\text{cm}}$  near 4.04 GeV are both around 0.3 nb. This corresponds to a  $\psi(4040)$  branching fraction of about 4%, which is lower than the predicted value of  $\sim 11\%$ . This branching fraction is of special interest because it determines the event rates available for studies of  $D_s$  decays.

The  $D^*\bar{D}^*$  mode has three independent decay amplitudes:  $^1P_1$ ,  $^5P_1$  and  $^5F_1$ . Since the c.m. energy is very near the  $D^*\bar{D}^*$  threshold, the  $^5F_1$  amplitude can probably be ignored, in which case the amplitude ratio is predicted to be  $^5P_1/^1P_1 = -2/\sqrt{5}$ .

		$\psi(4040)$		$\psi(4160)$		
Modes		BES-I[9, 10]	CLEO-c[4]	Mark-II[11]	Mark-III[12, 13]	CLEO-c[4]
$D\bar{D}$	$D^0 D^0$	$0.19 \pm 0.05$				
	$D^+ D^-$	$0.13 \pm 0.04$	$\sim 0.2$	$0.4 \pm 0.3$	$0.23 \pm 0.04 \pm 0.05$	$\sim 0.2$
$D^* \bar{D}$	$D^{*0} D^0$	$2.46 \pm 0.60$				
	$D^{*\pm} D^{\mp}$	$2.31 \pm 0.70$	$\sim 7$	$2.0 \pm 0.5$	$1.5 \pm 0.1 \pm 0.3$	$\sim 2$
$D^* \bar{D}^*$	$D^{*0} D^{*0}$	$2.07 \pm 0.40$				
	$D^{*\pm} D^{*\mp}$	$0.87 \pm 0.30$	$\sim 3.6$	$4.4 \pm 0.7$	$3.6 \pm 0.2 \pm 0.6$	$\sim 5$
$D_s^+ D_s^-$		$0.320 \pm 0.056 \pm 0.081$	$\sim 0.3$			$\sim 0.02$
$D_s^{*\pm} D_s^{\mp}$					$0.83 \pm 0.17 \pm 0.31$	$\sim 0.9$

Table 21.3: Charmed meson production cross sections at the  $\psi(4040)$  and  $\psi(4160)$  resonance peaks (in nb).

### $\psi(4160)$

The generally preferred charmonium assignment for the  $\psi(4160)$  is the  $2^3D_1$  state. Like the  $\psi(3770)$ , it may also have a significant  $S$ -wave  $c\bar{c}$  component, since it has a  $e^+e^-$  width that is larger than expected for a pure  $D$ -wave  $c\bar{c}$  state. There are five open-charm decay modes available for the  $\psi(4160)$ :  $D\bar{D}$ ,  $D^* \bar{D}$ ,  $D^* \bar{D}^*$ ,  $D_s \bar{D}_s$  and  $D_s^* \bar{D}_s$ . Experimental cross section results from Mark-II, Mark-III and CLEO-c are listed in Table 21.3. The leading mode is  $D^* \bar{D}^*$ , with a branching fraction that is greater than 50%, followed by substantial  $D^* \bar{D}$  and  $D_s^* \bar{D}_s$  modes, plus a weak  $D\bar{D}$  mode. The  $D_s \bar{D}_s$  cross section is very small.

The  $\psi(4160) \rightarrow D^* \bar{D}^*$  decay mode is interesting because of the three decay amplitudes allowed for this final state. For a pure  $D$ -wave  $c\bar{c}$  assignment for the  $\psi(4160)$ , the ratio of the two  $D^* \bar{D}^*$   $P$ -wave amplitudes,  ${}^5P_1 / {}^1P_1 = -1/\sqrt{5}$ , is independent of the radial wave function. The  ${}^5F_1$  amplitude is predicted to be the largest, whereas it is zero for an  $S$ -wave  $c\bar{c}$  assignment. A determination of these  $D^* \bar{D}^*$  decay amplitude ratios would provide an interesting test of the charmonium assignment for the  $\psi(4160)$ .

### $\psi(4415)$

The  $\psi(4415)$  is usually considered to be the  $4^3S_1$   $c\bar{c}$  state. There are more than ten kinematically allowed open-charm strong decay modes, seven with  $c\bar{n}$  meson states ( $n = u, d$ ), and three with  $c\bar{s}$ . To date, no experimental results on exclusive charmed hadronic decay modes of the  $\psi(4415)$  have been reported. Some of the theoretical predictions are:

- 1) The largest exclusive mode is predicted to be the  $D_1 \bar{D}$ ,  $S + P$ -wave meson combination. The  $D_1$  is the  $1^{++}$  axial mesons near 2.425 GeV. Since it is rather narrow ( $\Gamma \approx 20 - 30$  MeV) and decays dominantly to  $D^* \pi$ , the experimental signal for  $\psi(4415) \rightarrow D D^* \pi$  should be quite distinct.
- 2) The second-largest decay mode is predicted to be another  $S + P$ -wave meson mode, namely  $D_2^* \bar{D}$ . The  $D_2^*$  is moderately narrow and has significant branching fractions to both  $D^* \pi$  and  $D \pi$ ; the  $D_2^* \bar{D}$  mode of the  $\psi(4415)$  should be observable in both of these channels.

- 3) The  $D^*\bar{D}^*$  mode is predicted to have comparable strength to that for  $D_2^*\bar{D}$ . If the  $\psi(4415)$  is indeed predominantly an  $S$ -wave  $c\bar{c}$  state, the expected amplitude ratio would be  ${}^5P_1/{}^1P_1 = -2/\sqrt{5}$ , with a zero  ${}^5F_1$  amplitude.
- 4) It is interesting to note that the high mass tail of  $\psi(4415)$  decays may provide access to the recently discovered  $D_{s0}(2317)$ , even though the channel  $D_s^*D_{s0}(2317)$  has a threshold of 4429 MeV, which is 14 MeV above the nominal  $\psi(4415)$  mass. Since the decay  $\psi(4415) \rightarrow D_s^*D_{s0}(2317)$  would be purely  $S$ -wave, with no centrifugal barrier,  $D_{s0}(2317)$  production just above threshold, near  $E_{\text{cm}} = 4435$  MeV, might be significant.

### Angular distributions and correlations

The strong decays of the  $\psi(4040)$  and  $\psi(4160)$  vector states to  $D^*\bar{D}^*$  are of special interest, because in each case this is their only multi-amplitude decay mode. The decay to  $D\bar{D}$  and  $D^*\bar{D}$  are single amplitude modes,  ${}^1P_1$  and  ${}^3P_1$ , respectively, and not much is learned from angular distribution measurements for these channels. In contrast, decays to  $D^*\bar{D}^*$ , have three allowed amplitudes,  ${}^1P_1$ ,  ${}^5P_1$  and  ${}^5F_1$ , and an experimental determination of the ratios of these amplitudes can provide important tests of the decay model, in particular about the quantum numbers of the light  $q\bar{q}$  pair produced in the decay. In this section we give a brief description of the angular distribution in non-relativistic language.

$D\bar{D}$  production is purely  $P$ -wave with an amplitude

$$\mathcal{A}_{D\bar{D}} \propto \vec{\eta} \cdot \vec{p}, \quad (21.1.4)$$

where  $\vec{\eta}$  is the  $\gamma^*$  polarization vector and  $\vec{p}$  is the  $D$  meson three-momentum in the c.m. system. For unpolarized beams, the angular distribution is simply:

$$|\mathcal{A}_{D\bar{D}}|^2 \propto 1 - \cos^2 \theta = \sin^2 \theta. \quad (21.1.5)$$

For  $D^*\bar{D}$  (or  $\bar{D}^*D$ ) production,  $S = 1$ . To have the correct parity,  $L$  has to be odd, and, since  $J = 1$ , it cannot be greater than  $L = 2$ ; thus  $L = 1$ . The  $D^*\bar{D}$  decay amplitude has the form

$$\mathcal{A}_{D^*\bar{D}} \propto \vec{\eta} \cdot (\vec{p} \times \vec{\epsilon}). \quad (21.1.6)$$

The  $D^*$  decays either into  $D\pi$  or  $D\gamma$ , each with a single amplitude:

$$\begin{aligned} \mathcal{A}_{D^*\rightarrow D\pi} &\propto \vec{\epsilon} \cdot \vec{q}, \\ \mathcal{A}_{D^*\rightarrow D\gamma} &\propto \vec{\epsilon} \cdot (\hat{\mathbf{k}} \times \hat{\mathbf{E}}) \propto \vec{\epsilon} \cdot \hat{\mathbf{B}}, \end{aligned} \quad (21.1.7)$$

where  $\vec{\epsilon}$  is the  $D^*$  polarization vector,  $\vec{q}$  the pion momentum,  $\hat{\mathbf{k}}$  the  $\gamma$  direction, and  $\hat{\mathbf{E}}$  and  $\hat{\mathbf{B}}$  represent the photon's electric and magnetic polarization vectors, where

$$\sum_{\text{pol}} \hat{E}_i \hat{E}_j = \sum_{\text{pol}} \hat{B}_i \hat{B}_j = \delta_{ij} - \hat{\mathbf{k}}_i \hat{\mathbf{k}}_j. \quad (21.1.8)$$

The measureable angular distributions have the form

$$\begin{aligned} |\mathcal{A}_{D^*\bar{D}}|^2 &\propto 1 + \cos^2 \theta, \\ |\mathcal{A}_{D^*\bar{D}, D^*\rightarrow D\pi}|^2 &\propto 1 + \cos^2 \theta_\pi \propto 1 - \cos^2 \theta_{D\pi}, \\ |\mathcal{A}_{D^*\bar{D}, D^*\rightarrow D\gamma}|^2 &\propto 1 - \frac{1}{3} \cos^2 \theta_\gamma. \end{aligned} \quad (21.1.9)$$

For  $D^* \bar{D}^*$  production,  $S = 0, 1$  and  $2$  are possible. However, since  $P = (-1)^L$  and  $C = (-1)^{L+S}$ ,  $L$  has to be odd and  $S$  has to be even. If  $S = 2$ , then  $L = 1$  or  $3$ . For a purely  ${}^3S_1$   $c\bar{c}$  parent state, the amplitude for  $L = 3$  ( $F$ -wave) is zero. In any case, if the c.m. energy is near the  $D^* \bar{D}^*$  threshold, the  $F$ -wave term can be ignored because of the centrifugal barrier. Using  $\mathcal{A}_0$  and  $\mathcal{A}_2$  to denote the production amplitudes for  $S = 0$  and  $S = 2$  states, we have

$$\mathcal{A}_{D^* \bar{D}^*} = \mathcal{A}_0(\vec{\epsilon} \cdot \vec{\epsilon})(\vec{p} \cdot \vec{\eta}) + \mathcal{A}_2 \left[ \frac{1}{2}(\vec{\epsilon} \cdot \vec{p})(\vec{\epsilon} \cdot \vec{\eta}) + \frac{1}{2}(\vec{\epsilon} \cdot \vec{\eta})(\vec{\epsilon} \cdot \vec{p}) - \frac{1}{3}(\vec{\epsilon} \cdot \vec{\epsilon})(\vec{p} \cdot \vec{\eta}) \right], \quad (21.1.10)$$

where  $\vec{\epsilon}$  and  $\vec{\bar{\epsilon}}$  are the  $D^*$  and  $\bar{D}^*$  polarization vectors. The amplitudes are normalized in such a way that the total cross section is given by  $|\mathcal{A}_{D^* \bar{D}^*}|^2 \propto |\mathcal{A}_0|^2 + \frac{5}{9} |\mathcal{A}_2|^2$ . Then the production angular distribution has the form

$$|\mathcal{A}_{D^* \bar{D}^*}|^2 \propto 1 - \frac{|\mathcal{A}_2|^2 + 18 |\mathcal{A}_0|^2}{7 |\mathcal{A}_2|^2 + 18 |\mathcal{A}_0|^2} \cos^2 \theta. \quad (21.1.11)$$

The angular distributions for pions and photons produced in the process  $e^+ e^- \rightarrow D^* \bar{D}^* \rightarrow (D\pi_1)(\bar{D}\pi_2)$ ,  $(D\pi)(D\gamma)$ , and  $(D\gamma_1)(\bar{D}\gamma_2)$ , and their correlations are as follows [14]:

$$\begin{aligned} |\mathcal{A}_{D^* \bar{D}^*}|^2 &\propto \left(1 + \frac{1}{3} \cos^2 \theta_{\pi\pi}\right) |\mathcal{A}_2|^2 + 6 \cos^2 \theta_{\pi\pi} |\mathcal{A}_0|^2, \\ |\mathcal{A}_{D^* \bar{D}^*}|^2 &\propto \left(1 - \frac{1}{7} \cos^2 \theta_{\gamma\pi}\right) |\mathcal{A}_2|^2 + \frac{18}{7} (1 - \cos^2 \theta_{\gamma\pi}) |\mathcal{A}_0|^2, \\ |\mathcal{A}_{D^* \bar{D}^*}|^2 &\propto \left(1 + \frac{1}{13} \cos^2 \theta_{\gamma\gamma}\right) |\mathcal{A}_2|^2 + \frac{18}{13} (1 + \cos^2 \theta_{\gamma\gamma}) |\mathcal{A}_0|^2, \\ |\mathcal{A}_{D^* \bar{D}^*}|^2 &\propto \left(1 - \frac{21}{47} \cos^2 \theta_\pi\right) |\mathcal{A}_2|^2 + \frac{12}{47} |\mathcal{A}_0| |\mathcal{A}_2| \cos \varphi (1 - 3 \cos^2 \theta_\pi) + \frac{72}{47} |\mathcal{A}_0|^2, \\ |\mathcal{A}_{D^* \bar{D}^*}|^2 &\propto \left(1 + \frac{21}{73} \cos^2 \theta_\gamma\right) |\mathcal{A}_2|^2 + \frac{|\mathcal{A}_0| |\mathcal{A}_2|}{73} \cos \varphi (3 \cos^2 \theta_\gamma - 1) + \frac{144}{73} |\mathcal{A}_0|^2, \end{aligned} \quad (21.1.12)$$

where  $\varphi$  is the relative phase between the amplitudes  $\mathcal{A}_0$  and  $\mathcal{A}_2$ .

The two principal models currently used by theorists to study  $c\bar{c}$  decays to open charm are the  ${}^3P_0$  model [15] and the Cornell (timelike vector) model [16]. They give different predictions for the relative  $D^* \bar{D}^*$  decay amplitudes, which have not been tested experimentally. At *BES-III*, we can measure these amplitude ratios, which will guide the formulation of more accurate models for  $c\bar{c}$  strong decays and improve our general understanding of QCD strong-decay processes.

### 21.1.3 Charmed meson cross sections below the $D^* \bar{D}$ threshold

Near the open charm threshold, charmed mesons are produced in pairs, *i.e.*  $D^0 \bar{D}^0$ ,  $D^+ D^-$  and  $D_s^+ D_s^-$ , that are nearly at rest. Here the double-tag method can be applied to

obtain decay-mode-independent cross section measurements. For specific hadronic decay modes,  $i$  and  $j$ , the number of produced  $D\bar{D}$  pairs can be expressed as the number of single and double tags:

$$N_{D\bar{D}} = \begin{cases} \frac{1}{2} \times \frac{\mathcal{S}_i \times \mathcal{S}_j}{\mathcal{D}_{ij}} \times \frac{\epsilon_{ij}}{\epsilon_i \times \epsilon_j} & i \neq j \\ \frac{1}{4} \times \frac{\mathcal{S}_i^2}{\mathcal{D}_{ii}} \times \frac{\epsilon_{ii}}{\epsilon_i^2} & i = j, \end{cases} \quad (21.1.13)$$

where  $N_{D\bar{D}}$  is the total number of produced  $D\bar{D}$  pairs, summed over all decay modes,  $\mathcal{S}_i$  and  $\mathcal{D}_{ij}$  are the number of single and double tags, and  $\epsilon_i$  and  $\epsilon_{ij}$ ,  $\epsilon_{ii}$  are the detection efficiencies for the single and double tag decays.

Many systematic uncertainties cancel in the double-tag measurement. Applying the (reasonably good) approximations  $\frac{\epsilon_{ij}}{\epsilon_i \epsilon_j} \approx 1$ ,  $\frac{\epsilon_{ii}}{\epsilon_i^2} \approx 1$  to Eq. (21.1.13), and ignoring the error on the number of single tags, the precision on the number of produced charm meson pairs is estimated to be

$$\frac{\Delta N}{N} \approx \frac{1}{\sqrt{\sum \mathcal{D}_{ij}}} = \frac{1}{\sqrt{\mathcal{D}}}, \quad (21.1.14)$$

where  $\mathcal{D}$  presents the total number of double-tags.

At *BES-III*, about 400,000 and 200,000  $D^0$  and  $D^+$  double tags are expected to be reconstructed in a  $15 \text{ fb}^{-1}$  data sample accumulated at  $\sqrt{s} = 3.773 \text{ GeV}$ . Thus, the statistical error on the number of produced  $D\bar{D}$  pairs can be ignored. Ultimately, the dominant systematic uncertainty on the cross section measurement will be that from the luminosity ( $\mathcal{L}$ ) measurement, which is expected to be at the 1% level. For a  $3 \text{ fb}^{-1}$  data sample taken at  $4.03 \text{ GeV}$  or  $4.17 \text{ GeV}$ , about 750 and 2,200  $D_s$  double-tag events will be detected, and the corresponding statistic errors will be 2.0% or 1.2%. Statistical and systematic errors will contribute roughly equally to the  $D_s$  cross section measurement errors.

### 21.1.4 Charmed cross sections above the $D^*\bar{D}$ threshold

Both the  $\psi(4040)$  and  $\psi(4160)$  are above the  $D^*$  threshold and decay mainly into  $D^*$  final states. Since the hadronic decay modes of the  $D^*$  meson have a low  $Q$  value, the charmed meson momentum spectra can be used to distinguish the different production channels and measure their cross sections.

The  $D$ -meson momentum distributions are monochromatic for  $D\bar{D}$  production and for the “bachelor”  $D$  meson produced directly at the  $\psi(4040) \rightarrow D\bar{D}^*$  production point, but different for the “daughter”  $D$  mesons from  $D^*$  decays. Daughter  $D$  mesons from  $D^* \rightarrow \pi^0 D$  or  $\pi^+ D^0$  decays have a narrower momentum distribution than those for  $D^*$  decays to  $\gamma D$ . Figure 21.4 shows the momentum distributions for  $D^0$  and  $D^+$  mesons that are produced in  $\psi(4040) \rightarrow D\bar{D}^*$  (or  $\bar{D}D^*$ ) decays, where the contributions from the bachelor  $D$  mesons and the  $D^* \rightarrow \pi D$  and  $D^* \rightarrow \gamma D$  daughters are indicated.

#### The momentum distribution of $D$ mesons

The  $p_D$  distribution for  $D$  mesons produced by the decay of a  $D^*$  depends on the momentum of the parent  $D^*$  in the lab frame and the angle of emission of the  $D$  in the

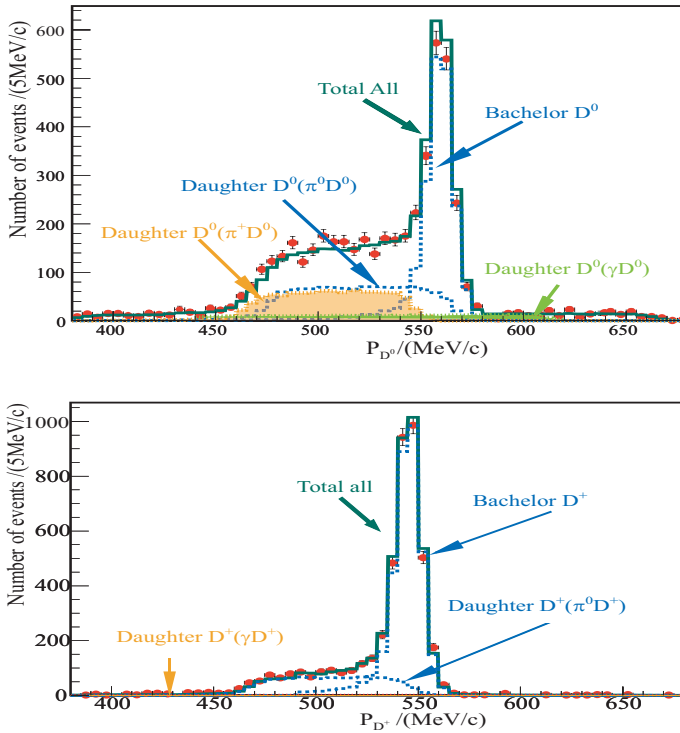


Figure 21.4: Simulated  $p_{D^0}$  and  $p_{D^+}$  distribution from  $D^*\bar{D}$  production at  $\sqrt{s} = 4.03\text{GeV}$ .

$D^*$  rest frame. In the case of  $D^*\bar{D}$ , the angular distribution of the  $D$  in the  $D^*$  frame can be uniquely predicted, while, in the case of  $D^*\bar{D}^*$ , it is much more complicated. Initial state radiation further distorts the shape of the  $p_D$  distribution by reducing the effective center-of-mass energy.

The shape of the distribution for  $p_D$  can be simulated with a Monte Carlo event generator [17, 18], with main contributions from the following channels:

$$p_{D^+} \rightarrow \begin{pmatrix} D^{*+}D^{*-} & D^{*\pm} \rightarrow \pi^0 D^{\pm} \\ D^{*+}D^{*-} & D^{*\pm} \rightarrow \gamma D^{\pm} \\ D^{*\pm}D^{\mp} & D^{*\pm} \rightarrow \pi^0 D^{\pm} \\ D^{*\pm}D^{\mp} & \text{Direct } D^{\mp} \\ D^{*\pm}D^{\mp} & D^{*\pm} \rightarrow \gamma D^{\pm} \\ D^+D^- & \text{Direct } D^{\pm} \end{pmatrix} \quad p_{D^0} \rightarrow \begin{pmatrix} D^{*+}D^{*-} & D^{*+} \rightarrow \pi^+ D^0 \\ D^{*0}\bar{D}^{*0} & D^{*0} \rightarrow \pi^0 D^0 \\ D^{*0}\bar{D}^{*0} & D^{*0} \rightarrow \gamma D^0 \\ D^{*\pm}D^{\mp} & D^{*\pm} \rightarrow \pi^{\pm} D^0 \\ D^{*0}\bar{D}^0 & D^{*0} \rightarrow \pi^0 D^0 \\ D^{*0}\bar{D}^0 & D^{*0} \rightarrow \gamma D^0 \\ D^{*0}\bar{D}^0 & \text{Direct } D^0 \\ D^0\bar{D}^0 & \text{Direct } D^0 \end{pmatrix} \quad (21.1.15)$$

Charmed meson production cross sections and  $D^*$  decay branching can be determined by simultaneous fits to the  $p_{D^0}$  and  $p_{D^+}$  distributions.

The  $p_D$  distributions are distorted by the effects of ISR and the  $\psi(3770)$ ,  $\psi(4040)$  and  $\psi(4160)$  line shapes. Systematic uncertainties can be estimated by varying the resonance parameters of the  $\psi$ 's in the MC generator. As shown in Table 21.1, the current values of the  $\psi(4040)$  and  $\psi(4160)$  widths have large uncertainties. In addition, the partial decay widths of the  $\psi$ 's to different charm meson pair channels have an energy dependence given

by the relation

$$\Gamma_i = \Gamma_i^0 \left( \frac{q}{q_0} \right)^{2L+1} \frac{m_0}{m}, \quad (21.1.16)$$

where  $q$  and  $q_0$  are the c.m. frame decay momenta in for  $E_{cm} = mc^2$  and  $m_0c^2$ , respectively, with the subscript 0 denoting the  $q$  and  $m$  values at the resonance peak, and the  $L$  is the orbital angular momentum.

The mass peaks of the three higher  $\psi$  resonances are close to each other and, since they have large total widths, interference between them (as well as with the continuum) can distort their lineshapes. Fine scan measurements can be used to investigate the effects of interference in each decay channel.

### Full reconstruction of $D\bar{D}$ events

In the discussion of  $D$  meson momentum spectra above the  $D^*$  production threshold, we have assumed that events containing charmed  $D$  mesons arise only from  $D\bar{D}^*$  and  $D^*\bar{D}^*$  production ( $D\bar{D}$  production is simple), so that the momentum of single detected  $D$  in an event can be used to infer that the recoiling system is either a monochromatic bachelor  $\bar{D}$ , a  $D^*$  (from  $D\bar{D}^*$  production), or a  $D^*\pi$  (or  $D^*\gamma$ ) combination for  $D^*\bar{D}^*$  production. Note that  $D^0$  tags can come from neutral  $D^{(*)}$  pair production or charged  $D^{(*)}$  pair production, while  $D^+$  tags come solely from charged  $D^{(*)}$  pair production, since neutral  $D^*$ 's are kinematically forbidden to decay to the charged  $D^\pm$  mesons. We assumed that the neutral  $D^*$  mesons decay to  $D^0$  mesons with a 100% branching fraction, and the charged  $D^*$  mesons decay to  $D^0$  meson with a decay fraction  $\text{Br}(D^{*+} \rightarrow \pi^+ D^0)$  and the correspondingly produced  $D^+$  mesons with a decay fraction  $1 - \text{Br}(D^{*+} \rightarrow \pi^+ D^0)$ . Table 21.4 lists the observed probability of single- and double-tags for different charmed  $D$  meson production channels.

Events containing either one or two reconstructed  $D$  mesons are selected. The momentum distributions of reconstructed  $D$  tags provide additional information to identify the  $D\bar{D}, D\bar{D}^*, D^*\bar{D}^*$  production channels. By comparing the observed number of single-tag  $D$  meson events with the number of partially reconstructed double-tag  $D$  meson events, we determined the different charmed  $D$  meson production rates using a  $\chi^2$  minimization fit.

To determine the individual branching ratios ( $B_i$ ) and the number of produced  $D\bar{D}^*$ ,  $D^*\bar{D}^*$  pairs ( $N = \sigma\mathcal{L}$ ), the observed number of single-tags( $S_i$ ) and double-tags( $D_{ij}$ ) is expected to be (see Table 21.4)

$$\left. \begin{array}{lcl} S_i^0 & = & 2N^0\epsilon_i B_i + N^+\epsilon_i B_i B_+^0 \\ S_i^+ & = & N^+\epsilon_i B_i + N^+\epsilon_i B_i (1 - B_+^0) \\ D_{ij}^{00} & = & \delta_{ij} N^0\epsilon_{ij} B_i B_j \\ D_{ij}^{++} & = & \delta_{ij} N^+\epsilon_{ij} B_i B_j (1 - B_+^0) \\ D_{ij}^{0+} & = & N^+\epsilon_{ij} B_i B_j B_+^0 \end{array} \right\} \quad \text{for } D\bar{D}^* \text{ production} \quad (21.1.17)$$

and

		Single Tags		Double Tags		
Modes		$D^0$	$D^+$	$D^0$ vs $D^0$	$D^+$ vs $D^-$	$D^0$ vs $D^-$
$D\bar{D}^*$	0	$2\epsilon_i B_i$	0	$\delta_{ij}\epsilon_{ij}B_iB_j$	0	0
	$\pm$	$\epsilon_i B_i B_0^+$	$\epsilon_i B_i (1 + B_+^+)$	0	$\delta_{ij}\epsilon_{ij}B_iB_jB_+^+$	$\epsilon_{ij}B_iB_jB_0^+$
$D^*\bar{D}^*$	0	$2\epsilon_i B_i$	0	$\delta_{ij}\epsilon_{ij}B_iB_j$	0	0
	$\pm$	$2\epsilon_i B_i B_0^+$	$2\epsilon_i B_i B_+^+$	$\delta_{ij}\epsilon_{ij}B_iB_j(B_0^+)^2$	$\delta_{ij}\epsilon_{ij}B_iB_j(B_+^+)^2$	$2\epsilon_{ij}B_iB_jB_0^+B_+^+$
$D\bar{D}$	0	$2\epsilon_i B_i$	0	$\delta_{ij}\epsilon_{ij}B_iB_j$	0	0
	$\pm$	0	$2\epsilon_i B_i$	0	$\delta_{ij}\epsilon_{ij}B_iB_j$	0

Table 21.4: The observation probability for single-tags and double-tags above charm threshold. Here,  $B_i, B_j$  are the decay fractions for  $D \rightarrow (i^{\text{th}}, j^{\text{th}})$  tag channels,  $\epsilon_i$  is the single-tag and  $\epsilon_{ij}$  the double-tag acceptance,  $B_0^0 = \text{Br}(D^{*+} \rightarrow \pi^+ D^0)$ ,  $B_+^+ = 1 - B_0^0$ , and  $\delta_{ij} = \begin{cases} 1 & (i=j) \\ 2 & (i \neq j) \end{cases}$ . The acceptance  $\epsilon$  is weighted by the detection efficiencies for  $D$  mesons originating from different  $D^*$  decay modes.

$$\left. \begin{array}{lcl} S_i^0 & = & 2N^0\epsilon_i B_i + 2N^+\epsilon_i B_i B_0^0 \\ S_i^+ & = & 2N^+\epsilon_i B_i (1 - B_0^0) \\ D_{ij}^{00} & = & \delta_{ij}(N^0\epsilon_{ij}B_iB_j + N^+\epsilon_{ij}B_iB_j(B_0^+)^2) \\ D_{ij}^{++} & = & \delta_{ij}N^+\epsilon_{ij}B_iB_j(1 - B_0^+)^2 \\ D_{ij}^{0+} & = & 2N^+\epsilon_{ij}B_iB_jB_0^0(1 - B_0^+) \end{array} \right\} \text{ for } D^*\bar{D}^* \text{ production,} \quad (21.1.18)$$

where  $N^0 = \sigma_{D^0\bar{D}^{*0}} \times \mathcal{L}$  &  $N^+ = \sigma_{D^\pm\bar{D}^{*\mp}} \times \mathcal{L}$  in Eq. (21.1.17),  $N^0 = \sigma_{D^{*0}\bar{D}^{*0}} \times \mathcal{L}$  &  $N^+ = \sigma_{D^{*\pm}\bar{D}^{*\mp}} \times L$  in Eq. (21.1.18),  $B_{i,j}$  are the individual branching fractions for  $D$  decay modes  $\{i, j\}$ ,  $\epsilon_i$  the efficiency for reconstructing a single-tag in the  $i^{\text{th}}$   $D$  decay mode,  $\epsilon_{ij}$  the reconstruction efficiency for  $D\bar{D}$ (from  $D\bar{D}^*$  and  $D^*\bar{D}^*$ ) decay mode  $\{i, j\}$ , and  $B_0^0 = \text{Br}(D^{*+} \rightarrow \pi^+ D^0)$ . The efficiencies are determined from a detailed Monte Carlo simulation of  $D\bar{D}^*$ ,  $D^*\bar{D}^*$  production and decay, including a full simulation of the detector response. Finally, we form a  $\chi^2$  expression:

$$\chi^2 = \sum_i \frac{(S_{\text{measure}}^i - S_{\text{predict}}^i)^2}{\sigma_{S_{\text{measure}}^i}^2} + \sum_{ij} \frac{(D_{\text{measure}}^{ij} - D_{\text{predict}}^{ij})^2}{\sigma_{D_{\text{measure}}^{ij}}^2}, \quad (21.1.19)$$

where the indices  $\{\text{measure}, \text{predict}\}$  represent for the number of tags obtained from the  $\{\text{measurement, prediction}\}$  and  $\sigma$  are the measurement errors. In the fit, one can extract the individual branching fractions ( $B_i$ ), and the number of produced  $D\bar{D}^*$  and  $D^*\bar{D}^*$  pairs ( $N = \sigma \mathcal{L}$ ).

### 21.1.5 Corrections to the observed cross sections

The Born cross section for charmed mesons are obtained by correcting the observed cross section for the effects of initial state radiation (ISR). A detailed discussion of ISR corrections can be found in the Section 4.2. For completeness, we provide here a brief description of the correction procedure.

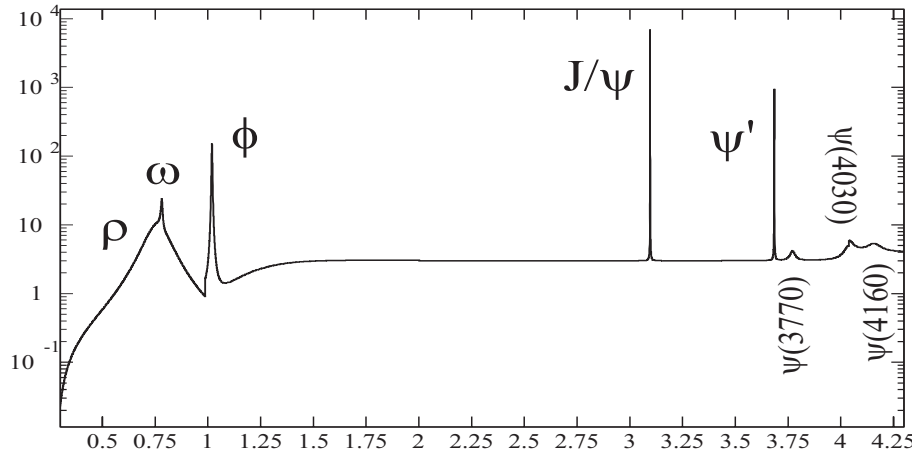


Figure 21.5: The Born cross section for  $e^+e^- \rightarrow$  hadrons from 0.3 GeV to 4.3 GeV (in units of  $R$ ).

The ISR correction is dependent on the cross section at all energies lower than the nominal c.m. energy. Kuraev and Fadin [19, 20, 21] give the observed cross section  $\sigma$  as an integral over the idealized radiatively corrected Born cross section  $\bar{\sigma}$ :

$$\sigma(s) = \int \bar{\sigma}(s(1-x)) F_{KF}(x, s),$$

where  $s = W^2$  and  $x = (W^2 - W_{\text{eff}}^2)/W^2$ ,  $W$  is the nominal c.m. energy,  $W_{\text{eff}}$  is the effective energy after ISR and  $F_{KF}(x, s)$  is the Kuraev-Fadin kernel function given by

$$F_{KF}(x, s) = tx^{t-1} \left[ 1 + \frac{3}{4}t + \frac{\alpha}{\pi} \left( \frac{\pi^2}{3} - \frac{1}{2} \right) + t^2 \left( \frac{9}{32} - \frac{\pi^2}{12} \right) \right] - t \left( 1 - \frac{x}{2} \right) + \frac{t^2}{8} \left[ 4(2-x) \ln \frac{1}{x} - \frac{1+3(1-x)^2}{x} \ln(1-x) - 6 + x \right], \quad (21.1.20)$$

where  $t = 2\frac{\alpha}{\pi} \left( \ln \frac{W^2}{m_e^2} - 1 \right)$ . Kuraev and Fadin claim a 0.1% accuracy for  $F_{KF}(x, s)$  [21]. The idealized Born cross section  $\bar{\sigma}$  for the charm region and below is sketched in Figure 21.5.

For a resonance, the Breit-Wigner amplitude and the cross section are given by

$$\mathcal{A}(W) = \frac{\sqrt{\kappa}}{W - M + i\Gamma/2} \quad (21.1.21)$$

$$\sigma(W) = |\mathcal{A}|^2 = \frac{\kappa}{(W - M)^2 + \Gamma^2/4},$$

where

$$\kappa = 3\pi\Gamma_{ee}\Gamma/M^2. \quad (21.1.22)$$

Note that the amplitude  $\mathcal{A}$  is complex, with a phase  $\phi_{\text{res}} = -\tan^{-1}[(\Gamma/2)/(W - M)]$  that starts near 0° at low  $W$ , passes through 90° at  $W = M$ , and approaches 180° at large  $W$ . If interference occurs between different overlapping  $\psi$  resonances with relative phases  $\alpha$ 's,

the total amplitude and the cross section is given by:

$$\mathcal{A}(W) = \sum_i \mathcal{A}_i \exp(i\alpha_i), \quad \sigma(W) = |\mathcal{A}|^2. \quad (21.1.23)$$

In BEPCII, synchrotron radiation and the replacement of the radiated energy by the RF cavities generates an energy spread in each beam, resulting in an essentially Gaussian distribution for the c.m. energy  $W'$  centered on the nominal  $W$  value

$$G(W, W') = \frac{1}{\sqrt{2\pi}\Delta} \exp\left[-\frac{(W - W')^2}{2\Delta^2}\right], \quad (21.1.24)$$

where  $\Delta$  is the rms c.m. energy spread. The final convolution has to be done numerically in order to include effects of the Breit-Wigner, the ISR tail, and the c.m. energy spread.

The observed partial width,  $\Gamma_{ee}$ , has to be corrected for all effects that contribute to  $1^{--} \rightarrow e^+e^-$ , including  $1^{--} \rightarrow e^+e^-\gamma$  decays. This correction will depend on the minimum detectable photon energy and, thus, the total scan width will not be equal to  $\Gamma_{tot}$ . In  $1^{--} \rightarrow e^+e^-(\gamma)$  decay, the divergences at the soft limit for photon emission and in the vertex correction cancel [22]. But in  $e^+e^- \rightarrow 1^{--}$  production there is no photon in the initial state and, thus, no cancelation. The correct procedure is to use the final state definition of  $\Gamma_{ee} = \Gamma(1^{--} \rightarrow e^+e^-(\gamma))$ , and to correct the lowest-order prediction for the  $e^+e^- \rightarrow 1^{--}$  process to account for the radiative effects that are included in the definition of  $\Gamma_{ee}$ :

$$\Gamma_{ee} = \Gamma_{ee}^0(1 + \delta_{vac}), \quad (21.1.25)$$

where  $\Gamma_{ee}$  is the experimental width,  $\Gamma_{ee}^0$  is the lowest-order width, and  $(1 + \delta_{vac})$  is the vacuum polarization factor that includes both leptonic and hadronic terms. Its variation from charm threshold to 4.14 GeV is less than  $\pm 2\%$ . To a reasonable approximation it can be treated as a constant with the value

$$(1 + \delta_{vac}) = 1.047 \pm 0.024. \quad (21.1.26)$$

## 21.2 $D$ -meson tagging

BEPCII will run near the charm threshold and provide unprecedented opportunities to study the physics of weak decay of charmed mesons. At the  $\psi(3770)$  resonance,  $D^0\bar{D}^0$  and  $D^+D^-$  pairs are produced with no other accompanying particles, thereby providing extremely clean and pure charmed-meson signals. The large production cross section at the peak of the  $\psi(3770)$ , its large decay fractions to charmed meson pairs, and high tagging efficiencies of *BES-III* will allow us to accumulate large samples of events where both  $D$  mesons are reconstructed. By applying the double-tag method to these event samples, many systematic uncertainties will cancel. The quantum coherence of the two produced  $D^0$  mesons from  $\psi(3770) \rightarrow D^0\bar{D}^0$  decays will provide opportunities to measure  $D^0 - \bar{D}^0$  mixing parameters, determine strong phases, and search for  $CP$  violation.

The general technique used for charm physics studies at the  $\psi(3770)$  is referred as tagging. Since the  $D\bar{D}$  are pair produced just above threshold, the identification of one  $D$  meson from a subset of tracks in an event guarantees that the remaining tracks have originated from the decay of the recoiling  $\bar{D}$ . The reconstructed  $D$  is referred to as the

tagged  $D$  or simply the tag, while everything not associated with the tag is referred to as the recoil. Once a tag is found, the recoil tracks can be examined for the decay mode of interest. Usually Cabibbo-favored hadronic decay modes with large branching ratios, such as  $D^0 \rightarrow K^-\pi^+(\sim 4\%)$ ,  $D^0 \rightarrow K^-\pi^+\pi^+\pi^-(\sim 8\%)$ ,  $D^0 \rightarrow K^-\pi^+\pi^0(\sim 14\%)$ ,  $D^+ \rightarrow K^-\pi^+\pi^+(\sim 9\%)$ ,  $D^+ \rightarrow \bar{K}^0\pi^+(\sim 3\%)$ ,  $D^+ \rightarrow \bar{K}^0\pi^+\pi^0(\sim 14\%)$ ,  $D^+ \rightarrow \bar{K}^0\pi^+\pi^+\pi^-(\sim 6\%)$ ,  $D^+ \rightarrow K^-\pi^+\pi^+\pi^0(\sim 6\%)$  are used for reconstructing tags. At the  $\psi(4040)$  or  $\psi(4160)$  energies,  $D_s^+$  mesons can be tagged using the  $D_s^+ \rightarrow K^-K^+\pi^+(\sim 5\%)$  and  $D_s^+ \rightarrow \bar{K}^0K^+(\sim 4\%)$  modes, and some  $D_s^+$  decays to final states containing an  $\eta$  or an  $\eta'$ .

### 21.2.1 Tag reconstruction

Tag reconstruction begins with the charged track selection. All charged tracks must have a good helix fit, and are required to be measured in the fiducial region of the drift chamber. Their parameters must be corrected for energy loss and multiple scattering according to the assigned mass hypotheses. Tracks not associated with  $K_S$  reconstruction are required to have originated from the interaction point. Kaons and pions are identified by the PID algorithm to reduce the combinatoric background.

Neutral kaon candidates are mainly reconstructed in the  $K_S \rightarrow \pi^+\pi^-$  decay mode. The decay vertex formed by the  $\pi^+\pi^-$  pair is required to be separated from the interaction point, and the momentum vector of  $\pi^+\pi^-$  pair must be aligned with the position vector from the interaction point to the decay vertex. The  $\pi^+\pi^-$  invariant mass is required to be consistent with the  $K_S$  mass. The track parameters and the error matrices are recalculated at the secondary vertex.  $K_L$  reconstruction will be useful in some double tag analyses. In this case, the recoil mass of all detected particles should be within the range of the  $K_L$  mass, and an interaction should be observed in a restricted angular region of the EMC or muon counters.

Neutral  $\pi^0$  mesons are reconstructed from  $\pi^0 \rightarrow \gamma\gamma$  decays using photons observed in the barrel and endcap regions of the EMC. In the identification of neutral tracks in the EMC, one has to distinguish genuine photons from a number of processes that can produce spurious showers. The major source of these “fake photons” arise from interactions of  $\pi$  or  $K$  mesons with the material before or in the EMC crystals; the secondary particles from these interactions can “split-off” and create energy clusters that are not associated to the original track’s shower by the pattern recognition algorithm. Other sources of fake photons are particle decays, back splash from particle interactions behind the EMC, beam-associated backgrounds and electronic noise. A shower is selected as an isolated photon by requiring a minimum energy deposit, e.g.  $E_\gamma > 40\text{MeV}$ , and a spatial separation from the nearest charged tracks. In addition,  $\eta/\eta'$  meson candidates can be reconstructed in the  $\eta \rightarrow \gamma\gamma$ ,  $\eta \rightarrow \pi^+\pi^-\pi^0$ ,  $\eta' \rightarrow \gamma\rho^0$  and  $\eta' \rightarrow \eta\pi^+\pi^-$  decay modes. For all these modes,  $3\sigma$  consistency with the  $\pi^0/\eta/\eta'$  mass is required, followed by a kinematic mass constraint.

Finally, for  $D$ -meson reconstruction, all tracks with consistent mass hypotheses and, if appropriate, reconstructed  $K_S$ ’s,  $\pi^0$ ’s and  $\eta/\eta'$ ’s are permuted to form the candidate combinations. To be accepted as a  $D$  tag, the candidate combination of final particles with a reconstructed total energy  $E_D$ , and total momentum  $p_D$  must fulfill the requirement that the energy difference,  $\Delta E = E_D - E_{\text{beam}}$ , is consistent with zero.

### 21.2.2 Beam constrained mass

The conventional method for observing resonant signals in particle physics analyses is by selecting a set of tracks and studying the invariant mass ( $M_{\text{inv}}$ ):

$$M_{\text{inv}} = \sqrt{\left(\sum_i E_i\right)^2 - \left(\sum_i \vec{p}_i\right)^2}, \quad (21.2.27)$$

where  $(E, \vec{p})_i$  are the energy and three-momentum of the track  $i$ . For reconstructing  $D$  decays at the  $\psi(3770)$  peak, the resolution of the invariant mass at *BES-III* is typically 6 to 8 MeV for modes containing only charged tracks and about 12 MeV for modes containing a single  $\pi^0$ . Improvement can be obtained by exploiting the kinematics of pair production of  $D$  mesons near threshold. Since the  $D$ 's are pair produced, each has an energy equal to that of the beam in the c.m. frame. Another quantity, known as the beam-constrained mass ( $M_{\text{bc}}$ ), can be constructed by replacing the energy of the  $D$  ( $E_D$  in Eq. 21.2.27) with the energy of the beam in the c.m. frame ( $E_{\text{beam}}$ ):

$$M_{\text{bc}} = \sqrt{E_{\text{beam}}^2 - \left(\sum_i \vec{p}_i\right)^2} = \sqrt{E_{\text{beam}}^2 - p_D^2}. \quad (21.2.28)$$

This quantity is simply a function of the total momentum of the decay products,  $p_D = \sum_i \vec{p}_i$ . The resolution of  $M_{\text{bc}}$  can be computed from

$$\delta M_{\text{bc}} = \frac{E_{\text{beam}}}{M_{\text{bc}}} \delta E_{\text{beam}} \oplus \frac{p_D}{M_{\text{bc}}} \delta p_D. \quad (21.2.29)$$

The energy spread of the BEPCII beam is small ( $\delta E_{\text{beam}} \sim 0.9$  MeV) as is the  $D$  meson momentum (at the  $\psi(3770)$ ,  $p_D (\simeq 270 \text{ MeV for } D^0 \text{ and } \simeq 242 \text{ MeV for } D^+)$  and its measurement ( $\delta p_D \simeq 5$  MeV). As a result, the  $M_{\text{bc}}$  resolution is of order 1.2–2 MeV.

Another advantage of having this second independent mass variable is in the reduction of misidentification background that it provides. The total energy (or the invariant mass) is sensitive to the mass hypotheses of the decay products, while the beam-constrained mass only relies on the track momentum (the measured momentum is dependent on the mass hypotheses only to the extent of a small correction for  $dE/dx$ ). Imposing a requirement on  $\Delta E$ , and leaving the  $M_{\text{bc}}$  value to be examined for a “signal peak,” or fitting both the  $\Delta E$  and  $M_{\text{bc}}$  distributions simultaneously can improve the signal-to-background ratio.

### 21.2.3 Multiple Counting

Sometimes one event could have two different track combinations that satisfy the tag candidate requirements. Such multiple counting can occur in two ways:

- 1) Two or more different tag channels can be reconstructed for a given event, for example, when both  $D$ 's in an event are reconstructed.
- 2) Two or more possible combinations of tracks can yield a consistent tag for a given channel; tag modes with higher multiplicity, such as  $D^+ \rightarrow \bar{K}^0 \pi^+ \pi^+ \pi^-$ , and those containing  $\pi^0$ 's tend to be more susceptible to this problem.

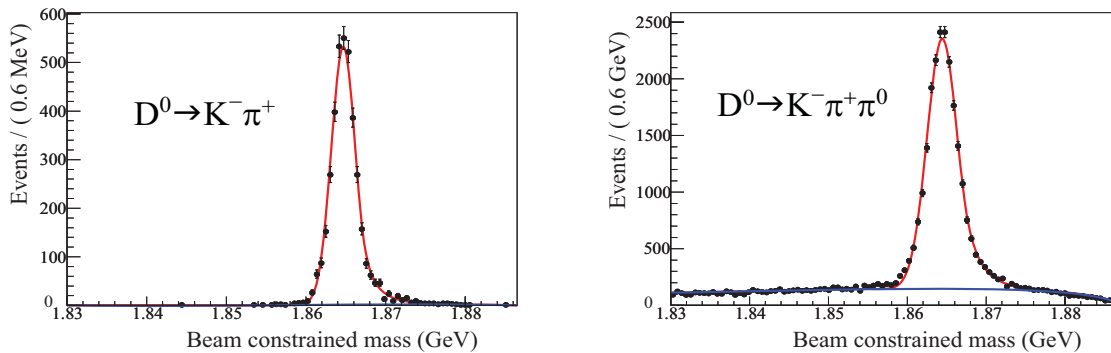


Figure 21.6: Beam constrained mass distributions for  $D^0 \rightarrow K^-\pi^+$  and  $D^0 \rightarrow K^-\pi^+\pi^0$  tags. The red curves show the sum of signal and background functions. The blue curves indicate the background fits.

To count the actual number of tagged events in an unbiased manner, the following criteria are used to select only one tag combination per event:

- 1) If more than one tag channel can be reconstructed, select the channel with the largest signal-to-noise ratio.
- 2) For all tags containing charged tracks only, if more than one combination of tracks form a tag, choose the combination whose lowest momentum track has a momentum higher than other combinations.
- 3) For all tags containing neutrals, if more than one combination of a photon pair can form a tag, choose the combination with the lowest  $\chi^2$  from the  $\pi^0$  fit, or choose the combination whose lowest energy track has an energy higher than that of the other combinations.

Items 2) and 3) are based on the fact that the tracking efficiency is higher for higher momentum/energy tracks, and the measurement is more reliable.

### Mass plot fitting

The distribution of beam-constrained masses for tag- $D$  candidates that survive the above-described selection procedure is shown in Fig. 21.6. The number of tags is determined by an extended unbinned maximum likelihood fit to a signal function on top of a background. The background shape is represented by the well known ARGUS function [23] which is an empirical formula to model the phase space of multi-body decays near threshold and is frequently used in  $B$  physics. The ARGUS function has the form:

$$\mathcal{B}(M_{bc}) = M_{bc} \left[ 1 - \left( \frac{M_{bc}}{E_{beam}} \right)^2 \right]^p \cdot \exp \left( c \left[ 1 - \left( \frac{M_{bc}}{E_{beam}} \right)^2 \right] \right), \quad (21.2.30)$$

where  $p$  is the power term (usually taken to be 0.5) and  $c$  is a scale factor for the exponential term. The shape parameters are usually determined by fitting  $M_{bc}$  distributions extracted from  $\Delta E$  sidebands.

There is a tail towards the high-mass end of the  $M_{bc}$  signal distribution that is caused by initial state radiation (ISR). The effects of ISR, the  $\psi(3770)$  resonance parameters and line-shape, the beam-energy spread, and the detector resolution can all contribute to the signal shape, which is usually taken to have the form [24]:

$$\mathcal{S}(M_{bc}) = \begin{cases} A \cdot \exp \left[ -\frac{1}{2} \left( \frac{M_{bc} - M_D}{\sigma_{M_{bc}}} \right)^2 \right] & \text{for } M_{bc} < M_D - \alpha \cdot \sigma_{M_{bc}} \\ A \cdot \frac{\left( \frac{n}{\alpha} \right)^n \exp \left( -\frac{1}{2} \alpha^2 \right)}{\left( \frac{M_{bc} - M_D}{\sigma_{M_{bc}}} + \frac{n}{\alpha} - \alpha \right)^n} & \text{for } M_{bc} > M_D - \alpha \cdot \sigma_{M_{bc}}, \end{cases} \quad (21.2.31)$$

which is similar to the form used to extract photon signals from electromagnetic calorimeters. In Eq. 21.2.31, the normalization constant  $A$  is related to the other parameters by

$$A^{-1} = \sigma_{M_{bc}} \cdot \left[ \frac{n}{\alpha} \cdot \frac{1}{n-1} \exp \left( -\frac{1}{2} \alpha^2 \right) + \sqrt{\frac{\pi}{2}} \left( 1 + \text{erf} \left( \frac{\alpha}{\sqrt{2}} \right) \right) \right], \quad (21.2.32)$$

where  $M_D$  is the "true" (or most likely) mass,  $\sigma_{M_{bc}}$  is the mass resolution, and  $n$  and  $\alpha$  are parameters governing the shape of the high mass tail.

# Chapter 22

## Leptonic, semileptonic $D(D_S)$ decays and CKM matrix elements

### 22.1 Leptonic Decays

#### 22.1.1 Theoretical Review<sup>1</sup>

Purely leptonic decays are the simplest and the cleanest decay modes of the pseudoscalar charged  $D^+$  meson. The hadronic dynamics is simply factorized into the decay constant  $f_D$ , which is defined as

$$\langle 0 | \bar{d} \gamma_\mu \gamma_5 c | D^+(p) \rangle = i f_{D^+} p_\mu. \quad (22.1.1)$$

The decays  $D^+ \rightarrow \ell^+ \nu_\ell$  proceed via the mutual annihilation of the  $c$ - and  $\bar{d}$ -quarks into a virtual  $W^+$  boson with a decay width given in the Standard Model (SM) by

$$\Gamma(D^+ \rightarrow \ell^+ \nu) = \frac{G_F^2}{8\pi} f_{D^+}^2 m_l^2 M_{D^+} \left( 1 - \frac{m_l^2}{M_{D^+}^2} \right) |V_{cd}|^2, \quad (22.1.2)$$

where  $M_{D^+}$  is the  $D^+$  mass,  $m_l$  is the mass of the final-state lepton,  $V_{cd}$  is the CKM matrix element,  $f_{D^+}$  is the decay constant and  $G_F$  is the Fermi coupling constant. Figure 22.1 shows the Feynman diagram for the  $D^+ \rightarrow l^+ \nu_\ell$  process. Because the  $D$  meson is a pseudoscalar, the decay is helicity suppressed; the decay rate is proportional to  $m_l^2$ . The dynamics are the same as that for  $\pi^- \rightarrow \mu \bar{\nu}_\mu$ , &  $e \bar{\nu}_e$ . Because of this helicity suppression,  $D^+ \rightarrow e^+ \nu$  is very small: the decay widths for  $D^+ \rightarrow \tau^+ \nu$ ,  $\mu^+ \nu$ , and  $e^+ \nu$  are expected to have relative values of  $2.65 : 1 : 2.3 \times 10^{-5}$ , respectively. Standard Model expectations for the branching fractions for the different leptonic decay modes of the  $D^+$  and  $D_s^+$  charmed mesons are listed in Table 22.1 [48].

Although,  $D^+ \rightarrow \mu^+ \nu$  has a smaller rate than  $D^+ \rightarrow \tau^+ \nu$ , it is the most favorable mode for experimental measurement because of the complications caused by the additional neutrino(s) produced in  $\tau$  decays. From Eq. 22.1.2, in the context of the SM, a measurement of  $D^+ \rightarrow \mu^+ \nu$  determines  $f_{D^+} |V_{cd}|$ . Thus, the value of  $|V_{cd}|$  is needed in order to extract  $f_{D^+}$ .

---

<sup>1</sup>By Ya-Dong Yang

Table 22.1: Predicted SM branching fractions for  $D^+$  and  $D_s$  purely leptonic decays assuming  $f_D = f_{D_s} = 200$  MeV,  $|V_{cd}| = 0.21$  and  $|V_{cs}| = 0.97$ .

Decay Mode	Branching fraction
$D^+ \rightarrow e^+ \nu_e$	$7.5 \times 10^{-9}$
$D^+ \rightarrow \mu^+ \nu_\mu$	$3.2 \times 10^{-4}$
$D^+ \rightarrow \tau^+ \nu_\tau$	$7.2 \times 10^{-4}$
$D_s^+ \rightarrow e^+ \nu_e$	$7.5 \times 10^{-8}$
$D_s^+ \rightarrow \mu^+ \nu_\mu$	$3.2 \times 10^{-3}$
$D_s^+ \rightarrow \tau^+ \nu_\tau$	$2.9 \times 10^{-2}$

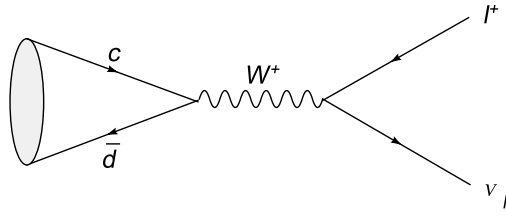


Figure 22.1: The Feynman diagram for  $D^+ \rightarrow l^+ \nu_\ell$

The magnitude of  $|V_{cd}|$  has been deduced from neutrino and anti-neutrino production of charmed particles on valence  $d$  quarks in fixed target experiments [25]. The current world-average value is [3]

$$|V_{cd}| = 0.224 \pm 0.012. \quad (22.1.3)$$

In the Wolfenstein parameterization of the CKM-matrix,  $V_{cd} = -V_{us}$  up to  $\mathcal{O}(\lambda^4)$ , where  $\lambda = |V_{us}|$ . With a  $281\text{pb}^{-1}$  data sample taken at the  $\psi(3770)$  resonance, the CLEO-c group determined [26]

$$\mathcal{B}(D^+ \rightarrow \mu^+ \nu) = (4.40 \pm 0.66^{+0.09}_{-0.12}) \times 10^{-4}. \quad (22.1.4)$$

Using  $|V_{cd}| = |V_{us}| = 0.2238 \pm 0.0029$ , this translates into [26]

$$f_{D^+} = (222.6 \pm 16.7^{+2.8}_{-3.4}) \text{MeV}. \quad (22.1.5)$$

In the literature,  $f_{D^+}$  has been extensively studied in a variety of theoretical approaches [27, 28]; it has been measured by the MARKIII [29], BES [30] and CLEO-c [26, 31] collaborations. The situation is summarized in Fig. 22.2. From this figure, we can see that the CLEO-c measurement agrees with the Lattice QCD calculations by the Fermilab Lattice, MILC and HPQCD Collaborations [32], which find  $f_{D^+} = 201 \pm 3 \pm 17$  MeV. Clearly, both the experimental measurements and theoretical predictions still lack sufficient precision to put SM predictions to a very stringent test.

The decay constant is a very fundamental parameter that can be used to test our knowledge of hadronic dynamics. For example,  $f_B$  is hard to determine experimentally because purely leptonic  $B^\pm$  decays are suppressed by the very small value of  $V_{ub} = (3.6 \pm 0.7) \times 10^{-3}$ . Thus, theoretical calculations on the Lattice, or with QCD Sum Rules, etc., are needed. However, a self-consistent calculation should include a prediction for  $f_D$ . If

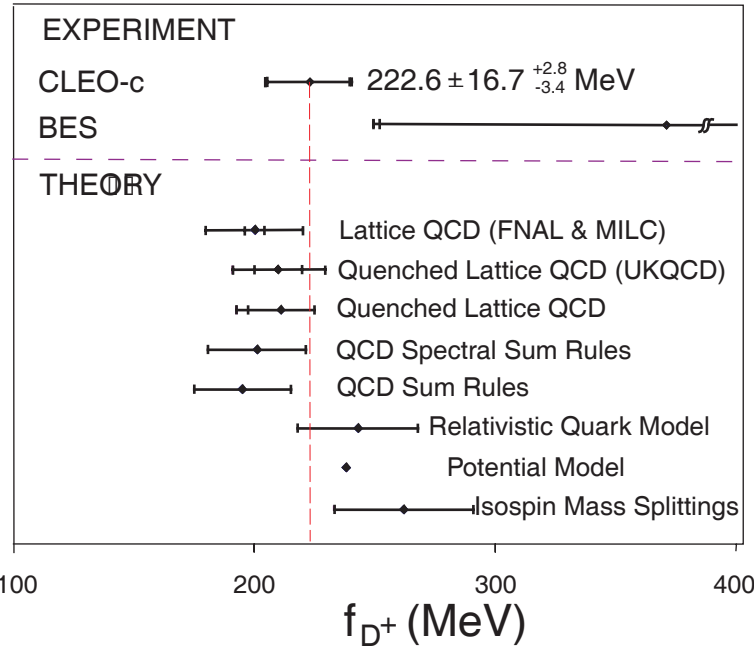


Figure 22.2: Summary of theoretical predictions and experimental results for  $f_{D^+}$

$f_D$  is known with good precision, one can validate theoretical calculations of  $f_B$ , which is a parameter of critical importance for  $B$  physics.

The purely leptonic decay  $D_s^+ \rightarrow \ell^+ \nu$  is very similar to  $D^+ \rightarrow \ell^+ \nu$ . However, it involves the larger CKM element  $V_{cs}$  and, thus, purely leptonic  $D_s^+$  decay rates are substantially larger than those for the corresponding  $D^+ \rightarrow \ell^+ \nu$  processes.

The value of  $|V_{cs}|$  can be obtained from  $W^+$  boson charm-tagged hadronic decays. In the SM, the branching fractions of the  $W^+$  boson depend on the six CKM elements  $V_{ij}$  ( $i=u, c$ ,  $j=d, s, b$ ). In terms of these six CKM elements, the leptonic branching ratio  $\mathcal{B}(W \rightarrow \ell \bar{\nu}_{ell})$  is given by [3]

$$\frac{1}{\mathcal{B}(W \rightarrow \ell \bar{\nu}_{\ell})} = 3 \left\{ 1 + \left[ 1 + \frac{\alpha_s(M_W^2)}{\pi} \right] \sum_{i,j} |V_{ij}|^2 \right\}. \quad (22.1.6)$$

Taking  $\alpha_s(M_W^2) = 0.121 \pm 0.002$ , and  $\mathcal{B}(W \rightarrow \ell \bar{\nu}_{ell}) = (10.69 \pm 0.06(\text{stat.}) \pm 0.07(\text{syst.}))\%$  from LEP measurements [3], we have

$$\sum_{i,j} |V_{ij}|^2 = 2.039 \pm 0.025 \pm 0.001. \quad (22.1.7)$$

Using experimental results from the PDG [3], one can get  $|V_{ud}|^2 + |V_{us}|^2 + |V_{ub}|^2 + |V_{cd}|^2 + |V_{cb}|^2 = 1.0477 \pm 0.0074$  [3]. Then the LEP result can be converted into a measurement of  $|V_{cs}|$

$$|V_{cs}| = 0.996 \pm 0.013. \quad (22.1.8)$$

With this value for  $|V_{cs}|$ , measurements of  $D_s^+ \rightarrow \ell^+ \nu$  decays can be used to determine  $f_{D_s}$ . At present, there are eight published measurements of  $D_s^+$  decaying to  $\mu^+ \nu_{\mu}$  and/or

$\tau^+\nu_\tau$ : WA75 [33], BES [34], E653 [35], L3 [36], CLEO [37], BEATRICE [38], OPAL [39], and ALEPH [40]. All of these experiments other than BES either explicitly or implicitly measure the leptonic branching ratio relative to the nonleptonic mode  $\mathcal{B}(D^+ \rightarrow \phi\pi^+)$  or relative to semileptonic  $D_s^+$  decays. The PDG weighted average for the leptonic branching fraction from all experiments other than BES is [3]

$$\mathcal{B}(D^+ \rightarrow \mu^+\nu_\mu) = 0.00547 \pm 0.00067 \pm 0.00132. \quad (22.1.9)$$

Since this average is  $1.5\sigma$  below the BES result of  $\mathcal{B}(D^+ \rightarrow \mu^+\nu_\mu) = 0.015^{+0.013+0.003}_{-0.006-0.002}$ , the PDG used the negative uncertainties of the BES measurement to recalculate the weighted average for all experiments, including BES, to be:

$$\mathcal{B}(D^+ \rightarrow \mu^+\nu_\mu) = 0.00596 \pm 0.00144. \quad (22.1.10)$$

Using this value, and including the relatively minor uncertainties on other parameters relevant to the decay, the world average  $D_s^+$  decay constant is extracted to be [3]

$$f_{D_s} = (267 \pm 33) \text{ MeV}. \quad (22.1.11)$$

### 22.1.2 Decay Constants<sup>2</sup>

#### The ratio of $f_{D^+}$ and $f_{D_s^+}$

The  $D^0$  decay constant is very important for interpreting measurements of  $D^0 - \bar{D}^0$  mixing, which is a good testing ground for the SM. Because of the smallness of the  $u$  and  $d$  quark masses, chiral symmetry gives

$$f_{D^0} = f_{D^\pm} \quad (22.1.12)$$

It should be noted that in the SM, the decay  $D_u^0 \rightarrow \mu^+\mu^+$  is strongly suppressed by the GIM mechanism; the expected branching fraction is less than  $10^{-12}$ . Any observation of this decay at present or near-future colliders will be a signal of new physics beyond the SM.

The ratio  $f_{D_s}/f_D$  is a very important quantity in flavor physics. It characterizes  $SU(3)_V$  breaking. If we take  $m_s, m_{u,d} \rightarrow 0$ , flavor  $SU(3)_V$  is an exact symmetry and  $f_{D_s}/f_D = 1$ . However, in nature  $m_s \gg m_{u,d}$ , and this ratio deviates from unity. To the one-loop level in Chiral Perturbation Theory, Grinstein *et al.*, [41] find

$$f_{D_s}/f_{D_d} = 1.2, \quad (22.1.13)$$

which is very nearly equal to  $f_K/f_\pi = 1.25$ . The relative values of the  $f_{D_s}/f_{D^\pm}$  and  $f_{B_s}/f_B$  ratios are characterized by the quantity  $R_1$  [42]:

$$R_1 = \frac{f_{B_s}/f_{B_d}}{f_{D_s}/f_{D_d}}, \quad (22.1.14)$$

and it has been shown that  $R_1$  deviates from unity by very small correction factors [43].

---

<sup>2</sup>By Ya-Dong Yang

It is known that the  $f_{B_s}/f_{B_d}$  ratio is a measurement of the relative strength of  $B_s - \bar{B}_s$  and  $B_d - \bar{B}_d$  mixing, which is parameterized by the ratio  $R_2$

$$R_2 = \frac{(\Delta M/\Gamma)_{B_s}}{(\Delta M/\Gamma)_{B_d}}. \quad (22.1.15)$$

Many uncertainties cancel out in the SM calculation of  $R_2$ :

$$R_2 = \frac{|V_{ts}|^2}{|V_{td}|^2} \frac{f_{B_s}^2}{f_{B_d}^2} \frac{B_{B_s}}{B_{B_d}}. \quad (22.1.16)$$

For example, the ratio of vacuum insertion parameters  $B_{B_s}/B_{B_d}$  is unity with very small corrections. Therefore, to a good approximation

$$R_2 = \frac{|V_{ts}|^2}{|V_{td}|^2} \frac{f_{D_s}^2}{f_D^2}. \quad (22.1.17)$$

It should be noted that leptonic decays of the  $B_s^0$ ,  $B_d^0$  and  $B^\pm$  are sensitive to New Physics that does not effect  $D$  mesons. Therefore, measurements of  $B^0 - \bar{B}^0$  and  $B_s^0 - \bar{B}_s^0$  mixing, in conjunction with precise values of  $f_{D_s}$  and  $f_D$ , will be very helpful in clarifying whether or not there is New Physics in  $B^0 - \bar{B}^0$  and  $B_s^0 - \bar{B}_s^0$  mixing.

### Theoretical extrapolations from $f_D$ to $f_B$

Heavy meson decay constants are among the simplest quantities that can be computed with Heavy Quark Effective Theory (HQET) [44].

In HQET, one can derive the relation

$$f_M \sqrt{m_M} = \hat{C}_{M_Q} F_{ren} + \mathcal{O}(1/m_Q), \quad (22.1.18)$$

where

$$\hat{C}_P(M_Q) = [\alpha_s(m_Q)]^{2/\beta_0} \left\{ 1 + \frac{\alpha_s(m_Q)}{\pi} \left( Z_{hl} + \frac{2}{3} \right) \right\}, \quad (22.1.19)$$

$$\hat{C}_V(M_Q) = [\alpha_s(m_Q)]^{2/\beta_0} \left\{ 1 + \frac{\alpha_s(m_Q)}{\pi} Z_{hl} \right\}, \quad (22.1.20)$$

$$Z_{hl} = 3 \frac{153 - 19n_f}{(33 - 2n_f)^2} - \frac{381 + 28\pi^2 - 30n_f}{36(33 - 2n_f)} - \frac{4}{3}. \quad (22.1.21)$$

This expresses the well known asymptotic-scaling law, rigorously derived in HQET, that  $f_M \sqrt{m_M}$  approaches a constant as  $m_M \rightarrow \infty$ . To leading order in  $\mathcal{O}(1/m_Q)$ , one finds that

$$r_1 = \frac{f_B}{f_D} = \sqrt{\frac{m_D}{m_B}} \left( \frac{\alpha_s(m_c)}{\alpha_s(m_b)} \right)^{6/25} \left\{ 1 + 0.894 \frac{\alpha_s(m_c) - \alpha_s(m_b)}{\pi} \right\}, \quad (22.1.22)$$

$$r_2 = \frac{f_V}{f_P} = 1 - \frac{\alpha_s(m_Q)}{3\pi}. \quad (22.1.23)$$

At subleading order, one must include  $1/m_Q$  and the  $SU(3)_V$  corrections. To the order of  $1/m_Q$ , one obtains

$$f_M \sqrt{m_M} = \hat{C}_{M_Q} F_{ren} \left\{ 1 + \frac{G_1(m_Q)}{m_Q} + \frac{2d_M}{m_Q} \left[ \hat{G}_2(m_Q) - \frac{\bar{\Lambda}}{12} \right] \right\}, \quad (22.1.24)$$

where  $d_P = 3$  and  $d_V = -1$ . The non-trivial hadronic parameters  $\hat{G}_i(m_Q)$  need to be computed using non-perturbative techniques. Using QCD sum rules, Ball [45] has estimated

$$\hat{G}_1(m_b) = -0.81 \pm 0.15 \text{GeV}, \quad \hat{G}_1(m_c) = -0.72 \pm 0.15 \text{GeV}, \quad (22.1.25)$$

and Neubert [46] finds

$$\hat{G}_2(m_b) = -26 \pm 4 \text{MeV}, \quad \hat{G}_2(m_c) = -0.44 \pm 7 \text{MeV}. \quad (22.1.26)$$

The  $SU(3)_V$ -violating correction to  $f_{B_s}/f_{f_B}$  is estimated to be

$$\frac{f_{B_s}}{f_B} = \sqrt{\frac{1 - (\frac{7}{3} + 3g^2)\frac{m_K^2}{16\pi^2 f^2} \ln \frac{m_K^2}{\mu^2}}{1 - \frac{2}{3}(1 - 3g^2)\frac{m_K^2}{16\pi^2 f^2} \ln \frac{m_K^2}{\mu^2}}} \approx 1.138, \quad (22.1.27)$$

for  $\mu = 1 \text{GeV}$ ,  $f = f_K$ ,  $g^2 \approx 0.4$ , and  $f_K = 1.25 f_\pi$ .

### Previous measurements of purely leptonic $D$ and $D_s$ decays

#### (a) Measurements of $\mathcal{B}(D^+ \rightarrow \mu\nu_\mu)$ and $f_{D^+}$

With data collected in the BES-I detector, BES measured  $f_D = (300^{+180+80}_{-150-40}) \text{ MeV}$  by fully reconstructing  $D^{*+}D^-$  events at  $\sqrt{s}=4.03 \text{ GeV}$ . They searched for  $D^- \rightarrow \mu^- \bar{\nu}_\mu$  events recoiling from a sample of tagged  $D^{*+} \rightarrow \pi^+ D^0$  with  $D^0 \rightarrow K^-\pi^+$  decays [49]. Subsequently, with the upgraded BESII detector, BES measured  $f_D$  again, in this case by reconstructing both  $D$  mesons in  $D^+D^-$  events produced close to threshold with data taken around  $\sqrt{s}=3.773 \text{ GeV}$ , and obtained the branching fraction value  $\mathcal{B}(D^+ \rightarrow \mu^+\nu) = (0.122^{+0.111}_{-0.053} \pm 0.010)\%$ , and a value for the decay constant of  $f_{D^+} = (371^{+129}_{-119} \pm 25) \text{ MeV}$  [50].

The MARK-III group determined an upper limit of  $f_D \leq 290 \text{ MeV}$  with data taken at  $3.770 \text{ GeV}$  at the SPEAR  $e^+e^-$  collider. The  $D^+ \rightarrow \mu^+\nu$  events were selected based on missing mass and momentum signatures [114]. Recently, the CLEO-c group made two measurements of the branching fraction for  $D^+ \rightarrow \mu^+\nu_\mu$ . In the first one, they used a  $60 \text{ pb}^{-1}$  data sample taken at  $\sqrt{s}=3.770 \text{ GeV}$  and found 8 events (including 1 background event). They selected events based on the measured missing mass  $M_{miss}^2 = (E_{beam} - E_\mu)^2 - (-p_{D^-} - p_\mu)^2$  and had a total systematic error of 16.4% [53]. The branching fraction was measured to be  $\mathcal{B}(D^+ \rightarrow \mu^+\nu_\mu) = (0.035 \pm 0.014 \pm 0.006)\%$  and  $f_{D^+}$  was determined to be  $(202 \pm 41 \pm 17) \text{ MeV}$ . Their second measurement was based on a  $281 \text{ pb}^{-1}$  data set, in which they found 50  $D^+ \rightarrow \mu^+\nu_\mu$  events (including  $2.81 \pm 0.30 \pm 0.27$  background events) on the recoil side of  $158, 354 \pm 496$   $D^-$  single-tags. The measured branching fraction is  $\mathcal{B}(D^+ \rightarrow \mu^+\nu_\mu) = (4.40 \pm 0.66^{+0.09}_{-0.12}) \times 10^{-4}$  from which they extract  $f_{D^+} = (222.6 \pm 16.7^{+2.8}_{-3.4}) \text{ MeV}$ . In this second measurement, they reduced the systematic

Table 22.2: Measured values of  $f_D$ .

Experiment	$E_{cm}$	Lum	Events	$B(D^+ \rightarrow \mu\nu_\mu)(\%)$	$f_D(MeV)$
BESI	4.03 GeV	$22.3 pb^{-1}$	1	$0.08^{+0.16+0.05}_{-0.05-0.02}$	$300^{+180+80}_{-150-40}$
BESII	3.773 GeV	33	$2.67 \pm 1.74$	$0.122^{+0.111}_{-0.053} \pm 0.10$	$371^{+129}_{-119} \pm 25$
MARKIII	3.773 GeV	9.3	0	$\leq 0.072(C.L. 90\%)$	$\leq 290 (C.L. 90\%)$
CLEOC	3.770 GeV	60	$7.0 \pm 2.8$	$0.035 \pm 0.014 \pm 0.006$	$202 \pm 41 \pm 17$
CLEOC	3.770 GeV	281	$47.2 \pm 7.1^{+0.3}_{-0.8}$	$0.044 \pm 0.0066^{+0.0009}_{-0.0012}$	$222.6 \pm 16.7^{+2.8}_{-3.4}$
PDG06 [3]				$0.044 \pm 0.007$	

Table 22.3: Measured values of  $f_{D_s}$ .

Experiment	$E_{cm}$	Lum	$B(D_s \rightarrow \mu\nu_\mu)(\%)$	$f_{D_s}(MeV)$
BESI	4.03 GeV	$22.3 pb^{-1}$	$1.5^{+1.3+0.3}_{-0.6-0.2}$	$430^{+150+40}_{-130-40}$
WA75	350 GeV		$0.4^{+0.18+0.08}_{-0.14-0.06} \pm 1.7$	$232 \pm 45 \pm 20 \pm 48$
E653	600 GeV		$0.30 \pm 0.12 \pm 0.06 \pm 0.05$	$194 \pm 35 \pm 20 \pm 14$
BEATRICE	350 GeV		$0.83 \pm 0.23 \pm 0.06 \pm 0.18$	$323 \pm 44 \pm 12 \pm 34$
CLEO	$\Upsilon(4S)$	$2.13 fb^{-1}$		$344 \pm 37 \pm 52 \pm 42$
CLEO	$\Upsilon(4S)$	$4.79 fb^{-1}$		$280 \pm 19 \pm 28 \pm 34$
PDG06[3]			$0.61 \pm 0.19$	

error to  $(^{+2.1}_{-2.5})\%$ . Most of this improvement came from a reduction in the uncertainty of the background contamination (from 15.4% to  $(^{+0.6}_{-1.7})\%$ ) [54]. Measured  $f_D$  values are summarized in Table 22.2.

### (b) Pioneering measurements of $\mathcal{B}(D_s \rightarrow \mu\nu_\mu)$ and $f_{D_s}$

The first measurement of leptonic  $D_s$  decays was the BES result  $\mathcal{B}(D_s \rightarrow \mu\nu) = (1.5^{+1.3+0.3}_{-0.6-0.2})\%$  from which they determined  $f_{D_s} = (430^{+150}_{-130} \pm 40)$  MeV. The measurement was done by fully reconstructing  $D_s^+ D_s^-$  events with the BESI detector operating at  $\sqrt{s}=4.03$  GeV. The  $D_s$  were tagged using the  $D_s \rightarrow \phi\pi, K^{*0}K, K^0K, \dots$  modes and the recoil systems were examined for  $D_s \rightarrow l\nu_l$  signals [51].

WA75 reported  $f_{D_s} = (232 \pm 45 \pm 20 \pm 48)$  MeV using muons from  $D_s^+$  leptonic decay seen in emulsion [55]. E653 determined a value of  $(194 \pm 35 \pm 20 \pm 14)$  MeV from one prong muon decays seen in an emulsion [56]. BEATRICE published a value of  $\mathcal{B}(D_s \rightarrow \mu\nu) = (0.83 \pm 0.23_{stat} \pm 0.06_{sys} \pm 0.18_{B(\phi\pi)})\%$  using  $\pi^-$  interactions on copper and tungsten targets. The resulting value for the  $D_s$  decay constant was  $f_{D_s} = 323 \pm 44 \pm 12 \pm 34$  MeV [57]. CLEO measured  $f_{D_s}$  twice, their first result was  $f_{D_s} = 344 \pm 37 \pm 52 \pm 42$  MeV and determined from the measured value of the ratio  $\Gamma(D_s^+ \rightarrow \mu^+\nu)/\Gamma(D_s^+ \rightarrow \phi\pi)$  from a  $2.13 fb^{-1}$  data sample taken at the  $\Upsilon(4S)$  [58]; later they presented an improved determination of  $f_{D_s}$  using a  $4.75 fb^{-1}$  data sample. Their later value is  $f_{D_s} = 280 \pm 19 \pm 28 \pm 34$  MeV [59].

Measured  $f_{D_s}$  values from these pioneering measurements are listed in Table 22.3. More recent results are discussed in the following section.

### 22.1.3 Probing for new physics in leptonic $D_{(s)}$ decays<sup>3</sup>

Purely leptonic decays of heavy mesons are of great interest both theoretically and experimentally. Measurements of the decays  $B^+ \rightarrow l^+ \nu$ ,  $D_s^+ \rightarrow l^+ \nu$  and  $D^+ \rightarrow l^+ \nu$ , provide an experimental determination of the product of CKM elements and decay constants. If the CKM element is measured from other reactions, the leptonic decays can access the decay constants, which can be used to test lattice QCD predictions for heavy quark systems.

In the Standard Model the purely leptonic decays  $B^+ \rightarrow l^+ \nu$ ,  $D^+ \rightarrow l^+ \nu$  and  $D_s^+ \rightarrow l^+ \nu$  proceed via annihilation of the meson's constituent quarks into virtual  $W^\pm$  boson. Akeroyd and Chen [60] point out that leptonic decay widths are modified by new physics. The charged Higgs bosons in the two  $SU(2)_L \times U(1)_Y$  Higgs doublets with hypercharge  $Y = 1$  model (2HDM) would modify the SM predictions for  $D^+$  and  $D_s^+$  leptonic decays [60]. The Feynman diagram for  $D_s^+ \rightarrow l^+ \nu$  is shown in Fig. 22.3. The tree-level partial width in the 2HDM is given by [60]

$$\Gamma(D_s^+ \rightarrow l^+ \nu) = \frac{G_F^2 m_{D_s^+} m_l^2 f_{D_s^+}^2}{8\pi} |V_{cs}|^2 \left(1 - \frac{m_l^2}{m_{D_s^+}^2}\right)^2 \times r_s, \quad (22.1.28)$$

where  $G_F = 1.16639 \times 10^{-5} \text{ GeV}^{-2}$  is the Fermi constant,  $m_l$  is the mass of the lepton,  $m_{D_s^+}$  is the mass of the  $D_s^+$  meson,  $V_{cs}$  is the Cabibbo-Kobayashi-Maskawa (CKM) matrix element, and  $f_{D_s^+}$  is the decay constant. In the 2HDM (with model-II type Yukawa couplings), the process is modified at tree level by the scaling factor  $r_s$ , given by [60]

$$\begin{aligned} r_s &= \left[1 - m_{D_s^+}^2 \frac{\tan^2 \beta}{m_{H^\pm}^2} \left(\frac{m_s}{m_c + m_s}\right)\right]^2 \\ &= \left[1 - m_{D_s^+}^2 R^2 \left(\frac{m_s}{m_c + m_s}\right)\right]^2, \end{aligned} \quad (22.1.29)$$

where  $m_{H^\pm}$  is the charged Higgs mass,  $m_c$  is the charm quark mass,  $m_s$  is the strange quark mass (for  $D^+$  decays, it is replaced by the  $d$ -quark mass,  $m_d$ ),  $\tan \beta$  is the ratio of the vacuum expectation values of the two Higgs doublets, and the  $H^\pm$  contribution to the decay rate depends on  $R = \frac{\tan \beta}{m_{H^\pm}}$ . The contribution from the  $H^\pm$  interferes destructively with the  $W^\pm$ -mediated SM diagram. As discussed in Ref. [61], the recent experimental measurements of  $\mathcal{B}(B^\pm \rightarrow \tau^\pm \nu_\tau)$  [62, 63] provide an upper limit of  $R < 0.29 \text{ GeV}^{-1}$  at 90% C.L.. For values of  $R$  in the interval  $0.20 < R < 0.30 \text{ GeV}^{-1}$ , the charged Higgs contribution could have a sizable effect on the  $D_s^+$  leptonic decay rate [60, 61].

For  $D^+$  leptonic decays,  $m_d \ll m_c$ , the modification is negligible and the scaling factor  $r_d \approx 1$ . However, in the case of the  $D_s^+$ , the scaling factor  $r_s$  may be sizable due to the non-negligible value of  $m_s/m_c$ . Although the contribution from new physics to the rate is small in comparison to the SM rate for  $D_s^+ \rightarrow l^+ \nu$  decays, measurable effects may be accessible since the decay rate for  $D_s^+ \rightarrow \mu^+ \nu_\mu$  is much larger than that for  $B$  leptonic decays, and can be measured with good precision.

Experimental measurements of the branching fraction for  $D^+ \rightarrow \mu \nu_\mu$  are summarized in Table 22.2 of the previous section. The most precise result is the CLEO-c measurement

<sup>3</sup>By Hai-Bo Li and Jia-Heng Zou

Table 22.4: Recent experimental results for  $\mathcal{B}(D_s^+ \rightarrow \mu\nu_\mu)$ ,  $\mathcal{B}(D_s^+ \rightarrow \tau\nu_\tau)$  and  $f_{D^+}$ . The decay constants are extracted from the measured branching ratios using  $|V_{cs}| = 0.9737$ , and a  $D_s^+$  lifetime of 0.50 ps [3] (from Ref. [61]).

Experiments	Decay mode	$\mathcal{B}$	$f_{D_s^+}$
CLEO-c [65]	$\mu\nu_\mu$	$(5.94 \pm 0.66 \pm 0.31) \times 10^{-3}$	$264 \pm 15 \pm 7$
CLEO-c [65]	$\tau\nu_\tau$	$(8.0 \pm 1.3 \pm 0.4) \times 10^{-2}$	$310 \pm 25 \pm 8$
CLEO-c [66]	$\tau\nu_\tau$	$(6.17 \pm 0.71 \pm 0.36) \times 10^{-2}$	$273 \pm 16 \pm 8$
CLEO-c combination [61]			$274 \pm 10 \pm 5$
Belle [67]	$\mu\nu_\mu$	$(6.44 \pm 0.76 \pm 0.52) \times 10^{-3}$	$275 \pm 16 \pm 12$
BaBar [68]	$\mu\nu_\mu$	$(6.74 \pm 0.83 \pm 0.26 \pm 0.66) \times 10^{-3}$	$283 \pm 17 \pm 7 \pm 14$
Our average			$276 \pm 9$

Table 22.5: Recent theoretical predictions for  $f_{D^+}$ ,  $f_{D_s^+}$  and  $f_{D_s^+}/f_{D^+}$  from lattice QCD calculations. The most precise calculation is from HPQCD+UKQCD [69], which determines  $D^+$  and  $D_s^+$  decay constants with 2% errors, four times better than experimental and previous theoretical results (from Ref. [61]).

Physical Model	$f_{D^+}$	$f_{D_s^+}$	$f_{D_s^+}/f_{D^+}$
Lattice (HPQCD+UKQCD) [69]	$208 \pm 4$	$241 \pm 3$	$1.164 \pm 0.011$
Lattice (FNAL+MILC+HPQCD) [70]	$201 \pm 3 \pm 17$	$249 \pm 3 \pm 16$	$1.24 \pm 0.01 \pm 0.07$
Quenched lattice (QCDSF) [71]	$206 \pm 6 \pm 3 \pm 22$	$220 \pm 6 \pm 5 \pm 11$	$1.07 \pm 0.02 \pm 0.02$
Quenched lattice (Taiwan) [72]	$235 \pm 8 \pm 14$	$266 \pm 10 \pm 18$	$1.13 \pm 0.02 \pm 0.05$
Quenched Lattice [73]	$210 \pm 10^{+17}_{-16}$	$236 \pm 8^{+17}_{-14}$	$1.13 \pm 0.02^{+0.04}_{-0.02}$
Experiment (world averages)	$223 \pm 17$ [61]	$276 \pm 9$	$1.23 \pm 0.10$ [61]

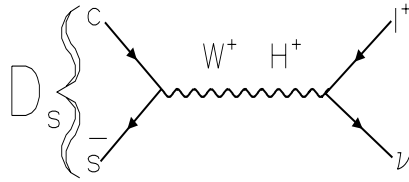


Figure 22.3: The tree-level annihilation diagram for pure  $D_s^+$  leptonic decays.

that is based on a  $281 \text{ pb}^{-1}$  data sample taken at the  $\psi(3770)$  peak. The measured decay rate of the  $D^+ \rightarrow \mu\nu_\mu$  is  $(4.40 \pm 0.66^{+0.09}_{-0.12}) \times 10^{-4}$  [64]. In the context of the SM, using the well measured  $D^+$  lifetime of  $1.040 \pm 0.007$  ps and assuming  $|V_{cd}| = |V_{us}| = 0.2238(29)$ , they determine [64]

$$(f_{D^+})_{\text{CLEO-c}} = (222.6 \pm 16.7^{+2.8}_{-3.4}) \text{ MeV.} \quad (22.1.30)$$

Recently, measurements of  $D_s^+ \rightarrow l^+\nu$  decays with precision levels comparable to that for  $D^+ \rightarrow \mu^+\nu$  decays have been reported by CLEOc [65, 66], BaBar [63] and Belle [67]; these are summarized in Table 22.4. For the  $D_s^+ \rightarrow \mu\nu_\mu$  decay mode, the combined decay rate from the CLEO-c, Belle and BaBar experiments is  $(6.26 \pm 0.43 \pm 0.25) \times 10^{-3}$ . For the  $D_s^+ \rightarrow \tau^+\nu_\tau$  decay mode, combining the two  $\tau$  decay channels ( $\tau^+ \rightarrow \pi^-\bar{\nu}_\tau$  and  $e^+\nu_e\bar{\nu}_\tau$ ) from CLEO-c [66], one obtains  $\mathcal{B}(D_s^+ \rightarrow \tau^+\nu_\tau) = (6.47 \pm 0.61 \pm 0.26)\%$ . Using the  $D_s^+$  lifetime of 0.50 ps and  $|V_{cs}| = 0.9737$  [3] in the SM relation, one determines the decay constant  $f_{D_s^+}$  from the  $D_s^+ \rightarrow \mu^+\nu_\mu$  mode to be

$$(f_{D_s^+})_{\text{exp}}^\mu = (272 \pm 11) \text{ MeV,} \quad (22.1.31)$$

and that from the  $D_s^+ \rightarrow \tau^+\nu_\tau$  decay mode to be

$$(f_{D_s^+})_{\text{exp}}^\tau = (285 \pm 15) \text{ MeV.} \quad (22.1.32)$$

The average of the  $\tau\nu_\tau$  and  $\mu\nu_\mu$  values is

$$(f_{D_s^+})_{\text{exp}} = (276 \pm 9) \text{ MeV.} \quad (22.1.33)$$

Table 22.5 summarizes recent lattice QCD predictions for the decay constants. The HPQCD+UKQCD collaboration claims better than 2% precision for their unquenched calculations:

$$\begin{aligned} (f_{D^+})_{\text{QCD}} &= (208 \pm 4) \text{ MeV,} \\ (f_{D_s^+})_{\text{QCD}} &= (241 \pm 3) \text{ MeV.} \end{aligned} \quad (22.1.34)$$

As pointed out in Ref. [74], there is a 15% ( $3.8\sigma$ ) discrepancy between the experimental and lattice QCD values of  $f_{D_s^+}$  (Eqs. 22.1.33 and 22.1.34). The discrepancy is seen in both the  $\tau\nu_\tau$  mode, where it is 18% ( $2.9\sigma$ ), and the  $\mu\nu_\mu$  where it is 13% ( $2.7\sigma$ ).

Equation 22.1.28 shows that the charged Higgs would lower the  $D_s^+$  decay rate relative to the SM prediction. However, the LQCD predicted value (Eq. 22.1.34) is *below* the measured value by more than  $3\sigma$ . This indicates that there is no value of  $m_{H^+}$  in

the 2HDM that can accommodate the measured  $f_{D_s^+}$  value. If we take the discrepancy seriously, there must be new physics that *enhances* the predicted leptonic decay rate.

Measurements of  $f_{D_s^+}$  and its world average are shown in Fig. 22.4 together with the LQCD prediction. With  $20 \text{ fb}^{-1}$  at  $E_{CM} = 4170 \text{ MeV}$ , the *BES-III* sensitivity for the measurement of the leptonic  $D_s^+$  decay branching fraction would be about 2% [75], which corresponds to a 1.0% uncertainty level for  $f_{D_s^+}$ , as indicated in Fig. 22.4. Assuming that the central value for the combined experimental  $f_{D_s^+}$  result persists, the discrepancy between the SM prediction and a *BES-III* measurement would be more than  $8\sigma$ , and a signal for new physics beyond the SM.

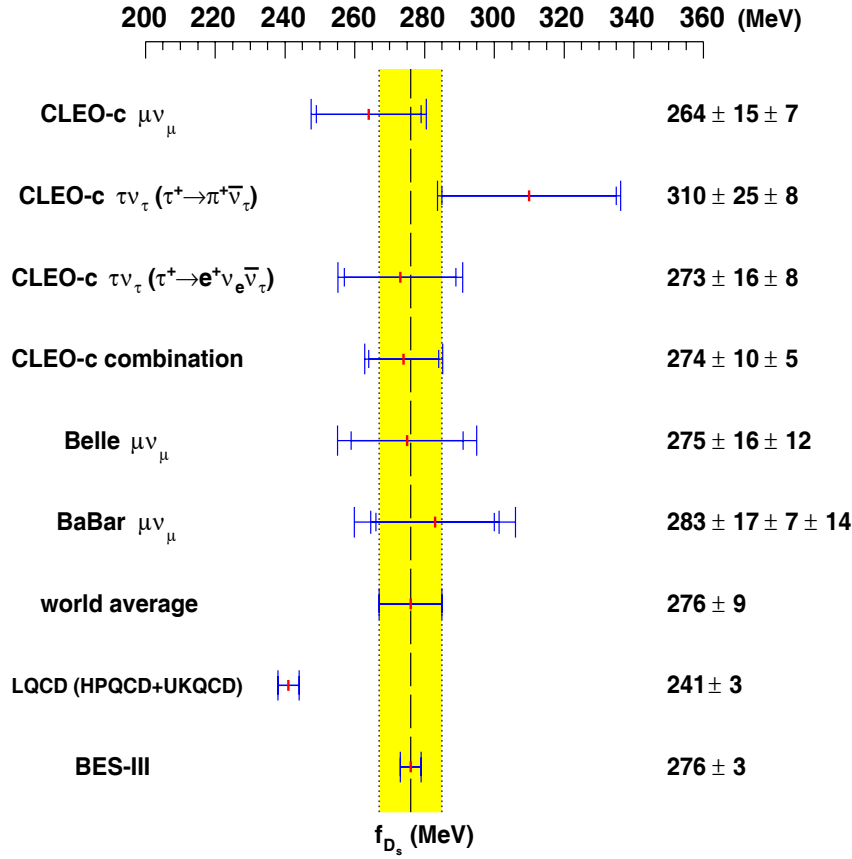


Figure 22.4: Values of  $f_{D_s^+}$  extracted from different experiments in the context of the SM. The world average is  $f_{D_s^+} = 276 \pm 9 \text{ MeV}$ , with an uncertainty of about 3.3%. The 1% *BES-III* sensitivity to  $f_{D_s^+}$  is indicated with the assumption that the current world average central value persists.

Another, more conservative approach, is to use the LQCD prediction for the ratio  $f_{D_s^+}/f_{D^+}$ , which is inherently more precise than those for the individual  $f_D$  values (c.f. the discussion in Sect. 22.1.2). A significant deviation of this ratio from the SM prediction would be a very robust sign of new physics beyond the SM.

Experimentally, the ratio  $f_{D_s^+}/f_{D^+}$  can be extracted from the measured ratio  $\mathcal{R}_\mu$  of

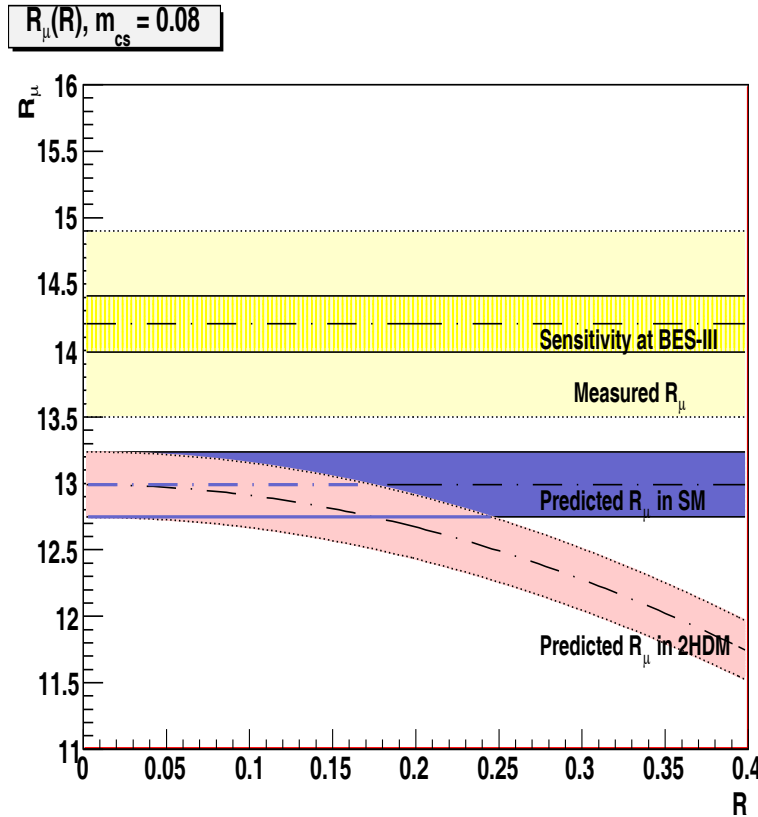


Figure 22.5:  $R_\mu$  as a function of  $R = \tan\beta/m_{H^\pm}$  for  $m_{sc} = m_s/(m_s + m_c) = 0.08$  and  $f_{D_s^+}/f_{D^+} = 1.164 \pm 0.011$  from LQCD calculations. The uncertainty on the theoretical prediction of  $R_\mu$  is shown as the gray band. The expected  $\pm 1\sigma$  *BES-III* uncertainty experimental range of  $R_\mu$  is indicated by the yellow band. The sensitivity for the measurement of the ratio  $R$  at *BES-III* is about 1.5% level is also shown with the assumption that the current central value for  $R_\mu$  persists.

the leptonic decay rates of the  $D_s^+$  and the  $D^+$ . In the SM, one has [60]:

$$R_\mu \equiv \frac{\mathcal{BR}(D_s^+ \rightarrow \mu^+ \nu)}{\mathcal{BR}(D^+ \rightarrow \mu^+ \nu)} = \left| \frac{f_{D_s^+}}{f_{D^+}} \right|^2 \left| \frac{V_{cs}}{V_{cd}} \right|^2 \frac{m_{D_s^+}}{m_{D^+}} \times \left( \frac{1 - m_\mu^2/m_{D_s^+}^2}{1 - m_\mu^2/m_{D^+}^2} \right) \times \frac{\tau_{D_s^+}}{\tau_{D^+}}. \quad (22.1.35)$$

In the case of the 2HDM, new physics only modifies the  $D_s^+$  terms, and the ratio  $R_\mu$  in Eq. 22.1.35 is corrected by a factor  $r_s$  defined in Eq. 22.1.29.

Using only CLEOc measurements and the SM relation, the experimental value for the  $f_{D_s^+}/f_{D^+}$  ratio is [61]

$$r_{D_s^+/D^+} \equiv \frac{f_{D_s^+}}{f_{D^+}} = 1.23 \pm 0.10. \quad (22.1.36)$$

The most precise LQCD prediction [69] is  $f_{D_s^+}/f_{D^+} = 1.164 \pm 0.011$ , which has a claimed precision that is better than 1%, and an order of magnitude better than the existing experimental measurement.

In Fig 22.5,  $\mathcal{R}_\mu$  is plotted as a function of  $R = \tan\beta/m_{H^\pm}$  for the case of the 2HDM, using  $m_{sc} = m_s/(m_s + m_c) = 0.08$  and  $f_{D_s^+}/f_{D^+} = 1.164 \pm 0.011$  from the LQCD calculation. The SM prediction is  $\mathcal{R}_\mu$  is  $(12.99 \pm 0.25)$ , where the error is from the uncertainty on the LCQCD prediction for  $f_{D_s^+}/f_{D^+}$ . Compared to the measured value  $\mathcal{R}_\mu = 14.2 \pm 0.7$ , we see that the SM prediction is almost 2 standard deviations low. If the LQCD calculation is reliable, this indicates that we need a modification to the SM that has constructive interference to accommodate the discrepancy [74]. It may be concluded that the 2HDM discussed in Ref. [60] is disfavored by the current data. It would be very interesting if the experimental precision on the  $f_{D_s^+}/f_{D^+}$  ratio could be improved to match the one percent level of the theoretical errors in the near future.

As discussed in the following Section, a MC study of the *BES-III* sensitivity for the  $\mathcal{R}_\mu$  ratio measurement indicates a precision about 5% for  $20 \text{ fb}^{-1}$  data samples taken at  $E_{CM} = 3773$  and  $4030 \text{ MeV}$  (Sect. 22.1.4). As mentioned in Sect. 21.1, the cross section for  $e^+e^- \rightarrow D_s^*\bar{D}_s$  at  $4.17 \text{ GeV}$  has been measured by CLEOc to be four times the cross section for  $e^+e^- \rightarrow D_s\bar{D}_s$  at  $4.03 \text{ GeV}$  [4]. If techniques that are currently being developed to tag  $D_s$  mesons produced in  $D_s^*\bar{D}_s$  final states are successful, and measurements from the  $D_s^+ \rightarrow \tau^+\nu_\tau$  are included, another factor of two precision will be gained by running at  $4.17 \text{ GeV}$ . Branching fraction errors of  $\sim 2\%$  translate into a  $\sim 1.5\%$  precision level on the  $f_{D_s^+}/f_{D^+}$  ratio.

## 22.1.4 Measurements of Leptonic Decays at *BES-III*<sup>4</sup>

The *BES-III* detector has very good  $\mu$  identification capabilities: the solid angle coverage of the Muon Chamber system is  $89\% \times 4\pi$ . Current *BES-III* plans include the accumulation of a total of  $20 \text{ fb}^{-1}$   $\psi(3770)$  data plus a smaller  $D_s^+D_s^-$  data sample at  $4.03 \text{ GeV}$  or a  $D_s^+D_s^{*-}$  sample at  $4.17 \text{ GeV}$ . By measuring the leptonic decays  $D^+ \rightarrow \mu^+\nu_\mu$  and  $D_s^+ \rightarrow \mu^+\nu_\mu$  in these data sets, *BES-III* will measure  $f_D$  and  $f_{D_s}$  with high precision.

### Monte Carlo samples and event selection

The decay constant,  $f_D$ , can be measured using data taken at the peak of the  $\psi(3770)$  where  $D\bar{D}$  mesons are produced in pairs. If we reconstruct a  $D^-$  from the  $D^+D^-$  pair (it is called a single-tag  $D^-$ ), the remaining tracks in the event must come from the “recoil  $D^+$ .” Single-tag  $D^-$  mesons can be reconstructed via hadronic decays  $D^- \rightarrow mKn\pi$ , and  $D^+ \rightarrow \mu^+\nu_\mu$  decay events can be isolated among the accompanying recoils.

According to the Eichten coupled-channel charmed meson production model [82], the peak of  $D_s^+D_s^-$  production cross section ( $R_{D_s^+D_s^-} \sim 0.1$ ) is around  $\sqrt{s} = 4.03 \text{ GeV}$ , which is just above the  $e^+e^- \rightarrow D_s^+D_s^-$  threshold, and below the threshold of  $D_s^+D_s^{*-}$  production. If data are taken around  $4.03 \text{ GeV}$ , leptonic  $D_s^+ \rightarrow \mu^+\nu_\mu$  events can be selected from among the recoil systems accompanying single-tag  $D_s^-$  mesons. The tagged  $D_s^-$  can be reconstructed via  $D_s^-$  hadronic decays such as  $D_s^- \rightarrow KK\pi(\phi\pi)$ ,  $\bar{K}^{*0}K(\bar{K}^{*0} \rightarrow K^-\pi^+)$ ,  $\bar{K}^0K(K_s^0 \rightarrow \pi^+\pi^-)$ ,  $KK\pi\pi$ , etc.

To study the *BES-III* capabilities for leptonic decay  $D^+ \rightarrow \mu^+\nu_\mu$  measurements, Monte Carlo  $e^+e^- \rightarrow D\bar{D}$  events are generated at  $3.773 \text{ GeV}$ , where the  $D$  and  $\bar{D}$  mesons are allowed to decay into all possible final states using branching fractions taken from the

<sup>4</sup>By Jiang-Chuan Chen, Jian Liu and Gang Rong

PDG [3]. These are simulated and reconstructed using BOSS version 6.02. A total of 5 million  $D\bar{D}$  Monte Carlo events were generated, which corresponds to a data sample with an integrated luminosity of about  $800 \text{ pb}^{-1}$ .

For the study of decay  $D_s^+ \rightarrow \mu^+ \nu_\mu$ , a  $D_s^+ D_s^-$  Monte Carlo sample was generated at a c.m. energy of 4.03 GeV. A total of  $1.2 \times 10^5$  ( $D_s^+ \rightarrow X$  versus  $D_s^- \rightarrow \phi\pi^-$ ) events were generated, which corresponds to a data sample with an integrated luminosity of about  $10 \text{ fb}^{-1}$ .

To select good events, charged tracks are required to satisfy a fiducial cut  $|\cos\theta| < 0.93$  and originate from the interaction region. For pion and kaon identification, a combined confidence level, calculated using the  $dE/dx$  and TOF measurements, is used. Neutral  $\pi^0$  and  $K_S^0$  mesons are reconstructed in their  $\pi^0 \rightarrow \gamma\gamma$  and  $K_S^0 \rightarrow \pi^+\pi^-$  decay modes.

### Single-tag $D^-$ and $D_s^-$ meson reconstruction

Single-tag  $D^-$  mesons are reconstructed in the four hadronic decay modes  $K^+\pi^-\pi^-$ ,  $K^+K^-\pi^-$ ,  $K^0\pi^-$  and  $K^+\pi^-\pi^-\pi^0$ . In order to reduce the background and improve the momentum resolution, a beam energy constraint is imposed on each  $mKn\pi$  combination of the  $D^-$  tag modes. The beam-constrained masses of the  $mKn\pi$  combinations are calculated using

$$M_{tag} = \sqrt{E_{beam}^2 - p_{mKn\pi}^2}, \quad (22.1.37)$$

where  $E_{beam}$  is the beam energy in the c.m. frame and  $p_{mKn\pi}$  is the total momentum of the  $mKn\pi$  combination. To suppress backgrounds from misidentified particles and fake photons, an  $M_{tag}$  signal region of  $\pm 3\sigma_{\Delta E}$  around the  $m_{D^-}$  is defined, where  $\Delta E = E_{mKn\pi} - E_{beam}$  and  $E_{mKn\pi}$  is the total energy of the  $mKn\pi$  combination.

Figure 22.6 shows the beam-constrained mass distributions for the four  $D^-$  tag modes  $K^+\pi^-\pi^-$ ,  $K^+K^-\pi^-$ ,  $K^0\pi^-$  and  $K^+\pi^-\pi^-\pi^0$ . The observed number of single-tag  $D^-$  mesons can be obtained from a maximum likelihood fit to the mass spectrum with a Gaussian function for the  $D$  signal and a special function [83, 84] to describe the background shape for each tag mode. The total number of single-tag  $D^-$  mesons is found to be  $N_{D^-} = 232,803.0 \pm 802$ .

Figure 22.7 shows the beam constrained mass distributions for the  $D_s^- \rightarrow \phi\pi^-$  tag mode from the MC  $D_s^+ D_s^-$  sample. A maximum likelihood fit to the mass spectrum with a Gaussian function for the  $D_s^-$  signal yields an observed number of single-tag  $D_s^-$  mesons of  $N_{D_s^-} = 26,793 \pm 318$ .

### Leptonic event selection

To select leptonic decay events from the recoils to the single-tag  $D^- (D_s^-)$  mesons, we require that the event satisfy the following criteria:

1. the event should not contain any isolated photons that are not used in the reconstruction of the single tag  $D^- (D_s^-)$  meson;
2. only one well reconstructed charged track is seen in the recoil side, and it should have a charge opposite that of the tag meson.

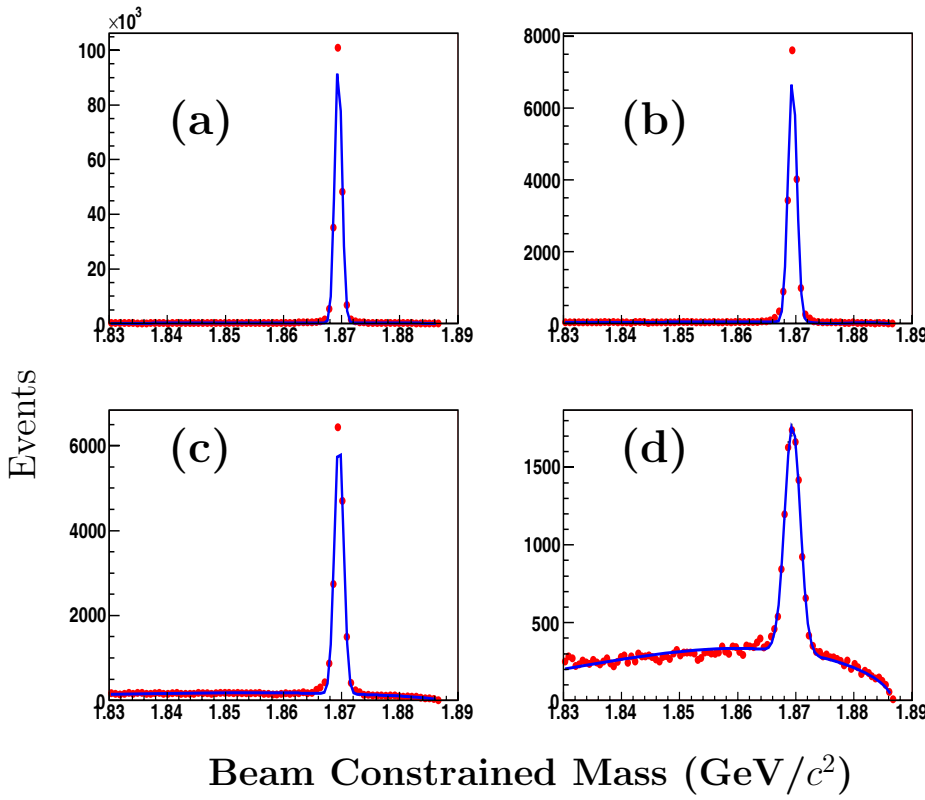


Figure 22.6: The beam constrained mass distributions for single tag  $\bar{D}^-$  candidates in the modes: (a)  $K^+\pi^-\pi^-$ , (b)  $K^0\pi^-$ , (c)  $K^-K^+\pi^-$  and (d)  $K^+\pi^-\pi^-\pi^0$ .

In the leptonic decay  $D^+(D_s^+) \rightarrow \mu^+\nu_\mu$ , the neutrino is undetected. Thus, the missing mass

$$M_{\text{miss}}^2 = E_{\text{miss}}^2 - p_{\text{miss}}^2,$$

where  $E_{\text{miss}} = E_{\text{cm}} - \sum \sqrt{\vec{p}_i^2 + m_i^2}$  and  $p_{\text{miss}} = -|\sum \vec{p}_i|$ , should be that of the undetected neutrino. Since the neutrino mass is (nearly) zero, the  $M_{\text{miss}}^2$  distribution should peak around zero. A further criterion requires that the momentum of the candidate muon track should be within the region  $(0.78, 1.08)$  GeV/ $c$  for  $D^+ \rightarrow \mu^+\nu_\mu$ , or  $(0.78, 1.22)$  GeV/ $c$  for  $D_s^+ \rightarrow \mu^+\nu_\mu$ , as shown in Fig. 22.8.

Figure 22.9 shows the  $M_{\text{miss}}^2$  distribution for the  $D^+ \rightarrow \mu^+\nu_\mu$  candidates on the recoil side of the four  $D^-$  tag modes; Fig. 22.10 shows the  $M_{\text{miss}}^2$  distribution for the  $D_s^+ \rightarrow \mu^+\nu_\mu$  candidates on the recoil side of the  $D_s^- \rightarrow \phi\pi^-$  tags. The number of signal events can be obtained from the  $M_{\text{miss}}^2$  distributions. A window within  $\pm 3\sigma_{M_{\text{miss}}^2}$  around zero is taken as the signal region, where  $\sigma_{M^2}$  is the standard deviation of the  $M_{\text{miss}}^2$  for the  $D^+$  ( $D_s^+$ ) sample. The numbers of the  $D^+ \rightarrow \mu^+\nu_\mu$  and  $D_s^+ \rightarrow \mu^+\nu_\mu$  candidates can be extracted from the events in the signal regions, where the large peaks near  $0.25$  GeV $^2$  for  $D^+$  and  $0.3$  GeV $^2$  for  $D_s^+$  in Figs. 22.9 and 22.10 are from the main background sources  $D^+ \rightarrow K_L\pi^+$  and  $D_s^+ \rightarrow K_L\pi^+$ . The total number of  $D^+ \rightarrow \mu^+\nu_\mu$  and  $D_s^+ \rightarrow \mu^+\nu_\mu$  candidates are determined to be  $91 \pm 9.5$  and  $63 \pm 7.9$ , respectively.

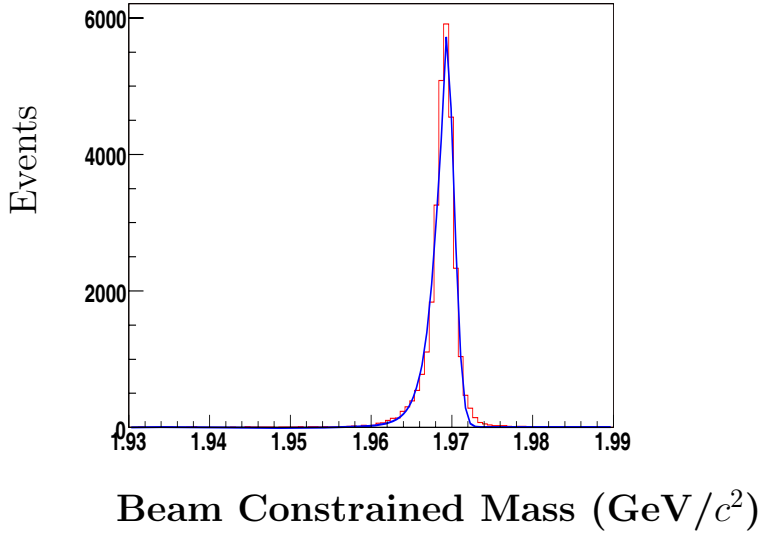


Figure 22.7: The fitted beam constrained masses for single-tag  $D_s^-$  candidates.

### Branching fractions for $D^+$ and $D_s^+$ leptonic decays

The detection efficiency for  $D^+ \rightarrow \mu^+ \nu_\mu$  and  $D_s^+ \rightarrow \mu^+ \nu_\mu$  leptonic decays can be estimated using MC events ( $D^+ \rightarrow \mu^+ \nu_\mu$  vs  $D_{\text{tag}}^-$ ) and ( $D_s^+ \rightarrow \mu^+ \nu_\mu$  vs  $D_s^-$  (tag)). They are  $53 \pm 1\%$  for  $D^+ \rightarrow \mu^+ \nu_\mu$  and  $52 \pm 1\%$  for  $D_s^+ \rightarrow \mu^+ \nu_\mu$ , respectively.

The branching fractions for  $D^+ \rightarrow \mu^+ \nu_\mu$  and  $D_s^+ \rightarrow \mu^+ \nu_\mu$  are determined using the relation:

$$\mathcal{B}(D_{(s)}^+ \rightarrow \mu^+ \nu_\mu) = \frac{N_{\mu^+}}{N_{D_{(s)}^{\text{tag}}} \times \epsilon_{D_{(s)}^+ \rightarrow \mu^+ \nu_\mu}}, \quad (22.1.38)$$

where  $N_{\mu^+}$  is the observed numbers of  $D^+$  or  $D_s^+ \rightarrow \mu^+ \nu_\mu$  events,  $N_{D_{(s)}^{\text{tag}}}$  are numbers of single-tag  $D^-$  or  $D_s^-$  mesons and  $\epsilon_{D_{(s)}^+ \rightarrow \mu^+ \nu_\mu}$  are the efficiencies. For the MC experiment, the branching fractions for the leptonic decays  $D^+ \rightarrow \mu^+ \nu_\mu$  and  $D_s^+ \rightarrow \mu^+ \nu_\mu$  are determined to be

$$\mathcal{B}(D^+ \rightarrow \mu^+ \nu_\mu) = (0.074 \pm 0.008)\% \text{ (input = 0.08\%)}$$

and

$$\mathcal{B}(D_s^+ \rightarrow \mu^+ \nu_\mu) = (0.452 \pm 0.057)\% \text{ (input = 0.40\%)}$$

The statistical error on  $\mathcal{B}(D^+ \rightarrow \mu^+ \nu_\mu)$  is about 10.5% for an integrated luminosity of  $800 \text{ pb}^{-1}$  at the  $\psi(3770)$  and four tag modes. This extrapolates to an error of  $\sim 2\%$  for a  $20 \text{ fb}^{-1}$  data sample and six tag modes  $K^+ \pi^- \pi^-$ ,  $K^+ K^- \pi^-$ ,  $K_S^0 \pi^-$ ,  $K^+ \pi^- \pi^- \pi^0$ ,  $K_S^0 \pi^- \pi^0$  and  $K_S^0 \pi^- \pi^- \pi^+$  (the PDG-2006 [3] uncertainty is about 16%). For  $\mathcal{B}(D_s^+ \rightarrow \mu^+ \nu_\mu)$ , the statistical error is about 12.5% for an integrated luminosity of  $10 \text{ fb}^{-1}$  of  $D_s^+ D_s^-$  data for one tag mode. This extrapolates to be about 5% for a  $20 \text{ fb}^{-1}$  sample and six tag modes  $\phi \pi^-$ ,  $K^{*0} K^-$ ,  $K_S K^-$ ,  $K_S^0 \pi^-$ ,  $K_S^0 K^+ \pi^- \pi^-$  and  $f_0 \pi^-$  (the PDG-2006 [3] uncertainty is about 31.1%).

As mentioned in Sect. 21.1, CLEOc has found that the cross section for  $e^+ e^- \rightarrow D_s^* \bar{D}_s$  at 4.17 GeV is a factor of four times the the  $e^+ e^- \rightarrow D_s \bar{D}_s$  cross section at 4.03 GeV [4]. If

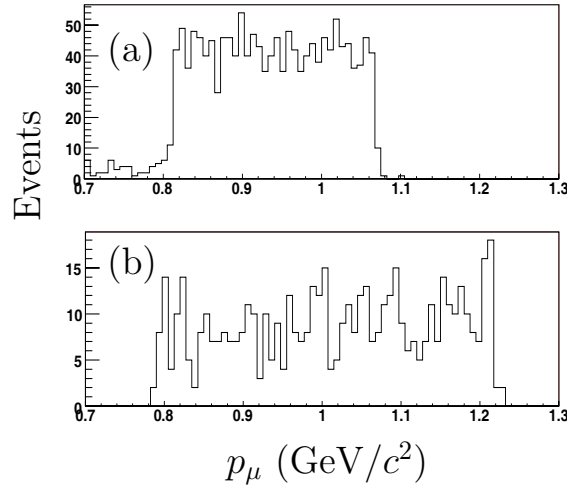


Figure 22.8: The candidate muon momentum distributions for (a)  $D^+ \rightarrow \mu^+ \nu_\mu$  and (b)  $D_s^+ \rightarrow \mu^+ \nu_\mu$ .

techniques being developed to tag  $D_s$  mesons produced in  $D_s^* \bar{D}_s$  final states are successful, another factor two in precision can be obtained, and branching ratio measurements for  $D^+ \rightarrow \mu^+ \nu_\mu$  and  $D_s^+ \rightarrow \mu^+ \nu_\mu$  at the  $\sim 2\%$  precision levels can be expected.

### Determination of $f_D$ and $f_{D_s}$

The decay constant  $f_D$  ( $f_{D_s}$ ) can be obtained by inserting the measured leptonic branching fractions, the mass of the muon, the mass of the  $D^+$  ( $D_s^+$ ) meson, the CKM matrix element  $|V_{cd}|$  ( $|V_{cs}|$ ), the Fermi coupling constant  $G_F$ , the lifetime of the  $D^+$  ( $D_s^+$ ) into Eq. 22.1.2. The systematic error on  $f_{D^+}$  ( $f_{D_s^+}$ ) are mainly due to uncertainties of the  $D^+$  ( $D_s^+$ ) lifetime,  $|V_{cd}|$  ( $|V_{cs}|$ ), and the measured branching fraction. The latter is due to the uncertainties in the track-finding efficiency, particle identification, photon selection, background estimation and the number of the single-tag  $D^-$  ( $D_s^-$ ) mesons. The expected errors on  $f_{D^+}$  and  $f_{D_s^+}$  are estimated using the relation

$$\frac{\delta f_{D_q}}{f_{D_q}} = \sqrt{\left(\frac{\Delta \tau_q}{2\tau_q}\right)^2 + \left(\frac{\Delta B}{2B}\right)^2 + \left(\frac{\Delta |V_{cq}|}{|V_{cq}|}\right)^2}, \quad (22.1.39)$$

where  $D_q = D + (D_s^+)$ ,  $\tau_q = \tau_{D^+}(\tau_{D_s^+})$  and  $V_{cq} = V_{cd}(V_{cs})$ . Table 22.6 lists the expected errors of  $f_{D^+}$  and  $f_{D_s^+}$  with  $20 \text{ fb}^{-1}$  data samples at *BES-III*.

Table 22.6: The expected errors on  $f_{D^+}$  and  $f_{D_s^+}$  from *BES-III* measurements with  $20 \text{ fb}^{-1}$  data samples.

Decays	Decay Const.	$\frac{\delta B}{B}$	$\frac{\delta \tau}{\tau}$ [3]	$\frac{\delta  V_{cq} }{ V_{cq} }$ [85]	$\frac{\delta f_{D_q}}{f_{D_q}}$
$D^+ \rightarrow \mu^+ \nu_\mu$	$f_{D^+}$	2%	0.6%	1.1%	1.5%
$D_s^+ \rightarrow \mu^+ \nu_\mu$	$f_{D_s^+}$	2%	1.0%	0.06%	1.3%

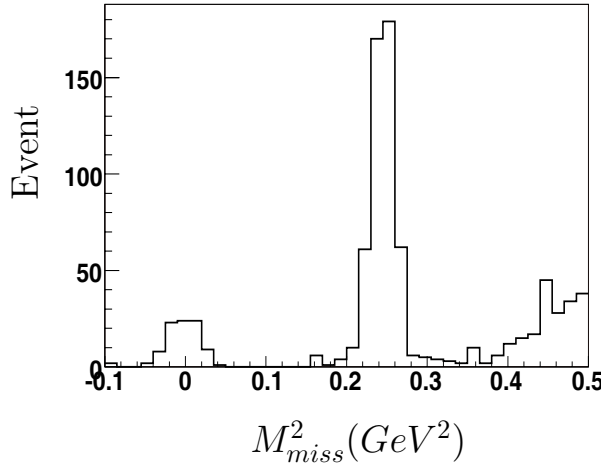


Figure 22.9: The  $M_{miss}^2$  distribution of the muon candidates on the recoil-side of the four  $D^-$  tag modes  $K^+\pi^-\pi^-$ ,  $K^+K^-\pi^-$ ,  $K_S^0\pi^-$  and  $K^+\pi^-\pi^-\pi^0$  (for a  $800\text{pb}^{-1}$  MC data sample).

## Conclusion

The decay constants  $f_D$  and  $f_{D_s}$  have been measured by many experiments but the precision of the measured values is still not sufficient for stringent tests of the SM. *BES-III* is expected to measure  $f_D$  and  $f_{D_s}$  with significantly improved precision. From a Monte Carlo study, we estimate that the statistical error for  $\mathcal{B}(D^+ \rightarrow \mu^+\nu_\mu)$  would be about  $\sim 2\%$  for a  $20\text{ fb}^{-1}$  sample with six tag modes  $K^+\pi^-\pi^-$ ,  $K^+K^-\pi^-$ ,  $K_S^0\pi^-$ ,  $K^+\pi^-\pi^-\pi^0$ ,  $K_S^0\pi^-\pi^0$  and  $K_S^0\pi^-\pi^-\pi^+$  (the PDG-2006 [3] uncertainty is about 16%); for  $\mathcal{B}(D_s^+ \rightarrow \mu^+\nu_\mu)$ , the statistical error is expected to be about  $\sim 5\%$  for a  $20\text{ fb}^{-1}$  data sample at 4.03 GeV with six tag modes  $\phi\pi^-$ ,  $K^{*0}K^-$ ,  $K_S^0\pi^-$ ,  $K_S^0K^-$ ,  $K_S^0K^+\pi^-\pi^-$  and  $f_0\pi^-$  (the PDG-2006 [3] uncertainty is about 31.1%). respectively. If techniques being developed to tag  $D_s$  mesons produced in  $D_s^*\bar{D}_s$  final states prove successful, the higher cross section for  $e^+e^- \rightarrow D_s^*\bar{D}_s$  at the 4.17 GeV cms energy can be exploited to gain as much as a factor of two improvement in statistical precision. Ultimate errors on  $f_D$  and  $f_{D_s}$  in the  $1 \sim 2\%$  range may be attainable.

## 22.2 Semileptonic Decays

### 22.2.1 Theoretical Review<sup>5</sup>

Charm mesons can decay into other hadrons by emitting a  $\ell^+\nu$  lepton pair via the weak interactions. At the quark level, this process is induced by the semileptonic charm quark decay:  $c \rightarrow q\ell^+\nu$ , where  $q = d, s$ . The light  $d$  or  $s$  daughter quark is bound to the initial light quark of the charm meson by the strong interaction to form a new hadron  $X$ , as depicted by the Feynman diagram of Fig. 22.11.

<sup>5</sup>By Mao-Zhi Yang

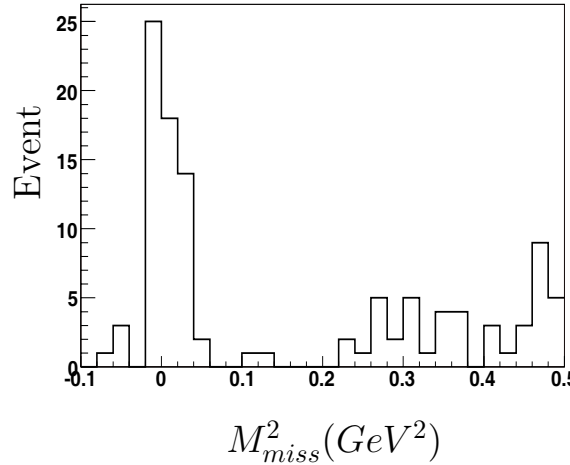


Figure 22.10: The  $M_{\text{miss}}^2$  distribution of the muon candidates on the recoil-side of the  $D_s^- \rightarrow \phi\pi^-$  tags (for a  $10 \text{ fb}^{-1}$  MC data sample).

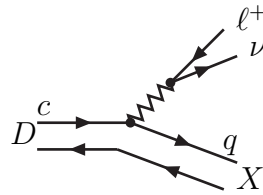


Figure 22.11: Feynman diagram for semileptonic D decay

In semileptonic decays, the two leptons do not feel the strong interaction, and are thus free of strong binding effects. Therefore, they can be factored out of the hadronic matrix element in the amplitude of the semileptonic decay process

$$A = \frac{G_F}{\sqrt{2}} V_{cq}^* \bar{\nu} \gamma_\mu (1 - \gamma_5) l \langle X | \bar{q} \gamma^\mu (1 - \gamma_5) c | D \rangle, \quad (22.2.40)$$

where all strong interactions are included in the hadronic matrix element  $\langle X | \bar{q} \gamma^\mu (1 - \gamma_5) c | D \rangle$ . The amplitude of the semileptonic decay process depends both on the hadronic matrix element and the quark-mixing parameter  $V_{cq}$ —the Cabibbo-Kobayashi-Maskawa (CKM) matrix element. Thus, the semileptonic charm meson decay process is a good laboratory for both studying the quark-mixing mechanism and testing theoretical techniques developed for calculating the hadronic matrix element.

The hadronic matrix element can be decomposed into several form factors according to its Lorentz structure. The form factors are generally controlled by non-perturbative dynamics, since perturbative QCD can not be applied directly. Several theoretical methods can be used to calculate these transition form factors, including: Lattice QCD [86, 87], QCD sum rules [88, 89, 90, 91, 92], light-cone sum rules [93], quark model [95, 96, 97, 98], light-front approach [99], and large-energy and heavy-quark-effective theory [100]. Among these, LQCD, QCD sum rules and LCSR are modeled on QCD.

Depending on the total quantum numbers of the daughter-quark system, the final hadron produced in the semileptonic decay process can be a pseudoscalar, vector, or scalar meson, etc. In the following, the charm meson decay to pseudoscalar, vector, or scalar meson processes are denoted as  $D \rightarrow P\ell^+\nu$ ,  $D \rightarrow V\ell^+\nu$ , and  $D \rightarrow S\ell^+\nu$ , respectively.

### (1) Transitions to pseudoscalar mesons $D \rightarrow P\ell^+\nu$

According to its Lorentz structure, the hadronic matrix element of  $D \rightarrow P$  transition process can be decomposed as

$$\langle P | \bar{q} \gamma^\mu (1 - \gamma_5) c | D \rangle = (p_1 + p_2)_\mu F_+(q^2) + (p_1 - p_2)_\mu F_-(q^2), \quad (22.2.41)$$

where  $p_1$  and  $p_2$  are the momenta of the initial  $D$  and final pseudoscalar mesons, respectively,  $q = p_1 - p_2$ , and  $F_+(q^2)$  and  $F_-(q^2)$  are the form factors. Equivalently, the decomposition can be expressed in the form

$$\langle P | \bar{q} \gamma^\mu (1 - \gamma_5) c | D \rangle = \left( p_1 + p_2 - \frac{m_D^2 - m_P^2}{q^2} q \right)_\mu F_+(q^2) + \frac{m_D^2 - m_P^2}{q^2} q_\mu F_0(q^2) \quad (22.2.42)$$

where  $F_0(q^2)$  and  $F_+(q^2)$  are the longitudinal and transverse form factors, respectively.

In general, the form factors in Eq. 22.2.42 can depend on all of the Lorentz scalars that can be formed from the two momenta  $p_1$  and  $p_2$ , i.e.,  $p_1^2$ ,  $p_2^2$  and  $p_1 \cdot p_2$ . However,  $p_1^2$  and  $p_2^2$  are not variables, they are the on-shell masses of the initial- and final-state particles. Therefore, the form factors can only depend on the Lorentz scalar  $p_1 \cdot p_2$ , which can equivalently be represented by  $q^2$ , according to the relation  $q^2 = p_1^2 - 2p_1 \cdot p_2 + p_2^2$ .

For the  $q^2$  dependence of the form factors, one usually assumes nearest-pole dominance [95]:

$$F_\pm(q^2) = \frac{F_\pm(0)}{1 - q^2/m_{\text{pole}}^2} \quad (22.2.43)$$

One can choose the value of  $m_{\text{pole}}$  as the mass of the nearest charm resonance with the same  $J^P$  as the hadronic weak current that induces the  $c \rightarrow q$  transition. This is only an assumption. In practice, one can also fit the data to obtain the effective pole mass. Any deviation from the mass of the nearest charm resonance will indicate the presence of contributions of the higher resonances. In this regard, one can also fit the data with the modified  $q^2$  distribution [101, 102]

$$F_\pm(q^2) = \frac{F_\pm(0)}{(1 - q^2/m_{D_{(s)}^*}^2)(1 - \alpha q^2/m_{D_{(s)}^*}^2)}, \quad (22.2.44)$$

where the parameter  $\alpha$  describes the deviation from the single resonance contribution.

In addition to the pole dominance ansatz discussed above, there is another model for the  $q^2$  dependence of the form factors that is commonly used in the literature [96, 97]:

$$F_\pm(q^2) = F_\pm(0) e^{\alpha q^2}. \quad (22.2.45)$$

Although this exponential form is quite different from the pole-dominance ansatz, it is difficult in practice to see the difference in cases where the final meson is heavy because

of the short range of  $q^2$  that is kinematically accessible. Experimentally, it is possible to distinguish between the  $q^2$  dependence of different models in decays to light final-state meson production, such as the  $D \rightarrow \pi$  transition.

Neglecting the lepton mass, the differential decay width of  $D \rightarrow P\ell^+\nu$  is given by

$$\frac{d\Gamma}{dq^2}(D \rightarrow P\ell^+\nu) = \frac{G_F^2}{192\pi^3 m_D^3} |V_{cq}|^2 [(m_D^2 + m_P^2 - q^2) - 4m_D^2 m_P^2]^{3/2} |F_+(q^2)|^2, \quad (22.2.46)$$

where only the  $F_+(q^2)$  form factor contributes. The contribution of  $F_-(q^2)$  is proportional to the squared lepton mass  $m_\ell^2$ , and is, therefore, neglected. The  $q^2$  distribution covers the range  $0 \leq q^2 \leq (m_D - m_P)^2$ . The branching ratio for the semileptonic decay can be obtained by integrating the differential decay width over the entire physical  $q^2$  range

$$Br(D \rightarrow P\ell^+\nu) = \tau_D \int_0^{(m_D - m_P)^2} dq^2 \frac{\Gamma}{dq^2}, \quad (22.2.47)$$

where  $\tau_D$  is the mean life time of the  $D$  meson.

The semileptonic decays  $D \rightarrow \pi\ell^+\nu$  and  $D \rightarrow K\ell^+\nu$  have been investigated both theoretically and experimentally. Theoretically the  $F_+^{D\pi}$  and  $F_+^{DK}$  form factors have been calculated in the quark model and with QCD sum rules, QCD light-cone sum rules (LCSR), lattice QCD (LQCD), etc. Some numerical results are summarized in Table 22.7. Existing BES collaboration data [103] are not precise enough to challenge these theoretical

Table 22.7: The  $F_+^{D\pi}(0)$  and  $F_+^{DK}(0)$  form factors.

	$F_+^{D\pi}(0)$	$F_+^{DK}(0)$
LQCD1[86]	$0.57 \pm 0.06^{+0.01}_{-0.00}$	$0.66 \pm 0.04^{+0.01}_{-0.00}$
	$0.57 \pm 0.06^{+0.02}_{-0.00}$	
LQCD2[87]	$0.64 \pm 0.03 \pm 0.06$	$0.73 \pm 0.03 \pm 0.07$
QCD SR[90]	$0.5 \pm 0.1$	$0.6^{+0.15}_{-0.10}$
LCSR[93]	$0.65 \pm 0.11$	$0.785 \pm 0.11$
LCSR[94]	$0.67 \pm 0.19$	$0.67 \pm 0.20$
Quark Model[98]	0.69	0.78
Light-Front[99]	0.67	
BES[103](Exp.)	$0.73 \pm 0.14 \pm 0.06$	$0.78 \pm 0.04 \pm 0.03$
CLEO[104](Exp.)	$\frac{ F_+^{D\pi}(0) ^2  V_{cd} ^2}{ F_+^{DK}(0) ^2  V_{cs} ^2} = 0.038^{+0.007+0.005}_{-0.007-0.003}$	
	Input $ V_{cd} ^2 /  V_{cs} ^2 = 0.052 \pm 0.001$ [3]	
	$\Rightarrow \frac{ F_+^{D\pi}(0) ^2}{ F_+^{DK}(0) ^2} = 0.86 \pm 0.07^{+0.06}_{-0.04} \pm 0.01$	

prediction. The precision will be highly improved by *BES-III*.

For the  $q^2$  dependence of the form factors, QCD sum rules confirm the pole dominance behavior for  $F_+^{D\pi}(q^2)$  and  $F_+^{DK}(q^2)$ . The fitted pole masses from QCD sum rules are:  $m_{\text{pole}}^{D \rightarrow \pi} = (1.95 \pm 0.10) \text{ GeV}$  and  $m_{\text{pole}}^{D \rightarrow K} = (1.81 \pm 0.10) \text{ GeV}$  [90], which are compatible with the experimental values  $m_{\text{pole}}^{D \rightarrow \pi} = 1.86^{+0.10+0.07}_{-0.06-0.03} \text{ GeV}$ ,  $m_{\text{pole}}^{D \rightarrow K} = 1.89 \pm 0.05^{+0.04}_{-0.03} \text{ GeV}$  [104].

The  $m_{\text{pole}}^{D \rightarrow \pi}$  value is consistent with the mass of the  $D^*$ , while  $m_{\text{pole}}^{D \rightarrow K}$  is definitely distinct from the mass of  $D_{(s)}^*$ . This indicates that the single pole behavior of  $F_+^{DK}(q^2)$  is the mean effect of a set of resonances in the  $c\bar{s}$  channel.

Using the modified pole form of Eq. 22.2.44, the value of  $\alpha$  for both  $D \rightarrow \pi$  and  $D \rightarrow K$  from LCSR is consistent with zero [93], which implies the strong dominance of the  $D_{(s)}^*$  pole. Experiment gives  $\alpha^{D \rightarrow \pi} = 0.37^{+0.20}_{-0.31} \pm 0.15$  and  $\alpha^{D \rightarrow K} = 0.36 \pm 0.10^{+0.03}_{-0.07} \pm 0.15$  [104]. The non-zero value of  $\alpha^{D \rightarrow K}$  suggests the existence of contributions beyond the pure  $D_s^*$  pole to  $F_+^{DK}(q^2)$ .

Different theoretical techniques predict slightly different  $q^2$  dependencies of the form factors. High precision experimental measurements of the partial decay width over different ranges of  $q^2$  will distinguish which method correctly describes the non-perturbative dynamics of QCD.

Table 22.8: Branching fractions for  $D^0 \rightarrow \pi^- \ell^+ \nu$  and  $D^0 \rightarrow K^- \ell^+ \nu$ .

	$Br(D^0 \rightarrow \pi^- \ell^+ \nu)(\%)$	$Br(D^0 \rightarrow K^- \ell^+ \nu)(\%)$
LQCD1[86]	$0.23 \pm 0.06$	$2.83 \pm 0.45$
	$0.24 \pm 0.06$	$2.99 \pm 0.45$
LQCD2[87]	$0.32 \pm 0.02 \pm 0.06 \pm 0.03$	$3.77 \pm 0.29 \pm 0.74 \pm 0.08$
QCD SR[90]	$0.16 \pm 0.03$	$2.7 \pm 0.6$
LCSR[93]	$0.27 \pm 0.10$	$3.6 \pm 1.4$
LCSR[94]	$0.30 \pm 0.09$	$3.9 \pm 1.2$
BES[103](Exp.)	$0.33 \pm 0.13 \pm 0.03$	$3.82 \pm 0.40 \pm 0.27$
CLEO[105](Exp.)	$0.262 \pm 0.025 \pm 0.008$	$3.44 \pm 0.10 \pm 0.10$

Theoretical calculations of the branching fractions for  $D^0 \rightarrow \pi^- \ell^+ \nu$  and  $D^0 \rightarrow K^- \ell^+ \nu$  are compared with current experimental data in Table 22.8. Most of the theoretical predictions are consistent with experimental data at the present level of precision, except for the results from QCD sum rules [90], which are somewhat lower than the experimental values.

Isospin invariance has been tested in  $D$  meson semileptonic decays [106]. Absolute branching fractions for  $D^+ \rightarrow \pi^0 e^+ \nu$  and  $D^+ \rightarrow \bar{K}^0 e^+ \nu$  are measured to be:  $Br(D^+ \rightarrow \pi^0 e^+ \nu) = (0.44 \pm 0.06 \pm 0.03)\%$ ,  $Br(D^+ \rightarrow \bar{K}^0 e^+ \nu) = (8.71 \pm 0.38 \pm 0.37)\%$ . The ratio of the decay widths  $D^0 \rightarrow K^- e^+ \nu$  and  $D^+ \rightarrow \bar{K}^0 e^+ \nu$  is  $\frac{\Gamma(D^0 \rightarrow K^- e^+ \nu)}{\Gamma(D^+ \rightarrow \bar{K}^0 e^+ \nu)} = 1.00 \pm 0.05 \pm 0.04$  and is consistent with the isospin invariance expectation for this ratio, which is unity. Thus, the experimental data confirms the applicability of isospin symmetry to  $D \rightarrow K \ell^+ \nu$  semileptonic decays.

The ratio of  $\frac{\Gamma(D^0 \rightarrow \pi^- e^+ \nu)}{2\Gamma(D^+ \rightarrow \pi^0 e^+ \nu)}$  is measured to be  $0.75^{+0.14}_{-0.11} \pm 0.04$  [106]. Isospin invariance says that this ratio should also be unity. The CLEO central values imply the presence of a large isospin breaking effect in the semileptonic decay of  $D \rightarrow \pi e^+ \nu$ . However, the present experimental error is too large to be conclusive. The precision will be improved by future *BES-III* measurements.

There are other  $D_{(s)}$  to pseudoscalar semileptonic decay channels that deserve further studies. The present theoretical calculations and experimental measurements are listed

Table 22.9: Branching fractions for  $D$  and  $D_s^+$  to  $\eta, \eta', K$  transitions.

channel	$Br(\%)$	Ref.
$D^+ \rightarrow \eta \ell^+ \nu$	0.10	Ref.[100] (double pole)
	0.15	Ref.[100] (single pole)
	$< 0.5$	Exp.[3]
$D^+ \rightarrow \eta' \ell^+ \nu$	0.016	Ref.[100] (double pole)
	0.019	Ref.[100] (single pole)
	$< 1.1$	Exp.[3]
$D_s^+ \rightarrow \eta \ell^+ \nu$	1.7	Ref.[100] (double pole)
	2.5	Ref.[100] (single pole)
	$2.3 \pm 0.4$	Ref.[91]
	$2.5 \pm 0.7$	Exp.[3]
$D_s^+ \rightarrow \eta' \ell^+ \nu$	0.61	Ref.[100] (double pole)
	0.74	Ref.[100] (single pole)
	$1.0 \pm 0.2$	Ref.[91]
	$0.89 \pm 0.33$	Exp.[3]
$D_s^+ \rightarrow K^0 \ell^+ \nu$	0.20	Ref.[100] (double pole)
	0.32	Ref.[100] (single pole)

in Table 22.9.

## (2) Transitions to vector mesons $D \rightarrow V \ell^+ \nu$

The Lorentz decomposition of the transition matrix element of  $D \rightarrow V$  is

$$\begin{aligned} \langle V(\varepsilon, p_2) | \bar{q} \gamma_\mu (1 - \gamma_5) c | D(p_1) \rangle &= \varepsilon_{\mu\nu\alpha\beta} \varepsilon^{*\nu} p_1^\alpha p_2^\beta \frac{2V(q^2)}{m_D + m_V} \\ &- i(\varepsilon_\mu^* - \frac{\varepsilon^* \cdot q}{q^2} q_\mu)(m_D + m_V) A_1(q^2) + i[(p_1 + p_2)_\mu - \frac{m_D^2 - m_V^2}{q^2} q_\mu] \\ &\times \varepsilon^* \cdot q \frac{A_2(q^2)}{m_D + m_V} - i \frac{2m_V \varepsilon^* \cdot q}{q^2} q_\mu A_0(q^2), \end{aligned} \quad (22.2.48)$$

where the form factor  $V(q^2)$  receives contributions from the vector current  $\bar{q} \gamma_\mu c$ , and the form factors  $A_{0,1,2}(q^2)$  from the axial-vector current  $\bar{q} \gamma_\mu \gamma_5 c$ .

The differential and total  $D \rightarrow V \ell^+ \nu$  decay rates can be calculated from the above decomposition of the hadronic matrix element. There are three polarization states for the  $V$  meson: one longitudinal state and two transverse states (right-handed and left-handed). The differential decay rate to a longitudinally polarized  $V$  meson is given by

$$\begin{aligned} \frac{d\Gamma_L}{dq^2} &= \frac{G_F^2 |V_{cq}|^2}{192\pi^3 m_D^3} \sqrt{\lambda(m_D^2, m_V^2, q^2)} \left| \frac{1}{2m_V} [(m_D^2 - m_V^2 - q^2) \right. \\ &\times (m_D + m_V) A_1(q^2) - \left. \frac{\lambda(m_D^2, m_V^2, q^2)}{m_D + m_V} A_2(q^2) \right|^2, \end{aligned} \quad (22.2.49)$$

where  $\lambda(m_D^2, m_V^2, q^2) \equiv (m_D^2 + m_V^2 - q^2)^2 - 4m_D^2 m_V^2$ .

The differential decay rates to the transverse states is given by

$$\frac{d\Gamma_T^\pm}{dq^2} = \frac{G_F^2 |V_{cq}|^2}{192\pi^3 m_D^3} q^2 \lambda(m_D^2, m_V^2, q^2)^{3/2} \left| \frac{V(q^2)}{m_D + m_V} \mp \frac{(m_D + m_V) A_1(q^2)}{\sqrt{\lambda(m_D^2, m_V^2, q^2)}} \right|^2, \quad (22.2.50)$$

where  $+$  and  $-$  correspond to the right- and left-handed states, respectively. Finally, the combined transverse and total differential decay rates are given by

$$\frac{d\Gamma_T}{dq^2} = \frac{d}{dq^2}(\Gamma_T^+ + \Gamma_T^-), \quad \frac{d\Gamma}{dq^2} = \frac{d}{dq^2}(\Gamma_L + \Gamma_T). \quad (22.2.51)$$

The vector meson is tagged by its decay products. For example, for  $D \rightarrow K^* \ell^+ \nu$ , the  $K^*$  is tagged according to its decay process  $K^* \rightarrow K\pi$ . The angular distribution for  $D \rightarrow K^* \ell^+ \nu$  ( $K^* \rightarrow K\pi$ ) is

$$\begin{aligned} \frac{d\Gamma}{dq^2 d\cos\theta_K d\cos\theta_\ell d\chi} &= \frac{3G_F^2 |V_{cs}|^2}{8(4\pi)^4} \frac{p_{K^*} q^2}{m_D^2} [(1 + \cos\theta_\ell)^2 \sin^2\theta_K |H_+(q^2)|^2 \\ &\quad + (1 - \cos\theta_\ell)^2 \sin^2\theta_K |H_-(q^2)|^2 - 4 \sin^2\theta_\ell \cos^2\theta_K |H_0(q^2)|^2 \\ &\quad + 4 \sin\theta_\ell (1 + \cos\theta_\ell) \sin\theta_K \cos\theta_K \cos\chi H_+(q^2) H_0(q^2) \\ &\quad - 4 \sin\theta_\ell (1 - \cos\theta_\ell) \sin\theta_K \cos\theta_K \cos\chi H_-(q^2) H_0(q^2) \\ &\quad - 2 \sin^2\theta_\ell \sin^2\theta_K \cos 2\chi H_+(q^2) H_-(q^2)] \\ &\quad \times Br(K^* \rightarrow K\pi), \end{aligned} \quad (22.2.52)$$

where  $\theta_\ell$  is the polar angle of the lepton in the rest frame of the  $\ell^+ \nu$  lepton pair,  $\theta_K$  the polar angle of the kaon in the  $K^*$  rest frame, and  $\chi$  is the relative angle between the  $D \rightarrow K^* \ell^+ \nu$  and  $K^* \rightarrow K\pi$  decay planes. The helicity functions  $H_+(q^2)$ ,  $H_-(q^2)$  and  $H_0(q^2)$  are

$$\begin{aligned} H_\pm(q^2) &= (m_D + m_{K\pi}) A_1(q^2) \mp \frac{\sqrt{\lambda(m_D^2, m_{K\pi}^2, q^2)}}{m_D + m_{K\pi}} \\ H_0(q^2) &= \frac{1}{2m_{K\pi}\sqrt{q^2}} \left[ (m_D^2 - m_{K\pi}^2 - q^2)(m_D + m_{K\pi}) A_1(q^2) \right. \\ &\quad \left. - \frac{\lambda(m_D^2, m_{K\pi}^2, q^2)}{m_D + m_{K\pi}} A_2(q^2) \right]. \end{aligned} \quad (22.2.53)$$

The  $D$  to vector meson transition form factors can be calculated by a variety of methods, such as the quark model (QM), QCD sum rules (SR), light-cone sum rules (LCSR), light-front approach (LF), etc. Some numerical results are collected in Table 22.10.

For some modes, different theoretical methods give consistent results, for others, different methods give different results. These different predictions provide opportunities to test the theoretical methods. However, it is difficult to measure the absolute values of  $D \rightarrow V$  transition form factors directly; usually experiments measure ratios of form factors. The ratios of the  $D \rightarrow V$  transition form factors are defined as

$$r_V \equiv \frac{V(0)}{A_1(0)}, \quad r_2 \equiv \frac{A_2(0)}{A_1(0)}. \quad (22.2.54)$$

Table 22.10: Form factors for  $D \rightarrow V$  transitions.

mode	$V(0)$	$A_0(0)$	$A_1(0)$	$A_2(0)$	Ref.
$D \rightarrow K^*$	0.82	0.47	0.57	0.75	QM [107]
	1.03		0.66	0.49	QM [98]
	$1.1 \pm 0.25$		$0.50 \pm 0.15$	$0.60 \pm 0.15$	SR[90]
	$0.8 \pm 0.10$		$0.59 \pm 0.10$	$0.55 \pm 0.08$	LCSR[94]
	0.99	1.12	0.62	0.31	Ref.[100]
$D \rightarrow \rho$	0.65	0.35	0.41	0.50	QM [107]
	0.90		0.59	0.49	QM [98]
	$1.0 \pm 0.2$		$0.5 \pm 0.2$	$0.4 \pm 0.1$	SR[90]
	$0.72 \pm 0.10$		$0.57 \pm 0.08$	$0.52 \pm 0.07$	LCSR[94]
	0.86	0.64	0.58	0.48	LF [99]
	1.05	1.32	0.61	0.31	Ref.[100]
$D \rightarrow \omega$	1.05	1.32	0.61	0.31	Ref.[100]
$D_s \rightarrow \phi$	1.10	1.02	0.61	0.32	Ref.[100]
	$1.21 \pm 0.33$	$0.42 \pm 0.12$	$0.55 \pm 0.15$	$0.59 \pm 0.17$	SR[92]
$D_s \rightarrow K^*$	1.16	1.19	0.60	0.33	Ref.[100]

Measured values of  $r_V$  and  $r_2$  for each decay mode can be compared with theoretical calculations to test the theoretical techniques (see Table 22.11).

The  $q^2$  dependence of the form factors can be calculated by theory. The QCD sum rule result shows that the behavior of  $V(q^2)$  and  $A_0(q^2)$  is compatible with the pole model [90, 92]

$$V(0) = \frac{V(0)}{1 - q^2/m_{\text{pole}}^V}, \quad A_0(0) = \frac{A_0(0)}{1 - q^2/m_{\text{pole}}^{A_0}}. \quad (22.2.55)$$

The fitted pole mass  $m_{\text{pole}}^V$  is consistent with the low-lying  $J^P = 1^-$  charmed meson resonance. While the  $q^2$  dependence of  $A_1(q^2)$  and  $A_2(q^2)$  is weak. This behavior implies that the pole-dominance assumption for  $A_1(q^2)$  and  $A_2(q^2)$  is inadequate.

Ratios of the polarized decay widths and total branching ratios of  $D \rightarrow V\ell^+\nu$  decays are shown in Table 22.12.

Isospin symmetry in  $D \rightarrow V\ell^+\nu$  decays can be tested by measuring  $\frac{\Gamma(D^0 \rightarrow K^{*-} \ell^+\nu)}{\Gamma(D^+ \rightarrow K^{*0} \ell^+\nu)}$  and  $\frac{\Gamma(D^0 \rightarrow \rho^- \ell^+\nu)}{2\Gamma(D^+ \rightarrow \rho^0 \ell^+\nu)}$ , which isospin invariance says should be unity. Deviations from unity provide measures of the degree of isospin breaking. CLEO measures:  $\frac{\Gamma(D^0 \rightarrow K^{*-} e^+\nu)}{\Gamma(D^+ \rightarrow K^{*0} e^+\nu)} = 0.98 \pm 0.08 \pm 0.04$  and  $\frac{\Gamma(D^0 \rightarrow \rho^- e^+\nu)}{2\Gamma(D^+ \rightarrow \rho^0 e^+\nu)} = 1.2_{-0.3}^{+0.4} \pm 0.1$  [106], both of which are consistent with unity. The former ratio implies that isospin symmetry in  $D \rightarrow K^*$  channel is a good symmetry at the few percentage level, while the latter needs significant improvement in precision to match that of the former.

### (3) Transitions to scalar mesons $D \rightarrow S\ell^+\nu$

A large number of scalar mesons have been found experimentally [3], including the:  $\sigma$  [or  $f_0(600)$ ],  $f_0(980)$ ,  $f_0(1370)$ ,  $f_0(1500)$ ,  $f_0(1710)$ ,  $a_0(980)$ ,  $a_0(1450)$ ,  $\kappa$ ,  $K_0^*(1430)$ ,

Table 22.11: Comparisons of  $r_V$  and  $r_2$  with experimental data.

mode	$r_V$	$r_2$	Ref.
$D \rightarrow K^*$	1.44	1.32	QM [107]
	2.10	1.35	QM [98]
	$2.2 \pm 0.2$	$1.2 \pm 0.2$	SR[90]
	$1.36 \pm 0.39$	$0.93 \pm 0.29$	LCSR[94]
	3.19	2.00	Ref.[100]
	$1.62 \pm 0.08$	$0.83 \pm 0.05$	Exp.[3]
$D \rightarrow \rho$	1.3	0.82	QM [107]
	1.84	1.20	QM [98]
	1.79	1.21	LF [99]
	3.39	1.97	Ref.[100]
	-	-	Exp.
$D \rightarrow \omega$	3.39	1.97	Ref.[100]
	-	-	Exp.
$D_s \rightarrow \phi$	3.44	1.91	Ref.[100]
	1.569	0.865	LF [99]
	$2.20 \pm 0.85$	$1.07 \pm 0.43$	SR[92]
	$1.92 \pm 0.32$	$1.60 \pm 0.24$	Exp.[3]
$D_s \rightarrow K^*$	3.52	1.82	Ref.[100]
	-	-	Exp.

etc. Their structure is still not well established theoretically. Suggestions about the composition of the scalar mesons include  $q\bar{q}$ ,  $q\bar{q}q\bar{q}$  and meson-meson bound states. To investigate the structure of the scalar mesons, a large amount of experimental data and theoretical studies are necessary.

Semileptonic  $D$  meson transitions to scalar mesons are important processes for studying the nature of scalars, because of the cleanliness of semileptonic decays as compared to hadronic decays.

The Lorentz decomposition of the hadronic matrix element of  $D \rightarrow S$  transition is

$$\langle S(p_2) | \bar{q} \gamma^\mu (1 - \gamma_5) c | D \rangle = i[(p_1 + p_2)^\mu F_+(q^2) + (p_1 - p_2)^\mu F_-(q^2)]. \quad (22.2.56)$$

The form factor  $F_-(q^2)$  does not contribute to the semileptonic decay amplitude in the limit of zero lepton mass. The differential decay width for  $D \rightarrow S\ell^+\nu$  in this limit is

$$\frac{d\Gamma}{dq^2} = \frac{G_F^2 |V_{Qq}|^2}{192\pi^3 m_D^3} F_+(q^2)^2 [(m_D^2 + m_S^2 - q^2)^2 - 4m_D^2 m_S^2]^{3/2}. \quad (22.2.57)$$

If the form factor is known, one can predict the decay width theoretically. The form factor not only depends on the dynamics of the strong binding effects, but also depends on the constituents of the scalar mesons. The  $D \rightarrow S$  transition form factors have been studied with QCD sum rules by treating the scalars as quark-antiquark bound states [108, 109]; the results are listed in Table 22.13.

Table 22.12: Ratios of the polarized decay widths and total branching fractions for  $D \rightarrow V\ell^+\nu$  decays.

mode	$\Gamma_L/\Gamma_T$	$Br(\%)$	Ref.
$D^0 \rightarrow K^{*-}\ell^+\nu$		4.0	QM [107]
	1.28	2.46	QM [98]
	$1.15 \pm 0.10$	$2.0 \pm 0.5$	LCSR[94]
	1.149	2.2	Ref.[100]
		$2.15 \pm 0.35$	Exp.[3]
$D^+ \rightarrow K^{*0}\ell^+\nu$	$0.86 \pm 0.06$	$4.0 \pm 1.6$	SR[90]
	1.13	5.6	Ref.[100]
		$5.73 \pm 0.35$	Exp.[3]
$D^0 \rightarrow \rho^-\ell^+\nu$		0.29	QM [107]
	1.16	0.17	QM [98]
	$1.17 \pm 0.09$	$0.14 \pm 0.035$	LCSR[94]
	1.10	0.20	Ref.[100]
	-	$0.194 \pm 0.039 \pm 0.013$	Exp.[105]
$D^+ \rightarrow \rho^0\ell^+\nu$	1.10	0.25	Ref.[100]
	-	$0.21 \pm 0.04 \pm 0.01$	Exp.[106]
$D^+ \rightarrow \omega\ell^+\nu$	1.10	0.25	Ref.[100]
	-	$0.16^{+0.07}_{-0.06} \pm 0.01$	Exp.[106]
$D_s^+ \rightarrow \phi\ell^+\nu$		2.5	QM [98]
	1.08	2.4	Ref.[100]
	$0.99 \pm 0.43$	$1.8 \pm 0.5$	SR[92]
	$0.72 \pm 0.18$	$2.0 \pm 0.5$	Exp.[3]
$D_s^+ \rightarrow K^{*0}\ell^+\nu$	1.21	0.19	QM [98]
	1.03	0.22	Ref.[100]
	-	-	Exp.

The  $q^2$  dependence of  $D \rightarrow S$  transition form factors calculated with QCD sum rules is consistent with the pole-model

$$F_+(q^2) = \frac{F_+(0)}{1 - q^2/m_{\text{pole}}^2}. \quad (22.2.58)$$

The fitted pole masses for each mode are [108, 109]

$$\begin{aligned} m_{\text{pole}}^{D\kappa} &= 2.05 \pm 0.15 \text{ GeV}, \\ m_{\text{pole}}^{DK_0^*} &= 2.9 \pm 0.3 \text{ GeV}, \\ m_{\text{pole}}^{D_s K_0^*} &= 1.96 \pm 0.12 \text{ GeV}. \end{aligned} \quad (22.2.59)$$

The total decay widths for each mode are

$$\Gamma(D \rightarrow \sigma\ell^+\nu) = (8.0 \pm 2.5) \times 10^{-16} \text{ GeV} [108],$$

Table 22.13: Form factors for  $D_{(s)} \rightarrow S\ell^+\nu$  decays.

mode	$F_+(0)$	Ref.
$D \rightarrow \sigma$	$0.50 \pm 0.07$	SR [108]
$D \rightarrow \kappa$	$0.52 \pm 0.03$	SR [108]
$D \rightarrow K_0^*(1430)$	$0.57 \pm 0.19$	SR [109]
$D_s \rightarrow K_0^*(1430)$	$0.51 \pm 0.20$	SR [109]

$$\begin{aligned}\Gamma(D \rightarrow \kappa\ell^+\nu) &= (5.5 \pm 1.0) \times 10^{-15} \text{ GeV} \text{ [108]}, \\ \Gamma(D \rightarrow K_0^*(1430)\ell^+\nu) &= (2.9_{-1.6}^{+2.3}) \times 10^{-16} \text{ GeV} \text{ [109]}, \\ \Gamma(D_s^+ \rightarrow K_0^*(1430)^0\ell^+\nu) &= (3.2_{-2.0}^{+3.0}) \times 10^{-17} \text{ GeV} \text{ [109]},\end{aligned}\quad (22.2.60)$$

and the corresponding branching fractions are

$$\begin{aligned}Br(D^+ \rightarrow \sigma\ell^+\nu) &= (1.26 \pm 0.40) \times 10^{-3}, \\ Br(D^0 \rightarrow \kappa^-\ell^+\nu) &= (3.43 \pm 0.62) \times 10^{-3},\end{aligned}\quad (22.2.61)$$

$$\begin{aligned}Br(D^+ \rightarrow \bar{\kappa}^0\ell^+\nu) &= (8.7 \pm 1.6) \times 10^{-3}, \\ Br(D^0 \rightarrow K_0^*(1430)^-\ell^+\nu) &= (1.8_{-1.0}^{+1.5}) \times 10^{-4}, \\ Br(D^+ \rightarrow \bar{K}_0^*(1430)^0\ell^+\nu) &= (4.6_{-2.6}^{+3.7}) \times 10^{-4}, \\ Br(D_s^+ \rightarrow K_0^*(1430)^0\ell^+\nu) &= (2.4_{-1.5}^{+2.2}) \times 10^{-5}.\end{aligned}\quad (22.2.62)$$

These numerical results indicate that many of the scalar semileptonic decay modes are rare. Measuring them experimentally will require large data sample. In return, however, these measurements will provide valuable information on the nature of the light scalar mesons. Such measurements are highly desired.

Other decay modes that are worth-while to measure are  $D \rightarrow f_0(980)\ell^+\nu$ ,  $D \rightarrow a_0(980)\ell^+\nu$ , etc.

#### (4) CKM matrix elements $V_{cd}$ and $V_{cs}$ in semileptonic $D$ decays

The CKM matrix elements are fundamental SM parameters that describe the mixing of quark fields due to the weak interaction. These parameters cannot be predicted from the basic SM theory, they must be measured by experiment. Measurements of the CKM matrix elements are important for understanding the dynamics of quark mixing and the source of  $CP$  violation. In theories with more than three generations of quarks, the CKM matrix provides phase parameters that generate non-SM  $CP$  violations.

Semileptonic  $D$  decays are sensitive to  $V_{cd}$  and  $V_{cs}$ . Precise branching fraction measurements for semileptonic  $D$  meson decays can improve the precision of  $V_{cd}$  and  $V_{cs}$ . The Particle Data Group (2004) gives magnitudes for  $V_{cd}$  and  $V_{cs}$  of [3]

$$|V_{cd}| = 0.224 \pm 0.012, \quad |V_{cs}| = 0.996 \pm 0.13. \quad (22.2.63)$$

The magnitude of  $|V_{cd}|$  is deduced from neutrino and antineutrino production of charm from valence  $d$  quarks. The present error on  $|V_{cd}|$  is about 5.4%. Values for  $|V_{cs}|$  obtained

from neutrino production of charm have errors that exceed 10% mainly because of theoretical uncertainties. The error of the present direct measurement value, given above, is about 13%. With the application of requirements for unitarity of the three-generation CKM matrix, the precision for  $|V_{cs}|$  can be greatly improved.

In *BES-III*, the absolute branching fractions for the semileptonic decay modes  $D \rightarrow \pi\ell^+\nu$ ,  $D \rightarrow K\ell^+\nu$ ,  $D \rightarrow \eta(\eta')\ell^+\nu$ ,  $D \rightarrow \rho\ell^+\nu$ ,  $D \rightarrow K^*\ell^+\nu$ ,  $D_s \rightarrow \phi\ell^+\nu$ , etc., will be measured with precisions at the 1% level. The form factor  $q^2$ -distribution slope will be as precise as 1.5% [110]. The differential decay width is proportional to squared product of  $|V_{cd(s)}|$  and the relevant semileptonic transition form factor  $F(q^2)$ :

$$\frac{d\Gamma(D \rightarrow X_{d,s}\ell^+\nu)}{dq^2} \propto |V_{cd(s)}|^2 |F(q^2)|^2. \quad (22.2.64)$$

High-precision values of  $|V_{cd(s)}|^2 |F(q^2)|^2$  can be extracted from precisely measured absolute branching fractions. This will lead to determinations of  $V_{cd}$  and  $V_{cs}$  with 1% precision if the form factors can be theoretically calculated at the 1.5% precision level. It is hoped that Lattice QCD can reach this level in next few years.

### 22.2.2 Exclusive Semileptonic Decays <sup>6</sup>

In exclusive semileptonic decays of  $D$  mesons, the effects of weak and strong interactions can be well separated theoretically. Therefore, these channels provide a good laboratory both for studying the quark-mixing mechanism and for testing theoretical techniques developed to calculate hadronic matrix elements.

At *BES-III*, we will collect a  $\psi(3770)$  data sample with an integrated luminosity of about  $\mathcal{L} = 20 \text{ fb}^{-1}$ , which will be enough to allow for systematic characterizations of the features of exclusive semileptonic  $D$  meson decays. The absolute branching fractions for many exclusive semileptonic decays of  $D$  mesons will be precisely measured, including:  $D^0 \rightarrow K^-\ell^+\nu_\ell$  ( $\ell = e$ , or  $\mu$ );  $D^0 \rightarrow \pi^-\ell^+\nu_\ell$ ;  $D^0 \rightarrow K^{*-}\ell^+\nu_\ell$ ,  $D^0 \rightarrow \rho^-\ell^+\nu_\ell$ ;  $D^+ \rightarrow \bar{K}^0\ell^+\nu_\ell$ ;  $D^+ \rightarrow \pi^0\ell^+\nu_\ell$ ;  $D^+ \rightarrow \bar{K}^{*0}\ell^+\nu_\ell$ ;  $D^+ \rightarrow \rho^0\ell^+\nu_\ell$ ;  $D^+ \rightarrow \omega\ell^+\nu_\ell$ ; etc. The magnitude of the CKM matrix element  $|V_{cs(d)}|$  can then be extracted with high precision. Here we describe a MC simulation of a measurement of the simplest pseudoscalar exclusive semileptonic decays:  $D^0 \rightarrow K^-e^+\nu_e$  and  $D^0 \rightarrow \pi^-e^+\nu_e$ , to demonstrate the experimental capabilities of *BES-III* in this area.

A Monte Carlo sample corresponding to an integrated luminosity of about  $800 \text{ pb}^{-1}$  at  $3.773 \text{ GeV}$  is used to simulate a measurement of the branching fractions for  $D^0 \rightarrow K^-e^+\nu_e$  and  $D^0 \rightarrow \pi^-e^+\nu_e$ . We first reconstruct single-tag  $\bar{D}^0$  mesons from the sample, and then select candidates for the semileptonic decays  $D^0 \rightarrow K^-e^+\nu_e$  and  $D^0 \rightarrow \pi^-e^+\nu_e$  in the system recoiling against the tag  $\bar{D}^0$  meson. We measure the branching fractions using a method previously used by BESII [83, 84]. The form factor  $|f_+^{K(\pi)}(0)|$ , the CKM matrix element  $|V_{cs(d)}|$ , and the ratio  $|V_{cd}|/|V_{cs}|$  are extracted. Based on the results of this simulation, we estimate the expected precision of these measurements for a  $20 \text{ fb}^{-1}$   $\psi(3770)$  data set.

---

<sup>6</sup>By Hui-Hui Liu, Hai-Long Ma and Gang Rong

## 1. Overview of the study of the decays $D^0 \rightarrow K^- e^+ \nu_e$ and $D^0 \rightarrow \pi^- e^+ \nu_e$

The exclusive semileptonic  $D^0 \rightarrow K^- e^+ \nu_e$  and  $D^0 \rightarrow \pi^- e^+ \nu_e$  decay final states contain only two easily reconstructed charged particles and have been studied by many different experiments [83, 111, 112, 113, 114, 115, 116, 117]. The measured branching fractions for  $D^0 \rightarrow K^- e^+ \nu_e$  and  $D^0 \rightarrow \pi^- e^+ \nu_e$  are summarized in Tables 22.14 and 22.15, respectively, including the number of signal events associated with each entry. In some experiments, the  $D^0 \rightarrow K^- e^+ \nu_e$  (or  $D^0 \rightarrow \pi^- e^+ \nu_e$ ) branching fractions are measured relative to the topologically similar mode  $D^0 \rightarrow K^- \pi^+$  (or  $D^0 \rightarrow K^- e^+ \nu_e$ ). Absolute branching fractions for  $D^0 \rightarrow K^- e^+ \nu_e$  and  $D^0 \rightarrow \pi^- e^+ \nu_e$  can be extracted by multiplying by the branching fraction of  $\mathcal{B}(D^0 \rightarrow K^- \pi^+)$  or  $\mathcal{B}(D^0 \rightarrow K^- e^+ \nu_e)$  [3]. In the tables, the first error is statistical, the second is systematic, and the third arises from the uncertainty in  $\mathcal{B}(D^0 \rightarrow K^- \pi^+)$  or  $\mathcal{B}(D^0 \rightarrow K^- e^+ \nu_e)$ . The relative errors of these branching fractions are 3.1% for  $\mathcal{B}(D^0 \rightarrow K^- e^+ \nu_e)$  and 6.8% for  $\mathcal{B}(D^0 \rightarrow \pi^- e^+ \nu_e)$ , with the most precise measurements coming from the CLEO Collaboration [115]. *BES-III* should be able to improve these errors significantly.

Table 22.14: Summary of measurements of the  $D^0 \rightarrow K^- e^+ \nu_e$  branching fraction from different experiments; here ‘absolute’ means that the branching fraction is made directly.

Experiment	Number of Events	Normalization Mode	Ratio of branching fraction	$\mathcal{B}(D^0 \rightarrow K^- e^+ \nu_e)$ (%)
E691 [111]	250	$\frac{D^0 \rightarrow K^- e^+ \nu_e}{D^0 \rightarrow K^- \pi^+}$	$0.91 \pm 0.07 \pm 0.11$	$3.46 \pm 0.27 \pm 0.42 \pm 0.08$
CLEO [112]	584	$\frac{D^0 \rightarrow K^- e^+ \nu_e}{D^0 \rightarrow K^- \pi^+}$	$0.90 \pm 0.06 \pm 0.06$	$3.42 \pm 0.23 \pm 0.23 \pm 0.08$
CLEOII [113]	2510	$\frac{D^0 \rightarrow K^- e^+ \nu_e}{D^0 \rightarrow K^- \pi^+}$	$0.978 \pm 0.027 \pm 0.044$	$3.72 \pm 0.10 \pm 0.17 \pm 0.09$
MARKIII [114]	55	absolute		$3.4 \pm 0.5 \pm 0.4$
BESII [83]	104	absolute		$3.82 \pm 0.40 \pm 0.27$
CLEOc [115]	1311	absolute		$3.44 \pm 0.10 \pm 0.10$
PDG average [3]				$3.51 \pm 0.11$

Table 22.15: Summary of measurements of the  $D^0 \rightarrow \pi^- e^+ \nu_e$  branching fraction from different experiments; here ‘absolute’ means that the branching fraction is made directly.

Experiment	Number of Events	Normalization Mode	Ratio of branching fraction	$\mathcal{B}(D^0 \rightarrow \pi^- e^+ \nu_e)$ (%)
CLEO [116]	87	$\frac{D^0 \rightarrow \pi^- e^+ \nu_e}{D^0 \rightarrow K^- e^+ \nu_e}$	$0.103 \pm 0.039 \pm 0.013$	$0.37 \pm 0.14 \pm 0.05 \pm 0.02$
E687 [117]	91 ( $e$ and $\mu$ )	$\frac{D^0 \rightarrow \pi^- e^+ \nu_e}{D^0 \rightarrow K^- l^+ \nu_l}$	$0.101 \pm 0.020 \pm 0.003$	$0.36 \pm 0.07 \pm 0.01 \pm 0.02$
MARKIII [114]	7	absolute		$0.39_{-0.11}^{+0.23} \pm 0.04$
BESII [83]	9	absolute		$0.33 \pm 0.13 \pm 0.03$
CLEOc [115]	117	absolute		$0.262 \pm 0.025 \pm 0.008$
PDG average [3]				$0.281 \pm 0.019$

## 2. Event simulation and selection

Monte Carlo  $e^+e^- \rightarrow D\bar{D}$  events are generated at 3.773 GeV, with the  $D$  and  $\bar{D}$  mesons allowed to decay into all possible final states with branching fractions taken from the PDG tables [3]. A total of 4.9 million  $D\bar{D}$  Monte Carlo events are generated, corresponding to an integrated luminosity of about  $800 \text{ pb}^{-1}$ . Events are fully simulated using the GEANT4 package and reconstructed using the *BES-III* software version BOSS 6.0.2.

To select good candidate events, we required at least two charged tracks are well reconstructed in the MDC. All charged tracks are required to satisfy a geometrical requirement  $|\cos\theta| < 0.93$ , where  $\theta$  is the polar angle with respect to the beam axis. Each track must originate from the interaction region, which is defined as  $V_{xy} < 1.0 \text{ cm}$  and  $|V_z| < 5.0 \text{ cm}$ , where  $V_{xy}$  and  $|V_z|$  are the distances of closest approach of the charged track in the  $xy$ -plane and  $z$  direction. Pions and kaons are identified using the  $dE/dx$  and TOF measurements, while neutral kaons are reconstructed through the decay  $K_S^0 \rightarrow \pi^+\pi^-$ . Neutral pions are reconstructed via their  $\pi^0 \rightarrow \gamma\gamma$  decay mode.

Single-tag  $\bar{D}^0$  mesons are reconstructed in four hadronic decay modes:  $K^+\pi^-$ ,  $K^+\pi^-\pi^-\pi^+$ ,  $K^+\pi^-\pi^0$  and  $K^0\pi^+\pi^-$ . The method used is similar to that described in Section 24.1.3.2. Figure 22.12 shows the resulting beam-constrained mass distributions for  $K^n\pi$  ( $n = 1, 2, 3$ ) modes for the single-tag  $\bar{D}^0$  mesons. A maximum likelihood fit to the mass spectrum with a Gaussian function representing the  $\bar{D}^0$  signal and a special background function [83, 84] yields the number of the single-tag  $\bar{D}^0$  mesons found in each mode. Their sum,  $N_{\bar{D}_i^0}$ , is the total number of reconstructed single-tag  $\bar{D}^0$  mesons. In each mass distribution, events within  $\pm 3\sigma_{M_{\bar{D}_i^0}}$  of the fitted  $\bar{D}^0$  mass  $M_{\bar{D}_i^0}$  value are defined as single-tag  $\bar{D}^0$  candidates, where  $\sigma_{M_{\bar{D}_i^0}}$  is the standard deviation of the mass spectrum for the  $i^{\text{th}}$  tag mode. The region outside of  $\pm 4\sigma_{M_{\bar{D}_i^0}}$  window around the fitted  $\bar{D}^0$  mass are used as a  $\bar{D}^0$  sideband sample for estimating the background in the  $\bar{D}^0$  signal region.

Candidate  $D^0 \rightarrow K^-e^+\nu_e$  and  $D^0 \rightarrow \pi^-e^+\nu_e$  decays are selected from the surviving tracks in the system recoiling against the tag  $\bar{D}^0$  mesons. We require that there are only two oppositely charged tracks, one of which is identified as an electron and the other as a kaon or pion. For modes other than  $K^0\pi^+\pi^-$ , the electron's charge is required to be opposite to the charm of the tag  $\bar{D}^0$ . In order to reduce background events from decays such as  $D^0 \rightarrow K^-\pi^0e^+(\mu^+)\nu_{e(\mu)}$  and  $D^0 \rightarrow K^-\pi^+\pi^0$ , we require that there are no extra charged tracks or isolated photons that have not been used in the reconstruction of the tag  $\bar{D}^0$  meson. There are still possible backgrounds for each semileptonic decay due to misidentified pions faking an electron. For example, the decay  $D^0 \rightarrow K^-\pi^+$  may be misidentified as  $D^0 \rightarrow K^-e^+\nu_e$ . These events are suppressed by requiring that the invariant mass of the  $K^-e^+$  combination is less than 1.8 GeV.

In semileptonic decays, there is one undetected massless neutrino. This can be reconstructed using the kinematic quantity

$$U_{\text{miss}} \equiv E_{\text{miss}} - p_{\text{miss}},$$

where  $E_{\text{miss}}$  and  $p_{\text{miss}}$  are the total energy and momentum of all the missing particles. The value of  $U_{\text{miss}}$  should be close to zero for correctly reconstructed signal events. Figure 22.13 shows the  $U_{\text{miss}}$  distribution for tagged  $D^0 \rightarrow K^-e^+\nu_e$  candidates. Figure 22.14 shows the  $U_{\text{miss}}$  distribution for  $D^0 \rightarrow \pi^-e^+\nu_e$  candidates where background from  $K^-$  misidentified

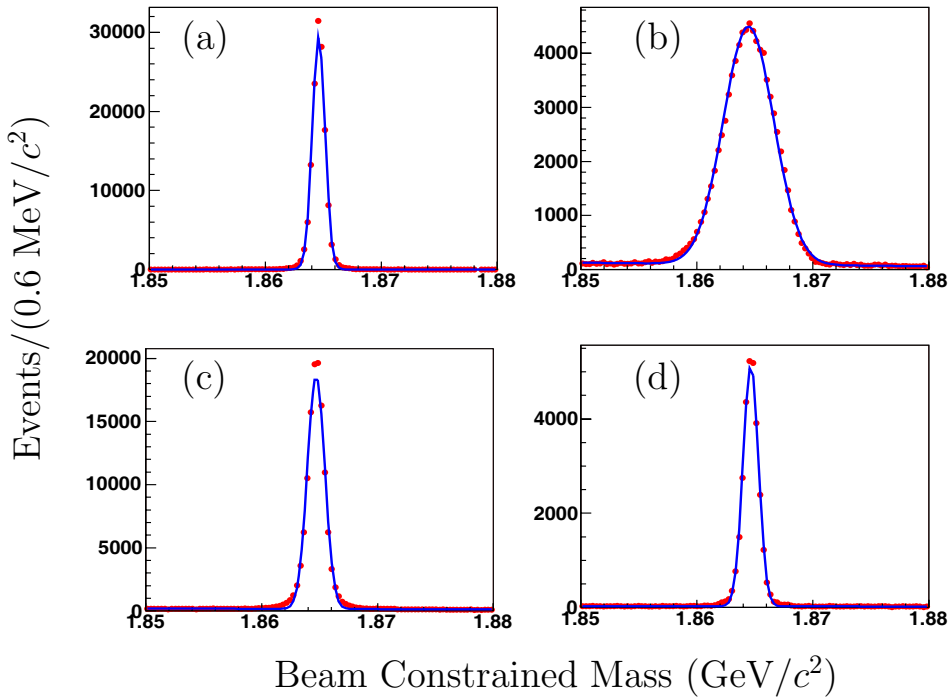


Figure 22.12: The beam constrained masses of the  $Kn\pi$  single-tag  $\bar{D}^0$  decay modes: (a)  $K^+\pi^-$ , (b)  $K^+\pi^-\pi^0$ , (c)  $K^+\pi^-\pi^-\pi^+$  and (d)  $K^0\pi^+\pi^-$ .

as  $\pi^-$  shows up as peak B. The signals around zero are the signals for  $D^0 \rightarrow K^-e^+\nu_e$  and  $D^0 \rightarrow \pi^-e^+\nu_e$ . Fitting each  $U_{miss}$  distribution with a Gaussian signal function and a polynomial background gives  $N_{D^0 \rightarrow K^-e^+\nu_e} = 5528 \pm 75$  and  $N_{D^0 \rightarrow \pi^-e^+\nu_e} = 707 \pm 27$ . There is no peak around zero observed in the  $U_{miss}$  distributions for selected events with tags in the  $\bar{D}^0$  sideband regions.

Monte Carlo studies show that the dominant background for  $D^0 \rightarrow K^-e^+\nu_e$  is from  $D^0 \rightarrow K^-\mu^+\nu_\mu$ , and the main background for  $D^0 \rightarrow \pi^-e^+\nu_e$  is from  $D^0 \rightarrow \pi^-\mu^+\nu_\mu$ ,  $D^0 \rightarrow K^-e^+\nu_e$  and  $D^0 \rightarrow \rho^-e^+\nu_e$  where the  $\mu^+(K^-)$  is misidentified as a  $e^+(\pi^-)$  and the  $\pi^0$  is missed. In addition to the tail of  $D^0 \rightarrow K^-e^+\nu_e$ , events in peak C are mainly from  $D^0 \rightarrow K^*-\pi^+$ ,  $K^{*-} \rightarrow K^-\pi^0$  and  $D^0 \rightarrow K^-\rho^+$ ,  $\rho^+ \rightarrow \pi^+\pi^0$  where the  $K^-\pi^+$  pair is misidentified as a  $\pi^-\pi^+$  pair the  $\pi^0$  is missed.

### 3. Branching fraction determinations

The  $D^0 \rightarrow K^-(\pi^-)e^+\nu_e$  branching fraction is determined from the relation

$$\mathcal{B}(D^0 \rightarrow K^-(\pi^-)e^+\nu_e) = \frac{N_{D^0 \rightarrow K^-(\pi^-)e^+\nu_e}}{N_{\bar{D}^0_{tag}} \times \epsilon_{D^0 \rightarrow K^-(\pi^-)e^+\nu_e}}, \quad (22.2.65)$$

where  $N_{D^0 \rightarrow K^-(\pi^-)e^+\nu_e}$  is the number of signal events,  $N_{\bar{D}^0_{tag}}$  is the total number of the single-tag  $\bar{D}^0$  mesons and  $\epsilon_{D^0 \rightarrow K^-(\pi^-)e^+\nu_e}$  is the MC-determined detection efficiency.

Inserting numbers into Eqn. 22.2.65, we obtain the branching fractions

$$\mathcal{B}(D^0 \rightarrow K^-(\pi^-)e^+\nu_e) = (3.41 \pm 0.05 \pm 0.03)\%,$$

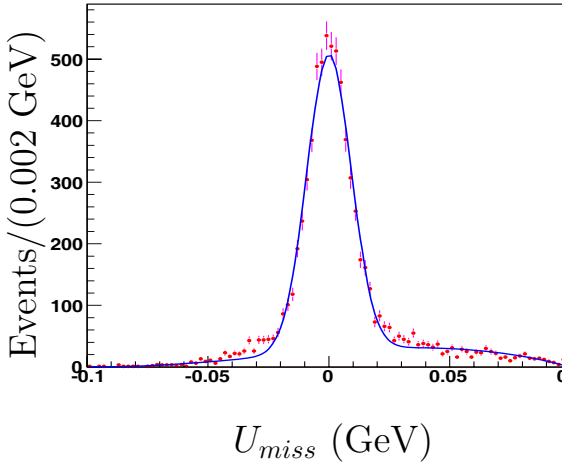


Figure 22.13: The  $U_{miss}$  distribution for  $D^0 \rightarrow K^- e^+ \nu_e$  candidate events.

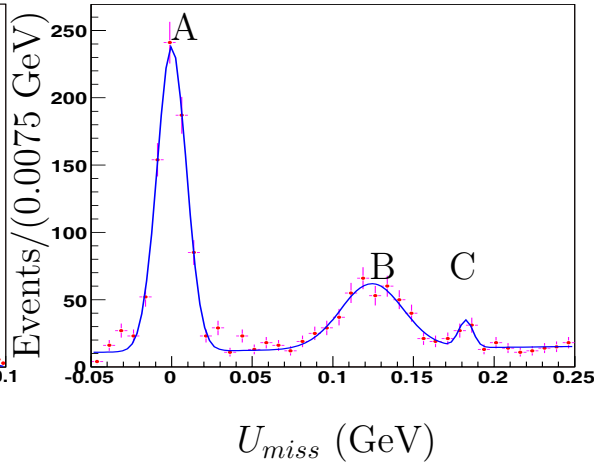


Figure 22.14: The  $U_{miss}$  distribution for  $D^0 \rightarrow \pi^- e^+ \nu_e$  candidate events.

$$\mathcal{B}(D^0 \rightarrow \pi^- e^+ \nu_e) = (0.409 \pm 0.015 \pm 0.04)\%,$$

where the first error is statistical and the second systematic. The systematic errors mainly arise from uncertainties in tracking simulation, particle identification, photon selection, fitting the  $U_{miss}$  distribution and the number of single-tag  $\bar{D}^0$  mesons. The total systematic error expected at *BES-III* is 1.0%.

By extrapolating the simulation results to  $20 \text{ fb}^{-1}$ , the expected statistical errors for *BES-III* measurements of  $\mathcal{B}(D^0 \rightarrow K^- e^+ \nu_e)$  and  $\mathcal{B}(D^0 \rightarrow \pi^- e^+ \nu_e)$  are estimated to be 0.3% and 0.7%, respectively, as shown in Table 22.16.

Table 22.16: Expected statistical errors for  $\mathcal{B}(D^0 \rightarrow K^- e^+ \nu_e)$  and  $\mathcal{B}(D^0 \rightarrow \pi^- e^+ \nu_e)$  at *BES-III*.

$\mathcal{L}$	$4 \text{ fb}^{-1}$	$20 \text{ fb}^{-1}$
$\frac{\Delta \mathcal{B}(D^0 \rightarrow K^- e^+ \nu_e)}{\mathcal{B}(D^0 \rightarrow K^- e^+ \nu_e)} \text{ stat.}$	0.6%	0.3%
$\frac{\Delta \mathcal{B}(D^0 \rightarrow \pi^- e^+ \nu_e)}{\mathcal{B}(D^0 \rightarrow \pi^- e^+ \nu_e)} \text{ stat.}$	1.6%	0.7%

#### 4. Form factors and CKM matrix elements

The semileptonic decay width for  $D^0 \rightarrow K^-(\pi^-)e^+\nu_e$  is related to the form factor  $|f_+^{K(\pi)}(0)|$  and the CKM matrix element  $|V_{cs(d)}|$  via the relations [83, 118, 119]

$$\Gamma(D^0 \rightarrow K^- e^+ \nu_e) = \frac{\mathcal{B}(D^0 \rightarrow K^- e^+ \nu_e)}{\tau_{D^0}} = 1.53 |V_{cs}|^2 |f_+^K(0)|^2 \times 10^{11} \text{ s}^{-1} \quad (22.2.66)$$

$$\Gamma(D^0 \rightarrow \pi^- e^+ \nu_e) = \frac{\mathcal{B}(D^0 \rightarrow \pi^- e^+ \nu_e)}{\tau_{D^0}} = 3.01 |V_{cs}|^2 |f_+^\pi(0)|^2 \times 10^{11} \text{ s}^{-1} \quad (22.2.67)$$

The form factors  $|f_+^K(0)|$  and  $|f_+^\pi(0)|$  can be extracted from the measured branching fractions and the lifetime of the  $D^0$  meson. Inserting the values  $|V_{cs}| = 0.996 \pm 0.013$  and  $|V_{cd}| = 0.224 \pm 0.012$  [3], the lifetime  $\tau_{D^0} = (410.1 \pm 1.5) \times 10^{-15}$ s and the branching fractions into Eqs. 22.2.66 and 22.2.67, the form factors are determined to be

$$|f_+^K(0)| = 0.74 \pm 0.01 \pm 0.01$$

and

$$|f_+^\pi(0)| = 0.81 \pm 0.04 \pm 0.04,$$

where the first error is statistical and the second systematic. In the form factor determination, the systematic error arises mainly from the uncertainties in the measured branching fractions ( $\Delta\mathcal{B}/\mathcal{B}$  is taken to be 1.0%), the lifetime  $\tau_{D^0}$  (0.4%), and the values of the CKM matrix elements  $|V_{cs(d)}|$  (1.3% for  $|V_{cs}|$  and 5.4% for  $|V_{cd}|$ ),

$$\frac{\Delta f_+^{K(\pi)}(0)}{f_+^{K(\pi)}(0)} = \sqrt{\left(\frac{\Delta\mathcal{B}}{2\mathcal{B}}\right)^2 + \left(\frac{\Delta\tau_{D^0}}{2\tau_{D^0}}\right)^2 + \left(\frac{\Delta V_{cs(d)}}{V_{cs(d)}}\right)^2}. \quad (22.2.68)$$

From this, the total systematic errors in the determination of  $f_+^{K(\pi)}(0)$  are estimated to be

$$\frac{\Delta f_+^K(0)}{f_+^K(0)} = 1.4\%,$$

and

$$\frac{\Delta f_+^\pi(0)}{f_+^\pi(0)} = 5.4\%,$$

and are dominated by the uncertainties in  $|V_{cs(d)}|$ , see Table 22.17.

Table 22.17: The errors in the determination of the  $|f_+^{K(\pi)}(0)|$  form factors with a  $20 \text{ fb}^{-1}$   $\psi(3770)$  data at *BES-III*.

	$\frac{\Delta\mathcal{B}}{2\mathcal{B}}$ stat.	$\frac{\Delta\mathcal{B}}{2\mathcal{B}}$ sys.	$\frac{\Delta\tau_{D^0}}{2\tau_{D^0}}$	$ V_{cs(d)} $	Total error
$ f_+^K(0) $	0.15%	0.5%	0.2%	1.3%	1.4%
$ f_+^\pi(0) $	0.35%	0.5%	0.2%	5.4%	5.4%

Using the measured branching fractions for  $D^0 \rightarrow K^- e^+ \nu_e$  and  $D^0 \rightarrow \pi^- e^+ \nu_e$ , and the predicted form factors  $f_+^K(0) = 0.66 \pm 0.04^{+0.01}_{-0.00}$  and  $f_+^\pi(0) = 0.57 \pm 0.06^{+0.01}_{-0.00}$  [120] from lattice QCD, we can extract the CKM matrix elements  $|V_{cs}|$  and  $|V_{cd}|$  from Eqs. 22.2.66 and 22.2.67:

$$|V_{cs}| = 1.12 \pm 0.06 \pm 0.02,$$

$$|V_{cd}| = 0.32 \pm 0.02 \pm 0.01,$$

where the first error is statistical and the second systematic. In the determinations of the CKM elements, the systematic error can be written as

$$\frac{\Delta V_{cs(d)}}{V_{cs(d)}} = \sqrt{\left(\frac{\Delta\mathcal{B}}{2\mathcal{B}}\right)^2 + \left(\frac{\Delta\tau_{D^0}}{2\tau_{D^0}}\right)^2 + \left(\frac{\Delta f_+^{K(\pi)}(0)}{f_+^{K(\pi)}(0)}\right)^2}. \quad (22.2.69)$$

In the next few years, the form factor uncertainties from lattice-QCD are expected to be about 1.5%, in which case the total systematic error in the determination of the CKM matrix element is estimated to be

$$\frac{\Delta V_{cs(d)}}{V_{cs(d)}} = 1.6\%,$$

and dominated by the uncertainty in  $|f_+^{K(\pi)}(0)|$  (see Table 22.18).

Table 22.18: The errors of in the determination of  $|V_{cs(d)}|$  with a  $20 \text{ fb}^{-1}$   $\psi(3770)$  data sample at *BES-III*.

	$\frac{\Delta \mathcal{B}}{2\mathcal{B} \text{ stat.}}$	$\frac{\Delta \mathcal{B}}{2\mathcal{B} \text{ sys.}}$	$\frac{\Delta \tau_{D^0}}{2\tau_{D^0}}$	$ f_+^{K(\pi)}(0) $	Total error
$ V_{cs} $	0.15%	0.5%	0.2%	1.5%	1.6%
$ V_{cd} $	0.35%	0.5%	0.2%	1.5%	1.6%

Combining Eqs. 22.2.66 and 22.2.67, the ratio of the  $D^0 \rightarrow K^- e^+ \nu_e$  and  $D^0 \rightarrow \pi^- e^+ \nu_e$  decay widths is related to the form factor  $|f_+^{K(\pi)}(0)|$  and the CKM matrix element  $|V_{cs(d)}|$  as

$$\frac{\mathcal{B}(D^0 \rightarrow \pi^- e^+ \nu_e)}{\mathcal{B}(D^0 \rightarrow K^- e^+ \nu_e)} = \frac{\Gamma(D^0 \rightarrow \pi^- e^+ \nu_e)}{\Gamma(D^0 \rightarrow K^- e^+ \nu_e)} = 1.967 \times \frac{|f_+^K(0)|^2}{|f_+^\pi(0)|^2} \frac{|V_{cd}|^2}{|V_{cs}|^2}. \quad (22.2.70)$$

Using the measured branching fractions for  $D^0 \rightarrow K^- e^+ \nu_e$  and  $D^0 \rightarrow \pi^- e^+ \nu_e$ , the ratio  $\frac{|f_+^K(0)|^2 |V_{cd}|^2}{|f_+^\pi(0)|^2 |V_{cs}|^2}$  is determined to be  $0.0615 \pm 0.0031 \pm 0.0006$ , where the first error is the statistical error, and the second systematic. In this ratio, some of the systematic uncertainties in the branching fraction measurements, such as the electron tracking simulation, particle identification, photon selection, and the number of the single-tag  $\bar{D}^0$  mesons cancel completely. In addition, the ratio is independent of the lifetime  $\tau_{D^0}$ . The remaining systematic error arises mainly from uncanceled uncertainties in the branching fraction measurements, including the  $K/\pi$  tracking simulation, particle identification, and fitting the  $U_{miss}$  distributions. The statistical error can be neglected in the case of  $20 \text{ fb}^{-1}$   $\psi(3770)$  data sample, while the total systematic error is estimated to be 1%.

If the error on the lattice QCD ratio of the form factors can reach the 1% level, the ratio  $|V_{cd}|/|V_{cs}|$  can be measured with a precision of 1.1% with a  $20 \text{ fb}^{-1}$   $\psi(3770)$  data sample. The  $|V_{cd}|/|V_{cs}|$  ratio measurement will be more precise than the individual  $|V_{cs}|$  and  $|V_{cd}|$  determinations.

### 22.2.3 Inclusive Semileptonic Decays <sup>7</sup>

With a Monte Carlo sample corresponding to an intergrated luminosity of about  $800 \text{ pb}^{-1}$  at  $3.773 \text{ GeV}$ , we developed analysis methods to measure branching fractions for inclusive semileptonic  $D$ -meson decays.

<sup>7</sup>By Hai-Long Ma, Hui-Hui Liu and Gang Rong

## 1. Overview of studies of inclusive semileptonic $D$ decays

The branching fractions for inclusive  $D$  semileptonic decays have been measured by many experiments [121, 122, 123, 124, 125, 126, 127]. The measured results for  $D^0 \rightarrow X e^+ \nu_e$ ,  $D^0 \rightarrow X \mu^+ \nu_\mu$  and  $D^+ \rightarrow X e^+ \nu_e$  are summarized in Tables 22.19, 22.21 and 22.20, respectively, along with the numbers of signal events associated with each entry.

The relative errors are 4.1% for  $D^0 \rightarrow X e^+ \nu_e$ , 12.3% for  $D^0 \rightarrow X \mu^+ \nu_\mu$ , and 11.0% for  $D^+ \rightarrow X e^+ \nu_e$ . Recently, the CLEO Collaboration reported a precision measurement of  $\mathcal{B}(D \rightarrow X e^+ \nu_e)$  [126]. However, there have only been a few  $\mathcal{B}(D \rightarrow X \mu^+ \nu_\mu)$  measurements reported during the thirty years that have passed since the discovery of the  $D$  mesons. Because of advantages provided by the unique capabilities of the *BES-III*  $\mu$  detection system, significant improvements of the  $\mathcal{B}(D \rightarrow X \mu^+ \nu_\mu)$  measurement can be expected.

Table 22.19: Summary of measurements of the branching fractions for  $D^0 \rightarrow X e^+ \nu_e$  from different experiments; here the superscript  <sup>$N$</sup>  indicates measurements that are not used in the PDG average.

Experiments	Number of Events	Comment	$\mathcal{B}(D^0 \rightarrow X e^+ \nu_e)$ (%)
ARGUS [121]	1670	$e^+ e^- \sim 10$ GeV	$6.9 \pm 0.3 \pm 0.5$
CLEOII [122]	4609	$e^+ e^- \sim \Upsilon(4S)$	$6.64 \pm 0.18 \pm 0.29$
MARKIII [123]	137	$e^+ e^- 3.77$ GeV	$7.5 \pm 1.1 \pm 0.4$
HYBR <sup><math>N</math></sup> [124]		$\pi p, pp$ 360, 400 GeV	$15 \pm 5$
MARKII <sup><math>N</math></sup> [125]	12	$e^+ e^- 3.771$ GeV	$5.5 \pm 3.7$
CLEOc <sup><math>N</math></sup> [126]	2246	$e^+ e^- 3.773$ GeV	$6.46 \pm 0.17 \pm 0.13$
PDG average [3]			$6.87 \pm 0.28$

Table 22.20: Summary of measurements of the branching fraction for  $D^+ \rightarrow X e^+ \nu_e$  from different experiments; here  <sup>$N$</sup>  indicates that the measurement is not used in the PDG average.

Experiments	Number of Events	Comment	$\mathcal{B}(D^+ \rightarrow X e^+ \nu_e)$ (%)
HYBR [124]		$\pi p, pp$ 360, 400 GeV	$20^{+9}_{-7}$
MARKIII [123]	158	$e^+ e^- 3.77$ GeV	$17.0 \pm 1.9 \pm 0.7$
MARKII [125]	23	$e^+ e^- 3.771$ GeV	$16.8 \pm 6.4$
DELCO <sup><math>N</math></sup> [127]		$e^+ e^- 3.77$ GeV	$22.0^{+4.4}_{-2.2}$
CLEOc <sup><math>N</math></sup> [126]	8798	$e^+ e^- 3.773$ GeV	$16.13 \pm 0.20 \pm 0.33$
PDG average [3]			$17.2 \pm 1.9$

Table 22.21: Summary of measurements of the branching fraction for  $D^0 \rightarrow X\mu^+\nu_\mu$  from different experiments.

Experiments	Number of Events	Comment	$\mathcal{B}(D^0 \rightarrow X\mu^+\nu_\mu)$ (%)
ARGUS [121]	310	$e^+e^- \sim 10 \text{ GeV}$	$6.0 \pm 0.9 \pm 1.2$
PDG average [3]			$6.5 \pm 0.8$

## 2. Analysis method for inclusive semileptonic $D$ decays

For  $D^0 \rightarrow Xe^+\nu_e$ , only three hadronic decays  $\bar{D}^0 \rightarrow K^+\pi^-$ ,  $\bar{D}^0 \rightarrow K^+\pi^-\pi^0$  and  $\bar{D}^0 \rightarrow K^+\pi^-\pi^-\pi^+$  are used to reconstruct single-tag  $\bar{D}^0$  mesons, since the mode  $\bar{D}^0 \rightarrow K^0\pi^+\pi^-$  does not determine the charm of the  $D^0$  meson. For  $D^+ \rightarrow Xe^+\nu_e$ , only the hadronic decay  $D^- \rightarrow K^+\pi^-\pi^-$  is used to reconstruct single-tag  $D^-$  mesons, since this mode has a large branching fraction and low background.

The resulting beam-constrained mass distributions for the  $Kn\pi$  ( $n = 1, 2, 3$ ) single-tag  $\bar{D}$  modes are shown in Fig. 22.15. A maximum likelihood fit to the mass spectrum with a Gaussian function representing the  $\bar{D}$  signal and a special background function [83, 84] yields the number of single-tag  $\bar{D}$  mesons for each mode.

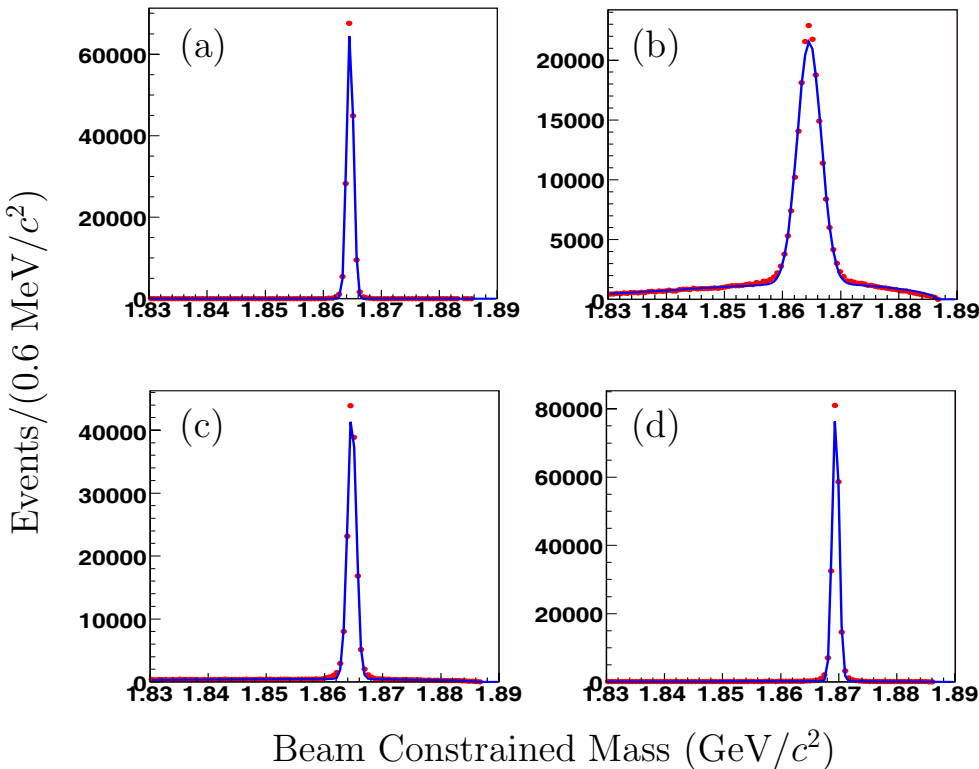


Figure 22.15: The beam constrained mass distributions for the  $Kn\pi$  single-tag  $\bar{D}$  modes: (a)  $\bar{D}^0 \rightarrow K^+\pi^-$ , (b)  $\bar{D}^0 \rightarrow K^+\pi^-\pi^0$ , (c)  $\bar{D}^0 \rightarrow K^+\pi^-\pi^-\pi^+$  and (d)  $D^- \rightarrow K^+\pi^-\pi^-$ .

In the system recoiling against the single-tag  $\bar{D}$  mesons, electrons, kaons and pions are selected from the surviving tracks. Electrons, kaons and pions are classified into right-sign and wrong-sign samples according to their charge-correlation relative to the flavor tag. Since the wrong-sign electrons are all from the background, they can be used to estimate the background level. The wrong-sign unfolded yield of electrons accounts for the the charge-symmetric background, which is mostly produced by  $\pi^0 \rightarrow \gamma e^+ e^-$  decays and  $\gamma$  conversions.

Figures 22.16(a) to (d') show the fitted beam constrained mass distributions for the  $Kn\pi$  single-tag combinations for events with one right-sign ((a)-(d)) or wrong-sign ((a')-(d')) electron observed in the system recoiling against the tag  $\bar{D}$  mesons. Because the detection efficiency for a particle and the probability of misidentifying a particle depends on momentum, we divide the momentum into  $n$  bins. The yield  $N_e^{\text{obs},i}$  of electrons in the  $i^{\text{th}}$  momentum bin is obtained by fitting to the corresponding mass spectrum. Similar analyses give the yields  $N_K^{\text{obs},i}$  and  $N_\pi^{\text{obs},i}$  of kaons and pions in each momentum range.

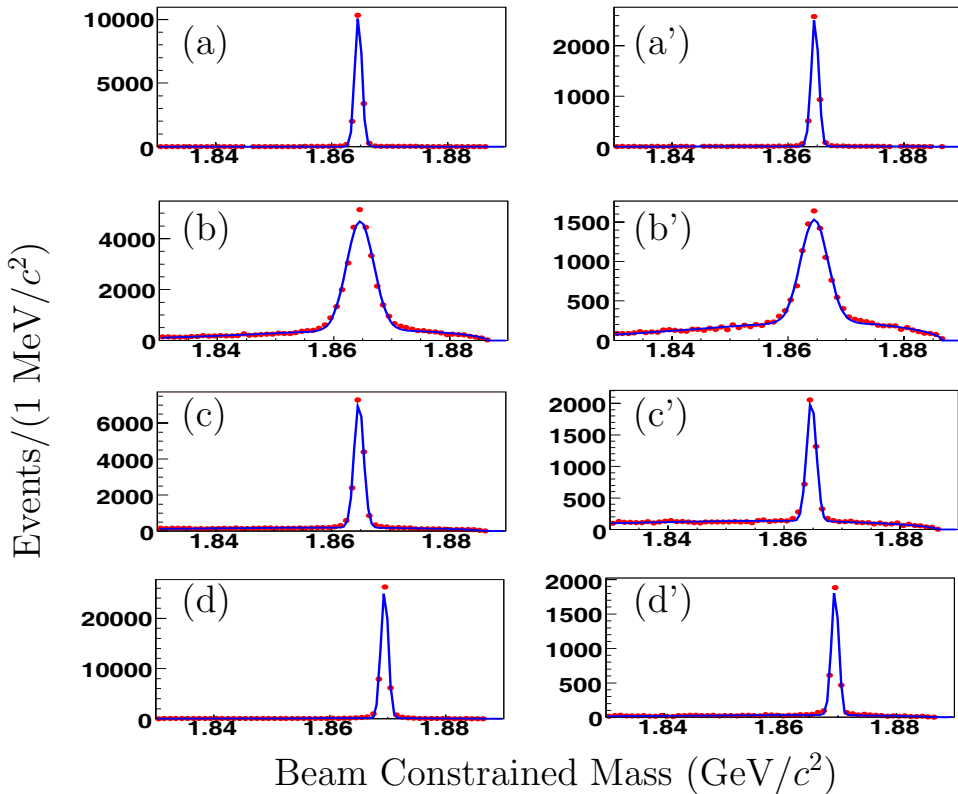


Figure 22.16: The fitted beam constrained mass distributions for  $Kn\pi$  tag  $D$  mesons with one electron observed in the recoil system: (a), (a')  $\bar{D}^0 \rightarrow K^+ \pi^-$ ; (b), (b')  $\bar{D}^0 \rightarrow K^+ \pi^- \pi^0$ ; (c), (c')  $\bar{D}^0 \rightarrow K^+ \pi^- \pi^- \pi^+$  and (d), (d')  $D^- \rightarrow K^+ \pi^- \pi^-$ ; here (a), (b), (c) and (d) are the right-sign events, while (a'), (b'), (c') and (d') are the wrong-sign events.

In the  $i^{\text{th}}$  momentum bin, the true number of electrons with the right-sign and wrong-

sign samples are obtained through an unfolding procedure, using the matrix:

$$\begin{pmatrix} N_e^{\text{obs},i} \\ N_K^{\text{obs},i} \\ N_\pi^{\text{obs},i} \end{pmatrix} = \begin{pmatrix} \epsilon_e^i & f_{\pi \rightarrow e}^i & f_{K \rightarrow e}^i \\ f_{e \rightarrow K}^i & \epsilon_K^i & f_{\pi \rightarrow K}^i \\ f_{e \rightarrow \pi}^i & f_{K \rightarrow \pi}^i & \epsilon_\pi^i \end{pmatrix} \begin{pmatrix} N_e^{\text{real},i} \\ N_K^{\text{real},i} \\ N_\pi^{\text{real},i} \end{pmatrix},$$

where  $N_e^{\text{obs},i}$ ,  $N_K^{\text{obs},i}$ ,  $N_\pi^{\text{obs},i}$  represent the numbers of the electrons, kaons and pions observed in the system recoiling against the tag  $\bar{D}$  meson;  $N_e^{\text{real},i}$ ,  $N_K^{\text{real},i}$ ,  $N_\pi^{\text{real},i}$  denote their corresponding true numbers; the efficiencies  $\epsilon_e^i$ ,  $\epsilon_K^i$ ,  $\epsilon_\pi^i$  account for the losses due to track finding, track selection criteria, and particle identification; the off-diagonal element  $f_{a \rightarrow b}^i$  is the probability of misidentifying particle type  $a$  as  $b$ . In analyses of real data, an electron sample selected from the radiative Bhabha scattering events, and kaon and pion samples selected from  $J/\psi \rightarrow \phi K^+ K^-$  and  $J/\psi \rightarrow \omega \pi^+ \pi^-$  events can be used to measure  $f_{a \rightarrow b}^i$ . In the simulation analysis, the efficiencies and the misidentification probabilities determined by Monte Carlo simulation for each kind of track is used. A detailed analysis of these particle samples give  $\epsilon_e^i$ ,  $\epsilon_K^i$ ,  $\epsilon_\pi^i$  and  $f_{a \rightarrow b}^i$  for each momentum bin.

Subtracting the number  $N_e^{\text{real},i}(R)$  of right-sign electrons by the number  $N_e^{\text{real},i}(W)$  of wrong-sign electrons, we obtain the net number of electrons in  $i^{\text{th}}$  momentum range,

$$N_e^{\text{real},i}(\text{net}) = N_e^{\text{real},i}(R) - N_e^{\text{real},i}(W).$$

Adding the net number of electrons in each momentum range yields the total net number  $N_{D \rightarrow X \ell^+ \nu_\ell}^{\text{net}}$  of electrons,

$$N_{D \rightarrow X \ell^+ \nu_\ell}^{\text{net}} = \sum_i^n N_e^{\text{real},i}(\text{net}).$$

### 3. Branching fractions

The branching fraction for  $D \rightarrow X \ell^+ \nu_\ell$  is determined from the relation

$$\mathcal{B}(D \rightarrow X \ell^+ \nu_\ell) = \frac{N_{D \rightarrow X \ell^+ \nu_\ell}^{\text{net}}}{N_{\bar{D}_{\text{tag}}} \times \epsilon_{D \rightarrow X \ell^+ \nu_\ell}}, \quad (22.2.71)$$

where  $N_{D \rightarrow X \ell^+ \nu_\ell}^{\text{net}}$  is the net number of  $D \rightarrow X \ell^+ \nu_\ell$  events,  $N_{\bar{D}_{\text{tag}}}$  is the total number of the single-tag  $D^-$  or  $\bar{D}^0$  mesons, and  $\epsilon_{D \rightarrow X \ell^+ \nu_\ell}$  is the detection efficiency. The detection efficiency is determined by Monte Carlo simulations for each single-tag  $\bar{D}$  mode, where the recoil  $D \rightarrow X \ell^+ \nu_\ell$  includes all exclusive semileptonic channels. A MC analysis procedure similar to that described above gives the detection efficiency. Inserting these numbers into Eqn. 22.2.71, we can obtain the branching fraction for the inclusive semileptonic decay.

In the  $D \rightarrow X \ell^+ \nu_\ell$  branching fraction measurement, the dominant systematic errors are due to uncertainties in the electron tracking simulation and particle identification, the efficiencies and misidentification probabilities, and the number of the single-tag  $\bar{D}$  mesons. As previously discussed, in the case of a  $20 \text{ fb}^{-1} \psi(3770)$  data sample, the statistical error can be neglected relative to the systematic error, which is expected to be at the 1.0% level.

#### 4. Determination of the ratio $\frac{\Gamma_{D^+}^{\text{SL}}}{\Gamma_{D^0}^{\text{SL}}}$

Using the measured branching fractions for the inclusive  $D$  semileptonic decays  $\mathcal{B}(D^+ \rightarrow X\ell^+\nu_\ell)$  and  $\mathcal{B}(D^0 \rightarrow X\ell^+\nu_\ell)$  in conjunction with the well measured lifetimes of the  $D^+$  and  $D^0$  mesons,  $\tau_{D^+} = (1040 \pm 7) \times 10^{-15}$  s and  $\tau_{D^0} = (410.1 \pm 1.5) \times 10^{-15}$  s, the ratio of the partial widths for the two inclusive semileptonic decays can be determined:

$$R = \frac{\Gamma_{D^+}^{\text{SL}}}{\Gamma_{D^0}^{\text{SL}}} = \frac{\mathcal{B}(D^+ \rightarrow X\ell^+\nu_\ell)/\tau_{D^+}}{\mathcal{B}(D^0 \rightarrow X\ell^+\nu_\ell)/\tau_{D^0}}. \quad (22.2.72)$$

In the determination of this ratio with a  $20 \text{ fb}^{-1}$   $\psi(3770)$  data sample, the statistical errors on  $\mathcal{B}(D \rightarrow X\ell^+\nu_\ell)$  can be neglected. The systematic error can be written as

$$\frac{\Delta R}{R} = \sqrt{\left(\frac{\Delta\tau_{D^+}}{\tau_{D^+}}\right)^2 + \left(\frac{\Delta\tau_{D^0}}{\tau_{D^0}}\right)^2 + \left(\frac{\Delta\mathcal{B}(D^+ \rightarrow X\ell^+\nu_\ell)}{\mathcal{B}(D^+ \rightarrow X\ell^+\nu_\ell)}\right)^2 + \left(\frac{\Delta\mathcal{B}(D^0 \rightarrow X\ell^+\nu_\ell)}{\mathcal{B}(D^0 \rightarrow X\ell^+\nu_\ell)}\right)^2}, \quad (22.2.73)$$

where the uncertainties in the lifetimes of  $D$  mesons are  $\Delta\tau_{D^+}/\tau_{D^+} = 0.7\%$  and  $\Delta\tau_{D^0}/\tau_{D^0} = 0.3\%$ , the uncanceled uncertainty in each measured branching fraction is conservatively taken to be  $\Delta\mathcal{B}(D \rightarrow X\ell^+\nu_\ell)/\mathcal{B}(D \rightarrow X\ell^+\nu_\ell) = 1.0\%$ . The resulting estimate of the total systematic error is about 1.6%.

## 22.3 Impact on CKM Measurements<sup>8</sup>

### 22.3.1 The Role of Charm in Precision CKM Physics

In the Standard Model (SM), quark-flavor mixing is described by the  $3 \times 3$  Cabibbo-Kobayashi-Maskawa (CKM) matrix  $V$  [128],

$$V = \begin{pmatrix} V_{ud} & V_{us} & V_{ub} \\ V_{cd} & V_{cs} & V_{cb} \\ V_{td} & V_{ts} & V_{tb} \end{pmatrix}. \quad (22.3.74)$$

Unitarity is the only, albeit powerful, constraint on  $V$ . Without loss of generality,  $V$  can be parameterized in terms of three mixing angles and one phase [3]:

$$V = \begin{pmatrix} c_{12}c_{13} & s_{12}c_{13} & s_{13}e^{-i\delta} \\ -s_{12}c_{23} - c_{12}s_{23}s_{13}e^{i\delta} & c_{12}c_{23} - s_{12}s_{23}s_{13}e^{i\delta} & s_{23}c_{13} \\ s_{12}s_{23} - c_{12}c_{23}s_{13}e^{i\delta} & -c_{12}s_{23} - s_{12}c_{23}s_{13}e^{i\delta} & c_{23}c_{13} \end{pmatrix}, \quad (22.3.75)$$

where  $c_{ij} \equiv \cos \theta_{ij}$  and  $s_{ij} \equiv \sin \theta_{ij}$  (for  $ij = 12, 23$  and  $13$ ). The irremovable phase  $\delta$  is the unique source of CP violation in quark flavor-changing processes within the SM.

The goal of precision CKM physics is threefold: (a) to measure the mixing and CP-violating parameters of  $V$  as accurately as possible; (b) to test the self-consistency of the CKM picture for quark mixing and CP violation; (c) to search for possible new physics beyond the CKM mechanism. It is, therefore, important to measure very precisely the

<sup>8</sup>J. Charles, S. Descotes-Genon, H. Lacker, H. B. Li, L. Roos, S. T'Jampens, Z. Z. Xing

various entries of the CKM matrix. A test of the self-consistency of the CKM picture is provided by unitarity conditions.

Charm physics may impact the study of the CKM matrix in various ways:

1. The current status of the first row (from direct measurements only) is:  $|V_{ud}|^2 + |V_{us}|^2 + |V_{ub}|^2 = 0.9992 \pm 0.0011$  [3]; *i.e.*, unitarity holds at the  $10^{-3}$  level. As for the second row, we have (from direct measurements only):  $|V_{cd}|^2 + |V_{cs}|^2 + |V_{cb}|^2 = 0.968 \pm 0.181$  [3], where the error is dominated by the theoretical uncertainty in  $|V_{cs}|$ .
2. The unitarity of  $V$  implies that  $|V_{us}| - |V_{cd}| = O(\lambda^5)$  [129], where  $\lambda \equiv \sin \theta_{12} \approx 0.22$  is the well-known Wolfenstein parameter [130]. At present, the best direct determination of  $|V_{cd}|$  is based on deep inelastic scattering of neutrinos and antineutrinos [3]:  $|V_{cd}| = 0.230 \pm 0.011$ , which has an error that is larger than that for  $|V_{us}|$  extracted from kaon semileptonic decays ( $|V_{us}| = 0.2257 \pm 0.0021$  [3]). Recent results on semileptonic  $K_{\ell 3}$  decays from NA38 are likely to change the value of  $|V_{us}|$  [131, 132], which will make more accurate determinations of  $|V_{cd}|$  and  $|V_{cs}|$  all the more interesting. Inconsistencies in the upper-left square of the CKM matrix would imply the existence of new physics.
3. If the elements in the first and second rows of  $V$  are all determined to a sufficiently high degree of precision, it is then possible to establish a “charming” unitarity triangle based on the orthogonality condition  $V_{ud}V_{cd}^* + V_{us}V_{cs}^* + V_{ub}V_{cb}^* = 0$ . That will be another (CP-conserving) way to cross-check the CKM mechanism for quark flavor mixing.
4. Reliable information on hadronic  $D$  and  $D_s$  decays (such as  $D^0 \rightarrow K\pi$  and  $D_s \rightarrow \phi\pi$ ) can be used to normalize results in  $B$  physics. It can also improve the understanding of  $B$ -decays into final states containing a charmed meson. For instance, comparing  $B^- \rightarrow D^0 K^-$  and  $B^- \rightarrow \bar{D}^0 K^-$  where  $D^0$  and  $\bar{D}^0$  both decay into  $K_s \pi^+ \pi^-$  provides a determination of  $\gamma$  that relies on models for the  $D$  decay [133]. The uncertainty on  $\gamma$  could be reduced to  $3^\circ$  with *BES-III* measurements of the relevant Dalitz plots in conjunction with measurements at  $B$ -machines.
5. Ratios of quantities related to charm and beauty mesons can be determined with a fairly good accuracy, in particular through lattice simulations. This allows for an interplay of charm and bottom physics in the era of high-precision heavy flavor physics, as exemplified in the next section.

### 22.3.2 Impact of BESIII measurements

#### The CKMfitter package

The CKMfitter package is a comprehensive tool for CKM matrix analysis. It allows the user to:

- quantify the agreement between theory (Standard Model or beyond) and experimental measurements;

- obtain the best estimate of a given set of theoretical parameters within a given theory (e.g., CKM parameters in the Standard Model).

In either case, a major issue for the fit of the CKM matrix is how to deal with the theoretical uncertainties. For most of the measured observables that enter into the fit, these uncertainties are non-negligible, or even dominate over the experimental ones. While experimental uncertainties can usually be considered as Gaussian, the meaning of the theoretical uncertainties is often not well defined (an exception consists in unquenched lattice QCD predictions). In the CKMfitter package, this issue is addressed by allowing theoretical parameters to vary only within the range defined by their uncertainties.

### The statistical approach

The CKMfitter package is based on the frequentist approach  $R$ fit, described in [134] and [135] and recalled here. The likelihood function  $\mathcal{L}$  is defined as the product of two components  $\mathcal{L}_{\text{exp}}$  and  $\mathcal{L}_{\text{theo}}$ :

$$\mathcal{L}(y_{\text{mod}}) = \mathcal{L}_{\text{exp}}(x_{\text{exp}} - x_{\text{theo}}(y_{\text{mod}})) \cdot \mathcal{L}_{\text{theo}}(y_{\text{QCD}}) .$$

where  $x_{\text{exp}}$  is a set of  $N_{\text{exp}}$  experimental measurements, and  $x_{\text{theo}}$  the  $N_{\text{exp}}$  corresponding theoretical predictions.  $x_{\text{theo}}$  depends on  $N_{\text{mod}}$  parameters  $y_{\text{mod}}$ , which are either free parameters of the theory (e.g., the CKM Matrix parameters) or, approximately known QCD related quantities (denoted  $y_{\text{QCD}}$ ). Each individual measurement entering into the  $\mathcal{L}_{\text{exp}}$  component is, in general, considered as Gaussian,<sup>9</sup> and correlations between variables, if known, are taken into account. The experimental systematics are added in quadrature to the statistical errors, whereas the theoretical systematics are dealt with through the theoretical component  $\mathcal{L}_{\text{theo}}$ . The uncertainties on the theoretical parameters  $y_{\text{QCD}}$  define the allowed range of values for each parameter. In other words, each individual likelihood component  $\mathcal{L}_{\text{theo}}(y_{\text{QCD}}(i))$  is one within the allowed range and zero outside. The fit is performed on all the parameters  $y_{\text{mod}}$  by minimizing  $\chi^2(y_{\text{mod}}) \equiv -2 \ln(\mathcal{L}(y_{\text{mod}}))$ . The minimum value is denoted  $\chi^2_{\text{min};y_{\text{mod}}}$ . One quantifies the agreement between theory and data by the probability to observe  $\chi^2$  values greater or equal to  $\chi^2_{\text{min};y_{\text{mod}}}$ . In the present study, we focus on a subset of the  $y_{\text{mod}}$  parameters, namely  $(\bar{\rho}, \bar{\eta})$ , defined as:

$$\bar{\rho} + i\bar{\eta} \equiv -\frac{V_{ud}V_{ub}^*}{V_{cd}V_{cb}^*}.$$

Let us denote  $a = (\bar{\rho}, \bar{\eta})$  and  $\mu$  the remaining parameters, such that  $y_{\text{mod}} = (a, \mu)$ . The minimum value  $\chi^2_{\text{min};\mu}(a)$  is computed for a set of fixed value  $a$ , while varying  $\mu$ . In the following graphics, we represent the Confidence Level obtained from  $\chi^2$  difference  $\Delta\chi^2(a) = \chi^2_{\text{min};\mu}(a) - \chi^2_{\text{min};y_{\text{mod}}}$ .

### The Global CKM Fit

---

<sup>9</sup>In the case of a non-Gaussian experimental errors, the exact description of the associated likelihood is directly used in the fit.

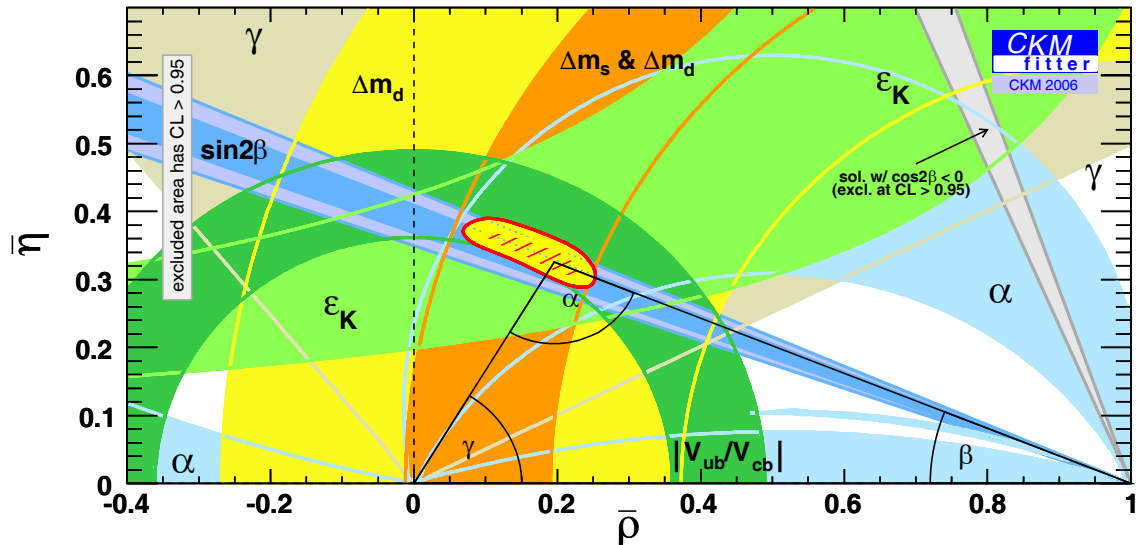


Figure 22.17: Individual constraints and the global CKM fit on the  $(\bar{\rho}, \bar{\eta})$  plane (as of Winter 2007). The shaded areas have 95% CL.

The inputs to the global fit are observables where the theoretical uncertainties are quantitatively under control in order to test the Standard Model:  $|V_{ud}|$ ,  $|V_{us}|$ ,  $|V_{cb}|$  (to fix the length scale of the UT and the constraints on  $A$  and  $\lambda$ ), and the following quantities that are particularly sensitive to  $(\bar{\rho}, \bar{\eta})$ , *i.e.*,  $|V_{ub}|$ ,  $\mathcal{B}(B \rightarrow \tau\nu)$ ,  $\varepsilon_K$ ,  $\Delta m_d$ ,  $\Delta m_d$  &  $\Delta m_s$ ,  $\sin 2\beta$ ,  $\cos 2\beta$ ,  $\alpha$  and  $\gamma$ .  $\lambda$  is determined from  $|V_{ud}|$  (superallowed nuclear transitions) and  $|V_{us}|$  (semileptonic kaon decays) to a combined precision of 0.5%.  $A$  is determined from  $|V_{cb}|$  (inclusive and exclusive semileptonic  $B$  decays) to a combined precision of about 1.7%. While  $\lambda$  and  $A$  are well-known, the parameters  $\bar{\rho}$  and  $\bar{\eta}$  are much more uncertain (about 20% for  $\bar{\rho}$  and 7% for  $\bar{\eta}$ ).

The main goal of CP-violation experiments is to over-constrain these parameters by measuring both the three angles and the sides of the  $B_d$  unitarity triangle and, possibly, to find inconsistencies suggesting the existence of physics beyond the SM. What is important is, thus, the capability of the CKM mechanism to describe flavor dynamics of many constraints from vastly different scales and not the measurement of the CKM phase's value *per se*. The unitarity triangle checks for the consistency of the information obtained from mixing with the information obtained from decay. This is only one of many tests of the CKM matrix. The strategy of placing all CKM constraints on the  $(\bar{\rho}, \bar{\eta})$  plane is a convenient way to compare the overconstraining measurements and a way to search for New Physics by looking for inconsistencies. The 95% CL of the individual constraints and the result of the global fit are displayed in Fig. 22.17. For the detailed inputs, see Ref. [135].

The  $\gamma$  and  $\alpha$  measurements together with  $|V_{ub}/V_{cb}|$  determine  $\bar{\rho}$  and  $\bar{\eta}$  from (effectively) tree-level processes, independently of mixing, and agree with the other loop-induced constraints. Present CKM fits provide a consistency check of the Standard Model hypothesis. The rather large allowed regions provided by each constraint individually (other than the angles) are mainly due to theoretical uncertainties from lattice QCD.

## The 2012 Prospective scenario

After the many measurements done by the  $B$ -factory and Tevatron experiments, the near future will be devoted to precision flavor physics in order to uncover physics beyond the Standard Model and to probe the flavour structure of new physics that may be discovered elsewhere. A crucial ingredient for precision measurements is to enhance or validate the theoretical control over QCD to reach the per cent level accuracy. The most promising tool is the simulation of QCD on the lattice, which needs to be confronted to precision measurements. The charm sector offers the possibility to validate forthcoming lattice QCD calculations at the few percent level. These can then be used to make precise measurements of CKM elements,  $|V_{cd}|$ ,  $|V_{cs}|$ ,  $|V_{ub}|$ ,  $|V_{cb}|$  and  $|V_{ts}|$ .

Charm physics opens an interesting window on the strong and weak sectors of the Standard Model. At the theoretical level, lattice simulations of QCD are a particularly relevant (and almost unique) tool to tackle charm dynamics, since the natural scales of these simulations lie between the strange and the charm quark masses. Therefore, lattice simulations can simulate almost directly charm dynamics, whereas they have to rely on extrapolations in the case of  $b$ -physics. In addition, they can help to reduce uncertainties in the computation of  $b$ -physics quantities [136], since many long-distance effects are similar in  $B$ - and  $D$ -observables, as can be checked explicitly using effective field theories (*e.g.*, Heavy Meson Chiral Perturbation Theory). In particular, there are ratios of quantities that are useful for precision physics in the charm and beauty sectors: these ratios are experimentally more accurately determined than absolute values, their estimate on the lattice does not suffer from large uncertainties related to the determination of an absolute scale, and they are less affected by the systematics from the extrapolation in quark masses. We, however, stress that the study of charm physics does not alleviate all of the difficulties encountered in lattice simulations (*e.g.*, finite volume effects, renormalisation issues).

For the prospective part, it is difficult to anticipate the progress in lattice simulations over the next five years [137]. For the present exercise, we take very rough estimates for theory uncertainties in 2012, and assume that the following accuracy can be obtained from  $B$ -machines (super- $B$  factories and LHCb)

$$\sin(2\beta) \rightarrow 0.011 \quad \alpha \rightarrow 5^\circ \quad \gamma \rightarrow 3^\circ \quad |V_{ub}| \rightarrow 4\% \quad |V_{cb}| \rightarrow 1.5\%. \quad (22.3.76)$$

$|V_{ub}|$  can be determined through either inclusive or exclusive processes. For the exclusive determination from  $Br(B \rightarrow \pi \ell \nu)$ , we take an uncertainty of 4% on the experimentally measured branching ratio and 4% for the lattice determination of  $F_{B \rightarrow \pi}$ . We assume that the inclusive extraction from  $Br(B \rightarrow X_u \ell \nu)$ , will provide a second determination of  $|V_{ub}|$  at 5%. The error on  $|V_{ub}|$  in Eq. (22.3.76) corresponds to an average of the two determinations (inclusive and exclusive). For the other relevant observables, the projected situation in 2012 for lattice and experiment is summarised in Table 22.22.

For the problem at hand, we propose to represent the combination of the CKM constraints in the plane that is relevant to the  $D$  meson Unitarity Triangle (DUT). In analogy with the exact and rephasing-invariant expression of  $(\bar{\rho}, \bar{\eta})$  [135] we define the coordinates of the apex of the DUT

$$\bar{\rho}_D + i \bar{\eta}_D \equiv -\frac{V_{ud} V_{cd}^*}{V_{us} V_{cs}^*} \quad (22.3.77)$$

where  $\bar{\rho}_D = 1 + \mathcal{O}(\lambda^4)$  and  $\bar{\eta}_D = \mathcal{O}(\lambda^4)$ . One can see that this triangle has two sides

Table 22.22: The projected precision for Lattice and experiments in 2012.

Observable	CKM	Had. param	Lattice error	Exp. error
$Br(B \rightarrow \tau\nu)$	$ V_{ub} $	$f_B$	4%	10%
$\Delta m_s$	$ V_{ts}V_{tb} $	$f_{Bs}\sqrt{B_{Bs}}$	3%	0.7%
$\frac{\Delta m_s}{\Delta m_d}$	$\left  \frac{V_{ts}}{V_{td}} \right $	$\xi$	1.5%	For $\Delta m_d$ : 0.8%
$\varepsilon_K$	$V_{qs}V_{qd}^*$	$B_K$	2%	0.4%

with length very close to 1 and a small side of order  $O(\lambda^4)$ , with angles  $\alpha_D = -\gamma$ ,  $\beta_D = \gamma + \pi + O(\lambda^4)$  and  $\gamma_D = O(\lambda^4)$ . The individual constraints as well as the combination from the usual observables are shown for 2012 in the  $(\bar{\rho}_D, \bar{\eta}_D)$  plane in Fig. 22.18.

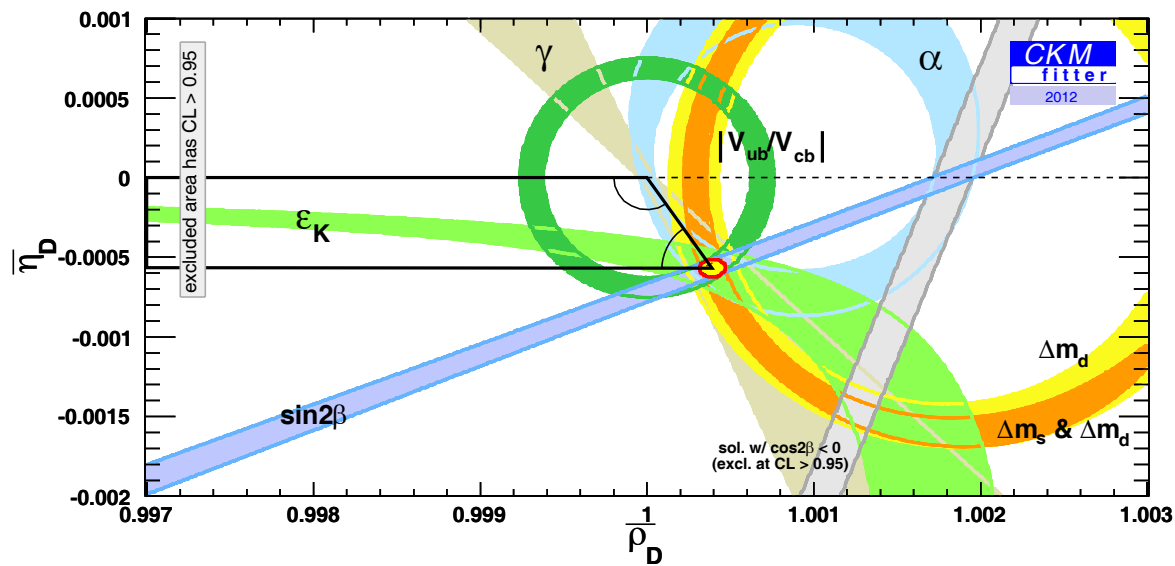


Figure 22.18: Individual constraints and the global CKM fit on the  $(\bar{\rho}_D, \bar{\eta}_D)$  plane (as of our prospective in 2012). The shaded areas have 95% CL. Only a part of the  $D$  Unitarity Triangle is visible (in black solid lines) : the two apices associated with large angles are shown, whereas the missing apex is situated at the origin, far away on the left.

For this prospective exercise, we only consider the impact of *BES-III* measurements for charm-related CKM matrix elements, which is less difficult to quantify than the more indirect one for  $B$ -physics quantities. For the charm-related CKM matrix elements, several observables can be of interest to determine  $|V_{cd}|$  and  $|V_{cs}|$  :

- Precision measurements of leptonic  $D$  and  $D_s$  decays can help determine the CKM matrix elements  $|V_{cd}|$  and  $|V_{cs}|$  provided that  $f_D$  and  $f_{D_s}$  are theoretically known to a good degree of accuracy.
- Precision measurements of semileptonic  $D$  and  $D_s$  decays can help determine the CKM matrix elements  $|V_{cd}|$  and  $|V_{cs}|$  to a good degree of accuracy, provided the relevant form factors are well predicted from lattice QCD and other theoretical models.

Assuming a  $20 \text{ fb}^{-1}$  data sample at the  $\psi(3770)$ , the uncertainties for *BES-III* experimental measurements can be estimated by considering both statistical and systematic errors (tracking, PID, and neutral particle reconstruction). We quote here the corresponding systematic uncertainties and perform a projection for the lattice errors in 2012. The expected situation is summarized in Table 22.23.

Table 22.23: Summary of lattice and experimental sensitivity in 2012.

Observable	CKM	Had. param	Lattice error	Exp. measure	Exp. error
$Br(D \rightarrow \ell\nu)$	$ V_{cd} $	$f_D$	2%	$f_D V_{cd} $	1.1%
$Br(D_s \rightarrow \ell\nu)$	$ V_{cs} $	$f_{Ds}$	1.5%	$f_{Ds} V_{cs} $	0.7%
$\frac{Br(D_s \rightarrow \ell\nu)}{Br(D \rightarrow \ell\nu)}$	$\frac{ V_{cs} }{ V_{cd} }$	$\frac{f_{Ds}}{f_D}$	1%	$\left  \frac{V_{cs}f_{Ds}}{V_{cd}f_D} \right $	0.8%
$d\Gamma(D^0 \rightarrow \pi^-)/ds$	$ V_{cd} $	$F_{D \rightarrow \pi}(0)$	4%	$ V_{cd} F_{D \rightarrow \pi}(0)$	0.6%
$d\Gamma(D^0 \rightarrow K^-)/ds$	$ V_{cs} $	$F_{D \rightarrow K}(0)$	3%	$ V_{cs} F_{D \rightarrow K}(0)$	0.5%
$d\Gamma(D_s \rightarrow K)/ds$	$ V_{cd} $	$F_{D_s \rightarrow K}(0)$	2%	$ V_{cd} F_{D_s \rightarrow K}(0)$	1.2%
$d\Gamma(D_s \rightarrow \phi)/ds$	$ V_{cs} $	$F_{D_s \rightarrow \phi}(0)$	1%	$ V_{cs} F_{D_s \rightarrow \phi}(0)$	0.8%

The most striking outcome of *BES-III* will be accurate measurements of quantities related to  $|V_{cd}|$ ,  $|V_{cs}|$  and their ratio. Currently, the best direct determination comes from dimuon production in deep-inelastic scattering of neutrinos and anti-neutrinos on nucleons for  $|V_{cd}|$  and from charm-tagged W decays for  $|V_{cs}|$  [3, 138]

$$|V_{cd}| = 0.230 \pm 0.011 \quad \sigma(|V_{cd}|)/|V_{cd}| = 5\% \quad (22.3.78)$$

$$|V_{cs}| = 0.97 \pm 0.09 \pm 0.07 \quad \sigma(|V_{cs}|)/|V_{cs}| = 12\%, \quad (22.3.79)$$

with little hope to improve on the accuracy in the case of  $|V_{cd}|$ . An alternative determination, which is superseding the previous one, comes from semileptonic  $D \rightarrow K\ell\nu$  and  $D \rightarrow \pi\ell\nu$  decays combined with lattice inputs for the form factors. The current CLEO-c data provide [139]:

$$|V_{cd}| = 0.213 \pm 0.008 \pm 0.021 \quad \sigma(|V_{cd}|)/|V_{cd}| = 11\% \quad (22.3.80)$$

$$|V_{cs}| = 0.957 \pm 0.017 \pm 0.093 \quad \sigma(|V_{cs}|)/|V_{cs}| = 10\%. \quad (22.3.81)$$

In 2012, with the inputs quoted above, the global fit from CKMfitter is expected to determine  $|V_{cd}|$  and  $|V_{cs}|$  with an accuracy of

$$\sigma(|V_{cd}|)/|V_{cd}| = 0.4\% \quad \sigma(|V_{cs}|)/|V_{cs}| = 0.02\% \quad (22.3.82)$$

$$\frac{\sigma(|V_{cd}|/|V_{cs}|)}{|V_{cd}|/|V_{cs}|} = 0.4\%. \quad (22.3.83)$$

We stress that these values are obtained assuming that the CKM mechanism is the only source for CP violation and including only the experimental inputs described in Sec. 22.3.2. In particular, these predictions are made without any direct experimental input on  $|V_{cd}|$  and  $|V_{cs}|$ . The main constraint comes from the accurate determination of  $|V_{ud}|$ , which, thanks to unitarity, fixes  $\lambda$  in the Wolfenstein parametrization and, thus, the two CKM matrix elements of interest.

This accuracy in the indirect determination from the global fit can be compared with the expected accuracy from *BES-III* and lattice QCD on the same CKM matrix elements from leptonic decays:

$$\sigma(|V_{cd}|)/|V_{cd}| = 2.3\% \quad \sigma(|V_{cs}|)/|V_{cs}| = 1.7\% \quad (22.3.84)$$

$$\frac{\sigma(|V_{cd}|/|V_{cs}|)}{|V_{cd}|/|V_{cs}|} = 1.3\%, \quad (22.3.85)$$

and from semileptonic decays (respectively  $D_s \rightarrow K$  and  $D_s \rightarrow \phi$ ):

$$\sigma(|V_{cd}|)/|V_{cd}| = 2.4\% \quad \sigma(|V_{cs}|)/|V_{cs}| = 1.3\%, \quad (22.3.86)$$

which means that the accuracy of leptonic and semileptonic measurements will allow a meaningful and detailed comparison with the CKMfitter predictions in a corner of the CKM matrix that has been tested only with a limited precision. This is particularly interesting in view of the recent hint of an anomaly in the  $s \rightarrow u$  weak current [131]: a disagreement between the predictions of the global fit and *BES-III* data supplemented by lattice results could provide a very valuable indication of physics beyond the Standard Model in the first two quark generations. This short and presumably very naive prospective exercise exemplifies how indirect methods (CKMfitter) and direct measurements (*BES-III*) can help each other to test the Standard Model in its less well-known aspects and which improvement can be expected from such combined analysis in the coming years.



# Chapter 23

## Hadronic $D(D_S)$ decays<sup>1</sup>

### 23.1 Present Status and Implication for QCD

The SM's electroweak phenomenology of charm-changing transitions appears dull, with the CKM parameters well known due to three-family unitarity constraints, the very slow  $D^0 - \bar{D}^0$  oscillation frequency, CP violating asymmetries that are small at best, and with loop-driven decays that are extremely rare and swamped by huge backgrounds due to long distance dynamics. Yet this very dullness can be utilized to gain new insights into nonperturbative dynamics, make progress in establishing theoretical control over them and calibrate the theoretical tools for  $B$  studies.

The issue at stake here is *not* whether QCD is the theory of the strong forces – there is no alternative – but our ability to perform calculations. Here charm hadrons can act as a bridge between the worlds of light flavours – as carried by  $u$ ,  $d$  and  $s$  quarks with masses lighter or at most comparable to  $\Lambda_{QCD}$  and described by chiral perturbation theory – and that of the *bona-fide* heavy  $b$  quark, with  $\Lambda_{QCD} \ll m_b$  and treatable by heavy quark theory. Only lattice QCD (LQCD) carries the promise for a truly quantitative treatment of charm hadrons that can be improved *systematically*. Furthermore LQCD is the only framework available that allows one to approach charm from lower as well as higher mass scales, which involves different aspects of nonperturbative dynamics and thus – if successful – would provide impressive validation.

At present, such a program can be carried most explicitly for exclusive semileptonic decays of charm hadrons, as described in detail in Sect. 26.2, especially since lattice QCD (LQCD) is reaching a stage where it can make rather accurate predictions for such modes. The theoretical challenges posed by nonleptonic decays are obviously more formidable. The complexities increase considerably for exclusive nonleptonic transitions, in particular because of the importance of final state interactions (FSI), which are much harder to bring under theoretical control even by using state-of-the-art LQCD.

Yet there are some strong motivations for obtaining a reliable description of exclusive nonleptonic charm decays:

- Their dynamics is largely determined by the transition region from the perturbative to the nonperturbative domain. Thus, we can gain novel insights there. One should also not give up hope for a future theoretical breakthrough in LQCD (or the

---

<sup>1</sup>By Yue-Liang Wu and Ming Zhong

advent of another similarly powerful theoretical technology) allowing us to extract numerically reliable lessons.

- The most sensitive probes for New Physics are CP asymmetries in nonleptonic channels. Search strategies and subsequent interpretations depend on hadronic matrix elements, FSI and their phases. As already indicated, we do not know how to compute them, yet one can profit here from a pragmatic exercise in ‘theoretical engineering:’ providing a phenomenological, yet comprehensive framework for a host of charm modes allows one to extract quantitative information on hadronic matrix elements and FSI phases and evaluate their reliability through overconstraints. The huge datasets already obtained by the  $B$  factories, CLEO-c and BESII and to be further expanded including also future *BES-III* studies will be of essential help here.
- Analogous decays of  $B$  mesons are being studied also as a means to extract the complex phase of  $V_{ub}$ . One could hope that  $D$  decays might serve as a validation analysis.
- Careful analysis of branching fractions can teach us novel lessons on light-flavour hadron spectroscopy, like on characteristics of resonances such as the scalar mesons, or on  $\eta$ - $\eta'$  mixing and possible non- $\bar{q}q$  components inside them.

## 23.2 Theoretical Review

### 23.2.1 The Effective Weak Hamiltonian

The theoretical description starts from constructing an effective  $\Delta C \neq 0$  Hamiltonian through an operator product expansion (OPE) in terms of *local* operators  $O_i$  and their coefficients  $c_i$ :

$$\langle f | \mathcal{H}_{\text{eff}} | D \rangle = \frac{G_F}{\sqrt{2}} V_{CKM} \sum_i c_i(\mu) \langle f | O_i | D \rangle(\mu) \quad (23.2.1)$$

The *auxiliary* scale  $\mu$  has been introduced – and this is a central element of the Wilsonian prescription for the OPE – to separate contributions from long- and short-distance dynamics: long distance  $> 1/\mu >$  short distance. Degrees of freedom with mass scales above  $\mu$  are integrated out into the coefficients  $c_i$  typically using perturbation theory, while degrees of freedom with scales below  $\mu$  remain dynamical and are contained in the operators  $O_i$ . Nonperturbative dynamics enters through their hadronic expectation values.

Observables, of course, cannot depend at all on the choice of  $\mu$ , *i.e.*, the  $\mu$  dependence of the coefficients has to cancel against that of the matrix elements when one does a complete calculation. However, in practice one has to keep the following in mind:

- The perturbatively treated coefficients also contain the strong coupling  $\alpha_S$ . To keep it in the perturbative domain, one needs

$$\mu \gg \Lambda_{QCD} \quad (23.2.2)$$

- Yet, at the same time, one does not want to choose too high a value for  $\mu$ , since it also provides the momentum cut-off in the hadronic wave function with which the matrix element is evaluated.

These two contravening requirements can be met by  $\mu \sim 1 - 1.5\text{GeV}$ , which happens to be close to the charmed quark mass. Thus  $\mu = m_c$  provides a reasonable ansatz. In practice one has to rely on additional approximations of various kinds, and these cause the computed rates to contain some sensitivity at least to  $\mu$ , which can, in turn, provide a gauge for the reliability of the result.

We do not know yet how to calculate these hadronic matrix elements from QCD's first principles in a numerically accurate way, although several different 'second generation' theoretical technologies have been brought to bear on them:  $1/N_C$  expansions, QCD sum rules and lattice QCD. While there is reasonable hope that the latter will be validated in (semi)leptonic  $D$  decays, exclusive nonleptonic transitions provide qualitatively new challenges.

While in the SM the weak decays are driven by charged currents, the intervention of QCD affects the strength of the charged current product and induces a product of effective neutral currents in a way that depends on  $\mu$ . For Cabibbo-allowed transitions, one can write down the effective weak Lagrangian

$$\mathcal{L}_{\text{eff}}^{\Delta C=1}(\mu = m_c) = -\frac{G_F}{\sqrt{2}} V_{ud} V_{cs}^* \cdot [c_- O_- + c_+ O_+] , \quad (23.2.3)$$

$$O_{\pm} = \frac{1}{2} [(\bar{s}_L \gamma_{\nu} c_L)(\bar{u}_L \gamma_{\nu} d_L)] \pm (\bar{u}_L \gamma_{\nu} c_L)(\bar{s}_L \gamma_{\nu} d_L) , \quad (23.2.4)$$

which is conveniently rewritten as:

$$\mathcal{L}_{\text{eff}}^{\Delta C=1}(\mu = m_c) = -\frac{G_F}{\sqrt{2}} V_{ud} V_{cs}^* \cdot [c_1 O_1 + c_2 O_2] ,$$

$$O_1 = (\bar{s}_L \gamma_{\nu} c_L)(\bar{u}_L \gamma_{\nu} d_L) , \quad O_2 = (\bar{u}_L \gamma_{\nu} c_L)(\bar{s}_L \gamma_{\nu} d_L) , \quad (23.2.5)$$

with

$$c_1 = \frac{1}{2}(c_+ + c_-) , \quad c_2 = \frac{1}{2}(c_+ - c_-) . \quad (23.2.6)$$

Using different schemes, one typically gets [140]:

$$c_1(m_c) = 1.25 \pm 0.03 , \quad c_2(m_c) = -0.48 \pm 0.05 . \quad (23.2.7)$$

### 23.2.2 Factorization and First Generation Theoretical Techniques

All decay amplitudes can then be expressed as linear combinations of two terms:

$$\mathcal{A}(D \rightarrow f) \propto a_1 \langle f | J_{\mu}^{(ch)} J'^{(ch)\mu} | D \rangle + a_2 \langle f | J_{\mu}^{(neut)} J'^{(neut)\mu} | D \rangle , \quad (23.2.8)$$

with

$$a_1 = c_1 + \xi c_2 , \quad a_2 = c_2 + \xi c_1 . \quad (23.2.9)$$

It should be noted that the quantities  $c_1$  and  $c_2$  on one hand and  $\xi$  on the other are of *completely different* origin despite their common appearance in  $a_1$  and  $a_2$ : while  $c_{1,2}$  are determined by short-distance dynamics and  $\xi$  parametrizes the impact of long distance dynamics on the size of matrix elements including effects due to FSI. Equation 23.2.9 contains two very important implicit assumptions, namely that the value of  $\xi$  is the same in the expressions for  $a_1$  and  $a_2$  and that it does not depend on the final state.

A very convenient ansatz is to write the nonleptonic transition matrix element as a product of two simpler matrix elements [141]

$$\langle f | J_\mu J'^\mu | D \rangle \equiv \langle f_1 f_2 | J_\mu J'^\mu | D \rangle \simeq \langle f_1 | J_\mu | 0 \rangle \langle f_2 | J'^\mu | D \rangle , \quad (23.2.10)$$

where  $f_1$  and  $f_2$  are "effective particles" that can contain any number of final state particles. The basic assumption here is that the color flow mediated by gluon exchanges *between* the two 'clusters'  $0 \rightarrow f_1$  and  $D \rightarrow f_2$  can be ignored and all the strong interaction effects lumped into two simpler transition amplitudes. Clearly this factorization ansatz can be only an approximation rather than an identity. One should also note that Eq. 23.2.10 is  $\mu$  dependent; i.e. changing the value of  $\mu$  will transform factorized contributions into non-factorized ones and *vice versa*. The best chance for this ansatz to represent a decent approximation is for the separation scale  $\mu$  to be around ordinary hadronic scales of about 1 GeV. This value happens to be close to  $m_c$ , yet that is a coincidence, since heavy quark masses are extraneous to QCD.

Besides these two types of diagrams, which are usually referred as color favored and color suppressed diagrams, other types of considerations are the weak annihilation (WA) contributions including annihilation and exchange diagrams where the matrix element is approximately written as

$$\langle f_1 f_2 | J_\mu J'^\mu | D \rangle \simeq \langle f_1 f_2 | J_\mu | 0 \rangle \langle 0 | J'^\mu | D \rangle . \quad (23.2.11)$$

Having assumed factorization, we have greatly restricted the number of free parameters. In principle at least, the amplitudes  $\langle f_1 | J_{i\mu} | 0 \rangle$  and  $\langle f_2 | J_i^\mu | D \rangle$  can be taken from (semi)leptonic  $D$  decay data, although in practice that information is augmented by some theoretical arguments. The two quantities  $a_{1,2}$  are then treated as free parameters fitted from experiment, although, in practice again, some theoretical judgment has to be applied concerning if and to what degree WA diagrams are included in addition to the spectator diagrams and corrections for FSI have to be applied.

Such an analysis was first carried out by Bauer, Stech and Wirbel (BSW) for charmed meson two-body decays, yielding [142]

$$a_1|_{exp} \simeq 1.2 \pm 0.1 , \quad a_2|_{exp} \simeq -0.5 \pm 0.1 , \quad (23.2.12)$$

to be compared with the theoretical expectations

$$a_1|_{QCD} \simeq 1.25 - 0.48\xi , \quad a_2|_{QCD} \simeq -0.48 + 1.25\xi . \quad (23.2.13)$$

It is remarkable that with just two fit parameters one can get a decent description of a host of nonleptonic rates. However one might say that those parameters have the wrong values: naively just counting colors one expects  $\xi \simeq 1/N_C = 1/3$  and thus  $a_1|_{QCD} \simeq 1.09$  and  $a_2|_{QCD} \simeq -0.06$ ; for  $a_2$  this is inconsistent with the experimental fit value.  $\xi \simeq 0$  would reconcile Eqs. 23.2.12 and 23.2.13.

### 23.2.3 The $1/N_C$ ansatz

The fit result  $\xi \simeq 0$  leads to an intriguing speculation that these weak two-body decays can be described more rigorously using  $1/N_C$  expansions [143]. These are invoked

to calculate hadronic matrix elements. The procedure is as follows: One employs the effective weak transition operator  $\mathcal{L}_{eff}(\Delta C = 1)$  given explicitly in Eq. 23.2.3; since it describes short distance dynamics, one has kept  $N_C = 3$  there. Then one expands the matrix element for a certain transition driven by these operators in  $1/N_C$

$$\mathcal{A}(D \rightarrow f) = \langle f | \mathcal{L}_{eff}(\Delta C = 1) | D \rangle = \sqrt{N_C} \left( b_0 + \frac{b_1}{N_C} + \mathcal{O}(1/N_C^2) \right). \quad (23.2.14)$$

Using the rules for  $1/N_C$  expansions, it is easy to show that the following simplifying properties hold for the leading  $1/N_C$  contributions:

- one has to consider *valence* quark wave functions only;
- *factorization* holds;
- *WA* has to be ignored as have FSI.

To leading order in  $1/N_C$ , only the term  $b_0$  is retained; then one has effectively  $\xi = 0$  since  $\xi \simeq 1/N_C$  represents a higher order contribution. However, the next-to-leading term  $b_1$  is, in general, beyond theoretical control.  $1/N_C$  expansions therefore do not enable us to decrease the uncertainties *systematically*.

The  $N_C \rightarrow \infty$  prescription is certainly a very compact one with transparent rules, and it provides a not-bad first approximation – but no more. One can ignore neither FSI nor WA completely.

### 23.2.4 Treatment with QCD sum rules

A treatment of  $D \rightarrow PP$  and  $D \rightarrow PV$  decays based on a judicious application of QCD sum rules was developed in a series of papers [144]. The authors analyzed four-point correlation functions between the weak Lagrangian  $\mathcal{L}(\Delta C = 1)$  and three currents. As usual, an OPE is applied to the correlation function in the Euclidean region; nonperturbative dynamics is incorporated through condensates  $\langle 0 | m \bar{q} q | 0 \rangle$ ,  $\langle 0 | G \cdot G | 0 \rangle$ , etc., the numerical values of which are extracted from other *light*-quark systems. They extrapolated their results to the Minkowskian domain through a (double) dispersion relation and succeeded in finding a stability range for matching it with phenomenological hadronic expressions.

The analysis has some nice features:

- ⊕ It has a clear basis in QCD, and includes, in principle at least, nonperturbative dynamics in a well defined way.
- ⊕ It incorporates different quark-level processes – external and internal  $W$  emission, WA and Pauli interference – in a natural manner.
- ⊕ It allows one to include nonfactorizable contributions systematically.

In practice, however, it suffers at the same time from some shortcomings:

- ⊖ The charm scale is not sufficiently high for one to have full confidence in the various extrapolations undertaken.
- ⊖ To make these very lengthy calculations at all manageable, some simplifying assumptions had to be made, like  $m_u = m_d = m_s = 0$  and  $SU(3)_{Fl}$  breaking beyond  $m_K > m_\pi$  had to be ignored; in particular  $\langle 0 | \bar{s} s | 0 \rangle = \langle 0 | \bar{d} d | 0 \rangle = \langle 0 | \bar{u} u | 0 \rangle$  was used. Thus, for example, one cannot expect  $SU(3)_{Fl}$  breaking to be reproduced correctly.

⊖ *Prominent* FSI that vary rapidly with the energy scale – like effects due to narrow resonances – cannot be described in this treatment; the extrapolation from the Euclidean to the Minkowskian domain amounts to some averaging or ‘smearing’ over energies.

A statement that the predictions did not provide an excellent fit to the data on about twenty-odd  $D^0$ ,  $D^+$  and  $D_s^+$  modes – while correct on the surface, especially when  $SU(3)_{Fl}$  breaking is involved – misses the main point:

- No *a priori* model assumption like factorization had to be made.
- In principle, the theoretical description does not contain any free parameters, although in practice there is some leeway in the size of some decay constants.

### 23.2.5 Modern Developments

As the data improved, the BSW prescription became inadequate, however most subsequent attempts to describe nonleptonic decays in the  $D$  system – except for the sum rules approach sketched above – use the assumption of naive factorization as a starting point.

Improvements and generalizations of the BSW description have been made in three areas:

1. Different parameterizations for the  $q^2$  dependence of the form factors are used and different evaluations of their normalization are made. This is similar to what was addressed in our discussion of exclusive semileptonic decays. One appealing suggestion is to use only those expressions for form factors that asymptotically – *i.e.* for  $m_c, m_s \rightarrow \infty$  – exhibit heavy quark symmetry.
2. Attempts have been made to incorporate FSI more reliably. Non-factorized contributions in general have been considered.
3. Contributions due to WA and Penguin operators have been included.

Two frameworks that are more firmly based on QCD than quark models have been developed to treat two-body decays of  $B$  mesons, namely ‘QCD factorization’ [145] and ‘pQCD’ [146]. While there is little reason to expect the more aggressive pQCD approach to work for charm decays, a treatment based on QCD factorization is worth a try despite the fact that the charm mass barely exceeds ordinary hadronic scales. To illustrate the present status, the branching fractions for  $D \rightarrow \pi\pi$  decays inferred from naive factorization and QCD factorization approaches are listed and compared with experimental data [147]:

$$BR(D^0 \rightarrow \pi^+ \pi^-) = \begin{cases} 1.86 \times 10^{-3}, & \text{(Naive Factorization)} \\ 1.69 \times 10^{-3}, & \text{(QCD Factorization)} \\ (1.364 \pm 0.032) \times 10^{-3}, & \text{(PDG06[3])} \end{cases}$$

$$BR(D^+ \rightarrow \pi^+ \pi^0) = \begin{cases} 1.68 \times 10^{-3}, & \text{(Naive Factorization)} \\ 1.94 \times 10^{-3}, & \text{(QCD Factorization)} \\ (1.28 \pm 0.09) \times 10^{-3}, & \text{(PDG06[3])} \end{cases}$$

$$BR(D^0 \rightarrow \pi^0 \pi^0) = \begin{cases} 2.44 \times 10^{-5}, & \text{(Naive Factorization)} \\ 2.06 \times 10^{-5}, & \text{(QCD Factorization)} \\ (7.9 \pm 0.8) \times 10^{-4}. & \text{(PDG06[3])} \end{cases}$$

Both the naive factorization and the QCD factorization predictions for  $D^0 \rightarrow \pi^+ \pi^-$  and  $D^+ \rightarrow \pi^+ \pi^0$  are of the same order as the experimental results, while the predictions for  $D^0 \rightarrow \pi^0 \pi^0$  are about forty times smaller than the experiment. For proper perspective one should note that the modes  $D^0 \rightarrow \pi^+ \pi^-$  and  $D^+ \rightarrow \pi^+ \pi^0$  are described by color-*favored* tree diagram  $T$ , whereas  $D^0 \rightarrow \pi^0 \pi^0$  is dominated by a color-*suppressed* tree diagram  $C$ . Non-factorizable corrections are found to be larger for the latter and, at present, are beyond theoretical control.

In summary, a theoretical description of exclusive nonleptonic decays of charmed mesons based on general principles is not yet possible. Even though the short distance contributions can be calculated and the effective weak Hamiltonian has been constructed at next-to-leading order, the evaluation of its matrix elements requires nonperturbative techniques. Some decent phenomenological descriptions have been achieved, but realistically few frameworks provide opportunities for systematic improvements, especially when they are applied to multi-body channels.

### 23.2.6 Symmetry Analysis

#### Isospin $SU(2)$ Symmetry

Symmetry-based arguments are a powerful weapon in our theoretical arsenal. Isospin invariance should hold at the  $\mathcal{O}(1\%)$  level, and no evidence to the contrary has been found. Taking two-body decays as an example, it leads to triangle relations among the decay amplitudes:

$$\mathcal{A}(D^0 \rightarrow \pi^+ \pi^-) + \sqrt{2} \mathcal{A}(D^0 \rightarrow \pi^0 \pi^0) - \sqrt{2} \mathcal{A}(D^+ \rightarrow \pi^+ \pi^0) = 0 , \quad (23.2.15)$$

$$\mathcal{A}(D^0 \rightarrow K^- \pi^+) + \sqrt{2} \mathcal{A}(D^0 \rightarrow \bar{K}^0 \pi^0) - \mathcal{A}(D^+ \rightarrow \bar{K}^0 \pi^+) = 0 , \quad (23.2.16)$$

$$\mathcal{A}(D^0 \rightarrow \pi^+ K^{*-}) + \sqrt{2} \mathcal{A}(D^0 \rightarrow \pi^0 \bar{K}^{*0}) - \mathcal{A}(D^+ \rightarrow \pi^+ \bar{K}^{*0}) = 0 , \quad (23.2.17)$$

$$\mathcal{A}(D^0 \rightarrow \rho^+ K^-) + \sqrt{2} \mathcal{A}(D^0 \rightarrow \rho^0 \bar{K}^0) - \mathcal{A}(D^+ \rightarrow \bar{K}^0 \rho^+) = 0 . \quad (23.2.18)$$

The measured rates tell us that these amplitudes possess large relative phases indicating strong FSI. Considering the three  $D \rightarrow \pi\pi$  modes, the transition amplitudes can be decomposed into

$$\mathcal{A}(D^0 \rightarrow \pi^+ \pi^-) = \sqrt{\frac{2}{3}} \mathcal{A}_0 + \sqrt{\frac{1}{3}} \mathcal{A}_2 , \quad (23.2.19)$$

$$\mathcal{A}(D^0 \rightarrow \pi^0 \pi^0) = \sqrt{\frac{1}{3}} \mathcal{A}_0 - \sqrt{\frac{2}{3}} \mathcal{A}_2 , \quad (23.2.20)$$

$$\mathcal{A}(D^+ \rightarrow \pi^+ \pi^0) = \sqrt{\frac{3}{2}} \mathcal{A}_2 . \quad (23.2.21)$$

The subscripts 0 and 2 of the  $\mathcal{A}$  describe the isospin  $I = 0$  and 2 components of the  $\pi\pi$  system. From the experimental data, the amplitude ratio  $|A_2/A_0|$  and the relative phase  $\delta = \delta_2 - \delta_0$  are determined to be [148]

$$|A_2/A_0| = 0.72 \pm 0.13 \pm 0.11 , \quad \cos \delta = 0.14 \pm 0.13 \pm 0.09 . \quad (23.2.22)$$

#### Flavor $SU(3)$ Symmetry and Its Breaking

It would seem tempting to argue that  $SU(3)$ -flavor symmetry holds to within, say, 20 - 30 %. This, however, does not seem to be the case, at least not for exclusive channels,

as can be read off most dramatically from the difference of the ratio

$$\frac{\mathcal{A}(D^0 \rightarrow K^+ K^-)}{\mathcal{A}(D^0 \rightarrow \pi^+ \pi^-)} \simeq 1.8 \quad (23.2.23)$$

from unity. This significant  $SU(3)$  symmetry violation may come from the finite strange quark mass, FSI and resonances [149]. There are indications, however, that for inclusive rates,  $SU(3)$ -flavor breaking does not exceed the 20% level [150].

## 23.3 Two-Body Decays

Two-body modes in charmed meson nonleptonic decays have drawn much attention since the 1980s because they have a number of advantages, in comparison with multi-body ones, including:

- Nonleptonic charm meson decays have been observed to proceed mainly via two-body channels, where a resonance is considered as a single body. A large accumulation of precise experimental data on two-body decays, including branching fractions for about 60 decay modes, is contained in the PDG tables [3].
- The phase space is trivial and the number of form factors are quite limited.
- There are fewer color sources in the form of quarks and antiquarks, and fewer different combinations of color flux tubes that can form.
- Quite a number of two-body modes allow for sizeable momentum transfers thereby, hopefully, reducing the predominance of long-distance dynamics.
- This is the one class of nonleptonic decays where one can harbor reasonable hopes of some success. It is not utopian to expect lattice QCD to treat these transitions some day in full generality. Such results will, however, only be reliable if obtained with the incorporation of fully dynamical fermions – i.e. without ”quenching” and without reliance on a  $1/m_c$  expansion.

### 23.3.1 Kinematics and Topologies of Amplitudes

In the center-of-mass frame, the differential decay rate for  $n$ -body charmed meson decay is

$$d\Gamma = \frac{1}{2m_D} \left( \prod_{i=1}^n \frac{d^3 p_i}{(2\pi)^3} \frac{1}{2E_i} \right) |\mathcal{A}(m_D \rightarrow \{p_1, p_2, \dots, p_n\})|^2 (2\pi)^4 \delta^4(p_D - \sum_{i=1}^n p_i). \quad (23.3.24)$$

If the number of final state particles is set to two, one can easily perform the integral over phase space to obtain the decay rate

$$\Gamma(D \rightarrow f_1 f_2) = \frac{p}{8\pi M_D^2} |\mathcal{A}|^2, \quad (23.3.25)$$

where

$$p = \frac{\sqrt{(M_D^2 - (m_1 + m_2)^2)(M_D^2 - (m_1 - m_2)^2)}}{2M_D}$$

denotes the center-of-mass 3-momentum of each final-state particle. The branching fraction for the  $D \rightarrow f_1 f_2$  transition is the ratio of this partial decay width to the full width of the  $D$  meson:

$$B(D \rightarrow f_1 f_2) = \frac{\Gamma(D \rightarrow f_1 f_2)}{\Gamma(D)}. \quad (23.3.26)$$

The amplitude  $\mathcal{A}$  can be decomposed into six distinct quark-graph topologies [151]: (1) color-favored tree amplitude  $T$ , (2) color-suppressed tree amplitude  $C$ , (3)  $W$ -exchange amplitude  $E$ , (4)  $W$ -annihilation amplitude  $A$ , (5) horizontal  $W$ -loop amplitude  $P$  and (6) vertical  $W$ -loop amplitude  $D$ . The penguin diagrams  $P$  and  $D$  play little role in practice because the relation of the CKM matrix elements  $V_{cs}^* V_{us} \approx -V_{cd}^* V_{ud}$  results in cancellations among them.

### 23.3.2 $D \rightarrow PP$ , $D \rightarrow PV$ and $D \rightarrow VV$ Decays

Among the experimental data on charm nonleptonic two-body decays, charmed mesons decaying to two pseudoscalar mesons ( $D \rightarrow PP$ ), to one pseudoscalar and one vector meson ( $D \rightarrow PV$ ) and to two vector mesons ( $D \rightarrow VV$ ) have the best precision. The light pseudoscalar and vector mesons are two classes of particles that are distinct because of their well established basic properties such as mass, lifetime, width, quark component and decay rate. The form factors for charmed mesons transforming to light pseudoscalar and vector mesons have been calculated in a variety of theoretical models. Based on the resulting form factors, most predictions on charmed meson semileptonic decays are consistent with experimental data, as discussed in Sect. 22.2.1. As a result,  $PP$ ,  $PV$  and  $VV$  decays are an ideal place to test the factorization assumption and develop an understanding of the mysteries of FSI and unfactorizable contributions.

Using the form factor definitions given in Eqs. 22.2.42 and 22.2.48, the four relevant amplitudes for  $D \rightarrow P_1 P_2$  in the factorization approach are:

$$T = i \frac{G_F}{\sqrt{2}} V_{q_1 q_2} V_{cq_3}^* a_1 f_{P_1} (m_D^2 - m_1^2) F_0^{D \rightarrow P_2} (m_1^2), \quad (23.3.27)$$

$$C = i \frac{G_F}{\sqrt{2}} V_{q_1 q_2} V_{cq_3}^* a_2 f_{P_1} (m_D^2 - m_2^2) F_0^{D \rightarrow P_2} (m_1^2), \quad (23.3.28)$$

$$E = i \frac{G_F}{\sqrt{2}} V_{q_1 q_2} V_{cq_3}^* a_2 f_D (m_1^2 - m_2^2) F_0^{P_1 P_2} (m_D^2), \quad (23.3.29)$$

$$A = i \frac{G_F}{\sqrt{2}} V_{q_1 q_2} V_{cq_3}^* a_1 f_D (m_1^2 - m_2^2) F_0^{P_1 P_2} (m_D^2). \quad (23.3.30)$$

The amplitudes for  $D \rightarrow PV$  are a little more complicated than  $D \rightarrow PP$ , since one has to distinguish terms where the spectator quark ends up in the pseudoscalar or vector particle in the final state. Using the subscripts  $P$  and  $V$  to distinguish between the cases where the spectator quark is in the pseudoscalar or vector final-state meson, respectively, one can read off the amplitudes:

$$T_V = 2 \frac{G_F}{\sqrt{2}} V_{q_1 q_2} V_{cq_3}^* a_1 f_P m_V (\varepsilon^* \cdot p_D) A_0^{D \rightarrow V} (m_P^2), \quad (23.3.31)$$

$$T_P = 2 \frac{G_F}{\sqrt{2}} V_{q_1 q_2} V_{cq_3}^* a_1 f_V m_V (\varepsilon^* \cdot p_D) F_+^{D \rightarrow P}(m_V^2), \quad (23.3.32)$$

$$C_V = 2 \frac{G_F}{\sqrt{2}} V_{q_1 q_2} V_{cq_3}^* a_2 f_V m_V (\varepsilon^* \cdot p_D) A_0^{D \rightarrow V}(m_P^2), \quad (23.3.33)$$

$$C_P = 2 \frac{G_F}{\sqrt{2}} V_{q_1 q_2} V_{cq_3}^* a_2 f_V m_V (\varepsilon^* \cdot p_D) F_+^{D \rightarrow P}(m_V^2), \quad (23.3.34)$$

$$E = 2 \frac{G_F}{\sqrt{2}} V_{q_1 q_2} V_{cq_3}^* a_2 f_D m_V (\varepsilon^* \cdot p_D) A_0^{PV}(m_D^2), \quad (23.3.35)$$

$$A = 2 \frac{G_F}{\sqrt{2}} V_{q_1 q_2} V_{cq_3}^* a_1 f_D m_V (\varepsilon^* \cdot p_D) A_0^{PV}(m_D^2). \quad (23.3.36)$$

Charm decays to two vector meson final states have a richer structure than those with at least one pseudoscalar in the final state. Here

$$\begin{aligned} T(D \rightarrow V_1 V_2) = & \frac{G_F}{\sqrt{2}} V_{q_1 q_2} V_{cq_3}^* a_1 [i f_{V_1} m_1 (m_D + m_2) A_1^{D \rightarrow V_2}(m_1^2) \varepsilon_1^* \cdot \varepsilon_2^* \\ & - i \frac{1}{m_D + m_2} f_{V_1} m_1 A_2^{D \rightarrow V_2}(m_1^2) \varepsilon_1^* \cdot (p_D + p_2) \varepsilon_2^* \cdot (p_D - p_2) \\ & - \frac{2}{m_D + m_2} f_{V_1} m_1 V^{D \rightarrow V_2}(m_1^2) \epsilon_{\mu\nu\alpha\beta} \varepsilon_1^{*\mu} \varepsilon_2^{*\nu} p_D^\alpha p_2^\beta], \end{aligned} \quad (23.3.37)$$

$$\begin{aligned} C(D \rightarrow V_1 V_2) = & \frac{G_F}{\sqrt{2}} V_{q_1 q_2} V_{cq_3}^* a_2 [i f_{V_1} m_1 (m_D + m_2) A_1^{D \rightarrow V_2}(m_1^2) \varepsilon_1^* \cdot \varepsilon_2^* \\ & - i \frac{1}{m_D + m_2} f_{V_1} m_1 A_2^{D \rightarrow V_2}(m_1^2) \varepsilon_1^* \cdot (p_D + p_2) \varepsilon_2^* \cdot (p_D - p_2) \\ & - \frac{2}{m_D + m_2} f_{V_1} m_1 V^{D \rightarrow V_2}(m_1^2) \epsilon_{\mu\nu\alpha\beta} \varepsilon_1^{*\mu} \varepsilon_2^{*\nu} p_D^\alpha p_2^\beta]. \end{aligned} \quad (23.3.38)$$

The terms proportional to  $A_1$ ,  $A_2$  and  $V$  represent  $S$ , longitudinal  $D$  and  $P$  waves respectively. The omitted expressions for exchange and annihilation topologies contain the vector-to-vector form factor.

From a long history of phenomenological analyses, we can draw some general conclusions on the factorization formalism that serve as guides for studies of the other charmed meson decay modes like those to two-body final states containing scalar ( $S$ ), axial-vector ( $A$ ) and tensor ( $T$ ) particles as well as multi-body final states.

- Nonfactorizable corrections that result from spectator interactions, FSI, resonance effects, etc., are known to be significant [152]. Some phenomenological models based on the one-particle-exchange method [153], resonance formation [154], and the combination of heavy quark effective theory and chiral perturbation theory [155] have been developed to try to get some insights into these corrections. Effects of  $q\bar{q}$  resonance formation are probably most important for hadronic charm decays, owing to the existence of an abundant spectrum of resonances that are known to exist at energies close to the mass of charmed mesons. Most of the resonance properties conform to unitarity and the effects of resonance-induced nonfactorizable contributions can be described in a model-independent manner in terms of the masses and decay widths of the contributing resonances [156].

- The parameters  $a_1$  and  $a_2$  were found to be non-universal and, instead, process or class dependent. For illustration purposes, we consider some examples

$$a_1(\mu) = c_1(\mu) + \left(\frac{1}{N_c} + \chi_1(\mu)\right)c_2(\mu) , \quad (23.3.39)$$

$$a_2(\mu) = c_2(\mu) + \left(\frac{1}{N_c} + \chi_2(\mu)\right)c_1(\mu) , \quad (23.3.40)$$

with  $\chi_1(\mu)$  and  $\chi_2(\mu)$  partially denoting nonfactorizable effects in the case of  $N_c = 3$ .  $\chi_2(\mu)$  has been determined to be [157]

$$\begin{aligned} \chi_2(D \rightarrow \bar{K}\pi) &\simeq -0.33 , \\ \chi_2(D \rightarrow \bar{K}^*\pi) &\simeq -(0.45 \sim 0.55) , \\ \chi_2(D \rightarrow \bar{K}^*\rho) &\simeq -(0.6 \sim 0.65) . \end{aligned} \quad (23.3.41)$$

- The light-meson to light-meson form factors involved in the above formulae are believed to be negligibly small. Thus, the factorization of the exchange and annihilation diagrams has no effect on the overall amplitudes. The main contributions from these diagrams may arise from the nonfactorizable parts. Through intermediate states, they relate to the tree diagram  $T$  and color-suppressed diagram  $C$  [156, 158]. As a consequence, they have sizable magnitudes that can be comparable to the  $T$  and  $C$  amplitudes and large strong phases relative to the  $T$  amplitude, as was demonstrated in a  $SU(3)$ -flavor symmetry analysis [159, 160]. This is especially true in the case of decay mode  $D^0 \rightarrow K^0\bar{K}^0$ , which proceeds completely via the  $E - E$  diagram representation, and the factorizable contribution is too trivial to be consistent with the experimentally measured branching fraction  $B = (7.1 \pm 1.9) \times 10^{-4}$ . Many studies have been performed on this decay [161] and they find that a nonfactorizable correction of the same order as that of the  $E$  diagram can account for the experimental results

Results from a variety of calculations for  $D \rightarrow PP$  decays are presented in Table 23.1; results for  $D \rightarrow PV$  decays are in Table 23.2. Note that all of these calculations have introduced some number of free parameters to describe the nonfactorizable contributions, and these are determined from fits to the experimental data. Results for  $D \rightarrow VV$  decays can be found in Refs. [155, 164, 165, 166].

### 23.3.3 $D \rightarrow SP$ Decays

Scalar meson production measurements in charm decays are now available from ARGUS [167], CLEO [168], E687 [169], E691 [170], E791 [171], FOCUS [172], and BaBar [173]. Specifically, the decays  $D \rightarrow f_0\pi(K)$ ,  $D \rightarrow a_0\pi(K)$ ,  $D \rightarrow \bar{K}_0^*\pi$  and  $D^+ \rightarrow \sigma\pi^+$  have been observed in Dalitz plot analysis of three-body decays. The results of various experiments are summarized in Table 23.3, where the products of  $\mathcal{B}(D \rightarrow SP_3)$  and  $\mathcal{B}(S \rightarrow P_1P_2)$  are listed. In order to extract the branching fractions for  $D \rightarrow f_0P$ , one should use the the result from a recent analysis [174]:  $\Gamma(f_0 \rightarrow \pi\pi) = (64 \pm 8)$  MeV,  $\Gamma(f_0 \rightarrow K\bar{K}) = (12 \pm 1)$  MeV and  $\Gamma_{f_0 \text{ total}} = (80 \pm 10)$  MeV. In this case one has

$$\mathcal{B}(f_0(980) \rightarrow K^+K^-) = 0.08 \pm 0.01 , \quad \mathcal{B}(f_0(980) \rightarrow \pi^+\pi^-) = 0.53 \pm 0.09 \quad (23.3.42)$$

Table 23.1: Predictions for  $D \rightarrow PP$  branching fractions ( $\times 10^{-2}$ ). Most decay modes involving a neutral K meson are given as  $K_S^0$  in PDG06 and  $\bar{K}^0$  in PDG04, which are presented as well.

Decay Modes	Buccella <i>et al.</i> [162]	Du <i>et al.</i> [153]	Wu <i>et al.</i> [163]	PDG 06/04
$D^0 \rightarrow K^-\pi^+$	3.847	3.72	3.79 ; 3.80	$3.80 \pm 0.07$
$\rightarrow \bar{K}^0\pi^0$	1.310	2.09	2.27 ; 2.24	$2.28 \pm 0.22$ (PDG04)
$\rightarrow \bar{K}^0\eta$			0.80 ; 0.81	$1.14 \pm 0.12$
$\rightarrow \bar{K}^0\eta'$			1.85 ; 1.88	$0.76 \pm 0.11$ (PDG04)
$\rightarrow \pi^+\pi^-$	0.151	0.149	0.144 ; 0.144	$0.38 \pm 0.06$
$\rightarrow \pi^0\pi^0$	0.115	0.106	0.078 ; 0.097	$1.87 \pm 0.28$ (PDG04)
$\rightarrow K^+K^-$	0.424	0.40	0.413 ; 0.413	$0.91 \pm 0.14$
$\rightarrow K^0\bar{K}^0$	0.130	0.0573	0.069 ; 0.062	$0.384 \pm 0.010$
$\rightarrow K^+\pi^-$	0.033	0.0141	0.0150 ; 0.0151	$0.071 \pm 0.019$ (PDG04)
$\rightarrow \eta\pi^0$			0.069 ; 0.068	$0.037 \pm 0.007$
$\rightarrow \eta'\pi^0$			0.088 ; 0.091	$0.0143 \pm 0.0004$
$\rightarrow \eta\eta$			0.011 ; 0.016	$0.056 \pm 0.014$
$\rightarrow \eta\eta'$			0.026 ; 0.030	—
$\rightarrow K^0\pi^0$	0.008	0.0284	0.002 ; 0.005	—
$\rightarrow K^0\eta$			0.001 ; 0.002	—
$\rightarrow K^0\eta'$			0.0 ; 0.0	—
$D^+ \rightarrow K^0\pi^+$	2.939		2.76 ; 2.76	$2.77 \pm 0.18$ (PDG04)
$\rightarrow \pi^+\pi^0$	0.185	0.18	0.25 ; 0.19	$1.47 \pm 0.06$
$\rightarrow \eta\pi^+$			0.34 ; 0.37	$0.128 \pm 0.009$
$\rightarrow \eta'\pi^+$			0.45 ; 0.42	$0.35 \pm 0.032$
$\rightarrow K^+\bar{K}^0$	0.764	0.64	0.62 ; 0.62	$0.53 \pm 0.11$
$\rightarrow K^0\pi^+$	0.053	0.0756	0.012 ; 0.026	$0.58 \pm 0.06$ (PDG04)
$\rightarrow K^+\pi^0$	0.055	0.0296	0.021 ; 0.023	$0.296 \pm 0.019$
$\rightarrow K^+\eta$			0.011 ; 0.012	$< 0.042$
$\rightarrow K^+\eta'$			0.005 ; 0.006	—
$D_s^+ \rightarrow K^0K^+$	4.623		3.06 ; 3.13	$4.4 \pm 0.9$
$\rightarrow \pi^+\eta$	1.131		1.05 ; 1.09	$2.11 \pm 0.35$
$\rightarrow \pi^+\eta'$			4.19 ; 4.43	$4.7 \pm 0.7$
$\rightarrow \pi^+K^0$	0.373		0.24 ; 0.26	$< 0.9$
$\rightarrow \pi^0K^+$	0.146		0.047 ; 0.090	—
$\rightarrow \eta K^+$	0.300		0.055 ; 0.040	—
$\rightarrow \eta'K^+$			0.090 ; 0.102	—
$\rightarrow K^+K^0$	0.012		0.014 ; 0.010	—

Table 23.2: Predictions for  $D \rightarrow PV$  branching fractions for  $D \rightarrow PV$  ( $\times 10^{-2}$ ). Most decay modes involving a neutral K meson are given as  $K_S^0$  in PDG06 and  $\bar{K}^0$  in PDG04, which are presented as well.

Decay Modes	Buccella <i>et al.</i> [162]	Du <i>et al.</i> [153]	Wu <i>et al.</i> [163]	PDG 06/04
$D^0 \rightarrow K^{*-} \pi^+$	4.656	5.22	5.93 ; 5.97	$5.9 \pm 0.4$ (PDG04)
$\rightarrow K^- \rho^+$	11.201	11.1	9.99 ; 9.90	$10.1 \pm 0.8$ (PDG04)
$\rightarrow \bar{K}^{*0} \pi^0$	3.208	2.72	2.72 ; 2.81	$2.8 \pm 0.4$ (PDG04)
$\rightarrow \bar{K}^0 \rho^0$	0.759	1.25	1.49 ; 1.25	$1.55_{-0.16}^{+0.12}$ (PDG04)
$\rightarrow \bar{K}^{*0} \eta$			1.50 ; 1.94	$1.8 \pm 0.4$ (PDG04)
$\rightarrow \bar{K}^0 \omega$	1.855		2.11 ; 1.80	$2.3 \pm 0.4$ (PDG04)
				$1.1 \pm 0.2$
$\rightarrow \bar{K}^0 \phi$			0.95 ; 0.90	$0.94 \pm 0.11$ (PDG04)
$\rightarrow K^+ K^{*-}$	0.290		0.25 ; 0.25	$0.20 \pm 0.11$
$\rightarrow K^- K^{*+}$	0.431		0.43 ; 0.43	$0.37 \pm 0.08$
$\rightarrow K^0 \bar{K}^{*0}$	0.052		0.08 ; 0.16	$< 0.17$ (PDG04)
				$< 0.08$
$\rightarrow \bar{K}^0 K^{*0}$	0.062		0.08 ; 0.16	$< 0.09$ (PDG04)
				$< 0.04$
$\rightarrow \pi^0 \phi$	0.105		0.12 ; 0.12	$0.074 \pm 0.005$
$\rightarrow \bar{K}^{*0} \eta'$			0.004 ; 0.003	$< 0.10$ (PDG04)
$\rightarrow \eta \phi$			0.035 ; 0.034	$0.014 \pm 0.004$
$\rightarrow \pi^+ \rho^-$	0.485	0.36	0.34 ; 0.35	$0.45 \pm 0.04$
$\rightarrow \pi^- \rho^+$	0.706	0.73	0.62 ; 0.61	$1.0 \pm 0.06$
$\rightarrow \pi^0 \rho^0$	0.216	0.11	0.19 ; 0.16	$0.32 \pm 0.04$
$\rightarrow \pi^0 \omega$	0.013		0.020 ; 0.003	$< 0.026$
$\rightarrow \eta \omega$			0.13 ; 0.10	
$\rightarrow \eta' \omega$			0.0007 ; 0.0003	
$\rightarrow \eta \rho^0$			0.0039 ; 0.0015	
$\rightarrow \eta' \rho^0$	0.039		0.012 ; 0.009	
$\rightarrow K^{*+} \pi^-$	0.025		0.029 ; 0.029	
$\rightarrow K^+ \rho^-$	0.004		0.016 ; 0.016	
$\rightarrow K^{*0} \pi^0$	0.008		0.0052 ; 0.0064	
$\rightarrow K^0 \rho^0$			0.0069 ; 0.0059	
$\rightarrow K^{*0} \eta$			0.0030 ; 0.0041	
$\rightarrow K^{*0} \eta'$			0.0 ; 0.0	
$\rightarrow K^0 \omega$	0.002		0.0076 ; 0.0056	
$\rightarrow K^0 \phi$			0.0 ; 0.0006	

Table 23.2: (*continued*) Predictions for  $D \rightarrow PV$  branching fractions ( $\times 10^{-2}$ ). Most decay modes involving a neutral K meson are given as  $K_S^0$  in PDG06 and  $\bar{K}^0$  in PDG04, which are presented as well.

Decay Modes	Buccella <i>et al.</i> [162]	Du <i>et al.</i> [153]	Wu <i>et al.</i> [163]	PDG 06/04
$D^+ \rightarrow K^{*0}\pi^+$	1.996		1.96 ; 1.96	$1.95 \pm 0.19$ (PDG04)
$\rightarrow \pi^+\phi$	0.619		0.64 ; 0.62	$0.65 \pm 0.07$
$\rightarrow \bar{K}^0\rho^+$	12.198	7.01	7.56 ; 8.43	$6.6 \pm 2.5$ (PDG04)
$\rightarrow \pi^+\rho^0$	0.104	0.13	0.088 ; 0.088	$0.107 \pm 0.011$
$\rightarrow K^+\bar{K}^{*0}$	0.436		0.44 ; 0.44	$0.43 \pm 0.06$ (PDG04)
$\rightarrow \bar{K}^0K^{*+}$	1.515		1.43 ; 1.25	$3.1 \pm 1.4$ (PDG04)
$\rightarrow K^+\rho^0$	0.029		0.030 ; 0.025	$0.025 \pm 0.007$
$\rightarrow K^{*0}\pi^+$	0.027		0.024 ; 0.022	$0.030 \pm 0.006$
$\rightarrow K^+\phi$			0.0066 ; 0.0067	$< 0.013$ (PDG04)
$\rightarrow \pi^+\omega$			0.57 ; 0.58	$< 0.034$
$\rightarrow \eta\rho^+$			0.24 ; 0.43	$< 0.7$
$\rightarrow \eta'\rho^+$			0.15 ; 0.15	$< 0.6$
$\rightarrow \pi^0\rho^+$	0.451	0.31	0.28 ; 0.35	
$\rightarrow K^0\rho^+$	0.042		0.025 ; 0.022	
$\rightarrow \pi^0K^{*+}$	0.057		0.037 ; 0.036	
$\rightarrow K^+\omega$			0.012 ; 0.011	
$\rightarrow K^{*+}\eta$			0.015 ; 0.015	
$\rightarrow K^{*+}\eta'$			0.00014 ; 0.00016	
$D_s^+ \rightarrow K^{*0}K^+$	4.812		3.34 ; 3.42	$3.3 \pm 0.9$ (PDG04)
$\rightarrow \bar{K}^0K^{*+}$	2.467		4.98 ; 4.66	$5.3 \pm 1.3$
$\rightarrow \pi^+\rho^0$			0.06 ; 0.06	$< 0.07$ (PDG04)
$\rightarrow \pi^+\phi$	4.552		3.08 ; 2.93	$4.4 \pm 0.6$
$\rightarrow \pi^+K^{*0}$	0.445		0.33 ; 0.35	$0.65 \pm 0.28$ (PDG04)
$\rightarrow K^+\rho^0$	0.198		0.12 ; 0.12	$0.26 \pm 0.07$
$\rightarrow K^+\phi$	0.008		0.032 ; 0.033	$< 0.06$
$\rightarrow K^+\omega$	0.178		0.40 ; 0.39	
$\rightarrow K^0\rho^+$	1.288		0.91 ; 0.77	
$\rightarrow \pi^0K^{*+}$	0.076		0.13 ; 0.13	
$\rightarrow \eta K^{*+}$	0.146		0.038 ; 0.047	
$\rightarrow \eta' K^{*+}$			0.068 ; 0.059	
$\rightarrow K^{*0}K^+$	0.006		0.0015 ; 0.0015	
$\rightarrow K^{*+}K^0$	0.018		0.0076 ; 0.0085	

For  $D \rightarrow a_0 P$ , one can apply the PDG average  $\Gamma(a_0 \rightarrow K\bar{K})/\Gamma(a_0 \rightarrow \pi\eta) = 0.183 \pm 0.024$  [3] to obtain

$$\begin{aligned}\mathcal{B}(a_0^0(980) \rightarrow \pi^0\eta) &= 0.845 \pm 0.017, \\ \mathcal{B}(a_0^+(980) \rightarrow K^+\bar{K}^0) &= \mathcal{B}(a_0^-(980) \rightarrow K^-K^0) = 0.155 \pm 0.017, \\ \mathcal{B}(a_0^0(980) \rightarrow K^+K^-) &= 0.078 \pm 0.009.\end{aligned}\quad (23.3.43)$$

For  $D \rightarrow K_0^*(1430)P$ , the branching fraction  $\mathcal{B}(K_0^*(1430) \rightarrow K^+\pi^-) = \frac{2}{3}(0.93 \pm 0.10)$  should be used [3]. Some scalar meson decays are not listed in the PDG tables. Precise measurements of these branching fractions would of great value for understanding charmed meson to scalar meson transitions.

The theoretical approaches to  $D \rightarrow SP$  are very similar to  $D \rightarrow PP$  except for the fact that the quark structure of the scalar mesons, especially the  $f_0(980)$  and  $a_0(980)$ , is still not well established. (For a recent review, see Ref. [3] and references therein). Thus, one faces a 'Scylla and Charybdis' dilemma with limited theoretical control on *both* the factorizable and nonfactorizable contributions. Still, there is no doubt that the study of charmed meson decays will provide a new avenue to the understanding of light scalar meson spectroscopy. One might resort to the knowledge gained from the  $D \rightarrow PP$  and  $D \rightarrow PV$  modes and try to gain some new understanding of some old puzzles related to the internal structure and parameters, *e.g.* the masses and widths, of light scalar mesons through the study of  $D \rightarrow SP$  [176, 177, 178]. Or *vice versa*: one could start with an assumed structure for the scalar mesons and make predictions for the decays [179, 180, 181]. Some of the theoretical results in the literature are given in Table 23.4. In either case, the following factorization formulae are useful:

$$T_S = -\frac{G_F}{\sqrt{2}} V_{q_1 q_2} V_{cq_3}^* a_1 f_P(m_D^2 - m_S^2) F_0^{D \rightarrow S}(m_P^2), \quad (23.3.44)$$

$$T_P = -\frac{G_F}{\sqrt{2}} V_{q_1 q_2} V_{cq_3}^* a_1 f_S(m_D^2 - m_P^2) F_0^{D \rightarrow P}(m_S^2), \quad (23.3.45)$$

$$C_S = -\frac{G_F}{\sqrt{2}} V_{q_1 q_2} V_{cq_3}^* a_2 f_P(m_D^2 - m_S^2) F_0^{D \rightarrow S}(m_P^2), \quad (23.3.46)$$

$$C_P = -\frac{G_F}{\sqrt{2}} V_{q_1 q_2} V_{cq_3}^* a_2 f_S(m_D^2 - m_P^2) F_0^{D \rightarrow P}(m_S^2). \quad (23.3.47)$$

### 23.3.4 $D \rightarrow AP$ Decays

There are two different types of axial vector mesons:  $^3P_1$  and  $^1P_1$ , with quantum numbers  $J^{PC} = 1^{++}$  and  $1^{+-}$ , respectively. The isovector non-strange axial vector mesons  $a_1(1260)$  and  $b_1(1235)$ , which correspond to  $^3P_1$  and  $^1P_1$ , respectively, cannot mix because of their opposite  $G$ -parities. However, the isodoublet strange mesons  $K_1(1270)$  and  $K_1(1400)$  are a mixture of  $^3P_1$  and  $^1P_1$  states due to the strange and non-strange light-quark mass difference. One usually expresses these as

$$\begin{aligned}K_1(1270) &= K_{1A} \sin \theta + K_{1B} \cos \theta, \\ K_1(1400) &= K_{1A} \cos \theta - K_{1B} \sin \theta,\end{aligned}\quad (23.3.48)$$

Table 23.3: Experimental branching fractions of various  $D \rightarrow SP$  decays measured by ARGUS, E687, E691, E791, CLEO, FOCUS and BaBar. For simplicity and convenience, mass identifications for the  $f_0(980)$ ,  $a_0(980)$  and  $K_0^*(1430)$  have been dropped.

Collaboration	$\mathcal{B}(D \rightarrow SP) \times \mathcal{B}(S \rightarrow P_1 P_2)$	$\mathcal{B}(D \rightarrow SP)$
PDG06	$\mathcal{B}(D^+ \rightarrow f_0 \pi^+) \mathcal{B}(f_0 \rightarrow \pi^+ \pi^-) = (2.1 \pm 0.5) \times 10^{-4}$	$\mathcal{B}(D^+ \rightarrow f_0 \pi^+) = (4.0 \pm 1.2) \times 10^{-4}$
E791	$\mathcal{B}(D^+ \rightarrow f_0 \pi^+) \mathcal{B}(f_0 \rightarrow \pi^+ \pi^-) = (1.9 \pm 0.5) \times 10^{-4}$	$\mathcal{B}(D^+ \rightarrow f_0 \pi^+) = (3.6 \pm 1.1) \times 10^{-4}$
FOCUS	$\mathcal{B}(D^+ \rightarrow f_0 K^+) \mathcal{B}(f_0 \rightarrow K^+ K^-) = (3.84 \pm 0.92) \times 10^{-5}$	$\mathcal{B}(D^+ \rightarrow f_0 K^+) = (4.8 \pm 1.3) \times 10^{-4}$
PDG06	$\mathcal{B}(D^+ \rightarrow f_0 K^+) \mathcal{B}(f_0 \rightarrow \pi^+ \pi^-) = (5.7 \pm 3.5) \times 10^{-5}$	$\mathcal{B}(D^+ \rightarrow f_0 K^+) = (1.1 \pm 0.7) \times 10^{-4}$
FOCUS	$\mathcal{B}(D^+ \rightarrow f_0 K^+) \mathcal{B}(f_0 \rightarrow \pi^+ \pi^-) = (6.12 \pm 3.65) \times 10^{-5}$	$\mathcal{B}(D^+ \rightarrow f_0 K^+) = (1.2 \pm 0.7) \times 10^{-4}$
FOCUS	$\mathcal{B}(D^+ \rightarrow a_0^0 \pi^+) \mathcal{B}(a_0^0 \rightarrow K^+ K^-) = (2.38 \pm 0.47) \times 10^{-3}$	$\mathcal{B}(D^+ \rightarrow a_0^0 \pi^+) = (3.1 \pm 0.7) \%$
E791	$\mathcal{B}(D^+ \rightarrow \sigma \pi^+) \mathcal{B}(\sigma \rightarrow \pi^+ \pi^-) = (1.4 \pm 0.3) \times 10^{-3}$	$\mathcal{B}(D^+ \rightarrow \sigma \pi^+) = (2.1 \pm 0.5) \times 10^{-3}$
E791	$\mathcal{B}(D^+ \rightarrow \kappa \pi^+) \mathcal{B}(\kappa \rightarrow K^- \pi^+) = (4.4 \pm 1.2) \%$	$\mathcal{B}(D^+ \rightarrow \kappa \pi^+) = (6.5 \pm 1.9) \%$
E691,E687	$\mathcal{B}(D^+ \rightarrow \bar{K}_0^{*0} \pi^+) \mathcal{B}(\bar{K}_0^{*0} \rightarrow K^- \pi^+) = (2.3 \pm 0.3) \%$	$\mathcal{B}(D^+ \rightarrow \bar{K}_0^{*0} \pi^+) = (3.7 \pm 0.6) \%$
PDG06	$\mathcal{B}(D^+ \rightarrow K_0^{*0} \pi^+) \mathcal{B}(K_0^{*0} \rightarrow K^- \pi^+) = (2.41 \pm 0.24) \%$	$\mathcal{B}(D^+ \rightarrow K_0^{*0} \pi^+) = (3.9 \pm 0.6) \%$
E791	$\mathcal{B}(D^+ \rightarrow \bar{K}_0^{*0} \pi^+) \mathcal{B}(\bar{K}_0^{*0} \rightarrow K^- \pi^+) = (1.14 \pm 0.16) \%$	$\mathcal{B}(D^+ \rightarrow \bar{K}_0^{*0} \pi^+) = (1.8 \pm 0.3) \%$
PDG06	$\mathcal{B}(D^+ \rightarrow \bar{K}_0^{*0} K^+) \mathcal{B}(K_0^{*0} \rightarrow K^- \pi^+) = (3.7 \pm 0.4) \times 10^{-3}$	$\mathcal{B}(D^+ \rightarrow \bar{K}_0^{*0} K^+) = (6.0 \pm 0.9) \times 10^{-3}$
PDG06	$\mathcal{B}(D^+ \rightarrow f_0(1370) \pi^+) \mathcal{B}(f_0(1370) \rightarrow \pi^+ \pi^-) = (8 \pm 6) \times 10^{-5}$	
FOCUS	$\mathcal{B}(D^+ \rightarrow f_0(1370) \pi^+) \mathcal{B}(f_0(1370) \rightarrow K^+ K^-) = (6.2 \pm 1.1) \times 10^{-4}$	
PDG06	$\mathcal{B}(D^0 \rightarrow \sigma \pi^0) \mathcal{B}(f_0 \rightarrow \pi^+ \pi^-) < 2.7 \times 10^{-5}$	$\mathcal{B}(D^0 \rightarrow \sigma \pi^0) < 4.1 \times 10^{-5}$
PDG06	$\mathcal{B}(D^0 \rightarrow f_0 \pi^0) \mathcal{B}(f_0 \rightarrow \pi^+ \pi^-) < 3.4 \times 10^{-6}$	$\mathcal{B}(D^0 \rightarrow f_0 \pi^0) < 6.4 \times 10^{-6}$
PDG06	$\mathcal{B}(D^0 \rightarrow f_0 K_s^0) \mathcal{B}(f_0 \rightarrow \pi^+ \pi^-) = (1.36^{+0.30}_{-0.22}) \times 10^{-3}$	$\mathcal{B}(D^0 \rightarrow f_0 K_s^0) = (2.6^{+0.7}_{-0.6}) \times 10^{-3}$
ARGUS,E687	$\mathcal{B}(D^0 \rightarrow f_0 \bar{K}^0) \mathcal{B}(f_0 \rightarrow \pi^+ \pi^-) = (3.2 \pm 0.9) \times 10^{-3}$	$\mathcal{B}(D^0 \rightarrow f_0 \bar{K}^0) = (6.0 \pm 2.0) \times 10^{-3}$
CLEO	$\mathcal{B}(D^0 \rightarrow f_0 \bar{K}^0) \mathcal{B}(f_0 \rightarrow \pi^+ \pi^-) = (2.5^{+0.8}_{-0.5}) \times 10^{-3}$	$\mathcal{B}(D^0 \rightarrow f_0 \bar{K}^0) = (4.7^{+1.7}_{-1.2}) \times 10^{-3}$
PDG06	$\mathcal{B}(D^0 \rightarrow f_0 K_s^0) \mathcal{B}(f_0 \rightarrow K^+ K^-) < 1.0 \times 10^{-4}$	$\mathcal{B}(D^0 \rightarrow f_0 K_s^0) < 1.3 \times 10^{-3}$
BaBar	$\mathcal{B}(D^0 \rightarrow f_0 \bar{K}^0) \mathcal{B}(f_0 \rightarrow K^+ K^-) = (1.2 \pm 0.9) \times 10^{-3}$	$\mathcal{B}(D^0 \rightarrow f_0 \bar{K}^0) = (1.5 \pm 1.1) \%$
PDG06	$\mathcal{B}(D^0 \rightarrow a_0^+ K^-) \mathcal{B}(a_0^+ \rightarrow K^+ K_s^0) = (6.1 \pm 1.8) \times 10^{-4}$	$\mathcal{B}(D^0 \rightarrow a_0^+ K^-) = (7.9 \pm 2.5) \%$
BaBar	$\mathcal{B}(D^0 \rightarrow a_0^+ K^-) \mathcal{B}(a_0^+ \rightarrow K^+ \bar{K}^0) = (3.3 \pm 0.8) \times 10^{-3}$	$\mathcal{B}(D^0 \rightarrow a_0^+ K^-) = (2.1 \pm 0.6) \%$
PDG06	$\mathcal{B}(D^0 \rightarrow a_0^- K^+) \mathcal{B}(a_0^- \rightarrow K^- K_s^0) < 1.1 \times 10^{-4}$	$\mathcal{B}(D^0 \rightarrow a_0^- K^+) < 1.4 \times 10^{-3}$
BaBar	$\mathcal{B}(D^0 \rightarrow a_0^- K^+) \mathcal{B}(a_0^- \rightarrow K^- \bar{K}^0) = (3.1 \pm 1.9) \times 10^{-4}$	$\mathcal{B}(D^0 \rightarrow a_0^- K^+) = (2.0 \pm 1.2) \times 10^{-3}$
PDG06	$\mathcal{B}(D^0 \rightarrow a_0^0 K_s^0) \mathcal{B}(a_0^0 \rightarrow K^+ K^-) = (3.0 \pm 0.4) \times 10^{-3}$	$\mathcal{B}(D^0 \rightarrow a_0^0 K_s^0) = (3.8 \pm 0.7) \%$
BaBar	$\mathcal{B}(D^0 \rightarrow a_0^0 \bar{K}^0) \mathcal{B}(a_0^0 \rightarrow K^+ K^-) = (5.9 \pm 1.3) \times 10^{-3}$	$\mathcal{B}(D^0 \rightarrow a_0^0 \bar{K}^0) = (7.6 \pm 1.9) \%$
BaBar	$\mathcal{B}(D^0 \rightarrow a_0^+ \pi^-) \mathcal{B}(a_0^+ \rightarrow K^+ \bar{K}^0) = (5.1 \pm 4.2) \times 10^{-4}$	$\mathcal{B}(D^0 \rightarrow a_0^+ \pi^-) = (3.3 \pm 2.7) \times 10^{-3}$
BaBar	$\mathcal{B}(D^0 \rightarrow a_0^- \pi^+) \mathcal{B}(a_0^- \rightarrow K^- K^0) = (1.43 \pm 1.19) \times 10^{-4}$	$\mathcal{B}(D^0 \rightarrow a_0^- \pi^+) = (9.2 \pm 7.7) \times 10^{-4}$
PDG06	$\mathcal{B}(D^0 \rightarrow K_0^{*-} \pi^+) \mathcal{B}(K_0^{*-} \rightarrow K_s^0 \pi^-) = (2.8^{+0.6}_{-0.4}) \times 10^{-3}$	$\mathcal{B}(D^0 \rightarrow K_0^{*-} \pi^+) = (9.0^{+2.3}_{-1.7}) \times 10^{-3}$
ARGUS,E687	$\mathcal{B}(D^0 \rightarrow K_0^{*-} \pi^+) \mathcal{B}(K_0^{*-} \rightarrow \bar{K}^0 \pi^-) = (7.3 \pm 1.6) \times 10^{-3}$	$\mathcal{B}(D^0 \rightarrow K_0^{*-} \pi^+) = (1.2 \pm 0.3) \%$
CLEO	$\mathcal{B}(D^0 \rightarrow K_0^{*-} \pi^+) \mathcal{B}(K_0^{*-} \rightarrow \bar{K}^0 \pi^-) = (4.3^{+1.9}_{-0.8}) \times 10^{-3}$	$\mathcal{B}(D^0 \rightarrow K_0^{*-} \pi^+) = (7.0^{+3.2}_{-1.5}) \times 10^{-3}$
PDG06	$\mathcal{B}(D^0 \rightarrow K_0^{*-} \pi^+) \mathcal{B}(K_0^{*-} \rightarrow K^- \pi^0) = (4.6 \pm 2.2) \times 10^{-3}$	$\mathcal{B}(D^0 \rightarrow K_0^{*-} \pi^+) = (1.5 \pm 0.7) \%$
CLEO	$\mathcal{B}(D^0 \rightarrow K_0^{*-} \pi^+) \mathcal{B}(K_0^{*-} \rightarrow K^- \pi^0) = (3.6 \pm 0.8) \times 10^{-3}$	$\mathcal{B}(D^0 \rightarrow K_0^{*-} \pi^+) = (1.2 \pm 0.3) \%$
PDG06	$\mathcal{B}(D^0 \rightarrow \bar{K}_0^{*0} \pi^0) \mathcal{B}(\bar{K}_0^{*0} \rightarrow K^- \pi^+) = (5.8^{+4.6}_{-1.5}) \times 10^{-3}$	$\mathcal{B}(D^0 \rightarrow \bar{K}_0^{*0} \pi^0) = (9.4^{+7.5}_{-2.6}) \times 10^{-3}$
CLEO	$\mathcal{B}(D^0 \rightarrow \bar{K}_0^{*0} \pi^0) \mathcal{B}(\bar{K}_0^{*0} \rightarrow K^- \pi^+) = (5.3^{+4.2}_{-1.4}) \times 10^{-3}$	$\mathcal{B}(D^0 \rightarrow \bar{K}_0^{*0} \pi^0) = (8.5^{+6.8}_{-2.5}) \times 10^{-3}$
PDG06	$\mathcal{B}(D^0 \rightarrow f_0(1370) K_s^0) \mathcal{B}(f_0(1370) \rightarrow \pi^+ \pi^-) = (2.5 \pm 0.6) \times 10^{-3}$	
PDG06	$\mathcal{B}(D^0 \rightarrow a_0 K_s^0) \mathcal{B}(a_0 \rightarrow \eta \pi^0) = (6.2 \pm 2.0) \times 10^{-3}$	
ARGUS,E687	$\mathcal{B}(D^0 \rightarrow f_0(1370) \bar{K}^0) \mathcal{B}(f_0(1370) \rightarrow \pi^+ \pi^-) = (4.7 \pm 1.4) \times 10^{-3}$	
CLEO	$\mathcal{B}(D^0 \rightarrow f_0(1370) \bar{K}^0) \mathcal{B}(f_0(1370) \rightarrow \pi^+ \pi^-) = (5.9^{+1.8}_{-2.7}) \times 10^{-3}$	
PDG06	$\mathcal{B}(D^0 \rightarrow f_0(1400) K_s^0) \mathcal{B}(f_0(1400) \rightarrow K^+ K^-) = (1.7 \pm 1.1) \times 10^{-4}$	
PDG06	$\mathcal{B}(D_s^+ \rightarrow f_0 \pi^+) \mathcal{B}(f_0 \rightarrow K^+ K^-) = (5.7 \pm 2.5) \times 10^{-3}$	$\mathcal{B}(D_s^+ \rightarrow f_0 \pi^+) = (7.1 \pm 3.2) \%$
E687	$\mathcal{B}(D_s^+ \rightarrow f_0 \pi^+) \mathcal{B}(f_0 \rightarrow K^+ K^-) = (4.9 \pm 2.3) \times 10^{-3}$	$\mathcal{B}(D_s^+ \rightarrow f_0 \pi^+) = (6.1 \pm 3.0) \%$
E791	$\mathcal{B}(D_s^+ \rightarrow f_0 \pi^+) \mathcal{B}(f_0 \rightarrow \pi^+ \pi^-) = (5.7 \pm 1.7) \times 10^{-3}$	$\mathcal{B}(D_s^+ \rightarrow f_0 \pi^+) = (1.1 \pm 0.4) \%$
FOCUS	$\mathcal{B}(D_s^+ \rightarrow f_0 \pi^+) \mathcal{B}(f_0 \rightarrow \pi^+ \pi^-) = (9.5 \pm 2.7) \times 10^{-3}$	$\mathcal{B}(D_s^+ \rightarrow f_0 \pi^+) = (1.8 \pm 0.6) \%$
FOCUS	$\mathcal{B}(D_s^+ \rightarrow f_0 \pi^+) \mathcal{B}(f_0 \rightarrow K^+ K^-) = (7.0 \pm 1.9) \times 10^{-3}$	$\mathcal{B}(D_s^+ \rightarrow f_0 \pi^+) = (8.8 \pm 2.6) \%$
FOCUS	$\mathcal{B}(D_s^+ \rightarrow f_0 K^+) \mathcal{B}(f_0 \rightarrow K^+ K^-) = (2.8 \pm 1.3) \times 10^{-4}$	$\mathcal{B}(D_s^+ \rightarrow f_0 K^+) = (3.5 \pm 1.7) \times 10^{-3}$
PDG06	$\mathcal{B}(D_s^+ \rightarrow \bar{K}_0^{*0} K^+) \mathcal{B}(\bar{K}_0^{*0} \rightarrow K^- \pi^+) = (4.8 \pm 2.5) \times 10^{-3}$	$\mathcal{B}(D_s^+ \rightarrow \bar{K}_0^{*0} K^+) = (7.7 \pm 4.1) \times 10^{-3}$
E687	$\mathcal{B}(D_s^+ \rightarrow \bar{K}_0^{*0} K^+) \mathcal{B}(\bar{K}_0^{*0} \rightarrow K^- \pi^+) = (4.3 \pm 2.5) \times 10^{-3}$	$\mathcal{B}(D_s^+ \rightarrow \bar{K}_0^{*0} K^+) = (6.9 \pm 4.1) \times 10^{-3}$
FOCUS	$\mathcal{B}(D_s^+ \rightarrow K_0^{*0} \pi^+) \mathcal{B}(K_0^{*0} \rightarrow K^+ \pi^-) = (1.4 \pm 0.8) \times 10^{-3}$	$\mathcal{B}(D_s^+ \rightarrow K_0^{*0} \pi^+) = (2.3 \pm 1.3) \times 10^{-3}$
E791	$\mathcal{B}(D_s^+ \rightarrow f_0(1370) \pi^+) \mathcal{B}(f_0(1370) \rightarrow \pi^+ \pi^-) = (3.3 \pm 1.2) \times 10^{-3}$	

Table 23.4: Branching fractions for various  $D \rightarrow SP$  decay modes. Experimental results are taken from Table 23.3.

Decay	Buccella <i>et al.</i> [179]	Cheng [178]	Experiment
$D^+ \rightarrow f_0 \pi^+$	$2.8 \times 10^{-4}$	$3.5 \times 10^{-4}$	$(3.6 \pm 1.1) \times 10^{-4}$
$\rightarrow f_0 K^+$	$2.3 \times 10^{-5}$	$2.2 \times 10^{-5}$	$\sim 10^{-4}$
$\rightarrow a_0^+ \bar{K}^0$	$6.4 \times 10^{-3}$	$1.7 \times 10^{-2}$	
$\rightarrow a_0^0 \pi^+$	$5.9 \times 10^{-4}$	$1.7 \times 10^{-3}$	$(3.1 \pm 0.7)\%$
$\rightarrow \sigma \pi^+$		input	$(2.1 \pm 0.5) \times 10^{-3}$
$\rightarrow \kappa \pi^+$		input	$(6.5 \pm 1.9)\%$
$\rightarrow \bar{K}_0^{*0} \pi^+$		input	$(1.8 \pm 0.3)\%$
$\rightarrow a_0^0 \pi^+$	$5.9 \times 10^{-4}$		
$\rightarrow a_0^+ \pi^0$	$1.2 \times 10^{-4}$		
$\rightarrow a_0^+ \eta$	$7.4 \times 10^{-4}$		
$\rightarrow a_0^0 K^+$	$6.2 \times 10^{-5}$		
$\rightarrow f_0 K^+$	$2.3 \times 10^{-5}$		
$D^0 \rightarrow f_0 \bar{K}^0$	$7.4 \times 10^{-4}$	input	$\sim 10^{-3} - 10^{-2}$
$\rightarrow a_0^+ K^-$	$7.8 \times 10^{-4}$	$1.1 \times 10^{-3}$	$(2.1 \pm 0.6)\%$
$\rightarrow a_0^0 \bar{K}^0$	$2.2 \times 10^{-3}$	$3.6 \times 10^{-3}$	$(7.6 \pm 1.9)\%$
$\rightarrow a_0^- K^+$	$4.0 \times 10^{-5}$	$7.9 \times 10^{-5}$	$(2.0 \pm 1.2) \times 10^{-3}$
$\rightarrow a_0^+ \pi^-$	$3.0 \times 10^{-5}$	$6.5 \times 10^{-5}$	$(3.3 \pm 2.7) \times 10^{-3}$
$\rightarrow a_0^- \pi^+$	$7.0 \times 10^{-4}$	$1.3 \times 10^{-3}$	$(9.2 \pm 7.7) \times 10^{-4}$
$\rightarrow K_0^{*-} \pi^+$		$1.1 \times 10^{-2}$	$\sim 10^{-3} - 10^{-2}$
$\rightarrow \bar{K}_0^{*0} \pi^0$		$3.7 \times 10^{-3}$	$(8.5^{+6.8}_{-2.5}) \times 10^{-3}$
$\rightarrow f_0 \pi^0$	$6.0 \times 10^{-6}$		
$\rightarrow f_0 \eta$	$4.0 \times 10^{-5}$		
$\rightarrow a_0^0 \pi^0$	$1.1 \times 10^{-4}$		
$\rightarrow a_0^0 \eta$	$1.5 \times 10^{-4}$		
$D_s^+ \rightarrow f_0 \pi^+$	1.1%	input	$(1.8 \pm 0.6)\%$
$\rightarrow f_0 K^+$	$6.9 \times 10^{-4}$	$1.2 \times 10^{-3}$	$(3.5 \pm 1.7) \times 10^{-3}$
$\rightarrow \bar{K}_0^{*0} K^+$		$1.5 \times 10^{-3}$	$(6.9 \pm 4.1) \times 10^{-3}$
$\rightarrow K_0^{*0} \pi^+$		$1.1 \times 10^{-3}$	$(2.3 \pm 1.3) \times 10^{-3}$
$\rightarrow a_0^+ K^0$	$3.0 \times 10^{-5}$		
$\rightarrow a_0^0 K^+$	$7.0 \times 10^{-5}$		
$\rightarrow a_0^+ \eta$	$7.0 \times 10^{-5}$		

where  $K_{1A}$  and  $K_{1B}$  are the strange partners of the  $a_1(1260)$  and  $b_1(1235)$ , respectively.

Two-body hadronic  $D \rightarrow AP$  decays have been studied in [182, 183, 184, 185, 186, 187, 188]. In the factorization approximation, the decay amplitudes are

$$T_A = 2 \frac{G_F}{\sqrt{2}} V_{q_1 q_2} V_{cq_3}^* a_1 f_P m_A (\varepsilon^* \cdot p_D) A_0^{D \rightarrow A}(m_P^2), \quad (23.3.49)$$

$$T_P = 2 \frac{G_F}{\sqrt{2}} V_{q_1 q_2} V_{cq_3}^* a_1 f_A m_A (\varepsilon^* \cdot p_D) F_+^{D \rightarrow P}(m_A^2), \quad (23.3.50)$$

$$C_A = 2 \frac{G_F}{\sqrt{2}} V_{q_1 q_2} V_{cq_3}^* a_2 f_P m_A (\varepsilon^* \cdot p_D) A_0^{D \rightarrow A}(m_P^2), \quad (23.3.51)$$

$$C_P = 2 \frac{G_F}{\sqrt{2}} V_{q_1 q_2} V_{cq_3}^* a_2 f_A m_A (\varepsilon^* \cdot p_D) F_+^{D \rightarrow P}(m_A^2). \quad (23.3.52)$$

When compared with experimental data, the predicted branching fractions derived from the factorizable contributions for  $D^0 \rightarrow K^- a_1^+$  and  $D^0 \rightarrow K_1^-(1270)\pi^+$  and those for  $D^0 \rightarrow \bar{K}^0 a_1^+$  and  $D^+ \rightarrow \bar{K}_1^0(1400)\pi^+$  in Refs. [182, 183, 184, 185, 186] are found to be too small by roughly factors of 5 and 2, respectively. One explanation is that the factorization approach may only be suitable for energetic two-body decays such as  $D \rightarrow PP$  and  $D \rightarrow PV$ ; for  $D \rightarrow AP$  there is very little energy release and the approximation is questionable, since the nonperturbative contributions are large. A recent analysis [188] that considers the sizable FSI effects indicated that the predictions, which are presented in Table 23.5 and Table 23.6, are improved greatly.

Table 23.5: Branching fractions for  $D \rightarrow K a_1(1260)$  and  $D \rightarrow K b_1(1235)$ . Decay modes involving a neutral K meson are given as  $K_S^0$  in PDG06 and  $\bar{K}^0$  in PDG04 which are presented as well.

Decay	Theory [188]		Experiment [3]
	without FSI	with FSI	
$D^+ \rightarrow K^0 a_1^+(1260)$	12.1%	12.1%	$(3.6 \pm 0.6)\%$ $(8.2 \pm 1.7)\%$ (PDG04)
$D^0 \rightarrow K^- a_1^+(1260)$	3.8%	6.2%	$(7.5 \pm 1.1)\%$
$D^0 \rightarrow \bar{K}^0 a_1^0(1260)$	$3.3 \times 10^{-4}$	$5.6 \times 10^{-4}$	$< 1.9\%$
$D^+ \rightarrow K^0 b_1^+(1235)$	$1.7 \times 10^{-3}$	$1.7 \times 10^{-3}$	
$D^0 \rightarrow K^- b_1^+(1235)$	$3.7 \times 10^{-6}$	$5.9 \times 10^{-6}$	
$D^0 \rightarrow \bar{K}^0 b_1^0(1235)$	$3.9 \times 10^{-4}$	$6.7 \times 10^{-4}$	

### 23.3.5 $D \rightarrow TP$ Decays

The  $J^P = 2^+$  tensor mesons  $f_2(1270)$ ,  $f'_2(1525)$ ,  $a_2(1320)$  and  $K_2^*(1430)$  form a  $SU(3)$   $1^3P_2$  nonet with quark content  $q\bar{q}$ . Hadronic charm decays to a pseudoscalar meson and a tensor meson  $f_2(1270)$ ,  $a_2(1320)$  or  $K_2^*(1430)$  were found in early experiments by ARGUS [167] and E687 [169], and more recently by E791 [171], CLEO [168], FOCUS [172] and BaBar [173], although some of these measurements do not have a compelling statistical significance. The results from various experiments are summarized in Table 23.7,

where the products of  $\mathcal{B}(D \rightarrow TP_3)$  and  $\mathcal{B}(T \rightarrow P_1P_2)$  are shown. It is evident that most of the  $D \rightarrow TP$  decays that are listed have branching fractions of order  $10^{-3}$ , even though some of them are Cabibbo-suppressed. In order to extract the branching ratios for  $D \rightarrow TP$  decays, one must use the branching fractions for the strong decays of the tensor mesons [3]:

$$\begin{aligned} \mathcal{B}(f_2(1270) \rightarrow \pi\pi) &= (84.7^{+2.5}_{-1.2})\%, & \mathcal{B}(f_2(1270) \rightarrow K\bar{K}) &= (4.6 \pm 0.4)\%, \\ \mathcal{B}(a_2(1320) \rightarrow K\bar{K}) &= (4.9 \pm 0.8)\%, & \mathcal{B}(K_2^*(1430) \rightarrow K\pi) &= (49.9 \pm 1.2)\% \\ & & & (23.3.54) \end{aligned}$$

Theoretical calculations based on the factorization hypothesis [189, 190, 191] are listed in Table 23.8, where one sees that most of the theoretical predictions are not consistent with experimental data. At first glance, some decays like  $D \rightarrow \bar{K}_2^*(1430)K$  and  $D^0 \rightarrow f_2'(1525)\bar{K}^0$  etc., appear to be kinematically not allowed since the total mass of the final state particles lies outside of the phase space for the decay. Nevertheless, they are possible because the tensor mesons have widths of order several hundred MeV [3].

### 23.3.6 Other Decay Modes

Measurements of other nonleptonic two-body modes, such as  $D \rightarrow AV$  etc., have been reported. The PDG table lists two fairly strong decay modes [3]:  $\mathcal{B}(D^+ \rightarrow \bar{K}^{*0}a_1(1260)^+) = (9.4 \pm 1.9) \times 10^{-3}$  and  $\mathcal{B}(D_s^+ \rightarrow \phi a_1(1260)^+) = (2.9 \pm 0.7)\%$ , even though the total mass of the final state mesons exceeds the available phase spaces. Given the relevant form factors, the branching fractions can be worked out in the factorization approach. However, one doubts the reliability of factorization for these modes because the nonfactorized corrections may be quite large at such small momentum transfers.

Table 23.6: Branching fractions for  $D \rightarrow K_1(1270)\pi$  and  $D \rightarrow K_1(1400)\pi$  calculated for various  $K_{1A} - K_{1B}$  mixing angles.

Decay	Theory [188]				Experiment [3]
	$-37^\circ$	$-58^\circ$	$37^\circ$	$58^\circ$	
$D^+ \rightarrow K_1^0(1270)\pi^+$	$6.4 \times 10^{-3}$	$7.8 \times 10^{-3}$	2.9%	4.7%	$< 7 \times 10^{-3}$
$D^+ \rightarrow \bar{K}_1^0(1400)\pi^+$	2.9%	4.0%	6.6%	6.6%	$(4.3 \pm 1.5)\%$
$D^0 \rightarrow K_1^-(1270)\pi^+$	$6.3 \times 10^{-3}$	$5.5 \times 10^{-3}$	$4.9 \times 10^{-4}$	$4.4 \times 10^{-5}$	$(1.12 \pm 0.31)\%$
$D^0 \rightarrow K_1^-(1400)\pi^+$	$3.7 \times 10^{-8}$	$4.2 \times 10^{-4}$	$3.0 \times 10^{-3}$	$3.2 \times 10^{-3}$	$< 1.2\%$
$D^0 \rightarrow \bar{K}_1^0(1270)\pi^0$	$8.4 \times 10^{-3}$	$8.4 \times 10^{-3}$	$8.4 \times 10^{-3}$	$8.4 \times 10^{-3}$	
$D^0 \rightarrow \bar{K}_1^0(1400)\pi^0$	$5.7 \times 10^{-3}$	$5.5 \times 10^{-3}$	$5.7 \times 10^{-3}$	$5.5 \times 10^{-3}$	$< 3.7\%$

Table 23.7: Experimental branching fractions for various  $D \rightarrow TP$  decays measured by BaBar, CLEO, E791, FOCUS and PDG06. For simplicity and convenience, we have dropped mass identifications for the  $f_2(1270)$ ,  $a_2(1320)$  and  $K_2^*(1430)$ .

Collaboration	$\mathcal{B}(D \rightarrow TP) \times \mathcal{B}(T \rightarrow P_1 P_2)$	$\mathcal{B}(D \rightarrow TP)$
PDG06	$\mathcal{B}(D^+ \rightarrow f_2 \pi^+) \mathcal{B}(f_2 \rightarrow \pi^+ \pi^-) = (4.8 \pm 1.3) \times 10^{-4}$	$\mathcal{B}(D^+ \rightarrow f_2 \pi^+) = (8.5 \pm 2.3) \times 10^{-4}$
E791	$\mathcal{B}(D^+ \rightarrow f_2 \pi^+) \mathcal{B}(f_2 \rightarrow \pi^+ \pi^-) = (6.0 \pm 1.1) \times 10^{-4}$	$\mathcal{B}(D^+ \rightarrow f_2 \pi^+) = (1.1 \pm 0.2) \times 10^{-3}$
FOCUS	$\mathcal{B}(D^+ \rightarrow f_2 \pi^+) \mathcal{B}(f_2 \rightarrow \pi^+ \pi^-) = (3.8 \pm 0.8) \times 10^{-5}$	$\mathcal{B}(D^+ \rightarrow f_2 \pi^+) = (6.8 \pm 1.4) \times 10^{-4}$
FOCUS	$\mathcal{B}(D^+ \rightarrow f_2 \pi^+) \mathcal{B}(f_2 \rightarrow K^+ K^-) = (7.0 \pm 1.9) \times 10^{-5}$	$\mathcal{B}(D^+ \rightarrow f_2 \pi^+) = (3.1 \pm 0.9) \times 10^{-3}$
PDG06	$\mathcal{B}(D^+ \rightarrow K_2^{*0} \pi^+) \mathcal{B}(K_2^{*0} \rightarrow K^+ \pi^-) = (5.2 \pm 3.5) \times 10^{-5}$	$\mathcal{B}(D^+ \rightarrow K_2^{*0} \pi^+) = (1.6 \pm 1.1) \times 10^{-4}$
E791	$\mathcal{B}(D^+ \rightarrow \bar{K}_2^{*0} \pi^+) \mathcal{B}(\bar{K}_2^{*0} \rightarrow K^- \pi^+) = (4.6 \pm 2.0) \times 10^{-4}$	$\mathcal{B}(D^+ \rightarrow \bar{K}_2^{*0} \pi^+) = (1.4 \pm 0.6) \times 10^{-3}$
PDG06	$\mathcal{B}(D^+ \rightarrow a_2^+ K_S^0) < 1.5 \times 10^{-3}$	
PDG06	$\mathcal{B}(D^0 \rightarrow f_2 K_S^0) \mathcal{B}(f_2 \rightarrow \pi^+ \pi^-) = (1.3^{+1.1}_{-0.7}) \times 10^{-4}$	$\mathcal{B}(D^0 \rightarrow f_2 K_S^0) = (2.3^{+2.0}_{-1.3}) \times 10^{-4}$
CLEO	$\mathcal{B}(D^0 \rightarrow f_2 \bar{K}^0) \mathcal{B}(f_2 \rightarrow \pi^+ \pi^-) = (1.6^{+2.4}_{-1.3}) \times 10^{-4}$	$\mathcal{B}(D^0 \rightarrow f_2 \bar{K}^0) = (2.8^{+4.3}_{-2.3}) \times 10^{-3}$
BaBar	$\mathcal{B}(D^0 \rightarrow a_2^- \pi^+) \mathcal{B}(a_2^- \rightarrow K^0 K^-) = (3.5 \pm 2.1) \times 10^{-5}$	$\mathcal{B}(D^0 \rightarrow a_2^- \pi^+) = (7.0 \pm 4.3) \times 10^{-4}$
PDG06	$\mathcal{B}(D^0 \rightarrow K_2^{*-} \pi^+) \mathcal{B}(K_2^{*-} \rightarrow K_S^0 \pi^-) = (3.2^{+2.1}_{-1.1}) \times 10^{-4}$	$\mathcal{B}(D^0 \rightarrow K_2^{*-} \pi^+) = (2.0^{+1.3}_{-0.7}) \times 10^{-3}$
CLEO	$\mathcal{B}(D^0 \rightarrow K_2^{*-} \pi^+) \mathcal{B}(K_2^{*-} \rightarrow \bar{K}^0 \pi^-) = (6.5^{+4.2}_{-2.2}) \times 10^{-4}$	$\mathcal{B}(D^0 \rightarrow K_2^{*-} \pi^+) = (2.0^{+1.3}_{-0.7}) \times 10^{-3}$
BaBar	$\mathcal{B}(D^0 \rightarrow K_2^{*+} K^-) \mathcal{B}(K_2^{*+} \rightarrow K^0 \pi^+) = (6.8 \pm 4.2) \times 10^{-4}$	$\mathcal{B}(D^0 \rightarrow K_2^{*+} K^-) = (2.0 \pm 1.3) \times 10^{-3}$
BaBar	$\mathcal{B}(D^0 \rightarrow \bar{K}_2^{*0} K^0) \mathcal{B}(\bar{K}_2^{*0} \rightarrow K^- \pi^+) = (6.6 \pm 2.7) \times 10^{-4}$	$\mathcal{B}(D^0 \rightarrow \bar{K}_2^{*0} K^0) = (2.0 \pm 0.8) \times 10^{-3}$
PDG06	$\mathcal{B}(D^0 \rightarrow a_2^+ K^-) < 2 \times 10^{-3}$	
PDG06	$\mathcal{B}(D_s^+ \rightarrow f_2 \pi^+) \mathcal{B}(f_2 \rightarrow \pi^+ \pi^-) = (1.2 \pm 0.7) \times 10^{-3}$	$\mathcal{B}(D_s^+ \rightarrow f_2 \pi^+) = (2.1 \pm 1.3) \times 10^{-3}$
E791	$\mathcal{B}(D_s^+ \rightarrow f_2 \pi^+) \mathcal{B}(f_2 \rightarrow \pi^+ \pi^-) = (2.0 \pm 0.7) \times 10^{-3}$	$\mathcal{B}(D_s^+ \rightarrow f_2 \pi^+) = (3.5 \pm 1.2) \times 10^{-3}$
FOCUS	$\mathcal{B}(D_s^+ \rightarrow f_2 \pi^+) \mathcal{B}(f_2 \rightarrow \pi^+ \pi^-) = (1.0 \pm 0.3) \times 10^{-3}$	$\mathcal{B}(D_s^+ \rightarrow f_2 \pi^+) = (1.8 \pm 0.5) \times 10^{-3}$
FOCUS	$\mathcal{B}(D_s^+ \rightarrow f_2 K^+) \mathcal{B}(f_2 \rightarrow \pi^+ \pi^-) = (2.0 \pm 1.3) \times 10^{-4}$	$\mathcal{B}(D_s^+ \rightarrow f_2 K^+) = (3.5 \pm 2.3) \times 10^{-4}$

Table 23.8: Branching fractions for various  $D \rightarrow TP$  decays. Experimental results are taken from Table 23.7.

Decay	Katoch <i>et al.</i> [189]	Muñoz <i>et al.</i> [190]	Cheng [191]		Experiment
			without FSIs	with FSIs	
$D^+ \rightarrow f_2(1270) \pi^+$		$7.97 \times 10^{-6}$	$2.9 \times 10^{-5}$	$2.2 \times 10^{-4}$	$(0.9 \pm 0.1) \times 10^{-3}$
$D^0 \rightarrow f_2(1270) \pi^0$		$2.47 \times 10^{-7}$			
$D^0 \rightarrow f_2(1270) \bar{K}^0$	$9.0 \times 10^{-5}$		$1.0 \times 10^{-4}$	$2.5 \times 10^{-4}$	$(4.5 \pm 1.7) \times 10^{-3}$
$D_s^+ \rightarrow f_2(1270) \pi^+$	$3.6 \times 10^{-4}$		$6.6 \times 10^{-5}$	$2.1 \times 10^{-3}$	$(2.1 \pm 0.5) \times 10^{-3}$
$\rightarrow f_2(1270) K^+$			$5.2 \times 10^{-6}$	$4.9 \times 10^{-5}$	$(3.5 \pm 2.3) \times 10^{-4}$
$D^+ \rightarrow f'_2(1525) \pi^+$		$7.18 \times 10^{-9}$	$1.4 \times 10^{-6}$	$3.7 \times 10^{-6}$	
$D^0 \rightarrow f'_2(1525) \pi^0$		$2.18 \times 10^{-10}$			
$D^0 \rightarrow f'_2(1525) \bar{K}^0$			$2.5 \times 10^{-7}$	$6.0 \times 10^{-7}$	
$D_s^+ \rightarrow f'_2(1525) \pi^+$	$1.3 \times 10^{-2}$		$1.6 \times 10^{-4}$	$1.5 \times 10^{-4}$	
$\rightarrow f'_2(1525) K^+$			$4.9 \times 10^{-6}$	$7.5 \times 10^{-6}$	
$D^+ \rightarrow a_2^+(1320) \pi^0$		$9.05 \times 10^{-7}$			
$D^+ \rightarrow a_2^0(1320) \pi^+$		$5.55 \times 10^{-6}$			
$D^+ \rightarrow a_2^+(1320) \bar{K}^0$	$1.1 \times 10^{-4}$		$1.3 \times 10^{-6}$	$1.3 \times 10^{-6}$	$< 3 \times 10^{-3}$
$D^0 \rightarrow a_2^-(1320) \pi^+$		$4.21 \times 10^{-6}$	$5.7 \times 10^{-6}$	$6.1 \times 10^{-6}$	$(7.0 \pm 4.3) \times 10^{-4}$
$\rightarrow a_2^0(1320) \pi^0$		$1.72 \times 10^{-7}$			
$\rightarrow a_2^+(1320) K^-$	0		0	$8.9 \times 10^{-8}$	$< 2 \times 10^{-3}$
$\rightarrow a_2^0(1320) \bar{K}^0$	$1.7 \times 10^{-5}$				
$D^+ \rightarrow K_2^{*0}(1430) \pi^+$	$9.9 \times 10^{-3}$		$2.6 \times 10^{-4}$	$2.6 \times 10^{-4}$	$(1.4 \pm 0.6) \times 10^{-3}$
$D^0 \rightarrow K_2^{*-}(1430) \pi^+$	$4.1 \times 10^{-3}$		$1.0 \times 10^{-4}$	$1.1 \times 10^{-4}$	$(2.0^{+1.3}_{-0.7}) \times 10^{-3}$
$\rightarrow \bar{K}_2^{*0}(1430) \pi^0$	0		0	$1.3 \times 10^{-5}$	$< 3.4 \times 10^{-3}$
$\rightarrow K_2^{*+}(1430) K^-$			0	$1.3 \times 10^{-6}$	$(2.0 \pm 1.3) \times 10^{-3}$
$\rightarrow \bar{K}_2^{*0}(1430) K^0$			0	$\sim 10^{-8}$	$(2.0 \pm 0.8) \times 10^{-3}$
$D_s^+ \rightarrow \bar{K}_2^{*0}(1430) K^+$	0				
$\rightarrow \bar{K}_2^{*+}(1430) \bar{K}^0$	$4.2 \times 10^{-5}$				

## 23.4 Three-Body Decays

### 23.4.1 Kinematics and Dalitz Plot

Starting from Eq. 23.3.24 and integrating over the solid angles, the decay rate for  $D \rightarrow M_1 M_2 M_3$  can be obtained

$$d\Gamma = \frac{1}{(2\pi)^3} \frac{1}{32m_D^3} |\mathcal{A}|^2 dm_{12}^2 dm_{23}^2 , \quad (23.4.55)$$

where  $m_{ij}$  is the invariant mass of particles  $i$  and  $j$ . For a given value of  $m_{12}^2$  in the range  $(m_1 + m_2)^2 \leq m_{12}^2 \leq (m_D - m_3)^2$ , the upper and lower bounds of  $m_{23}^2$  are determined

$$(m_{23}^2)_{max} = (E_2^* + E_3^*)^2 - (\sqrt{E_2^{*2} - m_2^2} - \sqrt{E_3^{*2} - m_3^2})^2 , \quad (23.4.56)$$

$$(m_{23}^2)_{min} = (E_2^* + E_3^*)^2 - (\sqrt{E_2^{*2} - m_2^2} + \sqrt{E_3^{*2} - m_3^2})^2 . \quad (23.4.57)$$

Here  $E_2^*$  and  $E_3^*$  are the respective energies of final state mesons  $M_2$  and  $M_3$  in the rest frames of  $M_1$  and  $M_2$ :

$$E_2^* = \frac{m_{12}^2 - m_1^2 + m_2^2}{2m_{12}} , \quad (23.4.58)$$

$$E_3^* = \frac{m_D^2 - m_{12}^2 - m_2^2}{2m_{12}} . \quad (23.4.59)$$

The scatter plot of  $m_{12}^2$  versus  $m_{23}^2$  is called the Dalitz plot. For a detailed introduction of Dalitz plot techniques, please refer to Chapter 4 and Ref. [192]. The amplitude  $|\mathcal{A}|^2$  of a nonresonant decay is parameterized as a constant without variation in magnitude or phase across the Dalitz plot, in which case the allowed region of the plot is uniformly populated with events. A nonuniformity with bands near the mass of the resonance in the plot will reflect the influence of a resonance contribution. One can find a review of Dalitz plot applications specific to charm decays in Ref. [193].

### 23.4.2 Resonant Three-Body Decays

Charmed meson three-body decays proceed dominantly via quasi-two-body decays containing an intermediate resonance state that subsequently decays into two particles. The analysis of these resonant decays using Dalitz plot techniques enables one to study the dynamical properties of various resonances. In theoretical studies, resonant decays are often divided into the product of two subprocesses:  $\mathcal{B}(D \rightarrow RM_3) \times \mathcal{B}(R \rightarrow M_1 M_2)$ , just as we have shown in Section 23.3. In this case we reduce the multi-body decay into a pair of two-body decays.

### 23.4.3 Nonresonant Three-Body Decays

The nonresonant contribution is usually a small fraction of the total three-body decay rate. Experimentally, they are hard to measure since the interference between nonresonant and quasi-two-body amplitudes makes it difficult to disentangle these two distinct

contributions and, then, extract the nonresonant one. Theoretically, the matrix element for  $D$  decaying into three mesons in general has two different formalisms in the factorization approximation that differ on how the three final mesons are distributed into two “clusters”.

For one type with a “cluster” where  $D$  transits to a light meson, one has

$$\langle M_1 M_2 M_3 | J_{i\mu} J_i'^\mu | D \rangle \sim \langle M_1 M_2 | J_{i\mu} | 0 \rangle \langle M_3 | J_i'^\mu | D \rangle. \quad (23.4.60)$$

Here it is evident that its contribution is negligibly small since the matrix element  $\langle M_1 M_2 | J_{i\mu} | 0 \rangle$ , which also appears in the factorizable contributions of weak annihilation in two-body decays, vanishes in the chiral limit.

For the other type of “clustering” where  $D$  transits to two light mesons, the factorized formula is

$$\langle M_1 M_2 M_3 | J_{i\mu} J_i'^\mu | D \rangle \sim \langle M_1 | J_{i\mu} | 0 \rangle \langle M_2 M_3 | J_i'^\mu | D \rangle, \quad (23.4.61)$$

where a matrix element  $\langle M_2 M_3 | J_i'^\mu | D \rangle$  is introduced. This has the general form [194]

$$\begin{aligned} \langle M_2(p_2) M_3(p_3) | J_i'^\mu | D(p_D) \rangle = & \quad i r (p_D - p_2 - p_3)^\mu + i \omega_+ (p_2 + p_3)^\mu + i \omega_- (p_3 - p_2)^\mu \\ & + h \epsilon^{\mu\nu\alpha\beta} p_{D\nu} (p_2 + p_3)_\alpha (p_3 - p_2)_\beta, \end{aligned} \quad (23.4.62)$$

where  $r$ ,  $\omega_\pm$  and  $h$  are form factors. In general these receive two distinct contributions: one from the point-like weak transition and the other from the pole diagrams that involve four-point strong vertices. Models based on chiral symmetry and heavy quark effective theory have been developed to make some estimates of them [194, 195, 196].

Charmed meson to three pseudoscalar nonresonant decays have been studied in the approach of an effective  $SU(4)_L \times SU(4)_R$  chiral Lagrangian [197, 198, 199, 200, 201]. For these, the predictions of the branching ratios are in general smaller than experimental measurements. With the advent of heavy meson chiral perturbation theory (HMChPT) [202, 203, 204], nonresonant  $D$  decays can be studied reliably at least in the kinematical region where the final pseudoscalar mesons are soft [205, 206, 207]. Some theoretical results are collected in Table 23.9.

#### 23.4.4 Beyond Three-Body Decays

Some multi-body charm meson decays, up to seven-body, have been experimentally measured [3]. However, the available theoretical tools lose much of their power when applied to genuine multi-body transitions. The kinematic structure and strong dynamics becomes more-and-more complicated and ultimately gets out of control when the number of final-state particles increases.

Table 23.9: Branching fractions (in %) for nonresonant three-body  $D$  decays from various models. Most decay modes involving a neutral K meson are given as  $K_S^0$  in PDG06 and  $\bar{K}^0$  in PDG04, which are presented as well.

Decay mode	Chau <i>et al.</i> [200]	Botella <i>et al.</i> [201]	Cheng <i>et al.</i> [207]	PDG 06/04
$D^0 \rightarrow \bar{K}^0 \pi^+ \pi^-$	0.13	0.19	0.03 ; 0.17	$0.026^{+0.059}_{-0.016}$ $0.054^{+0.120}_{-0.034}$ ( <i>pdg04</i> ) $1.13^{+0.54}_{-0.20}$
$\rightarrow K^- \pi^+ \pi^0$	0.18	0.76	0.61 ; 0.28	
$\rightarrow \bar{K}^0 K^+ K^-$	0.02	0.006	0.16 ; 0.01	
$\rightarrow \pi^+ \pi^- \pi^0$	0.04	0.11		
$\rightarrow K^+ K^- \pi^0$		0.013		
$\rightarrow K^0 K^- \pi^+$		0.007		
$\rightarrow \bar{K}^0 K^+ \pi^-$		0.013		$0.11 \pm 0.11$ $0.23 \pm 0.23$ ( <i>pdg04</i> ) $0.19^{+0.11}_{-0.08}$ $0.38^{+0.23}_{-0.19}$ ( <i>pdg04</i> ) $0.42 \pm 0.11$ $0.85 \pm 0.22$ ( <i>pdg04</i> )
$\rightarrow \bar{K}^0 \pi^0 \pi^0$				
$D^+ \rightarrow K^0 \pi^+ \pi^0$	0.76	1.9	1.5; 0.7	$0.9 \pm 0.7$ $1.3 \pm 1.1$ ( <i>pdg04</i> ) $9.0 \pm 0.7$
$\rightarrow K^- \pi^+ \pi^+$	1.71	0.95	6.5 ; 1.6	
$\rightarrow \pi^+ \pi^+ \pi^-$	0.15	0.19	0.50 ; 0.067	
$\rightarrow K^- K^+ \pi^+$	0.02	0.016	0.48 ; 0.004	
$\rightarrow K^+ \pi^+ \pi^-$		0.0032		
$\rightarrow K^+ K^+ K^-$		$1.58 \times 10^{-5}$		
$\rightarrow \pi^+ \eta \eta$		0.016 ; 0.032		
$\rightarrow \pi^+ \eta \eta'$		0.032		
$D_s^+ \rightarrow K^- K^+ \pi^+$	0.42	0.32	1.0 ; 0.69	
$\rightarrow \pi^+ \pi^+ \pi^-$	$5 \times 10^{-5}$	$4.7 \times 10^{-4}$		
$\rightarrow \pi^+ \pi^0 \eta$		1.1 ; 0.95		
$\rightarrow \pi^+ \pi^0 \eta'$		0.158		
$\rightarrow K^+ \pi^+ \pi^-$		0.047		
				$< 5$ $< 1.8$ $0.1 \pm 0.04$



# Chapter 24

## Charm baryon production and decays<sup>1</sup>

### 24.1 Introduction

In the past years many new excited charmed baryon states have been discovered by BaBar, Belle and CLEO. In particular,  $B$  factories have provided a very rich source of charmed baryons both from  $B$  decays and from the continuum  $e^+e^- \rightarrow c\bar{c}$ . A new chapter for the charmed baryon spectroscopy is opened by the rich mass spectrum and the relatively narrow widths of the excited states. Experimentally and theoretically, it is important to identify the quantum numbers of these new states and understand their properties. Since the pseudoscalar mesons involved in the strong decays of charmed baryons are soft, the charmed baryon system offers an excellent ground for testing the ideas and predictions of heavy quark symmetry of the heavy quark and chiral symmetry of the light quarks.

The observation of the lifetime differences among the charmed mesons  $D^+$ ,  $D^0$  and charmed baryons is very interesting since it was realized very early that the naive parton model gives the same lifetimes for all heavy particles containing a heavy quark  $Q$ , while experimentally, the lifetimes of  $\Xi_c^+$  and  $\Omega_c^0$  differ by a factor of six ! This implies the importance of the underlying mechanisms such as  $W$ -exchange and Pauli interference due to the identical quarks produced in the heavy quark decay and in the wavefunction of the charmed baryons. With the advent of heavy quark effective theory, it was recognized in early nineties that nonperturbative corrections to the parton picture can be systematically expanded in powers of  $1/m_Q$ . Within the QCD-based heavy quark expansion framework, some phenomenological assumptions can be turned into some coherent and quantitative statements and nonperturbative effects can be systematically studied.

Contrary to the significant progress made over the last 20 years or so in the studies of the heavy meson weak decay, advancement in the arena of heavy baryons is relatively slow. Nevertheless, the experimental measurements of the charmed baryon hadronic weak decays have been pushed to the Cabibbo-suppressed level. Many new data emerged can be used to test a handful of phenomenological models available in the literature. Apart from the complication due to the presence of three quarks in the baryon, a major

---

<sup>1</sup>By Hai-Yang Cheng

disparity between charmed baryon and charmed meson decays is that while the latter is usually dominated by factorizable amplitudes, the former receives sizable nonfactorizable contributions from  $W$ -exchange diagrams which are not subject to color and helicity suppression. Besides the dynamical models, there are also some considerations based on the symmetry argument and the quark diagram scheme.

The exclusive semileptonic decays of charmed baryons like  $\Lambda_c^+ \rightarrow \Lambda e^+(\mu^+) \nu_e$ ,  $\Xi_c^+ \rightarrow \Xi^0 e^+ \nu_e$  and  $\Xi_c^0 \rightarrow \Xi^- e^+ \nu_e$  have been observed experimentally. Their rates depend on the heavy baryon to the light baryon transition form factors. Experimentally, the only information available so far is the form-factor ratio measured in the semileptonic decay  $\Lambda_c \rightarrow \Lambda e \bar{\nu}$ .

Although radiative decays are well measured in the charmed meson sector, e.g.  $D^* \rightarrow D\gamma$  and  $D_s^+ \rightarrow D_s^+ \gamma$ , only three of the radiative modes in the charmed baryon sector have been observed, namely,  $\Xi_c'^0 \rightarrow \Xi_c^0 \gamma$ ,  $\Xi_c^+ \rightarrow \Xi_c^+ \gamma$  and  $\Omega_c^{*0} \rightarrow \Omega_c^0 \gamma$ . Charm flavor is conserved in these electromagnetic charmed baryon decays. However, it will be difficult to measure the rates of these decays because these states are too narrow to be experimentally resolvable. There are also charm-flavor-conserving weak radiative decays such as  $\Xi_c \rightarrow \Lambda_c \gamma$  and  $\Omega_c \rightarrow \Xi_c \gamma$ . In these decays, weak radiative transitions arise from the diquark sector of the heavy baryon whereas the heavy quark behaves as a “spectator”. The charm-flavor-violating weak radiative decays, e.g.,  $\Lambda_c^+ \rightarrow \Sigma^+ \gamma$  and  $\Xi_c^0 \rightarrow \Xi^0 \gamma$ , arise from the  $W$ -exchange diagram accompanied by a photon emission from the external quark.

Two excellent review articles on charmed baryons can be found in Refs. [208, 209].

## 24.2 Production of charmed baryons at *BES-III*

Production and decays of the charmed baryons can be studied at *BES-III* once its center-of-mass energy  $\sqrt{s}$  is upgraded to the level above 4.6 GeV. In order to estimate the number of charmed baryon events produced at *BES-III*, it is necessary to know its luminosity, the cross section  $\sigma(e^+e^- \rightarrow c\bar{c})$  at the energies of interest and the fragmentation function of the  $c$  quark into the charmed baryon.

## 24.3 Spectroscopy

Charmed baryon spectroscopy provides an ideal place for studying the dynamics of the light quarks in the environment of a heavy quark. The charmed baryon of interest contains a charmed quark and two light quarks, which we will often refer to as a diquark. Each light quark is a triplet of the flavor SU(3). Since  $\mathbf{3} \times \mathbf{3} = \bar{\mathbf{3}} + \mathbf{6}$ , there are two different SU(3) multiplets of charmed baryons: a symmetric sextet **6** and an antisymmetric antitriplet **3**. For the ground-state  $s$ -wave baryons in the quark model, the symmetries in the flavor and spin of the diquarks are correlated. Consequently, the diquark in the flavor-symmetric sextet has spin 1, while the diquark in the flavor-antisymmetric antitriplet has spin 0. When the diquark combines with the charmed quark, the sextet contains both spin 1/2 and spin 3/2 charmed baryons. However, the antitriplet contains only spin 1/2 ones. More specifically, the  $\Lambda_c^+$ ,  $\Xi_c^+$  and  $\Xi_c^0$  form a **3** representation and they all decay weakly. The  $\Omega_c^0$ ,  $\Xi_c'^+$ ,  $\Xi_c'^0$  and  $\Sigma_c^{++,+,0}$  form a **6** representation; among them, only  $\Omega_c^0$  decays weakly.

Note that we follow the Particle Data Group (PDG) [3] to use a prime to distinguish the  $\Xi_c$  in the **6** from the one in the  $\bar{\mathbf{3}}$ .

The lowest-lying orbital excited baryon states are the  $p$ -wave charmed baryons with their quantum numbers listed in Table 24.1. Although the separate spin angular momentum  $S_\ell$  and orbital angular momentum  $L_\ell$  of the light degrees of freedom are not well defined, they are included for guidance from the quark model. In the heavy quark limit, the spin of the charmed quark  $S_c$  and the total angular momentum of the two light quarks  $J_\ell = S_\ell + L_\ell$  are separately conserved. It is convenient to use them to enumerate the spectrum of states. There are two types of  $L_\ell = 1$  orbital excited charmed baryon states: states with the unit of orbital angular momentum between the diquark and the charmed quark, and states with the unit of orbital angular momentum between the two light quarks. The orbital wave function of the former (latter) is symmetric (antisymmetric) under the exchange of two light quarks. To see this, one can define two independent relative momenta  $\mathbf{k} = \frac{1}{2}(\mathbf{p}_1 - \mathbf{p}_2)$  and  $\mathbf{K} = \frac{1}{2}(\mathbf{p}_1 - \mathbf{p}_2 - 2\mathbf{p}_c)$  from the two light quark momenta  $\mathbf{p}_1, \mathbf{p}_2$  and the heavy quark momentum  $\mathbf{p}_c$ . (In the heavy quark limit,  $\mathbf{p}_c$  can be set to zero.) Denoting the quantum numbers  $L_k$  and  $L_K$  as the eigenvalues of  $\mathbf{L}_k^2$  and  $\mathbf{L}_K^2$ , the  $k$ -orbital momentum  $L_k$  describes relative orbital excitations of the two light quarks, and the  $K$ -orbital momentum  $L_K$  describes orbital excitations of the center of the mass of the two light quarks relative to the heavy quark [208]. The  $p$ -wave heavy baryon can be either in the  $(L_k = 0, L_K = 1)$   $K$ -state or the  $(L_k = 1, L_K = 0)$   $k$ -state. It is obvious that the orbital  $K$ -state ( $k$ -state) is symmetric (antisymmetric) under the interchange of  $\mathbf{p}_1$  and  $\mathbf{p}_2$ .

Table 24.1: The  $p$ -wave charmed baryons and their quantum numbers, where  $S_\ell$  ( $J_\ell$ ) is the total spin (angular momentum) of the two light quarks. The quantum number in the subscript labels  $J_\ell$ . The quantum number in parentheses is referred to the spin of the baryon. In the quark model, the upper (lower) four multiplets have even (odd) orbital wave functions under the permutation of the two light quarks. That is,  $L_\ell$  for the former is referred to the orbital angular momentum between the diquark and the charmed quark, while  $L_\ell$  for the latter is the orbital angular momentum between the two light quarks. The explicit quark model wave functions for  $p$ -wave charmed baryons can be found in [210].

State	SU(3)	$S_\ell$	$L_\ell$	$J_\ell^{P_\ell}$	State	SU(3)	$S_\ell$	$L_\ell$	$J_\ell^{P_\ell}$
$\Lambda_{c1}(\frac{1}{2}, \frac{3}{2})$	<b>3</b>	0	1	$1^-$	$\Xi_{c1}(\frac{1}{2}, \frac{3}{2})$	<b>3</b>	0	1	$1^-$
$\Sigma_{c0}(\frac{1}{2})$	<b>6</b>	1	1	$0^-$	$\Xi'_{c0}(\frac{1}{2})$	<b>6</b>	1	1	$0^-$
$\Sigma_{c1}(\frac{1}{2}, \frac{3}{2})$	<b>6</b>	1	1	$1^-$	$\Xi'_{c1}(\frac{1}{2}, \frac{3}{2})$	<b>6</b>	1	1	$1^-$
$\Sigma_{c2}(\frac{3}{2}, \frac{5}{2})$	<b>6</b>	1	1	$2^-$	$\Xi'_{c2}(\frac{3}{2}, \frac{5}{2})$	<b>6</b>	1	1	$2^-$
$\tilde{\Sigma}_{c1}(\frac{1}{2}, \frac{3}{2})$	<b>6</b>	0	1	$1^-$	$\tilde{\Xi}'_{c1}(\frac{1}{2}, \frac{3}{2})$	<b>6</b>	0	1	$1^-$
$\tilde{\Lambda}_{c0}(\frac{1}{2})$	<b>3</b>	1	1	$0^-$	$\tilde{\Xi}_{c0}(\frac{1}{2})$	<b>3</b>	1	1	$0^-$
$\tilde{\Lambda}_{c1}(\frac{1}{2}, \frac{3}{2})$	<b>3</b>	1	1	$1^-$	$\tilde{\Xi}_{c1}(\frac{1}{2}, \frac{3}{2})$	<b>3</b>	1	1	$1^-$
$\tilde{\Lambda}_{c2}(\frac{3}{2}, \frac{5}{2})$	<b>3</b>	1	1	$2^-$	$\tilde{\Xi}_{c2}(\frac{3}{2}, \frac{5}{2})$	<b>3</b>	1	1	$2^-$

The observed mass spectra and decay widths of charmed baryons are summarized

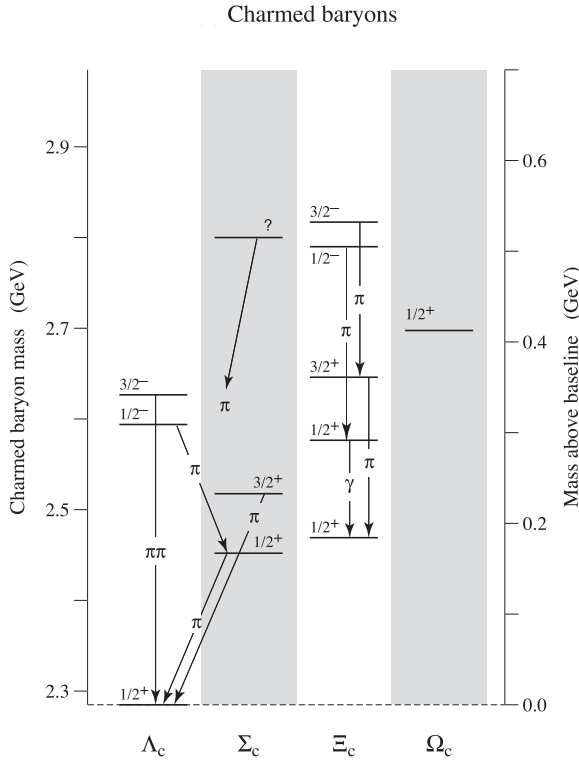


Figure 24.1: Charmed baryons and some of their orbital excitations [3].

in Table 24.2 (see also Fig. 24.1).  $B$  factories have provided a very rich source of charmed baryons both from  $B$  decays and from the continuum  $e^+e^- \rightarrow c\bar{c}$ . For example, several new excited charmed baryon states such as  $\Lambda_c(2765)^+$ ,  $\Lambda_c(2880)^+$ ,  $\Lambda_c(2940)^+$ ,  $\Xi_c(2815)$ ,  $\Xi_c(2980)$  and  $\Xi_c(3077)$  have been measured recently and they are not still not in the list of 2006 Particle Data Group [3]. By now, the  $J^P = \frac{1}{2}^+$  and  $\frac{1}{2}^- \bar{\mathbf{3}}$  states:  $(\Lambda_c^+, \Xi_c^+, \Xi_c^0)$ ,  $(\Lambda_c(2593)^+, \Xi_c(2790)^+, \Xi_c(2790)^0)$ , and  $J^P = \frac{1}{2}^+$  and  $\frac{3}{2}^+ \mathbf{6}$  states:  $(\Omega_c, \Sigma_c, \Xi_c')$ ,  $(\Omega_c^*, \Sigma_c^*, \Xi_c^*)$  are established. Notice that except for the parity of the lightest  $\Lambda_c^+$ , none of the other  $J^P$  quantum numbers given in Table 24.2 has been measured. One has to rely on the quark model to determine the  $J^P$  assignments.

In the following we discuss some of the new excited charmed baryon states:

- The highest  $\Lambda_c(2940)^+$  was first discovered by BaBar in the  $D^0 p$  decay mode [211] and confirmed by Belle in the decays  $\Sigma_c^0 \pi^+$ ,  $\Sigma_c^{++} \pi^-$  which subsequently decay into  $\Lambda_c^+ \pi^+ \pi^-$  [212, 213]. The state  $\Lambda_c(2880)^+$  first observed by CLEO [214] in  $\Lambda_c^+ \pi^+ \pi^-$  was also seen by BaBar in the  $D^0 p$  spectrum [211]. It was originally conjectured that, based on its narrow width,  $\Lambda_c(2880)^+$  might be a  $\tilde{\Lambda}_{c0}^+(\frac{1}{2})$  state [214]. Recently, Belle has studied the experimental constraint on the  $J^P$  quantum numbers of  $\Lambda_c(2880)^+$  [212]. The angular analysis of  $\Lambda_c(2880)^+ \rightarrow \Sigma_c^{0,++} \pi^\pm$  indicates that  $J = 5/2$  is favored over  $J = 1/2$  or  $3/2$ , while the study of the resonant structure of  $\Lambda_c(2880)^+ \rightarrow \Lambda_c^+ \pi^+ \pi^-$  implies the existence of the  $\Sigma_c^* \pi$  intermediate states and  $\Gamma(\Sigma_c^* \pi^\pm) / \Gamma(\Sigma_c \pi^\pm) = (24.1 \pm 6.4^{+1.1}_{-4.5})\%$ . This value is in agreement with heavy quark symmetry predictions [215] and favors the  $5/2^+$  over the  $5/2^-$  assignment.<sup>2</sup> There-

<sup>2</sup>Strictly speaking, the argument in favor of the  $5/2^+$  assignment is reached in [212] by considering

Table 24.2: Mass spectra and decay widths (in units of MeV) of charmed baryons. Experimental values are taken from the Particle Data Group [3] except  $\Lambda_c(2880)$ ,  $\Lambda_c(2940)$ ,  $\Xi_c(2980)^{+,0}$ ,  $\Xi_c(3077)^{+,0}$  and  $\Omega_c(2768)$  for which we use the most recent available BaBar and Belle measurements.

State	Quark content	$J^P$	Mass	Width
$\Lambda_c^+$	$udc$	$\frac{1}{2}^+$	$2286.46 \pm 0.14$	
$\Lambda_c(2593)^+$	$udc$	$\frac{1}{2}^-$	$2595.4 \pm 0.6$	$3.6^{+2.0}_{-1.3}$
$\Lambda_c(2625)^+$	$udc$	$\frac{3}{2}^-$	$2628.1 \pm 0.6$	$< 1.9$
$\Lambda_c(2765)^+$	$udc$	??	$2766.6 \pm 2.4$	50
$\Lambda_c(2880)^+$	$udc$	$\frac{5}{2}^+$	$2881.5 \pm 0.3$	$5.5 \pm 0.6$
$\Lambda_c(2940)^+$	$udc$	??	$2938.8 \pm 1.1$	$13.0 \pm 5.0$
$\Sigma_c(2455)^{++}$	$uuc$	$\frac{1}{2}^+$	$2454.02 \pm 0.18$	$2.23 \pm 0.30$
$\Sigma_c(2455)^+$	$udc$	$\frac{1}{2}^+$	$2452.9 \pm 0.4$	$< 4.6$
$\Sigma_c(2455)^0$	$ddc$	$\frac{1}{2}^+$	$2453.76 \pm 0.18$	$2.2 \pm 0.4$
$\Sigma_c(2520)^{++}$	$uuc$	$\frac{3}{2}^+$	$2518.4 \pm 0.6$	$14.9 \pm 1.9$
$\Sigma_c(2520)^+$	$udc$	$\frac{3}{2}^+$	$2517.5 \pm 2.3$	$< 17$
$\Sigma_c(2520)^0$	$ddc$	$\frac{3}{2}^+$	$2518.0 \pm 0.5$	$16.1 \pm 2.1$
$\Sigma_c(2800)^{++}$	$uuc$	??	$2801^{+4}_{-6}$	$75^{+22}_{-17}$
$\Sigma_c(2800)^+$	$udc$	??	$2792^{+14}_{-5}$	$62^{+60}_{-40}$
$\Sigma_c(2800)^0$	$ddc$	??	$2802^{+4}_{-7}$	$61^{+28}_{-18}$
$\Xi_c^+$	$usc$	$\frac{1}{2}^+$	$2467.9 \pm 0.4$	
$\Xi_c^0$	$dsc$	$\frac{1}{2}^+$	$2471.0 \pm 0.4$	
$\Xi_c'^+$	$usc$	$\frac{1}{2}^+$	$2575.7 \pm 3.1$	
$\Xi_c'^0$	$dsc$	$\frac{1}{2}^+$	$2578.0 \pm 2.9$	
$\Xi_c(2645)^+$	$usc$	$\frac{3}{2}^+$	$2646.6 \pm 1.4$	$< 3.1$
$\Xi_c(2645)^0$	$dsc$	$\frac{3}{2}^+$	$2646.1 \pm 1.2$	$< 5.5$
$\Xi_c(2790)^+$	$usc$	$\frac{1}{2}^-$	$2789.2 \pm 3.2$	$< 15$
$\Xi_c(2790)^0$	$dsc$	$\frac{1}{2}^-$	$2791.9 \pm 3.3$	$< 12$
$\Xi_c(2815)^+$	$usc$	$\frac{3}{2}^-$	$2816.5 \pm 1.2$	$< 3.5$
$\Xi_c(2815)^0$	$dsc$	$\frac{3}{2}^-$	$2818.2 \pm 2.1$	$< 6.5$
$\Xi_c(2980)^+$	$usc$	??	$2971.1 \pm 1.7$	$25.2 \pm 3.0$
$\Xi_c(2980)^0$	$dsc$	??	$2977.1 \pm 9.5$	43.5
$\Xi_c(3077)^+$	$usc$	??	$3076.5 \pm 0.6$	$6.2 \pm 1.1$
$\Xi_c(3077)^0$	$dsc$	??	$3082.8 \pm 2.3$	$5.2 \pm 3.6$
$\Omega_c^0$	$ssc$	$\frac{1}{2}^+$	$2697.5 \pm 2.6$	
$\Omega_c(2768)^0$	$ssc$	$\frac{3}{2}^+$	$2768.3 \pm 3.0$	

fore, it is not a  $\tilde{\Lambda}_{c2}^+(\frac{5}{2})$  state either. Since  $J_\ell = 2, S_\ell = 0, L = 2$  for the diquark system of  $\Lambda_c(2880)^+$ , this is the first observation of a  $d$ -wave charmed baryon. It is interesting to notice that, based on the diquark idea, the assignment  $J^P = 5/2^+$  has already been predicted in [217] for the state  $\Lambda_c(2880)$  before the Belle experiment. As for  $\Lambda_c(2980)^+$ , it was recently argued that it is an exotic molecular state of  $D^{*0}$  and  $p$  [218].

- The new charmed strange baryons  $\Xi_c(2980)^+$  and  $\Xi_c(3077)^+$  that decay into  $\Lambda_c^+ K^- \pi^+$  were first observed by Belle [219] and confirmed by BaBar [220]. In the recent BaBar measurement [220], the  $\Xi_c(2980)^+$  is found to decay resonantly through the intermediate state  $\Sigma_c(2455)^{++} K^-$  with  $4.9\sigma$  significance and non-resonantly to  $\Lambda_c^+ K^- \pi^+$  with  $4.1\sigma$  significance. With  $5.8\sigma$  significance, the  $\Xi_c(3077)^+$  is found to decay resonantly through  $\Sigma_c(2455)^{++} K^-$ , and with  $4.6\sigma$  significance, it is found to decay through  $\Sigma_c(2520)^{++} K^-$ . The significance of the signal for the non-resonant decay  $\Xi_c(3077)^+ \rightarrow \Lambda_c^+ K^- \pi^+$  is  $1.4\sigma$ .
- The highest isotriplet charmed baryons  $\Sigma_c(2800)^{++,+,0}$  decaying into  $\Lambda_c^+ \pi$  were first measured by Belle [221]. They are most likely to be the  $J^P = 3/2^-$   $\Sigma_{c2}$  states because the  $\Sigma_{c2}(\frac{3}{2})$  baryon decays principally into the  $\Lambda_c \pi$  system in a  $D$ -wave, while  $\Sigma_{c1}(\frac{3}{2})$  decays mainly into the two pion system  $\Lambda_c \pi \pi$ . The state  $\Sigma_{c0}(\frac{1}{2})$  can decay into  $\Lambda_c \pi$  in an  $S$ -wave, but it is very broad with width of order 406 MeV [216]. Experimentally, it will be very difficult to observe it.
- The new  $3/2^+$   $\Omega_c(2768)$  was recently observed by BaBar in the electromagnetic decay  $\Omega_c(2768) \rightarrow \Omega_c \gamma$  [222]. With this new observation, the  $3/2^+$  sextet is finally completed.
- Evidence of double charm states has been reported by SELEX in  $\Xi_{cc}(3519)^+ \rightarrow \Lambda_c^+ K^- \pi^+$  [223]. Further observations of  $\Xi_{cc}^{++} \rightarrow \Lambda_c^+ K^- \pi^+ \pi^+$  and  $\Xi_{cc}^+ \rightarrow p D^+ K^-$  were also announced by SELEX [224]. However, none of the double charm states discovered by SELEX has been confirmed by FOCUS, BaBar [225] and Belle [213] despite the  $10^6$   $\Lambda_c$  events produced in  $B$  factories versus 1630  $\Lambda_c$  events observed at SELEX.

Charmed baryon spectroscopy has been studied extensively in various models. The interested readers are referred to Ref. [226] for further references. In heavy quark effective theory, the mass splittings between spin- $\frac{3}{2}$  and spin- $\frac{1}{2}$  sextet charmed baryon multiplets are governed by the chromomagnetic interactions so that

$$m_{\Sigma_c^*} - m_{\Sigma_c} = m_{\Xi_c'^*} - m_{\Xi_c'} = m_{\Omega_c^*} - m_{\Omega_c}, \quad (24.3.1)$$

up to corrections of  $1/m_c$ . This relation is borne out by experiment:  $m_{\Sigma_c^{*+}} - m_{\Sigma_c^+} = 64.6 \pm 2.3$  MeV,  $m_{\Xi_c'^*} - m_{\Xi_c^+} = 70.9 \pm 3.4$  MeV and  $m_{\Omega_c^*} - m_{\Omega_c} = 70.8 \pm 1.5$  MeV.

---

only the  $F$ -wave contribution and neglecting the  $P$ -wave contribution to  $\Lambda_c(2880)^+ \rightarrow \Sigma_c^* \pi$  (see [216] for more discussions).

## 24.4 Strong decays

Due to the rich mass spectrum and the relatively narrow widths of the excited states, the charmed baryon system offers an excellent ground for testing the ideas and predictions of heavy quark symmetry and light flavor SU(3) symmetry. The pseudoscalar mesons involved in the strong decays of charmed baryons such as  $\Sigma_c \rightarrow \Lambda_c \pi$  are soft. Therefore, heavy quark symmetry of the heavy quark and chiral symmetry of the light quarks will have interesting implications for the low-energy dynamics of heavy baryons interacting with the Goldstone bosons.

The strong decays of charmed baryons are most conveniently described by the heavy hadron chiral Lagrangians in which heavy quark symmetry and chiral symmetry are incorporated [202, 203]. The Lagrangian involves two coupling constants  $g_1$  and  $g_2$  for  $P$ -wave transitions between  $s$ -wave and  $s$ -wave baryons [202], six couplings  $h_2 - h_7$  for the  $S$ -wave transitions between  $s$ -wave and  $p$ -wave baryons, and eight couplings  $h_8 - h_{15}$  for the  $D$ -wave transitions between  $s$ -wave and  $p$ -wave baryons [210]. The general chiral Lagrangian for heavy baryons coupling to the pseudoscalar mesons can be expressed compactly in terms of superfields. We will not write down the relevant Lagrangians here; instead the reader is referred to Eqs. (3.1) and (3.3) of Ref. [210]. Nevertheless, we list some of the partial widths derived from the Lagrangian [210]:

$$\begin{aligned}
\Gamma(\Sigma_c^* \rightarrow \Sigma_c \pi) &= \frac{g_1^2}{2\pi f_\pi^2} \frac{m_{\Sigma_c}}{m_{\Sigma_c^*}} p_\pi^3, & \Gamma(\Sigma_c \rightarrow \Lambda_c \pi) &= \frac{g_2^2}{2\pi f_\pi^2} \frac{m_{\Lambda_c}}{m_{\Sigma_c}} p_\pi^3, \\
\Gamma(\Lambda_{c1}(1/2) \rightarrow \Sigma_c \pi) &= \frac{h_2^2}{2\pi f_\pi^2} \frac{m_{\Sigma_c}}{m_{\Lambda_{c1}}} E_c^2 \pi_\pi, & \Gamma(\Sigma_{c0}(1/2) \rightarrow \Lambda_c \pi) &= \frac{h_3^2}{2\pi f_\pi^2} \frac{m_{\Lambda_c}}{m_{\Sigma_{c0}}} E_\pi^2 p_\pi, \\
\Gamma(\Sigma_{c1}(1/2) \rightarrow \Sigma_c \pi) &= \frac{h_4^2}{4\pi f_\pi^2} \frac{m_{\Sigma_c}}{m_{\Sigma_{c1}}} E_\pi^2 p_\pi, & \Gamma(\tilde{\Sigma}_{c1}(1/2) \rightarrow \Sigma_c \pi) &= \frac{h_5^2}{4\pi f_\pi^2} \frac{m_{\Sigma_c}}{m_{\tilde{\Sigma}_{c1}}} E_\pi^2 p_\pi, \\
\Gamma(\tilde{\Xi}_{c0}(1/2) \rightarrow \Xi_c \pi) &= \frac{h_6^2}{2\pi f_\pi^2} \frac{m_{\Xi_c}}{m_{\tilde{\Xi}_{c0}}} E_\pi^2 p_\pi, & \Gamma(\tilde{\Lambda}_{c1}(1/2) \rightarrow \Sigma_c \pi) &= \frac{h_7^2}{2\pi f_\pi^2} \frac{m_{\Sigma_c}}{m_{\tilde{\Lambda}_{c1}}} E_\pi^2 p_\pi,
\end{aligned} \tag{24.4.2}$$

where  $p_\pi$  is the pion's momentum and  $f_\pi = 132$  MeV. Unfortunately, the decay  $\Sigma_c^* \rightarrow \Sigma_c \pi$  is kinematically prohibited since the mass difference between  $\Sigma_c^*$  and  $\Sigma_c$  is only of order 65 MeV. Consequently, the coupling  $g_1$  cannot be extracted directly from the strong decays of heavy baryons.

### 24.4.1 Strong decays of $s$ -wave charmed baryons

In the framework of heavy hadron chiral perturbation theory (HHChPT), one can use some measurements as input to fix the coupling  $g_2$  which, in turn, can be used to predict the rates of other strong decays. We shall use  $\Sigma_c \rightarrow \Lambda_c \pi$  as input [3]

$$\Gamma(\Sigma_c^{++}) = \Gamma(\Sigma_c^{++} \rightarrow \Lambda_c^+ \pi^+) = 2.23 \pm 0.30 \text{ MeV.} \tag{24.4.3}$$

From which we obtain

$$|g_2| = 0.605^{+0.039}_{-0.043}, \tag{24.4.4}$$

Table 24.3: Decay widths (in units of MeV) of  $s$ -wave charmed baryons. Theoretical predictions of [229] are taken from Table IV of [230].

Decay	HHChPT	Tawfiq et al. [229]	Ivanov et al. [230]	Huang et al. [231]	Albertus et al. [232]	Expt. [3]
$\Sigma_c^{++} \rightarrow \Lambda_c^+ \pi^+$	input	$1.51 \pm 0.17$	$2.85 \pm 0.19$	2.5	$2.41 \pm 0.07$	$2.23 \pm 0.30$
$\Sigma_c^+ \rightarrow \Lambda_c^+ \pi^0$	$2.6 \pm 0.4$	$1.56 \pm 0.17$	$3.63 \pm 0.27$	3.2	$2.79 \pm 0.08$	$< 4.6$
$\Sigma_c^0 \rightarrow \Lambda_c^+ \pi^-$	$2.2 \pm 0.3$	$1.44 \pm 0.16$	$2.65 \pm 0.19$	2.4	$2.37 \pm 0.07$	$2.2 \pm 0.4$
$\Sigma_c(2520)^{++} \rightarrow \Lambda_c^+ \pi^+$	$16.7 \pm 2.3$	$11.77 \pm 1.27$	$21.99 \pm 0.87$	8.2	$17.52 \pm 0.75$	$14.9 \pm 1.9$
$\Sigma_c(2520)^+ \rightarrow \Lambda_c^+ \pi^0$	$17.4 \pm 2.3$			8.6	$17.31 \pm 0.74$	$< 17$
$\Sigma_c(2520)^0 \rightarrow \Lambda_c^+ \pi^-$	$16.6 \pm 2.2$	$11.37 \pm 1.22$	$21.21 \pm 0.81$	8.2	$16.90 \pm 0.72$	$16.1 \pm 2.1$
$\Xi_c(2645)^+ \rightarrow \Xi_c^{0,+} \pi^{+,0}$	$2.8 \pm 0.4$	$1.76 \pm 0.14$	$3.04 \pm 0.37$		$3.18 \pm 0.10$	$< 3.1$
$\Xi_c(2645)^0 \rightarrow \Xi_c^{+,0} \pi^{-,0}$	$2.9 \pm 0.4$	$1.83 \pm 0.06$	$3.12 \pm 0.33$		$3.03 \pm 0.10$	$< 5.5$

where we have neglected the tiny contributions from electromagnetic decays. Note that  $|g_2|$  obtained from  $\Sigma_c^0 \rightarrow \Lambda_c^+ \pi^-$  has the same central value as Eq. (24.4.4) except that the errors are slightly large. If  $\Sigma_c^* \rightarrow \Lambda_c \pi$  decays are employed as input, we will obtain  $|g_2| = 0.57 \pm 0.04$  from  $\Sigma_c^{*++} \rightarrow \Lambda_c^+ \pi^+$  and  $0.60 \pm 0.04$  from  $\Sigma_c^{*0} \rightarrow \Lambda_c^+ \pi^-$ . Hence, it is preferable to use the measurement of  $\Sigma_c^{++} \rightarrow \Lambda_c^+ \pi^+$  to fix  $|g_2|$ .<sup>3</sup>

As pointed out in [202], within in the framework of the non-relativistic quark model, the couplings  $g_1$  and  $g_2$  can be related to  $g_A^q$ , the axial-vector coupling in a single quark transition of  $u \rightarrow d$ , via

$$g_1 = \frac{4}{3} g_A^q, \quad g_2 = \sqrt{\frac{2}{3}} g_A^q. \quad (24.4.5)$$

Using  $g_A^q = 0.75$  which is required to reproduce the correct value of  $g_A^N = 1.25$ , we obtain

$$g_1 = 1, \quad g_2 = 0.61. \quad (24.4.6)$$

Hence, the quark model prediction is in good agreement with experiment, but deviates  $2\sigma$  from the large- $N_c$  argument:  $|g_2| = g_A^N / \sqrt{2} = 0.88$  [228]. Applying (24.4.4) leads to (see also Table 24.3)

$$\begin{aligned} \Gamma(\Xi_c'^{*+}) = \Gamma(\Xi_c'^{*+} \rightarrow \Xi_c^+ \pi^0, \Xi_c^0 \pi^+) &= \frac{g_2^2}{4\pi f_\pi^2} \left( \frac{1}{2} \frac{m_{\Xi_c^+}}{m_{\Xi_c'^+}} p_\pi^3 + \frac{m_{\Xi_c^0}}{m_{\Xi_c'^0}} p_\pi^3 \right) = (2.8 \pm 0.4) \text{ MeV}, \\ \Gamma(\Xi_c'^{*0}) = \Gamma(\Xi_c'^{*0} \rightarrow \Xi_c^+ \pi^-, \Xi_c^0 \pi^0) &= \frac{g_2^2}{4\pi f_\pi^2} \left( \frac{m_{\Xi_c^+}}{m_{\Xi_c'^0}} p_\pi^3 + \frac{1}{2} \frac{m_{\Xi_c^0}}{m_{\Xi_c'^0}} p_\pi^3 \right) = (2.9 \pm 0.4) \text{ MeV}. \end{aligned} \quad (24.4.7)$$

Note that we have neglected the effect of  $\Xi_c - \Xi_c'$  mixing in calculations (for recent considerations, see [233, 234]). Therefore, the predicted total width of  $\Xi_c'^{*+}$  is in the vicinity of the current limit  $\Gamma(\Xi_c'^{*+}) < 3.1$  MeV [235].

It is clear from Table 24.3 that the predicted widths of  $\Sigma_c^{++}$  and  $\Sigma_c^0$  by HHChPT are in good agreement with experiment. The strong decay width of  $\Sigma_c$  is smaller than that of  $\Sigma_c^*$  by a factor of  $\sim 7$ , although they will become the same in the limit of heavy quark

<sup>3</sup>For previous efforts of extracting  $g_2$  from experiment using HHChPT, see [227, 210].

Table 24.4: Same as Table 24.3 except for  $p$ -wave charmed baryons [216].

Decay	HHChPT	Tawfiq et al. [229]	Ivanov et al. [230]	Huang et al. [231]	Zhu [236]	Expt. [3]
$\Lambda_c(2593)^+ \rightarrow (\Sigma_c^+ \pi \pi)_R$	input			2.5		$2.63^{+1.56}_{-1.09}$
$\Lambda_c(2593)^+ \rightarrow \Sigma_c^{++} \pi^-$	$0.62^{+0.37}_{-0.26}$	$1.47 \pm 0.57$	$0.79 \pm 0.09$	$0.55^{+1.3}_{-0.55}$	0.64	$0.65^{+0.41}_{-0.30}$
$\Lambda_c(2593)^+ \rightarrow \Sigma_c^0 \pi^+$	$0.67^{+0.40}_{-0.28}$	$1.78 \pm 0.70$	$0.83 \pm 0.09$	$0.89 \pm 0.86$	0.86	$0.67^{+0.41}_{-0.30}$
$\Lambda_c(2593)^+ \rightarrow \Sigma_c^+ \pi^0$	$1.34^{+0.79}_{-0.55}$	$1.18 \pm 0.46$	$0.98 \pm 0.12$	$1.7 \pm 0.49$	1.2	
$\Lambda_c(2625)^+ \rightarrow \Sigma_c^{++} \pi^-$	$\leq 0.011$	$0.44 \pm 0.23$	$0.076 \pm 0.009$	0.013	0.011	$< 0.10$
$\Lambda_c(2625)^+ \rightarrow \Sigma_c^0 \pi^+$	$\leq 0.015$	$0.47 \pm 0.25$	$0.080 \pm 0.009$	0.013	0.011	$< 0.09$
$\Lambda_c(2625)^+ \rightarrow \Sigma_c^+ \pi^0$	$\leq 0.011$	$0.42 \pm 0.22$	$0.095 \pm 0.012$	0.013	0.011	
$\Lambda_c(2625)^+ \rightarrow \Lambda_c^+ \pi \pi$	$\leq 0.21$			0.11		$< 1.9$
$\Sigma_c(2800)^{++} \rightarrow \Lambda_c \pi, \Sigma_c^{(*)} \pi$	input					$75^{+22}_{-17}$
$\Sigma_c(2800)^+ \rightarrow \Lambda_c \pi, \Sigma_c^{(*)} \pi$	input					$62^{+60}_{-40}$
$\Sigma_c(2800)^0 \rightarrow \Lambda_c \pi, \Sigma_c^{(*)} \pi$	input					$61^{+28}_{-18}$
$\Xi_c(2790)^+ \rightarrow \Xi_c'^0 \pi^{+,0}$	$7.7^{+4.5}_{-3.2}$					$< 15$
$\Xi_c(2790)^0 \rightarrow \Xi_c'^+ \pi^{-,0}$	$8.1^{+4.8}_{-3.4}$					$< 12$
$\Xi_c(2815)^+ \rightarrow \Xi_c'^+ \pi^{0,+}$	$3.2^{+1.9}_{-1.3}$	$2.35 \pm 0.93$	$0.70 \pm 0.04$			$< 3.5$
$\Xi_c(2815)^0 \rightarrow \Xi_c'^+ \pi^{-,0}$	$3.5^{+2.0}_{-1.4}$					$< 6.5$

symmetry. This is ascribed to the fact that the pion's momentum is around 90 MeV in the decay  $\Sigma_c \rightarrow \Lambda_c \pi$  while it is two times bigger in  $\Sigma_c^* \rightarrow \Lambda_c \pi$ . Since  $\Sigma_c$  states are significantly narrower than their spin-3/2 counterparts, this explains why the measurement of their widths came out much later. Instead of using the data to fix the coupling constants in a model-independent manner, there exist some calculations of couplings in various models such as the relativistic light-front model [229], the relativistic three-quark model [230] and light-cone sum rules [231, 236]. The results are summarized in Table 24.3.

It is worth remarking that although the coupling  $g_1$  cannot be determined directly from the strong decay such as  $\Sigma_c^* \rightarrow \Sigma_c \pi$ , some information of  $g_1$  can be learned from the radiative decay  $\Xi_c'^* \rightarrow \Xi_c^0 \gamma$ , which is prohibited at tree level by SU(3) symmetry but can be induced by chiral loops. A measurement of  $\Gamma(\Xi_c'^* \rightarrow \Xi_c^0 \gamma)$  will yield two possible solutions for  $g_1$ . Assuming the validity of the quark model relations among different coupling constants, the experimental value of  $g_2$  implies  $|g_1| = 0.93 \pm 0.16$  [227].

#### 24.4.2 Strong decays of $p$ -wave charmed baryons

Some of the  $S$ -wave and  $D$ -wave couplings of  $p$ -wave baryons to  $s$ -wave baryons can be determined. In principle, the coupling  $h_2$  is readily extracted from  $\Lambda_c(2593)^+ \rightarrow \Sigma_c^0 \pi^+$  with  $\Lambda_c(2593)^+$  identified as  $\Lambda_{c1}(\frac{1}{2})^+$ . However, since  $\Lambda_c(2593)^+ \rightarrow \Sigma_c \pi$  is kinematically barely allowed, the finite width effects of the intermediate resonant states will become important [237].

Pole contributions to the decays  $\Lambda_c(2593)^+, \Lambda_c(2625)^+ \rightarrow \Lambda_c^+ \pi \pi$  have been considered in [238, 231, 210] with the finite width effects included. The intermediate states of interest are  $\Sigma_c$  and  $\Sigma_c^*$  poles. The resonant contribution arises from the  $\Sigma_c$  pole, while the non-resonant term receives a contribution from the  $\Sigma_c^*$  pole. (Since  $\Lambda_c(2593)^+, \Lambda_c(2625)^+ \rightarrow \Lambda_c^* \pi$  are not kinematically allowed, the  $\Sigma_c^*$  pole is not a resonant contribution.) The decay rates thus depend on two coupling constants  $h_2$  and  $h_8$ . The decay rate for the process  $\Lambda_{c1}^+(2593) \rightarrow \Lambda_c^+ \pi^+ \pi^-$  can be calculated in the framework of heavy hadron chiral

perturbation theory to be [216]

$$\begin{aligned}\Gamma(\Lambda_c(2593) \rightarrow \Lambda_c^+ \pi\pi) &= 14.48h_2^2 + 27.54h_8^2 - 3.11h_2h_8, \\ \Gamma(\Lambda_c(2625) \rightarrow \Lambda_c^+ \pi\pi) &= 0.648h_2^2 + 0.143 \times 10^6 h_8^2 - 28.6h_2h_8.\end{aligned}\quad (24.4.8)$$

It is clear that the limit on  $\Gamma(\Lambda_c(2625))$  gives an upper bound on  $h_8$  of order  $10^{-3}$  (in units of  $\text{MeV}^{-1}$ ), whereas the decay width of  $\Lambda_c(2593)$  is entirely governed by the coupling  $h_2$ . This indicates that the direct non-resonant  $\Lambda_c^+ \pi\pi$  cannot be described by the  $\Sigma_c^*$  pole alone. Identifying the calculated  $\Gamma(\Lambda_c(2593) \rightarrow \Lambda_c^+ \pi\pi)$  with the resonant one, we find

$$|h_2| = 0.427_{-0.100}^{+0.111}, \quad |h_8| \leq 3.57 \times 10^{-3}. \quad (24.4.9)$$

Assuming that the total decay width of the  $\Lambda_c(2593)$  is saturated by the resonant  $\Lambda_c^+ \pi\pi$  3-body decays, Pirjol and Yan obtained  $|h_2| = 0.572_{-0.197}^{+0.322}$  and  $|h_8| \leq (3.50 - 3.68) \times 10^{-3} \text{ MeV}^{-1}$  [210]. Using the updated hadron masses and  $\Gamma(\Lambda_c(2593) \rightarrow \Lambda_c^+ \pi\pi)$ ,<sup>4</sup> we find  $|h_2| = 0.499_{-0.100}^{+0.134}$ . Taking into account the fact that the  $\Sigma_c$  and  $\Sigma_c^*$  poles only describe the resonant contributions to the total width of  $\Lambda_c(2593)$ , we finally reach the  $h_2$  value given in (24.4.9). Taking into account the threshold (or finite width) effect in the strong decay  $\Lambda_c(2593)^+ \rightarrow \Lambda_c \pi\pi$ , a slightly small coupling  $h_2^2 = 0.24_{-0.11}^{+0.23}$  is obtained in [237]. For the spin- $\frac{3}{2}$  state  $\Lambda_c(2625)$ , its decay is dominated by the three-body channel  $\Lambda_c^+ \pi\pi$  as the major two-body decay  $\Sigma_c \pi$  is a  $D$ -wave one.

Some information on the coupling  $h_{10}$  can be inferred from the strong decays of  $\Lambda_c(2800)$ . As noticed in passing, the states  $\Sigma_c(2800)^{++,+,0}$  are most likely to be  $\Sigma_{c2}(\frac{3}{2})$ . Assuming their widths are dominated by the two-body modes  $\Lambda_c \pi$ ,  $\Sigma_c \pi$  and  $\Lambda_c^* \pi$ , we have [210]

$$\begin{aligned}\Gamma\left(\Sigma_{c2}(\frac{3}{2})^{++}\right) &\approx \Gamma\left(\Sigma_{c2}(\frac{3}{2})^{++} \rightarrow \Lambda_c^+ \pi^+\right) + \Gamma\left(\Sigma_{c2}(\frac{3}{2})^{++} \rightarrow \Sigma_c^+ \pi^+\right) + \\ &\quad \Gamma\left(\Sigma_{c2}(\frac{3}{2})^{++} \rightarrow \Sigma_c^{*+} \pi^+\right) \\ &= \frac{4h_{10}^2}{15\pi f_\pi^2} \frac{m_{\Lambda_c}}{m_{\Sigma_{c2}}} p_c^5 + \frac{h_{11}^2}{10\pi f_\pi^2} \frac{m_{\Sigma_c}}{m_{\Sigma_{c2}}} p_c^5 + \frac{h_{11}^2}{10\pi f_\pi^2} \frac{m_{\Sigma_c^*}}{m_{\Sigma_{c2}}} p_c^5,\end{aligned}\quad (24.4.10)$$

and similar expressions for  $\Sigma_c(2800)^+$  and  $\Sigma_c(2800)^0$ . Using the quark model relation  $h_{11}^2 = 2h_{10}^2$  [see also Eq. (24.4.13)] and the measured widths of  $\Sigma_c(2800)^{++,+,0}$  (Table 24.2), we obtain

$$|h_{10}| = (0.85_{-0.08}^{+0.11}) \times 10^{-3} \text{ MeV}^{-1}. \quad (24.4.11)$$

Since the state  $\Lambda_{c1}(\frac{3}{2})$  is broader, even a small mixing of  $\Lambda_{c2}(\frac{3}{2})$  with  $\Lambda_{c1}(\frac{3}{2})$  could enhance the decay width of the former [210]. In this case, the above value for  $h_{10}$  should be regarded as an upper limit of  $|h_{10}|$ . Using the quark model relation  $|h_8| = |h_{10}|$  (see Eq. (24.4.13) below), the calculated partial widths of  $\Lambda_c(2625)^+$  are shown in Table 24.4.

The  $\Xi_c(2790)$  and  $\Xi_c(2815)$  baryons form a doublet  $\Xi_{c1}(\frac{1}{2}, \frac{3}{2})$ .  $\Xi_c(2790)$  decays to  $\Xi_c' \pi$ , while  $\Xi_c(2815)$  decays to  $\Xi_c \pi\pi$ , resonating through  $\Xi_c^*$ , i.e.  $\Xi_c(2645)$ . Using the coupling  $h_2$  obtained (24.4.9) and the experimental observation that the  $\Xi_c \pi\pi$  mode in

<sup>4</sup>The CLEO result  $\Gamma(\Lambda_c(2593)) = 3.9_{-1.6}^{+2.4} \text{ MeV}$  [239] is used in [210] to fix  $h_2$ .

$\Xi_c(2815)$  decays is consistent with being entirely via  $\Xi_c(2645)\pi$ , the predicted  $\Xi_c(2790)$  and  $\Xi_c(2815)$  widths are shown in Table 24.4 and they are consistent with the current experimental limits.

Couplings other than  $h_2$  and  $h_{10}$  can be related to each other via the quark model. The  $S$ -wave couplings between the  $s$ -wave and the  $p$ -wave baryons are related by [210]

$$\frac{|h_3|}{|h_4|} = \frac{\sqrt{3}}{2}, \quad \frac{|h_2|}{|h_4|} = \frac{1}{2}, \quad \frac{|h_5|}{|h_6|} = \frac{2}{\sqrt{3}}, \quad \frac{|h_5|}{|h_7|} = 1. \quad (24.4.12)$$

The  $D$ -wave couplings satisfy the relations

$$|h_8| = |h_9| = |h_{10}|, \quad \frac{|h_{11}|}{|h_{10}|} = \frac{|h_{15}|}{|h_{14}|} = \sqrt{2}, \quad \frac{|h_{12}|}{|h_{13}|} = 2, \quad \frac{|h_{14}|}{|h_{13}|} = 1. \quad (24.4.13)$$

The reader is referred to Ref. [210] for further details.

## 24.5 Lifetimes

The lifetime differences among the charmed mesons  $D^+$ ,  $D^0$  and charmed baryons have been studied extensively both experimentally and theoretically since the late 1970s. It was realized very early that the naive parton model gives the same lifetimes for all heavy particles containing a heavy quark  $Q$  and that the underlying mechanism for the decay width differences and the lifetime hierarchy of heavy hadrons comes mainly from the spectator effects like  $W$ -exchange and Pauli interference due to the identical quarks produced in the heavy quark decay and in the charmed baryons (for a review, see [240, 209, 241]). The spectator effects were expressed in 1980s in terms of local four-quark operators by relating the total widths to the imaginary part of certain forward scattering amplitudes [242, 243, 244]. (The spectator effects for charmed baryons were first studied in [245].) With the advent of heavy quark effective theory (HQET), it was recognized in early 1990s that nonperturbative corrections to the parton picture can be systematically expanded in powers of  $1/m_Q$  [246, 247]. Subsequently, it was demonstrated that this  $1/m_Q$  expansion is applicable not only to global quantities such as lifetimes, but also to local quantities, e.g. the lepton spectrum in the semileptonic decays of heavy hadrons [248]. Therefore, the above-mentioned phenomenological work in 1980s acquired a firm theoretical footing in 1990s, namely the heavy quark expansion (HQE), which is a generalization of the operator product expansion (OPE) in  $1/m_Q$ . Within this QCD-based framework, some phenomenological assumptions can be turned into some coherent and quantitative statements and nonperturbative effects can be systematically studied.

Based on the OPE approach for the analysis of inclusive weak decays, the inclusive rate of the charmed baryon is schematically represented by

$$\Gamma(\mathcal{B}_c \rightarrow f) = \frac{G_F^2 m_c^5}{192\pi^3} V_{\text{CKM}} \left( A_0 + \frac{A_2}{m_c^2} + \frac{A_3}{m_c^3} + \mathcal{O}\left(\frac{1}{m_c^4}\right) \right). \quad (24.5.14)$$

The  $A_0$  term comes from the  $c$  quark decay and is common to all charmed hadrons. There is no linear  $1/m_Q$  corrections to the inclusive decay rate due to the lack of gauge-invariant dimension-four operators [249, 246], a consequence known as Luke's theorem [250]. Non-perturbative corrections start at order  $1/m_Q^2$  and they are model independent. Spectator

effects in inclusive decays due to the Pauli interference and  $W$ -exchange contributions account for  $1/m_c^3$  corrections and they have two eminent features: First, the estimate of spectator effects is model dependent; the hadronic four-quark matrix elements are usually evaluated by assuming the factorization approximation for mesons and the quark model for baryons. Second, there is a two-body phase-space enhancement factor of  $16\pi^2$  for spectator effects relative to the three-body phase space for heavy quark decay. This implies that spectator effects, being of order  $1/m_c^3$ , are comparable to and even exceed the  $1/m_c^2$  terms.

The lifetimes of charmed baryons are measured to be [3]

$$\begin{aligned}\tau(\Lambda_c^+) &= (200 \pm 6) \times 10^{-15} \text{ s}, & \tau(\Xi_c^+) &= (442 \pm 26) \times 10^{-15} \text{ s}, \\ \tau(\Xi_c^0) &= (112_{-10}^{+13}) \times 10^{-15} \text{ s}, & \tau(\Omega_c^0) &= (69 \pm 12) \times 10^{-15} \text{ s}.\end{aligned}\quad (24.5.15)$$

As we shall see below, the lifetime hierarchy  $\tau(\Xi_c^+) > \tau(\Lambda_c^+) > \tau(\Xi_c^0) > \tau(\Omega_c^0)$  is qualitatively understandable in the OPE approach but not quantitatively.

In general, the total width of the charmed baryon  $\mathcal{B}_c$  receives contributions from inclusive nonleptonic and semileptonic decays:  $\Gamma(\mathcal{B}_c) = \Gamma_{\text{NL}}(\mathcal{B}_c) + \Gamma_{\text{SL}}(\mathcal{B}_c)$ . The nonleptonic contribution can be decomposed into

$$\Gamma_{\text{NL}}(\mathcal{B}_c) = \Gamma^{\text{dec}}(\mathcal{B}_c) + \Gamma^{\text{ann}}(\mathcal{B}_c) + \Gamma_-^{\text{int}}(\mathcal{B}_c) + \Gamma_+^{\text{int}}(\mathcal{B}_c), \quad (24.5.16)$$

corresponding to the  $c$ -quark decay, the  $W$ -exchange contribution, destructive and constructive Pauli interferences. It is known that the inclusive decay rate is governed by the imaginary part of an effective nonlocal forward transition operator  $T$ . Therefore,  $\Gamma^{\text{dec}}$  corresponds to the imaginary part of Fig. 24.2(a) sandwiched between the same  $\mathcal{B}_c$  states. At the Cabibbo-allowed level,  $\Gamma^{\text{dec}}$  represents the decay rate of  $c \rightarrow s u \bar{d}$ , and  $\Gamma^{\text{ann}}$  denotes the contribution due to the  $W$ -exchange diagram  $cd \rightarrow us$ . The interference  $\Gamma_-^{\text{int}}$  ( $\Gamma_+^{\text{int}}$ ) arises from the destructive (constructive) interference between the  $u$  ( $s$ ) quark produced in the  $c$ -quark decay and the spectator  $u$  ( $s$ ) quark in the charmed baryon  $\mathcal{B}_c$ . Notice that the constructive Pauli interference is unique to the charmed baryon sector as it does not occur in the bottom baryon sector. From the quark content of the charmed baryons (see Table 24.2), it is clear that at the Cabibbo-allowed level, the destructive interference occurs in  $\Lambda_c^+$  and  $\Xi_c^+$  decays, while  $\Xi_c^+, \Xi_c^0$  and  $\Omega_c^0$  can have  $\Gamma_+^{\text{int}}$ . Since  $\Omega_c^0$  contains two  $s$  quarks, it is natural to expect that  $\Gamma_+^{\text{int}}(\Omega_c^0) \gg \Gamma_+^{\text{int}}(\Xi_c)$ .  $W$ -exchange occurs only for  $\Xi_c^0$  and  $\Lambda_c^+$  at the same Cabibbo-allowed level. In the heavy quark expansion approach, the above-mentioned spectator effects can be described in terms of the matrix elements of local four-quark operators.

Within this QCD-based heavy quark expansion approach, some phenomenological assumptions can be turned into some coherent and quantitative statements and non-perturbative effects can be systematically studied. To begin with, we write down the general expressions for the inclusive decay widths of charmed hadrons. Under the heavy quark expansion, the inclusive nonleptonic decay rate of a charmed baryon  $\mathcal{B}_c$  is given by [246, 247]

$$\Gamma_{\text{NL}}(\mathcal{B}_c) = \frac{G_F^2 m_c^5}{192\pi^3} N_c V_{\text{CKM}} \frac{1}{2m_{\mathcal{B}_c}} \left\{ \left( c_1^2 + c_2^2 + \frac{2c_1 c_2}{N_c} \right) \left[ I_0(x, 0, 0) \langle \mathcal{B}_c | \bar{c}c | \mathcal{B}_c \rangle \right. \right.$$

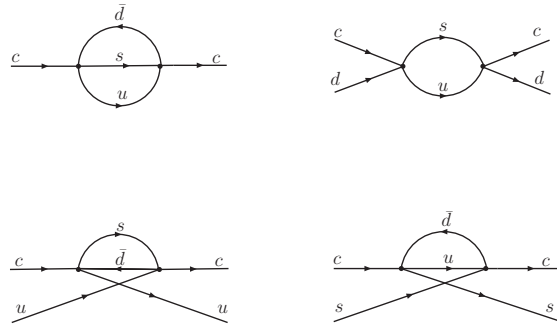


Figure 24.2: Contributions to nonleptonic decay rates of charmed baryons from four-quark operators: (a)  $c$ -quark decay, (b)  $W$ -exchange, (c) destructive Pauli interference and (d) constructive interference.

$$\begin{aligned}
 & - \frac{1}{m_c^2} I_1(x, 0, 0) \langle \mathcal{B}_c | \bar{c} \sigma \cdot G c | \mathcal{B}_c \rangle \Big] - \frac{4}{m_c^2} \frac{2c_1 c_2}{N_c} I_2(x, 0, 0) \langle \mathcal{B}_c | \bar{c} \sigma \cdot G c | \mathcal{B}_c \rangle \Big\} \\
 & + \frac{1}{2m_{\mathcal{B}_c}} \langle \mathcal{B}_c | \mathcal{L}_{\text{spec}} | \mathcal{B}_c \rangle + \mathcal{O} \left( \frac{1}{m_c^4} \right), \tag{24.5.17}
 \end{aligned}$$

where  $\sigma \cdot G = \sigma_{\mu\nu} G^{\mu\nu}$ ,  $x = (m_s/m_c)^2$ ,  $N_c$  is the number of colors,  $c_1$ ,  $c_2$  are Wilson coefficient functions,  $N_c = 3$  is the number of color and  $V_{\text{CKM}}$  takes care of the relevant CKM matrix elements. In the above equation,  $I_{0,1,2}$  are phase-space factors

$$\begin{aligned}
 I_0(x, 0, 0) &= (1 - x^2)(1 - 8x + x^2) - 12x^2 \ln x, \\
 I_1(x, 0, 0) &= \frac{1}{2}(2 - x \frac{d}{dx}) I_0(x, 0, 0) = (1 - x)^4, \\
 I_2(x, 0, 0) &= (1 - x)^3, \tag{24.5.18}
 \end{aligned}$$

for  $c \rightarrow su\bar{d}$  transition.

In heavy quark effective theory, the two-body matrix element  $\langle \mathcal{B}_c | \bar{c} c | \mathcal{B}_c \rangle$  in Eq. (24.5.17) can be recast to

$$\frac{\langle \mathcal{B}_c | \bar{c} c | \mathcal{B}_c \rangle}{2m_{\mathcal{B}_c}} = 1 - \frac{K_H}{2m_c^2} + \frac{G_H}{2m_c^2}, \tag{24.5.19}$$

with

$$\begin{aligned}
 K_H &\equiv -\frac{1}{2m_{\mathcal{B}_c}} \langle \mathcal{B}_c | \bar{c} (iD_{\perp})^2 c | \mathcal{B}_c \rangle = -\lambda_1, \\
 G_H &\equiv \frac{1}{2m_{\mathcal{B}_c}} \langle \mathcal{B}_c | \bar{c} \frac{1}{2} \sigma \cdot G c | \mathcal{B}_c \rangle = d_H \lambda_2, \tag{24.5.20}
 \end{aligned}$$

where  $d_H = 0$  for the antitriplet baryon and  $d_H = 4$  for the spin- $\frac{1}{2}$  sextet baryon. It should be stressed that the expression (24.5.19) is model independent and it contains nonperturbative kinetic and chromomagnetic effects which are usually absent in the quark model calculations. The nonperturbative HQET parameters  $\lambda_1$  and  $\lambda_2$  are independent of the heavy quark mass. Numerically, we shall use  $\lambda_1^{\text{baryon}} = -(0.4 \pm 0.2) \text{ GeV}^2$  [251] and  $\lambda_2^{\text{baryon}} = 0.055 \text{ GeV}^2$  for charmed baryons [252]. Spectator effects in inclusive decays

of charmed hadrons are described by the dimension-six four-quark operators  $\mathcal{L}_{\text{spec}}$  in Eq. (24.5.17) at order  $1/m_c^3$ . Its complete expression can be found in, for example, Eq. (2.4) of [252].

For inclusive semileptonic decays, there is an additional spectator effect in charmed-baryon semileptonic decay originating from the Pauli interference of the  $s$  quark for charmed baryons  $\Xi_c$  and  $\Omega_c$  [253]. The general expression of the inclusive semileptonic widths is given by

$$\begin{aligned}\Gamma_{\text{SL}}(\mathcal{B}_c) &= \frac{G_F^2 m_c^5}{192\pi^3} V_{\text{CKM}} \frac{\eta(x, x_\ell, 0)}{2m_{\mathcal{B}_c}} \left[ I_0(x, 0, 0) \langle \mathcal{B}_c | \bar{c}c | \mathcal{B}_c \rangle - \frac{1}{m_c^2} I_1(x, 0, 0) \langle \mathcal{B}_c | \bar{c}\sigma \cdot Gc | \mathcal{B}_c \rangle \right] \\ &- \frac{G_F^2 m_c^2}{6\pi} |V_{cs}|^2 \frac{1}{2m_{\mathcal{B}_c}} (1-x)^2 \left[ (1 + \frac{x}{2})(\bar{c}s)(\bar{s}c) - (1 + 2x)\bar{c}(1 - \gamma_5)s\bar{s}(1 + \gamma_5)c \right],\end{aligned}\quad (24.5.21)$$

where  $\eta(x, x_\ell, 0)$  with  $x_\ell = (m_\ell/m_Q)^2$  is the QCD radiative correction to the semileptonic decay rate and its general analytic expression is given in [254]. Since both nonleptonic and semileptonic decay widths scale with the fifth power of the charmed quark mass, it is very important to fix the value of  $m_c$ . It is found that the experimental values for  $D^+$  and  $D^0$  semileptonic widths [3] can be fitted by the quark pole mass  $m_c = 1.6$  GeV. Taking  $m_s = 170$  MeV, we obtain the charmed-baryon semileptonic decay rates

$$\begin{aligned}\Gamma(\Lambda_c \rightarrow X e \bar{\nu}) &= \Gamma(\Xi_c \rightarrow X e \bar{\nu}) = 1.533 \times 10^{-13} \text{ GeV}, \\ \Gamma(\Omega_c \rightarrow X e \bar{\nu}) &= 1.308 \times 10^{-13} \text{ GeV}.\end{aligned}\quad (24.5.22)$$

The prediction (24.5.22) for the  $\Lambda_c$  baryon is in good agreement with experiment [3]

$$\Gamma(\Lambda_c \rightarrow X e \bar{\nu})_{\text{expt}} = (1.480 \pm 0.559) \times 10^{-13} \text{ GeV}. \quad (24.5.23)$$

We shall see below that the Pauli interference effect in the semileptonic decays of  $\Xi_c$  and  $\Omega_c$  can be very significant, in particular for the latter.

The baryon matrix element of the four-quark operator  $\langle \mathcal{B}_c | (\bar{c}q_1)(\bar{q}_2 q_3) | \mathcal{B}_c \rangle$  with  $(\bar{q}_1 q_2) = \bar{q}_1 \gamma_\mu (1 - \gamma_5) q_2$  is customarily evaluated using the quark model. In the non-relativistic quark model (for early related studies, see [242, 243]), the matrix element is governed by the charmed baryon wave function at origin,  $|\psi_{cq}^{\mathcal{B}_c}(0)|^2$ , which can be related to the charmed meson wave function  $|\psi_{cq}^D(0)|^2$ . For example, the hyperfine splittings between  $\Sigma_c^*$  and  $\Sigma_c$ , and between  $D^*$  and  $D$  separately yield [255]

$$|\psi_{cq}^{\Lambda_c}(0)|^2 = |\psi_{cq}^{\Sigma_c}(0)|^2 = \frac{4}{3} \frac{m_{\Sigma_c^*} - m_{\Sigma_c}}{m_{D^*} - m_D} |\psi_{cq}^D(0)|^2. \quad (24.5.24)$$

This relation is supposed to be robust as  $|\psi_{cq}(0)|^2$  determined in this manner does not depend on the strong coupling  $\alpha_s$  and the light quark mass  $m_q$  directly. Defining

$$|\psi_{cq}^{\mathcal{B}_c}(0)|^2 = r_{\mathcal{B}_c} |\psi_{cq}^D(0)|^2, \quad (24.5.25)$$

we have

$$r_{\Lambda_c} = \frac{4}{3} \frac{m_{\Sigma_c^*} - m_{\Sigma_c}}{m_{D^*} - m_D}, \quad r_{\Xi_c} = \frac{4}{3} \frac{m_{\Xi_c^*} - m_{\Xi_c'}}{m_{D^*} - m_D}, \quad r_{\Omega_c} = \frac{4}{3} \frac{m_{\Omega_c^*} - m_{\Omega_c}}{m_{D^*} - m_D}. \quad (24.5.26)$$

In terms of the parameter  $r_{\mathcal{B}_c} |\psi_{cq}^D(0)|^2$  we have [252]

$$\begin{aligned}
\Gamma^{\text{ann}}(\Lambda_c) &= \frac{G_F^2 m_c^2}{\pi} r_{\Lambda_c} (1-x)^2 \left( \eta(c_1^2 + c_2^2) - 2c_1 c_2 \right) |\psi^D(0)|^2, \\
\Gamma_-^{\text{int}}(\Lambda_c) &= -\frac{G_F^2 m_c^2}{4\pi} r_{\Lambda_c} (1-x)^2 (1+x) \left( \eta c_1^2 - 2c_1 c_2 - N_c c_2^2 \right) |\psi^D(0)|^2, \\
\Gamma^{\text{ann}}(\Xi_c)/r_{\Xi_c} &= \Gamma^{\text{ann}}(\Lambda_c)/r_{\Lambda_c}, \quad \Gamma_-^{\text{int}}(\Xi_c^+)/r_{\Xi_c} = \Gamma_-^{\text{int}}(\Lambda_c)/r_{\Lambda_c}, \\
\Gamma_+^{\text{int}}(\Xi_c) &= -\frac{G_F^2 m_c^2}{4\pi} r_{\Xi_c} (1-x^2) (1+x) \left( \eta c_2^2 - 2c_1 c_2 - N_c c_1^2 \right) |\psi^D(0)|^2, \\
\Gamma_+^{\text{int}}(\Omega_c) &= -\frac{G_F^2 m_c^2}{6\pi} r_{\Omega_c} (1-x^2) (5+x) \left( \eta c_2^2 - 2c_1 c_2 - N_c c_1^2 \right) |\psi^D(0)|^2, \\
\Gamma^{\text{ann}}(\Omega_c) &= 6 \frac{G_F^2 m_c^2}{\pi} r_{\Omega_c} (1-x^2) \left( \eta(c_1^2 + c_2^2) - 2c_1 c_2 \right) |\psi^D(0)|^2, \\
\Gamma^{\text{int}}(\Xi_c \rightarrow X e \bar{\nu}) &= \frac{G_F^2 m_c^2}{4\pi} r_{\Xi_c} (1-x^2) (1+x) |\psi^D(0)|^2, \\
\Gamma^{\text{int}}(\Omega_c \rightarrow X e \bar{\nu}) &= \frac{G_F^2 m_c^2}{6\pi} r_{\Omega_c} (1-x^2) (5+x) |\psi^D(0)|^2,
\end{aligned} \tag{24.5.27}$$

where the parameter  $\eta$  is introduced via

$$\langle \mathcal{B}_c | (\bar{c}c)(\bar{q}q) | \mathcal{B}_c \rangle = -\eta \langle \mathcal{B}_c | (\bar{c}q)(\bar{q}c) | \mathcal{B}_c \rangle, \tag{24.5.28}$$

so that  $\eta = 1$  in the valence quark approximation. In the zero light quark mass limit ( $x = 0$ ) and in the valence quark approximation, the reader can check that results of (24.5.27) are in agreement with those obtained in Refs. [242, 243, 256] except the Cabibbo-suppressed  $W$ -exchange contribution to  $\Omega_c^0$ ,  $\Gamma^{\text{ann}}(\Omega_c)$ . We have a coefficient of 6 arising from the matrix element  $\langle \Omega_c | (\bar{c}s)(\bar{s}c) | \Omega_c \rangle = -6 |\psi_{cs}^{\Omega_c}(0)|^2 (2m_{\Omega_c})$  [252], while the coefficient is claimed to be  $\frac{10}{3}$  in [256].

Neglecting the small difference between  $r_{\Lambda_c}$ ,  $r_{\Xi_c}$  and  $r_{\Omega_c}$  and setting  $x = 0$ , the inclusive nonleptonic rates of charmed baryons in the valence quark approximation have the expressions:

$$\begin{aligned}
\Gamma_{\text{NL}}(\Lambda_c^+) &= \Gamma^{\text{dec}}(\Lambda_c^+) + \cos_C^2 \Gamma^{\text{ann}} + \Gamma_-^{\text{int}} + \sin_C^2 \Gamma_+^{\text{int}}, \\
\Gamma_{\text{NL}}(\Xi_c^+) &= \Gamma^{\text{dec}}(\Xi_c^+) + \sin_C^2 \Gamma^{\text{ann}} + \Gamma_-^{\text{int}} + \cos_C^2 \Gamma_+^{\text{int}}, \\
\Gamma_{\text{NL}}(\Xi_c^0) &= \Gamma^{\text{dec}}(\Xi_c^0) + \Gamma^{\text{ann}} + \Gamma_-^{\text{int}} + \Gamma_+^{\text{int}}, \\
\Gamma_{\text{NL}}(\Omega_c^0) &= \Gamma^{\text{dec}}(\Omega_c^0) + 6 \sin_C^2 \Gamma^{\text{ann}} + \frac{10}{3} \cos_C^2 \Gamma_+^{\text{int}},
\end{aligned} \tag{24.5.29}$$

with  $\theta_C$  being the Cabibbo angle.

Assuming the  $D$  meson wavefunction at the origin squared  $|\psi_{cq}^D(0)|^2$  being given by  $\frac{1}{12} f_D^2 m_D$ , we obtain  $|\psi^{\Lambda_c}(0)|^2 = 7.5 \times 10^{-3} \text{ GeV}^3$  for  $f_D = 220 \text{ MeV}$ .<sup>5</sup> To proceed to the numerical calculations, we use the Wilson coefficients  $c_1(\mu) = 1.35$  and  $c_2(\mu) = -0.64$  evaluated at the scale  $\mu = 1.25 \text{ GeV}$ . Since  $\eta = 1$  in the valence-quark approximation and since the wavefunction squared ratio  $r$  is evaluated using the quark model, it is reasonable to assume that the NQM and the valence-quark approximation are most reliable when

<sup>5</sup>The recent CLEO measurement of  $D^+ \rightarrow \mu^+ \nu$  yields  $f_{D^+} = 222.6 \pm 16.7^{+2.8}_{-3.4} \text{ MeV}$  [257].

Table 24.5: Various contributions to the decay rates (in units of  $10^{-12}$  GeV) of charmed baryons. The charmed meson wavefunction at the origin squared  $|\psi^D(0)|^2$  is taken to be  $\frac{1}{12}f_D^2m_D$ . Experimental values are taken from [3].

	$\Gamma^{\text{dec}}$	$\Gamma^{\text{ann}}$	$\Gamma_-^{\text{int}}$	$\Gamma_+^{\text{int}}$	$\Gamma_{\text{SL}}$	$\Gamma^{\text{tot}}$	$\tau(10^{-13}s)$	$\tau_{\text{expt}}(10^{-13}s)$
$\Lambda_c^+$	1.006	1.342	-0.196		0.323	2.492	2.64	$2.00 \pm 0.06$
$\Xi_c^+$	1.006	0.071	-0.203	0.364	0.547	1.785	3.68	$4.42 \pm 0.26$
$\Xi_c^0$	1.006	1.466		0.385	0.547	3.404	1.93	$1.12^{+0.13}_{-0.10}$
$\Omega_c^0$	1.132	0.439		1.241	1.039	3.851	1.71	$0.69 \pm 0.12$

the baryon matrix elements are evaluated at a typical hadronic scale  $\mu_{\text{had}}$ . As shown in [258], the parameters  $\eta$  and  $r$  renormalized at two different scales are related via the renormalization group equation, from which we obtain  $\eta(\mu) \simeq 0.74\eta(\mu_{\text{had}}) \simeq 0.74$  and  $r(\mu) \simeq 1.36r(\mu_{\text{had}})$  [252].

The results of calculations are summarized in Table 24.5. It is clear that the lifetime pattern

$$\tau(\Xi_c^+) > \tau(\Lambda_c^+) > \tau(\Xi_c^0) > \tau(\Omega_c^0) \quad (24.5.30)$$

is in accordance with experiment. This lifetime hierarchy is qualitatively understandable. The  $\Xi_c^+$  baryon is longest-lived among charmed baryons because of the smallness of  $W$ -exchange and partial cancellation between constructive and destructive Pauli interferences, while  $\Omega_c$  is shortest-lived due to the presence of two  $s$  quarks in the  $\Omega_c$  that renders the contribution of  $\Gamma_+^{\text{int}}$  largely enhanced. From Eq. (24.5.27) we also see that  $\Gamma_+^{\text{int}}$  is always positive,  $\Gamma_-^{\text{int}}$  is negative and that the constructive interference is larger than the magnitude of the destructive one. This explains why  $\tau(\Xi_c^+) > \tau(\Lambda_c^+)$ . It is also clear from Table 24.5 that, although the qualitative feature of the lifetime pattern is comprehensive, the quantitative estimates of charmed baryon lifetimes and their ratios are still rather poor.

In [256], a much larger charmed baryon wave function at the origin is employed. This is based on the argument originally advocated in [241]. The physical charmed meson decay constant  $f_D$  is related to the asymptotic static value  $F_D$  via

$$f_D = F_D \left( 1 - \frac{|\mu|}{m_c} + \mathcal{O}\left(\frac{1}{m_c^2}\right) \right). \quad (24.5.31)$$

It was argued in [241] that one should not use the physical value of  $f_D$  when relating  $|\psi^{\mathcal{B}_c}(0)|^2$  to  $|\psi^D(0)|^2$  for reason of consistency since the widths have been calculated through order  $1/m_c^3$  only. Hence, the part of  $f_D$  which is not suppressed by  $1/m_c$  should not be taken into account. However, if we use  $F_D \sim 2f_D$  for the wave function  $|\psi^D(0)|^2$ , we find that the predicted lifetimes of charmed baryons become too short compared to experiment except  $\Omega_c^0$ . By contrast, using  $|\psi^{\Lambda_c}(0)|^2 = 2.62 \times 10^{-2} \text{ GeV}^3$  and the so-called hybrid renormalization, lifetimes  $\tau(\Lambda_c^+) = 2.39$ ,  $\tau(\Xi_c^+) = 2.51$ ,  $\tau(\Xi_c^0) = 0.96$  and  $\tau(\Omega_c^0) = 0.61$  in units of  $10^{-13}s$  are obtained in [256]. They are in better agreement with

the data except  $\Xi_c^+$ . The predicted ratio  $\tau(\Xi_c^+)/\tau(\Lambda_c^+) = 1.05$  is too small compared to the experimental value of  $2.21 \pm 0.15$ . By inspecting Eq. (24.5.29), it seems to be very difficult to enhance the ratio by a factor of 2.

In short, when the lifetimes of charmed baryons are analyzed within the framework of the heavy quark expansion, the qualitative feature of the lifetime pattern is understandable, but a quantitative description of charmed baryon lifetimes is still lack. This may be ascribed to the following possibilities:

1. Unlike the semileptonic decays, the heavy quark expansion in inclusive nonleptonic decays cannot be justified by analytic continuation into the complex plane and local duality has to be assumed in order to apply the OPE directly in the physical region. This may suggest a significant violation of quark-hadron local duality in the charm sector.
2. Since the  $c$  quark is not heavy enough, it casts doubts on the validity of heavy quark expansion for inclusive charm decays. This point can be illustrated by the following example. It is well known that the observed lifetime difference between the  $D^+$  and  $D^0$  is ascribed to the destructive interference in  $D^+$  decays and/or the constructive  $W$ -exchange contribution to  $D^0$  decays. However, there is a serious problem with the evaluation of the destructive Pauli interference  $\Gamma^{\text{int}}(D^+)$  in  $D^+$ . A direct calculation analogous to  $\Gamma^{\text{int}}(\mathcal{B}_c)$  in the charmed baryon sector indicates that  $\Gamma^{\text{int}}(D^+)$  overcomes the  $c$  quark decay rate so that the resulting nonleptonic decay width of  $D^+$  becomes negative [241, 341]. This certainly does not make sense. This example clearly indicates that the  $1/m_c$  expansion in charm decay is not well convergent and sensible, to say the least. It is not clear if the situation is improved even after higher dimension terms are included.
3. To overcome the aforementioned difficulty with  $\Gamma^{\text{int}}(D^+)$ , it has been conjectured in [241] that higher-dimension corrections amount to replacing  $m_c$  by  $m_D$  in the expansion parameter  $f_D^2 m_D/m_c^3$ , so that it becomes  $f_D^2/m_D^2$ . As a consequence, the destructive Pauli interference will be reduced by a factor of  $(m_c/m_D)^3$ . By the same token, the Pauli interference in charmed baryon decay may also be subject to the same effect. Another way of alleviating the problem is to realize that the usual local four-quark operators are derived in the heavy quark limit so that the effect of spectator light quarks can be neglected. Since the charmed quark is not heavy enough, it is very important, as stressed by Chernyak [259], to take into account the nonzero momentum of spectator quarks in charm decay. In the framework of heavy quark expansion, this spectator effect can be regarded as higher order  $1/m_c$  corrections.
4. One of the major theoretical uncertainties comes from the evaluation of the four-quark matrix elements. One can hope that lattice QCD will provide a better handle on those quantities.

## 24.6 Hadronic weak decays

Contrary to the significant progress made over the last 20 years or so in the studies of the heavy meson weak decay, advancement in the arena of heavy baryons, both theoretical and experimental, has been relatively slow. This is partly due to the smaller baryon production cross section and the shorter lifetimes of heavy baryons. From the theoretical point of view, baryons being made out of three quarks, in contrast to two quarks for mesons, bring along several essential complications. First of all, the factorization approximation that the hadronic matrix element is factorized into the product of two matrix elements of single currents and that the nonfactorizable term such as the  $W$ -exchange contribution is negligible relative to the factorizable one is known empirically to be working reasonably well for describing the nonleptonic weak decays of heavy mesons. However, this approximation is *a priori* not directly applicable to the charmed baryon case as  $W$ -exchange there, manifested as pole diagrams, is no longer subject to helicity and color suppression. This is different from the naive color suppression of internal  $W$ -emission. It is known in the heavy meson case that nonfactorizable contributions will render the color suppression of internal  $W$ -emission ineffective. However, the  $W$ -exchange in baryon decays is not subject to color suppression even in the absence of nonfactorizable terms. A simple way to see this is to consider the large- $N_c$  limit. Although the  $W$ -exchange diagram is down by a factor of  $1/N_c$  relative to the external  $W$ -emission one, it is compensated by the fact that the baryon contains  $N_c$  quarks in the limit of large  $N_c$ , thus allowing  $N_c$  different possibilities for  $W$  exchange between heavy and light quarks [260]. That is, the pole contribution can be as important as the factorizable one. The experimental measurement of the decay modes  $\Lambda_c^+ \rightarrow \Sigma^0 \pi^+$ ,  $\Sigma^+ \pi^0$  and  $\Lambda_c^+ \rightarrow \Xi^0 K^+$ , which do not receive any factorizable contributions, indicates that  $W$ -exchange indeed plays an essential role in charmed baryon decays. Second, there are more possibilities in drawing the quark diagram amplitudes as depicted in Fig. 24.3; in general there exist two distinct internal  $W$ -emissions and several different  $W$ -exchange diagrams which will be discussed in more detail shortly.

Historically, the two-body nonleptonic weak decays of charmed baryons were first studied by utilizing the same technique of current algebra as in the case of hyperon decays [261]. However, the use of the soft-meson theorem makes sense only if the emitted meson is of the pseudoscalar type and its momentum is soft enough. Obviously, the pseudoscalar-meson final state in charmed baryon decay is far from being “soft”. Therefore, it is not appropriate to make the soft meson limit. It is no longer justified to apply current algebra to heavy-baryon weak decays, especially for  $s$ -wave amplitudes. Thus one has to go back to the original pole model, which is nevertheless reduced to current algebra in the soft pseudoscalar-meson limit, to deal with nonfactorizable contributions. The merit of the pole model is obvious: Its use is very general and is not limited to the soft meson limit and to the pseudoscalar-meson final state. Of course, the price we have to pay is that it requires the knowledge of the negative-parity baryon poles for the parity-violating transition. This also explains why the theoretical study of nonleptonic decays of heavy baryons is much more difficult than the hyperon and heavy meson decays.

The nonfactorizable pole contributions to hadronic weak decays of charmed baryons have been studied in the literature [262, 263, 264]. In general, nonfactorizable  $s$ - and  $p$ -wave amplitudes for  $\frac{1}{2}^+ \rightarrow \frac{1}{2}^+ + P(V)$  decays ( $P$ : pseudoscalar meson,  $V$ : vector

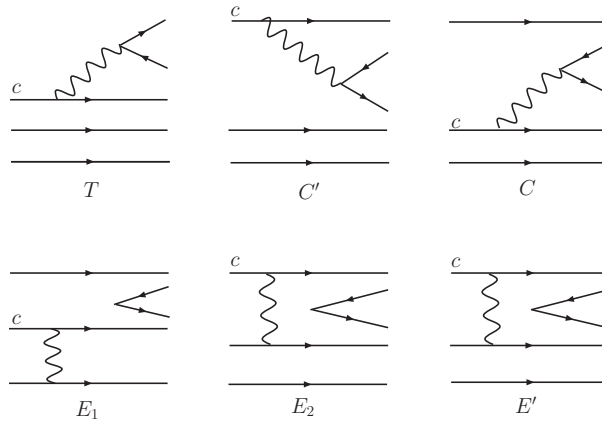


Figure 24.3: Quark diagrams for charmed baryon decays

meson), for example, are dominated by  $\frac{1}{2}^-$  low-lying baryon resonances and  $\frac{1}{2}^+$  ground-state baryon poles, respectively. However, the estimation of pole amplitudes is a difficult and nontrivial task since it involves weak baryon matrix elements and strong coupling constants of  $\frac{1}{2}^+$  and  $\frac{1}{2}^-$  baryon states. This is the case in particular for  $s$ -wave terms as we know very little about the  $\frac{1}{2}^-$  states. As a consequence, the evaluation of pole diagrams is far more uncertain than the factorizable terms. In short,  $W$ -exchange plays a dramatic role in the charmed baryon case and it even dominates over the spectator contribution in hadronic decays of  $\Lambda_c^+$  and  $\Xi_c^0$  [265].

Since the light quarks of the charmed baryon can undergo weak transitions, one can also have charm-flavor-conserving weak decays, e.g.,  $\Xi_c \rightarrow \Lambda_c \pi$  and  $\Omega_c \rightarrow \Xi_c \pi$ , where the charm quark behaves as a spectator. This special class of weak decays usually can be calculated more reliably than the conventional charmed baryon weak decays.

### 24.6.1 Quark-diagram scheme

Besides dynamical model calculations, it is useful to study the nonleptonic weak decays in a way which is as model independent as possible. The two-body nonleptonic decays of charmed baryons have been analyzed in terms of SU(3)-irreducible-representation amplitudes [266, 267]. However, the quark-diagram scheme (i.e., analyzing the decays in terms of quark-diagram amplitudes) has the advantage that it is more intuitive and easier for implementing model calculations. It has been successfully applied to the hadronic weak decays of charmed and bottom mesons [268, 269]. It has provided a framework with which we not only can do the least-model-dependent data analysis and give predictions but also make evaluations of theoretical model calculations.

A general formulation of the quark-diagram scheme for the nonleptonic weak decays of charmed baryons has been given in [270] (see also [271]). The general quark diagrams shown in Fig. 24.3 are: the external  $W$ -emission tree diagram  $T$ , internal  $W$ -emission diagrams  $C$  and  $C'$ ,  $W$ -exchange diagrams  $E_1$ ,  $E_2$  and  $E'$  (see Fig. 2 of [270] for notation and for details). There are also penguin-type quark diagrams which are presumably negligible in charm decays due to GIM cancellation. The quark diagram amplitudes  $T$ ,  $C$ ,  $C' \dots$  etc. in each type of hadronic decays are in general not the same. For octet

baryons in the final state, each of the  $W$ -exchange amplitudes has two more independent types: the symmetric and the antisymmetric, for example,  $E_{1A}$ ,  $E_{2A}$ ,  $E_{2S}$ ,  $E'_A$  and  $E'_S$  [270]. The antiquark produced from the charmed quark decay  $c \rightarrow q_1 q_2 \bar{q}_3$  in diagram  $C'$  can combine with  $q_1$  or  $q_2$  to form an outgoing meson. Consequently, diagram  $C'$  contains factorizable contributions but  $C$  does not. It should be stressed that all quark graphs used in this approach are topological with all the strong interactions included, i.e. gluon lines are included in all possible ways. Hence, they are *not* Feynman graphs. Moreover, final-state interactions are also classified in the same manner. A good example is the reaction  $D^0 \rightarrow \bar{K}^0 \phi$ , which can be produced via final-state rescattering even in the absence of the  $W$ -exchange diagram. Then it was shown in [269] that this rescattering diagram belongs to the generic  $W$ -exchange topology.

Since the two spectator light quarks in the heavy baryon are antisymmetrized in the antitriplet charmed baryon  $\mathcal{B}_c(\bar{\mathbf{3}})$  and the wave function of the decuplet baryon  $\mathcal{B}(\mathbf{10})$  is totally symmetric, it is clear that factorizable amplitudes  $T$  and  $C'$  cannot contribute to the decays of type  $\mathcal{B}_c(\bar{\mathbf{3}}) \rightarrow \mathcal{B}(\mathbf{10}) + M(\mathbf{8})$ ; it receives contributions only from the  $W$ -exchange and penguin-type diagrams (see Fig. 1 of [270]). Examples are  $\Lambda_c^+ \rightarrow \Delta^{++} K^-, \Sigma^{*+} \rho^0, \Sigma^{*+} \eta, \Xi^{*0} K^+$  and  $\Xi_c^0 \rightarrow \Sigma^{*+} \bar{K}^0$ . They can only proceed via  $W$ -exchange. Hence, the experimental observation of them implies that the  $W$ -exchange mechanism plays a significant role in charmed baryon decays. The quark diagram amplitudes for all two-body decays of (Cabibbo-allowed, singly suppressed and doubly suppressed)  $\Lambda_c^+, \Xi_c^{+,0}$  and  $\Omega_c^0$  are listed in [270]. In the SU(3) limit, there exist many relations among various charmed baryon decay amplitudes, see [270] for detail. For charmed baryon decays, there are only a few decay modes which proceed through factorizable external or internal  $W$ -emission diagram, namely, Cabibbo-allowed  $\Omega_c^0 \rightarrow \Omega^- \pi^+(\rho^+)$ ,  $\Xi^{*0} \bar{K}^0(\bar{K}^{*0})$  and Cabibbo-suppressed  $\Lambda_c^+ \rightarrow p\phi$ .

### 24.6.2 Dynamical model calculation

To proceed we first consider the Cabibbo-allowed decays  $\mathcal{B}_c(\frac{1}{2}^+) \rightarrow \mathcal{B}(\frac{1}{2}^+) + P(V)$ . The general amplitudes are

$$\begin{aligned} M[\mathcal{B}_i(1/2^+) \rightarrow \mathcal{B}_f(1/2^+) + P] &= i\bar{u}_f(p_f)(A + B\gamma_5)u_i(p_i), \\ M[\mathcal{B}_i(1/2^+) \rightarrow \mathcal{B}_f(1/2^+) + V] &= \bar{u}_f(p_f)\varepsilon^{*\mu}[A_1\gamma_\mu\gamma_5 + A_2(p_f)_\mu\gamma_5 + B_1\gamma_\mu + B_2(p_f)_\mu]u_i(p_i), \end{aligned} \quad (24.6.32)$$

where  $\varepsilon_\mu$  is the polarization vector of the vector meson,  $A$ ,  $(B, B_1, B_2)$  and  $A_2$  are  $s$ -wave,  $p$ -wave and  $d$ -wave amplitudes, respectively, and  $A_1$  consists of both  $s$ -wave and  $d$ -wave ones. The QCD-corrected weak Hamiltonian responsible for Cabibbo-allowed hadronic decays of charmed baryons reads

$$\mathcal{H}_W = \frac{G_F}{\sqrt{2}} V_{cs} V_{ud}^* (c_1 O_1 + c_2 O_2), \quad (24.6.33)$$

where  $O_1 = (\bar{s}c)(\bar{u}d)$  and  $O_2 = (\bar{s}d)(\bar{u}c)$  with  $(\bar{q}_1 q_2) \equiv \bar{q}_1 \gamma_\mu (1 - \gamma_5) q_2$ . From the expression of  $O_{1,2}$ , it is clear that factorization occurs if the final-state meson is  $\pi^+(\rho^+)$  or  $\bar{K}^0(\bar{K}^{*0})$ . Explicitly,

$$A^{\text{fac}}(\mathcal{B}_i \rightarrow \mathcal{B}_f + \pi^+) = \lambda a_1 f_P(m_i - m_f) f_1(m_\pi^2),$$

$$\begin{aligned}
B^{\text{fac}}(\mathcal{B}_i \rightarrow \mathcal{B}_f + \pi^+) &= \lambda a_1 f_P(m_i + m_f) g_1(m_\pi^2), \\
A^{\text{fac}}(\mathcal{B}_i \rightarrow \mathcal{B}_f + \bar{K}^0) &= \lambda a_2 f_P(m_i - m_f) f_1(m_K^2), \\
B^{\text{fac}}(\mathcal{B}_i \rightarrow \mathcal{B}_f + \bar{K}^0) &= \lambda a_2 f_P(m_i + m_f) g_1(m_K^2),
\end{aligned} \tag{24.6.34}$$

and

$$\begin{aligned}
A_1^{\text{fac}}(\mathcal{B}_i \rightarrow \mathcal{B}_f + \rho^+) &= -\lambda a_1 f_\rho m_\rho [g_1(m_\rho^2) + g_2(m_\rho^2)(m_i - m_f)], \\
A_2^{\text{fac}}(\mathcal{B}_i \rightarrow \mathcal{B}_f + \rho^+) &= -2\lambda a_1 f_\rho m_\rho g_2(m_\rho^2), \\
B_1^{\text{fac}}(\mathcal{B}_i \rightarrow \mathcal{B}_f + \rho^+) &= \lambda a_1 f_\rho m_\rho [f_1(m_\rho^2) - f_2(m_\rho^2)(m_i + m_f)], \\
B_2^{\text{fac}}(\mathcal{B}_i \rightarrow \mathcal{B}_f + \rho^+) &= 2\lambda a_1 f_\rho m_\rho f_2(m_\rho^2),
\end{aligned}$$

and similar expressions for  $\mathcal{B}_i \rightarrow \mathcal{B}_f + \bar{K}^{*0}$ , where  $\lambda = G_F V_{cs} V_{ud}^* / \sqrt{2}$ ,  $f_i$  and  $g_i$  are the form factors defined by ( $q = p_i - p_f$ )

$$\begin{aligned}
\langle \mathcal{B}_f(p_f) | V_\mu - A_\mu | \mathcal{B}_i(p_i) \rangle &= \bar{u}_f(p_f) [f_1(q^2) \gamma_\mu + i f_2(q^2) \sigma_{\mu\nu} q^\nu + f_3(q^2) q_\mu \\
&\quad - (g_1(q^2) \gamma_\mu + i g_2(q^2) \sigma_{\mu\nu} q^\nu + g_3(q^2) q_\mu) \gamma_5] u_i(p_i).
\end{aligned} \tag{24.6.35}$$

In the naive factorization approach, the coefficients  $a_1$  for the external  $W$ -emission amplitude and  $a_2$  for internal  $W$ -emission are given by  $(c_1 + \frac{c_2}{N_c})$  and  $(c_2 + \frac{c_1}{N_c})$ , respectively. However, we have learned from charmed meson decays that the naive factorization approach never works for the decay rate of color-suppressed decay modes, though it usually operates for color-allowed decays. Empirically, it was learned in the 1980s that if the Fierz-transformed terms characterized by  $1/N_c$  are dropped, the discrepancy between theory and experiment is greatly improved [272]. This leads to the so-called large- $N_c$  approach for describing hadronic  $D$  decays [273]. Theoretically, explicit calculations based on the QCD sum-rule analysis [274] indicate that the Fierz terms are indeed largely compensated by the nonfactorizable corrections.

As the discrepancy between theory and experiment for charmed meson decays gets much improved in the  $1/N_c$  expansion method, it is natural to ask if this scenario also works in the baryon sector? This issue can be settled down by the experimental measurement of the Cabibbo-suppressed mode  $\Lambda_c^+ \rightarrow p\phi$ , which receives contributions only from the factorizable diagrams. As pointed out in [262], the large- $N_c$  predicted rate is in good agreement with the measured value. By contrast, its decay rate predicted by the naive factorization approximation is too small by a factor of 15. Therefore, the  $1/N_c$  approach also works for the factorizable amplitude of charmed baryon decays. This also implies that the inclusion of nonfactorizable contributions is inevitable and necessary. If nonfactorizable effects amount to a redefinition of the effective parameters  $a_1, a_2$  and are universal (i.e., channel-independent) in charm decays, then we still have a new factorization scheme with the universal parameters  $a_1, a_2$  to be determined from experiment. Throughout this paper, we will thus treat  $a_1$  and  $a_2$  as free effective parameters.

At the hadronic level, the decay amplitudes for quark diagrams  $T$  and  $C'$  are conventionally evaluated using the factorization approximation. How do we tackle with the remaining nonfactorizable diagrams  $C, E_1, E_2, E'$ ? One popular approach is to consider the contributions from all possible intermediate states. Among all possible pole contributions, including resonances and continuum states, one usually focuses on the most

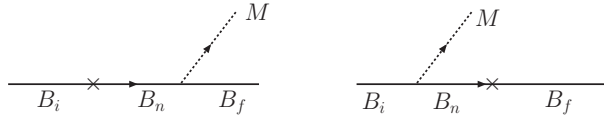


Figure 24.4: Pole diagrams for charmed baryon decay  $\mathcal{B}_i \rightarrow \mathcal{B}_f + M$ .

important poles such as the low-lying  $\frac{1}{2}^+, \frac{1}{2}^-$  states, known as pole approximation. More specifically, the  $s$ -wave amplitude is dominated by the low-lying  $1/2^-$  resonances and the  $p$ -wave one governed by the ground-state  $1/2^+$  poles (see Fig. 24.4):

$$\begin{aligned} A^{\text{nf}} &= - \sum_{\mathcal{B}_n^*(1/2^-)} \left( \frac{g_{\mathcal{B}_f \mathcal{B}_{n^*} P} b_{n^* i}}{m_i - m_{n^*}} + \frac{b_{f n^*} g_{\mathcal{B}_{n^*} \mathcal{B}_i P}}{m_f - m_{n^*}} \right) + \dots, \\ B^{\text{nf}} &= - \sum_{\mathcal{B}_n} \left( \frac{g_{\mathcal{B}_f \mathcal{B}_n P} a_{ni}}{m_i - m_n} + \frac{a_{fn} g_{\mathcal{B}_n \mathcal{B}_i P}}{m_f - m_n} \right) + \dots, \end{aligned} \quad (24.6.36)$$

where  $A^{\text{nf}}$  and  $B^{\text{nf}}$  are the nonfactorizable  $s$ - and  $p$ -wave amplitudes of  $\mathcal{B}_c \rightarrow \mathcal{B}P$ , respectively, ellipses in Eq.(24.6.36) denote other pole contributions which are negligible for our purposes, and  $a_{ij}$  as well as  $b_{i^*j}$  are the baryon-baryon matrix elements defined by

$$\langle \mathcal{B}_i | \mathcal{H}_W | \mathcal{B}_j \rangle = \bar{u}_i (a_{ij} - b_{ij} \gamma_5) u_j, \quad \langle \mathcal{B}_i^*(1/2^-) | \mathcal{H}_W^{\text{PV}} | \mathcal{B}_j \rangle = i b_{i^*j} \bar{u}_i u_j, \quad (24.6.37)$$

with  $b_{ji^*} = -b_{i^*j}$ . Evidently, the calculation of  $s$ -wave amplitudes is more difficult than the  $p$ -wave owing to the troublesome negative-parity baryon resonances which are not well understood in the quark model. In [262, 263], the form factors appearing in factorizable amplitudes and the strong coupling constants and baryon transition matrix elements relevant to nonfactorizable contributions are evaluated using the MIT bag model [275]. Two of the pole model calculations for branching ratios [263, 264] are displayed in Table 24.6. The study of charmed baryon hadronic decays in [276] is similar to [263, 264] except that the effect of  $W$ -exchange is parametrized in terms of the baryon wave function at origin. Sharma and Verma [276] defined a parameter  $r = |\psi^{\mathcal{B}_c}(0)|^2 / |\psi^{\mathcal{B}}(0)|^2$  and argued that its value is close to 1.4. A variant of the pole model has been considered in [277] in which the effects of pole-model-induced SU(4) symmetry breaking in parity-conserving and parity-violating amplitudes are studied.

Instead of decomposing the decay amplitude into products of strong couplings and two-body weak transitions, Körner and Krämer [260] have analyzed the nonleptonic weak processes using the spin-flavor structure of the effective Hamiltonian and the wave functions of baryons and mesons described by the covariant quark model. The nonfactorizable amplitudes are then obtained in terms of two wave function overlap parameters  $H_2$  and  $H_3$ , which are in turn determined by fitting to the experimental data of  $\Lambda_c^+ \rightarrow p \bar{K}^0$  and  $\Lambda_c^+ \rightarrow \Lambda \pi^+$ , respectively. Despite the absence of first-principles calculation of the parameters  $H_2$  and  $H_3$ , this quark model approach has fruitful predictions for not only  $\mathcal{B}_c \rightarrow \mathcal{B} + P$ , but also  $\mathcal{B}_c \rightarrow \mathcal{B} + V$ ,  $\mathcal{B}^*(3/2^+) + P$  and  $\mathcal{B}^*(3/2^+) + V$  decays. Another advantage of this analysis is that each amplitude has one-to-one quark-diagram interpretation. While the overlap integrals are treated as phenomenological parameters to be determined from a fit to the data, Ivanov *et al.* [278] developed a microscopic approach to the overlap integrals by specifying the form of the hadron-quark transition vertex including the explicit momentum dependence of the Lorentz scalar part of this vertex.

Table 24.6: Branching ratios of Cabibbo-allowed  $\mathcal{B}_c \rightarrow \mathcal{B} + P$  decays in various models. Results of [260, 264, 263] have been normalized using the current world averages of charmed baryon lifetimes [3]. Branching ratios cited from [276] are for  $\phi_{\eta-\eta'} = -23^\circ$  and  $r = 1.4$ . The experimental branching fraction for  $\Xi_c^+ \rightarrow \Xi^0 \pi^+$  is relative to  $\Xi_c^+ \rightarrow \Xi^- \pi^+ \pi^+$ .

Decay	Körner, Krämer [260]	Xu, Kamal [264]	Cheng, Tseng [263]	Ivanov et al. [278]	Żenczy- kowski[277]	Sharma [276]	Expt. [3]
$\Lambda_c^+ \rightarrow \Lambda \pi^+$	input	1.62	0.88	0.79	0.54	1.12	$0.90 \pm 0.28$
$\Lambda_c^+ \rightarrow \Sigma^0 \pi^+$	0.32	0.34	0.72	0.88	0.41	1.34	$0.99 \pm 0.32$
$\Lambda_c^+ \rightarrow \Sigma^+ \pi^0$	0.32	0.34	0.72	0.88	0.41	1.34	$1.00 \pm 0.34$
$\Lambda_c^+ \rightarrow \Sigma^+ \eta$	0.16			0.11	0.94	0.57	$0.48 \pm 0.17$
$\Lambda_c^+ \rightarrow \Sigma^+ \eta'$	1.28			0.12	0.12	0.10	
$\Lambda_c^+ \rightarrow p K^0$	input	1.20	1.26	2.06	1.79	1.64	$2.3 \pm 0.6$
$\Lambda_c^+ \rightarrow \Xi^0 K^+$	0.26	0.10		0.31	0.36	0.13	$0.39 \pm 0.14$
$\Xi_c^+ \rightarrow \Sigma^+ K^0$	6.45	0.44	0.84	3.08	1.56	0.04	
$\Xi_c^+ \rightarrow \Xi^0 \pi^+$	3.54	3.36	3.93	4.40	1.59	0.53	$0.55 \pm 0.16$
$\Xi_c^0 \rightarrow \Lambda K^0$	0.12	0.37	0.27	0.42	0.35	0.54	seen
$\Xi_c^0 \rightarrow \Sigma^0 K^0$	1.18	0.11	0.13	0.20	0.11	0.07	
$\Xi_c^0 \rightarrow \Sigma^+ K^-$	0.12	0.12		0.27	0.36	0.12	
$\Xi_c^0 \rightarrow \Xi^0 \pi^0$	0.03	0.56	0.28	0.04	0.69	0.87	
$\Xi_c^0 \rightarrow \Xi^0 \eta$	0.24			0.28	0.01	0.22	
$\Xi_c^0 \rightarrow \Xi^0 \eta'$	0.85			0.31	0.09	0.06	
$\Xi_c^0 \rightarrow \Xi^- \pi^+$	1.04	1.74	1.25	1.22	0.61	2.46	seen
$\Omega_c^0 \rightarrow \Xi^0 K^0$	1.21		0.09	0.02			

Table 24.7: The predicted asymmetry parameter  $\alpha$  for Cabibbo-allowed  $\mathcal{B}_c \rightarrow \mathcal{B} + P$  decays in various models. Results cited from [276] are for  $\phi_{\eta-\eta'} = -23^\circ$  and  $r = 1.4$ .

Decay	Körner, Krämer [260]	Xu, Kamal [264]	Cheng, Tseng [263]	Ivanov et al. [278]	Żenczy- kowski[277]	Sharma, [276]	Expt. [3]
$\Lambda_c^+ \rightarrow \Lambda \pi^+$	-0.70	-0.67	-0.95	-0.95	-0.99	-0.99	$-0.91 \pm 0.15$
$\Lambda_c^+ \rightarrow \Sigma^0 \pi^+$	0.70	0.92	0.78	0.43	0.39	-0.31	
$\Lambda_c^+ \rightarrow \Sigma^+ \pi^0$	0.71	0.92	0.78	0.43	0.39	-0.31	$-0.45 \pm 0.32$
$\Lambda_c^+ \rightarrow \Sigma^+ \eta$	0.33			0.55	0	-0.91	
$\Lambda_c^+ \rightarrow \Sigma^+ \eta'$	-0.45			-0.05	-0.91	0.78	
$\Lambda_c^+ \rightarrow p K^0$	-1.0	0.51	-0.49	-0.97	-0.66	-0.99	
$\Lambda_c^+ \rightarrow \Xi^0 K^+$	0	0		0	0	0	
$\Xi_c^+ \rightarrow \Sigma^+ K^0$	-1.0	0.24	-0.09	-0.99	1.00	0.54	
$\Xi_c^+ \rightarrow \Xi^0 \pi^+$	-0.78	-0.81	-0.77	-1.0	1.00	-0.27	
$\Xi_c^0 \rightarrow \Lambda K^0$	-0.76	1.0	-0.73	-0.75	-0.29	-0.79	
$\Xi_c^0 \rightarrow \Sigma^0 K^0$	-0.96	-0.99	-0.59	-0.55	-0.50	0.48	
$\Xi_c^0 \rightarrow \Sigma^+ K^-$	0	0		0	0	0	
$\Xi_c^0 \rightarrow \Xi^0 \pi^0$	0.92	0.92	-0.54	0.94	0.21	-0.80	
$\Xi_c^0 \rightarrow \Xi^0 \eta$	-0.92			-1.0	-0.04	0.21	
$\Xi_c^0 \rightarrow \Xi^0 \eta'$	-0.38			-0.32	-1.00	0.80	
$\Xi_c^0 \rightarrow \Xi^- \pi^+$	-0.38	-0.38	-0.99	-0.84	-0.79	-0.97	$-0.6 \pm 0.4$
$\Omega_c^0 \rightarrow \Xi^0 K^0$	0.51		-0.93	-0.81			

Table 24.8: Branching ratios of Cabibbo-allowed  $\mathcal{B}_c \rightarrow \mathcal{B} + V$  decays in various models. The experimental value denoted by the superscript \* is the branching ratio relative to  $\Xi_c^+ \rightarrow \Xi^- \pi^+ \pi^+$ .

Decay	Körner, Krämer [260]	Żenczykowski [277]	Cheng, Tseng [262]	Experiment [3]
$\Lambda_c^+ \rightarrow \Lambda \rho^+$	19.08	1.80	2.6	$< 5$
$\Lambda_c^+ \rightarrow \Sigma^0 \rho^+$	3.14	1.56	0.19	$0.99 \pm 0.32$
$\Lambda_c^+ \rightarrow \Sigma^+ \rho^0$	3.12	1.56	0.19	$< 1.4$
$\Lambda_c^+ \rightarrow \Sigma^+ \omega$	4.02	1.10		$2.7 \pm 1.0$
$\Lambda_c^+ \rightarrow \Sigma^+ \phi$	0.26	0.11		$0.32 \pm 0.10$
$\Lambda_c^+ \rightarrow p K^{*0}$	3.08	5.03	3.3	$1.6 \pm 0.5$
$\Lambda_c^+ \rightarrow \Xi^0 K^{*+}$	0.12	0.11		$0.39 \pm 0.14$
$\Xi_c^+ \rightarrow \Sigma^+ K^{*0}$	2.34	7.38		$0.81 \pm 0.15^*$
$\Xi_c^+ \rightarrow \Xi^0 \rho^+$	95.83	5.48		
$\Xi_c^0 \rightarrow \Lambda K^{*0}$	1.12	1.15		
$\Xi_c^0 \rightarrow \Sigma^0 K^{*0}$	0.62	0.77		
$\Xi_c^0 \rightarrow \Sigma^+ K^{*-}$	0.39	0.37		
$\Xi_c^0 \rightarrow \Xi^0 \rho^0$	1.71	1.22		
$\Xi_c^0 \rightarrow \Xi^0 \omega$	2.33	0.15		
$\Xi_c^0 \rightarrow \Xi^0 \phi$	0.18	0.10		
$\Xi_c^0 \rightarrow \Xi^- \rho^+$	12.29	1.50		
$\Omega_c^0 \rightarrow \Xi^0 K^{*0}$	0.59			

Table 24.9: Branching ratios and decay asymmetries (in parentheses) of Cabibbo-allowed  $\mathcal{B}_c \rightarrow \mathcal{B}(3/2^+) + P(V)$  decays in various models. Experimental values denoted by the superscript \* are the branching ratios relative to  $\Xi_c^+ \rightarrow \Xi^-\pi^+\pi^+$ . The model calculations of Xu and Kamal are done in two different schemes [281].

Decay	Körner, Krämer [260]	Xu & Kamal [281]	Cheng [282]	Experiment [3]
$\Lambda_c^+ \rightarrow \Delta^{++}K^-$	2.70	1.00(0.00); 1.04(0.43)		$0.86 \pm 0.30$
$\Lambda_c^+ \rightarrow \Delta^+K^0$	0.90	0.34(0.00); 0.34(0.43)		$0.99 \pm 0.32$
$\Lambda_c^+ \rightarrow \Xi^{*0}K^+$	0.50	0.08(0.00); 0.08(0.25)		$0.26 \pm 0.10$
$\Lambda_c^+ \rightarrow \Sigma^{*+}\pi^0$	0.50	0.22(0.00); 0.24(0.40)		
$\Lambda_c^+ \rightarrow \Sigma^{*0}\pi^+$	0.50	0.22(0.00); 0.24(0.40)		
$\Lambda_c^+ \rightarrow \Sigma^{*+}\eta$	0.54			$0.85 \pm 0.33$
$\Xi_c^+ \rightarrow \Sigma^{*+}K^0$	0	0		$1.0 \pm 0.5^*$
$\Xi_c^+ \rightarrow \Xi^{*0}\pi^+$	0	0		$< 0.1^*$
$\Xi_c^0 \rightarrow \Omega^-K^+$	0.34	0.15(0.00); 0.16(0.27)		seen
$\Xi_c^0 \rightarrow \Sigma^{*0}K^0$	0.25	0.09(0.00); 0.10(0.43)		
$\Xi_c^0 \rightarrow \Sigma^{*+}K^-$	0.49	0.18(0.00); 0.19(0.43)		
$\Xi_c^0 \rightarrow \Xi^{*0}\pi^0$	0.28	0.12(0.00); 0.13(0.40)		
$\Xi_c^0 \rightarrow \Xi^{*-}\pi^+$	0.56	0.25(0.00); 0.27(0.40)		
$\Omega_c^0 \rightarrow \Omega^-\pi^+$	$0.35a_1^2$	$1.47a_1^2(0); 1.44a_1^2(0)$	$0.92a_1^2(0.17)$	seen
$\Omega_c^0 \rightarrow \Xi^{*0}K^0$	$0.40a_2^2$	$0.69a_2^2(0); 0.61a_2^2(0)$	$1.06a_2^2(0.35)$	
$\Omega_c^0 \rightarrow \Omega^-\rho^+$	$2.02a_1^2$	$8.02a_1^2(-0.08); 7.82a_2^2(-0.21)$	$3.23a_1^2(0.43)$	
$\Omega_c^0 \rightarrow \Xi^{*0}K^{*0}$	$2.28a_2^2$	$3.15a_2^2(-0.09); 1.13a_2^2(-0.27)$	$1.60a_2^2(0.28)$	

### 24.6.3 Discussions

Various model predictions of the branching ratios and decay asymmetries for Cabibbo-allowed  $\mathcal{B}_c \rightarrow \mathcal{B} + P(V)$  decays are summarized in Tables 24.6-24.9. In the following we shall first discuss the decay asymmetry parameter  $\alpha$  and then turn to the decay rates.

#### Decay asymmetry

A very useful information is provided by the study of the polarization of the daughter baryon  $\mathcal{B}'$  in the decay  $\mathcal{B} \rightarrow \mathcal{B}'\pi$ . Its general expression is given by

$$\mathbf{P}_{\mathcal{B}'} = \frac{(\alpha_{\mathcal{B}} + \mathbf{P}_{\mathcal{B}} \cdot \mathbf{n})\mathbf{n} + \beta_{\mathcal{B}}(\mathbf{n} \times \mathbf{P}_{\mathcal{B}}) + \gamma_{\mathcal{B}}\mathbf{n} \times (\mathbf{n} \times \mathbf{P}_{\mathcal{B}})}{1 + \alpha_{\mathcal{B}}\mathbf{P}_{\mathcal{B}} \cdot \mathbf{n}}, \quad (24.6.38)$$

where  $\mathbf{P}_{\mathcal{B}}$  is the parent baryon polarization,  $\alpha_{\mathcal{B}}$ ,  $\beta_{\mathcal{B}}$  and  $\gamma_{\mathcal{B}}$  are the parent baryon asymmetry parameters and  $\mathbf{n}$  is a unit vector along the daughter baryon  $\mathcal{B}'$  in the parent baryon frame. If the parent baryon is unpolarized, the above equation reduces to  $\mathbf{P}_{\mathcal{B}'} = \alpha_{\mathcal{B}}\mathbf{n}$ , which implies that the baryon  $\mathcal{B}'$  obtained from the decay of the unpolarized baryon  $\mathcal{B}$  is longitudinally polarized by the amount of  $\alpha_{\mathcal{B}}$ . The transverse polarization components are measured by the parameters  $\beta_{\mathcal{B}}$  and  $\gamma_{\mathcal{B}}$ . In terms of the  $s$ - and  $p$ -wave amplitudes in Eq. (24.6.32), the baryon parameters have the expressions

$$\alpha = \frac{2\text{Re}(S^*P)}{|S|^2 + |P|^2}, \quad \beta = \frac{2\text{Im}(S^*P)}{|S|^2 + |P|^2}, \quad \gamma = \frac{|S|^2 - |P|^2}{|S|^2 + |P|^2}, \quad (24.6.39)$$

where

$$S = \sqrt{2m_{\mathcal{B}'}(E' + m_{\mathcal{B}'})} A, \quad P = \sqrt{2m_{\mathcal{B}'}(E' - m_{\mathcal{B}'})} B. \quad (24.6.40)$$

When  $CP$  is conserved and final-state interactions are negligible,  $\beta$  vanishes. Since the sign of  $\alpha_{\mathcal{B}}$  depends on the relative sign between  $s$ - and  $p$ -wave amplitudes, the measurement of  $\alpha$  can be used to discriminate between different models.

The model predictions for the decay asymmetry  $\alpha$  in  $\Lambda_c^+ \rightarrow \Lambda\pi^+$  range from  $-0.67$  to  $-0.99$  (see Table 24.7). The current world average of  $\alpha$  is  $-0.91 \pm 0.15$  [3], while the most recent measurement is  $-0.78 \pm 0.16 \pm 0.19$  by FOCUS [279]. The agreement between theory and experiment implies the  $V - A$  structure of the decay process  $\Lambda_c^+ \rightarrow \Lambda\pi^+$ .

It is evident from Table 24.7 that all the models except one model in [276] predict a positive decay asymmetry for the decay  $\Lambda_c^+ \rightarrow \Sigma^+\pi^0$ . Therefore, the measurement of  $\alpha = -0.45 \pm 0.31 \pm 0.06$  by CLEO [280] is a big surprise. If the negative sign of  $\alpha$  is confirmed in the future, this will imply an opposite sign between  $s$ -wave and  $p$ -wave amplitudes for this decay, contrary to the model expectation. The implication of this has been discussed in detail in [262]. Since the error of the previous CLEO measurement is very large, it is crucial to have more accurate measurements of the decay asymmetry for  $\Lambda_c^+ \rightarrow \Sigma^+\pi^0$ .

The decays  $\Lambda_c^+ \rightarrow \Xi^0K^+$  and  $\Xi_c^0 \rightarrow \Sigma^+K^-$  share some common features that they can proceed via  $W$ -exchange [270] and that their  $s$ -wave amplitudes are very small. As a consequence, their decay asymmetries are expected to be very tiny. Indeed, all the existing models predict vanishing  $s$ -wave amplitude and hence  $\alpha = 0$  (cf. Table 24.7).

### $\Lambda_c^+$ decays

Experimentally, nearly all the branching ratios of the  $\Lambda_c^+$  are measured relative to the  $pK^-\pi^+$  mode. Some Cabibbo-suppressed modes such as  $\Lambda_c^+ \rightarrow \Lambda K^+$  and  $\Lambda_c^+ \rightarrow \Sigma^0K^+$  have been recently measured by BaBar [283]. Theoretically, only one model [284] gives predictions for the Cabibbo-suppressed decays.

The first measured Cabibbo-suppressed mode  $\Lambda_c^+ \rightarrow p\phi$  is of particular interest because it receives contributions only from the factorizable diagram and is expected to be color suppressed in the naive factorization approach. An updated calculation in [285] yields

$$\mathcal{B}(\Lambda_c^+ \rightarrow p\phi) = 2.26 \times 10^{-3} a_2^2, \quad \alpha(\Lambda_c^+ \rightarrow p\phi) = -0.10. \quad (24.6.41)$$

From the experimental measurement  $\mathcal{B}(\Lambda_c^+ \rightarrow p\phi) = (8.2 \pm 2.7) \times 10^{-4}$  [3], it follows that

$$|a_2|_{\text{expt}} = 0.60 \pm 0.10. \quad (24.6.42)$$

This is in excellent agreement with the  $1/N_c$  approach where  $a_2 = c_2(m_c) = -0.59$ .

### $\Xi_c^+$ decays

No absolute branching ratios have been measured. The branching ratios listed in Tables 24.6 and 24.8 are the ones relative to  $\Xi_c^+ \rightarrow \Xi^-\pi^+\pi^+$ . Several Cabibbo-suppressed decay modes such as  $p\bar{K}^{*0}$ ,  $\Sigma^+\phi$  and  $\Xi(1690)K^+$  have been observed.

The Cabibbo-allowed decays  $\Xi_c^+ \rightarrow \mathcal{B}(3/2^+) + P$  have been studied and they are believed to be forbidden as they do not receive factorizable and  $1/2^\pm$  pole contributions

[281, 260]. However, the  $\Sigma^{*+}\bar{K}^0$  mode was seen by FOCUS before [286] and this may indicate the importance of pole contributions beyond low-lying  $1/2^\pm$  intermediate states.

### $\Xi_c^0$ decays

No absolute branching ratios have been measured so far. However, there are several measurements of ratios of branching fractions, for example [3],

$$R_1 = \frac{\Gamma(\Xi_c^0 \rightarrow \Lambda K_S^0)}{\Gamma(\Xi_c^0 \rightarrow \Xi^-\pi^+)} = 0.21 \pm 0.02 \pm 0.02, \quad R_2 = \frac{\Gamma(\Xi_c^0 \rightarrow \Omega^-K^+)}{\Gamma(\Xi_c^0 \rightarrow \Xi^-\pi^+)} = 0.297 \pm 0.024. \quad (24.6.43)$$

Most models predict a ratio of  $R_1$  smaller than 0.18 except the model of Żenczykowski [277] which yields  $R_1 = 0.29$  due to the small predicted rate of  $\Xi_c^0 \rightarrow \Xi^-\pi^+$  (see Table 24.6). The model of Körner and Krämer [260] predicts  $R_2 = 0.33$  (Table 24.9), in agreement with experiment, but its prediction  $R_1 = 0.06$  is too small compared to the data.

### $\Omega_c^0$ decays

One of the unique features of the  $\Omega_c^0$  decay is that the decay  $\Omega_c^0 \rightarrow \Omega^-\pi^+$  proceeds only via external  $W$ -emission, while  $\Omega_c^0 \rightarrow \Xi^{*0}\bar{K}^0$  proceeds via the factorizable internal  $W$ -emission diagram  $C'$ . The general amplitudes for  $\mathcal{B}_c \rightarrow B^*(\frac{3}{2}^+) + P(V)$  are:

$$\begin{aligned} M[\mathcal{B}_i \rightarrow \mathcal{B}_f^*(3/2^+) + P] &= iq_\mu \bar{u}_f^\mu(p_f)(C + D\gamma_5)u_i(p_i), \\ M[\mathcal{B}_i \rightarrow \mathcal{B}_f^*(3/2^+) + V] &= \bar{u}_f^\nu(p_f)\varepsilon^{*\mu}[g_{\nu\mu}(C_1 + D_1\gamma_5) \\ &\quad + p_{1\nu}\gamma_\mu(C_2 + D_2\gamma_5) + p_{1\nu}p_{2\mu}(C_3 + D_3\gamma_5)]u_i(p_i), \end{aligned} \quad (24.6.44)$$

with  $u^\mu$  being the Rarita-Schwinger vector spinor for a spin- $\frac{3}{2}$  particle. Various model predictions of Cabibbo-allowed  $\Omega_c^0 \rightarrow \mathcal{B}(3/2^+) + P(V)$  are displayed in Table 24.9 with the unknown parameters  $a_1$  and  $a_2$ . From the decay  $\Lambda_c^+ \rightarrow p\phi$  we learn that  $|a_2| = 0.60 \pm 0.10$ . Notice a sign difference of  $\alpha$  for  $\Omega_c \rightarrow \frac{3}{2}^+ + V$  in [281] and [282]. It seems to us that the sign of  $A_i$  and  $B_i$  in Eq. (58) of [281] should be flipped. A consequence of this sign change will render  $\alpha$  positive in  $\Omega_c \rightarrow \frac{3}{2}^+ + V$  decay. In the model of Xu and Kamal [281], the  $D$ -wave amplitude in Eq. (24.6.44) and hence the parameter  $\alpha$  vanishes in the decay  $\Omega_c \rightarrow \frac{3}{2}^+ + P$  due to the fact that the vector current is conserved at all  $q^2$  in their scheme 1 and at  $q^2 = 0$  in scheme 2.

#### 24.6.4 Charm-flavor-conserving weak decays

There is a special class of weak decays of charmed baryons which can be studied in a reliable way, namely, heavy-flavor-conserving nonleptonic decays. Some examples are the singly Cabibbo-suppressed decays  $\Xi_c \rightarrow \Lambda_c\pi$  and  $\Omega_c \rightarrow \Xi_c'\pi$ . The idea is simple: In these decays only the light quarks inside the heavy baryon will participate in weak interactions; that is, while the two light quarks undergo weak transitions, the heavy quark behaves as a “spectator”. As the emitted light mesons are soft, the  $\Delta S = 1$  weak interactions among light quarks can be handled by the well known short-distance effective Hamiltonian. The

Table 24.10: Predicted semileptonic decay rates (in units of  $10^{10} s^{-1}$ ) and decay asymmetries (second entry) in various models. Dipole  $q^2$  dependence for form factors is assumed whenever the form-factor momentum dependence is not calculated in the model. Predictions of [289] are obtained in the non-relativistic quark model and the MIT bag model (in parentheses).

Process	Pérez-Marcial et al. [289]	Singleton [290]	Cheng, Tseng [285]	Ivanov [291]	Luo [292]	Marques de Carvalho [293]	Huang, Wang [294]	Expt. [3]
$\Lambda_c^+ \rightarrow \Lambda^0 e^+ \nu_e$	11.2 (7.7)	9.8	7.1	7.22 -0.812	7.0	$13.2 \pm 1.8$ -1	$10.9 \pm 3.0$ -0.88 $\pm 0.03$	$10.5 \pm 3.0$ -0.86 $\pm 0.04$
$\Xi_c^0 \rightarrow \Xi^- e^+ \nu_e$	18.1 (12.5)	8.5	7.4	8.16	9.7			seen
$\Xi_c^+ \rightarrow \Xi^0 e^+ \nu_e$	18.4 (12.7)	8.5	7.4	8.16	9.7			seen

synthesis of heavy-quark and chiral symmetries provides a natural setting for investigating these reactions [287]. The weak decays  $\Xi_Q \rightarrow \Lambda_Q \pi$  with  $Q = c, b$  were also studied in [288].

The combined symmetries of heavy and light quarks severely restricts the weak interactions allowed. In the symmetry limit, it is found that there cannot be  $\mathcal{B}_{\bar{3}} - \mathcal{B}_6$  and  $\mathcal{B}_6^* - \mathcal{B}_6$  nonleptonic weak transitions. Symmetries alone permit three types of transitions:  $\mathcal{B}_{\bar{3}} - \mathcal{B}_{\bar{3}}$ ,  $\mathcal{B}_6 - \mathcal{B}_6$  and  $\mathcal{B}_6^* - \mathcal{B}_6$  transitions. However, in both the MIT bag and diquark models, only  $\mathcal{B}_{\bar{3}} - \mathcal{B}_{\bar{3}}$  transitions have nonzero amplitudes.

The predicted rates are [287]

$$\begin{aligned} \Gamma(\Xi_c^0 \rightarrow \Lambda_c^+ \pi^-) &= 1.7 \times 10^{-15} \text{ GeV}, & \Gamma(\Xi_c^+ \rightarrow \Lambda_c^+ \pi^0) &= 1.0 \times 10^{-15} \text{ GeV}, \\ \Gamma(\Omega_c^0 \rightarrow \Xi_c^+ \pi^-) &= 4.3 \times 10^{-17} \text{ GeV}, \end{aligned} \quad (24.6.45)$$

and the corresponding branching ratios are

$$\begin{aligned} \mathcal{B}(\Xi_c^0 \rightarrow \Lambda_c^+ \pi^-) &= 2.9 \times 10^{-4}, & \mathcal{B}(\Xi_c^+ \rightarrow \Lambda_c^+ \pi^0) &= 6.7 \times 10^{-4}, \\ \mathcal{B}(\Omega_c^0 \rightarrow \Xi_c^+ \pi^-) &= 4.5 \times 10^{-6}. \end{aligned} \quad (24.6.46)$$

As stated above, the  $\mathcal{B}_6 - \mathcal{B}_6$  transition  $\Omega_c^0 \rightarrow \Xi_c^+ \pi^-$  vanishes in the chiral limit. It receives a finite factorizable contribution as a result of symmetry-breaking effect. At any rate, the predicted branching ratios for the charm-flavor-conserving decays  $\Xi_c^0 \rightarrow \Lambda_c^+ \pi^-$  and  $\Xi_c^+ \rightarrow \Lambda_c^+ \pi^0$  are of order  $10^{-3} \sim 10^{-4}$  and should be readily accessible in the near future.

## 24.7 Semileptonic decays

The exclusive semileptonic decays of charmed baryons:  $\Lambda_c^+ \rightarrow \Lambda e^+(\mu^+) \nu_e$ ,  $\Xi_c^+ \rightarrow \Xi^0 e^+ \nu_e$  and  $\Xi_c^0 \rightarrow \Xi^- e^+ \nu_e$  have been observed experimentally. Their rates depend on the  $\mathcal{B}_c \rightarrow \mathcal{B}$  form factors  $f_i(q^2)$  and  $g_i(q^2)$  ( $i = 1, 2, 3$ ) defined in Eq. (24.6.35). These form factors have been evaluated in the non-relativistic quark model [289, 290, 285], the MIT bag model [289], the relativistic quark model [291], the light-front quark model [292] and QCD sum rules [293, 294]. Experimentally, the only information available so far is the

form-factor ratio measured in the semileptonic decay  $\Lambda_c \rightarrow \Lambda e \bar{\nu}$ . In the heavy quark limit, the six  $\Lambda_c \rightarrow \Lambda$  form factors are reduced to two:

$$\langle \Lambda(p) | \bar{s} \gamma_\mu (1 - \gamma_5) c | \Lambda_c(v) \rangle = \bar{u}_\Lambda (F_1^{\Lambda_c \Lambda}(v \cdot p) + \not{v} F_2^{\Lambda_c \Lambda}(v \cdot p)) \gamma_\mu (1 - \gamma_5) u_{\Lambda_c}. \quad (24.7.47)$$

Assuming a dipole  $q^2$  behavior for form factors, the ratio  $R = \tilde{F}_2^{\Lambda_c \Lambda} / \tilde{F}_1^{\Lambda_c \Lambda}$  is measured by CLEO to be [295]

$$R = -0.31 \pm 0.05 \pm 0.04. \quad (24.7.48)$$

Various model predictions of the charmed baryon semileptonic decay rates and decay asymmetries are shown in Table 24.10. Dipole  $q^2$  dependence for form factors is assumed whenever the form factor momentum dependence is not available in the model. The predicted rates cited from [289] include QCD corrections. However, as stressed in [208], it seems that QCD effects computed in [289] are unrealistically too large. Moreover, the calculated heavy-heavy baryon form factors in [289] at zero recoil do not satisfy the constraints imposed by heavy quark symmetry [285]. From Table 24.10 we see that the computed branching ratios of  $\Lambda_c^+ \rightarrow \Lambda e^+ \nu$  lie in the range  $1.4\% \sim 2.6\%$ , in agreement with experiment,  $(2.1 \pm 0.6)\%$  [3]. Branching ratios of  $\Xi_c^0 \rightarrow \Xi^- e^+ \nu$  and  $\Xi_c^+ \rightarrow \Xi^0 e^+ \nu$  are predicted to fall into the ranges  $(0.8 \sim 2.0)\%$  and  $(3.3 \sim 8.1)\%$ , respectively. Experimentally, only the ratios of the branching fractions are available so far [3]

$$\frac{\Gamma(\Xi_c^+ \rightarrow \Xi^0 e^+ \nu)}{\Gamma(\Xi_c^+ \rightarrow \Xi^- \pi^+ \pi^+)} = 2.3 \pm 0.6^{+0.3}_{-0.6}, \quad \frac{\Gamma(\Xi_c^0 \rightarrow \Xi^- e^+ \nu)}{\Gamma(\Xi_c^0 \rightarrow \Xi^- \pi^+)} = 3.1 \pm 1.0^{+0.3}_{-0.5}. \quad (24.7.49)$$

## 24.8 Electromagnetic and Weak Radiative decays

Although radiative decays are well measured in the charmed meson sector, e.g.  $D^* \rightarrow D\gamma$  and  $D_s^+ \rightarrow D_s^+ \gamma$ , only three of the radiative modes in the charmed baryon sector have been seen, namely,  $\Xi_c'^0 \rightarrow \Xi_c^0 \gamma$ ,  $\Xi_c'^+ \rightarrow \Xi_c^+ \gamma$  and  $\Omega_c^{*0} \rightarrow \Omega_c^0 \gamma$ . This is understandable because  $m_{\Xi_c'} - m_{\Xi_c} \approx 107$  MeV and  $m_{\Omega_c^*} - m_{\Omega_c} \approx 71$  MeV. Hence,  $\Xi_c'$  and  $\Omega_c^*$  are governed by the electromagnetic decays. However, it will be difficult to measure the rates of these decays because these states are too narrow to be experimentally resolvable. Nevertheless, we shall systematically study the two-body electromagnetic decays of charmed baryons and also weak radiative decays.

### 24.8.1 Electromagnetic decays

In the baryon sector, the following two-body electromagnetic decays are of interest:

$$\begin{aligned} B_6 \rightarrow B_{\bar{3}} + \gamma &: \Sigma_c \rightarrow \Lambda_c + \gamma, \quad \Xi_c' \rightarrow \Xi_c + \gamma, \\ B_6^* \rightarrow B_{\bar{3}} + \gamma &: \Sigma_c^* \rightarrow \Lambda_c + \gamma, \quad \Xi_c'^* \rightarrow \Xi_c + \gamma, \\ B_6^* \rightarrow B_6 + \gamma &: \Sigma_c^* \rightarrow \Sigma_c + \gamma, \quad \Xi_c'^* \rightarrow \Xi_c' + \gamma, \quad \Omega_c^* \rightarrow \Omega_c + \gamma, \end{aligned} \quad (24.8.50)$$

where we have denoted the spin  $\frac{1}{2}$  baryons as  $B_6$  and  $B_{\bar{3}}$  for a symmetric sextet **6** and antisymmetric antitriplet **3̄**, respectively, and the spin  $\frac{3}{2}$  baryon by  $B_6^*$ .

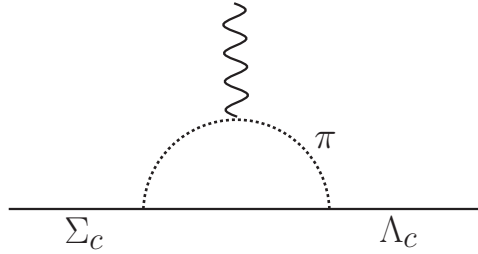


Figure 24.5: Chiral loop contribution to the E2 amplitude of  $\Sigma_c^* \rightarrow \Lambda_c \gamma$ .

An ideal theoretical framework for studying the above-mentioned electromagnetic decays is provided by the formalism in which the heavy quark symmetry and the chiral symmetry of light quarks are combined [202, 203]. When supplemented by the nonrelativistic quark model, the formalism determines completely the low energy dynamics of heavy hadrons. The electromagnetic interactions of heavy hadrons consist of two distinct contributions: one from gauging electromagnetically the chirally invariant strong interaction Lagrangians for heavy mesons and baryons given in [202, 203], and the other from the anomalous magnetic moment couplings of the heavy particles. The heavy quark symmetry reduces the number of free parameters needed to describe the magnetic couplings to the photon. There are two undetermined parameters for the ground state heavy baryons. All these parameters are related simply to the magnetic moments of the light quarks in the nonrelativistic quark model. However, the charmed quark is not particularly heavy ( $m_c \simeq 1.6$  GeV), and it carries a charge of  $\frac{2}{3}e$ . Consequently, the contribution from its magnetic moment cannot be neglected. The chiral and electromagnetic gauge-invariant Lagrangian for heavy baryons can be found in Eqs. (3.8) and (3.9) of [296].

The amplitudes of electromagnetic decays are given by [296]

$$\begin{aligned} A(B_6 \rightarrow B_{\bar{3}} + \gamma) &= i\eta_1 \bar{u}_3 \sigma_{\mu\nu} k^\mu \varepsilon^\nu u_6, \\ A(B_6^* \rightarrow B_{\bar{3}} + \gamma) &= i\eta_2 \epsilon_{\mu\nu\alpha\beta} \bar{u}_3 \gamma^\nu k^\alpha \varepsilon^\beta u^\mu, \\ A(B_6^* \rightarrow B_6 + \gamma) &= i\eta_3 \epsilon_{\mu\nu\alpha\beta} \bar{u}_6 \gamma^\nu k^\alpha \varepsilon^\beta u^\mu, \end{aligned} \quad (24.8.51)$$

where  $k_\mu$  is the photon 4-momentum and  $\varepsilon_\mu$  is the polarization 4-vector. The corresponding decay rates are [296]

$$\begin{aligned} \Gamma(B_6 \rightarrow B_{\bar{3}} + \gamma) &= \eta_1^2 \frac{k^3}{\pi}, \\ \Gamma(B_6^* \rightarrow B_{\bar{3}} + \gamma) &= \eta_2^2 \frac{k^3}{3\pi} \frac{3m_i^2 + m_f^2}{4m_i^2}, \\ \Gamma(B_6^* \rightarrow B_6 + \gamma) &= \eta_3^2 \frac{k^3}{3\pi} \frac{3m_i^2 + m_f^2}{4m_i^2}, \end{aligned} \quad (24.8.52)$$

where  $m_i$  ( $m_f$ ) is the mass of the parent (daughter) baryon.

The coupling constants  $\eta_i$  can be calculated using the quark model [296]; some of them are

$$\eta_1(\Sigma_c^+ \rightarrow \Lambda_c^+) = \frac{e}{6\sqrt{3}} \left( \frac{2}{M_u} + \frac{1}{M_d} \right), \quad \eta_2(\Sigma_c^{*+} \rightarrow \Lambda_c^+) = \frac{e}{3\sqrt{6}} \left( \frac{2}{M_u} + \frac{1}{M_d} \right),$$

Table 24.11: Electromagnetic decay rates (in units of keV) of charmed baryons.

Decay	HHChPT +QM [227, 296]	Ivanov et al. [291]	Bañuls et al. [297]	Tawfiq et al. [298]	Experiment [3]
$\Sigma_c^+ \rightarrow \Lambda_c^+ \gamma$	88	$60.7 \pm 1.5$		87	
$\Sigma_c^{*++} \rightarrow \Sigma_c^{++} \gamma$	1.4			3.04	
$\Sigma_c^{*+} \rightarrow \Sigma_c^+ \gamma$	0.002	$0.14 \pm 0.004$		0.19	
$\Sigma_c^{*+} \rightarrow \Lambda_c^+ \gamma$	147	$151 \pm 4$			
$\Sigma_c^{*0} \rightarrow \Lambda_c^0 \gamma$	1.2			0.76	
$\Xi_c'^+ \rightarrow \Xi_c^+ \gamma$	16	$12.7 \pm 1.5$			seen
$\Xi_c'^0 \rightarrow \Xi_c^0 \gamma$	0.3	$0.17 \pm 0.02$	$1.2 \pm 0.7$		seen
$\Xi_c'^{*+} \rightarrow \Xi_c^+ \gamma$	54	$54 \pm 3$			
$\Xi_c'^{*0} \rightarrow \Xi_c^0 \gamma$	1.1	$0.68 \pm 0.04$	$5.1 \pm 2.7$		
$\Omega_c^{*0} \rightarrow \Omega_c^0 \gamma$	0.9				seen

$$\begin{aligned}
\eta_3(\Sigma_c^{*++} \rightarrow \Sigma_c^{++}) &= \frac{2\sqrt{2}e}{9} \left( \frac{1}{M_u} - \frac{1}{M_c} \right), & \eta_3(\Sigma_c^{*0} \rightarrow \Sigma_c^0) &= \frac{2\sqrt{2}e}{9} \left( -\frac{1}{2M_d} - \frac{1}{M_c} \right), \\
\eta_3(\Sigma_c^{*+} \rightarrow \Sigma_c^+) &= \frac{\sqrt{2}e}{9} \left( \frac{1}{M_u} - \frac{1}{2M_d} - \frac{2}{M_c} \right), & \eta_3(\Xi_c'^{*+} \rightarrow \Xi_c^+) &= \frac{e}{3\sqrt{6}} \left( \frac{2}{M_u} + \frac{1}{M_s} \right), \\
\eta_3(\Xi_c'^{*0} \rightarrow \Xi_c^0) &= \frac{e}{3\sqrt{6}} \left( -\frac{1}{M_d} + \frac{1}{M_s} \right), & \eta_3(\Omega_c^{*0} \rightarrow \Omega_c^0) &= \frac{2\sqrt{2}e}{9} \left( -\frac{1}{2M_s} - \frac{1}{M_c} \right).
\end{aligned} \tag{24.8.53}$$

Using the constituent quark masses,  $M_u = 338$  MeV,  $M_d = 322$  MeV and  $M_s = 510$  MeV [3], the calculated results are summarized in the second column of Table 24.11. A similar procedure is followed in [298] where the heavy quark symmetry is supplemented with light-diquark symmetries to calculate the widths of  $\Sigma_c^+ \rightarrow \Lambda_c^+ \gamma$  and  $\Sigma_c^* \rightarrow \Sigma_c \gamma$ . The authors of [291] apply the relativistic quark model to predict various electromagnetic decays of charmed baryons. Besides the magnetic dipole (M1) transition, the author of [299] also considered and estimated the electric quadrupole (E2) amplitude for  $\Sigma_c^{*+} \rightarrow \Lambda_c^+ \gamma$  arising from the chiral loop correction (Fig. 24.5). A detailed analysis of the E2 contributions was presented in [297]. The E2 amplitudes appear at different higher orders for the three kinds of decays:  $\mathcal{O}(1/\Lambda_\chi^2)$  for  $B_6^* \rightarrow B_6 + \gamma$ ,  $\mathcal{O}(1/m_Q \Lambda_\chi^2)$  for  $B_6^* \rightarrow B_{\bar{3}} + \gamma$  and  $\mathcal{O}(1/m_Q^3 \Lambda_\chi^2)$  for  $B_6 \rightarrow B_{\bar{3}} + \gamma$ . Therefore, the E2 contribution to  $B_6 \rightarrow B_{\bar{3}} + \gamma$  is completely negligible.

Chiral-loop corrections to the M1 electromagnetic decays and to the strong decays of heavy baryons have been computed at the one loop order in [300]. The leading chiral-loop effects we found are nonanalytic in the forms of  $m/\Lambda_\chi$  and  $(m^2/\Lambda_\chi^2) \ln(\Lambda^2/m^2)$  (or  $m_q^{1/2}$  and  $m_q \ln m_q$ , with  $m_q$  being the light quark mass). Some results are [300]

$$\Gamma(\Sigma_c^+ \rightarrow \Lambda_c^+ \gamma) = 112 \text{ keV}, \quad \Gamma(\Xi_c'^+ \rightarrow \Xi_c^+ \gamma) = 29 \text{ keV}, \quad \Gamma(\Xi_c'^0 \rightarrow \Xi_c^0 \gamma) = 0.15 \text{ keV}, \tag{24.8.54}$$

which should be compared with the corresponding quark-model results: 88 keV, 16 keV and 0.3 keV (Table 24.11).

The electromagnetic decay  $\Xi_c'^* \rightarrow \Xi_c^0 \gamma$  is of special interest. It has been advocated in [301] that a measurement of its branching ratio will determine one of the coupling constants in HHChPT, namely,  $g_1$ . The radiative decay  $\Xi_c'^* \rightarrow \Xi_c^0 \gamma$  is forbidden at tree level in SU(3) limit [see Eq. (24.8.53)]. In heavy baryon chiral perturbation theory, this radiative decay is induced via chiral loops where SU(3) symmetry is broken by the light current quark masses. By identifying the chiral loop contribution to  $\Xi_c'^* \rightarrow \Xi_c^0 \gamma$  with the quark model prediction given in Eq. (24.8.53), it was found in [227] that one of the two possible solutions is in accord with the quark model expectation for  $g_1$ .

For the electromagnetic decays of  $p$ -wave charmed baryons, the search of  $\Lambda_c(2593)^+ \rightarrow \Lambda_c^+ \gamma$  and  $\Lambda_c^+(2625)^+ \rightarrow \Lambda_c^+ \gamma$  has been failed so far. On the theoretical side, the interested reader is referred to Refs. [298, 291, 301, 236, 238, 302] for more details.

The electromagnetic decays considered so far do not test critically the heavy quark symmetry nor the chiral symmetry. The results follow simply from the quark model. There are examples in which both the heavy quark symmetry and the chiral symmetry enter in a crucial way. These are the radiative decays of heavy baryons involving an emitted pion. Some examples which are kinematically allowed are

$$\Sigma_c \rightarrow \Lambda_c \pi \gamma, \quad \Sigma_c^* \rightarrow \Lambda_c \pi \gamma, \quad \Sigma_c^* \rightarrow \Sigma_c \pi \gamma, \quad \Xi_c^* \rightarrow \Xi_c \pi \gamma. \quad (24.8.55)$$

For an analysis of the decay  $\Sigma_c \rightarrow \Lambda_c \pi \gamma$ , see [296].

### 24.8.2 Weak radiative decays

At the quark level, there are three different types of processes which can contribute to the weak radiative decays of heavy hadrons, namely, single-, two- and three-quark transitions [304]. The single-quark transition mechanism comes from the so-called electromagnetic penguin diagram. Unfortunately, the penguin process  $c \rightarrow u \gamma$  is very suppressed and hence it plays no role in charmed hadron radiative decays. There are two contributions from the two-quark transitions: one from the  $W$ -exchange diagram accompanied by a photon emission from the external quark, and the other from the same  $W$ -exchange diagram but with a photon radiated from the  $W$  boson. The latter is typically suppressed by a factor of  $m_q k / M_W^2$  ( $k$  being the photon energy) as compared to the former bremsstrahlung process [303]. For charmed baryons, the Cabibbo-allowed decay modes via  $c\bar{u} \rightarrow s\bar{d}\gamma$  (Fig. 24.6) or  $cd \rightarrow us\gamma$  are

$$\Lambda_c^+ \rightarrow \Sigma^+ \gamma, \quad \Xi_c^0 \rightarrow \Xi^0 \gamma. \quad (24.8.56)$$

Finally, the three-quark transition involving  $W$ -exchange between two quarks and a photon emission by the third quark is quite suppressed because of very small probability of finding three quarks in adequate kinematic matching with the baryons [304, 305].

The general amplitude of the weak radiative baryon decay reads

$$A(\mathcal{B}_i \rightarrow \mathcal{B}_f \gamma) = i\bar{u}_f(a + b\gamma_5)\sigma_{\mu\nu}\varepsilon^\mu k^\nu u_i, \quad (24.8.57)$$

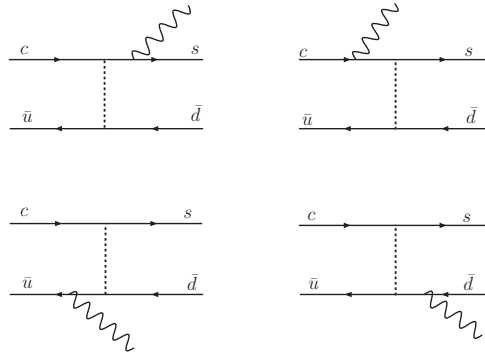


Figure 24.6:  $W$ -exchange diagrams contributing to the quark-quark bremsstrahlung process  $c + \bar{u} \rightarrow s + \bar{d} + \gamma$ . The  $W$ -annihilation type diagrams are not shown here.

where  $a$  and  $b$  are parity-conserving and -violating amplitudes, respectively. The corresponding decay rate is

$$\Gamma(\mathcal{B}_i \rightarrow \mathcal{B}_f \gamma) = \frac{1}{8\pi} \left( \frac{m_i^2 - m_f^2}{m_i} \right)^3 (|a|^2 + |b|^2). \quad (24.8.58)$$

Nonpenguin weak radiative decays of charmed baryons such as those in (24.8.56) are characterized by emission of a hard photon and the presence of a highly virtual intermediate quark between the electromagnetic and weak vertices. It has been shown in [306] that these features should make possible to analyze these processes by perturbative QCD; that is, these processes are describable by an effective local and gauge invariant Lagrangian:

$$\mathcal{H}_{\text{eff}}(c\bar{u} \rightarrow s\bar{d}\gamma) = \frac{G_F}{2\sqrt{2}} V_{cs} V_{ud}^* (c_+ O_+^F + c_- O_-^F), \quad (24.8.59)$$

with

$$O_{\pm}^F(c\bar{u} \rightarrow s\bar{d}\gamma) = \frac{e}{m_i^2 - m_f^2} \left\{ \left( e_s \frac{m_f}{m_s} + e_u \frac{m_i}{m_u} \right) \left( \tilde{F}_{\mu\nu} + iF_{\mu\nu} \right) O_{\pm}^{\mu\nu} \right. \quad (24.8.60)$$

$$\left. - \left( e_d \frac{m_f}{m_d} + e_c \frac{m_i}{m_c} \right) \left( \tilde{F}_{\mu\nu} - iF_{\mu\nu} \right) O_{\mp}^{\mu\nu} \right\}, \quad (24.8.61)$$

where  $m_i = m_c + m_u$ ,  $m_f = m_s + m_d$ ,  $\tilde{F}_{\mu\nu} \equiv \frac{1}{2} \epsilon_{\mu\nu\alpha\beta} F^{\alpha\beta}$  and

$$O_{\pm}^{\mu\nu} = \bar{s}\gamma^{\mu}(1 - \gamma_5)c\bar{u}\gamma^{\nu}(1 - \gamma_5)d \pm \bar{s}\gamma^{\mu}(1 - \gamma_5)d\bar{u}\gamma^{\nu}(1 - \gamma_5)c. \quad (24.8.62)$$

For the charmed baryon radiative decays, one needs to evaluate the matrix element  $\langle \mathcal{B}_f | O_{\pm}^{\mu\nu} | \mathcal{B}_i \rangle$ . Since the quark-model wave functions best resemble the hadronic states in the frame where both baryons are static, the static MIT bag model [275] was thus adopted in [306] for the calculation. The predictions are

$$\mathcal{B}(\Lambda_c^+ \rightarrow \Sigma^+ \gamma) = 4.9 \times 10^{-5}, \quad \alpha(\Lambda_c^+ \rightarrow \Sigma^+ \gamma) = -0.86,$$

$$\mathcal{B}(\Xi_c^0 \rightarrow \Xi^0 \gamma) = 3.6 \times 10^{-5}, \quad \alpha(\Xi_c^0 \rightarrow \Xi^0 \gamma) = -0.86. \quad (24.8.63)$$

A different analysis of the same decays was carried out in [307] with the results

$$\begin{aligned} \mathcal{B}(\Lambda_c^+ \rightarrow \Sigma^+ \gamma) &= 2.8 \times 10^{-4}, & \alpha(\Lambda_c^+ \rightarrow \Sigma^+ \gamma) &= 0.02, \\ \mathcal{B}(\Xi_c^0 \rightarrow \Xi^0 \gamma) &= 1.5 \times 10^{-4}, & \alpha(\Xi_c^0 \rightarrow \Xi^0 \gamma) &= -0.01. \end{aligned} \quad (24.8.64)$$

Evidently, these predictions (especially the decay asymmetry) are very different from the ones obtained in [306].

Finally, it is worth remarking that, in analog to the heavy-flavor-conserving nonleptonic weak decays as discussed above, there is a special class of weak radiative decays in which heavy flavor is conserved. Some examples are  $\Xi_c \rightarrow \Lambda_c \gamma$  and  $\Omega_c \rightarrow \Xi_c \gamma$ . In these decays, weak radiative transitions arise from the diquark sector of the heavy baryon whereas the heavy quark behaves as a spectator. However, the dynamics of these radiative decays is more complicated than their counterpart in nonleptonic weak decays, e.g.,  $\Xi_c \rightarrow \Lambda_c \pi$ . In any event, it deserves a detailed study.

# Chapter 25

## $D^0 - \bar{D}^0$ Mixing

Meson-antimeson oscillations have been of central importance in the evolution of the Standard Model (SM) and in searches for new physics. This is based on two seminal features [1]: (a) In such oscillations quantum mechanical effects will build up over macroscopic distances, which makes tiny mass differences measurable. (b) Oscillations and the rare decay reactions  $s \rightarrow dl^+l^-$ ,  $s \rightarrow d\nu\bar{\nu}$ ,  $b \rightarrow s\gamma$ , and  $b \rightarrow sl^+l^-$  are driven by flavor changing neutral currents (FCNC), which are highly suppressed in the SM, where they are given by 1-loop processes.

A program of searches for new physics in charm is complementary to the corresponding programs in bottom or strange systems, since the situation is fundamentally different for neutral  $D$  mesons built from the *up*-type quark  $c$ . For example,  $D^0 - \bar{D}^0$  mixing or FCNC decays are sensitive to the dynamics of ultra-heavy down-type particles. Although, the  $D^0 - \bar{D}^0$  oscillations have to be rather slow in the SM, large statistics usually available in charm physics experiment makes it possible to probe small effects that might be generated by the presence of new physics particles and interactions.

On the other hand,  $D^0 - \bar{D}^0$  oscillations can be generated at second order in  $SU(3)_{Fl}$  breaking from long-distance contributions. As discussed below, within the SM  $D^0 - \bar{D}^0$  oscillations are driven by long distance dynamics, over which our theoretical control is rather limited. It is quite difficult to make the statement that these oscillations are slow. Nevertheless, it is mandatory to probe  $D^0 - \bar{D}^0$  oscillations as sensitively as possible; while their observation by themselves might not provide conclusive proof for the intervention of New Physics, it is an essential element in searches for  $CP$  violation, where such conclusive proof can be obtained.

### 25.1 Theoretical Review<sup>1</sup>

#### 25.1.1 Oscillation Formalism: the Phenomenology

It has become customary to use the terms ‘oscillations’ and ‘mixing’ in an interchangeable way. This is unfortunate. For while the two terms describe phenomena that are related, they are of a different nature with ‘mixing’ denoting the more general concept and ‘oscillations’ the more specific one.

---

<sup>1</sup>by Edited by I. I. Bigi and H. B. Li

*Mixing* means that classically distinct states are not necessarily so in quantum mechanics and therefore can *interfere*. For example in atomic physics wave functions are said to be *mixtures* of ‘right’ and ‘wrong’ components whose interference generates parity odd observables; it is the weak neutral current that induces such wrong parity components. Mass eigenstates of quarks (and leptons) contain components of different flavors giving rise to the non-diagonal CKM (or PMNS) matrix described below. This is usually referred to as quark mixing. Such mixing creates a plethora of observable effects.

The most intriguing mixings arise when the violation of a certain quantum number – like strangeness – leads to stationary or mass eigenstates that are not eigenstates of that quantum number. This induces *oscillations* like matter-antimatter oscillations discussed above or neutron-antineutron oscillations or neutrino oscillations. *Oscillations* thus require *mixing*, but go beyond it in the sense that they generate transitions with a very peculiar time evolution, namely an oscillatory one rather than the usual exponentially damped one.

The time evolution of the  $D^0 - \bar{D}^0$  system is described by the Schrödinger-like equation as

$$i\frac{\partial}{\partial t} \begin{pmatrix} D^0(t) \\ \bar{D}^0(t) \end{pmatrix} = \left(\mathbf{M} - \frac{i}{2}\mathbf{\Gamma}\right) \begin{pmatrix} D^0(t) \\ \bar{D}^0(t) \end{pmatrix}, \quad (25.1.1)$$

where the  $\mathbf{M}$  and  $\mathbf{\Gamma}$  matrices are Hermitian, and are defined as

$$\left(\mathbf{M} - \frac{i}{2}\mathbf{\Gamma}\right) = \begin{pmatrix} M_{11} - \frac{i}{2}\Gamma_{11} & M_{12} - \frac{i}{2}\Gamma_{12} \\ M_{12}^* - \frac{i}{2}\Gamma_{12}^* & M_{22} - \frac{i}{2}\Gamma_{22} \end{pmatrix}. \quad (25.1.2)$$

*CPT* invariance imposes

$$M_{11} = M_{22} \equiv M, \quad \Gamma_{11} = \Gamma_{22} \equiv \Gamma. \quad (25.1.3)$$

The off-diagonal elements of these matrices describe the dispersive and absorptive parts of  $D^0 - \bar{D}^0$  mixing (for details see Ref. [308]). The two eigenstates  $D_1$  and  $D_2$  of the effective Hamiltonian matrix ( $\mathbf{M} - \frac{i}{2}\mathbf{\Gamma}$ ) are given by

$$|D_1\rangle = \frac{1}{\sqrt{|p|^2 + |q|^2}}(p|D^0\rangle + q|\bar{D}^0\rangle), \quad |D_2\rangle = \frac{1}{\sqrt{|p|^2 + |q|^2}}(p|D^0\rangle - q|\bar{D}^0\rangle). \quad (25.1.4)$$

The corresponding eigenvalues are

$$\lambda_{D_1} \equiv m_1 - \frac{i}{2}\Gamma_1 = \left(M - \frac{i}{2}\Gamma\right) + \frac{q}{p} \left(M_{12} - \frac{i}{2}\Gamma_{12}\right), \quad (25.1.5)$$

$$\lambda_{D_2} \equiv m_2 - \frac{i}{2}\Gamma_2 = \left(M - \frac{i}{2}\Gamma\right) - \frac{q}{p} \left(M_{12} - \frac{i}{2}\Gamma_{12}\right), \quad (25.1.6)$$

where  $m_1(m_2)$  and  $\Gamma_1(\Gamma_2)$  are the mass and width of  $D_1$  ( $D_2$ ), respectively, and

$$\frac{q}{p} = \left(\frac{M_{12}^* - \frac{i}{2}\Gamma_{12}^*}{M_{12} - \frac{i}{2}\Gamma_{12}}\right)^{1/2}. \quad (25.1.7)$$

From Eqs. 25.1.5 and 25.1.6, one can get the differences in mass and width:

$$\Delta m \equiv m_2 - m_1 = -2\text{Re} \left[ \frac{q}{p} \left(M_{12} - \frac{i}{2}\Gamma_{12}\right) \right], \quad (25.1.8)$$

$$\Delta\Gamma \equiv \Gamma_2 - \Gamma_1 = -2\text{Im} \left[ \frac{q}{p} (M_{12} - \frac{i}{2}\Gamma_{12}) \right]. \quad (25.1.9)$$

The subscripts are mere labels at this point. We have chosen the definitions of  $\Delta M$  and  $\Delta\Gamma$  such that when applied to the kaon sector with  $K_S = K_1$  and  $K_L = K_2$ , we get both differences positive.

A pure  $D^0$  state generated at  $t = 0$  could decay to  $K^+\pi^-$  state either by  $D^0 - \overline{D}^0$  mixing or by DCSD, and the two amplitudes may interfere. The time evolutions of  $|D_1\rangle$  and  $|D_2\rangle$  are given by

$$|D_i\rangle = e_i |D_i\rangle, \quad e_i = e^{-im_i t - \frac{1}{2}\Gamma_i t}, \quad (i = 1, 2). \quad (25.1.10)$$

Under the phase convention  $CP|D^0\rangle = |\overline{D}^0\rangle$ , a state that is purely  $|D^0\rangle$  ( $|\overline{D}^0\rangle$ ) prepared by the strong interaction at  $t = 0$  will evolve to  $|D_{\text{phys}}^0(t)\rangle$  ( $|\overline{D}_{\text{phys}}^0(t)\rangle$ ):

$$|D_{\text{phys}}^0(t)\rangle = g_+(t)|D^0\rangle + \frac{q}{p}g_-(t)|\overline{D}^0\rangle, \quad (25.1.11)$$

$$|\overline{D}_{\text{phys}}^0(t)\rangle = \frac{p}{q}g_-(t)|D^0\rangle + g_+(t)|\overline{D}^0\rangle, \quad (25.1.12)$$

where

$$g_{\pm}(t) = \frac{1}{2}(e_1 \pm e_2). \quad (25.1.13)$$

The probability to find a  $\overline{D}^0$  at time  $t$  in an initially pure  $D^0$  beam is given by

$$|\langle \overline{D}^0 | D_{\text{phys}}^0(t) \rangle| = \frac{1}{4} \left| \frac{q}{p} \right|^2 e^{-\Gamma_2 t} \left( 1 + e^{-\Delta\Gamma t} - 2e^{-\frac{1}{2}\Delta\Gamma t} \cos\Delta m t \right). \quad (25.1.14)$$

While the flavour of the initial meson is tagged by its production, the flavour of the final meson is inferred from its decay.

There are two dimensionless ratios describing the interplay between oscillations and decays:

$$x \equiv \frac{\Delta m}{\Gamma}, \quad y \equiv \frac{\Delta\Gamma}{2\Gamma}, \quad (25.1.15)$$

where  $\Gamma \equiv (\Gamma_1 + \Gamma_2)/2$  is the averaged  $D^0$  width.

### 25.1.2 Time-dependent Rate for Incoherent $D$ Decays

Searches for mixing attempt to identify the process  $|D^0\rangle \rightarrow |\overline{D}^0\rangle$  ( $|\overline{D}^0\rangle \rightarrow |D^0\rangle$ ) by analyzing the decay products of a particle known to be created as a  $|D^0\rangle$  ( $|\overline{D}^0\rangle$ ). In practice, this means reconstructing the state  $|f\rangle$  in an attempt to observe

$$|D^0\rangle \rightarrow |\overline{D}^0\rangle \rightarrow |f\rangle \quad (25.1.16)$$

The difficulty comes from the fact that for hadronic systems, the decay

$$|D^0\rangle \rightarrow |f\rangle \quad (25.1.17)$$

can occur directly, without any mixing at all. Distinguishing process (25.1.16) from (25.1.17) is the primary goal of  $D$  mixing searches, and it relies on the fact that the decay-time distribution of the final state  $|f\rangle$  is different for the two processes. The most sensitivity to mixing will occur when the amplitude for process (25.1.17) is as small as possible and, therefore, doubly Cabibbo-suppressed (DCS) decays are chosen for this type of analysis.

Let us define  $A_f \equiv \langle f | \mathcal{H} | D^0 \rangle$ ,  $\bar{A}_f \equiv \langle f | \mathcal{H} | \bar{D}^0 \rangle$  with  $\rho_f \equiv \frac{\bar{A}_f}{A_f}$ ; and  $A_{\bar{f}} \equiv \langle \bar{f} | \mathcal{H} | D^0 \rangle$ ,  $\bar{A}_{\bar{f}} \equiv \langle \bar{f} | \mathcal{H} | \bar{D}^0 \rangle$  with  $\bar{\rho}_{\bar{f}} \equiv \frac{A_{\bar{f}}}{\bar{A}_{\bar{f}}}$ . Now the time-dependent *wrong sign* decay amplitude for states of initially pure  $|D^0\rangle$  ( $|\bar{D}^0\rangle$ ) to decay to  $|f\rangle$  ( $|\bar{f}\rangle$ ) is given by (with  $f = K^+ \pi^-$  and  $|\bar{f}\rangle \equiv CP|f\rangle$ )

$$A(|D_{\text{phys}}^0(t) \rightarrow f\rangle) = \frac{q}{p} \bar{A}_f [\lambda_f^{-1} g_+(t) + g_-(t)], \quad (25.1.18)$$

and

$$A(|\bar{D}_{\text{phys}}^0(t) \rightarrow \bar{f}\rangle) = \frac{p}{q} A_{\bar{f}} [\lambda_{\bar{f}} g_-(t) + g_+(t)], \quad (25.1.19)$$

where

$$\lambda_f \equiv \frac{q}{p} \frac{\bar{A}_f}{A_f} \equiv \frac{q}{p} \rho_f, \quad \lambda_{\bar{f}} \equiv \frac{q}{p} \frac{\bar{A}_{\bar{f}}}{A_{\bar{f}}} \equiv \frac{q}{p} \bar{\rho}_{\bar{f}}. \quad (25.1.20)$$

and

$$\frac{q}{p} = (1 + A_M) e^{i\phi}. \quad (25.1.21)$$

In order to describe the three types of  $CP$  violation in a convenient way, one can also parameterize  $\lambda_f$  ( $\lambda_{\bar{f}}$ ) as [309, 310]

$$\lambda_f \equiv \frac{q}{p} \frac{\bar{A}_f}{A_f} = \frac{(1 + A_M)}{\sqrt{R_D}(1 + A_D)} e^{i(\delta + \phi)}, \quad (25.1.22)$$

$$\lambda_{\bar{f}} \equiv \frac{q}{p} \frac{\bar{A}_{\bar{f}}}{A_{\bar{f}}} = \frac{\sqrt{R_D}(1 + A_M)}{(1 + A_D)} e^{-i(\delta - \phi)}, \quad (25.1.23)$$

where  $|q|/|p| = (1 + A_M)$  and  $|\bar{A}_f|/|A_f| = \sqrt{R_D}(1 + A_D)$ , and  $\delta$  is the strong phase difference between  $\bar{A}_f$  and  $A_f$ . Here  $\phi$  represents the convention-independent weak phase difference between the ratio of decay amplitudes and the mixing matrix. In Chapter 26, we will use these definitions to describe the three types of  $CP$  violation in detail. In the limit of  $CP$  conservation,  $A_M$ ,  $A_D$  and  $\phi$  are all zero.

It is usual to normalize the *wrong sign* decay distributions to the integrated rate of *right sign* decays and to express time in units of the precisely measured  $D^0$  mean lifetime,  $\bar{\tau}_{D^0} = 1/\Gamma = 2/(\Gamma_1 + \Gamma_2)$ . Therefore the time-dependent rates of production of the *wrong sign* final states relative to the integrated *right sign* states are:

$$r(t) = \left| \frac{q}{p} \right|^2 \left| \lambda_f^{-1} g_+(t) + g_-(t) \right|^2, \quad (25.1.24)$$

and

$$\bar{r}(t) = \left| \frac{p}{q} \right|^2 \left| \lambda_{\bar{f}} g_-(t) + g_+(t) \right|^2. \quad (25.1.25)$$

We will expand  $r(t)$  and  $\bar{r}(t)$  to second order in time for the modes where the ratio of the decay amplitudes  $R_D = |A_f/\bar{A}_f|^2$  is very small (it is the ratio of double-cabibbo-favored (DCS) decay rate and cabibbo-favored (CF) decay rate).

### 25.1.3 Standard Model Predictions for Oscillation Parameters

Oscillations arise from  $\Delta C = 2$  interactions that generate off-diagonal terms in mass matrix as in Eq. 25.1.2 for  $D^0$  and  $\bar{D}^0$  mesons. The expansion of the off-diagonal terms in the neutral  $D$  mass matrix to second order in perturbation theory is

$$M_{12} = \langle \bar{D}^0 | \mathcal{H}_w^{\Delta C=2} | D^0 \rangle + P \sum_n \frac{\langle \bar{D}^0 | \mathcal{H}_w^{\Delta C=1} | n \rangle \langle n | \mathcal{H}_w^{\Delta C=1} | D^0 \rangle}{m_D^2 - E_n^2}, \quad (25.1.26)$$

$$\Gamma_{12} = \sum_n \rho_n \langle \bar{D}^0 | \mathcal{H}_w^{\Delta C=1} | n \rangle \langle n | \mathcal{H}_w^{\Delta C=1} | D^0 \rangle, \quad (25.1.27)$$

where the sum runs over all relevant intermediate states (virtual ones for  $M_{12}$  and real ones for  $\Gamma_{12}$ ),  $P$  denotes the principle value, and  $\rho_n$  is the density of the states  $n$ .

The operator in the first term  $-\mathcal{H}_w^{\Delta C=2}$  is a *local* one at scale  $\mu \sim m_D$ , so it contributes to the  $M_{12}$  (but not to the  $\Gamma_{12}$ ) part of the generalized mass matrix. New Physics could induce such a contribution of potentially significant size. The SM generates such a term, namely from the quark box diagram with  $b$  quarks as internal quarks, yet it is truly tiny due to its highly suppressed CKM parameters. The second term in Eq. 25.1.26 comes from a double insertion of  $\Delta C = 1$  operators; it contributes to both  $M_{12}$  and  $\Gamma_{12}$ . The dominant SM contribution comes from here as described below; here New Physics could make a significant contribution to  $M_{12}$ .

BES-III-20050721-1

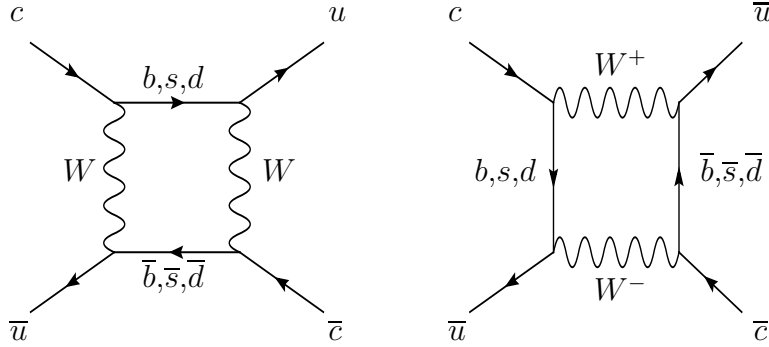


Figure 25.1: Standard Model box diagrams of flavor-changing neutral currents contributing to  $D^0 - \bar{D}^0$  mixing at the quark level.

#### Short-Distance Contribution to $x$ and $y$

In the SM there is a *bona fide* short-distance  $\Delta C = 2$  operator, which is inferred from the quark box diagram with  $b$  quarks as the intermediate quarks, see Fig. 25.1. The effects due to intermediate  $b$  quarks are evaluated in a straightforward way since they are far off-shell [311]:

$$\Delta m^{b\bar{b}} \simeq -\frac{G_F^2 m_b^2}{8\pi^2} |V_{cb}^* V_{ub}|^2 \frac{\langle D^0 | (\bar{u} \gamma_\mu (1 - \gamma_5) c) (\bar{u} \gamma_\mu (1 - \gamma_5) c) | \bar{D}^0 \rangle}{2M_D}; \quad (25.1.28)$$

however they are highly suppressed by the tiny CKM parameters. Using factorization to estimate the matrix element one finds  $x^{b\bar{b}} \sim 10^{-6}$ . Loops with one  $b$  and one light quark likewise are suppressed.

For the light intermediate quarks –  $d, s$  – the momentum scale is set by the *external* mass  $m_c$ . However, it is highly GIM suppressed

$$\Delta m^{(s,d)} \simeq -\frac{G_F^2 m_c^2}{8\pi^2} |V_{cs}^* V_{us}|^2 \frac{(m_s^2 - m_d^2)^2}{m_c^4} \times \frac{\langle D^0 | (\bar{u}\gamma_\mu(1-\gamma_5)c)(\bar{u}\gamma_\mu(1-\gamma_5)c) + (\bar{u}(1+\gamma_5)c)(\bar{u}(1+\gamma_5)c) | \bar{D}^0 \rangle}{2M_D} \quad (25.1.29)$$

In contrast to  $K^0 - \bar{K}^0$  and  $B^0 - \bar{B}^0$  mixing, the internal quarks in the box diagrams here are down-type quarks. The  $b$ -quark contribution, which would give, in principle, the largest GIM violation, is suppressed by small CKM mixing factors  $V_{cb}^* V_{ub}$ . The leading contribution, as shown in Eq. 25.1.29, is given by the strange quark and therefore results in a very effective GIM suppression.

The contribution to  $\Delta\Gamma$  from the bare quark box is greatly suppressed by a factor  $m_s^6$ . The GIM mass insertions yield a factor  $m_s^4$ . Contrary to a claim in Ref. [312], the additional factor of  $m_s^2$  is *not* due to helicity suppression – the GIM factors already take care of that effect; it is of an accidental nature: it arises because the weak currents are purely  $V - A$  and only in four dimensions. Including radiative QCD corrections to the box diagram yields contributions  $\propto m_s^4 \alpha_S / \pi$ . Numerically one finds:

$$y^{box} \ll x^{box} \simeq (10^{-6}) - (10^{-5}). \quad (25.1.30)$$

### Long-distance Contribution to $x$ and $y$

BES-III-20050721

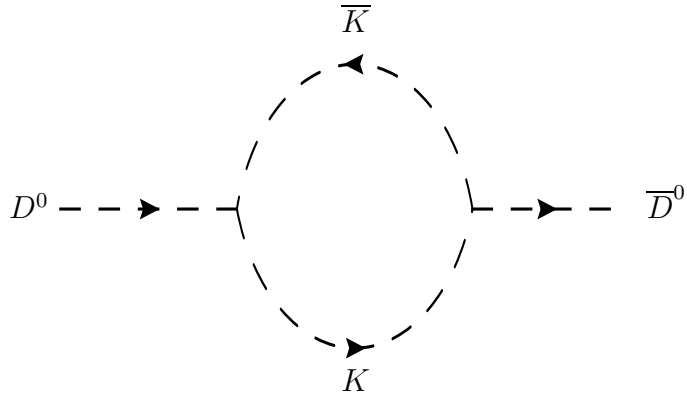


Figure 25.2: A hadron-level diagram of a long-distance physics contribution to  $D^0 - \bar{D}^0$  mixing.

The long-distance contributions to  $D^0 - \bar{D}^0$  oscillations are inherently non-perturbative, and we have not yet learned how to calculate them from first principles. It is, however,

extremely important to estimate their size in order to understand the origin of a possible experimental observation. These contributions come from transitions to final states  $|f\rangle$  that are accessible to both  $|D^0\rangle$  and  $|\overline{D}^0\rangle$ . For example, Fig. 25.2 illustrates a contribution to mixing from transitions to two pseudoscalars. GIM cancellations are such that they become complete in the  $SU(3)_{FL}$  limit; i.e., no oscillations can occur then.

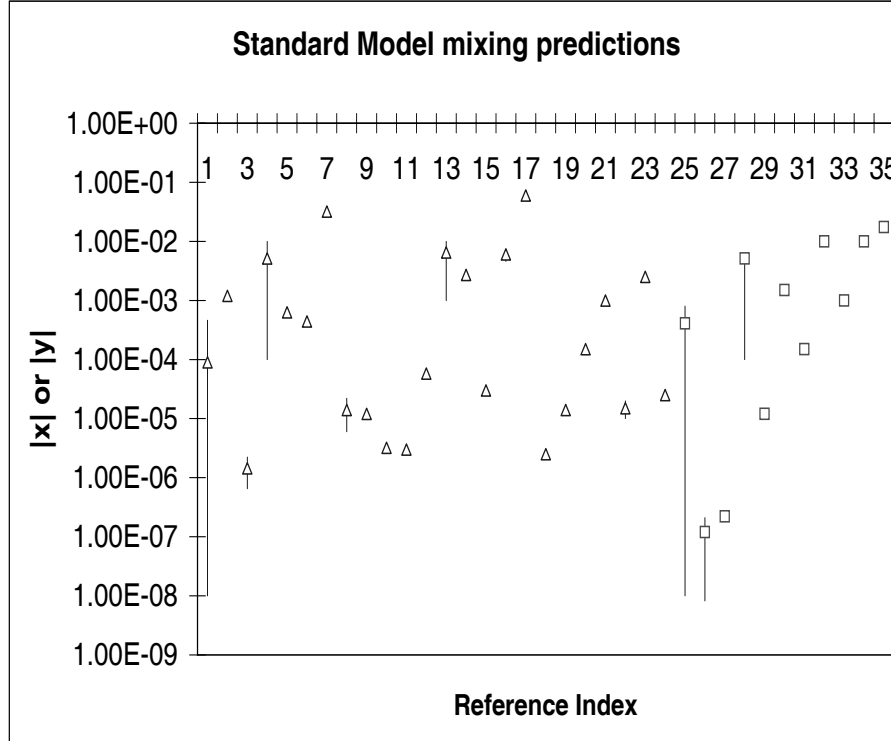


Figure 25.3: Standard Model predictions for  $|x|$  (open triangles) and  $|y|$  (open squares). Horizontal line references are tabulated in Table 4 in Ref. [313].

Within the SM  $x$  and  $y$  are generated only at second order in  $SU(3)_F$  breaking,

$$x, y \sim \sin^2 \theta_C \times [SU(3) \text{ breaking}]^2, \quad (25.1.31)$$

where  $\theta_C$  is the Cabibbo angle. The SM predictions for  $x$  and  $y$  thus depend crucially on estimating the size of  $SU(3)_F$  breaking. Although  $y$  is expected to be determined by SM processes, its value nevertheless affects significantly the sensitivity to new physics of experimental analyses of  $D$  mixing [314]. This circumstance would lead to the naive estimate

$$x, y \sim \sin^2 \theta_C \times \left( \frac{m_s}{\Lambda_{\text{hadron}}} \right)^2 \leq O(10^{-3}), \quad (25.1.32)$$

with  $\Lambda_{\text{hadron}} \sim O(1)$  GeV a typical hadronic scale. Beyond this simple estimate, there are two main approaches to estimating the long-distance contributions to mixing: an *inclusive* approach using an operator product expansion (OPE), and an *exclusive* approach that sums over intermediate hadronic states using experimental data. Neither approach yields accurate predictions.

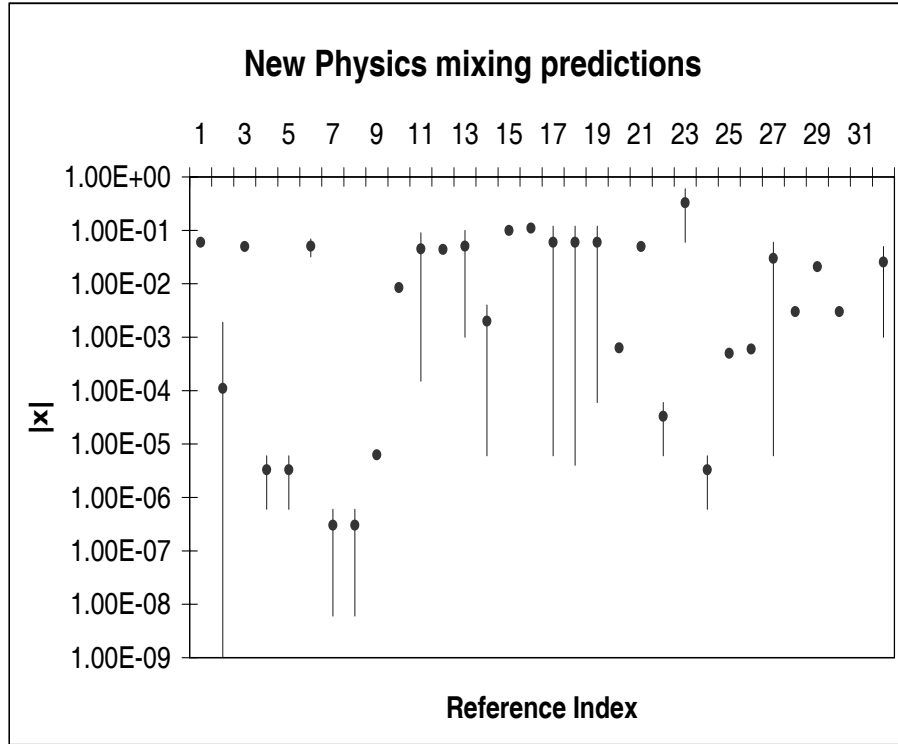


Figure 25.4: New Physics predictions for  $|x|$ . Horizontal line references are tabulated in Table 5 in Ref. [313].

The *inclusive* approach applies Heavy-Quark Expansions (HQE) to calculate contributions to  $D$  oscillations, an approach first taken by Georgi [315] and later extended by others [316, 317]. There are two main assumptions. The first is that the mass of the  $c$ -quark is large,  $m_c \gg \Lambda_{\text{hadr.}}$ . The second is that one can construct local quark-level operators that can be applied to hadron-level processes, i.e. that quark-hadron duality is applicable already at the charm scale. Then  $x$  and  $y$  are evaluated through the OPE as an expansion in powers of  $(\Lambda_{\text{hadr.}}/m_c)$ . The result of this type of approach is [317]

$$x \sim y \sim O(10^{-3}). \quad (25.1.33)$$

The *exclusive* approach takes all of the known hadronic states common to  $|D^0\rangle$  and  $|\bar{D}^0\rangle$ , and groups them both according to their respective  $SU(3)_F$  multiplets and to the number of particles in the final state. An example of such a set would be  $(\pi^+\pi^-, \pi^+K^-, K^+K^-, K^+\pi^-)$ . In the limit of a perfect  $SU(3)_F$  symmetry, the individual contributions within each of these groups would cancel, and there would be no mixing. If one knows the relative amplitudes and strong phases for these states, calculations of  $x$  and  $y$  can be done for each multiplet. For the example set above, this calculation gives a small contribution due to cancellations, a reasonable result since all of the states in the set are far from threshold and not affected as much by phase space considerations. Contributions to  $x$  are not required to be on-shell, so in this case there is no symmetry breaking caused by limited phase space. If one assumes that all of the sets contribute incoherently in roughly

the same amount, one concludes that [311]

$$x \leq O(10^{-3}). \quad (25.1.34)$$

By contrast, contributions to  $y$  are due to on-shell states, so phase space is a significant source of symmetry breaking. Considering phase space as the only source of symmetry breaking, one can calculate the contribution to  $y$  of each of the final state multiplets for which there is data using the measured masses of the final-particles [313]. The largest calculable contribution comes from the final-state multiplet comprising four pseudoscalars, whose elements are either near the production threshold with relatively large branching fractions, or are above threshold and entirely absent. This ansatz leads to [313]

$$y \leq O(10^{-2}). \quad (25.1.35)$$

The results from these two methods should not be seen as inconsistent. Rather they indicate the range of uncertainty, which can be phrased as follows: While the best a priori SM estimate yields  $x, y \sim O(10^{-3})$ , we cannot conclude that values as ‘high’ as  $10^{-2}$  would necessarily establish the intervention of New Physics. To be more specific: while the presence of New Physics can enhance  $x$  to its present upper bound of few  $\times 10^{-2}$ , it should not affect  $y$  in a significant way, since  $\Delta\Gamma$  is generated from *on-shell* transitions. The minimal requirement for any claim of New Physics thus is  $x|_{\text{experim}} \gg y|_{\text{experim}}$ . This appears as a rather iffy scenario at present. Nevertheless, it is mandatory to probe for oscillations with as much sensitivity as possible for three main reasons: (i) With oscillations being an intriguing quantum mechanical phenomenon their observation carries intrinsic intellectual value. (ii) We might be only one breakthrough in our computational control over nonperturbative dynamics away from making precise predictions. (iii) Last and most importantly:  $CP$  asymmetries that involve oscillations – see Sect. 26.4 below – would conclusively establish the existence of New Physics. Having an independent measurement of those oscillations would provide a most powerful validation of such asymmetries.

In summary: to the best of our present knowledge even values for  $x$  and  $y$  as ‘high’ as 0.01 could be due entirely to SM dynamics of otherwise little interest. It is likewise possible that a large or even dominant part of  $x \sim 0.01$  in particular is due to New Physics. While one should never rule out a theoretical breakthrough, we are less than confident that even the usual panacea, namely lattice QCD, can provide a sufficiently fine instrument in the foreseeable future.

Yet despite this lack of an unequivocal statement from theory, one wants to probe these oscillations as accurately as possible, even in the absence of the aforementioned breakthrough, since they represent an intriguing quantum mechanical phenomenon and – on the more practical side – constitute an important ingredient for  $CP$  asymmetries arising in  $D^0$  decays due to New Physics as explained in the next Chapter.

## 25.2 Experimental Review<sup>2</sup>

$D^0 - \overline{D}^0$  mixing and  $CP$  violation in charm sector have been searched for by various experimental facilities with different techniques. The principal production processes are

---

<sup>2</sup>by Edited by D. M. Asner and H. B. Li

$e^+e^- \rightarrow c\bar{c}$  at center of mass energy from threshold up to  $Z^0$  boson peak, hadroproduction at both fixed-target experiments and the Fermilab Tevatron, photoproduction and so on. The cross sections vary from a few nb to microbarns for photoproduction, and to order of a millibarn at the Tevatron. However, the ratio of signal to background cross section range from 1:1 in  $e^+e^-$  annihilation to 1:500 at the Tevatron as listed in Table 25.1.

Table 25.1: Summary of recent charm experiments including: techniques, luminosity, charm production cross section and signal to noise ratio.

Experiment	Beam	Lumin. ( $\text{cm}^{-2}\text{s}^{-1}$ )	Cross-Section	#events $c\bar{c}$ Per year	$\sigma(c\bar{c})/\sigma_{Total}$
BaBar	$e^+e^- (\Upsilon(4S))$	$3 \times 10^{33}$	1.3 nb	$40 \times 10^6$	$\sim 1/5$
Belle	$e^+e^- (\Upsilon(4S))$	$3 \times 10^{33}$	1.3 nb	$40 \times 10^6$	$\sim 1/5$
CLEO-c	$e^+e^- (\psi(3770))$	$2 \times 10^{32}$	6.4 nb	$6.4 \times 10^6$	$\sim 1$
BES-III	$e^+e^- (\psi(3770))$	$1 \times 10^{33}$	6.4 nb	$32 \times 10^6$	$\sim 1$
LHC-b	$pp(\sqrt{s} = 14 \text{ TeV})$	$2 \times 10^{32}$	1.0 mb	$1 \times 10^{11}$	$\sim 1/100$

The techniques that can be used to search for mixing can be roughly divided into four classes: mixing in semi-leptonic decays, time-dependent measurements in wrong-sign decays to hadronic non- $CP$  eigenstates, decays to  $CP$  eigenstates and mixing measurements via quantum coherence at threshold.

### 25.2.1 Semileptonic Decays

The manifestation of  $D^0$  mixing in semileptonic decays is relatively simple, since such transitions are flavor specific in the standard model or some of its extensions. Because of the flavor specificity of  $D^0 \rightarrow l^+ X^-$  and  $\bar{D}^0 \rightarrow l^- X^+$ , it is not necessary to study the time-dependent  $D$  decay modes.

In semileptonic  $D$  decays, the wrong-sign decay amplitudes  $A_f = \bar{A}_{\bar{f}} = 0$ . Then in the limit of weak mixing, where  $|ix + y| \ll 1$ , from Eq. 25.1.24,  $r(t)$  is given by

$$r(t) = \left| \frac{q}{p} \right|^2 |g_-(t)|^2 \sim \frac{e^t}{4} (x^2 + y^2) t^2 \left| \frac{q}{p} \right|^2, \quad (25.2.36)$$

In the limit of  $CP$  conservation,  $r(t) = \bar{r}(t)$ , and integrating Eq. 25.2.36 over all time gives

$$R_M = \int_0^\infty r(t) dt = \left| \frac{q}{p} \right|^2 \frac{x^2 + y^2}{2 + x^2 + y^2} \simeq \frac{x^2 + y^2}{2}, \quad (25.2.37)$$

The traditional method of looking for *like-sign*  $\mu^\pm \mu^\pm$  pairs is an example at fixed target experiments [320, 321, 322]. However, in  $e^+e^-$  experiments, such as those at a  $B$  factory, there are enough kinematic constraints to infer the neutrino momentum. Specifically, momentum conservation prescribes  $P_\nu = P_{CM} - P_{\pi_s Kl} - P_{\text{rest}}$  [318], where  $P_{CM}$  is the four-momentum of the  $e^+e^-$  center-of-mass (CM) system,  $\pi_s$ ,  $K$ , and  $l$  are daughters from decay  $D^*+ \rightarrow D^0 \pi_s \rightarrow \pi_s Kl\nu$ , and  $P_{\text{rest}}$  is the four-momentum of the remaining particles in the event. In  $B$ -factory experiments, the magnitude of  $|P_{\text{rest}}|$  is rescaled to satisfy  $(P_{CM} - P_{\text{rest}})^2 = m_{D^*}^2$  and, after this rescaling, the direction of  $\overrightarrow{p_{\text{rest}}}$  is adjusted

Table 25.2: Results for  $R_M$  in  $D^0$  semileptonic decays from HFAG [319].

Year	Experiment	Final states	$R_M$ (%)
1996	E791 [323]	$K^+e^-\bar{\nu}$	$0.11^{+0.30+0.00}_{-0.27-0.014}$
2005	CLEO-II.V [324]	$K^{(*)+}e^-\bar{\nu}$	$0.16 \pm 0.29 \pm 0.29$
2004	BaBar [325]	$K^{(*)+}e^-\bar{\nu}$	$0.23 \pm 0.12 \pm 0.04$
2005	Belle [318]	$K^{(*)+}e^-\bar{\nu}$	$0.02 \pm 0.047 \pm 0.014$
2007	BaBar [326]	$K^{(*)+}e^-\bar{\nu}$	$0.004^{+0.070}_{-0.060}$
Average from HFAG [319]			$0.0173 \pm 0.0387$ (CL=0.965)

to satisfy  $P_\nu^2 (= m_\nu^2) = 0$ . Table 25.2 gives a summary of the experimental status of  $R_M$  measurements in semileptonic decays.

The best places to use the semileptonic method are probably at *BES-III* and CLEO-c operating near the charm threshold. The idea is to search for  $e^+e^- \rightarrow \psi(3770) \rightarrow D^0\bar{D}^0 \rightarrow (K^-l^+\nu)(K^-l^+\nu)$  or  $e^+e^- \rightarrow D^-\bar{D}^{*+} \rightarrow (K^+\pi^-\pi^-)(K^+l^-\nu) + \pi_s$ . The latter is probably the only process where the semileptonic method does not suffer from a large background, since there is only one neutrino missing in the entire event, threshold kinematic constraints should provide a clean signal.

However, it has been pointed out that one can not claim a  $D^0$  mixing signal based on the semileptonic decay alone (unless accompanied by information on the decay time of  $D^0$  which is possible at a  $B$  factory). Bigi [327] pointed out that an observation of a signal on  $D^0 \rightarrow l^-X^+$  establishes only that a certain selection rule is violated in the processes where the charm quantum number is changed, namely, the rule  $\Delta C = -\Delta Q_l$  where  $Q_l$  denotes leptonic charge. This violation can occur either through  $D^0 - \bar{D}^0$  mixing (with the unique attribute of the decay time-dependence of mixing), or through new physics beyond the SM (which could be independent of time). Nevertheless, one can always use this method to set an upper limit for mixing.

### 25.2.2 Hadronic Final States

*Wrong-sign* hadronic decay modes can occur either through  $D^0 - \bar{D}^0$  mixing or through DCSD as illustrated in Eqs. 25.1.16 and 25.1.17. The major complication for this method is the need to distinguish between DCSD and mixing. In principle, there are at least three ways to distinguish between DCSD and mixing candidates experimentally: (1) use the difference in the decay time-dependence [331, 330]; (2) use the possible difference in the resonance substructure between DCSD and mixing events on the Dalitz plot in three-body  $D^0 \rightarrow K^+\pi^-\pi^0$  decay [333], or multi-body decays, like  $D^0 \rightarrow K^+\pi^-\pi^+\pi^-$ , etc.; (3) use the quantum correlations between the production and decay processes at the  $\psi(3770)$  peak [327, 334]. Method (1) is popular at  $B$  factory since the  $D^0$  is highly boosted, so its decay time information can be used. Method (2) requires knowledge of the structures of the DCSD decay on the Dalitz plots, which can be done at both a  $B$  factory and a  $\tau$ -charm factory. Method (3) can be done by *BES-III* at charm threshold region. In this subsection, we only discuss method (1), specifically. Method (2) and (3) are discussed later.

According to Eq. 25.1.24, one has:

$$r(t) = \left| \frac{q}{p} \right|^2 (\lambda_f^{-2} g_+^2(t) + \lambda_f^{-1} g_+(t) g_-^*(t) + (\lambda_f^{-1})^* g_+^*(t) g_-(t) + g_-^2(t)), \quad (25.2.38)$$

We can simplify Eq. 25.2.38 under the assumption of small mixing,  $|ix + y| \ll 1$ , and express

$$\begin{aligned} \lambda_f^{-2} g_+^2(t) &= |\lambda_f^{-1}|^2 \frac{e^{-t}}{2} [\cosh(yt) + \cos(xt)] \\ &\simeq |\lambda_f^{-1}|^2 e^{-t}, \end{aligned} \quad (25.2.39)$$

$$\begin{aligned} g_-^2(t) &= \frac{e^{-t}}{2} [\cosh(yt) - \cos(xt)] \\ &\simeq e^{-t} \left( \frac{x^2 + y^2}{4} \right) t^2, \end{aligned} \quad (25.2.40)$$

and

$$\begin{aligned} &\lambda_f^{-1} g_+(t) g_-^*(t) + (\lambda_f^{-1})^* g_+^*(t) g_-(t) \\ &= \frac{e^{-t}}{2} (e^{-i(\delta+\phi)} (\sinh(yt) - i \sin(xt)) + e^{i(\delta+\phi)} (\sinh(yt) + i \sin(xt))) \\ &\simeq |\lambda_f^{-1}| e^{-t} (y \cos(\delta + \phi) - x \sin(\delta + \phi)) t. \end{aligned} \quad (25.2.41)$$

If we define

$$y'_\pm \equiv y' \cos\phi \pm x' \sin\phi = y \cos(\delta \mp \phi) - x \sin(\delta \mp \phi), \quad (25.2.42)$$

where

$$y' \equiv y \cos\delta - x \sin\delta, \quad x' \equiv x \cos\delta + y \sin\delta, \quad (25.2.43)$$

and combine Eqs. 25.1.22, 25.2.39, 25.2.40 and 25.2.41 in the limit of  $CP$  conservation ( $A_D = 0$ ,  $A_M = 0$  and  $\phi = 0$ ), we obtain the standard form for the time-dependent decay rate, including  $D$  mixing:

$$r(t) = \bar{r}(t) = e^{-t} \left( R_D + \sqrt{R_D} y' t + \frac{1}{2} R_M t^2 \right) \quad (25.2.44)$$

The above wrong-sign decay rate includes three components: one from the DCSD, another from mixing, and one from the interference between DCSD and mixing. The time-integrated wrong-sign rate relative to the integrated right-sign rate is

$$R_{WS} = \int_0^\infty r(t) dt = R_D + \sqrt{R_D} y' + \frac{1}{2} R_M. \quad (25.2.45)$$

As shown in Eq. 25.2.44,  $D$  mixing is characterized in the decay rate by a small deviation from a pure exponential. In order to have the most sensitivity to  $(x^2 + y^2)$ , a decay channel for which  $R_D$  is relatively small is desirable. The analysis technique benefits

Table 25.3: Results for  $R_{WS}$  and  $R_D$  in  $D^0 \rightarrow K^+\pi^-$ , where it is assumed that there is no mixing and no  $CP$  violation in DCSD decays.

Experiments	comments	$R_{WS}$ (%)	$R_D$ (%)
E791 [328]	500 GeV $\pi^-N$ interactions	$0.68^{+0.34}_{-0.33} \pm 0.07$	–
CLEO [310]	$9.0 \text{ fb}^{-1}$ near $\Upsilon(4S)$	$0.332^{+0.063}_{-0.065} \pm 0.040$	$0.47^{+0.11}_{-0.12} \pm 0.040$
FOCUS [329]	$\gamma$ BeO	$0.429 \pm 0.063 \pm 0.028$	$0.381^{+0.167}_{-0.163} \pm 0.092$
Belle [330]	$400 \text{ fb}^{-1}$ near $\Upsilon(4S)$	$0.377 \pm 0.008 \pm 0.005$	$0.364 \pm 0.017$
BaBar [331]	$384 \text{ fb}^{-1}$ near $\Upsilon(4S)$	–	$0.303 \pm 0.016 \pm 0.010$
CDF [332]	$0.35 \text{ fb}^{-1}$ at $\sqrt{s} = 1.96 \text{ TeV}$	$0.405 \pm 0.021 \pm 0.011$	–

Table 25.4:  $D^0 \rightarrow K^+\pi^-$  results for  $x'^2$  and  $y'$  from HFAG [319]. These results assume no  $CPV$ .

Experiment	comments	$x'^2$ (%)	$y'$ (%)
CLEO [310]	$9.0 \text{ fb}^{-1}$ near $\Upsilon(4S)$	$0.0 \pm 1.5 \pm 0.2$	$-2.3^{+1.3}_{-1.4} \pm 0.3$
Belle [330]	$400 \text{ fb}^{-1}$ near $\Upsilon(4S)$	$0.018^{+0.021}_{-0.023}$	$0.06^{+0.40}_{-0.39}$
BaBar [331]	$384 \text{ fb}^{-1}$ near $\Upsilon(4S)$	$-0.022 \pm 0.030 \pm 0.021$	$0.97 \pm 0.44 \pm 0.31$

from the ability to compare the signal distribution, given by Eq. 25.2.44, to the CF decay distribution, which may be treated as pure exponential. In this way, systematic bias is significantly limited.

The ratios  $R_{WS}$  and  $R_D$  are the most readily accessible experimental quantities. Table 25.3 gives recent measurements of  $R_{WS}$  and  $R_D$  ifor  $D^0 \rightarrow K^+\pi^-$  decays.

The interference causes the measured  $x$  and  $y$  to be rotated through an angle  $\delta$ , the phase difference between the DCS and CF decay processes. By measuring the time dependence of the decay rate it is possible to sort out the mixing from the DCS decay. At  $B$  factory and the CLEO experiments, wrong-sign candidate events of the types  $D^0 \rightarrow K^+\pi^-$  and  $\overline{D}^0 \rightarrow K^-\pi^+$  are selected by requiring the soft  $\pi_s$  from the  $D^*$  decay and the daughter  $K$  of the  $D^0$  to have identical charge (wrong-sign tag). In order to determine the wrong-sign and right-sign yields, two powerful distinguishing variables are used by Belle,  $M_{K\pi}$  and the released energy  $Q \equiv M^* - M_{K\pi} - m_{\pi_s}$ , where  $M^*$  is the reconstructed mass of the  $K^+\pi^-\pi_s^+$  system,  $M_{K\pi}$  is the reconstructed mass of  $K^+\pi^-$  system, and  $m_{\pi_s}$  is the charged pion mass. In comparison, the BaBar and CLEO experiments used the mass difference  $\delta m = M^* - M_{K\pi}$ . To detect a deviation from an exponential decay in wrong-sign events, a likelihood fit to the distribution of the reconstructed proper decay time  $t$  is performed for each experiment. The likelihood fit includes a signal and a background component and models each as the convolution of a decay-time distribution and a resolution function.

Results for  $x'^2$  and  $y'$  from several experiments are listed in Table 25.4. While no experiment claims an effect, it is interesting that the Belle result is consistent with no mixing only at the 3.9% C.L. [330]. Figure 25.5 shows the 95% C.L. region in the  $x'^2$ - $y'$  plane from HFAG [319]. The significance of the oscillation effect exceeds  $4\sigma$ .

Mixing has also been searched for in the wrong-sign multibody final states  $K^+\pi^-\pi^0$  and  $K^+\pi^-\pi^+\pi^-$  [335, 336, 337]. Using  $281 \text{ fb}^{-1}$  of data, Belle has done a time-integrated

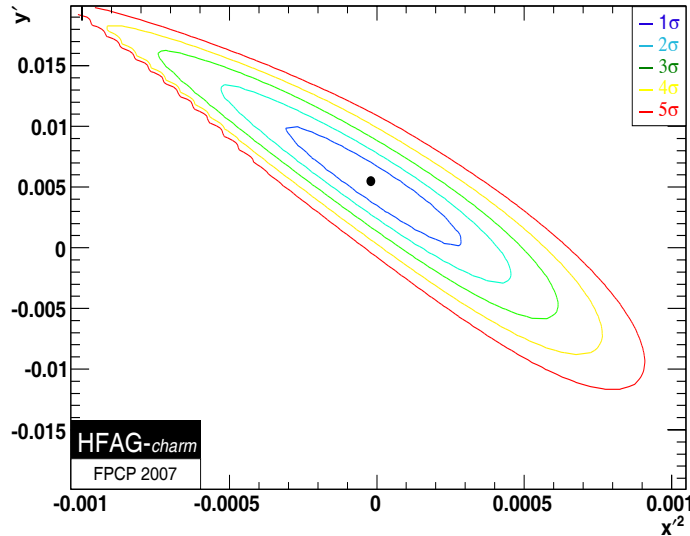


Figure 25.5: Contours (1 through 5 $\sigma$ ) of the allowed region in the  $x'^2$  vs  $y'$  plane are shown for  $D^0 \rightarrow K^+ \pi^-$  decay by combining BaBar and Belle's results. The significance of the oscillation effect exceeds 4 $\sigma$ .

analysis, and measured the time-independent ratio of wrong-sign to right-sign decays. The results are  $R_{WS} = (0.229 \pm 0.015^{+0.013}_{-0.009})\%$  for the  $D^0 \rightarrow K^+ \pi^- \pi^0$  and  $R_{WS} = (0.320 \pm 0.018^{+0.018}_{-0.013})\%$  for the  $D^0 \rightarrow K^+ \pi^- \pi^+ \pi^-$ .

BaBar reported a measurement of the mixing rate  $R_M$  in the decay  $D^0 \rightarrow K^+ \pi^- \pi^0$  based on a time-dependent analysis [333]. There are two key motivations to select  $D^0 \rightarrow K^+ \pi^- \pi^0$ : (1) one expects the Dalitz-plot structure of DCS decay to differ from that of CF decay. We note that DCS decays proceed primarily through the resonance  $D^0 \rightarrow K^{*+} \pi^-$ ,  $K^{*0} \pi^0$ , while CF decays proceed primarily through the resonance  $D^0 \rightarrow K^- \rho^+$ . The measurement sensitivity to  $R_M$  is increased by selecting regions of the Dalitz plot where CF decays contribute with a large amplitude relative to the corresponding DCS decays. (2) The time-integrated mixing rate  $R_M = (x^2 + y^2)/2$  is independent of the decay mode and is expected to be consistent between different mixing measurement methods. The sensitive regions of the phase space (i.e., the Dalitz plot) are selected by removing the  $K^*$  resonance. In the limit of  $CP$  conservation, the time-dependent ratio of wrong-sign to right-sign is expressed approximately as:

$$R_{WS} = \tilde{R}_D + \alpha \sqrt{\tilde{R}_D} \tilde{y}' t + \frac{1}{2} R_M t^2 \quad (25.2.46)$$

$$0 \leq \alpha \leq 1,$$

where the tilde indicates quantities that have been integrated over any choice of phase space regions. Here  $\tilde{R}_D$  is the integrated DCS ratio of DCS decays to CF decays;  $\tilde{y}' = y \cos \tilde{\delta} - x \sin \tilde{\delta}$ ,  $\tilde{\delta}$  is an unknown integrated strong-phase difference between the CF and the DCS decay amplitudes;  $\alpha$  is a suppression factor that accounts for possible strong-phase variations over the regions. The time-integrated mixing rate  $R_M$  is independent of decay mode. By fitting the proper time distribution, they get the results  $R_M = (0.023^{+0.018}_{-0.014} \pm 0.004)\%$  and  $\tilde{R}_D = (0.164^{+0.026}_{-0.022} \pm 0.012)\%$  with the assumption of  $CP$

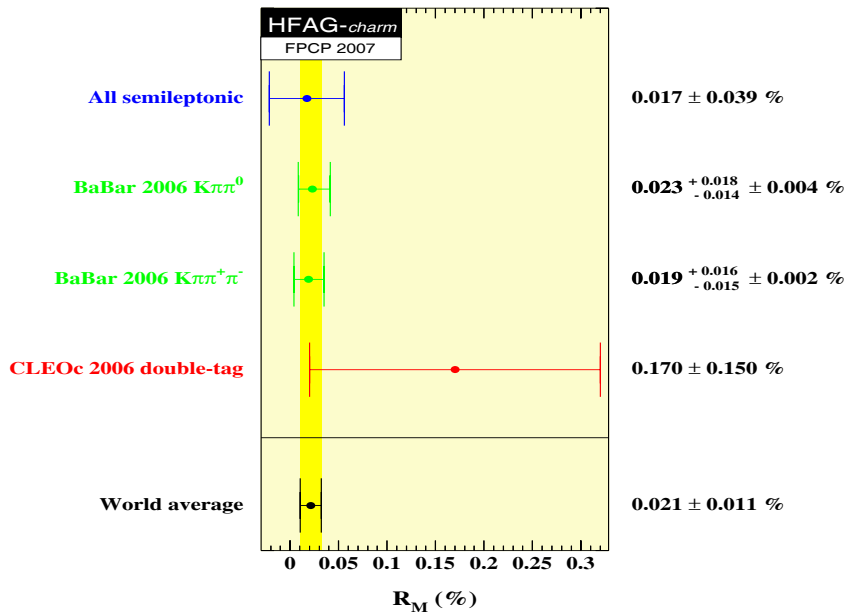


Figure 25.6:  $R_M$  combination: the world averaged  $R_M$  by combining the results of semileptonic  $D$  decays and these from the wrong-sign multibody final states.

invariance. An upper limit is established as  $R_M < 0.054\%$  at the 95% confidence level. They conclude that the observed data are consistent with no mixing at the 4.5% confidence level. Using a similar method and idea, BaBar also measured the time-integrated mixing rate  $R_M$  in  $D^0 \rightarrow K^+ \pi^- \pi^+ \pi^-$  decay mode. Assuming  $CP$  conservation, they get  $R_M = (0.019_{-0.015}^{+0.016} \pm 0.002)\%$ , and  $R_M < 0.048\%$  at 95% C.L.. Furthermore, they combined results from both decay modes, and found that  $R_M = (0.020_{-0.010}^{+0.011})\%$  and  $R_M < 0.042\%$  at 95% C.L. which is the best limit with current data. The combined data sets are consistent with the no-mixing hypothesis with 2.1% confidence.

By combining the results of semileptonic  $D$  decays and these from the wrong-sign multibody final states, one can obtain the world averaged  $R_M$  shown in Fig. 25.6. The averaged mixing rate is  $R_{Ms} = (0.021 \pm 0.011)\%$  with  $CL = 0.795$ .

### 25.2.3 $CP$ Eigenstates

$D^0$  mixing parameters can be measured by comparing the lifetimes extracted from the analysis of  $D$  decays into the  $CP$ -even and  $CP$ -odd final states. When the final state is a  $CP$  eigenstate  $f$  (i.e.,  $|\bar{f}\rangle \equiv CP|f\rangle = \pm|f\rangle$ ), such as  $K^+ K^-$ ,  $\pi^+ \pi^-$  and  $K_S \pi^0$ , there is no strong phase difference between  $\bar{A}_f$  and  $A_f$ . Assuming  $|\bar{A}_f| = |A_f|$  (no direct  $CP$  violation),  $\lambda_f = -|q|/|p|e^{i\phi}$  and  $\lambda_{\bar{f}} = -|p|/|q|e^{-i\phi}$ , where  $\phi$  is the weak phase difference. Inserting these terms into Eqs. 25.1.24 and 25.1.25 gives

$$R(D^0 \rightarrow K^+ K^-) \simeq |A_{K^+ K^-}|^2 e^{-t} e^{-|q/p|(y \cos \phi - x \sin \phi)t}, \quad (25.2.47)$$

and

$$R(\bar{D}^0 \rightarrow K^+ K^-) \simeq |A_{K^+ K^-}|^2 e^{-t} e^{-|p/q|(y \cos \phi + x \sin \phi)t}. \quad (25.2.48)$$

Equations 25.2.47 and 25.2.48 imply that the measured  $D^0$  and  $\bar{D}^0$  inverse lifetimes are slightly different each other. We define

$$y_{CP} = \frac{\tau_{D^0 \rightarrow K^-\pi^+}}{\tau_{D^0 \rightarrow K^+K^-}} - 1 = \frac{|q|}{|p|}(y\cos\phi - x\sin\phi), \quad (25.2.49)$$

for  $D^0$  decays, and for  $\bar{D}^0$  decays, it is

$$y_{CP} = \frac{\tau_{\bar{D}^0 \rightarrow K^+\pi^-}}{\tau_{\bar{D}^0 \rightarrow K^+K^-}} - 1 = \frac{|p|}{|q|}(y\cos\phi + x\sin\phi). \quad (25.2.50)$$

For  $|q/p| = 1$ , i.e., no  $CP$  violation in mixing,  $y_{CP} = y\cos\phi$  for samples with equal numbers of  $D^0$  and  $\bar{D}^0$  decays. If, in addition,  $\phi = 0$  (no  $CP$  violation),  $y_{CP} = y$ .

One can also combine the two  $D \rightarrow K^+K^-$  modes. To understand the consequences of such an analysis, one has to consider the relative weight of  $D^0$  and  $\bar{D}^0$  in the sample. We define  $A_{\text{prod}}$  as the production asymmetry of  $D^0$  and  $\bar{D}^0$ :

$$A_{\text{prod}} = \frac{N(D^0) - N(\bar{D}^0)}{N(D^0) + N(\bar{D}^0)}. \quad (25.2.51)$$

Then

$$\begin{aligned} y_{CP} &= \frac{\tau_{D^0 \rightarrow K^-\pi^+}}{\tau_{D \rightarrow K^+K^-}} - 1 \\ &= y\cos\phi \left[ \frac{1}{2} \left( \left| \frac{p}{q} \right| + \left| \frac{q}{p} \right| \right) + \frac{A_{\text{prod}}}{2} \left( \left| \frac{p}{q} \right| - \left| \frac{q}{p} \right| \right) \right] \\ &\quad - x\sin\phi \left[ \frac{1}{2} \left( \left| \frac{p}{q} \right| - \left| \frac{q}{p} \right| \right) + \frac{A_{\text{prod}}}{2} \left( \left| \frac{p}{q} \right| + \left| \frac{q}{p} \right| \right) \right], \end{aligned} \quad (25.2.52)$$

Table 25.5: Summary of  $y_{CP}$  results.

Year	Experiment	comments	$y_{CP}(\%)$
2000	FOCUS [338]	$\gamma N$ interactions	$3.4 \pm 1.4 \pm 0.7$
2002	CLEO [339]	$9.0 \text{ fb}^{-1}$ near $\Upsilon(4S)$	$-1.2 \pm 2.5 \pm 1.4$
2002	Belle [340]	$23.4 \text{ fb}^{-1}$ near $\Upsilon(4S)$ ; no $D^*$ tag	$-0.5 \pm 1.0 \pm 0.8$
2007	Belle [342]	$540 \text{ fb}^{-1}$ near $\Upsilon(4S)$	$1.31 \pm 0.32 \pm 0.25$
2007	BaBar [344]	$384 \text{ fb}^{-1}$ near $\Upsilon(4S)$	$1.03 \pm 0.33 \pm 0.19$
	Average		$1.132 \pm 0.266$

The value of  $y_{CP}$  is determined from the difference in slopes of the decay-time distributions for the  $D^0 \rightarrow K^-\pi^+$  sample, which is an equal mixture of  $CP$ -even and  $CP$ -odd final states, and the  $D^0 \rightarrow K^+K^-$  or  $\pi^+\pi^-$  samples, which are  $CP$ -even final states. An unbinned maximum likelihood fit to the distribution of the reconstructed proper time  $t$  of the  $D^0$  candidates is performed. To date, five experiments have measured  $y_{CP}$ , as listed in Table 25.5.

Since it requires a fit to the proper-time distribution, this method can not be applied at the *BES-III* and CLEO-c experiments, which operate near the open charm threshold.

### 25.2.4 Mixing parameters from a Dalitz Plot analysis

The first time-dependent Dalitz plot analysis was done by CLEO for the  $D^0 \rightarrow K_S \pi^+ \pi^-$  decay mode [347]. In 2007, Belle also presented results with a  $540 \text{ fb}^{-1}$  data sample at the  $\Upsilon(4S)$  peak [348]. They use a self-conjugate final state that is not a  $CP$  eigenstate as reflected by substructures with either  $L = 0$  ( $CP$ -even) or  $L = 1$  ( $CP$ -odd) in the three body decay. The decay rate to  $K_S \pi^+ \pi^-$  with  $(m_{K_S \pi^-}^2, m_{\pi^+ \pi^-}^2)$  at time  $t$  of a particle tagged as  $|D^0\rangle$  at  $t = 0$  is

$$d\Gamma(m_{K\pi}^2, m_{\pi\pi}^2, t) = \frac{1}{256\pi^3 M^3} |\mathcal{M}|^2 dm_{K\pi}^2 dm_{\pi\pi}^2, \quad (25.2.53)$$

where  $\mathcal{M} = \langle f | H | D^0(t) \rangle$ , and  $\langle f | = \langle K_S \pi^+ \pi^- (m_{K_S \pi^-}^2, m_{\pi^+ \pi^-}^2) |$ . An expression for  $|D^0(t)\rangle$  is given in Eq. 25.1.11.

The decay channels can be collected into those that are  $CP$ -even or  $CP$ -odd (with amplitudes  $\text{Amp}_+$  or  $\overline{\text{Amp}}_-$ ) and to those that are  $D^0$  or  $\overline{D}^0$  flavor eigenstates (with amplitudes  $\text{Amp}_f$  or  $\overline{\text{Amp}}_f$ ):

$$\langle f | \mathcal{H} | D_{+, -} \rangle = \sum a_j e^{i\delta_j} \mathcal{A}_{+, -}^j = p \text{Amp}_{+, -}; \quad (25.2.54)$$

$$\langle \overline{f} | \mathcal{H} | D_{+, -} \rangle = \sum a_j e^{i\delta_j} \overline{\mathcal{A}}_{+, -}^j = q \overline{\text{Amp}}_{+, -}; \quad (25.2.55)$$

$$\langle f | \mathcal{H} | D^0 \rangle = \sum a_j e^{i\delta_j} \mathcal{A}^j = \text{Amp}_f; \quad (25.2.56)$$

$$\langle \overline{f} | \mathcal{H} | \overline{D}^0 \rangle = \sum a_j e^{i\delta_j} \overline{\mathcal{A}}^j = p \overline{\text{Amp}}_f. \quad (25.2.57)$$

Here  $a_j$  and  $\delta_j$  are the explicitly  $CP$  conserving amplitudes and relative strong phases (Ref. [346] fixes  $a_\rho = 1$  and  $\delta_\rho = 0$ ; all other strong phases are relative to the  $\rho$  amplitude) for the  $j^{\text{th}}$  quasi-two-body state.  $\mathcal{A}_{+, -}^j = \mathcal{A}_{+, -}^j(m_{K_S \pi^-}^2, m_{\pi^+ \pi^-}^2)$  is the Breit-Wigner amplitude for resonance  $j$  with  $D$  decay to  $CP = +$  or  $CP = -$  quasi-two-body contributions. In Ref. [346], CLEO considered the following ten modes:  $K^{*-} \pi^+$ ,  $K_0^*(1430)^- \pi^+$ ,  $K_2^*(1430)^- \pi^+$ ,  $K^*(1680)^- \pi^+$ ,  $K_S \rho$ ,  $K_S \omega$ ,  $K_S f_0(980)$ ,  $K_S f_2(1270)$ ,  $K_S f_0(1370)$ , and the "wrong-sign"  $K^{*+} \pi^-$  plus a small non-resonant component. Collecting terms with similar time dependence and combining Eqs. 25.1.11 and 25.1.12, one finds

$$\begin{aligned} \mathcal{M} &= \langle f | \mathcal{H} | D^0(t) \rangle = \frac{1}{2p} (\langle f | \mathcal{H} | D_1(t) \rangle + \langle f | \mathcal{H} | D_2 \rangle) \\ &= \frac{1}{2p} (\langle f | \mathcal{H} | (pD^0 + q\overline{D}^0) \rangle e_1(t) + \langle f | \mathcal{H} | (pD^0 - q\overline{D}^0) \rangle e_2(t)) \\ &= \frac{1}{2p} ([p(\text{Amp}_f + \text{Amp}_+) + q(\overline{\text{Amp}}_f + \overline{\text{Amp}}_+)] e_1(t) \\ &\quad + [p(\text{Amp}_f + \text{Amp}_-) - q(\overline{\text{Amp}}_f + \overline{\text{Amp}}_-)] e_2(t)) \\ &= \frac{1}{2} [(1 + \chi_f) \text{Amp}_f + (1 + \chi_+) \text{Amp}_+] e_1(t) \\ &\quad + [(1 - \chi_f) \text{Amp}_f + (1 - \chi_-) \text{Amp}_-] e_2(t)) \\ &\equiv e_1(t) A_1 + e_2 A_2, \end{aligned} \quad (25.2.58)$$

and

$$\begin{aligned}
\mathcal{M} &= \langle \bar{f} | \mathcal{H} | \bar{D}^0(t) \rangle = \frac{1}{2q} (\langle \bar{f} | \mathcal{H} | D_1(t) \rangle - \langle \bar{f} | \mathcal{H} | D_2 \rangle) \\
&= \frac{1}{2} ([(\chi_{\bar{f}}^{-1} + 1) \overline{\text{Amp}}_{\bar{f}} + (\chi_{+}^{-1} + 1) \overline{\text{Amp}}_{+}] e_1(t) \\
&\quad - [(\chi_{\bar{f}}^{-1} - 1) \overline{\text{Amp}}_{\bar{f}} + (\chi_{-}^{-1} - 1) \overline{\text{Amp}}_{-}] e_2(t)) \\
&\equiv e_1(t) \overline{A}_1 + e_2 \overline{A}_2,
\end{aligned} \tag{25.2.59}$$

for  $D^0$  and  $\bar{D}^0$ , respectively. The CLEO experiment defines

$$\chi_f = \frac{q \overline{\text{Amp}}_f}{p \text{Amp}_f} = \left| \frac{\overline{\text{Amp}}_f}{\text{Amp}_f} \right| (1 + A_M) e^{i(\delta + \phi)} \tag{25.2.60}$$

$$\chi_{\bar{f}} = \frac{q \overline{\text{Amp}}_{\bar{f}}}{p \text{Amp}_{\bar{f}}} = \left| \frac{\overline{\text{Amp}}_{\bar{f}}}{\text{Amp}_{\bar{f}}} \right| (1 + A_M) e^{-i(\delta - \phi)} \tag{25.2.61}$$

$$\chi_{\pm} = \pm \frac{q \overline{\text{Amp}}_{\pm}}{p \text{Amp}_{\pm}} = \pm \left| \frac{\overline{\text{Amp}}_{\pm}}{\text{Amp}_{\pm}} \right| (1 + A_M) e^{\pm i\phi}, \tag{25.2.62}$$

where  $\delta$  is the relative strong phase between  $D^0$  and  $\bar{D}^0$  to  $K_S \pi^+ \pi^-$  and, in the limit of  $CP$  conservation, the real  $CP$ -violating parameters,  $A_D$  and  $\phi$ , are zero. Squaring the amplitude and factoring out the time-dependent functions yields

$$|\mathcal{M}|^2 = |e_1(t)|^2 |A_1|^2 + |e_2(t)|^2 |A_2|^2 + 2\text{Re}[e_1(t) e_2^*(t) A_1 A_2^*]. \tag{25.2.63}$$

$$|\overline{\mathcal{M}}|^2 = |e_1(t)|^2 |\overline{A}_1|^2 + |e_2(t)|^2 |\overline{A}_2|^2 + 2\text{Re}[e_1(t) e_2^*(t) \overline{A}_1 \overline{A}_2^*]. \tag{25.2.64}$$

The time-dependent terms are given explicitly by

$$|e_1(t)|^2 = e^{\Gamma_1 t} = e^{-\Gamma(1-y)t}, \tag{25.2.65}$$

$$|e_2(t)|^2 = e^{\Gamma_2 t} = e^{-\Gamma(1+y)t}, \tag{25.2.66}$$

$$\begin{aligned}
e_1(t) e_2^*(t) &= e^{-\lambda_{D_1} t} e^{+\lambda_{D_2} t} = e^{-\Gamma(1+ix)t}, \\
&= e^{\Gamma t} (\cos(\Delta m t) - i \sin(\Delta m t)).
\end{aligned} \tag{25.2.67}$$

Experimentally,  $y$  modifies the lifetime of certain contributions to the Dalitz plot while  $x$  introduces a sinusoidal rate variation. Then,  $|\mathcal{M}|^2$  can be expressed as

$$\begin{aligned}
|\mathcal{M}|^2 &= |A_1|^2 e^{-\Gamma(1-y)t} + |A_2|^2 e^{-\Gamma(1+y)t} \\
&\quad + 2e^{\Gamma t} (\text{Re} A_1 A_2^* \cos(\Delta m t) + \text{Im} A_1 A_2^* \sin(\Delta m t)).
\end{aligned} \tag{25.2.68}$$

Using the above probability density function, CLEO does an unbinned maximum likelihood fit to the Dalitz plot and the time  $t$  distribution to determine  $a_j$ ,  $\delta_j$ ,  $x$  and  $y$ . There is a systematic uncertainty arising from the decay model, *i.e.*, one must decide which intermediate states to include in the fit. Equation 25.2.68 depends linearly on  $x$  ( $x < 1$ ) and is, therefore, sensitive to the sign of  $x$ . The fit results are listed in Table 25.6.

Table 25.6: Results for mixing parameters from  $t$ -dependent fits to the  $D^0 \rightarrow K_S^0 \pi^+ \pi^-$  Dalitz plot. For CLEO's results, the errors are statistical, experimental systematic, and decay model systematic, respectively.

Year/Exp.	Param.	Result (%)	Comment
2005/CLEO II.V [347]	$x$	$1.9^{+3.2}_{-3.3} \pm 0.4 \pm 0.4$	$9.0 \text{ fb}^{-1}$ near $\Upsilon(4S)$
	$y$	$-1.4 \pm 2.4 \pm 0.8 \pm 0.4$	
2007/Belle [348]	$x$	$0.80 \pm 0.29 \pm 0.17$	$540 \text{ fb}^{-1}$ near $\Upsilon(4S)$
	$y$	$0.33 \pm 0.24 \pm 0.15$	
Average	$x$	$0.811 \pm 0.334$	$CL = 0.74$
	$y$	$0.309 \pm 0.281$	$CL = 0.50$

The first significant results in  $D^0 \rightarrow K_S \pi^+ \pi^-$  are from Belle [348] as listed in Table 25.6. This is  $2.7\sigma$  from the non-mixing hypothesis. The 95% CL intervals are  $0 < x < 0.016$  and  $-0.0035 < y < 0.010$ .

The analysis relies on the amplitude throughout the Dalitz plot, but its modelling has only been tested so far with rates. In the region of the Dalitz plot corresponding to large  $K^{**}$  masses ( $K^{**}$  denotes heavy kaon states which decay to  $K_S \pi$ ) the ratio of the DCS and CF rates is significantly enhanced in the Belle model [348] compared to that for  $D \rightarrow K\pi$ . While this is possible theoretically, it is less pronounced in the BaBar model [349, 350]. Data on  $CP$ -tagged  $D \rightarrow K_S \pi^+ \pi^-$  decays expected soon from CLEO-c and *BES-III* could help reduce the uncertainties. With more data, one can also attempt a model-independent analysis, as in the extraction of the CKM angle  $\gamma$  [351].

In summary, combining all experimental results obtained without allowing for  $CP$  violation, HFAG finds a  $5.7\sigma$  signal for  $D^0 - \bar{D}^0$  mixing, with the projections [319]

$$x = (8.7^{+3.0}_{-3.4}) \times 10^{-3}, \quad y = (6.6 \pm 2.1) \times 10^{-3}. \quad (25.2.69)$$

In Fig. 25.7, the overall likelihood function with contours (1 through  $5\sigma$ ) for the allowed region in the  $x$  vs  $y$  plane from HFAG is shown [319].

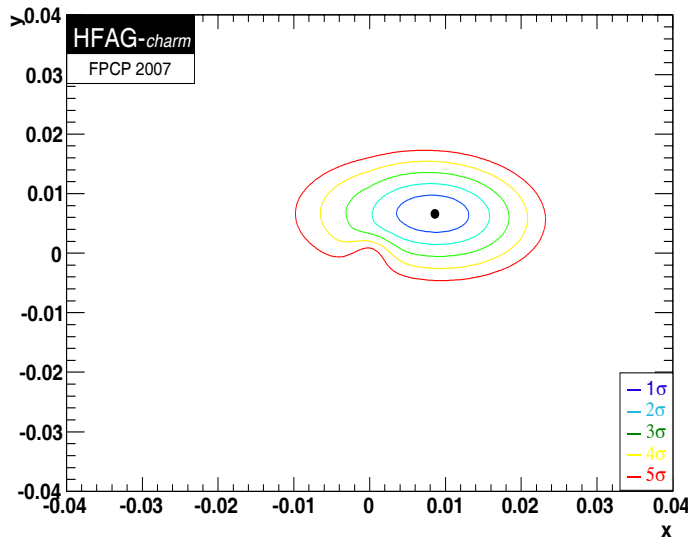


Figure 25.7: Contours (1 through  $5\sigma$ ) of the allowed region in the  $x$  vs  $y$  plane are shown from HFAG by combining all results. The significance of the oscillation effect is about  $5.7\sigma$ .

### 25.3 Measurements at the $\psi(3770)$ peak<sup>3</sup>

At *BES-III*,  $\psi(3770)$  decays will provide another opportunity to search for  $D^0 - \bar{D}^0$  mixing and to investigate sources of  $CP$  violation in the charm system. The amplitude for  $\psi(3770)$  decaying to  $D^0\bar{D}^0$  is  $\langle D^0\bar{D}^0 | \mathcal{H} | \psi(3770) \rangle$ , and the  $D^0\bar{D}^0$  final-state system has charge parity  $C = -1$ , which can be expressed as

$$|D^0\bar{D}^0\rangle^{C=-1} = \frac{1}{\sqrt{2}}[|D^0\rangle|\bar{D}^0\rangle - |\bar{D}^0\rangle|D^0\rangle]. \quad (25.3.70)$$

Even though there is a weak current contribution to  $\psi(3770) \rightarrow D^0\bar{D}^0$  decay that may not conserve charge-parity, the  $D^0\bar{D}^0$  pair can still not be in a  $C = +1$  state. The reason is that the relative orbital angular momentum of the  $D^0\bar{D}^0$  pair must be  $L = 1$  because of angular momentum conservation, and a boson-pair with  $L = 1$  must be in an anti-symmetric state; the anti-symmetric state of a particle-anti-particle pair must have  $C = -1$ . The  $D^0$  and  $\bar{D}^0$  mesons will, therefore, be entangled with the same quantum numbers as the parent resonance.

In general, as shown in Ref. [352], a  $D^0\bar{D}^0$  pair produced via a virtual photon in the reaction  $e^+e^- \rightarrow D^0\bar{D}^0 + m\gamma + n\pi^0$  is in a  $C = (-1)^{m+1}$  state. Thus, at the  $\psi(3770)$ , where no additional fragmentation particles are produced, there can only be  $C = -1$ , while at energies above  $D^*\bar{D}$  threshold, both  $C = -1$  and  $C = +1$  eigenstates can be accessed, such as  $e^+e^- \rightarrow \psi(4140) \rightarrow \gamma(D^0\bar{D}^0)_{C=+1}$  or  $\pi^0(D^0\bar{D}^0)_{C=-1}$ .

We now consider decays of these correlated systems into various final states, and look in particular for interference effects that depend on  $\delta$ . In all cases, we integrate with

<sup>3</sup>Edited by H. B. Li

respect to the proper time, since the vertex separation at a symmetric  $e^+e^-$  “charm factory” is likely to be problematic. Xing [353] and Gronau *et al.* [354] have considered time-integrated decays into correlated pairs of states, including some effects of a non-zero final state phase difference. In Ref. [354], Gronau *et al.* derived general expressions for time-integrated decay rates into a pair of final states  $f_1$  and  $f_2$ , from  $C = -1$  and  $C = +1$   $D^0\overline{D}^0$  states:

$$\Gamma^{C=-1}(f_1, f_2) = \frac{1}{2}|a^-|^2 \left[ \frac{1}{1-y^2} + \frac{1}{1+x^2} \right] + \frac{1}{2}|b^-|^2 \left[ \frac{1}{1-y^2} - \frac{1}{1+x^2} \right], \quad (25.3.71)$$

$$\begin{aligned} \Gamma^{C=+1}(f_1, f_2) = & \frac{1}{2}|a^+|^2 \left[ \frac{1+y^2}{(1-y^2)^2} + \frac{1-x^2}{(1+x^2)^2} \right] \\ & + \frac{1}{2}|b^+|^2 \left[ \frac{1+y^2}{(1-y^2)^2} - \frac{1}{(1-x^2)^2} \right] \\ & + 2\mathcal{R}e \left\{ a^{+*}b^+ \left[ \frac{y}{(1-y^2)^2} + \frac{ix}{(1+x^2)^2} \right] \right\}, \end{aligned} \quad (25.3.72)$$

where

$$a^\pm = \langle f_1 | D^0 \rangle \langle f_2 | \overline{D}^0 \rangle \pm \langle f_1 | \overline{D}^0 \rangle \langle f_2 | D^0 \rangle, \quad (25.3.73)$$

$$b^\pm = \langle f_1 | D^0 \rangle \langle f_2 | D^0 \rangle \pm \langle f_1 | \overline{D}^0 \rangle \langle f_2 | \overline{D}^0 \rangle. \quad (25.3.74)$$

These can be easily generalized to allow for  $CP$  violation [354]:

$$a^\pm = \frac{p}{q} A_1 A_2 (\lambda_2 \pm \lambda_1), \quad (25.3.75)$$

$$b^\pm = \frac{p}{q} A_1 A_2 (1 \pm \lambda_1 \lambda_2), \quad (25.3.76)$$

where

$$A_i \equiv \langle f_i | D^0 \rangle, \quad \overline{A}_i \equiv \langle f_i | \overline{D}^0 \rangle, \quad \lambda_i \equiv \frac{q}{p} \frac{\overline{A}_i}{A_i}. \quad (25.3.77)$$

The quantities in the above equation are discussed in detail in Sect. 25.1.2.

Following Refs. [353, 354, 355, 356], we consider the following categories of  $D^0$  and  $\overline{D}^0$  final states:

- Hadronic final states,  $f$  or  $\overline{f}$ , but not  $CP$  eigenstates, such as  $K^-\pi^+$ , which is produced via CF  $D^0$  transitions or DCS  $\overline{D}^0$  transitions;
- Semileptonic or pure leptonic final states,  $l^+$  or  $l^-$ , which, in the absence of mixing, tag unambiguously the flavor of the parent  $D$ ;
- $CP$ -even ( $S_+$ ) and  $CP$ -odd ( $S_-$ ) eigenstates, respectively.

We discuss different final states in the context of the assumption of  $CP$  conservation. Taking into account  $x, y \ll 1$ , keeping terms up to order  $x^2, y^2$  and  $R_D$  ( $R_D$  is the ratio between DCS and CF decay rate as defined in Eq. 25.1.23), and neglecting  $CP$  violation in decay and mixing, one gets the following results for various cases [354]

$C = -1$   $D^0\bar{D}^0$  states:

- $(K^-\pi^+)(K^-\pi^+)$ :

$$\Gamma^{C=-1}(K^-\pi^+)(K^-\pi^+) = \frac{1}{2}A^4|1 - R_D e^{-2i\delta}|^2(x^2 + y^2) \approx \frac{1}{2}A^4(x^2 + y^2), \quad (25.3.78)$$

where  $A = |\langle K^-\pi^+ | D^0 \rangle|$  is the real-valued decay amplitude. This process serves to measure mixing effects.

- $(K^-\pi^+)(K^+\pi^-)$ :

$$\Gamma^{C=-1}(K^-\pi^+)(K^+\pi^-) = A^4 \left[ 1 - 2R_D \cos 2\delta - \frac{1}{2}(x^2 - y^2) \right]. \quad (25.3.79)$$

This process is not sensitive to the mixing measurements since  $x$  and  $y$  are small. It can be used as a normalization for the previous case.

- $(K^-\pi^+)(S_\chi)$ :

$$\Gamma^{C=-1}(K^-\pi^+)(S_\chi) = A^2 A_{S_\chi}^2 |1 + \chi \sqrt{R_D} e^{-i\delta}|^2 (1 + y^2) \approx A^2 A_{S_\chi}^2 (1 + 2\chi \sqrt{R_D} \cos \delta), \quad (25.3.80)$$

where  $S_\chi \chi = \pm 1$  denotes  $CP$  eigenstate decays. In the  $SU(3)_{fl}$  limit  $R_D = \tan^4 \theta_C \approx 0.0025$ . By comparing the rate for  $\chi = +1$  final states, such as  $K^+K^-$ , and  $\chi = -1$  final states, such as  $K_S$  ( $\pi^0$  or  $\omega, \phi$ ), one can measure  $\cos \delta$ .

- $(K^-\pi^+)(l^-X)$ :

At the  $\psi(3770)$  peak, using a leptonic  $\bar{D}^0$  flavor tag and defining  $A_{l^-} = \langle l^- X | \bar{D}^0 \rangle$ , one finds [354, 353]

$$\Gamma^{C=-1}(K^-\pi^+)(l^- X) = A^2 A_{l^-}^2 \left[ 1 - \frac{1}{2}(x^2 - y^2) \right]. \quad (25.3.81)$$

This process is not sensitive to mixing parameters and serves as a normalization for the next process.

- $(K^-\pi^+)(l^+X)$ :

$$\Gamma^{C=-1}(K^-\pi^+)(l^+ X) = A^2 A_{l^+}^2 \left[ R_D + \frac{1}{2}(x^2 + y^2) \right]. \quad (25.3.82)$$

where  $A_{l^+} = \langle l^+ X | D^0 \rangle = A_{l^-}$ . This process is interesting if  $x^2, y^2$  and  $R_D$  are of comparable in size. But, as mentioned above, it is likely that  $x^2, y^2 \ll R_D$  in which case this process can be used to measure  $R_D$ .

- $(S_\chi)(l^+X)$ :

$$\Gamma^{C=-1}(S_\chi)(l^+X) = A_{S_\chi}^2 A_{l^+}^2 (1 + y^2). \quad (25.3.83)$$

Here  $A_{S_\chi}^2$  is already of order  $\sqrt{R_D}$ . This process serves as a normalization for the others.

$C = +1$   $D^0\overline{D}^0$  states:

- $(K^-\pi^+)(K^-\pi^+)$ .

$$\Gamma^{C=+1}(K^-\pi^+)(K^-\pi^+) = 4A^4 \left[ R_D + \sqrt{R_D}y' + \frac{3}{8}(x^2 + y^2) \right]. \quad (25.3.84)$$

In this case, the three terms ( $R_D$ ,  $y'$  and  $R_M$ ) may be measurable. However, in most SM estimates  $x$  and  $y$  are considerably smaller than a percent [357]. If this is the case, the last term in Eq. 25.3.84 may be inaccessible even though evidence exists for a non-zero  $\sqrt{R_D}y'$  term. Moreover, we need an independent determination of  $\delta$ , which can be obtained from Eq. 25.3.80.

- $(K^-\pi^+)(K^+\pi^-)$ :

$$\Gamma^{C=+1}(K^-\pi^+)(K^+\pi^-) = A^4 \left[ 1 + 2R_D \cos 2\delta + 4\sqrt{R_D}(y \cos \delta + x \sin \delta) - \frac{3}{2}(x^2 - y^2) \right]. \quad (25.3.85)$$

Here the correction terms are probably unmeasurable and, so, this process can serve as a normalization for comparison with the previous one.

- $(K^-\pi^+)(S_\chi)$ :

$$\Gamma^{C=+1}(K^-\pi^+)(S_\chi) \approx A^2 A_{S_\chi}^2 (1 - 2\chi \sqrt{R_D} \cos \delta) (1 - 2\chi y). \quad (25.3.86)$$

This process provides information that constrains  $\cos \delta$  if  $R_D$  and  $y$  are known.

- $(K^-\pi^+)(l^-X)$ :

$$\Gamma^{C=+1}(K^-\pi^+)(l^-X) = A^2 A_{l^-}^2 \left[ 1 + 2\sqrt{R_D}(y \cos \delta + x \sin \delta) - \frac{3}{2}(x^2 - y^2) \right]. \quad (25.3.87)$$

- $(K^-\pi^+)(l^+X)$ :

$$\Gamma^{C=+1}(K^-\pi^+)(l^+X) = A^2 A_{l^+}^2 \left[ R_D + 2\sqrt{R_D}y' + \frac{3}{2}(x^2 + y^2) \right]. \quad (25.3.88)$$

### 25.3.1 The mixing rate: $R_M$

The *BES-III* experiment at BEPCII will search for  $D^0 - \bar{D}^0$  mixing at the  $\psi(3770)$  by observing semileptonic modes of  $D^0$ 's:

$$\frac{N(l^\pm l^\pm)}{N(l^\pm l^\mp)} = \frac{x^2 + y^2}{2} = R_M, \quad (25.3.89)$$

hadronic decay modes:

$$\frac{N[(K^-\pi^+)(K^-\pi^+)]}{N[(K^-\pi^+)(K^+\pi^-)]} \approx \frac{x^2 + y^2}{2} = R_M. \quad (25.3.90)$$

and for cases where one final state is hadronic and the other semileptonic:

$$\frac{N[(l^+)(K^-\pi^+)]}{N[(l^+)(K^+\pi^-)]} \approx \frac{x^2 + y^2}{2} + R_D, \quad (25.3.91)$$

where  $R_D$  is defined in Eq. 25.1.23.

The measurement of  $R_M$  can be performed unambiguously using the reactions:

$$\begin{aligned} (i) \quad & e^+e^- \rightarrow \psi(3770) \rightarrow D^0\bar{D}^0 \rightarrow (K^\pm\pi^\mp)(K^\pm\pi^\mp), \\ (ii) \quad & e^+e^- \rightarrow \psi(3770) \rightarrow D^0\bar{D}^0 \rightarrow (K^-e^+\nu)(K^-e^+\nu), \\ (iii) \quad & e^+e^- \rightarrow D^-D^{*+} \rightarrow (K^+\pi^-\pi^-)(\pi_{soft}^+ [K^+e^-\nu]). \end{aligned} \quad (25.3.92)$$

The observation of reaction (i) would be definite evidence for the existence of  $D^0 - \bar{D}^0$  mixing since the final state  $(K^\pm\pi^\mp)(K^\pm\pi^\mp)$  can not be produced from DCS decay due to quantum statistics [308, 327]. In particular, the initial  $D^0\bar{D}^0$  pair is in an odd eigenstate of  $C$ , which precludes, in the absence of mixing between the  $D^0$  and  $\bar{D}^0$  over time, the formation of a symmetric state, which is required by Bose statistics for decays to the same final state. This final state is also very appealing experimentally, because it involves a two-body decay of both charm mesons, with energetic charged particles in the final state that form an overconstrained system. Particle identification is crucial in this measurement: if both the kaon and pion are misidentified in one of the two  $D$ -meson decays in the event, it is impossible to discern whether or not mixing has occurred. At *BES-III*, with an expected integrated luminosity of  $20 \text{ fb}^{-1}$  at the  $\psi(3770)$  peak, the sensitivity will be  $\sqrt{R_M} \simeq 0.4\%$ , but only if the particle identification capabilities are adequate. If it were possible to obtain  $500 \text{ fb}^{-1}$  at the  $\psi(3770)$ , the sensitivity would be  $\sqrt{R_M} \simeq 0.08\%$  [1].

Reactions (ii) and (iii) offer unambiguous evidence for mixing in that the mixing would be seen in semileptonic decays for which there is no DCS decay contamination. Since the time-evolution is not measured, the observation of Reactions (ii) and (iii) would actually indicate a violation of the SM selection rule relating the change in charm to the change in leptonic charge [327].

In Table 25.7, the sensitivity for  $R_M$  measurements in different decay modes are estimated for a four year run at BEPCII (*i.e.*,  $20 \text{ fb}^{-1}$ ).

In the limit of  $CP$  conservation, the combined measurements of  $x$  from  $D^0 \rightarrow K_S\pi\pi$  and  $y_{CP}$  from Belle [358], gives  $R_M = (1.18 \pm 0.6) \times 10^{-4}$ . With  $20 \text{ fb}^{-1}$  of data at *BES-III*,

Table 25.7: The sensitivity for  $R_M$  measurements at BESIII with different decay modes for a four year run at BESPCII

$D^0\bar{D}^0$ Mixing		
Reaction	Events Right Sign	Sensitivity of $R_M$
$\psi(3770) \rightarrow (K^-\pi^+)(K^-\pi^+)$	10,3600	$1 \times 10^{-4}$
$\psi(3770) \rightarrow (K^-e^+\nu)(K^-e^+\nu)$	8,8705	
$\psi(3770) \rightarrow (K^-e^+\nu)(K^-\mu^+\nu)$	8,0617	$3.7 \times 10^{-4}$
$\psi(3770) \rightarrow (K^-\mu^+\nu)(K^-\mu^+\nu)$	7,3268	
$D^{*+}D^- \rightarrow [\pi_s^+(K^+e^-\bar{\nu})(K^+\pi^-\pi^-)]$	76000	
$D^{*+}D^- \rightarrow [\pi_s^+(K^+\mu^-\bar{\nu})(K^+\pi^-\pi^-)]$	60000	
$D^{*+}D^- \rightarrow [\pi_s^+(K^+e^-\bar{\nu})(\text{other } D^- \text{ tag})]$	60000	$4.7 \times 10^{-5}$
$D^{*+}D^- \rightarrow [\pi_s^+(K^+\mu^-\bar{\nu})(\text{other } D^- \text{ tag})]$	60000	

Table 25.8: The expected mixing signal for  $N_{sig} = N(K^\pm\pi^\mp)(K^\pm\pi^\mp)$ , background  $N_{bkg}$ , and the Poisson probability  $P(n)$  for  $10 \text{ fb}^{-1}$  and  $20 \text{ fb}^{-1}$  BES-III data samples at the  $\psi(3770)$  peak. Here, we assume a mixing rate of  $R_M = 1.18 \times 10^{-4}$ .

	$10 \text{ fb}^{-1} (\psi(3770))$ 36 million $D^0\bar{D}^0$	$20 \text{ fb}^{-1} (\psi(3770))$ 72 million $D^0\bar{D}^0$
$N_{sig}$	1.5	3.0
$N_{bkg}$	0.3	0.6
$P(n = 0)$	15.7%	2.5%
$P(n = 1)$	29.1%	9.1%
$P(n = 2)$	26.9%	16.9%
$P(n = 3)$	16.6%	20.9%
$P(n = 4)$	7.7%	19.3%
$P(n = 5)$	2.8%	14.3%
$P(n = 6)$	0.9%	8.8%
$P(n = 7)$	0.2%	4.7%
$P(n = 8)$	0.1%	2.2%
$P(n = 9)$	0.01%	0.9%

about 12 events for the precess  $D^0\bar{D}^0 \rightarrow (K^\pm\pi^\mp)(K^\pm\pi^\mp)$  will be produced. Only 3.0 events are expected to be observed, on average, because the *BES-III* detection efficiency for a four-charged-particle final state is about 25%. The background contamination due to double particle misidentification in the same sample is estimated to be about 0.6 events. Table 25.8 lists the expected mixing signal for  $N_{sig} = N(K^\pm\pi^\mp)(K^\pm\pi^\mp)$ , background  $N_{bkg}$ , and the Poisson probability  $P(n)$ , where  $n$  is the possible number of events that are observed in the experiment. In Table 25.8, we assume  $R_M = 1.18 \times 10^{-4}$ , and the expected numbers of mixing signal events are estimated for  $10\text{fb}^{-1}$  and  $20\text{fb}^{-1}$  data samples.

### 25.3.2 Lifetime differences and the strong phase $\delta_{K\pi}$

Doubly Cabibbo suppressed (DCS) decays of the  $D^0$  mesons, and  $D^0$  mixing, give rise to identical final states. The two processes can only be distinguished by their different time dependence or, at the  $\psi(3770)$  peak, by taking advantage of effects due to quantum statistics as discussed in Sect. 25.3.1. In Eq. 25.2.45 of Sect. 25.2.2, the wrong-sign decay rate relative to the right-sign rate is defined as

$$R_{WS} = R_D + \sqrt{R_D}y' + \frac{1}{2}R_M. \quad (25.3.93)$$

In absence of mixing,  $R_{WS} = R_D = |A_f/\bar{A}_f|^2$ . In general, the ratio of DCS decay rate relative to CF decay rate is  $R_D \sim \tan^4\theta_C \sim 0.25\%$ , where  $\theta_C$  is the Cabibbo angle. However, as pointed out in Ref. [308],  $\tan^4\theta_C$  is not the only suppression factor. Final state interactions can cause the ratio to be different for each final state, such as  $R_D \sim 2.1 \times \tan^4\theta_C$  for  $D^0 \rightarrow K^+\pi^-$ , while  $R_D \sim 0.45 \times \tan^4\theta_C$  for  $D^0 \rightarrow K^+\rho^-$ .

One can also measure  $R_D$  in the multibody channels  $D^0 \rightarrow K^+\pi^-\pi^0$  and  $D^0 \rightarrow K^+\pi^-\pi^+\pi^+$  as discussed in Sect. 25.2.2.

At the  $\psi(3770)$  peak, semileptonic decays can be used to tag hadronic decays on the recoil side. Using Eq. 25.3.91 and neglecting mixing effects, one has [354]

$$\frac{N[(l^+)(K^-\pi^+)]}{N[(l^+)(K^+\pi^-)]} \sim R_D. \quad (25.3.94)$$

Since it is likely that  $x^2, y^2 \ll R_D$ , this process can be used to measure  $R_D$  directly.

In the limit of  $SU(3)_{fl}$  symmetry,  $A_{K^+\pi^-} = \langle K^+\pi^- | \mathcal{H} | D^0 \rangle$  and  $\bar{A}_{K^+\pi^-} = \langle K^+\pi^- | \mathcal{H} | \bar{D}^0 \rangle$  ( $A_{K^-\pi^+} = \langle K^-\pi^+ | \mathcal{H} | D^0 \rangle$  and  $\bar{A}_{K^-\pi^+} = \langle K^-\pi^+ | \mathcal{H} | \bar{D}^0 \rangle$ ) are simply related by CKM factors,  $A_{K^+\pi^-} = (V_{cd}V_{us}^*/V_{cs}V_{ud}^*)\bar{A}_{K^+\pi^-}$  [354]. In particular,  $A_{K^+\pi^-}$  and  $\bar{A}_{K^+\pi^-}$  have the same strong phase. But  $SU(3)_{fl}$  symmetry is broken; according to the recent measurements from the  $B$  factories, the ratio [309]:

$$\mathcal{R} = \frac{\mathcal{BR}(D^0 \rightarrow K^+\pi^-)}{\mathcal{BR}(\bar{D}^0 \rightarrow K^+\pi^-)} \left| \frac{V_{ud}V_{cs}^*}{V_{us}V_{cd}^*} \right|^2, \quad (25.3.95)$$

which is unity in the  $SU(3)_{fl}$  symmetry limit, is measured to be [3]

$$\mathcal{R}_{exp} = 1.21 \pm 0.03. \quad (25.3.96)$$

Since  $SU(3)_{fl}$  is apparently broken in  $D \rightarrow K\pi$  decays at the level of 20%, the strong phase  $\delta$  should be non-zero. Recently, a time-dependent analysis of  $D \rightarrow K\pi$  has been performed based on a  $384 \text{ fb}^{-1}$  data sample at the  $\Upsilon(4S)$  [359]. With the assumption of  $CP$  conservation, the following neutral  $D$  mixing results are obtained [359]:

$$\begin{aligned} R_D &= (3.03 \pm 0.16 \pm 0.10) \times 10^{-3}; \\ x'^2 &= (-0.22 \pm 0.30 \pm 0.21) \times 10^{-3}; \\ y' &= (9.7 \pm 4.4 \pm 3.1) \times 10^{-3}. \end{aligned} \quad (25.3.97)$$

Table 25.9: Current experimental results. The quoted errors are the quadrature sum of the statistical and systematic contributions.

Parameter	BaBar ( $\times 10^{-3}$ )	Belle( $\times 10^{-3}$ )	Technique
$x'^2$	$-0.22 \pm 0.37$ [359]	$0.18^{+0.21}_{-0.23}$ [362]	$K\pi$
$y'$	$9.7 \pm 5.4$ [359]	$0.6^{+4.0}_{-3.9}$ [362]	$K\pi$
$R_D$	$3.03 \pm 0.19$ [359]	$3.64 \pm 0.17$ [362]	$K\pi$
$y_{CP}$	-	$13.1 \pm 4.1$ [360]	$K^+K^-$ , $\pi^+\pi^-$
$x$	-	$8.0 \pm 3.4$ [363]	$K_S\pi^+\pi^-$
$y$	-	$3.3 \pm 2.8$ [363]	$K_S\pi^+\pi^-$

The results are inconsistent with the non-mixing hypothesis with a significance of 3.9 standard deviations. The BaBar and Belle results for the  $y'$  measurement using  $D \rightarrow K\pi$  agree within 2 standard deviations (see Table 25.9). As indicated in Eq. 25.3.96, the strong phase  $\delta$  should be non-zero as a result of  $SU(3)_{fl}$  violation. In order to extract the direct mixing parameters,  $x$  and  $y$ , the strong phase difference has to be known. However, it is hard to do this at the  $B$  factories in a model-independent way [354, 1]. To extract the strong phase  $\delta$  we need  $CP$  tagged  $D^0$  decays near the  $D\bar{D}$  threshold, as discussed in Ref. [354]. Here, we investigate existing information on the strong phase  $\delta$  from recent  $B$  factory results for different decay modes. This can give us some idea about *BES-III*'s sensitivity for measuring the strong phase.

In Ref [360], Belle reported results for  $y_{CP} = \frac{\tau(D^0 \rightarrow K^+\pi^-)}{\tau(D^0 \rightarrow f_{CP})} - 1$ , where  $f_{CP} = K^+K^-$  and  $\pi^+\pi^-$ ,

$$y_{CP} = (13.1 \pm 3.2 \pm 2.5) \times 10^{-3}. \quad (25.3.98)$$

This result is about a  $3.2\sigma$  significant deviation from zero (non-mixing). In the limit of  $CP$  symmetry,  $y_{CP} = y$  [364, 365]. In the decay of  $D^0 \rightarrow K_S\pi^+\pi^-$ , Belle did a Dalitz plot (DP) analysis [363] and obtained the direct mixing parameters  $x$  and  $y$  as

$$x = (8.0 \pm 3.4) \times 10^{-3}, \quad y = (3.3 \pm 2.8) \times 10^{-3}, \quad (25.3.99)$$

where the errors include both statistic and systematic uncertainties. Since the parameterizations of the resonances contributing to the Dalitz plot (DP) are model-dependent, the results suffer from large systematic uncertainties. In their analysis, they see a  $2.4\sigma$  significant deviation from non-mixing. Here, we use the value of  $x$  measured in the DP

analysis for further discussion. Once  $y$ ,  $y'$  and  $x$  are known, it is straightforward to extract the strong phase difference between the DCS and CF  $D^0 \rightarrow K\pi$  decay amplitudes. Using the measured central values of  $x$ ,  $y_{CP}(\approx y)$ , and  $y'$  as input parameters, we find a two-fold ambiguous solution for  $\tan\delta$ :

$$\tan\delta = 0.35 \pm 0.63, \text{ or } -7.14 \pm 29.13, \quad (25.3.100)$$

corresponding to  $(19 \pm 32)^\circ$  and  $(-82^\circ \pm 30)^\circ$ , respectively.

In order to extract the mixing parameter  $y$  at the  $\psi(3770)$  peak, one can make use of rates for exclusive  $D^0\bar{D}^0$  combinations, where both the  $D^0$  final states are specified (known as double tags or DT), as well as inclusive rates, where either the  $D^0$  or  $\bar{D}^0$  is identified and the other  $D^0$  decays generically (known as single tags or ST). With the DT technique [367, 368], one can fully exploit the quantum correlations in the  $C = -1$   $D^0\bar{D}^0$  pairs produced from  $\psi(3770)$  decays [327, 308, 366].<sup>4</sup>

For the ST sample, in the limit of  $CP$  conservation, the rate of  $D^0$  decays into a  $CP$  eigenstate is given as [366]:

$$\Gamma_{f_\eta} \equiv \Gamma(D^0 \rightarrow f_\eta) = 2A_{f_\eta}^2 [1 - \eta y], \quad (25.3.101)$$

where  $f_\eta$  is a  $CP$  eigenstate with eigenvalue  $\eta = \pm 1$ , and  $A_{f_\eta} = |\langle f_\eta | \mathcal{H} | D^0 \rangle|$  is the real-valued decay amplitude.

For the DT case, Xing [353] and Gronau *et. al.* [354] have considered time-integrated decays into correlated pairs of states, including the effects of non-zero final state phase difference. As discussed in Ref. [354], the rate of  $(D^0\bar{D}^0)^{C=-1} \rightarrow (l^\pm X)(f_\eta)$  is given as [354]:

$$\begin{aligned} \Gamma_{l;f_\eta} \equiv \Gamma[(l^\pm X)(f_\eta)] &= A_{l^\pm X}^2 A_{f_\eta}^2 (1 + y^2) \\ &\approx A_{l^\pm X}^2 A_{f_\eta}^2, \end{aligned} \quad (25.3.102)$$

where  $A_{l^\pm X} = |\langle l^\pm X | \mathcal{H} | D^0 \rangle|$  is the real-valued amplitude for semileptonic decays; here, we have neglected the  $y^2$  term since  $y \ll 1$ .

For  $C = -1$  initial  $D^0\bar{D}^0$  states,  $y$  can be expressed in terms of ratios of DT rates and double ratios of ST rates to DT rates [366]:

$$y = \frac{1}{4} \left( \frac{\Gamma_{l;f_+} \Gamma_{f_-}}{\Gamma_{l;f_-} \Gamma_{f_+}} - \frac{\Gamma_{l;f_-} \Gamma_{f_+}}{\Gamma_{l;f_+} \Gamma_{f_-}} \right). \quad (25.3.103)$$

For a small  $y$ , its error,  $\Delta(y)$ , is approximately  $1/\sqrt{N_{l^\pm X}}$ , where  $N_{l^\pm X}$  is the total number of  $(l^\pm X)$  events tagged with  $CP$ -even and  $CP$ -odd eigenstates. The number  $N_{l^\pm X}$  of  $CP$  tagged events is related to the total number of  $D^0\bar{D}^0$  pairs  $N(D^0\bar{D}^0)$  through  $N_{l^\pm X} \approx N(D^0\bar{D}^0) [\mathcal{BR}(D^0 \rightarrow l^\pm + X) \times \mathcal{BR}(D^0 \rightarrow f_\pm) \times \epsilon_{tag}] \approx 1.5 \times 10^{-3} N(D^0\bar{D}^0)$ , here we take the branching ratio-times-efficiency factor  $(\mathcal{BR}(D^0 \rightarrow f_\pm) \times \epsilon_{tag})$  for tagging  $CP$  eigenstates to be 1.1% (the total branching ratio into  $CP$  eigenstates is larger than about 5% [3]). We find

$$\Delta(y) = \frac{\pm 26}{\sqrt{N(D^0\bar{D}^0)}} = \pm 0.003. \quad (25.3.104)$$

<sup>4</sup>The DT technique can also be used at energies above the  $\psi(3770)$  to exploit quantum correlations in  $C = -1$  and  $C = +1$   $D^0\bar{D}^0$  pairs produced, respectively, via the reactions  $e^+e^- \rightarrow D^0\bar{D}^0(n\pi^0)$  and  $e^+e^- \rightarrow D^0\bar{D}^0\gamma(n\pi^0)$ .

If we take the central value of  $y$  from the Belle measurement of  $y_{CP}$  [360], we infer that at the *BES-III* experiment [76], with a  $20\text{fb}^{-1}$  data sample taken at the  $\psi(3770)$  peak, the significance of the  $y$  measurement would be around  $4.3\sigma$ .

We can also take advantage of the coherence of the  $D^0$  mesons produced at the  $\psi(3770)$  peak to extract the strong phase difference  $\delta$  between DCS and CF decay amplitudes [354, 366]. Because the  $CP$  properties of the final states produced in the decay of the  $\psi(3770)$  are anti-correlated [327, 308], one  $D^0$  state decaying into a final state with definite  $CP$  properties immediately identifies or tags the  $CP$  properties of the other side. As discussed in Ref. [354], the process of one  $D^0$  decaying to  $K^-\pi^+$ , while the other  $D^0$  decaying to a  $CP$  eigenstate  $f_\eta$  can be described as

$$\begin{aligned}\Gamma_{K\pi;f_\eta} \equiv \Gamma[(K^-\pi^+)(f_\eta)] &\approx A^2 A_{f_\eta}^2 |1 + \eta \sqrt{R_D} e^{-i\delta}|^2 \\ &\approx A^2 A_{f_\eta}^2 (1 + 2\eta \sqrt{R_D} \cos\delta),\end{aligned}\tag{25.3.105}$$

where  $A = |\langle K^-\pi^+ | \mathcal{H} | D^0 \rangle|$  and  $A_{f_\eta} = |\langle f_\eta | \mathcal{H} | D^0 \rangle|$  are the real-valued decay amplitudes, and we have neglected the  $y^2$  terms in Eq. 25.3.105. In order to estimate the total sample of events needed to perform a useful measurement of  $\delta$ , we use the asymmetry [1, 354]

$$\mathcal{A} \equiv \frac{\Gamma_{K\pi;f_+} - \Gamma_{K\pi;f_-}}{\Gamma_{K\pi;f_+} + \Gamma_{K\pi;f_-}},\tag{25.3.106}$$

where  $\Gamma_{K\pi;f_\pm}$ , defined in Eq. 25.3.105, is the rate for the  $\psi(3770) \rightarrow D^0 \bar{D}^0$  configuration to decay into a  $K\pi$  flavor eigenstate and a  $CP$ -eigenstate  $f_\pm$ . Equation 25.3.105 implies a small asymmetry:  $\mathcal{A} = 2\sqrt{R_D} \cos\delta$ . In general, a small asymmetry, has an error  $\Delta\mathcal{A}$  that is approximately  $1/\sqrt{N_{K^-\pi^+}}$ , where  $N_{K^-\pi^+}$  is the total number of events tagged with  $CP$ -even and  $CP$ -odd eigenstates. Thus one obtains

$$\Delta(\cos\delta) \approx \frac{1}{2\sqrt{R_D} \sqrt{N_{K^-\pi^+}}}.\tag{25.3.107}$$

The expected number of  $CP$ -tagged events,  $N_{K^-\pi^+}$ , can be connected to the total number of  $D^0 \bar{D}^0$  pairs  $N(D^0 \bar{D}^0)$  through  $N_{K^-\pi^+} \approx N(D^0 \bar{D}^0) \mathcal{BR}(D^0 \rightarrow K^-\pi^+) \times \mathcal{BR}(D^0 \rightarrow f_\pm) \times \epsilon_{tag} \approx 4.2 \times 10^{-4} N(D^0 \bar{D}^0)$  [354], where, as in Ref [354], we take the branching ratio-times-efficiency factor to be  $\mathcal{BR}(D^0 \rightarrow f_\pm) \times \epsilon_{tag} = 1.1\%$ . Using the measured value of  $R_D = (3.03 \pm 0.19) \times 10^{-3}$  and  $\mathcal{BR}(D^0 \rightarrow K^-\pi^+) = 3.8\%$  [3], one finds [354]

$$\Delta(\cos\delta) \approx \frac{\pm 444}{\sqrt{N(D^0 \bar{D}^0)}}.\tag{25.3.108}$$

At *BES-III*, about  $72 \times 10^6 D^0 \bar{D}^0$  pairs will be collected in a four year run at the  $\psi(3770)$ . Considering both  $K^-\pi^+$  and  $K^+\pi^-$  final states, we estimate that an accuracy level of about 0.04 for  $\cos\delta$  can be reached. Figure 25.8 shows the expected error of the strong phase  $\delta$  for various central values of  $\cos\delta$ . With the expected error of  $\Delta(\cos\delta) = \pm 0.04$ , the sensitivity to the strong phase *angle* varies with the physical value of  $\cos\delta$ . For  $\delta = 19^\circ$  and  $-82^\circ$ , the expected errors would be  $\Delta(\delta) = \pm 8.7^\circ$  and  $\pm 2.9^\circ$ , respectively.

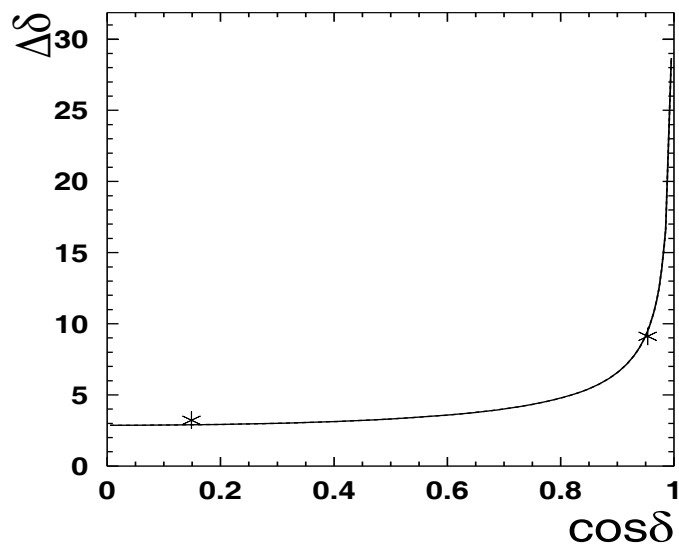


Figure 25.8: An illustrative plot of the expected error ( $\Delta\delta$ ) on the strong phase angle, in degrees, for various central values of  $\cos\delta$ . The expected *BES-III* error on  $\cos\delta$  is 0.04 for a  $20 \text{ fb}^{-1}$  data sample taken at the  $\psi(3770)$  peak. The asterisks correspond to  $\delta = 19^0$  and  $-82^0$ .

# Chapter 26

## CP and T Violation<sup>1</sup>

The violation of the  $CP$  symmetry, where  $C$  and  $P$  are the charge-conjugation and parity-transformation operators, respectively, is one of the fundamental and most exciting phenomena in particle physics. Although weak interactions are not invariant under  $P$  (and  $C$ ) transformations, as discovered in 1957, it was believed for several years that the product  $CP$  was preserved. However, in 1964, it was discovered through the observation of  $K_L \rightarrow \pi^+\pi^-$  decays that weak interactions are not invariant under  $CP$  transformations [370]. After this discovery, many observations show us that  $CP$  violation has been established in both  $K$  and  $B$  systems [371]. All these measurements are consistent with the Kobayashi-Maskawa (KM) picture of  $CP$  violation.

However, people still believe that there must be new sources of  $CP$  violation beyond the SM prediction for, at least, the following two reasons:

- *The baryon asymmetry of the Universe:*

Baryogenesis is a consequence of  $CP$  violating processes [372]. Therefore, the present baryon number, which is accurately deduced from Big Bang Nucleosynthesis (BBN) and Cosmic Microwave Background Radiation (CMBR) constraints,

$$Y_B \equiv \frac{n_B - n_{\bar{B}}}{s} \approx 9 \times 10^{-11}, \quad (26.0.1)$$

is essentially a  $CP$  violating observable. The surprising point is that the KM mechanism for  $CP$  violation fails to account for it [371].

- *Non-vanishing neutrino masses:*

It is also interesting to note that the evidence for non-vanishing neutrino masses that has emerged over the last few years points towards an origin beyond the SM [374], raising the question of having  $CP$  violation in the neutrino sector, which could be studied, in the more distant future, at a dedicated neutrino factory [375].

It would be very interesting to look for  $CP$  violation in the  $D$  system; most factors favour dedicated searches for  $CP$  violation in Charm transitions:

- New physics might be just around the corner, since baryogenesis implies the existence of New Physics (NP) in  $CP$  violation dynamics. It will be of interest to

---

<sup>1</sup>By Ikaros Bigi and Hai-Bo Li

undertake dedicated searches for  $CP$  asymmetries in Charm decays, where the SM predicts very small effects, *i.e.* smaller than  $\mathcal{O}(10^{-3})$ , and they can arise only in *singly Cabibbo-suppressed* (SCS) transitions. Significantly larger values would signal NP. Any asymmetry in CF and DCS decays requires the intervention of NP (except for  $D^\pm \rightarrow K_S \pi^\pm$  [1], where the  $CP$  impurity in  $K_S$  induces an asymmetry of  $3.3 \times 10^{-3}$ ).

- Secondly, the neutral  $D$  system is the only one where the external up-sector quarks are involved. Thus it probes models in which the up-sector plays a special role, such as supersymmetric models with alignment [373, 376] and, more generally, models in which CKM mixing is generated in the up sector.
- Third, SCS decays are sensitive to new-physics contributions to penguin and dipole operators. As far as this point is concerned, among all hadronic  $D$  decays, the SCS decays ( $c \rightarrow u\bar{q}\bar{q}$ ) are uniquely sensitive to new contributions to  $\Delta C = 1$  QCD penguin and chromomagnetic dipole operators [377, 378]. In particular, such contributions would affect neither CF ( $c \rightarrow s\bar{d}u$ ) nor the DCS ( $c \rightarrow d\bar{s}u$ ) decays.
- There is a rich assortment of light resonances in the  $D$  mass region and, thus, final state interactions involving these resonances are expected to be important sources of strong phase shifts that are necessary for producing direct  $CP$  violation.
- Decays to final states of more than two pseudoscalar or one pseudoscalar and one vector mesons contain more dynamical information than that given by their partial widths. Dalitz plot analyses can exhibit  $CP$  asymmetries that might be considerably larger than those from decay rates only [379].

$CP$  asymmetries in integrated partial widths depend on hadronic matrix elements and (strong) phase shifts, neither of which can be predicted accurately. However the craft of theoretical engineering can be practised with profit here. One makes an ansatz for the general form of the matrix elements and phase shifts that are included in the description of  $D \rightarrow PP, PV, VV$  etc. channels, where  $P$  and  $V$  denote pseudoscalar and vector mesons, and fits them to the measured branching ratios on the Cabibbo-allowed, once- and twice-Cabibbo-forbidden levels. If one has sufficiently accurate and comprehensive data, one can use these fitted values of the hadronic parameters to predict  $CP$  asymmetries. Such analyses have been undertaken in the past [380], but the data base was not as broad and precise as one would like [379]. CLEO-c and *BES-III* measurements will certainly lift such studies to a new level of reliability.

## 26.1 Formalism and Review

In order to discuss the  $CP$  violation in neutral  $D$  system, we use the following notations as described in the previous sections:

$$\begin{aligned}\tau &\equiv \Gamma_D t, \quad \Gamma_D \equiv \frac{\Gamma_{D_H} + \Gamma_{D_L}}{2}, \\ A_f &\equiv A(D^0 \rightarrow f), \quad \overline{A}_f \equiv A(\overline{D}^0 \rightarrow f),\end{aligned}$$

$$\begin{aligned}
A_{\bar{f}} &\equiv A(D^0 \rightarrow \bar{f}), \quad \bar{A}_{\bar{f}} \equiv A(\bar{D}^0 \rightarrow \bar{f}), \\
x &\equiv \frac{\Delta m_D}{\Gamma_D} \equiv \frac{m_{D_H} - m_{D_L}}{\Gamma_D}, \quad y \equiv \frac{\Delta \Gamma_D}{2\Gamma_D} \equiv \frac{\Gamma_{D_H} - \Gamma_{D_L}}{2\Gamma_D}, \\
\lambda_f &\equiv \frac{q \bar{A}_f}{p A_f}, \quad A_M \equiv \left| \frac{q}{p} \right| - 1, \quad R_f \equiv \left| \frac{\bar{A}_f}{A_f} \right|,
\end{aligned} \tag{26.1.2}$$

where  $D_H$  and  $D_L$  stand for the heavy and light mass eigenstates, and  $q$  and  $p$  are defined in Eq. 25.1.4. We distinguish three types of  $CP$ -violation effects in neutral  $D$  meson decays:

- $CP$  violation in decay is defined by

$$\left| \frac{\bar{A}_{\bar{f}}}{A_f} \right| \neq 1. \tag{26.1.3}$$

In the charged  $D$  decays without mixing effects, it is the only possible source of  $CP$  asymmetries:

- $CP$  violation in mixing is defined as

$$\left| \frac{q}{p} \right| \neq 1. \tag{26.1.4}$$

In charged-current semileptonic decays of neutral  $D$ ,  $|A_{l+X}| = |\bar{A}_{l-X}|$  and  $A_{l-X} = \bar{A}_{l+X} = 0$  in the SM and most of the reasonable extensions of SM, where  $|p|/|q| \neq 1$  would be the only source of  $CP$  violation. This can be measured in the asymmetry of “wrong-sign” decays induced by oscillations.

- $CP$ -violation in the interference between a decay without mixing,  $D^0 \rightarrow f$ , and a decay with mixing,  $D^0 \rightarrow \bar{D}^0 \rightarrow f$ , and is defined by

$$\text{Im} \left( \frac{q \bar{A}_f}{p A_f} \right) \neq 0. \tag{26.1.5}$$

This form of  $CP$  violation can be observed in the asymmetry of  $D^0$  and  $\bar{D}^0$  decays into common final states, such as  $CP$  eigenstates  $f_{CP}$ .

Example of these three different types of  $CP$  violation are given in the following sections.

There are several ways to study  $CP$  violation in charm decays [402]: we can look for direct  $CP$  violation, even in charged decays; we can look for  $CP$  violation via mixing;  $T$  violation can be examined in 4-body  $D$  meson decays, assuming  $CPT$  conservation, by measuring triple-product correlations [403]; the quantum coherence present in correlated  $D^0 \bar{D}^0$  decays of the  $\psi(3770)$  can be exploited [404].

Most existing  $CP$  limits are for direct  $CP$  violation. A few results from CLEO, BaBar and Belle experiments consider  $CP$  violation in mixing. Tables 26.1 and 26.2 are summaries of measurements of  $CP$  violations in neutral  $D$  and charged  $D$  decays, respectively. No evidence for  $CP$  violation is observed and all results are consistent with the SM expectations.

Large samples of  $D$  mesons will be available at the *BES-III* experiment. One year's running at *BES-III* will provide an intrinsic statistical precision of  $< 1.0\%$ . For this purpose, one has to pay great attention to systematic biases. Initial-state asymmetries and detector asymmetries will be the main concerns.

Finally, in Table 26.3, we list results of  $CP$  violation measurements done by looking at  $D^0$  lifetime asymmetries for different decay modes.

Year	Experiment	Decay Mode	$A_{CP}(\%)$
2007	BABAR [381]	$D^0 \rightarrow K^+ K^-$	$+0.00 \pm 0.34 \pm 0.13$
2005	CDF [382]	$D^0 \rightarrow K^+ K^-$	$+2.0 \pm 1.2 \pm 0.6$
2002	CLEO [383]	$D^0 \rightarrow K^+ K^-$	$+0.0 \pm 2.2 \pm 0.8$
2000	FOCUS [384]	$D^0 \rightarrow K^+ K^-$	$-0.1 \pm 2.2 \pm 1.5$
1998	E791 [385]	$D^0 \rightarrow K^+ K^-$	$-1.0 \pm 4.9 \pm 1.2$
1995	CLEO [386]	$D^0 \rightarrow K^+ K^-$	$+8.0 \pm 6.1$
1994	E687 [387]	$D^0 \rightarrow K^+ K^-$	$+2.4 \pm 8.4$
	Average	$D^0 \rightarrow K^+ K^-$	$+0.15 \pm 0.34$
2007	BABAR [381]	$D^0 \rightarrow \pi^+ \pi^-$	$-0.24 \pm 0.52 \pm 0.22$
2005	CDF [382]	$D^0 \rightarrow \pi^+ \pi^-$	$1.0 \pm 1.3 \pm 0.6$
2002	CLEO [388]	$D^0 \rightarrow \pi^+ \pi^-$	$+1.9 \pm 3.2 \pm 0.8$
2000	FOCUS [384]	$D^0 \rightarrow \pi^+ \pi^-$	$+4.8 \pm 3.9 \pm 2.5$
1998	E791 [385]	$D^0 \rightarrow \pi^+ \pi^-$	$-4.9 \pm 7.8 \pm 3.0$
	Average	$D^0 \rightarrow \pi^+ \pi^-$	$+0.02 \pm 0.51$
2001	CLEO [389]	$D^0 \rightarrow K_S K_S$	$-23 \pm 19$
2005	CLEO [390]	$D^0 \rightarrow \pi^+ \pi^- \pi^0$	$1^{+9}_{-7} \pm 8$
2001	CLEO [389]	$D^0 \rightarrow K_S \pi^0$	$+0.1 \pm 1.3$
2007	CLEO-c [391]	$D^0 \rightarrow K^- \pi^+ \pi^0$	$+0.2 \pm 0.4 \pm 0.8$
2001	CLEO [392]	$D^0 \rightarrow K^- \pi^+ \pi^0$	$-3.1 \pm 8.6$
	Average	$D^0 \rightarrow K^- \pi^+ \pi^0$	$+0.16 \pm 0.89$
2005	Belle [393]	$D^0 \rightarrow K^+ \pi^- \pi^0$	$-0.6 \pm 5.3$
2001	CLEO [394]	$D^0 \rightarrow K^+ \pi^- \pi^0$	$+9.0^{+25}_{-22}$
	Average	$D^0 \rightarrow K^+ \pi^- \pi^0$	$-0.14 \pm 5.17$
2004	CLEO [395]	$D^0 \rightarrow K_S \pi^+ \pi^-$	$-0.9 \pm 2.1^{+1.0+1.3}_{-4.3-3.7}$
2005	Belle [393]	$D^0 \rightarrow K^+ \pi^- \pi^+ \pi^-$	$-1.8 \pm 4.4$
2005	FOCUS [396]	$D^0 \rightarrow K^+ K^- \pi^+ \pi^-$	$-8.2 \pm 5.6 \pm 4.7$

Table 26.1: Measurements of  $CP$  violating asymmetries in neutral  $D$  decays in different modes. The averaged results are from HFAG.

## 26.2 $CP$ Violation in $D^0 - \bar{D}^0$ Mixing

A mixing  $CP$  asymmetry can be best isolated in semileptonic decays of neutral  $D$  mesons, as discussed in Ref. [405]. In the case of the  $D^0$  meson, this can be measured as

Year	Experiment	Decay Mode	$A_{CP}(\%)$
2007	CLEO-c [391]	$D^+ \rightarrow K_S \pi^+$	$-0.6 \pm 1.0 \pm 0.3$
2002	FOCUS [397]	$D^+ \rightarrow K_S \pi^+$	$-1.6 \pm 1.5 \pm 0.9$
	Average	$D^+ \rightarrow K_S \pi^+$	$-0.86 \pm 0.90$
2002	FOCUS [397]	$D^+ \rightarrow K_S K^+$	$+7.1 \pm 6.1 \pm 1.2$
1997	E791 [398]	$D^+ \rightarrow \pi^+ \pi^- \pi^+$	$-1.7 \pm 4.2$
2007	CLEO-c [391]	$D^+ \rightarrow K^- \pi^+ \pi^+$	$-0.5 \pm 0.4 \pm 0.9$
2007	CLEO-c [391]	$D^+ \rightarrow K_S \pi^+ \pi^0$	$+0.3 \pm 0.9 \pm 0.3$
2007	CLEO-c [391]	$D^+ \rightarrow K^+ K^- \pi^+$	$-0.1 \pm 1.5 \pm 0.8$
2005	BaBar [399]	$D^+ \rightarrow K^+ K^- \pi^+$	$1.4 \pm 1.0 \pm 0.8$
2000	FOCUS [384]	$D^+ \rightarrow K^+ K^- \pi^+$	$+0.6 \pm 1.1 \pm 0.5$
1997	E791 [398]	$D^+ \rightarrow K^+ K^- \pi^+$	$-1.4 \pm 2.9$
1994	E687 [387]	$D^0 \rightarrow K^+ K^- \pi^+$	$-3.1 \pm 6.8$
	Average	$D^0 \rightarrow K^+ K^- \pi^+$	$+0.59 \pm 0.75$
2007	CLEO-c [391]	$D^+ \rightarrow K^- \pi^+ \pi^- \pi^0$	$+1.0 \pm 0.9 \pm 0.9$
2007	CLEO-c [391]	$D^+ \rightarrow K_S \pi^+ \pi^+ \pi^-$	$+0.1 \pm 1.1 \pm 0.6$
2005	FOCUS [396]	$D^0 \rightarrow K_S K^+ \pi^+ \pi^-$	$-4.2 \pm 6.4 \pm 2.2$
2005	BaBar [399]	$D^+ \rightarrow \phi \pi^+$	$0.2 \pm 1.5 \pm 0.6$
2005	BaBar [399]	$D^+ \rightarrow \bar{K}^{*0} K^+$	$0.9 \pm 1.7 \pm 0.7$

Table 26.2: Measurements of  $CP$  violating asymmetries in charged  $D$  decays in different modes. The averaged results are from HFAG.

Year	Experiment	Decay Mode	$(\tau_{\bar{D}^0} - \tau_{D^0})/(\tau_{\bar{D}^0} + \tau_{D^0})(\%)$
2007	Belle [400]	$D^0 \rightarrow K^+ K^-$ and $\pi^+ \pi^-$	$+0.010 \pm 0.300 \pm 0.150$
2007	Babar [401]	$D^0 \rightarrow K^+ K^-$ and $\pi^+ \pi^-$	$+0.260 \pm 0.360 \pm 0.080$
	Average	$D^0 \rightarrow K^+ K^-$ and $\pi^+ \pi^-$	$+0.123 \pm 0.248$

Table 26.3:  $CP$  lifetime asymmetries in  $D^0$  decay modes.

an asymmetry of “wrong-sign” decays ( $A_{SL}$ ):

$$\begin{aligned} A_{SL} &\equiv \frac{\Gamma(\overline{D}^0(t)_{\text{phys}} \rightarrow l^+ X) - \Gamma(D^0(t)_{\text{phys}} \rightarrow l^- X)}{\Gamma(\overline{D}^0(t)_{\text{phys}} \rightarrow l^+ X) + \Gamma(D^0(t)_{\text{phys}} \rightarrow l^- X)} \\ &= \frac{1 - |q/p|^4}{1 + |q/p|^4}. \end{aligned} \quad (26.2.6)$$

Here  $\overline{D}^0(0)_{\text{phys}} = \overline{D}^0$  and  $D^0(0)_{\text{phys}} = D^0$ . Note that all the final states in Eq. 26.2.6 contain “wrong-sign” leptons and can only be reached via  $D^0 - \overline{D}^0$  oscillations. This asymmetry represents the difference between the rates for  $\overline{D}^0 \rightarrow D^0 \rightarrow l^+ X$  and  $D^0 \rightarrow \overline{D}^0 \rightarrow l^- X$ . If the phases in the  $\overline{D}^0 \rightarrow D^0$  and  $D^0 \rightarrow \overline{D}^0$  transition amplitudes differ from each other, a non-vanishing  $CP$  violation follows. This asymmetry is expected to be tiny, both in the SM and many of its extensions. The corresponding observable has been studied in semileptonic decays of neutral  $K$  and  $B$  mesons. Since  $A_{SL}$  is controlled by  $(\Delta\Gamma/\Delta M)\sin\phi_{\text{weak}}$ , it is predicted to be small in both cases, albeit for different reasons: (i) while  $(\Delta\Gamma_K/\Delta M_K) \sim 1$ , one has  $\sin\phi_{\text{weak}}^K \ll 1$  leading to  $A_{SL}^K = \delta_l \simeq (3.32 \pm 0.06) \cdot 10^{-3}$  as observed; (ii) for  $B^0$  mesons, one has  $(\Delta\Gamma_B/\Delta M_B) \ll 1$  leading to  $A_{SL}^B < 10^{-3}$ .

For  $D^0$ , on the other hand, both  $\Delta M_D$  and  $\Delta\Gamma_D$  are small, but  $\Delta\Gamma_D/\Delta M_D$  is not: present data indicate it is about unity or even larger.  $A_{SL}$  is given by the smaller of  $\Delta\Gamma_D/\Delta M_D$  or its inverse multiplied by  $\sin\phi_{\text{weak}}^D$ , which might not be that small: *i.e.*, while the rate for ‘wrong-sign’ leptons is certainly small in semileptonic decays of neutral  $D$  mesons, their  $CP$  asymmetry might not be if New Physics intervenes to induce a non-zero value for  $\phi_{\text{weak}}^D$ .

At the  $\psi(3770)$  peak, this kind of  $CP$ -violating signal can manifest itself in like-sign dilepton events of  $(D^0\overline{D}^0)$  pairs:

$$A_{SL} \equiv \frac{R(l_1^+ X, l_2^+ X) - R(l_1^- X, l_2^- X)}{R(l_1^+ X, l_2^+ X) + R(l_1^- X, l_2^- X)} = \frac{1 - |q/p|^4}{1 + |q/p|^4}, \quad (26.2.7)$$

where  $R(l_1^+ X, l_2^+ X)$  and  $R(l_1^- X, l_2^- X)$  are the production rates for the like-sign dileptons at the  $\psi(3770)$ , as defined in Ref. [406]. Note that this asymmetry is not only independent of the time distributions, but also independent of the charge-conjugation parity  $C$  of the  $(D^0\overline{D}^0)$  pair. Thus, it can be measured using time-integrated dilepton events at either the  $\psi(3770)$  or  $\psi(4170)$  resonances.

## 26.3 $CP$ Violation in Decay

Decay  $CP$  violation (also called “direct  $CP$  violation”) occurs when the absolute value of the decay amplitude  $A_f$  for  $D$  decaying to a final state  $f$  is different from the one for the corresponding  $CP$ -conjugated amplitude, *i.e.*  $|A_f| \neq |\overline{A}_{\overline{f}}|$ . This kind of  $CP$  violation would be induced by  $\Delta C = 1$  effective operators, and could produce asymmetries in both charged and neutral  $D$  decays. For charged  $D$  meson decays, where mixing effects are absent, this is the only possible observable  $CP$  asymmetry;

$$A_{f^\pm}^{CP} \equiv \frac{\Gamma(D^- \rightarrow f^-) - \Gamma(D^+ \rightarrow f^+)}{\Gamma(D^- \rightarrow f^-) + \Gamma(D^+ \rightarrow f^+)} = \frac{|\overline{A}_{f^-}/A_{f^+}|^2 - 1}{|\overline{A}_{f^-}/A_{f^+}|^2 + 1}, \quad (26.3.8)$$

where  $\Gamma_{f^\pm}$  represents the  $D^\pm \rightarrow f^\pm$  decay rate. A two-component decay amplitude with weak and strong phase differences is required for this type of  $CP$  violation. If, for example, there are two such contributions,  $A_f = a_1 + a_2$ , we have

$$\begin{aligned} A_f &= |a_1|e^{+i\phi_T}[1 + r_f e^{i(\Delta_f + \theta_f)}], \\ \overline{A_f} &= |a_1|e^{-i\phi_T}[1 + r_f e^{i(\Delta_f - \theta_f)}], \end{aligned} \quad (26.3.9)$$

where  $\Delta_f$  corresponds to the strong phase difference and  $\theta_f$  corresponds to the weak phase difference between the  $CP$ -conserving ( $a_1$  from tree level contribution in the SM) and  $CP$ -violating parts of the decay amplitude and  $r_f$  represents the small ratio,  $r_f = |a_2|/|a_1|$ ;  $\phi_T$  is the weak phase from the SM tree-level contribution.

It is straightforward to evaluate the  $CP$  asymmetry for charged  $D$  decays:

$$A_{f^\pm}^{CP} = -\frac{2|r_f|\sin(\Delta_f)\sin(\theta_f)}{1 + |r_f|^2 + 2|r_f|\cos(\Delta_f)\cos(\theta_f)}. \quad (26.3.10)$$

No reliable model-independent predictions exist for  $\Delta_f$ ; it is believed that it could be quite large due to the abundance of light-quark resonances in the vicinity of the  $D$ -meson mass that can induce large final-state interaction (FSI) phases. The quantity of most interest to theory is the weak phase difference  $\theta_f$ . Its extraction from the asymmetry requires, however, that the amplitude ratio  $r_f$  and the strong phase difference  $\Delta_f$  are known. Both quantities are difficult to calculate due to non-perturbative hadronic parameters. In the SM, relative weak phases can obtain in SCS decays via, for instance, interference between spectator and penguin amplitudes. Since the most optimistic model-dependent estimates put the SM predictions for the asymmetry  $A^{CP} < 0.1\%$  [407], an observation of any  $CP$ -violating signal in the current round of experiments would be a sign of new physics.

Specific model calculations [408] for  $D \rightarrow K\bar{K}$ ,  $\pi\pi$ ,  $K^*\bar{K}$ , three-body modes, etc. yield this order-of-magnitude effect. New physics could enter, for example, via large phases in the penguin diagram. These could produce asymmetries of the order of 1% or larger. On the other hand, CF decays do not have two amplitudes with different weak phases and, therefore, their  $CP$  asymmetries are zero in the SM. Some new physics scenarios may provide extra phases that could give asymmetries as large as 1%.

## 26.4 $CP$ Violation in the interference between decays with and without mixing

This type of  $CP$  violation is possible for common final states to which both  $D^0$  and  $\overline{D}^0$  can decay. It is usually associated with the relative phase between mixing and decay contributions as described in Eq. 26.1.5. It can be studied with both time-dependent and time-integrated asymmetries.

### (1) $CP$ eigenstate

In general, for a  $CP$  even (odd) eigenstate, the decay amplitudes can be written as

$$\begin{aligned} A_f &= |a_1|e^{+i\phi_T}[1 + r_f e^{i(\Delta_f + \theta_f)}], \\ \overline{A_f} &= \eta_f^{CP} \times \overline{A_f} = \eta_f^{CP} |a_1|e^{-i\phi_T}[1 + r_f e^{i(\Delta_f - \theta_f)}], \end{aligned} \quad (26.4.11)$$

where  $\eta_f^{CP} = +(-)$  for a  $CP$  even (odd) state and we have used  $CP|D^0\rangle = -|\overline{D}^0\rangle$ . Neglecting  $r_f$  in Eq. 26.4.11,  $\lambda_f$  can be written as

$$\begin{aligned}\lambda_f &\equiv -\eta_f^{CP} R_m e^{i\phi}, \\ \overline{\lambda}_f &\equiv -\eta_f^{CP} R_m^{-1} e^{-i\phi},\end{aligned}\quad (26.4.12)$$

where  $\phi$  is the relative weak phase between the mixing amplitude and the decay amplitude, and  $R_m = |q/p|$ . The time-integrated  $CP$  asymmetry for a final  $CP$  eigenstate  $f$  is defined as:

$$A_f^{CP} \equiv \frac{\Gamma(D^0 \rightarrow f) - \Gamma(\overline{D}^0 \rightarrow f)}{\Gamma(D^0 \rightarrow f) + \Gamma(\overline{D}^0 \rightarrow f)}. \quad (26.4.13)$$

Given experimental constraints, one can take  $x, y, r_f \ll 1$  and expand to the leading order in these parameters, and get [377]:

$$A_f^{CP} = 2r_f \sin \Delta_f \sin \theta_f - \eta_f^{CP} \frac{y}{2} (R_m - R_m^{-1}) \cos \phi + \eta_f^{CP} \frac{x}{2} (R_m + R_m^{-1}) \sin \phi, \quad (26.4.14)$$

where the first term represents  $CP$  violation in the decay, the second term is related to  $CP$  violation in mixing, and the third term is for  $CP$  violation in the interference between mixing and decay amplitudes. If  $CP$  violation in mixing and decay is neglected, one has:

$$A_f^{CP} \approx \eta_f^{CP} x \sin \phi. \quad (26.4.15)$$

The above discussion is only for incoherent  $D^0\overline{D}^0$  decays. In the case of  $D^0\overline{D}^0$  produced coherently at *BES-III*, the  $D^0\overline{D}^0$  pair system is in a state with charge parity  $C = \eta$ , which can be defined as [378, 406]

$$|D^0\overline{D}^0\rangle^{C=\eta} = \frac{1}{\sqrt{2}} \left[ |D^0\rangle|\overline{D}^0\rangle + \eta |\overline{D}^0\rangle|D^0\rangle \right], \quad (26.4.16)$$

where  $\eta$  is the charge conjugation parity or orbital angular momentum of the  $D^0\overline{D}^0$  pair. Thus, it is easy to see that  $D^0\overline{D}^0$  occur in a  $P$ -wave ( $L = 1$ ) in the reactions

$$\begin{aligned}e^+e^- &\rightarrow \gamma^* \rightarrow D^0\overline{D}^0, \\ e^+e^- &\rightarrow \gamma^* \rightarrow D^0\overline{D}^{*0}, D^{*0}\overline{D}^0 \rightarrow D^0\overline{D}^0\pi^0, \\ e^+e^- &\rightarrow \gamma^* \rightarrow D^{*0}\overline{D}^{*0} \rightarrow D^0\overline{D}^0\pi^0\pi^0,\end{aligned}\quad (26.4.17)$$

and in an  $S$ -wave ( $L = 0$ ) in the reactions

$$\begin{aligned}e^+e^- &\rightarrow \gamma^* \rightarrow D^0\overline{D}^{*0}, D^{*0}\overline{D}^0 \rightarrow D^0\overline{D}^0\gamma, \\ e^+e^- &\rightarrow \gamma^* \rightarrow D^{*0}\overline{D}^{*0} \rightarrow D^0\overline{D}^0\gamma\pi^0.\end{aligned}\quad (26.4.18)$$

One can use the semileptonic decay of one  $D$  meson to tag the other  $D$  decaying to a  $CP$  eigenstate  $f$ . We define the leptonic-tagged  $CP$  asymmetry  $A_{fl\pm}^{CP}$  as

$$A_{fl\pm}^{CP} = \frac{R(l^-X, f) - R(l^+X, f)}{R(l^-X, f) + R(l^+X, f)} = \frac{N(l^-X, f) - N(l^+X, f)}{N(l^-X, f) + N(l^+X, f)}, \quad (26.4.19)$$

where  $R(l^- X, f)$  and  $R(l^+ X, f)$  are the time integrated decay rates of  $|D^0 \bar{D}^0\rangle^{C=\eta}$  into  $(l^- X, f)$  and  $(l^+ X, f)$  final states, respectively, and are defined as [378]:

$$R(l^- X, f) = \int_0^\infty dt_1 dt_2 |\langle (l^- X, f) | \mathcal{H} | D^0 \bar{D}^0 \rangle^{C=\eta}|^2, \quad (26.4.20)$$

$$R(l^+ X, f) = \int_0^\infty dt_1 dt_2 |\langle (l^+ X, f) | \mathcal{H} | D^0 \bar{D}^0 \rangle^{C=\eta}|^2, \quad (26.4.21)$$

and are proportional to the numbers of lepton-tagged  $D^0(\bar{D}^0) \rightarrow f$  events,  $N(l^- X, f)$  and  $N(l^+ X, f)$ . After a complicated calculation, Du finds [378]:

$$A_{fl^\pm}^{CP} = (1 + \eta) \eta_f^{CP} \left[ -\frac{y}{2} (R_m - R_m^{-1}) \cos\phi + \frac{x}{2} (R_m + R_m^{-1}) \sin\phi \right]. \quad (26.4.22)$$

Comparing Eqs. 26.4.22 and 26.4.14, and neglecting  $CP$  violation in the decay (namely, the first term in Eq. 26.4.14 is zero), Du finds that  $A_{fl^\pm}^{CP}$  is just twice as large as  $A_f^{CP}$  when charge conjugation parity (or the orbital angular momentum  $L$ ) is even. In Table 26.4, we present an estimate of the number of all lepton-tagged events of the type  $K(\pi)e\nu$  and  $K(\pi)\mu\nu$  — where the neutrino is the only missing particle — with  $CP$ -eigenstates that can be collected in a year of running at  $\sqrt{s} = 4.17$  GeV with luminosity of  $\mathcal{L} = 10^{33} \text{ cm}^{-2} \text{ sec}^{-1}$ . The chain of the reactions considered is  $e^+ e^- \rightarrow \gamma^* \rightarrow D^0 \bar{D}^{*0}$ ,  $D^{*0} \bar{D}^0 \rightarrow D^0 \bar{D}^0 \gamma$  and  $(D^0 \bar{D}^0) \rightarrow (l^\pm X, f)$ . An estimated production cross-section of  $\sigma(e^+ e^- \rightarrow D^0 \bar{D}^{*0}) = 2.6 \text{ nb}$  is used and the branching ratio for the decay  $D^{*0} \rightarrow D^0 \gamma$  is taken to be 38%. The  $CP$ -eigenstate branching ratios are taken from PDG2006 [3]. The efficiencies are estimated based on solid angle and PID criteria. All the numbers are normalized via the branching ratios and efficiencies for the above decay chain. As the results in Table 26.4 indicate, there will be a total of about 10K events and the observed  $CP$  asymmetry,  $A_{fl^\pm}^{CP}$ , could be measured with an accuracy of 1.2%.

Eigenstate	$\eta_f^{CP}$	Branching Ratio(%)	Efficiency	$D^0 \bar{D}^0 \gamma$ Events
$K^+ K^-$	+1	$(0.38 \pm 0.01)$	0.50	1040
$\pi^+ \pi^-$	+1	$(0.14 \pm 0.003)$	0.80	460
$K_S K_S$	+1	$(0.037 \pm 0.001)$	0.26	30
$\rho^0 \pi^0$	+1	$(0.32 \pm 0.04)$	0.70	3140
$\pi^0 \pi^0$	+1	$(0.079 \pm 0.008)$	0.50	500
$K_S \pi^0$	-1	$(1.14 \pm 0.12)$	0.26	770
$K_S \eta$	-1	$(0.38 \pm 0.06)$	0.12	290
$K_S \rho^0$	-1	$(0.75 \pm 0.07)$	0.42	460
$K_S \phi$	-1	$(0.42 \pm 0.032)$	0.05	60
$K_S \omega$	-1	$(1.10 \pm 0.20)$	0.06	320

Table 26.4: Estimates of the numbers of fully reconstructed lepton-tagged  $CP$ -eigenstate decays in a one year at *BES-III*.

## (2) Non-*CP* eigenstate

Another promising channel for probing *CP* symmetry is  $D^0(t) \rightarrow K^+ \pi^-$ . Since this mode is doubly Cabibbo suppressed, it should *a priori* exhibit a higher sensitivity to a New Physics amplitude. Furthermore it cannot exhibit a direct *CP* violation in the SM.

$$\frac{\Gamma(D^0(t) \rightarrow K^+ \pi^-)}{\Gamma(D^0(t) \rightarrow K^- \pi^+)} = \left| \frac{T(D^0 \rightarrow K^+ \pi^-)}{T(D^0 \rightarrow K^- \pi^+)} \right|^2 \times \quad (26.4.23)$$

$$\left[ 1 + \left( \frac{t}{\tau_D} \right)^2 \left( \frac{x^2 + y^2}{4 \operatorname{tg}^2 \theta_C} \right) \left| \frac{q}{p} \right|^2 |\hat{\rho}_{K\pi}|^2 + \left( \frac{t}{\tau_D} \right) \left| \frac{q}{p} \right| |\hat{\rho}_{K\pi}| \left( \frac{y' \cos \phi_{K\pi} + x' \sin \phi_{K\pi}}{\operatorname{tg}^2 \theta_C} \right), \right]$$

$$\frac{\Gamma(\bar{D}^0(t) \rightarrow K^- \pi^+)}{\Gamma(\bar{D}^0(t) \rightarrow K^+ \pi^-)} = \left| \frac{T(\bar{D}^0 \rightarrow K^- \pi^+)}{T(\bar{D}^0 \rightarrow K^+ \pi^-)} \right|^2 \times \quad (26.4.24)$$

$$\left[ 1 + \left( \frac{t}{\tau_D} \right)^2 \left( \frac{x^2 + y^2}{4 \operatorname{tg}^2 \theta_C} \right) \left| \frac{p}{q} \right|^2 |\hat{\rho}_{K\pi}|^2 + \left( \frac{t}{\tau_D} \right) \left| \frac{p}{q} \right| |\hat{\rho}_{K\pi}| \left( \frac{y' \cos \phi_{K\pi} - x' \sin \phi_{K\pi}}{\operatorname{tg}^2 \theta_C} \right), \right]$$

with

$$\begin{aligned} \frac{q}{p} \frac{T(D^0 \rightarrow K^+ \pi^-)}{T(D^0 \rightarrow K^- \pi^+)} &\equiv -\frac{1}{\operatorname{tg}^2 \theta_C} (1 + A_M) |\hat{\rho}_{K\pi}| e^{-i(\delta - \phi_{K\pi})}, \\ \frac{q}{p} \frac{T(\bar{D}^0 \rightarrow K^- \pi^+)}{T(\bar{D}^0 \rightarrow K^+ \pi^-)} &\equiv -\frac{1}{\operatorname{tg}^2 \theta_C} \frac{1}{1 + A_M} |\hat{\rho}_{K\pi}| e^{-i(\delta + \phi_{K\pi})}, \end{aligned} \quad (26.4.25)$$

yielding an asymmetry

$$\frac{\Gamma(D^0(t) \rightarrow K^+ \pi^-) - \Gamma(\bar{D}^0(t) \rightarrow K^- \pi^+)}{\Gamma(D^0(t) \rightarrow K^+ \pi^-) + \Gamma(\bar{D}^0(t) \rightarrow K^- \pi^+)} \simeq$$

$$\left( \frac{t}{\tau_D} \right) |\hat{\rho}_{K\pi}| \left( \frac{y' \cos \phi_{K\pi} A_M + x' \sin \phi_{K\pi}}{\operatorname{tg}^2 \theta_C} \right) - \left( \frac{t}{\tau_D} \right)^2 |\hat{\rho}_{K\pi}|^2 \frac{A_M (x^2 + y^2)}{2 \operatorname{tg}^4 \theta_C}. \quad (26.4.26)$$

Here we have again assumed for simplicity  $|A_M| \ll 1$  ( $|q|/|p| = 1 + A_M$ ),  $\rho_{K\pi} = \frac{A(D^0 \rightarrow K^+ \pi^-)}{A(D^0(t) \rightarrow K^- \pi^+)}$  and *no direct CP violation*.

BaBar has searched for a time dependent *CP* asymmetry in  $D^0 \rightarrow K^+ \pi^-$  vs.  $\bar{D}^0(t) \rightarrow K^- \pi^+$ , but has not found any evidence for it at about the 1% level [409]. However, with  $x'$  and  $y'$  capped at about 1%, no nontrivial bound can be placed on the weak phase  $\phi_{K\pi}$  that could be induced by New Physics. On the other hand, a further increase in experimental sensitivity might reveal a signal.

## 26.5 Rate of the *CP* Violation in the Coherent $D^0 \bar{D}^0$ Pair

Let us consider the reaction:

$$e^+ e^- \rightarrow \psi(3770) \rightarrow D^0 \bar{D}^0 \rightarrow f_a f_b, \quad (26.5.27)$$

where  $f_a$  and  $f_b$  represent  $CP$  eigenstates with the same  $CP$  parity, i.e.

$$\begin{aligned} CP|f_a\rangle &= \eta_a|f_a\rangle, \\ CP|f_b\rangle &= \eta_b|f_b\rangle, \\ \eta_a\eta_b &= +1. \end{aligned} \quad (26.5.28)$$

The process in Eq. 26.5.27 can proceed only in the presence of  $CP$  violation, because:

$$CP|\psi(3770)\rangle = +|\psi(3770)\rangle, \quad (26.5.29)$$

whereas

$$CP|f_a f_b\rangle = \eta_a \eta_b (-1)^{l=1} |f_a f_b\rangle = -|f_a f_b\rangle. \quad (26.5.30)$$

Thus  $CP(\text{initial}) \neq CP(\text{final})$ , and  $CP$  invariance is broken. More explicitly, for  $x \ll 1$  one has:

$$\begin{aligned} \text{BR}(\psi(3770) \rightarrow D^0 \bar{D}^0 \rightarrow f_a f_b) &\simeq \text{BR}(D \rightarrow f_a) \text{BR}(D \rightarrow f_b) \cdot \\ &\left[ (2+x^2) \left| \frac{q}{p} \right|^2 |\bar{\rho}(f_a) - \bar{\rho}(f_b)|^2 + x^2 \left| 1 - \frac{q}{p} \bar{\rho}(f_a) \frac{q}{p} \bar{\rho}(f_b) \right|^2 \right], \end{aligned} \quad (26.5.31)$$

where  $\bar{\rho}(f)$  is defined in Eq. 25.1.20 of Sect. 25.1.2. The second contribution in the square brackets can occur only via oscillations, but includes  $f_a = f_b$ ; moreover it is heavily suppressed by  $x^2 \leq 10^{-4}$  making it practically unobservable. The first term arises even with  $x = 0$ , yet requires  $f_a \neq f_b$ . It is possible that the  $|\bar{\rho}(f_a) - \bar{\rho}(f_b)|^2$  term provides a larger signal for  $CP$  violation than that from either the  $|1 - |\rho(f_a)|^2|$  or  $|1 - |\rho(f_b)|^2|$  terms. Equation 26.5.31 also holds when the final states are not  $CP$  eigenstates, as long as the modes are common to  $D^0$  and  $\bar{D}^0$ . Consider, for example,  $e^+ e^- \rightarrow D^0 \bar{D}^0 \rightarrow f_a f_b$  with  $f_a = K^+ K^-$ ,  $f_b = K^\pm \pi^\mp$ . Measurements of these rates would yield unique information on the strong phase shifts.

Note that all these arguments cannot be applied for  $D$  decays into vector states  $D \rightarrow V_1 V_2$ . These decay modes, in contrast to  $D \rightarrow PP$  and  $PV$ , are described by more than one independent amplitude. Therefore, the process  $e^+ e^- \rightarrow D^0 \bar{D}^0 \rightarrow (K^* \rho)(K^* \rho)$  can occur even in the absence of mixing and  $CP$  violation, since the two decays could be described by different combinations of decay amplitudes. Analyses of these decays could yield useful information on final state interactions in these decay modes.

Table 26.5 summarizes the sensitivities of measurements of  $CP$  asymmetries in coherent  $D^0 \bar{D}^0$  decays into  $CP$  eigenstates at *BES-III*.

## 26.6 *T* Violation

### 26.6.1 Triple-Product Correlation in $D$ Decays

There are other types of  $CP$ -violating effects that can also reveal the presence of new physics, namely Triple-product (TP) correlations [412]. These take the form  $\vec{v}_1 \cdot (\vec{v}_2 \times \vec{v}_3)$ , where each  $\vec{v}_i$  is a spin or momentum vector. Since  $T(\vec{v}_i) = -\vec{v}_i$ , these TP's are odd under time reversal ( $T$ ) and, hence, by the  $CPT$  theorem, also constitute potential signals for

CP Violation		
Reaction	Event	Comment
$D^{*0}\bar{D}^0 \rightarrow [\gamma_s(\text{semileptonic})(CP \text{ eigenstates})]$	26280	Measure mixing-dependent $CP$ violation Asymmetry determined to 1%
$\psi(3770) \rightarrow (\text{semileptonic})(CP \text{ eigenstates})$	136000	Measure magnitude of $CP$ violating amplitude to 0.5 %
$\psi(3770) \rightarrow (CP\pm \text{ eigenstates})(CP\pm \text{ eigenstates})$	16000	Sensitive to phase of direct $CP$ violating amplitude (1.0%)

Table 26.5: Summary of  $CP$  violation measurements using coherent  $D^0\bar{D}^0$  decays to  $CP$  eigenstates at *BES-III*

$CP$  violation. One can construct the non-zero TP by measuring the non-zero value of the asymmetry:

$$A_T \equiv \frac{\Gamma(\vec{v}_1 \cdot (\vec{v}_2 \times \vec{v}_3) > 0) - \Gamma(\vec{v}_1 \cdot (\vec{v}_2 \times \vec{v}_3) < 0)}{\Gamma(\vec{v}_1 \cdot (\vec{v}_2 \times \vec{v}_3) > 0) + \Gamma(\vec{v}_1 \cdot (\vec{v}_2 \times \vec{v}_3) < 0)}, \quad (26.6.32)$$

where  $\Gamma$  is the decay rate for a given process. However, a non-vanishing value for  $A_T$  is not necessarily due to the  $T$  transformation. This is because, in addition to reversing spins and momenta, the time reversal symmetry  $T$  also exchanges the initial and final states. In particular, non-zero TP correlations can be due to final state interactions, even if there is no  $CP$  violation. One typically finds

$$A_T \propto \sin(\phi + \delta), \quad (26.6.33)$$

where  $\phi$  is a weak,  $CP$ -violating phase and  $\delta$  is a strong phase. From this we see that if  $\delta \neq 0$ , a TP correlation will appear, even without  $CP$  violation. To perform a stringent test of  $CP$  invariance, one has to also measure  $\bar{A}_T$  for the  $CP$ -conjugate decay process. One then gets a  $T$ -violating asymmetry:

$$\mathcal{A}_T^{CP} \equiv \frac{1}{2}(A_T + \bar{A}_T). \quad (26.6.34)$$

This is a true  $T$ -violating signal that is non-zero only if  $\phi \neq 0$ .

In fact, TP asymmetries are similar to direct  $CP$  asymmetries in two ways [413]: (i) they are both obtained by comparing a signal in a given decay with the corresponding signal in the  $CP$ -transformed process, and (ii) they both need the interference between two different decay amplitudes. However, there is one important difference between the direct  $CP$  and TP asymmetries. The direct  $CP$  asymmetry can be written

$$A_{dir}^{CP} \propto \sin\phi\sin\delta, \quad (26.6.35)$$

while, for the true  $T$ -violating asymmetry is given by

$$\mathcal{A}_T^{CP} \propto \sin\phi\cos\delta. \quad (26.6.36)$$

The key point here is that one can produce a direct  $CP$  asymmetry only if there is a non-zero strong-phase difference between the two decay amplitudes. However, TP asymmetries are maximal when the strong phase difference is zero. Thus, it may be more promising to look for TP asymmetries than direct  $CP$  asymmetries in  $D$  and  $B$  decays.

Consider the weak decay of a  $D$  meson to two vector mesons,  $D \rightarrow V_1(k_1, \epsilon_1)V_2(k_2, \epsilon_2)$ , where  $k_1$  and  $\epsilon_1$  ( $k_2$  and  $\epsilon_2$ ) denote the polarization and momentum of  $V_1$  ( $V_2$ ). For example, in the decay of  $D^+ \rightarrow \bar{K}^{*0}(k_1, \epsilon_1)K^{*+}(k_2, \epsilon_2)$ , one can study the triple correlation

$$A_T = \frac{N(k_1 \cdot (\epsilon_1 \times \epsilon_2) > 0) - N(k_1 \cdot (\epsilon_1 \times \epsilon_2) < 0)}{N(k_1 \cdot (\epsilon_1 \times \epsilon_2) > 0) + N(k_1 \cdot (\epsilon_1 \times \epsilon_2) < 0)} \quad (26.6.37)$$

and the true  $T$  asymmetry,  $\mathcal{A}_T^{CP} \equiv \frac{1}{2}(A_T + \bar{A}_T)$ , can be studied by considering the  $CP$  conjugate decay mode  $D^- \rightarrow K^{*0}K^{*-}$ .  $CP$  symmetry is violated if  $\mathcal{A}_T^{CP} \neq 0$ .

The only reported experimental search for  $T$ -odd asymmetries is from FOCUS in the  $D^0 \rightarrow K^+K^-\pi^+\pi^-$  and  $D_S \rightarrow \bar{K}^0K^-\pi^+$  decay modes, as listed in Table 26.6. No evidence for a  $T$ -odd asymmetry is observed. The large *BES-III* data samples are expected to provide enhanced sensitivity to possible  $T$ -violating asymmetries.

Year	Experiment	Decay Mode	$A_T^{CP}(\%)$
2005	FOCUS [396]	$D^0 \rightarrow K^+K^-\pi^+\pi^-$	$1.0 \pm 5.7 \pm 3.7$
2005	FOCUS [396]	$D^+ \rightarrow \bar{K}^0K^-\pi^+\pi^-$	$2.3 \pm 6.2 \pm 2.2$
2005	FOCUS [396]	$D_S \rightarrow \bar{K}^0K^-\pi^+$	$-3.6 \pm 6.7 \pm 2.3$

Table 26.6:  $T$ -violating asymmetries in  $D$  meson decays from the FOCUS experiment.

## 26.6.2 Searches for $CP$ Violation via $T$ -odd moments in $D$ decays<sup>2</sup>

Decays to final states of *more than* two pseudoscalar or one pseudoscalar and one vector mesons contain more dynamical information than given by their partial widths; their distributions as described by Dalitz plots or  $T$ -odd moments can exhibit  $CP$  asymmetries that can be considerably larger than those for the integrated partial width. Final state interactions, while not necessary for the emergence of such effects, can fake a signal; however, these can be disentangled by comparing  $T$ -odd moments for  $CP$  conjugate modes, as explained below.

All  $CP$  asymmetries observed to date in  $K_L$  and  $B_d$  decays concern partial widths –  $\Gamma(P \rightarrow f) \neq \Gamma(\bar{P} \rightarrow \bar{f})$  – except for one. The notable exception, namely the  $T$ -odd moment found in the rare mode  $K_L \rightarrow \pi^+\pi^-e^+e^-$ , can teach us important lessons for future searches in charm decays. Define  $\phi$  as the angle between the planes spanned by the two pions and the two leptons in the  $K_L$  restframe:

$$\phi \equiv \angle(\vec{n}_l, \vec{n}_\pi), \quad \vec{n}_l = \vec{p}_{e^+} \times \vec{p}_{e^-} / |\vec{p}_{e^+} \times \vec{p}_{e^-}|, \quad \vec{n}_\pi = \vec{p}_{\pi^+} \times \vec{p}_{\pi^-} / |\vec{p}_{\pi^+} \times \vec{p}_{\pi^-}|. \quad (26.6.38)$$

One analyzes the decay rate as a function of  $\phi$ :

$$\frac{d\Gamma}{d\phi} = \Gamma_1 \cos^2 \phi + \Gamma_2 \sin^2 \phi + \Gamma_3 \cos \phi \sin \phi. \quad (26.6.39)$$

<sup>2</sup>By Ikaros Bigi

Since

$$\cos\phi \sin\phi = (\vec{n}_l \times \vec{n}_\pi) \cdot (\vec{p}_{\pi^+} + \vec{p}_{\pi^-})(\vec{n}_l \cdot \vec{n}_\pi) / |\vec{p}_{\pi^+} + \vec{p}_{\pi^-}|, \quad (26.6.40)$$

one notes that

$$\cos\phi \sin\phi \xrightarrow{T,CP} -\cos\phi \sin\phi \quad (26.6.41)$$

under both  $T$  and  $CP$  transformations; i.e. the observable  $\Gamma_3$  represents a  $T$ - and  $CP$ -odd correlation. It can be projected out by comparing the  $\phi$  distribution integrated over two quadrants:

$$A = \frac{\int_0^{\pi/2} d\phi \frac{d\Gamma}{d\phi} - \int_{\pi/2}^{\pi} d\phi \frac{d\Gamma}{d\phi}}{\int_0^{\pi} d\phi \frac{d\Gamma}{d\phi}} = \frac{2\Gamma_3}{\pi(\Gamma_1 + \Gamma_2)}. \quad (26.6.42)$$

It was first measured by KTEV and then confirmed by NA48 [3]:

$$A = (13.7 \pm 1.5)\%. \quad (26.6.43)$$

$A \neq 0$  is induced by  $\epsilon_K$ , the  $CP$  violation in the  $K^0 - \bar{K}^0$  mass matrix, leading to the prediction [414]

$$A = (14.3 \pm 1.3)\%. \quad (26.6.44)$$

The observed value for the  $T$  odd moment  $A$  is fully consistent with  $T$  violation.

It is actually easy to see how this sizable forward-backward asymmetry is generated from the tiny quantity  $|\eta_{+-}| \simeq 0.0023$ . For  $K_L \rightarrow \pi^+ \pi^- e^+ e^-$  is driven by the two subprocesses

$$K_L \xrightarrow{CP \& \Delta S=1} \pi^+ \pi^- \xrightarrow{E1} \pi^+ \pi^- \gamma^* \rightarrow \pi^+ \pi^- e^+ e^- \quad (26.6.45)$$

$$K_L \xrightarrow{M1 \& \Delta S=1} \pi^+ \pi^- \gamma^* \rightarrow \pi^+ \pi^- e^+ e^-, \quad (26.6.46)$$

where the first reaction is suppressed, since it requires  $CP$  violation in  $K_L \rightarrow 2\pi$ , as is the second one, since it involves an  $M1$  transition. Those two *a priori* very different suppression mechanisms happen to yield comparable amplitudes, which thus generate a sizable interference. The price one pays is the small branching ratio, namely  $\text{BR}(K_L \rightarrow \pi^+ \pi^- e^+ e^-) = (3.32 \pm 0.14 \pm 0.28) \cdot 10^{-7}$ . *I.e.*, one has ‘traded away’ rate for a much larger asymmetry.

$D$  decays can be treated in an analogous way [415]. Consider the Cabibbo-suppressed channel <sup>3</sup>

$$\overset{(-)}{D} \rightarrow K\bar{K}\pi^+\pi^- \quad (26.6.47)$$

and now define  $\phi$  as the angle between the  $K\bar{K}$  and  $\pi^+\pi^-$  planes. Then one has

$$\frac{d\Gamma}{d\phi}(D \rightarrow K\bar{K}\pi^+\pi^-) = \Gamma_1 \cos^2\phi + \Gamma_2 \sin^2\phi + \Gamma_3 \cos\phi \sin\phi, \quad (26.6.48)$$

$$\frac{d\Gamma}{d\phi}(\bar{D} \rightarrow K\bar{K}\pi^+\pi^-) = \bar{\Gamma}_1 \cos^2\phi + \bar{\Gamma}_2 \sin^2\phi + \bar{\Gamma}_3 \cos\phi \sin\phi. \quad (26.6.49)$$

The partial width for  $D[\bar{D}] \rightarrow K\bar{K}\pi^+\pi^-$  is given by  $\Gamma_{1,2} [\bar{\Gamma}_{1,2}]$ ;  $\Gamma_1 \neq \bar{\Gamma}_1$  or  $\Gamma_2 \neq \bar{\Gamma}_2$  represents direct  $CP$  violation in the partial width.  $\Gamma_3 \& \bar{\Gamma}_3$  constitute  $T$  odd correlations.

<sup>3</sup>This mode can exhibit direct  $CP$  violation even within the SM.

By themselves, they do not necessarily indicate *CP* violation, since they can be induced by strong final state interactions. However

$$\Gamma_3 \neq \bar{\Gamma}_3 \implies \text{CP violation!} \quad (26.6.50)$$

It is quite possible, or even likely, that a difference in  $\Gamma_3$  *vs.*  $\bar{\Gamma}_3$  is significantly larger than in  $\Gamma_1$  *vs.*  $\bar{\Gamma}_1$  or  $\Gamma_2$  *vs.*  $\bar{\Gamma}_2$ . Furthermore, one can expect that differences in detection efficiencies can be handled by comparing  $\Gamma_3$  with  $\Gamma_{1,2}$  and  $\bar{\Gamma}_3$  with  $\bar{\Gamma}_{1,2}$ . A pioneering search for such an effect has been undertaken by FOCUS [416].

The recent evidence observed for  $D^0 - \bar{D}^0$  oscillations even suggests that the *T* odd moments  $\Gamma_3$  and  $\bar{\Gamma}_3$  would show a *time dependence* [417].



# Chapter 27

## Rare and Forbidden Charm Decays<sup>1</sup>

### 27.1 Introduction

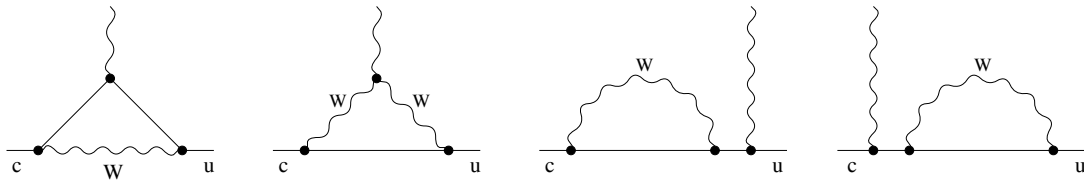
The remarkably successful Standard Model of particle physics describes matter's most basic elements and the forces through which they interact. Physicists have tested its predictions to better than 1% precision. Yet despite its many successes, we know the SM is not the whole story. The questions of so-called fine-tuning, mass hierarchy, etc. remain unexplained. Testing the SM is one of the most important missions in particle physics. One important feature of the SM is the absence of FCNC at tree level. Generally, FCNC processes begin at one-loop level and are GIM suppressed. They have proven to be powerful tools for probing the structure of electro-weak interactions. Examples are rare  $K$  and  $B$  decays and oscillations that induced by penguin or box Feynman diagrams. Because of the large top quark mass, the GIM suppression is mild for down-type quarks. For charm quark FCNC processes, however, only down type quarks can propagate in the loop, as a result, the GIM suppression is very strong and SM predictions for FCNC are very tiny, and beyond the sensitivities of any running or planned experiment. Thus, searches for these decays would be sensitive probes of new, beyond the SM physics. However, long distance contributions, which are not always reliably calculable, could be considerably larger than SM short distance effects.

Potentially interesting decays include: (i)  $D \rightarrow V\gamma$  ( $V = \rho, \omega, \phi, \dots$ ), (ii)  $D \rightarrow X\ell^+\ell^-$  ( $X = \pi, K, \eta, \rho, \omega, \phi, \dots$ ), (iii)  $D \rightarrow X\nu_\ell\bar{\nu}_\ell$  ( $X = \pi, K, \eta, \dots$ ), (iv)  $D \rightarrow \gamma\gamma$ , and (v)  $D \rightarrow \ell^+\ell^-$ .

There have been many attempts to calculate both short- and long-distance contributions to these decays as reliably as possible in both the SM and possible new physics scenarios that potentially have large effects. In a number of cases, extensions of the SM can give contributions that are sometimes orders of magnitude larger than those of the SM [418]. In order to establish the existence of a clean window for observation of new physics in a given observable in rare charm decays, SM contributions first should be made clear. In this regard, it is very important to include long-distance contributions due to the propagation of light quarks, although they are hard to calculate with analytical methods. In the following, we review these decays in the context of the SM and then look at them in new physics models.

---

<sup>1</sup>By Hai-Bo Li and Ya-Dong Yang

Figure 27.1: One-loop diagrams inducing the  $c \rightarrow u\gamma$ 

## 27.2 Rare charm decays in the SM

In principle, the task of producing SM predictions for FCNC  $D$  meson decays is straightforward. There are two components to the analysis: short-distance (SD) and long-distance (LD), which must be separately calculated. It is known that the SD contribution can be calculated in a well defined framework, but phenomenological methods have to be resorted to for LD contributions.

### 27.2.1 Radiative charm decays

Radiative decay modes with one photon include  $D \rightarrow V\gamma$ ,  $D_s \rightarrow V\gamma$  and  $D \rightarrow X_u\gamma$ . The short distance effective Hamiltonian for  $\bar{c} \rightarrow \bar{u} + \gamma$  starts from the one-loop diagrams shown in Fig. 27.2.1 and gives

$$L_{int} = -\frac{4G_F}{\sqrt{2}} A \frac{e}{16\pi^2} m_c (\bar{u} \sigma_{\mu\nu} P_R c) F^{\mu\nu}, \quad (27.2.1)$$

with

$$\Delta A_{1\text{ loop}} \simeq -\frac{5}{24} \sum_{q=d,s,b} V_{cq}^* V_{uq} \left( \frac{m_q}{M_W} \right)^2. \quad (27.2.2)$$

The CKM factors in the above equation have very different orders of magnitude:

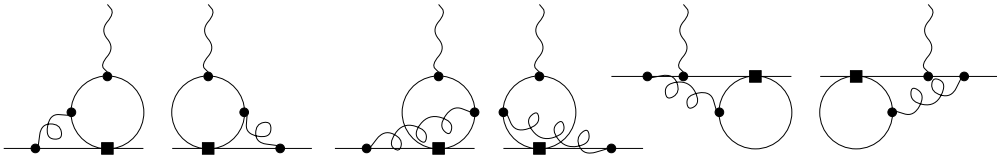
$$|V_{cd}^* V_{ud}| \simeq |V_{cs}^* V_{us}| \simeq 0.22 \quad \text{and} \quad |V_{cb}^* V_{ub}| \simeq (1.3 \pm 0.4) \times 10^{-4}. \quad (27.2.3)$$

Consequently,  $|\Delta A_{1\text{ loop}}| \sim 2 \times 10^{-7}$ . The extraordinary smallness of this number is due to the tiny factors  $(m_q/M_W)^2$  for the light quarks and the small CKM elements governing the  $b$ -quark contributions.

Since the important suppression factors are independent of gauge couplings, it is possible that higher orders in perturbation theory give dominant contributions to the radiative amplitude considered above because they may not suffer from the same dramatic suppression factors and are reduced only by powers of the gauge couplings.

With RGE, one can re-sum short distance QCD corrections in the leading logarithmic approximation which results in the effective Hamiltonian

$$H_{eff}(m_b > \mu > m_c) = \frac{4G_F}{\sqrt{2}} \sum_{q=d,s} V_{cq}^* V_{uq} [C_1(\mu) O_1^q + C_2(\mu) O_2^q + \sum_{i=3}^8 C_i(\mu) O_i], \quad (27.2.4)$$

Figure 27.2: Two-loop diagrams for the  $c \rightarrow u\gamma$ 

where

$$O_1^q = (\bar{u}_\alpha \gamma_\mu P_L q_\beta)(\bar{q}_\alpha \gamma^\mu P_L c_\beta), \quad q = d, s, b \quad (27.2.5)$$

$$O_2^q = (\bar{u}_\alpha \gamma_\mu P_L q_\alpha)(\bar{q}_\beta \gamma^\mu P_L c_\beta), \quad q = d, s, b \quad (27.2.6)$$

$$O_7 = \frac{e}{16\pi^2} m_c (\bar{u}_\alpha \sigma_{\mu\nu} P_R c_\alpha) F^{\mu\nu}. \quad (27.2.7)$$

The Wilson co-efficients  $C_i$  and remaining operators  $O_i$  are given explicitly in Ref. [419]. It is found that the leading logarithmic QCD correction will enhance the  $c \rightarrow u\gamma$  by more than one order-of-magnitude:

$$|\Delta A_{LLA}| = [0.001C_1(m_b) + 0.055C_2(m_b)] |V_{cb}^* V_{ub}| = 0.060 |V_{cb}^* V_{ub}| \simeq (8 \pm 3) \times 10^{-6}. \quad (27.2.8)$$

Moreover, when the two loop contributions depicted in Fig. 27.2.1 are included, one finds that the strength of  $c \rightarrow u\gamma$  is further enhanced by more than two orders-of-magnitude

$$|A| = |V_{cs}^* V_{us}| \frac{\alpha(m_c)}{4\pi} (0.86 \pm 0.19) = (4.7 \pm 1.0) \times 10^{-3}. \quad (27.2.9)$$

After these surprising enhancements, the predicted branching ratio ( $\mathcal{B}$ ) for  $c \rightarrow u\gamma$  is found to be  $\sim 10^{-8}$ . However, even this is very small compared to long-distance contributions from the  $s$  and  $u$  channel poles from nearby states and VMD contributions from  $\rho$ ,  $\omega$ , and  $\phi$ . These estimates suffer from uncertainties from several sources. The mass  $m_c$  is too large for the chiral symmetry approximation and it is too small for the HQET approximation. Thus, one has to resort to inspired guesswork [419, 420, 421]. In any case, the end results seem reasonable and agree with recent measurements. The branching fractions are in the range of  $10^{-5}$  to  $10^{-7}$ . The recent measurement of  $\mathcal{B}(D^0 \rightarrow \phi^0 \gamma) \sim 2.6 \times 10^{-5}$  by Belle [422] is well within the expected range. However, it would be extremely hard to extract the small short-distance contributions.

## 27.2.2 GIM-suppressed decays

### The short-distance component

Short-distance amplitudes are concerned with the QCD degrees of freedom (quarks, gluons) and any relevant additional fields (leptons, photons). Thus, the short-distance part of the  $D \rightarrow X_u \ell^+ \ell^-$  amplitude involves the quark process  $c \rightarrow u \ell^+ \ell^-$ . It is usually most natural to employ an effective description in which the weak Hamiltonian is expressed in terms of local multiquark operators and Wilson coefficients [423]. For example, the

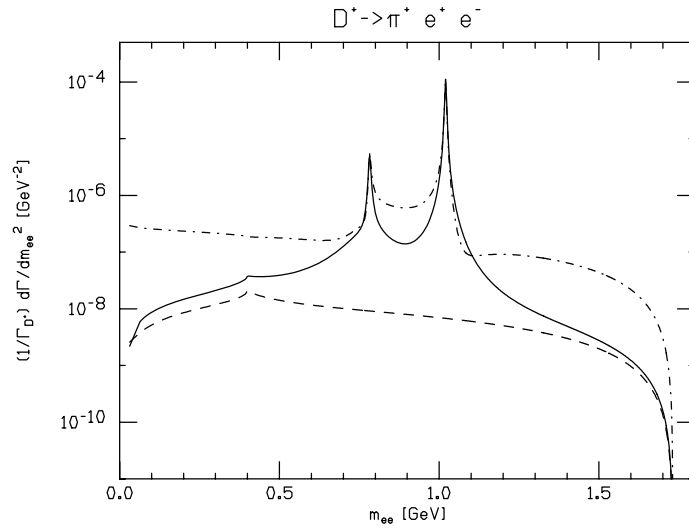


Figure 27.3: Predicted dilepton mass distributions for  $D^+ \rightarrow \pi^+ e^+ e^-$ . The dashed (solid) line is the short-distance (total) SM contribution. The dot-dashed line is the  $R$ -parity violating SUSY contribution.

effective Hamiltonian for  $c \rightarrow u\ell^+\ell^-$  with renormalization scale  $\mu$  in the range  $m_b \geq \mu \geq m_c$  is <sup>2</sup>

$$\mathcal{H}_{\text{eff}}^{c \rightarrow u\ell^+\ell^-} = -\frac{4G_F}{\sqrt{2}} \left[ \sum_{i=1}^2 \left( \sum_{q=d,s} C_i^{(q)}(\mu) \mathcal{O}_i^{(q)}(\mu) \right) + \sum_{i=3}^{10} C'_i(\mu) \mathcal{O}'_i(\mu) \right] . \quad (27.2.10)$$

In the above expression,  $\mathcal{O}_{1,2}^{(q)}$  are four-quark current-current operators,  $\mathcal{O}'_{3-6}$  are the QCD penguin operators,  $\mathcal{O}_7$  ( $\mathcal{O}_8$ ) is the electromagnetic (chromomagnetic) dipole operator and  $\mathcal{O}_{9,10}$  explicitly couple quark and lepton currents. For example, we have

$$\mathcal{O}'_7 = \frac{e}{16\pi^2} m_c (\bar{u}_L \sigma_{\mu\nu} c_R) F^{\mu\nu} , \quad \mathcal{O}'_9 = \frac{e^2}{16\pi^2} (\bar{u}_L \gamma_\mu c_L) (\bar{\ell} \gamma^\mu \ell) . \quad (27.2.11)$$

The famous Inami-Lim functions [424] contribute to the Wilson coefficients  $C_{7-10}$  at scale  $\mu = M_W$ .

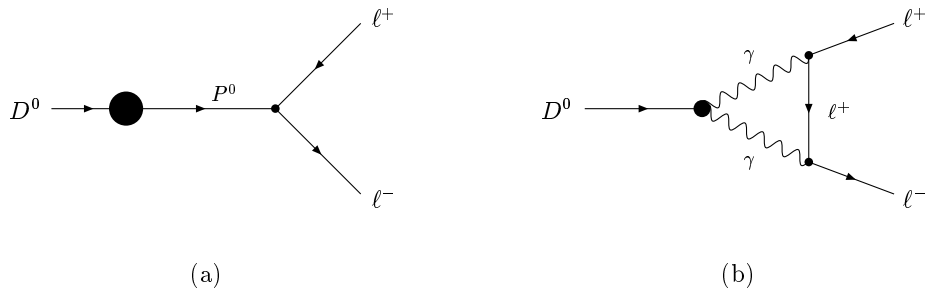
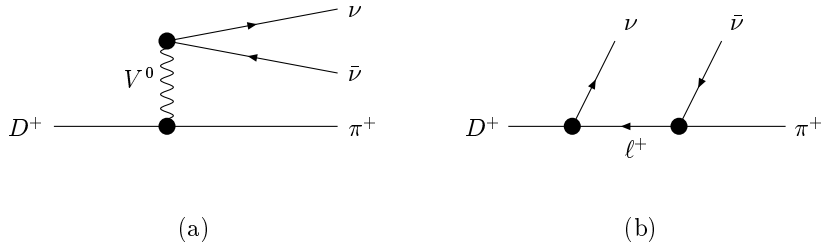
Figure 27.3 displays the predicted dilepton mass spectrum for  $D^+ \rightarrow \pi^+ \ell^+ \ell^-$ . Several distinct kinds of contributions are included. The short-distance SM component corresponds to the dashed line, which is seen to lie beneath the other two curves. For reference, we note the predicted ‘short distance’ *inclusive* branching ratio,

$$\mathcal{Br}_{D^+ \rightarrow \pi^+ e^+ e^-}^{(\text{sd})} \simeq 2 \times 10^{-8} . \quad (27.2.12)$$

### The long-distance component

The long-distance component to a transition amplitude is often cast in terms of hadronic entities rather than the underlying quark and gluonic degrees of freedom. For

<sup>2</sup>Quantities with primes have had the explicit  $b$ -quark contributions integrated out

Figure 27.4: Long distance contributions to  $D^0 \rightarrow \ell^+ \ell^-$ .Figure 27.5: Long distance contributions to  $D^+ \rightarrow \pi^+ \ell^+ \ell^-$ .

charm decays, the long-distance amplitudes are typically important but difficult to determine with any rigor. There are generally several long-distance mechanisms for a given transition, *e.g.* as indicated for  $D^0 \rightarrow \ell^+ \ell^-$  in Fig. 27.2.2 and for  $D^+ \rightarrow \pi^+ \bar{\nu}\nu$  in Fig. 27.2.2.

We return to the case of  $D^+ \rightarrow \pi^+ \ell^+ \ell^-$  depicted in Fig. 27.3. The solid curve represents the *total* SM signal, summed over both SD and LD contributions. In this case the LD component dominates, and from studying the dilepton mass distribution we can see what is happening. The peaks in the solid curve must correspond to intermediate resonances ( $\phi$ , etc.). The corresponding Feynman graph would be analogous to that in Fig. 27.2.2 (b) in which the final state neutrino pair is replaced by a charged lepton pair. One finds numerically that

$$\mathcal{B}r_{D^+ \rightarrow \pi^+ e^+ e^-}^{(\text{SM})} \simeq \mathcal{B}r_{D^+ \rightarrow \pi^+ e^+ e^-}^{(\text{LD})} \simeq 2 \times 10^{-6} . \quad (27.2.13)$$

### The Standard Model Predictions

In an analysis based in part on existing literature [425], both SD and LD amplitudes for a number of FCNC  $D$ -meson transitions have been calculated [418]. Results are collected in Table 27.1. As stated earlier, the current database for processes appearing in Table 27.1 consists entirely of upper bounds (or in the case of  $D^0 \rightarrow \gamma\gamma$  no data entry at all). In all cases, existing experimental bounds are much larger than the SM predictions, so there is no conflict between the two. For some cases (*e.g.*  $D \rightarrow \pi \ell^+ \ell^-$ ) the gap between SM theory and experiment is not so large and there is hope for detection in the near future. In other cases (*e.g.*  $D^0 \rightarrow \ell^+ \ell^-$ ) the gap is enormous, leaving plenty of opportunities for signals from New Physics to appear. This point is sometimes not fully appreciated and,

thus, warrants some emphasis. It is why, for example, attempts to detect  $\Delta M_D$  via  $D^0$ - $\bar{D}^0$  mixing experiments are so important.

Table 27.1: Standard Model predictions and current experimental limits for the branching fractions due to short and long distance contributions for various rare  $D$  meson decays.

Decay Mode	Experimental Limit	$\mathcal{B}r_{S.D.}$	$\mathcal{B}r_{L.D.}$
$D^+ \rightarrow X_u^+ e^+ e^-$		$2 \times 10^{-8}$	
$D^+ \rightarrow \pi^+ e^+ e^-$	$< 4.5 \times 10^{-5}$		$2 \times 10^{-6}$
$D^+ \rightarrow \pi^+ \mu^+ \mu^-$	$< 1.5 \times 10^{-5}$		$1.9 \times 10^{-6}$
$D^+ \rightarrow \rho^+ e^+ e^-$	$< 1.0 \times 10^{-4}$		$4.5 \times 10^{-6}$
$D^0 \rightarrow X_u^0 + e^+ e^-$		$0.8 \times 10^{-8}$	
$D^0 \rightarrow \pi^0 e^+ e^-$	$< 6.6 \times 10^{-5}$		$0.8 \times 10^{-6}$
$D^0 \rightarrow \rho^0 e^+ e^-$	$< 5.8 \times 10^{-4}$		$1.8 \times 10^{-6}$
$D^0 \rightarrow \rho^0 \mu^+ \mu^-$	$< 2.3 \times 10^{-4}$		$1.8 \times 10^{-6}$
$D^+ \rightarrow X_u^+ \nu \bar{\nu}$		$1.2 \times 10^{-15}$	
$D^+ \rightarrow \pi^+ \nu \bar{\nu}$			$5 \times 10^{-16}$
$D^0 \rightarrow \bar{K}^0 \nu \bar{\nu}$			$2.4 \times 10^{-16}$
$D_s \rightarrow \pi^+ \nu \bar{\nu}$			$8 \times 10^{-15}$
$D^0 \rightarrow \gamma \gamma$		$4 \times 10^{-10}$	$\text{few} \times 10^{-8}$
$D^0 \rightarrow \mu^+ \mu^-$	$< 3.3 \times 10^{-6}$	$1.3 \times 10^{-19}$	$\text{few} \times 10^{-13}$
$D^0 \rightarrow e^+ e^-$	$< 1.3 \times 10^{-5}$	$(2.3 - 4.7) \times 10^{-24}$	
$D^0 \rightarrow \mu^\pm e^\mp$	$< 8.1 \times 10^{-6}$	0	0
$D^+ \rightarrow \pi^+ \mu^\pm e^\mp$	$< 3.4 \times 10^{-5}$	0	0
$D^0 \rightarrow \rho^0 \mu^\pm e^\mp$	$< 4.9 \times 10^{-5}$	0	0

## 27.3 New Physics Analysis

There is a wide collection of possible New Physics models leading to FCNC  $D$ -meson transitions. Among those considered in Ref. [418] are (i) Supersymmetry (SUSY):  $R$ -parity conserving,  $R$ -parity violating, (ii) Extra Degrees of Freedom: Higgs bosons, Gauge bosons, Fermions, Spatial dimensions, (iii) Strong Dynamics: Extended technicolor, Top-condensation.

We restrict most of our attention to the case of supersymmetry and add a few remarks on the topic of large extra dimensions. The SUSY discussion divides naturally according to how the  $R$ -parity  $R_P$  is treated, where

$$R_P = (-)^{3(B-L)+2S} = \begin{cases} +1 & (\text{particle}) \\ -1 & (\text{sparticle}) \end{cases} \quad (27.3.14)$$

### 27.3.1 $R$ -parity conserving SUSY

$R$ -parity conserving SUSY will contribute to charm FCNC amplitudes via loops. To calculate  $R$ -parity conserving SUSY contributions, the so-called *mass insertion approximation*

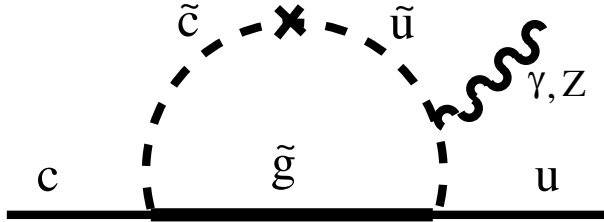


Figure 27.6: A typical contribution to  $c \rightarrow u$  FCNC transitions in the MSSM. The cross denotes one mass insertion  $(\delta_{12}^u)_{\lambda\lambda'}$  and  $\lambda, \lambda'$  are helicity labels.

mation is always employed [426]; this is oriented towards phenomenological studies and is also model independent. Let us first describe what is actually done and then provide a brief explanation of the underlying rationale.

In this approach, a squark propagator becomes modified by a mass insertion (*e.g.* the ‘ $\times$ ’ in Fig. 27.3.1 that changes the squark flavor) [426, 427]. For convenience, one expands the squark propagator in powers of the dimensionless quantity  $(\delta_{ij}^u)_{\lambda\lambda'}$ ,

$$(\delta_{ij}^u)_{\lambda\lambda'} = \frac{(M_{ij}^u)^2_{\lambda\lambda'}}{M_{\tilde{q}}^2} , \quad (27.3.15)$$

where  $i \neq j$  are generation indices,  $\lambda, \lambda'$  denote the chirality,  $(M_{ij}^u)^2$  are the off-diagonal elements of the up-type squark mass matrix and  $M_{\tilde{q}}$  represents the average squark mass. The exchange of squarks in loops thus leads to FCNC through diagrams such as the one in Fig. 27.3.1. The role of experiment is either to detect the predicted (SUSY-induced) FCNC signal or to constrain the contributing  $(\delta_{ij}^u)_{\lambda\lambda'}$ .

This topic is actually part of the super-CKM problem. If one works in a basis that diagonalizes the fermion mass matrices, then sfermion mass matrices (and thus sfermion propagators) will generally be nondiagonal. As a result, flavor-changing processes can occur. One can use phenomenology to restrict these FCNC phenomena. The  $Q = -1/3$  sector has yielded fairly strong constraints but thus far only  $D^0$ - $\bar{D}^0$  mixing has been used to limit the  $Q = +2/3$  sector. In the analysis of Ref. [418], charm FCNCs have been taken to be as large as allowed by the  $D$ -mixing upper bounds.

For the decays  $D \rightarrow X_u \ell^+ \ell^-$  discussed above in Sect. 27.2.2, the gluino contributions will occur additively relative to those from the SM and, so, we can write for the Wilson coefficients,

$$C_i = C_i^{(\text{SM})} + C_i^{\tilde{g}} . \quad (27.3.16)$$

To get some feeling for the dependence on the  $(\delta_{12}^u)_{\lambda\lambda'}$  parameters, we display the examples

$$C_7^{\tilde{g}} \propto (\delta_{12}^u)_{\text{LL}} \text{ and } (\delta_{12}^u)_{\text{LR}} , \quad C_9^{\tilde{g}} \propto (\delta_{12}^u)_{\text{LL}} , \quad (27.3.17)$$

whereas for quark helicities opposite<sup>3</sup> to those in the operators of Eq. (27.2.11), one finds

$$\hat{C}_7^{\tilde{g}} \propto (\delta_{12}^u)_{\text{RR}} \text{ and } (\delta_{12}^u)_{\text{LR}} , \quad \hat{C}_9^{\tilde{g}} \propto (\delta_{12}^u)_{\text{RR}} . \quad (27.3.18)$$

Moreover, the term in  $\hat{C}_7^{\tilde{g}}$  that contains  $(\delta_{12}^u)_{\text{LR}}$  experiences the enhancement factor  $M_{\tilde{g}}/m_c$ .

<sup>3</sup>We use the notation  $\hat{C}$  for the associated Wilson coefficients.

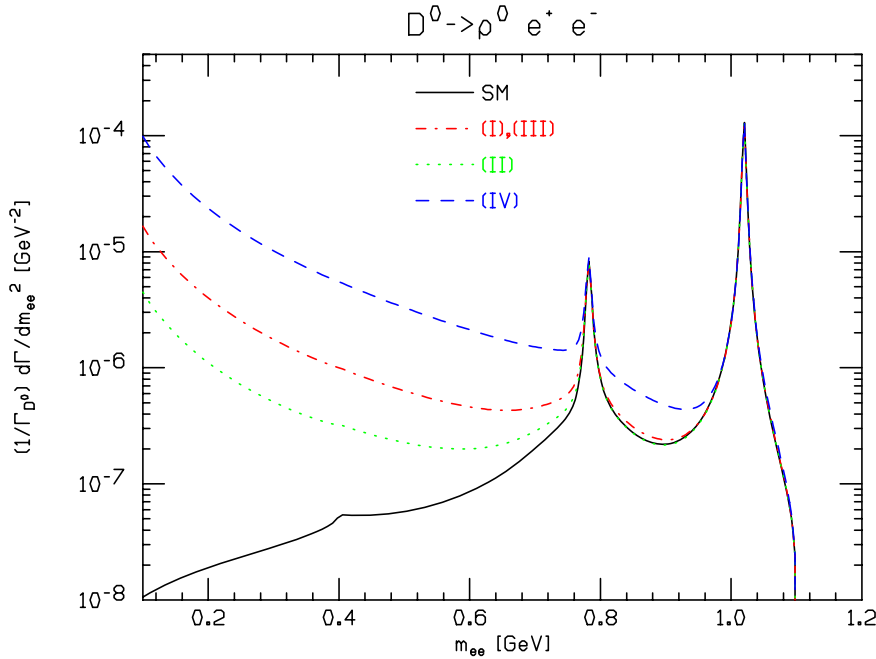


Figure 27.7: Dilepton mass distributions for  $D^0 \rightarrow \rho^0 e^+ e^-$  in the mass insertion approximation of MSSM. The SM prediction (solid curve) is provided for reference and the MSSM curves refer to (i)  $M_{\tilde{g}} = M_{\tilde{q}} = 250$  GeV, (ii)  $M_{\tilde{g}} = 2M_{\tilde{q}} = 500$  GeV, (iii)  $M_{\tilde{g}} = M_{\tilde{q}} = 1000$  GeV and (iv)  $M_{\tilde{g}} = M_{\tilde{q}}/2 = 250$  GeV.

The effects in  $c \rightarrow u\ell^+\ell^-$  are studied numerically for the range of masses: (I)  $M_{\tilde{g}} = M_{\tilde{q}} = 250$  GeV, (II)  $M_{\tilde{g}} = 2M_{\tilde{q}} = 500$  GeV, (III)  $M_{\tilde{g}} = M_{\tilde{q}} = 1000$  GeV and (IV)  $M_{\tilde{g}} = (1/2)M_{\tilde{q}} = 250$  GeV. For some  $D \rightarrow X_u\ell^+\ell^-$  modes, the effect of the squark-gluino contributions can be large relative to the SM component, both in the total branching ratio and for certain kinematic regions of the dilepton mass. The mode  $D^0 \rightarrow \rho^0 e^+ e^-$  is given in Fig. 27.7. This figure demonstrates the importance of measuring the low  $m_{\ell^+\ell^-}$  part of the dilepton mass spectrum.

### 27.3.2 $R$ -parity violating SUSY

The effect of assuming that  $R$ -parity can be violated is to allow additional interactions between particles and sparticles. Ignoring bilinear terms that are not relevant to our discussion of FCNC effects, we introduce the  $R$ -parity violating (RPV) super-potential of trilinear couplings,

$$\mathcal{W}_{R_p} = \epsilon_{ab} \left[ \frac{1}{2} \lambda_{ijk} L_i^a L_j^b \bar{E}_k + \lambda'_{ijk} L_i^a Q_j^b \bar{D}_k + \frac{1}{2} \epsilon_{\alpha\beta\gamma} \lambda''_{ijk} \bar{U}_i^\alpha \bar{D}_j^\beta \bar{D}_k^\gamma \right] , \quad (27.3.19)$$

where  $L$ ,  $Q$ ,  $\bar{E}$ ,  $\bar{U}$  and  $\bar{D}$  are the standard chiral super-fields of the MSSM and  $i, j, k$  are generation indices. The quantities  $\lambda_{ijk}$ ,  $\lambda'_{ijk}$  and  $\lambda''_{ijk}$  are *a priori* arbitrary couplings with a total of  $9 + 27 + 9 = 45$  unknown parameters in the theory.

The presence of RPV means that *tree-level* amplitudes become possible in which a virtual sparticle propagates from one of the trilinear vertices in Eq. 27.3.19 to another.

In order to avoid significant FCNC signals (which would be in contradiction with current experimental limits), bounds must be placed on the (unknown) coupling parameters. As experimental probes become more sensitive, the bounds become ever tighter. In particular, the FCNC sector probed by charm decays involves the  $\{\lambda'_{ijk}\}$ . Introducing matrices  $\mathcal{U}_L$ ,  $\mathcal{D}_R$  to rotate left-handed up-quark fields and right-handed down-quark fields to the mass basis, we obtain for the relevant part of the superpotential

$$\mathcal{W}_{\lambda'} = \tilde{\lambda}'_{ijk} \left[ -\tilde{e}_L^i \bar{d}_R^k u_L^j - \tilde{u}_L^j \bar{d}_R^k e_L^i - (\bar{d}_R^k)^* (\bar{e}_L^i)^c u_L^j + \dots \right] , \quad (27.3.20)$$

where neutrino interactions are not shown, and we define

$$\tilde{\lambda}'_{ijk} \equiv \lambda'_{irs} \mathcal{U}_{rj}^L \mathcal{D}_{sk}^{*R} . \quad (27.3.21)$$

Some bounds on the  $\{\tilde{\lambda}'_{ijk}\}$  are already available from data on such diverse sources as charged-current universality, the ratio  $\Gamma_{\pi \rightarrow e \nu_e} / \Gamma_{\pi \rightarrow \mu \nu_\mu}$ , the semileptonic decay  $D \rightarrow K \ell \nu_\ell$ , etc. [429]. The additional experimental implications of the preceding formalism are considered:

(i) For the decay  $D^+ \rightarrow \pi^+ e^+ e^-$ , the effect of RPV is displayed as the dot-dash line in Fig. 27.3. Here the effect is proportional to  $\tilde{\lambda}'_{11k} \cdot \tilde{\lambda}'_{12k}$  and we have employed existing limits on these couplings. Although the effect on the branching ratio is not large, the dilepton spectrum away from resonance poles is seen to be sensitive to the RPV contributions. This case is not optimal because the current experimental limit on  $\mathcal{Br}_{D^+ \rightarrow \pi^+ e^+ e^-}$  is well above the dot-dash curve.

(ii) For  $D^+ \rightarrow \pi^+ \mu^+ \mu^-$ , the current experimental limit on  $\mathcal{Br}_{D^+ \rightarrow \pi^+ \mu^+ \mu^-}$  actually provides the new bound

$$\tilde{\lambda}'_{11k} \cdot \tilde{\lambda}'_{12k} \leq 0.004 . \quad (27.3.22)$$

(iii) Another interesting mode is  $D^0 \rightarrow \mu^+ \mu^-$ . Upon using the bound of Eq. (27.3.22) we obtain

$$\mathcal{Br}_{D^0 \rightarrow \mu^+ \mu^-}^{\mathcal{R}_p} < 3.5 \times 10^{-6} \left( \frac{\tilde{\lambda}'_{12k}}{0.04} \right)^2 \left( \frac{\tilde{\lambda}'_{11k}}{0.02} \right)^2 . \quad (27.3.23)$$

A modest improvement of the existing limit on  $\mathcal{Br}_{D^0 \rightarrow \mu^+ \mu^-}$  will yield a new bound on the product  $\tilde{\lambda}'_{11k} \cdot \tilde{\lambda}'_{12k}$ .

(iv) Lepton flavor violating processes are allowed by the RPV Lagrangian. One example is the mode  $D^0 \rightarrow e^+ \mu^-$ , for which existing parameter bounds predict

$$\mathcal{Br}_{D^0 \rightarrow \mu^+ e^-}^{\mathcal{R}_p} < 0.5 \times 10^{-6} \times \left[ \left( \frac{\tilde{\lambda}'_{11k}}{0.02} \right) \left( \frac{\tilde{\lambda}'_{22k}}{0.21} \right) + \left( \frac{\tilde{\lambda}'_{21k}}{0.06} \right) \left( \frac{\tilde{\lambda}'_{12k}}{0.04} \right) \right] . \quad (27.3.24)$$

An order-of-magnitude improvement in  $\mathcal{Br}_{D^0 \rightarrow \mu^+ e^-}^{\mathcal{R}_p}$  will provide a new bound on the above combination of RPV couplings.

### 27.3.3 Large Extra Dimensions

For several years, the study of large extra dimensions ('large' means much greater than the Planck scale) has been an area of intense study. This approach might hold the

solution of the hierarchy problem while having verifiable consequences at the TeV scale or less. Regarding the subject of rare charm decays, one's reaction might be to ask *How could extra dimensions possibly affect the decays of ordinary hadrons?*. We provide a few examples in the following.

Suppose the spacetime of our world amounts to a  $3 + 1$  brane which together with a manifold of additional dimensions (the bulk) is part of some higher-dimensional space. A field  $\Theta$  that can propagate in a large extra dimension will exhibit a Kaluza-Klein (KK) tower of states  $\{\Theta_n\}$ , detection of which would signal existence of the extra dimension. Given our ignorance regarding properties of the bulk or of which fields are allowed to propagate in it, one naturally considers a variety of different models.

Assume, for example, the existence of an extra dimension of scale  $1/R \sim 10^{-4}$  eV such that the gravitational field (denote it simply as  $G$ ) alone can propagate in the extra dimension [430]. There are then bulk-graviton KK states  $\{G_n\}$  which couple to matter. In principle there will be FCNC transitions  $c \rightarrow u G_n$  and, since the  $\{G_n\}$  remain undetected, there will be apparent missing energy. However this mechanism leads to too small a rate to be observable.

Another possibility that has been studied is that the scale of the extra dimension is  $1/R \sim 1$  TeV and that SM gauge fields propagate in the bulk [431]. However, precision electroweak data constrain the mass of the first gauge KK excitation to be in excess of 4 TeV [432] and, thus, their contributions to rare decays are small [433].

More elaborate constructions, such as allowing fermion fields to propagate in the five-dimensional bulk of the Randall-Sundrum localized-gravity model [434], are currently being actively explored [435]. Interesting issues remain and a good deal more study deserves to be done.

## 27.4 Summary

FCNC charm decays are very rare in the SM due to the strong GIM suppression. In sharp contrast to  $B \rightarrow X_s \gamma, K^* \gamma$ , the SD contributions in radiative charm decays are much smaller than the LD contributions in the SM, which makes the extraction SD contribution from future measurements of  $D \rightarrow X_u \gamma$  and  $D \rightarrow V \gamma$  more complicated. Although the LD contributions still dominate the rates, just as in the radiative decays, there are decays modes such as  $D \rightarrow \pi \ell^+ \ell^-$  and  $D \rightarrow \rho \ell^+ \ell^-$  where it is possible to access the SD physics away from the resonance contributions in the low di-lepton invariant mass region. As illustrated in Figs. 27.3 and 27.7, for low di-lepton mass the sum of long and short distance effects leaves a large window where the physics beyond the SM can be observed.

In summary, the FCNC modes are most sensitive to the effects of some new physics scenarios. If the sensitivity of experiment could reach below  $10^{-6}$ , these new physics effects could be tightly constrained. Such an experimental sensitivity, of course, makes many radiative  $D$  decays accessible. However, these may not illuminate short distance physics.

Past searches have set upper limits for the dielectron and dimuon decay modes [3]. In Table 27.2 and Table 27.3, the current limits and expected sensitivities at *BES-III* are summarized for  $D^+$  and  $D^0$ , respectively. Detailed descriptions of rare charm decays can

be found in Refs [440, 441]. Charmed meson radiative decays are also very important to understand final state interaction that may enhance the decay rates. In Refs. [440, 441], the decay rates of  $D \rightarrow V\gamma$  ( $V$  can be  $\phi$ ,  $\omega$ ,  $\rho$  and  $K^*$  ) are estimated to be in the  $10^{-5} - 10^{-6}$  range, which can be reached at *BES-III*.

Mode	Reference Experiment	Best Upper limits( $10^{-6}$ )	<i>BES-III</i> ( $\times 10^{-8}$ )
$\pi^+ e^+ e^-$	CLEO-c [436]	7.4	5.6
$\pi^+ \mu^+ \mu^-$	FOCUS [437]	8.8	8.7
$\pi^+ \mu^+ e^-$	E791 [438]	34	5.9
$\pi^- e^+ e^+$	CLEO-c [436]	3.6	5.6
$\pi^- \mu^+ \mu^+$	FOCUS [437]	4.8	8.7
$\pi^- \mu^+ e^+$	E791 [438]	50	5.9
$K^+ e^+ e^-$	CLEO-c [436]	6.2	6.7
$K^+ \mu^+ \mu^-$	FOCUS [437]	9.2	10.5
$K^+ \mu^+ e^-$	E791 [438]	68	8.3
$K^- e^+ e^+$	CLEO-c [436]	4.5	6.7
$K^- \mu^+ \mu^+$	FOCUS [437]	13	10.4
$K^- \mu^+ e^+$	E687 [439]	130	8.3

Table 27.2: Current and projected 90%-CL upper limits on rare  $D^+$  decay modes at *BES-III* with a  $20 \text{ fb}^{-1}$  data sample taken at the  $\psi(3770)$  peak.

Mode	Reference Experiment	Best Upper limits( $10^{-6}$ )	<i>BES-III</i> ( $\times 10^{-8}$ )
$\gamma\gamma$	CLEO [442]	28	5.0
$\mu^+\mu^-$	D0 [444]	2.4	17.0
$\mu^+e^-$	E791 [438]	8.1	4.3
$e^+e^-$	E791 [438]	6.2	2.4
$\pi^0\mu^+\mu^-$	E653 [445]	180	12.3
$\pi^0\mu^+e^+$	CLEO [443]	86	9.7
$\pi^0e^+e^-$	CLEO [443]	45	7.9
$K_S\mu^+\mu^-$	E653 [445]	260	10.6
$K_S\mu^+e^-$	CLEO [443]	100	9.6
$K_S e^+e^-$	CLEO [443]	110	7.5
$\eta\mu^+\mu^-$	CLEO [443]	530	15.0
$\eta\mu^+e^-$	CLEO [443]	100	12.0
$\eta e^+e^-$	CLEO [443]	110	10.0

Table 27.3: Current and projected 90%-CL upper limits on rare  $D^0$  decay modes at *BES-III* with a  $20 \text{ fb}^{-1}$  data sample taken at the  $\psi(3770)$  peak.

# Bibliography

- [1] S. Bianco, F. Fabbri, D. Benson, I. Bigi, "A Cicerone for the Physics of Charm", *La Riv.d. Nuov.Cim.* **26** (2003); G. Burdman, I. Shipsey, " $D^0 - \bar{D}^0$  Oscillations and Rare Charm Decays", *Ann.Rev.Nucl.Part.Sci.* **53** (2003).
- [2] T. Barnes, S. Godfrey and E. S. Swanson, arXiv:hep-ph/0505002
- [3] W.M. Yao et. al. (Particle Data Group), *J. Phys. G* **33** (2006) 1.
- [4] R. Poling, arXiv:hep-ex/0606016
- [5] E. Eichten, *et al.* *Phys. Rev. D* **21**, 203 (1980)
- [6] J. Adler *et al.* *Phys. Rev. Lett.* **60**, 89 (1988)
- [7] K. L. He, J. Y. Zhang, W. G. Li, BES analysis Note.
- [8] Q. He *et al.* *Phys. Rev. Lett.* **95**, 121801 (2005)
- [9] J. Z. Bai *et al.* *Phys. Rev. D* **52**, 3781 (1995)
- [10] H. W. Zhao, PhD. thesis(in Chinese), 1997;K. L. He, PhD. thesis (in Chinese), 1999.
- [11] M. W. Coles *et al.* *Phys. Rev. D* **26**, 2190 (1982)
- [12] J. Adler *et al.* *Phys. Lett. B* **208**, 152 (1988)
- [13] G. Blaylock *et al.* *Phys. Rev. Lett.* **58**, 2171 (1987)
- [14] N. Cahn, B. Kayser, *Phys. Rev. D* **22**, 2752 (1980)
- [15] T. Barnes, S. Godfrey and E. S. Swanson, *Phys. Rev. D* **72**, 054026 (2005)
- [16] E. J. Eichten, K. Lane and C. Quigg, *Phys. Rev. D* **73**, 014014 (2006), *Phys. Rev. D* **73**, 079903 (2006)
- [17] S. Jadach, B. F. L. Ward, Z. Was, *Phys. Rev. D* **63**, 113009 (2001)
- [18] <http://www.slac.stanford.edu/~lange/EvtGen>, David Lange and Anders Ryd, proceeding of CHEP98, 1998.
- [19] E. A. Kuraev and V. S. Fadin, *Sov. J. Nucl. Phys.* 41, 466(1985).

- [20] G. Altareli and G. Martinelli, CERN Yellow Report 86-02(1986)47; O. Nicrosini and L. Trentadue, *Phys. Lett. B* **196**, 551 (1987).
- [21] F. A. Berends, G. Burgers and W. L. van Neeren, *Nucl. Phys. B* **297**, 429 (1988); *Nucl. Phys. B* **304**, 921 (1986).
- [22] T. Kinoshita, *J. Math. Phys.* **3**, 650(1962); T. D. Lee and M. Nauenberg, *Phys. Rev. B* **133**, 1549(1964).
- [23] H. Albrecht *et al.* *Phys. Lett. B* **241**(1990)278.
- [24] T. Skwarnicki, "A study of the Radiative Cascade Transitions between the Upsilon-Prime and Upsilon Resonances", DESY F31-86-02(thesis, unpublished) (1986)
- [25] H. Abramowicz *et al.*, *Z. Phys. C* **15**, 19(1982); S. A. Rabinowitz *et al.*, *Phys. Rev. Lett.* **70**, 134(1993); A. O. Bazarko *et al.*, *Z. Phys. C* **65**, 189(1995).
- [26] M. Artuso *et al.*, CLEO Collaboration, hep-ex/0508057.
- [27] T. W. Chiu *et al.*, *Phys.Lett. B* **624** (2005) 31, hep-ph/0506266;  
L. Lellouch and C.J. Lin, *Phys.Rev. D* **64**, 094501(2001), hep-ph/0011086.  
D. Becirevic, *Phys.Rev. D* **60**, 074501(1999). hep-lat/9811003;
- [28] S. Narison, hep-ph/0202200;  
A. Penin and M. Steinhauser, *Phys. Rev. D* **65**, 054006(2002), hep-ph/0108110  
D. Ebert *et al.*, *Mod.Phys.Lett. A* **17** (2002) 803, hep-ph/0204167;  
Z. G. Wang, *Nucl. Phys. A* **744**, 156(2004), hep-ph/0403259;  
L. Salcedo *et al.*, hep-ph/0311008, *Braz. J. Phys.* **34** (2004) 297;  
J. Amundson, *Phys. Rev. D* **47**, 3059(1993), hep-ph/9207235.
- [29] J. Adler *et al.*, MARKIII Collaboration, *Phys. Rev. Lett.* **60**, 1375 (1988).
- [30] J.Z. Bai *et al.*, *Phys.Lett. B* **429** (1998) 188; M. Ablikim *et al.*, *Phys.Lett. B* **610**, 183(2005), hep-ex/0410050.
- [31] G. Bonvicini *et al.*, CLEO Collaboration, *Phys.Rev. D* **70**, 112004(2004), hep-ex/0411050
- [32] C. Aubin *et al.*, *Phys. Rev. Lett.* **95** (2005) 122002, hep-lat/0506030.
- [33] S. Aoki *et al.*, WA75 Collaboration, *Prog. Theo. Part.* **89**, 131(1993).
- [34] J.Z. Bai *et al.*, BES Collaboration, *Phys. Rev. Lett.* **74**, 4599(1995).
- [35] K. Kodama, *et al.*, E653 Collaboration, *Phys. Lett. B* **382**, 299(1996).
- [36] M. Acciarri *et al.*, L3 Collaboration, *Phys. Lett. B* **396**, 327(1997).
- [37] M. Chada *et al.*, *Phy. Rev. D* **58**, 032002(1998).

- [38] Y. Alexandrov *et al.*, BEATRICE Collaboration, Phys. Lett. B478, 31(2000).
- [39] G. Abbiendi *et al.*, OPAL Collaboration, Phy. Lett. B516, 236(2001)
- [40] A. Heister *et al.*, ALEPH Collaboration, Phys. Lett. B528, 1(2002).
- [41] B. Grinstein *et al.*, Nucl. Phys. B380, 369(1992); A. Falk, Phys. Lett. B305, 268(1993).
- [42] R. J. Oakes, Phys.Rev.Lett.73, 381(1994)
- [43] T. Huang, Z.H. Li and C. W. Luo, Phys. Lett. B391, 451(1997); D.S. Huang and G. H. Kim, Phys. Lett. B367, 353(1996); Phys. Rev. D53, 3659(1996).
- [44] For a review, M. Neubert, Phys. Rep. 245, 259(1994) and references therein. For a comprehensive book, A. Manohar and M.B. Wise, Heavy Quark Physics, CAMBRIDGE MONOGRAPHS ON PARTICLE PHYSICS, NUCLEAR PHYSICS AND COSMOLOGY, 10.
- [45] P. Ball, Nucl. Phys. B421, 593(1994), hep-ph/9312325.
- [46] M. Neubert, Phys. Rev. D46, 1076(1992).
- [47] J.L. Rosner, Phys. Rev. **D42** (1990) 3732.
- [48] J. D. Richman and P. R. Burchat, Rev. of Mod. Phys. **67** (1995) 893.
- [49] J.Z. Bai *et al* Phy. Lett. **B429** (1998) 188.
- [50] M. Ablikim *et al* Phy. Lett. **B610** (2005) 183.
- [51] J.Z. Bai *et al* Phy. Rev. Lett. **74** (1995) 4599.
- [52] J. Adler *et al* (MARKIII), Phy. Rev. Lett. **60** (1988) 1375.
- [53] G. Bonvicini *et al*. (CLEOC), Phy. Rev. **D70** (2004) 112004.
- [54] M. Artuso *et al* (CLEOC), Phy. Rev. Lett. **95** (2005) 251801.
- [55] S. Aoki *et al* (WA75), Prog. Theo. Phys. **89** (1993) 131.
- [56] K. Kodama *et al* (Fermilab E653), Phy. Lett. **B382** (1996) 299.
- [57] Y. Alexandrov Phy. Lett. **B478** (2000) 31.
- [58] D. Acosta *et al.* (CLEO) Phys. Rev. **D49** (1994) 5690.
- [59] M. Chada *et al.* (CLEO) **58** (1998) 032002.
- [60] A. G. Akeroyd and C.-H. Chen, Phys. Rev. **D 75**, 075004 (2007); A. G. Akeroyd, Prog. Theor. Phys. **111**, 295 (2004).
- [61] J. L. Rosner and S. Stone, arXiv:0802.1043v2 [hep-ex].

- [62] K. Ikado *et al.*, (Belle Collaboration), Phys. Rev. Lett. **97**, 251802 (2006).
- [63] B. Aubert *et al.*, (BaBar Collaboration) [arXiv:0705.1820]; B. Aubert *et al.*, (BaBar Collaboration), Phys. Rev. **D76**, 052002(2007).
- [64] M. Artuso *et al.*, (CLEO Collab.), Phys. Rev. Lett. **95**, 251801 (2005).
- [65] M. Artuso *et al.*, (CLEO Collab.), Phys. Rev. Lett. **99**, 071802 (2007).
- [66] K.M. Ecklund *et al.*, (CLEO Collab.), [arXiv:0712.1175] (2007).
- [67] K. Abe *et al.*, (Belle Collab.), [arXiv:0709.1340] (2007).
- [68] B. Aubert *et al.*, (BABAR Collab.), Phys. Rev. Lett. **98**, 141801 (2007).
- [69] E. Follana *et al.*, (HPQCD and UKQCD Collabs.), [arXiv:0706.1726](2007).
- [70] C. Aubin *et al.*, (MILC Collaboration), Phys. Rev. Lett. **95**, 122002 (2005).
- [71] A. Ali Khan *et al.*, (QCDSF Collaboration), Phys. Lett. **B652**, 150 (2007).
- [72] T. W. Chiu *et al.*, Phys. Lett. **B624**, 31 (2005).
- [73] L. Lellouch and C.-J. Lin (UKQCD Collaboration), Phys. Rev. **D64**, 094501 (2001).
- [74] B. A. Dobrescu and A. S. Kronfeld, [arXiv:0803.0512][hep-ph].
- [75] H. B. Li, Nucl. Phys. **B** Proc. Suppl. **162**, 312 (2006).
- [76] BES-III Collaboration, "The Preliminary Design Report of the BESIII Detector", Report No. IHEP-BEPCII-SB-13.
- [77] R. Poling, Invited talk at 4th Flavor Physics and CP Violation Conference (FPCP 2006), Vancouver, British Columbia, Canada, 9-12 Apr 2006. In the Proceedings of 4th Flavor Physics and CP Violation Conference (FPCP 2006), Vancouver, British Columbia, Canada, 9-12 Apr 2006, [hep-ex/0606016].
- [78] T. K. Pedlar, *et al.*, (CLEO Collab.), Phys. Rev. **D 76**, 072002 (2007).
- [79] D. M. Asner, Proceedings of the CHARM2007 Workshop, Ithaca, NY, August 5-8, 2007, [arXiv:0711.3044].
- [80] Q. He, *et al.*, (CLEO Collab.), Phys. Rev. Lett. **95**, 121801 (2005) [Erratum-ibid. **96**, 199903(2006)].
- [81] G. Burdman, J. T. Goldman and D. Wyler, Phys. Rev. **D 51**, 111 (1995).
- [82] E. Eichten *et al.* **D21** (1980) 203.
- [83] M. Ablikim et al., (BES Collab.) Phys.Lett. **B597** (2004) 39, hep-ex/04060.
- [84] M. Ablikim et al., (BES Collab.) Phys.Lett. **B608** (2005) 24.

- [85] J. Charles et al., (CKMfitter Group) *Eur. Phys. J. C* **41**,(2005) 1-131
- [86] A. Abada et al., *Nucl Phys.* B619 (2001)565.
- [87] C. Aubin et al., *Phys. Rev. Lett.* 94 (2005) 011601.
- [88] M.A. Shifman, A.I. Vainshtein and V.I. Zakharov, *Nucl. Phys.* B147 (1979) 385; 448.
- [89] T.M. Aliev, V.L. Eletskii, and Ya. I. Kogan, *Sov. J. Nucl. Phys.* 40 (1984) 527; A.A. Ovchinnikov and V.A. Slobodenyyuk, *Z. Phys.* C44 (1989) 433; V.N. Baier and Grozin, *Z. Phys.* C47 (1990) 669; A.A. Ovchinnikov, *Sov. J. Nucl. Phys.* 50 (1989) 519.
- [90] P. Ball, V.M. Braun and H.G. Dosch, *Phys. Rev.* D44 (1991) 3567; P. Ball, *Phys. Rev.* D48 (1993) 3190.
- [91] P. Colangelo and F. De Fazio, *Phys. Lett. B* 520 (2001) 78.
- [92] D.S. Du, J.W. Li and M.Z. Yang, *Eur. Phys. J. C*37 (2004) 173.
- [93] A. Khodjamirian, R. Rückl, S. Weinzierl, C.W. Winhart, O. Yakovlev, *Phys. Rev.* D62 (2000) 114002.
- [94] W.Y. Wang, Y.L. Wu and M. Zhong, *Phys. Rev.* D.67 (2003) 014024.
- [95] M. Wirbel, B. Stech and M. Bauer, *Z. Phys.* C29 (1985) 637; M. Bauer, B. Stech and M. Wirbel, *Z. Phys.* C34 (1987) 103.
- [96] N. Isgur, D. Scora, B. Grinstein and M.B. Wise, *Phys. Rev.* D39 (1989) 799.
- [97] D. Scora and N. Isgur, *Phys. Rev.* D52 (1995) 2783.
- [98] D. Melikhov and B. Stech, *Phys. Rev.* D62 (2000) 014006.
- [99] H.Y. Cheng, C.K. Chua and C.W. Hwang, *Phys. Rev.* D69 (2004) 074025.
- [100] S. Fajfer and J. Kamenik, *Phys. Rev.* D71 (2005) 014020; and *Phys. Rev.* D72 (2005) 034029.
- [101] D. Becirevic and A. Kaidalov, *Phys. Lett.* B478 (2000) 417.
- [102] A. Khodjamirian, R. Rückle, S. Weinzierl, C.W. Winhart, and O. Yakovlev, *Phys. Rev.* D62 (2000) 114002
- [103] M. Ablikim et al. (BES Collaboration), *Phys. Lett.* B597 (2004) 39.
- [104] G.S. Huang et al. (CLEO Collaboration), *Phys. Rev. Lett.* 94 (2005) 011802.
- [105] T.E. Coan et al. (CLEO Collaboration), *Phys. Rev. Lett.* 95 (2005) 181802.
- [106] G.S. Huang et al. (CLEO Collaboration), *Phys. Rev. Lett.* 95 (2005) 181801.
- [107] X.H. Guo and T. Huang, *Phys. Rev.* D43 (1991) 2931.

- [108] H.G. Dosch, E.M. Ferreira, F.S. Navarra, and M. Nielsen, Phys. Rev. D 65 (2002) 114002.
- [109] M.Z. Yang, Phys. Rev. D 73 (2006) 034027; Erratum-ibid, D73 (2006) 079901.
- [110] Haibo Li, eprint hep-ex/0605004.
- [111] E691 Collaboration, J. C. Anjos, et al., Phys. Rev. Lett. 62 (1989) 1587.
- [112] CLEO Collaboration, G. Crawford, et al., Phys. Rev. D 44 (1991) 3394.
- [113] CLEOII Collaboration, A. Bean, et al., Phys. Lett. B 317 (1993) 647.
- [114] MARKIII Collaboration, J. Adler, et al., Phys. Rev. Lett. 62 (1989) 1821.
- [115] CLEOc Collaboration, T. E. Coan, et al., Phys. Rev. Lett. 95 (2005) 181802.
- [116] CLEOc Collaboration, F. Butler, et al., Phys. Rev. D 52 (1995) 2656.
- [117] E687 Collaboration, P. L. Frabetti, et al., Phys. Lett. B 382 (1996) 312.
- [118] R. J. Morrison, M. S. Witherell, Annu. Rev. Part. Sci. 39 (1989) 183.
- [119] M. Ablikim, J. C. Chen, G. Rong, D. H. Zhang, HEP & NP 29(1) (2005) 5.
- [120] A. Abada et al., Nucl. Phys. B 619 (2001) 565.
- [121] ARGUS Collaboration, H. Albrecht, et al., Phys. Lett. B 374 (1996) 249.
- [122] CLEOII Collaboration, Y. Kubota, et al., Phys. Rev. D 54 (1996) 2994.
- [123] MARKIII Collaboration, R. M. Baltrusaitis, et al., Phys. Rev. Lett. 54 (1985) 1976.
- [124] LEBC-EHS Collaboration, M. Aguilar-Benitez, et al., Z. Phys. C 36 (1987) 551.
- [125] MARKIII Collaboration, R. H. Schindler, et al., Phys. Rev. D. 24 (1981) 78.
- [126] CLEOc Collaboration, N. E. Adam, et al., hep-ex/0604044.
- [127] DLCO Collaboration, W. Bacino et al., Phys. Rev. Lett. 45 (1980) 329.
- [128] N. Cabibbo, Phys. Rev. Lett. **10**, 531 (1963); M. Kobayashi and T. Maskawa, Prog. Theor. Phys. **49**, 652 (1973).
- [129] Z.Z. Xing, *On testing unitarity of the quark mixing matrix*, Nucl. Phys. B (Proc. Suppl.) **50**, 24 (1996).
- [130] L. Wolfenstein, Phys. Rev. Lett. **51**, 1945 (1983).
- [131] M. Veltri, *NA48 results on kaon and hyperon decays relevant to  $-V(us)$* , hep-ex/0703007, talk given at the 4th International Workshop on the CKM Unitarity Triangle, Nagoya, Japan, December 12-16, 2006.

- [132] E. Blucher *et al.*, arXiv:hep-ph/0512039. Proceedings of 3rd Workshop on the Unitarity Triangle: CKM 2005, San Diego, California, March 15-18, 2005.
- [133] M. Gronau, Y. Grossman, Z. Surujon, and J. Zupan, hep-ph/0702011; and references therein.
- [134] “A New Approach to a Global Fit of the CKM Matrix”, H. Höcker, H. Lacker, S. Laplace and F. Le Diberder Eur. Phys. J. C21, 225-259 (2001) LAL 06/01 [hep-ph/0104062]
- [135] CKMfitter Group (J. Charles et al.), *CP Violation and the CKM Matrix: Assessing the Impact of the Asymmetric B Factories*, Eur. Phys. J. C41, 1-131 (2005), [hep-ph/0406184], updated results and plots available at: <http://ckmfitter.in2p3.fr>
- [136] D. Asner, plenary talk given at the 4th International Workshop on the CKM Unitarity Triangle, Nagoya, Japan, December 12 - 16, 2006.
- [137] V. Lubicz, *CKM fit and Lattice QCD*, IV SuperB Workshop (13-15/11/06, Frascati).  
S. Sharpe, *Weak decays of light hadrons*, Lattice QCD: Present and Future (14-16/04/04, Orsay).  
F. Jegerlehner *et al.*, *Requirements for high performance computing for lattice QCD: Report of the ECFA working panel*, CERN-2000-002.
- [138] S. Eidelman *et al.* [Particle Data Group], Phys. Lett. B **592** (2004) 1.
- [139] A. Hocker and Z. Ligeti, hep-ph/0605217.
- [140] G. Buchalla, A.J. Buras and M.E. Lautenbacher, Rev. Mod. Phys. **68**, 1125 (1996).
- [141] J. Schwinger, Phys. Rev. Lett. **12** (1965) 630; R. P. Feynman, in *Symmetries in Particle Physics*, ed. A. Zichichi, (Academic Press, 1965), p.167; O. Haan, B. Stech, Nucl. Phys. B **22**, 448 (1970).
- [142] M. Bauer, B. Stech and M. Wirbel, Z. Phys. C**34**, 103 (1987).
- [143] A.J. Buras, J.M. Gerard, R. Rückl, Nucl. Phys. **B268**, 16 (1986).
- [144] B. Blok, M. Shifman, *Yad.Fiz.* **45** (1987) 211, 478, 841.
- [145] M. Beneke, G. Buchalla, M. Neubert and C.T. Sachrajda, Phys. Rev. Lett. **83**, 1914 (1999); M. Beneke, G. Buchalla, M. Neubert and C.T. Sachrajda, Nucl. Phys. **B591** (2000) 313.
- [146] H.N. Li and H.L. Yu, Phys. Rev. Lett. **74**, 4388 (1995); Yong-Yeon Keum, Hsiang-nan Li, A.I. Sanda, Phys. Lett. **B504**, 6 (2001); Y.Y. Keum, Hsiang-Nan Li, A.I. Sanda, Phys. Rev. **D63**, 054008 (2001).
- [147] X. Y. Wu, X. G. Yin, D. B. Chen, Y. Q. Guo, Y. Zeng, Mod. Phys. Lett. **A19**, 1623 (2004).
- [148] CLEO Collaboration, M. Selen *et al.*, Phys. Rev. Lett. **71**, 1973 (1993).

- [149] L.L. Chau and H.Y. Cheng, Phys. Lett. **B333**, 514 (1994); M. Gronau and D. Pirjol, Phys. Rev. **D62**, 077301 (2000).
- [150] S. Bianco, F.L. Fabbri, D. Benson, I. Bigi, Riv. Nuovo Cim. **26N7**, 1 (2003).
- [151] L.L. Chau and H.Y. Cheng, Phys. Rev. Lett. **56**, 1655 (1986); Phys. Rev. **D36**, 137 (1987); Phys. Lett. **B222**, 285 (1989); Mod. Phys. Lett. **A4**, 877 (1989); L.L. Chau, Phys. Rep. **95**, 1 (1983); M. Gronau, O.F. Hernández, D. London and J.L. Rosner, Phys. Rev. **D50**, 4529 (1994); *ibid.* **52**, 6356, 6374 (1995).
- [152] X.Q. Li and B.S. Zou, Phys. Lett. **B399**, 297 (1997); S. Fajfer and J. Zupan, Int. J. Mod. Phys. **A14**, 4161 (1999); S. Fajfer, A. Prapotnik, P. Singer and J. Zupan, Phys. Rev. **D68**, 094012 (2003).
- [153] M. Ablikim, D.S. Du and M.Z. Yang, Phys. Lett. **B536**, 34 (2002); J.W. Li, M.Z. Yang and D.S. Du, hep-ph/0206154; M. Ablikim, D.S. Du and M.Z. Yang, hep-ph/0211413.
- [154] F. Buccella *et al.*, Z. Phys. C **55**, 243 (1992); Phys. Lett. B **302**, 319 (1993); Phys. Rev. **D51**, 3478 (1995); Phys. Lett. **B379**, 249 (1996).
- [155] B. Bajc, S. Fajfer, R.J. Oakes and S. Prelovšek, Phys. Rev. D **56**, 7207 (1997).
- [156] P. Zenczykowski, Acta Phys. Polon. **B28**, 1605 (1997).
- [157] H.Y. Cheng, Phys. Lett. **B335**, 428 (1994).
- [158] H.Y. Cheng, Eur. Phys. J. **C26**, 551 (2003).
- [159] J.L. Rosner, Phys. Rev. **D60**, 114026 (1999).
- [160] C.W. Chiang, Z. Luo, and J.L. Rosner, Phys. Rev. **D67**, 014001 (2003).
- [161] Y.S. Dai *et al.*, Phys. Rev. D **60**, 014014 (1999); J.M. Gerard, J. Pastieau, J. Weyers, Phys. Lett. B **436**, 363 (1998); P. Zenczykowski, Phys. Lett. B **460**, 390 (1999); K. Terasaki, Phys. Rev. D **59**, 114001 (1999); J.O. Eeg, S. Fajfer, J. Zupan, Phys. Rev. D **64**, 034010 (2001).
- [162] M. Lusignoli and A. Pugliese, hep-ph/0210071.
- [163] Y. L. Wu, M. Zhong and Y. F. Zhou, Eur. Phys. J. **C42**, 391 (2005).
- [164] A.N. Kamal, R.C. Verma and N. Sinha, Phys. Rev. D **43**, 843 (1991).
- [165] P. Bedaque, A. Das and V.S. Mathur, Phys. Rev. D **49**, 269 (1994).
- [166] I. Hinchliffe and T.A. Kaeding, Phys. Rev. D **54**, 914 (1996).
- [167] ARGUS Collaboration, H. Albrecht *et al.*, Phys. Lett. **B308**, 435 (1993).
- [168] CLEO Collaboration, H. Muramatsu *et al.*, Phys. Rev. Lett. **89**, 251802 (2002), *ibid.* **90**, 059901(E) (2003) ; S. Kopp *et al.*, Phys. Rev. **D63**, 092001 (2001).

- [169] E687 Collaboration, P.L. Frabetti *et al.*, Phys. Lett. **B351**, 591 (1995);*ibid.* **B331**, 217 (1994).
- [170] E691 Collaboration, J.C. Anjos *et al.*, Phys. Rev. **D48**, 56 (1993).
- [171] E791 Collaboration, E.M. Aitala *et al.*, Phys. Rev. Lett. **89**, 121801 (2002);*ibid.* **86**, 765 (2001);*ibid.* **86**, 770 (2001).
- [172] FOCUS Collaboration, J.M. Link *et al.*, Phys. Lett. **B541**, 227 (2002); talk presented by S. Erba at the DPF Meeting of the American Physical Society at Williamsburg, Virginia, May 24-28, 2002; talk presented by S. Malvezzi at ICHEP2002, Amsterdam, July 24-31, 2002; K. Stenson, hep-ex/0111083.
- [173] BaBar Collaboration, B. Aubert *et al.*, hep-ex/0207089.
- [174] V.V. Anisovich, V.A. Nikonov and A.V. Sarantsev, Phys. Atom. Nucl. **65**, 1545 (2002).
- [175] S. Spanier and N.A. Törnqvist, "Note on scalar mesons" in W.-M. Yao *et al.* (Particle Data Group), J. Phys. G **33**, 1 (2006).
- [176] A. Deandrea, R. Gatto, G. Nardulli, A.D. Polosa and N.A. Tornqvist, Phys. Lett. B **502**, 79 (2001).
- [177] F. Kleefeld, E. van Beveren, G. Rupp, M.D. Scadron, Phys. Rev. D **66**, 034007 (2002).
- [178] H.Y. Cheng, Phys. Rev. D **67**, 034024 (2003).
- [179] F. Buccella, M. Lusignoli, A. Pugliese, Phys. Lett. B **379**, 249 (1996).
- [180] R. Gatto, G. Nardulli, A.D. Polosa, N.A. Tornqvist, Phys. Lett. B **494**, 168 (2000).
- [181] I. Bediaga and M. Nielsen, Phys. Rev. D **68**, 036001 (2003).
- [182] A.N. Kamal and R.C. Verma, Phys. Rev. D**45**, 982 (1992).
- [183] X.Y. Pham and X.C. Vu, Phys. Rev. D**46**, 261 (1992).
- [184] T.N. Pham, Phys. Rev. D**46**, 2976 (1992).
- [185] A.N. Kamal, Q.P. Xu, and A. Czarnecki, Phys. Rev. D**49**, 1330 (1994).
- [186] A.C. Katoch and R.C. Verma, J. Phys. G**21**, 525 (1995).
- [187] H.J. Lipkin, Phys. Lett. B**515**, 81 (2001).
- [188] H.Y. Cheng, Phys. Rev. D**67**, 094007 (2003).
- [189] A.C. Katoch and R.C. Verma, Phys. Rev. D **49**, 1645 (1994); **55**, 7315(E) (1997).
- [190] J.H. Muñoz, A.A. Rojas and G. L. Castro, Phys. Rev. D **59**, 077504 (1999).

- [191] H.Y. Cheng, Phys. Rev. D **68**, 014015 (2003).
- [192] D. Asner, "Dalitz Plot Analysis Formalism" in W.-M. Yao *et al.* (Particle Data Group), J. Phys. G **33**, 1 (2006).
- [193] D. Asner, "Review of Charm Dalitz Plot Analyses" in W.-M. Yao *et al.* (Particle Data Group), J. Phys. G **33**, 1 (2006).
- [194] C.L.Y. Lee, M. Lu, and M.B. Wise, Phys. Rev. D**46**, 5040 (1992).
- [195] J. Schechter, A. Subbaraman, S. Surya, Int. J. Mod. Phys. A**9**, 3773 (1994).
- [196] B. Bajc, S. Fajfer, R.J. Oakes, T.N. Pham, Phys. Rev. D**58**, 054009 (1998).
- [197] P. Singer, Phys. Rev. D**16**, 2304 (1977); Nuovo Cim. **42A**, 25 (1977).
- [198] Yu. L. Kalinovsk and V.N. Pervushin, Sov. J. Nucl. Phys. **29**, 225 (1979).
- [199] H.Y. Cheng, Z. Phys. C**32**, 243 (1986).
- [200] L.L. Chau and H.Y. Cheng, Phys. Rev. D**41**, 1510 (1990).
- [201] F.J. Botella, S. Noguera, and J. Portolés, Phys. Lett. B**360**, 101 (1995).
- [202] T.M. Yan, H.Y. Cheng, C.Y. Cheung, G.L. Lin, Y.C. Lin, and H.L. Yu, Phys. Rev. D**46**, 1148 (1992); **55**, 5851(E) (1997).
- [203] M.B. Wise, Phys. Rev. D **45**, 2188 (1992); G. Burdman and J. Donoghue, Phys. Lett. B **280**, 287 (1992).
- [204] G. Burdman and J.F. Donoghue, Phys. Lett. B**280**, 287 (1992).
- [205] D.X. Zhang, Phys. Lett. B**382**, 421 (1996).
- [206] A.N. Ivanov and N.I. Troitskaya, Nuovo Cim. A**111**, 85 (1998).
- [207] H. Y. Cheng and K. C. Yang, Phys. Rev. D**66**, 054015 (2002).
- [208] J.G. Körner, M. Krämer, and D. Pirjol, Prog. Part. Nucl. Phys. **33**, 787 (1994) [hep-ph/9406359].
- [209] S. Bianco, F.L. Fabbri, D. Benson, and I.I. Bigi, Riv. Nuovo Cim. **26**, #7-8 (2003) [hep-ex/0309021].
- [210] D. Pirjol and T.M. Yan, Phys. Rev. D **56**, 5483 (1997).
- [211] BaBar Collaboration, B. Aubert *et al.*, Phys. Rev. Lett. **98**, 012001 (2007).
- [212] Belle Collaboration, R. Mizuk *et al.*, Phys. Rev. Lett. **98**, 262001 (2007).
- [213] R. Mizuk, talk presented at the XXXIIIth International Conference on High Energy Physics, July 26-August 2, 2006, Moscow, Russia.

- [214] CLEO collaboration, M. Artuso *et al.*, Phys. Rev. Lett. **86**, 4479 (2001).
- [215] N. Isgur and M.B. Wise, Phys. Rev. Lett. **66**, 1130 (1991).
- [216] H.Y. Cheng and C.K. Chua, Phys. Rev. **D 75**, 014006 (2007).
- [217] A. Selem, *A Diquark Interpretation of the Structure and Energies of Hadrons*, Senior thesis, M.I.T. (2005); A. Selem and F. Wilczek, hep-ph/0602128.
- [218] X.G. He, X.Q. Li, X. Liu, and X.Q. Zeng, Eur. Phys. J. **C 51**, 883 (2007).
- [219] Belle Collaboration, R. Chistov *et al.*, Phys. Rev. Lett. **97**, 162001 (2006).
- [220] BaBar Collaboration, B. Aubert *et al.*, hep-ex/0607042
- [221] Belle Collaboration, R. Mizuk *et al.*, Phys. Rev. Lett. **94**, 122002 (2005).
- [222] BaBar Collaboration, B. Aubert *et al.*, Phys. Rev. Lett. **97**, 232001 (2006).
- [223] SELEX Collaboration, M. Mattson *et al.*, Phys. Rev. Lett. **89**, 112001 (2002).
- [224] SELEX Collaboration, A. Ocherashvili *et al.*, Phys. Lett. B **628**, 18 (2005).
- [225] BaBar Collaboration, B. Aubert *et al.*, Phys. Rev. **D 74**, 011103 (2006).
- [226] S. Migura, D. Merten, B. Metsch, and H.R. Petry, Eur. Phys. J. A **28**, 41 (2006); D. Ebert, R.N. Faustov, and V.O. Galkin, Phys. Rev. D **66**, 014502 (2005); D.W. Wang and M.Q. Huang, Phys. Rev. D **68**, 034019 (2003); E. Jenkins, Phys. Rev. D **54**, 4515 (1996); *ibid.* **55**, 10 (1997); S. Capstick and N. Isgur, Phys. Rev. D **34**, 2809 (1986); L.A. Copley, N. Isgur, and G. Karl, Phys. Rev. D **20**, 768 (1979).
- [227] H.Y. Cheng, Phys. Lett. B **399**, 281 (1997).
- [228] Z. Guralnik, M. Luke, and A.V. Manohar, Nucl. Phys. **B390**, 474 (1993); E. Jenkins, Phys. Lett. B **315**, 431 (1993).
- [229] S. Tawfiq, P.J. O'Donnell, and J.G. Körner, Phys. Rev. D **58**, 054010 (1998).
- [230] M.A. Ivanov, J.G. Körner, V.E. Lyubovitskij, and A.G. Rusetsky, Phys. Rev. D **60**, 094002 (1999).
- [231] M.Q. Huang, Y.B. Dai, and C.S. Huang, Phys. Rev. D **52**, 3986 (1995); Phys. Rev. D **55**, 7317(E) (1997).
- [232] C. Albertus, Hernández, J. Nieves, and J.M. Verde-Velasco, Phys. Rev. D **72**, 094022 (2005).
- [233] C.G. Boyd, M. Lu, and M.J. Savage, Phys. Rev. D **55**, 5474 (1997).
- [234] T. Ito and Y. Matsui, Prog. Theor. Phys. **96**, 659 (1996).
- [235] CLEO Collaboration, P. Avery *et al.*, Phys. Rev. Lett. **75**, 4364 (1995); L. Gibbons *et al.*, Phys. Rev. Lett. **77**, 810 (1996).

- [236] S.L. Zhu, Phys. Rev. D **61**, 114019 (2000).
- [237] A.E. Blechman, A.F. Falk, D. Pirjol, and J.M. Yelton, Phys. Rev. D **67**, 074033 (2003).
- [238] P. Cho, Phys. Rev. D **50**, 3295 (1994).
- [239] CLEO Collaboration, K.W. Edwards *et al.*, Phys. Rev. Lett. **74**, 3331 (1995).
- [240] I.I. Bigi, hep-ph/9508408, hep-ph/9612293; G. Bellini, I.I. Bigi, and P.J. Dornan, Phys. Rep. **289**, 1 (1997).
- [241] B. Blok and M. Shifman, in *Proceedings of the Third Workshop on the Physics at a Tau-Charm Factory*, Marbella, Spain, June 1993, eds. J. Kirkby and R. Kirkby (Editions Frontieres, 1994) [hep-ph/9311331].
- [242] N. Bilić, B. Guberina, and J. Trampetić, Nucl. Phys. B **248**, 261 (1984).
- [243] B. Guberina, R. Rückl, and J. Trampetić, Z. Phys. C **33**, 297 (1986).
- [244] M.A. Shifman and M.B. Voloshin, Sov. J. Nucl. Phys. **41**, 120 (1985); Sov. Phys. JETP **64**, 698 (1986).
- [245] R. Rückl, Phys. Lett. B **120**, 449 (1983).
- [246] I.I. Bigi, N.G. Uraltsev, and A.I. Vainshtein, Phys. Lett. B **293**, 430 (1992); B **297**, 477(E) (1992).
- [247] B. Blok and M. Shifman, Nucl. Phys. B **399**, 441 (1993); B **399**, 459 (1993).
- [248] I.I. Bigi, M. Shifman, N.G. Uraltsev, and A. Vainshtein, Phys. Rev. Lett. **71**, 496 (1993); A. Manohar and M.B. Wise, Phys. Rev. D **49**, 1310 (1994); B. Blok, L. Koyrakh, M. Shifman, and A. Vainshtein, Phys. Rev. D **49**, 3356 (1994).
- [249] J. Chay, H. Georgi, and B. Grinstein, Phys. Lett. B **247**, 399 (1990); J. Chay and S.J. Rey, Z. Phys. C **68**, 431 (1995).
- [250] M.E. Luke, Phys. Lett. B **252**, 447 (1990).
- [251] For a review of the nonperturbative HQET parameters, see M. Neubert, Int. J. Mod. Phys. A **11**, 4173 (1996).
- [252] H.Y. Cheng, Phys. Rev. D **56**, 2783 (1997).
- [253] M.B. Voloshin, Phys. Lett. B **385**, 369 (1996).
- [254] Q. Hokim and X.Y. Pham, Phys. Lett. B **122**, 297 (1983).
- [255] J.L. Rosner, Phys. Lett. B **379**, 267 (1996).
- [256] B. Guberina and B. Melić, Eur. Phys. J. C **2**, 697 (1998).
- [257] CLEO Collaboration, M. Artuso *et al.*, Phys. Rev. Lett. **95**, 251801 (2005).

- [258] M. Neubert and C.T. Sachrajda, Nucl. Phys. B **483**, 339 (1997).
- [259] V. Chernyak, Nucl. Phys. **B457**, 96 (1995).
- [260] J.G. Körner and M. Krämer, Z. Phys. C **55**, 659 (1992).
- [261] J.G. Körner, G. Kramer, and J. Willrodt, Phys. Lett. B **78**, 492 (1978); Z. Phys. C **2**, 117 (1979); B. Guberina, D. Tadić, and J. Trampetić, Z. Phys. C **13**, 251 (1982); F. Hussain and M.D. Scadron, Nuovo Cimento, A **79**, 248 (1984); F. Hussain and K. Khan, *ibid.* A **88**, 213 (1985); R.E. Karlsen and M.D. Scadron, Europhys. Lett. **14**, 319 (1991); D. Ebert and W. Kallies, Phys. Lett. B **131**, 183 (1983); B **148**, 502(E) (1984); Yad. Fiz. **40**, 1250 (1984); Z. Phys. C **29**, 643 (1985); H.Y. Cheng, Z. Phys. C **29**, 453 (1985); Yu.L. Kalinovsky, V.N. Pervushin, G.G. Takhtamyshev, and N.A. Sarikov, Sov. J. Part. Nucl. **19**, 47 (1988); S. Pakvasa, S.F. Tuan, and S.P. Rosen, Phys. Rev. D **42**, 3746 (1990); G. Kaur and M.P. Khanna, Phys. Rev. D **44**, 182 (1991); *ibid.* D **45**, 3024 (1992); G. Turan and J.O. Eeg, Z. Phys. C **51**, 599 (1991).
- [262] H.Y. Cheng and B. Tseng, Phys. Rev. D **46**, 1042 (1992); D **55**, 1697(E) (1997).
- [263] H.Y. Cheng and B. Tseng, Phys. Rev. D **48**, 4188 (1993).
- [264] Q.P. Xu and A.N. Kamal, Phys. Rev. D **46**, 270 (1992).
- [265] H.Y. Cheng, Phys. Lett. B **289**, 455 (1992).
- [266] M.J. Savage and R.P. Springer, Phys. Rev. D **42**, 1527 (1990).
- [267] S.M. Sheikholeslami, M.P. Khanna, and R.C. Verma, Phys. Rev. D **43**, 170 (1991); M.P. Khanna and R.C. Verma, Phys. Rev. D **53**, 3723 (1996).
- [268] L.L. Chau, in *Proceedings of the VPI Workshop on Weak Interactions*, AIP Conf. Proc. No. 72, Particles and Fields, Subseries No. 23, eds. G.B. Collins, L.N. Chang, J.R. Ficence, Blacksburg, Virginia, December 3–6, 1980; Phys. Rep. **95**, 1 (1983).
- [269] L.L. Chau and H.Y. Cheng, Phys. Rev. Lett. **56**, 1655 (1986); Phys. Rev. D **36**, 137 (1987); *ibid.* D **39**, 2788 (1989); Phys. Lett. B **222**, 285 (1987); Mod. Phys. Lett. A **4**, 877 (1989).
- [270] L.L. Chau, H.Y. Cheng, and B. Tseng, Phys. Rev. D **54**, 2132 (1996).
- [271] Y. Kohara, Phys. Rev. D **44**, 2799 (1991).
- [272] M. Fukugita, T. Inami, N. Sakai, and S. Yazaki, Phys. Lett. B **72**, 237 (1977); D. Tadić and J. Trampetić, *ibid.* B **114**, 179 (1982); M. Bauer and B. Stech, *ibid.* B **152**, 380 (1985).
- [273] A.J. Buras, J.-M. Gérard, and R. Rückl, Nucl. Phys. **B268**, 16 (1986).
- [274] B. Blok and M. Shifman, Sov. J. Nucl. Phys. **45**, 35, 301, 522 (1987).
- [275] A. Chodos, R.L. Jaffe, K. Johnson, and C.B. Thorn, Phys. Rev. D **10**, 2599 (1974); T. DeGrand, R.L. Jaffe, K. Johnson, and J. Kiskis, Phys. Rev. D **12**, 2060 (1975).

- [276] K.K. Sharma and R.C. Verma, Eur. Phys. J. C **7**, 217 (1999).
- [277] P. Żenczykowski, Phys. Rev. D **50**, 5787, 3285, 402 (1994).
- [278] M.A. Ivanov, J.G. Körner, V.E. Lyubovitskij, and A.G. Tusetsky, Phys. Rev. D **57**, 1 (1998).
- [279] FOCUS Collaboration, J.M. Link *et al.*, Phys. Lett. B **634**, 165 (2006).
- [280] CLEO Collaboration, M. Bishai *et al.*, Phys. Lett. B **350**, 256 (1995).
- [281] Q.P. Xu and A.N. Kamal, Phys. Rev. D **46**, 3836 (1992).
- [282] H.Y. Cheng, Phys. Rev. D **56**, 2799 (1997).
- [283] BaBar Collaboration, B. Aubert *et al.*, Phys. Rev. D **75**, 052002 (2007).
- [284] T. Uppal, R.C. Verma, and M.P. Khana, Phys. Rev. D **49**, 3417 (1994).
- [285] H.Y. Cheng and B. Tseng, Phys. Rev. D **53**, 1457 (1996); Phys. Rev. D **55**, 1697(E) (1997).
- [286] FOCUS Collaboration, J.M. Link *et al.*, Phys. Lett. B **571**, 139 (2003).
- [287] H.Y. Cheng, C.Y. Cheung, G.L. Lin, Y.C. Lin, T.M. Yan, and H.L. Yu Phys. Rev. D **46**, 5060 (1992).
- [288] M.B. Voloshin, Phys. Lett. B **476**, 297 (2000).
- [289] R. Pérez-Marcial, R. Huerta, A. Garcia, and M. Avila-Aoki, Phys. Rev. D **40**, 2955 (1989); *ibid.* D **44**, 2203(E) (1991).
- [290] R. Singleton, Phys. Rev. D **43**, 2939 (1991).
- [291] M.A. Ivanov, V.E. Lyubovitskij, J.G. Körner, and P. Kroll, Phys. Rev. D **56**, 348 (1998).
- [292] C.W. Luo, Eur. Phys. J. C **1**, 235 (1998).
- [293] R.S. Marques de Carvalho *et al.*, Phys. Rev. D **60**, 034009 (1999).
- [294] M.Q. Huang and D.W. Wang, hep-ph/0608170.
- [295] CLEO Collaboration, J.W. Hinson *et al.*, Phys. Rev. Lett. **94**, 191801 (2005).
- [296] H.Y. Cheng, C.Y. Cheung, G.L. Lin, Y.C. Lin, T.M. Yan, and H.L. Yu Phys. Rev. D **47**, 1030 (1993).
- [297] M.C. Bañuls, A. Pich, and I. Scimemi, Phys. Rev. D **61**, 094009 (2000).
- [298] S. Tawfiq, J.G. Körner, and P.J. O'Donnell, Phys. Rev. D **63**, 034005 (2001).
- [299] M.J. Savage, Phys. Lett. B **345**, 61 (1995).

- [300] H.Y. Cheng, C.Y. Cheung, G.L. Lin, Y.C. Lin, T.M. Yan, and H.L. Yu Phys. Rev. D **49**, 5857 (1994).
- [301] M. Lu, M.J. Savage, and J. Walden, Phys. Lett. B **369**, 337 (1996).
- [302] Z.A. Baccouche, C.K. Chow, T.D. Cohen, and B.A. Gelman, Nucl. Phys. A **696**, 638 (2001).
- [303] A.N. Kamal and Riazuddin, Phys. Rev. D **28**, 2317 (1983).
- [304] A.N. Kamal and R.C. Verma, Phys. Rev. D **26**, 190 (1982).
- [305] L.C. Hua, Phys. Rev. D **26**, 199 (1982).
- [306] H.Y. Cheng, C.Y. Cheung, G.L. Lin, Y.C. Lin, T.M. Yan, and H.L. Yu Phys. Rev. D **51**, 1199 (1995).
- [307] T. Uppal and R.C. Verma, Phys. Rev. D **47**, 2858 (1993).
- [308] I. I. Bigi and A. I. Sanda, Phys. Lett. B **171**, 320 (1986).
- [309] A. F. Falk, Y. Nir, and A. Petrov, JHEP12, 019 (1999); Y. Nir, Lectures given at 27th SLAC Summer Institute on Particle Physics: *CP* violation in and beyond the Standard Model (SSI 99), Stanford, California, 7-16 Jul. 1999. Published in Trieste 1999, *Particle Physics*, pp. 165-243.
- [310] CLEO Collaboration, R. Godang, *et al.*, Phys. Rev. Lett. **84**, 5038 (2000).
- [311] S. Bianco, F. Fabbri, D. Benson, I. Bigi, *la Riv. Nuov. Cim.* **26** # 7& 8 (2003).
- [312] A. F. Falk *et al.*, Phys. Rev. **D65**, 054034 (2002).
- [313] A. A. Petrov, hep-ph/0311371; for the most updated version, see <http://www.physics.wayne.edu/~apetrov/mixing/>.
- [314] S. Bergmann, *et al.*, Phys. Lett. **B 486**, 418(2000).
- [315] H. Gorgia, Phys. Lett. **B 297**, 353 (1992).
- [316] T. Ohl *et al.*, Nucl. Phys. **B 403**, 605 (1993).
- [317] I. I. Bigi and N. Uraltsev, Nucl. Phys. **B 592**, (92 (2001).
- [318] Belle Collaboration, U. Bitenc, *et al.*, Phys. Rev. **D 72**, 071101() (2005).
- [319] [http://www.slac.stanford.edu/xorg/hfag/charm/FPCP07/results\\_mixing.html](http://www.slac.stanford.edu/xorg/hfag/charm/FPCP07/results_mixing.html)
- [320] J. J. Aubert, *et al.*, Phys. Lett. **B 106**, 419 (1981).
- [321] A. Benvenuti, *et al.*, Phys. Lett. **B 158**, 531 (1985).
- [322] W. C. Louis *et al.*, Phys. Rev. Lett. **56**, 1027 (1986).

- [323] E791, E. M. Aitala *et al.*, Phys. Rev. Lett. **77**, 2384 (1996).
- [324] CLEO Collaboration, C. Cawlfie, *et al.*, Phys. Rev. **D 71**, 077101 (2005).
- [325] BaBar Collaboration, B. Aubert, *et al.*, Phys. Rev. **D 70**, 091102(R) (2004).
- [326] BaBar Collaboration, B. Aubert, *et al.*, arXiv:0705.0704v2 [hep-ex].
- [327] I. I. Bigi, in: *Proceed. of the Tau-Charm Workshop*, L.V. Beers (ed.), SLAC-Report-343, 1989, p. 169.
- [328] E791 Collaboration, Phys. Rev. **D57**, 13 (1998).
- [329] FOCUS, J. M. Link, *et al.*, Phys. Lett. **B 618**, 23 (2005).
- [330] Belle Collaboration, L. Zhang *et al.*, Phys. Rev. Lett. **96**, 151801 (2006); Belle Collaboration, J. Li *et al.*, Phys. Rev. Lett. **94**, 071801 (2005).
- [331] BaBar Collaboration, B. Aubert, *et al.*, Phys. Rev. Lett. **98**, 211802 (2007).
- [332] CDF Collaboration, A. Abulencia, *et al.*, hep-ex/0605027.
- [333] M. G. Wilson, hep-ex/0605046; BaBar Collaboration, B. Aubert, *et al.*, hep-ex/0607090.
- [334] D. Asner, W. M. Sun, *Phys. Rev. D73* (2006) 034024.
- [335] FNAL-E791, E. M. Aitala *et al.*, Phys. Rev. **D57**, 13 (1998).
- [336] CLEO Collaboration, G. Brandenburg *et al.*, Phys. Rev. Lett. **87**, 071802 (2001); CLEO, S. A. Dytman *et al.*, Phys. Rev. **D 64**, 111101 (2001).
- [337] Belle Collaboration, X. C. Tian *et al.*, Phys. Rev. Lett. **95**, 231801 (2005).
- [338] J. Link *et al.*, (FOCUS), Phys. Lett. **B485**, 62(2000).
- [339] S. E. Csorna, *et al.*, (CLEO), Phys. Rev. D **65**, 092001 (2002).
- [340] K. Abe, *et al.* (Belle), Phys. Rev. Lett. **88**, 162001 (2002).
- [341] K. Abe, *et al.*, (Belle), "Measurement of the  $D^0 - \overline{D}^0$  Lifetime Difference Using  $D^0 \rightarrow K\pi/KK$  Decays", submitted to Lepton-Photon Conference [Belle-CONF-347] (2003).
- [342] M. Staric *et al.*, Phys. Rev. Lett. **98**, 211803 (2007).
- [343] B. Aubert, *et al.*, (BaBar), Phys. Rev. Lett. **71**, 077101 (2005).
- [344] B. Aubert, *et al.*, (BaBar), arXiv:0712.2249v1 [hep-ex].
- [345] B. Aubert, *et al.*, (BaBar), Phys. Rev. Lett. **91**, 121801 (2003).
- [346] D. M. Asner, *et al.*, (CLEO), Phys. Rev. D **72**, 012001 (2005).

- [347] H. Muramatsu *et al.*, (CLEO), Phys. Rev. Lett. **89**, 251802(2002).
- [348] L. M. Zhang, *et al.*, (BELLE), Phys. Rev. Lett. **99**, 131803 (2007).
- [349] B. Aubert, *et al.*, (BaBar),hep-ex/0607104.
- [350] Z. Ligeti, "Mixing and  $CP$  violation in the  $D^0$  and  $B_s^0$  systems", arXiv:0706.0919 [hep-ph], (2007).
- [351] A. Giri, Y. Grossman, A. Soffer and J. Zupan, Phys. Rev. **D 68** 054018 (2003).
- [352] M. Goldhaber and J. L. Rosner, Phys. Rev. **D 15**, 1254 (1977).
- [353] Z. Z. Xing, Phys. Rev. **D 53**, 204 (1996); Z. Z. Xing, Phys. Lett. **B 372**, 317 (1996); Z. Z. Xing, Phys. Lett. **B 379**, 257 (1996); Z. Z. Xing, Phys. Rev. **D 55**, 196 (1997); Z. Z. Xing, Phys. Lett. **B 463**, 323 (1999).
- [354] M. Gronau, Y. Grossman, and J. Rosner, Phys. Lett. **B 508**, 37 (2001).
- [355] D. Atwood and A. A. Petrov, Phys. Rev. **D 71**, 054032 (2005).
- [356] D. M. Asner and W. M. Sun, Phys. Rev. **D 73**, 034024 (2006).
- [357] H. Nelson, Talk given at the 19th International Symposium on Lepton and Photon Interactions at High-Energies, Stanford, CA, 9-14 August, 1999, UCSB-HEP-99-08, hep-ex/9908021.
- [358] X. D. Cheng *et. al.*, arXiv:0704.0120 [hep-ex]
- [359] B. Aubert, *et. al.*, (BaBar Collaboration), hep-ex/0703020.
- [360] K. Abe *et. al.*, (Belle Collaboration), hep-ex/0703036.
- [361] Y. Nir, hep-ph/0703235.
- [362] L. M. Zhang *et. al.*, (Belle Collaboration), Phys. Rev. Lett. **96**, 151801 (2006).
- [363] M. Staric, Talk given at the 42th Renocontres De Moriond On Electroweak Interactions And Unified Theories, March 10-17, 2007, La Thuile, Italy.
- [364] S. Bergmann, Y. Grossman, Z. Ligeti, Y. Nir and A. A. Petrov, Phys. Lett. **B486**, 418(2000).
- [365] D. Atwood, A. A. Petrov, Phys. Rev. **D71**, 054032 (2005).
- [366] D. M. Asner and W. M. Sun Phys. Rev. **D73**, 034024 (2006);D. M. Asner *et. al.*, Int. J. Mod. Phys. **A21**, 5456 (2006); W. M. Sun, hep-ex/0603031, AIP Conf. Proc. 842:693-695 (2006).
- [367] R. M. Baltrusaitis, *et. al.*, (MARK III Collaboration), Phys. Rev. Lett. **56**, 2140(1986).
- [368] J. Adler, *et. al.*, (MARK III Collaboration), Phys. Rev. Lett. **60**, 89 (1988).

- [369] Y. Z. Sun *et. al.*, to appear at HEP & NP **31**, 1 (2007).
- [370] J. H. Christenson, J. W. Croin, V. L. Fitch and R. Turlay, Phys. Rev. Lett. **13**, 138 (1964).
- [371] Y. Nir, hep-ph/0510413.
- [372] A. D. Sakharov, Pisma Zh. Eksp. Teor. Fiz. 5, 32 (1967) [JETP Lett. **5**, 24 (1967)].
- [373] Y. Nir and N. Seiberg, Phys. Lett. **B309**, 337 (1993).
- [374] G. Altarelli and F. Feruglio, hep-ph/0306265.
- [375] A. De Rujula, M. B. Gavela and P. Hernandez, Nucl. Phys. **B547**, 21 (1999); K. Dick, M. Freund, M. Lindner and A. Romanino, Nucl. Phys. **B562**, 29 (1999); P. Huber, M. Lindner, M. Rolinec, T. Schwetz and W. Winter, hep-ph/0403068.
- [376] M. Leurer, Y. Nir and N. Seiberg, Nucl. Phys. **B420**, 468 (1994).
- [377] Y. Grossman, A. L. Kagan and Y. Nir, hep-ph/0609178.
- [378] D. S. Du, hep-ph/0608313;
- [379] I. I. Bigi, Talk at the first International Workshop on  $\tau$ -Charm Physics (Charm2006), 6-7 June 2006, Beijing, hep-ph/0608073.
- [380] F. Buccella *et al.*, hep-ph/9411286.
- [381] B. Aubert *et al.* (BABAR Collab.), Preprint arXiv:0709.2715 (2007).
- [382] D. Acosta *et al.* (CDF Collaboration), Phys. Rev. Lett. **94**, 122001(2005).
- [383] S. E. Csorna *et al.* (CLEO Collab.), Phys. Rev. D 65, 092001 (2002).
- [384] J. M. Link *et al.* (FOCUS Collab.), Phys. Lett. B 491, 232 (2000), Erratum-ibid. B495: 443 (2000).
- [385] E. M. Aitala *et al.* (E791 Collab.), Phys. Lett. B 421, 405 (1998).
- [386] J. E. Bartelt *et al.* (CLEO Collab.), Phys. Rev. D 52, 4860 (1995).
- [387] P. L. Frabetti *et al.* (E687 Collab.), Phys. Rev. D 50, 2953 (1994).
- [388] S. E. Csorna *et al.* (CLEO Collab.), Phys. Rev. D 65, 092001 (2002).
- [389] G. Bonvicini *et al.* (CLEO Collab.), Phys. Rev. D 63, 071101 (2001).
- [390] D. Cronin-Hennessy, *et al.* (CLEO Collaboration), Phys. Rev. **D72**, 031102 (2005).
- [391] S. Dobbs *et al.* (CLEO Collab.), Preprint arXiv:0709.3783 (2007).
- [392] S. Kopp, *et al.* (CLEO Collaboration), Phys. Rev. **D63**, 092001 (2001).
- [393] X. C. Tian, *et al.* (Belle Collaboration), Phys. Rev. Lett. **95**, 231801 (2005).

- [394] G. Brandenburg *et al.* (CLEO Collab.), Phys. Rev. Lett. 87, 071802 (2001).
- [395] D. M. Asner *et al.* (CLEO Collaboration), Phys. Rev. **D70**, 091101 (2004).
- [396] J. M. Link *et al.* (FOCUS Collaboration), Phys. Lett. **B622**, 239 (2005).
- [397] J. M. Link *et al.* (FOCUS Collab.), Phys. Rev. Lett. 88, 041602 (2002), Erratum-  
ibid. 88: 159903(2002).
- [398] E. M. Aitala *et al.* (E791 Collab.), Phys. Lett. B 403, 377 (1997).
- [399] B. Aubert *et al.*, (BaBar Collaboration), Phys. Rev. **D71**, 091101 (2005).
- [400] M. Staric *et al.* (BELLE Collab.), Phys. Rev. Lett. 98, 211803 (2007).
- [401] B. Aubert *et al.* (BABAR Collab.), Preprint arXiv:0712.2249 (2007).
- [402] A. A. Petrov, Nucl. Phys. Proc. Suppl. **142**, 333 (2005) [hep-ph/0409130].
- [403] I. I. Bigi, Talk in KAON2001: International Conference on  $CP$  violation, (2001) [hep-ph/0107102].
- [404] D. Cinabro, "Interference Effects in  $D$  Meson Decays" Presented at Flavor Physics and  $CP$  Violation, April 9-12, 2006, Vancouver, BC, Canada.
- [405] A. J. Buras, hep-ph/0505175.
- [406] H. B. Li and M. Z. Yang, Phys. Rev. **D74**, 094016 (2006).
- [407] F. Buccella, M. Lusignoli, and A. Pugliese, Phys. Lett. **B379**, 249 (1996).
- [408] F. Buccella, *et al.* Phys. Lett. **B302**, 319 (1993).
- [409] The BaBar Collab., B. Aubert *et al.*, hep-ex/0703020.
- [410] R. H. Dalitz, Phil. Mag. 44, 1068 (1953).
- [411] J. D. Jackson, Nuovo Cim. 34, 1644 (1964).
- [412] B. Kayser, Nucl. Phys. B (Proc. Suppl.) **13**, 487 (1990); G. Valencia, Phys. Rev. **D 39**, 3339 (1989).
- [413] A. Datta and A. London, Int. J. of Mod. Phys. **A 19**, 2505 (2004).
- [414] L.M. Sehgal and M. Wanninger, *Phys. Rev. D46* (1992) 1035; *Phys. Rev. D46* (1992) 5209 (E); see also the earlier papers: A.D. Dolgov and L.A. Ponomarev, *Sov. J. Nucl. Phys.* **4** (1967) 262; D.P. Majumdar and J. Smith; *Phys. Rev.* **187** (1969) 2039.
- [415] I.I. Bigi, in: *Proceed. of the International Workshop on Tau-Charm Physics*', Beijing (China), June 2006, *Intern. Journ. of Mod. Physics A* **21** (2006) 5404.
- [416] FOCUS Collab., J.M. Link *et al.*, *Phys. Lett. B622* (2005) 239.

- [417] I.I. Bigi, hep-ph/0703132.
- [418] G. Burdman, E. Golowich, J. Hewett and S. Pakvasa, Phys. Rev. **D66**, 014009(2002). And references therein.
- [419] G. Burdman, E. Golowich, J. Hewett and S. Pakvasa, Phys. Rev. **D52**, 6383 (1995).
- [420] C. Greub, T. Hurth, M. Misiak, and D. Wyler, Phys. Lett. B382, 415 (1996).
- [421] C. Bajc, S. Fajfer and R. Oakes, Phys. Rev. D54, 5883 (1996); S. Fajfer, S. Prevlosek and P. Singer, Eur. Phys. J. C6, 471 (1999).
- [422] O. Tajima et. al. (the Belle Collaboration), Phys. Rev. Lett. 92, 101803 (2004).
- [423] G. Buchalla, A. J. Buras and M. E. Lautenbacher, Rev. Mod. Phys. **68**, 1125 (1996).
- [424] T. Inami and C.S. Lim, Prog. Theor. Phys. **65**, 1772 (1981).
- [425] Such references include C. Greub *et al.*, Phys. Lett. **B382**, 415 (1996); C-H. V. Chang, G-L. Lin and Y-P. Yao, Phys. Lett. **B415**, 395 (1997); L. Reina, G. Ricciardi and A. Soni, Phys. Rev. **D56**, 5805 (1997); D. Choudhury and J. Ellis, Phys. Lett. **B433**, 102 (1998); S. Fajfer, P. Singer and J. Zupan, Phys. Rev. **D64**, 074008 (2001); C. S. Lim, T. Morozumi and A. I. Sanda, Phys. Lett. **B218**, 343 (1989); N.G. Deshpande, J. Trampetic, and K. Panrose, Phys. Rev. **D39**, 1461 (1989); P. Singer and D.-X. Zhang, Phys. Rev. **D55**, R1127 (1997).
- [426] L.J. Hall, V.A. Kostelecky, and S. Raby, Nucl. Phys. **B267**, 415 (1986).
- [427] For a comprehensive study of FCNC effects in supersymmetry see, S. Bertolini, F. Borzumati, A. Masiero, and G. Ridolfi, Nucl. Phys. **B193**, 591 (1991); F. Gabbiani, E. Gabrielli, A. Masiero and L. Silvestrini, Nucl. Phys. **B477**, 321 (1996); J.L. Hewett and J.D. Wells, Phys. Rev. **D55**, 5549 (1997); P. Cho, M. Misiak, and D. Wyler, Phys. Rev. **D54**, 3329 (1996). For a review see M. Misiak, S. Pokorski and J. Rosiek, in “*Heavy Flavors II*”, eds. A.J. Buras and M. Lindner, Adv. Ser. Direct. High Energy Phys. **15**, 795 (1998).
- [428] *E.g.*, see J. Ellis and D.V. Nanopoulos, Phys. Lett. **110B**, 44 (1982).
- [429] For a recent review, see, B. C. Allanach, A. Dedes and H. K. Dreiner, Phys. Rev. **D60**, 075014 (1999).
- [430] N. Arkani-Hamed, S. Dimopoulos, and G. Dvali, Phys. Lett. **B429**, 263 (1998), and Phys. Rev. **D59**, 086004 (1999); I. Antoniadis, N. Arkani-Hamed, S. Dimopoulos, and G. Dvali, Phys. Lett. **B436**, 257 (1998).
- [431] I. Antoniadis, Phys. Lett. **B246**, 377 (1990); J. Lykken, Phys. Rev. **D54**, 3693 (1996); E. Witten, Nucl. Phys. **B471**, 135 (1996); P. Horava and E. Witten, Nucl. Phys. **B460**, 506 (1996), *ibid.*, **B475**, 94 (1996).
- [432] T.G. Rizzo and J.D. Wells, Phys. Rev. **D61**, 016007 (2000); P. Nath and M. Yamaguchi, Phys. Rev. **D60**, 116006 (1999); M. Masip and A. Pomarol, Phys. Rev. **D60**, 096005 (1999); W.J. Marciano, Phys. Rev. **D60**, 093006 (1999).

- [433] See, for example, K. Agashe, N.G. Deshpande, G.H. Wu, Phys. Lett. **B514**, 309 (2001).
- [434] L. Randall and R. Sundrum, Phys. Rev. Lett. **83**, 3370 1999 , and *ibid.*, 4690, (1999).
- [435] J.L. Hewett, F.J. Petriello, and T.G. Rizzo, SLAC-PUB-9146; arXiv:hep-ph/0203091.
- [436] Q. He *et al.*, Phys. Rev. Lett. **95** (2005) 221802.
- [437] J. M. Link *et al.*, Phys. Lett. **B572** (2003) 21.
- [438] E. M. Aitala *et al.*, Phys. Lett. **B462** (1999) 401.
- [439] P. L. Frabetti *et al.*, Phys. Lett. **B398** (1997) 239.
- [440] G. Burdman *et al.*, Phys. Rev. **D52** (1995) 6383; Phys. Rev. **D66** (2002) 014009.
- [441] G. Burdman and I. Shipsey, Ann. Rev. Nucl. Part. Sci. **53** (2003) 431; S. Bianco, F. L. Fabbri, D. Benson and I. Bigi, Riv. Nuovo Cim. **26N7** (2003) 1.
- [442] T. E. Coan *et al.*, Phys. Rev. Lett. **90** (2003) 101801.
- [443] A. Freyberger *et al.*, Phys. Rev. Lett. **76** (1996) 3065; erratum, Phys. Rev. Lett. **77** (1996) 2147.
- [444] A. Korn *et al.*, hep-ex/0305054.
- [445] K. Kodama *et al.*, Phys. Lett. **B345** (1995) 85.



# Part VI

## $\tau$ Physics

### Conveners

Antonio Pich, Changzheng Yuan

### Contributors

I. I. Bigi, I. R. Boyko, D. Dedovich, C. D. Fu,  
X. H. Mo, A. Pich, A. Stahl, Y. K. Wang,  
and C. Z. Yuan



# Chapter 28

## Tau Physics near Threshold<sup>1</sup>

### 28.1 Introduction

The tau-charm factory currently under construction at the Institute of High Energy Physics in Beijing will give us excellent opportunities for interesting physics with tau leptons. Such an  $e^+e^-$  collider, running in the energy regime of the tau and charm thresholds, will produce large samples of tau leptons. It could produce up to 50 million tau pairs per year, but this is not the real advantage of the tau-charm factory. Today the  $B$ -factories have tau samples of several hundred million tau pairs and the LHC will produce  $10^{12}$  tau pairs per year even at low luminosity. The advantages of the tau-charm factory are the excellent experimental conditions that will allow the experiments to analyze many aspects of the tau decays with low systematics. Aspects that are hardly accessible at other machines.

The cross section for the production of tau pairs rises above threshold like

$$\sigma(s) = \frac{4\pi\alpha^2}{3s} \beta \frac{3 - \beta^2}{2}, \quad (28.1.1)$$

where  $s$  is the center-of-mass energy and  $\beta$  the velocity of one of the tau leptons in the overall rest frame. The formula is the result of a first-order calculation. More detailed calculations are available [1]. The main backgrounds are the production of light quark pairs ( $u$ -,  $d$ -, and  $s$ -quarks) with a cross section of approximately 173.6 nbarn/ $s$  ( $s$  in GeV $^2$ ) and charm production. For tau physics there are four interesting running points in this region:

- 1)  $\sqrt{s} = 3.50$  GeV

This energy is just below the production threshold for tau pairs. It allows one to measure and investigate the light quark background. The experimentally determined background at this point can be extrapolated to the other running points with the help of a Monte Carlo program. The background varies only slightly with the center-of-mass energy and no significant systematic error is expected from the extrapolation.

- 2)  $\sqrt{s} = 3.55$  GeV

This is right at the production threshold and the tau leptons are produced at rest.

---

<sup>1</sup>By Achim Stahl

The cross section is different from zero due to the Coulomb attraction between the  $\tau^+$  and  $\tau^-$ . The cross section at threshold is 0.1 nbarn for ideal beams. For a realistic number the energy spread of the machine must be taken into account. This is the ideal energy for the study of tau decays as explained in the following section.

- 3)  $\sqrt{s} = 3.69$  GeV

This is an energy above the  $\Psi(2S)$ , but still below the production threshold for open charm. The tau cross section has risen to 2.4 nbarn. The background situation is as good as at point 2, but the tau leptons are no longer produced at rest. The kinematic identification described in the following section will not work here.

- 4)  $\sqrt{s} = 4.25$  GeV

At this energy the cross section for tau production is at its maximum (3.5 nbarn). But here there is substantial charm background on top of the light quark background.

## 28.2 Tau Production at Threshold

Data taking right at the tau production threshold, where the tau leptons are produced at rest, is the most favored situation. In addition to its two leptonic decay modes, the tau lepton decays with a branching fraction of 64.8% [2] into a tau neutrino plus hadrons. The decay can be summarized as a two-body decay  $\tau^- \rightarrow \nu_\tau \text{had}^-$  where the hadronic system  $\text{had}^-$  might fragment into several mesons.<sup>2</sup> This description is kinematically correct even if no identifiable intermediate resonance is present. As a consequence, the hadronic system has a fixed energy and momentum in the tau rest frame:

$$E_{\text{had}}^* = \frac{m_\tau^2 + m_{\text{had}}^2}{2 m_\tau}, \quad p_{\text{had}}^* = \frac{m_\tau^2 - m_{\text{had}}^2}{2 m_\tau}, \quad (28.2.2)$$

where  $m_\tau = 1776.99$  MeV is the mass of the tau lepton and  $m_{\text{had}}$  the invariant mass of the hadronic system in this particular decay. A mass of the tau neutrino in the sub-eV range is negligible in this context. At the production threshold, the tau leptons are at rest in the center-of-mass system and the hadron energy in this system is directly given by  $E_{\text{had}}^*$ . Above threshold the energy of the hadronic system is given by

$$E_{\text{had}} = \gamma E_{\text{had}}^* + \beta \gamma p_{\text{had}}^* \cos \theta^*, \quad (28.2.3)$$

with the Lorentz factors  $\beta$  and  $\gamma$  and the unknown decay angle  $\theta^*$ . The monoenergetic spectrum at threshold broadens under the influence of the angle  $\theta^*$ . For example, for a  $\rho$  meson with mass of 770 MeV, the the  $E_{\text{had}}^* = 1055$  MeV value at threshold is smeared out to have a  $\pm 24$  MeV width for production just 1 MeV above threshold. The kinematic constraint rapidly vanishes with increasing center-of-mass energy.

Two-body kinematics at threshold provide powerful possibilities to distinguish different hadronic decay channels from kinematics only. In simple decays such as, for example,  $\tau^- \rightarrow K^- \nu_\tau$  (branching ratio 0.691 %) the kaons must have a fixed energy or momentum

---

<sup>2</sup>All arguments apply similarly to the  $\tau^+$

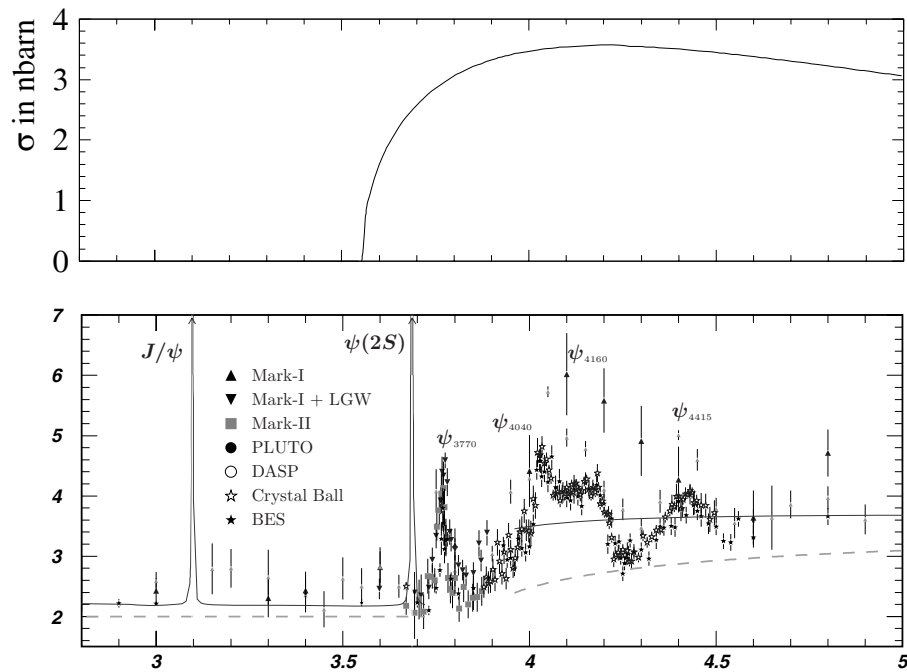


Figure 28.1: Top: Production cross section for tau pairs. Bottom: The  $R$ -ratio showing the expected background from quark production (from PDG). Cross section and  $R$ -ratio are shown versus the center-of-mass energy in GeV on identical scales.

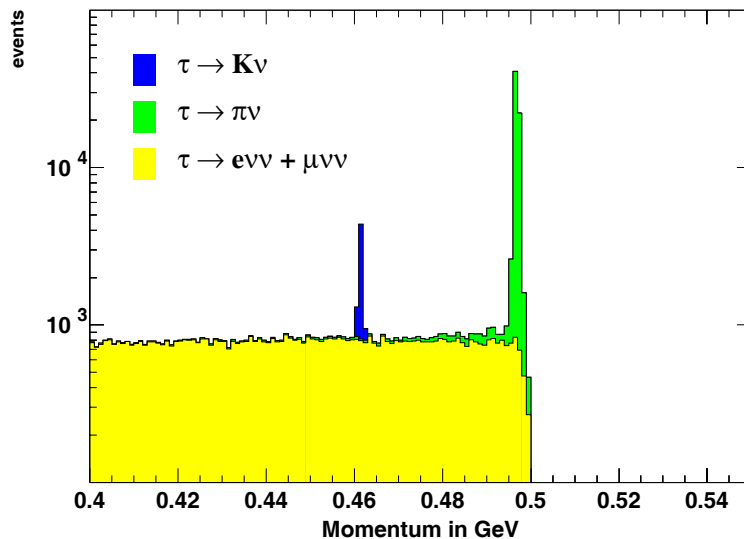


Figure 28.2: Momentum spectrum of charged tracks from tau leptons produced at rest at the production threshold. No particle identification applied.

in the center-of-mass system. Figure 28.2 shows the expected spectrum derived from a fast simulation of 300.000 events generated with TAUOLA [3]. A momentum resolution of  $\Delta p/p = 0.32\% \times p \oplus 0.37\%$  with the two terms added in quadrature is used, similar to the expected resolution of the *BES-III* detector. No particle identification is applied. All negative tracks in the events are considered. For clarity, the plot shows only the background from the leptonic decays (branching ratio of 35.3 %) and  $\tau^- \rightarrow \pi^- \nu_\tau$  (branching ratio 10.90 %). The others are small. The peak for the kaon decay is very well separated from the decay to the pion.

In more complicated decays, the detector records certain particles from the decays of the two tau leptons and measures their momenta. To identify the decay of the  $\tau^-$  a hypothesis is formed about which particles belong to its decay and what their identity is (whether they are pions or kaons). The invariant mass is calculated under this hypothesis and then  $E_{\text{had}}$  can be predicted from Eq. 28.2.2. The hypothesis is correct only if the predicted energy of the hadronic system matches the measured one. Figure 28.3 illustrates the identification. It shows the difference of the measured and the predicted energy. Again 300,000 events generated with TAUOLA are processed through a fast simulation with the same momentum resolution for charged tracks as above and an energy resolution for neutral pions of  $\Delta E/E = 2\%/\sqrt[4]{E} \oplus 2.5\%$ . Only the most energetic neutral pion in an event is considered; the others are assumed to be lost. A simple model for the creation of fake  $\pi^0$ 's from charged hadrons is also included in the simulation. Again, the signal can be well separated from the background without any particle identification.

Because of these kinematic properties, running directly at threshold (point 2 in section 28.1) is the preferred configuration for a number of tau physics measurements.

## 28.3 Physics Opportunities

The tau physics opportunities at a tau-charm factory are numerous, even compared to the high statistics of the *B*-factories. For many measurements, statistics are not the problem; efficiency, background and resolution are the main issues. For these measurements, the tau-charm factory is in a better situation. A list of measurements that a tau-charm factory should be able to improve significantly is given below.

- Measurement of the non-strange spectral function with low background and much improved mass resolution.
- First measurement of the strange spectral function with good statistics. Separation into vector and axial-vector parts through a detailed analysis of all decay modes. This improvement, together with the first point, will reduce the uncertainties of the measurement of the strong coupling constant  $\alpha_s$  from tau decays.
- Identification and measurement of second-class currents and Wess-Zumino anomalies.
- Tests of calculations from chiral perturbation theory at low  $Q^2$  and a determination of their range of validity.

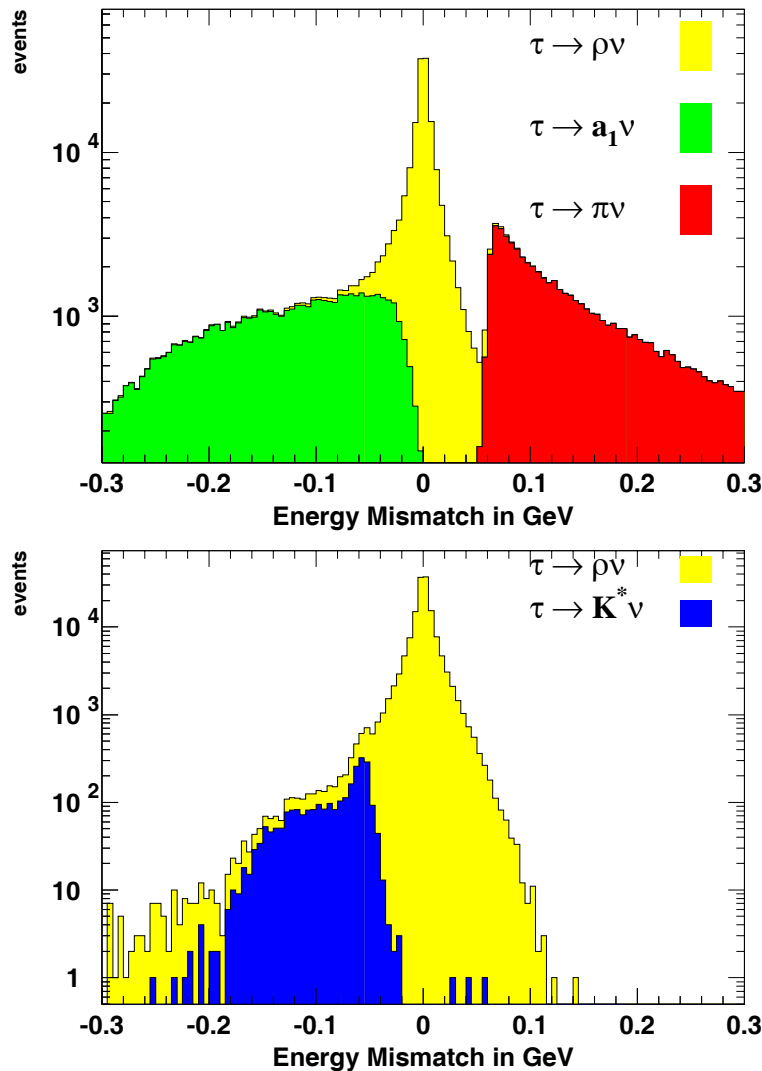


Figure 28.3: Measured energy minus predicted energy for a  $\tau^- \rightarrow \pi^- \pi^0 \nu_\tau$  hypothesis for negative charged tracks and the most energetic  $\pi^0$  in the events. The two plots show the signal together with the main backgrounds. No particle identification has been applied.

- Many branching ratios can be improved, especially those with charged kaons.
- Some exclusive channels provide good opportunities for spectroscopy of light mesons, for example the measurement of the mass and width of the charged and neutral  $\rho$  mesons.
- It would be interesting to improve the knowledge on the tau mass which is currently dominated by the BES-II measurement [4]. This would imply the reduction of all systematics including the knowledge of the energy spread of the machine and its stability.
- The measurement of the Michel parameters can be improved for the leptonic decays and the hadronic decays due to higher statistics combined with lower background. This is especially interesting as the LHC might tell us for what kind of new currents we are looking for.
- Other more exotic topics might be the search for a deviation of the g-factor of the tau lepton from 2 or the search for  $CP$  violation in tau decays.

Measurements that cannot be improved at a tau-charm factory are the tau lifetime, the neutral current couplings, the mass of the tau neutrino, a search for very rare or forbidden decays, or a search for  $CP$ -violation in the *production* of tau leptons.

## 28.4 Running Strategy

The tau-charm factory is a machine that can do very interesting physics in several areas and a running strategy must balance the requests of the different communities of users. Two months of running for tau physics should be sufficient during the initial operation of the machine and below threshold.

Running on threshold would produce 100,000 very clean tau pairs. From kinematically tagged decays one should be able to study the particle identification (time-of-flight,  $dE/dx$ , calorimeter, etc.), to understand the efficiencies, purities, and resolution, and to tune the detector simulation. A few physics analysis can already be improved from this data set, for example the  $\tau^- \rightarrow K^- \nu_\tau$  branching ratio or the  $\tau^- \rightarrow K^- \pi^0 \nu_\tau$  mass spectrum.

Running below threshold is necessary to understand the background from the production of light quarks and to tune the corresponding Monte Carlo generators. Once this has been done, the Monte Carlo can be used to subtract the background at the other running points.

The understanding of the identification of the tau leptons and their decay modes from the initial running at threshold will enable the collaboration to use luminosity collected at a later stage at higher energies for charm physics to do some of the tau measurements. The experience gained during the initial running at threshold will be a good basis to decide how much more luminosity one would like to accumulate at the tau threshold at some later stage.

# Chapter 29

## Tau Decays

### 29.1 Hadronic $\tau$ Decays

The pure leptonic or semileptonic character of  $\tau$  decays provides a clean laboratory for performing very precise tests of the electroweak gauge structure at the 0.1% to 1% level. Moreover, hadronic  $\tau$  decays turn out to be a beautiful laboratory for studying strong interaction effects at low energies [5, 6, 7, 8]. Accurate determinations of the QCD coupling and the strange quark mass have been obtained with  $\tau$ -decay data. More recently, a very competitive estimate of the quark mixing  $|V_{us}|$  has been also extracted from Cabibbo suppressed  $\tau$  decays.

The excellent experimental conditions offered by the tau-charm factory will allow for further analyses of many aspects of  $\tau$  physics with low systematics. The BEPCII collider could produce large statistical samples as many as 50 million  $\tau^+\tau^-$  pairs per year, providing the opportunity for an extensive programme of high-precision measurements with  $\tau$  leptons. The  $B$ -factories have already produced much larger data samples, which will be further increased at LHC and, if approved, at future Super- $B$  factories. However, the threshold region makes possible a much better control of backgrounds and systematic errors for a number of measurements. Thus, the tau-charm factory combines the optimum conditions to perform a number of very accurate measurements.

#### 29.1.1 A Laboratory for QCD<sup>1</sup>

The inclusive character of the total  $\tau$  hadronic width renders possible an accurate calculation of the ratio [( $\gamma$ ) represents additional photons or lepton pairs]

$$R_\tau \equiv \frac{\Gamma[\tau^- \rightarrow \nu_\tau \text{ hadrons}(\gamma)]}{\Gamma[\tau^- \rightarrow \nu_\tau e^- \bar{\nu}_e(\gamma)]} = R_{\tau,V} + R_{\tau,A} + R_{\tau,S}, \quad (29.1.1)$$

using analyticity constraints and the Operator Product Expansion [9, 10, 11, 12, 13]. One can separately compute the contributions associated with specific quark currents.  $R_{\tau,V}$  and  $R_{\tau,A}$  correspond to the Cabibbo-allowed decays through the vector and axial-vector currents, while  $R_{\tau,S}$  contains the remaining Cabibbo-suppressed contributions.

---

<sup>1</sup>By Antonio Pich

The theoretical prediction for  $R_{\tau,V+A}$  can be expressed as [11]

$$R_{\tau,V+A} = N_C |V_{ud}|^2 S_{EW} \{1 + \delta_P + \delta_{NP}\}, \quad (29.1.2)$$

where  $N_C = 3$  denotes the number of quark colours and  $S_{EW} = 1.0201 \pm 0.0003$  contains the electroweak radiative corrections [14]. The dominant correction ( $\sim 20\%$ ) is the perturbative QCD contribution  $\delta_P$ , which is fully known to  $O(\alpha_s^3)$  [11] and includes a resummation of the most important higher-order effects [12].

Non-perturbative contributions are suppressed by six powers of the  $\tau$  mass [11] and, therefore, are very small. Their numerical size has been determined from the invariant-mass distribution of the final hadrons in  $\tau$  decay, through the study of weighted integrals that can be calculated theoretically in the same way as  $R_\tau$  [15]:

$$R_\tau^{kl} \equiv \int_0^{m_\tau^2} ds \left(1 - \frac{s}{m_\tau^2}\right)^k \left(\frac{s}{m_\tau^2}\right)^l \frac{dR_\tau}{ds}. \quad (29.1.3)$$

The predicted suppression [11] of the non-perturbative corrections has been confirmed by ALEPH [16], CLEO [17] and OPAL [18]. The most recent analysis [16] gives

$$\delta_{NP} = -0.0043 \pm 0.0019. \quad (29.1.4)$$

The QCD prediction for  $R_{\tau,V+A}$  is then completely dominated by the perturbative contribution; non-perturbative effects being smaller than the perturbative uncertainties from uncalculated higher-order corrections. The result turns out to be very sensitive to the value of  $\alpha_s(m_\tau^2)$ , thereby allowing for an accurate determination of the fundamental QCD coupling [10, 11]. The experimental measurement  $R_{\tau,V+A} = 3.471 \pm 0.011$  implies [19]

$$\alpha_s(m_\tau^2) = 0.345 \pm 0.004_{\text{exp}} \pm 0.009_{\text{th}}. \quad (29.1.5)$$

The strong coupling measured at the  $\tau$  mass scale is significantly larger than the values obtained at higher energies. From the hadronic decays of the  $Z$ , one gets  $\alpha_s(M_Z^2) = 0.1186 \pm 0.0027$  [20], which differs from the  $\tau$  decay measurement by more than twenty standard deviations. After evolution up to the scale  $M_Z$  [21], the strong coupling constant in Eq. 29.1.5 decreases to [19]

$$\alpha_s(M_Z^2) = 0.1215 \pm 0.0012, \quad (29.1.6)$$

in excellent agreement with the direct measurements at the  $Z$  peak and with a similar accuracy. The comparison of these two determinations of  $\alpha_s$  in two extreme energy regimes,  $m_\tau$  and  $M_Z$ , provides a beautiful test of the predicted running of the QCD coupling; *i.e.*, a very significant experimental verification of *asymptotic freedom*.

With  $\alpha_s(m_\tau^2)$  fixed to the value in Eq. 29.1.5, the same theoretical framework gives definite predictions for the semi-inclusive  $\tau$  decay widths  $R_{\tau,V}$ ,  $R_{\tau,A}$  and  $R_{\tau,S}$ , in good agreement with the experimental measurements. Moreover, using the measured invariant mass distributions, one can study (for each separate  $V$ ,  $A$  and  $S$  component) the integrated moments defined in Eq. 29.1.3, with arbitrary weight functions and/or varying the upper end of integration in the range  $s_0 \leq m_\tau^2$ . This allows one to investigate many non-perturbative aspects of the strong interactions [22]. For instance,  $R_{\tau,V} - R_{\tau,A}$  is a pure non-perturbative quantity; basic QCD properties force the associated mass distribution to obey

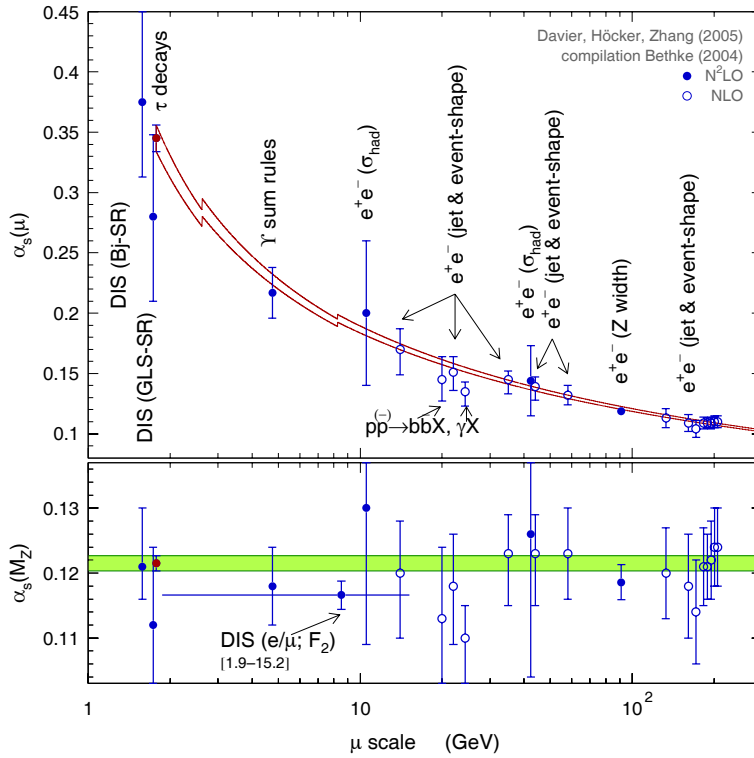


Figure 29.1: Measured values of  $\alpha_s$  at different scales. The curves show the energy dependence predicted by QCD, using  $\alpha_s(m_\tau^2)$  as input. The corresponding extrapolated  $\alpha_s(M_Z^2)$  values are shown at the bottom, where the shaded band displays the  $\tau$  decay result [19].

a series of chiral sum rules [22, 23], which relate the  $\tau$  measurements with low-energy non-perturbative observables such as the pion decay constant  $f_\pi$  or the electromagnetic pion mass difference  $m_{\pi^\pm} - m_{\pi^0}$ . One can also extract the non-perturbative contributions to the OPE of the QCD vector and axial-vector current correlators. The determination of these effects is needed to perform many theoretical predictions of other important observables, such as, for instance, the kaon  $CP$ -violating ratio  $\varepsilon'/\varepsilon$ . The measured vector spectral distribution can also be used to estimate the hadronic vacuum polarization contribution to  $\alpha(M_Z)$  and to the muon anomalous magnetic moment.

### 29.1.2 Determinations of $m_s$ and $V_{us}$ in Hadronic $\tau$ Decays<sup>2</sup>

Separate measurements of the  $|\Delta S| = 0$  and  $|\Delta S| = 1$   $\tau$  decay widths will allow us to pin down the  $SU(3)_{fl}$  breaking effects induced by the strange quark mass [24, 25, 26, 27, 28, 29, 30], through the differences [25]

$$\delta R_\tau^{kl} \equiv \frac{R_{\tau,V+A}^{kl}}{|V_{ud}|^2} - \frac{R_{\tau,S}^{kl}}{|V_{us}|^2} \approx 24 \frac{m_s^2(m_\tau^2)}{m_\tau^2} \Delta_{kl}(\alpha_s) - 48\pi^2 \frac{\delta O_4}{m_\tau^4} Q_{kl}(\alpha_s). \quad (29.1.7)$$

The perturbative QCD corrections  $\Delta_{kl}(\alpha_s)$  and  $Q_{kl}(\alpha_s)$  are known to  $O(\alpha_s^3)$  and  $O(\alpha_s^2)$ , respectively [25, 30]. Since the longitudinal contribution to  $\Delta_{kl}(\alpha_s)$  does not converge well,

<sup>2</sup>By A. Pich

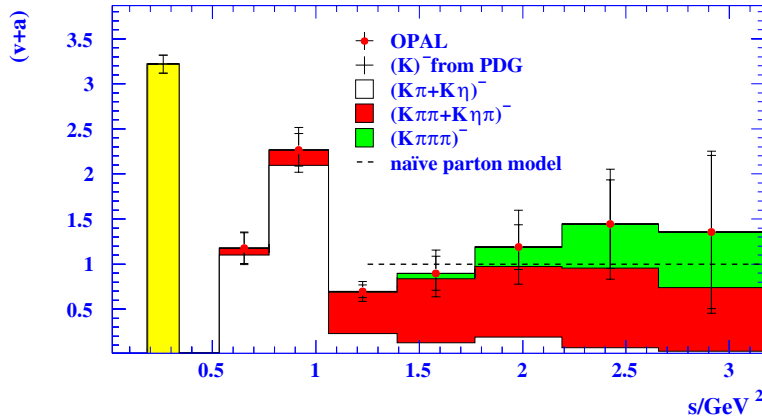


Figure 29.2: The OPAL measurement of the spectral distribution in  $|\Delta S| = 1$   $\tau$  decays [32].

the  $J = 0$  QCD expression is replaced by its corresponding phenomenological hadronic parametrization [29], which is much more precise because it is strongly dominated by the well known kaon pole. The small non-perturbative contribution,  $\delta O_4 \equiv \langle 0 | m_s \bar{s}s - m_d \bar{d}d | 0 \rangle = -(1.5 \pm 0.4) \times 10^{-3} \text{ GeV}^4$ , has been estimated with Chiral Perturbation Theory techniques [25].

From the measured moments  $\delta R_\tau^{k0}$  ( $k = 0, 1, 2, 3, 4$ ) [31, 32], it is possible to determine the strange quark mass; however, the extracted value depends sensitively on the modulus of the Cabibbo–Kobayashi–Maskawa matrix element  $|V_{us}|$ . It appears, then, more natural to turn things around and, with an input for  $m_s$  obtained from other sources, determine  $|V_{us}|$  [29]. The most sensitive moment is  $\delta R_\tau^{00}$ :

$$|V_{us}|^2 = \frac{R_{\tau,S}^{(0,0)}}{\frac{R_{\tau,V+A}^{(0,0)}}{|V_{ud}|^2} - \delta R_{\tau,\text{th}}^{(0,0)}}. \quad (29.1.8)$$

Using  $m_s(2 \text{ GeV}) = (94 \pm 6) \text{ MeV}$ , which includes the most recent determinations of  $m_s$  from lattice and QCD Sum Rules [33], one obtains  $\delta R_{\tau,\text{th}}^{00} = 0.240 \pm 0.032$  [29]. This prediction is much smaller than  $R_{\tau,V+A}^{(0,0)} / |V_{ud}|^2$ , making the theoretical uncertainty in Eq. 29.1.8 negligible in comparison with the experimental inputs  $R_{\tau,V+A}^{(0,0)} = 3.471 \pm 0.011$  and  $R_{\tau,S}^{(0,0)} = 0.1686 \pm 0.0047$  [19]. Taking  $|V_{ud}| = 0.97377 \pm 0.00027$  [2], one gets [29]

$$|V_{us}| = 0.2220 \pm 0.0031_{\text{exp}} \pm 0.0011_{\text{th}}. \quad (29.1.9)$$

This result is competitive with the standard  $K_{e3}$  determination,  $|V_{us}| = 0.2234 \pm 0.0024$  [34]. The precision should be considerably improved in the near future because the error is dominated by the experimental uncertainty, which can be reduced with the much better data samples from BaBar, Belle and *BES-III*. Thus,  $\tau$  data has the potential to provide the best determination of  $|V_{us}|$ .

With future high-precision  $\tau$  data, a simultaneous fit of  $m_s$  and  $|V_{us}|$  should also become possible. A better understanding of the perturbative QCD corrections  $\Delta_{kl}(\alpha_s)$  would be very helpful to improve the precision on  $m_s$  [28, 29].

### 29.1.3 Tau Hadronic Spectral Functions<sup>3</sup>

Hadronic tau decays give unique possibilities for performing detailed investigations of hadronic production from the QCD vacuum through the determination of *spectral functions*. Spectral functions play an important role in the understanding of hadron dynamics in the intermediate energy range and provide the basic input for QCD studies and for calculation of the low-energy contributions from the hadronic vacuum polarization.

#### Definition

The spectral function  $v_1(a_1, a_0)$ , where subscript refers to the spin of hadronic system, is defined for a non-strange ( $\Delta S = 0$ ) or strange ( $\Delta S = 1$ ) vector (axial-vector) tau decay channel  $V^- \nu_\tau$  ( $A^- \nu_\tau$ ), and is obtained by dividing the invariant mass-squared distribution  $(1/N_{V/A})(dN_{V/A}/ds)$  by the appropriate kinematic factor and is normalized by the ratio of vector/axial vector branching fraction  $\mathcal{B}(\tau \rightarrow V^-/A^- \nu_\tau)$  to the branching fraction of the decay to a massless lepton (electron) ::

$$v_1/a_1 = \frac{m_\tau^2}{6|V_{CKM}|^2 S_{EW}} \frac{\mathcal{B}(\tau \rightarrow V^-/A^- \nu_\tau)}{\mathcal{B}(\tau \rightarrow e^- \nu_e \nu_\tau)} \frac{dN_{V/A}}{N_{V/A} ds} \left[ \left(1 - \frac{s}{m_\tau^2}\right)^2 \left(1 + \frac{2s}{m_\tau^2}\right) \right]^{-1}, \quad (29.1.10)$$

$$a_0 = \frac{m_\tau^2}{6|V_{CKM}|^2 S_{EW}} \frac{\mathcal{B}(\tau \rightarrow \pi^- \nu_\tau)}{\mathcal{B}(\tau \rightarrow e^- \nu_e \nu_\tau)} \frac{dN_A}{N_A ds} \left(1 - \frac{s}{m_\tau^2}\right)^{-2}. \quad (29.1.11)$$

Here  $S_{EW}$  is the electroweak radiative correction factor that is introduced in the previous section. Due to the conserved vector current (CVC), there is no  $J = 0$  contribution to the vector spectral function; the only contribution to  $a_0$  is assumed to be from the pion pole, with  $dN_A/N_A ds = \delta(s - m_\pi^2)$ .

Using unitarity and analyticity, the spectral functions are connected to the imaginary parts of the two-point correlation (hadronic vacuum polarization) functions [35, 36]

$$\begin{aligned} \Pi_{i,j,U}^\mu(q^2) &\equiv \int d^4x e^{iqx} \langle 0 | T(U_{ij}^\mu(x) U_{ij}^\mu(0)^+) | 0 \rangle \\ &= (-g^{\mu\nu} q^2 + q^\mu q^\nu) \Pi_{ij,U}^{(1)}(q^2) + q^\mu q^\nu \Pi_{ij,U}^{(0)}(q^2), \end{aligned} \quad (29.1.12)$$

of vector ( $U_{ij}^{\mu\nu} = V_{ij}^\nu = \bar{q}_j \gamma^\mu q_i$ ) or axial-vector ( $U_{ij}^\mu = V_{ij}^\mu = \bar{q}_j \gamma^\mu \gamma_5 q_i$ ) quark currents for time-like momenta-squared  $q^2 > 0$ . The polarization functions  $\Pi_{i,j,U}^{\mu\nu}(s)$  have a branch cut along the real axis in the complex  $s = q^2$  plane. Their imaginary parts give the spectral functions defined in Eq. 29.1.10. For non-strange currents:

$$\begin{aligned} \text{Im} \Pi_{\bar{u}d,V/A}^{(1)}(s) &= \frac{1}{2\pi} v_1/a_1(s), \\ \text{Im} \Pi_{\bar{u}d,A}^{(0)}(s) &= \frac{1}{2\pi} v_1/a_0(s). \end{aligned} \quad (29.1.13)$$

---

<sup>3</sup>By I. Boyko and D. Dedovich

Analytic functions  $\Pi^{(J)}ij, U(q^2)$  obey the dispersion relation

$$\Pi^{(J)}ij, U(q^2) = \frac{1}{\pi} \int_0^\infty ds \frac{Im\Pi_{ij,U}^{(J)}(s)}{s - q^2 - i\epsilon}. \quad (29.1.14)$$

This dispersion relation allows one to connect the experimentally accessible spectral functions to the correlation functions  $\Pi^{(J)}ij, U(q^2)$ , which can be derived from QCD theory and are used for theoretical calculations of total cross sections and decay widths.

### Tau spectral functions and electron-positron annihilation data

In the limit of isospin invariance, the vector current is conserved (CVC), so that the spectral function for a vector  $\tau$  decay mode  $X^-\nu_\tau$  in a given isospin state for the hadronic system is related to the  $e^+e^-$  annihilation cross section of the corresponding isovector final state  $X^0$  :

$$\sigma_{e^+e^- \rightarrow X^0}^{I=1}(s) = \frac{4\pi\alpha^2}{s} v_{1,X^-}(s), \quad (29.1.15)$$

where  $\alpha$  is the electromagnetic fine structure constant. In reality, isospin symmetry is broken, particularly due to electromagnetic effects, and corrections must be applied to compare (and combine)  $\tau$ -decay and  $e^+e^-$  data. A more complete review and further references about sources and value of the symmetry breaking can be found in Refs. [37, 38]. A comparison of two-pion spectral functions obtained from tau decays and  $e^+e^-$  data is shown in Fig. 29.3, which is taken from Ref. [38]. Here it is evident that, although the absolute difference is relatively small, there is a clear discrepancy between data, especially above the  $\rho$  peak. Another, more “quantitative” way to compare spectral functions is to use  $e^+e^-$  data to calculate hadronic tau branching fractions. For the most studied decay,  $\tau \rightarrow \nu_\tau \pi^0 \pi^0$ , different authors [37, 38, 39] give  $\tau - e^+e^-$  discrepancies in the range  $2.9\sigma - 4.5\sigma$  with differences depending mainly on which  $e^+e^-$  data are included in the analysis, while in all cases the  $\tau$ -decay data are dominated by the ALEPH results. In a recent work [40], a new calculation of isospin breaking corrections is presented, and this reduces the discrepancies mentioned above to  $2.6\sigma$  and substantially improves the agreement between the shapes of spectral functions obtained from  $\tau$ -decay and  $e^+e^-$  annihilation. Nevertheless, the situation is still far from the “good agreement” state. In addition, the predicted value for the anomalous muon magnetic moment  $g_\mu - 2$  calculated using combined the  $\tau$  and  $e^+e^-$  data is now  $3.6\sigma$  away from the most precise measurement. Thus, we now face a very intriguing situation: differences between predictions and measurements are substantial on one side, but still too small to be a sign of new physics on the other side; new reliable measurements will be very useful.

### Measurement of Tau Hadronic Spectral Functions at **BES-III**

Experimental tau physics data can be divided into two main groups: Data produced at LEP have low background and high selection efficiency, but are statistically limited. Data from  $B$ -factories have almost unlimited statistics, but much worse background conditions due to relatively low multiplicity of hadronic events and the high ratio of the inclusive hadron and the tau-pair production cross-sections. The **BES-III** experiment has

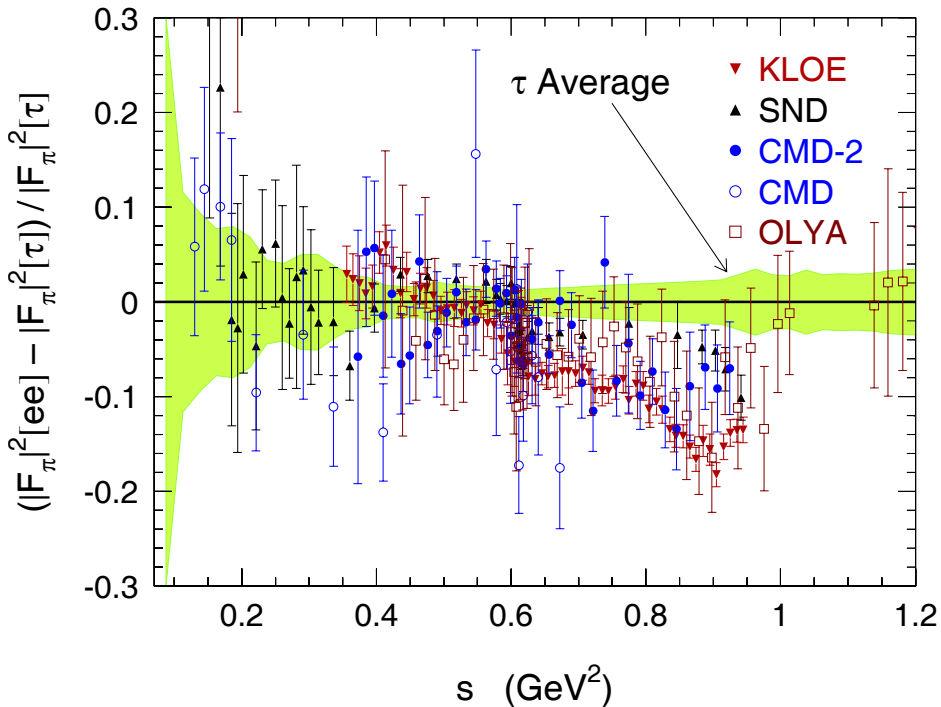


Figure 29.3: Relative comparison of the isospin-breaking-corrected  $\tau$  data (world average) and  $\pi^+\pi^-$  spectral function from  $e^+e^-$  annihilation, expressed as a ratio to the  $\tau$  spectral function. The shaded band gives the uncertainty on the  $\tau$  spectral function.

no advantage over the  $B$ -factories when working at the charmonium resonances. On the other hand, a dedicated “tau” run at an energy slightly below the  $\psi(2S)$  resonance would allow a combination of high statistics and excellent background conditions. Using leptonic  $\tau$ -decay tagging in combination with the usual kinematic selection criteria (high missing momenta, acollinearity and accomplanarity, broken  $P_t$  balance) will make it is possible to select an extremely clean sample of  $\tau$  decays, with backgrounds well below 1%. Another obvious advantage of using lepton-tagged events is that that the selection (in)efficiency causes no bias in the measured values, and only affects the available statistics. Thus, if more strict selection criteria are used, we can say that “we are buying low systematics with statistics.” The table below gives a comparison of *BES-III* and *ALEPH* experimental conditions for  $\tau$  hadronic branching measurements and spectral functions determinations. The *BES-III* values are computed assuming a three-month dedicated tau run and an 80% tagging efficiency.

	<b>ALEPH</b>	<b>BES-III</b>
$\tau$ -decays selected	$\sim 327000$	$1.6 \times 10^6$
$\tau \rightarrow \pi\pi_0\nu_\tau$ decays selected	$\sim 81000$	$\sim 280\,000$
external background	1.2%	< 1%
hadronic mass reconstruction accuracy	$\sim 80$ MeV	< 50 MeV

Another very important consideration is the neutral hadron ( $\pi^0$  most of all) identifi-

cation efficiency. A preliminary simulation shows that the single  $\pi^0$  registration efficiency for the *BES-III* detector will be about 95% for decays that are within the acceptance of the calorimeter, which is at least as good as that for ALEPH. It should be noted that the tau leptons in LEP events are highly boosted and this results in a large number of merged or overlapped clusters in electromagnetic calorimeters, which require a very complicated (and, therefore, vulnerable to error) analysis. At *BES-III*, the  $\tau$  decay products are distributed almost uniformly throughout the detector. The main contribution to the neutral pion reconstruction inefficiency will be due to the geometrical acceptance (95%), which can be calculated with high accuracy and should not result in a substantial systematic error. Another attractive possibility is related to the determination of strange spectral functions. At LEP experiments, kaons were identified only on a statistical basis. At *BES-III*, kaons produced in tau decay will have momenta below 0.8 GeV/c, *i.e.* in the momentum range where they can be selected with high purity by the TOF and  $dE/dX$  measurements.

Thus, a three-month dedicated tau run at *BES-III* has a good chance of providing the most accurate measurements of the hadronic spectral functions.

## 29.2 Leptonic Tau decays

The precise measurement of the different exclusive  $\tau$  decays provides very valuable information to test the Standard Model, both in the electroweak and strong sectors. The threshold region, with its kinematical advantages and low backgrounds, makes accurate studies of the lowest-multiplicity decay modes possible.

### 29.2.1 Leptonic Decays and Universality Tests<sup>4</sup>

The leptonic decays  $\tau^- \rightarrow l^- \bar{\nu}_l \nu_\tau$  ( $l = e, \mu$ ) are theoretically understood at the level of the electroweak radiative corrections. Within the Standard Model

$$\Gamma_{\tau \rightarrow l} \equiv \Gamma(\tau^- \rightarrow \nu_\tau l^- \bar{\nu}_l) = \frac{G_F^2 m_\tau^5}{192\pi^3} f\left(\frac{m_l^2}{m_\tau^2}\right) r_{EW}, \quad (29.2.16)$$

where  $f(x) = 1 - 8x + 8x^3 - x^4 - 12x^2 \log x$ . The factor  $r_{EW}$  takes into account radiative corrections not included in the Fermi coupling constant  $G_F$ , and the non-local structure of the  $W$  propagator [14]; these effects are quite small [ $\alpha(m_\tau) = 1/133.3$ ]:

$$r_{EW} = \left[1 + \frac{\alpha(m_\tau)}{2\pi} \left(\frac{25}{4} - \pi^2\right)\right] \left[1 + \frac{3}{5} \frac{m_\tau^2}{M_W^2} - 2 \frac{m_l^2}{M_W^2}\right] = 0.9960. \quad (29.2.17)$$

Using the value of  $G_F$  measured in  $\mu$  decay in Eq. (29.2.16), yields a relation between the  $\tau$  lifetime and the leptonic branching ratios:

$$B_{\tau \rightarrow e} \equiv \text{Br}(\tau^- \rightarrow e^- \bar{\nu}_e \nu_\tau) = \frac{B_{\tau \rightarrow \mu}}{0.972564 \pm 0.000010} = \frac{\tau_\tau}{(1632.1 \pm 1.4) \times 10^{-15} \text{ s}}. \quad (29.2.18)$$

Here the quoted errors reflect the present uncertainty of 0.3 MeV in the value of  $m_\tau$ .

---

<sup>4</sup>A. Pich

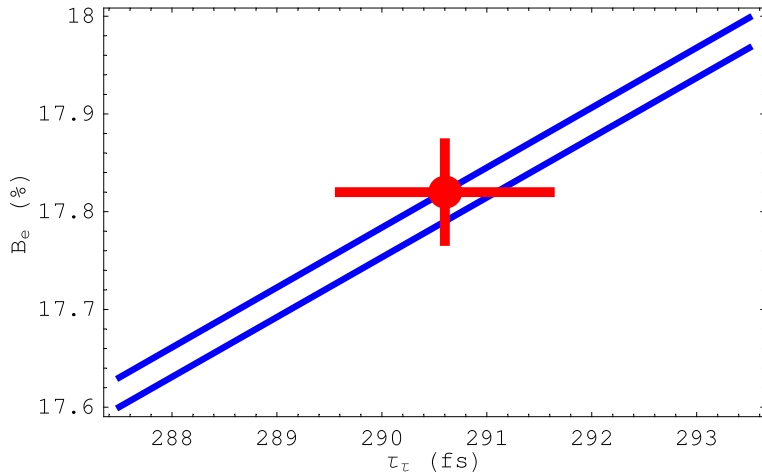


Figure 29.4: The relation between  $B_{\tau \rightarrow e}$  and  $\tau_\tau$ . The diagonal band corresponds to Eq. (29.2.18).

Table 29.1: Present constraints on  $|g_l/g_\nu|$  [7, 34].

	$B_{\tau \rightarrow e} \tau_\mu / \tau_\tau$	$\Gamma_{\tau \rightarrow \pi} / \Gamma_{\pi \rightarrow \mu}$	$\Gamma_{\tau \rightarrow K} / \Gamma_{K \rightarrow \mu}$	$B_{W \rightarrow \tau} / B_{W \rightarrow \mu}$
$ g_\tau/g_\mu $	$1.0004 \pm 0.0022$	$0.996 \pm 0.005$	$0.979 \pm 0.017$	$1.039 \pm 0.013$
	$B_{\tau \rightarrow \mu} / B_{\tau \rightarrow e}$	$B_{\pi \rightarrow \mu} / B_{\pi \rightarrow e}$	$B_{K \rightarrow \mu} / B_{K \rightarrow e}$	$B_{K \rightarrow \pi \mu} / B_{K \rightarrow \pi e}$
$ g_\mu/g_e $	$1.0000 \pm 0.0020$	$1.0017 \pm 0.0015$	$1.012 \pm 0.009$	$1.0002 \pm 0.0026$
	$B_{W \rightarrow \mu} / B_{W \rightarrow e}$	$ g_\tau/g_e $	$B_{\tau \rightarrow \mu} \tau_\mu / \tau_\tau$	$B_{W \rightarrow \tau} / B_{W \rightarrow e}$
$ g_\mu/g_e $	$0.997 \pm 0.010$		$1.0004 \pm 0.0023$	$1.036 \pm 0.014$

The predicted value of  $B_{\tau \rightarrow \mu} / B_{\tau \rightarrow e}$  is in excellent agreement with the measured ratio  $B_{\tau \rightarrow \mu} / B_{\tau \rightarrow e} = 0.9725 \pm 0.0039$ . As shown in Fig. 29.4, the relation between  $B_{\tau \rightarrow e}$  and  $\tau_\tau$  is also well satisfied by the present data. Note that this relation is very sensitive to the value of the  $\tau$  mass [ $\Gamma_{\tau \rightarrow l} \propto m_\tau^5$ ].

These measurements can be used to test the universality of the  $W$  couplings to the leptonic charged currents, *i.e.*  $g_e = g_\mu = g_\tau \equiv g$ . The  $B_{\tau \rightarrow \mu} / B_{\tau \rightarrow e}$  ratio constraints  $|g_\mu/g_e|$ , while the  $B_{\tau \rightarrow e} / \tau_\tau$  relation provides information on  $|g_\tau/g_\mu|$ . As shown in Table 29.1, the present data verify the universality of the leptonic charged-current couplings to the 0.2% level.<sup>5</sup>

The  $\tau$  leptonic branching fractions and the  $\tau$  lifetime are known with a precision of 0.3%. Slightly improved lifetime measurements are expected from BaBar and Belle. For comparison, the  $\mu$  lifetime is known with an accuracy of  $10^{-5}$ , which should be further improved to  $10^{-6}$  by the MuLan experiment at PSI [41].

Universality tests also require a precise determination of  $m_\tau^5$ , which is only known to the 0.08% level. Two new preliminary measurements of the  $\tau$  mass have been presented

<sup>5</sup> $\text{Br}(W \rightarrow \nu_\tau \tau)$  is  $2.1\sigma/2.7\sigma$  larger than  $\text{Br}(W \rightarrow \nu_e e / \nu_\mu \mu)$ . The stringent limits on  $|g_\tau/g_{e,\mu}|$  from  $W$ -mediated decays makes it unlikely that this is a real physical effect.

recently:

$$m_\tau = \begin{cases} 1776.71 \pm 0.13 \pm 0.35 \text{ MeV} & [\text{Belle}], \\ 1776.80_{-0.23}^{+0.25} \pm 0.15 \text{ MeV} & [\text{KEDR}]. \end{cases} \quad (29.2.19)$$

The Belle value [42] is based on a pseudomass analysis of  $\tau \rightarrow \nu_\tau 3\pi$  decays, while the KEDR result [43] comes from a measurement of  $\tau^+ \tau^-$  threshold production, taking advantage of a precise energy calibration through the resonance depolarization method. In both cases the achieved precision is getting close to the present BES-I dominated value,  $m_\tau = 1776.99_{-0.26}^{+0.29}$  [2]. KEDR aims to obtain a final accuracy of 0.15 MeV. A precision of better than 0.1 MeV should be easily achieved at *BES-III* [44], through a detailed analysis of  $\sigma(e^+e^- \rightarrow \tau^+\tau^-)$  at threshold [1, 45, 46], as discussed in detail in Chapt. 30.

### 29.2.2 Lorentz Structure<sup>6</sup>

With high statistics, the leptonic  $\tau$  decay modes provide opportunities to investigate the Lorentz structure of the decay amplitude, through the analysis of the energy and angular distribution of the final charged lepton. The most general, local, derivative-free, lepton-number conserving, four-lepton interaction Hamiltonian, consistent with locality and Lorentz invariance [47, 48, 49, 50],

$$\mathcal{H} = 4 \frac{G_{ll}}{\sqrt{2}} \sum_{n,\epsilon,\omega} g_{\epsilon\omega}^n \left[ \overline{l}_\epsilon \Gamma^n (\nu_{l'})_\sigma \right] \left[ \overline{(\nu_l)_\lambda} \Gamma_n l_\omega \right], \quad (29.2.20)$$

contains ten complex coupling constants or, since a common phase is arbitrary, nineteen independent real parameters that could be different for each leptonic decay. The sub-indices  $\epsilon, \omega, \sigma, \lambda$  label the chiralities (left-handed, right-handed) of the corresponding fermions, and  $n$  the type of interaction: scalar ( $I$ ), vector ( $\gamma^\mu$ ) and tensor ( $\sigma^{\mu\nu}/\sqrt{2}$ ). For given  $n, \epsilon, \omega$ , the neutrino chiralities  $\sigma$  and  $\lambda$  are uniquely determined.

Taking out a common factor  $G_{ll}$ , which is determined by the total decay rate, the coupling constants  $g_{\epsilon\omega}^n$  are normalized to [49]

$$1 = \frac{1}{4} \left( |g_{RR}^S|^2 + |g_{RL}^S|^2 + |g_{LR}^S|^2 + |g_{LL}^S|^2 \right) + 3 \left( |g_{RL}^T|^2 + |g_{LR}^T|^2 \right) + \left( |g_{RR}^V|^2 + |g_{RL}^V|^2 + |g_{LR}^V|^2 + |g_{LL}^V|^2 \right). \quad (29.2.21)$$

In the Standard Model,  $g_{LL}^V = 1$  and all the other  $g_{\epsilon\omega}^n = 0$ . The sums of all contributions in Eq. 29.2.21 with identical initial and final chiralities,  $\mathcal{Q}_{\epsilon\omega}$ , can be interpreted as the probabilities for the decay of an  $\omega$ -handed  $l^-$  into an  $\epsilon$ -handed daughter lepton. Upper bounds on any of these (positive-semidefinite) probabilities translate into corresponding limits for all couplings with the given chiralities. The measurement of the  $\tau$  polarization is possible due to the fact that the spins of the  $\tau^+ \tau^-$  pair produced in  $e^+e^-$  annihilation are strongly correlated. Table 29.2 shows the present 90% C.L. experimental bounds on the  $g_{\epsilon\omega}^n$  couplings.

---

<sup>6</sup>By A. Pich

Table 29.2: 90% C.L. experimental bounds [2] for the normalized  $\tau$ -decay couplings  $g_{\epsilon\omega}^n \equiv g_{\epsilon\omega}^n/N^n$ , where  $N^n \equiv \max(|g_{\epsilon\omega}^n|) = 2, 1, 1/\sqrt{3}$  for  $n = S, V, T$ .

$\tau^- \rightarrow e^- \bar{\nu}_e \nu_\tau$			
$ g_{RR}^S  < 0.70$	$ g_{LR}^S  < 0.99$	$ g_{RL}^S  < 2.01$	$ g_{LL}^S  < 2.01$
$ g_{RR}^V  < 0.17$	$ g_{LR}^V  < 0.13$	$ g_{RL}^V  < 0.52$	$ g_{LL}^V  < 1.01$
$ g_{RR}^T  \equiv 0$	$ g_{LR}^T  < 0.08$	$ g_{RL}^T  < 0.51$	$ g_{LL}^T  \equiv 0$
$\tau^- \rightarrow \mu^- \bar{\nu}_\mu \nu_\tau$			
$ g_{RR}^S  < 0.72$	$ g_{LR}^S  < 0.95$	$ g_{RL}^S  < 2.01$	$ g_{LL}^S  < 2.01$
$ g_{RR}^V  < 0.18$	$ g_{LR}^V  < 0.12$	$ g_{RL}^V  < 0.52$	$ g_{LL}^V  < 1.01$
$ g_{RR}^T  \equiv 0$	$ g_{LR}^T  < 0.08$	$ g_{RL}^T  < 0.51$	$ g_{LL}^T  \equiv 0$

### 29.2.3 Study of the Lorentz structure at **BES-III**<sup>7</sup>

#### Michel parameters

The coupling constants,  $g_{\epsilon\omega}^n$  in Eq. 29.2.20, can be experimentally accessed via the energy spectra of the daughter leptons from tau decays. The polarization of the daughter leptons usually cannot be measured; however the polarization of the tau lepton  $P_\tau$  in principle can be measured through its decay spectra. Under these assumptions the spectrum of the tau decays predicted by Eq. 29.2.20 can be parametrized at the Born level by the following sum of polynomials  $h_i$ :

$$\frac{1}{\Gamma} \frac{d\Gamma}{dx_\ell} = h_0(x_\ell) + \eta h_\eta(x_\ell) + \rho h_\rho(x_\ell) - P_\tau [\xi h_\xi(x_\ell) + \xi\delta h_{\xi\delta}(x_\ell)], \quad (29.2.22)$$

where  $P_\tau$  is the average tau polarization and  $x_\ell = E_\ell/E_{max}$  is the “reduced energy” of the daughter lepton, or the ratio of its energy to the maximum possible energy. Examples of the polynomials  $h_i$  are illustrated in Fig. 29.5.

The coefficients  $\eta, \rho, \xi, \xi\delta$ , known as the Michel parameters [51], are bilinear combinations of the coupling constants in Eq. 29.2.20. The four Michel parameters carry the full information on the coupling constants that can be extracted from the decay spectra of the tau leptons (without the measurement of the polarisation of the final state leptons).

In the Standard Model, the Michel parameters are predicted to be:  $\rho = 0.75$ ;  $\eta = 0$ ;  $\xi = 1$ ;  $\xi\delta = 0.75$ . An observation of different values of the Michel parameters would indicate a violation of the Standard Model.

#### Anomalous tensor coupling

The parametrization presented in Eq. 29.2.20 is based on certain assumptions; namely it assumes the Hamiltonian to be lepton-number conserving, derivative-free, local, Lorentz invariant, and a 4-fermion point interaction. While most of these assumptions are quite

<sup>7</sup>By Igor R. Boyko. and Dedovich Dima

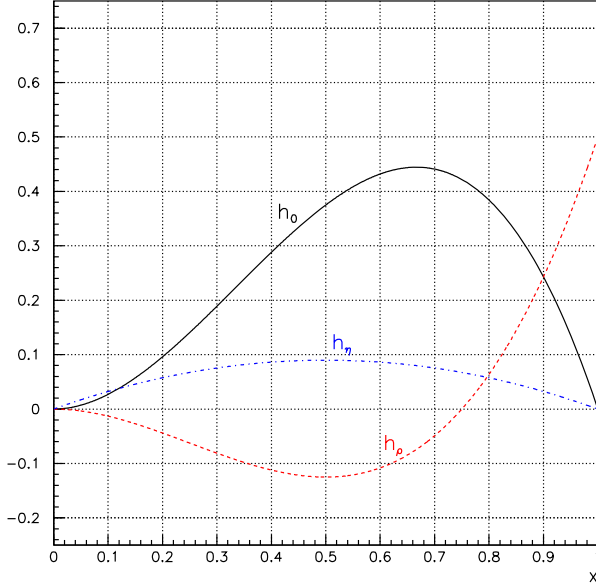


Figure 29.5: The shapes of polynomial functions  $h_i$  for the Michel parametrisation of tau decays.

natural, there is no fundamental reason to assume that the interaction Lagrangian does not include derivatives.

An anomalous interaction involving derivatives (which can only be a tensor interaction) can be represented in the following form [52]:

$$\mathcal{L} = \frac{g}{\sqrt{2}} W^\alpha \left\{ \bar{\tau} \gamma_\alpha \frac{1 - \gamma^5}{2} \nu + \frac{\kappa_\tau^W}{2m_\tau} \partial_\beta \left( \bar{\tau} \sigma_{\alpha\beta} \frac{1 - \gamma^5}{2} \nu \right) \right\} + \text{h.c.}, \quad (29.2.23)$$

where  $\kappa_\tau^W$  is the strength of the anomalous coupling. Such an anomalous interaction can be studied through the possible distortions of the energy spectra of tau decays. Since the Lagrangian of Eq. 29.2.23 explicitly contains derivatives, the distortions of the energy spectra can not be described in terms of the known Michel parameters.

The matrix element for the purely leptonic tau decays then takes the form:

$$\mathcal{M} = \frac{4G}{\sqrt{2}} \langle \bar{v}_l | \gamma_\alpha | v_{\bar{\nu}_l} \rangle \left( \langle \bar{v}_{\nu_\tau} | \gamma_\alpha | u_{\tau_L} \rangle - i \frac{\kappa_\tau^W}{2m_\tau} q_\beta \langle \bar{v}_{\nu_\tau} | \sigma_{\alpha\beta} | u_{\tau_R} \rangle \right), \quad (29.2.24)$$

where  $q$  is the four-momentum of the  $W$ . The first summand in Eq. 29.2.24 is the Standard Model prediction, while the second one is the contribution of the anomalous coupling. (In the framework of the Standard Model  $\kappa_\tau^W = 0$ .) In principle, both the anomalous coupling  $\kappa_\tau^W$  and the “standard” couplings  $g_{ij}^\gamma$  can take non-Standard Model values simultaneously. In this case the first summand in (29.2.24) has to be replaced by the full parametrisation of Eq. 29.2.20.

Like the case of Michel parameters, the contribution of the anomalous tensor coupling can be also parametrized in terms of the polynomials. The approximate shape of the

energy spectrum is

$$\frac{1}{\Gamma} \frac{d\Gamma}{dx_\ell} \sim x_\ell^2 \cdot (-2x_\ell + 3 + 2 \cdot \kappa_\tau^W \cdot x_\ell). \quad (29.2.25)$$

Figure 29.6 compares the deviations of the decay spectrum from the Standard Model prediction for non-Standard Model values of  $\kappa_\tau^W$  and the Michel parameter  $\rho$ . One can see that the change in shape is significantly different for the two cases, which makes it possible to measure the two parameters simultaneously.

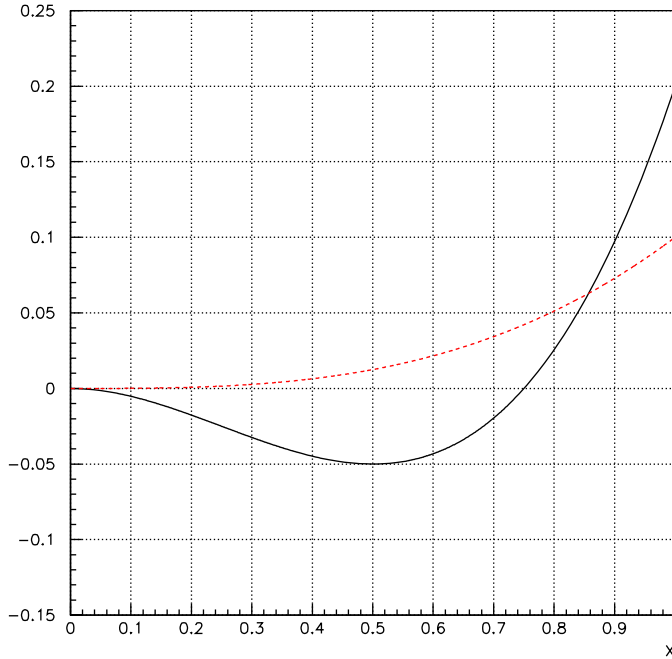


Figure 29.6: The deviation of the spectrum of leptons from tau decays from the Standard Model prediction. Dashed line: for the non-zero value of the anomalous tensor coupling. Solid line: for  $\rho \neq 0.75$ .

### Measurement of Michel parameters and search for an anomalous tensor coupling

The Michel parameters have been extensively measured in tau lepton decays by many experiments. The current experimental uncertainty on the parameter  $\rho$  is about 0.008 and for  $\eta$  the uncertainty is 0.07. To date, the anomalous tensor coupling has only been studied by the DELPHI experiment. The coupling constant  $\kappa_\tau^W$  was measured with a precision of 0.04 and was found to be consistent with zero.

The *BES-III* experiment will have an abundant sample of tau lepton decays and an accurately measured energy spectrum. This will provide an excellent possibility to improve significantly the current knowledge on the Lorentz structure in tau decays. This section

presents a Monte-Carlo estimate of the possible reach of *BES-III* for measurements of the Michel parameters and in the search for the anomalous tensor coupling. For simplicity, only two Michel parameters  $\rho$  and  $\eta$  are considered.

The simulation was based on version 5.1 of the *BES-III* software. The events were generated at a c.m. energy of 3.69 GeV, where background from hadronic events is minimal. The following samples were simulated: 100K Bhabha scattering events  $ee \rightarrow ee$ ; 20K dimuon events  $ee \rightarrow \mu\mu$ ; 100K hadronic events  $ee \rightarrow qq$ . The total number of simulated tau pair events was 100K. The simulated signal was limited to the decay channel  $ee \rightarrow \tau\tau \rightarrow e\mu$  (+ neutrinos). This channel represents only about 3% of the total tau pairs, but these are rather easy events to select. The possible inclusion of hadronic tau decays can increase the available statistics significantly, therefore the results presented in this section can be considered as a conservative estimate of the *BES-III* reach.

The analysis was restricted to the angular region  $|\cos\theta| < 0.83$ . The event selection was based on the particle identification. Exactly two reconstructed charged particles were required in the event. One of them was required to be identified as an electron and the other had to be a muon. The main criterion for particle identification was based on the  $dE/dx$  pull variable, *i.e.* the deviation of the measured  $dE/dx$  value from the expected one, expressed in units of the  $dE/dx$  uncertainty. Figure 29.7 shows the pulls for the muon and electron hypotheses for the electron and muon candidates. One can see that the dimuon and Bhabha events are rejected very efficiently.

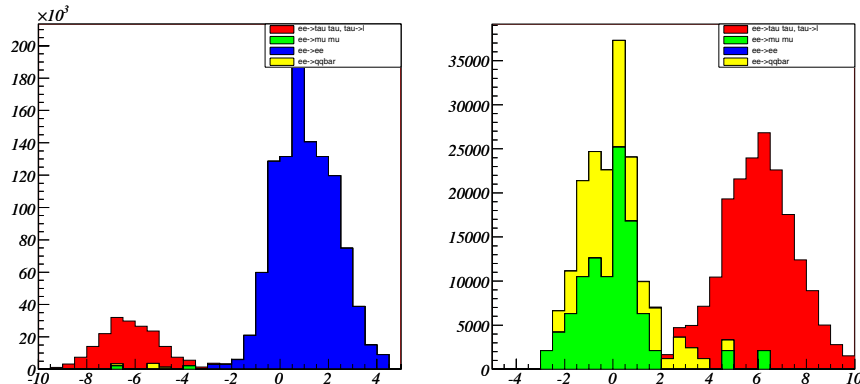


Figure 29.7: Left: the muon hypothesis pull for the electron candidate. Right: the electron hypothesis pull for the muon candidate. The selection cuts were +3 for the electron candidate and -3 for the muon candidate.

Several additional cuts were applied for further background suppression. The electron and muon candidates were required to be identified as such by the electromagnetic calorimeter (EMC) and muon chambers, respectively. Figure 29.8 illustrates the selection criteria. In addition, TOF information was used to reject protons and kaons from hadronic events in the momentum regions where  $dE/dx$  of these particles is close to that of electrons.

The signal selection efficiency was found to be about 30% (with respect to the full solid angle). For an integrated luminosity of 5  $\text{fb}^{-1}$ , this efficiency corresponds to 180K

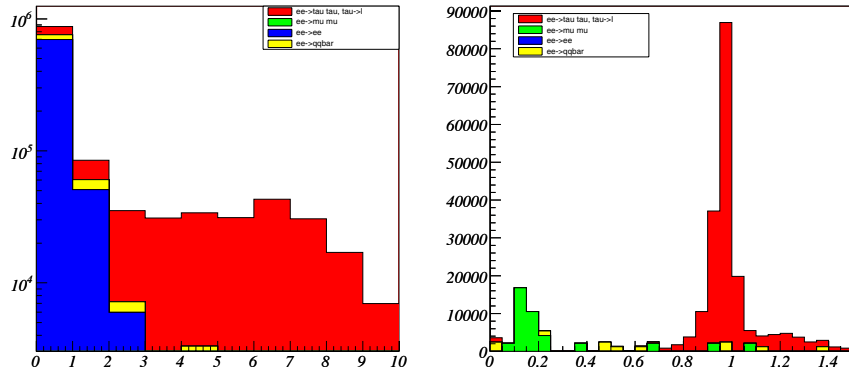


Figure 29.8: Left: the number of hits in muon chambers associated with the muon candidates. Right: the relative electromagnetic energy deposition  $E/P$  in the EMC for the electron candidates. The selection cuts were:  $N_{HIT} \geq 3$  for muons and  $E/P > 0.8$  for electrons.

selected signal events. The residual background is 6%, about half of which are hadronic events  $ee \rightarrow qq$ . The momentum spectra of the selected electron and muon candidates are presented in Fig. 29.9

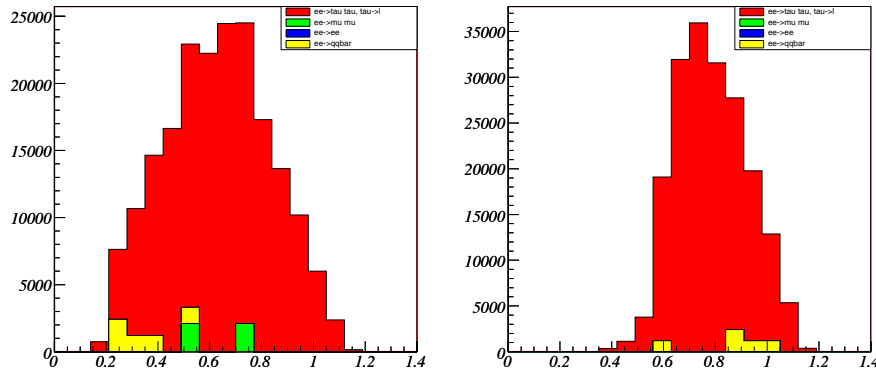


Figure 29.9: The momentum spectra of the selected muon (left) and electron (right) candidates. The statistics corresponds to a  $5 \text{ fb}^{-1}$  data sample.

The spectra of reconstructed momenta of electrons and muons from tau decays were fitted to the expectations for different values of the Michel parameter  $\rho$  and the anomalous coupling constant  $\kappa_\tau^W$ . The statistical uncertainties of the fit parameters are:

$$\sigma(\rho) = 0.003$$

$$\sigma(\eta) = 0.02$$

$$\sigma(\kappa_\tau^W) = 0.002$$

The statistical errors correspond to a  $5 \text{ fb}^{-1}$  data sample collected at a c.m. energy of  $3.69 \text{ GeV}$ .

### Summary

The *BES-III* experiment will provide excellent opportunities to study the Lorentz structure of tau decays, including the measurements of the Michel parameters and a search for an anomalous tensor coupling. Conservative estimates based on Monte-Carlo simulation of leptonic tau decays suggest that the current precision on the Michel parameters can be improved by factors of 2-4, and the limits on the anomalous coupling constant  $\kappa_\tau^W$  can be improved by at least a factor of 10 with a  $5 \text{ fb}^{-1}$  data sample collected at  $E_{cm} = 3.69 \text{ GeV}$ . The inclusion of hadronic tau decays into analysis would significantly improve the precision.

## 29.3 Semileptonic Decays<sup>8</sup>

### 29.3.1 Two-body Semileptonic Decays

The  $\tau$  is the only known lepton massive enough to decay into hadrons. Its semileptonic decays are, thus, ideally suited for studying the hadronic weak currents in very clean conditions. The decay  $\tau^- \rightarrow \nu_\tau H^-$  probes the matrix element of the left-handed charged current between the vacuum and the final hadronic state  $H^-$ .

For the decay modes with lowest multiplicity,  $\tau^- \rightarrow \nu_\tau \pi^-$  and  $\tau^- \rightarrow \nu_\tau K^-$ , the relevant matrix elements (the so-called decay constants  $f_{\pi, K}$ ) are already known from the measured decays  $\pi^- \rightarrow \mu^- \bar{\nu}_\mu$  and  $K^- \rightarrow \mu^- \bar{\nu}_\mu$ . The corresponding  $\tau$  decay widths can then be accurately predicted:

$$R_{\tau/\pi} \equiv \frac{\Gamma(\tau^- \rightarrow \nu_\tau \pi^-)}{\Gamma(\pi^- \rightarrow \mu^- \bar{\nu}_\mu)} = \left| \frac{g_\tau}{g_\mu} \right|^2 \frac{m_\tau^3}{2m_\pi m_\mu^2} \frac{(1 - m_\pi^2/m_\tau^2)^2}{(1 - m_\mu^2/m_\pi^2)^2} (1 + \delta R_{\tau/\pi}), \quad (29.3.26)$$

$$R_{\tau/K} \equiv \frac{\Gamma(\tau^- \rightarrow \nu_\tau K^-)}{\Gamma(K^- \rightarrow \mu^- \bar{\nu}_\mu)} = \left| \frac{g_\tau}{g_\mu} \right|^2 \frac{m_\tau^3}{2m_K m_\mu^2} \frac{(1 - m_K^2/m_\tau^2)^2}{(1 - m_\mu^2/m_K^2)^2} (1 + \delta R_{\tau/K}). \quad (29.3.27)$$

Owing to the different energy scales involved, the radiative corrections to the  $\tau^- \rightarrow \nu_\tau \pi^-/K^-$  amplitudes are, however, not the same as the corresponding effects in  $\pi^-/K^- \rightarrow \mu^- \bar{\nu}_\mu$ . The relative corrections have been estimated [53, 54] to be:

$$\delta R_{\tau/\pi} = (0.16 \pm 0.14)\%, \quad \delta R_{\tau/K} = (0.90 \pm 0.22)\%. \quad (29.3.28)$$

Using these numbers, the measured  $\tau^- \rightarrow \pi^- \nu_\tau$  and  $\tau^- \rightarrow K^- \nu_\tau$  decay rates imply the  $|g_\tau/g_\mu|$  ratios given in Table 29.1.

Assuming universality in the  $W^\pm$  quark couplings, these decay modes determine the ratio [2, 33]

$$\frac{|V_{us}| f_K}{|V_{ud}| f_\pi} = \begin{cases} 0.27618 \pm 0.00048 & [\Gamma_{K/\pi \rightarrow \nu_\mu \mu}], \\ 0.267 \pm 0.005 & [\Gamma_{\tau \rightarrow \nu_\tau K/\pi}]. \end{cases} \quad (29.3.29)$$

The very different accuracies reflect the present poor precision on  $\Gamma(\tau^- \rightarrow \nu_\tau K^-)$ . *BES-III* could considerably improve the measurements of the  $\tau^- \rightarrow \nu_\tau K^-$  and  $\tau^- \rightarrow \nu_\tau \pi^-$  branching ratios. The monochromatic kinematics of the final hadron at threshold will make possible a clean separation of each decay mode and, therefore, excellent accuracy.

### 29.3.2 Decays into Two Hadrons

For the two-pion final state, the hadronic matrix element is parameterized in terms of the so-called pion form factor [ $s \equiv (p_{\pi^-} + p_{\pi^0})^2$ ]:

$$\langle \pi^- \pi^0 | \bar{d} \gamma^\mu u | 0 \rangle \equiv \sqrt{2} F_\pi(s) (p_{\pi^-} - p_{\pi^0})^\mu. \quad (29.3.30)$$

A dynamical understanding of the pion form factor can be achieved [55, 56, 57, 58], using analyticity, unitarity and some general properties of QCD, such as chiral symmetry

---

<sup>8</sup>By A. Pich

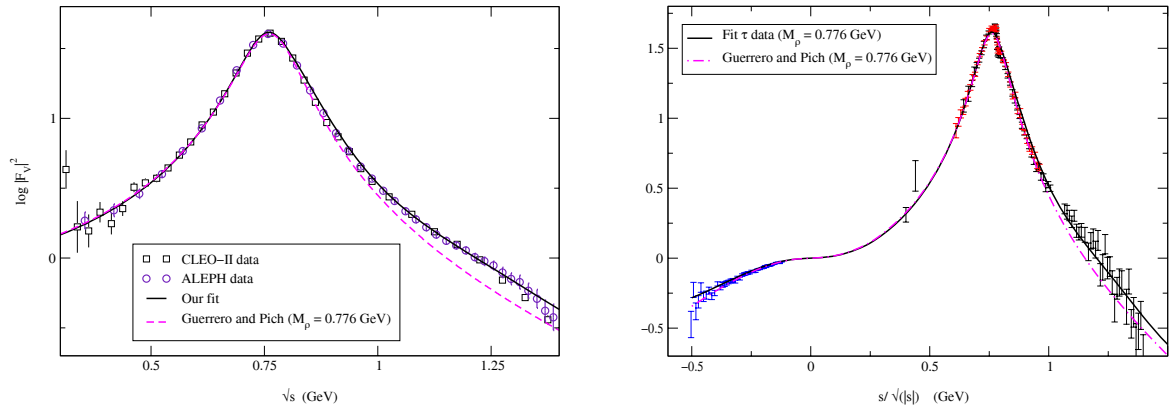


Figure 29.10: The pion form factor from  $\tau$  data [62, 63] (left) and  $e^+e^-$  data [64, 65] (right), compared with theoretical predictions [55, 56]. The dashed lines correspond to the expression in Eq. 29.3.31.

[59] and the short-distance asymptotic behavior [60, 61]. Putting all these fundamental ingredients together, one gets the result [56]

$$F_\pi(s) = \frac{M_\rho^2}{M_\rho^2 - s - iM_\rho\Gamma_\rho(s)} \exp \left\{ -\frac{s \operatorname{Re} A(s)}{96\pi^2 f_\pi^2} \right\}, \quad (29.3.31)$$

where

$$A(s) \equiv \log \left( \frac{m_\pi^2}{M_\rho^2} \right) + 8 \frac{m_\pi^2}{s} - \frac{5}{3} + \sigma_\pi^3 \log \left( \frac{\sigma_\pi + 1}{\sigma_\pi - 1} \right) \quad (29.3.32)$$

contains the one-loop chiral logarithms,  $\sigma_\pi \equiv \sqrt{1 - 4m_\pi^2/s}$  and the off-shell  $\rho$  width [56, 57] is given by  $\Gamma_\rho(s) = \theta(s - 4m_\pi^2) \sigma_\pi^3 M_\rho s / (96\pi f_\pi^2)$ . This prediction, which only depends on  $M_\rho$ ,  $m_\pi$  and the pion decay constant  $f_\pi$ , is compared with the data in Fig. 29.10. The agreement is rather impressive and extends to negative  $s$  values, where the  $e^-\pi$  elastic data applies.

The small effects of heavier  $\rho$  resonance contributions and additional next-to-leading order  $1/N_C$  corrections can be easily included, at the price of having some free parameters that decrease the predictive power [55, 58]. This gives a better description of the  $\rho'$  shoulder around 1.2 GeV (continuous lines in Fig. 29.10). A clear signal for the  $\rho''(1700)$  resonance in  $\tau^- \rightarrow \nu_\tau \pi^- \pi^0$  events has been reported by Belle (see Fig. 29.11), with a data sample 20 times larger than that of previous experiments [66].

The  $\tau^- \rightarrow \nu_\tau \pi^- \pi^0$  decay amplitude can be related through an isospin rotation with the isovector piece of  $e^+e^- \rightarrow \pi^+\pi^-$ . Thus, for  $s < m_\tau^2$ ,  $F_\pi(s)$  can be obtained from the two sets of data. At present, there exists a serious discrepancy between  $e^+e^-$  and  $\tau$  data. From  $e^+e^-$  data one predicts  $\operatorname{Br}(\tau \rightarrow \nu_\tau 2\pi) = (24.48 \pm 0.18)\%$ , which is  $4.5\sigma$  smaller than the direct  $\tau$  measurement  $(25.40 \pm 0.10)\%$  [67]. This discrepancy translates into two different estimates of the hadronic vacuum polarization to the anomalous magnetic moment of the muon; while the  $e^+e^-$  data leads to a theoretical prediction for  $(g-2)_\mu$  which is  $3.3\sigma$  below the BNL-E821 measurement, the prediction obtained from the  $\tau$  data is in much better agreement ( $0.9\sigma$ ) with the experimental value [7].

Clearly, new precise  $e^+e^-$  and  $\tau$  data sets are needed. The present experimental situation is very unsatisfactory, showing internal inconsistencies among different  $e^+e^-$

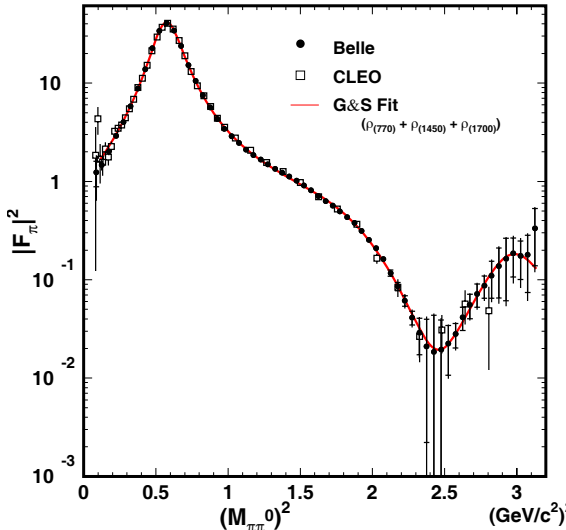


Figure 29.11: Preliminary Belle measurements of the pion form factor from  $\tau^- \rightarrow \nu_\tau \pi^- \pi^0$  decays [66].

and  $\tau$  measurements. The KLOE  $e^+e^-$  invariant-mass distribution does not agree with CMD2 and SND, while the most recent Belle measurement of the  $\tau$  decay spectrum [66] slightly disagrees with ALEPH and CLEO [67]. The accurate measurement of  $F_\pi(s)$  at *BES-III* could clarify this important issue.

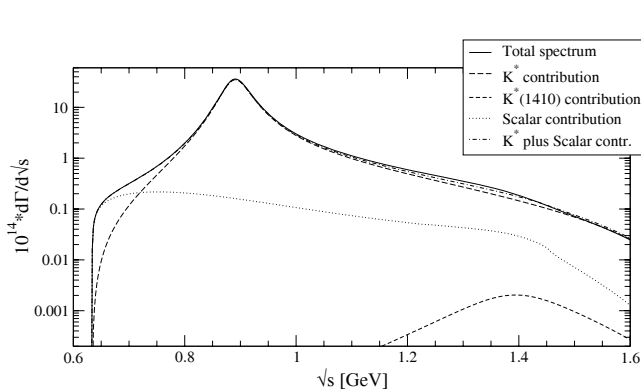


Figure 29.12: Predicted  $\tau \rightarrow \nu_\tau K\pi$  distribution, together with the separate contributions from the  $K^*(892)$  and  $K^*(1410)$  vector mesons as well as the scalar component residing in  $F_0^{K\pi}(s)$  [68].

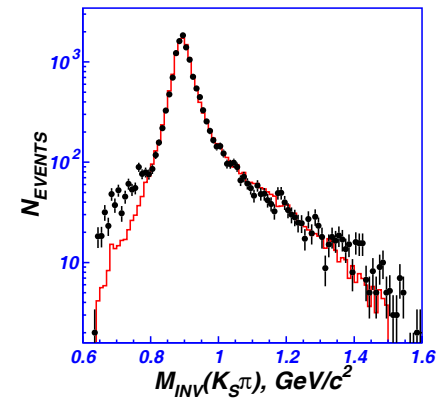


Figure 29.13:  $K_S\pi$  invariant-mass distribution from BELLE  $\tau \rightarrow \nu_\tau K_S\pi$  events. The histogram shows the expected  $K^*(892)$  contribution [70].

More recently, the decay  $\tau \rightarrow \nu_\tau K\pi$  has been studied in Ref. [68]. The hadronic spectrum, shown in Fig. 29.12, is characterized by two form factors,

$$\frac{d\Gamma_{K\pi}}{d\sqrt{s}} = \frac{G_F^2 |V_{us}|^2 m_\tau^3}{32\pi^3 s} \left(1 - \frac{s}{m_\tau^2}\right)^2 \left[ \left(1 + 2 \frac{s}{m_\tau^2}\right) q_{K\pi}^3 |F_+^{K\pi}(s)|^2 + \frac{3\Delta_{K\pi}^2}{4s} q_{K\pi} |F_0^{K\pi}(s)|^2 \right], \quad (29.3.33)$$

where  $q_{K\pi} = \frac{1}{2\sqrt{s}} \lambda^{1/2}(s, m_K^2, m_\pi^2)$  and  $\Delta_{K\pi} = m_K^2 - m_\pi^2$ . The vector form factor  $F_+^{K\pi}(s)$

has been described in an analogous way to  $F_\pi(s)$ , while the scalar component  $F_0^{K\pi}(s)$  takes into account additional information from  $K\pi$  scattering data through dispersion relations [33, 69]. The decay width is dominated by the  $K^*(892)$  contribution, with a predicted branching ratio  $\text{Br}[\tau \rightarrow \nu_\tau K^*] = (1.253 \pm 0.078)\%$ , while the scalar component is found to be  $\text{Br}[\tau \rightarrow \nu_\tau(K\pi)_{\text{S-wave}}] = (3.88 \pm 0.19) \cdot 10^{-4}$ .

Preliminary measurements of the  $\tau^- \rightarrow \nu_\tau K_S \pi^-$  (Belle [70]) and  $\tau^- \rightarrow \nu_\tau K^- \pi^0$  (BaBar [71]) distributions show clear evidence for the scalar contribution at low invariant masses and a  $K^*(1410)$  vector component at large  $s$  (see Fig. 29.13).

The dynamical structure of other hadronic final states can be investigated in a similar way. The  $\tau \rightarrow \nu_\tau 3\pi$  decay mode was studied in Ref. [72], where a theoretical description of the measured structure functions [73, 74, 16] was provided. A detailed analysis of other  $\tau$  decay modes into three final pseudoscalar mesons is in progress [75]. The more complicated  $\tau \rightarrow \nu_\tau 4\pi$  and  $e^+e^- \rightarrow 4\pi$  transitions have also been studied [76]. Accurate experimental measurements of the hadronic decay distributions would provide a very valuable data set to perform important tests of QCD in the non-perturbative regime. Violation in  $\tau$

## 29.4 Search for $CP$ Violation in $\tau$ decays<sup>9</sup>

There are two powerful motivations for probing  $CP$  symmetry in lepton decays:

- The discovery of  $CP$  asymmetries in  $B$  decays that are close to 100 % in a sense ‘de-mystifies’  $CP$  violation, in that it established that complex  $CP$  phases are not intrinsically small and can even be close to 90 degrees. This de-mystification would be completed, if  $CP$  violation were found in the decays of leptons as well.
- We know that CKM dynamics, which is so successful in describing quark flavour transitions, is utterly irrelevant to baryogenesis. There are actually intriguing arguments for baryogenesis being merely a secondary effect driven by primary leptogenesis [77]. To make the latter less speculative, one has to find  $CP$  violation in leptodynamics.

The strength of these motivations has been well recognized in the community, as can be seen from the planned experiments to measure  $CP$  violation in neutrino oscillations and the ongoing heroic efforts to find an electron EDM. Yet there are other avenues to this goal as well that certainly are at least as challenging, namely to probe  $CP$  symmetry in  $\tau$  decays. There is also a less orthodox probe, namely attempting to extract an EDM for  $\tau$  leptons from  $e^+e^- \rightarrow \tau^+\tau^-$ . It is understood that the Standard Model does not produce an observable effect here. One should also note that one is searching for a  $CP$ -odd effect in an *electromagnetic* production process unlike in  $\tau$  decays, which are controlled by the weak force.

The betting line is that  $\tau$  decays – next to the electron EDM and  $\nu$  oscillations – provide the best stage to search for manifestations of  $CP$  breaking leptodynamics. There exists a considerable literature on the subject started by discussions on a tau-charm factory more than a decade ago [78, 79, 80, 81], which has recently attracted renewed interest recently [82, 83, 84, 85] especially stressing the following points:

---

<sup>9</sup>By I. I. Bigi

- There are many more decay channels for tau leptons than for muons, making the constraints imposed by  $CPT$  symmetry much less restrictive.
- The  $\tau$  lepton has sizable rates into multibody final states. Due to their nontrivial kinematics, asymmetries can emerge in the final-state distributions, where they are likely to be significantly larger than in the integrated widths. The channel

$$K_L \rightarrow \pi^+ \pi^- e^+ e^-$$

illustrates this point. It commands only the tiny branching ratio of  $3 \cdot 10^{-7}$ . The forward-backward asymmetry  $\langle A \rangle$  in the angle between the  $\pi^+ \pi^-$  and  $e^+ e^-$  planes constitutes a  $CP$ -odd observable. It has been measured by KTeV and NA48 to be truly large, namely about 13 %, although it is driven by the small value of  $|\epsilon_K| \sim 0.002$ . One can, thus, trade branching ratio for the size of a  $CP$  asymmetry.

- New Physics in the form of multi-Higgs models can contribute on the tree-level, such as the SM W exchange.
- Some of the channels could exhibit enhanced sensitivity to New Physics.
- Having polarized  $\tau$  leptons provides a powerful handle on  $CP$  asymmetries as well as control over systematics.

These features will be explained in more detail below. It seems clear that such measurements can be performed only in  $e^+ e^-$  annihilation, *i.e.* at *BES-III*, the existing  $B$  factories, or better still at a Super-Flavour factory. There one has the added advantage that one can realistically obtain highly polarized  $\tau$  leptons: This can be achieved directly by having the electron beam longitudinally polarized or more indirectly even with unpolarized beams by using the spin alignment of the produced  $\tau$  pair to ‘tag’ the spin of the  $\tau$  under study by the decay of the other  $\tau$  like  $\tau \rightarrow \nu \rho$ .

#### 29.4.1 $\tau \rightarrow \nu K \pi$

The most promising channels for exhibiting  $CP$  asymmetries are  $\tau^- \rightarrow \nu K_S \pi^-$ ,  $\nu K^- \pi^0$  [81]:

- Due to the heaviness of the lepton and quark flavours they are most sensitive to nonminimal Higgs dynamics while being Cabibbo suppressed in the SM.
- They can show asymmetries in the final state distributions.

The SM does generate a  $CP$  asymmetry in  $\tau$  decays that should be observable. Based on known physics one can reliably predict a  $CP$  asymmetry [82]:

$$\frac{\Gamma(\tau^+ \rightarrow K_S \pi^+ \bar{\nu}) - \Gamma(\tau^- \rightarrow K_S \pi^- \nu)}{\Gamma(\tau^+ \rightarrow K_S \pi^+ \bar{\nu}) + \Gamma(\tau^- \rightarrow K_S \pi^- \nu)} = (3.27 \pm 0.12) \times 10^{-3} \quad (29.4.34)$$

due to  $K_S$ ’s preference for antimatter over matter. Strictly speaking, this prediction is more general than the SM: no matter what produces the  $CP$  impurity in the  $K_S$  wave

function, the effect underlying Eq. 29.4.34 has to be present, while of course not affecting  $\tau^\mp \rightarrow \nu K^\mp \pi^0$ .

To generate a  $CP$  asymmetry, one needs two different amplitudes that contribute coherently. This requirement is satisfied, since the  $K\pi$  system can be produced from the (QCD) vacuum in a vector and scalar configuration with form factors  $F_V$  and  $F_S$ , respectively. Both are present in the data, with the vector component (mainly in the form of the  $K^*$ ) dominant as expected [6]. Within the SM, there is no weak phase between them at any observable level, yet it can readily be provided by a charged Higgs exchange in non-minimal Higgs models, which contribute to  $F_S$ .

A few general remarks on the phenomenology might be helpful to set the stage. For a  $CP$  violation in the underlying weak dynamics to generate an observable asymmetry in partial widths or energy distributions, one also needs a relative strong phase between the two amplitudes:

$$\Gamma(\tau^- \rightarrow \nu K^- \pi^0) - \Gamma(\tau^+ \rightarrow \bar{\nu} K^+ \pi^0), \frac{d}{dE_K} \Gamma(\tau^- \rightarrow \nu K^- \pi^0) - \frac{d}{dE_K} \Gamma(\tau^+ \rightarrow \bar{\nu} K^+ \pi^0) \propto \text{Im}(F_H F_V^*) \text{Im} g_H g_W^*, \quad (29.4.35)$$

where  $F_H$  denotes the Higgs contribution to  $F_S$  and  $g_H$  its weak coupling. This should not represent a serious restriction, since the  $K\pi$  system is produced in a mass range with several resonances. If, on the other hand, one is searching for a  $T$ -odd correlation such as

$$O_T \equiv \langle \vec{\sigma}_\tau \cdot (\vec{p}_K \times \vec{p}_\pi) \rangle, \quad (29.4.36)$$

then  $CP$  violation can surface even *without* a relative strong phase

$$O_T \propto \text{Re}(F_H F_V^*) \text{Im} g_H g_W^*. \quad (29.4.37)$$

However, there is a caveat: final state interactions can generate  $T$ -odd moments even from  $T$ -invariant dynamics, where one has

$$O_T \propto \text{Im}(F_H F_V^*) \text{Re} g_H g_W^*. \quad (29.4.38)$$

Fortunately one can differentiate between the two scenarios of Eqs. 29.4.37 and 29.4.38 at *BES-III* by comparing directly the  $T$ -odd moments for the  $CP$ -conjugate pair  $\tau^+$  and  $\tau^-$ :

$$O_T(\tau^+) \neq O_T(\tau^-) \implies CP \text{ violation!} \quad (29.4.39)$$

A few numerical scenarios might illuminate the situation: a Higgs amplitude 1% or 0.1% the strength of the SM  $W$ -exchange amplitude – the former [latter] contributing [mainly] to  $F_S$  [ $F_V$ ] – is safely in the ‘noise’ of present measurements of partial widths; yet it could conceivably create a  $CP$  asymmetry as large 1% or 0.1%, respectively. More generally a  $CP$ -odd observable in a SM allowed process is merely *linear* in a New Physics amplitude, since the SM provides the other amplitude. On the other hand SM-forbidden transitions – say lepton-flavour violation as in  $\tau \rightarrow \mu\gamma$  – have to be *quadratic* in the New Physics amplitude.

$$CP - \text{odd} \propto |T_{SM}^* T_{NP}| \text{ vs. LFV} \propto |T_{NP}|^2 \quad (29.4.40)$$

Probing  $CP$  symmetry on the 0.1% level in  $\tau \rightarrow \nu K\pi$  thus has roughly the same sensitivity for a New Physics amplitude as searching for  $\text{BR}(\tau \rightarrow \mu\gamma)$  on the  $10^{-8}$  level.

CLEO has undertaken a pioneering search for a  $CP$  asymmetry in the angular distribution of  $\tau \rightarrow \nu K_S \pi$  placing an upper bound of a few percent [86].

### 29.4.2 Other $\tau$ decay modes

It appears unlikely that analogous asymmetries could be observed in the Cabibbo allowed channel  $\tau \rightarrow \nu\pi\pi$ , yet detailed studies of  $\tau\nu 3\pi/4\pi$  look promising, also because the more complex final state allows one to form  $T$ -odd correlations with unpolarized  $\tau$  leptons; on the other hand, decays of polarized  $\tau$  leptons might exhibit much larger  $CP$  asymmetries [83].

Particular attention should be paid to  $\tau \rightarrow \nu K 2\pi$ , which has potentially very significant additional advantages:

- ⊕: One can interfere *vector* with *axial vector*  $K 2\pi$  configurations.
- ⊕: The larger number of kinematical variables and of specific channels should provide more internal cross checks of systematic uncertainties such as detection efficiencies for positive vs. negative particles.



# Chapter 30

## $\tau$ mass near threshold<sup>1</sup>

### 30.1 Introduction

The mass of the  $\tau$  lepton is a fundamental parameter of the Standard Model; many experiments [87, 88, 89, 90, 91, 92, 93, 94, 95, 96] have measured it as shown in Fig. 30.1. Experimentally, the depolarization technique developed by the KEDR collaboration has been used to realize a highly accurate beam energy calibration — at the level of one part in  $10^6$  for c.m. energies near the  $\tau$  mass threshold [97]— while theoretically, accurate calculations have claimed precisions at the level of one part in  $10^4$  for the near-threshold  $\tau$ -pair production cross section [103, 105, 107, 99]. Large  $\tau$ -pair data samples are expected at *BES-III* and, therefore, it is of great interest to understand how accurate a  $\tau$  mass measurement we can look forward to having in the near future.

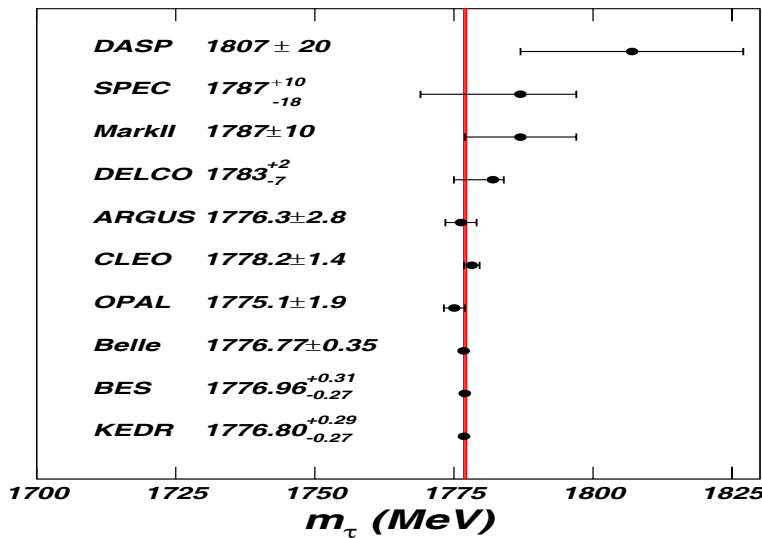


Figure 30.1: A comparison of different measurements of the  $\tau$  mass. The vertical line indicates the current world average value:  $1776.99^{+0.29}_{-0.26}$  MeV [2], which is the averaged result of the measurements from Refs. [90, 91, 92, 93, 94].

<sup>1</sup>By Xiao-Hu Mo, Y. K. Wang, C. Z. Yuan and C. D. Fu

Usually, either pseudomass and threshold-scan methods are employed to measure the  $\tau$  mass. The scan method adopted by the BES-I collaboration achieved the most accurate single measurement of the  $\tau$  mass [92]:

$$m_\tau = 1776.96^{+0.18+0.25}_{-0.21-0.17} \text{ MeV} . \quad (30.1.1)$$

Note that the relative statistical ( $1.6 \times 10^{-4}$ ) and systematic ( $1.7 \times 10^{-4}$ ) uncertainties are comparable in magnitude, improvements are needed in both categories.

## 30.2 Statistical Optimization

### 30.2.1 Methodology

We need to develop a scheme that provides the most precise  $\tau$  mass measurement one can achieve given a specific period of data-taking time or, equivalently, a given amount of integrated luminosity. A sampling technique is utilized to simulate various data taking possibilities, among which the optimal one is to be found. The likelihood function for a given scheme is constructed as [92, 108, 109]:

$$LF(m_\tau) = \prod_i^n \frac{\mu_i^{N_i} e^{-\mu_i}}{N_i!} , \quad (30.2.2)$$

where  $N_i$  is the observed number of  $\tau^+\tau^-$  events detected in the  $e\mu$  final state<sup>2</sup> at the c.m. energy scan point  $i$  and  $\mu_i$  is the expected number of events given by

$$\mu_i(m_\tau) = [\epsilon \cdot B_{e\mu} \cdot \sigma_{exp}(m_\tau, E_{cm}^i) + \sigma_{BG}] \cdot \mathcal{L}_i . \quad (30.2.3)$$

In Eq. (30.2.3),  $\mathcal{L}_i$  is the integrated luminosity at  $i^{\text{th}}$  point,  $\epsilon$  is the overall detection efficiency for the  $e\mu$  final states (including the trigger and event selection efficiencies),  $B_{e\mu}$  is the combined branching ratio for decays  $\tau^+ \rightarrow e^+ \nu_e \bar{\nu}_\tau$  and  $\tau^- \rightarrow \mu^- \bar{\nu}_\mu \nu_\tau$  (or the corresponding charge conjugate mode) and  $\sigma_{exp}$  is the experimentally observed cross section, which has the form [98]

$$\sigma_{exp}(s, m_\tau, \Delta) = \int_0^\infty d\sqrt{s'} G(\sqrt{s'}, \sqrt{s}) \int_0^{1-\frac{4m_\tau^2}{s'}} dx F(x, s') \frac{\bar{\sigma}(s'(1-x), m_\tau)}{|1 - \Pi(s'(1-x))|^2} . \quad (30.2.4)$$

Here  $\sqrt{s}$  is the c.m. energy;  $F(x, s)$  is the initial-state radiation factor [98],  $\Pi$  is the vacuum polarization factor [99, 100, 101], and  $G(\sqrt{s'}, \sqrt{s})$ , which is usually treated as a Gaussian distribution [102], depicts the energy spread of the  $e^+e^-$  collider. The production cross section  $\bar{\sigma}$  can be expressed as<sup>3</sup>

$$\bar{\sigma}(v) = \frac{2\pi\alpha^2}{3s} v(3 - v^2) F_c(v) \left( 1 + \frac{\alpha}{\pi} S(v) - \frac{\pi\alpha}{2v} + h(v) \right) , \quad (30.2.5)$$

<sup>2</sup>For simplicity only the  $e\mu$  channel is considered at this time; the statistical significance will be improved if more channels are taken into account, see Sect. 30.2.4 for a detailed discussion.

<sup>3</sup>Here the Voloshin's formula in Ref. [103] is adopted. This takes into account: (a) radiation from the initial electron and positron; (b) vacuum polarization of the time-like photon; (c) corrections to the special density of the electromagnetic current of the tau leptons; and (d) the interference between the effects (a)-(c) which start from the relative order  $\alpha^2$ .

Here  $v = \sqrt{1 - 4m_\tau^2/s}$  is the velocity of either of the  $\tau$  leptons in the c.m. frame and  $F_c(v)$  is the so-called Coulomb factor, which is defined as

$$F_c(v) = \frac{\pi\alpha/v}{1 - \exp(-\pi\alpha/v)} . \quad (30.2.6)$$

A description of the correction function  $S(v)$  can be found in Schwinger's textbook [104]:

$$\begin{aligned} S(v) = & \frac{1}{v} \left\{ (1 + v^2) \left[ \frac{\pi^2}{6} + \ln\left(\frac{1+v}{2}\right) \ln\left(\frac{1+v}{1-v}\right) + 2\text{Li}_2\left(\frac{1-v}{1+v}\right) + 2\text{Li}_2\left(\frac{1+v}{2}\right) \right. \right. \\ & - 2\text{Li}_2\left(\frac{1-v}{2}\right) - 4\text{Li}_2(v) + \text{Li}_2(v^2) \left. \right] \\ & + \left[ \frac{11}{8}(1 + v^2) - 3v + \frac{1}{2} \frac{v^4}{(3 - v^2)} \right] \ln\left(\frac{1+v}{1-v}\right) \\ & \left. + 6v \ln\left(\frac{1+v}{2}\right) - 4v \ln v + \frac{3}{4}v \frac{(5 - 3v^2)}{(3 - v^2)} \right\} , \end{aligned} \quad (30.2.7)$$

with

$$\text{Li}_2(x) = - \int_0^x \ln(1-t)dt/t = \sum_{n=1}^{\infty} x^n/n^2.$$

The correction function  $h(v)$  is expressed in terms of a double integral [103, 105]:

$$h(v) = \frac{2\alpha}{3\pi} \left[ -2\lambda \text{Im} \int_0^\infty dt \int_1^\infty dx \left( \frac{1+t}{t} \right)^{i\lambda} \frac{(t + izxv^{-1})^{i\lambda-1}}{(t + 1 + izxv^{-1})^{i\lambda+1}} \left( 1 + \frac{1}{2x^2} \right) \frac{\sqrt{x^2 - 1}}{x^2} \right] , \quad (30.2.8)$$

with

$$z = m_e/m_\tau , \quad \lambda = \frac{\alpha}{2v} .$$

The function  $h(v)$  contains corrections from two sources: the so-called hard correction due to a finite radiative effect in the  $\tau$  electromagnetic vertex at the threshold, and from the modification of the Coulomb interaction due to running of the coupling  $\alpha$ , which is described by the Uehling-Serber radiative correction to the potential [106].

In the following study, we take  $\epsilon = 14.2\%$  [110], the c.m. energy spread<sup>4</sup>  $\Delta = 1.4$  MeV and  $B_{e\mu} = 0.06194$  [2]. We neglect the corresponding uncertainties, which are left for the systematic study. As for  $\sigma_{BG}$ , previous experience [108] indicates that  $\sigma_{BG} \approx 0.024 \text{ pb}^{-1}$ , which is small compared to the  $\tau^+\tau^-$  production cross section near threshold of ( $\simeq 0.1 \text{ nb}^{-1}$ ). In any case, a large data sample can be taken below the threshold to determine  $\sigma_{BG}$  accurately. For simplicity, we set  $\sigma_{BG}$  to be zero, which means it is background free. In fact, if  $\sigma_{BG}$  is a constant, it has no effect on the optimization of the data taking strategy.

Since we want to optimize the accuracy of the  $m_\tau$  measurement, the value of  $\tau$  mass itself is assumed to be known. In fact, the optimal number of points and the luminosity

<sup>4</sup>The c.m. energy spread is calculated from the empirical formula:  $\Delta = (0.16203E_{cm}^2/4 + 0.89638) \times 10^{-3}$  GeV, which gives  $\Delta = 1.4$  MeV at  $E_{cm} = 1.77699$  GeV [110].

distribution among these points are correlated. To resolve this dilemma, we use an iterative procedure: we start from a simple distribution and look for the optimal number of points; we then look for an optimal distribution; with such a distribution, we then reoptimize the number of points.

### 30.2.2 First Optimization

As a starting point, we study an energy interval that is evenly divided, *viz.*

$$E_i = E_0 + i \times \delta E, \quad (i = 1, 2, \dots, N_{pt}). \quad (30.2.9)$$

Here the initial point is  $E_0 = 3.545$  GeV, the final point is  $E_f = 3.595$  GeV and the fixed step is  $\delta E = (E_f - E_0)/N_{pt}$ , where  $N_{pt}$  is the number of energy points. The total luminosity is distributed equally ( $\mathcal{L}_i = \mathcal{L}_{tot}/N_{pt}$ ) at each point,<sup>5</sup> and the fitted  $m_\tau$  and corresponding uncertainty  $S_{m_\tau}^2(m_\tau)$  using Eq. (30.2.2) is averaged over all the samplings ( $N_{samp}$ ) for each  $N_{pt}$  value in order to suppress or reduce the statistical fluctuation [111]:

$$\bar{m}_\tau^i = \frac{1}{N_{samp}} \sum_{j=1}^{N_{samp}} m_{\tau j}^i, \quad (30.2.10)$$

$$S_{m_\tau}^2(m_\tau^i) = \frac{1}{N_{samp} - 1} \sum_{j=1}^{N_{samp}} (m_{\tau j}^i - \bar{m}_\tau^i)^2. \quad (30.2.11)$$

Here  $i$  indicates the scheme being tested while  $j$  indicates the sampling times, which is 500 in this study.

Using the experiment parameters  $\epsilon$ ,  $\Delta$ , and  $B_{e\mu}$  given in Sect. 30.2.1 and setting  $\mathcal{L}_{tot} = 30 \text{ pb}^{-1}$ , we obtain the fitted results for  $N_{pt}$  ranging from 3 to 20 shown in Figs. 30.2(a) and (b), where  $\Delta m_\tau = \bar{m}_\tau - m_\tau^0$ , the difference between the average fitted  $m_\tau$  and the input value ( $m_\tau^0 = 1776.99$  MeV according to PDG06 [2]), and  $S_{m_\tau}$  is the corresponding *rms* uncertainty.

The  $\Delta m_\tau$  values, shown as the dots in Fig. 30.2(a), indicate the fit bias due to the limited number of events. With increased luminosity (and increased number of events), the bias tends to zero. This point is demonstrated more clearly in a separate study of the variation of  $\Delta m_\tau$  with luminosity, discussed below (in reference to Table 30.1).

For the fit uncertainties,  $S_{m_\tau}$ , two points should be noted: first,  $S_{m_\tau}$  is much larger than absolute value of the bias  $|\Delta m_\tau|$ . Thus, from the point view of accuracy, the optimization of the former is much more crucial than that of the latter. Therefore, in the following study  $S_{m_\tau}$  is used as the goodness-of-fit quantity. Second, it is evident in Fig. 30.2(b) that taking very few data points yields a large uncertainty, while having many points makes no contribution to the improvement of the accuracy. From the figure one can see that  $N_{pt} = 5$  is near the optimal number of measurement points for the evenly-divided-distribution scheme.

<sup>5</sup>Another scheme is to apportion the total number of events evenly at each point, the luminosity at each point is determined by relation  $\mathcal{L}_i = \mathcal{L}_{tot}/(\sigma_i \cdot \sum 1/\sigma_i)$  with  $\sigma_i$  denotes the cross section at  $i$ -th point. This scheme leads to the same final conclusion of this study.

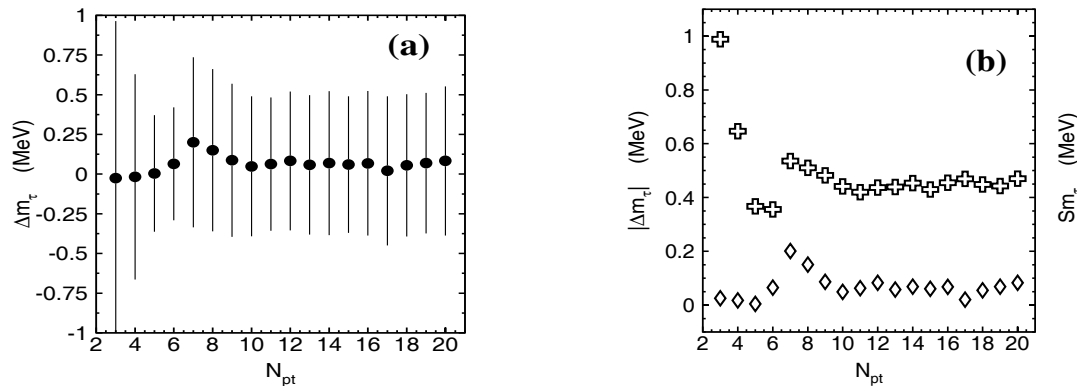


Figure 30.2: The variation of  $\Delta m_\tau$  (and  $|\Delta m_\tau|$ ) and  $S_{m_\tau}$  versus the number of measurement points  $N_{pt}$ . In (a) the dots and bars represent  $\Delta m_\tau$  and  $S_{m_\tau}$ , respectively. In (b) the diamonds denote  $|\Delta m_\tau|$  and the crosses  $S_{m_\tau}$ .

With five points, we search further for ways to minimize the fit uncertainty. Without any theoretical considerations, a sampling technique is employed and the energy points are distributed randomly over the chosen interval. In a total of 200 samplings, the one with the smallest uncertainty has  $S_{m_\tau} = 0.152$  MeV and the one with the greatest uncertainty has  $S_{m_\tau} = 1.516$  MeV. The two extreme distributions are indicated in Fig. 30.3. It is apparent that the small uncertainty measurement has scan points that are crowded near the threshold, while the scheme with the large uncertainty has scan points that are far from the threshold.<sup>6</sup> Intuitively, one expects that the smallest uncertainty occurs at energies near the point where the derivative of the cross section is largest. This must be, therefore, close to the optimal position for data taking, as discussed in the next section.

### 30.2.3 Second Optimization

Based on the previous study, we embark on studies to determine (a) the energy region most sensitive to the fit uncertainty, (b) the optimal number of points that should be taken in that region, and (c) the locations of the optimal points.

#### Optimal region

To hunt for the most sensitive energy region, two regions are defined as shown in Fig. 30.4(a): region *I* ( $E_{cm} \subset (3.553, 3.558)$  GeV), where the derivative is greater than 75% of its maximum value and region *II* ( $E_{cm} \subset (3.565, 3.595)$  GeV), where the variation of the derivative is smoother than it is in region *I*.

To confirm the afore-mentioned speculation, two schemes are designed. In the first scheme, two points are taken in region *I*, one at 3.55398 GeV as the threshold point and the other at 3.5548 GeV corresponding to the energy point where the derivative of the cross section is largest. In addition points are taken in the region *II*, with the number of points  $N_{pt}$  is varied from 1 to 20, with each point having a luminosity of  $5 \text{ pb}^{-1}$ . The fit results for this scheme, displayed as crosses in Fig. 30.4(b), show no improvement in

<sup>6</sup>For both schemes, the lowest energy point in Fig. 30.3 corresponds to an expected number of events of zero, since they are below threshold.

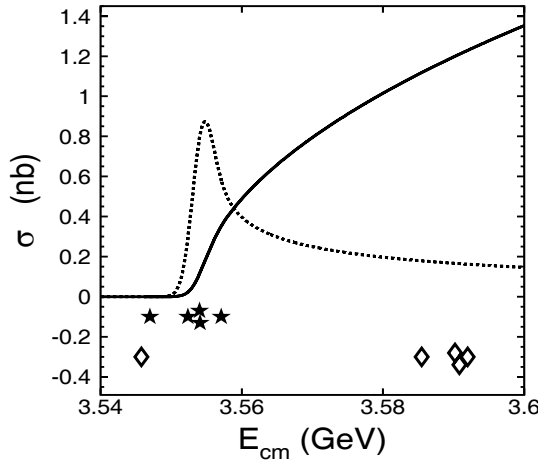


Figure 30.3: The distributions of the data taking points for the schemes with the smallest (denoted by stars) and largest (denoted by diamonds) values of  $S_{m_\tau}$ . The solid curve is the calculated observed cross section, and the dashed line the corresponding derivative of the cross section with respect to energy (with a scale factor of  $10^{-2}$ ).

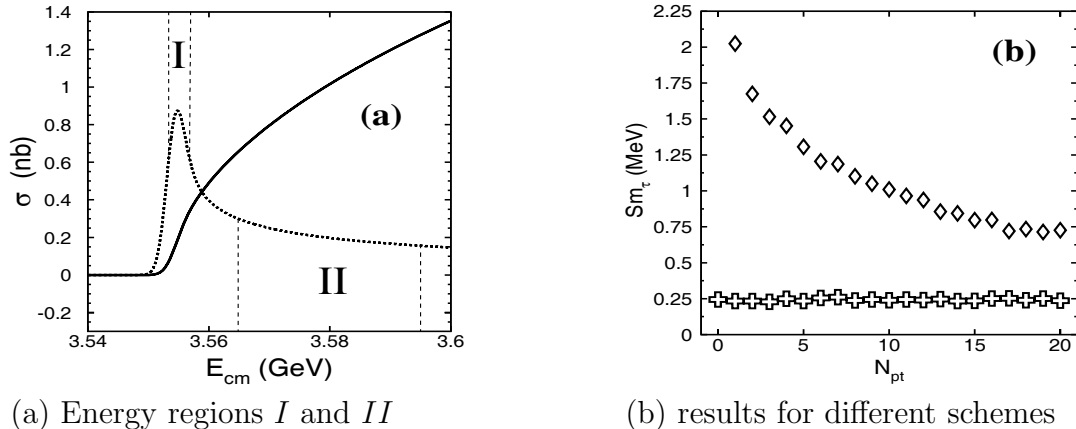


Figure 30.4: (a) The locations of the energy subregions  $I$  and  $II$ , with different derivative features. Here the solid line denotes the observed cross section and the dashed line the corresponding derivative value (with a scale factor of  $10^{-2}$ ). (b) The fit uncertainties for the two measurement schemes, the crosses and the diamonds denote, respectively, the results for the first and second schemes as described in the text.

precision resulting from an increased number of data points in region  $II$  ( $S_{m_\tau}$  stays very near 0.25 MeV for any number of points). To further examine this point, we investigated a second scheme, which only uses energy points in region  $II$ , again with  $N_{pt}$  varied from 1 to 20. The fit results for this scheme are displayed as diamonds in Fig. 30.4(b). As expected, with the increasing number of points,  $S_{m_\tau}$  decreases, but even with 20 points spread over region  $II$ , the value of  $S_{m_\tau} = 0.7256$  MeV is still much larger than that of  $S_{m_\tau}$  with only two points in region  $I$ . From this we conclude that the data taken at energy points within region  $I$  are much more useful for optimal data taking.

## Optimal position

In this subsection, we investigate the number of energy points that are optimal in the large derivative region ( $I$ ). Using a procedure similar to that described in Sect. 30.2.2, the total luminosity  $\mathcal{L}_{tot} = 45 \text{ pb}^{-1}$  is evenly distributed into  $N_{pt}$  points ( $N_{pt} = 1, 2, \dots, 6$ ) inside the energy region between 3.553 GeV and 3.557 GeV. The results for  $S_{m_\tau}$  are shown in Fig. 30.5, where it is seen that the number of points has a weak effect on the final uncertainty. In other words, within the large derivative region, a single point is sufficient to give a small uncertainty. This is easy to understand since there is only one free parameter ( $m_\tau$ ) to be fit in the  $\tau^+\tau^-$  production cross section, even one measurement will fix the normalization of the curve. The larger the derivative, the more sensitivity to the mass of  $\tau$  lepton.

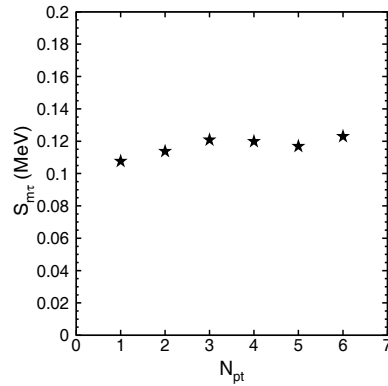


Figure 30.5: The relation between  $S_{m_\tau}$  and the number of measurement points within the energy region between 3.553 GeV and 3.555 GeV.

If one point is enough, an immediate question is where is the optimal point located? To answer this, a one-point scan with the luminosity  $\mathcal{L}_{tot} = 45 \text{ pb}^{-1}$  was made and the results are shown in Figs. 30.6(a) and (b). As indicated in previous study, the small uncertainty is near the peak of the derivative. Actually, the most precise result,  $S_{m_\tau} = 0.105$  MeV, is obtained at the  $m_\tau$  threshold, at 3.55398 MeV; the measurement taken right at the peak of the cross section derivative,  $S_{m_\tau}$  is slightly worse. In addition, the study indicates that within a 2 MeV region the variation of  $S_{m_\tau}$  is fairly small (from 0.105 MeV to 0.127 MeV), which is very good for actual data taking.

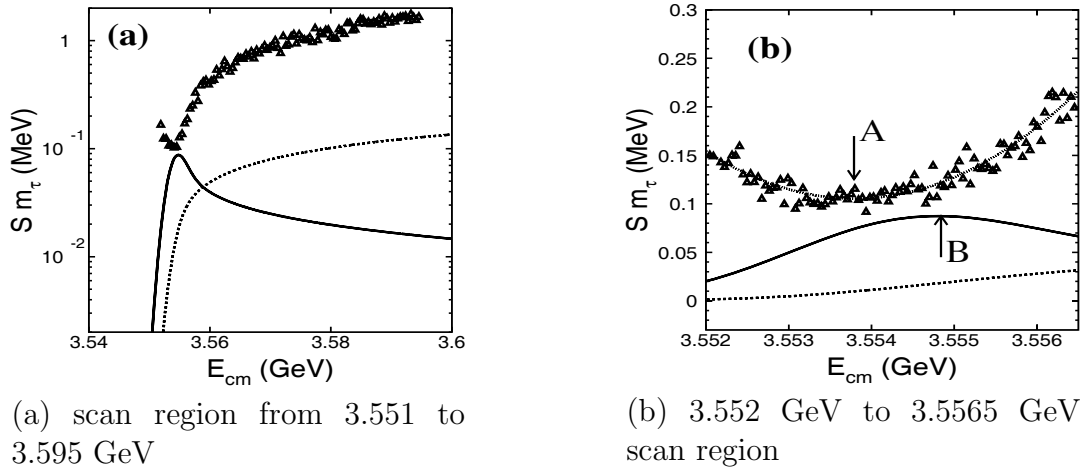


Figure 30.6: The variation of  $S_{m_\tau}$  versus energy from a one-point measurement with  $\mathcal{L}_{tot} = 45 \text{ pb}^{-1}$ . (a) over the scan region from 3.551 GeV to 3.595 GeV (b) over the scan region from 3.5533 GeV to 3.55694 GeV. The solid line denotes the cross section derivative with a scale factor of  $10^{-3}$  and the dashed line the observed cross section with a scale factor of  $10^{-1}$ .

### luminosity and uncertainty

The last question we investigate is the relation between the uncertainty and the luminosity. For the fit with one point in the large-derivative region, results are listed in Table 30.1. The second and third column present the results at  $E_{cm} = 3.55398 \text{ GeV}$ , corresponding to the threshold while the last two columns give the results at  $3.55484 \text{ GeV}$ , corresponding to the point with the largest cross section derivative. From the results in Table 30.1, we see that the precision is inversely proportional to the luminosity and a luminosity of  $63 \text{ pb}^{-1}$  is sufficient to provide an accuracy of less than 0.1 MeV.

#### 30.2.4 Discussion

At *BES-III*, the design peak luminosity is around  $1 \text{ nb}^{-1}\text{s}^{-1}$ . If the average luminosity is taken to be 50% of the peak value, two-days of data taking will give to a statistical uncertainty of less than 0.1 MeV. Notice that this evaluation is solely for  $e\mu$ -tagged event, other channels, such as  $ee$ ,  $e\mu$ ,  $eh$ ,  $\mu\mu$ ,  $\mu h$  and  $hh$  will have at least five times the number of  $e\mu$ -tagged events [108, 92], and these can significantly improve the uncertainty. Therefore at *BES-III*, a one-week data-taking run will lead to a statistical uncertainty of order 0.017 MeV.

### 30.3 Systematic uncertainty

In this section systematic uncertainties on  $m_\tau$  measurements will be examined, including the theoretical accuracy, energy spread, energy scale, luminosity, efficiency, backgrounds, etc.

Table 30.1: The relation between luminosity and uncertainty.

$L_{tot}$ ( $\text{pb}^{-1}$ )	$E_{cm} = 3.55398 \text{ GeV}$		$E_{cm} = 3.5548 \text{ GeV}$	
	$Sm_\tau$ (MeV)	$\Delta m_\tau$ (MeV)	$Sm_\tau$ (MeV)	$\Delta m_\tau$ (MeV)
9	0.24874	0.02931	0.29240	0.02114
18	0.16926	0.01550	0.19635	0.00756
27	0.14024	0.01234	0.15670	0.00475
36	0.12130	0.00812	0.14384	0.00504
45	0.10653	0.00824	0.12717	0.00292
54	0.09783	0.00717	0.10714	-0.00037
63	0.09035	0.00726	0.09923	-0.00003
72	0.08424	0.00520	0.09297	0.00008
100	0.06781	0.00129	0.07876	-0.00002
1000	0.02146	0.00016	0.02515	0
10000	0.00684	0	0.00805	0

### 30.3.1 Theoretical accuracy

The experimentally observed cross section has the form [98]

$$\begin{aligned} \sigma_{exp}(m_\tau, s, \Delta) &= \int_0^\infty d\sqrt{s'} G(\sqrt{s'}, \sqrt{s}) \\ &\times \int_0^{1-\frac{4m_\tau^2}{s'}} dx F(x, s') \frac{\bar{\sigma}(s'(1-x), m_\tau)}{|1 - \Pi(s'(1-x))|^2}, \end{aligned} \quad (30.3.12)$$

where  $s = E_{cm}^2$ ,  $F(x, s)$  is the initial state radiation factor [98],  $\Pi$  is the vacuum polarization factor [99, 100, 101], and  $G(\sqrt{s'}, \sqrt{s})$ , describes the energy-spread of the  $e^+e^-$  collider, which is usually treated as a Gaussian function [102]. As mentioned in Sect. 30.1, the high-accuracy calculations of the production cross section ( $\bar{\sigma}$ ) have only recently become available. Voloshin's improved formulae [103] are used here; the production cross section (denoted as  $\bar{\sigma}^*$ ) used in the BES-I  $m_\tau$  fit was based on Voloshin's earlier results [109]. The relative differences in the cross sections calculated with the two sets of Voloshin's formulae are shown in Fig. 30.7.

To estimate the effect due to theoretical calculation accuracy, the fitted  $\tau$  masses by using the two formulae are compared. The comparison shows the uncertainty due to this effect is at the level of  $10^{-3}$  MeV.

### 30.3.2 Energy spread

As indicated in Eq. (30.3.12), the experimentally measured cross section  $\sigma_{exp}$  depends on the energy spread ( $\Delta$ ); the effect on the  $m_\tau$  measurement is considered here.

In fact, the value of  $\Delta$  in the  $\tau$  threshold region is usually interpolated from the energy

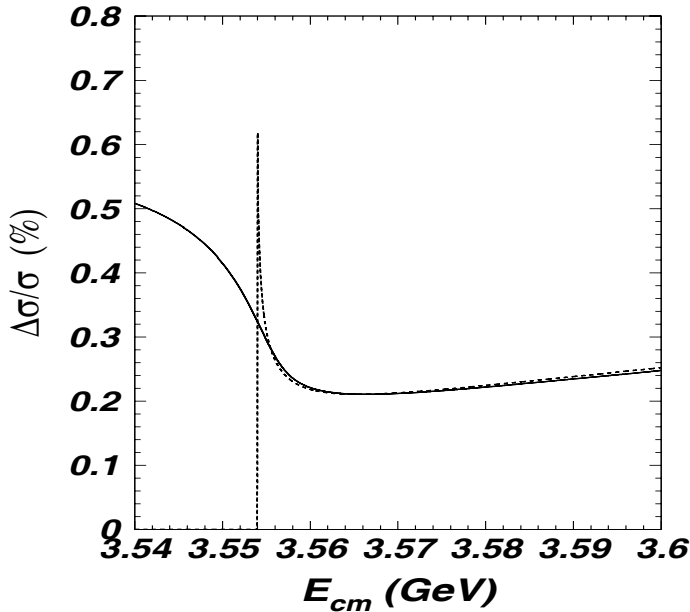


Figure 30.7: The relative differences of the latest and previous cross section calculations from Voloshin [110]. The result that includes effects of the beam energy spread ( $\sigma_{exp}$ ) are shown as the solid line. Results without beam energy effects ( $\bar{\sigma}$ ) are shown as the dashed line.

spreads measured at the  $J/\psi$  ( $\Delta_{J/\psi}$ ) and  $\psi'$  ( $\Delta_{\psi'}$ ) regions, assuming the relation

$$\frac{\Delta - \Delta_{J/\psi}}{\Delta_{\psi'} - \Delta_{J/\psi}} = \frac{f(E) - f(E_{J/\psi})}{f(E_{\psi'}) - f(E_{J/\psi})}. \quad (30.3.13)$$

It is assumed that  $\Delta \propto f(E)$ , where  $f(E)$  denotes the dependence of  $\Delta$  on the beam energy  $E_{cm}$ . Since a rigorous form for  $f(E)$  is not available, a generic form is assumed:

$$f(E) = a \cdot E + b \cdot E^2 + c \cdot E^3, \quad (30.3.14)$$

and linear, quadratic, cubic or a mixed-type of energy-dependence is used. At BES-I, the fit results give  $\delta m_\tau < 1.5 \times 10^{-3}$  MeV. Even if  $\Delta$  is artificially changed to  $3\Delta$  the fit indicates that  $\delta m_\tau < 6 \times 10^{-3}$  MeV.

### 30.3.3 Energy scale

In the BES-I measurement, precisely known mass values of the  $J/\psi$  ( $M_{J/\psi}$ ) and the  $\psi'$  ( $M_{\psi'}$ ) were used as the scale to calibrate the energies in  $\tau$  ( $E_\tau$ ) threshold region,

$$\frac{E_\tau - E_{J/\psi}}{E_{\psi'} - E_{J/\psi}} = \frac{E_s - M_{J/\psi}}{M_{\psi'} - M_{J/\psi}}, \quad (30.3.15)$$

where  $E_s$  is the scaled energy value. If the energy and mass peak have only a small relative shift  $\delta$ , which in actuality are at the level of  $10^{-4}$ , the relation can be written as

$$\frac{E_s - M_{J/\psi}}{M_{\psi'} - M_{J/\psi}} = \frac{\delta_s - \delta_{J/\psi}}{\delta_{\psi'} - \delta_{J/\psi}}. \quad (30.3.16)$$

Similar to the energy spread, if we could assume  $\delta \propto f(E)$ , the uncertainty due to the energy scale would only be about  $8 \times 10^{-3}$  MeV.

However, the relation  $\delta \propto f(E)$  is merely a speculation and probably not a safe assumption. At present, there are two approaches to determine the absolute energy scale directly, one is depolarization and the other is Compton back-scattering, both were developed by the KEDR group [96].

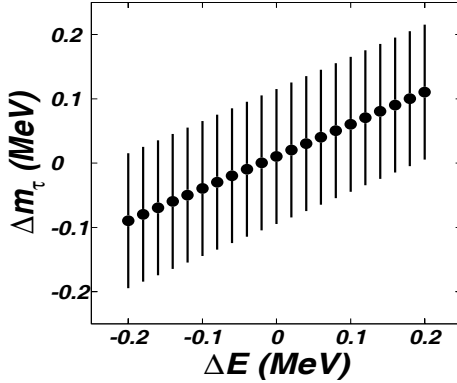


Figure 30.8: The effects of uncertainty in the absolute energy calibration on  $m_\tau$  measurement.

It is proposed to adopt the Compton back-scattering technique to measure the BEPCII beam energies. The relative precision of this technique is expected to be at the  $5 \times 10^{-5}$  level, which directly translates to a systematic uncertainty on  $m_\tau$  of  $5 \times 10^{-5}$  (relative error) or 0.09 MeV (absolute error). This error is an order-of-magnitude larger than the combined error from other sources, which is  $8 \times 10^{-3}$  MeV. Since the uncertainty of the energy scale will transfer directly to the final  $m_\tau$  measurement as displayed in Fig. 30.8, the absolute calibration of energy scale is the bottleneck for the  $m_\tau$  measurement.

### 30.3.4 Other factors

The systematic uncertainties due to other experimental factors are quantified by reasonable variations of the corresponding quantities, as listed in Table 30.2. The total uncertainty is estimated to be at the level of 0.1 MeV.

## 30.4 Energy measurement at *BES-III*

As we mentioned above, the absolute energy calibration plays a crucial role in the  $\tau$  mass measurement. A technique based on the Compton back-scattering principle is proposed to measure the BEPCII beam energies with high precision.

The detection system would be located at the north interaction point (IP) of the BEPCII storage ring as shown in Figs. 30.9 and 30.10.

The proposed beam energy measurement system (denoted as energy detector in Fig. 30.9) is comprised of the following parts:

1. the laser source and optics system;

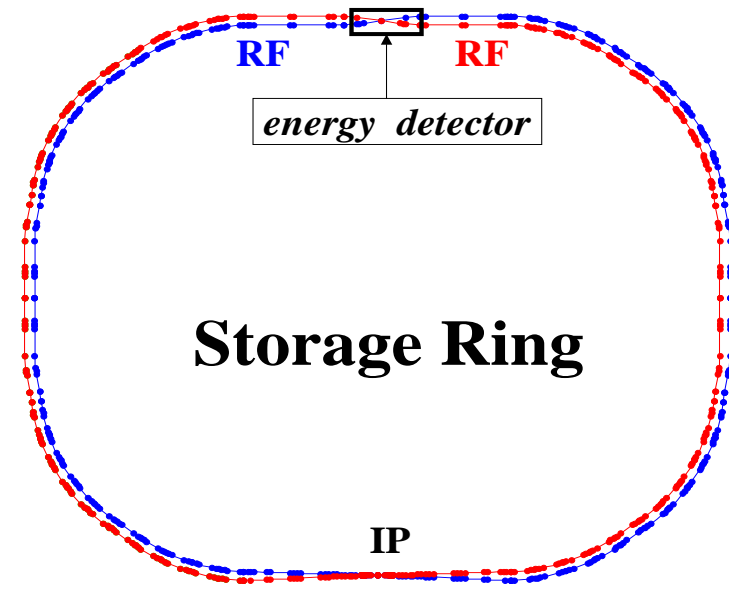


Figure 30.9: The location of the energy measurement system at in BEPCII.

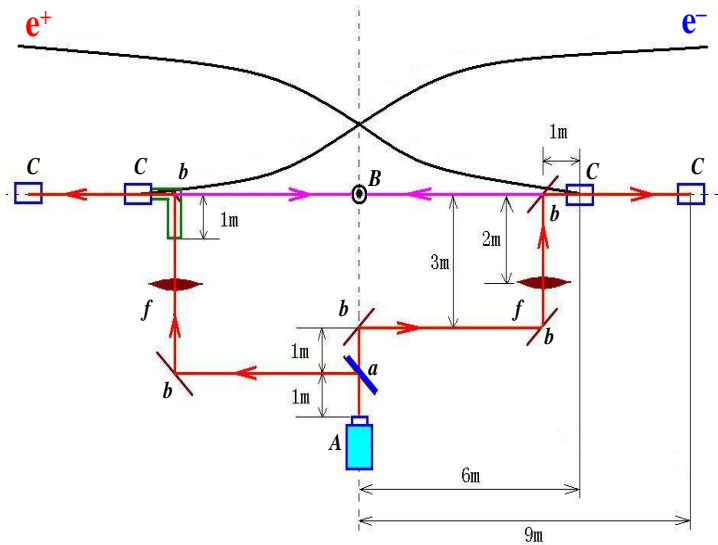


Figure 30.10: A schematic diagram of the layout for the energy measurement system. The two black curved lines denote the positron and electron beams. The bottle-like box (*A*) indicates the laser source; the circled dot (*B*) indicates the HPGe detector; rectangles (*C*) denote BEPCII bending magnets; *a* indicates a half-transmissive/half-reflective lens; *b*'s indicate reflective lenses and *f*'s indicate focusing lenses.

Table 30.2: Systematic uncertainties for  $m_\tau$  measurement.

Source	$\delta m_\tau$ ( $10^{-3}$ MeV)	$\delta m_\tau/m_\tau$ ( $10^{-6}$ )
Luminosity (2%)	14.0	7.9
Efficiency (2%)	14.0	7.9
Branching Fraction (0.5%)	3.5	2.0
Background (10%)	1.7	1.0
Energy spread (30%)	3.0	1.7
Theoretical accuracy	3.0	1.7
Energy scale	100	56.3
Summation	102	57.5

2. the interaction regions where the laser beams collides with the electron or positron beam;
3. a high purity Geranium detector (HPGe) to measure back-scattering high energy  $\gamma$ -rays or  $X$ -rays.

In the following subsections, we will describe each subsystem. In operation, the energy measured at the north IP has to be corrected for synchrotron radiation produced by the beams when the travel to the collision point in the south intersection point. This is at the level of 200 keV, with a corresponding uncertainty that is less than 10%, or, equivalently, 20 keV.

### 30.4.1 Laser source and optics system

A simple and extensively used expression for a laser beam amplitude is [112]

$$\psi(x, y, z) = C \cdot \exp \left[ -\frac{x^2 + y^2}{r^2(z)} \right] \cdot \exp [i\theta(x, y, z)] . \quad (30.4.17)$$

Here  $\psi(x, y, z)$  describes a TEM<sub>00</sub> mode Gaussian beam, where TEM is the abbreviation for transverse electric and magnetic wave. In Eq. (30.4.17),  $\theta(x, y, z)$  is a phase factor and  $r(z)$  is a function of  $z$  (the propagation distance):

$$r(z) = r_0 \sqrt{1 + \left( \frac{z}{z_0} \right)^2}, \quad z_0 = \frac{\pi r_0}{\lambda} , \quad (30.4.18)$$

where  $r_0$  is the waist width of laser beam given at  $z = 0$  and  $\lambda$  is the wavelength of the laser beam. Using Eq. (30.4.17), we obtain the photon density in the laser beam to be

$$\rho_\gamma = |\psi(x, y, z)|^2 = \rho_0 \cdot f_\gamma(x, y, z), \quad f_\gamma(x, y, z) = \exp \left[ -\frac{2(x^2 + y^2)}{r^2(z)} \right] . \quad (30.4.19)$$

To determine the constant  $\rho_0$  ( $= C^2$ ) in Eq. (30.4.19), we consider the differential relation between the laser power ( $P$ ) and the photon density:

$$dP = \omega_\gamma \cdot \rho_\gamma \cdot \Delta S \cdot c , \quad (30.4.20)$$

where  $\omega_\gamma$  is the energy of laser beam,  $c$  the velocity of light, and  $\Delta S$  is a cross-sectional area element of the laser beam. Integrating the above relation:

$$P = \int dP = \omega_\gamma \cdot \rho_0 \cdot c \int \int f_\gamma(x, y, z) dx dy ,$$

we find

$$P = \rho_0 \cdot (\omega_\gamma \cdot c \cdot \pi \cdot r^2(z)) ,$$

or

$$\rho_0 = \frac{P}{\omega_\gamma \cdot c \cdot \pi \cdot r^2(z)} . \quad (30.4.21)$$

From dimensional analysis, we notice that  $\rho_0$  has dimension of inverse volume, so the photon density  $\rho_\gamma$  is actually a volume density distribution.

### 30.4.2 Electron beam

Similarly, the density function for the electron (positive or negative) beam can be expressed as

$$\rho_e = \rho'_0 \cdot f_e(x, y, z), \quad f_e(x, y, z) = \exp \left[ - \left( \frac{x^2}{\sigma_x^2} + \frac{y^2}{\sigma_y^2} \right) \right] , \quad (30.4.22)$$

where  $\sigma_x$  and  $\sigma_y$  are standard deviations of electron beam in  $x$  and  $y$  directions, respectively;  $\rho'_0$  is the normalization factor which is determined by the differential relation between the current intensity ( $I$ ) and electron density:

$$dI = e \cdot \rho_e \cdot \Delta S \cdot u_e , \quad (30.4.23)$$

where  $e$  is the electron charge,  $u_e$  is the velocity of electron beam, and  $\Delta S$  is a cross-sectional area element of the electron beam. From the integration of the above relation:

$$I = \int dI = e \cdot \rho'_0 \cdot u_e \int \int f_e(x, y, z) dx dy ,$$

we get

$$P = \rho'_0 \cdot (u_e \cdot e \cdot \pi \cdot \sigma_x \sigma_y) ,$$

or

$$\rho'_0 = \frac{I}{u_e \cdot e \cdot \pi \cdot \sigma_x \sigma_y} . \quad (30.4.24)$$

From dimensional analysis, we notice that  $\rho'_0$  has dimension of inverse volume, so the electron density  $\rho_e$  is actually a volume density distribution.

### 30.4.3 Compton back-scattering principle

The interaction of the electron and laser beams is described by the Compton back-scattering principle [113, 114]. The energy of the back-scattered photon ( $\omega_2$ ) is

$$\omega_2 = \frac{\omega_1(1 - \beta \cos \phi_1)}{1 - \beta \cos \phi_2 + \frac{\omega_1}{\gamma m}(1 - \cos[\phi_1 - \phi_2])} . \quad (30.4.25)$$

When unpolarized light is scattered by unpolarized electrons and neither the spin of the residual electron nor the polarization of the final photon are observed, the differential cross section can be expressed in terms of relativistic invariants as

$$\frac{d\sigma}{dt} = 2\pi r_0^2 \frac{1}{(mx_1)^2} \left\{ 4y(1+y) - \frac{x_1}{x_2} - \frac{x_2}{x_1} \right\} , \quad (30.4.26)$$

where  $r_0$  is the classical electron radius and

$$x_1 = 2\gamma \frac{\omega_1}{m} (1 - \beta \cos \phi_1) , \quad (30.4.27)$$

$$x_2 = -2\gamma \frac{\omega_2}{m} (1 - \beta \cos \phi_2) , \quad (30.4.28)$$

$$y = \frac{1}{x_1} + \frac{1}{x_2} . \quad (30.4.29)$$

In a scattering experiment,  $s$  (and therefore  $x_1$ ) is fixed by the energies of the initial electron and photon. The total cross section is obtained from Eq. (30.4.26) using  $t = -m^2(x_1 + x_2)$  and integrating over  $x_2$  at a fixed value of  $x_1$

$$\sigma = 2\pi r_0^2 \frac{1}{x_1} \left\{ \left( 1 - \frac{4}{x_1} - \frac{8}{x_1^2} \right) \ln(1+x_1) + \frac{1}{2} + \frac{8}{x_1} - \frac{1}{2(1+x_1)^2} \right\} , \quad (30.4.30)$$

When observed in the laboratory, however, the Lorentz transformation concentrates the photon flux into a small cone with half-angle  $\phi_2$  of the order of  $1/\gamma$ , which increases the photon flux at backward scattering angles. In Ref. [115], the differential cross section per unit solid angle is given by

$$\frac{d\sigma}{d\Omega} = 2r_0^2 \left( \frac{\omega_2}{mx_1} \right)^2 \left\{ 4y(1+y) - \frac{x_1}{x_2} - \frac{x_2}{x_1} \right\} . \quad (30.4.31)$$

The formulae in Eqs. 30.4.30 and 30.4.31 are used below to calculate the interaction rate between the laser beam and the high energy electron beam.

#### 30.4.4 A simple simulation

Based on the principles introduced above, we establish a simplified system to simulate the procedure of the absolute energy measurement. We evaluate the intensity of the back-scattered photons and simulate the detected photon energy distribution. Finally, the precision of the beam energy measurement is obtained.

The intensity of back-scattered photons can be calculated by the following formula:

$$N_\gamma = u_e \sigma_T \cdot \int \int \int \rho_\gamma \cdot \rho_e \, dx dy dz \quad (30.4.32)$$

where  $\rho_\gamma$  denotes the volume density of the laser beam described by Eqs. 30.4.19 and 30.4.21;  $\rho_e$  is the volume density of the electron beam described by Eqs. 30.4.22 and 30.4.24;  $\sigma_T$  is the total cross section given in Eq. 30.4.31 (or approximately by Eq. 30.4.30). We can rewrite the above equation as:

$$N_\gamma = \frac{PI\sigma_T}{\omega_\gamma \cdot c \cdot e \cdot \pi^2} \int \int \int \frac{1}{r^2(z)} f_\gamma \cdot f_e \, dx dy dz . \quad (30.4.33)$$

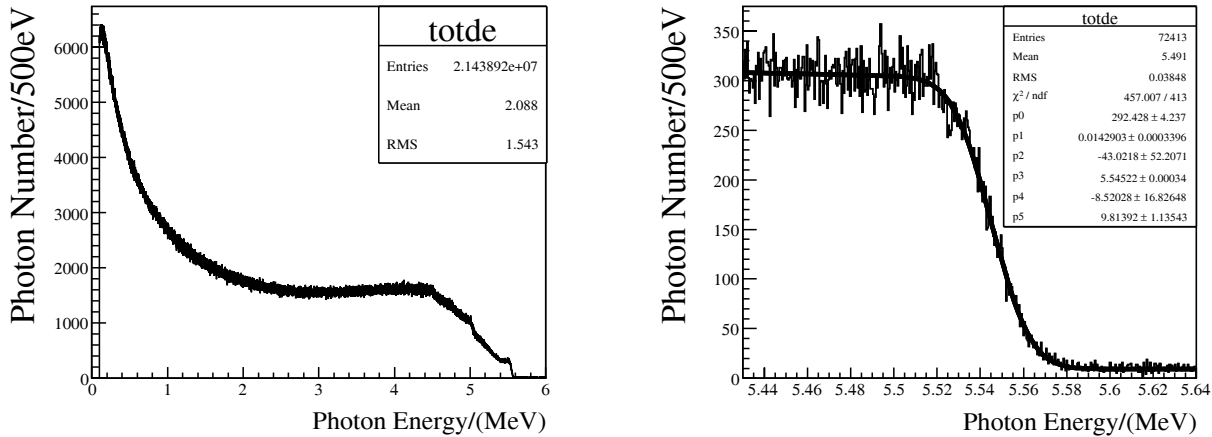
Inserting the parameters provided in Table 30.3 into Eq. 30.4.33, we find

$$N_\gamma = 2.7 \times 10^8 s^{-1} .$$

Table 30.3: Some input parameters for the laser and electron beam.

laser beam	electron beam
power $P = 50$ W	$I = 9.8$ mA
wave-length $\lambda = 10.59 \mu m$	$\sigma_x = 1.6$ mm
laser energy $\omega_\gamma = 0.117$ eV	$\sigma_y = 0.16$ mm
waist radius $r_0 = 2$ mm	$\sigma_z = 15$ mm

The detection of the back-scattered photons in the HPGe is simulated using the GEANT4 package [116]. Figure 30.11 shows the photon energy spectrum, where a clear Compton edge is evident; this edge is used to measure the absolute beam energy.



(a) The detected photon energy spectrum between 0 and 6 MeV.

(b) the detected photon energy spectrum between 5.43 MeV and 5.64 MeV

Figure 30.11: The simulated photon energy spectrum measured by the HPGe detector.

The edge of the Compton spectrum is fitted with the six parameter function [117]:

$$g(x, \vec{p}) = \frac{1}{2} (p_2(x - p_0) + p_3) \cdot \text{erfc} \left[ \frac{x - p_0}{\sqrt{2}p_1} \right] - \frac{p_1 p_2}{\sqrt{2\pi}} \cdot \exp \left[ -\frac{(x - p_0)^2}{2p_1^2} \right] + p_4(x - p_0) + p_5 , \quad (30.4.34)$$

where  $p_0$  is the edge position;  $p_1$  is the edge width;  $p_2$  is the left slope;  $p_3$  is the edge amplitude;  $p_4$  is the right slope; and  $p_5$  is the background. The  $p_0$  parameter gives the information about the average electron beam energy during the data acquisition period, while  $p_1$  is mostly coupled to the electron beam energy spread.

In addition to the simple simulation described above, a number of factors have to be taken into account in a real measurement, including: the effect of the focusing system on the laser beam, the dynamics and trajectories of the electron beam, the calibration of the HPGe detector, etc., in order to estimate the accuracy of the beam energy measurement.

## 30.5 Summary

The statistical and systematic uncertainties of a  $m_\tau$  measurement at *BES-III* are studied based on previous experience and recent theoretical calculations. Monte Carlo simulation and sampling techniques are employed to obtain an optimal data taking strategy. It is found that:

1. the optimal measurement energy is located near the point with the largest derivative of the cross section with respect to energy;
2. one measurement point in this region is sufficient to provide the smallest statistical error for a given amount of integrated luminosity;
3. an integrated luminosity of  $63 \text{ pb}^{-1}$  will produce a statistical accuracy that is better than 0.1 MeV.

In addition, many factors have been taken into account to estimate possible systematic uncertainties. The expected total relative error is at the level of  $5.8 \times 10^{-5}$ . The absolute calibration of energy scale will be crucial for further improvement of the accuracy of the  $m_\tau$  measurement. If the laser back-scattering technique is applied at *BES-III*, an ultimate systematic uncertainty of around 0.09 MeV could be achieved.



# Bibliography

- [1] P. Ruiz-Femenía and A. Pich, Nucl. Phys. B (Proc. Suppl.) 121 (2003) 205 [arXiv:hep-ph/0210003].
- [2] W.-M. Yao et al., *The Review of Particle Physics*, J. Phys. G 33 (2006) 1.
- [3] S. Jadach et al., Comp. Phys. Comm. 76 (1993) 361.
- [4] J. Z. Bai et al., Phys. Rev. D 53 (1996) 20.
- [5] A. Pich, *Tau Physics*, in *Heavy Flavours II*, eds. A.J. Buras and M. Lindner, Advanced Series on Directions in High Energy Physics, Vol. 15 (World Scientific, Singapore, 1998), p. 453.
- [6] A. Pich, *Theoretical Overview on Tau Physics*, Int. J. Mod. Phys. A 21 (2006) 5652.
- [7] A. Pich, *Tau Physics 2006: Summary & Outlook*, arXiv:hep-ph/0702074.
- [8] A. Stahl, *Physics with Tau Leptons*, Springer Tracts in Modern Physics 160 (Springer, Berlin, 2000).
- [9] E. Braaten, Phys. Rev. Lett. 60 (1988) 1606; Phys. Rev. D 39 (1989) 1458.
- [10] S. Narison and A. Pich, Phys. Lett. B 211 (1988) 183.
- [11] E. Braaten, S. Narison and A. Pich, Nucl. Phys. B 373 (1992) 581.
- [12] F. Le Diberder and A. Pich, Phys. Lett. B 286 (1992) 147. A.A. Pivovarov, Z. Phys. C 53 (1992) 461.
- [13] A. Pich, Nucl. Phys. B (Proc. Suppl.) 39B,C (1995) 326.
- [14] W.J. Marciano and A. Sirlin, Phys. Rev. Lett. 61 (1988) 1815. E. Braaten and C.S. Li, Phys. Rev. D 42 (1990) 3888. J. Erler, arXiv:hep-ph/0211345.
- [15] F. Le Diberder and A. Pich, Phys. Lett. B 289 (1992) 165.
- [16] ALEPH Collab., Phys. Rep. 421 (2005) 191; Eur. Phys. J. C 4 (1998) 409; Phys. Lett. B 307 (1993) 209.
- [17] CLEO Collab., Phys. Lett. B 356 (1995) 580.
- [18] OPAL Collab., Eur. Phys. J. C 7 (1999) 571.

- [19] M. Davier, A. Höcker and Z. Zhang, Rev. Mod. Phys. 78 (2006) 1043.
- [20] The LEP Collaborations ALEPH, DELPHI, L3, OPAL and the LEP Electroweak Working Group, arXiv:hep-ph/0612034; <http://www.cern.ch/LEPEWWG>.
- [21] G. Rodrigo, A. Pich and A. Santamaria, Phys. Lett. B 424 (1998) 367.
- [22] A. Pich, *QCD Tests from Tau Decay Data*, Proc. Tau-Charm Factory Workshop (SLAC, 1989), ed. L.V. Beers, SLAC-Report-343 (1989) p. 416.
- [23] S. Weinberg, Phys. Rev. Lett. 18 (1967) 507. T. Das et al., Phys. Rev. Lett. 18 (1967) 759.
- [24] M. Davier, Nucl. Phys. B (Proc. Suppl.) 55C (1997) 395.
- [25] A. Pich and J. Prades, JHEP 9910 (1999) 004; 9806 (1998) 013.
- [26] S. Chen et al., Eur. Phys. J. C 22 (2001) 31.
- [27] K.G. Chetyrkin, J.H. Kühn and A.A. Pivovarov, Nucl. Phys. B 533 (1998) 473. J.G. Körner, F. Krajewski and A.A. Pivovarov, Eur. Phys. J. C 20 (2001) 259.
- [28] K. Maltman and C.E. Wolfe, Phys. Lett. B 639 (2006) 283; arXiv:hep-ph/0701037. J. Kambor and K. Maltman, Phys. Rev. D 62 (2000) 093023; 64 (2001) 093014. K. Maltman, Phys. Rev. D 58 (1998) 093015.
- [29] E. Gámiz et al., Phys. Rev. Lett. 94 (2005) 011803; JHEP 0301 (2003) 060; arXiv:hep-ph/0612154.
- [30] P.A. Baikov, K.G. Chetyrkin and J.H. Kühn, Phys. Rev. Lett. 95 (2005) 012003.
- [31] ALEPH Collab., Eur. Phys. J. C 11 (1999) 599; 10 (1999) 1.
- [32] OPAL Collab., Eur. Phys. J. C 35 (2004) 437.
- [33] M. Jamin, J.A. Oller and A. Pich, Phys. Rev. D 74 (2006) 074009.
- [34] A. Pich, arXiv:0705.4264 [hep-ph].
- [35] E.Braaten, S.Narisson, A.Pich, Nucl. Phys. **B373** (1992) 581
- [36] A.Pich, Nucl. Phys. **B39** (Proc.Suppl.) (1995) 326
- [37] ALEPH Coll., S. Schael et al., Phys.Rept. **421** (2005) 191
- [38] M.Davier, A.Hocker, Z.Zhang, arXive:hep-ph/0507078 (2006)
- [39] M.Davier, Nucl. Phys. **B169** (Proc.Suppl.) (2007) 288
- [40] M.Davier, ‘Status of the tau spectral function data and their role for g-2’ , talk on Workshop on the Muon Magnetic Dipole Moment, 2007
- [41] MuLan Collaboration, arXiv:0704.1981 [hep-ex].

- [42] M. Shapkin, TAU06 proceedings.
- [43] KEDR Collab., arXiv:hep-ex/0611046.
- [44] X.H. Mo, TAU06 proceedings.
- [45] P. Ruiz-Femenía and A. Pich, Phys. Rev. D 64 (2001) 053001.
- [46] M.B. Voloshin, Phys. Lett. B 556 (2003) 153. B.H. Smith and M.B. Voloshin, Phys. Lett. B 324 (1994) 117; 333 (1994) 564.
- [47] L. Michel, Proc. Phys. Soc. A 63 (1950) 514, 1371. C. Bouchiat and L. Michel, Phys. Rev. 106 (1957) 170. T. Kinoshita and A. Sirlin, Phys. Rev. 107 (1957) 593; 108 (1957) 844.
- [48] F. Scheck, *Leptons, Hadrons and Nuclei* (North-Holland, Amsterdam, 1983); Phys. Rep. 44 (1978) 187.
- [49] W. Fetscher, H.-J. Gerber and K.F. Johnson, Phys. Lett. B 173 (1986) 102. W. Fetscher and H.-J. Gerber, *Precision Measurements in Muon and Tau Decays*, in *Precision Tests of the Standard Electroweak Model*, ed. P. Langacker, Advanced Series on Directions in High Energy Physics – Vol. 14 (World Scientific, Singapore, 1995), p. 657.
- [50] A. Pich and J.P. Silva, Phys. Rev. D 52 (1995) 4006.
- [51] L. Michel, Proc. Phys. Soc. A63 (1950) 514; C. Bouchiat and L. Michel, Phys. Rev. 106 (1957) 170.
- [52] M. Chizhov, hep-ph/9612399
- [53] W.J. Marciano and A. Sirlin, Phys. Rev. Lett. 71 (1993) 3629.
- [54] R. Decker and M. Finkemeier, Nucl. Phys. B 438 (1995) 17.
- [55] A. Pich and J. Portolés, Phys. Rev. D 63 (2001) 093005; Nucl. Phys. B (Proc. Suppl.) 121 (2003) 179.
- [56] F. Guerrero and A. Pich, Phys. Lett. B 412 (1997) 382.
- [57] D. Gómez-Dumm, A. Pich and J. Portolés, Phys. Rev. D 62 (2000) 054014.
- [58] J.J. Sanz-Cillero and A. Pich, Eur. Phys. J. C 27 (2003) 587. I. Rosell, J.J. Sanz-Cillero and A. Pich, JHEP 0408 (2004) 042.
- [59] J. Gasser and H. Leutwyler, Nucl. Phys. B 250 (1985) 465, 517, 539. G. Ecker, Prog. Part. Nucl. Phys. 35 (1995) 1. A. Pich, Rep. Prog. Phys. 58 (1995) 563. V. Bernard and U.-G. Meissner, arXiv:hep-ph/0611231.
- [60] G. Ecker et al., Nucl. Phys. B 321 (1989) 311; Phys. Lett. B 233 (1989) 425.
- [61] A. Pich, arXiv:hep-ph/0205030.

- [62] ALEPH Collab., Z. Phys. C 76 (1997) 15.
- [63] CLEO Collab., Phys. Rev. D 61 (2000) 112002.
- [64] L.M. Barkov et al., Nucl. Phys. B 256 (1985) 365.
- [65] S.R. Amendolia et al., Nucl. Phys. B 277 (1986) 168.
- [66] M. Fujikawa, TAU06 proceedings.
- [67] M. Davier et al., Eur. Phys. J. C 27 (2003) 497; 31 (2003) 503. M. Davier, arXiv:hep-ph/0701163.
- [68] M. Jamin, A. Pich and J. Portolés, Phys. Lett. B 640 (2006) 176.
- [69] M. Jamin, J.A. Oller and A. Pich, Nucl. Phys. B 622 (2002) 279; 587 (2000) 331.
- [70] B.A. Shwartz, TAU06 proceedings.
- [71] I.M. Nugent, TAU06 proceedings.
- [72] D. Gómez–Dumm, A. Pich and J. Portolés, Phys. Rev. D 69 (2004) 073002.
- [73] CLEO Collab., Phys. Rev. D 61 (2000) 052004, 012002.
- [74] OPAL Collab., Z. Phys. C 75 (1997) 593.
- [75] J. Portolés, arXiv:hep-ph/0702132.
- [76] G. Ecker and R. Unterdorfer, Eur. Phys. J. C 24 (2002) 535.
- [77] W. Buchmüller, R.D. Peccei, T. Yanagida, Ann. Rev. Nucl. Part. Sci. 55 (2005) 311.
- [78] Y.S. Tsai, in: Stanford Tau Charm 1989:0387-393 (QCD183:T3:1989).
- [79] Y.S. Tsai, Phys. Rev. D51 (1995) 3172.
- [80] J.H. Kühn, E. Mirkes, Z. Phys. C56 (1992); Erratum, *ibid.* C67 (1995) 364.
- [81] J.H. Kühn, E. Mirkes, Phys. Lett. B398 (1997) 407.
- [82] I.I. Bigi, A.I. Sanda, Phys. Lett. B625 (2005) 47.
- [83] A. Datta *et al.*, hep-ph/0610162.
- [84] J. Bernabeu *et al.*, Nucl. Phys. B763 (2007) 283.
- [85] D. Delepine *et al.*, Phys. Rev. D74 (2006) 056004.
- [86] S. Anderson *et al.* [CLEO Collaboration], Phys. Rev. Lett. 81 (1998) 3823.
- [87] DASP Collaboration, R. Brandelik *et al.*, Phys. Lett. B73 (1978) 109.

- [88] W. Bartel *et al.*, Phys. Lett. B77 (1978) 331.
- [89] C.A. Blocker, Ph.D. Thesis, LBL-Report 10801 (1980).
- [90] W. Bacino *et al.*, Phys. Rev. Lett. 41 (1978) 13.
- [91] ARGUS Collaboration, H. Albrecht *et al.*, Phys. Lett. B292 (1992) 221.
- [92] BES Collaboration, J.Z. Bai *et al.*, Phys. Rev. D53 (1996) 20.
- [93] CLEO Collaboration, A. Anastassov *et al.*, Phys. Rev. D55 (1997) 2559; Phys. Rev. D58 (1998) 119904 (Erratum).
- [94] OPAL Collaboration, G. Abbiendi *et al.*, Phys. Lett. B492 (2000) 23.
- [95] M. Shapkin, “Measurement of the mass of the tau-lepton”, report at this conference.
- [96] B. Shwartz, “New precise determination of the tau lepton mass at the KEDR detector”, report at this conference.
- [97] A. Bogomyagkov *et al.*, “Research of Possibility to use Beam Polarization for Absolute Energy Calibration in High-precision Measurement of Tau Lepton Mass at VEPP-4M.”, Presented at the 9th European Particle Accelerator Conference (EPAC 2004), Lucerne, Switzerland, July 5-9, 2004.
- [98] E.A. Kuraev and V.S. Fadimi, Sov. J. Nucl. Phys. 41 (1985) 466; G. Altarelli and G. Martinelli, CERN 86-02 (1986) 47; O. Nicrosini and L. Trentadue, Phys. Lett. B196 (1987) 551; F.A. Berends, G. Burgers and W.L. Neerven, Nucl. Phys. B297 (1988) 429; Nucl. Phys. B304 (1988) 921.
- [99] P. Ruiz-Femenía and A. Pich, Phys. Rev. D64 (2001) 053001.
- [100] F.A. Berends, K.J.F. Gaemers and R. Gastmans, Nucl. Phys. B57 (1973) 381; F.A. Berends and G.J. Komen, Phys. Lett. B63 (1976) 432.
- [101] G. Rodrigo, A. Pich and A. Santamaria, hep-ph/9707747.
- [102] P. Wang, C.Z. Yuan, X.H. Mo and D.H. Zhang, Phys. Lett. B593 (2004) 89.
- [103] M. B. Voloshin, Phys. Lett. B556, 153 (2003).
- [104] Schwinger J. Particles, Sorces and Fields (Volume II), 1973
- [105] B. H. Smith and M.B. Voloshin, Phys. Lett. B324 (1994) 117; Phys. Lett. B333 (1994) 564, Erratum.
- [106] Berestetskii V B, Lifshits E M and Pitaevskii L P. Quantum Electrodynamics. Pergamon, 1982
- [107] A. Pich, “Perspectives on Tau-Charm Factory Physics” in Proceedings of the 3rd Workshop on the Tau-Charm Factory, Marbella, Spain, 1993, edited by J. Kirkby and R. Kirkby (Editions Frontieres, Gif-sur-Yvete, 1994), p. 767.

- [108] BES Collaboration, J.Z. Bai *et al.*, Phys. Rev. Lett. 69 (1992) 3021.
- [109] BES Collaboration, J.Z. Bai *et al.*, HEP& NP, 16, 343 (1992).
- [110] Y.K. Wang, X.H. Mo, C.Z. Yuan and J.P. Liu, “Measurement of  $\tau$  mass based on improved theoretical calculations”, to be published in HEP& NP.
- [111] S. Brandt, Data Analysis (3rd ed.), Springer-Verlag, New York, 1999.
- [112] W.S.C. Chang, *Principles of Lasers and Optics*, Cambridge University Press, 2005.
- [113] P. Rullhusen, X. Artru, P. Dhez, *Novel Radiation Sources Using Relativistic Electrons*, World Scientific Publishing, 1998.
- [114] L.D Landau and E.M. Lifshitz, *Course of theoretical Physics*, Vol4.PartI, *Relativistic Quantum Mechanics*, Pergamon, 1971.
- [115] J.M. Rauch and F. Rohrlich, *The Theory of Photons and Electrons*, Addison-Wesley, 1959.
- [116] GEANT4 package, <http://cern.ch/geant4>.
- [117] N. Muchnoi, S. Nikitin, V. Zhilich, *FAST AND PRECISE BEAM ENERGY MONITOR BASED ON THE COMPTON BACKSCATTERING AT THE VEPP-4M COLLIDER*, EPAC-2006 report.

## Acknowledgements

We acknowledge the encouragement and strong support from IHEP director He-sheng Chen and former IHEP directors Zhi-peng Zheng and Ming-han Ye. We also benefited from excellent advice and many useful suggestions from BES-II spokespersons Wei-guo Li and Fred Harris, and former CLEO-c spokesperson Ian Shipsey. Ying-hua Jia provided valuable assistance to all phases of the preparation of this document. This work is supported in part by the National Natural Science Foundation of China under contracts Nos. 10491300, 10225524, 10225525, 10425523, 10575108, 10521003, 10735080, 10675131, 10605031 (IHEP), the Chinese Academy of Sciences under contract Nos. KJ95T-03 and KJCX3-SYW-N2, the 100 Talents Program of CAS under Contract Nos. U-11, U-24, U-25, and the Knowledge Innovation Project of CAS under Contract Nos. U-602, the Research and Development Project of Important Scientific Equipment of CAS under contracts No. H7292330S7, the National Natural Science Foundation of China under Contract Nos. 10775179, 10491306 (GUCAS), the National Natural Science Foundation of China under Contract Nos. 10625521, 10721063 (Peking University), the National Natural Science Foundation of China under Contract Nos. 10225522, 10775077, 10635030 (Tsinghua University), the Department of Energy under Contract No. DE-FG02-04ER41291 (U Hawaii), U.S. National Science Foundation through grant NSF-PHY-0244786 at the University of Tennessee, U.S. Department of Energy under contract DE-AC05-00OR22725 at Oak Ridge National Laboratory, the NSF under grant number PHY-0355098 (Univ. of Notre Dame), the European Network Flavianet under contract MRTN-CT-2006-035482, the network Flavianet MRTN-CT-2006-035482, the MEC (Spain) under grant Nos. FPA2007-60275, FPA2007-60323, the Spanish Consolider-Ingenio 2010 Programme CPAN (CSD2007-00042), the catalan grant SGR2005-00916, the ANR contract ANR-06-JCJC-0056, the EU Contract No. MRTN-CT-2006-035482, “FLAVIAnet”, the National Science Council of Taiwan, the RFBR-NSFC grant No. 06-02-39009, and the grant of President of Russian Federation MK-2952.2006.2.



# Appendix A

## Statistics in HEP data analysis<sup>1</sup>

This Appendix introduces an overview of two aspects of statistical methods used in High Energy Physics (HEP)- parameter estimation and hypothesis testing. For the detail, it is recommended to refer to the relevant textbooks [1, 2, 3] and literatures [4], and references quoted in this Appendix. In an experiment of HEP, an observable  $x$  usually is a random variable, its *pdf* is expressed as  $f(x, \theta)$  with parameter  $\theta$ , what the experiment obtained is an sample of  $x$ :  $\vec{x} = (x_1, \dots, x_n)^T$ . The task of the statistical inference is based on the sample of data to determine the value and error, or a confidence interval at given confidence level for the parameter  $\theta$ , or infer observable's *pdf*  $f(x, \theta)$ .

### A.1 Parameter estimation

Parameter  $\theta$  is estimated with a function of sample of observed data:  $\hat{\theta}(x_1, \dots, x_n)$ , which is called an estimator of  $\theta$ . The sample of observed data  $\vec{x} = (x_1, \dots, x_n)^T$  is also a random variable, the value of the estimator to a specific measurement of  $(x_1, \dots, x_n)^T$  is called an estimate. Throughout this Appendix, we will use same notation to denote estimate and estimator. An good estimator should have properties of consistency, unbiasedness and high efficiency.

The consistency means when the size of the data sample  $(x_1, \dots, x_n)$  goes to infinity, the estimator  $\hat{\theta}$  converges to the true value of parameter  $\theta$ .

The bias of an estimator is defined as the difference of the expectation of the estimator and the true value  $\theta$ :  $E(\hat{\theta}) = \theta + b(\theta)$ . The unbiasedness is a property of an estimator in finite sample, namely, it is required  $E(\hat{\theta}) = \theta$ . If it has to be estimated with a biased estimator, then the bias  $b$  of the estimator should be known or can be obtained by some way.

The efficiency is a measure of the variance of an estimator. Under the regularity conditions, namely, if the range of  $\vec{x}$  is independent of  $\theta$  and the first and second derivatives of the sample's joint *pdf* - Likelihood function  $L(\vec{x}|\theta) = \prod_{i=1}^n f(x_i, \theta)$  - with respect to  $\theta$  exist, there exists a lower bound on the variance of the estimates derived from an estimator, which is called the minimum variance bound MVB, given by Cramer-Rao

---

<sup>1</sup>By Yong-Sheng Zhu

inequality:

$$MVB = \frac{(1 + \frac{\partial b}{\partial \theta})}{I(\theta)}, \quad (\text{A.1.1})$$

where  $I(\theta)$  is the Fisher information:

$$I(\theta) = E[(\frac{\partial \ln L}{\partial \theta})^2] = \int (\frac{\partial \ln L}{\partial \theta})^2 \cdot L d\vec{x} = E[-\frac{\partial^2 \ln L}{\partial \theta^2}] = \int (-\frac{\partial^2 \ln L}{\partial \theta^2}) \cdot L d\vec{x}. \quad (\text{A.1.2})$$

The efficiency of an estimator  $\hat{\theta}$  is defined as  $e(\hat{\theta}) = MVB/V(\hat{\theta})$ . Apparently, we hope the efficiency of the used estimator is close or equal to 1.

The mean-square error (MSE) of an estimator is a convenient quantity which combine the uncertainties in an estimator due to bias and variance:

$$MSE = E[(\hat{\theta} - \theta)^2] = V(\hat{\theta}) + b^2. \quad (\text{A.1.3})$$

### A.1.1 Estimators for mean and variance

Suppose we are interested in the expectation  $\mu$  of an observable  $x$  (random variable) and its variance,  $\sigma^2$ . We have a set of  $n$  independent measurements  $x_i$ , which have same unknown expectation  $\mu$  and common unknown variance  $\sigma^2$ . This corresponds to, for instance, a set of  $n$  measurements for an observable  $x$  in an experiment. Then their consistent and unbiased estimate are the sample mean  $\bar{x}$  and sample variance  $S^2$ , respectively:

$$\hat{\mu} = \bar{x} = \frac{1}{n} \sum_{i=1}^n x_i, \quad (\text{A.1.4})$$

$$\hat{\sigma}^2 = S^2 = \frac{1}{n-1} \sum_{i=1}^n (x_i - \bar{x})^2. \quad (\text{A.1.5})$$

The variance of  $\hat{\mu}$  is  $\sigma^2/n$ , while the variance of  $\hat{\sigma}^2$  is

$$V(\hat{\sigma}^2) = \frac{1}{n} (m_4 - \frac{n-3}{n-1} \sigma^4), \quad (\text{A.1.6})$$

where  $m_4$  is the 4th central moment of  $x$ .

For the known  $\mu$ , the consistent, unbiased estimator of variance is

$$\hat{\sigma}^2 = \frac{1}{n} \sum_{i=1}^n (x_i - \mu)^2, \quad (\text{A.1.7})$$

which gives a somewhat better estimator of  $\sigma^2$  compared with Eq. A.1.5 for unknown  $\mu$  case. For the binomial, Poisson and Gaussian variables  $x_i$ , which are often used in data analysis, the sample mean is an efficient estimator for  $\mu$ ; For the normal variables, Eq. A.1.7 is an efficient estimator of  $\sigma^2$  in the case of known  $\mu$ , and sample variance  $S^2$  is an asymptotic efficient estimator for  $\sigma^2$ .

For the Gaussian distributed  $x_i$ , Eq. A.1.6 becomes  $V(\hat{\sigma}^2) = 2\sigma^4/(n-1)$  for any  $n \geq 2$ , and for large  $n$  the standard deviation of  $\hat{\sigma}$  (the "error of the error") is  $\sigma/\sqrt{2n}$ .

If the  $x_i$  have different, known variance  $\sigma_i^2$ , which corresponds to the situation that different experiments measure the same quantity with different uncertainties. Assume  $x_i$  can be considered as a measurement of the Gaussian distributed variable  $N(\mu, \sigma_i^2)$ , then the unbiased estimator of the physics quantity  $\mu$  is a weighted average

$$\hat{\mu} = \frac{1}{\omega} \sum_{i=1}^n \omega_i x_i, \quad (\text{A.1.8})$$

where  $\omega_i = 1/\sigma_i^2$ ,  $\omega = \sum_i \omega_i$ , and the standard deviation of  $\hat{\mu}$  is  $1/\sqrt{\omega}$ .

### A.1.2 The method of maximum likelihood(ML)

From the statistical point of view, the method of maximum likelihood (ML) is the most important general method of estimation, as the ML estimator of parameter has many good properties.

#### The ML estimators for parameter and its error

Suppose  $x_i, i = 1, \dots, n$  are the  $n$  independent measurements of a random variable  $x$  with the pdf  $f(x, \vec{\theta})$ , where  $\vec{\theta} = (\theta_1, \dots, \theta_k)^T$  are  $k$  parameters to be determined, then the ML estimators  $\hat{\vec{\theta}}(x_1, \dots, x_n)$  are the values of  $\vec{\theta}$  that maximize the likelihood function

$$L(\vec{x}|\hat{\vec{\theta}}) = \prod_{i=1}^n f(x_i; \vec{\theta}). \quad (\text{A.1.9})$$

Since both  $\ln L$  and  $L$  are maximized for the same parameters values  $\vec{\theta}$  and it is usually easier to work with  $\ln L$ , therefore, the ML estimators can be found by solving the likelihood equations

$$\frac{\partial \ln L}{\partial \theta_i} = 0, \quad i = 1, \dots, k. \quad (\text{A.1.10})$$

The ML estimator is invariant under change of parameter, namely, under an one-to-one change of parameters from  $\vec{\theta}$  to  $\vec{\eta}$ , the ML estimators  $\hat{\vec{\theta}}$  transform to  $\hat{\vec{\eta}}(\hat{\vec{\theta}}) : \hat{\vec{\eta}}(\hat{\vec{\theta}}) = \vec{\eta}(\hat{\vec{\theta}})$ . Moreover, the ML estimators are asymptotic unbiased. When the likelihood function satisfies the regularity conditions, the ML estimators are consistent estimators. If there exist the efficient estimators for parameters or their functions, then the efficient estimators must be the ML estimators, and the likelihood equations give the unique solutions; while if the efficient estimators do not exist, the ML estimators give possibly minimum variance for  $\vec{\theta}$ . For large size  $n$  and the likelihood function satisfies the regularity conditions,  $\hat{\vec{\theta}}$  asymptotically distributed as a normal variable with the mean being the true values  $\vec{\theta}$  and the variances reach the MVB.

The ML estimators give only the values of the parameters. To know the errors of the parameters, one has to know the variances of parameters. The expression of the covariance between parameters  $\hat{\theta}_i$  and  $\hat{\theta}_j$  for any size of sample  $n$  is

$$V_{ij}(\hat{\vec{\theta}}) = \int (\hat{\theta}_i - \theta_i)(\hat{\theta}_j - \theta_j) L(\vec{x}|\hat{\vec{\theta}}) d\vec{x}, \quad i, j = 1, \dots, k. \quad (\text{A.1.11})$$

The calculation of this integral is sometimes troublesome, however, in general, it can be calculated with numerical method in any case.

For the case that  $\hat{\theta}$  is an efficient estimator of single parameter, following equation is applicable for any size of sample  $n$ :

$$V(\hat{\theta}) = \frac{(1 + \frac{\partial b}{\partial \theta})^2}{(-\frac{\partial^2 \ln L}{\partial \theta^2})_{\theta=\hat{\theta}}}; \quad (\text{A.1.12})$$

In particular, if  $\hat{\theta}$  is an unbiased efficient estimator

$$V(\hat{\theta}) = \frac{1}{(-\frac{\partial^2 \ln L}{\partial \theta^2})_{\theta=\hat{\theta}}}. \quad (\text{A.1.13})$$

For multi-parameters and large  $n$ , if there exists a set of  $k$  jointly sufficient statistics  $t_1, \dots, t_k$  for the  $k$  parameters  $\theta_1, \dots, \theta_k$ , the inverse of the covariance matrix  $V_{ij} = \text{cov}(\hat{\theta}_i, \hat{\theta}_j)$  for a set of ML estimators can be calculated by

$$V_{ij}^{-1}(\hat{\vec{\theta}}) = \left(-\frac{\partial^2 \ln L}{\partial \theta_i \partial \theta_j}\right)_{\vec{\theta}=\hat{\vec{\theta}}}, \quad i, j = 1, \dots, k. \quad (\text{A.1.14})$$

Besides, for large  $n$  and the likelihood function satisfying the regularity conditions, the ML estimators  $\hat{\vec{\theta}}$  asymptotically distributed as a multi-dimensional normal variable, then one has

$$V_{ij}^{-1}(\hat{\vec{\theta}}) = E\left(-\frac{\partial^2 \ln L(\vec{x}|\vec{\theta})}{\partial \theta_i \partial \theta_j}\right)_{\vec{\theta}=\hat{\vec{\theta}}} = \int \left(-\frac{\partial^2 \ln L(\vec{x}|\vec{\theta})}{\partial \theta_i \partial \theta_j}\right)_{\vec{\theta}=\hat{\vec{\theta}}} \cdot L d\vec{x}, \quad i, j = 1, \dots, k; \quad (\text{A.1.15})$$

or, one can use the *pdf* of the random variable  $x$  to calculate the covariance matrix:

$$V_{ij}^{-1}(\hat{\vec{\theta}}) = n \int \frac{1}{f} \left(\frac{\partial f}{\partial \theta_i}\right) \left(\frac{\partial f}{\partial \theta_j}\right) dx, \quad i, j = 1, \dots, k. \quad (\text{A.1.16})$$

Wherein, the last equation uses only the *pdf* of the random variable  $x$  and does not need the measured data sample, which is particularly useful in the design stage of an experiment.

If the observable  $x$  is a normal random variable, or the size of sample  $n$  is sufficiently large, then the likelihood function is an asymptotically normal distribution and  $\ln L$  is a parabolic function, a numerically equivalent way of determining  $s$ -standard-deviation errors is from the contour given by the  $\vec{\theta}'$  such that

$$\ln L(\vec{\theta}') = \ln L_{\max} - \frac{s^2}{2}, \quad (\text{A.1.17})$$

where  $L_{\max}$  is the value of  $\ln L$  at the solution point. The extreme limits of this contour on the  $\theta_i$  axis give an  $s$ -standard-deviation likelihood interval for  $\theta_i$ . In the case  $\ln L$  is not a parabolic function, the approximate 1-standard-deviation likelihood interval can also be estimated by this equation, and it will give an asymmetric positive and negative errors for each parameter, namely,  $\sigma^+(\theta_i) \neq \sigma^-(\theta_i)$ ,  $i = 1, \dots, k$ .

### The ML method for binned data

In the case that the size  $n$  of data sample  $\vec{x} = (x_1, \dots, x_n)^T$  is sufficiently large, the measurements often are expressed as a histogram binned data. For constant  $n$ , the likelihood function (joint *pdf*) of  $n_i (i = 1, \dots, m)$  measurement values appearing in  $i$ -th bin is expressed as a multinomial distribution

$$L(n_1, \dots, n_m | \vec{\theta}) = n! \prod_{i=1}^m \frac{1}{n_i!} p_i^{n_i}. \quad (\text{A.1.18})$$

The probability of one measurement value appearing in  $i$ -th bin is calculated with *pdf*  $f(x | \vec{\theta})$

$$p_i = p_i(\vec{\theta}) = \int_{\Delta x_i} f(x | \vec{\theta}) dx. \quad (\text{A.1.19})$$

Then the likelihood equation becomes

$$\left( \frac{\partial \ln L}{\partial \theta_i} \right)_{\vec{\theta}=\hat{\vec{\theta}}} = \frac{\partial}{\partial \theta_i} \left[ \sum_{i=1}^m n_i \ln p_i(\vec{\theta}) \right]_{\vec{\theta}=\hat{\vec{\theta}}} = 0, \quad i = 1, \dots, m, \quad (\text{A.1.20})$$

Solving this set of equations gives the ML estimators  $\hat{\vec{\theta}}$ .

### The extended ML method

If the size  $n$  of data sample is not a constant but a Poisson random variable with the expectation  $\nu$ , then the likelihood function is the product of usual likelihood function and the Poisson probability of observing  $n$  events

$$L(\nu, \vec{\theta}) = \frac{\nu^n}{n!} e^{-\nu} \prod_{i=1}^n f(x_i, \vec{\theta}), \quad (\text{A.1.21})$$

which is called the extended likelihood function [5]. Then the solutions of the likelihood equations

$$\frac{\partial \ln L(\nu, \vec{\theta})}{\partial \theta_j} = 0, \quad j = 1, \dots, k, \quad (\text{A.1.22})$$

$$\frac{\partial \ln L(\nu, \vec{\theta})}{\partial \nu} = 0 \quad (\text{A.1.23})$$

give the ML estimators  $\hat{\vec{\theta}}$ .

In the case that  $\nu$  is irrelevant to  $\vec{\theta}$ ,  $\frac{\partial \ln L(\nu, \vec{\theta})}{\partial \nu} = 0$  gives  $\hat{\nu} = n$ , the solutions of Eq. A.22 give the same  $\hat{\vec{\theta}}$  as those from Eqs. A.1.9, A.1.10. If  $\nu$  is a function of  $\vec{\theta}$ , the likelihood function becomes (dropping terms irrelevant to  $\vec{\theta}$ )

$$\ln L(\vec{\theta}) = -\nu(\vec{\theta}) + \sum_{i=1}^n \ln [\nu(\vec{\theta}) \cdot f(x_i, \vec{\theta})]. \quad (\text{A.1.24})$$

The variances of the ML estimators  $\hat{\vec{\theta}}$  derived from the extended likelihood function are usually smaller than those from usual likelihood function because the former uses the information from both  $n$  and  $\vec{x}$ .

For the binned data, the extended likelihood function is

$$L(n_1, \dots, n_m | \vec{\theta}) = \prod_{i=1}^m \frac{1}{n_i!} \nu_i^{n_i} e^{-\nu_i}, \quad (\text{A.1.25})$$

where the expectation of  $n_i$ ,  $\nu_i$ , is

$$\nu_i = \nu \int_{\Delta x_i} f(x | \vec{\theta}) dx, \quad \nu = \sum_{i=1}^m \nu_i. \quad (\text{A.1.26})$$

In the case that  $\nu$  is irrelevant to  $\vec{\theta}$ , the likelihood equations become

$$\frac{\partial \ln L}{\partial \theta_j} \Big|_{\vec{\theta}=\hat{\vec{\theta}}} = \frac{\partial}{\partial \theta_j} \left[ \sum_{i=1}^m n_i \ln \nu_i \right]_{\vec{\theta}=\hat{\vec{\theta}}} = 0, \quad j = 1, \dots, m, \quad (\text{A.1.27})$$

which has the same form of Eq. A.1.20 with  $p_i(\vec{\theta})$  replaced by  $\nu_i(\vec{\theta})$ , and  $\hat{\nu} = n$ . If  $\nu$  is a function of  $\vec{\theta}$ , then the likelihood equations are

$$\frac{\partial \ln L}{\partial \theta_j} \Big|_{\vec{\theta}=\hat{\vec{\theta}}} = \frac{\partial}{\partial \theta_j} \left[ \sum_{i=1}^m n_i \ln \nu_i - \nu \right]_{\vec{\theta}=\hat{\vec{\theta}}} = 0, \quad j = 1, \dots, m. \quad (\text{A.1.28})$$

The variances of the ML estimators  $\hat{\vec{\theta}}$  derived from these equations are usually smaller than those from usual likelihood function because the random property of  $n$  has been taken into account here.

### Combining measurements with ML method

Suppose the observations in two independent experiments are  $\vec{x} = (x_1, \dots, x_l)^T$  and  $\vec{y} = (y_1, \dots, y_m)^T$ , and their pdf  $f_x(x, \vec{\theta})$  and  $f_y(y, \vec{\theta})$ , depend on same parameters  $\vec{\theta}$ , which are the quantities to be measured in the experiments. The joint likelihood function of these two experiments are

$$L(\vec{x}, \vec{y}; \vec{\theta}) = L(\vec{x}; \vec{\theta}) \cdot L(\vec{y}; \vec{\theta}) = \prod_{i=1}^l f_x(x_i, \vec{\theta}) \prod_{j=1}^m f_y(y_j, \vec{\theta}). \quad (\text{A.1.29})$$

Solving the likelihood equations of this likelihood function with respect to parameters  $\vec{\theta}$  and obtaining the ML estimator  $\hat{\vec{\theta}}$  gives the combined measurement of these two experiments for parameters  $\vec{\theta}$ .

In the case  $f_x(x, \theta)$  and  $f_y(y, \theta)$  are Gaussians and the parameter  $\theta$  is the mean of Gaussians, the combined estimator of the parameter and its variance have simple forms:

$$\hat{\theta} = \left( \frac{\theta_x}{\sigma_x^2} + \frac{\theta_y}{\sigma_y^2} \right) / \left( \frac{1}{\sigma_x^2} + \frac{1}{\sigma_y^2} \right), \quad (\text{A.1.30})$$

$$V(\hat{\theta}) = 1/(\frac{1}{\sigma_x^2} + \frac{1}{\sigma_y^2}), \quad (\text{A.1.31})$$

where  $\theta_x$  and  $\sigma_x$  are the measured value of parameter  $\theta$  and its error from experiment  $x$ , respectively. Above expressions can be directly extended to the situation of multi-experiments.

If the likelihood function is unknown, and only the results of parameter  $\theta$  and its errors,  $\theta_i, \sigma_i^+, \sigma_i^-$ , are reported in each experiment, the combined results for parameter  $\theta$  and its errors of multi-experiments can be deduced with the method suggested by R. Barlow [6]. The essence of the method is using the measured values  $\theta_i, \sigma_i^+, \sigma_i^-$  to construct an approximate parametric likelihood function for each experiment. The *variable width Gaussians* are concluded as the best approximation for our purpose. The likelihood function can be approximated as

$$\ln L(\theta_i|\theta) = -\frac{(\theta - \theta_i)^2}{2V_i(\theta)}, \quad (\text{A.1.32})$$

where the true value of parameter is  $\theta$ , and the measured value is  $\theta_i$  in  $i$ -th experiment. For the *linear  $\sigma$  parametrization*, we have

$$V_i(\theta) = [\sigma_i(\theta)]^2, \quad \sigma_i(\theta) = \sigma_i + \sigma'_i(\theta - \theta_i), \quad (\text{A.1.33})$$

$$\sigma_i = \frac{2\sigma_i^+ \sigma_i^-}{\sigma_i^+ + \sigma_i^-}, \quad \sigma'_i = \frac{\sigma_i^+ - \sigma_i^-}{\sigma_i^+ + \sigma_i^-}, \quad (\text{A.1.34})$$

where  $\sigma_i^+, \sigma_i^-$  are the measured positive and negative errors of  $\theta_i$  in  $i$ -th experiment. For the *linear  $V$  parametrization*,

$$V_i(\theta) = V_i + V'_i(\theta - \theta_i), \quad (\text{A.1.35})$$

$$V_i = \sigma_i^+ \sigma_i^-, \quad V'_i = \sigma_i^+ - \sigma_i^-. \quad (\text{A.1.36})$$

Thus, the joint likelihood function of multi-experiments for parameter  $\theta$  is approximately

$$\ln L(\theta) = -\frac{1}{2} \sum_i \frac{(\theta - \theta_i)^2}{V_i(\theta)}. \quad (\text{A.1.37})$$

The best estimate of  $\theta$ ,  $\hat{\theta}$ , is determined by the maximum of above likelihood function. For the linear  $\sigma$  form, the solution is

$$\hat{\theta} = \sum_i \omega_i \theta_i / \sum_i \omega_i, \quad (\text{A.1.38})$$

$$\omega_i = \frac{\sigma_i}{[\sigma_i + \sigma'_i(\hat{\theta} - \theta_i)]^3}. \quad (\text{A.1.39})$$

For the linear  $V$  form, the solution is

$$\hat{\theta} = \sum_i \omega_i [\theta_i - \frac{V'_i}{2V_i} (\hat{\theta} - \theta_i)^2] / \sum_i \omega_i, \quad (\text{A.1.40})$$

$$\omega_i = \frac{V_i}{[V_i + V'_i(\hat{\theta} - \theta_i)]^2}. \quad (\text{A.1.41})$$

Two sets of equations shown above are non-linear for  $\hat{\theta}$  and the solution must be found by iteration. The  $\Delta \ln L = 0.5$  points of the likelihood function in Eq. A.1.37 are used to determine the positive and negative errors for  $\hat{\theta}$ , which also need to be determined numerically. The program of combining results from multi-experiments using parametrization likelihood function has been coded, and obtainable under <http://www.slac.stanford.edu/~barlow/statistics.html>.

### A.1.3 The method of least squares(LS)

#### The LS estimator for parameter and its error

Suppose  $n$  observations  $\vec{y} = (y_1, \dots, y_n)^T$  are measured at  $n$  points  $\vec{x} = (x_1, \dots, x_n)^T$ , the covariance matrix of observations  $\vec{y}$  is expressed as  $V_{ij} = \text{cov}(y_i, y_j)$ , and the true values of  $\vec{y}$ ,  $\vec{\eta}$ , are described by model  $\eta_i = f(x_i, \vec{\theta})$ ,  $i = 1, \dots, n$ , where  $\vec{\theta} = (\theta_1, \dots, \theta_k)^T$  are the parameters to be determined. The least squares (LS) estimators of  $\vec{\theta}$ ,  $\hat{\vec{\theta}}$ , can be found by minimizing the LS function  $Q^2(\vec{\theta})$  with respect to  $\vec{\theta}$ :

$$Q^2(\vec{\theta}) = (\vec{y} - \vec{\eta}(\vec{\theta}))^T V^{-1} (\vec{y} - \vec{\eta}(\vec{\theta})) = \sum_{i=1}^n \sum_{j=1}^n (y_i - \eta_i) V_{ij}^{-1} (y_j - \eta_j). \quad (\text{A.1.42})$$

In the case of  $y_i, i = 1, \dots, n$  being  $n$  independent measurements, the LS function has simple form

$$Q^2(\vec{\theta}) = \sum_{i=1}^n \frac{(y_i - \eta_i)^2}{\sigma_i^2}, \quad (\text{A.1.43})$$

where  $\sigma_i$  is the error of  $y_i$ . An usual case is  $y_i$  is a Poisson variable, then  $\sigma_i^2$  can be approximated by  $y_i$  or its predicted value  $\eta_i$ . If  $y_i, i = 1, \dots, n$  are  $n$  independent Gaussians,  $y_i \sim N(\eta_i, \sigma_i^2)$ , the likelihood function of  $\vec{y}$  is  $L(\vec{\theta}) \propto \exp[-\frac{1}{2} \sum_{i=1}^n (\frac{y_i - \eta_i}{\sigma_i})^2]$ . In this case maximizing  $L(\vec{\theta})$  with respect to parameters  $\vec{\theta}$  is equivalent to minimizing the LS function  $Q^2(\vec{\theta}) = \sum_{i=1}^n \frac{(y_i - \eta_i)^2}{\sigma_i^2}$ , namely, the estimators of ML and LS methods for  $\vec{\theta}$  are identical.

For the linear LS model, *i.e.*  $f(x_i, \vec{\theta})$  is the linear function of  $\vec{\theta}$ :

$$f(x_i, \vec{\theta}) = \sum_{j=1}^k a_{ij} \theta_j, \quad i = 1, \dots, n, \quad k < n, \quad (\text{A.1.44})$$

where  $a_{ij}$  equals  $x_i^{j-1}$  or is the  $(j-1)$ -th Legendre polynomial of  $x_i$ , minimizing the LS function  $Q^2(\vec{\theta})$  simplified to solve a set of  $k$  linear equations. Define  $a_{ij}$  being the elements of a  $n \times k$  matrix  $A$ , minimizing the LS function  $Q^2(\vec{\theta})$  gives the LS estimator of parameters  $\vec{\theta}$ :

$$\hat{\vec{\theta}} = (A^T V^{-1} A)^{-1} A^T V^{-1} \vec{y}, \quad (\text{A.1.45})$$

the covariance matrix of  $\hat{\vec{\theta}}$  is

$$V(\hat{\vec{\theta}}) = (A^T V^{-1} A)^{-1}, \quad (\text{A.1.46})$$

or equivalently

$$(V^{-1}(\hat{\vec{\theta}}))_{ij} = \frac{1}{2} \frac{\partial^2 Q^2}{\partial \theta_i \partial \theta_j} \Big|_{\vec{\theta}=\hat{\vec{\theta}}} = \sum_{l,m=1}^n a_{li} a_{mj} (V^{-1})_{lm}, \quad i, j = 1, \dots, k. \quad (\text{A.1.47})$$

If  $y_i, i = 1, \dots, n$  are independent each other, the non-diagonal elements equal to zeros, then the above equation is simplified to

$$(V^{-1}(\hat{\vec{\theta}}))_{ij} = \sum_{m=1}^n a_{mi} a_{mj} / \sigma_m^2, \quad i, j = 1, \dots, k. \quad (\text{A.1.48})$$

The linear LS estimators provide the exact solutions for parameters  $\vec{\theta}$ , and they are unique and unbiased, and have minimum variances.

Expanding  $Q^2(\vec{\theta})$  about  $\hat{\vec{\theta}}$ , one finds that the contour in parameter space defined by

$$Q^2(\vec{\theta}) = Q^2(\hat{\vec{\theta}}) + s^2 = Q_{\min}^2 + s^2 \quad (\text{A.1.49})$$

has tangent planes located at plus or minus  $s$ - standard deviation from the LS estimates  $\hat{\vec{\theta}}$ .

For the linear LS model, if the observations  $\vec{y}$  are multi-normal variables, the minimum of the LS function  $Q^2(\vec{\theta})$

$$Q_{\min}^2(\vec{\theta}) = \sum_{i=1}^n \sum_{j=1}^n (y_i - \hat{\eta}_i) V_{ij}^{-1} (y_j - \hat{\eta}_j) \quad (\text{A.1.50})$$

is a  $\chi^2$  variable with degree of freedom of  $n - k$ . This means the  $Q_{\min}^2$  obtained by LS method is a quantitative measure of the consistency between the measured values  $\vec{y}$  and their fitted value  $\hat{\vec{\eta}}$ , *i.e.*, the  $Q_{\min}^2$  represents the goodness of fit (see section A.3.1., goodness of fit tests).

For the non-linear LS model, *i.e.*  $f(x_i, \vec{\theta})$  is the non-linear function of  $\vec{\theta}$ , usually the minimizing of the LS function  $Q^2(\vec{\theta})$  is implemented via iteration procedure to obtain an approximate solution of  $\hat{\vec{\theta}}$ . The non-linear LS estimator is a biased estimator, its variance does not reach MVB, and the exact distribution of  $Q_{\min}^2$  is unknown. However, if  $n$  is sufficiently large, the LS estimator is asymptotically unbiased, and its  $Q_{\min}^2$  is approximately a  $\chi^2$  variable.

### The LS method for binned data

For sufficiently large size  $n$  of data sample  $\vec{x} = (x_1, \dots, x_n)^T$  and the measurements expressed as a histogram binned data, assuming the observed number of measurements in  $i$ -th bin is  $n_i, i = 1, \dots, m$ , and its corresponding expectation from assumed model is

$$f_i(\vec{\theta}) = np_i, \quad p_i(\vec{\theta}) = \int_{\Delta x_i} g(x|\vec{\theta}) dx, \quad (\text{A.1.51})$$

where  $g(x|\vec{\theta})$  is the *pdf* of observable  $x$  and  $\vec{\theta}$  are the parameters to be determined. The normalization  $\sum_{i=1}^m p_i = 1$  requires

$$\sum_{i=1}^m n_i = \sum_{i=1}^m f_i(\vec{\theta}) = n. \quad (\text{A.1.52})$$

It can be proved for a given  $n$ , the LS function  $Q^2(\vec{\theta})$  is of the form

$$Q^2(\vec{\theta}) = \sum_{i=1}^m \frac{(n_i - np_i)^2}{np_i} = \sum_{i=1}^m \frac{(n_i - f_i)^2}{f_i}. \quad (\text{A.1.53})$$

The  $f_i$  in the denominator can be approximated by  $n_i$ . Minimizing this LS function leads to the LS estimates for parameters  $\vec{\theta}$ , which usually needs to be implemented by numerical iteration procedure. The  $n_i$  is a Poisson variable with the expectation  $np_i$ , if  $n$  is sufficiently large,  $n_i$  can be approximated by a Gaussian, then  $(n_i - f_i)/\sqrt{f_i}$  or  $(n_i - f_i)/\sqrt{n_i}$  is approximately a standard normal variable, therefore, the  $Q^2_{min}(\vec{\theta})$  distributed approximately as a  $\chi^2(m - 1)$  variable, where the degree of freedom of  $m - 1$  is due to the existence of a constraint equation A.1.52.

### General LS estimation with constraints

Often in the estimation problem there exist a set of constraint equations between the true values of observations  $\eta_i, i = 1, \dots, n$ . The typical example is in the kinematic analysis of a particle reaction or decay, the momentum and energy conservation laws constitute a set of restrictions relating the various momenta and angles for the particle combination defining the kinematic hypothesis. Some of the quantities have been measured to a certain accuracy (say, the momenta and angles of curved tracks), and some are completely unknown (the variables for an unseen particle). The purpose of the LS estimation is to investigate the kinematic hypothesis: for a successful minimization the constraint equations will supply estimates for the unmeasured variables as well as "improved measurements" for the measured quantities.

Assume  $\vec{y} = (y_1, \dots, y_n)^T$  are the measured values with covariant matrix  $V(\vec{y})$ , let the true values of  $\vec{y}$  be  $\vec{\eta}$ . In addition, we have a set of  $J$  unmeasurable variables  $\vec{\xi} = (\xi_1, \dots, \xi_J)^T$ . The  $n$  measurable and  $J$  unmeasurable variables are related and have to satisfy a set of  $K$  constraint equations

$$f_k(\vec{\eta}, \vec{\xi}) = 0, \quad k = 1, \dots, K.$$

According to the LS principle, we should adopt as the best estimates of the unknown  $\vec{\eta}$  and  $\vec{\xi}$  those values for which

$$Q^2(\vec{\eta}) = (\vec{y} - \vec{\eta})^T V^{-1}(\vec{y}) (\vec{y} - \vec{\eta}) = \text{minimum}, \quad (\text{A.1.54})$$

$$f(\vec{\eta}, \vec{\xi}) = \vec{0}. \quad (\text{A.1.55})$$

Usually the method of the Lagrangian multipliers are used to solve above equations. We introduce  $K$  additional unknowns  $\vec{\lambda} = (\lambda_1, \dots, \lambda_K)^T$  and rephrase the problem by requiring

$$Q^2(\vec{\eta}, \vec{\xi}, \vec{\lambda}) = (\vec{y} - \vec{\eta})^T V^{-1}(\vec{y}) (\vec{y} - \vec{\eta}) + 2\vec{\lambda}^T \vec{f}(\vec{\eta}, \vec{\xi}) = \text{minimum}. \quad (\text{A.1.56})$$

We have now a total of  $n + J + K$  unknowns. When the derivatives of  $Q^2$  with respect to all unknowns are put equal to zero we get following set of equations

$$V^{-1}(\vec{y})(\vec{y} - \vec{\eta}) + F_\eta^T \vec{\lambda} = \vec{0}, \quad (\text{A.1.57})$$

$$F_\xi^T \vec{\lambda} = \vec{0}, \quad (\text{A.1.58})$$

$$\vec{f}(\vec{\eta}, \vec{\xi}) = \vec{0}, \quad (\text{A.1.59})$$

where the matrices  $F_\eta$  (of dimension  $K \times N$ ) and  $F_\xi$  (of dimension  $K \times J$ ) are defined by

$$(F_\eta)_{ki} \equiv \frac{\partial f_k}{\partial \eta_i}, \quad (F_\xi)_{kj} \equiv \frac{\partial f_k}{\partial \xi_j}. \quad (\text{A.1.60})$$

The solution of this set of equations for the  $n + J + K$  unknowns and their errors must in general case be found by iterations, producing successively better approximations.

In the linear LS estimation problem for the  $n$  measurable and  $J$  unmeasurable variables which are related and have to satisfy a set of  $K$  constraint equations, if the measured values  $\vec{y} = (y_1, \dots, y_n)^T$  is a multi-normal variable, the  $Q_{min}^2$  is a  $\chi^2$  variable with the degree of freedom  $(K - J)$ . For the non-linear LS estimation problem of non-linear constraint equations, and/or  $\vec{y}$  is not a multi-normal variable, the  $Q_{min}^2$  may be approximated by  $\chi^2(K - J)$ .

The momentum-energy conservation laws constitute a set of 4 constraint equations. If all the particle's parameters in a reaction or a decay process have been measured (no unmeasurable variables) and the momentum-energy conservation laws are applied to obtain better values of particles parameters (4C kinematic fit), the  $Q_{min}^2$  of the LS estimator is then an approximate  $\chi^2(4)$  variable. If there exist  $J$  unmeasurable variables and  $r$  intermediate resonances which promptly decayed to observed final state particles, and the invariant masses of daughter particles of these resonances are constrained to their mother particles' masses, then the  $Q_{min}^2$  is approximately a  $\chi^2(4 + r - J)$  variable.

## A.2 Interval estimation, confidence interval and upper limit

The task of the interval estimation is to locate a region which contains the true value of the parameter  $\theta$  to be studied with a probability  $\gamma$ . This region is called the confidence interval with coverage probability  $\gamma$ . When the goal of an experiment is to determine a parameter  $\theta$ , the result is usually expressed by quoting, in addition to the point estimate, some sort of confidence interval which reflects the statistical precision of the measurement. In the simplest case this can be given by the parameter's estimated value  $\hat{\theta}$  plus/minus an estimate of the standard deviation of  $\hat{\theta}$ ,  $\sigma_{\hat{\theta}}$ . If the parameter  $\theta$  has boundary (without losing generality, we assume it is lower boundary with the value zero throughout this Appendix), and the estimate of  $\theta$  in an experiment is close to this boundary, then the determination of the interval estimation is difficult and needs to be treated in special way.

### A.2.1 Frequentist confidence interval

#### Neyman method for confidence interval

Confidence interval refers to frequentist interval obtained with a procedure due to Neyman [7]. Consider a *pdf*  $f(x; \theta)$  where  $x$  represents the measurement of the experiment and  $\theta$  the unknown parameter for which we want to construct a confidence interval. The variable  $x$  could (and often does) represent an estimator of  $\theta$ . Using  $f(x; \theta)$  we can find for a pre-specified probability  $\gamma = 1 - \alpha$  and for every value of  $\theta$  a set of values  $x_1(\theta, \alpha)$  and  $x_2(\theta, \alpha)$  such that

$$P(x_1 < x < x_2; \theta) = 1 - \alpha \equiv \gamma = \int_{x_1}^{x_2} f(x; \theta) dx. \quad (\text{A.2.61})$$

This is illustrated in Fig. A.1: a horizontal line segment  $[x_1(\theta, \alpha), x_2(\theta, \alpha)]$  is drawn for representative values of  $\theta$ . The union of such intervals for all values of  $\theta$ , designated in

the figure as  $D(\alpha)$ , is known as the confidence belt. Typically the curves  $x_1(\theta, \alpha)$  and  $x_2(\theta, \alpha)$  are monotonic functions of  $\theta$ , which we assume for this discussion.

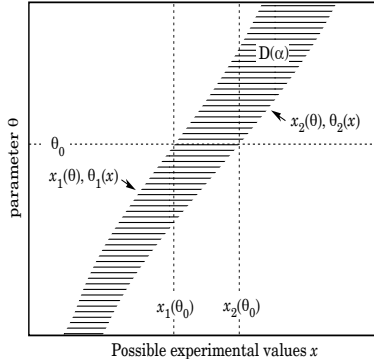


Figure A.1: Construction of the confidence belt

Upon performing an experiment to measure  $x$  and obtaining a value  $x_0$ , one draws a vertical line through  $x_0$ . The confidence interval for  $\theta$  is the set of all values of  $\theta$  for which the corresponding line segment  $[x_1(\theta, \alpha), x_2(\theta, \alpha)]$  is intersected by this vertical line. Such confidence intervals are said to have a confidence level (CL) equal to  $\gamma = 1 - \alpha$ .

Now suppose that the true value of  $\theta$  is  $\theta_0$ , indicated in the figure. We see from the figure that  $\theta_0$  lies between  $\theta_1(x)$  and  $\theta_2(x)$  if and only if  $x$  lies between  $x_1(\theta_0)$  and  $x_2(\theta_0)$ . The two events thus have the same probability, and since this is true for any value  $\theta_0$ , we can drop the subscript 0 and obtain

$$\gamma = 1 - \alpha = P(x_1(\theta) < x < x_2(\theta)) = P(\theta_2(x) < \theta < \theta_1(x)). \quad (\text{A.2.62})$$

In this probability statement  $\theta_1(x)$  and  $\theta_2(x)$ , *i.e.*, the endpoints of the interval, are the random variables and  $\theta$  is an unknown constant. If the experiment were to be repeated a large number of times, the interval  $[\theta_1, \theta_2]$  would vary, covering the fixed value  $\theta$  in a fraction  $\gamma = 1 - \alpha$  of the experiments.

The condition of coverage probability does not determine  $x_1$  and  $x_2$  uniquely and additional criteria are needed. The most common criterion is to choose central intervals such that the probabilities below  $x_1$  and above  $x_2$  are each  $\alpha/2$ . In other cases one may want to report only an upper or lower limit, then the probability excluded below  $x_1$  or above  $x_2$  can be set to zero.

When the observed random variable  $x$  is continuous, the coverage probability obtained with the Neyman construction is  $\gamma = 1 - \alpha$ , regardless of the true value of the parameter. If  $x$  is discrete, however, it is not possible to find segments  $[x_1(\theta, \alpha), x_2(\theta, \alpha)]$  that satisfy Eq. A.2.62 exactly for all values of  $\theta$ . By convention one constructs the confidence belt requiring the probability  $P(x_1 < x < x_2)$  to be greater than or equal to  $\gamma = 1 - \alpha$ . This gives confidence intervals that include the true parameter with a probability greater than or equal to  $\gamma = 1 - \alpha$ .

## Gaussian distributed measurements

An important example of constructing a confidence interval is when the data consist of a single random variable  $x$  that follow a Gaussian distribution; this is often the case when

$x$  represents an estimator for a parameter and one has a sufficiently large data sample. If there is more than one parameter being estimated, the multivariate Gaussian is used. For the univariate case with known  $\sigma$ ,

$$\gamma = 1 - \alpha = \frac{1}{\sqrt{2\pi\sigma}} \int_{\mu-\delta}^{\mu+\delta} e^{-(x-\mu)^2/2\sigma^2} dx = \text{erf}\left(\frac{\delta}{\sqrt{2}\sigma}\right) \quad (\text{A.2.63})$$

is the probability that the measured value  $x$  will fall within  $\pm\delta$  of the true value  $\mu$ . From the symmetry of the Gaussian with respect to  $x$  and  $\mu$ , this is also the probability for the interval  $x \pm \delta$  to include  $\mu$ . The choice  $\delta = \sigma$  gives an interval called the standard error which has  $\gamma = 1 - \alpha = 68.27\%$  if  $\sigma$  is known. Values of  $\alpha$  for other frequently used choices of  $\delta$  are given in Table A.1. The relation of  $\alpha$  and  $\delta$  can be also represented by the cumulated distribution function for the  $\chi^2$  distribution for  $\chi^2 = (\delta/\sigma)^2$  and  $n = 1$  degree of freedom:

$$\gamma = 1 - \alpha = F(\chi^2; n = 1). \quad (\text{A.2.64})$$

For multivariate measurements of, say,  $n$  parameter estimates  $\vec{\theta} = (\hat{\theta}_1, \dots, \hat{\theta}_n)^T$ , one

Table A.1: Area of the tails  $\alpha$  outside  $\pm\delta$  from the mean of a Gaussian distribution.

$\alpha$	$\delta$	$\alpha$	$\delta$
0.3173	$1\sigma$	0.2	$1.28\sigma$
0.0455	$2\sigma$	0.1	$1.64\sigma$
0.0027	$3\sigma$	0.05	$1.96\sigma$
$6.3 \times 10^{-5}$	$4\sigma$	0.01	$2.58\sigma$
$5.7 \times 10^{-7}$	$5\sigma$	0.001	$3.29\sigma$
$2.0 \times 10^{-9}$	$6\sigma$	0.0001	$3.89\sigma$

requires the full covariance matrix  $V_{ij} = \text{cov}(\hat{\theta}_i, \hat{\theta}_j)$ , which can be estimated by ML or LS method.

If the parameters  $\vec{\theta}$  are estimated with the ML method, for sufficient large  $n$  and the likelihood function satisfies the regularity conditions, the likelihood function distributed asymptotically as a multi-Gaussian, then we have

$$\ln L(\vec{\theta}) = \ln L_{\max} - Q(\vec{\theta})/2, \quad (\text{A.2.65})$$

where  $Q(\vec{\theta}) = (\vec{\theta} - \hat{\vec{\theta}})^T V^{-1}(\vec{\theta})(\vec{\theta} - \hat{\vec{\theta}})$  is asymptotically a  $\chi^2(k)$  variable, and  $k$  is the dimension of  $\vec{\theta}$ . The intersection contour of super-plane  $\ln L = \ln L_{\max} - Q_{\gamma}/2$  and super-surface  $\ln L(\vec{\theta})$  forms the boundary of the confidence region of  $\vec{\theta}$  with coverage probability of  $\gamma = 1 - \alpha$ , which is calculated by the cumulated  $\chi^2$  function

$$\gamma = 1 - \alpha = P(Q \leq Q_{\gamma}) = \int_0^{Q_{\gamma}} \chi^2(Q; \nu = k) dQ = F_{\alpha}(Q_{\gamma}; \nu = k). \quad (\text{A.2.66})$$

In the case that the parameters  $\vec{\theta}$  are estimated with LS method, for linear LS estimator and multi-Gaussian measurements, we have

$$Q^2(\vec{\theta}) = Q_{\min}^2 + Q_{LS}^2, \quad (\text{A.2.67})$$

where  $Q_{LS}^2(\vec{\theta}) = (\vec{\theta} - \hat{\vec{\theta}})^T V^{-1}(\vec{\theta})(\vec{\theta} - \hat{\vec{\theta}})$  is a  $\chi^2(k)$  variable and  $k$  is the dimension of  $\vec{\theta}$  for non-constraint LS estimation, and the dimension of  $\vec{\theta}$  minus the number of independent linear constraint equations for constraint LS case. The intersection contour of super-plane  $Q^2(\vec{\theta}) = Q_{min}^2 + Q_\gamma$  and super-surface  $Q^2(\vec{\theta})$  forms the boundary of the confidence region of  $\vec{\theta}$  with coverage probability of  $\gamma \equiv 1 - \alpha$ , which is also calculated by Eq. A.2.66. Values of  $Q_\gamma$  for  $k = 1, 2, 3$  are given in Table A.2 for several values of the coverage probability  $\gamma = 1 - \alpha$ .

Table A.2:  $Q_\gamma$  for  $k = 1, 2, 3$  corresponding to a coverage probability  $\gamma = 1 - \alpha$  in the large data sample limit.

$\gamma(\%)$	k=1	k=2	k=3
68.27	1.00	2.30	3.53
90.	2.71	4.61	6.25
95.	3.84	5.99	7.82
95.45	4.00	6.18	8.03
99.	6.63	9.21	11.34
99.73	9.00	11.83	14.16

If the mentioned conditions are not fully satisfied, the confidence region determined by Eqs. A.2.65 and A.2.67 are not exact but an approximate one.

The ML method has an advantage that is easier to calculate the confidence region for combining several independent measurements of same parameters. Assume  $N$  independent measurements give likelihood functions  $\ln L_i(\vec{\theta})$ ,  $i = 1, \dots, N$ , then the combined likelihood function is simply

$$\ln L(\vec{\theta}) = \sum_i^N \ln L_i(\vec{\theta}). \quad (\text{A.2.68})$$

Then using this likelihood functions in Eq. A.2.65 can give the confidence region with coverage probability  $\gamma$  for combined estimate  $\hat{\vec{\theta}}$ .

### Poisson distributed measurements

If  $n$  represents the number of events produced in a reaction with cross section  $\sigma$ , say in a fixed integrated luminosity  $L$ , then it follows a Poisson distribution with mean  $s = \sigma L$  in the case there is no background. Therefore, to determine the cross section of a reaction or the branching ratio of a decay process in terms of the number of observed events, the interval estimation of Poisson distributed data must be met. The probability of observing  $n$  events of the Poisson distribution with the mean  $s$  is

$$P(n, s) = \frac{s^n e^{-s}}{n!}. \quad (\text{A.2.69})$$

The upper and lower (one sided) limits on the mean  $s$  can be found from the Neyman procedure to be

$$s_{lo} = \frac{1}{2} F_{\chi^2}^{-1}(\alpha_{lo}; 2n), \quad (\text{A.2.70})$$

$$s_{up} = \frac{1}{2} F_{\chi^2}^{-1}(1 - \alpha_{up}); 2(n + 1)), \quad (\text{A.2.71})$$

where the upper and lower limits are at confidence levels of  $1 - \alpha_{lo}$  and  $1 - \alpha_{up}$ , respectively, and  $F_{\chi^2}^{-1}$  is the quantile of the  $\chi^2$  distribution (inverse of the cumulative distribution). The quantiles  $F_{\chi^2}^{-1}$  can be obtained from standard tables or from the CERNLIB routine CHISIN. For central confidence intervals at CL  $1 - \alpha$ , set  $\alpha_{lo} = \alpha_{up} = \alpha/2$ . Values for confidence levels of 90% and 95% are shown in Table A.3.

Table A.3: Lower and upper (one-sided) limits for the mean  $s$  of a Poisson variable given  $n$  observed events in the absence of background, for CL of 90% and 95%

$n$	$1 - \alpha = 90\%$		$1 - \alpha = 95\%$	
	$s_{lo}$	$s_{up}$	$s_{lo}$	$s_{up}$
0		2.30		3.00
1	0.105	3.89	0.051	4.74
2	0.532	5.32	0.355	6.30
3	1.10	6.68	0.818	7.75
4	1.74	7.99	1.37	9.15
5	2.43	9.27	1.97	10.51
6	3.15	10.53	2.61	11.84
7	3.89	11.77	3.29	13.15
8	4.66	12.99	3.98	14.43
9	5.43	14.21	4.70	15.71
10	6.22	15.41	5.43	16.96

If the number of observed events  $n$  contains both signal and background events, which are Poisson variables with mean  $s$  and  $b$ , respectively, then we have

$$P(n, s) = \frac{(s + b)^n e^{-(s+b)}}{n!}. \quad (\text{A.2.72})$$

For a specific value of  $s$ , the upper and lower limit of the central confidence region,  $[n_l, n_u]$ , and the lower limit of the upper confidence belt,  $n_{l0}$ , at given confidence level  $\gamma = 1 - \alpha$  can be determined by

$$\sum_{n=0}^{n_l} P(n, s) \leq \frac{\alpha}{2}, \quad \sum_{n=n_u+1}^{\infty} P(n, s) \leq \frac{\alpha}{2}, \quad (\text{A.2.73})$$

$$\sum_{n=0}^{n_{l0}} P(n, s) \leq \alpha, \quad (\text{A.2.74})$$

respectively. For all  $s$  values, such calculations give the confidence belts for central region and upper confidence belt. The inequality sign is to ensure the actual coverage greater or equal to the given coverage in the discrete variable case.

## Confidence interval near the physics boundary

A number of issues arise in the construction and interpretation of confidence intervals when the parameter can only take on values in a restricted range. An important sample is where the mean of a Gaussian variable is constrained on physical grounds to be non-negative. This arises, for example, when the square of the neutrino mass is estimated from  $\hat{m}^2 = \hat{E}^2 - \hat{p}^2$ , where  $\hat{E}$  and  $\hat{p}$  are independent, Gaussian distributed estimates of the energy and momentum. Although the true  $m^2$  is constrained to be positive, random errors in  $\hat{E}$  and  $\hat{p}$  can easily lead to negative values for the estimate  $\hat{m}^2$ .

If one uses the prescription given above for Gaussian distributed measurements, which says to construct the interval by taking the estimate plus/minus one standard deviation, then this can give intervals that are partially or entirely in the unphysical region. In fact, by following strictly the Neyman construction for the central confidence interval, one finds that the interval is truncated below zero; nevertheless an extremely small or even a zero-length interval can result.

An additional important example is where the experiment consists of counting a certain number of events,  $n$ , which is assumed to be Poisson distributed. Suppose the expectation value  $E(n) = \mu$  is equal to  $s + b$ , where  $s$  and  $b$  are the means for signal and background processes, and assume further that  $b$  is a known constant. Then  $\hat{s} = n - b$  is an unbiased estimator for  $s$ . Depending on true magnitudes of  $s$  and  $b$ , the estimate  $\hat{s}$  can easily fall in the negative region. Similar to the Gaussian case with the positive mean, the central confidence interval or even the upper limit for  $s$  may be of zero length.

An additional difficulty arises when a parameter estimate is not significantly far away from the boundary, in which case it is natural to report a one-sided confidence interval (often an upper limit). It is straightforward to force the Neyman prescription to produce only an upper limit by setting  $x_2 = \infty$  in Eq. A.2.61. Then  $x_1$  is uniquely determined and the upper limit can be obtained. If, however, the data come out such that the parameter estimate is not so close to the boundary, one might wish to report a central (*i.e.*, two-sided) confidence interval. As pointed out by Feldman and Cousins [8], however, if the decision to report an upper limit or two-sided interval is made by looking at the data ("flip-flopping"), then the resulting intervals will not in general cover the parameter with the probability  $1 - \alpha$ .

With the confidence intervals suggested by Feldman and Cousins [8], the prescription determines whether the interval is one- or two-sided in a way which preserves the coverage probability. Intervals with this property are said to be unified. Furthermore, this prescription is such that null intervals do not occur. For a given choice of  $1 - \alpha$ , if the parameter estimate is sufficiently close to the boundary, then the method gives an one-sided limit. In the case of a Poisson variable in the presence of background, for example, this would occur if the number of observed events is compatible with the expected background. For parameter estimates increasingly far away from the boundary, *i.e.*, for increasing signal significance, the interval makes a smooth transition from one- to two-sided, and far away from the boundary one obtains a central interval. The intervals according to this method for the mean of Poisson variable in the absence of background are given in Table A.4.

The intervals constructed according to the unified procedure in Ref. [8] for a Poisson variable  $n$  consisting of signal and background have the property that for  $n = 0$  observed events, the upper limit decreases for increasing expected background. This is counter-

Table A.4: Unified confidence interval  $[s_1, s_2]$  for a mean  $s$  of a Poisson variable given  $n$  observed events in the absence of background, for CL of 90% and 95%

$n$	$1 - \alpha = 90\%$		$1 - \alpha = 95\%$	
	$s_1$	$s_2$	$s_1$	$s_2$
0	0.00	2.44	0.00	3.09
1	0.11	4.36	0.05	5.14
2	0.53	5.91	0.36	6.72
3	1.10	7.42	0.82	8.25
4	1.47	8.60	1.37	9.76
5	1.84	9.99	1.84	11.26
6	2.21	11.47	2.21	12.75
7	3.56	12.53	2.58	13.81
8	3.96	13.90	2.94	15.29
9	4.36	15.30	4.36	16.77
10	5.50	16.50	4.75	17.82

intuitive, since it is known that if  $n = 0$  for the experiment in question, then no background was observed, and therefore one may argue that the expected background should not be relevant. Roe and Woodroffe [9] proposed a solution to this problem by using such a fact that, given an observation  $n$ , the background  $b$  can not be larger than  $n$  in any case. Therefore, the usual Poisson *pdf* should be replaced by a conditional *pdf*, and then this conditional *pdf* is used to construct the confidence intervals following Feldman and Cousins' procedure.

### Confidence interval incorporating systematic uncertainties

A modification of the Neyman method incorporating systematic uncertainty of the signal detection efficiency has been proposed by Highland and Cousins [10], in which a "semi-Bayesian" approach is adopted, where an average over the probability of the detection efficiency is performed. This method is of limited accuracy in the limit of high relative systematic uncertainties. On the other hand, an entirely frequentist approach has been proposed for the uncertainty in the background rate prediction [11]. This approach is based on a two-dimensional confidence belt construction and likelihood ratio hypothesis testing and treats the uncertainty in the background as a statistical uncertainty rather than as a systematic one. Recently, Conrad *et al* extend the method of confidence belt construction proposed in [12] to include systematic uncertainties in both the signal and background efficiencies as well as systematic uncertainty of background expectation prediction. It takes into account the systematic uncertainties by assuming a *pdf* which parameterizes our knowledge on the uncertainties and integrating over this *pdf*. This method, combining classical and Bayesian elements, is referred to as semi-Bayesian approach. A FORTRAN program, POLE, has been coded to calculate the confidence intervals for a maximum of observed events of 100 and a maximum signal expectation of 50 [13].

### A.2.2 Bayesian credible interval

In Bayesian approach one has to assume a prior *pdf* of an unknown parameter and then perform an experiment to update the prior distribution. The prior *pdf* reflects the experimenter's subjective degree of belief about unknown parameter before the measurement was carried out. The updated prior, called posterior *pdf*, is used to draw inference on unknown parameter. This updating is done with the use of Bayes theorem [14]. Assuming that  $n$  represents the number of observed events,  $s$  is the expectation of the number of signal events which is unknown and to be inferred,  $p(n|s)$  is the conditional *pdf* of observing  $n$  events with given signal  $s$ ,  $\pi(s)$  is the prior *pdf*, the Bayes theorem gives the posterior *pdf*:

$$h(s|n) = \frac{p(n|s)\pi(s)}{\int_0^\infty p(n|s)\pi(s)ds}. \quad (\text{A.2.75})$$

Here the lower limit of the integral is zero, which is the possible minimum of the signal expectation. Using this posterior *pdf*, one can calculate a Bayesian credible interval for the signal expectation  $s$  at given credible level  $CL = 1 - \alpha$  :

$$1 - \alpha = \int_{s_L}^{s_U} h(s|n)ds. \quad (\text{A.2.76})$$

However, such intervals are not uniquely determined. Often, the highest posterior density (HPD) credible interval  $I$  is chosen, which is determined in following way:

$$1 - \alpha = \int_I h(s|n)ds, \quad h(s_1|n) \geq h(s_2|n) \quad \text{for any } s_1 \in I \text{ and } s_2 \notin I. \quad (\text{A.2.77})$$

The upper limit of the signal expectation  $s$  at given credible level  $CL = 1 - \alpha$ ,  $s_{UP}$ , is naturally given by:

$$1 - \alpha = \int_0^{s_{UP}} h(s|n)ds. \quad (\text{A.2.78})$$

The nice feature of the Bayesian approach is that the zero value of an upper limit  $s_{UP}$  always corresponds to the zero value of credible level  $CL = 1 - \alpha$ , which is not necessarily true for the classical approach. The most important issue is to determine a prior *pdf* of the parameter. This is an issue which brings most of controversies into Bayesian methods. An important question is that if one should use an *informative* prior, *i.e.*, a prior which incorporates results of previous experiments, or a *non-informative* prior, *i.e.*, a prior which claims total ignorance. The major objection against informative prior is based on such argument: if we assume a prior which incorporates results of previous experiments, then our measurement will not be independent, hence, we will not be able to combine our results with previous results by taking a weighted average.

Thus, we only discuss the Bayesian inference that assumes a non-informative prior *pdf* for the non-negative parameter of a Poisson distribution. For the case that in the "signal region" where the signal events resides, the number of signal events is a Poisson variable with unknown expectation  $s$ , and the number of background events is a Poisson variable with expectation  $b$ , the conditional *pdf* of observing total events  $n$ ,  $p(s|n)$ , can be represented by

$$P(s|n) = \frac{(s+b)^n e^{-(s+b)}}{n!}. \quad (\text{A.2.79})$$

To deduce the posterior *pdf*, one has to assume a prior *pdf*. Bayes stated that, the non-informative prior for any parameter must be flat [14]. This statement does not based on any strict mathematical argument, but merely his intuition. The obvious weakness of Bayes prior *pdf* is that if one can assume a flat distribution of an unknown parameter, then one can also assume a flat distribution for any function of this parameter, and these two prior functions are apparently not identical. Jeffreys [15], [16], Jaynes [17], and Box *et al* [18] derived the non-informative priors from first principle to resolve this problem, which are proportional to  $1/\theta$  and  $1/\sqrt{\theta}$ , respectively, where  $\theta$  is the unknown parameter. Comments on these non-informative priors can be found in Refs. [19], [20]. For the *pdf* shown by Eq. A.2.79, the corresponding priors are proportional to  $1/(s+b)$  and  $1/\sqrt{s+b}$ . In general, we can use a prior *pdf* of

$$\pi(s) \propto \frac{1}{(s+b)^m}, \quad s \geq 0, \quad 0 \leq m \leq 1, \quad (\text{A.2.80})$$

where  $m = 0$  corresponds to Bayes prior,  $m = 0.5$  to  $1/\sqrt{s+b}$  prior, and  $m = 1$  to  $1/(s+b)$  prior. One can choose  $m$  value as he/she thinks appropriate, however, it should be always kept in mind that different  $m$  value will give different answer for the credible interval and upper limit. Expected coverage and length of credible intervals constructed with these three priors and with the Neyman construction and unified approach can be found in Ref. [20]. It has been shown that the  $1/\sqrt{s+b}$  prior is the most versatile choice among the Bayesian methods, it provides a reasonable mean coverage for the credible interval and upper limit for Poisson observable.

Substituting  $p(n|s)$  of Eq. A.2.79 and  $\pi(s)$  of Eq. A.2.80 into Eq. A.2.75, the posterior *pdf* is then given by

$$h(s|n) = \frac{(s+b)^{n-m} e^{-(s+b)}}{\Gamma(n-m+1, b)}, \quad (\text{A.2.81})$$

where

$$\Gamma(x, b) = \int_0^\infty s^{x-1} e^{-s} ds, \quad x > 0, b > 0 \quad (\text{A.2.82})$$

is an incomplete gamma function.

In the case that the systematic uncertainties of the signal efficiency and background expectation can be neglected, the signal expectation  $s$  is an unknown constant and the background expectation  $b$  is a known value. The Bayesian HPD credible interval at given credible level  $1 - \alpha$  can be obtained by substituting the posterior *pdf* of Eq. A.2.81 into Eq. A.2.77, while the Bayesian upper limit can be calculated by substituting the posterior *pdf* of Eq. A.2.81 into Eq. A.2.78:

$$\alpha = \frac{\Gamma(n-m+1, s_{UP}+b)}{\Gamma(n-m+1, b)}. \quad (\text{A.2.83})$$

If the flat prior  $m = 0$  is used, Eq. A.2.83 turns into

$$\alpha = e^{-s_{UP}} \cdot \frac{\sum_{k=0}^n \frac{(s_{UP}+b)^k}{k!}}{\sum_{k=0}^n \frac{b^k}{k!}}. \quad (\text{A.2.84})$$

The upper limit  $s_{UP}$  at given credible level  $1 - \alpha$  can be acquired by solving Eq. A.2.83 or Eq. A.2.84 numerically from measured values of  $n$  and  $b$ . Eq. A.2.84 has been recommended by PDG [4], therefore, widely used in particle physics experiments. However, from statistics point of view, the  $1/\sqrt{s+b}$  prior seems to be a more appropriate non-informative prior as mentioned above, therefore, using Eq. A.2.83 with  $m = 0.5$  to determine  $s_{UP}$  seems a reasonable choice.

Now we turn to the question of inclusion of systematic uncertainties. First we consider only the uncertainty of background expectation is present, and the distribution of the background expectation is represented by a pdf  $f_{b'}(b, \sigma_b)$  with the mean  $b$  and standard deviation  $\sigma_b$ . The conditional pdf expressed by Eq. A.2.79 now is modified to

$$q(n|s)_b = \int_0^\infty p(n|s)_{b'} \cdot f_{b'}(b, \sigma_b) db', \quad (\text{A.2.85})$$

where  $p(n|s)_{b'}$  has the same expression in Eq. A.2.79 with  $b$  replaced by  $b'$ .

Next we take into account the uncertainties of the signal efficiency and background expectation simultaneously, and consider they are independent each other. The distribution of the signal relative efficiency  $\varepsilon$  (with respect to the nominal signal detection efficiency) is described by a pdf  $f_\varepsilon(1, \sigma_\varepsilon)$  with the mean 1 and standard deviation  $\sigma_\varepsilon$ . The conditional pdf described by Eq. A.2.79 is then further modified to

$$q(n|s)_b = \int_0^\infty \int_0^\infty p(n|s\varepsilon)_{b'} f_{b'}(b, \sigma_b) f_\varepsilon(1, \sigma_\varepsilon) db' d\varepsilon, \quad (\text{A.2.86})$$

where  $p(n|s\varepsilon)_{b'}$  represents that in Eq. A.2.79  $b$  is replaced by  $b'$ , and  $s$  by  $s\varepsilon$ . One notices that the lower limits of integrals in Eqs. A.2.85, A.2.86 are all zeros, which are the possible minimum value of any efficiencies and number of background events.

Using  $q(s|n)_b$  in Eqs. A.2.85, A.2.86 to construct posterior pdf

$$h(s|n) = \frac{q(n|s)_b \pi(s)}{\int_0^\infty q(n|s)_b \pi(s) ds}, \quad (\text{A.2.87})$$

one can calculate the Bayesian HPD credible interval or upper limit  $s_{UP}$  on  $s$  at any given credible level with inclusion of systematic uncertainties in terms of Eq. A.2.77 or A.2.78.

An method to calculate the Bayesian HPD credible interval or upper limit at given credible level with or without inclusion of systematic uncertainties in pure Bayesian approach has been described in ref. [21], [22]. It has been implemented as a FORTRAN program, BPOCI (Bayesian POissonian Credible Interval) [22].

### A.3 Tests of hypotheses

In addition to estimating parameters, one often wants to assess the validity of certain statements concerning the data's underlying distribution. Hypothesis tests provide a rule for accepting or rejecting hypotheses depending on the outcome of a measurement. We restrict ourselves here to discuss the Goodness-of-fit tests - one of the non-parametric tests, which deals with questions of the functional form for the distribution of the data and gives the probability to obtain a level of incompatibility with a certain hypothesis

that is greater than or equal to the level observed with the actual data. Two methods will be stated: Pearson's  $\chi^2$  test and Kolmogorov-Smirnov test, which is applicable for the large and small size of the measured data sample, respectively. Finally, we have a section to discuss an important concept in particle physics experiment-the statistical significance of signal.

### A.3.1 Goodness-of-fit test

#### Pearson's $\chi^2$ test

We assume that  $n$  observations on the variable  $x$  belong to  $N$  mutually exclusive classes, such as successive intervals in a histogram, non-overlapping regions in two-dimensional plot, etc. The number of events  $n_1, n_2, \dots, n_N$  in the different classes will then be multinomially distributed, with probabilities  $p_i$  for the individual classes as determined by the underlying distribution  $f(x)$  for continuous variable  $x$ :

$$p_i = \int_{\Delta x_i} f(x) dx, \quad i = 1, 2, \dots, N,$$

or  $q_j = P(x = x_j), j = 1, 2, \dots$  for discrete variable  $x$ :

$$p_i = \sum_{j, x_j \in \Delta x_i} q_j, \quad i = 1, 2, \dots, N,$$

where  $\Delta x_i$  represents the  $i$ -th interval. The hypothesis we wish to test specifies the class probabilities according to a certain prescription,

$$H_0 : p_i = p_{0i}, \quad i = 1, 2, \dots, N, \quad (\text{A.3.88})$$

where

$$\sum_{i=1}^N p_{0i} = 1, \quad (\text{A.3.89})$$

is the overall normalization and

$$p_{0i} = \int_{\Delta x_i} f_0(x) dx, \quad \text{or} \quad p_{0i} = \sum_{j, x_j \in \Delta x_i} q_{0j}.$$

Therefore, what we wish to test is if the distribution of the observation  $f(x)$  or  $q_j$  is consistent with the assigned distribution  $f_0(x)$  or  $q_{0j}$ , or equivalently, if the hypothesis  $H_0$  is accepted by the observed data, given that the total number in all classes is  $n$ ? To test whether the set of predicted numbers  $np_{0i}$  is compatible with the set of observed numbers  $n_i$  we take as our test statistic the quantity

$$X^2 = \sum_{i=1}^N \frac{(n_i - np_{0i})^2}{np_{0i}} = \frac{1}{n} \sum_{i=1}^N \frac{n_i^2}{p_{0i}} - n. \quad (\text{A.3.90})$$

When  $H_0$  is true this statistic is approximately  $\chi^2(N - 1)$  distributed. This is called the Pearson theorem.

If  $H_0$  is true and the experiment is repeated many times under the same conditions with  $n$  observations, the actual values obtained for  $X^2$ ,  $X_{obs}^2$ , will therefore be distributed nearly like  $\chi^2(N - 1)$ ; in particular, the mean value for  $X_{obs}^2$  will be  $\simeq N - 1$  and the variance  $\simeq 2(N - 1)$ . If, on the other hand,  $H_0$  is not true, the expectation for each  $n_i$  is not  $np_{0i}$ , and the sum of terms  $(n_i - np_{0i})^2/np_{0i}$  will tend to become on the average larger than if  $H_0$  were true. Hence it seems reasonable to reject  $H_0$  if  $X_{obs}^2$  becomes too large. The criteria to reject  $H_0$  at *significance level*  $\alpha$  is

$$X_{obs}^2 > \chi_{\alpha}^2(N - 1), \quad (\text{A.3.91})$$

where  $\chi_{\alpha}^2(N - 1)$  is determined by the  $\chi^2(N - 1)$  *pdf*  $f(y; N - 1)$  such that

$$\alpha = \int_{\chi_{\alpha}^2(N-1)}^{\infty} f(y; N - 1) dy.$$

Often, the model which to describe the distribution of the measured data includes  $L$  unknown parameters. For a Least-Square estimation we know that the comparison between data and fitted model is made using the  $\chi^2$  distribution with a number of degrees of freedom equal to the number of independent observations minus the number of independent parameters estimated. This procedure is exact only in the limit of infinitely many observations and with a linear parameter dependence; otherwise it is an approximation. Thus, if there are  $L$  parameters in  $H_0$  which are estimated by the *LS* method and  $N$  classes subject to an overall normalization condition, Pearson's  $\chi^2$  test for goodness-of-fit consists in comparing the fitted (minimum) value  $X_{min}^2$  to the  $\chi^2$  distribution with  $(N - 1 - L)$  degrees of freedom.

### Kolmogorov-Smirnov test

The Kolmogorov-Smirnov (KS) test avoids the binning of individual observations and may be more sensitive to the data, and is superior to the  $\chi^2$  test in particular for small samples and has many nice properties when applied to problems in which no parameters are estimated.

Given  $n$  independent observations on the variable  $x$  we form an *ordered sample* by arranging the observations in ascending order of magnitude,  $x_1, x_2, \dots, x_n$ . The cumulative distribution for this sample of size  $n$  is now defined by

$$S_n(x) = \begin{cases} 0, & x < x_i, \\ \frac{i}{n}, & x_i \leq x \leq x_{i+1}, \\ 1, & x \geq x_n. \end{cases} \quad (\text{A.3.92})$$

Thus  $S_n(x)$  is an increasing step function with a step of height  $1/n$  at each of the observational points  $x_1, x_2, \dots, x_n$ .

The KS test involves a comparison between the observed cumulative distribution function  $S_n(x)$  for the data sample and the cumulative distribution function  $F_0(x)$  which is determined by some theoretical model. We state the null hypothesis as

$$H_0 : S_n(x) = F_0(x). \quad (\text{A.3.93})$$

For  $H_0$  true one expects that the difference between  $S_n(x)$  and  $F_0(x)$  at any point should be reasonably small. The KS test looks at the difference  $S_n(x) - F_0(x)$  at all observed points and takes the maximum of the absolute value of this quantity,  $D_n$ , as a test statistic

$$D_n = \max |S_n(x) - F_0(x)|. \quad (\text{A.3.94})$$

It can be shown that provided no parameter in  $F_0(x)$  has been determined from the data, and assuming  $H_0$  true, the variable  $D_n$  has a distribution which is independent of  $F_0(x)$ , *i.e.*  $D_n$  is *distribution free*. This holds irrespective of the sample size.

For continuous variable  $x$  and finite  $n$ , the  $D_n$  has the distribution of [23]

$$P(D_n < z + \frac{1}{2n}) = \begin{cases} 0, & z \leq 0, \\ \int_{\frac{1}{2n}-z}^{\frac{1}{2n}+z} \int_{\frac{3}{2n}-z}^{\frac{3}{2n}+z} \cdots \int_{\frac{2n-1}{2n}-z}^{\frac{2n-1}{2n}+z} f(y_1, \dots, y_n) dy_1 \cdots dy_n, & 0 < z < 1 - \frac{1}{2n} \\ 1, & z \geq 1 - \frac{1}{2n}, \end{cases} \quad (\text{A.3.95})$$

where

$$f(y_1, \dots, y_n) = \begin{cases} n!, & \text{when } 0 < y_1 < \cdots < y_n < 1, \\ 0, & \text{others.} \end{cases} \quad (\text{A.3.96})$$

For large  $n$  the  $D_n$  has the cumulative distribution of

$$\lim_{n \rightarrow \infty} P(D_n \leq \frac{z}{\sqrt{n}}) = 1 - 2 \sum_{r=1}^{\infty} (-1)^{r-1} e^{-2r^2 z^2}, \quad (z > 0). \quad (\text{A.3.97})$$

This relation is approximately valid at  $n \simeq 80$ .

If  $H_0$  is true, the  $D_n$  tends to be small, while if  $H_0$  is not true, the  $D_n$  tends to be larger than if  $H_0$  were true. Hence it seems reasonable to reject  $H_0$  if  $D_n$  becomes too large. The criteria to reject  $H_0$  at significance level  $\alpha$  is

$$P(D_n > D_{n,\alpha}). \quad (\text{A.3.98})$$

A table in the Appendix of the book [2] or [3] gives the critical values  $D_{n,\alpha}$  at 5 different significance level  $\alpha$  for  $n \leq 100$ , and the approximate expression for  $n > 100$ .

### A.3.2 Statistical significance of signal

The statistical significance of a signal in an experiment of particle physics is to quantify the degree of confidence that the observation in the experiment either confirm or disprove a null hypothesis  $H_0$ , in favor of an alternative hypothesis  $H_1$ . Usually the  $H_0$  stands for known or background processes, while the alternative hypothesis  $H_1$  stands for a new or a signal process plus background processes with respective production cross section. This concept is very useful for usual measurements that one can have an intuitive estimation, to what extent one can believe the observed phenomena are due to backgrounds or a signal. It becomes crucial for measurements which claim a new discovery or a new signal. As a convention in particle physics experiment, the "5 $\sigma$ " standard, namely the statistical significance  $S \geq 5$  is required to define the sensitivity for discovery; while in the cases  $S \geq 3$  ( $S \geq 2$ ), one may claim that the observed signal has strong (weak) evidence.

However, as pointed out in Ref. [24], the concept of the statistical significance has not been employed consistently in the most important discoveries made over the last quarter century. Also, the definitions of the statistical significance in different measurements differ from each other. Listed below are various definitions for the statistical significance in counting experiment (see, for example, refs. [25] [26] [19]):

$$S_1 = (n - b)/\sqrt{b}, \quad (\text{A.3.99})$$

$$S_2 = (n - b)/\sqrt{n}, \quad (\text{A.3.100})$$

$$S_{12} = \sqrt{n}/\sqrt{b}, \quad (\text{A.3.101})$$

$$S_{B1} = S_1 - k(\alpha)\sqrt{n/b}, \quad (\text{A.3.102})$$

$$S_{B12} = 2S_{12} - k(\alpha), \quad (\text{A.3.103})$$

$$\int_{-\infty}^{S_N} N(0, 1)dx = \sum_{i=0}^{n-1} e^{-b} \frac{b^i}{i!}, \quad (\text{A.3.104})$$

where  $n$  is the total number of the observed events, which is the Poisson variable with the expectation  $s + b$ ,  $s$  is the expected number of signal events to be searched, while  $b$  is the known expected number of Poisson distributed background events. All numbers are counted in the "signal region" where the searched signal events are supposed to appear. In equations A.3.102 and A.3.103 the  $k(\alpha)$  is a factor related to the  $\alpha$  that the corresponding statistical significance assumes  $1 - \alpha$  acceptance for positive decision about signal observation, and  $k(0.5) = 0, k(0.25) = 0.66, k(0.1) = 1.28, k(0.05) = 1.64$ , etc [26]. In equation A.3.104,  $N(0, 1)$  is a notation for the standard normal function. On the other hand, the measurements in particle physics often examine statistical variables that are continuous in nature. Actually, to identify a sample of events enriched in the signal process, it is often important to take into account the entire distribution of a given variable for a set of events, rather than just to count the events within a given signal region of values. In this situation, I. Narsky [19] gives a definition of the statistical significance via likelihood function

$$S_L = \sqrt{-2 \ln L(b)/L(s + b)} \quad (\text{A.3.105})$$

under the assumption that  $-2 \ln L(b)/L(s + b)$  distributes as  $\chi^2$  function with degree of freedom of 1.

Upon above situation, it is clear that we desire to have a self-consistent definition for statistical significance, which can avoid the ambiguity that the same  $S$  value in different measurements may imply virtually different statistical significance, and can be suitable for both counting experiment and continuous test statistics.

### Definition of the statistical significance

In the PDG [4], the  $p$ -value is defined to quantify the level of agreement between the experimental data and a hypothesis. Assume an experiment makes a measurement for test statistic  $t$  being equal to  $t_{obs}$ , and  $t$  has a probability density function  $g(t|H_0)$  if a null hypothesis  $H_0$  is true. We further assume that large  $t$  values correspond to poor

agreement between the null hypothesis  $H_0$  and data, then the  $p$ –value of an experiment would be

$$p(t_{obs}) = P(t > t_{obs} | H_0) = \int_{t_{obs}}^{\infty} g(t | H_0) dt. \quad (\text{A.3.106})$$

A very small  $p$ –value tends to reject the null hypothesis  $H_0$ .

Since the  $p$ –value of an experiment provides a measure of the consistency between the  $H_0$  hypothesis and the measurement, Zhu [27] define the statistical significance  $S$  in terms of the  $p$ –value in the following form

$$\int_{-S}^S N(0, 1) dx = 1 - p(t_{obs}) \quad (\text{A.3.107})$$

under the assumption that the null hypothesis  $H_0$  represents that the observed events can be described merely by background processes. A small  $p$ –value (larger  $t_{obs}$ ) corresponds to poor agreement between  $H_0$  and data, in this case one would get a large signal significance  $S$  by this expression. The left side of equation A.3.107 represents the integral probability of the normal distribution in the region within  $S$  standard deviation ( $S\sigma$ ). In such a definition, some correlated  $S$  and  $p$ –values are listed in Table A.5.

Table A.5: *Statistical Significance  $S$  and correlated  $p$ –value.*

$S$	$p$ –value
1	0.3173
2	0.0455
3	0.0027
4	$6.3 \times 10^{-5}$
5	$5.7 \times 10^{-7}$
6	$2.0 \times 10^{-9}$

### Statistical significance in counting experiment

A group of particle physics experiment involves the search for new phenomena or signal by observing a unique class of events that can not be described by background processes. One can address this problem to that of a "counting experiment", where one identifies a class of events using well-defined criteria, counts up the number of observed events, and estimates the average rate of events contributed by various backgrounds in the signal region, where the signal events (if exist) will be clustered. Assume in an experiment, the number of signal events in the signal region is a Poisson variable with the expectation  $s$ , while the number of events from backgrounds is a Poisson variable with a known expectation  $b$ , then the observed number of events distributes as the Poisson variable with the expectation  $s + b$ . If the experiment observed  $n_{obs}$  events in the signal region, then the  $p$ –value is

$$p(n_{obs}) = P(n > n_{obs} | H_0) = \sum_{n=n_{obs}}^{\infty} \frac{b^n}{n!} e^{-b} \quad (\text{A.3.108})$$

$$= 1 - \sum_{n=0}^{n_{obs}-1} \frac{b^n}{n!} e^{-b}.$$

Substituting this relation to equation A.3.107, one immediately has

$$\int_{-S}^S N(0, 1) dx = \sum_{n=0}^{n_{obs}-1} \frac{b^n}{n!} e^{-b} \quad (\text{A.3.109})$$

Then, the signal significance  $S$  can be easily determined. Comparing this equation with equation A.3.104 given by Ref. [19], we found the lower limit of the integral is different.

### Statistical significance in continuous test statistics

The general problem in this situation can be addressed as follows. Suppose we identify a class of events using well-defined criteria, which are characterized by a set of  $n$  observations  $x_1, \dots, x_n$  for a random variable  $x$ . In addition, one wish to test a hypothesis which predicts the probability density function of  $x$ , say  $f(x|\vec{\theta})$ , where  $\vec{\theta} = (\theta_1, \theta_2, \dots, \theta_k)$  is a set of parameters which need to be estimated from the data. Then the problem is to define a statistic that gives a measure of the consistency of the distribution of data with the distribution given by the hypothesis.

To be concrete, we consider the random variable  $x$  is, say, an invariant mass, and the  $n$  observations  $x_1, \dots, x_n$  give an experimental distribution of  $x$ . Assuming parameters  $\vec{\theta} = (\theta_1, \dots, \theta_k) \equiv (\vec{\theta}_s; \vec{\theta}_b)$ , where  $\vec{\theta}_s$  and  $\vec{\theta}_b$  represent the parameters belong to signal (say, a resonance) and backgrounds contribution, respectively. We assume the null hypothesis  $H_0$  stands for that the experimental distribution of  $x$  can be described merely by the background processes, namely, the null hypothesis  $H_0$  specifies fixed values for a subset of parameters  $\vec{\theta}_s$ . Therefore, the parameters  $\vec{\theta}$  are restricted to lie in a subspace  $\omega$  of its total space  $\Omega$ . On the basis of a data sample of size  $n$  from  $f(x|\vec{\theta})$  we want to test the hypothesis  $H_0 : \vec{\theta}$  belongs to  $\omega$ . Given the observations  $x_1, \dots, x_n$ , the likelihood function is  $L = \prod_{i=1}^n f(x_i|\vec{\theta})$ . The maximum of this function over the total space  $\Omega$  is denoted by  $L(\hat{\Omega})$ ; while within the subspace  $\omega$  the maximum of the likelihood function is denoted by  $L(\hat{\omega})$ , then we define the likelihood-ratio  $\lambda \equiv L(\hat{\omega})/L(\hat{\Omega})$ . It can be shown that for  $H_0$  true, the statistic

$$t \equiv -2 \ln \lambda \equiv 2(\ln L_{max}(s+b) - \ln L_{max}(b)) \quad (\text{A.3.110})$$

is distributed as  $\chi^2(r)$  where  $r$  is the difference in the number of degrees of freedom between the  $H_1$  and  $H_0$  hypotheses [1]. In equation A.3.110 we use  $\ln L_{max}(s+b)$  and  $\ln L_{max}(b)$  denoting  $L(\hat{\Omega})$  and  $L(\hat{\omega})$ , respectively. If  $\lambda$  turns out to be in the neighborhood of 1, the null hypothesis  $H_0$  is such that it renders  $L(\hat{\omega})$  close to the maximum  $L(\hat{\Omega})$ , and hence  $H_0$  will have a large probability of being true. On the other hand, a small value of  $\lambda$  will indicates that  $H_0$  is unlikely. Therefore, the critical region of  $\lambda$  is in the neighborhood of 0, corresponding to large value of statistic  $t$ . If the measured value of  $t$  in an experiment is  $t_{obs}$ , from equation A.3.106 we have  $p$ -value

$$p(t_{obs}) = \int_{t_{obs}}^{\infty} \chi^2(t; r) dt. \quad (\text{A.3.111})$$

Therefore, in terms of equation A.3.107, one can calculate the signal significance according to following expression:

$$\int_{-S}^S N(0, 1)dx = 1 - p(t_{obs}) = \int_0^{t_{obs}} \chi^2(t; r)dt. \quad (\text{A.3.112})$$

For the case of  $r = 1$ , we have

$$\begin{aligned} \int_{-S}^S N(0, 1)dx &= \int_0^{t_{obs}} \chi^2(t; 1)dt \\ &= 2 \int_0^{\sqrt{t_{obs}}} N(0, 1)dx. \end{aligned} \quad (\text{A.3.113})$$

and immediately obtain

$$\begin{aligned} S &= \sqrt{t_{obs}} \\ &= [2(\ln L_{max}(s + b) - \ln L_{max}(b))]^{1/2}, \end{aligned} \quad (\text{A.3.114})$$

which is identical to the equation A.3.105 given by Ref. [19].



# Bibliography

- [1] W.T. Eadie *et al*, Statistical methods in experimental physics, North-Holland publishing Co., Amsterdam, 1971; F. James, Statistical methods in experimental physics, 2nd ed., World Scientific Publishing Co., 2007.
- [2] A. Frodesen *et al*, Probability and Statistics in particle physics, Universitetsforlaget, Bergen-Oslo-Tromsø, 1979.
- [3] Yongsheng Zhu, Probability and statistics in experimental physics, 2nd edition, Academic Press, Beijing, 2006.
- [4] Particle Data Group, W.-M. Yao *et al*, Journal of Physics G, **33**, 1 (2006).
- [5] G. Cowan, Statistical data analysis, Oxford Univ. Press Inc., New York, 1998.
- [6] R. Barlow, arXiv Physics/0406120, 2004.
- [7] J. Neyman, Phil. Trans. Royal Soc. London, Series A, **236**, 333 (1937)
- [8] G. Feldman and R.D. Cousins, Phys. Rev. **D57**, 3873 (1998).
- [9] B.P. Roe and M.B. Woodroffe, Phys. Rev. **D63**, 013009 (2001).
- [10] R.D. Cousins and V.L. Highland, Nucl. Instr. Meth. in Phys. Res. **A320**, 331 (1992).
- [11] W.A. Rolke and A.M. Lopez, Nucl. Instr. Meth. in Phys. Res. **A458**, 745 (2001).
- [12] J. Conrad *et al*, Phys. Rev. **D67**, 012002 (2003).
- [13] <http://www3.tsl.uu.se/~conrad/pole.html>.
- [14] T. Bayes, Phil. Trans. Roy. Soc., **53**, 370 (1763).
- [15] H. Jeffreys, Theory of probability, 3rd edition, Clarendon, Oxford, 1961.
- [16] H. Jeffreys, Proc. of the Royal Soc. of London, **A 196**, 453 (1946).
- [17] H. Jaynes, IEEE Trans. on System Sci. and Cyber. **SSC-4**, 3, 227 (1968).
- [18] G.E.P. Box and G.C. Tiao, Bayesian Inference in Statistical Analysis, Wiley Classics, 1992.
- [19] I. Narsky, Nucl.Intr.Meth. **A450**, 444 (2000).

- [20] I. Narsky, arXiv: hep-ex/0005019 (2000).
- [21] Yongsheng Zhu, Nucl.Instr.Meth. **A578**, 322 (2007).
- [22] Yongsheng Zhu, <http://ihep.ac.cn/lunwen/zhuys/BPOCI/BPOCI.html>.
- [23] V. Rohatgi, An introduction to probability theory and mathematical statistics, John Wiley & Sons, New York, 1976.
- [24] P.K. Sinervo, Proc of Conf. "Advanced statistical techniques in particle physics", Durham, UK, 18-22 March, 2002, p64.
- [25] S.I. Bityukov *et al*, Nucl.Intr.Meth. **A452**, 518 (2000)
- [26] S.I. Bityukov *et al*, Proc of Conf. "Advanced statistical techniques in particle physics", Durham, UK, 18-22 March, 2002, p77.
- [27] Yongsheng Zhu, HEP&NP, **30**, 331 (2006)